XXVII RUSSIAN PARTICLE ACCELERATORS CONFERENCE

RuPAC-2021

26 September – 2 October 2021
Resort Hotel "Dubna" , Alushta, Crimea

JOINT INSTITUTE FOR NUCLEAR RESEARCH

PROGRAM COMMITTEE:
I. Meshkov (JINR) – Chairman
B. Sharkov (JINR) – Co-Chairman
A. Philippov (JINR) – Scientific Secretary
E. Ahmanova (JINR) – Secretary
S. Ivanov (NRC KI - IHEP)
S. Polozov (NRNU MEPhI)
V. Korchuganov (NRC KI)
E. Levichev (BINP SB RAS)
Yu. Gavrish (JSC NIIEFA)
N. Zavyalov (RFNC-VNIIEF)
V. Parkhomchuk (BINP SB RAS)
A. Feshchenko (INR RAS)
T. Kulevoy (NRC KI - ITEP)
D. Ovsyannikov (SPBU)
L. Kravchuk (INR RAS)
O. Lebedev (NRC KI - IHEP)

SUPERVISORY COMMITTEE:
G. Trubnikov (JINR) – Chairman
B. Sharkov (JINR) – Co-Chairman
B. Gikal (JINR)
S. Dmitriev (JINR)
I. Meshkov (JINR)
G. Shirkov (JINR)

ORGANISING COMMITTEE:
G. Sharkov (JINR) – Co-Chairman
B. Gikal (JINR) – Co-Chairman
S. Yakovenko (JINR) – Deputy chairman
O. Belova (JINR) – Secretary
D. Kamanin (JINR)
M. Kuzin (BINP SB RAS)
A. Popeko (JINR)
A. Philippov (JINR)
M. Kazarinov (JINR)
R. Pivin (JINR)

Joint Institute for Nuclear Research
Scientific Council of Russian Academy of Sciences
on Charged Particle Accelerators

Email: rupac21@jinr.ru
The conference website: httpp://rupac21.jinr.ru
The photo was taken from: https://e-news.su





ITECH


INTECH
VAT
00-200-24-80




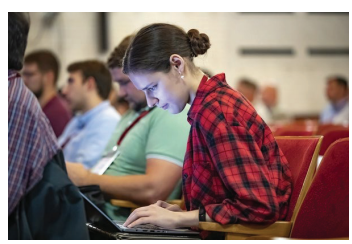

PREFACE

The XXVII Russian Particle Accelerator Conference (RuPAC 2021) was held in Alushta, Russia on September 26 — October 2, 2021. It was co-organized by the Scientific Council of Russian Academy of Sciences for Charged Particle Accelerators and Joint Institute for Nuclear Research (JINR, Dubna). The year of this Conference, 2021, is notable for the JINR, the JINR celebrate its 65th anniversary.

The goal of the event was to facilitate information interchange and discussion of various aspects of accelerator science and technology, beam physics, new accelerator development, upgrade of existing facilities, and use of accelerators for basic and applied research.

The scientific program covered the conventional topics: Modern trends in accelerator technology, Colliders, Beam dynamics in accelerators and storage rings, cooling methods, new methods of acceleration, Cyclic and linear accelerators of high intensity, Heavy ion accelerators, Synchrotron radiation sources and free electron lasers, Magnetic systems, power supply systems and accelerator vacuum systems, Superconducting technologies in accelerators, Accelerating structures and powerful radio engineering, Control and diagnostic systems, Ion sources and electron guns, Accelerators for medicine and engineering applications, Problems of radiation safety at accelerators.

The RuPAC 2021 was attended by about 135 participants (and 12 on-line) from 25 organizations, both home (21) and foreign (4) labs. 9 invited talks (3 on-line), 49 contributed oral reports (9 on-line) and 133 posters were presented at the Conference.

The Organizing Committee decided to maintain the Conference tradition of awarding the best youth's scientific works (for authors aged below 35, inclusive). The laureates were nominated by the Selection Jury formed at the Conference from representatives of Russian accelerator laboratories and chaired by Prof. Valery Telnov (BINP of SB RAS, Novosibirsk, Russia). This year, the Selection Committee decided to award 4 full diplomas, one of which is collective. The personal contest winners are listed alphabetically after collective ones in the table to follow.

Name	Affiliation	Report
The team of the Superconducting Magnets & Technology Department of LHEP, JINR	JINR, Dubna	For series reports presented at the Conference on the production of the superconducting magnets of the NICA complex
Gikal Kirill	JINR, Dubna	Peculiarities of Producing ^{48}Ca, ^{48}Ti, ^{52}Cr Beams at the DC-280 Cyclotron
Gorelyshev Ivan	JINR, Dubna	NICA Stochastic Cooling System: Designing and Modeling
Osina Yulia	NIIEFA, St. Petersburg	Cyclotron of Multicharged Ions

The success of the RuPAC 2021 can be attributed to the collaborative efforts of the Program and Organizing Committees, and, of course, to all of the participants themselves.

Participants of the Conference from Russian accelerator centers and Universities and from several foreign accelerator centers enjoyed fruitful discussions at oral and poster presentations regardless to the coronavirus infection (COVID-19).

Trubnikov Grigory, Chair of the Supervisory Committee
Igor Meshkov, Chair of the Program Committee
Boris Sharkov, Co-Chair of the Program Committee
Shirkov Grigory, Chair of the Organizing Committee

ORGANIZED BY

Joint Institute for Nuclear Research, Dubna
Scientific Council of Russian Academy of Sciences on Charged Particle Accelerators.

SUPERVISORY COMMITTEE

G. Trubnikov (JINR), Chairman
B. Sharkov (JINR), Co-Chairman
B. Gikal (JINR)
S. Dmitriev (JINR)
I. Meshkov (JINR)
G. Shirkov (JINR)

PROGRAM COMMITTEE

I. Meshkov (JINR), Chairman
B. Sharkov (JINR), Co-Chairman
A. Philippov (JINR), Scientific Secretary
E. Ahmanova (JINR), Secretary
S. Ivanov (IHEP, NRC KI)
S. Polozov (NRNU MEPhI)
V. Korchuganov (NRC KI)
E. Levichev (BINP SB RAS)
Yu. Gavrish (JSC NIIEFA)
N. Zavyalov (RFNC-VNIIEF)
V. Parkhomchuk (BINP SB RAS)
A. Feshchenko (INR RAS)
T. Kulevoy (ITEP, NRC KI)
D. Ovsyannikov (SPBU)
L. Kravchuk (INR RAS)
O. Lebedev (IHEP, NRC KI)

ORGANISING COMMITTEE

G. Shirkov (JINR), Co-Chairman
B. Gikal (JINR), Co-Chairman
S. Yakovenko (JINR), Deputy chairman
O. Belova (JINR), Secretary
D. Kamanin (JINR)
M. Kuzin (BINP SB RAS)
A. Popeko (JINR)
A. Philippov (JINR)
M. Kazarinov (JINR)
R. Pivin (JINR)

Contents

Preface i
Foreword . . . iii
Committees . . . iv
Contents . . . v

Papers 1
MOX02 – Development and Implementation of Bunch Shape Instrumentation for Ion Linacs . . . 1
MOY01 – The NICA Complex Injection Facility . . . 7
MOY02 – NICA Ion Coolider at JINR . . . 12
MOY05 – Linear Induction Accelerator LIA-2 Upgrade . . . 17
MOB01 – Status of U-70 . . . 20
TUX01 – Status of the HIAF Accelerator Facility in China . . . 23
TUY01 – VEPP-2000 Collider Complex Operation in 2019-2021 Runs . . . 28
TUA01 – VEPP-4M Electron Positron Collider Operation at High Energy . . . 34
TUA02 – Current Status of VEPP-5 Injection Complex . . . 37
TUB02 – NICA Collider Magnetic Field Correction System . . . 41
TUB03 – Methods and Systematic Errors for Searching for the Electric Dipole Moment of Charged Particle Using a Storage Ring . . . 44
TUB04 – Development of the Electron Cooling System for NICA Collider . . . 48
TUB07 – The Conceptual Design of the 7.5 MeV/u Light Ion Injector . . . 51
TUC01 – Status of the Kurchatov Synchrotron Radiation Source . . . 55
TUC03 – Development of Powerful Long-Pulse THz-Band FEL Driven by Linear Induction Accelerator . . . 58
WEA01 – Beam Transfer Systems of NICA Facility: from HILAC to Booster . . . 61
WEA02 – Acceleration the Beams of He and Fe14+ Ions by HILAC and its Injection into NICA Booster in its Second Run . . . 65
WEA03 – 200 MeV Linac Development for the SKIF Light Source Injector . . . 68
WEB02 – Magnetic Field Measurements for the NICA Collider Magnets and FAIR Quadrupole Units . . . 71
WEB03 – First Experience of Production and Testing the Superconducting Quadrupole and Corrector Magnets for the SIS100 Heavy Ion Accelerator of FAIR . . . 75
WED04 – Precise Analysis of Beam Optics at the VEPP-4M by Turn-by-Turn Betatron Phase Advance Measurement . . . 79
WED05 – Nondestructive Diagnostics of Accelerated Ion Beams With MCP-Based Detectors at the Accelerator Complex NICA. Experimental Results and Prospects . . . 82
THA01 – Status of the SC HWR Cavities Production for NICA Project . . . 85
THC03 – Numerical Simulations of Space Charge Dominated Beam Dynamics in Experimentally Optimized PITZ RF Photogun . . . 89
FRA01 – Peculiarities of Producing 48Ca, 48Ti, 52Cr Beams at the DC-280 Cyclotron . . . 93
FRA02 – Cyclotron of Multicharged Ions . . . 96
FRA03 – Simulation and Design of the Permanent Magnet Multipole for DC140 . . . 99
FRA04 – The Experimental Research of Cyclotron DC-280 Beam Parameters . . . 102
FRA05 – Cyclotron System C-250 . . . 105
FRB01 – Advances in the Development of a Vacuum Insulated Tandem Accelerator and Its Applications . . . 108
FRB02 – Accelerators of ELV Series: Current Status and Further Development . . . 111
FRB03 – Upgrated the Extraction Device of Focused Electron Beam Into the Atmosphere . . . 114
FRB04 – A Linear Accelerator for Proton Therapy . . . 117
FRB05 – Updated Status of Protom Synchrotrons for Radiation Therapy . . . 120
FRB06 – The Results Obtained on "Radiobiological Stand" Facility, Working with the Extracted Carbon Ion Beam of the U-70 Accelerator . . . 124
FRB07 – Transmission Studies With Ion Beams Within FAMA . . . 127
FRC01 – Neutron Field Measurements by GFPC Based Monitors at the Carbon Beam of IHEP U-70 Proton Synchrotron . . . 129
MOPSA02 – Experimental Tests of CW Resonance Accelerator With 7.5 MeV High Intensity Electron Beam 132
MOPSA03 – Calculations of Ion Dynamics and Elecrodynamics Characteristics of 800 KeV/nucleon RFQ 135
MOPSA04 – The Tuning of RF Parameters of 40 MHz RFQ . . . 139

MOPSA06 – Parameters of the Normal Conducting Accelerating Structure for the Up to 1 GeV Hadron Linacs . . . 142
MOPSA07 – 200 MeV Linear Electron Accelerator - Pre-Injector for a New Kurchatov Synchrotron Radiation Source . . . 145
MOPSA08 – Beam Dynamics Simulation in a Linear Electron Accelerator - Injector for the 4th Generation Specialized Synchrotron Radiation Source USSR . . . 149
MOPSA11 – Room Temperature Folding Segment for a Transfer of Multiple Charge States Uranium Ions Between Sections of Linac-100 . . . 153
MOPSA13 – Computer Simulation of the Mechanical Behavior of the FFS Superconducting Quadrupole Coil . . . 156
MOPSA14 – Production of Superconducting Magnets for the NICA Collider at JINR . . . 159
MOPSA15 – Thermodynamic Characteristics of the Superconducting Quadrupole Magnets of the NICA Booster Synchrotron . . . 162
MOPSA16 – Design and Characteristics of Cryostat for Testing of Low-Beta 325 MHz Half-Wave Resonators 165
MOPSA17 – Automated System for Heating High-Vacuum Elements of Superconducting Synchrotrons of the NICA Complex . . . 168
MOPSA23 – Machine Learning for the Storage Ring Optimization . . . 169
MOPSA29 – Applied Research Stations and New Beam Transfer Lines at the NICA Accelerator Complex 172
MOPSA39 – Application of a Scintillation Detector for Periodic Monitoring of Beam Parameters at Medical Proton Therapy Complex "Prometheus" . . . 176
MOPSA40 – The PIPLAN Proton-Carbon Ion Radiation Therapy Planning System . . . 179
MOPSA41 – Effect of a Proton Beam from a Linear Accelerator for Radiation Therapy . . . 182
MOPSA42 – Compact S-Band Accelerating Structure for Medical Applications . . . 186
MOPSA44 – Conceptual Project of Proton Beam Lines in the Nuclear Medicine Project of the "Kurchatov Institute" - PNPI . . . 189
MOPSA45 – Experimental Simulation of Volume Repainting Technique at Proton Synchrotron in Context of Spot Scanning Proton Therapy . . . 192
MOPSA46 – Preliminary Design Study of the Gantry for the Proton Radiotherapy Center NRC "Kurchatov Institute" . . . 196
MOPSA47 – Verification of a Beam of Epithermal Neutrons for Boron-Neutron Capture Therapy . . . 199
MOPSA48 – Simulation of the Electrostatic Deflector of DC140 Cyclotron . . . 202
MOPSA49 – DC140 Cyclotron, Trajectory Analysis of Beam Acceleration and Extraction . . . 205
MOPSA50 – Axial Injection System of DC140 Cyclotron of FLNR JINR . . . 209
MOPSA51 – The Extraction System of DC140 Cyclotron . . . 213
MOPSA52 – Modeling of the Magnetic System of the Cyclotron of Multicharged Ions . . . 216
MOPSA53 – Focusing Properties of the Magnetic Structure of Isochronous Cyclotrons With Large Spiraling Angle of Pole Tips . . . 219
MOPSA54 – Calculation of Dose Fields and Energy Spectra of Secondary Radiation in the Extraction Zone of a Synchrotron Accelerator for Protons With Energies Up to 700 MeV . . . 222
MOPSA55 – Beam-induced Background Simulations for the CMS Experiment at the LHC . . . 225
MOPSA56 – Upgrades of a Vacuum Insulated Tandem Accelerator for Obtaining Required Voltage Without Breakdowns . . . 228
MOPSA57 – Experimental Investigation the Synthetic Crystal Diamond Plates of Methods of Positron Annihilation Spectroscopy . . . 231
MOPSA58 – Sources of Ultrashort X-Ray Pulses in the Investigation of the Structure and Dynamics of Nanosystems . . . 234
TUPSB04 – Features of the Electronic Cooling System of the NICA Booster . . . 236
TUPSB05 – Longitudinal Impedance of the NICA Collider Ring and Ion Beam Stability . . . 239
TUPSB07 – Particle Collimation in the NICA Collider . . . 242
TUPSB08 – Magneto-Optical Structure of the NICA Collider With High Critical Energy . . . 245
TUPSB09 – Resonance Slow Extraction From Ion Synchrotron for Technological Application . . . 248
TUPSB10 – Modeling of the Spin-Navigator Method for Manipulating the Beam Polarization in a Spin-Transparent Storage Ring . . . 251
TUPSB11 – Numerical Investigation of the Robustness of Spin-Navigator Polarization Control Method in a Spin-Transparent Storage Ring . . . 254
TUPSB12 – Development of a Program Code for Calculation of Charged Particle Dynamics in RFQ . . . 256

TUPSB13 – Charged Particle Dynamics Optimization in Discrete Systems . . . 259
TUPSB16 – Calculation and Optimization of High-Energy Beam Transfer Lines by the Monte Carlo Method 262
TUPSB17 – Investigations of Charge Particle Dynamics in Space Charge Fields . . . 265
TUPSB20 – Selection of a System for Correcting the Energy Spread of Relativistic Electron Bunches for a Free Electron Laser . . . 268
TUPSB21 – System for Correcting the Longitudinal Length of Electron Bunches for Generation a Free Electron Laser . . . 271
TUPSB22 – Wakefield Undulator Based on a Sinusoidal Dielectric Waveguide . . . 274
TUPSB25 – Storage Ring Design and Beam Instabilities Investigation for MEPhI's Photon Source . . . 277
TUPSB26 – Lattice Options With Reverse Bending Magnets for USSR HMBA Storage Ring . . . 280
TUPSB28 – X-ray Thomson Inverse Scattering from Periodically Modulated Laser Pulses . . . 283
TUPSB29 – Geant4 for Inverse Compton Radiation Source Simulations . . . 286
TUPSB32 – Emission of Photons at the Interaction of a High-Energy Positron Beam with a Periodically Deformed Crystal . . . 289
TUPSB33 – 2.5 GeV Booster Synchrotron for a New Kurchatov Synchrotron Radiation Source . . . 293
TUPSB34 – New Lattice Design for Kurchatov Synchrotron Radiation Source . . . 297
TUPSB35 – 3D Simulation Study and Optimization of Magnetic System of DECRIS Ion Source with the Pumping Frequency 28 GHz . . . 300
TUPSB36 – High Intensity Calcium, Chromium and Titanium Ion Beams from the Permanent Magnet ECR Ion Source DECRIS-PM . . . 303
TUPSB37 – Modernization of the ECR Ion Source DECRIS-2M. Results of the First Tests. . . . 307
TUPSB38 – Magnetic System With Variable Characteristics for a 2.45 GHz ECRIS . . . 310
TUPSB39 – Study of Space Charge Compensation Process of a 400 KeV Pulsed Hydrogen Ion Beam . . . 313
TUPSB40 – He Ion Source for the NICA Injection Complex . . . 316
TUPSB43 – Optimization of the RF-Gun With Photocathode at Operating Frequency 2800 MHz for the New Injection Linac for USSR Project . . . 319
TUPSB44 – Design and Simulation of an S-Band RF Photogun for a New Injector of the Accelerator Linac-200 at JINR . . . 322
TUPSB47 – Stability Conditions for a Penning Trap with Rotating Quadrupole or Dipole Electric Fields . 324
TUPSB48 – Optimization of the Geometric Characteristics of the Laser Beam in a Multi-Pass Scheme of Nonlinear Amplification of the Master Oscillator Illumination . . . 327
TUPSB51 – Measurement of Neutron Field Functionals Around a Neutron Converter of 50 GeV Protons 330
TUPSB52 – Measurement of the Argon Ion Current Accompanying at the Accelerating Source of Epithermal Neutrons . . . 334
TUPSB53 – Measurement of Parameters of Neutron Radiation on the Accelerator-Based Epithermal Neutron Source . . . 337
WEPSC01 – Unit for Matching a Driving Waveguide With a Cavity . . . 340
WEPSC03 – Multipactor Discharge in Short 5-Gap 80 MHz IH Structures . . . 343
WEPSC04 – Accelerating Structure of 8 MeV Electron Linac . . . 346
WEPSC05 – Modeling of the Energy Compression System SLED for the LINAC-200 Accelerator . . . 349
WEPSC06 – Asess Input Data Uncertainties in Thermal-Mechanical Calculations of the Outlet Window Membrane of the LUE-200 Accelerator . . . 352
WEPSC07 – Medium Energy Ions Transport Channel for a Pulsed Linear Accelerator . . . 355
WEPSC08 – Vacuum Condition Simulations for Vacuum Chambers of Synchrotron Radiation Source . . . 358
WEPSC10 – Optimization of Accelerators Vacuum Structures Pumping . . . 361
WEPSC12 – Preliminary Calculation of the Power Coupler for the SYLA Storage Ring RF Cavity . . . 364
WEPSC13 – Accelerating Cavities with HOM Damping for USSR-4 Storage Ring . . . 367
WEPSC14 – Booster RF System First Beam Tests . . . 370
WEPSC15 – Barrier Station RF1 of the NICA Collider. Design Features and Influence on Beam Dynamics 373
WEPSC16 – Numerical Research of Design Solutions for the Bending Magnets of the Electron Beam Facility GESA-1M . . . 376
WEPSC17 – Vibrating Wire System for Fiducialization NICA Booster Superconducting Quadrupole Magnets 379
WEPSC18 – Serial Magnetic Measurements of the NICA Collider Twin-Aperture Dipoles. The Main Results 383
WEPSC20 – Magnets Design for 2.5 GeV Booster Synchrotron . . . 386
WEPSC21 – Light Ion Accelerator Magnets . . . 390
WEPSC28 – Optical Diagnostics of 1 MeV Proton Beam in Argon Stripping Target of a Tandem Accelerator 393

WEPSC29 – Diagnostics of the Proton Beam Position Using the Luminescence of a Lithium Neutron-Generating Target . . . 396
WEPSC30 – Measurement of the Phase Portrait of a 2 MeV Proton Beam Along Beam Transfer Line . . 399
WEPSC31 – 2D-Tomography of the Proton Beam in the Vacuum Insulated Tandem Accelerator 402
WEPSC32 – Proton Beam Size Diagnostics Used in the Vacuum Insulated Tandem Accelerator 404
WEPSC33 – Increasing Quality of Experiment Interpretation in Real-Time for the Tandem Accelerator . . 407
WEPSC34 – Treatment of the Results Measurement of Profile Beam Using Wire Scanners at Accelerator U-70 IHEP . . . 410
WEPSC36 – Simulation of the Coherent Radiation Interferometry for the Beam Temporal Structure Diagnostics . . . 413
WEPSC39 – Data Collection, Archiving and Monitoring System for U70 Synchrotron 417
WEPSC40 – Detection of Anomalies in BPM Signals at the VEPP-4M 420
WEPSC42 – RF Cavity Based Charge Detector for a Low Charge Ultra Sort Singe Electron Bunch Measurement . . . 423
WEPSC44 – Beam Loss Monitoring System for the SKIF Synchrotron Light Source 426
WEPSC45 – Measurement of the Electron Beam Spectrum by the Absorbing Filters Method During a Single Pulse . . . 430
WEPSC50 – Enhancement of Transverse Beam Phase Space Analysis by Tomography Method at INR Linac 433
WEPSC51 – Concept of Decision Support System for INR RAS Linac Beam Tuning 436
WEPSC55 – Development of the Low Intensity Extraction Beam Control System at Protom Synchrotron for Proton Radiography Implementation . . . 439
WEPSC56 – Beam Parameters Measurement and Control Software Tools for VEPP-5 Injection Complex Damping Ring . . . 443
WEPSC57 – System of on-Line Energy Control of Electron Beam for Accelerator 446

Appendices **449**
List of Authors . . . 449
Institutes List . . . 459
Participants List . . . 468

ISBN: 978-3-95450-240-0 ISSN: 2673-5539 doi:10.18429/JACoW-RuPAC2021-MOX02

DEVELOPMENT AND IMPLEMENTATION OF BUNCH SHAPE INSTRUMENTATION FOR ION LINACS*

S. A. Gavrilov†, A. V. Feschenko, V. A. Gaidash,
Institute for Nuclear Research of the Russian Academy of Sciences, Moscow, Troitsk, Russia

Abstract

A longitudinal charge distribution in beam bunches, so-called bunch shape, is one of the most important and difficult to measure characteristics of a beam in ion linear accelerators. Despite the variety of approaches only the methods using low energy secondary electrons emitted, when the beam passes through a thin target, found practical application. The most common beam instrumentation, based on this method, became Bunch Shape Monitor (BSM) developed in INR RAS. The monitor provides direct measurements of bunch shape and bunch longitudinal halo, allows to carry out such complex diagnostic procedures as longitudinal emittance measurements, amplitude and phase setting of accelerating fields and observation of bunch shape evolution in time to check the overall quality of longitudinal tuning of the accelerator.

The principle of the monitor operation, design features, ultimate parameters and limitations are discussed. Several modifications of the monitor with implementation peculiarities are described as well as lots of measurement results at different ion linacs with a variety of beam parameters. New challenges for bunch shape instrumentation to satisfy demands of forthcoming linacs are also characterized.

INTRODUCTION

The main requirement for bunch shape measurements is phase resolution. In ion linacs for typical bunch phase duration range from several degrees to several tens of degrees the resolution of 1° looks adequate. The corresponding temporal resolution, for example for 350 MHz, equals to ~8 ps.

In ion beams, as opposite to electron ones, an attempt to extract information on bunch shape through beam electromagnetic field results in aggravation of phase resolution due to large longitudinal extent of the particle field. The problem can be overcome if one localizes a longitudinal space passing through which the bunch transmits information on its shape.

This approach can be implemented if a longitudinally small target is inserted into the beam and some type of radiation due to interaction of the beam with this target is detected. Different types of radiation are used or proposed to be used [1-5], however low energy secondary electrons are used most extensively. The distinctive feature of these electrons is a weak dependence of their properties both on type and energy of primary particles, so the detectors can be used for almost any ion beam.

Among the characteristics of low energy secondary emission, influencing the parameters of the bunch shape monitor, one can point initial energy and angular distributions as well as time dispersion or delay of the emission. Time dispersion establishes a fundamental limitation on the resolution of the detector. The value of time dispersion for metals is estimated theoretically to be about $10^{-15}\div10^{-14}$ s [6], which is negligible from the point of view of bunch shape measurements. The experimental results of time dispersion measurements give not exact value but its upper limit. It was shown that the upper limit does not exceed $(4\pm2)\cdot10^{-12}$ s [7].

Operation of bunch shape monitors with low energy secondary electrons is based on coherent transformation of a time structure of the analyzed beam into a spatial distribution of secondary electrons through RF modulation. The first real detectors described in [8, 9] use RF modulation in energy or in other words a longitudinal modulation. Another possibility is using a transverse scanning [10]. The electrons are modulated in transverse direction and deflected depending on their phase. Spatial separation is obtained after a drift space.

BUNCH SHAPE MONITOR OF INR RAS

Principle of Operation

The first real BSM with transverse scanning of low energy secondary electrons, developed and fabricated in INR, has been described in [11, 12].

The operation principle of BSM with up-to-date design can be described briefly with the reference to Fig. 1.

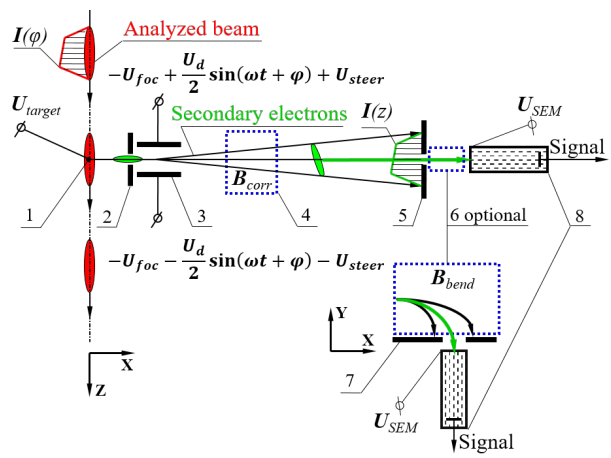

Figure 1: BSM scheme: 1 – tungsten wire target, 2 – inlet collimator, 3 – RF-deflector, 4 – correcting magnet, 5 – outlet collimator, 6 – optional bending magnet, 7 – registration collimator, 8 – electron detector.

* Work was awarded the Veksler Prize 2021 of RAS
† s.gavrilov@gmail.com

ISBN: 978-3-95450-240-0 ISSN: 2673-5539 doi:10.18429/JACoW-RuPAC2021-MOX02

The series of bunches of the beam under study crosses the wire target 1 which is at a high negative potential (U_{target} about -10 kV). The target represents a tungsten wire of 0.1 mm diameter. Interaction of the beam with the target results in emission of low energy secondary electrons. The electrons are accelerated by electrostatic field and move almost radially away from the target. A fraction of the electrons passes through input collimator 2 and enters RF deflector 3 operating at a frequency equal to or multiple of the linac accelerating field frequency. Deflection of the electrons at the exit of the RF deflector depends on their phase with respect to deflecting field. Downstream of the drift distance the electrons are spatially separated and their coordinates are dependent on phase of the deflecting field. Temporal structure of the analyzed ion beam is initially transformed into that of secondary electrons and then into spatial distribution of the electrons. The intensity of the electrons at a fixed coordinate is proportional to the intensity of the primary beam at a fixed point along the bunch. These electrons are separated by outlet collimator 5 and their intensity is measured with electron detector 8. Adjusting the deflecting field phase with respect to accelerator RF reference, one can obtain a longitudinal distribution of charge in the bunches of the analyzed beam.

Main Parameters

The most important characteristic of BSM is its phase resolution. We define phase resolution by a simple relation $\Delta\varphi = \Delta Z / nZ_{\max}$, where $Z_{\max}$ is the amplitude of electron displacement at collimator 5 plane, n is a harmonic number of the deflecting field with respect to the fundamental bunch array frequency and ΔZ is a full width at a half maximum of the electron beam at the collimator 5 for zero phase duration bunches of the analyzed beam. To decrease ΔZ and hence to improve the resolution the electron beam must be focused by additionally applying focusing potential U_{foc} to the deflector electrodes. To steer the electron beam additional potential difference U_{steer} is also applied between the deflector electrodes. Evidently the size of the collimator should not exceed ΔZ. Otherwise the size of the collimator is to be used in the above formula instead of electron beam size ΔZ.

The value of maximum displacement $Z_{\max}$ can be both calculated and found experimentally. As for the ΔZ value, its finding is not a trivial task. To find the value of ΔZ for the purpose of phase resolution evaluation both theoretical and experimental data are used. Initially focusing properties of the detector can be found experimentally using thermal electrons. Heating the wire target made of tungsten, it is possible to visually observe the thermal electron beam on the phosphor covering the front surface of the plates of collimator 5 through the viewing port. The size of the focused beam of secondary electrons can be measured by adjusting the steering voltage U_{steer} for the turned off RF deflecting field. After that computer simulations can be done to find the value of ΔZ for real parameters of the low energy secondary electrons taking into account a real spatial distribution of the deflecting field. Sometimes instead of full width at a half maximum a double rms size is used.

Another important characteristic is an ability of measuring small intensities. This feature is especially important for longitudinal halo measurements. Using a secondary electron multiplier as an electron beam detector 8 enables the measurements to be done within 5 orders of intensity magnitude.

The limitation of BSM use for high intensities is due to two reasons. The first one is target heating. In case of tungsten target before its destruction the overheating is manifested as arising of thermal electron current. A bunch substrate increasing within the beam pulse is observed when bunch behaviour within the beam pulse is measured.

The second limitation is effect of space charge of the analysed beam.

Influence of Analyzed Beam Space Charge

All the estimations described above are done with the assumption of a zero-intensity analysed beam, while a space charge of the real beam can strongly influence the secondary electrons trajectories and result in phase resolution deterioration [13-14].

As an example, the results of simulations for ESS proton linac for different beam currents are presented in Fig. 2. The phase resolution is given as a function of a longitudinal coordinate along the bunch. The bunch head is at the left side in the figure.

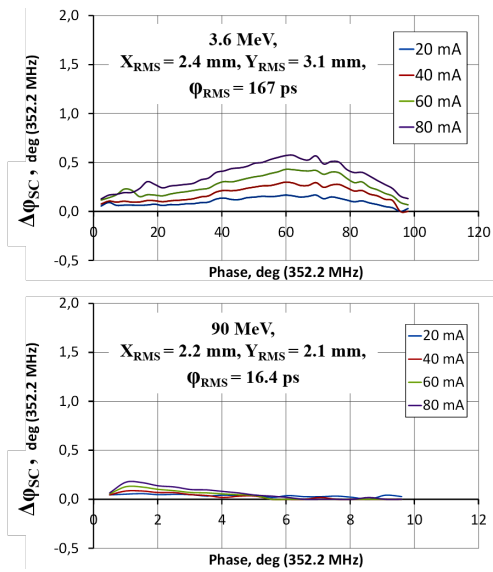

Figure 2: Space charge effect for various beam currents.

Also the energy modulation of secondary electrons by the space charge can result in a phase reading error, when the measured phase coordinate along the bunch does not correspond to the real one.

ISBN: 978-3-95450-240-0 ISSN: 2673-5539 doi:10.18429/JACoW-RuPAC2021-MOX02

MODIFICATIONS OF BUNCH SHAPE MONITOR

Additionally to the basic detector above described there are three BSM modifications: BSM for H^- beams, Bunch Length and Velocity Detector (BLVD) and Three Dimensional Bunch Shape Monitor (3D-BSM).

BSM for H- Minus Beams

In case of H^- beam a fraction of the detached electrons after interaction with the BSM target gets into the secondary electron channel of BSM and the detected signal represents a superposition of signals due to low energy secondary electrons and the detached electrons. The effect has been analyzed in [15]. The energy of the detached electrons differs from that of low energy secondary electrons so the two groups of the electrons can be effectively separated. BSM for H^- beam includes additional element – bending magnet located between the outlet collimator and the electron detector.

Bunch Length and Velocity Detector

BLVD is a BSM, which can be mechanically translated along the beam line [16]. In this detector a time of flight method of energy measurements is implemented. The translation results in a shift in phase of the observed distribution. Measuring the value of the translation and the value of the shift one can find an average velocity of the beam. The accuracy of bunch shape measurements for this detector is the same as for normal BSM. Special procedure of velocity measurement enables to decrease systematic error to ±0.1%. Total error of velocity measurements is typically within ±(0.3÷0.4)%.

Three-Dimensional Bunch Shape Monitor

3D-BSM is aimed to measure a three-dimensional distribution of charge in bunches [17]. Due to high strength and concentration of electric field near the wire target the electrons move almost perpendicular to its axis with very small displacement along the wire in the area between the target and the input collimator. Additional slit perpendicular to the target installed outside the beam enables to separate the secondary electrons emitted from a fixed coordinate along the wire. For fixed position of the wire and fixe position of the additional slit the intensity of the electrons passed through the slit is proportional to beam intensity at the fixed transverse coordinate. The phase distribution of the separated electrons is measured in the same manner as in basic BSM. Moving the target and the slit and each time measuring longitudinal distribution one can obtain a three-dimensional distribution of charge in bunches.

COMMISSIONING EXPERIENCE

The first BSM with transverse scanning of low energy secondary electrons has been developed and built in INR in the eighties and the first measurements has been done in 1988 during commissioning of INR linac. Since that time BSMs of various modifications have been developed and built for several accelerators (Table 1). It should be noted that the detectors of this type have also been developed in other laboratories [18-20].

Table 1: BSM Commissioning History

Year	LINAC	Beam commissioning	Quantity
1988	INR RAS	H^+ (20, 100 MeV)	1 BSM
1993	SSC RFQ	H^- (2.5 MeV)	1 BSM
1994	CERN LINAC3	Pb^{27+}(0.25, 4.2 MeV/u)	1 BLVD
1996	CERN LINAC2	H^+ (50 MeV)	1 3D-BSM
1996	JHP RFQ	H^- (3 MeV)	1 BLVD
1997	DESY	H^- (10, 30, 50 MeV)	2 BSMs + 1 BLVD
1997	INR RAS	H^+ (160 MeV)	1 BLVD
1999-2000	CERN LINAC2	H^+ (10, 30 MeV)	2 BSMs
2003-2010	SNS ORNL	H^- (7.5, ~90, ~180, ~1000 MeV)	8 BSMs
2012-2016	CERN LINAC4	H^- (3÷160 MeV)	2 BSMs
2012	J-PARC	H^- (~200 MeV)	3 BSMs
2016	LANSCE	H^+, H^- (0.75, ~70 MeV)	2 BSMs
2016	GSI-FAIR	Ar^{9+}(3.5 MeV/u)	1 BSM
2019	FRIB	Ar^{9+}(20 MeV/u)	1 BSM
2021	GSI-FAIR	Ar^{9+}(1.4÷7 MeV/u), H^+ (3÷70 MeV)	2 BSMs
2022	ESS	H^+ (3.6, 90 MeV)	2 BSMs
2022	MYRRHA	H^+ (1.5, 5.9 MeV)	1 BSM

MAIN BSM COMPONENTS

Typical BSM components [21] are RF and HV systems, secondary electron detection system, control system as well as magnetic shield and corrector.

RF System

The system includes RF deflector, RF amplifier and phase shifter. Depending on BSM design features both fundamental bunch array frequency and higher harmonics are used. The deflector is combined with the electrostatic lens thus enabling simultaneous focusing and RF-scanning of the electrons. Typically, BSM deflectors are RF-cavities, based on parallel wire lines with capacitive plates. An electrical length of the deflectors is usually λ/4 or λ/2. To improve the uniformity of both deflecting and focusing fields in Y-direction, thus improving a phase resolution, the new λ-type symmetric cavity has been developed for BSM-ESS [22]. The uniformity of the field in a zone of the electron beam passage is an order of magnitude better for the symmetric type (Fig. 3).

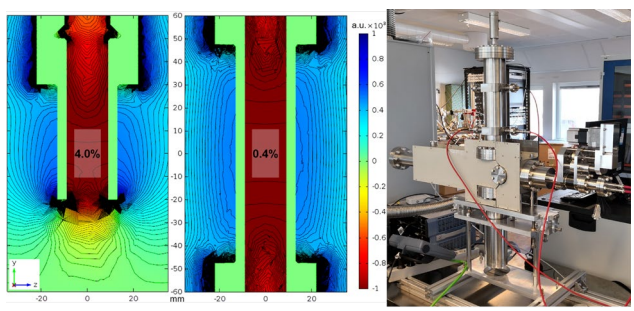

Figure 3: RF-field E_Z-component distribution in YZ-plane of λ/2- and λ-type BSM deflectors and photo of BSM-ESS with the implemented λ-type deflector.

Typical value of RF power required for deflector excitation is near 10 W and ~20 W for symmetric deflector type. Phase of the deflecting field is normally adjusted from pulse to pulse and the most suitable are voltage controlled electronic phase shifters.

ISBN: 978-3-95450-240-0 ISSN: 2673-5539 doi:10.18429/JACoW-RuPAC2021-MOX02

HV System

The HV system is intended to supply HV potentials to the target and electrostatic lens as well as to secondary electron multiplier. Typical value of target potential is −10 kV. To provide BSM tuning with thermal electrons a filament source is foreseen at HV target potential. To provide steering of the electrons an adjustable voltage difference of several hundred volts must be superimposed on focusing potential.

Electron Detection System

Secondary electron multipliers are most widely used. In this single channel system only one phase point is detected for a fixed phase setting hence multiple beam pulses are required for bunch shape measurement.

The detection system of 3D-BSM uses 30-channel electron collector thus enabling the measurement of the whole longitudinal distribution to be done per single beam pulse.

Control System

In principle any type of control system can be used. However the most recent our developments are based on LabVIEW platform with the use of National Instruments control modules NI USB-6363 and NI-9264.

Magnetic Shield and Corrector

Often BSMs are installed in a close vicinity of magnetic focusing elements with strong fringe fields both static and alternating. In this case a magnetic shield must be used to provide a non-distorted e-beam transport inside BSM. Typical BSM shield represents a sectional jacket made of low-carbon steel with interior surfaces covered with a foil made of a cobalt-iron alloy with high μ_r. Figure 4 shows the effect of the BSM shield on the fringe field of a quad located close to the BSM-ESS. Better results can be obtained if additional screens are added upstream and downstream of BSM. In this case the remnant fields decrease to the level less than the Earth's magnetic field, and their influence will be negligible.

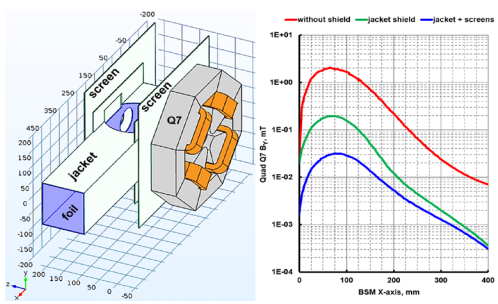

Figure 4: BSM shield design and the quad B_Y distribution.

An influence of remnant static magnetic fields inside the standard shield as well as unavoidable misalignments can be compensated for Z-direction by adjusting the steering voltage U_{steer} and for other directions with the help of additional magnetic corrector with superposition of dipole and quadrupole magnetic fields [23]: the dipole field moves the electron beam along Y-axis and the quadrupole field enables to adjust the tilt of the e-beam in YZ-plane (Fig. 5).

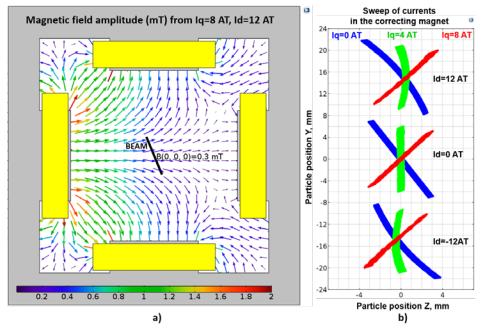

Figure 5: (a) Magnetic corrector with fields superposition. (b) E-beam in the plane of the outlet collimator for different quadrupole Iq and dipole Id coil currents.

SOME EXPERIMENTAL RESULTS

Normally different phase points are measured for different beam pulses and the signal is digitized within the beam pulse. It is implied that bunches are reproducible from pulse to pulse though can vary within the beam pulses. BSM allows to observe an evolution of charge longitudinal distribution in bunches within a beam pulse. Figure 6 demonstrates an evolution of bunch shape observed at the initial stage of CERN Linac-4 commissioning, when the beam loading compensation was insufficient.

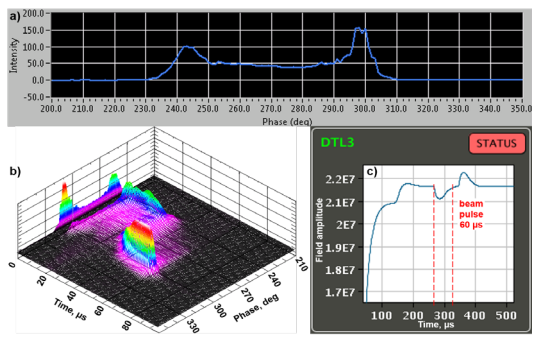

Figure 6: Experimental data from CERN Linac-4. a) A bunch shape with 1° resolution. b) Evolution of a bunch shape during a beam pulse. c) DTL3 field amplitude with the beam.

Data about evolution in time can be used as a generalized criterion of correct operation of all accelerator systems influencing on the longitudinal beam dynamics, including accelerating field parameters (Fig. 7).

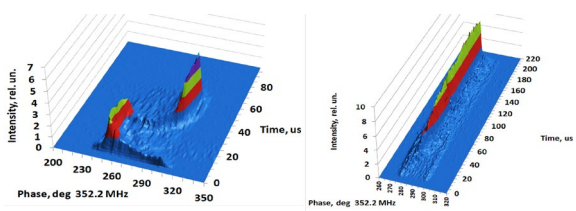

Figure 7: Behavior of bunch shape in time at the exit of CERN Linac-4 during commissioning (left) and for normal operation (right).

ISBN: 978-3-95450-240-0 ISSN: 2673-5539 doi:10.18429/JACoW-RuPAC2021-MOX02

If the measurements are done with increased gains of secondary electron multiplier a longitudinal halo can be observed [24,25] (Fig. 8).

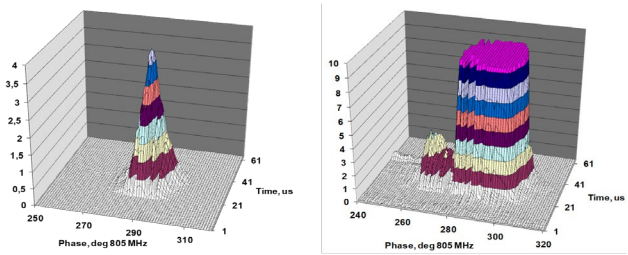

Figure 8: Observation of bunch longitudinal halo in the first SNS CCL: left – nominal SEM-gain, right – 160 times larger gain.

Bunch shape measurements can be used also for restoration of longitudinal emittance (Fig. 9), setting of accelerating field parameters, longitudinal matching etc.

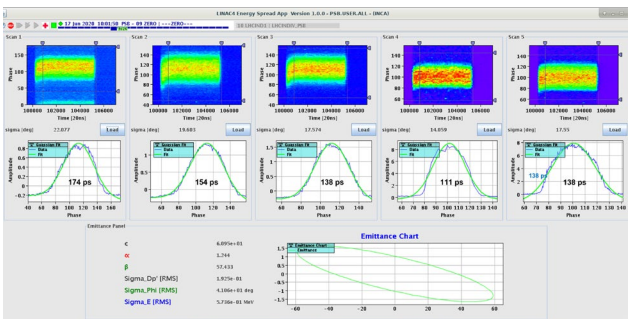

Figure 9: Longitudinal phase ellipse at the entrance of CERN PS Booster [26].

CONCLUSIONS

Bunch Shape Monitors being developed in INR RAS since eighties have become a new class of precise beam instrumentation for longitudinal beam parameters measurements and beam dynamics studies in ion linacs. They enable to obtain the results with the resolution unachievable with other conventional instrumentation. As an example Fig. 10 demonstrated the results of bunch shape measurements made with phase probes, fast current transformer and BSM [27].

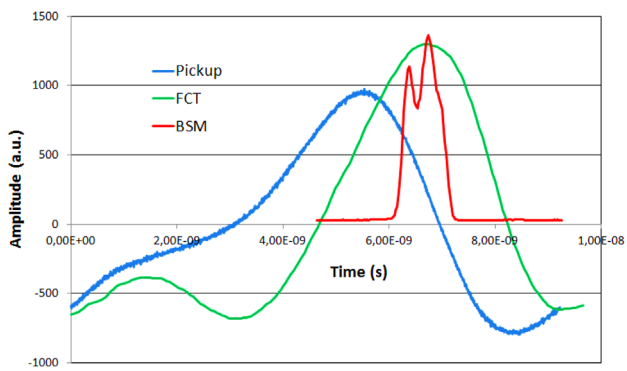

Figure 10: Bunch shapes of identical bunches of 3.5 Mev/u Ar9+ beam in GSI cw-Linac prototype measured with three different detectors.

REFERENCES

[1] A. S. Artiomov, A. K. Gevorkov, V. V. Limar, V. P. Sidorov, and N. G. Vaganov, "Method and Apparatus for Multifunctional Nonperturbing Diagnostics of H- Beams", in *Proc. 14th Particle Accelerator Conf. (PAC'91),* San Francisco, CA, USA, May 1991, pp. 1573-1576.

[2] S. Assadi, "SNS Transverse and Longitudinal Laser Profile Monitors Design, Implementation and Results", in *Proc. 10th European Particle Accelerator Conf. (EPAC'06)*, Edinburgh, UK, Jun. 2006, paper THPCH156, p. 3161.

[3] Y. Liu *et al.*, "Laser Based Diagnostics for Measuring H- Beam Parameters", in *Proc. 24th Particle Accelerator Conf. (PAC'11)*, New York, NY, USA, Mar.-Apr. 2011, paper WEOCN1, pp. 1433-1437.

[4] P. N. Ostroumov, A. Barcikowski, A. Delannoy, S. A. Kondrashev, and J. A. Nolen, "Bunch Length Detector Based on X-Ray Produced Photoelectrons", in *Proc. 23rd Particle Accelerator Conf. (PAC'09)*, Vancouver, Canada, May 2009, paper TU3GRC04, pp. 751-753.

[5] P. Forck and C. Dorn, "Measurements with a Novel Non-Intercepting Bunch Shape Monitor at the High Current GSI-LINAC", in *Proc. 7th European Workshop on Beam Diagnostics and Instrumentation for Particle Accelerators (DIPAC'05)*, Lyon, France, Jun. 2005, paper POM010, p. 48.

[6] I. M. Bronstein, B. S. Fraiman, "Secondary Electron Emission", Moscow, Nauka, 1969 (in Russian).

[7] E. W. Ernst, H. V. Foerster, "Time dispersion of secondary emission", *Journal of Appl. Phys.*, v. 26, No. 6, pp. 781-782, 1955.

[8] R. L. Witkover, "A non-destructive bunch length monitor for a proton linear accelerator", *Nucl. Instrum. Meth.*, v. 137, No. 2, pp. 203-211, 1976.

[9] A. Tron, A. Feschenko, "A monitor of proton beam phase distribution in linear resonance accelerator", in *Proc. 7th all union meeting on particle accelerators,* Dubna, USSR, 1981, v. 2, p. 125 (in Russian).

[10] I. A. Prudnikov, USSR invention license, H05h7/00, No.174281 (in Russian).

[11] A. V. Feschenko and P. N. Ostroumov, "Bunch Shape Measuring Technique and its Application for an Ion Linac Tuning", in *Proc. 1986 Linear Accelerator Conf. (LINAC'86)*, Stanford, CA, USA, Jun. 1986, paper WE3-30, pp. 323-327.

[12] A. V. Feschenko, P. N. Ostroumov, "Bunch shape measurements at the INR linac", in Proc. Workshop on Advanced Beam Instrumentation, KEK, Tsukuba, Japan, April 1991, pp. 235-245.

[13] A. V. Feschenko and V. A. Moiseev, "Space Charge Effects in Bunch Shape Monitors", in *Proc. 20th Linear Accelerator Conf. (LINAC'00)*, Monterey, CA, USA, Aug. 2000, paper MOC13, p. 178.

[14] A. Feschenko and V. A. Moiseev, "Peculiarities of Bunch Shape Measurements of High Intensity Ion Beams", in *Proc. 1st Int. Particle Accelerator Conf. (IPAC'10)*, Kyoto, Japan, May 2010, paper MOPE041, pp. 1065-1067.

[15] A. Denisov, A. Feschenko, and A. Aleksandrov, "Peculiarities Of Bunch Shape Measurements Of H-Minus Beams In Linear Accelerators", in *Proc. 21st Russian Particle Accelerator Conf. (RuPAC'08)*, Zvenigorod, Russia, Sep.-Oct. 2008, paper WEEAU02, p. 298.

ISBN: 978-3-95450-240-0 ISSN: 2673-5539 doi:10.18429/JACoW-RuPAC2021-MOX02

[16] P. N. Ostroumov, A. V. Feschenko, V. A. Gaidach, S. A. Krioukov, A. A. Menshov, and A. Ueno, "Bunch Length and Velocity Measurement of the JHP-RFQ Beam with INR BLVD", in *Proc. 19th Int. Linac Conf. (LINAC'98)*, Chicago, IL, USA, Aug. 1998, paper TH4061, pp. 905-907.

[17] S. K. Esin *et al.,* "A three dimensional bunch shape monitor for the CERN proton linac", in *Proc. 18th Linear Accelerator Conf. (LINAC'96)*, Geneva, Switzerland, Aug. 1996, paper MOP53, p. 193.

[18] E. S. McCrory, C. W. Schmidt, and A. V. Feschenko, "Use of INR-Style Bunch-Length Detector in the Fermilab Linac", in *Proc. 1992 Linear Accelerator Conf. (LINAC'92)*, Ottawa, Canada, Aug. 1992, paper TH4-21, pp. 662-664.

[19] N. Y. Vinogradov *et al.*, "Bunch Shape Measurement of CW Heavy-Ion Beam", in *Proc. 21st Linear Accelerator Conf. (LINAC'02)*, Gyeongju, Korea, Aug. 2002, paper MO411, pp. 61-63.

[20] N. Y. Vinogradov *et al.,* "A detector of bunch time structure for cw heavy-ion beams", *Nucl. Instrum. Meth.* A 526, p. 206, 2004.

[21] S. Gavrilov *et al.,* "Bunch Shape Monitors for modern ion linacs", *JINST* v. 12 p. 12014, 2017.

[22] S. A. Gavrilov, D. A. Chermoshentsev, and A. Feschenko, "Development, Fabrication and Laboratory Tests of Bunch Shape Monitors for ESS Linac", in *Proc. 7th Int. Beam Instrumentation Conf. (IBIC'18)*, Shanghai, China, Sep. 2018, pp. 407-409. doi:10.18429/JACoW-IBIC2018-WEPA17

[23] S. A. Gavrilov and A. Feschenko, "Design and Development of Bunch Shape Monitor for FRIB MSU", in *Proc. 6th Int. Beam Instrumentation Conf. (IBIC'17)*, Grand Rapids, MI, USA, Aug. 2017, pp. 179-181. doi:10.18429/JACoW-IBIC2017-TUPCC13

[24] J. Tan, G. Bellodi, A. Feschenko, and S. A. Gavrilov, "Results from the CERN LINAC4 Longitudinal Bunch Shape Monitor", in *Proc. 7th Int. Beam Instrumentation Conf. (IBIC'18)*, Shanghai, China, Sep. 2018, pp. 415-419. doi:10.18429/JACoW-IBIC2018-WEPA19

[25] A. Feschenko *et al.*, "Longitudinal Beam Parameters Study in the SNS Linac", in *Proc. 22nd Particle Accelerator Conf. (PAC'07)*, Albuquerque, NM, USA, Jun. 2007, paper THOAAB01, pp. 2608-2610.

[26] J. Tan, "LINAC4 diagnostics experience during commissioning", *in Proc. ARIES workshop "Experiences during hadron linac commissioning"*, Jan. 2021, https://agenda.ciemat.es/event/1229/contributions/2276/

[27] T. Sieber *et al.,* "Bunch Shape Measurements at the GSI CW-Linac Prototype", in Proc. 9th Int. Particle Accelerator Conf. (IPAC'18), Vancouver, Canada, Apr.-May 2018, pp. 2091. doi:10.18429/JACoW-IPAC2018-WEPAK006

ISBN: 978-3-95450-240-0 ISSN: 2673-5539 doi:10.18429/JACoW-RuPAC2021-MOY01

THE NICA COMPLEX INJECTION FACILITY

A. Butenko †, H. Khodzhibagiyan, S. Kostromin, I. Meshkov, A. Sidorin, E. Syresin, G. Trubnikov, A. Tuzikov, Joint Institute for Nuclear Research, Dubna, Russia

Abstract

The Nuclotron-based Ion Collider fAcility (NICA) is under construction in JINR. The NICA goals are providing of colliding beams for studies of hot and dense strongly interacting baryonic matter and spin physics. The NICA complex injection facility consists of following accelerators: Alvarez-type linac LU-20 of light ions up to 5 MeV/u; heavy ion linac HILAC with RFQ and IH DTL sections at energy 3.2 MeV/u; superconducting Booster synchrotron at energy up 578 MeV/u; superconducting synchrotron Nuclotron at gold ion energy 3.85 GeV/u. In the nearest future the old LU-20 will be substituted by a new light ion linac for acceleration of 2<A/z<3 ions up to 7 MeV/u with additional two acceleration sections for protons, first IH section for 13 MeV and the second one - superconducting for 20 MeV. The status of NICA injection facility is under discussion.

NICA INJECTION COMPLEX

The NICA accelerator complex [1,2] is constructed and commissioned at JINR. NICA experiments shall be performed in search of the mixed phase of baryonic matter and nature of nucleon/particle spin. The new NICA accelerator complex will permit implementing experiments in the following modes: with the Nuclotron ion beams extracted at a fixed target; with colliding ion beams in the collider; with colliding ion-proton beams; with colliding beams of polarized protons and deuterons. The main elements of the NICA complex are an injection complex, which includes a set of ion sources and two linear accelerators, the superconducting acting Booster, the superconducting acting synchrotron Nuclotron, a Collider composed of two superconducting rings with two beam interaction points, a Multi-Purpose Detector (MPD) and a Spin Physics Detector (SPD) and beam transport channels.

The injection complex [1] is divided on two injection chains: one is used for heavy ions, other - for protons and light ions. The light ion injection chain includes laser ion source (LIS) and source of polarized ions (SPI), linear accelerator LU-20, Nuclotron and transfer line LU-20-Nuclotron. The heavy ion injection chain consists from electron string ion source (ESIS), laser ion source, plasma ion source, the acting Heavy Ion Linac (HILAC), transfer line HILAC-Booster, superconducting acting synchrotron Booster, transfer line Booster-Nuclotron and acting superconducting synchrotron Nuclotron.

INJECTION CHAIN FOR LIGHT IONS

The linear accelerator LU-20, which is under operation since 1974, accelerates protons and ions from few sources: the laser source and the source of polarized ions - protons and deuterons. SPI was constructed by JINR-INR RAS collaboration. The beam current of polarized deuterons corresponds to 2 mA. During 2009 - 2018 years completely modernized all of the main systems of the Linac: RF power amplifiers (5MW/pulse), drift tubes power supply (PS), beam diagnostics, HV terminal, fore-injector, LLRF system, synchronization system, vacuum system, PS system of the injection line. At the LU-20 exit, the energy of ions is 5 MeV/n. At present time, the LU-20 beam is injected directly into the Nuclotron through transfer line Lu-20-Nuclotron. The HV injector of linac LU-20 has been replaced in 2016 by RFQ (Fig. 1) [1,3] with beam matching channels. The RFQ was constructed by JINR, ITEP of NRC "Kurchatov Institute", NRNU MEPHI, VNIITF collaboration. The new buncher constructed by ITEP of NRC "Kurchatov Institute" was installed between RFQ and LU-20 in 2017. Installation of new buncher permited to increase the heavy ion beam current by 5 times in Nuclotron 55 run in 2018.

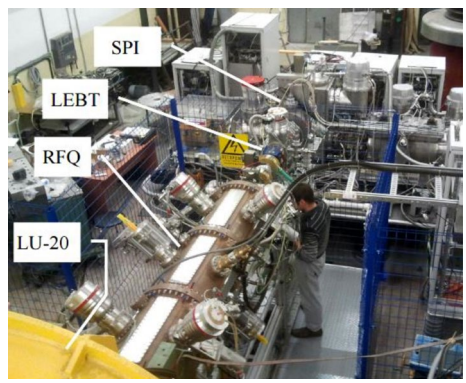

Figure 1: New fore-injector for LU-20.

The design of new Light Ion Linac (LILAc) was started in 2017 to replace the LU-20 in NICA injection complex. LILAc consists of three sections: warm injection section applied for acceleration of light ions and protons up to energy 7 MeV/n [4], warm medium energy section used for proton acceleration up to energy 13 MeV [4] and superconducting HWR sections [5], which provides proton acceleration up to energy 20 MeV. The LILAC should provide beam current of 5 emA. The construction of first light ion section [4] at ion energy 7 MeV/n was started in 2018 by Bevatech (Germany), it should be delivered in JINR in 2023. The next step of the LILAc project – design of a middle energy section and HWR superconducting sections.

The increased beam energy of LILAc is required for future researches with polarized proton beams. The operating frequency of the LILAc is equal to 162.5 MHz for first two sections and 325 MHz for HWR section. The two superconducting HWRs (Fig. 2) were constructed by Russian-Belarusian collaboration with participation of JINR, NRNU MEPhI, INP BSU and PTI NASB.

ISBN: 978-3-95450-240-0 ISSN: 2673-5539 doi:10.18429/JACoW-RuPAC2021-MOY01

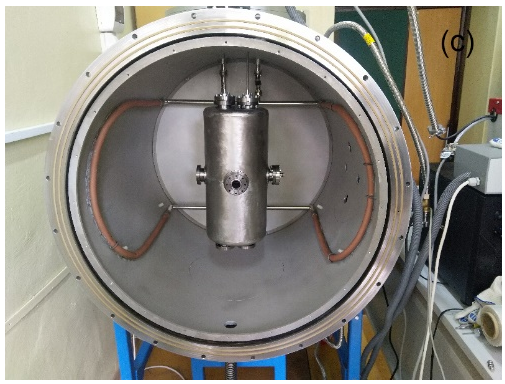

Figure 2: Niobium cavity inside of testing cryostat.

INJECTION CHAIN FOR HEAVY IONS

The second linear accelerator of NICA injection complex— a new heavy-ion linear accelerator (Heavy Ion Linac, HILAc) [1,6] (Fig. 3) constructed by JINR-Bevatech collaboration is under exploitation since 2016. It is aimed to accelerate heavy ions injected from KRION-6T, a superconducting electron-string heavy ion source. At the present time KRION-6T produces 5×10^8 Au^{31+} and 2×10^8 $^{209}Bi^{27+}$ ions.

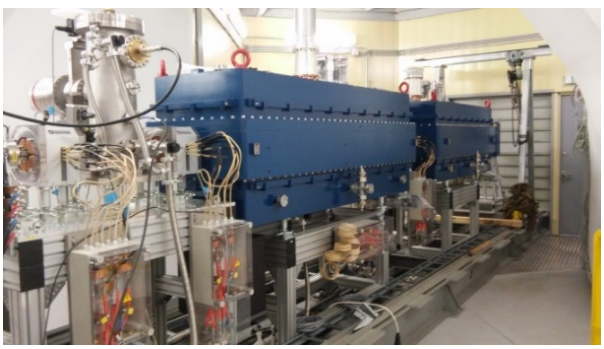

Figure 3: Heavy ion linear accelerator.

This ion source will be used at injection in Booster in 2022. Upgraded version of KRION-N with $^{197}Au^{31+}$ or $^{209}Bi^{35+}$ ion intensity up 2×10^9 particles per pulse will be constructed in 2022 for Collider experiments. The energy of ions at the exit from HILAc is 3.2 MeV/n, while the beam intensity amounts to 2×10^9 particles per pulse or 10 emA, repetition rate is 10 Hz. The HILAc consists of three sections: RFQ and two IH sections. The RFQ is a 4-rod structure operating at 100.625 MHz. The RFQ and each IH section are powered by 140 kW and 340 kW solid state amplifiers.

Especially for the test of the Booster [7] the plasma source generating a single component He^{1+} beam was created. The efficiency of beam transportation through second and third IH sections was 78.5% (Fig. 4). The maximal ion $^4He^{1+}$ beam current at HILAC entrance during first Booster runs corresponds to project value 10 mA. During second Booster run the $^4He^{1+}$and $^{56}Fe^{14+}$ ions produced in plasma and laser ion sources were accelerated in HILAC and injected in Booster.

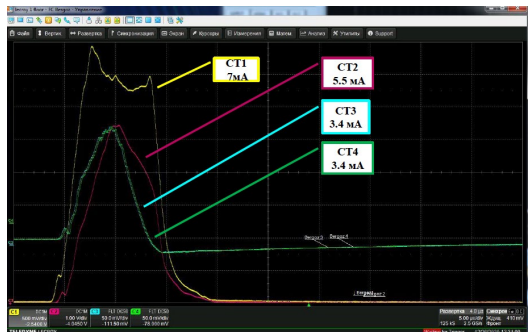

Figure 4: Signals of current transformers CT: CT1 at RFQ exit, CT2 at IH2 exit, CT2-at the middle of transfer line HILAC-Booster, CT3 at transfer line exit.

The transfer line from HILAC to Booster (Fig. 5) [8] consists of 2 dipole magnets, 7 quadrupole lenses, 6 stirrers magnets, debuncher, collimator, vacuum and diagnostic equipment. The debuncher constructed by Bevatech reduces relative ion momentum spread after HILAc from 5×10^{-3} to 10^{-3}. The collimation diaphragm in transport channel provides separation of ions with required charge $^{197}Au^{31+}$ from parasitic ions with another charges. The assembling of transfer line was done in 2020. The achieved efficiency of beam transportation during first Booster beam run was of 90% at beam current at the HILAC exit of 4 mA, this value was sufficient for the first experiments [7]. The measured beam profiles (Fig. 6) is in agreement with beam sizes obtained from channel optic simulations.

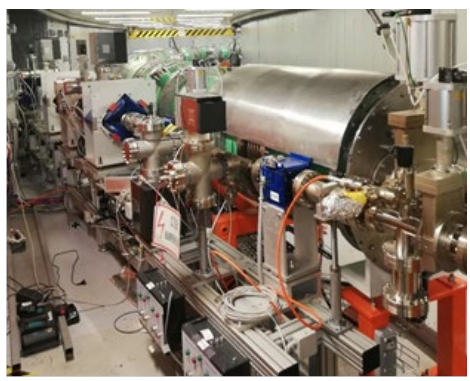

Figure 5: Transport channel HILAC-Booster.

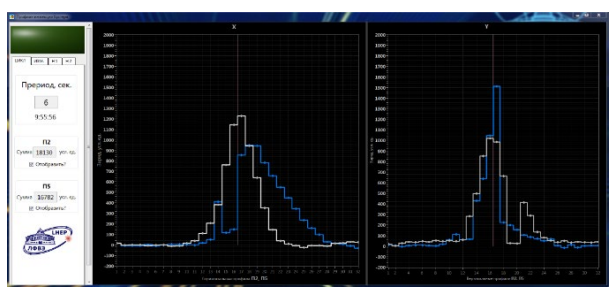

Figure 6: Beam profiles measured by PM2 and PM5.

The Booster [1] is a superconducting synchrotron intended for accelerating heavy ions to an energy of 600 MeV/n. The magnetic structure of the Booster with a 211-m-long circumference is mounted inside the yoke of the Synchrophasotron magnet.

ISBN: 978-3-95450-240-0 ISSN: 2673-5539 doi:10.18429/JACoW-RuPAC2021-MOY01

Figure 7: Booster ring inside Synchrophasatron yoke.

The main goals of the Booster are accumulation of $2 \cdot 10^9$ Au^{31+} ions, acceleration of heavy ions up to the energy 578 MeV/n required for effective stripping, and forming of the required beam emittance with the electron cooling system. The Booster has a four-fold symmetry lattice with DFO periodic cells. Each quadrant of the Booster has ten dipole magnets, six focusing and six defocusing quadrupole lenses, and multipole corrector magnets. All Booster dipole magnets and quadrupole lenses were fabricated and tested at JINR.

The Booster power supply system provides consecutive connection of dipole magnets, quadrupole focusing and defocusing lenses. The main powerful source of the power supply system forms a current of up to 12.1 kA with the required magnetic field ramp of 1,2 T/s. Two additional power supply sources are intended for flexible adjustment of the Booster working point.

The beam injection system of the Booster consists of an electrostatic septum and three electric kickers.

The Booster RF system provide 10 kV of acceleration voltage. The operating frequency range of the stations is from 587 kHz to 2526 kHz.

The electron cooling system has the maximal electron energy of 60 keV.

The Booster beam extraction system consists of a magnetic kicker, two magnetic septa, a stripping station and a closed orbit bump subsystem. The ions accelerated in the Booster are extracted and transported along a magnetic channel, and on their way, they cross a stripped target. The channel consists of five dipole magnets, eight quadrupole lenses, three correctors, separation septa, and diagnostic and vacuum equipment.

The installation of the Booster cryomagnetic equipment (Fig. 7) was started in September 2018. The first technical Booster run was done in November-December 2020.

At the first stage the insulating vacuum volume and beam pipe were assembled and tested. After this the cooling of cryomagnetic system, commissioning of thermometry, quench protection systems, tuning of power supply and HILAC-Booster beam transfer line systems were done. Then the beam was injected into the Booster [7] on the plateau of the magnetic field corresponding to the injection energy. The beam circulation was achieved without activation of the orbit correction system.

Turn-by-turn measurements were used for the injection optimization. The signals from two nearest BPMs and virtual model of the injection section permitted to calculate linear optics and closed orbit position in the injection point depending on the quadrupole settings (Fig. 8). The efficiency of beam pass through injection section was achieved at the level of about 75%.

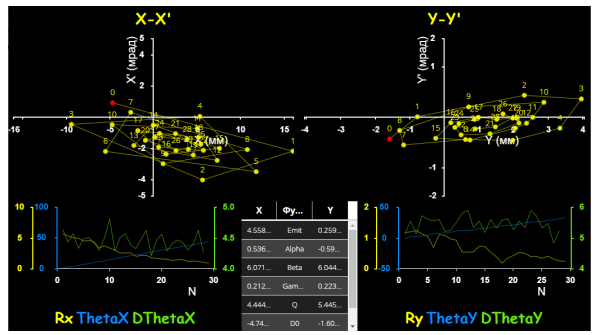

Figure 8: Turn-by-turn measurements of the linear optics and closed orbit position in the injection point.

After the orbit correction and tuning of the injection system the intensity of the $^4He^{1+}$ circulating beam was increased up to 7×10^{10} ions (Fig. 9). The charge of these ions is equal to charge of 2×10^9 Au^{31+} ions. Life time of ions corresponds to 1.3 s or equivalent average residual gas pressure 2×10^{-8} Pa.

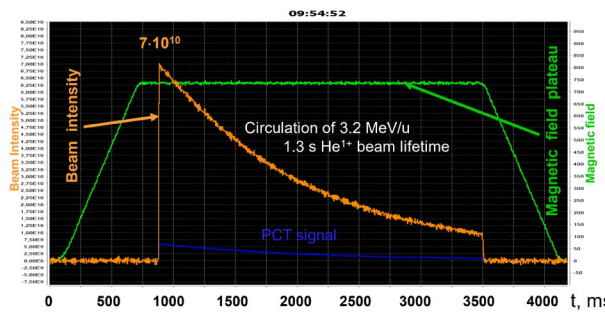

Figure 9: PCT signal, beam intensity and magnetic field time dependencies during the cycle.

The beam current transformer signal at ion acceleration up energy of 100 MeV/n is shown in Fig. 10. The choice of maximal ion energy was defined by the radiation safety conditions at Booster operation without beam extraction.

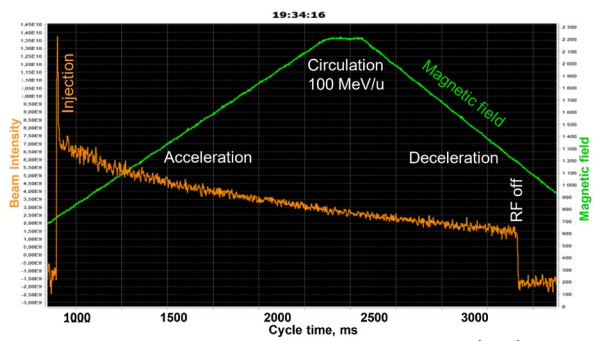

Figure 10: Beam current transformer signal at $^4He^{1+}$ ion acceleration.

During second run of the Booster in September 2021 the beams of ions $^4He^{1+}$ and $^{56}Fe^{14+}$ with mass-to-charge ratio A/Z=4 and intensity up 4×10^{10} and 4×10^8 correspondently were injected in to the Booster, bunched on the injection

ISBN: 978-3-95450-240-0 ISSN: 2673-5539 doi:10.18429/JACoW-RuPAC2021-MOY01

table of magnetic field on fifth RF harmonic, then accelerated up to 65 MeV/u where recaptured with first RF harmonic and again accelerated. The $^{56}Fe^{14+}$ ions were accelerated up to project energy – 578 MeV/n (Fig. 11).

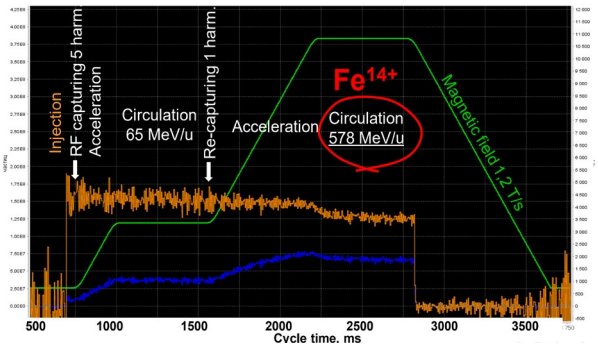

Figure 11: Beam current transformer signal at $^{56}Fe^{14+}$ ion acceleration.

The main results of the second cycle of the Booster beam commissioning are following: the beam injection efficiency with adiabatic capturing at 5 harmonic at efficiency is higher than 95%; accelerating up to 65 MeV/u, where recaptured with 1 RF harmonic with efficiency closed to 100%; acceleration up to project energy of 578 MeV/u with dB/dt = 1.2 T/s; ultra-high vacuum in beam pipe ($^{4}He^{+1}$ ion life-time more than 10 s), electron cooling of ions at energy 3.2 MeV/n, beam extraction to transfer line Booster-Nuclotron and transportation in this transfer line with total transfer efficiency of 70%.

The $^{4}He^{1+}$ ion life (Fig. 12) during second Booster run corresponds to 10.8 s. The equivalent residual gas pressure is about 5×10^{-9} Pa. The relative concentration of residual gases like CO and H_2O in warm Booster sections was several times less during second run in comparison with first one.

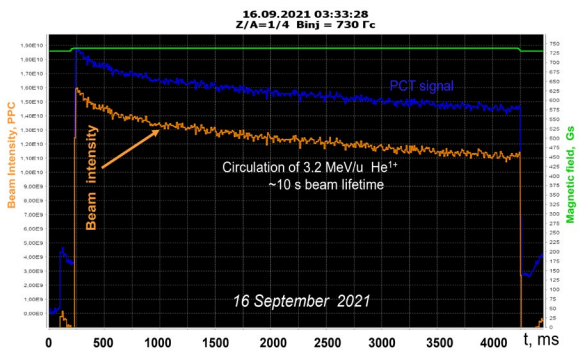

Figure 12: Beam current transformer signal at $^{4}He^{1+}$ ion energy 3.2 MeV/u.

The electron cooling of $^{56}Fe^{14+}$ ions was first time realized during second Booster run. The relative momentum spread of cooled ions is equal to 4×10^{-4}. Transverse cooling time at beam emittance reduction in e-times corresponds to 1,4 s.

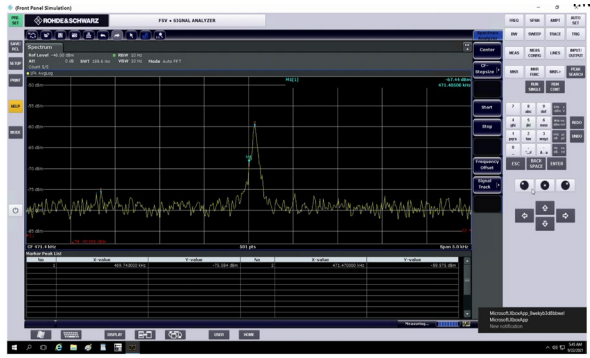

Figure 13: Schottky noise signal at 4 harmonic of revolution frequency and ion energy 3.2 MeV/u.

The cryomagnetic and power supply systems were tested at the design magnetic field cycle during first Booster run (Fig. 14). The magnetic cycle has three plateaus: for injection, electron cooling and beam extraction. The achieved ramping rate 1.2 T/s of the magnetic field corresponds to the project value (Fig. 14). The achieved maximum magnetic field of 1.8 T also equal to the project value.

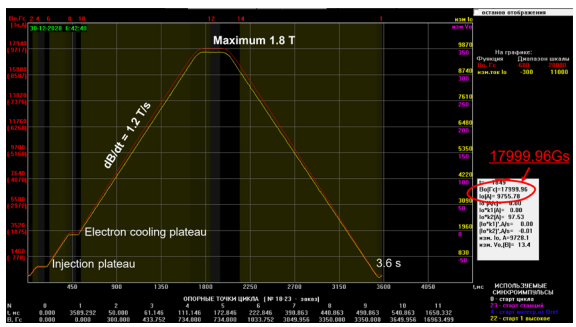

Figure 14: The Booster magnetic field cycle at design parameters.

The Booster beam extraction system [8] consists of a magnetic kicker, two magnetic septa, a stripping station and a closed orbit bump subsystem including four lattice dipoles with five additional HTS current leads. The Booster beam extraction system together with transfer line Booster-Nuclotron (Fig. 15) was fabricated by BINP SB RAS. The first beam experiments with extracted $^{4}He^{1+}$ and $^{56}Fe^{14+}$ ion beams were performed during second Booster beam run. The total efficiency of beam extraction from Booster and transportation in transfer line Booster–Nuclotron corresponds to about 70%.

Figure 15: The Booster-Nuclotron transfer line.

ISBN: 978-3-95450-240-0 ISSN: 2673-5539 doi:10.18429/JACoW-RuPAC2021-MOY01

THE NUCLOTRON

The linear accelerator LU-20, which is under operation

The upgraded Nuclotron [9] accelerates protons, polarized deuterons and ions to a maximum energy depending of the sort of particles. The maximum ion energy corresponds to 5.2 GeV/n at present time (Table 1).

Table 1: Main Parameters of Nuclotron Beams

Parameter	Project	Status, 2020
Max. magn. field, T	2	2 (1.7 routine)
B-field ramp, T/s	1	0.8 (0.7 routine)
particles	p – U, d↑	p↑, d↑, p – Xe
Maximum energy, GeV/u	12 (p), 5.8 (d) 4.5 $^{197}Au^{79+}$	5.2 (d, C), 3.6 (Ar^{16+})
Intensity, ions/cycl	10^{11} (p,d), 2×10^{9} (A > 100)	d 4×10^{10} (2×10^{10} routine) $^{7}Li^{3+}3\times10^{9}$ C^{6+} 2×10^{9} $Ar^{16+}1\times10^{6}$ $Kr^{26+}2\times10^{5}$ $Xe^{42+}1\times10^{4}$

The polarized deuteron beams were obtained at intensity up 2×10^{9} ppp in Nuclotron runs 53 and 54 with SPI in 2016-2018 (Table 1). The polarized proton beams were formed first time at intensity 10^{8} ppp in Nuclotron 54 run in 2017. The injection with RF adiabatic capture at efficiency of 80%. was used in two last Nuclotron runs 54 and 55 in 2017 and 2018. The run 55 in 2018 was performed with acceleration of C^{6+}, Ar^{16+} and Kr^{26+} (Fig.16) ion beams (Table 1). The resonant stochastic extraction (RF knockout technique) was realized in the run 55 in 2018.

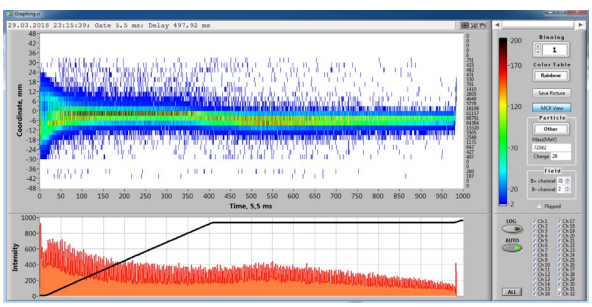

Figure 16: The size and beam intensity of extracted from Nuclotron Kr^{26+} ion beam.

The installation in the Nuclotron of the Booster beam injection system and the Collider fast extraction system are required for its operation as the main synchrotron of the NICA complex. The kicker and Lambertson magnet (Fig. 17) should be installed for injection section in end 2021 or in beginning 2022.

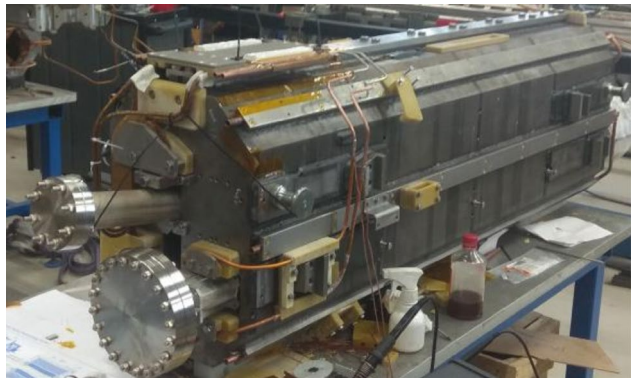

Figure 17: The Nuclotron Lambertson magnet for injection section.

REFERENCES

[1] Technical Project of NICA Acceleration Complex, Dubna, 2015.

[2] V.D. Kekelidze R. Lednicky, V.A. Matveev *et al.*, Three stages of the NICA accelerator complex, *Eur. Phys. J. A*, v.52:211, p.390, 2016. doi:10.1088/1742-6596/668/1/012023

[3] V.A. Andreev, A.I. Balabin, A.V. Butenko *et al.*, *Problems of Atomic Science and Technology. Series: Nuclear Physics Investigation*, v.6, no7, pp.943-946, 2016.

[4] H. Höltermann, M. Basten, B. Koubek *et al.*, "Light Ion Linear Accelerator up to 7 AMeV for NICA", in *Proc. RuPAC'18*, Protvino, Russia, Oct. 2018, paper WECAMH02, pp. 68-71. doi: 10.18429/JACoW-RUPAC2018-WECAMH02.

[5] D. Bychanok, A Sukhotski, S Huseu *et al.*, "Control of electromagnetic properties during prototyping, fabrication and operation of low-β 325 MHz half-wave resonators", *Journal of Physics D: Applied Physics*, vol. 54, no. 10, p. 255502, Apr. 2021. doi:10.1088/1361-6463/abf168.

[6] A.M. Bazanov, A.V. Butenko, B.V. Golovenckiy *et al.*, "Commissioning of the new heavy ion linac at the NICA project, in *Proc.IPAC17*, Copenhagen, Denmark, May 2017, paper TUPVA116, pp.2362-2364.

[7] A. Butenko, N. Agapov, A. Alfeev *et al.,* "First Experiments with Accelerated Ion Beams in the Booster of NICA Accelerator Complex", presented at the *12th Int. Particle Accelerator Conf. (IPAC'21),* Campinas, Brazil, May 2021, paper MOPAB025.

[8] A.V. Butenko, V.I. Volkov, C. Yu. Kolesnikov *et al.,* "Beam transport channels and beam injection and extraction systems of the NICA accelerator complex", *Nuclei and Letters*, v.13, pp.966-977, 2016. doi:10.1134/S1547477116070190.

[9] E.M. Syresin, N.N. Agapov, A.V. Alfeev *et al.*, "Nuclotron Development for NICA Acceleration Complex", in *Proc. IPAC 19*, Melbourne, Australia, May 2019, paper THXXPLM1, pp.3396-3398. doi: 10.18429/JACoW-IPAC2019-THXXPLM1

ISBN: 978-3-95450-240-0 ISSN: 2673-5539 doi:10.18429/JACoW-RuPAC2021-MOY02

NICA ION COLLIDER AT JINR

E. Syresin, N. Agapov, A. Alfeev, V. Andreev, A. Baldin, A. Bazanov, O. Brovko, V. Bugaev, A. Butenko, A. Galimov, I. Gorelyshev, D. Donets, E.D. Donets, E.E. Donets, A. Eliseev, G. Filatov, V. Fimushkin, B. Golovenskiy, E. Gorbachev, A. Govorov, A. Grebentsov, E. Ivanov, V. Karpinsky, V. Kekelidze, A. Kirichenko, H. Khodzhibagiyan, A. Kobets, V. Kobets, A. Konstantinov, S. Korovkin, S. Kostromin, O. Kozlov, K. Levterov, D. Lyuosev, A. Malyshev, A. Martynov, S. Melnikov, I. Meshkov, V. Mikhailov, Yu. Mitrophanova, V. Monchinsky, A. Nesterov, A. Osipenkov, K. Osipov, R. Pivin, A. Philippov, D. Ponkin, S. Romanov, P. Rukojatkin, I. Shirikov, A. Shurygin, A. Sidorin, V. Slepnev, A. Slivin, G. Trubnikov, A. Tuzikov, B. Vasilishin, V.Volkov, Joint Institute for Nuclear Research, Dubna , Russia

Abstract

The Nuclotron-based Ion Collider fAcility (NICA) [1-5] is under construction in JINR. The NICA goals are providing of colliding beams for studies of hot and dense strongly interacting baryonic matter and spin physics. The accelerator facility of Collider NICA consists of following elements: acting Alvarez-type linac LU-20 of light ions at energy 5 MeV/u, constructed a new light ion linac of light ions at energy 7 MeV/u and protons at energy 13 MeV, new acting heavy ion linac HILAC with RFQ and IH DTL sections at energy 3.2 MeV/u, new acting superconducting Booster synchrotron at energy up 600 MeV/u, acting superconducting synchrotron Nuclotron at gold ion energy 4.5 GeV/n and two Collider storage rings with two interaction points. The status of acceleration complex NICA is under discussion.

INJECTION ACCELERATOR COMPLEX NICA FOR HEAVY ION MODE

The injection accelerator complex NICA for heavy ion mode [2] involves following accelerators: a new heavy-ion linear accelerator (Heavy Ion Linac, HILAC) constructed by JINR-Bevatech collaboration is under exploitation since 2016. It will accelerate heavy ions such as $^{197}Au^{31+}$ and $^{209}Bi^{35+}$ injected from KRION-6T, a superconducting electron-string heavy ion source, constructed by JINR. At present time KRION-6T produces $8\cdot10^8$ Au^{31+} ions and $9\cdot10^8$ $^{209}Bi^{35+}$ ions during three pulses of extracted beam. This ion source will be used at injection in Booster in 2022. Upgraded version of KRION-N with $^{197}Au^{31+}$ or $^{209}Bi^{35+}$ion intensity up $2.5\cdot10^9$ particles per pulse will be constructed in 2022 for Collider experiments. The energy of ions at the exit from HILAC is 3.2 MeV/n, while the beam intensity amounts to 2×10^9 particles per pulse or 10 emA, repetition rate is 10 Hz. The HILAC consists of three sections: RFQ and two IH sections. The RFQ is a 4-rod structure operating at 100.625 MHz. The RFQ and each IH section are powered by 140 kW and 340 kW solid state amplifiers. The acceleration of $^{12}C^{2+}$ ions with mass-charge ratio of A/Z=6, produced in laser ion source, was performed at first HILAC tests. Especially for the test run of the Booster the plasma source generating a single component $^4He^{1+}$ (A/Z = 4) beam was created. The maximal ion $^4He^{1+}$ beam current at HILAC entrance during first Booster runs corresponds to project value 10 mA, efficiency of beam transportation through second and third IH sections was 78.5%. During second Booster run the $^4He^{1+}$and $^{56}Fe^{14+}$ ions produced in plasma and laser ion sources were accelerated in HILAC and injected in Booster.

The transfer line from HILAC to Booster [*2*] (Fig. 1) consists of 2 dipole magnets, 7 quadrupole lenses, 6 steerers magnets, debuncher, collimator, vacuum and diagnostic equipment. The transfer line from HILAC to Booster was under operation since autumn 2020. The achieved efficiency of the beam transmission in HILAC – Booster transfer line was about 90% at the beam current of 4 mA.

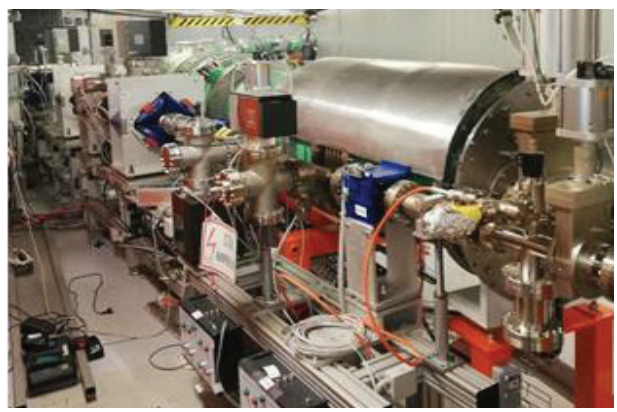

Figure 1: Transport channel HILAC-Booster.

The Booster [1-5] is a superconducting synchrotron intended for accelerating heavy ions up to energy of 578 MeV/u. The magnetic structure of the Booster with a 211 m - long circumference is mounted in tunnel inside the huge iron yoke of the Synchrophasotron magnet (Fig. 2). The main goals of the Booster are accumulation of $2\cdot10^9$ $^{197}Au^{31+}$ or $^{209}Bi^{35+}$ ions, acceleration of heavy ions up to the energy 578 MeV/u required for effective stripping, and forming of the required beam emittance with the electron cooling system.

ISBN: 978-3-95450-240-0 ISSN: 2673-5539 doi:10.18429/JACoW-RuPAC2021-MOY02

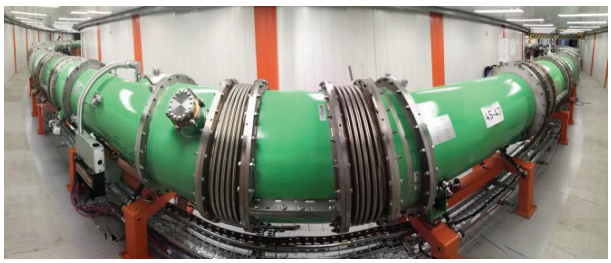

Figure 2: Booster ring in the tunnel inside the Synchrophasotron iron yoke.

The Booster operation was started in end of 2020 [6,7]. The circulated in Booster ion $^{4}He^{1+}$ beam at intensity 7×10^{10} corresponds to equivalent project intensity $2\cdot10^{9}$ $^{197}Au^{31+}$ ions. During second run in September 2021 the beams of ions $^{4}He^{1+}$ and $^{56}Fe^{14+}$ with mass-charge ratio A/Z=4 and intensity up $4\cdot10^{10}$ and $4\cdot10^{8}$ correspondently were injected in Booster, bunched on the injection table of magnetic field on fives RF harmonic and then accelerated up energy 65 MeV/n, where they were rebunched on first RF harmonic and again accelerated. The $^{56}Fe^{14}$ ions were accelerated up energy of 578 MeV/n.

The Booster beam extraction system [2] consists of a magnetic kicker, two magnetic septa, a stripping station and a closed orbit bump subsystem including four lattice dipoles with five additional HTS current leads. The Booster beam extraction system together with transfer line Booster Nuclotron (Fig. 3) was fabricated by BINP SB RAS. The first beam experiments with extracted $^{4}He^{1+}$ and $^{56}Fe^{14+}$ ion beams were performed during second Booster beam run.

Figure 3: The transfer line Booster – Nuclotron.

The installation in Nuclotron of beam injection system from the Booster and fast extraction system in Collider [2] are required for its operation as the main synchrotron of the NICA complex. The installation of kickers and Lamberson magnets for Nuclotron injection section is planned in autumn 2021. The operation of Collider NICA injection chain HILAC-Booster-Nuclotron is planned in December 2021-January 2022.

The magnetic system of room-temperature transfer lines from Nuclotron to Collider rings [2,5] was fabricated by French company Sigma Phi. The transfer line lattice contains 27 dipoles, 28 quadrupoles, 33 steerers and set of beam diagnostics devices. The installation of magnet is planned to start in end of 2021. The channel magnets are powered in pulsed mode. The power supplies of magnets will be delivered in JINR in summer 2022.

COLLIDER RINGS

The Collider [1-5] consists of two storage rings with two interaction points (IPs). Its main parameters (Table 1) are as follows: the magnetic rigidity is up to 45 T·m; the residual gas pressure in the beam chamber is not high than 10^{-10} Torr; the maximum field in dipole magnets is 1.8 T; the kinetic energy of gold nuclei ranges from 1 to 4.5 GeV/n; the beam axes coincide at the interaction section (zero intersection angle); and the average luminosity is 10^{27} cm^{-2} s^{-1} for gold ions. The rings of the Collider are identical in shape to a racetrack — two arcs are connected by two long straight section (109 m each). The circumference of each ring is 503.04 m.

The dipole magnets (Fig. 4) and lenses in the arcs are combined into 12 cells of the so-called FODO structure separated by straight sections. The total number of the horizontal dipole magnets in the arcs of both rings corresponds to 80 and 8 vertical dipole magnets for two IP regions. The magnets of both rings in the arcs are situated one above another; their axes are separated vertically by 320 mm. Upon passing the section bringing them together, the particle bunches along the upper and lower rings travel along a common straight trajectory toward each other to collide at two interaction points (IPs). The magnets in the arcs have common yokes, but their construction permits controlling the field in each of the rings separately.

Figure 4: Collider dipole magnet.

ISBN: 978-3-95450-240-0 ISSN: 2673-5539 doi:10.18429/JACoW-RuPAC2021-MOY02

Table 1: Main Parameters of the NICA Accelerator Complex

Parameter	Value		
Ring circumference, m	503,04		
Number of bunches	22		
Rms bunch length, m	0.6		
Beta-function in the IP, m	0.6		
Betatron tunes, Q_x/Q_y	9.44/9.44		
Ring acceptance, π·mm·mrad	40		
Longitudinal acceptance	±0.01		
Ion energy, GeV/n	1	3	4.5
Ion number per bunch	$3.2{\cdot}10^8$	$2.9{\cdot}10^9$	$3.1{\cdot}10^9$
Rms dp/p, 10^{-3}	0.55	1.15	1.5
Rms emittance, π·mm·mrad	1.3/1.3	1.3/1.1	1.3/1.0
Luminosity, $cm^{-2}s^{-1}$	$0.8{\cdot}10^{25}$	$0.8{\cdot}10^{27}$	10^{27}
IBS growth time, sec	160	460	2000

The all arc dipole magnets were produced and tested on a cryogenic test bench. The results of cryogenic tests are given in Fig. 5. The measurements of magnet effective length are illustrated by Fig. 6.

The total number of the lenses is equal to 86 in the arcs and the straight sections and 12 lenses of final focus sections. Single-aperture lenses are installed along final focus sections to provide that both beams are focused at the IP.

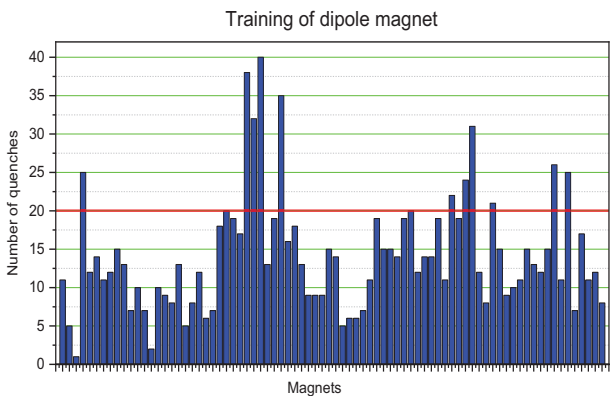

Figure 5: Cryogenic training of dipole magnets.

Three power supplies are used in Collider for all dipole magnets and quadrupole lenses. The Collider main power supply provides consecutive connection of dipole magnets, quadrupole focusing and defocusing lenses at maximum current of 10.7 kA. The second power supply is used for all lenses, and third one is intended only for D lenses. The powers of second and third power supplies are by one order less than power of main power supply. At transition from working point 9.44 to 9.1 the power supply current is variated in all quadrupole lenses on -300 A (except lenses of final focuses) and on 9A for D-lenses. The length of each pair of quadrupole lenses was optimized in straight sections for this case. Additionally, each pair of lenses in straight section and each final focus lens has individual power supply with correction current up 300A.

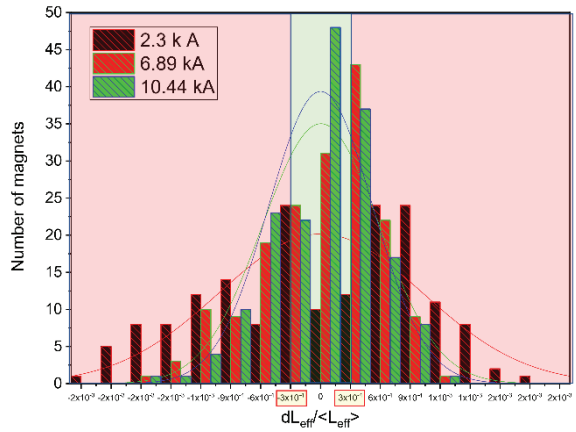

Figure 6: Arc dipole magnet distribution related to their effective lengths.

Methods for cooling of charged particle beams represent the key accelerator technologies, which are critical for achieving the design parameters of the complex. The electron cooling system [2] for the NICA Collider at an electron energy of 2.5 MeV is intended for accumulation and bunch formation at the ion kinetic energies in the range of 1.0–4.5 GeV/n. Construction of the electron cooling system was started in BINP SB RAS in 2016. The assembling of cooling system in JINR will be started in winter 2022.

Table 2: Electron Cooling Parametetrs

Parameter	Value
Electron energy, MeV	0.2 – 2.5
Energy instability, ΔE/E	$\leq 1{\cdot}10^{-4}$
Electron beam current, A	0.1 – 1.0
Cooling section length, m	6.0
Solenoid magnetic field, T	0.05 – 0.2
Field inhomogeneity, ΔB/B	$\leq 1{\cdot}10^{-5}$

The main goal of using stochastic cooling system (SCS) in colliding ion beam experiments in the Collider NICA is to achieve and maintain design luminosities of $10^{27}cm^{-2}c^{-1}$ in the beam energy range from 3 to 4.5 GeV / u. The stochastic cooling system [2] of the NICA Collider must provide ion cooling of up to $3.1{\cdot}10^9$ ions in a bunch, which corresponds to an effective number $8{\cdot}10^{11}$ of ions. To achieve the design cooling time, an SCS with the frequency bandwidth 0.7–3.2 GHz is necessary. The SCS is a broadband microwave feedback system via the beam and in the main configuration consists of 6 channels for longitudinal, horizontal and vertical cooling, respectively for each Collider ring. In the basic configuration, the SCS consists only

ISBN: 978-3-95450-240-0 ISSN: 2673-5539 doi:10.18429/JACoW-RuPAC2021-MOY02

of longitudinal cooling channels. Each channel has the following main components: pickup, cascade of preamplifiers, signal transmission lines, electronics for control, power amplifiers, kicker. As pickups and kickers, a ring structure with a slot coupling is taken as the basis. The unit cell of this structure is a ring with eight azimuthally distributed sensor loops Several rings are combined by microstrip boards, summing the signal in each of the azimuthal directions.

Table 3: Stochastic Cooling Parametetrs

Longitudinal cooling method	Filter
Passband, GHz	0.7 – 3.2
Beam distance from pickup to kicker, m	183.5-191.5
Phase advance from pickup to kicker, deg	1340-1360
Ion energy $^{197}Au^{79+}$, GeV/u	3.0
Slip-factor from pickup to kicker	0.0294
Revolution slip-factor	0.0362
Pickup/kicker coupling impedance, Ω	200/800
Gain, dB	75 – 79
Peak power at kicker, W	3·200
Pickup/noise temperature, K	300/40

Three RF systems with 26 cavities of the acceleration radio-frequency voltage will be applied for ion accumulation and formation of ion bunches [2,5] with the necessary parameters in the Collider. Accumulation of the beam of the required intensity is planned to be realized in the longitudinal phase space with the use of the 'technique of barrier RF1 voltages' (Fig. 7) and of stochastic or electron cooling of the particles being accumulated. The burrier bucket technique also will be used for ion acceleration in the rings

The RF1 system generates 2 pairs of ±5 kV pulses (accelerating and decelerating in each pair) at the bunch revolution frequency thus forming two separatrices – injection and stack. A bunch from the Nuclotron is captured into the injection separatrix, circulates in the ring until wo pulses separating separatrices are switched off and the injected bunch merges with the stack. The accumulated ions trapped between the two barrier pulses may be accelerated, if necessary, by ±0.3 kV meander voltage generated by the RF1 as well. The RF1 system is actually an induction accelerator composed by 20 inductor sections: 15 are used to form the barriers, 3 generate accelerating meander voltage and 2 passive damping sections correct voltage shape. Each active section is driven by a pair of pulse generators. An inductor section consists of a magnetic core made from the amorphous magnetic alloy and glued between the two water cooled copper plates.

Figure 7: Burrier bucket RF1 cavity.

When the necessary ion intensity is achieved, the beam is bunched the RF2 system (Table 4, Fig. 8) at voltage up to 25 kV of the 22nd harmonics of the rotation frequency with the subsequent takeover by the RF3 system (Table 4) of the 66th harmonics. This permits 22 short bunches to be formed, which is necessary in order to achieve high luminosity. The maximal RF3 voltage corresponds to 125 kV. The RF2 and RF3 systems additionally will be used for an ion acceleration in rings from injection energy up to energy required for Collider experiments. The RF2 and RF3 cavities are of coaxial type which makes the cavity diameter small enough to fit in between the two Collider rings separated by 320 mm only. In order to decrease the length down to an acceptable value the cavity is heavily loaded by a mushroom-like capacitor. Due to the wide operating frequency range (12%) the cavity has four capacitive tuners. The RF solid state amplifiers developed by Russian firm TRIADA are used for RF2 and RF3 systems.

Table 4: Parameters of RF2 and RF3 Cavities

Value	RF2	RF3
Harmonic	22	66
Frequency, MHz	11.484÷ 12.914	34.452÷ 38.742
Rsh,Ohms	$3.12 \cdot 10^5$	$2.68 \cdot 10^6$
Q	3900	6700
Rate of cavity frequency variation, kHz/s	14.7	25.7
RF voltage, kV	25	125
Number of cavities per ring	4	8

ISBN: 978-3-95450-240-0 ISSN: 2673-5539 doi:10.18429/JACoW-RuPAC2021-MOY02

The construction of three RF systems was started in 2016-2017 in BINP SB RAS. Two RF1 and four RF2 cavities will be installed in JINR in beginning of 2022. Additional 4 RF2 and 16 RF3 cavities will be commissioned for extension collider version in end of 2022.

Figure 8: Prototype of RF2 cavity.

The beam injection system is designed for single-turn injection of heavy nuclei into Collider rings with minimal losses. Systems' elements are placed inside the cryostat in straight sections located in the arch of the half-ring E of Collider. The main elements of the beam injection system are septum and kicker magnets, as well as a closed-orbit bump subsystem consisting of Collider lattice dipole magnets with additional current leads. Septum magnets are used to enter the beam into the vacuum chambers of the Collider rings. Kicker magnets are used to land the beam onto a closed orbit. In order to weaken the requirements for kicker magnets, the circulating beam is shifted to the knives of the septum magnets of the injection system, for which local closed orbit bumps are created at the beam entry sites in Collider. The beam injection system now is under design, its fabrication and installation is planned in autumn 2022.

The beam dumping from Collider is carried out by a set of kicker and septum magnets mounted symmetrically to the system of beam injection in the ring with the opposite direction of particle motion. The beams are dumped in the directions opposite to the directions of beam injection into Collider rings. Kicker magnets throw circulating beams into septum magnets, which complete the extraction of the beams from the Collider rings. The beam extraction system is designed now, its fabrication is planed in 2022, commissioning of this system should be done in 2023.

The beam diagnostic system (Table 5) involves pick-up electrodes, strip line monitor, current transformers, Q-meter for tune measurements, ionization profile monitor, Schottky pick-up electrodes, beam loss monitor. The diagnostic equipment is under construction; their installation is planned in 2022.

The feedback system is used for suppression of the coherent transverse beam oscillations: damping of coherent transverse oscillations, arising from injection errors, damping of coherent transverse instabilities, excitation of coherent transverse oscillations at betatron tune measurements. The feedback system is under construction; their installation is planned in autumn 2022.

Table 5: Beam Diagnostic System

Pick-up near F lenses (X)	24
Pick-up near D lenses (Z)	24
Pick-up in straight sections (X/Z)	20
Parametric current transformer (Bergoz	1
Fast current transformer (Bergoz)	2
Betatron tune measurements (Q-meter)	1
Ionization profile monitor	3
Schottky pick-up electrode	1
Strip pick-up monitor	2
Beam loss monitors (for both rings)	68

The beam collimation system in each Collider ring consists of foil section for scattering of ions with the large betatron amplitudes and four catchers for x and y coordinates. This system is fabricated now; their installation is planned in end 2022.

REFERENCES

[1] G. V. Trubnikov *et al.,* "Project of the Nuclotron-based Ion Collider Facility (NICA) at JINR", in *Proc. 11th European Particle Accelerator Conf. (EPAC'08),* Genoa, Italy, Jun. 2008, paper WEPP029, pp. 2581-2583.

[2] Technical Project of NICA Acceleration Complex, Dubna, 2015.

[3] V.D. Kekelidze, R. Lednicky, V.A. Matveev, I.N. Meshkov, A.S. Sorin and G.V. Trubnikov, "Three stages of the NICA accelerator complex", *Eur. Phys. J.* A52: 211, 2016.

[4] N.N. Agapov, *et al.*, "Relativistic nuclear physics in JINR: from Synchrophasotron to Collider NICA", *Phys. Usp.*, v.59, p. 383. 2016.

[5] E. Syresin *et al.*, "Status of Accelerator Complex NICA", in *Proc. 26th Russian Particle Accelerator Conf. (RuPAC'18)*, Protvino, Russia, Oct. 2018, pp. 12-16. doi:10.18429/JACoW-RUPAC2018-MOXMH03

[6] A. V. Butenko *et al.,* "First Experiments with Accelerated Ion Beams in the Booster of NICA Accelerator Complex", presented at the *12th Int. Particle Accelerator Conf. (IPAC'21),* Campinas, Brazil, May 2021, paper MOPAB025.

[7] A V Butenko, *et.al.,* "Vacuum conditions and beam lifetime of single charged He ions in Booster NICA (first run)", *Exper. Theor. Phys. Letters*, v.113, p.752. 2021.

ISBN: 978-3-95450-240-0 ISSN: 2673-5539 doi:10.18429/JACoW-RuPAC2021-MOY05

LINEAR INDUCTION ACCELERATOR LIA-2 UPGRADE

D. Starostenko†, A. Akimov, P. Bak, D. Bolkhovityanov, V. Fedorov, Ya. Kulenko, G. Kuznetsov, P. Logachev, D. Nikiforov, A. Petrenko, O. Pavlov, A. Pavlenko, Budker Institute of Nuclear Physics SB RAS, Novosibirsk, Russia
A. Ahmetov, A. Chernitsa, O. Nikitin, A. Kargin, P. Kolesnikov, S. Khrenkov, D. Petrov, Russian Federal Nuclear Center – Zababakhin All-Russia Research Institute of Technical Physics, Snezhinsk, Russia

Abstract

X-ray facilities based on a linear induction accelerator are designed to study of high density objects. It requires the high-current electron beam to obtain a small spot and bright x-ray source using a conversion target. The electrons source in such facilities is injectors capable generate pulses with a duration from tens of nanoseconds to several microseconds and a current of several kA. The transportation and focusing of high-current beams into diameter about 1 mm is difficult due to the space charge phenomena. In the similar induction accelerators (AIRIX [1], DARHT [2], FXR, etc.), auto-emission cathodes are used to obtain high-current electron beams. The use of a thermionic cathode, in compared to auto-emission cathode, provides stable generation of several pulses with a time interval of several microseconds, but makes high requirements on the injector vacuum system: not less than 10^{-7} Torr [3].

Dispenser Cathode

The cathode assembly is an integral part of any beam source system. Elements of the cathode assembly, such as a heater or internal components, not formally effects on the beam dynamics. However, the uniformity of heating of the cathode surface, is very important for the uniformity of emission. To develop of this issue, the thermal calculations of cathode heating system were performed in order to optimize the cathode assembly. In particular, the homogeneity of the temperature distribution along the surface of cathode core was studied. This is important for high quality beam forming.

3D-modeling was performed using COMSOL Multiphysics software platform. In simulation of heat exchange by radiation between solids in vacuum the module "Surface-to-surface radiation" was used. A 3D-model of the cathode assembly was used as the initial geometry. All calculations were made for a stationary thermal conditions. The appearance of the modified cathode assembly is shown in Fig. 1.

At power 2500 W, the heater temperature reaches 1500 °C, the cathode surface temperature is about 1000 °C. The asymmetrical shape of the heater (Fig. 2) leads to an increase in the local zone by 4 degrees, which is an acceptable value (Fig. 3).

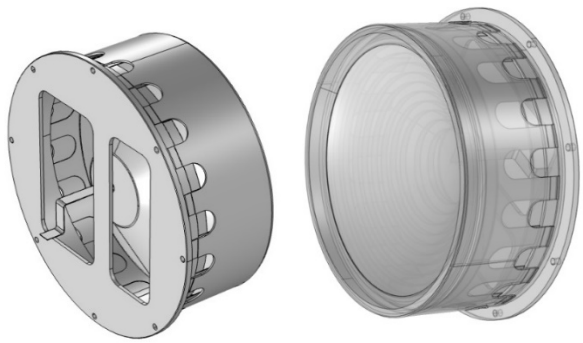

Figure 1: The cathode assembly.

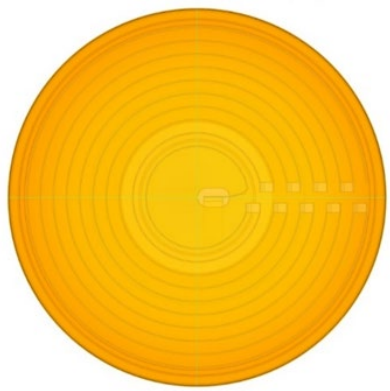

Figure 2: The cathode model for simulate heating process in COMSOL to estimate the temperature distribution along the surface.

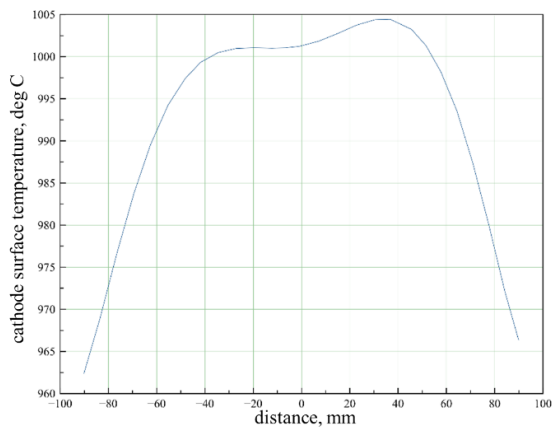

Figure 3: Cathode surface temperature distribution in horizontal section.

† d.a.starostenko@inp.nsk.su

ISBN: 978-3-95450-240-0 ISSN: 2673-5539 doi:10.18429/JACoW-RuPAC2021-MOY05

Dispenser Cathode in Double-Pulse Mode

Generation of two pulses with a short time interval using the dispenser cathode is not difficult, because there is no plasma in the cathode region after the first pulse. As shown in Fig. 4, both current pulses have approximately the same shape and the first pulse does not effect on the second. The time interval between pulses is 4 μs.

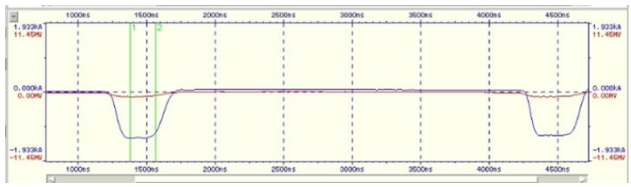

Figure 4: Double-pulse mode at 1.5 MeV, current is 1.25 kA, time delay is 4 μs.

Beam Dynamics Simulation

Currently, few different codes have been developed to simulate high-current electron beams in accelerator. To correctly take into account the space charge, it is necessary to simulate with a large number of macroparticles, while the computation time is long, even when using high-performance computing technologies. A simple alternative for simulation with macroparticles can be a code based on the envelope equation for an axially symmetric beam with the uniform distribution. This "K-V envelope code" was developed at the BINP SB RAS.

For simulation of the beam dynamic in LIA-2 the REDPIC [4] code and the K-V envelope code were used. The equation of motion with space charge is:

$$r'' + k_s r - \frac{P}{r} - \frac{\epsilon^2}{r^3} = 0.$$

Here we consider a round beam with a radius r and the uniform distribution of space charge density, $P = \frac{2I}{I_a \beta^3 \gamma^3}$ is the generalized beam perveance, $I_a = 17$ кА, ϵ is the beam emittance, $k_s = (\frac{eB_z}{2mc\beta\gamma})^2$ is the rigidity of solenoidal lenses, β is the particle velocity and γ is the Lorentz factor.

In Fig. 5 the comparison of simulations using the K-V envelope codes (black dotted line) and REDPIC (blue filling) is shown. Simulation in the REDPIC program was carried out with uniform transverse distribution and pulse duration is about 200 ns. The character time of solving with such parameters is about 4 hours. In the K-V envelope code (dashed line), it takes a few seconds to integrate the envelope equation with longitudinal step about 1mm. The results of simulations by different codes demonstrate a good agreement.

The LIA-2 magnetic system consists of three pulse shielded solenoids, with length 217 mm and maximal field up to 2 kG, and final focusing solenoidal lens with length 60 mm and maximal field 4.5 kG. The main task of magnetic system is beam transportation from the cathode to the target assembly without current losses and high-quality focusing.

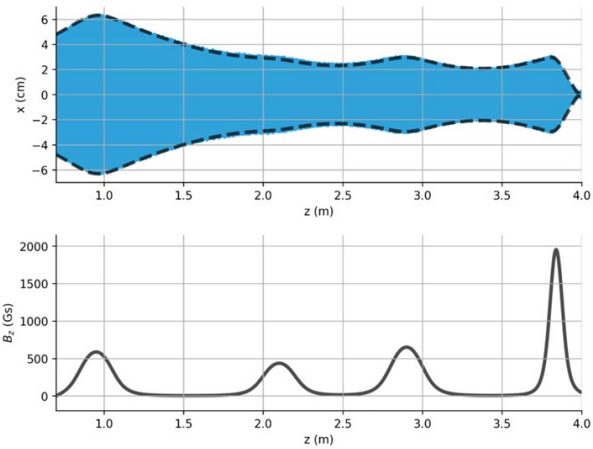

Figure 5: A comparison of simulations using the K-V envelope code (black dotted line) and REDPIC (blue filling). The bottom line shows the longitudinal distribution of magnetic field.

The spherical aberration in final focusing lens doesn't allow to focus large-diameter beam at the entrance of lens to the required size of 1 mm. Spherical aberration leads to the fact that particles with different distance from lens axis have different focusing length (Fig. 6).

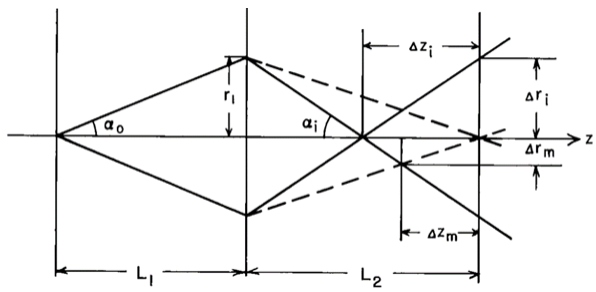

Figure 6: Schematic representation of particle trajectories when passing through a thin lens with spherical aberration.

For achieving of spot size less than 1 mm the beam size at the entrance to the final focusing lens with aberration was estimated. Consider the final focusing lens with following parameters in Table 1.

Table 1: Final Focusing Lens Specifications

Parameters	
Length	60 mm
Aperture radius	60 mm
Magnetic fields	Up to 4 kG

The results of simulation with UltraSAM code for parallel round beam without space charge for different beam radius are presented at Fig. 7. Table 2 shows the values of Δr_{min} depending on the beam size r_a at the lens entrance, obtained analytically and using simulation in the UltraSAM program.

ISBN: 978-3-95450-240-0 ISSN: 2673-5539 doi:10.18429/JACoW-RuPAC2021-MOY05

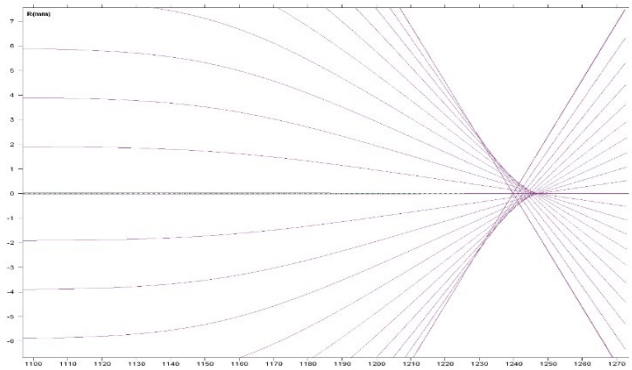

Figure 7: Simulation of the beam trajectories at final focusing lens.

Table 2: Comparison Results

r_a, mm	UltraSAM $\Delta r_{min}, mm$	Analytical calc. $\Delta r_{min}, mm$
25	0.88	0.71
20	0.41	0.35
15	0.19	0.16
10	0.05	0.04

The difference between the simulation results and the analytical estimation is within 20%, which can be explained with errors in numerical simulations of small beam size in the crossover. Nevertheless, it can be concluded that beam radius r_a should be not above 20 mm at the entrance of final focusing lens.

LIA-2 Magnetic System Optimization

For avoiding of the effect of spherical aberration in final focusing lens on the focal spot size the beam size at the lens entrance should be adjusted. The installation of additional solenoidal lens before the final lens is the possible solutions of this problem (Fig. 8).

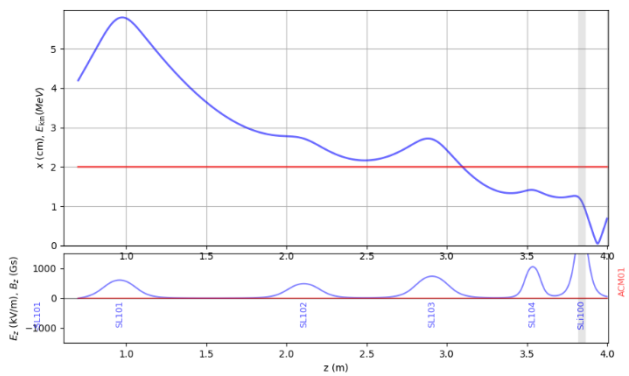

Figure 8: Resulting envelope and magnetic field longitudinal distribution.

Simulation with K-V envelope code shows that additional lens allows varying the beam size at final focusing lens entrance in the wide range and allows satisfying the requirement for beam size described above.

New Design for Diagnostics and Vacuum Chamber before Conversion Target

An upgraded version of the beam transfer channel has been developed, including a new current transformer, a transient radiation sensor for measuring the transverse beam profile, and an additional lens between the third and final lenses (Fig. 9).

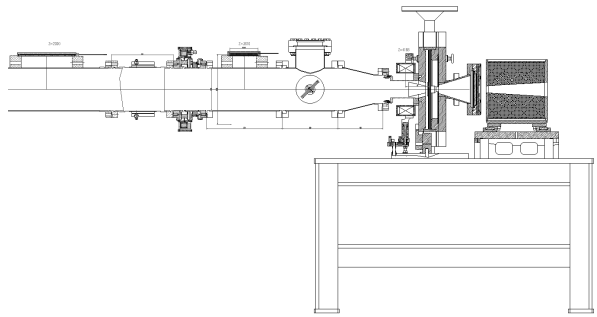

Figure 9: New version of the beam transfer channel.

It allows to visually observe the transverse profile and size of beam, measure the main beam parameters, reduce influence of spherical aberration, and simplify the adjustment of magnetic system for the beam focusing in the conversion target.

CONCLUSION

New version of cathode was manufactured and successfully installed in the LIA-2.

"K-V envelope code" has been developed that allows in a few seconds to simulate the beam envelope with space charge phenomena and spherical aberration of the final lens.

The new transport channel with additional diagnostic elements with aperture 152 mm was proposed for measuring of transverse profile and other beam parameters.

ACKNOWLEDGEMENTS

This work is supported by State Atomic Energy Corporation Rosatom, Russian Federation.

REFERENCES

[1] Ph. Eyharts *et al.,* "Status of the AIRIX Induction Accelerator", in *Proc. 16th Particle Accelerator Conf. (PAC'95),* Dallas, TX, USA, May 1995, paper TAE09. DOI:10.1109/PAC.1995.505176

[2] M.J. Burns, B.E. Carlsten, *et al.* "DARHT accelerators update and plans for initial operation", *in Proc. PAC'99*, Volume 1, Publisher IEEE, DOI:10.1109/PAC.1999.795776

[3] K. Takayama, Richard J. Briggs «Induction Accelerators», year 2010, 119-120 p.

[4] A.V. Novokhatski, "REDPIC", Computer Simulation of Radiation Field Dynamics in Accelerating Structures, 502 Preprint INP 82-157 (1982).

ISBN: 978-3-95450-240-0 ISSN: 2673-5539 doi:10.18429/JACoW-RuPAC2021-MOB01

STATUS OF U70

V. Kalinin†, Yu. Antipov, A. Afonin, N. Ignashin, S. Ivanov, V. Lapygin, O. Lebedev, A. Maksimov, Yu. Milichenko, A Soldatov, S. Strekalovskikh, S. Sytov, N. Tyurin, D. Vasiliev A. Zaitsev
NRC "Kurchatov Institute"– IHEP (Institute for High Energy Physics)
Protvino, Moscow Region, 142281, Russia

Abstract

The report overviews present status of the Accelerator Complex U-70 at IHEP of NRC "Kurchatov Institute" (Protvino). The emphasis is put on the recent activity and upgrades implemented since the previous conference RuPAC-2018, in a run-by-run chronological ordering.

History of the foregoing activity is recorded sequentially in [1].

GENERALITIES

The entire Accelerator Complex U70 comprises four machines — 2 linear (I100, URAL30) and 2 circular (U1.5, U70) accelerators. Proton mode (default) employs a cascade of URAL30–U1.5–U70, while the light-ion (carbon) one — that of I100–U1.5–U70.

Since the previous conference RuPAC-2018, the U70 complex operated for five runs in total. Table 2 lists their calendar data. The second run of 2021 is being planned for October–December of 2021.

Details of the routine operation and upgrades through years 2018–21 are reported in what follows, run by run.

RUN 2018-2

The run lasted from October 01 till December 12 2018 in the two modes and with four beam energies — proton (0.7 and 50 GeV) and carbon (250 and 456 MeV/u).

At the 1st half of proton mode, 50 GeV proton beam was directed to applied research at the radiographic facility.

To this end, the facility was fed with the fast-extracted bunched beam with equal bunches of $3–4\cdot10^{11}$ ppb.(see Fig. 1) To attain electric energy conserving operation, the flattop length was cut short to 0.6 sec.

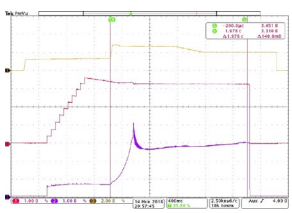

Figure 1: Fast extraction to radiographic facility. Traces from top to bottom: envelope of RF electric field, beam DC current; bunch peak current.

At the 2nd half of the proton mode, research activity was focus to expand the range of the working beam intermediate energy in U-70 (350÷1320 MeV for proton and 250÷455 MeV/u for carbon). The presence of extracted beams of intermediate energies opens up new possibilities for proton radiography, radiobiological studies, etc. To this end, the U70 magnet lattice was toggled to regulated power supply unit [2]. Magnetic cycle for slowing down (from 1320 to 700 MeV) proton beam was created. Proton bunch from U1.5 ($1.8\cdot10^{11}$ ppb) was injected in U-70 on the injection plateau (356 Gs) then, after adjustment RF and magnet field correction systems, was slowed down to 0.7 GeV and circulating at extraction plateau (230 Gs) ($1.2\cdot10^{11}$ ppb). All efforts to decrease extraction plateau field (less than 230 Gs) lead to rapid loss of all beam intensity. Same research was repeated in carbon mode. In this case, carbon beam was slowed down from 456 MeV/u to 250 MeV/u and circulating at extraction plateau (250 Gs).

Closer to end of the run the regulated power supply unit was switched to the DC mode at 455 MeV/u, the main ring being operated as beam storage and stretcher ring at flatbottom DC magnetic field. The beam was extracted slowly with a stochastic extraction scheme [3] capable of yielding 0.6 s long square-wave spills. The in-out transfer ratio amounted 55-57%, close the top expected value of around 68% The beam was used for applied radiobiological and biophysical research (see Fig. 2) by teams from four institutes listed in the 2nd row of Table 1.

Figure 2: Screenshot of the Radio-Biological Workbench work monitor.

RUN 2019-1

It was an intermediate-energy ad hoc one-month long run dedicated to the several sequential tasks:

First, to provide more time for studies and finer tuning of deceleration regime (455÷180 MeV/u).

Second, obtain the regimes of deceleration, of circulation and slow extraction of a beam of carbon nuclei two different energies 300 and 200 MeV/u.

Third, testing new irradiation field-forming system based on electromagnetic wobbler magnets. Testing new

†vakalinin@ihep.ru

ISBN: 978-3-95450-240-0 ISSN: 2673-5539 doi:10.18429/JACoW-RuPAC2021-MOB01

144-channel mosaic ionization chamber for spatial transverse (x, y)-pattern.

All the tasks accomplished successfully (see Fig. 3, Fig. 4).

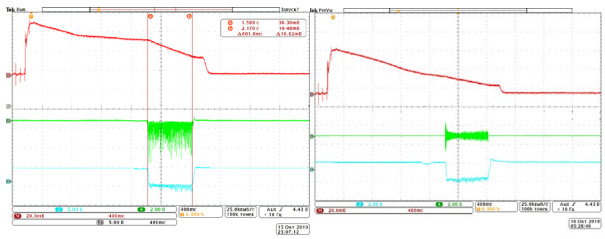

Figure 3: Slow extraction of 300 MeV/u (left) and 200 MeV/u (right) carbon beam. Traces from top to bottom: Beam DC current, ionization chamber in the head of BTL#25 (left) or deflecting noise (right). feedback signal for noise AM.

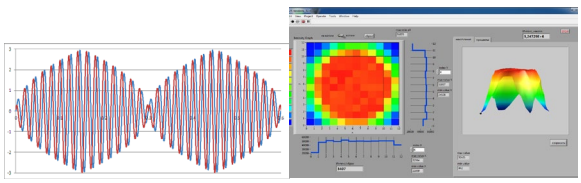

Figure 4: Wobbler electromagnets spiral sweep mode. Currents (left) and Spatial transverse (x, y)-pattern (right).

After accomplished R&D tasks the beam (455 MeV/u, $3.0 \div 4.6 \cdot 10^9$ ipp) was used for applied radiobiological and biophysical research by teams from institutes listed in the 3[d] row of Table 1.

RUN 2019-2

The run went on from October 19 till November 24, 2019. The complex was engaged in two modes — proton (50 GeV) and carbon (200÷455 MeV/u) ones.

At proton mode, the 50 GeV proton beam was used for both, applied and fundamental research.

To this end, the flattop (0.67 sec) accommodated two sequential slots 0.150 sec and 0.52 sec.

The 1[st] slot was serviced by the first fast extraction at radiographic facility (top-priority beam consumer that called for beam intensity of $3.0 \div 4.5 \cdot 10^{11}$ ppb. Beam structure was either single-bunch or multi-bunch with an arbitrary orbit filling with equal bunches, on demand.), while the 2[nd] one — by second fast extraction at NEUTRON facility (Fig. 5). When NEUTRON facility finished on 2[nd] slot beam fed SPASCHARM (BTL #14 via IT#24), VES (BTL #4 via IT#27), (FODS (BTL #22 via CD#19) or SVD (BTL #22 via CD#19) in parallel (Fig. 6). In their captions and in what follows, BTL is a Beam Transfer Line, IT is an Internal Target, CD is a bent-Crystal Deflector, all numbered by the # of the relevant (host) straight section (SS) in the U70 lattice. Traditionally now, the run had ended with the 455 MeV/u carbon beam mode for radio-biological studies. The beam (455 MeV/u and 300 MeV/u) was used for applied radiobiological and biophysical research by teams from institutes listed in the four row of Table 1.

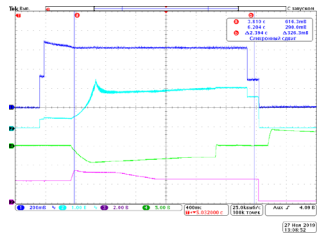

Figure 5: Sequential beam sharing at flattop with two fast extractions. Traces from top to bottom: beam DC current; bunch peak current, B-field ramp rate, envelope of RF electric field.

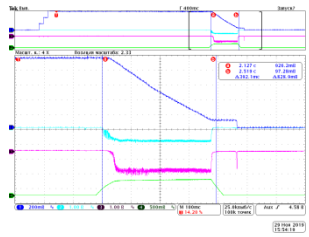

Figure 6: Parallel beam sharing (50 GeV, $8 \cdot 10^{11}$ ppp net). Traces from top to bottom: beam DC current, spill of secondary particles beam from IT ## 24 and 27, driving current of the enclosing orbit bump between ## 24 and 30.

RUN 2020-1

In course of this run, U70 was again employed in two modes — proton (50 GeV) and carbon (456 MeV/u) ones. To meet beam user demand, proton mode of the run was broken into 3 segments with different priorities assigned either to fundamental or to applied fixed-target research. These used to call for a non-compliant set of beam structure, extractions and the BTLs involved.

During first segment of proton part the azimuthally uniform (de-bunched) 50 GeV proton beam was used for fundamental physics at three experimental facilities. The top-energy slow stochastic extraction has fed the OKA (BTL#8), SPIN (BTL#8(21)) and FODS (BTL#22 via CD#30) facility with $3 \div 3.5 \cdot 10^{11}$ protons per a low-ripple spill (0.45 s long) at the flattop (Fig. 7).

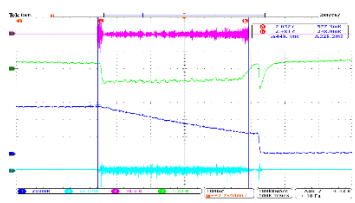

Figure 7: Slow stochastic extraction at the flattop. Traces from top to bottom: phase noise, beam feedback signal for AM-modulation of the noise, beam DC current, spill of secondary particles beam from CD # 30.

During second segment beam used for an applied research with the proton radiographic (top priority) and NEUTRON facility, the U70 was operated in single- and multi-bunch modes with (3–4.5) 10^{11} ppb.

ISBN: 978-3-95450-240-0 ISSN: 2673-5539 doi:10.18429/JACoW-RuPAC2021-MOB01

During third segment beam used for an applied research with the proton radiographic (top priority) facility and SPASCHARM (BTL #14 via IT#24), VES (BTL #4 via IT#27) and HYPERON (BTL #18 via IT#35) in parallel.

At carbon mode, the regime of deceleration and slow extraction of a beam of carbon nuclei with an energy of 350 MeV was prepared. 256-channel mosaic ionization chamber for spatial transverse (x, y)-pattern was tested. After R&D session, the beam (455 MeV/u) was used for applied radiobiological and biophysical research by teams from institutes listed in the five row of Table 1.

RUN 2021-1

It was the first spring run since 2018. The run went on from February 24 till April 30, 2021. The complex was engaged in two modes — proton (50 GeV) and carbon (200÷455 MeV/u) ones.

The proton mode was similar to the RUN 2019-2. As at RUN 2019-2, the flattop (0.67 sec) accommodated two sequential slots 0.150 sec and 0.52 sec.

The 1st slot was serviced by the first fast extraction at radiographic facility (top-priority), while the 2nd one — by second fast extraction at NEUTRON and SPIN (via CD#30) facility. When NEUTRON and SPIN facility finished on 2nd slot beam fed SPASCHARM (BTL #14 via IT#24), HYPERON (BTL #18 via IT#35), VES (BTL #4 via IT#27) or ISTRA (BTL #4 via CD#27) in parallel.

At R&D session of carbon mode, all 6 regimes 455, 400 (new regime), 350, 300, 250 (new regime) and 200 MeV/u was prepared for applied radiobiological and biophysical research by teams from institutes listed in the five row of Table 1.

UPGRADING THE POWER SUPPLY PLANT OF THE U1.5 RING MAGNET

Upgraded power supply plant of the U1.5 ring magnet now includes new modular electrical substation (10 kV, 30 Mw), new capacitor bank (15 kV, 28 mF), a set of non-standard electrical equipment with Automated Process Control System (APSC). Upgraded power supply plant of the U1.5 ring magnet has been working since RUN-2020-1.

CONCLUSION

Accelerator Complex U70 at IHEP of NRC "Kurchatov Institute" continues its routine operation for fixed-target physics and applications and has accomplished five regular machine runs since the previous conference RuPAC-2018, refer to Table 2.

Table 1: Engagement of the Off-Site Institutions in Carbon-Beam Sub-Runs

Institution	2018-2	2019-1	2019-2	2020-1	2021-1
MRRC of NMRCR, http://mrrc.nmicr.ru	+	+	+	+	+
ITEB of RAS, web.iteb.psn.ru	+	+	+	+	+
IBMP of RAS, www.imbp.ru	+	+	+	+	
FMBC of FMBA, fmbafmbc.ru		+	+		
JINR, www.jinr.ru		+			
VNIIFTRI, www.vniiftri.ru		+	+		
MEPHI, https://mephi.ru/				+	
IMB of BAS, www.bio21.bas.bg	+				

REFERENCES

[1] S. Ivanov, *et al.*, "Status of U70" in *Proc. 26th Russian Particle Accelerator Conf. (RuPAC'18)*, Protvino, Russia, Oct. 2018, pp. 55-59.

[2] An. Markin, V. Kalinin, O. Lebedev, D. Hmaruk, "Upgrading of the power supply for magnet U70 synchrotron", in *Proc. 26th Russian Particle Accelerator Conf. (RuPAC'18)*, Protvino, Russia, Oct. 2018, pp. 335-336.

[3] S. Ivanov, *et al.*, "Slow Extraction of a Carbon-Nuclei Beam from the U-70 Synchrotron", *Instruments and Experimental Techniques* vol. 64, May 26, 2021, pp. 343-351.

Table 2: Five Runs of the U70 in Between RuPAC-2018 and -2021

Run	2018-2	2019-1	2019-2	2020-1	2021-1
Launching linac URAL30, booster U1.5 and U70 sequentially (I100 in parallel with a delay)	October, 01	September, 16	October, 19	October, 19	February, 24
Beam in the U70 ring since	November, 06	October, 07	November, 24	November, 21	March, 24
Fixed-target physics program with extracted top-energy beams (either of protons or of carbon nuclei)	November,12 – 20, 9 days	-	November,25-December, 2, 8 days	November,26-December, 15, 20 days	March, 29 – April, 12, 45 day
No. of multiple beam users (of which the 1st priority ones)	4 (4)	4 (4)	11 (6)	12(8)	10(9)
MD sessions and R&D on beam and accelerator physics, days	19	13	6	18	12
Light-ion acceleration program, intermediate energy only	November,21–December,12,17½ days	October,07–27, 20½ days	December, 03–12, 9½ days	December, 16–30, 14½ days	April, 13–30, 17½ day

ISBN: 978-3-95450-240-0 ISSN: 2673-5539 doi:10.18429/JACoW-RuPAC2021-TUX01

STATUS OF THE HIAF ACCELERATOR FACILITY IN CHINA*

L. J. Mao, J. C. Yang†, D. Q. Gao, Y. He, G. D. Shen, L. N. Sheng, L. T. Sun, Z. Xu, Y. Q. Yang, Y. J. Yuan and HIAF project team, IMP CAS, Lanzhou, China

Abstract

The High Intensity heavy-ion Accelerator Facility (HIAF) is under constructed at IMP in China. The HIAF main feature is to provide high intensity heavy ion beam pulse. A rapid acceleration in the booster synchrotron ring (BRing) with the ramping rate of 12 T/s is used. The challenges are related to the systems injector, RF cavities, power supplies, vacuum, magnets, etc. Works on key prototypes of the HIAF accelerator are ongoing at IMP. In this paper, an overview of the status and perspective of the HIAF project is reported.

INTRODUCTION

The High Intensity heavy-ion Accelerator Facility (HIAF) is a new accelerator under construction at the Institute of Modern Physics (IMP) in China [1]. It is designed to provide intense primary heavy ion beams for nuclear and atomic physics. The facility consists mainly of a superconducting electron-cyclotron-resonance (SECR) ion source, a continuous wave (CW) superconducting ion linac (iLinac), a booster synchrotron (BRing) and a high precision spectrometer ring (SRing). A fragment separator (HFRS) is also used as a beam line to connect BRing and SRing. Six experimental terminals will be built in phase-I at HIAF. The layout of the HIAF accelerator was shown in Fig. 1. The main parameters are listed in Table 1.

The construction of the HIAF project was started officially in December 23rd, 2018. Up to now, roughly 50% of civil construction is finished. The first component of SECR is planned to equip in the tunnel in the middle of 2022. The first beam will be accelerated at BRing in the middle of 2025. A Day-one experiment is proposed before the end of 2025. A brief time schedule of HIAF construction is shown in Fig. 2.

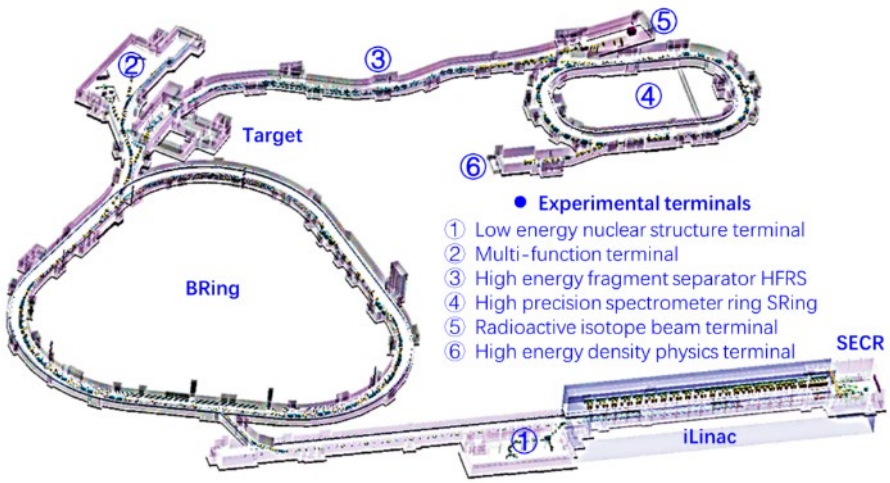

Figure 1: Layout of the HIAF project.

Table 1: Main Parameters of the HIAF Accelerators

	SECR	iLinac	BRing	HFRS	SRing
Length / circumference (m)	---	114	569	192	277
Final energy of U (MeV/u)	0.014 (U^{35+})	17 (U^{35+})	835 (U^{35+})	800 (U^{92+})	800 (U^{92+})
Max. magnetic rigidity (Tm)	---	---	34	25	15
Max. beam intensity of U	50 pμA (U^{35+})	28 pμA (U^{35+})	10^{11}ppp (U^{35+})		10^{10}ppp (U^{92+})
Operation mode	DC	CW or pulse	fast ramping (12T/s, 3Hz)	Momentum-resolution 1100	DC or deceleration
Emittance or Acceptance (H/V, π·mm·mrad, dp/p)		5 / 5	200/100, 0.5%	±30mrad(H)/±15 mrad(V), ±2%	40/40, 1.5%, normal mode

Currently, most of the prototypes related to the HIAF technical challenges have being manufactured or tested. In this paper, the status and perspectives of the HIAF project are presented. The developments and test results of hardware are reported.

* Work supported by the National Development and Reform Commission, China
† yangjch@impcas.ac.cn.

ISBN: 978-3-95450-240-0 ISSN: 2673-5539 doi:10.18429/JACoW-RuPAC2021-TUX01

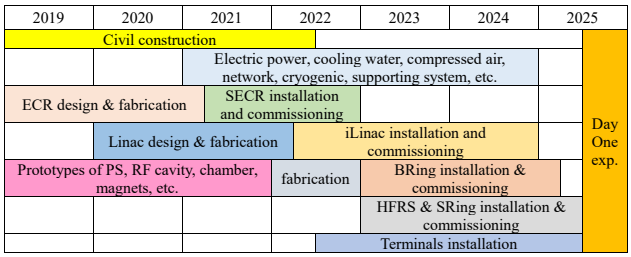

Figure 2: Time schedule of the HIAF construction.

ION SOURCE

Pulsed 50 pμA (~1 ms) U^{35+} ion beam from SECR is required in the HIAF project, which is 5 times higher than the present records of the 3rd generation ECR ion source. It can only be met by sources operating at higher magnetic field and microwave frequency. SECR incorporates with a Nb_3Sn high field superconducting magnet and a quasi-optical 45 GHz gyrotron microwave system, as shown in Fig. 3. The main parameters are listed in Table 2. The biggest challenge lies in the design and fabrication of the Nb_3Sn magnet. A promising cold mass design has been completed by a collaboration with LBNL, as shown in Fig. 3. Up to now, a 1/2 cold-mass prototypes related to critical technologies have be fabricated and tested. The full-sized cold-mass completion is scheduled in 2020 [2].

Table2: Typical Parameters of SECR

Specs.	Unit	SECR
Frequency	GHz	45
RF power	kW	20
Chamber ID	Mm	>Φ140
Mirror fields	T	≥6.4/3.2
B_{rad}	T	≥3.2
B_{max} in conductor	T	11.8
Magnet coils	---	Nb_3Sn
Cooling capacity at 4.2 K	W	>10

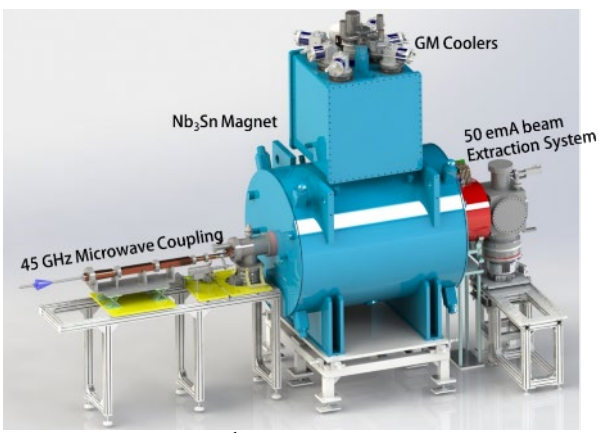

Figure 3: the 4th generation ion source SECR.

The microwave power transmission coupling and ECR heating are critical issues. Based on the present ion source SECRAL-2 at IMP, a study with a 45 GHz gyrotron microwave system by GYCOM Ltd was reported [3]. The transmission lines combined quasi-optical mirror and wave guide mode converter are manufactured. The 45 GHz microwave power at TE_{01} mode has been fed into SECRAL-2 and got the first stable 45 GHz ECR plasma and Xenon beam.

LINAC INJECTOR

The iLinac is used as the injector of BRing and the main accelerator for the low energy nuclear structure terminal. That's why a CW superconducting linac is proposed in HIAF. Two types of accelerating structures in 17 cryomodules are used to achieve the energy of 17 MeV/u for U^{35+} ion beam. The first 6 cryomodules with QWR007 cavities is used to accelerate U^{35+} ions to 5.4 MeV/u. The rest cryomodules are installed with HWR015 cavities. These cavities will be made based on the experience of the CiADS project. A layout of iLinac is shown in Fig. 4. LEBT, RFQ and MEBT locate between SECR and iLinac.

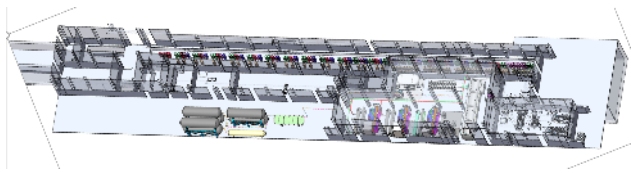

Figure 4: 3-D view of iLinac. SECR locates on left side. The physical design has been finished.

BOOSTER SYNCHROTRON

BRing is the key component of the HIAF project. It is designed with a maximum magnetic rigidity of 34 Tm, which is intended for the storage of U^{35+} ions to an intensity of 2×10^{11} particles with the energy of 835 MeV/u. The BRing lattice and its beta function and dispersion function is shown in Fig. 5. The ionization processes with residual gas particles is the main issue with respect to potential beam loss. Therefore, the lattice design is to localize the beam loss at certain positions to install collimators. It has a three-folding symmetry lattice with DBA (double bend achromat) structure. BRing offers a transverse acceptance of 200 / 100 π·mm·mrad to overcome space charge limits of high intensity beams. It is operated below the transition energy to avoid beam loss by transition-energy crossing [4].

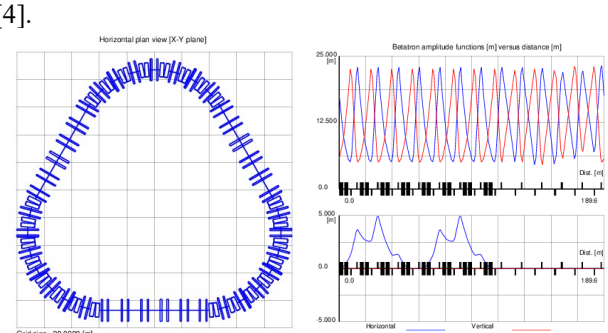

Figure 5: Bring lattice structure and its beta function and dispersion function (one cell).

The present currents reached from the high current source and linac need no stacking by the electron cooling. To obtain a high average beam intensity and avoid space charge limits, transverse phase space painting (4-D) is im-

ISBN: 978-3-95450-240-0 ISSN: 2673-5539 doi:10.18429/JACoW-RuPAC2021-TUX01

plemented for beam accumulation and a rapid ramping cycle is used to reduce the integral ionization cross section. Related prototypes as tilted electrostatic septum, ceramic-lined thin-wall vacuum chamber, fast-cycling power supply and magnetic alloy (MA) acceleration cavities are developed for BRing.

Transverse Phase Space Painting Injection

In the 4-D painting injection scheme, the closed orbit is moved with the horizontal and vertical injection bumps as functions of time. Unlike the injection using charge exchange implemented in proton machine (SNS, J-PARC), a tilted corner septum is used for both transverse phase places simultaneously injection in BRing. Low-loss and low phase space dilution are basic requirements. Injection begins with both horizontal and vertical bump close to the centroid of injection beam, and then gradually move away from it. Both the horizontal and vertical emittance are painted from small to large [5]. Figure 6 shows the particle invariant distribution at the end of injection and its evolution up to 1000 turns. The simulation is performed with U^{35+} ions at the injection energy of 17 MeV/u. The total emittance and momentum spread of iLinac beam are 5 π·mm·mrad and ±0.2%, respectively. The space charge effect is included in the simulation. Due to a small gap between the closed orbit and the injection point, the injection efficiency is small at the beginning. A "hollow" beam in horizontal and vertical phase space is obtained after the injection. However, such a beam profile is susceptible to transverse coupling due to space charge forces in simulation. Finally, the particle emittance reaches a Gaussian-like distribution in both phase spaces.

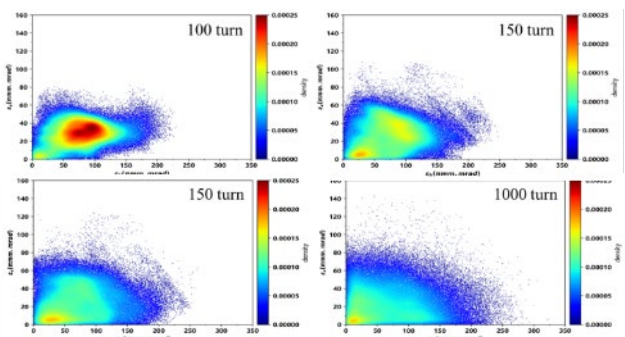

Figure 6: particle invariant distribution after 4-D painting injection.

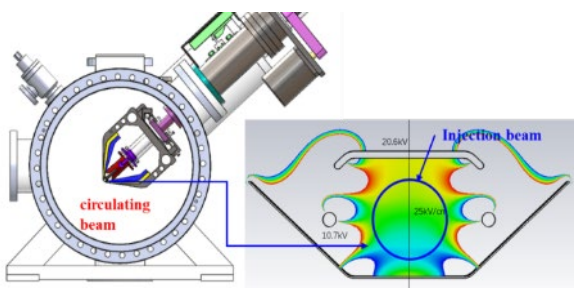

Figure 7: Corner septum cross section and its field map.

A corner electrostatic septum is used to deflect the injection beam to the closed orbit, as shown in Fig. 7. The septum wire with the thickness of 0.1 mm is tilted by 40° to combine the horizontal and vertical injection. To reduce beam loss on the wire, a U-like shape anode is designed. The anode together with two auxiliary electrodes are used to optimize the electric field for injection beam. The field homogeneity better than 5% is achieved in the injection region.

Fast Ramping

Since the cross sections of ionization are decreasing significantly with ion energies, the integral cross section can be kept very small with a fast ramping rate. Rapid accelerating was proposed and tested at SIS18 in 2005, shown an optimistic result for minimum beam loss and dynamic vacuum effect. In BRing, a ramping rate of 12T/s is needed for optimising the space charge limits and collimators. Therefore, a dipole power supply with a rate of 38 kA/s and maximum current of 4 kA is desired. One power supply can be used for 4 dipoles connected in series and 12 groups are needed in BRing. A full-energy storage technology is developed to reduce its power consumption. The analytic modelling optimal control with kinetic inductance fine turning method is used in the control system, to improve the precision of current ramping. A prototype was already tested at IMP. The maximum current of 5.1 kA was obtained in a solenoid load with the ramping rate of 40 kA/s, as shown in Fig. 8. The output current average tracking error is around 5×10^{-4}, which meets the requirements of BRing. Next, the prototype will be tested with BRing dipoles, to study its properties in operation.

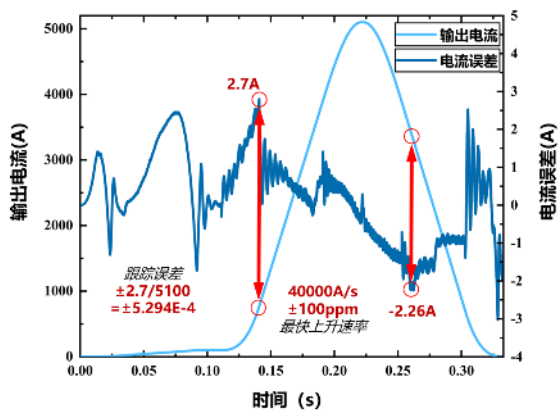

Figure 8: current curve of fast ramping power supply.

High accelerating voltage up to 240 kV is used in the fast ramping of BRing, which will be provided by new MA acceleration cavities. The quality factor (*Q value*) is set at 0.45 to cover a wide frequency range of 0.3 to 2 MHz. A typical acceleration process of $^{78}Kr^{19+}$ is shown in Fig. 9. There are four stages. The first capture stage is used to capture the coasting beam after 4-D multi-turn painting injection. Usually two or even more bunches are obtained in the first capture stage, since a high harmonic should be used at such low injection energies. At the acceleration stage, the maximum ramping rate is 12 T/s, corresponding to the maximum RF voltage of 240 kV. At the de-bunching stage, the RF voltage decreases to zero rapidly, a coasting beam is obtained again in BRing. Two extraction schemes are designed in BRing. The slow extraction mode starts at the end

ISBN: 978-3-95450-240-0 ISSN: 2673-5539 doi:10.18429/JACoW-RuPAC2021-TUX01

of de-bunching. In the fast extraction mode, additional second capture stage is needed, to make only one bunch in BRing. the extraction starts at the end of the second capture stage.

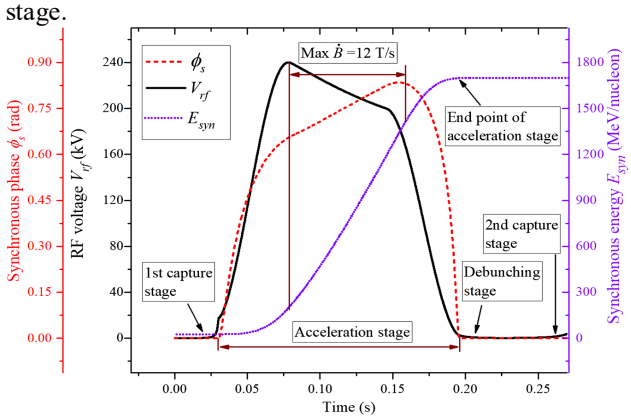

Figure 9: Corner septum cross section and its field map.

The fast ramping of the magnets induces eddy currents in the vacuum chamber wall, which could make a distortion of magnetic field. Ceramic-lined thin-wall vacuum chamber is a good solution to reduce the eddy current effect. A stainless steel with the thickness of 0.3 mm is used for the BRing vacuum chamber. To withstand the atmospheric pressure, the thin wall vacuum chamber is supported by ceramic rings inside. The ceramic rings are made by yttrium stabilized zirconia, which has very good mechanical strength and toughness. the ceramic rings are coated with a 1 μm Au film to reduce the beam impedance and the desorption rate of the ceramic surface. Compared to the similar chamber with reinforced ribs, the gap size of the dipole decreases significantly. A prototype of 3 m length dipole chamber has been tested, as shown in Fig. 10. The pressure is about 1.07×10^{-9} Pa, which basically meets the BRing requirement.

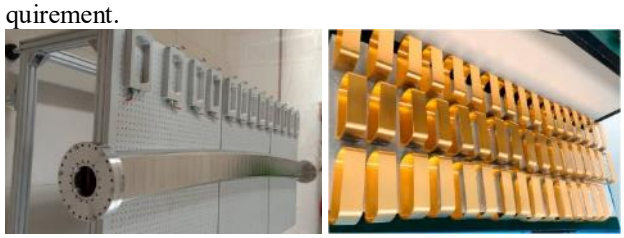

Figure 10: ceramic-lined thin-wall vacuum chamber for BRing dipole (left) and the ceramic rings inside.

SPECTROMETER RING

SRing is designed as a multi-function experimental storage ring, which can be operated in three modes. Firstly, it will be used as an isochronous mass spectrometer (IMS mode) with two TOF detectors for short-lived neutron-rich nuclei. Secondly, it is used to collect and cool long-lived rare isotopes for nuclear experiments, or accumulate and extract highly-charged stable ions for high energy density physics (normal mode). Thirdly, it can be used to store H-like, He-like or other special charge state ions for internal target experiments (target mode). Ions can be decelerated to tens MeV in this mode. Details are available in [6].

A 450 keV magnetized DC electron cooler is used to boost the luminosity of internal target experiments, and proposed to accumulate isotopes with stochastic cooling and barrier bucket system [7]. The cooler is designed based on changes of the 300 keV cooler at IMP, which was made by BINP in 2004 [8]. An 8.0 m cooling section is used with the longitudinal magnetic field of 0.15 T. A pan-cake solenoid is easy to have high precise magnetic field with the homogeneity better than 10^{-4}, but the correct coils will produce transverse components at edges. Figure 11 shows that the coils of the cooling section, the gun and the collector have been tested at IMP.

(a)

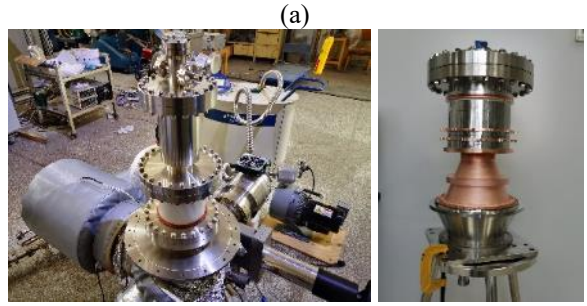

(b) (c)

Figure 11: the coils, the gun and the collector for 450 keV cooler.

FRAGMENT SEPARATOR

The High energy Fragment Separator (HFRS) is an in-flight separator at relativistic energy. The schematic layout is shown in Fig. 12. A primary beam from BRing hits the target at PF0. The rare isotopes produced by projectile fragmentation or fission will be collected and purified by the HFRS with the Bρ-ΔE-Bρ method. The magnetic rigidity up to 25 Tm can be operated in HFRS. The large acceptance including the angular acceptances ±30 mrad (H) / ±15 mrad (V) and the momentum acceptance ±2% provides a high collecting efficiency. A two-stage structure is used in HFRS design. The pre-separator is used to dump the primary beams and undesired fragments. The main separator is used to identify the rare isotopes. Details of the HFRS design can be found in [9]. Currently, the target is under-construction at workshop. A prototype of CCT coils is tested at IMP. Figure 13 shows the photos of CCT coils.

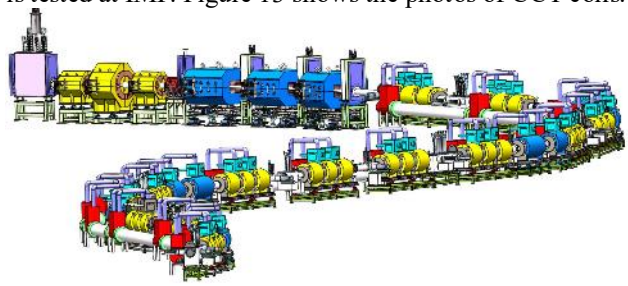

Figure 12: 3-D view of HFRS (a part).

ISBN: 978-3-95450-240-0 ISSN: 2673-5539 doi:10.18429/JACoW-RuPAC2021-TUX01

Figure 13: a prototype of CCT coil.

CONCLUSION

The HIAF project is the biggest heavy ion accelerator project under-construction in China. There are several challenges related to the ion source, the linac, the RF cavities, the power supplies and so on. In past few years, the HIAF project team have developed several prototypes and obtained test results. The HIAF construction will be benefit on these works. The commissioning of the accelerator complex is planned in 2025.

ACKNOWLEDGEMENTS

We thank all the colleagues working on the HIAF project for their valuable contributions on this article.

REFERENCES

[1] J.C.Yang *et.al., Nucl. Instr. Meth.* B 317, 263, 2013.

[2] L. Sun *et.al., IEEE Transactions on Applied Superconductivity*, 28 (3), 4101606, 2018.

[3] J.W. Guo *et.al., AIP Conference Proceedings*, 090001, 2018.

[4] L. Peng *et.al., Nucl. Instr. Meth.* A 920, pp. 14-21, 2019.

[5] C.R. Prior, G.H. Rees, *Nucl. Instr. Meth.* A415 357-362, 1998.

[6] B.Wu, *et.al., Nucl. Instr. Meth.* A 881, pp. 27-35, 2018.

[7] L. J. Mao *et al.,* "The Electron Cooling System for the HIAF Project in China", in *Proc. 12th Workshop on Beam Cooling and Related Topics (COOL'19),* Novosibirsk, Russia, Sep. 2019, pp. 14-17. doi:10.18429/JACoW-COOL2019-MOZ01

[8] V. B. Reva *et al.,* "Commissioning of Electron Cooler EC-300", in *Proc. 9th European Particle Accelerator Conf. (EPAC'04)*, Lucerne, Switzerland, Jul. 2004, paper TUPLT120, pp. 1419-1421.

[9] L.N.Sheng, *et.al., Nucl. Instr. Meth.* B 469, pp. 1-9, 2021.

ISBN: 978-3-95450-240-0 ISSN: 2673-5539 doi:10.18429/JACoW-RuPAC2021-TUY01

VEPP-2000 COLLIDER OPERATION IN 2019–2021 RUNS: CHALLENGES AND RESULTS*

M. Timoshenko†, Yu. Aktershev, O. Belikov, D. Berkaev, D. Burenkov, V. Denisov, V. Druzhinin, K. Gorchakov, G. Karpov, A. Kasaev, A. Kirpotin, S. Kladov[1], I. Koop[1], A. Kupurzhanov, G. Kurkin, M. Lyalin[1], A. Lysenko, S. Motygin, A. Otboev, A. Pavlenko[1], E. Perevedentsev[1], V. Prosvetov, S. Rastigeev, Yu. Rogovsky, A. Semenov[1], A. Senchenko[1], L. Serdakov, D. Shatilov, P. Shatunov, Yu. Shatunov[1], D. Shwartz[1], V. Yudin, I. Zemlyansky, Yu. Zharinov
Budker Institute of Nuclear Physics, Novosibirsk, Russia
[1]also at Novosibirsk State University (NSU), Novosibirsk, Russia

Abstract

VEPP-2000 is the only electron-positron collider operating with a round beam that permits to increase the limit of beam-beam effects. VEPP-2000 is the compact collider with circumference of 24.39 m which has record design luminosity of 1×10^{32} cm^{-2} s^{-1} per bunch at energy up to 1 GeV and record achieved luminosity of 5×10^{31} cm^{-2} s^{-1} at energy of 500 MeV, magnetic fields in superconducting solenoids is 13 T and 2.4 T in the bending magnets. Collider complex experimental program of 2019–2021 was focused on several energy ranges. Energy range was (180–300) MeV in the second half of 2019, in the first half of 2020 we worked in (935–970) MeV, in the first half of 2021 that was (970–1003.5) MeV. Data taking was carried out by CMD-3 and SND detectors, the operation efficiency is compared with previous runs. Luminosity was limited by beam-beam effects. 2021 year was clouded by vacuum accident and subsequent intensive degassing using beam synchrotron radiation.

INTRODUCTION

We present in this paper an overview of VEPP-2000 electron-positron collider, operation chronology and statistics. In spite of problems connected with some vacuum accident and also with Anti COVID measures, luminosity records at operation energy ranges have been achieved. Data taking was also successful comparable to previous years level. This factor was provided by using several instruments for increasing peak luminosity such as Beam-shaker and lattice optimization. The analysis of operation time for data taking by collider detectors have been done and some solution for increasing the rate of collecting integral luminosity are in plans and have already been implementing.

VEPP-2000 OVERVIEW

VEPP-2000 is a compact electron-positron single rind collider [1] equipped with electron-positron booster ring [2] (Fig. 1) operating at bunch energy range (160–1000 MeV). Booster is feeded with particles by BINP Injection complex [3] at 430 MeV energy (until recently it was 390 MeV). Table 1 shows main parameters of the collider.

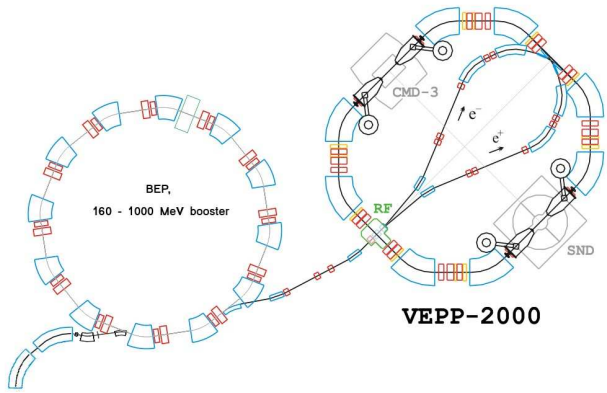

Figure 1: VEPP-2000 complex layout.

Table 1: VEPP-2000 Design Main Parameters at E= 1 GeV

Parameter	Value
Circumference, C	24.39 m
Energy range, E	160–1000 MeV
Number of bunches	1×1
Number of particles per bunch, N	1×10^{11}
Betatron functions at IP, $\beta^*_{x,y}$	8.5 cm
Betatron tunes, $\nu_{x,y}$	4.1; 2.1
Beam emittance, $\varepsilon_{x,y}$	1.4×10^{-7} m rad
Beam–beam parameters, $\xi_{x,z}$	0.1
Luminosity, L	1×10^{32} cm^{-2} s^{-1}

Round Beam Concept

Uniqueness and feature of VEPP-2000 collider is realization of Round Beam Concept [4, 5]. This factor allowed VEPP-2000 to have high luminosity and to make particles' dynamic one-dimensional although still non-linear. The concept applies several requirements to collider lattice:

- Head-on collisions (zero crossing angle)
- Small and equal β functions at IP ($\beta^*_x = \beta^*_y$).
- Equal beam emittances ($\varepsilon_x = \varepsilon_y$).
- Equal fractional parts of betatron tunes ($\nu_x = \nu_y$).

* The reported study was partly funded by RFBR, project number 20-32-90217
† tim94max@gmail.com

ISBN: 978-3-95450-240-0 ISSN: 2673-5539 doi:10.18429/JACoW-RuPAC2021-TUY01

Experimental Program

Collider hosts two particle detectors, Spherical Neutral Detector (SND) and Cryogenic Magnetic Detector (CMD-3), placed into dispersion-free low-beta straights. Both detectors deals with measurement of cross section of annihilation of electron-positron pairs into hadrons, each detector has special experimental program [6, 7].

SND:

- Measurements of ω, ρ and ϕ (782, 770 and 1020 MeV)
- Looking for $e^+e^- \to \eta$ (547.853 ± 0.024 MeV)

CMD-3:

- Birth nucleon-antinucleon pairs $e^+e^- \to N\bar{N}$
- Processes: $e^+e^- \to \eta'$, $e^+e^- \to \pi^0$, $e^+e^- \to D^{*0}$

Luminosity integral depending on bunch energy is depicted on Fig. 2.

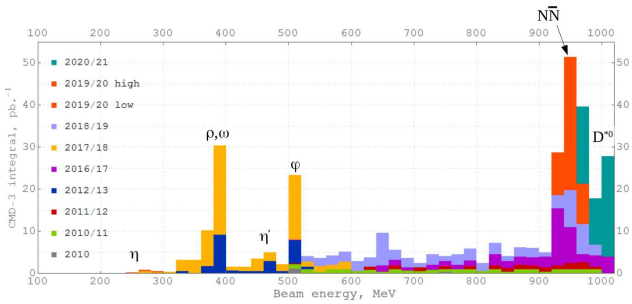

Figure 2: Luminosity integral for all the time.

OPERATION CHRONOLOGY

Run usually continues from 1st of September to 1st of July of the next year. In the "turning on" period of VEPP-2000 collider complex the power, control and beam diagnostic systems are tuned, soft is upgraded and operating mode of BINP Injection Complex is set up for work with two colliders (VEPP-2000 and VEPP-4 [8]). In the "luminosity" period bunches permanently (in perfect case) circulate in collider and data taking by detectors is carried out. Lets look at two operating run chronology separately. Hereinafter analysis is carried out using CMD-3 data.

2019–2020 Run

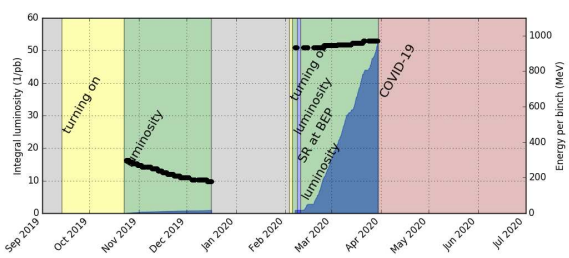

Figure 3: Chronology 2019–2020.

This operation run started at September 2019 and, after a month of tuning, collider has been operating for data taking by detectors ("luminosity") at low bunch energy range (180–300 MeV per bunch) from mid October to mid December. After that and further technical shut down in beginning of March the collider continued operation at high energy range (935–970 MeV per bunch) before shut down in connection with Anti COVID measure (see Fig. 3).

In addition to routine data taking, during this run several days were spent on serving the synchrotron radiation (SR) material science experiments at the BEP storage ring. The experiments are dedicated the sudy of in-vacuum properties (desorption, secondary electron emission) of the vacuum chamber wall covering under the SR treatment for HL-LHC research and development program [9]. In this regime BEP operates exclusively as SR source being unable to supply beams to VEPP-2000 collider.

2020–2021 Run

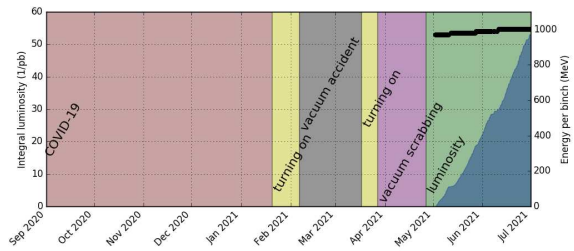

Figure 4: Chronology 2020–2021.

This run started in mid February 2020. In turning on process vacuum accident took place: hole in the vacuum chamber of BEP–VEPP positron transfer line has been burnt by arc discharge inside pre-injection pulse magnet. It resulted in collider vacuum volume depressurization. After pumping out beam lifetime was dramatically limited by gas photo stimulated desorption from vacuum volume surface [10]. Degassing (vacuum scrabbing by intensive beam synchrotron radiation) was required for decreasing coefficient of the desorption (see Fig. 4).

This process took almost month (beam energy was 700 MeV and dose achieved was 87 A h) and after that data taking was continued at previous run final energy point 970 MeV.

LUMINOSITY TIME STATISTICS

If we look at the statistics of operating in the "luminosity" mode we met similar pictures. In 2019–2020 and 2020–2021 runs VEPP-2000 operated 2530 and 1440 hours for luminosity respectively, and the distribution of operating and dead time is depicted on Figs. 5 and 6.

"Smooth operation" work looks like the Fig. 7: BEP stores beams without interruption and almost constant intensity bunches circulate in VEPP-2000.

"Liquid He refill" corresponds to the replenishment of liquid helium (LHe) in four superconducting solenoids' cryostats. This process now is impossible without an access

ISBN: 978-3-95450-240-0 ISSN: 2673-5539 doi:10.18429/JACoW-RuPAC2021-TUY01

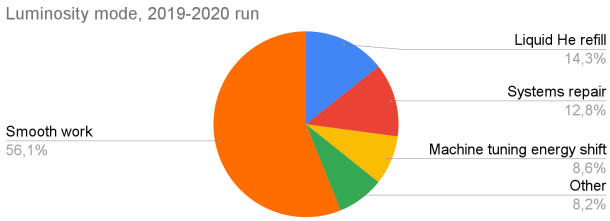

Figure 5: Luminosity mode, 2019–2020 run.

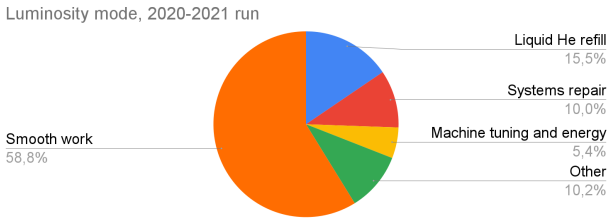

Figure 6: Luminosity mode, 2020–2021 run.

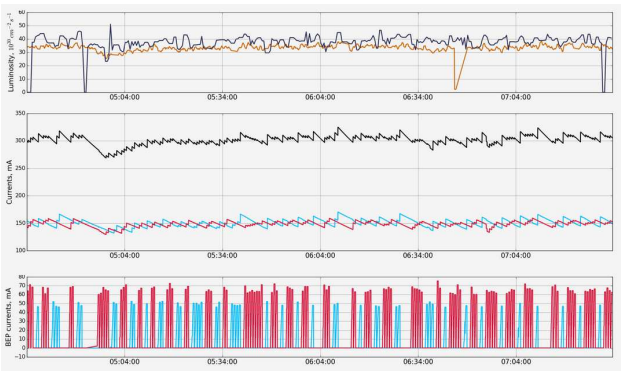

Figure 7: Smooth work.

to experimental hall that means beams abort and interruption of regular operation thus affecting the daily luminosity integral rate. This daily stop takes from 1 to 4 hours every morning, depending on logistics.

"Systems repair" is for time spent for removal of malfunctions of various accelerator complex subsystems. To mitigate this factor the modernization program is developed, for example for power supplies, and being implemented gradually.

"Machine tuning and energy" is the optimization machine lattice for luminosity and beam dynamics, and changing beam energy according to experimental program.

"Other" reasons of dead time is due to problems outside of VEPP-2000 complex. For example: Injection complex tuning, instabilities of water station work, power interruption. Also including here are quenches in solenoids:

- 5 times at 2019–2020 run
- 7 times at 2020–2021 run

Quenches occurred mostly at high bunch energies due to failed injection when beam dump took place. Quenches in the some solenoid usually resulted in almost total evaporation LHe from its cryostat. For reducing this factor which again demanded time-consuming LHe refill testing of the quench-protection system were carried out and stabilization measure of it was took.

According to the diagrams we can make rough estimation of operation and dead time due to main significant reasons: see Table 2.

Table 2: Smooth Luminosity Operation and Dead Time

Work	Persent
Smooth work	60
Liquid helium	15
System repair	12
Machine tuning and energy shift	8

For decreasing dead time some ways potentially are available.

INCREASING OPERATION EFFICIENCY

Project "Helium Outside"

To save data taking time there is an expensive concept of placing liquid helium volume inside the experimental hall which will be connected with solenoids cryostats and its input will be located outside the hall. Thus helium refill will take place without complex operation interruption saving about 15 % operation time. The concept is under consideration and its advisability is estimated now.

Systems Upgrade

During all the VEPP-2000 complex lifetime both the software and hardware is upgraded gradually. For example new 300 A/20 V power supplies for all the collider quadrupole magnets are developed by BINP lab and in production now at BINP workshop. Four of them have been already installed and operates reliably. The power supplies for regular pulsed quadrupole magnets for transfer line between BEP and VEPP-2000 rings are planned to be changed in order to increase the beam injection stability. The prototype of pulse power supply developed for NICA project by BINP will be used for series production.

Machine Tuning and Beam Diagnostic Improvement

Machine Tuning Process of tuning collider lattice is realized by analysis of response matrix singular value decomposition (SVD) using data from 16 CCD-cameras and 4 electrostatic BMPs [11]. This process is needed when change of energy point takes place and now it takes much time. In plans there are:

- development more automated methods for doing lattice and orbit correction
- revealing diagnostic optics defects
- more close investigation of non-linear effects (including beam-beam) influencing the dynamic aperture

ISBN: 978-3-95450-240-0 ISSN: 2673-5539 doi:10.18429/JACoW-RuPAC2021-TUY01

Beam Diagnostic Improvement For better understanding beam injection processes and for studying beam dynamics and also beam-beam effects new optical diagnostic system based on beam synchrotron radiation detection is developed. The system includes avalanche photodiode array with low relaxation time [12] as sensible element that provides turn-by-turn measurements of one-dimensional section of beam transfer profile. Prototype of this system was tested with different scales of beam image and different conditions: at stationary beam circulation and synchronized with kicks of variable amplitude. Combination of two described orthogonal arrays is planned to be installed at the single VEPP-2000 SR output in order to carry out measurements in horizontal and vertical planes simultaneously.

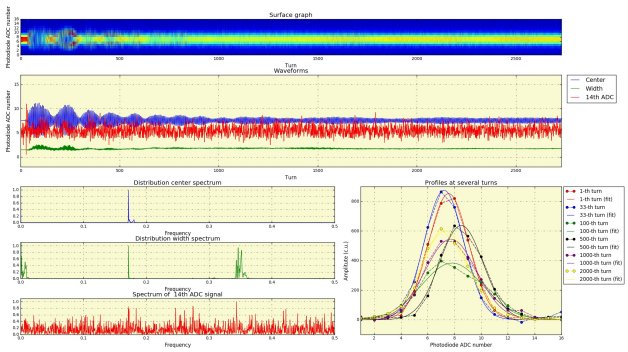

Figure 8: View of test application.

Test software application was developed for visualization measurements (Fig. 8). This soft can parse output file of signals from 16 arrays' photodiode during 2730 turns and makes graphs. Illustrating at the graphs are:

- Color two-dimentional diogram of turns history
- Oscillograms of center and weight of Gaussian distribution fit and also modulated signal from one of the 16 diodes
- Spectra of these oscillograms
- Profiles and their fit at several turns

Typical transverse VEPP-2000 beam size is 0.6–1.7 mm (standard deviation σ of Gaussian distribution) depending on operation energy and other factors. Thus optical table (Fig. 9) with wide movement range was designed allowing beam image to be scaled from 8 to 20 σ for full σ range. This factor provide ability of changing balance either to have high resolution or to observe high amplitude oscillation.

Current status of the optical table is under development.

BEAM-BASED POSITIONING TESTS

For example, mentioned above SVD method was applied to beam-based positioning tests of solenoids. VEPP-2000 solenoids consists of three different superconducting coils. The misalignment of solenoids not only provides the closed orbit distortions but also is harmful for dynamic aperture reduction due to strong nonlinear fringe fields.

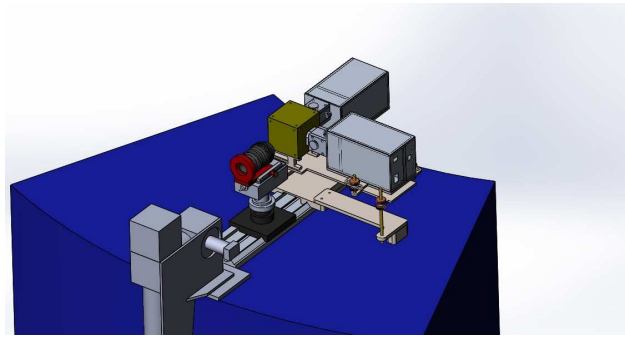

Figure 9: Optical table.

In the recent paper [13] the test study of solenoids positioning reconstruction procedure based on a circulating beam orbit responses was presented. Test measurement reveal that coils are effectively misaligned to each other, even inner and outer coils in the single solenoid. By now there is no clear explanation of this phenomena since huge shifts can be hardly tolerated by mechanical assembly. It also couldn't be explained with winding inaccuracy since the coils consists of thousands turns. At the same time, this observation probably can shed the light on confusion of early magnets alignment attempts at the commissioning stage.

ACHIEVED LUMINOSITY

During discussed above experimental runs VEPP-2000 peak luminosity record breaking have been done in both operation energy ranges.

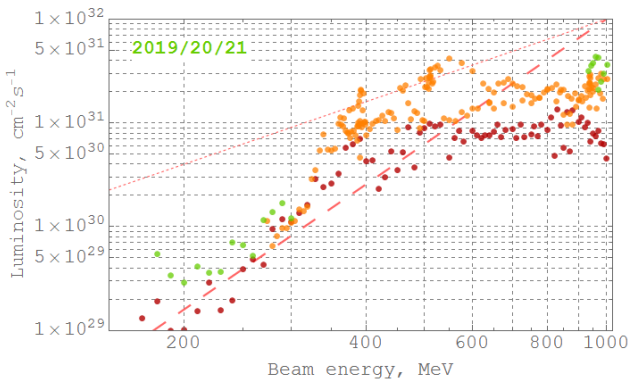

Figure 10: Peak luminosity. Red points correspond 2010–2013 run, orange points correspond 2017–2018 run after injection chain upgrade [14].

Dashed trend lines at the graph (Fig. 10) show two calculated luminosity dependencies on bunch energy. Short dashed line corresponds fixed β-function at IP (β^*), long dashed line corresponds variable β^* when its value was increased in such a way that bunch size takes as more aperture as possible.

Luminosity at low energy is limited by IBS (intra-beam scattering), small DA and low beam lifetime and also flip-flop effect which has threshold character depending on beam intensity. This device is a square pulse generator

ISBN: 978-3-95450-240-0 ISSN: 2673-5539 doi:10.18429/JACoW-RuPAC2021-TUY01

which applies amplified signals to additional kicker plates for shaking bunches increasing effectively emittance and suppressing flip-flop effect [15].

At high energy record values have been achieved only by precise lattice tuning.

The highest luminosity $L_{max} = 5 \times 10^{31}\,cm^{-2}\,s^{-1}$ in the VEPP-2000 history has been achieved at energy of 550 MeV in 2017–2018 run and at 950 MeV in 2019–2020 run (Fig. 10), while the design value is $L_{proj} = 1 \times 10^{32}\,cm^{-2}\,s^{-1}$.

RESULTS

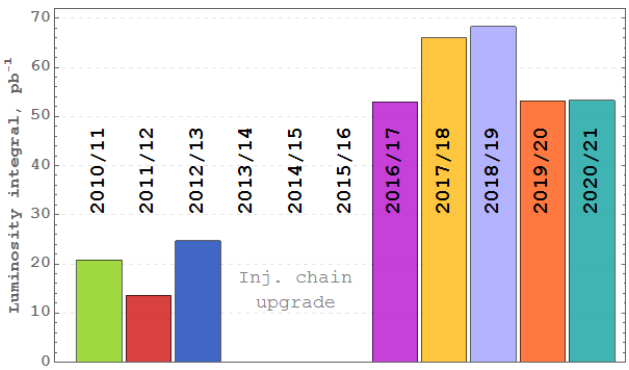

Figure 11: Total luminosity integral.

In spite of challenges and difficulties the luminosity integral comparable to previous runs has been collected (Fig. 11). It is worth noting that rates of data collection were higher (Fig. 12).

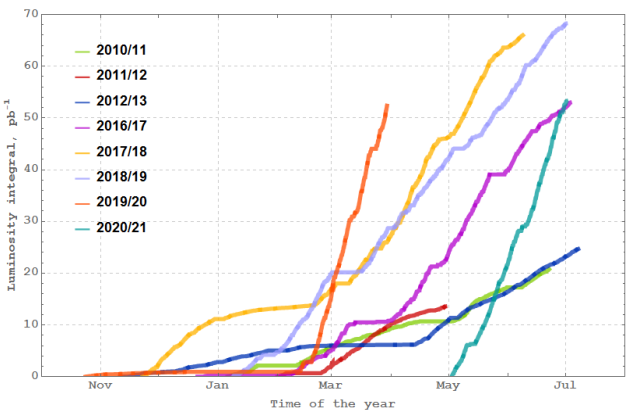

Figure 12: Data taking dynamics.

The total luminosity integral collected by each detector at VEPP-2000 achieved the value of 350 pb^{-1} with a target of 1 fb^{-1} foreseen for physical program completion.

ACKNOWLEDGEMENT

The reported study was partly funded by RFBR, project number 20-32-90217.

REFERENCES

[1] Yu. M. Shatunov *et al.*, "Project of a new electron positron collider VEPP-2000", in *Proc. of the 7th European Particle Accelerator Conf. (EPAC'2000)*, Vienna, Austria, June 2000, pp. 439–441.

[2] D. Shwartz *et al.*, "Booster of Electrons and Positrons (BEP) Upgrade to 1 GeV", in *Proc. of the 5th International Particle Accelerator Conf. (IPAC'2014)*, Dresden, Germany, 2014, paper MOPRO018, pp. 102–104.

[3] Yu. Maltseva *et al.*, "VEPP-5 Injection Complex: new possibilities for BINP electron-positron colliders", in *Proc. of the 9th International Particle Accelerator Conf. (IPAC'18)*, Vancouver, Canada, 2018, paper MOPMK011, pp. 371–373.

[4] V. V. Danilov et al., "The Concept of Round Colliding Beams", in *Proc. of the 5th European Particle Accelerator Conf. (EPAC'96)*, Sitges, Spain, Jun. 1996, paper MOP007L, pp. 1149–1151.

[5] D. Shwartz, *et al.*, "Implementation of round colliding beams concept at VEPP-2000", in *Proc. of the 58th ICFA Advanced Beam Dynamics Workshop on High Luminosity Circular e^+e^- Colliders (eeFACT2016)*, Daresbury, UK, Oct. 2016, paper MOT3AH3, pp. 32–38

[6] V. Druzhinin *et al.*, "Study of e^+e^- annihilation into hadrons with the SND detector at the VEPP-2000 collider", *Proceedings of Science*, vol. EPS-HEP2019, p. 509, Nov. 2020

[7] A. E. Ryzhenenkov *et al.*, "Overview of the CMD-3 recent results", *Journal of Physics: Conference Series*, vol. 152, p. 012009, 2020 Conference Series, Apr. 2020

[8] P. A. Piminov *et al.*, "Current status of the VEPP-4 accelerator facility", *Phys. Part. Nuclei Lett.*, vol. 17, pp. 938–950, Dec. 2020

[9] A. A. Krasnov, V. V. Anashin, A. M. Semenov, D. B. Shwartz, "Synchrotron radiation beamline installed at BINP to study the High Luminosity LHC vacuum system", in *Proc. 25th Russian Particle Accelerator Conference, (RuPAC2016)*, Saint Petersburg, Russia, Nov 2016, paper THPSC017, pp. 572–574.

[10] A. Semenov *et al.*, "Vacuum system of VEPP-2000 accelerator complex", *Journal of Instrumentation*, vol. 14, p. 10030, Oct. 2019

[11] A. L. Romanov *et al.*, "Round Beam Lattice Correction using Response Matrix at VEPP-2000", *in Proc. 1st Int. Particle Accelerator Conf. (IPAC'10)*, Kyoto, Japan, May 2010, paper THPE014, pp. 4542–4544.

[12] First Sensor APD Array Data Sheet, Part Description 16AA0.13-9 SMD, Order №3001187 https://www.first-sensor.com

[13] D. Shwartz, "Final focusing solenoids beam-based positioning test", in *Proc. 12th International Particle Accelerator Conf. (IPAC'21),* Campinas, SP, Brazil, 2021, paper TUPAB003, pp. 1330–1333.

[14] D. Berkaev *et al.*, "Comissioning of upgraded VEPP-2000 injection chain", in *Proc. of the 7th International Particle Accelerator Conf. (IPAC2016)*, Busan, Korea, May. 2016, paper THPOR018, 3811–3813.

ISBN: 978-3-95450-240-0 ISSN: 2673-5539 doi:10.18429/JACoW-RuPAC2021-TUY01

[15] D. Shwartz *et al.*, "Round colliding beams at VEPP-2000 with extreme tuneshifts", in *Proc. of the 62nd ICFA Advanced Beam Dynamics Workshop on High Luminosity Circular e^+e^- Colliders (eeFACT'2018)*, Hong Kong, China, 2018, paper MOYBA01, pp. 34–40.

ISBN: 978-3-95450-240-0 ISSN: 2673-5539 doi:10.18429/JACoW-RuPAC2021-TUA01

VEPP-4M COLLIDER OPERATION AT HIGH ENERGY

P. A. Piminov†, G. N. Baranov, A. V. Bogomyagkov, V. M. Borin, V. L. Dorokhov, S. E. Karnaev, K. Yu. Karyukina, V. A. Kiselev, E. B. Levichev, O. I. Meshkov, S. I. Mishnev, I. A. Morozov, I. B. Nikolaev, O. N. Okunev, E. A. Simonov, A. G. Shamov, S. V. Sinyatkin, E. V. Starostina, C. Yu. Todyshev, V. N. Zhilich, A. A. Zhukov, A. N. Zhuravlev,
Budker Institute of Nuclear Physics SB RAS, Novosibirsk, Russia

Abstract

From 2018 HEP experiments at the VEPP-4M collider with the KEDR detector were carried out in the high energy range (higher than 2 GeV). VEPP-4M is an electron positron collider in the beam energy range from 1 to 6 GeV. KEDR is the universal magnetic detector with 6 kGs longitudinal field and the particle tagging system for selection of gamma-gamma interaction. The paper discusses recent experimental activity of the VEPP-4M: the hadron cross section measurement from 2.3 to 3.5 GeV, ϒ(1S) meson searching, gamma-gamma physics luminosity run, synchrotron radiation, etc. Also the beam energy measurement by the resonance depolarization method using the laser polarimeter has been presented.

INTRODUCTION

The multipurpose accelerator complex VEPP-4 [1] is used for high energy physics (HEP) experiments at electron positron collider VEPP-4M with KEDR detector [2], experiments with synchrotron radiation (SR) at VEPP-3 and VEPP-4M [3], nuclear physics experiments at Deuteron facility [4], experiments with extracted hard gamma beams (~ 0.1÷3 GeV) at Test Beam Facility for detector physics [5] and accelerator physics researches. The VEPP-4 facility is shown schematically on Fig. 1. On the figure SR is experimental halls for synchrotron radiation researches and ROKK-1M is an experimental hall for the Test Beam Facility and the laser polarimeter.

The VEPP-3 is storage ring with 74 m length and beam energy from 400 MeV to 2 GeV. It has its own experimental program and is used also for the particle acceleration and the particle polarization for VEPP-4M. The transport channel from VEPP-3 to VEPP-4M is pulse with 1.9 GeV maximum energy.

The VEPP-4M ring is a racetrack of 366 m length with single magnetic turn for electron and positron beams. The beam energy range is from 0.9 to 6.0 GeV. Four vertical bumps by 4 electrostatic plates in each allow circulating of 2 electron and 2 positron bunches. The beams are collided in main interaction point after the injection and the acceleration. For radiation beam control 2 Robinson gradient wigglers two dipole 3-pole wigglers at 2 T are used. The vertical digital feedback suppresses single-bunch instability and the analog RF feedback suppresses the multibunch longitudinal instability. All this allows increasing the beam currents and the beam lifetime at low energies and obtaining threshold currents for the beam-beam.

† piminov@inp.nsk.su

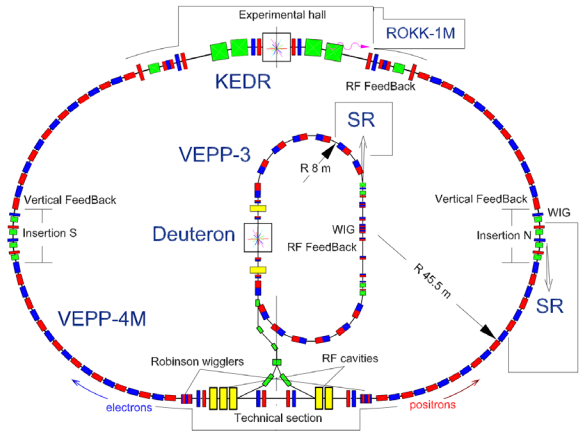

Figure 1: VEPP-4 layout.

The maximum acceleration rate is 20 MeV/s. RF system has 5 cavities and operates at 180 MHz frequency (222 harmonic number) and 4.5 MV maximal voltage.

Parameters of VEPP-4M for different energies are given in Table 1. The red colour marks out nearest goals.

Table 1: Parameters of VEPP-4M for Different Energies

Energy	2.3	3.5	4.75	GeV
Betatron tunes		8.54/7.57		
Nat. chroms		–14/–20		
Comp. factor		0.0168		
Hor. emit.	42	100	180	nm·rad
Energy spread	3.7	6.5	7.5	$\cdot 10^{-4}$
Bunch length		4		cm
Beam	2x2	2x2	1x1→2x2	
Bunch current	6	9→12	9→12	mA
Luminosity	0.5	1.2→2.0	0.5→1.4	$\cdot 10^{31}$ cm^{-2} s^{-1}

HIGH ENERGY PHYSICS EXPERIMENT

Since 2018 KEDR experimental program in the high energy range of VEPP-4M was started. It requires the beam acceleration in the collider. The beam injection and the acceleration take during 30 minutes and the luminosity time is 2 hours.

Hadron Cross Section scan from 2.3 to 3.5 GeV

The first goal of the KEDR physical program was measurement of the hadron cross section (R-scan) from 2.3 to 3.5 GeV in 17 points. The total luminosity integral is 13.7 pb^{-1}. The beam energy measurement is not required. The beam energy stability in each point is 5 MeV.

The R values are critical in various precision tests of the Standard Model. The energy region 4.6÷7 GeV, where KEDR data has been collected, gives small contribution

ISBN: 978-3-95450-240-0 ISSN: 2673-5539 doi:10.18429/JACoW-RuPAC2021-TUA01

to the anomalous magnetic moment of the muon, it is of about 1%. At the same time this energy range provides 10% into the hadronic contribution to the running the electromagnetic coupling constant $\alpha(M_z^2)$ and the corresponding contribution of the uncertainty is about 15%. In addition, when considering the energy region above 5.2 GeV and up to upsilon resonances, theoretical calculations based on pQCD are usually used. New measurements of KEDR will allow the use of experimental data up to 7 GeV.

Gamma-Gamma Physics

In 2021 the luminosity run for gamma-gamma physics [2] was started. For the experiment the particle tagging system (TS) of the KEDR is used. It allows registration of the scattered electron positron pair after two photons interaction. The final focus quadrupoles and two special bending magnets of the collider form the focusing magnetic spectrometer. The scattered electrons or positrons with the energy loss from 0.02 to 0.6 of the beam energy are registered by one of the four modules of the TS. The module consists of six double layers of the drift tubes and the two-coordinate GEM detector in front of them.

For the first stage we plan to collect 50÷100 pb^{-1} at the energy range 3.5÷4.7 GeV. It provides (a) the measurement of the total cross section for the process gamma-gamma → hadrons within the invariant mass range 1÷4 GeV and study physical characteristics of events (multiplicity, spectra, etc) and (b) study exclusive gamma-gamma processes at low invariant masses (≤1 GeV) which are approachless for B-factories due to the trigger conditions. Based on the results of the first stage we will evaluate the possibility for the larger luminosity integral and further gamma-gamma investigations. In particular, the study of charmed resonances η_c, $\chi_{0,2}$, η_c (2S), etc.

At present time the luminosity is collected at 3.5 GeV where we hope will be achieved the maximum luminosity of VEPP-4M (higher that $2\cdot10^{31}$ cm$^{-2}\cdot$s^{-1}). Now the maximum peak luminosity is $1.2\cdot10^{31}$ cm$^{-2}\cdot$s^{-1}, the integral luminosity is 177 nb^{-1} per 12 hours and 1.4 pb^{-1} per a week. The total recorded luminosity integral is 10 pb^{-1}.

ϒ(1S)-Meson

In June 2021 the luminosity run at 4.75 GeV for searching ϒ(1S) meson has been made. Unfortunately the beam energy calibration in this range was unsuccessful due to the spin resonance. Using the main dipole field control using NMR technique ϒ(1S) meson was founded in during 12 hours with 42 nb^{-1} luminosity integral in 8 points in 10 MeV energy range. After the position of the peak has been determined 190 nb^{-1} in 10 points has been collected. The final results is shown on Fig. 2 where E_{set} is the collider magnetic system energy or magnetic rigidity which is calculated by the control system. Knowing the rest mass of ϒ(1S) from PDG, the energy offset was fitted.

The main goal of the experiment is to demonstrate the possibility of operation of the collider and detector at this energy. Also background conditions have been inspected. The beam energy spread was checked in this experiment. The energy position of Y(1S) meson is marker for the laser polarimeter tuning and the radiation polarization obtaining at this energy.

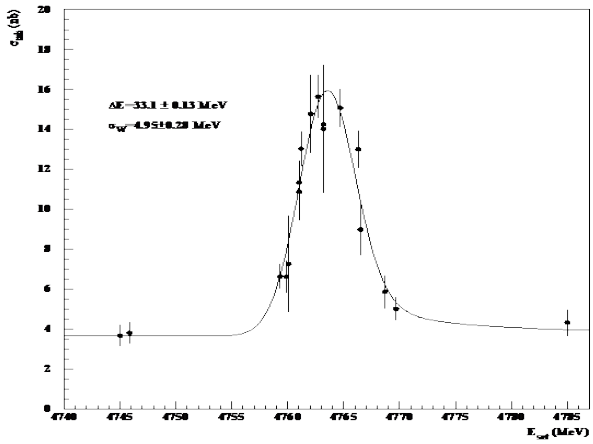

Figure 2: The Y(1S) scan.

SYNCHROTRON RADIATION

For SR experiments special runs are organized [3]. Normally, 25% of complex operation time is dedicated for SR and 75% for HEP. During SR runs experiments are performed simultaneously at VEPP-3 (1.2 or 2.0 GeV) and VEPP-4M (1.9 2.5 and 4.5 GeV). For experiments with hard X-rays [6] on VEPP-4M at 4.5 GeV 9-pole 1.9 T hybrid wiggler is used [7]. In standard operation mode, two 10 mA electron bunches separated by half of the turn or 610 ns are used. Multi-bunch operation mode is available with full loading (up to 23 bunches separated by 50 ns).

LASER POLARIMETER

An experiment on Upsilon-meson mass measurement requires beam energy calibration by resonance depolarization method with beam polarization determination. We developed a laser polarimeter based on the Compton scattering [8]. Circularly polarized (with the help of the Pockels cell and the λ/4 phase plate) photons from the 527-nm Nd:YLF laser are scattered at the polarized electron beam with a 2-kHz repetition rate and detected through the 12 mm thick lead converter by the GEM two-coordinate detector. Pockels cell toggles left-right laser beam polarization for each laser pulse. In order to deterine electron beam polarization we apply join fit to the left and right two-dimentional distributions of registered photons using Compton differential cross section convoluted with angular spread of electron momentum (Fig. 3).

ISBN: 978-3-95450-240-0 ISSN: 2673-5539 doi:10.18429/JACoW-RuPAC2021-TUA01

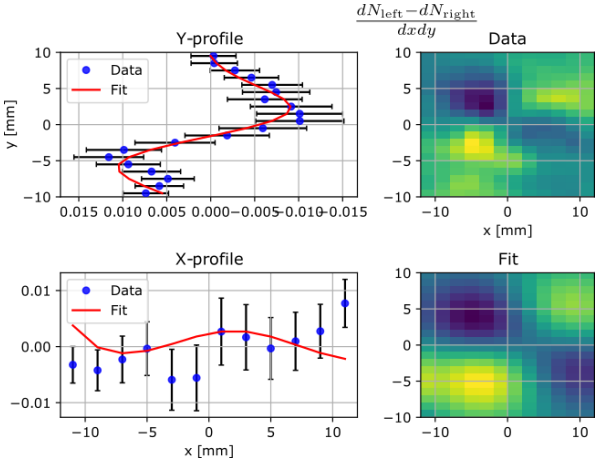

Figure 3: The result of the two-dimentional join fit to the left and right distributions of the scattered photons. The vertical (Y) projection shows Compton back scattering asymmetry due to vertical polarization of electron beam appearance

The energy calibration by resonance depolarization method at the energy 4.1 GeV (Fig. 4) shows highest possible electron beam polarization (93%) according to Sokolov-Ternov theory. Obtaining polarization at the 4.7 GeV (ϒ(1S)-meson energy) which is our main goal is difficult due to depolarizing spin-betatron resonances. In order to increase accuracy of polarization/energy measurement we are developing new water-cooling copper mirror. This mirror will result in better laser focusing on electron bunch thus Compton scattering rate will increase.

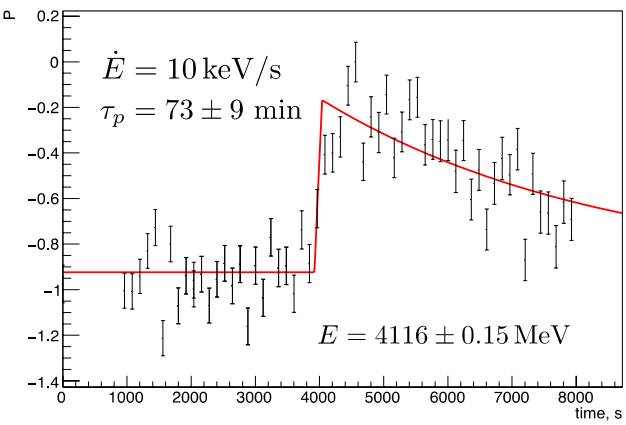

Figure 4: The beam energy calibration at 4.1 GeV.

UPGRADE

For operation at high energy main subsystems has been upgraded (RF system, beam and optical diagnostics, control and protection system, engineering infrastructure, etc).

Currently, the maximum operation energy is 4.75 GeV. It is limited by the arc elements power supply (PS) system. To increase maximum energy of the VEPP-4M collider up to 6 GeV a new 10 kA 70 V thyristor PS is installed to feed 66 main magnets connected in series. PS has output current stability of better than 0.01% at the maximum current. Now this PS is in commissioning stage.

One of troubles limiting the beam current is low power of the high voltage generators of the electrostatic system. There is a photocurrent from electrostatic plates due to synchrotron radiation. The photocurrent and the voltage between electrostatic plates increase with increasing the beam energy. At energies above 3 GeV the power of the generators isn't enough and the voltage drops down and the beam is lost. Three years ago four new generators (30 kV 10 mA) were installed in Insertion N (see Fig. 1). Now others generator has been made and now they are commissioning.

CONCLUSION

HEP experiments at VEPP-4V collider with KEDR detector at energy high range are continued. The hadron cross section from 2.3 to 3.5 GeV beam energy has been finished. The luminosity run for gamma-gamma physics at 3.5 GeV using the particle tagging system is continuing. Preliminary searching of ϒ(1S) meson at 4.75 GeV has been finished successfully. It demonstrates a possibility of the collider and the detector performance at high energy. Development of resonant depolarization technique using laser polarimeter system for absolute energy calibration at energies higher than 3 GeV is continued. Radiate polarization and depolarization of electron beam at 4.1 GeV has been obtained. Synchrotron radiation runs have been performed periodically. Various subsystems are being upgraded to allow experiments at maximum energy.

REFERENCES

[1] P. A. Piminov *et al,* "Current Status of the VEPP-4 Accelerator Facility", *Phys. Part. Nucl. Lett.* 17(7), 2020, pp.938-850.

[2] V. V. Anashin *et al,* "The KEDR detector", *Phys. Part. Nucl.* vol. 44 no. 4, 657-702, 2013. DOI:10.1134/S1063779613040035.

[3] P. A. Piminov *et al,* "Synchrotron radiation research and application at VEPP-4", *Physics Procedia* 84, 19 26, 2016. DOI:10.1016/j.phpro.2016.11.005.

[4] D. M. Nikolenko, "Experiments with internal targets at the VEPP-3 electron storage ring", *Physics of Atomic Nuclei,* 73, 8, 2010, p. 1322-1338, DOI:10.1134/S1063778810080065

[5] V. S. Bobrovnikov *et al.,* "Extracted electron and gamma beams in BINP", *JINST* 9 C08022, 2014. DOI:10.1088/1748-0221/9/08/C08022.

[6] G.Baranov *et al,* "Experiments with Synchrotron Radiation at the VEPP-4M", *Journal of Surface Investigation,* 14, 1, pp. 150-154, 2020. DOI:10.1134/S1027451020020032.

[7] G. N. Baranov *et al,* "Hybrid Nine-Pole Wiggler as a Source of Hard X-ray Radiation at the VEPP-4 Accelerator Complex", *Journal of Surface Investigation,* 2020, 14(6), 1290-1293, DOI: 10.1134/S1027451020060269.

[8] V. E. Blinov *et al,* "Status of laser polarimeter at VEPP-4M", *JINST* 15 (2020) C08024, DOI:10.1088/1748-0221/15/08/C08024.

ISBN: 978-3-95450-240-0 ISSN: 2673-5539 doi:10.18429/JACoW-RuPAC2021-TUA02

CURRENT STATUS OF VEPP-5 INJECTION COMPLEX

Yu.I. Maltseva*[1], A. Andrianov[1], K. Astrelina, V. Balakin[1], A. Barnyakov, A.M. Batrakov, O.V. Belikov, D.E. Berkaev, D. Bolkhovityanov, F.A. Emanov[1], A. Frolov, G. Karpov, A. Kasaev, A.A. Kondakov, N. Kot, E.S. Kotov[1], G. Ya. Kurkin, R. Lapik, N. Lebedev[1], A. Levichev[1], A. Yu. Martynovsky, P. Martyshkin, S. V. Motygin, A. Murasev, V. Muslivets, D. Nikiforov[1], A. Pavlenko[1], A. Pilan, Yu. Rogovsky[1], S. Samoylov, A.G. Tribendis[2], S. Vasiliev, V. Yudin,
Budker Institute of Nuclear Physics SB RAS, Novosibirsk, Russia
[1]also at Novosibirsk State University, Novosibirsk, Russia
[2]also at Novosibirsk State Technical University, Novosibirsk, Russia

Abstract

VEPP-5 Injection Complex (IC) supplies VEPP-2000 and VEPP-4 colliders at Budker Institute of Nuclear Physics (BINP, Russia) with high energy electron and positron beams. Since 2016 the IC has shown the ability to support operation of both colliders routinely with maximum positron storage rate of $1.7 \cdot 10^{10}$ e+/s. Stable operation at the energy of 430 MeV has been reached. Research on further improvements on the IC performance is carried out. In particular control system was improved, additional beam diagnostics systems were developed, monitoring of RF system was upgraded. In this paper, the latest achieved IC performance, operational results and prospects are presented.

INTRODUCTION

Since 2016 the IC [1,2] has supplying the VEPP-2000 [3] and VEPP-4 [4] facilities with high energy electron and positron beams. The layout of BINP colliders together with IC is shown in Fig. 1.

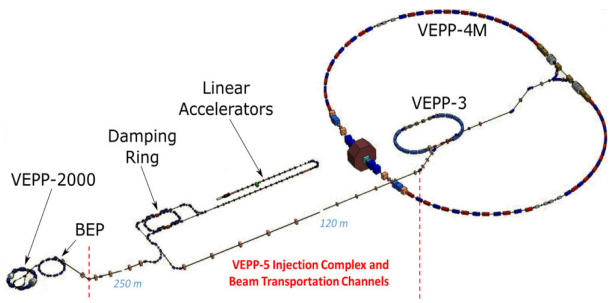

Figure 1: Layout of BINP accelerator facilities.

The IC consists of electron and positron S-band linacs with achieved energies of 280 MeV and 430 MeV, respectively, and the damping ring (DR) alternately storing both electron and positron beams. Then beams are transported to users via the set of K-500 beam transfer lines. Main IC parameters are presented in Table 1.

During the 2020/2021 run malfunction of positron solenoid reduced the positron storage rate, however by proper tuning the beam orbit and optimizing the regime-switching procedures positron storage rate of $0.9 \cdot 10^{10}$ e+/s was reached.

* yu.i.maltseva@inp.nsk.su

Table 1: Main IC Parameters

Parameter	Value
Linac energy e-, e+ (reached)	280, 430 MeV
Linac RF frequency	2855.5 MHz
Energy spread e-, e+	±1%, ±3%
Linac repetition rate	up to 12.5 Hz
Extr. repetition rate	up to 1 Hz
Design horizontal emittance	$2.3 \cdot 10^{-6}$ rad·cm
Design vertical emittance	$0.5 \cdot 10^{-6}$ rad·cm
DR energy (design)	510 MeV
DR RF frequency	11.94 MHz
DR circumference	27.4 m
DR design current	30 mA
e+ storage rate (reached)	$1.7 \cdot 10^{10}$ /s
Damping time@510MeV(h/v/l)	11/18/12 ms

In terms of beam charge and injection repetition rate, VEPP-2000 collider imposes strict requirements on the IC performance. It requires constant beam injection due to small beam lifetime of 500 s. In order to achieve the desired luminosity a new portion of 10^{10} particles at least every 50 s has to be injected into the main ring. To meet these requirements switching between electron and positron beams in the IC was minimized up to 5 s by tuning both linacs to achieve equal energy for electron and positron beams, while keeping the DR operation mode to be constant. K-500 transfer line magnets and power supplies limit minimal switching time between the particle types to at least 30 s.

Due to small conversion efficiency for positron production, positron storage rate and extraction from the DR are the main concern. Considering achieved positron storage rate of $0.9 \cdot 10^{10}$ e+/s and transfer losses of up to 50-60 %, remaining time of 20 s to supply 10^{10} particles into VEPP-2000 main ring is sufficient. Thus, the IC meets the VEPP-2000 requirements. However, further improvement on the IC performance are essential for its reliable operation.

The IC has four operating modes: electron or positron production for VEPP-2000 or VEPP-4. The switching between these modes is automated with simple asynchronous state machine, 12 transitions between K-500 modes in order to reliably remagnetize its elements are utilized. Currently the IC is able to automatically supply the VEPP-2000 with all

ISBN: 978-3-95450-240-0 ISSN: 2673-5539 doi:10.18429/JACoW-RuPAC2021-TUA02

types of particles, but switching to VEPP-4 is still performed by operator request. More detailed description on operation modes can be found in paper [5].

PERFORMANCE 2020/2021

Reliability

During 2020/2021 run the IC was operated for over 7000 hrs with 50/50% user's ratio. Maintenance work took 10 % of the operation time, most of the system failures were caused by outdated electronics of the klystron modulators. The amount of failures due to magnetic system power supplies was decreased by their partial replacement: 9 of 500 A and 8 of 1000 A power supplies have been replaced in 2019/2020.

More delicate and accurate linac tuning has allowed us to reach energy beam of 430 MeV. Previously reached energy was 390 MeV. Energy increase leads to better injection efficiency in the DR and increase beam life time at the injection in VEPP-3. Positron solenoid malfunction reduced maximum achieved positron storage rate by the factor of 2.

New Electron Gun Cathode

In 2019/2020 a new cathode assembly with pulse current of 7.25 A and pulse duration of 7.3 ns was installed. Previous cathode had 5 A pulses with 3 ns duration. In the beginning of 2020 cathode heater current was reduced in order to extend cathode lifetime. Then in the middle of 2020 gun grid modulator was replaced with one with shorter pulses, and now gun provides about $1.5 \cdot 10^{11}$ electrons per pulse as shown in Fig. 2.

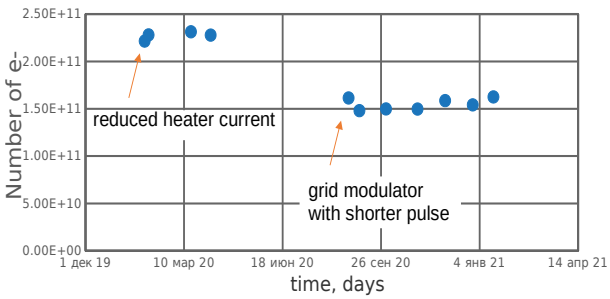

Figure 2: Cathode performance in 2020/2021 run.

Positron Solenoid Malfunction

In October 2019 positron solenoid was damaged resulting in decreasing the IC productivity by the factor of 2. And single e+ injection value in the DR equals to $0.8 \cdot 10^9$. The solenoid can only be replaced as a whole unit including conversion system and the 1st e+ RF section. New solenoid design with no gaps between coils, hence better field quality, is under development. Designed magnetic field is shown in Fig. 3. Mechanical design and construction of the solenoid is planned for 2021/2022 run.

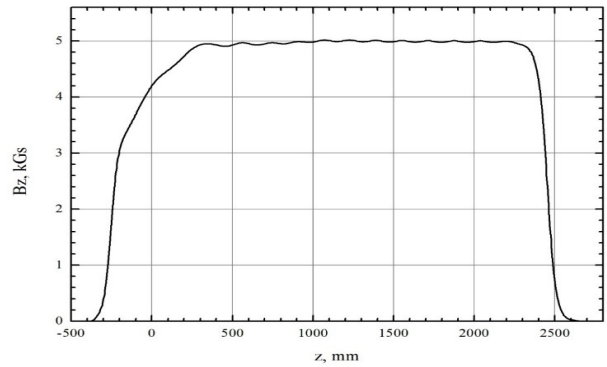

Figure 3: Designed magnetic field profile of a new positron solenoid.

IMPROVEMENTS

In order to provide better IC performance and operation stability several significant improvements of the IC systems were performed and further improvements are under consideration.

Beam Loss Monitor System

Fiber-based beam loss diagnostics system was developed and two beam loss monitors were installed at the DR extraction channels to both user directions (see Fig. 4). They allow online monitoring of beam loss distributions along the K-500 transfer lines. Devices are fully integrated in the IC control system and used in a routine operation [6, 7].

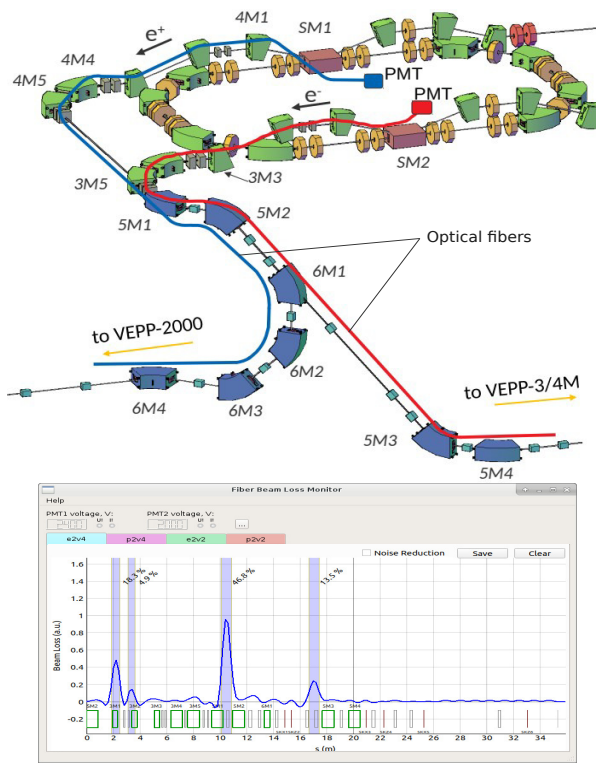

Figure 4: Beam loss monitor layout.

ISBN: 978-3-95450-240-0 ISSN: 2673-5539 doi:10.18429/JACoW-RuPAC2021-TUA02

Linac RF Monitoring System

For simultaneous monitoring all main points of the linac RF system, 10 new ADC250x4 assembled in one VME64 crate with L-timer [8, 9] were developed at BINP and installed. Measurement point layout of RF signal is shown in Fig. 5. L-timer was adapted to operate with the IC master generator and synchronization system as clock and start signals and read all ADC signals simultaneously. The RF monitoring system is fully integrated into the IC software. More automatic data preprocessing is now under consideration.

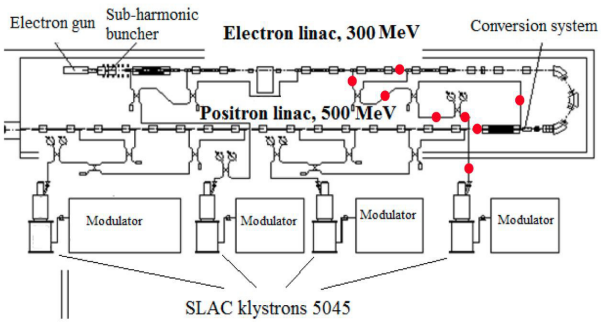

Figure 5: Measurement point layout of linac RF system.

Control System

The IC software is based on CXv4 framework [10], control software set is constantly improved [11]. The recent changes are the following:

- Many base framework improvements were implemented;
- Server-side device/channel bridging, used to easily interface beam user control systems;
- EPICS and TANGO client modules for CX;
- Improved Python bindings for CX client libraries;
- Improved CX-connected Qt widgets set;
- Improved database tools for machine configuration, configuration files generation;
- Improved machine state snapshot storage and manipulation programs;
- Improved automatic and data preprocessing software;
- Developed a software set for the DR optic measurements and studies;
- Developed few data preprocessing services and operators front-end applications.

Full automatic operation with VEPP-2000 is performed. Switching to VEPP-4 is still performed by operator request, but full automatic operation with both colliders is under development.

Injection Efficiency

Several programs for measurement and correction of the DR parameters were developed. They allow orbit correction, betetron tune and optics measurements. Injection efficiency study was performed using new software for tune control [12]. Tune scan was performed and optimal working point for the DR was determined, as shown in Fig. 6.

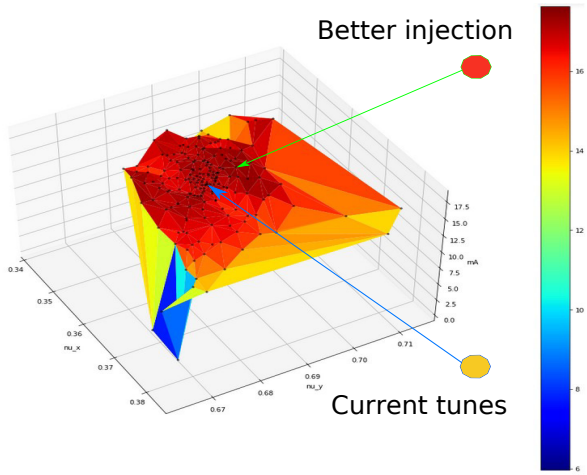

Figure 6: Amount of captured positrons in the DR vs tunes.

Beam Diagnostics for Injection Channels

To improve injection efficiency in the DR, we propose to use additional beam diagnostics in both injection channels: 6 and 3 BPMs for the e+ and e- channels, respectively [13]. Layout of proposed BPMs is shown in Fig. 7. New set of BPMs should decrease additional losses related to trajectory or optics mismatch.

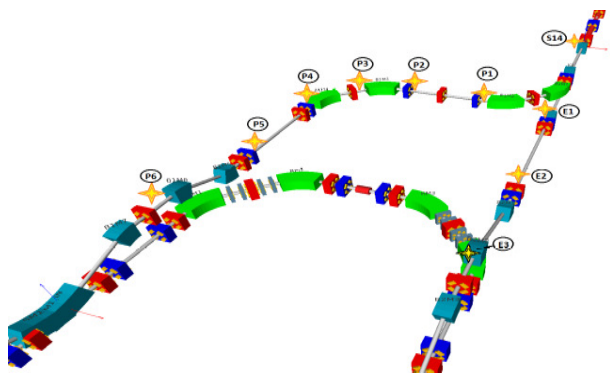

Figure 7: Layout of proposed BPMs for the DR injection channels.

CONCLUSION

Over the past five years, the IC successfully has been supplying both BINP colliders simultaneously. Maximum positron storage rate of $1.7 \cdot 10^{10}$ e+/s was achieved prior to positron solenoid malfunction. Stable IC operation at the energy of 430 MeV has been reached. New 10 A electron gun was installed. Positron solenoid replacement is planned for 2021/2022 run. Significant improvements on beam loss monitor system, RF monitoring system, control system were performed. Further IC performance and operation stability improvements are under consideration.

ISBN: 978-3-95450-240-0 ISSN: 2673-5539 doi:10.18429/JACoW-RuPAC2021-TUA02

REFERENCES

[1] F. A. Emanov *et al.*, "Status of VEPP-5 Injection Complex", presented at the *12th Int. Particle Accelerator Conf. (IPAC'21)*, Campinas, Brazil, May 2021, paper THPAB021.

[2] K. Astrelina et al., Current Status and Planned Upgrades of the VEPP-5 Injection Complex, *Phys. Part. Nuclei Lett.* 17, 409–414 (2020). doi:10.1134/S1547477120040056

[3] M.V. Timoshenko *et al.*, Status of VEPP-2000 BINP Electron–Positron Collider, *Phys. Part. Nuclei Lett.* 17, 419–424 (2020). doi:10.1134/S1547477120040457

[4] A.N. Zhuravlev *et al.*, Current Status of the VEPP-4 Accelerator Facility, *Phys. Part. Nuclei Lett.* 17, 938–950 (2020). doi:10.1134/S1547477120070067

[5] D. Berkaev *et al.*, "VEPP-5 Injection Complex: Two Colliders Operation Experience", in *Proc. 8th Int. Particle Accelerator Conf. (IPAC'17)*, Copenhagen, Denmark, May 2017, pp. 2982-2984. doi:10.18429/JACoW-IPAC2017-WEPIK026

[6] Maltseva Yu.I., Prisekin V.G., Frolov A.R., Beam Loss Measurements Using the Cherenkov Effect in Optical Fiber for the BINP e+e- Injection Complex, in *Proc. 8th Int. Beam Instrumentation Conf. (IBIC'19)*, Malmö, Sweden, Sep. 2019, pp. 233-237. doi:10.18429/JACoW-IBIC2019-TUA003

[7] Maltseva Yu.I. *et al.*,"Distributed beam loss monitor based on the Cherenkov effect in an optical fiber", *Physics-Uspekhi*, vol. 58, pp. 516–519, 2015. doi:10.3367/ufne.0185.201505m.0553

[8] G. A. Fatkin *et al.*, "New VME-Based Hardware for Automation in BINP", in *Proc. 16th Int. Conf. on Accelerator and Large Experimental Physics Control Systems (ICALEPCS'17)*, Barcelona, Spain, Oct. 2017, pp. 1294-1297. doi:10.18429/JACoW-ICALEPCS2017-THMPL10

[9] E. S. Kotov *et al.*, "VME Based Digitizers for Waveform Monitoring System of Linear Induction Accelerator (LIA-20)", in *Proc. 16th Int. Conf. on Accelerator and Large Experimental Physics Control Systems (ICALEPCS'17)*, Barcelona, Spain, Oct. 2017, pp. 1291-1293. doi:10.18429/JACoW-ICALEPCS2017-THMPL09

[10] D. Bolkhovityanov, P. B. Cheblakov, and F. A. Emanov, "CXv4, a Modular Control System", in *Proc. 15th Int. Conf. on Accelerator and Large Experimental Physics Control Systems (ICALEPCS'15)*, Melbourne, Australia, Oct. 2015, pp. 915-918. doi:10.18429/JACoW-ICALEPCS2015-WEPGF093

[11] F. A. Emanov, D. E. Berkaev, D. Yu. Bolkhovityanov VEPP-5 Injection Complex Control-System Software, *Phys. Part. Nuclei Lett.* 15, 953–955 (2018). doi:10.1134/S1547477118070312

[12] V. V. Balakin, F. A. Emanov, D. E. Berkaev, "Beam Parameters Control and Operation Software Tools for VEPP-5 Injection Complex Damping Ring", presented at the *27th Russian Particle Accelerator Conf. (RuPAC'21)*, Alushta, Russia, Sept.-Oct. 2021, paper WEPSC56, this conference.

[13] K. V. Astrelina and F. A. Emanov, "Consideration the Prospects of Beam Diagnostic System Upgrade in the Transport Channels of Injection Complex VEPP-5", presented at the *12th Int. Particle Accelerator Conf. (IPAC'21)*, Campinas, Brazil, May 2021, paper MOPAB272.

ISBN: 978-3-95450-240-0 ISSN: 2673-5539 doi:10.18429/JACoW-RuPAC2021-TUB02

NICA COLLIDER MAGNETIC FIELD CORRECTION SYSTEM

M. M. Shandov*, H. G. Khodzhibagiyan, S. A. Kostromin[1], O. S. Kozlov, I. Yu. Nikolaichuk, T. Parfylo, A. V. Phillippov, A. V. Tuzikov, Joint Institute for Nuclear Research, Dubna, Russia
[1]also at Saint Petersburg University, Saint-Petersburg, Russia

Abstract

The NICA Collider is a new superconducting facility that has two storage rings, each of about 503 m in circumference, which is under construction at the Joint Institute for Nuclear Research, Dubna, Russia. The influence of the fringe fields and misalignments of the lattice magnets, the field imperfections and natural chromaticity should be corrected by the magnetic field correction system. The layout and technical specification of the magnetic field correction system, the main parameters, arrangements and the field calculations and measurement results of the corrector magnets are presented. The results of dynamic aperture calculation at working energies are shown.

INTRODUCTION

NICA (Nuclotron-based Ion Collider fAcility) is a new accelerator complex currently under construction at the Joint Institute for Nuclear Research, Dubna, Russia. One of the main goals of the NICA project is experimental studies of dense nuclear (baryonic) matter [1]. Two arcs and two straight sections with two interaction points compose the Collider lattice [2]. The FODO optics with 12 periods is chosen for the arc structure. The twin-aperture superconducting dipoles and quadrupoles with the distance between beams 320 mm [3] are used in FODO cells (see Fig. 1). The correction system includes 124 corrector magnets for each beam (46 in arcs and 16 in straight sections) and 8 corrector magnets combined for 2 beams (in interaction point regions), in total 132 corrector magnets.

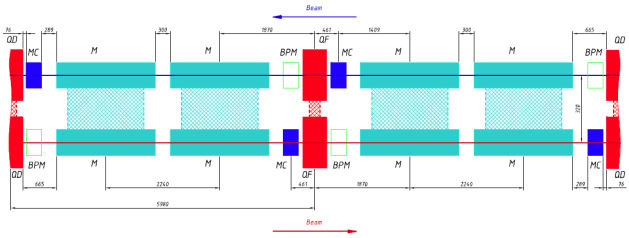

Figure 1: FODO-cell of the NICA Collider.

MAGNETIC FIELD CORRECTION SYSTEM

Corrector magnets are installed in each module of the quadrupole magnet (see Fig. 1, MC) except for special corrector magnets in straight sections of the Collider. As it was shown in [4], the designed lattice structure and the magnetic field correction system of the NICA Collider are made it possible to reach the design parameters. In addition, a dynamic aperture (DA) 8 -9 σ was reached. The main limitation of the dynamic aperture is the effect of the fringe fields (FF) of quadrupole magnets (see Fig. 2). At the present time, a tuning mode for compensation of the betatron tune coupling, ring chromaticity and fringe fields influence have been found. The current state of the results of calculating the beam dynamics for the NICA Collider was carried out in [5].

Random and systematic errors should be compensated by the correction system. The field imperfections, the deviation of magnetic field integrals, the influence of the FF and misalignments of lattice magnets are the sources of systematic errors. In addition, the natural chromaticity and betatron tune coupling are should be compensated too. The main aims for the magnetic field correction system are presented in Table 1. More details can be found in [6].

Table 1: Goals of the Correction System

Field Type	Correction Goal	Field Strength
Normal dipole	Hor. orbit	0.15 T
Skew dipole	Vert. orbit	0.15 T
Normal quadrupole	Betatron tune	3 T/m
Skew quadrupole	Motion coupl.	3 T/m
Normal sextupole	Ring chrom.	175 T/m^2
Normal octupole	DA correction	1300 T/m^3
Normal dodecapole	DA correction	125 000 T/m^5

CORRECTOR MAGNETS

The design of the corrector magnets is based on the Nuclotron corrector magnets. In general, these are superconducting magnets with sector coils and an iron yoke (see Fig. 3). The cooling of the superconducting coils is carried out by an inner cooling cylinder (see Fig. 3, 1). The positioning and electrical insulation of the superconducting coils are carried out with spacer cylinders (see Fig. 3, 2). Structurally, the corrector magnets are separated in 10 groups according to the type of the installed coils. The design of the magnet, the main characteristics and the results of 2D FEM field calculation were presented in [6].

The DA value is reduced to 6 -7 σ based on the results of 3D FEM field calculation of final focusing quadrupole magnets, in particular, by the integral value of the allowed harmonics B_5. For this reason, a special dodecapole corrector magnet has been developed. The superconducting coil with a cooling spacer is mounted directly on the surface of the beam pipe in the centre of the central final focusing

* shandov@jinr.ru

ISBN: 978-3-95450-240-0 ISSN: 2673-5539 doi:10.18429/JACoW-RuPAC2021-TUB02

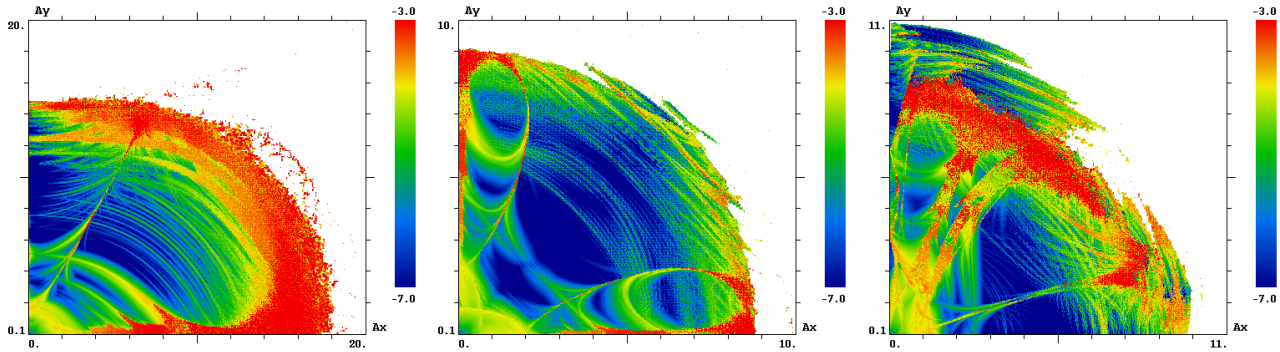

Figure 2: FMA results from the DA calculation (in normalized betatron amplitudes): no FF (left), including FF (center), including FF and correction (right).

quadrupole magnet. An iron yoke is not provided for this type of the corrector magnets.

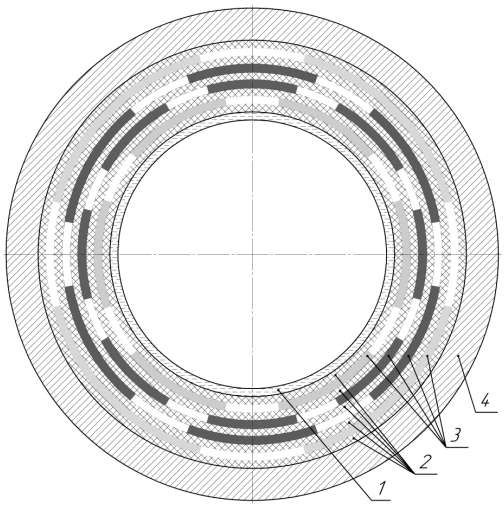

Figure 3: The cross-section view of the corrector magnet: (1) cooling cylinder, (2) spacer cylinder, (3) coils, (4) iron yoke.

The production of the corrector magnets has been organized in the SCM&T Department of LHEP, JINR, Dubna, Russia [7]. At this time, 68.9 % of the corrector magnets have been produced. The procedure of magnetic measurements was carried out for each magnet at an operating temperature of ≈4.6 K. The Hall probe is installed on the surface (R=46 mm) of the magnetic measurement system for quadrupole magnets in the centre of the corrector magnet (see Fig. 4) [6].

Table 2: Magnetic Measurement Results (R_{ref} = 46 mm)

Harmonica	Measurement	2D FEM
Dipole (B_0)	0.1270	0.1390
Sextupole (B_2)	0.0970	0.0957
Octupole (B_2)	0.0189	0.0212

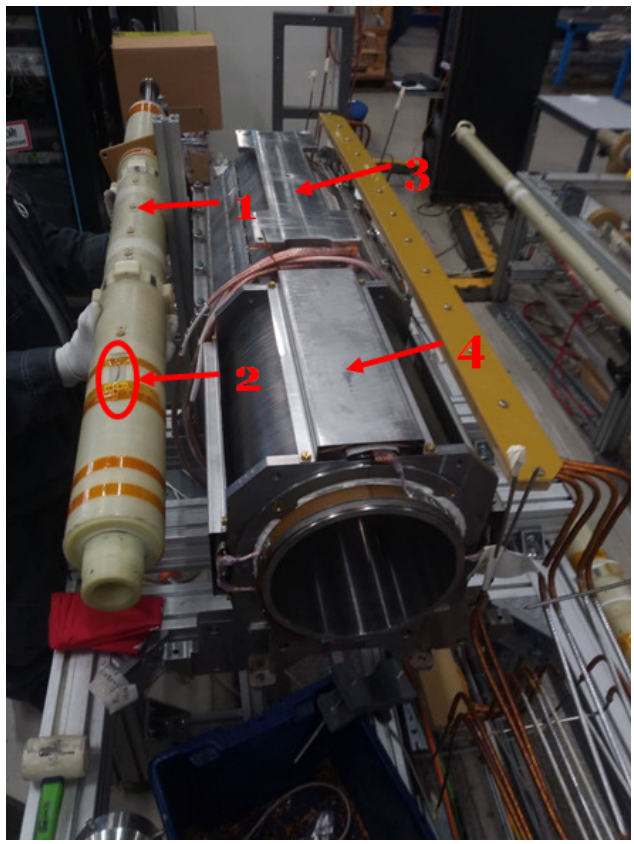

Figure 4: Magnetic measurement probe for quadrupole magnets: (1) probe, (2) Hall sensor, (3) quadrupole magnet, (4) corrector magnet.

The functional relationship of the radial component of the magnetic field from the angular position $B_r(\theta)$ from the Hall probe (three measurements and the mean value) and from the 2D FEM calculation for the fifth group of corrector magnets are shown in Figure 5 and Table 2. Individual power supplies and operating currents of the coils were used according to the technical specification. As it can be seen, a correlation was observed between the measured and the calculated results. It should be emphasized, that the offset of the the axis of

ISBN: 978-3-95450-240-0 ISSN: 2673-5539 doi:10.18429/JACoW-RuPAC2021-TUB02

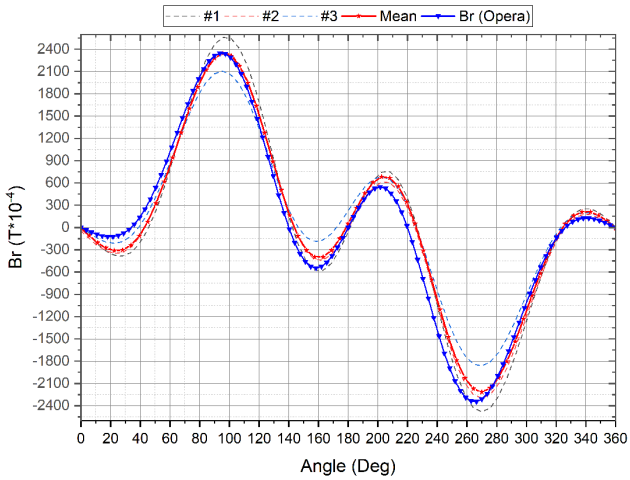

Figure 5: Radial component of the magnetic field vs. angular position.

the magnetic measurement probe to the magnetic axis and the difference between the designed and actual turns in the coils are the main sources of discrepancy between the 2D FEM calculation and the measurement results. Thus, based on the data of magnetic measurements, the offset between the corrector and quadrupole magnet axes can be calculated.

At present time, 100 % of the dipole (including reserves) and 34.8 % of the quadrupole magnets for the NICA Collider have passed the magnetic measurement procedure [8]. The search for a tuning mode of the magnetic field correction system based on these data is made our plans.

CONCLUSION

At the moment, the development of the NICA Collider magnetic field correction system has been completed. This system of the NICA Collider allows to reach the design parameters. The random and systematic errors should be compensated by the correction system. The development and serial production of the Collider corrector magnets has been started at JINR. The analytical and 2D FEM calculations were performed in the magnet centre. The FEM calculation tacking into account all sources of systematic errors, the 3D analytical and FEM models are made our plans. Magnetic measurements were carried out for 68.9 % of the Collider corrector magnets with a system based on the Hall probe. The experience of establishing the Booster corrector was taken into account when developing the design and technology of the collider correctors.

ACKNOWLEDGEMENTS

The authors would like to thank those who support our tests at JINR, especially the staff of the SCM&T Department of LHEP, the staff of the design department of LHEP, Anna Glebova for proofreading the paper and Dmitriy Shatilov for the consultation on using the Lifetrac tracking code.

REFERENCES

[1] E. Syresin *et al.*, “Status of Accelerator Complex NICA”, in *Proc. 26th Russian Particle Accelerator Conf. (RuPAC’18)*, Protvino, Russia, Oct. 2018, pp. 12–16. doi:10.18429/JACoW-RUPAC2018-MOXMH03

[2] E. Syresin *et al.*, “NICA Ion Collider at JINR”, presented at the 27th Russian Particle Accelerator Conf. (RuPAC’21), Alushta, Crimea, 26 September to 02 October 2021, paper MOY02, this conference.

[3] H. G. Khodzhibagiyan *et al.*, “Superconducting Magnets for the NICA Accelerator Complex in Dubna”, IEEE Trans. Appl. Supercond. **21** (2010) no.3, 5613210 doi:10.1109/TASC.2010.2081334

[4] S. A. Kostromin *et al.*, “Optimization the Optical Structure of the NICA Collider”, Phys. Part. Nuclei Lett. **17** (2020) doi:10.1134/S1547477120040263

[5] S. Kostromin *et al.*, “NICA Heavy Ion Collider Beam Dynamics”, presented at the 27th Russian Particle Accelerator Conf. (RuPAC’21), Alushta, Crimea, 26 September to 02 October 2021, paper TUB01, this conference.

[6] M. M. Shandov *et al.*, “Correctors’ Magnets for the NICA Booster and Collider”, Phys. Part. Nuclei Lett. **17** (2020) doi:10.1134/S154747712004041X

[7] D. Nikiforov *et al.*, “SC Magnets for Project of NICA”, presented at the 27th Russian Particle Accelerator Conf. (RuPAC’21), Alushta, Crimea, 26 September to 02 October 2021, paper WEB01, this conference.

[8] D. Zolotykh *et al.*, “Serial MM of the NICA Collider Twin-Aperture Dipoles. The Main Results”, presented at the 27th Russian Particle Accelerator Conf. (RuPAC’21), Alushta, Crimea, 26 September to 02 October 2021, paper WEPSC18, this conference.

ISBN: 978-3-95450-240-0 ISSN: 2673-5539 doi:10.18429/JACoW-RuPAC2021-TUB03

METHOD AND SYSTEMATIC ERRORS FOR SEARCHING FOR THE ELECTRIC DIPOLE MOMENT OF CHARGED PARTICLE USING A STORAGE RING

Y. Senichev, A. Aksentyev, A. Melnikov, Institute for Nuclear Research of Russian Academy of Sciences, Moscow 117312, Russia

Abstract

One of possible arguments for CP-invariant violation is the existence of non-vanishing electric dipole moments (EDM) of elementary particles [1]. To search for the EDM the BNL proposed to construct a special ring implementing the frozen spin mode in order to detect the EDM signal. Since systematic errors determine the sensitivity of a method, this article analyses some major methods proposed for searching for the EDM from the point of view of this problem. The frequency domain method (FDM) proposed by the authors does not require a special accelerator for deuterons and requires spin precession frequency measurements only. The method has four features: the total spin precession frequency due both to the electric and the magnetic dipole moments in an imperfect ring in the longitudinal-vertical plane is measured at an absolute statistic error value of ~10^{-7} rad/sec in one ring filling; the ring elements position remain unchanged when changing the beam circulation direction from clockwise (CW) to counter-clockwise (CCW); calibration of the effective Lorentz factor by means of spin precession frequency measurements in the horizontal plane is carried out alternately in each CW and CCW procedure; the approximate relationship between the spin precession frequency components is set to exclude them from mixing to the expected EDM signal at a statistical sensitivity level approaching 10^{-29} e cm. The FDM solves the problem of systematic errors, and can be applied in the NICA facility.

ORIGINAL IDEA

The idea of searching for electric dipole moment of the proton and deuteron using polarized beams in a storage ring is based on "the frozen spin" method and was originally proposed at Brookhaven National Laboratory (BNL) [2]. The concept of the "frozen spin" lattice consists of deflectors with electric and magnetic fields incorporated in one element, in which the spin vector of the reference particle is always orientated along the momentum. This is clearly evident from the Thomas–Bargmann–Michel–Telegdi equation:

$$\frac{d\vec{S}}{dt} = \vec{S} \times \left(\vec{\Omega}_{mdm} + \vec{\Omega}_{edm}\right),$$

$$\vec{\Omega}_{mdm} = \frac{e}{m\gamma}\left\{(\gamma G + 1) - \left(\gamma G + \frac{\gamma}{\gamma+1}\right)\frac{\vec{\beta}\times\vec{E}}{c}\right\}, \quad (1)$$

$$\vec{\Omega}_{edm} = \frac{e\eta}{2m}\left(\vec{\beta} \times \vec{B} + \frac{\vec{E}}{c}\right), \; G = \frac{g-2}{2} \quad ,$$

where G is the anomalous magnetic moment, g is the gyromagnetic ratio, Ω_{mdm} is the spin precession frequency due to the magnetic dipole moment (hereinafter referred to as MDM precession), Ω_{edm} is the spin precession frequency due to the electrical dipole moment (hereinafter referred to as EDM precession), and η is the dimensionless coefficient defined in (1) by the relation $d = \eta e\hbar/4mc$. The advantages of purely electrostatic machines are especially evident at the "magic" energy, when:

$$G - 1/\left(\gamma_{mag}^2 - 1\right) = 0, \quad (2)$$

and the spin vector initially oriented in the longitudinal direction rotates in the horizontal plane with the same frequency as the momentum Ω_p, i.e., $\Omega_{mdm} - \Omega_p = 0$.

In the case of deuterons with $G = -0.142$ the only possible method is a storage ring with both electric and magnetic fields [3]. This can be done by applying a radial electric field E_r to balance the vertical magnetic field B_v contribution to Ω_{mdm}^p, as shown in Eq. (1):

$$E_r = \frac{GBc\beta\gamma^2}{1-G\beta^2\gamma^2} \approx GB_v c\beta\gamma^2. \quad (3)$$

Thus, for both protons and deuterons there is a general idea of how to construct a ring, but this is realized with the help of different types of deflectors.

METODS OF EDM MEASUREMENT

for searching for the EDM are determined by the success of solving the problem of systematic errors. From this point of view, there are currently three promising methods of searching for the electric dipole moment of protons and deuterons: BNL "frozen spin" method [2], Koop's "spin wheel" method [3] and Frequency Domain method (FDM) [4]. Basically, their difference is delineated by how the problem of systematic errors is solved.

BNL "Frozen Spin" Metod

First, we will consider the "frozen spin" method [2]. In common case the orientation of the spin in 3D space is determined by three frequency projections of spin precession due to magnetic dipole moment $\Omega_r, \Omega_y, \Omega_z$ and electric dipole moment Ω_{edm}:

$$\Omega = \sqrt{(\Omega_{edm} + \Omega_r)^2 + \Omega_y^2 + \Omega_z^2}. \quad (4)$$

ISBN: 978-3-95450-240-0 ISSN: 2673-5539 doi:10.18429/JACoW-RuPAC2021-TUB03

The main idea of the "frozen" spin concept is to create such a configuration of external fields that in an ideal accelerator without imperfection of elements of the storage ring the spin orientation changes only due to the presence of the electric dipole moment Ω_{edm}, that is at $\Omega_r, \Omega_y, \Omega_z \ll \Omega_{edm}$ we have $\Omega \approx \Omega_{edm}$. However, in a non-ideal storage ring with imperfection, when $\Omega_r \neq 0, \Omega_y \neq 0, \Omega_z \neq 0$, the spin changes in accordance with:

$$\tilde{S}_y = \sqrt{\left(\frac{\Omega_y \Omega_z}{\Omega^2}\right)^2 + \left(\frac{\Omega_r + \Omega_{edm}}{\Omega}\right)^2}\, sin(\alpha + \phi), \alpha = \Omega \cdot t \quad (5)$$

In BNL method the deviation of the spin vector in the vertical plane is measured, that is, the amplitude of the changing part of the signal $\tilde{S}_y$. Expecting it at the level of $\tilde{S}_y \approx 10^{-6} rad$ after $t \approx 1000$ sec and assuming that it is necessary to correct all misalignments to such a magnitude $\Omega_y, \Omega_z, \Omega_r << \Omega_{edm}$, that is the contribution will be determined only by the EDM signal. However, each of the residual frequencies $\Omega_y, \Omega_z, \Omega_r$ plays its own negative role as a systematic error. The most important factor determining systematic errors is the presence of errors in the installation of the elements (imperfections) of the ring, which leads to the appearance of vertical E_v and radial B_r components of the electric and magnetic fields, respectively. They both change the spin components in the vertical plane, in which the EDM signal is expected, and create the systematic errors that imitate the EDM signal. Even if we assume that the vertical component of the Lorentz force averaged over the ring F_v is equal to exactly zero due to the ideal adjustment of fields in elements of the ring to provide the stable motion [5],

$$\overline{F_v} = e\left(\overline{vB_r} - \overline{E_v}\right) = 0,. \quad (6)$$

we would still observe a non-zero rotation of the spin in the vertical plane, that is to say the "fake EDM" signal. Assuming that n number of arbitrary elements of length L are installed on the ring with the rms vertical error $\langle \delta h \rangle$ and that the condition (6) for them is fulfilled, one computes the standard deviation of the MDM spin precession frequency in the vertical plane defined by the radial axis:

$$\langle \Omega_{r,mdm} \rangle = \frac{e}{m\gamma} \cdot \frac{G+1}{\gamma} \cdot \frac{\langle B_r \rangle}{\sqrt{n}}. \quad (7)$$

where $\langle B_r \rangle$ is the rms value of the radial magnetic field. In the given case $\Omega_{r,mdm}$ and Ω_r are the same. The value of the radial component of the field $\langle B_r \rangle = B_v \cdot \langle \delta h \rangle / L$ is thus determined by (a) the slope of the magnet in the transverse plane defined by the longitudinal axis and (b) the vertical component of the magnetic field B_v. If we assume a realistic rms value of the installation error of an arbitrary magnet $\langle \delta h \rangle$=100μ, the spin precession frequency in the vertical plane will be on the order of $\langle \Omega_{r,mdm} \rangle$ ≈100 rad/sec when the size of the magnets is L ≈1 m and the total number of elements on the ring is $n \approx 100$. To solve this problem in the BNL method it was suggested the procedure of injecting two beams in the ring in two opposite directions, clockwise (CW) and counter-clockwise (CCW) [5]. If in the CW direction the deviations of the spin-vector from the horizontal plane due to the MDM and the EDM add up, then they subtract in the case of the CCW circulating beam. Adding the CW and CCW results together, the EDM can be separated from a systematic error arising due to the MDM. However, in the case of a deuteron ring, the magnetic component of the Lorentz force depends on the direction of motion, which therefore means that the polarity of the magnetic field needs to be changed when the direction of injection is different. This is a fundamental problem for the implementation of the CW-CCW procedure in the deuteron case.

Another unresolved problem from our point of view is the so-called geometric phase effect. If the frequencies $\Omega_y, \Omega_z, \Omega_r$ (see 4,5) in all three planes are of equal order of magnitude and close in value, but not equal to zero, then the invariant spin axis is completely undefined, that is, in each element of ring the spin rotates around the most pronounced axis with an indefinite amplitude. The effect of mixing the frequencies with the frequency of the EDM occurs, which, despite the use of two beams moving in opposite directions clockwise CW and counter clockwise CCW, eliminates the certainty of the measurements. This effect is called the "geometric phase" and it remains unresolved in the BNL method. Eq. (1)].

Koop's "Spin Wheel" Metod

Now we need to discuss the idea of Koop's "spin wheel" method. This method uses a transverse magnetic field instead of the CW-CCW procedure, causing the spin-vector to rotate in the vertical plane perpendicular to it first in the clockwise and then the counter-clockwise direction. Quoting I. Koop, we can formulate the basic concept of the "spin wheel" method. The idea of the method is to apply a relatively strong radial magnetic field B_y to provide for rapid spin rotation in the vertical plane, say about 0.1÷1 Hz instead of 10^{-9} Hz, as in the frozen spin scenario. If one controls the accompanied beam orbit splitting with a required accuracy, then it is possible to extract the EDM contribution to a measured spin precession rate just comparing runs with a positive $\langle z1 \rangle - \langle z2 \rangle = +\Delta$ and negative $\langle z1 \rangle - \langle z2 \rangle = -\Delta$ orbit separation. Measuring the spin precession frequency $\Omega_x(\pm\Delta)$in the vertical plane one obtains

$$\Omega_{edm} = \frac{\Omega_x(+\Delta) + \Omega_x(-\Delta)}{2} \text{ at } \Omega_r = \Omega_{r,mdm} \pm \Omega_{B_x} \quad (8)$$

$$\Omega_x(\pm\Delta) = (\Omega_{edm} + \Omega_r)\sqrt{1 + (\Omega_y^2 + \Omega_z^2)/(\Omega_{edm} + \Omega_r)}$$

The author makes an estimate of the contribution of the average radial magnetic field at a level of 10^{-13} Gauss, which produces a mimic effect comparable with the EDM at the level $d = 10^{-29}$ e·cm. According to D. Kawall, the accompanying beam orbit splitting is on the order of 10^{-12}m. Here the author supposes two things: (1) that they

ISBN: 978-3-95450-240-0 ISSN: 2673-5539 doi:10.18429/JACoW-RuPAC2021-TUB03

can measure the average value of the orbit with an accuracy of 10^{-12} m using SQUIDs and (2) that the MDM spin precession frequency is completely determined by the average orbit, hence $\Omega_x(+\Delta) = \Omega_x(-\Delta)$. We disagree with assumption (1) on the grounds that such an orbit displacement measurement accuracy has never been shown experimentally, and we believe assumption (2) to be wrong because the spin precession frequency of a bunched beam in the presence of an RF field depends on the beam orbit length, but not the average orbit shift Δ. Besides, it is not clear how one can eliminate the contribution from the MDM frequency Ω_x^{mdm} arising due to imperfections. Assuming $\Omega_y, \Omega_z << \Omega_{B_x}$ we get

$$\frac{\Omega_x(+\Delta)+\Omega_x(-\Delta)}{2} = \Omega_{edm} + \Omega_r^{mdm}, \quad (9)$$

but not Ω_{edm}. This is only possible if $\Omega_r^{mdm} = 0$. This conclusion is obvious, since two terms Ω_x^{mdm} and Ω_{B_x} are aligned with the EDM.

FREQUENCY DOMAIN METHOD

In FDM [4] only spin precession frequency measurements are involved and at an accuracy that already has been experimentally verified [6]. The method is based on four fundamental features: the total spin precession frequency due to the electric and magnetic dipole moments in an imperfect ring in a vertical plane is measured at an absolute statistic error value of ~10^{-7} rad/sec for one ring filling; a position of the ring elements is unchanged from clockwise (CW) to counter-clockwise (CCW) procedures; the calibration of the effective Lorentz factor using the spin precession frequency measurement in the horizontal plane is carried out alternately in each CW and CCW procedure; the approximate relationship between the frequencies of the spin in different planes is set to exclude them from mixing to the vertical frequency of the expected EDM signal at a statistical sensitivity level approaching 10^{-29} e cm. The total spin precession frequency in the vertical plane is measured with a clockwise direction of the beam $\Omega_{CW} = \Omega_{r,mdm}^{CW} + \Omega_{edm}$ and compared with counterclockwise measurements $\Omega_{CCW} = -\Omega_{r,mdm}^{CCW} + \Omega_{edm}$. The sum of the frequencies of these two signals $\Omega_{edm} = (\Omega_{CW} + \Omega_{CCW})/2 + (\Omega_{r,mdm}^{CCW} - \Omega_{r,mdm}^{CW})/2$ allows one to identify the frequency of the EDM signal, which in turn converts into the EDM value. However, given an accuracy of the EDM measurement it is completely determined how exactly the condition $\Omega_{r,mdm}^{CCW} = \Omega_{r,mdm}^{CW}$ must be fulfilled after changing the polarity of the magnetic field. We must therefore reformulate the global problem regarding how to restore the conditions for the equal contribution of the MDM spin frequency. Studying the spin-orbital dynamics of the beam, we introduced a fundamental parameter, the effective Lorentz factor $\gamma_{eff} = \gamma_s + \beta_s^2\gamma_s \cdot \Delta\delta_{eq}$, which determines the spin precession in 3D space [4,7]:

$$\Delta\delta_{eq} = \frac{\gamma_s^2}{\gamma_s^2\alpha_0 - 1}\left[\frac{\delta_m^2}{2}\left(\alpha_1 - \frac{\alpha_0}{\gamma_s^2} + \frac{1}{\gamma_s^4}\right) + \left(\frac{\Delta L}{L}\right)_\beta\right], \quad (10)$$

where $\Delta\delta_{eq}$ is the deviation of the equilibrium level (average value) of momentum due to the orbit increasing in length in the transverse plane $(\Delta L/L)_\beta$ and due to synchrotron oscillation with amplitude δ_m, α_0, α_1 are the zero and first order momentum compaction factors, while γ_s is the Lorentz factor of the synchronous particle. Using γ_{eff}, we can assert: two particles are assumed to be the same, or, equivalently, the beams are identical in terms of spin behaviour if they have the same effective Lorentz factor averaged over all particles in the beam. This ensures it is no longer necessary to obtain a coincidence of trajectories, but instead only requires the condition of equality γ_{eff} for the CW and CCW beams. In this regard, before changing the polarity, we must calibrate the effective Lorentz factor. Calibration of the effective Lorentz factor is done via measuring spin precession in the horizontal plane where we have no contribution from Ω_{edm}. For that purpose, a special transverse spin rotator Wien filter is used in order to suppress the spin precession in the vertical plane without beam trajectory perturbation together with a small detuning of the beam energy from the magic value. This procedure allows one to change the direction of the invariant spin axis from horizontal to vertical. Using the fact that ν_s is an injective function of γ_{eff}, it follows that there exists a unique value, γ_{eff} at which the polarization vector is frozen with respect to the beam's momentum vector in the horizontal plane, i.e., ν_s = 0 in the rest frame. Since the tilt of the spin precession axis is the same for the CW and the CCW beams, $\lim_{\nu_s^{CCW} - \nu_s^{CW} \to 0} \Omega_{r,mdm}^{CCW} - \Omega_{r,mdm}^{CW} \to 0$. After calibrating the effective Lorentz factor, we turn off the Wien filter transferring the invariant spin precession axis from horizontal to vertical position and measure $\Omega_{CW} = \Omega_{r,mdm}^{CW} + \Omega_{edm}$.

Another important problem, the "geometric phase" (GP) error, is the accumulation of spin rotation in the vertical y–z plane caused by non-commuting rotations in the horizontal x–z and transverse vertical x–y planes. Formulated in the frequency domain language, it is a result of a lack of a definite direction of the spin precession axis. Our goal in minimizing the GP effect is to make the Ω_{edm} contribution to $\Omega = \left((\Omega_{edm} + \Omega_r)^2 + \Omega_y^2 + \Omega_z^2\right)^{1/2}$ much larger than that of Ω_y and Ω_z. That is, we have to fulfil the requirement $(\Omega_{edm} + \Omega_r)^2 > \frac{1}{2}\frac{\Omega_y^2+\Omega_z^2}{\Omega_{edm}}$. According to this equation, the restriction occurs at the values of Ω_y and Ω_z, which should have less of an effect on the total frequency Ω than the EDM: $\frac{\Omega_y^2+\Omega_z^2}{2\Omega_r} < \Omega_{edm}$. Since we expect the Ω_r in the range of 50 to 100 rad/sec, it follows that making Ω_y and Ω_z. < 10−3 rad/sec is sufficient to minimize the GP error to below the Ω_{edm} value. Note that the solution of the GP problem does not require knowledge of the precise values of Ω_y and Ω_z, they just have to be small.

Thus, FDM has significant advantages over the two methods discussed above: the method is based on measuring the spin precession frequency and the problems of the geometric phase and the transition from CW to CCW are solved.

ISBN: 978-3-95450-240-0 ISSN: 2673-5539 doi:10.18429/JACoW-RuPAC2021-TUB03

REFERENCES

[1] A. Sakharov. *J. Exp. Theor. Phys.*, vol.5, 24- 26, 1967.

[2] F.J.M. Farley, *et al*., Phys. Rev. Lett. 93, 052001, 2004.

[3] I.A. Koop, *Phys. Scr.* 014034, 2015.

[4] Y. Senichev, A. Aksentev, A. Ivanov and E. Valetov, "Frequency domain method of the search for the deuteron electric dipole moment in a storage ring with imperfections", Preprint 2017, arxiv:1711.06512 [physics.acc-ph]

[5] D. Anastassopoulos *et al.*, "AGS Proposal: Search for a permanent electric dipole moment of the deuteron nucleus at the 10^{-29} e cm level", BNL, 2008.

[6] Z. Bagdasarian *et al*., *Phys. Rev. ST Accel. Beams* 17, 052803, 2014.

[7] Y Senichev, R. Maier, D. Zyuzin, "Spin tune decoherence effects in electro-magnetic structures", in *Proc. 4th Int. Particle Accelerator Conf.(IPAC 2013),* Shanghai, China, May 2013, pp.2579-81. ISBN 978-3-95450-122-9

ISBN: 978-3-95450-240-0 ISSN: 2673-5539 doi:10.18429/JACoW-RuPAC2021-TUB04

DEVELOPMENT OF THE ELECTRON COOLING SYSTEM FOR NICA COLLIDER

M. Bryzgunov, A. Bubley, A. Denisov, A. Goncharov, V. Gosteev, V. Panasyuk, V. Parkhomchuk, V. Reva[1], A. Batrakov, E. Bekhtenev[1], O. Belikov, V. Chekavinskiy, M. Fedotov, K. Gorchakov, I. Gusev, I. Ilyin, A. Ivanov[1], G. Karpov, M. Kondaurov, N. Kremnev[1], D. Pureskin, A. Putmakov, D. Senkov, K. Shtro, D. Skorobogatov, R. Vakhrushev, A. Zharikov
Budker Institute of Nuclear Physics, Novosibirsk, Russia
[1]also at Novosibirsk State University, Novosibirsk, Russia

Abstract

The high voltage electron cooling system for the NICA collider is now under development in the Budker Institute of Nuclear Physics (Russia). The aim of the cooler is to increase ion beams intensity during accumulation and to decrease both longitudinal and transverse emittances of colliding beams during experiment in order to increase luminosity. Status of its development and results of tests of the cooler elements are described in the article.

INTRODUCTION

The NICA project is aimed to provide experiments with highly compressed baryonic matter with the help of colliding ion beams. In order to achieve project luminosity it is planned to use electron and stochastic cooling, which will help both during accumulation (to increase beam intensity) and during experiment (to compensate beam's emittance grow due to beam-beam effects, intra-beam scattering etc.).

Budker INP has big experience in production of electron cooling systems for different energies and now it develops project of high voltage electron cooling system (HV ECS) for the NICA. In Fig. 1 a 3-D model of the ECS is shown. Its design is based on design of HV electron cooler for COSY, produced by BINP [1]. The system consists of two almost independent coolers, which cool both colliding beams. Each cooler consists of high voltage system (which is placed in high pressure vessel, filled with SF_6, and which contains electron gun, electron collector, electrostatic tubes and HV power supplies), cooling section and transport channels (consisting of linear and bend magnets). Electron beam, emitted by cathode in electron gun, is accelerated by electrostatic tube to working energy. After that, it moves through transport cannel to the cooling section, where it interacts with ion beam. After the cooling section it moves back (through another transport channel) to high voltage system where it is decelerated and absorbed by collector surface. Such not standard scheme of ECS with whole high voltage system in one vessel is usual for high energy electron coolers and besides the COSY cooler it was realized on 4.3 MeV Fermilab electron cooler of the Recycler ring [2].

On whole trajectory from gun to collector electron beam moves in longitudinal magnetic field, which provides transverse focusing of the beam. In the cooling section longitudinal field provides, so-called, "fast" (or magnetized) electron cooling [3].

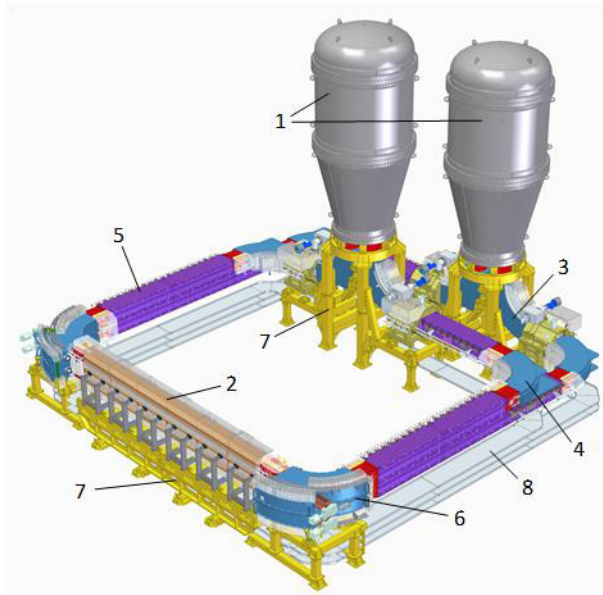

Figure 1: 3D model of the electron cooling system for NICA collider. 1 – high-voltage vessels, 2 – cooling section, 3 – vertical bend, 4 – horizontal bends, 5 – linear sections, 6 – toroid magnet, 7 – supports, 8 – cable channels.

HIGH VOLTAGE SYSTEM

The HV system of the cooler (Fig. 2) generally consists of HV column and HV terminal on its top. The column consists of 42 identical sections (Fig. 3). Each section contains 2 HV power supplies (up to 30 kV), connected in series, magnetic coils for longitudinal field, power supplies for coils and control electronics. The sections are separated from each other with insulating (plastic) supports. Section height is 48 mm, period is 64 mm. Connection of every section with control computer is realized with the help of wireless interface ZigBee. All sections are powered with the help of cascade transformer [4]. For this purpose each section of the transformer has small winding.

Two electrostatic tubes are installed in magnetic coils for beam acceleration and deceleration.

ISBN: 978-3-95450-240-0 ISSN: 2673-5539 doi:10.18429/JACoW-RuPAC2021-TUB04

In the centre of the column there is a special middle section of about 30 cm height, which contains magnetic elements and does not contains HV power sources. This section was added for diagnostic reasons (with BPMs) and for additional vacuum pumping.

High voltage terminal contains electron gun, collector, two solenoids (for gun and collector) and control electronics. The terminal is powered by upper winding of the cascade transformer.

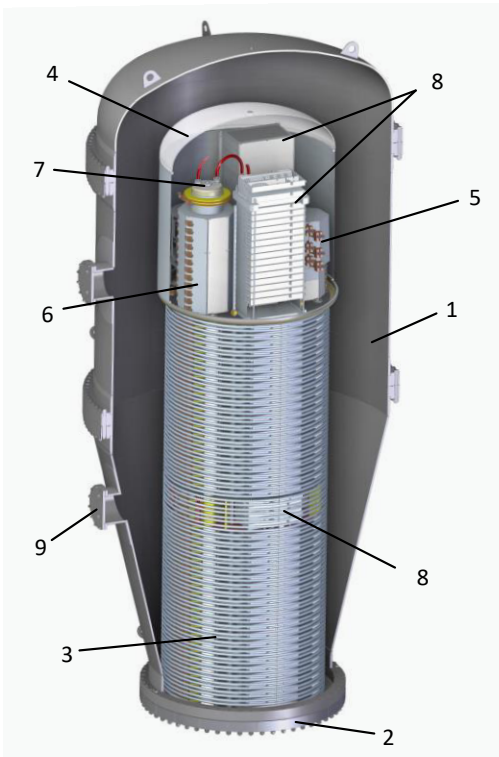

Figure 2: High voltage system of the electron cooler for NICA collider. 1 – pressure vessel, 2 – bottom flange, 3 – high voltage column, 4 – high voltage terminal, 5 – electron gun solenoid, 6 – electron collector solenoid, 7 – collector, 8 – middle section, 9 – side flange.

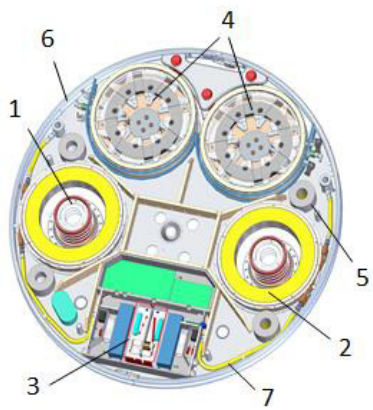

Figure 3: High-voltage section. 1 – electrostatic tube, 2 – magnetic coil, 3 – electronics unit, 4 – sections of cascade transformers, 5 – insulating supports, 6 – external ring, 7 – oil tubes.

In the COSY cooler one transformer was used for powering both column (consisting of 33 sections) and terminal. But efficiency of power transfer by cascade transformer decreases with increase of number of sections and, from experience, achieved during operation with the cooler, it look, that COSY variant is close to limits. In the NICA cooler it was decided to use 2 transformers in parallel: one for column and one for terminal.

CASCADE TRANSFORMER

The transformer consists of alternating ceramic and metal rings (Fig. 4). Inside the metal ring there is a magnetic circuit with two high-voltage sectioned windings and one winding under the potential of the magnetic circuit to power HV section. One high-voltage winding serves to transfer power to the next stage up, the other winding for connection with the lower section of the transformer.

The design of the cascade transformer is similar to the design of the COSY transformer, however, some changes have been made to improve its performance and simplify the manufacturing process. In particular, the primary and secondary windings are divided into 4 groups of 8 turns, instead of 2 groups of 14 turns. The metal rings are produced of aluminium instead of copper-covered stainless steel. Under the windings, directly on the core, a ring of thin fiberglass with a copper coating is placed to set the potential to the core.

To test the new design of the transformer, a 3-section prototype was made. According to the results of measurements, the parameters of the transformer are similar to parameters of the transformer of the COSY cooler. After the tests production of the transformer was started. Fig. 4 (c) shows first transformer after assembling.

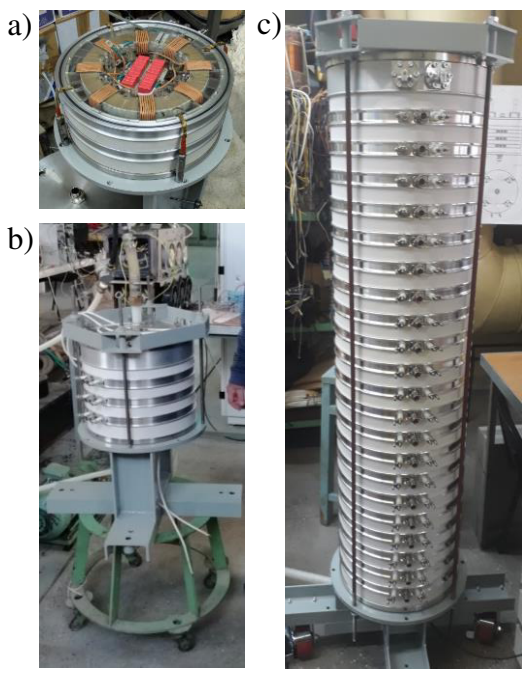

Figure 4: Cascade transformer production: a) transformer prototype during assembling, b) assembled prototype during tests, c) cascade transformer of the cooler.

ISBN: 978-3-95450-240-0 ISSN: 2673-5539 doi:10.18429/JACoW-RuPAC2021-TUB04

"GUN-COLLECTOR" TEST BENCH

Since ion beam diameter in the NICA is small, it was decided to decrease cathode diameter from 3 cm (as it was in previous coolers, produced by BINP) to 1 cm. For this purpose a new gun was constructed and special test bench was built for its testing (Fig. 5). The main magnetic element of the test bench is straight solenoid. Vacuum chamber with gun and collector is installed along solenoid's axis. For beam measurement the vacuum chamber contains special diagnostic node with wire profile monitor and BPM inside. The monitor provides measurements both electrical signal and optical (due to wire heating by electron beam).

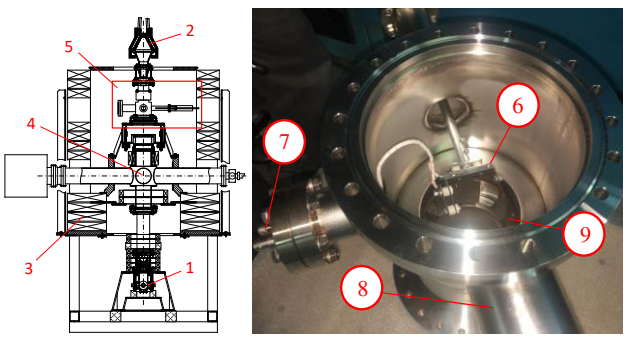

Figure 5: "Gun-collector" test bench (left) and diagnostic node of the test bench (right). 1 – electron gun, 2 – electron collector, 3 – solenoid, 4 – vacuum chamber, 5 – diagnostic node, 6 – wire support of the monitor, 7 – electric feedtroughs for the monitor, 8 – tube for vacuum window, 9 – BPM.

From electron cooling theory one can obtain, that cooling rate is inversely proportional to ion velocity to the 3-rd power [3]. As result, particles with smaller betatron amplitudes are cooled faster, then those with higher amplitudes. This can result is appearance of overcooled centre of ion beam.

According to [5], the controllability of electron current density profile is essential to prevent instability development in ion beams caused by overcooling of beam centre. By increasing electron emission from the cathode edges using the control electrode, the emission from the centre of the cathode can be suppressed by the space charge electrical field. In this case, the electron beam becomes "hollow". The cooling rate for ions with small amplitudes of betatron oscillations decreases; therefore, the ion beam cools more evenly.

Because of this, one of the most important goal of the test bench is testing the ability to vary the beam profile. On Fig. 6 first results of beam profiles measurements for different regimes of gun work are shown (the measurements are made from electrical signal). One can see, that the gun provides effective control of the beam. The results generally prove calculation results [6].

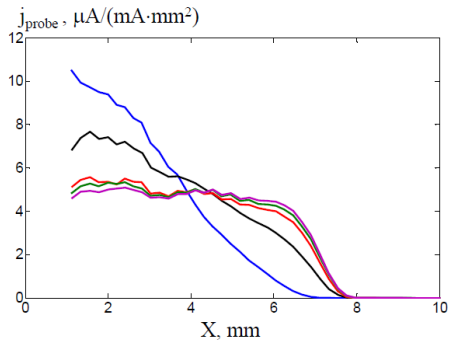

Figure 6: Beam profiles for different regimes of gun work.

CONCLUSION

Budker INP is actively developing project of the high voltage electron cooling system for the NICA collider. The most part of the design stage is passed and many elements of the cooler are already produced. At the same time, prototypes of some critical elements are produced and tested. Some prototypes (such as electron gun), are still being tested.

REFERENCES

[1] V. B. Reva et al., "COSY 2 MeV Cooler: Design, Diagnostic and Commissioning", in *Proc. 5th Int. Particle Accelerator Conf. (IPAC'14)*, Dresden, Germany, Jun. 2014, pp. 777-779. doi:10.18429/JACoW-IPAC2014-MOPRI075

[2] S. Nagaitsev, L. Prost, A. Shemyakin, "Fermilab 4.3 MeV electron cooler", https://arxiv.org/abs/1411.6994

[3] V.V. Parkhomchuk, A.N. Skrinsky, "Electron cooling: 35 years of development", *Physics–Uspekhi* 43:5, pp. 433–452, 200. doi: 10.1070/PU2000v043n05ABEH000741

[4] M. Bryzgunov *et al.*, "Energy transfer in the high-voltage electron cooler for the COSY synchrotron ring", *Instruments and Experimental Technics*, vol. 58, pp. 181-189, 2015. doi: 10.1134/S0020441215020165

[5] V. V. Parkhomchuk, "Development of a new generation of coolers with a hollow electron beam end electrostatic bending", in *Proc. of International Workshop on Beam Cooling and Related Topics (COOL05)*, Galena, Illinois, U.S.A., September 2005, paper CP821, pp. 249-258.

[6] A. P. Denisov *et al.*, "Design of a Compact Electron Gun for the High-Voltage Electron Cooling System of the NICA Collider", in *Proc. 12th Workshop on Beam Cooling and Related Topics (COOL'19)*, Novosibirsk, Russia, Sep. 2019, pp. 18-21. doi:10.18429/JACoW-COOL2019-MOA02

ISBN: 978-3-95450-240-0 ISSN: 2673-5539 doi:10.18429/JACoW-RuPAC2021-TUB07

THE CONCEPTUAL DESIGN OF THE 7.5 MeV/U LIGHT ION INJECTOR

S.M. Polozov, A.E. Aksentyev, M.M. Bulgacheva, O.A. Deryabochkin, M.S. Dmitriyev, V.V. Dmitriyeva, M.V. Dyakonov, V.S. Dyubkov, A.V. Gerasimenko, A.A. Gorchakov, M.A. Gusarova, M.A. Guzov, E.N. Indiushnii, O.A. Ivanov, A.M. Korshunov, K.I. Kozlovskiy, A.S. Krasnov, M.V. Lalayan, Y.Y. Lozeev, T.A. Lozeeva, A.I. Makarov, S.V. Matsievskiy, A.P. Melekhov, O.V. Murygin, R.E. Nemchenko, G.G. Novikov, A.E. Novozhilov, A.S. Panishev, V.N. Pashentsev, E.A. Plotnikov, A.G. Ponomarenko, A.V. Prokopenko, V.I. Rashchikov, A.V. Samoshin, A.A. Savchik, V.L. Shatokhin, A.E. Shikanov, K.D. Smirnov, G.A. Tsarev, S.A. Tumanov, I.A. Yurin, M.I. Zhigailova
National Research Nuclear University - Moscow Engineering Physics Institute, Moscow, Russia
N.V. Zavyalov, M.L. Smetanin, A.V. Telnov
RFNC-VNIIEF, Sarov, Nizhniy Novgorod region, Russia

Abstract

The new linac for light ion beam injection is under development at MEPhI. Such linac was proposed for acceleration of 7.5 MeV/nucleon ion beam with A/Z=1-3.5 and current up to 5 mA for proton and 0.4 pmA for light ions. The linac general layout will include two types of ion sources: ECR ion source for proton and He ions and laser ion source for ions form Li to O. Following the LEBT ions will be bunched and accelerated to the final energy using RFQ section and 14 IH-cavities. These IH-cavities will be identical (divided into two groups) and independently phased. All cavities will operate on 81.25 MHz. Results of the beam dynamics simulations and the cavities design will be presented in the report.

INTRODUCTION

Starting 2018 the new ion synchrotron complex is under development at RFNC-VNIIEF, Sarov. New complex will include booster and storage rings, two injectors LU1 (protons and light ions) and LU2 (heavy ions, designing at NRC Kurchatov Institute - ITEP) and many experimental channels. MEPhI is duty for LU1 linac which will accelerate ions from protons to oxygen up to energy of 7.5 MeV/nucleon with mass-to charge ratio A/Z<3.5.

LU1 linac will include two types of ion sources: ECR for protons and He beam and laser ion source for ions from Li to O. Both types of ion sources will be doubled to growth the reliability of the linac operation. All accelerating and bunching cavities will operate on the same frequency of 81.25 MHz. The low energy beam transport channel (LEBT) will be complex to compose beams from four ion sources. LEBT also will include buncher B1 for beams pre-bunching before the RFQ and first beam diagnostics devices block. RFQ will bunch and accelerate beam up to 820 keV/nucleon and should to provide the beam capturing coefficient not less than 90 % for all types of ions. Following RFQ section and medium energy transport line MEBT1 two groups of short 5-gaps independently feeded IH-cavities will be placed. The geometric velocity β_g will be constant for the group of cavities to reduce the linac cost. As it was shown due to the beam dynamics simulation it will be enough to have two groups of cavities with β_g=0.057 and 0.099 (six and eight cavities for the first and the second groups correspondently) to achieve the final beam energy of 7.5 MeV/nucleon. The second buncher B2 will be added to MEBT1 to control the bunch length and to chop the bunch tail. Two groups of cavities will also separated by short transport line MEBT2 includes one reserve buncher B3.

After acceleration the beam should be rotated at the angle ~40 degrees at the high-energy transport line (HEBT). After junction with the direct HEBT of LU2 the beam will start to prepare for injection into the storage ring. Note that it is planned to inject the continuous beam into the booster ring and we should to use a debuncher in HEBT for this aim

Finally, we will have 19 accelerating and bunching cavities for LU1 in total, they will operating on the same frequency of 81.25 MHz. The linac total length is about 40 m (without HEBT). All cavities will feed by solid state amplifiers.

ION SOURCES

As it was noted above LU1 linac will include four ion sources: two ECR and two laser ion sources. The key difficulty for the ECR design is the aim to generate both protons and He^{2+} ions in the same source and to have the necessary beam intensity. The operating frequency of 2450 MHz was choused for ECR due to availability of magnetrons and successful experience of its operation at MEPhI [1]. The magnet system for ECR was chosen basing on solid state magnets with mechanical motion of the sextupole trap and end rings. The simulation shows that the necessary p^+ and He^{2+} beam intensity will be achieved.

New laser ion source will be also designed basing on the old prototype operation experience. The laser ion source operates at MEPhI more that 30 years. It is used to generate different ion beams having single chatge state- and it was used to test the proposed technical solutions and to verify our analytical estimations for multi-charged beams. Unfortunately, the ion source is now equipped by low power (<450 mJ) laser, that prevents to generate multi-charged ions because this energy is lower that the

ISBN: 978-3-95450-240-0 ISSN: 2673-5539 doi:10.18429/JACoW-RuPAC2021-TUB07

ionization potential for the second electron. New plasma chamber was also designed to operate with different types of targets in the same session, Fig. 1. Two step motors will provide both "slow-step" motion of the target to replace the injured point and to change the target to the different material. Such design gives us the possibility to operate with eight targets.

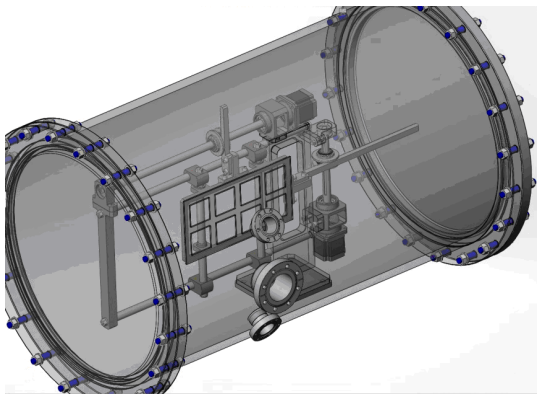

Figure 1: Discharge chamber for new laser ion (form Li to O) source.

RFQ SECTION

The RFQ section will be used both for beam bunching and following acceleration up to energy of 820 keV/nucleon. It was shown that the current transmission coefficient can be increased up to 95-97 % for all types of ions by means of short low field pre-buncher installed before RFQ, Fig. 2. The beam dynamics simulation was done using BEAMDULAC-RFQ code designed at MEPhI [2-6]. The pre-buncher using also provides two times lower output energy spectrum.

The four-vane RFQ cavity with magnetic coupling windows [7] was proposed for LU1. Such type of the cavity has compact design, it is comparatively simple for tuning and such linac was successfully designed, constructed and operated as the for-injector of the JINR Nuclotron-NICA complex [8-9]. The design of the RFQ cavity is shown in Fig. 3. The total length of the cavity is about 5 m. 12 plungers will be used for the operating frequency tuning, this number is enough to shift the frequency at the wide band of ±300 kHz. The RF design of the RFQ cavity will be discussed more detail in [10-11]. All necessary simulations of the cavity are close to finish and we plan to start the manufacturing of one cavity sector next year.

IH-CAVITIES

The beam dynamics for the regular part of LU1 was studied by the combination of analytical methods and numerical simulation as it was proposed in [12-14]. As known the synchronism condition violates for such system of cavities with constant geometrical velocity and more accurate treatment of the phase slipping is necessary to achieve correct results of the beam dynamics simulation. The beam dynamics simulation shows that the regular part of the linac will consists of two groups of IH-cavities with geometrical velocities βg=0.057 (six 5-gap cavities) and 0.099 (eight 5-gap cavities) to achieve the final energy of 7.5 MeV/nucleon. Results of the beam dynamics simulation are shown in Figs. 4 and 5. Fig. 4 illustrates the slipping factor inside the groups of cavities. Longitudinal and transverse phase spaces before the first cavity, after cavities No. 6 and No. 14 are shown in Fig. 5.

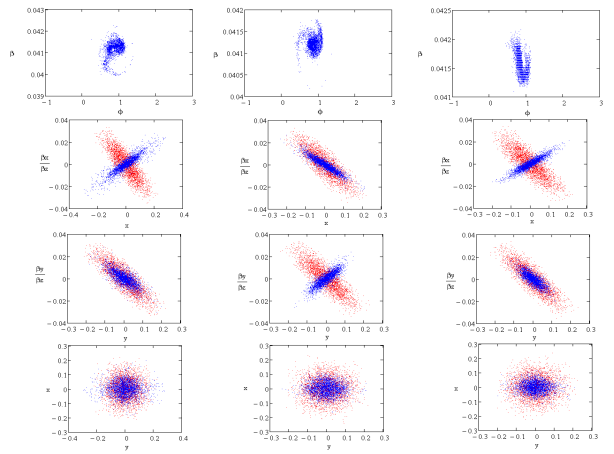

Figure 2: Beam dynamics simulation results for LU1 RFQ: A/Z=1, I=10 mA (at left), A/Z =2.0, I=1 мА (at center), A/Z=3.5, I=1 мА; all simulation were done with pre-buncher before RFQ; it are shown (top-to-bottom): longitudinal emittance, transverse emittances and the beam cross-section; all parameters are plotted by red color for the front-end of the RFQ and by blue color for the output.

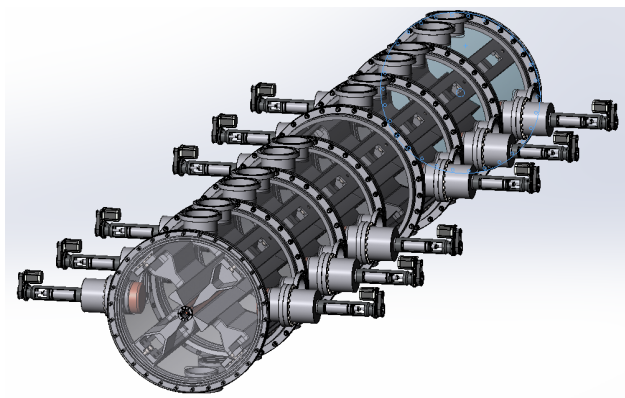

Figure 3: RFQ cavity design.

Further electrodynamics, thermal and mechanical simulations of IH-cavities were done and we start to prepare the construction of the full-scale model of first group cavity. The model of the cavity is shown in Fig. 6, it includes all necessary elements as well as vacuum and RF ports, plungers, vacuum valves, etc. Note that all mechanical tuning elements are placed inside of the cavity.

ISBN: 978-3-95450-240-0 ISSN: 2673-5539 doi:10.18429/JACoW-RuPAC2021-TUB07

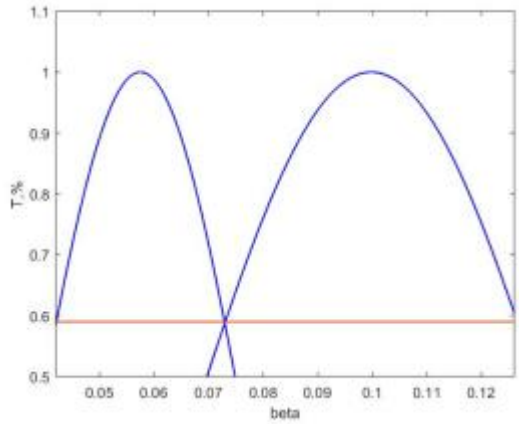

Figure 4: Slipping factor for the regular part of LU1, it includes 14 IH-cavities divided into two groups

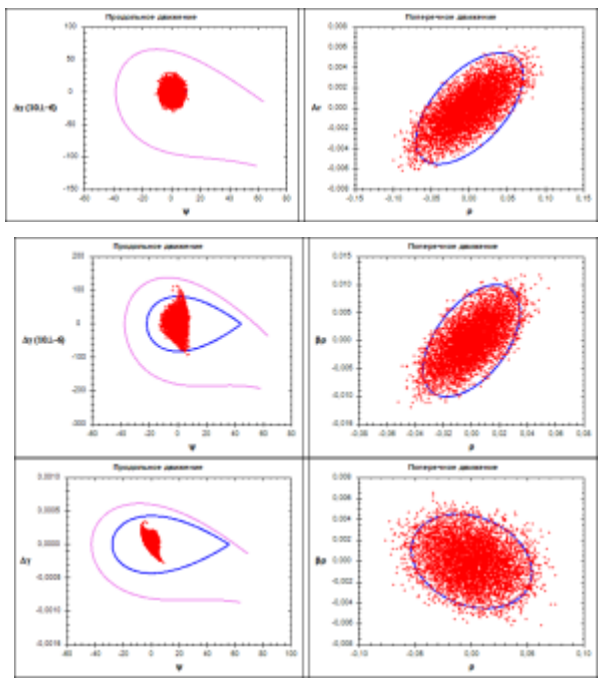

Figure 5: Beam dynamics simulation results for the regular part of LU1; longitudinal and transverse phase spaces are shown before the first cavity, after cavities No. 6 and No. 14.

BEAM TRANSPORT CHANNELS

LU1 will include four main beam transport channels (LEBT, MEBT1, MEBT2, HEBT) and 12 short channels between IH-cavities (with quadrupole doublets). The beam dynamics simulation for the transport channels shows that we can use one type of pulse quadrupoles for all channels and the maximal necessary gradient will be not higher than 22 T/m. The pulse regime provides us the low operation power and gives us possibility to use lenses without water cooling of coils. Channels will also include five dipoles, three in LEBT to join beams generated by four ion sources and two in HEBT. Please find the information about beamlines and magnets in [15].

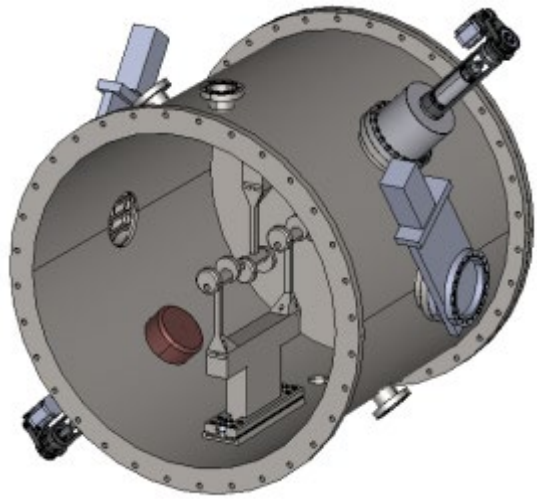

Figure 6: IH-cavity design.

VACUUM, CONTROL, DIAGNOSTICS

LU1 will be equipped by all necessary systems as well as vacuum, power, diagnostics, control, mechanic supports, etc. The vacuum system for LU1 is discussed in [16]. The control system of the new VNIIEF synchrotron complex is planned to build using high-level platform TANGO, but local control system for LU1 will be much more simple and will include data server and control server as well as control racks for all linac systems. Beam diagnostics is now a key point for successful accelerator commissioning and operation. It is planned that LU1 will include four main diagnostics blocks located in LEBT, MEBT1, MEBT2 and HEBT. We plan to use slit grids, paper port and Allison scanner to control the beam emittance and a bunch shape monitor also (all these components will be developed at INP RAS). Also we plan to use ~15 beam position monitors and ~18 current transformers to control the current parameters along the linac.

CONCLUSION

New injector LU1 is now under development for VNIIEF synchrotron complex under R&D. Such linac will accelerate light ions from protons to oxygen up to energy of 7.5 MeV/nucleon. Main features of LU1 were discussed in the paper as well as the beam dynamics simulation results. Cavities (RFQ, IH type and bunchers) preliminary design is close to finish today and we hope that tests of RFQ and IH-cavity prototypes will start next year.

REFERENCES

[1] M. Dmitriyev *et al.*, "Magnetic System With Variable Characteristics for a 2.45 GHz ECRIS", presented at the 27th Russian Particle Accelerator Conf. (RuPAC'21), Alushta, Russia, September 2021, paper TUPSB38, this conference, 2021.

ISBN: 978-3-95450-240-0 ISSN: 2673-5539 doi:10.18429/JACoW-RuPAC2021-TUB07

[2] E.S. Masunov, S.M. Polozov, "The new version of BEAMDULAC code for high intensity ion beam dynamics", *Prob. of Atomic Sci. and Tech., Series Nuclear Physics Investigations,* N 3 (47), pp. 119-121, 2006.

[3] E.S. Masunov, S.M. Polozov, "BEAMDULAC code for numerical simulation of 3D beam dynamics in a high-intensity undulator linac", *Nucl. Instrum. Methods Phys. Res., Sect. A*, 558, pp. 184–187, 2006.

[4] S.M. Polozov, "Ion beam space charge neutralization using for beam intensity increase in linacs", *Prob. of Atomic Sci. and Tech., Series Nuclear Physics Investigations*, 3 (79), pp. 131-136, 2012.

[5] S.M. Polozov *et al.*, "Beam Dynamics Simulations and Code Comparison for a New CW RFQ Design", Proc. of the 57th ICFA Advanced Beam Dynamics Workshop on High-Intensity, High Brightness and High Power Hadron Beams, HB'2016, pp. 188-190, 2016. doi:10.18429/JACoW-HB2016-MOPL004

[6] S.M. Polozov *et al.*, "Beam Dynamics Study for the New CW RFQ", Proc. of RuPAC'16, 2016, pp. 267-269. doi:10.18429/JACoW-RuPAC2016-TUPSA026

[7] V.A. Andreev, Patent US5483130, 1996.

[8] V.A. Andreev *et al.*, "Reconstruction of light and polarized ion beam injection system of JINR Nuclotron-NICA accelerator complex", *Prob. of Atomic Sci. and Tech., Series Nuclear Physics Investigations*, 6 (88), 8-12, 2013.

[9] A.V. Butenko *et al.*, "Commissioning of New Light Ion RFQ Linac and First Nuclotron Run with New Injector", Proc. of RuPAC'16, 153-155, 2016. doi:10.18429/JACoW-RuPAC2016-FRCAMH02

[10] M.A. Guzov *et al.*, "The Beam Dynamics and Elecrodynamics Characteristics of 800 keV/nucleon RFQ", presented at the 27th Russian Particle Accelerator Conf. (RuPAC'21), Alushta, Russia, September 2021, paper MOPSA03, this conference.

[11] S.M. Polozov *et al.*, "Optimization of the RFQ Electrode Construction for Multipactor Discharge Prevention", presented at the 27th Russian Particle Accelerator Conf. (RuPAC'21), Alushta, Russia, September 2021, paper WEPSC11, this conference.

[12] A.V. Samoshin, "Complex Approach of Beam Dynamics Investigation in SC LINAC", *Prob. of Atomic Sci. and Tech., Series Nuclear Physics Investigations*, 4 (80), 78 – 82, 2012.

[13] E. S. Masunov, A.V. Samoshin, "Beam focusing in a linear ion accelerator consisting of a periodic sequence of independently phased superconducting cavities", *Tech. Phys.*, 55, Issue 7, 1028-1035, 2010.

[14] E. S. Masunov, A.V. Samoshin, "Investigation of beam dynamics in a linear superconducting heavy-ion accelerator", *At. Energy*, 108, Issue 2, 141-153, 2010.

[15] I. Yurin *et al.*, "Light Ion Accelerator Magnets", presented at RuPAC'21, presented at the 27th Russian Particle Accelerator Conf. (RuPAC'21), Alushta, Russia, September 2021, paper WEPSC21, this conference.

[16] V.L. Shatokhin *et al.*, "Optimization of Accelerators Vacuum Structures Pumping", presented at the 27th Russian Particle Accelerator Conf. (RuPAC'21), Alushta, Russia, September 2021, paper WEPSC10, this conference.

ISBN: 978-3-95450-240-0 ISSN: 2673-5539 doi:10.18429/JACoW-RuPAC2021-TUC01

STATUS OF THE KURCHATOV SYNCHROTRON RADIATION SOURCE

V. Korchuganov, A. Belkov, Y. Fomin, E. Kaportsev, Yu. Krylov, V. Moiseev, K. Moseev, N. Moseiko, D. Odintsov, S. Pesterev, A. Smygacheva, A. Stirin, V. Ushakov, A. Valentinov
NRC Kurchatov Institute, Akademika Kurchatova Sq., 1, Moscow, 123182 Russia

Abstract

The Kurchatov synchrotron radiation source goes on to operate in the range of synchrotron radiation from VUV up to hard X-ray. An electron current achieves 120 mA at 2.5 GeV, up to 12 experimental stations may function simultaneously. Improvement of the facility according Federal Program of KSRS modernization is in progress. Two 3 Tesla superconducting wigglers have been installed at main ring at 2019. They were tested with small electron beam current at 2020-2021. Wigglers' influence on beam parameters is much closed to calculated value. Vacuum system has been upgraded at 2020. In 2021 control system will be completely modified. Manufacturing of third 181 MHz RF generator, new preliminary amplification cascades and new waveguides for all three generators continues in Budker Institute (Novosibirsk). Preparation of great modernization of the whole facility according Federal Program for science infrastructure development has been started.

INTRODUCTION

A 2.5 GeV electron storage ring Siberia-2 is a main source of synchrotron radiation (SR) at Kurchatov Synchrotron Radiation Source (KSRS) facility. A magnetic structure of Siberia-2 provides 98 nm·rad horizontal emittance of an electron beam, electron current achieves 150 mA. At present Federal KSRS modernization program (below – Program 1) is in progress, it was prolonged till 2022. Within the scope of Program 1 a third 181 MHz RF generator was manufactured in addition to two existing generators of Siberia-2. Besides 2 new identical superconducting wigglers (SCW) with 3 Tesla maximal magnetic field were put in operation during 2019 – 2021. They were tested with small electron beam. In 2019 – 2020 a modernization of vacuum system was completed, now control system modernization is close to completion.

At 2020 a preparing to deep KSRS modernization has been started according to Federal Program for Scientific Infrastructure Development (below – Program 2). As a result of Program 2 all KSRS accelerators must be replaced to new ones. New main 2.5 GeV KSRS ring should have horizontal emittance less than 3 nm·rad and top-up injection from booster synchrotron. Only RF system, SCWs and SR beamlines will be retained from old KSRS equipment. Because of Program 2 appearance some items were cancelled from Program1.

OPERATIONAL STATISTICS

As a rule Siberia-2 operates for SR users during 9 months per year. It functions during 3 or 4 weeks in around-the-clock mode from Monday to Saturday. Then one week of preventive maintenance and machine tuning follows. Usually there is one beam storing per day. Storing of 150 mA takes approximately one hour, then energy ramping occurs for 3 minutes with 2 - 3 % loss of current. Then beam current slowly decreases down to 40 – 50 mA so new storing is needed. Beam lifetime at 2.5 GeV depends on vacuum level and beam integral accumulated from the moment of last vacuum chamber violation.

As a result of KSRS development a stable facility operation was achieved during last several years (see Table 1, values for 2021 correspond to first half of the year.). But prominent decrease of these values occurred in 2020. Mostly it was caused by coronavirus pandemic which lead to KSRS shutdown at April-May and December. A long summer break for vacuum system modernization was one more reason. Finally initial plan for duration of users' work was completed only by 55% (in comparison with 100 – 110% during previous 4 years). Activity of SR users also was lower for the same reasons. But in 2021 all values became close to normal ones.

Table 1: Statistics of Siberia-2 Operation for last 4 Years

Parameter	2018	2019	2020	2021
Time for users, hours	3035	2728	1202	1706
Beam current integral, A·hours	227.1	200.1	88.8	105.0
Average number of stations in use	7.4	7.4	5.6	10.6
Average current, mA	74.8	73.4	73.9	61.5

FEDERAL KSRS MODERNIZATION PROGRAM (PROGRAM 1)

KSRS modernization according Program 1 should not change overall scheme of the facility, all magnetic elements are the same. The facility still consists of two storage rings (Siberia-1 and Siberia-2), linac and two

ISBN: 978-3-95450-240-0 ISSN: 2673-5539 doi:10.18429/JACoW-RuPAC2021-TUC01

transport lines. Realization of Program 1 has been longed till the end of 2022. Some points of Program 1 are described below.

RF System

RF system modernization includes: manufacturing of third RF generators for Siberia-2 and modernization of preliminary amplification cascades of two existing RF generators; manufacturing of low and high voltage supply racks; racks with control equipment; new waveguides. All three RF generators will be identical. All new parts of RF system were produced in Budker Institute of Nuclear Physics (BINP, Novosibirsk). They will be sent to Kurchatov Institute at the end of 2021. An assembling of RF equipment is included to Program 2 as well as production of supplying and cooling service lines and electricity supply system.

Vacuum System

KSRS vacuum system has got a lot of new equipment. 15 new pneumatic-drive vacuum valves were installed at Siberia-2, one as minimum for every straight section, two for injection section and for sections with superconducting wigglers. Now there is a possibility to produce repair of the chamber only at separate regions. Before it only RF cavities could be isolated. Four valves were installed at beam transport lines. Siberia-2 has got 21 new BPMs in addition to 24 old ones. Five new BPMs mounted on transport line from Siberia-1 to Siberia-2 instead of four BPMs with old design. Most of ion pumps were replaced at Siberia-2, titanium evaporation units were updated in all ion pumps. Also modernization includes new vacuum meters, bells, mass-spectrometers, new aluminum vacuum chambers for Siberia-2 straight sections.

Two new superconducting wigglers SCW2 and SCW3 (2 or 3 means a number of Siberia-2 superperiod) were installed in 2019 summer. Additional photon absorber was added to SCW straight section in order to protect wiggler vacuum chamber from synchrotron radiation from previous bending magnet. At the same time part of vacuum chambers near old wiggler SCW1 was replaced in order to increase vertical aperture for SR beam from SCW1. All other works were made in 2020. An outgassing of Siberia-2 vacuum chamber was done after all; electron current value and beam lifetime sufficient for SR users were achieved at November of 2020.

New Superconducting wigglers

BINP produced for KSRS two identical superconducting wigglers in 2019 [1]. Maximal magnetic field of SCW equals 3 Tesla with 48 mm period. Wiggler's magnet consists of 54 poles: 50 central poles with nominal field 3 T and 4 side poles. SCWs were transported to KSRS and tested outside Siberia-2 shielding. Nominal field was achieved successfully. After that wigglers were installed on Siberia-2. View on SCW3 is presented on Fig. 1. Simultaneously special technological area was constructed for installing of wiggler's equipment (power supplies, compressors, water cooling systems and computers). The area is situated at the level of the shielding roof inside the ring. Tracks for helium flexlines, feeding and control cables, from the technological area to wigglers were also mounted.

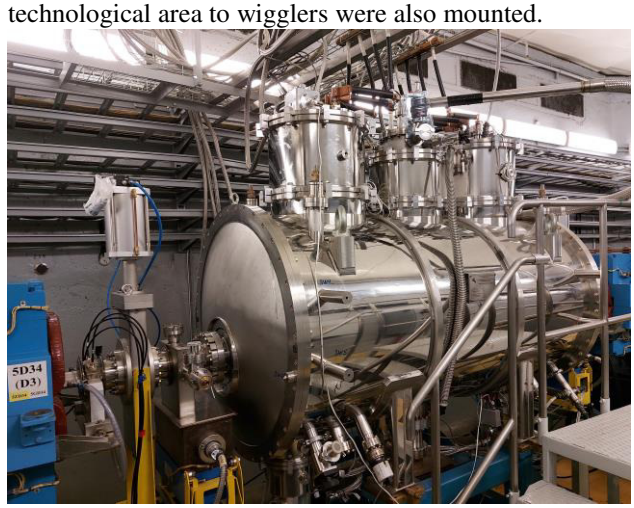

Figure 1: New 3 Tesla wiggler on Siberia-2 (SCW3).

At the beginning of 2020 SCW3 was tested with 3 T with electron beam, two wigglers were tested simultaneously in 2021 after assembling of all supplying equipment. Electron current didn't exceed 4 mA. Larger current is not possible yet, because there are not adequate photon absorbers in SCW's beamlines. Absorbers inside Siberia-2 vacuum chamber are not dedicated for great SR power density from wigglers. The power density can achieve 1000 W/mrad in the center of SR beam for 100 mA electron current at 2.5 GeV. Total emitted SR power will be 4.2 kW in this case.

Wigglers strongly effects on beam dynamics in the machine. They cause vertical betatron tune shift, changes in betatron functions, horizontal emittance, power losses per turn and energy spread in the beam. In order to minimize wigglers' influence SCW are installed in dispersion-free straight section with small vertical betatron function.

Figure 2 presents dependence of betatron tune shifts on magnetic field in SCWs during its separate operation. Then they are work together a total betatron tune shift is coincide with sum of individual values with good accuracy. A dependence of vertical betatron tune shift on SCW field is close to quadratic one. It corresponds to theory if vertical betatron function in the center of SCW equals 0.75 m (SCW2) and 0.8 m (SCW3).

The wigglers cause closed orbit distortion at all machine azimuths. Maximal horizontal orbit distortion (60 microns at 3 T in both SCWs) is relatively small in comparison with beam size. Besides it can be decreased by changing proportions of supplying currents. Vertical orbit distortion achieved 450 microns at 3 T in both wigglers. It means discrepancy between physical and magnetic axes of the wigglers. Vertical shift of magnetic axe is equal to 2 – 2.5 mm. It is rather big value in comparison with vertical aperture of SCW's vacuum chamber (10 mm). However such orbit distortion can be

ISBN: 978-3-95450-240-0 ISSN: 2673-5539 doi:10.18429/JACoW-RuPAC2021-TUC01

corrected by dipole correctors of the ring. Besides correction of the wiggler's vertical position may be done.

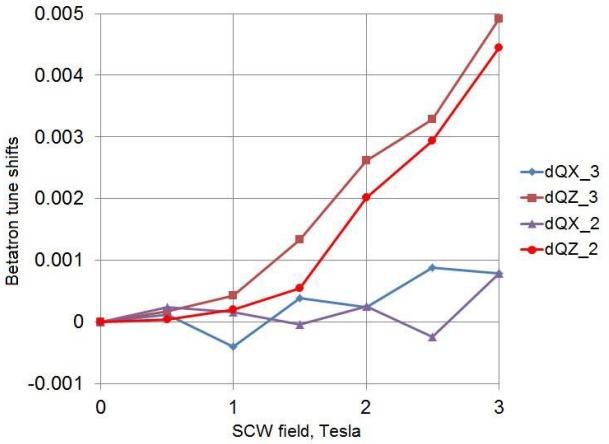

Figure 2: Dependence of betatron tune shifts dQX (horizontal plane) and dQZ (vertical plane) on wiggler's field during separate operation of SCW2 and SCW3.

KSRS control System

KSRS control system provides management of more than 2000 executive channels and 5000 measuring ones. At present control system includes two great parts: one part under control of CitectSCADA server (most of the equipment), second under control of PC CANServer (magnets and RF generator of Siberia-2 injection complex, pulse synchronization). Second part so far uses old CAMAC modules. Closed orbit in Siberia-2 and beam position in transport line are also measured independently. CANbus is preferably used to connect hardware. Main ideas of the modernization are to organize unified control system under management of modern version of CitectSCADA, to proceed to Ethernet links and optic cables for pulse synchronization. Modern control system has to ensure stable and reliable operation of KSRS, to increase useful beam parameters for SR users. It should contain new subsystems and hardware listed below:

- For vacuum system: 65 new modules BUP-M for ion pumps control, 12 new racks in Siberia-2 hall for Ti evaporation units and vacuum valves control.
- For RF system: new modules for all RF generators control, measurement of RF power in waveguides and temperature of RF cavities.
- New pulse synchronization system using optic cables, removal of CAMAC modules.
- For magnet system: 60 new modules BUK-M for high- and low-current power supplies control.
- New thermal stabilizing scheme for linac structure.
- Additional modules Libera Brilliance for Siberia-2 closed orbit measurement, 5 new modules Libera Spark for trajectory measurements in electron transport line. 7 new racks for Libera modules in Siberia-2 hall. All these modules are manufactured by International Technology (Slovenia).
- New server hardware and terminal devices.
- System for integrating pulse magnets' supply currents.

Also new control system has to include KSRS subsystems that were modernized earlier:

- Control of movable SR absorbers.
- Themperature control system.
- System of unified time.
- Pulse magnets' power supplies.
- Wigglers' control systems.
- Electron beam current measurement.

New control system software should provide reliable management of all KSRS subsystems, execution of necessary operation algorithms, collecting, transporting, representation, storing of all data, and notification about emergency situations.

FEDERAL PROGRAM FOR SCIENTIFIC INFRASTRUCTURE DEVELOPMENT (PROGRAM 2)

The Program 2 has to be finished in 2027. According to this Program all KSRS accelerators must be dismounted and be replaced with new ones. Instead of Siberia-2 with 98 nm·rad horizontal emittance new SR source should appear with emittance less than 3 nm·rad. A booster synchrotron will be used as injector to new ring. Injection is planned on working energy 2.5 GeV with 1 second cycle. New linear accelerator with energy 200 MeV will serve as injector for the booster synchrotron. More details of Program 2 are presented in [2]. Part of modern KSRS equipment will stay in new facility: RF system (after modernization according Program 1), superconducting wigglers, SR beamlines and part of control system modules. After Program 2 appearance several items of modernization were moved from Program 1 to Program 2. Among them mounting of new RF generator and waveguides, water cooling system, electric power supply system should be mentioned. Because of Program 2 appearance some items of Program 1 was eliminated. For example, modernization of high-current power supplies was cancelled.

CONCLUSION

KSRS is keeping on working effectively for SR users. Present modernization has to provide improvement of facility parameters. As a result of global modernization according to Federal Program of Scientific Infrastructure Development new bright source of synchrotron radiation will be created.

REFERENCES

[1] V.Korchuganov *et al.*, "New Superconducting Wigglers for KSRS", in *Proc. RUPAC'18*, Protvino, Russia, Oct.2018, pp.407-409. doi:10.18429/JACoW-RUPAC2018-THPSC04

[2] V.Korchuganov *et al.*, "Concept of a New Kurchatov Synchrotron Radiation Source", presented at RUPAC'21, Alushta, Russia, Sep.2021 paper TUC02, this conference.

ISBN: 978-3-95450-240-0 ISSN: 2673-5539 doi:10.18429/JACoW-RuPAC2021-TUC03

DEVELOPMENT OF POWERFUL LONG-PULSE THz-BAND FEL DRIVEN BY LINEAR INDUCTION ACCELERATOR*

N. Yu. Peskov†, V. I. Belousov, N. S. Ginzburg, D. I. Sobolev and V. Yu. Zaslavsky,
Institute of Applied Physics, Russian Academy of Sciences, Nizhny Novgorod, Russia
A. V. Arzhannikov, D. A. Nikiforov, E. S. Sandalov, S. L. Sinitsky,
D. I. Skovorodin, A. A. Starostenko, and K. I. Zhivankov
Budker Institute of Nuclear Physics, Russian Academy of Sciences, Novosibirsk, Russia

Abstract

Project of high-power long-pulse sub-THz to THz-band FEL is under development based on the linac "LIU" of the new generation forming 5 - 20 MeV / 2 kA / 200 ns electron beam. The aim of this project is to achieve a record sub-GW power level and pulse energy content up to 10 - 100 J at the specified frequency ranges. In the present paper, results of electron-optical experiments on the formation of an electron beam with parameters acceptable to drive the FEL are discussed. Helical pulse undulators were elaborated for pumping operating transverse oscillations of the beam electrons. As a key component of the electrodynamic system of the FEL-oscillator, the possibility of using advanced Bragg resonators based on the coupling of propagating and quasi-cutoff waves, which are capable to provide stable narrow-band generation under conditions of substantial oversize of the interaction space, is analyzed.

INTRODUCTION

Project of free-electron laser (FEL) is under development in collaboration between BINP RAS (Novosibirsk) and IAP RAS (Nizhny Novgorod) based on a new generation of induction linac "LIU" 5 - 20 MeV / 2 kA / 200 ns implemented in recent years at BINP RAS [1]. The use of such beam makes it possible to realize ultra-high power long-pulse FEL operating from sub-THz to THz frequency range [2]. Principal problems in realization of this generator include: (a) formation of the relativistic electron beam (REB) with parameters acceptable for operation in the short-wavelength ranges, (b) development of undulator for pumping operating transverse oscillations in the beam, and (c) elaboration of electrodynamic system that can provide stable narrow-band oscillation regime in a strongly oversized interaction space.

Initial proof-of-principle experiments are planned to start at the "LIU-5" accelerator in the 0.3 THz frequency range, with prospects of transition to 0.6 THz range and higher frequencies after positive results would be demonstrated. In the paper, the design parameters of the FEL project are discussed. Results of electron-optical experiments on the beam formation are presented. Structural elements of the FEL magnetic system based on helical undulator and a guide solenoid that provides intense beam transportation were elaborated. An electrodynamic system was proposed exploiting a new modification of oversized Bragg structures, so-called advanced Bragg structures, which have significantly improved selective properties. Structures of such type were designed with the diameter of 20 and 40 wavelengths for operation in specified frequency ranges.

RESULTS OF ELECTRON-OPTICAL EXPERIMENTS AT THE LINAC "LIU"

The experimental basis for realization of the novel FEL scheme is the "LIU-5" accelerator complex [1] comprising a 2 MeV thermionic injector and the induction accelerating sections (total number of 8 with the acceleration of ~ 0.4 MeV each), which finally provide formation of 5 MeV beam with the current of up to 2 kA, duration of 200 ns and diameter of ~ 4 cm at the output. Beam focusing between these sections is provided by the pulsed magnetic lenses of ~ 0.2 T.

To conduct experiments on sub-THz /THz generation in the FEL, it is necessary to perform a significant compression over the beam cross-section from the size given above to the required diameter D_{beam} ~ 5 - 7 mm and further transportation of the beam along the interaction region of about 1 - 1.5 m without loss of current. Based on the existing electron-optical system of the "LIU-5", the beam injection into the undulator was designed using magnetic lens of the accelerator and focusing pulsed solenoid of ~ 0.4 T. Simulations of the beam dynamics in this magnetic system were carried out using WARP code (which takes into account the electric and magnetic fields of an intense REB) and demonstrated possibility to compress the beam with measured emittance to the diameter needed to drive the FEL (see Fig. 1).

Schematic of experiments on the injection of an electron beam formed by the linac "LIU-5" into the FEL electron-optical system and its further transportation is shown in Fig. 1. As a result of the experiments, the required beam compression was realized. Beam current transmission through the vacuum channel was obtained with an efficiency of about 90%, which, however, was accompanied by reduction in the beam pulse duration to 80 - 100 ns due to the cutting of its leading and trailing edges. Currently, additional tuning of the accelerator and the magnetic system is being carried out, which should allow transportation of the compressed beam through the FEL interaction space to be close to 100% without beam pulse shortening. In this case, according to the simulation, energy spread in the beam is expected to be less than 1%.

* Work supported by the Russian Science Foundation, grant 19-12-00212
† peskov@ipfran.ru

ISBN: 978-3-95450-240-0 ISSN: 2673-5539 doi:10.18429/JACoW-RuPAC2021-TUC03

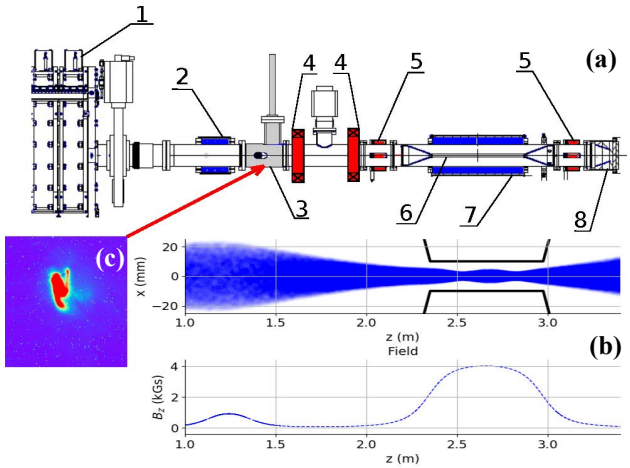

Figure 1: (a) Scheme of beam compression experiment: 1 - output accelerating module of the linac "LIU-5", 2 - matching pulsed magnetic lens, 3 - transient radiation detector, 4 - dipole correctors, 5 - beam position detectors, 6 - vacuum chamber, 7 - guide solenoid and 8 - beam collector. (b) Results of simulations of the beam dynamics in the compression system using the WARP code (the beam envelope is shown). (c) The image of the beam on the transient radiation detector at the entrance of the compression system.

DESIGN OF PULSED HELICAL UNDULATOR AND GUIDE SOLENOID

Constructing the pulsed undulators, we applied our experience accumulated in the previous FEM experiments, which were successfully realized up to now in the millimeter wavelength bands in collaboration between IAP RAS and JINR (Dubna) [3]. To improve the uniformity of the transverse magnetic field distribution over the undulator cross-section and increase the ratio: magnetic field amplitude to current in the windings, we exploited a bifilar helical configuration composed of the four conductors (see Fig. 2a), in which the conductors with the same current direction are positioned at an azimuthal angle of $\varphi \sim 60°$ to each other [4]. For pumping operating bounce oscillations in magnetically-guided REBs, undulators with adiabatically up-tapered section are traditionally applied at the entrance. For realization of such an input (and output) section of the undulator, an "optimized" tapered configuration was developed, based on the simultaneous application of two methods: (i) increasing the distance of the conductors from the axis using a conical section, and (ii) approaching the conductors with the currents of opposite directions in the winding. Sample of the undulator, which implements the proposed "optimized" profiling, is shown in Fig.2a. Results of 3D simulations demonstrate that an undulator with such an input section provides smooth rise of the magnetic field amplitude with no parasitic spatial "spikes", which was confirmed by the "cold" magnetic measurements (Fig. 2b).

The so-called reverse guide field regime [5, 6] was chosen for the FEL operation, which, according to the simulation [3], possesses a low sensitivity to the initial spread of the REB parameters and provides a high-quality helical beam formation in the slowly up-tapered undulator entrance. Simulations demonstrated that in this regime amplitude of "parasitic" cyclotron oscillations never exceeded 2 - 3% of the operating bounce oscillations acquired by the electrons in the entire range of designed values of the guide and the undulator fields. As the theoretical analysis shows, these beams allow for implementation of the sub-THz/THz FEL with relatively high electron efficiency.

DESIGN AND TESTING OF ADVANCED BRAGG RESONATORS

One of the key problems in realization of the FEL-oscillator is development of an electrodynamic system that can provide stable narrow-band oscillation regime in a strongly oversized interaction space. Moreover, for transportation of intense electron beam, which is realized currently at the "LIU-5" accelerator, the resonator diameter D should in orders exceeds the radiation wavelength λ when operating from sub-THz to THz band, i.e. $D/\lambda \sim 20$ to 50.

This problem can be solved using advanced Bragg structures based on coupling of the propagating and quasi-cutoff waves. For realization of such coupling, the corrugation period should be approximately twice as long as in "conventional" structures. Involvement of a quasi-cutoff wave in the feedback loop, similarly to gyrotrons or orotrons, results in significant purification of transverse mode spectrum of the resonator under the substantial oversize parameter and improvement of selective properties in comparison with the Bragg structures of "conventional" type. Thus, FELs based on advanced Bragg resonators combine the advantages of the gyrotrons (high selectivity over the transverse mode index) with those of relativistic oscillators (operation at short wavelength

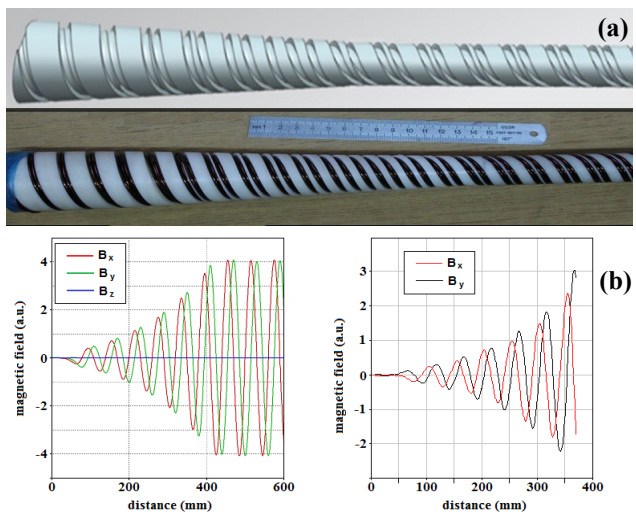

Figure 2: (a) Photograph of 3D model (top) and experimental prototype (bottom) of the "improved" undulator with a period d_u = 6 см, and (b) results of 3D simulations (left) and "cold" measurements (right) of longitudinal structure of magnetic field at the undulator entrance.

ISBN: 978-3-95450-240-0 ISSN: 2673-5539 doi:10.18429/JACoW-RuPAC2021-TUC03

bands with high pulsed power level). According to the theoretical analysis carried out in the frame of averaged models as well as to the 3D simulations, advanced Bragg structures allow selective excitation of the operating mode at the transverse sizes sufficient for realization of FELs up to THz frequencies [7].

Results of 3D simulations (code CST Microwave Studio) of cylindrical advanced Bragg structures in the ranges of 0.3 THz and 0.6 THz are shown in Fig. 3a and Fig. 4. These structures have approximately the same diameter of ~ 20 mm acceptable for transportation of the beam formed at the "LIU-5" accelerator. The oversize factor D/λ of these structures is about 20 and 40, respectively and their feedback loop is formed by two counter-propagating $TE_{1,1}$ waves (the forward propagating wave of this type is chosen to be an operating one) and cutoff waves of $TE_{1,20}$ and $TE_{1,40}$ types. Simulations demonstrate that even with such large transverse dimensions, novel Bragg structures provide selective reflection for the operating mode with an efficiency of ~ 80 - 90% in power. Results of "cold" electrodynamic tests of advanced Bragg structure carried out at 0.3 THz band coincide with the simulations and confirm the existence of effective narrow-band reflection in the designed frequency range (Fig. 3b).

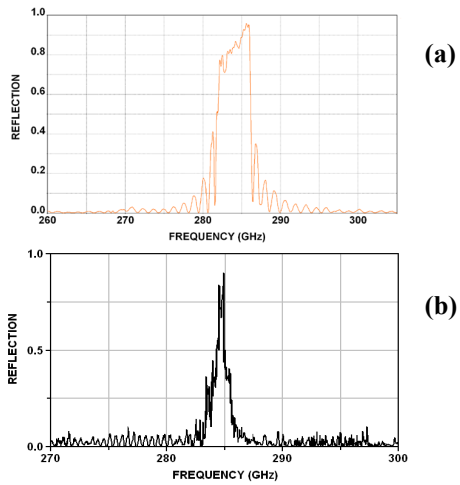

Figure 3: Results of (a) 3D simulations and (b) "cold" tests of advanced Bragg structure having oversize factor $Ø/\lambda$ ~ 20 and operating at 0.3 THz band (feedback loop $TE_{1,1} \leftrightarrow TE_{1,20\ -\ cutoff} \leftrightarrow TE_{1,1}$, length l_{ad} = 10 cm, corrugation period d_{ad} = 1.05 mm and depth r_{ad} = 0.3 mm).

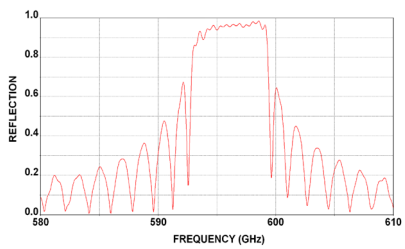

Figure 4: Results of 3D CST simulations of advanced Bragg structure with oversize factor D/λ ~ 40 in the frequency band of 0.6 THz (l_{ad} = 7.5 см, d_{ad} = 0.5 мм, r_{ad} = 0.3 мм, feedback loop $TE_{1,1} \leftrightarrow TE_{1,40\text{-cutoff}} \leftrightarrow TE_{1,1}$).

CONCLUSION

Summarizing, theoretical studies of electrodynamic, magnetic, and electron-optical systems, simulations of processes of formation of intense REBs and their interaction with RF-waves in new high-selective electrodynamic systems allowed developing the project of powerful FEL operating from sub-THz to THz bands based on the linac "LIU". The key components for experimental realization of these FEL-oscillators have been designed and studied in "cold" tests. Assembly of the installation components was started for their full-scale tests.

It is important to underline that operability of novel components of electron-optical ("optimized" helical undulator) and electrodynamic (advanced Bragg structures) systems were studied in the proof-of-principle experiment carried out in collaboration between IAP RAS and JINR (Dubna) based on the induction linac "LIU-3000" 0.8 MeV / 200 A / 200 ns. In these experiments [8], high-efficiency FEM-oscillator was realized at W-band, and stable narrow-band operation was demonstrated under the transverse oversize factor D/λ ~ 5. Increase in the radiation frequency in the JINR-IAP FEM was limited by the electron beam energy at this accelerator and the achievable undulator periods. Meanwhile, this FEM-oscillator can be considered as a prototype for the FEL project, which is in progress in the frame of BINP - IAP cooperation based on linacs of the new generation.

REFERENCES

[1] D.A. Nikiforov *et al*, "High-current electron-beam transport in the LIA-5 Linear Induction Accelerator", *Phys. of Particles and Nuclei Lett.*, vol.17(2), pp.197-203, 2020.

[2] A.V. Arzhannikov *et al*, "Powerful long-pulse THz-band Bragg FEL based on linear induction accelerator", in *Proc. of the 44th Int. Conf. on Infrared, Mm and THz Waves (IRMMW-THz 2019)*, Paris, France, Sept. 2019, p.5864231.

[3] N.Yu. Peskov *et al*, "Powerful narrow-band Free-Electron Masers based on linear induction accelerators", *Radiophys. and Quant. Electron.*, vol.63, no.12, pp.1032-1081, 2020.

[4] N.Yu. Peskov *et al*, "Powerful FEM-oscillators with advanced Bragg resonators operating in a single mode regime from Ka- to W-band", *Proc. of the 41th Int. Conf. on Infrared, Mm and THz Waves (IRMMW-THz 2016)*, Copenhagen, Denmark, Sept. 2016, p.F2E.01.

[5] A.A. Kaminsky *et al*, "Experiments on the efficiency increase of FEL amplifier on the base of LIU-3000", *Particle Accelerators*, vol.33, pp.189-195, 1990.

[6] M.E. Conde and G. Bekefi, "Experimental study of a 33.3 GHz free electron laser amplifier with a reversed axial guide magnetic field", *Phys. Rev. Lett.*, vol.67, no.22, pp.3082-3085, 1991.

[7] N.Yu. Peskov *et al*, "Oversized advanced bragg resonators for powerful long-pulse FEL of subteraherts frequency range", *Radiophys. and Quant. Electr.*, vol.63, no.5-6, pp.542-546, 2020.

[8] N.Yu. Peskov *et al*, "Powerful oversized W-band FEM with advanced Bragg resonator based on coupling of propagating and cutoff waves", *Appl. Phys. Lett.*, vol.116, p.213505, 2020.

ISBN: 978-3-95450-240-0 ISSN: 2673-5539 doi:10.18429/JACoW-RuPAC2021-WEA01

BEAM TRANSFER SYSTEMS OF NICA FACILITY: FROM HILAC TO BOOSTER

A. Tuzikov†, A. Bazanov, A. Butenko, D. Donets, A. Fateev, A. Galimov, B. Golovenskiy, E. Gorbachev, A. Govorov, S. Kolesnikov, A. Kozlov, K. Levterov, D. Lyuosev, I. Meshkov, H. Nazlev, A. Petukhov, D. Ponkin, G. Sedykh, V. Seleznev, I. Shirikov, V. Shvetsov, A. Sidorin, A. Sidorov, A. Svidetelev, E. Syresin, V. Tyulkin, Joint Institute for Nuclear Research, Dubna, Russia

Abstract

New accelerator complex is being constructed by Joint Institute for Nuclear Research (Dubna, Russia) in frame of Nuclotron-based Ion Collider fAcility (NICA) project. The NICA layout includes new Booster and existing Nuclotron synchrotrons as parts of the heavy ion injection chain of the NICA Collider as well as beam transport lines which are the important link for the whole accelerator facility. Designs and current status of beam transfer systems in the beginning part of the NICA complex, which are partially commissioned, are presented in this paper.

INTRODUCTION

The Nuclotron-based Ion Collider fAcility (NICA) including new accelerator complex [1, 2] is constructed in Joint Institute for Nuclear Research (Dubna, Russia). In frame of the NICA project the existing superconducting synchrotron Nuclotron which is under operation since 1993 was modernized to match the project specifications [3, 4] and the new accelerators - the heavy ion linear accelerator (HILAC) and the superconducting Booster synchrotron [5] – as well as systems of beam transfer between these accelerators had been created and commissioned in 2016-2021 [6-9].

In the paper, design and current status of creation and commissioning of the first of connecting links of the heavy ion injection chain of the NICA Collider - beam transfer systems from the HILAC to the Booster - are given.

BEAM TRANSFER FROM HILAC TO BOOSTER

The beam transfer of heavy ions (Au^{31+} is chosen as reference ions) from the HILAC into the Booster ring at energy of 3.2 MeV/n is fulfilled by means of a beam transport channel and devices of a beam injection system of the synchrotron [10-13]. The ion-optical system of the beam transport channel and the beam injection system provide beam injection by several methods for accumulation of ions in the Booster with required intensity. Main methods of beam injection are single-turn, multi-turn (up to three turns) and multiple injections (twice or triple injection repetitions with rate of 10 Hz). Accumulation of ions is based on betatron stacking in the horizontal phase plane of the Booster synchrotron. To be able to inject beams by three given methods, the beam injection system of the Booster has a set of devices containing the electrostatic septum ESS and three electric kickers, or modules of inflector plates IP1 – IP3. The beam transport channel from HILAC to the Booster [14] contains 2 dipole and 7 quadrupole magnets, 6 steerers, a debuncher and extended set of beam diagnostics devices including Faraday cups, fast and AC current transformers, shoe-box and button pick-ups, a phase probe, multi-wire profile monitors (see Fig. 1). The ion-optical system of the channel provides beam debunching and betatron matching of ion beams of the target charge state with the Booster lattice functions as well as separation and collimation of neighbor parasitic charge states of ions. It is designed to be flexible enough to maintain required beam parameters at the channel exit for different working points of the Booster as well as for different initial beam parameters at the exit of the HILAC. The beam transfer systems also have options useful to fill more compact the phase space of the Booster by injected ions: rapid change of electric fields inside the kickers and variation of electric fields of the septum and magnetic fields of the channel's magnets in intervals between beam injections during multiple injection.

The HILAC-Booster beam transport channel is located in the median plane of the synchrotron and connected to the Booster at the entrance of the electrostatic septum ESS. The septum ESS and the kicker IP2 [15] are placed in the 1st straight section of the Booster ring (see Fig. 2) which is under room-temperature conditions. The kickers IP1 and IP3 are located in the vicinity of the 1st straight section and placed inside the Booster cryostat.

EQUIPMENT

Dipole, quadrupole and steering magnets of the channel are room-temperature. Dipoles and quadrupoles are powered in pulsed mode. Pulsed power supplies developed and assembled at JINR provide twice-triple repetitions of pulses to maintain multiple injection and also allow to realize dynamical retuning of the channel. 2D steerers have DC power supplies. Optional DC power supply is also used for the dipoles to obtain high stability of magnetic fields.

The 4-gap debuncher was produced as a part of Bevatech (Germany) project on design and creation of the HILAC. The debuncher is integrated into the HILAC RF system.

The electrostatic septum with length of 1.9 m is a pair of curved anode and cathode with curvature radii of 11.535 m and 11.5 m correspondingly installed inside a vacuum box. High voltage up to 130 kV is applied to the cathode while the anode is grounded. HV power supply maintains capability to vary the voltage in intervals between beam injections during multiple injection in the range to 10 kV.

† tuzikov@jinr.ru

ISBN: 978-3-95450-240-0 ISSN: 2673-5539 doi:10.18429/JACoW-RuPAC2021-WEA01

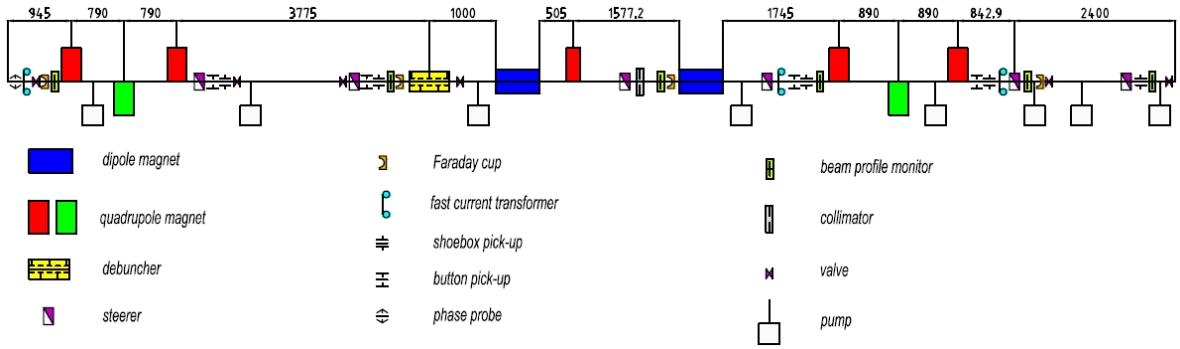

Figure 1: Layout of the HILAC-Booster beam transport channel. Beam direction is from left to right.

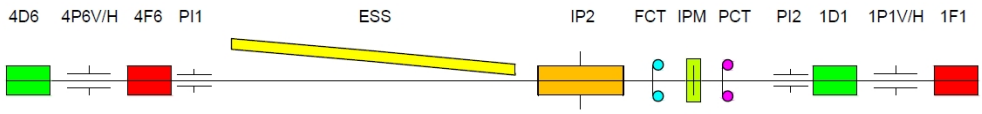

Figure 2: Layout of the 1st straight section of the Booster. Notation: 1D1, 1F1, 4D6, 4F6 – quadrupole lenses, FCT – fast current transformer, PCT – parametric (DC) current transformer, IPM – ionization profile monitor, 1P1V/H, 4P6V/H – lattice vertical/horizontal pick-ups, PI1, PI2 – additional vertical/horizontal pick-ups for beam injection tuning.

The electric kickers IP1 – IP3 are pairs of inflector plates installed vertically inside vacuum chambers parallel to the Booster axis. In turn the chambers of the cryogenic modules IP1 and IP3 are places inside cryostats. The IP1 and IP3 are designed on maximum voltage up to 65 kV while the module IP2 has maximum voltage of 50 kV. Five pulsed power supplies [16] provide independent unipolar charging/discharging of each of the inflector plates excluding one of the plates of the module IP1. Two modes of power supply system operation are maintained: the single-plateau pulse mode with charging of one plate of the kicker only and the double-plateau pulse mode with charging of both plates and asynchronous discharging of them which leads to rapid jump of electric field.

COMMISSIONING AND FIRST RUNS WITH BEAMS

At present all the beam transport channel equipment except one multi-wire profile monitor and a collimator of ions of parasitic charge states was manufactured and most of them is mounted (see Fig. 3) and tested on the channel during three stages of the channel mounting performed in 2019-2021.

Figure 3: The beginning section of the HILAC-Booster beam transport channel.

Manufacturing of all the modules of inflector plates as well as the electrostatic septum is also finished and the start configuration of the beam injection system providing the single-turn injection of a beam is assembled on the Booster ring in 2020. It includes the module of inflector plates IP3 with one pulsed power supply feeding the primary plate of the module (see Fig. 4) and the electrostatic septum with the module of inflector plates IP2 (see Fig. 5).

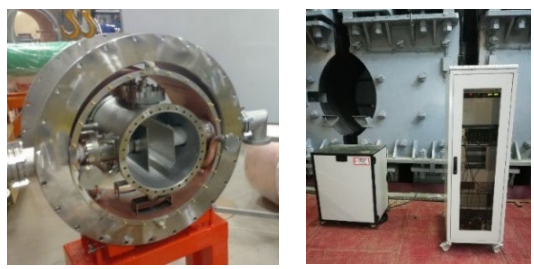

Figure 4: The module of inflector plates IP3 before mounting into the Booster (left) and racks of power supply and control of the IP3 near the Booster tunnel (right).

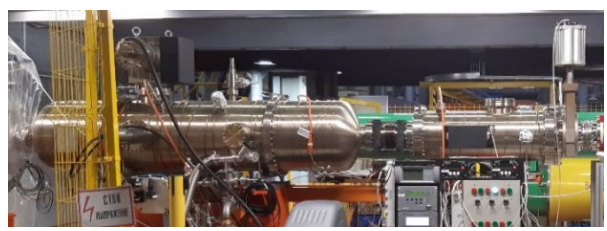

Figure 5: The electrostatic septum (left vacuum box) and the module of inflector plates IP2 (right vacuum box).

The first ion beam in the HILAC-Booster beam transport channel was transported during the short run of the HILAC on December 2019 after finish of the first stage of mounting when a beam had been observed in the last Faraday cup of the channel.

The first run of the Booster was hold on December 2020. At start of the run, after vacuum pumping of the insulating volume and beam pipes of the Booster, the equipment of the beam injection system had been tested and the septum

ISBN: 978-3-95450-240-0 ISSN: 2673-5539 doi:10.18429/JACoW-RuPAC2021-WEA01

has reached the design value of voltage 130 kV. On the IP3 the voltage of 62 kV which is close to the design one has been also obtained.

During the run the He^{1+} ion beam had been successfully transported in the channel with transmission efficiency of more than 90%, injected into the Booster ring and a beam circulation was obtained without activation of the closed orbit correction system of the Booster. Injection was achieved with the tuning of the beam injection system close to the designed one: voltage of the ESS - 74 kV vs. 72 kV, voltage of the IP3 - 38 kV vs. 40 kV.

During the runs on December 2020 and September 2021, tuning of a beam transmission through the final section of the channel and the beam injection devices ESS and IP2 was resulted in transmission efficiency about 90% and then the following methodic of fine tuning of beam injection was tested. The main idea of the methodic is that the closed orbit (CO) may be locally corrected (by means of steerers located in vicinity of the 1st straight section) in order to get intersection of the CO and a trajectory of the injecting beam in the center of the module IP3 that allows to inject a beam directly onto the corrected CO with minimal deviations from the Booster axis. The first step is to obtain a beam circulation during first several turns by tuning of the Booster magnetic field, the working point and the CO correction system. Then turn-by-turn measurement of the injected beam positions and angles at the septum exit during first N turns is performed by processing signals from two pick-ups neighbour to the 1st straight section: the pair PI1 and PI2 (at present these pick-ups are not installed yet into the Booster) or the pair 1P1 and 4P6 (which were used in the first Booster runs). Phase coordinates of the injected beam at the septum exit are calculated by solving the matrix equations [Eq. (1)].

$$\begin{cases} X_{2,i} = M_{sep\to 2} \cdot M_{1\to sep} \cdot X_{1,i} \\ X_{sep,i} = M_{1\to sep} \cdot X_{1,i} \end{cases} \quad (1)$$

Here $X_{1/2/sep,i}$ – vectors of phase coordinates of a beam in the 1st or 2nd pick-up or the septum exit after i^{th} turn where $x_{1/2,i}$ and $y_{1/2,i}$ are measured beam positions in the pick-ups; $M_{1\to sep}$ and $M_{sep\to 2}$ – transfer matrices from the 1st pick-up to the septum exit and from the septum exit to the 2nd pick-up correspondingly.

As a result of the measurements, ellipse-shaped figures may be plotted representing coherent oscillations of a beam after injection (see Fig. 6) and parameters of the Booster ring at the septum exit such as phase coordinates of CO X_{CO} and lattice functions β_x, α_x as well as betatron tunes Q_x may be evaluated by processing the set of turn-by-turn measured phase coordinates (see [Eqs. (2-4)]). Brackets $\langle\ \rangle$ in [Eqs. (2-3)] mean averaging over turns.

$$X_{CO} = \langle X_{sep,i} \rangle, \quad (2)$$

$$\begin{pmatrix} \beta_x & -\alpha_x \\ -\alpha_x & \gamma_x \end{pmatrix} = \frac{\langle (X_{sep,i}-X_{CO})\cdot(X_{sep,i}-X_{CO})^T \rangle}{\sqrt{\det\langle (X_{sep,i}-X_{CO})\cdot(X_{sep,i}-X_{CO})^T \rangle}} \quad (3)$$

$$Q_x = \left\langle \arctan\left(\beta_x \frac{x'_{i-1}}{x_{i-1}} + \alpha_x\right) - \arctan\left(\beta_x \frac{x'_i}{x_i} + \alpha_x\right) \right\rangle \quad (4)$$

The estimated parameters permits to find initial positions (x_0, x'_0) of the injected beam at start of the 1st turn which are calculated by [Eq. (5)] (analogously for y).

$$\varphi_0 = Q_x - \arctan\left(\beta_x \frac{x'_1}{x_1} + \alpha_x\right),$$

$$x_0 = \sqrt{2\,\beta_x\, I_x}\cos\varphi_0,$$

$$x'_0 = \sqrt{\frac{2\,I_x}{\beta_x}}(\sin\varphi_0 - \alpha_x \cos\varphi_0). \quad (5)$$

Knowing phase coordinates of both CO and the injected beam, one can firstly tune the septum and the IP3 to shift the initial position of the injected beam closer to the Booster axis and then correct the orbit by local bump to shift CO into the initial position of the injected beam. Iteration of these steps permits to tune the beam injection with minimal amplitudes of coherent oscillations.

During the run on September 2021 the beam injection with amplitude of coherent oscillations less than 4 mm was obtained. In Fig. 6 results of tuning of injection of Fe^{14+} beam are presented.

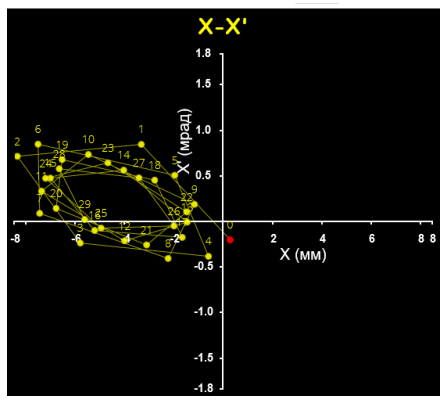

Figure 6: Phase trajectories of horizontal coherent oscillations of the injected Fe^{14+} beam at the exit of the electrostatic septum. Red point is the calculated initial position of the injected beam. Phase coordinates are given in mm and mrad.

CONCLUSION

Start configuration of the HILAC-Booster beam transfer systems has been manufactured and commissioned in 2019-2021. The first two runs of the Booster allow to test the systems with beams of He^{1+} and Fe^{14+} ions and beam transmission from HILAC to the Booster was achieved at level not less than 80%. Methodic of fine tuning of the beam injection providing minimization of coherent oscillations after injection has been proposed and successfully tried out.

ISBN: 978-3-95450-240-0 ISSN: 2673-5539 doi:10.18429/JACoW-RuPAC2021-WEA01

REFERENCES

[1] Ed. I. Meshkov, G. Trubnikov, *Technical Project of NICA Acceleration Complex*. JINR, Dubna, Russia, 2015.

[2] V. D. Kekelidze *et al.*, "Three stages of the NICA accelerator complex", *Eur. Phys. J. A*, vol. 52:211, p. 390, 2016. doi:10.1088/1742-6596/668/1/012023

[3] A. Eliseev *et al.*, "Results of the Nuclotron upgrade program", in *Proc. IPAC'11*, San Sebastián, Spain, Sep. 2011, paper WEPS013, pp. 2508-2510.

[4] E. Syresin *et al.*, "Nuclotron development for NICA acceleration complex", in *Proc. IPAC'19*, Melbourne, Australia, May 2019, pp. 3396-3398. doi:10.18429/JACoW-IPAC2019-THXXPLM1

[5] A. Tuzikov *et al.*, "Booster Synchrotron at NICA Accelerator Complex", in *Proc. RuPAC'16*, St. Petersburg, Russia, Nov. 2016, pp. 160-162. doi:10.18429/JACoW-RuPAC2016-FRCAMH05

[6] A.V. Butenko *et al.*, "Commissioning of the New Heavy Ion Linac at the NICA Project", in *Proc. IPAC'17*, Copenhagen, Denmark, May 2017, pp. 2362-2365. doi: 10.18429/JACoW-IPAC2017-TUPVA116

[7] V. Akimov *et al.*, "Acceleration of He^+ beams for injection into NICA Booster during its first run", in *Proc. IPAC'21*, Campinas, SP, Brazil, May 2021, pp. 3016-3019. doi:10.18429/JACoW-IPAC2021-WEPAB176

[8] A. Butenko *et al.*, "First experiments with accelerated ion beams in the Booster of the NICA accelerator complex", in *Proc. IPAC'21*, Campinas, SP, Brazil, May 2021, pp. 123-125. doi:10.18429/JACoW-IPAC2021-MOPAB025

[9] A. Butenko *et al.*, "The NICA Complex Injection Facility", presented at RuPAC'21, Alushta, Russia, Sep. 2021, paper MOY01, this conference.

[10] V. Volkov, I. Meshkov, V. Mikhailov, G. Trubnikov, A. Tuzikov, and A. Fateev, "Conceptual design of the system of heavy-ion beam injection into the booster of the NICA accelerator complex", *Phys. Part. Nucl. Lett.*, vol. 11, p. 675, 2014. doi:10.1134/S1547477114050276

[11] A. V. Butenko *et al.*, "Beam transport channels and beam injection and extraction systems of the NICA accelerator complex", *Phys. Part. Nucl. Lett.*, vol. 13, p. 966, 2016. doi:10.1134/S1547477114050276

[12] A. Tuzikov *et al.*, "Beam Transfer From Heavy-Ion Linear Accelerator HILAC Into Booster of NICA Accelerator Complex", in *Proc. RuPAC'16*, St. Petersburg, Russia, Nov. 2016, pp. 443-445. doi:10.18429/JACoW-RUPAC2016-WEPSB037

[13] A. Tuzikov *et al.*, "Heavy Ion Injection Chain of NICA Collider", in *Proc. RuPAC'18*, Protvino, Russia, Oct. 2018, pp. 52-54. doi:10.18429/JACoW-RUPAC2018-TUCDMH01

[14] A. Bogatov *et al.*, "HILAC-Booster transport channel: The magnetic elements power supply and beam profile measurements", in *AIP Conference Proceedings 2163, 080002,* Oct. 2019. doi:10.1063/1.5130117

[15] V. V. Kosukhin, A. I. Sidorov, A. V. Tuzikov, and V. S. Shvetsov, "Module of Elements for Beam Injection into the Booster of the NICA Accelerator Complex", *Phys. Part. Nucl. Lett.*, vol. 15, p. 903, 2018. doi: 10.1134/S1547477118070439

[16] V. Bulanov, E. Gorbachev, N. Lebedev, A. Tuzikov, and A. Fateev, "A conceptual design of a power-supply system of deflecting plates for multivariate injection into the NICA accelerator complex booster", *Phys. Part. Nucl. Lett.*, vol. 11, p. 695, 2014. doi:10.1134/S1547477114050100

ISBN: 978-3-95450-240-0 ISSN: 2673-5539 doi:10.18429/JACoW-RuPAC2021-WEA02

ACCELERATION THE BEAMS OF He^+ AND Fe^{14+} IONS BY HILAC AND ITS INJECTION INTO NICA BOOSTER IN ITS SECOND RUN

V. Akimov, A. Bazanov, A. Butenko, A. Galimov, A. Govorov, B. Golovenskiy, D. Donets, D. Egorov, V. Kobets, A. Kovalenko, K. Levterov, D. Letkin, D. Leushin, D. Lyuosev, A. Martynov, V. Mialkovsky, V. Monchinskiy, D. Ponkin, A. Sidorin, E. Syresin, I. Shirikov, G. Trubnikov, A. Tuzikov, Joint Institute for Nuclear Research, Dubna, Moscow region, Russia
H. Höltermann, U. Ratzinger, A. Schempp, H. Podlech, BEVATECH GmbH, Frankfurt, Germany

Abstract

Injector of NICA accelerating facility based on the Heavy Ion Linear Accelerator (HILAC) is aimed to inject the heavy ions having atomic number A≈200 and ratio A/Z ≤ 6.25 produced by ESIS ion source accelerated up to the 3.2 MeV for the injection into superconducting synchrotron (SC) Booster. The project output energy of HILAC was verified on commissioning in 2018 using the beams of carbon ions produced with the Laser Ion Source and having ratio A/Z=6 that is close to the project one. Beams of He^{1+} ions were injected into Booster in its first run and accelerated in 2020. In 2021 ions of Fe^{14+} produced with the LIS were injected and accelerated up to 200 MeV/u. Beam formation of Fe ions and perspectives of using LIS for the production the ions with high atomic mass A and ratio A/Z matching to HILAC input parameters are described.

HEAVY ION LINEAR INJECTOR

Heavy ion injector of the NICA project is based on the heavy ion linear accelerator (HILAC) and aimed to be injector of gold ions into SC Booster synchrotron of the NICA facility. The main features of it are presented in the Table 1.

Table 1: Main Features of HILAC

	HILAC
Species of ions	Au^{31+}
Z/A	≥ 0.16
Input energy	17 keV/u
Output energy	3.2 MeV/u
Beam current, mA	10
Operating frequency, MHz	100.625
Beam transmission rate, %	98

The accelerator is based on 4-rod RFQ [1] and IH DTL cavities with the KONUS accelerating structure inside [2]. Output energy of the HILAC was verified on its commissioning in 2015-2018 [3,4]. The beams of carbon ions C^{2+} having mass-to-charge ratio A/Z=6 that was close to the project value 6.25 were accelerated. Transverse strong focusing featured for KONUS was provided by two doublets and two triplets. RF power supply system is based on the solid state amplifiers: 140 kW for RFQ, two 340 kW amplifiers for IH1 and IH2 and two 4 kW for rebuncher and debuncher.

LLRF system designed and commissioned in collaboration with ITEP [2] provided five continuous sin input signals for RF amplifiers up to 1V amplitude. Output RF power of the amplifier is tuned by the amplitude of the input signals. Phase shifting between LLRF signals is tuned with accuracy 0.1°. Level of RF power inside each cavity was controlled by the pickups signals monitoring.

HELIUM ION SOURCE

The beams of He^+ ions produced with the ion source developed in LHEP JINR were used for the first run of SC synchrotron Booster. For designing helium ion source the proton ion sources described in [3,4] were taken as a prototype. Ion source with cold magnetron cathode and magnetic plasma compression produced ~90% of He^+ ions (see Fig. 1). There are three basic space emay be attributed to plasma generator: space of auxiliary discharge between magnetron cathode and magnetron anode, space of the basic discharge between magnetron cathode and anode, and area of plasma expansion.

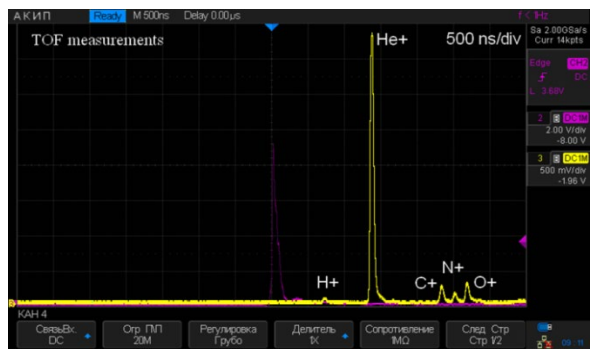

Figure 1: TOF spectrum of the ions at the output of the helium ion source.

LASER ION SOURCE

Laser ion source, developed as the ion source for Alvarez linac LU-20 at the JINR Laboratory of High energy physics in 1983, is based on a CO_2 laser operating in Q-fixed mode. The radiation flux density at the target is estimated as ~10^{10} W/cm² and is enough to produce light ions having mass-to-charge ratio A/Z≤ 3 that is the limit value for the acceleration in LU-20. Range of accelerated ions provided with LIS is various enough: $^6Li^{3+}$, $^7Li^{3+}$,

ISBN: 978-3-95450-240-0 ISSN: 2673-5539 doi:10.18429/JACoW-RuPAC2021-WEA02

B^{4+}, C^{4+}, N^{5+}, O^{6+}, F^{7+}, Mg^{8+}, Si^{11+}. Because of degradation of RF system and problem of RF breakdowns inside LU-20 cavity a necessity was growing up to reduce A/Z ratio of the ions being injected into accelerator. Direct way to do it was to increase flux density of the focused laser radiation on the surface of the target material in order to rise up the number if the ions in higher charge state. For this purpose, CO_2 laser was replaced with the Nd-YAG laser having pulsed energy 1.0 J and pulse duration 10 ns. The expected laser radiation flux density at the target was estimated ~10^{13} W/cm² [5]. Carbon ions C^{5+} produced with the upgraded laser ion source were successfully injected and accelerated in SC synchrotron Nuclotron in accelerating run with satisfied intensity taking extra work of LU-20 RF system and breakdown troubles off. Beams of C^{6+} ions also passed through injection chain successfully but were unstable for application.

Commissioning of heavy ions injector based on HILAC [6,7] opened possibility of acceleration the ions having mass-to-charge ratio A/Z≤ 6.25 at the atomic mass value A high enough. Test bench researches of the laser plasma produced with the Nd-YAG laser were done to find out the high charge states of the carbon and ferrum ions. Presence of C^{6+} and Fe^{16+} ions having almost the same ionization energy 490 eV was observed surely. Moreover, the ions of Fe^{17+} requiring for its appearance ionization energy 1263 eV were observed also (see Fig. 2) [5], so one may expect to accelerate by HILAC the beams of ions having atomic number close to 90.

Beam matching for the RFQ input provided with the LEBT consisting of two focusing electrodes, electrostatic accelerating tube, two short solenoids and XY-steerer.

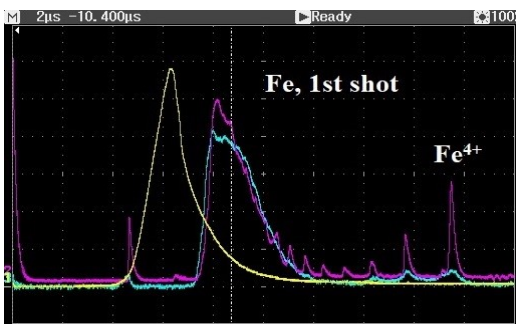

Figure 2: TOF spectrum of the ions at the output of the laser ion source, white vertical line is TOF marker for Fe^{16+}, lilac - SEM detector signals, blue - collected signal at the SEM input, yellow - collected signal at the analyzer input.

ACCELERATION THE BEAMS OF HELIUM AND FERRUM IONS BY HILAC AND INJECTION INTO BOOSTER

For the first run of SC synchrotron Booster the beams of one species He^+ having mass-to-charge ratio A/Z=4 were accelerated by HILAC up to injection energy 3.2 MeV/u and injected in Booster [8]. The intensity $7 \cdot 10^{10}$ of the ions accumulated in the ring per one pulse of injection and accelerated up to 100 MeV/u was achieved [9]. Beam diagnostic system included four current transformer, three phase probes, beam profile monitors and shoebox pickups (see Fig. 3). Beam transmission was estimated with the current transformers signals placed consequentially behind RFQ, IH2 and behind second bending magnet (see Fig. 3).

The second accelerating run of NICA Booster started from the He^+ ions acceleration. Ions current duration at the ion source output was 50-60 us. Duration of the ions current at the RFQ input was controlled by HV pulse applied to the focusing electrode used for modulation and tuned in range 1-30 us taking into account that one turn of ions circulation at the injection energy takes ~8 us and three-turn injection is projected. Transmission 50% was observed for 7 mA beam current (see Fig. 4) at the 8 us duration at the RFQ output. Significant beam loading took place in three accelerating cavities of HILAC (see Fig. 5).

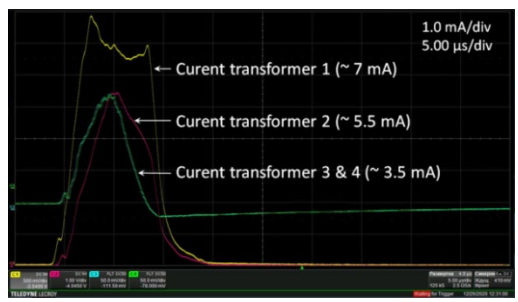

Figure 4: Current transformer signals of He^+ beam, 7 mA-RFQ output, 5.5 mA-IH2 output, 3.5 mA –behind QT4 triplet.

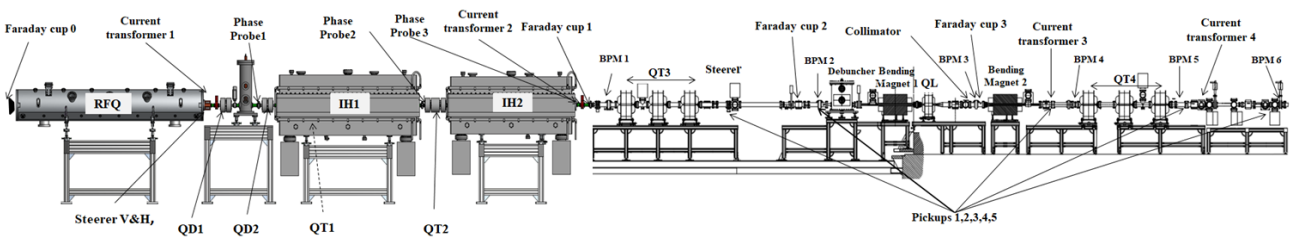

Figure 3: Beam diagnostic units arranged along HILAC.

ISBN: 978-3-95450-240-0 ISSN: 2673-5539 doi:10.18429/JACoW-RuPAC2021-WEA02

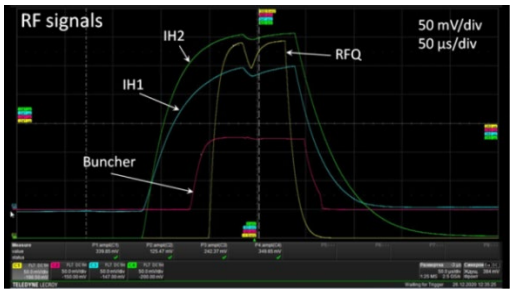

Figure 5: RF beam loading in the HILAC cavities caused with the He^+ beam.

Beams of He^+ ions were following by acceleration of Fe^{14+} ions generated with the LIS. On changing ion source HILAC tunings had not been changed because of identical mass-to-charge ratio A/Z=4 both for He^+ and Fe^{14+} ions. Ions Fe^{14+} current duration ~1-2 us featured for LIS was observed through injection chain and beam transmission was rather less (See Fig.6). No RF loading in HILAC cavities were detected except for a little one in RFQ cavity.

The detected signals of RFQ, IH1 and IH2 pickups (see Figs. 4,5) were observed synchronously to the presented beam currents signals (see Figs. 6,7). One should underline that all run time was spent for the Booster tuning and injector could not been tuned accurately.

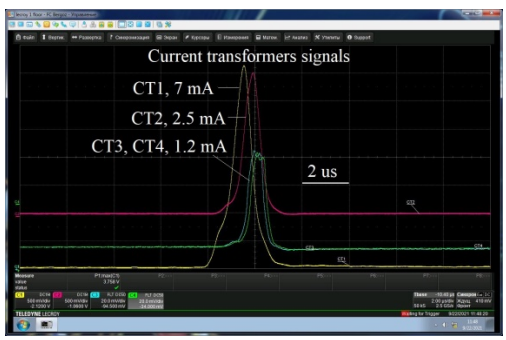

Figure 6: Current transformer signals of Fe^{14+} beam, 7 mA-RFQ output, 2.5 mA-IH2 output,1.5 mA –behind QT4 triplet.

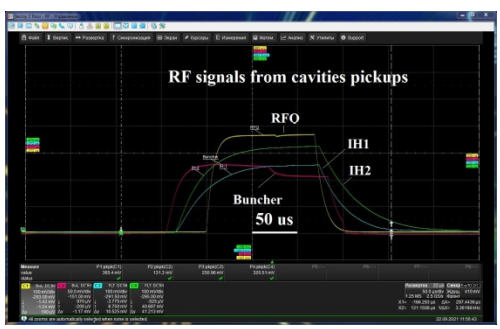

Figure 7: RF beam loading in the HILAC cavities caused with the Fe^{14+} beam.

CONCLUSION

In the second accelerating run of NICA Booster commissioning in September 2021 heavy ion injector based on HILAC injected the beams of ions He^+ and Fe^{14+} into Booster ring where they were accelerated up to 578 MeV/u. He^+ ions were provided with the developed helium ion source with cold magnetron cathode and magnetic plasma compression. For the first time the beams of Fe^{14+} ions having mass-to-charge ratio A/Z=4 produced with the LIS could be accelerated and injected in synchrotron ring due to the commissioned heavy ion linear accelerator HILAC. Upgraded LIS based on a Nd-YAG laser in tandem with HILAC make it possible to expect the possibility to generate, accelerate and inject into Booster the ions having atomic number A up to ~90. Searching for the best tuning of heavy ion injector and compensation of beam loading are needed.

REFERENCES

[1] U. Ratzinger, H. Hähnel, R. Tiede, J. Kaiser, A. Almomani, "Combined zero degree structure beam dynamics and applications", *Phy. Rev. Special Topics - Accelerators and Beams,* 22, 2019. doi: 10.1103/PhysRevAccelBeams.22.114801.

[2] A.V. Butenko *et al.*, "Development of NICA Injection Complex", in *Proc. 5th Int. Particle Accelerator Conf. (IPAC'14)*, Dresden, Germany, June 2014, pp. 2103-2105, doi:10.18429/JACoW-IPAC2014-WEPRO067

[3] L. Veresov, O. Veresov, "Ion Source with a Cold Magnetron Cathode and Magnetic Plasma Compression", *Technical Physics,* 48, pp. 1338-1345, 2003. doi:10.1134/1.1620132.

[4] B.A. Frolov, O.K. Belyaev, E.A. Konoplev, and A.M. Korotkov, "Magnetron Proton Source", in *Proc. RUPAC'18*, Protvino, Russia, Oct 2018, pp. 501-503. doi:10.18429/JACoW-RUPAC2018-THPSC48

[5] A.M. Bazanov, "Laser ion source in injection facility of NICA project", *Phys.Scripta* 95, 5, p. 055307, 2020. doi: 10.1088/1402-4896/ab7aa8

[6] A.V. Butenko *et al.*, "Commissioning of the New Heavy Ion Linac at the NICA Project", in *Proc. 25th Russian Particle Accelerator Conf. (RuPAC'16)*, St. Petersburg, Russia, Nov. 2016, paper FRCAMH03, pp. 156-159, 2016.

[7] A.V. Butenko *et al.*, "Injection Complex Development for the NICA-project at JINR", in *Proc. LINAC'18*, Beijing, China, Sep. 2018, pp. 663-665. doi:10.18429/JACoW-LINAC2018-TH1P02

[8] V. Akimov *et al.*, "Acceleration of He^+ beams for injection into NICA Booster during its first run", in *Proc. IPAC'21*, May 2020, Campinas, SP, Brazil. doi:10.18429/JACoW-IPAC2021-WEPAB176

[9] V. Akimov *et al.*, "First experiments with accelerated ion beams in the Booster of the NICA accelerator complex" in *Proc. IPAC'21,* May 2020, Campinas, SP, Brazil. doi: 10.18429/JACoW-IPAC2021-MOPAB025

ISBN: 978-3-95450-240-0 ISSN: 2673-5539 doi:10.18429/JACoW-RuPAC2021-WEA03

200 MeV LINAC DEVELOPMENT FOR THE SKIF LIGHT SOURCE INJECTOR

A. Andrianov, M. Arsentyeva†, A. Barnyakov, D. Chekmenev, A. Levichev, O. Meshkov, D. Nikiforov, O. Pavlov, I. Pivovarov, S. Samoylov, V. Volkov
Budker Institute of Nuclear Physics SB RAS, Novosibirsk, Russia

Abstract

A new synchrotron light source SKIF of the 4th generation is construction at Budker institute of nuclear physics (Novosibirsk, Russia). It consists of the main ring, the booster ring and the linear accelerator. This paper presents design of the linear accelerator which is expected to provide electron beams with the energy of 200 MeV. Construction of the linear accelerator is discussed. Description of the linear accelerator main systems is presented.

INTRODUCTION

The SKIF light source is designed for the top-up injection to the main ring from the booster ring at the electron energy of 3 GeV. The linear accelerator is designed based on the injector technical requirements and BINP experience at the linac development. Electron linac with the energy of 200 MeV is similar to that of the Injection complex VEPP-5 [1]. The booster synchrotron with the maximum energy of 3 GeV is a modification of the synchrotron designed by BINP for NSLS II [2].

In the main operation mode the SKIF storage ring will be supplied by approximately 500 bunches with the total current of 400 mA. There is also a possibility to work in other modes depending on the requirements of the light source users. Table 1 presents required parameters of the electron beam to be obtained at the linear accelerator.

Table 1: Requirements for the Electron Beam Parameters

Parameter	Value
Operating energy	200 MeV
Energy spread (RMS)	1%
Injection rate	1 Hz
Bunch period	5.6 ns
Number of bunches	55
Single bunch charge	0.3 nC
Horizontal emittance at 200 MeV	150 nm

Figure 1 presents layout of the linear accelerator. The injection rate is 1 Hz and the operating frequency of the RF gun is 178.5 MHz while the booster and storage rings operate at 357 MHz. Thus, it is supposed that a single linac beam consisting of 55 electron bunches fills every second separatrix and after the phase shift next bunch train fills other separatrices. After the gun the beam passes through the bunching channel which consists of the third harmonic cavity, the solenoids and the preaccelerator. Three klystrons Canon E3730A with the peak power of 50 MW are used as RF power sources for the preaccelerator and five regular accelerating structures. Linac ends by the diagnostic channel with the magnet spectrometer and the Faraday cup.

ELECTRON GUN

RF gun which is an electron source for the linac has an operating frequency 178.5 MHz and is planned to be built on the cathode-grid assembly. Using this scheme allows one to perform modulation of the cathode current, providing variation of the bunch charge.

Parameters of the RF gun cavity are shown in Table 2. At the electric field amplitude on the axis of 13 MV/m it is possible to extract electron bunches with the charge up to 1.1 nC (Fig. 2, left) while the average particle energy is about 0.6-0.7 MeV.

Table 2: RF Gun Parameters

Parameter	Value
Operating frequency	178.5 MHz
Electric field amplitude	13 MV/m
Injection rate	1 Hz
Pulse power	500 kW
Quality factor	10300

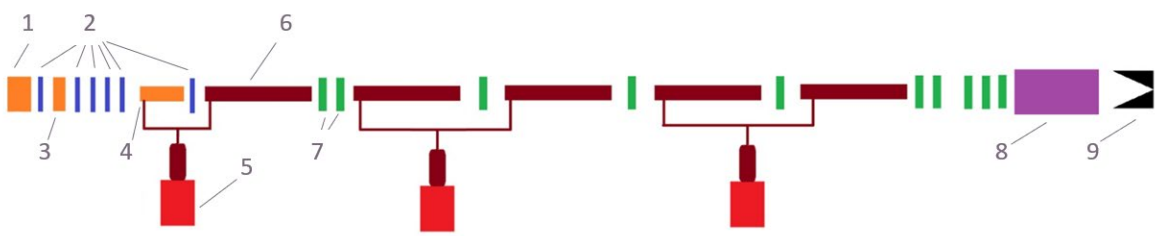

Figure 1: Layout of the linac. 1 – electron gun, 2 – solenoids, 3 – 535 MHz buncher, 4 – preaccelerator, 5 – klystrons, 6 – regular accelerating structures, 7 – quadruple lenses, 8 – spectrometer, 9 – Faraday cup.

† M.V.Arsentyeva@inp.nsk.su

ISBN: 978-3-95450-240-0 ISSN: 2673-5539 doi:10.18429/JACoW-RuPAC2021-WEA03

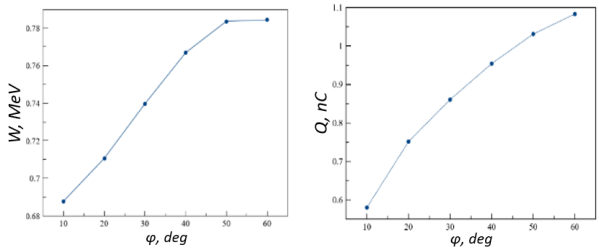

Figure 2: Left – dependence of the electron average energy on the injection phase, right – bunch charge dependence on the injection phase.

SYSTEM OF BUNCHING AND PREACCELERATION

The beam is emitted from the RF gun at the bunching phase, for the linearization of the bunching forces the third harmonic cavity is to be used. The bunching cavity operates at the frequency of 535 MHz with the electric field amplitude of about 2.5 MV/m.

After the third harmonic cavity the beam is injected to the preaccelerator which is a part of the linac regular accelerating structure. It consists of two wave type transformers and accelerating cells. Due to the beam injection energy of 0.6 MeV there is no need in the optimization of first accelerating cells. The preaccelerator input power is 10 MW, providing the electron energy of about 3 MeV.

System of beam bunching includes also solenoids, their parameters are given in Table 3.

Table 3: Parameters of the Bunching Channel Solenoids

Magnet	Qty	L, mm	B_{max}, kGs
Solenoids of the bunching channel	5	100	0.65
Preaccelerator solenoids	2	250	1.0
Matching solenoid	1	100	1.5

MAGNET SYSTEM

Besides solenoids in the beginning of the linac, its magnet system includes also two-dimensional dipole correctors of the beam trajectory. There are 8 small correctors in the bunching channel and 6 correctors with the yoke in linac regular part. Parameters of the dipole correctors are shown in Table 4.

Table 4: Parameters of the Dipole Correctors

Magnet	Qty	L, mm	B_{max}, kGs
Small correctors	8	140	0.021
Correctors with a yoke	6	140	0.5

For the regular linac part seven quadruple lenses are provided, there is also a triplet of quadruple lenses in the diagnostics channel (Fig. 1). Quadruple lens parameters are given in Table 5.

Table 5: Parameters of the Quadruple Lenses

Magnet	Qty	L, mm	G_{max}, kGs/cm
Quadruple lenses in the regular linac	7	100	1.2
Quadruple lenses in the diagnostics channel	3	150	1.2

ACCELERATING STRUCTURES

Linear accelerator includes five disk loaded regular accelerating structures (Fig. 3) operating at the $2\pi/3$ mode with the frequency of 2856 MHz. Accelerating structure parameters are shown in Table 6.

Table 6: Parameters of the Accelerating Structures

Parameter	Value
Operating frequency	2856 MHz
Quality factor	13000
Period	34.99 mm
Cell diameter	83.75 mm
Diaphragm thickness	6 mm
Length	2.93 m
Shunt impedance	51 Ohm/m
Phase velocity	c
Group velocity	0.021 c
Filling time	0.456 mcs

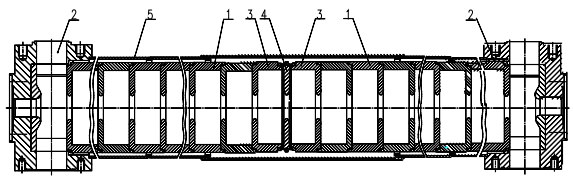

Figure 3: Disk loaded waveguide accelerating structure: 1 – accelerating cell, 2 – wave type transformer, 3–junction cell, 4 – junction diaphragm, 5 – cooling shielding.

With the input power of 40 MW in the first accelerating structure, the beam increases its energy by about 50 MeV. In other accelerating structures with the input power of 25 MW the beam energy gain is about 40 MeV. Corresponding electric field distributions in the structures are given in Fig. 4.

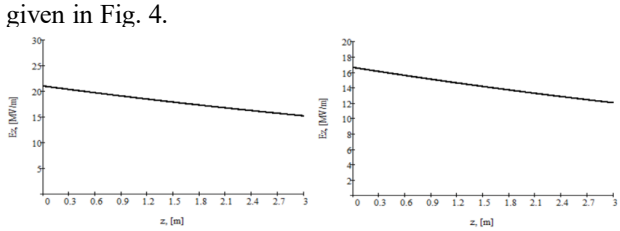

Figure 4: Electric field distribution along the accelerating structure. Left – input power of 40 MW, right – input power of 25 MW.

ISBN: 978-3-95450-240-0 ISSN: 2673-5539 doi:10.18429/JACoW-RuPAC2021-WEA03

DIAGNOSTICS

Measurement of the beam current will be performed by 3 fast current transformers (FCT). Beam position control and transverse profile registration are to be carried out by 9 fluorescent screens. Beam longitudinal profile along the bunching channel is to be measured with the help of 3 Cherenkov sensors. Seven beam position monitors are provided, the linac ends by the magnet spectrometer with the Faraday cup in the radiation shielding.

WAVEGUIDE SYSTEM

Figure 5 presents the waveguide scheme for the distribution of the klystron RF power in the linac beginning. The klystron power is divided with the help of 7 dB coupler in the ratio 1:4 between the preaccelerator and the regular accelerating structure, the couplers for the power measurements are provided. There are also phase shifters for both accelerating structure while the preaccelerator input power is to be adjusted with the help of the attenuator. Waveguide schemes for other accelerating structures consist of the same elements besides the 7 dB coupler and the attenuator.

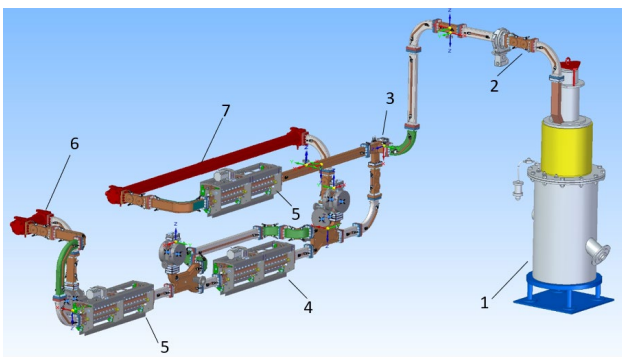

Figure 5: Waveguide system for the linac beginning. 1 – klystron, 2 – power measurement couplers, 3 – 7 dB coupler, 4 – attenuator, 5 – phase shifters, 6 – preaccelerator, 7 – accelerating structure.

BEAM DYNAMICS SIMULATIONS

Beam dynamics simulation in linear accelerator with the described systems were performed using ASTRA [3]. There are no particles loss during the acceleration, the beam transverse size in the linac is shown in Fig. 6. Beam parameters and its distribution in the longitudinal phase space are shown in Fig. 7 and Table 7, correspondingly.

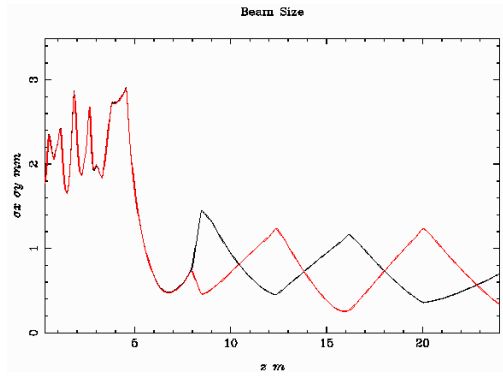

Figure 6: Beam transverse size evolution in the linac.

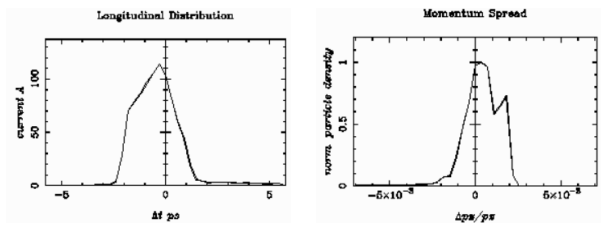

Figure 7: Longitudinal phase space of the beam at the linac output.

Table 7: Parameters of the Accelerated Beam

Parameter	Value
Energy	200 MeV
Energy spread (RMS)	0.3 %
Horizontal emittance	50 nm
Single bunch charge	0.3 nC

CONCLUSION

The linear accelerator of electrons with the energy of 200 MeV was designed as a part of the injector for the SKIF light source. Simulations of the beam dynamics show parameters of the accelerated beam to meet the requirements.

REFERENCES

[1] Yu. Maltseva *et al.*, "VEPP-5 Injection Complex: New Possibilities for BINP Electron-Positron Colliders", in *Proc. 9th Int. Particle Accelerator Conf. (IPAC'18)*, Vancouver, Canada, Apr.-May 2018, pp. 371-373. doi:10.18429/JACoW-IPAC2018-MOPMK011

[2] S. M. Gurov *et al.*, "Status of NSLS-II Booster", in *Proc. 24th Particle Accelerator Conf. (PAC'11)*, New York, NY, USA, Mar.-Apr. 2011, paper WEP201, pp. 1864-1866.

[3] https://www.desy.de/~mpyflo/

ISBN: 978-3-95450-240-0 ISSN: 2673-5539 doi:10.18429/JACoW-RuPAC2021-WEB02

MAGNETIC FIELD MEASUREMENTS FOR THE NICA COLLIDER MAGNETS AND FAIR QUADRUPOLE UNITS

A. V. Shemchuk†, V. V. Borisov, I. I. Donguzov, O. M. Golubitsky, H. G. Khodzhibagiyan, B. Kondratiev, S. A. Kostromin, D. I. Khramov, A. V. Kudashkin, T. Parfylo, M. M. Shandov, E. V. Zolotykh, D. A. Zolotykh,
JINR, Dubna, Moscow Region, Russia

Abstract

The magnetic system of the NICA collider includes 86 quadrupole and 80 dipole twin-aperture superconducting magnets. The serial production and testing of the dipole magnets was completed in the summer of 2021. The tests of the quadrupole magnets of the collider and the quadrupole units of the FAIR project have successfully entered the phase of serial assembly and testing at the Joint Institute for Nuclear Research (VBLHEP JINR). One of the important testing tasks is to measure the characteristics of the magnetic field of magnets. The article describes the state of magnetic measurements and the main results of magnetic measurements of NICA collider magnets, quadrupole units of the FAIR project, as well as plans for measuring the following types of magnets of the NICA project.

INTRODUCTION

NICA (Nuclotron-based Ion Collider fAcility) is a new acceleration-storage complex[1]. It is under construction in JINR. In parallel with the NICA project, the FAIR project is being implemented in Darmstadt, Germany, of which the SIS100 accelerator is a part [2]. The SIS100 accelerator includes 166 quadrupole units of various configurations. For quadrupole units, it is necessary to measure these parameters of the magnetic field:

- Integral of the mainl field component (GL).
- Effective length (L_{eff}).
- Roll angle (α).
- Position of magnetic axis (dz, dy).
- Relative harmonics up to 10^{th}.

At the moment, 25 units have successfully passed cryogenic tests.

Collider includes 86 quadrupole and 80 dipole twin-aperture superconducting magnets. Manufacturing of 80 main and 6 reserve magnets is finished now. To carry out magnetic measurements, the method of rotating harmonic coils, described in articles [3], [4] was chosen. It is necessary to measure the parameters of the magnetic field such as:

- Field in the center of the dipole ($B_1(0)$).
- Effective length (L_{eff}).
- Magnetic field angle (α).
- Relative harmonics up to 10^{th}.

Dipoles were tested at the ambient and operating (4.5 K) temperatures. Maximal operating current at operating temperature is 10.44 kA for NICA collider and 11.5 kA for SIS100 quadrupole units.

MAGNETIC MEASUREMENTS SYSTEMS (MMS)

Figure 1 shows the progress of magnetic measurements. For serial magnetic measurements, 4 stands are used, 3 for measurements at room temperature, 1 for measurements in cryogenic conditions. The total number of magnetometers is 15 pcs.

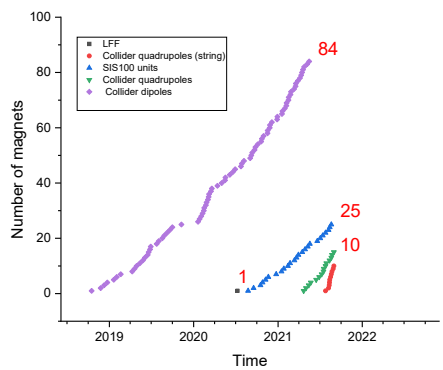

Figure 1: The progress of magnetic measurements.

For measurements of quadrupole magnets of both the NICA and FAIR projects, in addition to the method of rotating harmonic coils, the method of a vibrating string is used.

MMS for NICA Collider Dipoles

During the measurements, 6 serial magnetometers (see Fig. 2) were created to measure the collider dipole magnets. 2 magnetometers are used in the area of warm magnetic measurements, and 4 magnetometers on the cryogenic stand. A detailed description of the measurement system and design of the magnetometer is presented in [5].

The statistics of parameters of magnetic field are presented in the results (see Fig. 7, Fig. 8, Fig. 9).

† shemchuk@jinr.ru

ISBN: 978-3-95450-240-0 ISSN: 2673-5539 doi:10.18429/JACoW-RuPAC2021-WEB02

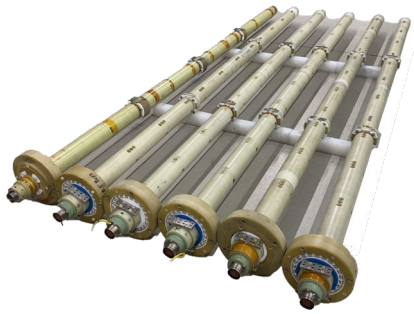

Figure 2: Serial magnetometers for collider dipole magnets.

Key features of magnetometers:

- The production time of 1 magnetometer: 60 days.
- Each magnetometer is relative calibrated on a reference magnet.
- The assembly is carried out under the control of a control measuring machine (0.050 mm).
- The accuracy of the measuring system does not exceed the TK tolerance.

MMS for NICA Collider Quadrupoles

At the moment, 6 serial magnetometers are taking part in the measurements. Each magnetometer is equipped with a hall sensor for measuring correctors, which are mounted on a quadrupole magnet.

Figure 3 shows a stand of warm (I=100 A) magnetic measurements. The concept of magnetometers, as well as the control and data acquisition system, is similar to that used in [3] and [5].

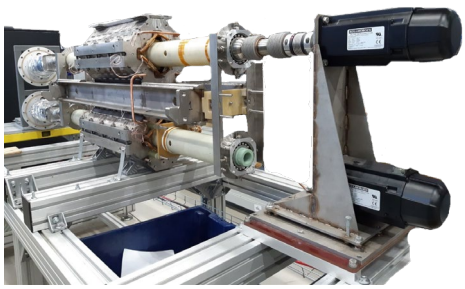

Figure 3: Warm magnetic measurement stand.

The key features of the magnetometer are similar to those for collider dipole magnets.

MMS for FAIR Quadrupole Units

The design of a magnetometer for quadrupole units is based on the design of magnetometers for collider quadrupoles. The main differences are:

- The production time of 1 magnetometer: 90 days.
- The magnetometer is equipped with a system for monitoring the position of the axis of rotation.
- 4 ceramic bearings. 2 of them are double-row self-aligning.

Figure 4 shows a 3D model of a quadrupole unit with an installed magnetometer.

The statistics of parameters of magnetic field are presented in the results (see Fig. 11, Fig. 12).

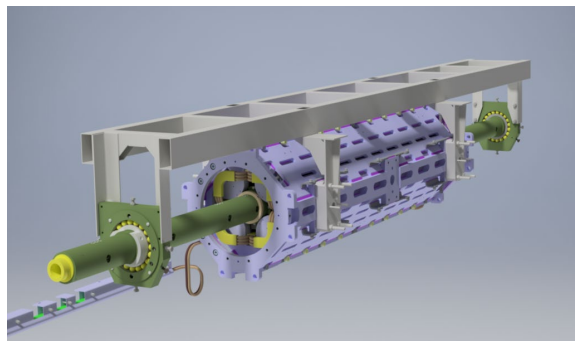

Figure 4: Serial magnetometer for FAIR quadrupole units.

POLE GEOMETRY CONTROL SYSTEMS

Since the field for magnets for the NICA and FAIR projects is formed by an iron yoke, the exact measurement of the geometry of the poles and their mutual position is of particular interest.

Pole Gap Measurement System for NICA collider dipoles

The system (see Fig. 5) was developed and assembled at JINR. It allows measuring the interpolar gap of the collider two-aperture dipole magnets with an accuracy of no worse than 0.005 mm.

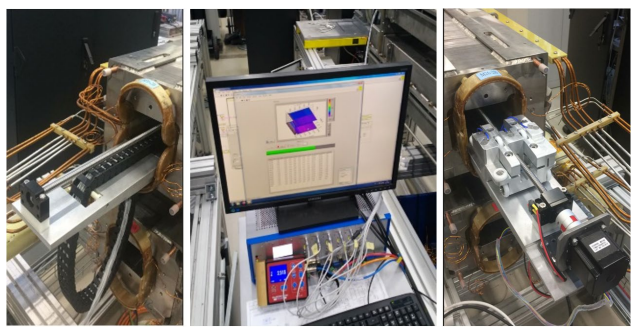

Figure 5: PCB harmonic coils for FAIR qadrupole untit magnetometer.

The main element of the system is 6 MicroEpsilon capacitive sensors with a measurement range of 0 - 1.2 mm.

Thus, by measuring the geometry of the poles, it is possible to carry out a comparative analysis of the results of measuring the geometry of the poles and the results of magnetic measurements.

Hyperbolic Profile Measurement System for FAIR Quadrupole Units

The concept of the system is similar to that described above. The measuring card contains 20 capacitive sensors, which allow measuring the hyperbolic profile of a quadrupole unit with an accuracy of no worse than 0.005 mm.

The main elements of the system are shown in Fig. 6. The statistical measurement results are shown in Fig. 10.

ISBN: 978-3-95450-240-0 ISSN: 2673-5539 doi:10.18429/JACoW-RuPAC2021-WEB02

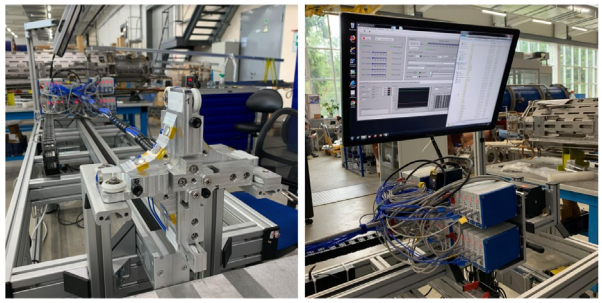

Figure 6: Hyperbolic profile measurement system for FAIR quadrupole units.

RESULTS

Below are the results of magnetic measurements for dipole and quadrupole magnets of the NICA project, as well as measurements of the interpole gap of dipole magnets.

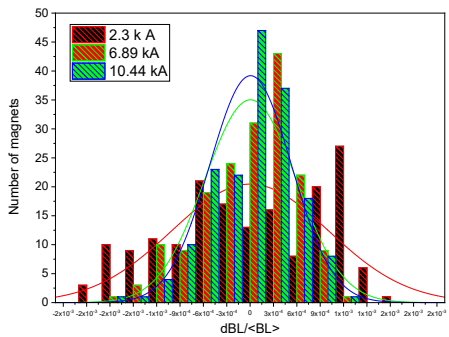

Figure 7: Relative spread of the integral of the magnetic field for dipole magnets of the NICA project.

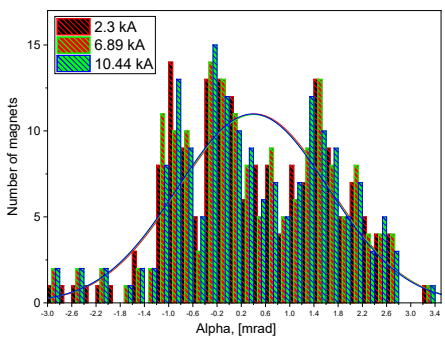

Figure 8: Integral angle of the magnetic field of the dipole magnets of the NICA booster

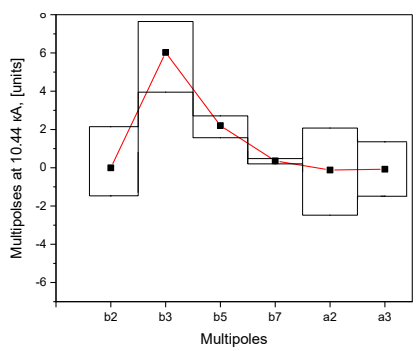

Figure 9: Multipoles for dipole magnets of the NICA project.

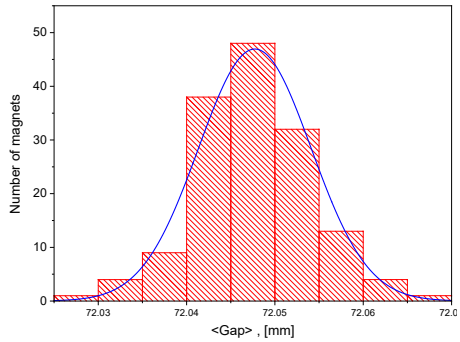

Figure 10: Interpolar gap for dipole magnets of the NICA project.

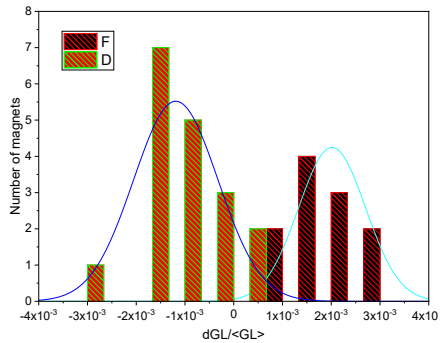

Figure 11: Relative spread of the integral of the magnetic field for quadrupole magnets of the NICA project.

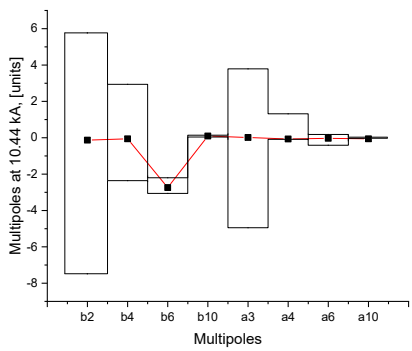

Figure 12: Multipoles for quadrupole magnets of the NICA project.

CONCLUSION

Magnetic measurements performed:

- 100 % collider dipole magnets.
- 35 % collider quadrupole magnets.
- 15 % SIS100 quadrupole units.

Total created magnetometers:

- 16 serial magnetometers of various configurations.

Measuring stands put into operation:

- 6 stands for measuring magnetic field parameters.
- 2 stands for measuring the geometry of magnets.

REFERENCES

[1] Technical Project of NICA Acceleration Complex, Dubna, 2015.

ISBN: 978-3-95450-240-0 ISSN: 2673-5539 doi:10.18429/JACoW-RuPAC2021-WEB02

[2] E. S. Fischer, E. Floch, J. Macavei, P. Schnizer, P. G. Akishin, and A. Mierau, "Design and Operation Parameters of the Superconducting Main Magnets for the SIS100 Accelerator of FAIR", in *Proc. 2nd Int. Particle Accelerator Conf. (IPAC'11),* San Sebastian, Spain, Sep. 2011, paper WEPO024, pp. 2451-2453.

[3] A. V. Shemchuk *et al.*, "Serial Magnetic Measurements for the NICA Quadruple Magnets of the NICA Booster Synchrotron", in *Proc. 9th Int. Particle Accelerator Conf. (IPAC'18)*, Vancouver, Canada, Apr.-May 2018, pp. 3649-3652. doi:10.18429/JACoW-IPAC2018-THPAL014.

[4] V. V. Borisov *et al.*, "Magnetic Measurements of NICA Booster Dipoles", in *Proc. 8th Int. Particle Accelerator Conf. (IPAC'17)*, Copenhagen, Denmark, May 2017, pp. 3458-3460. doi:10.18429/JACoW-IPAC2017-WEPVA087.

[5] M. M. Shandov *et al.*, "The Present Status of the Magnetic Measurements of the NICA Collider Twin-Aperture Dipoles", in *Proc. 26th Russian Particle Accelerator Conf. (RuPAC'18)*, Protvino, Russia, Oct. 2018, pp. 349-352. doi:10.18429/JACoW-RUPAC2018-WEPSB32.

ISBN: 978-3-95450-240-0 ISSN: 2673-5539 doi:10.18429/JACoW-RuPAC2021-WEB03

FIRST EXPERIENCE OF PRODUCTION AND TESTING THE SUPERCONDUCTING QUADRUPOLE AND CORRECTOR MAGNETS FOR THE SIS100 HEAVY ION ACCELERATOR OF FAIR

E. Fischer, H. Khodzhibagiyan, D. Nikiforov, V. Borisov, T. Parfylo, Y. Bespalov, D. Khramov, B. Kondratiev, M. Petrov, A. Shemchuk, JINR, Dubna, Russia
A. Waldt, A. Bleile, GSI, Darmstadt, Germany

Abstract

The fast-cycling superconducting SIS100 heavy ion accelerator is the designated working horse of the international Facility for Antiproton and Ion Research (FAIR) under construction at GSI in Darmstadt, Germany [1].

The main dipoles will ramp with 4 T/s and with a repetition frequency of 1 Hz up to a maximum magnetic field of 1.9 T. The field gradient of the main quadrupole will reach 27.77 T/m. The integral magnetic field length of the horizontal/vertical steerer and of the chromaticity sextupole corrector magnets will provide 0.403/0.41 m and 0.383 m, respectively. The series production of the high current quadrupoles and of the individually ramped low current corrector magnets was started in 2020 at the JINR in Dubna and is planned to be completed in 2023. We present the technological challenges that must be solved from production of the first magnets toward a stable and high-rate series production with reliably magnet quality as well as the first test results at operation conditions.

INTRODUCTION

The international scientific center FAIR will provide high intensity beams of ions and antiprotons for experiments in nuclear, atomic and plasma physics 0. The operation modes of the FAIR facility will facilitate four experiments simultaneously. Beside the reference Uranium and proton beams, acceleration of all other ion species is foreseen. The SIS100 synchrotron has a magnetic rigidity of 100 T·m. The high repetition rate of its acceleration cycles up to 1 Hz requires fast-ramped superconducting magnets with high dynamic heat load which must be cooled steadily. The SIS100 dipole and quadrupole magnets as well as the magnets for the NICA project [2] were designed based on the fast-cycling super-ferric magnets for the Nuclotron synchrotron at JINR in Dubna [3-8]. The production and test facility [2] of SC magnets for the NICA and FAIR project at the Laboratory of High Energy Physics of JINR was commissioned by end of 2016. For production and testing of the superconducting magnets a detailed quality assurance system was introduced, various sets of geometrical and magnetic measurement equipment were developed, methodically optimized 0, 0 and the high-resolution data analysis processing was adjusted.

THE CRYOMAGNETIC COMPONENTS

The synchrotron ring has a circumference of 1.1 km consists of six sections with cryomagnetic components, bypass lines and electrical supply systems, shown in Fig. 1. In each sector there are 9 quadrupole doubled modules (QDM) of the arc-section type, two QDM of the arc-termination type, 18 dipole modules (DPM) and 2 missing DPM. The basic ion optic cell is 12.9 m long and built of the dipole – dipole – defocusing quadrupole – focusing quadrupole structure (DP – DP – QD – QF). Besides the 108 main dipoles there are three families of quadrupoles, powered in their own electrical circuits – F1, F2, QD.

The operation modes of the accelerator are planned to vary in a wide parameter range of magnetic field amplitude, ramp rate and repetition frequency 0.

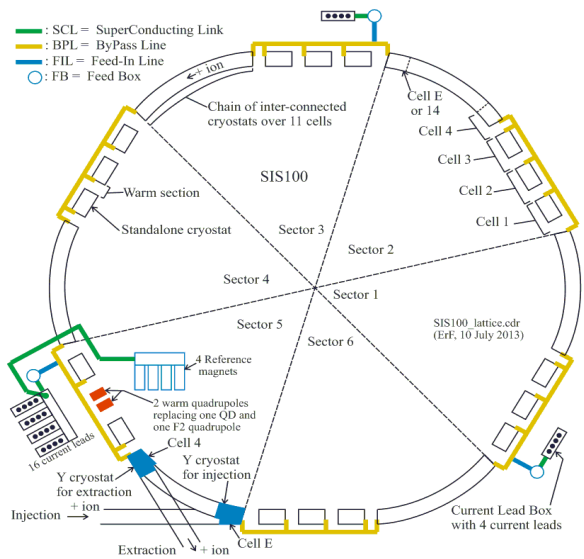

Figure 1: Scheme of the six sections of the synchrotron ring with Bypass Lines, the cryogenic and electrical supply systems.

The cryomagnetic modules have 11 different types of QDM, always containing two quadrupole units (QPU). Two QPU are mounted on a common girder system and combined with additional components of the vacuum system or a collimator. A QPU is a combination of a quadrupole magnet with different corrector magnets or also with a beam position monitor, mounted on the quadrupole as one cold mass. The detailed schema of the modules and units is given in Table 1. In this paper we present the results for the magnet parts of units VQD, SF2B and SF1B. The assembly with beam position monitors as well as their integration into a complete doublet configuration (here 2.5 or 1.7B) is not part of the working contract between JINR and the GSI/FAIR company and remains in the responsibility of the latter.

ISBN: 978-3-95450-240-0 ISSN: 2673-5539 doi:10.18429/JACoW-RuPAC2021-WEB03

Table 1: Quadrupole Units and Doublet Modules

Unit Configuration			*Doublet Configuration*		
Upstream	Centre	Downstream	Joined Name	Short Name	Quantity
QDB	-TRP-	SF2	QDB-TRP-SF2	2.123	15
QDBs	-TRP-	SF2s	QDBs-TRP-SF2s	2.13s	2
QDBb	-T-	SF2Mb	QDBb-T-SF2Mb	2.4	5
QDBx	-T-	SF2Mx	QDBx-T-SF2Mx	2.4x	1
VQD	**-CR-**	**SF2B**	**VQD-CR-SF2B**	**2.5**	**6**
BQD	-C-	SF1H	BQD-C-SF1H	1.6A	12
VQD	-CR-	SF1B	VQD-CR-SF1B	1.7B	12
BQD	-C-	SF2H	BQD-C-SF2H	2.8C	12
BQD	-CR-	SF2J	BQD-CR-SF2J	2.9D	12
MQDb	-C-	SF1Bb	MQDb-C-SF1Bb	1.E	5
MQDi	-C-	SF1Bi	MQDi-C-SF1Bi	1.Ei	1
			Total		**83**

The abbreviations in Table 1 are the following: QD – Defocusing quadrupole, F1 – Focusing quad. 1, F2 – Focusing quad. 2, B – Beam position monitor, V – Vertical chromaticity Sextupole, H – Horizontal chromaticity Sextupole, S – Steering magnet, M – Multipole corrector magnet, J – gamma-jump Quadrupole, C – Cryo-ion-catcher (collimator), T – Drift tube, b – modified busbars, i – injection Y cryostat, x – extraction Y cryostat, s – Star shape chamber, P – Cryo-sorption-pump, R – Roughing with cold-warm transition (CWT).

QUADRUPOLES AND CORRECTOR MAGNETS

All superconducting quadrupole and corrector magnets of SIS100 were contracted to be manufactured and tested in Dubna. The Nuclotron-type design — a cold, window-frame iron yoke with a coil made of hollow superconducting cable — was chosen for the SIS100 magnets. For the low current corrector magnets, a Nuclotron-type cable utilizing electrically insulated strands, was chosen. The main characteristics and the number of series magnets are given in Table 2. The cross sections of the sextupole (window frame design) and of the steerer (cosine-theta design) are illustrated in Fig. 2.

Table 2: Characteristics of the Magnets

Characteristic	Lattice Quadrupole	Corrector magnet		
		Multipole (Q/S/O)	Steerer	Chrom. Sextupole
Number of magnets	166	12	84	42
Max. field strength, T/m^{n-1}	27.77	0.75/25/333,3	0.37	232
Effective magnetic length, m	1.264	0.75	0.403/0.41	0.383
Aperture diameter, mm	100	150	135	120
Operation current	10512	250/246/240	245/241	252
Magnet weight, kg	850	200	120	145

Status of the Series Production

The iron yokes for all the quadrupoles, sextupoles and steerers were already produced by industry (STP, Minsk) and passed the incoming inspection at JINR. The superconducting coils are manufactured in Dubna and had passed the quality inspection for 20 %, 25 % and 50 % of the overall amount of the quadrupoles, sextupoles and steerers respectively. Using these components all magnets of the series type 2.5 (12 QPUs) and 33 % of series type 1.7B were completed, assembled to units, tested and delivered to FAIR by end of August 2021. The next 8 QPU are in preparation for shipment until end of October.

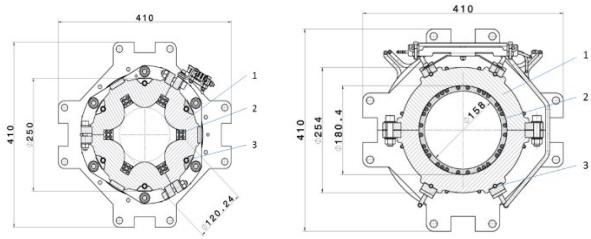

Figure 2: Cross sections of the sextupole (left) and of the steerer (right).

Test Results and Reproducibility

The details of the cryogenic procedures and the magnetic measurement systems are presented in 0-0.

The field quality of window frame magnets is dominated by the accuracy of yoke geometry to about 90 %. The geometry of the poles is checked with a dedicate gauge equipped with 20 capacitive sensors (see Fig. 3 for a typical example, yoke Nr. 142). The data are well within the tolerance limit of ±50 µm. Such a quality was found for all quadrupole apertures.

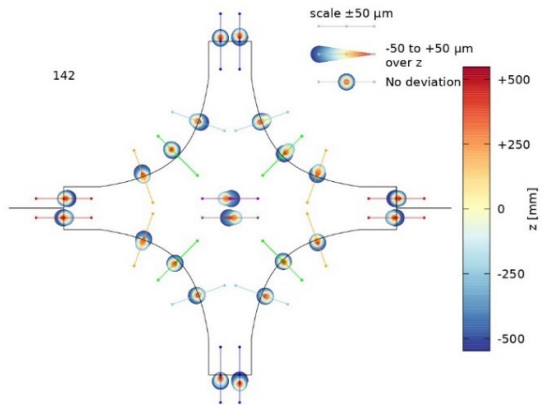

Figure 3: Geometrical measurement results for the real aperture along the yoke length compared to the designed contour.

A vibrating wire system was used for fiducialization of the quadrupoles 0. The precise knowledge of coordinates and direction of the magnetic axis with respect to the yoke symmetry and the reference points is a crucial requirement for the doublet conception: Both QPUs must be fixed finally on a common girder structure with exact mutual alignment of their magnetic axes. This alignment must hold unchanged even during an occasionally vacuum crash or other operation faults.

The horizontal y- and vertical z-position of the magnetic axis in the midplane of the quadrupole are presented in Fig. 4 for subsequent produced 22 quadrupoles. The data are showing a good reproducibility along the series production. For about 90 % the geometrical and magnetic axes do not differ more than ± 0.15 mm. Similar results were obtained for the respective pitch and yaw angles values and for their distribution along the production sequence (see Fig. 5).

ISBN: 978-3-95450-240-0 ISSN: 2673-5539 doi:10.18429/JACoW-RuPAC2021-WEB03

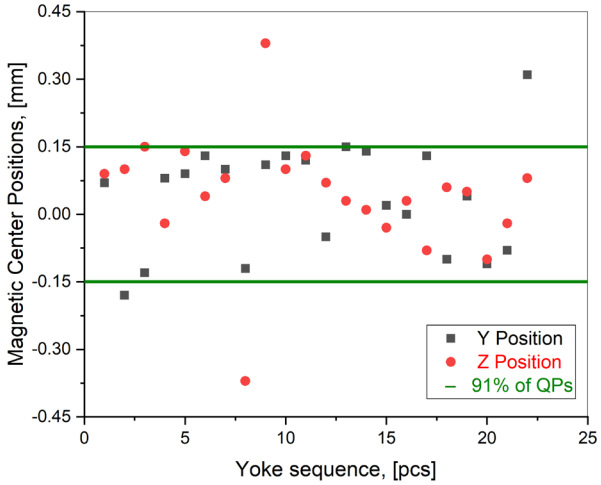

Figure 4: Positions of the magnetic axes with respect to the geometrical center of the quadrupoles for the first produces QPUs.

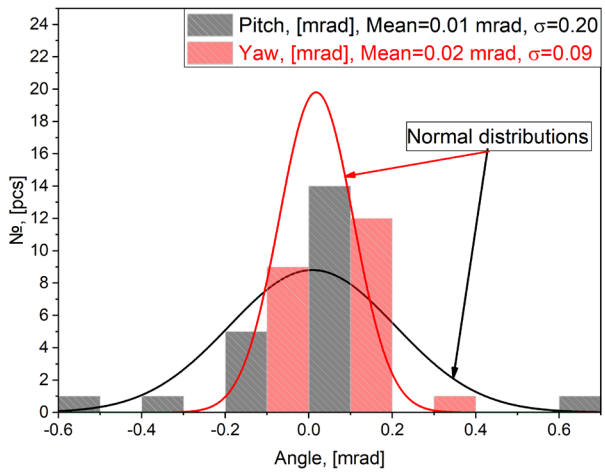

Figure 5: Distribution of the magnetic axes (pitch and yaw) for the statistics of the first 22 Quadrupoles.

The magnetic field quality of the magnets was measured by rotating coil assemblies both at ambient and at helium temperatures. Following the cooling down of the units during about 70…80 hours the preliminary magnet training had shown, that on average the magnets reach their operation current after 2…3 quenches. Their heat release during the various AC-operation modes was also reproducible within ± 10 %. The typical current dependence of integral transfer functions (ITF) of the quadrupoles and their respective statistical distribution are shown in Fig. 6. Similar good results were obtained for the ITFs of the steerers and sextupoles showing a data spread along the production sequence within ± 0.6 % and ± 0.2 % respectively. The relative variation of the magnetic length of the quadrupoles over series production is about $1 \cdot 10^{-3}$. The quadrupole series statistics for the measured multipoles is summarized in Fig. 7. It was found that b6 is the only significant multipole and reproduces for all the measured quadrupoles within ± 1 unit.

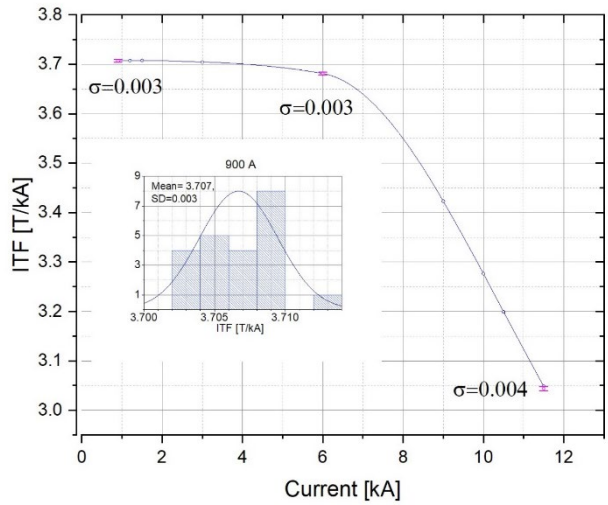

Figure 6: Current dependence of Integral transfer functions of the quadrupoles. The inset graph gives der distribution for 22 series magnets at 900 A.

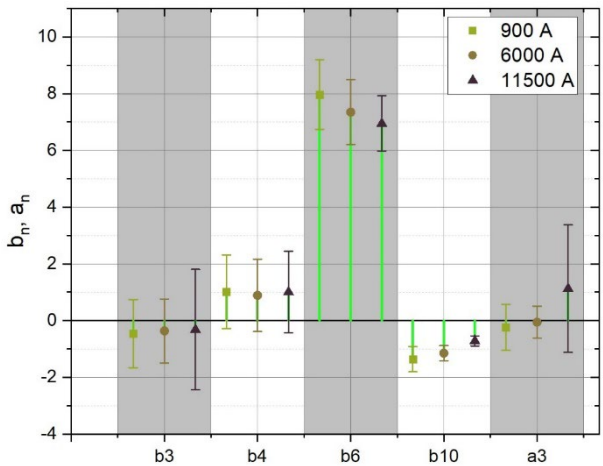

Figure 7: Integral multipoles of 22 quadrupole magnets and their variation within the series sequence.

CONCLUSION

The series production of the superconducting quadrupole and corrector units for the SIS100 of FAIR was started successful at the JINR, Dubna. Twenty quadrupole units were already assembled, tested up to 20 % above operation parameters and delivered to Darmstadt. The next eight units are under preparation for shipment in October 2021. The first unit series 2.5 was completed in March this year, the second series 1.7B will also be finished this year. JINR had established an effective and stable production and testing scenario for the Quadrupole units. The optimization of the production technology and detailed methodological adjustment of the measurement techniques resulted in the proven and continuously high quality of the series magnets.

REFERENCES

[1] FAIR at GSI, http://www.gsi.de

[2] Nuclotron–based ion collider facility, http://nica.jinr.ru

ISBN: 978-3-95450-240-0 ISSN: 2673-5539 doi:10.18429/JACoW-RuPAC2021-WEB03

[3] H. Khodzhibagiyan *et al.,* "The concept of a superconducting magnet system for the Nuclotron", in *Proc. of ICEC12*, Southampton, 1988, p. 841. DOI:10.1088/1757-899X/502/1/012112.

[4] A. Kovalenko *et al.,* "New Results on Minimizing AC Power Losses in a Fast Cycling 2 T Superferric Dipole with a Cold Yoke", *IEEE Trans. Appl. Supercond.* 16, 338–341, 2006. DOI:10.1109/TASC.2006.873341

[5] V. V. Borisov *et al.,* "Magnetic Field Performance of the First Serial Quadrupole Units for the SIS100 Synchrotron of FAIR", presented at the 12th Int. Particle Accelerator Conf. (IPAC'21), Campinas, Brazil, May 2021, paper TUPAB383. doi:10.18429/JACoW-IPAC2021-TUPAB383.

[6] D. Nikiforov *et al.,* "SC Magnets for Project of NICA", presented at the 27th Russian Particle Accelerator conference (RuPAC'21), Alushta, Russia, September 2021, paper WEB01, this conference.

[7] A. Shemchuk *et al.,* "Magnetic Field Measurements for the Collider Magnets and FAIR Quadrupole Units", presented at the 27th Russian Particle Accelerator conference (RuPAC'21), Alushta, Russia, September 2021, paper WEB02, this conference.

[8] T. Parfylo *et al.,* "Vibrating Wire System for Fiducialization NICA Booster Superconducting Quadrupole Magnets", presented at the 27th Russian Particle Accelerator conference (RuPAC'21), Alushta, Russia, September 2021, paper WEPSC17, this conference.

ISBN: 978-3-95450-240-0 ISSN: 2673-5539 doi:10.18429/JACoW-RuPAC2021-WED04

PRECISE ANALYSIS OF BEAM OPTICS AT THE VEPP-4M BY TURN-BY-TURN BETATRON PHASE ADVANCE MEASUREMENT

I.A. Morozov*, P.A. Piminov, I.S. Yakimov, BINP SB RAS, Novosibirsk, Russia

Abstract

Turn-by-turn (TbT) beam centroid signals can be used to evaluate various relevant accelerator parameters including betatron frequencies and optical functions. Accurate estimation of parameters and corresponding variances are important to drive accelerator lattice correction. Signals acquired from beam position monitors (BPMs) are limited by beam decoherence and BPM resolution. Therefore, it is important to obtain accurate estimations from available data. Several methods based on harmonic analysis of TbT data are compared and applied to the VEPP-4M experimental signals. The accuracy of betatron frequency, amplitude, and phase measurements are investigated. Optical functions obtained from amplitudes and phases are compared.

INTRODUCTION

The VEPP-4M is an electron-positron collider operating in 1 GeV to 6 GeV beam energy range [1]. The VEPP-4M storage ring is equipped with 54 dual-plane BPMs [2] capable of performing accurate TbT measurements. TbT data is acquired by excitation of the circulating beam with impulse kickers. In Fig. 1 the optical functions of the VEPP-4M ring are shown along with corresponding BPM positions.

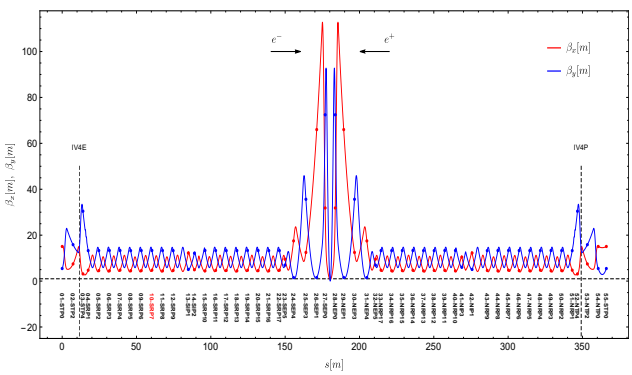

Figure 1: The VEPP-4M lattice functions.

Harmonic analysis [3] can be used to obtain frequency and optics from TbT data. Previously, optics measurements were based only on the computation of β functions from amplitudes. In this paper, the extension of the optics measurement procedure is described. It includes the addition of TbT data processing, anomaly detection and BPM noise estimation. The frequency measurement algorithm has been tuned. Statistical error propagation has been added to the computation of BPM signal parameters. Optics measurement from phase has been performed for the first time at the VEPP-4M. This provides an additional tool to check optics measurement from amplitude and to study BPM calibrations. Both methods with statistical error propagation will allow more accurate lattice correction. Experimental results of optics measurement are reported.

* I.A.Morozov@inp.nsk.su

VEPP-4M TBT PROCESSING LOOP

In Fig. 2 TbT analysis workflow at the VEPP-4M is shown. First, detection of anomalies in TbT signals is performed [4], and anomalies are flagged. After anomaly detection, TbT filtering is performed. Noise estimation using optimal SVD truncation [5] is performed for each BPM signal. The frequency for each BPM is computed from its interpolated spectrum maximum. For known frequencies, amplitudes and phases are computed for each BPM with statistical error propagation. Amplitudes and phases are then used to compute linear optics.

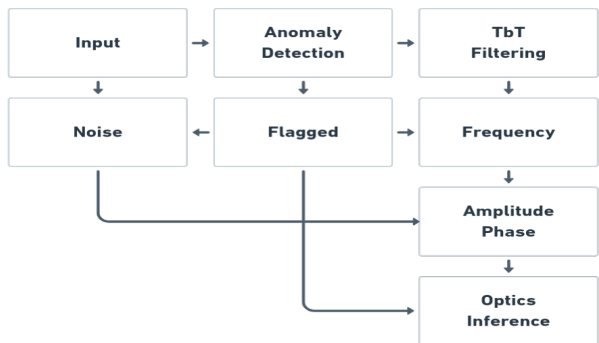

Figure 2: The VEPP-4M TbT processing loop.

We have tested several different techniques for TbT data noise cleaning. One of the common options is to used truncated SVD applied to the full TbT matrix. For the VEPP-4M case, the optimal rank of truncated representation was found to be eight. Another option is to apply Robust PCA [6] to the full TbT matrix. This method was found to introduce a bias for estimated amplitudes and phases, but no bias was observed in frequencies. Both SVD and Robust PCA can be applied to individual BPM signals. In this case each signal $x = [x_1\ x_2\ x_3\ x_4\ x_5\ x_6]$ is represented using Hankel matrix:

$$X = \begin{bmatrix} x_1 & x_2 & x_3 \\ x_2 & x_3 & x_4 \\ x_3 & x_4 & x_5 \\ x_4 & x_5 & x_6 \end{bmatrix}$$

Truncated SVD or Robust PCA can be applied to this signal representation. The filtered signal is then reconstructed as the mean of skew diagonals.

ISBN: 978-3-95450-240-0 ISSN: 2673-5539 doi:10.18429/JACoW-RuPAC2021-WED04

BPM NOISE ESTIMATION

BPM noise study was performed for experimental TbT data obtained with impulse kick excitation. Each BPM signal noise was estimated using Hankel matrix representation and optimal SVD truncation. In Fig. 3 the dependence on the beam current of the estimated noise is shown. Top plots show results for 100 successive kicks for two particular BPMs. After each 20 kicks TbT data without excitation were acquired (SOFT). Hollow points correspond to the noise estimation as the standard deviation for these cases. The bottom plots show noise estimation for 10 successive kick measurements for all BPMs. On average, noise is at the level of 40 µm for the horizontal plane and 35 µm for the vertical one. Noise estimations are used for statistical error propagation in amplitude, phase and optics computation.

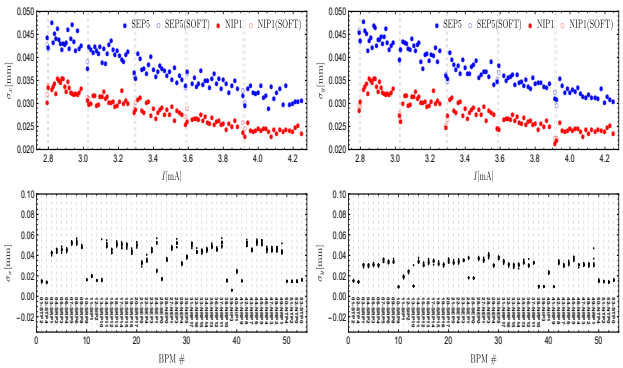

Figure 3: BPM noise estimation. Estimated noise vs the beam current for selected BPMs (top plots). Estimated noise for all BPMs @ 2 mA (bottom plots).

FREQUENCY MEASUREMENT

Previously, frequency measurement was configured to provide accuracy of 10^{-4}. This is related to magnetic system stability and is sufficient for optics measurements. For nonlinear beam dynamics studies, a more accurate measurement was desired. Several methods based on the interpolated spectrum were tested including the effect of windowing.

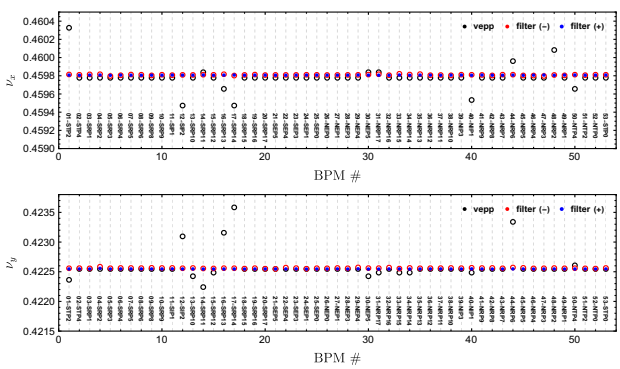

Figure 4: An example of frequency measurement with (blue) and without (red) signal filtering in comparison with the previous system (black).

In Fig. 4 an example of frequency measurement is shown. The spread of frequencies across BPMs is $5 \cdot 10^{-6}$ without filtering and close to 10^{-6} with filtering. Cosine window was used in both cases.

AMPLITUDE AND PHASE MEASUREMENT

For known frequencies, corresponding amplitudes and phases can be computed using convolution. The results of phase measurements are shown in Fig. 5 and Fig. 6. The accuracy of phase measument is better than 5 % and average deviation from the model is 15 %. For amplitude, the accuracy is 2 % and 3 % for horizontal and vertical planes.

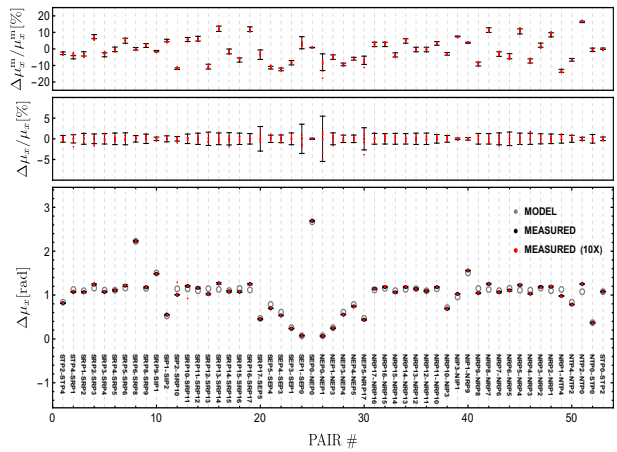

Figure 5: Measured phase advance between successive BPM pairs for the horizontal plane. Deviation from model (top) for a single measurement with statistical errors (black) and 10 successive measurements (red). Spread of phase advance (middle) for 10 measurements (red) and a single measument with statistical errors. Absolute phase advance (bottom) for model (gray), 10 measurements (red) and a single measument (black).

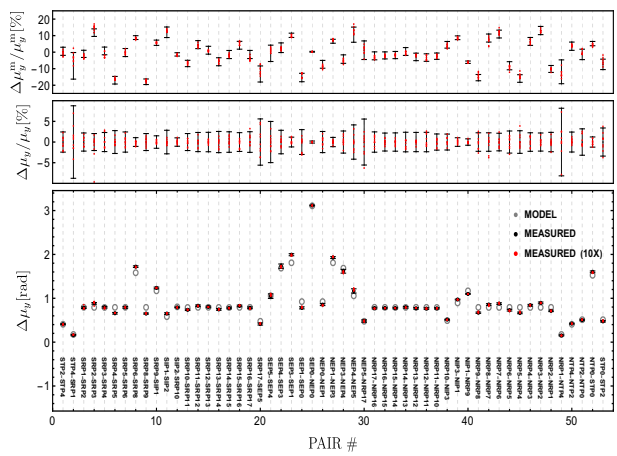

Figure 6: Measured phase advance between successive BPM pairs for the vertical plane.

ISBN: 978-3-95450-240-0 ISSN: 2673-5539 doi:10.18429/JACoW-RuPAC2021-WED04

OPTICS MEASUREMENT

In Fig. 7 the results of optics measurement from amplitude are shown. The average deviation from the model is around 15 %, and the spread between measurements is 5 %. For measurements from phase (Fig. 8), the average deviation from the model is also around 15 %. Spread in this case is close to 10 %. Here, the best adjacent triplets were used for optics computation. We have also tested using a combination of several different triplets. In this case, the spread from 10 measurements was around 5 %.

Comparison of two methods is shown in Fig. 9. Both methods are around 15 % off from the model. The ratio of β functions is within 15 %.

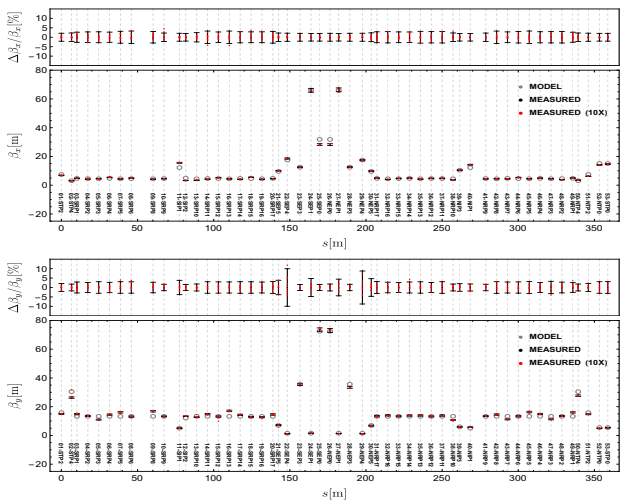

Figure 7: Optics measurement from amplitude. Top plots shows spread from 10 measurements (red) with a single measurement with errors (black). Comparison with model optics (bottom plots).

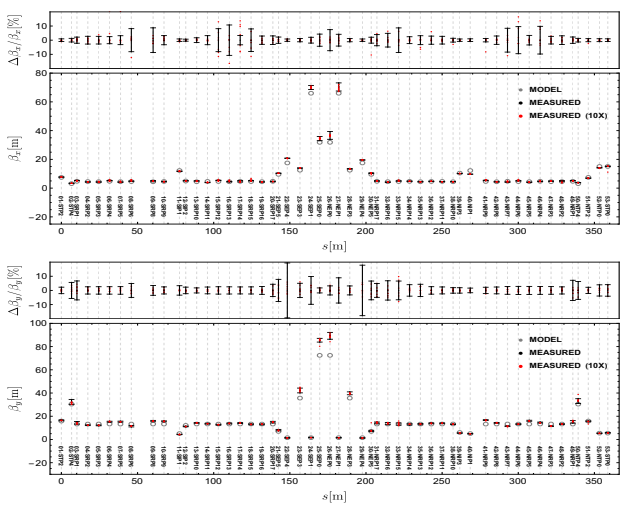

Figure 8: Optics measurement from phase. Top plots shows spread from 10 measurements (red) with a single measurement with errors (black). Comparison with model optics (bottom plots).

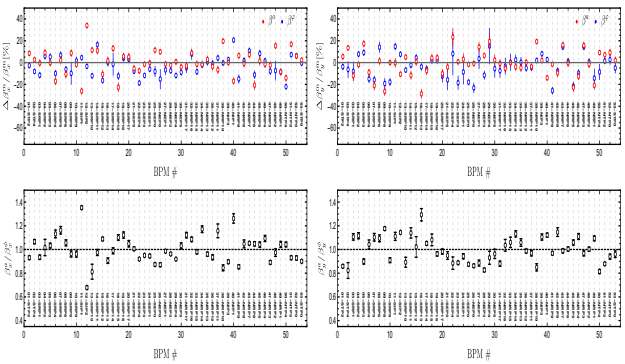

Figure 9: Comparison of optics from amplitude and phase. Deviation from model for optics from amplitude (red) and phase (blue). Ratio of β functions (bottom plots).

CONCLUSION

The improved TbT analysis workflow was verified at the VEPP-4M. An anomaly detection system and TbT data filtering were introduced. BPM noise studies were performed using noise estimation based on optimal SVD truncation. The estimated noise agrees with the results from measurements without excitation. An improved frequency estimation procedure was implemented. The frequency spread close to 10^{-6} was archived across BPMs in a single measurement. This allows a more accurate study of nonlinear dynamics at the VEPP-4M. The spread of amplitudes and phases from successive measurements is less than 5 % and around 5 %. Single measurement statistical errors match the observed spread. Two methods of optics computations were performed and compared. Both methods are around 15 % off from the model. The difference between methods is also close to 15 % on average. Phase advance measurements are planned to be added to the optics correction. A detailed BPM calibration study is scheduled for the new season.

REFERENCES

[1] P. Piminov *et al.*, "Vepp-4m collider operation in high energy," *Proceedings of the 12th International Particle Accelerator Conference, IPAC2021, Campinas, Brazil*, May 2021.

[2] E. A. Bekhtenev and G. V. Karpov, "Bpm system for vepp-4m collider," *Physics of Particles and Nuclei Letters*, vol. 15, no. 7, pp. 929–932, Dec. 2018. DOI: 10.1134/S1547477118070154.

[3] R. Tomás, M. Aiba, A. Franchi, and U. Iriso, "Review of linear optics measurement and correction for charged particle accelerators," *Phys. Rev. Accel. Beams*, vol. 20, p. 054 801, 5 May 2017. DOI: 10.1103/PhysRevAccelBeams.20.054801.

[4] I. Morozov and P. Piminov, "Detection of anomalies in bpm signals at the vepp-4m," *Proceedings of the 17th Russian Particle Accelerator Conference, RUPAC2021, Alushta, Russia*, Oct. 2021, this conference.

[5] M. Gavish and D. L. Donoho, "The optimal hard threshold for singular values is 4/sqrt(3)," *IEEE Transactions on Information Theory*, vol. 60, no. 8, pp. 5040–5053, Aug. 2014. DOI: 10.1109/TIT.2014.2323359.

[6] E. J. Candès, X. Li, Y. Ma, and J. Wright, "Robust principal component analysis?" *J. ACM*, vol. 58, no. 3, May 2011. DOI: 10.1145/1970392.1970395.

ISBN: 978-3-95450-240-0 ISSN: 2673-5539 doi:10.18429/JACoW-RuPAC2021-WED05

NONDESTRUCTIVE DIAGNOSTICS OF ACCELERATED ION BEAMS WITH MCP-BASED DETECTORS AT THE ACCELERATOR COMPLEX NICA. EXPERIMENTAL RESULTS AND PROSPECTS

A. A. Baldin†, V. I. Astakhov, A. V. Beloborodov, D. N. Bogoslovsky, A. N. Fedorov, P. R. Kharyuzov, A. P. Kharyuzova, D. S. Korovkin, A. B. Safonov, Joint Institute for Nuclear Research, Dubna, Russia

Abstract

Non-destructive ion beam detectors based on micro-channel plates are presented. The design of two-coordinate profilometer situated in the high vacuum volume of the Booster ring is discussed. Experimental data on registration of circulating beam of the Booster in the second run (September 2021) are presented. The possibility of adjustment of the electron cooling system with the help of this detector based on the obtained experimental data is discussed.

INTRODUCTION

Obviously, development of nondestructive diagnostic systems for both circulating and extracted beams is one of the most important tasks at the acceleration complex NICA [1]. One can speak of nondestructive systems of two types: the first one registers electromagnetic radiation, and the second one registers interaction of beam ions with molecules of residual gas in the vacuum chamber of the accelerator.

This paper considers some first results of operation of the nondestructive diagnostic system implemented at the Booster put in operation at the end of 2020. This diagnostic system provides registration of the space-time beam structure directly inside the Booster vacuum chamber at the input point from HILAC.

A similar system is situated in the Nuclotron ring and at the extracted beam line of Nuclotron (see Fig. 1) [2, 3, 4, 5].

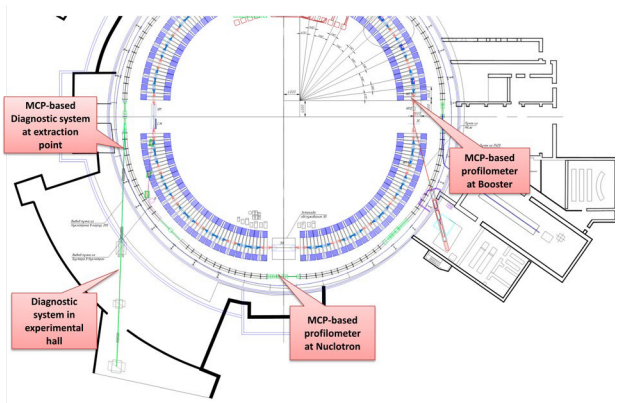

Figure 1: Schematic diagram of diagnostic system locations at the Booster and Nuclotron.

* This work was supported in part by the Russian Foundation for Basic Research, project no.18-02-40097.
† an.baldin@mail.ru

NUMERICAL STUDY OF MCP-BASED DETECTOR

The drawing of the MCP-based profilometers mounted inside the chamber is shown in Fig. 2.

This detector geometry implemented in the Booster chamber was used in the software CST for simulation of the detector operation.

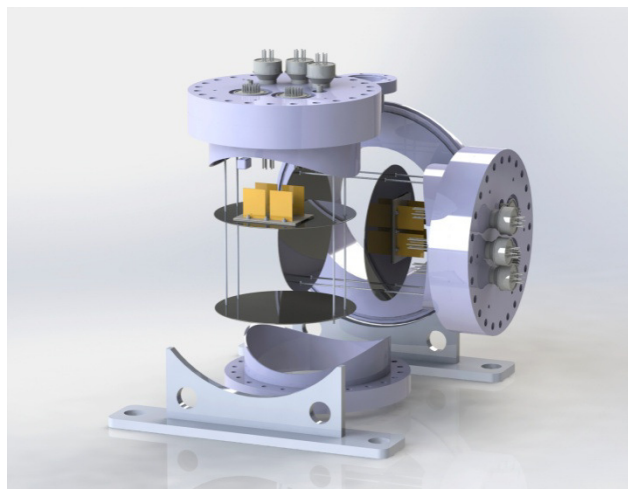

Figure 2: Assembly drawing of MCP-based profilometers mounted on vacuum flanges.

CST is designated for simulation of a wide range of electromagnetic interactions, including construction of electrostatic models and charged particle tracking in simulated fields. The study presented here used the solvers "E-Static" and "Particle Tracking" of the module "Statics and low frequency" CST. The real geometry of the existing detectors was input in the simulation.

The physics of the simulated processes is as follows. accelerated charged particles, passing the ion beam line, ionize residual gas. The number of ions produced in unit volume is proportional to the beam intensity, residual gas pressure, and squared ion charge. These ions are accelerated by electrostatic field toward the chevron assembly of the MCP detector and are registered by the detector to give the space-time parameters of the beam.

In the simulation, ionized particles were distributed uniformly over the whole detector volume and their trajectories were traced in the electrostatic system of the detector. It was found out that the electrostatic systems of the X and Y profilometers distort the electrostatic field and, as a consequence, ion trajectories inside the vacuum

ISBN: 978-3-95450-240-0 ISSN: 2673-5539 doi:10.18429/JACoW-RuPAC2021-WED05

chamber. The shape of electrodes was specially adjusted numerically in order to reduce this distortion. The repulsive electrode was bent with a radius of 180 mm from the center at an angle of 45° to the beam axis; the cuts for plate fastening and detectors were shifted by 20 mm along the beam from the center of the unit. Also, the special absorbers in the form of rectangular plates along the beam axis were added to the electrostatic system of detector. These absorbers cut off ions produced beyond the working region of the detector; the working voltage at the absorbers was 2.2 kV. The detectors used at the Booster were manufactured according to this numerically found optimal shape.

The detector resolution was also determined in the simulation as the root mean square deviation of the coordinate calculated for all tracks. The resolution in both X and Y directions was found to be not worse than 0.3 mm.

MEASUREMENTS OF BEAM SPATIAL DISTRIBUTION WITH MCP-BASED DETECTOR

The photo of the MCP-based detectors used at the Booster is shown in Fig. 3.

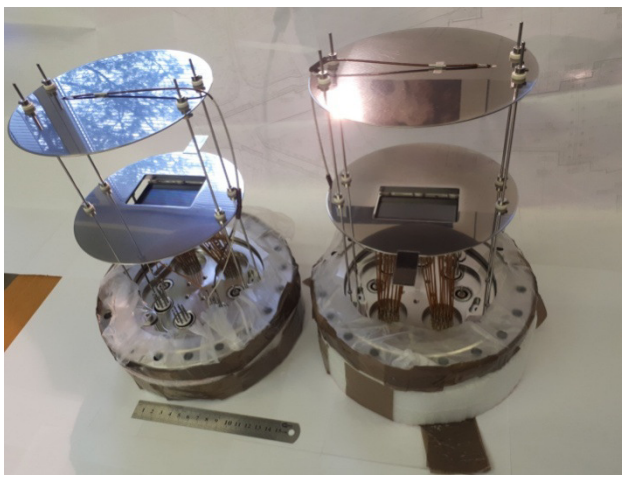

Figure 3: Photo of the two MCP-based detectors installed at the Booster for X and Y profile measurement.

The electron cooling system of the Booster beam was tested in run 2 (September, 2021). The MCP-based detectors shown above were installed at the Booster and used in this run for beam diagnostics. The detector system provided measurement of the beam profile in the X and Y directions. The electron cooling system was tested in the course of injection with $^{14+}$Fe beam. The electron velocity corresponding to the velocity of beam ions was about 1.85 keV.

The plots below: Fig. 4, Fig. 5, and Fig. 6 show the dynamic profile of the beam with and without the electron cooling system. It can be seen that the electron cooling has a noticeable beam narrowing effect.

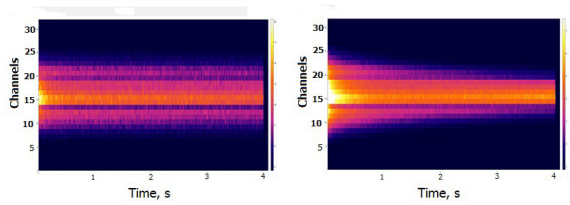

(a) (b)

Figure 4: Y profile of 14+Fe beam as a function of time: (a) without electron cooling; (b) with electron cooling. The working electron cooling voltage is 1.83 keV.

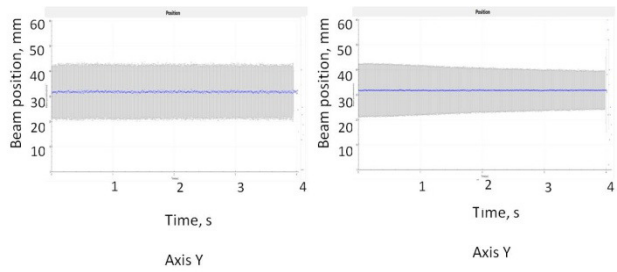

(a) (b)

Figure 5: Y position of $^{14+}$Fe beam as a function of time: (a) without electron cooling; (b) with electron cooling. The working electron cooling voltage is 1.83 keV.

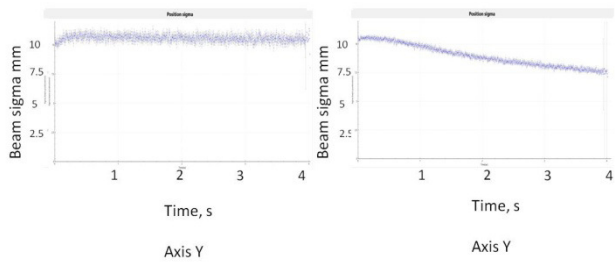

(a) (b)

Figure 6: Dispersion of $^{14+}$Fe beam as a function of time: (a) without electron cooling; (b) with electron cooling. The working electron cooling voltage is 1.83 keV.

Similar results were obtained for both X and Y directions at different electron beam energies and currents.

MEASUREMENTS OF TIME RESOLUTION WITH MCP-BASED DETECTOR

It was already shown earlier [6] that the MCP-based detector is capable of measuring first turns and even the beam structure within one beam revolution.

Figure 7 shows the beam dynamics for the first 125 turns of the beam after injection measured in run 2 of the Booster, which corresponds to a time slice of 1 μs.

Regular beam oscillations in the transverse direction with a frequency of about 12 kHz can be clearly observed.

ISBN: 978-3-95450-240-0 ISSN: 2673-5539 doi:10.18429/JACoW-RuPAC2021-WED05

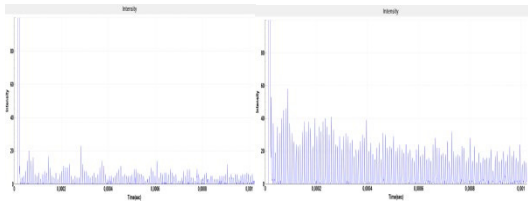

(a) (b)

Figure 7: $^{14+}$Fe beam intensity as a function of time immediately after injection in run 2 of the Booster: (a) along X (horizontal); (b) along Y (vertical).

Figure 8 shows the beam dynamics for the first 250 turns of the beam after injection measured in run 2 of the Booster. It can be clearly seen that the above mentioned oscillations die out after the first hundred of turns.

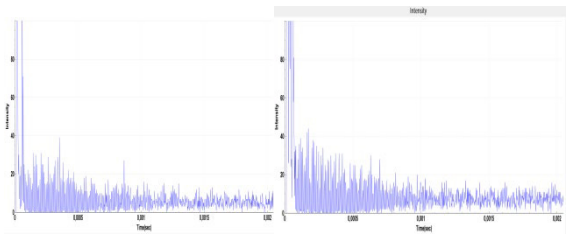

(a) (b)

Figure 8: $^{14+}$Fe beam intensity as a function of time immediately after injection in run 2 of the Booster: (a) along X (horizontal); (b) along Y (vertical).

This illustrates the potential of application of this detector for adjustment of injection and optimization of the beam capture in acceleration cycle at the initial stage of acceleration.

The data acquisition system for these detectors is based on the electronic module TIC-64 developed by our team. This module represents a counter with buffer memory based on FPGA. This module, with a synchro-pulse from the accelerator, remotely sets the time delay for measurements and records pulse counts in 64 channels with given time intervals from hundreds ns to seconds.

ACKNOWLEDGEMENTS

This work was supported in part by the Russian Foundation for Basic Research, project no.18-02-40097.

We thank I.N. Meshkov, A.V. Butenko, E.M. Syresin V.M. Slepnev for helpful discussions, and A.R. Galimov and A.M. Bazanov for technical support with high vacuum equipment.

REFERENCES

[1] V. Kekelidze *et al.*, "The NICA project at JINR Dubna", in *Proc. 2nd International Conference on New Frontiers in Physics (ICNFP 2013)*, Colymbari, Crete, Greece, Aug. 28 - Sep. 5, 2013, pp. 00127. DOI: 10.1051/epjconf/20147100127.

[2] A. A. Baldin *et al.*, "Diagnostic system for circulating beam of Nuclotron based on MCP", *JINR Rapid Commun.*, no. 2[82], pp. 15-22,1997.

[3] A. A. Baldin *et al.*, "The MCP based detector for monitoring space-time characteristics of the Nuclotron circulating beam", *Phys. Part. Nucl. Lett.*, vol. 11 no.2(186), pp. 209-218,2014.

[4] A. Baldin *et al.*, "Proposals for a new type of microchannel plate based vertex detector", *Nucl. Instrum. Methods A.*, vol. 323 no.2(186), pp. 439-444,1992. doi: 10.1016/0168-9002(92)90329-3.

[5] G. Feofilov *et al.*, "Development and tests of MCP based timing and multiplicity detector for MIPs", *Phys. Part. Nucl. Lett.*, vol. 14 no.1, pp. 150-159,2017.

[6] A. Baldin *et al.*, "Fast beam-beam collisions monitor for experiments at NICA", *Nucl. Instrum. Methods A*, vol. 958, 162154,2020. doi:10.1016/j.nima.2019.04.108.

ISBN: 978-3-95450-240-0 ISSN: 2673-5539 doi:10.18429/JACoW-RuPAC2021-THA01

STATUS OF THE SC HWR CAVITIES PRODUCTION FOR NICA PROJECT

A. Butenko, E. Syresin, G. Trubnikov, D. Nikiforov, JINR, Dubna, Russia
M. Gusarova[1], M. Lalayan[1], S. Matsievskiy[1], R. Nemchenko, S. Polozov,
N. Sobenin, V. Shatokhin[1], NRNU MEPhI, Moscow, Russia
D. Bychanok[2], A. Sukhotski, S. Huseu, S. Maksimenko, INP BSU, Minsk, Belarus
A. Shvedov, S. Yurevich, V. Petrakovsky, A. Pokrovsky, I. Pobol, V. Zaleski, PTI NASB, Minsk, Belarus
[1]also at JINR, Dubna, Russia [2]also at TSU, Tomsk, Russia

Abstract

Since 2015 the superconducting (SC) linac-injector development for Nuclotron NICA (JINR, Dubna, Russia) is carried out by the collaboration of JINR, NRNU MEPhI, INP BSU, PTI NASB. This new SC linac is to accelerate protons up to 20 MeV and light ions to 7.5 MeV/u with possible energy upgrade up to 50 MeV for proton beam. This paper reports the current status of the development and manufacturing of superconducting accelerating cavities for a new linear accelerator of the injection complex of the Nuclotron-NICA project.

INTRODUCTION

Nuclotron-based Ion Collider fAcility (NICA) is new accelerator complex under construction at JINR [1-5]. It was proposed for ion collision and high-density matter study. NICA facility will include the existing ion synchrotron Nuclotron together with new booster and two collider rings being under construction. The injection system of Nuclotron-NICA was upgraded in 2011-2016. The pulse DC linac forinjector of Alvarez-type DTL LU-20 was replaced by the new RFQ developed and commissioned by JINR, ITEP and MEPhI [6]. New RFQ linac can accelerate ions with charge-to-mass ratio Z/A>0.3. The first technical session of Nuclotron with new injector was ended on 2016 [7]. The LU-20 with new RFQ for-injector is used for p, p↑, d, d↑, He, C and Li ions acceleration till now. The other heavy ion linac for particles with Z/A=1/8-1/6 was developed by joint team of JINR, Frankfurt University and BEVATECH and commissioned in 2016.

It must be noted that LU-20 operation causes many technical issues because of its age: it was commissioned in 1972. The possibility of LU-20 replacement by the new linac of 20 MeV energy for protons [8-12] and 7.5 MeV/nucleon for deuterium beam is discussed now. Project also include an option of the proton beam energy upgrade up to 50 MeV by installing several cavities in additional section. New linac will include a number of superconducting (SC) cavities.

The general layout of new light ion linac (LILac) for the NICA collider is presented in Fig. 1 [13]. LILac consists of 5 cavities: RFQ, re-buncher, two Interdigital H-mode Drift-Tube-Linacs (IH-1 and IH-2) and a de- buncher [14]. The operating frequency is 162.5 MHz and the final energy at the IH-2 exit is 7 MeV/u. After IH-2 the beam is transported towards the Nuclotron (bending magnets shown in blue). SPI stands for Source of Polarized Ions [15]. In future the extension of LILac is expected with normal-conductive cavities up to 13 MeV/u (marked green) and followed by SC HWR 1 cavities (light blue at Fig. 1) up to 20 MeV for protons and to 7.5 MeV/u light ions and by SC HWR 2 cavities up to 50 MeV for protons [16].

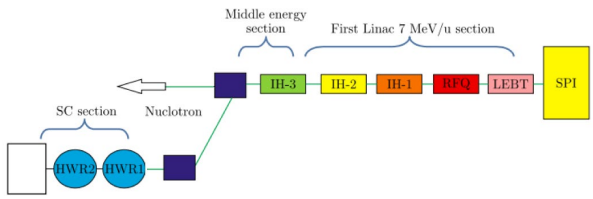

Figure 1: The Light Ion Linac.

The problem with SC cavities and SC linac construction for Nuclotron-NICA was the absence of SRF technology in Russia. The development of the SRF technologies is the key task of the new Russian - Belarusian collaboration launched in March 2015. For testing purposes, the test beamline is proposed with two HWR1 cavities installed. A test cryostat for two cavities HWR 1 is developing now by a joint team of JINR, GSI (Germany) and BEVATECH (Germany). Cryostat for 4 cavities HWR 1 is developing by JINR and IMP (China).

BEAM DYNAMICS AND FR DESIGN

The beam dynamics simulation for superconducting part of the first linac layout was done using BEAMDULAC-SCL code designed at MEPhI [17-19]. According to the fourth version of SC linac design developed the accelerator is divided into two groups of cavities HWR 1 and HWR 2 with geometric velocities β_G = 0.21 and 0.314. First group HWR 1 at β_G = 0.21 accelerates protons to 20 MeV and light ions to 7.5 MeV/u. Second group HWR 2 at β_G = 0.314 accelerates particles up to 50 MeV.

The beam dynamics of proton and deuterium ions beam was studied at [9]. Parameters of the first group of cavities (HWR 1) are shown in Table 1.

Considerations on the SC cavity types choice and their RF design done at MEPhI and JINR are presented in detail in [20]. HWR cavities were proposed because they could provide proper consent to electrodynamic parameters and beam dynamics [16, 20].

The operating frequency of SC sections is 325 MHz. Different concurring HWR cavity designs were considered one with ordinary cylinder-shaped central conductor and the second with cone-shaped one [21]. Geometric and electrodynamics parameters of the cavities are presented in Table 2.

ISBN: 978-3-95450-240-0 ISSN: 2673-5539 doi:10.18429/JACoW-RuPAC2021-THA01

Table 1: Current Parameters of the HWR1 Group of SC Linac for Proton and Deuterium Beams Acceleration

Cavity group	0 *	1**	2**	0 *	1**	2**
	Proton beam			Deuterium beam		
β_g	0.12		0.21	0.12		0.21
F, MHz	162.5		325	162.5		325
T, %	24.0		24.0	24.0		24.0
N_{gap}	2		2x2**	2		2x2***
L_{res}, m	0.222		0.39	0.222		0.39
L_{sol}, m	0.2		0.2	0.2		0.2
L_{gap}, m	0.1		0.1	0.1		0.1
L_{per}, m	0.622		0.79	0.622		0.79
N_{per}	3	8	8	3	8	8
L, m	1.87	4.98	6.32	1.87	4.98	6.32
E_{acc}, MV/m	4.50	5.86	6.4	4.50	5.86	6.4
U_{res}, MV	1.0	1.3	1.25	1.0	1.3	1.25
Φ, deg	–20	–20	–20	–20	–20	-90
B_{sol}, T	1.35	1.3	1.9	1.8	2.0	1.0
W_{in}, MeV	2.5	4.9	13.47	2.5	3.65	8.3
β_{in}	0.073	0.102	0.168	0.073	0.088	0.133
W_{out}, MeV	4.9	13.47	31.0	3.65	8.3	8.3
β_{out}	0.102	0.168	0.251	0.088	0.133	0.133
K_T, %	100	100	100	100	100	100

* these cavities are normal conducting;
** SC cavities;
*** two 2-gap HWR per one period.

The operating frequency of SC sections is 325 MHz. Different concurring HWR cavity designs were considered one with ordinary cylinder-shaped central conductor and the second with cone-shaped one [21]. Geometric and electrodynamics parameters of the cavities are presented in Table 2.

It was shown that both designs satisfy the requirements for the accelerating gradient. The second design with the conical central conductor cavity has much better performance with respect to multipactor discharge. This discharge is observed for coaxial cavities for low RF field levels and leads to the conditioning time increase.

Table 2: RF Parameters of 325 MHz HWR for $\beta g = 0.21$

Parameter	Value	
HWR type	Cylindrical	Conical
Operating frequency, f, MHz	325	
Geometrical velocity, β_g	0.21	
Cavity height, mm	431	474
Cavity radius, mm	97	97
Ratio of the peak electric surface field to the accelerating field, E_p/E_{acc}	6.5	5.9
Ratio of the peak surface magnetic field to the accelerating field, B_p/E_{acc}, mT/(MV/m)	10.2	9.6
Effective shunt impedance, R_{sh}/Q_0, Ohm	298	306
Geometric factor, $G=R_s/Q$, Ohm	57	57

Cavity body design was done by PTI NASB and MEPhI research groups taking into account thermal and mechanical cavity performance considerations during cooldown. Cavity was designed in classical coaxial HWR configuration with integrated helium vessel [22, 23]. PTI NASB production facility expertise in deep-drawing and EB welding of high purity niobium allowed us to choice in favor of more complicated but yet much more promising design with conical inner conductor. HWR cavity with integrated cryostat vessel design is presented on Fig. 2.

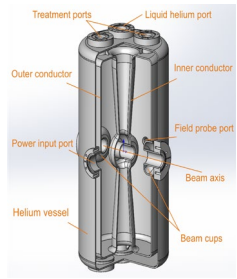

Figure 2: The Light Ion Linac SC cavity design.

COPPER PROTOTYPE

Design study and manufacturing of copper prototype cavity (Fig. 3) were carried out from 2019 to 2020 at PTI NANB and INP BSU. Tooling for hydroforming of central conductor parts, side beam ports and housing covers were developed. The cavity was assembled using the clamping system shown in Fig. 3a, that allowed one to align, precisely adjust and securely fix cavity parts before welding. This clamping system also was used for cavity RF performance intermediate measurements as shown in Fig. 3c.

Copper prototype cavity (see Fig. 4) was manufactured and tested in 2020 [24]. Resonant frequency measurements and vacuum tests showed cavity desired performance [25]. Intermediate measurements and frequency control procedure used at production site allowed us to get the necessary frequency value. This multistage tuning took us several weeks as the cavity parts were manufactured and matched. Cavity RF test port reflection and resonant frequency dependence on temperature are presented on Fig. 5.

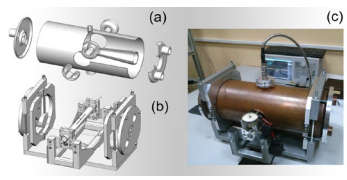

Figure 3: (a) Six parts of the cavity body, (b) assembling frame and (c) complete assembly with fixtures for RF measurements.

Copper prototype cavity (see Fig. 4) was manufactured and tested in 2020 [24]. Resonant frequency measurements and vacuum tests showed cavity desired performance [25]. Intermediate measurements and frequency control procedure used at production site allowed us to get the necessary frequency value. This multistage tuning took us several weeks as the cavity parts were manufactured and matched. Cavity RF test port reflection and resonant frequency dependence on temperature are presented on Fig. 5.

Plunger with precise mechanical actuator for slow frequency tune was developed and manufactured at INP BSU. [25]. Tuner design and prototype manufactured are shown on Fig. 6. This tuner was successfully tested on copper cavity and showed to deliver 13 kHz/mm frequency shift.

ISBN: 978-3-95450-240-0 ISSN: 2673-5539 doi:10.18429/JACoW-RuPAC2021-THA01

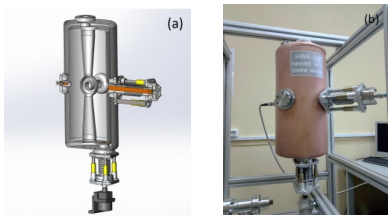

Figure 4: (a) 3D model of the coaxial half-wave resonator with field probe, power input antennas and plunger-based frequency tuning system; (b) manufactured copper prototype [24].

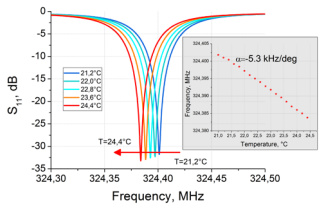

Figure 5: The reflection coefficient S_{11} for the power input in the critical coupling conditions for different ambient temperatures; (inset) resonant frequency dependence on temperature.

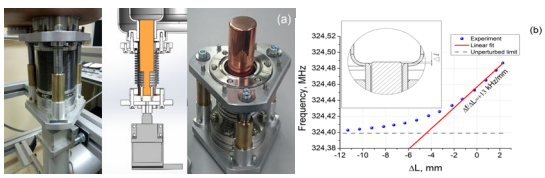

Figure 6: (a) The slow frequency tuning system; (b) experimentally measured frequency shift Δf vs plunger penetration depth ΔL [25].

NIOBIUM CAVITY PRODUCTION

Pilot full performance SC cavity is being manufactured in 2020-2021. The cavity is made of RRR300 bulk niobium and has titanium cryogenic vessel permanently attached. Technology of niobium sheets deep drawing, hydroforming, electron beam welding at several production facilities at Minsk were developed. The intermediate frequency measurements and control of niobium cavity (Fig. 7) were performed based on copper prototype-based experience. Fig. 8 illustrates the Nb cavity core sealed and equipped for RF and vacuum tests. Weld seals leak rate was under 3.8×10^{-9} Pa·m^3/s. Cavity outer shell for cryogenic system was made of titanium and welded to the cavity. Cavity low power RF tests at room temperature were carried out [26] and showed the expected results.

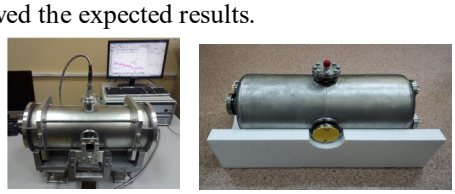

Figure 7: Niobium cavity core under intermediate RF test and cavity Nb core with outer Ti shell assembly.

Cryostat for cavity testing was developed in collaboration of JINR and INP BSU, Fig. 8 [27]. At September 2021 first tests of cavity cooled down to liquid nitrogen temperature were done. Resonant frequency shift measured during cooldown at selected temperatures is shown on Fig. 9. Helium tests are scheduled to the end of 2021.

As soon as the first cavity tests would be fully completed two cavities for Nuclotron-NICA injector will be made. Their production is already launched, Fig. 10 shows two sets of Nb parts for these cavities.

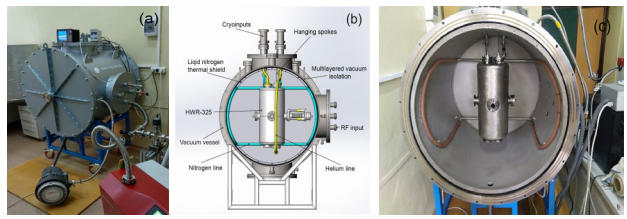

Figure 8: (a) Fabricated test cryostat, (b) the main parts and subsystems of the cryostat, (c) test cryostat with a cavity inside [27].

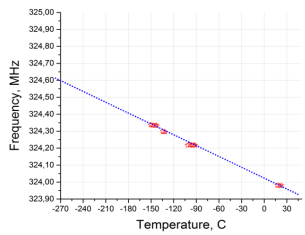

Figure 9: Resonant frequency vs. temperature dependence measured during cavity cooldown.

Figure 10: Nb parts for two Nuclotron-NICA cavities.

CONCLUSION

HWR SC cavity with frequency tuner for Nuclotron-NICA injector was designed. Dedicated tooling and technologies were developed and certified for production of high performance SC cavities. Core parts are made of high RRR bulk niobum sheets by deep drawing and hydroforming and then electron beam welded. Titanium cryogenic shell is permanently attached to cavity core. Full production line procedures for intermediate measuring, testing and adjustment of cavity parts was developed. Cryostat for cavity tests under L-He temperature was designed and manufactured.

Copper prototype and niobium pilot cavity were manufactured. Vacuum and low power RF tests at room temperature and Liquid-N_2 conditions were carried out and showed the cavity expected performance. Production of two Nb cavities for NICA beamline is launched.

Next steps scheduled to 2021/2022 will be cavity cold tests at 4K and fast frequency tuning system development [28].

ISBN: 978-3-95450-240-0 ISSN: 2673-5539 doi:10.18429/JACoW-RuPAC2021-THA01

REFERENCES

[1] G. Trubnikov, N. Agapov, V. Alexandrov *et al.*, "Project of the Nuclotron-Based Ion Collider Facility (Nica) at JINR", in *Proc. IPAC'10*, Kyoto, Japan, May 2010, paper MOPD011, pp. 693-695.

[2] O. Kozlov, H. Khodzhibagiyan *et al.*, "Design of the NICA Collider Rings", in *Proc. IPAC'11*, San Sebastián, Spain., Sep. 2001, paper TUPZ005, pp. 1807-1809.

[3] A.V. Butenko, E.E. Donets, *et al.*, "Development of the NICA Injection Facility", in *Proc. IPAC'13*, Shanghai, China, May 2013, paper THPWO069, pp. 3915-3917.

[4] A.V. Butenko, E.E. Donets et *al.*, "Development of NICA Injection Complex", in *Proc. IPAC'14*, Dresden, Germany, June 2014, paper WEPRO067, pp. 2103-2105. doi:10.18429/JACoW-IPAC2014-WEPRO067

[5] A.V. Butenko, A.M. Bazanov, D.E. Donets et *al.*, "Commissioning of New Light Ion RFQ Linac and First Nuclotron Run with New Injector", in *Proc. IPAC'17*, Copenhagen, Denmark, May 2010, paper TUPVA117, pp. 2366-2368.

[6] V.A. Andreev, A.I. Balabin, A.V. Butenko et *al.*, "Reconstruction of light and polarized ion beam injection system of JINR Nuclotron-NICA accelerator complex", *Problems of Atomic Science and Technology. Series: Nucl. Physics Investigations*, vol. 6, no. 88, pp. 8-12, 2013.

[7] A.V. Butenko, A.M. Bazanov, D.E. Donets et *al.*, "Commissioning of New Light Ion RFQ Linac and First Nuclotron Run with New Injector", in *Proc. RuPAC'16*, St. Petersburg, Russia, Nov. 2016, paper FRCAMH02, pp. 153-155. doi:10.18429/JACoW-RuPAC2016-FRCAMH02

[8] G.V. Trubnikov, T.V. Kulevoy, S.M. Polozov et *al.*, "The Perspective of a Superconducting Linac for Nuclotron Complex Modernization", *PEPAN Letters*, vol. 13, no. 7, pp. 1418-1424, 2016.

[9] G.V. Trubnikov, T.V. Kulevoy, S.M. Polozov et *al.*, "Beam Dynamics Study for the New CW RFQ", in *Proc. RuPAC'16*, St. Petersburg, Russia, Nov. 2016, pp. 267-269.

[10] M. Gusarova, T. Kulevoy, M.V. Lalayan et *al.*, "QWR resonator Cavities Electrodynamics Simulations for new Nuclotron-NICA Injector", in *Proc. RuPAC'16*, St. Petersburg, Russia, Nov. 2016, paper TUPSA028, pp. 275.

[11] G.V. Trubnikov, A.V. Butenko, N. Emelianov, et *al.*, "Status of R&D on New Superconducting Injector Linac for Nuclotron-NICA", in *Proc. IPAC'17*, Copenhagen, Denmark, May 2017, paper WEPVA014, pp. 3282-3285.

[12] G.V. Trubnikov, T.V. Kulevoy, S.M. Polozov et *al.*, "New Superconducting Linac Injector Project for Nuclotron-Nica: Current Results", in *Proc. RuPAC'16*, St. Petersburg, Russia, Nov. 2016, paper THPSC041, pp. 626-628.

[13] A.M. Bazanov, A.V. Butenko et *al.*, "The New Light-Ion Linac for the NICA Collider", *AIP Conference Proceedings*, vol. 2163, iss. 1, p. 080001, 2019. doi:10.1063/1.5130116

[14]. H. Höltermann, M. Basten, B. Koubek et *al.*, "Light Ion Linear Accelerator up to 7 AMeV for NICA", in *Proc. RuPAC'18*, Protvino, Russia, Oct. 2018, paper WECAMH02, pp. 68-71. doi: 10.18429/JACoW-RUPAC2018-WECAMH02

[15] V. Fimushkin, A. Kovalenko, A. Belov, et *al.*, "SPI for the JINR accelerator complex," in *Proc. PSTP'2015*, Bochum, Germany, Sep. 2015, p. 041.

[16] S.M. Polozov et *al.*, "Status of R&D on New Superconducting Injector Linac for Nuclotron-NICA", in *Proc. HB'18*, Daejeon, Korea, June 2018, paper TUA2WC02, pp. 83-87. doi:10.18429/JACoW-HB2018-TUA2WC02

[17] A.V. Samoshin, "Complex approach of beam dynamic investigation in SC linac", *Problems of atomic science and technology*, vol. 4, no. 80, pp. 78–82, 2012.

[18] E. S. Masunov, A. V. Samoshin, "Beam focusing in a linear ion accelerator consisting of a periodic sequence of independently phased superconducting cavities", *Technical Physics*, vol. 55, iss. 7, pp. 1028-1035, 2010. doi:10.1134/s1063784210070182

[19] E. S. Masunov, A. V. Samoshin, "Investigation of beam dynamics in a linear superconducting heavy-ion accelerator", *Atomic Energy*, vol. 108, iss. 2, pp. 141-153, 2010.

[20] M.A. Gusarova, D.V. Surkov, K.V.Taletskiy et *al.*, "Selection of the Type of Accelerating Structures for the Second Group of Cavity SC Linac Nuclotron-NICA", in *Proc. SRF'2017*, Lanzhou, China, July 2017, paper MOPB034, pp.125-127. doi: 10.18429/JACoW-SRF2017-MOPB034

[21] A.V. Butenko, N.E. Emelianov, A.O. Sidorin et *al.*, "Status of R&D on New Superconducting Injector Linac for Nuclotron-NICA", in *Proc. HB'18*, Daejeon, Korea, June 2018, paper TUA2WC02, pp. 83-87. doi:10.18429/JACoW-HB2018-TUA2WC02

[22] A. Facco, F. Scarpa, D. Zenere et *al.*,V. "Low- and intermediate-beta, 352 MHz superconducting half-wave resonators for high power hadron acceleration", *Phys. Rev. ST Accel. Beams*, 9, Nov. 2006, p.110101. doi:10.1103/PhysRevSTAB.9.110101

[23] J. R. Delayen, C. L. Bohn and C. T. Roches, "Niobium resonator development for high-brightness ion beam acceleration," in IEEE Transactions on Magnetics, vol. 27, no. 2, pp. 1924-1927, March 1991, doi: 10.1109/20.133578

[24] D.Bychanok, A Sukhotski, S Huseu et *al.*, "Control of electromagnetic properties during prototyping, fabrication and operation of low-β 325 MHz half-wave resonators", *Journal of Physics D: Applied Physics*, vol. 54, no. 10, p. 255502, Apr. 2021. doi: 10.1088/1361-6463/abf168

[25] D. Bychanok, A. Sukhotski, S. Huseu et *al.*, "Design, characteristics and dynamic properties of mobile plunger-based frequency tuning system for coaxial half wave resonators", in *Proc. IPAC'2021*, Campinas, SP, Brazil, May 2021, paper MOPAB363, pp. 1129-1131. doi:10.18429/JACoW-IPAC2021-MOPAB363

[26] D. Bychanok, E. Vasilevich, A. Sukhotski et *al.*, "Comparison of electromagnetic properties during fabrication of copper and niobium prototypes of 325 MHz coaxial half-wave resonator", presented at SRF'2021, Virtual Conference, June 2021, paper WEPCAV010.

[27] D. Bychanok, S. Huseu, E.Vasilevich et *al.*, "Design and characteristics of cryostat for testing of low-betta 325 MHz Half-Wave resonators", presented at RuPAC'2021, Alushta, Crimea, Sep. 2021, paper MOPSA16, this conference.

[28] R.E. Nemchenko, M.A Gusarova, "Development of a Frequency Control Device for a Superconducting Half-Wave Resonator", *Phys. Atom. Nuclei*, vol 83, no. 10,pp. 1482–1483, 2020. doi: 10.1134/S1063778820100178

ISBN: 978-3-95450-240-0 ISSN: 2673-5539 doi:10.18429/JACoW-RuPAC2021-THC03

NUMERICAL SIMULATIONS OF SPACE CHARGE DOMINATED BEAM DYNAMICS IN EXPERIMENTALLY OPTIMIZED PITZ RF PHOTOGUN *

S.M. Polozov, V.I. Rashchikov†, NRNU(MEPhI) - NRC «Kurchatov Institute», Moscow, Russia

Abstract

Discrepancies between experimental data and computer simulation results of picosecond highly charged beam photoemission are discussed. New space charge limited emission numerical model with positively charged ions arising in the cathode region and dynamically changing during the emission is presented. Estimates on the time characteristics of the charge migrating process in the semiconductor region are given. The numerical results are compared with the results of other numerical models and with experimental observations at the Photo Injector Test facility at DESY in Zeuthen (PITZ).

INTRODUCTION

High brightness electron sources are key components necessary for the successful operation of modern free electron lasers, new sources of synchrotron radiation and lepton colliders. For such facilities, it is required to have a rather high bunch charge (~nC), a very small transverse normalized emittance (< 1 mm×mrad), rather short bunches (~ 1÷20 ps), and a small energy spread (<1 %). For example, for the European X-ray Free Electron Laser (European XFEL) photo gun, electron bunches with a charge of 1 nC/bunch and a normalized transverse emittance < 0.9 mm×mrad should be generated by an RF gun operating with a Cs_2Te photocathode at a high electric field on the cathode surface (~ 60 MV/m) and repetition rate up to 27,000 pulses per second. Detailed studies of the photoemission process are crucial for understanding the beam dynamics in space charge dominated photo injectors, without which it is difficult to achieve the high brightness.

TEST FACILITY AND SIMULATION MODEL

The Photo Injector Test facility at DESY in Zeuthen (PITZ) develops and optimizes high brightness photo injectors for more than 20 years [1].

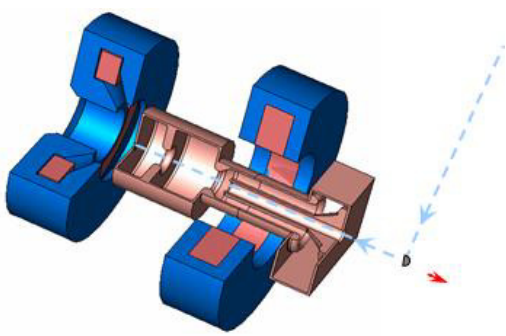

Figure 1: PITZ RF gun scheme.

The PITZ L-band 1.6-cell RF-gun (Fig. 1) consists of a 1.3 GHz copper cavity operated in π-mode fed by a coaxial RF power coupler and supplied with a pair of focusing solenoids. A molybdenum cathode plug with Cs_2Te film is inserted in the cavity back wall using a load-lock vacuum system.

For precise description of the space charge dominated dynamics in the RF-photogun beam measurements and computer simulations have been performed. Discrepancies between experimental data and simulation results have been observed for these measurements [2-3]. The results of experimental studies on the bunch charge production and transverse emittance optimization revealed that the limiting current of the emitted beam obtained experimentally cannot be reproduced by ASTRA simulations [4] using the parameters of the experimental setup. The ASTRA code, used for these simulations, is one of the few in the world optimized to solve beam dynamics problems associated with photoemission and photoguns. In order to bring beam dynamics simulations closer to the experimental results the photoemission model for a space charge dominated regime has to be improved. A typical schematic of a semiconductor photocathode is illustrated by Fig. 2.

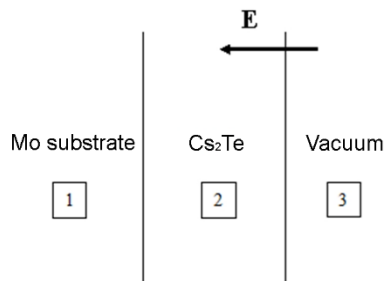

Figure 2: Photocathode model.

It consists of three regions: 1- molybdenum substrate, 2 - Cs_2Te film (< 0.1μm), 3- vacuum. Since the photocathode is located in a strong electric field, the penetration of the field into the semiconductor film should be taken into account. With a field strength of $E \sim 10^7$ V/m on the cathode surface, it is necessary to create the following surface charge density σ to compensate this field inside the film:

$$E = \frac{\sigma}{2\varepsilon\varepsilon_0} = \frac{qN}{2\varepsilon\varepsilon_0},$$

where N is the surface charge density, ε and ε_0 is the dielectric permittivity of the photocathode film and vacuum respectively, q is a particle charge. Hence, assuming ε ~10, we obtain the surface charge density at the cathode $N \sim 10^{11}$ cm^{-2}. If the average concentration of carriers in a semiconductor is $n \sim 10^{15}$ cm^{-3} then the required number of charges is obtained at a thickness of $d = \frac{N}{n} \sim 1$μm. That is, the field penetrates to a depth that is significantly greater

* The reported study was partly funded by RFBR, project 19-29-12036
† VIRashchikov@mephi.ru

ISBN: 978-3-95450-240-0 ISSN: 2673-5539 doi:10.18429/JACoW-RuPAC2021-THC03

than the thickness of the semiconductor film, i.e. the electric field easily reaches the substrate.

In the standard steady-state photo emission model, electrons generated by a laser pulse leave the cathode, and the magnitude of the emission current is limited either by the space charge field of the emitted electrons including the image charge (when the total electric field on the semiconductor surface is equal to zero), or by the emissivity of the photocathode (the laser power and the cathode quantum efficiency).

Ongoing to picosecond laser pulse durations, which are necessary to obtain short electron bunches, the picture changes. In this case the regions of the substrate and the semiconductor should be considered separately. The electrons produced by the laser pulse are in a strong electric field E, which, as shown above, easily penetrates the film and quickly leaves it. It is easy to show that within the time t ~ 1 ps the electron velocities v reach

$$v = \frac{eEt}{\varepsilon\gamma m} \approx 10^6 \text{ m/s}$$

and the electrons move by the distance of the order of one micron, which is significantly greater than the thickness of the semiconductor. Since the number of free electrons in region 2 is limited, the rate of their influx will be determined by the difference in carrier concentrations, determined according to Fick's first law by the expression $\vec{j} = \rho\vec{v} = -eD\ grad\ n$,where ρ - is the charge density, D is the diffusion coefficient of the particle, n is the electron concentration. The diffusion coefficient D is related to the mobility of charge carriers by the Einstein's relation. For electrons it reads as

$$D = \frac{kT}{e}\mu,$$

where k is the Boltzmann constant and T is the temperature. Since the diffusion velocity is less than the drift one, the positive charge will dominate in the region 2 (Fig. 2).

Thus, the region 2 turns out to be positively charged, and the amount of charge will dynamically change and be determined by the rate of outflow and inflow of electrons into the semiconductor region. The presence of such a charge inside the film can significantly increase a space charge limited emission current in the case of high charge density picosecond bunches.

SIMULATION RESULTS

The developed model is based on the 2.5 dimensional finite difference-time domain (FDTD) particle-in-cell (PIC) code SUMA [5]. This code has been tested and widely used to model various physical processes [6-9]. Part of the code responsible for the charged particles emission was modified according to our understanding of the physical process [10-11]. In the proposed model in the region 2 (semiconductor film), the number of electrons arising in the process of photoemission is equal to the number of positive charges. As the electrons (Q-) move to the region 3, positive charges (Q+) will dominate in the region 2, but their amount will be less than the number of electrons escaping from the region $Q^+ = Q^-(t)e^{-t/\tau}$. Partial compensation of the positive charge in the region 2 (defined by the positive charge relaxation time τ) is associated with the influx of electrons from neighbouring regions and is caused by the resulting difference in carrier concentrations.

The time dependence of the cathode emissivity corresponded to the temporal profile of the laser pulse, which has 21.5 ps FWHM and ~2 ps rise/fall times.

A transverse charge density distribution during emission is uniform up to a given radius, and then falls off according to the Gauss's law.

The time dependence of the electron charge emitted by the cathode is shown in Fig. 3.

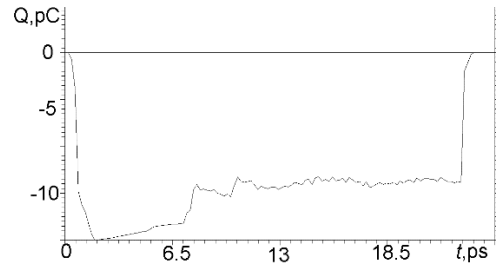

Figure 3: Emitted charge.

The time dependence of the positive charge remained in the region 2 is presented in Fig. 4.

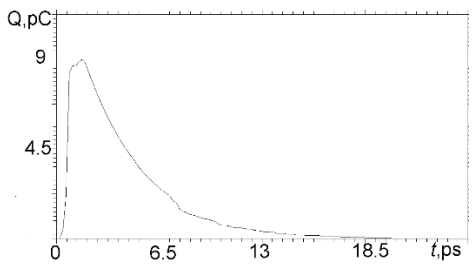

Figure 4: Positive charge, remained in semiconductor.

The presence of a positive charge in the region 2 significantly changes the emission process at a high charge density of the bunch at the photocathode. Figure 5 shows the shape variation of the electron bunch current emitted from the photocathode with increasing of the initial charge (or laser pulse energy) on it without taking into account (top row of plots) and taking into account (bottom row of plots) the presence of the positive charge in the region 2.

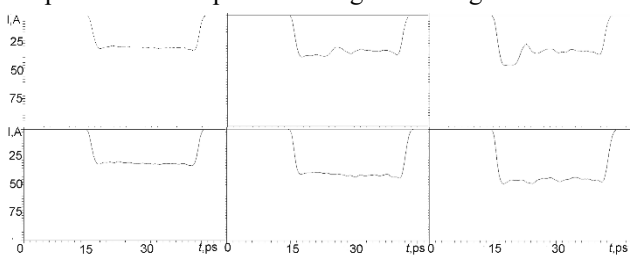

Figure 5: Current pulse from the photocathode with increasing charge (0.4 nC, 0.7 nC, 1.0 nC) without (top row of plots) and with taking into account positive charge on semiconductor (bottom row of plots).

It can be seen that in the old model, which does not consider the presence of a dynamically changing positive

ISBN: 978-3-95450-240-0 ISSN: 2673-5539 doi:10.18429/JACoW-RuPAC2021-THC03

charge in the region 2, with a laser pulse energy increase the beam current amplitude stops growing and the shape is distorted, which can be explained by the formation of a virtual cathode. If the appearance of a positive charge in the region 2 (new model) is taken into account, the picture changes. With an increase of the laser pulse energy the amount of positive charge Q^+ increases as well, and as a results, the photocurrent amplitude continues to grow, and the bunch current profile distortion is significantly smaller. This behavior can be explained by the partial compensation of the space charge forces of the emitted electrons by the increased amount of positive charge in the region 2.

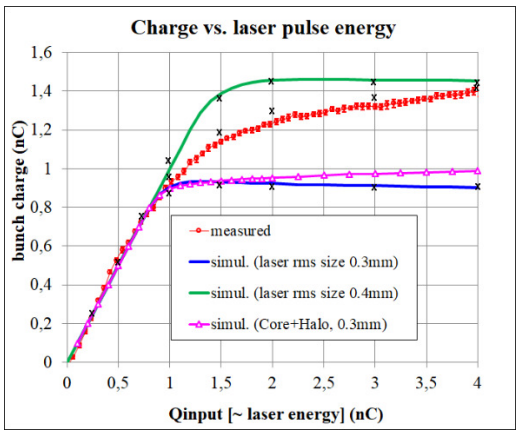

Figure 6: Emission curves measured at PITZ (red curve) compared to the simulation results from ASTRA (green, blue and magenta curves) and from SUMA (crosses).

Figure 6 shows dependence of the bunch charge on the laser pulse energy, measured and calculated by the ASTRA code for different transverse laser pulse distributions [3]. The blue and green curves correspond to the beam $\sigma_{xy} = \sqrt{\sigma_x \sigma_Y}$ size of 0.3 mm and 0.4 mm, the magenta curve depicts the results of the applied transverse core+halo laser distribution model [12], and the red curve shows the experimental curve. As it could be seen, due to the strong space charge effect, the ASTRA results cannot reproduce the experimentally obtained current values from the cathode. Increasing of the rms spot size used in ASTRA simulations from the experimental 0.3 mm by ~30% (to 0.4 mm) leads to the higher saturation level of the emission, but the simulated curve does not follow the measured one. Results of SUMA simulations are shown in Fig. 6 with crosses. Cross-check with the old emission model are in a good agreement with corresponding ASTRA simulations. The newly implemented photoemission model employing the positive charge within the Cs_2Te photocathode film yields significantly better agreement with the experimental data.

Parameter $\tau = 4 \cdot 10^{-12}$ is fitted for one point of the experimental emission curve and fixed as a material constant in all further calculations. This gives us confidence in the validity of the model applied.

Figure 7 shows experimental studies on the RF field influence on the emitted bunch charge [13] supplied with corresponding SUMA results on it.

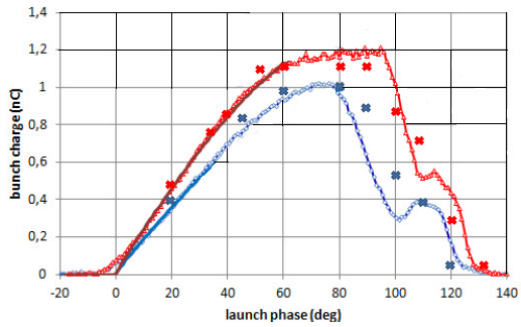

Figure 7: RF lunch phase influence. $E_{cathode,max}$=62 MV/m (red curve) and $E_{cathode,max}$=47.6 MV/m (blue curve). Crosses mark the SUMA calculation results.

Figure 8 shows the beam transverse emittance evolution along the gun. Its strong changes are visible in the initial stage, when the electron velocities are not yet high and the space charge forces influence is most significant.

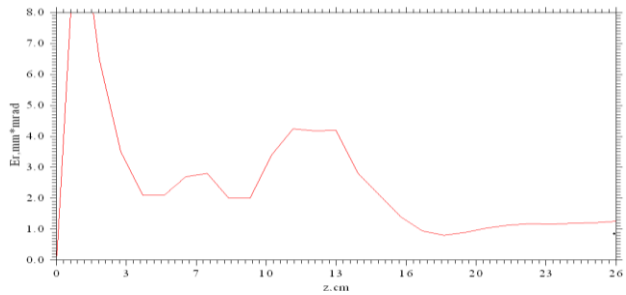

Figure 8: Transverse emittance along the gun.

CONCLUSION

A new model of the photoemission from a semiconductor photocathode in a space charge dominated regime was proposed and implemented in the SUMA code. It implies a finite rate of the positive charge flow inside the photocathode film which (partially) compensates the space charge field of the emitted electrons. The new model was applied to the experimental data from the PITZ RF photogun operated in a space charge dominated regime corresponding to the high brightness performance of the photoinjector. The results show better agreement of the newly proposed model with experimental data than the old model. Further investigations are ongoing.

REFERENCES

[1] M. Krasilnikov *et al.*, "Experimentally minimized beam emittance from an L-band photoinjector", *Phys. Rev. Accel. Beams*, vol. 15, p. 100701, 2012.

[2] S. Rimjaem *et al.*, "Optimizations of transverse projected emittance at the photo-injector test facility at DESY, location Zeuthen", *Nucl. Instrum. Methods,* vol. 671, pp. 62-75, 2012. doi:10.1016/j.nima.2011.12.101

[3] M. Krasilnikov, Y. Chen, and F. Stephan, "Studies of space charge dominated electron photoemission at PITZ". *J. Phys.: Conf. Ser.,* vol. 1238, p.012064, 2019

[4] K. Floettmann, "ASTRA particle tracking code", http://www.desy.de/~mpyflo/

[5] V.I. Rashchikov, "Electromagnetic field calculation in complex geometry structures", *Problems of Atomic Science and*

ISBN: 978-3-95450-240-0 ISSN: 2673-5539 doi:10.18429/JACoW-RuPAC2021-THC03

Technology. Series: Nuclear Physics Investigations, vol. 10 (18), pp. 50–53, 1990

[6] S.M. Polozov and V.I. Rashchikov, "Longitudinal motion stability of electrons inside the plasma channel of LPWA", *Cybernetics and Physics,* vol. 7 (4), pp. 228–232, 2018.

[7] V.I. Rashchikov and A.N. Didenko, "High power microwave generation in virtual cathode systems", *1991 IEEE Particle Accelerator Conference*, pp. 3111–3113, 1991

[8] A.N. Didenko, V.I. Rashchikov and V.E. Fortov, "Mechanism of generation of high-intensity terahertz radiation under the action of high-power laser pulsed on a target". *Technical Physics*, vol. 56, (10), pp. 1535–1538, 2011.

[9] V.I. Rashchikov and A.E. Shikanov, "Compact plasma reflex triode for neutron generation", *IEEE Transactions on Plasma Science*, vol. 47 (2), pp. 1279–1282, 2019.

[10] S.M. Polozov, V.I. Rashchikov. "Simulation studies on the radiofrequency gun saturated emission", *Cybernetics and physics,* Vol. 9, no. 2, pp.103–10, 2019.

[11] S.M. Polozov, V.I. Rashchikov, M. Krasilnikov," An Improved Model for Photoemission of Space Charge Dominated Picosecond Electron Bunches: Theory and Experiment", *in Proc. of 12th Int. Particle Acc. Conf. (IPAC2021)*, Campinas, SP, Brazil, 24–28 May 2021, https://doi.org/10.18429/JACoW-IPAC2021-WEPAB101

[12] M. Krasilnikov et al., Investigations on Electron Beam Imperfections at PITZ, *in Proc. of Linear Accelerator Conference (LINAC'16)*, East Lansing, MI, USA, 25-30 September 2016, https://doi.org/10.18429/JACoW-LINAC2016-MOPLR013

[13] M. Krasilnikov "Measurements and modelling of space charge assisted photoemission at PITZ", Physics of Photocathodes for Photoinjectors Workshop to be held at Cornell University in October 8-10, 2012.

ISBN: 978-3-95450-240-0 ISSN: 2673-5539 doi:10.18429/JACoW-RuPAC2021-FRA01

PECULIARITIES OF PRODUCING ^{48}CA, ^{48}TI, ^{52}CR BEAMS AT THE DC-280 CYCLOTRON

K.B. Gikal†, S. L. Bogomolov, I. A. Ivanenko, N. Yu. Kazarinov, V. I. Lisov, A. A. Protasov, D.K. Pugachev, V.A. Semin, Joint Institute for Nuclear Research, Dubna, Russia

Abstract

The main task of the new accelerator is implementation of the long-term program of researches on the SHE Factory aimed on synthesis of new elements (Z≥119) and detailed studying of nuclear- physical and chemical properties of earlier opened 112-118 ones. The first beam of $^{84}Kr^{+14}$ ions was accelerated in the DC-280 on December 26, 2018 and extracted to the ion transport channel on January 17, 2019. In March 2019, beams of accelerated $^{84}Kr^{+14}$ ions with intensity of 1.36 pμA and $^{12}C^{+2}$ ions with and intensity of 10 pμA were extracted from the DC-280 to the beam transport channel with energy about 5.8 MeV/nucleon. In 2020-2021 years, beams of $^{48}Ca^{7+,10+}$ ions with intensity up to 10,6 pμA were accelerated and 7,1 pμA were extracted from the DC-280 to the beam transport channel with energy in range 4,51 - 5,29 MeV/nucleon. In 2021 year, beams of accelerated $^{52}Cr^{10+}$ ions with intensity up to 2,6 pμA were extracted from the DC-280 to the beam transport channel with energy 5,05 MeV/nucleon and beams of $^{48}Ti^{7+,10+}$ with intensity up to 1 pμA with energy 4,94 MeV/nucleon.

DC-280 DESCRIPTION

DC-280 is the accelerated ions source for experiments on synthesis of super heavy elements [1]. It is part of Super Heavy Element (SHE) Factory which was created in FLNR in JINR. It is isochronous cyclotron designed for acceleration of ion with mass to charge ratio from 4.5 to 8 to energy from 4 to 8 MeV/n. Main parameters design and achieved present in Table 1.

Table 1: Main Parametrs of DC-280 Cyclotron

parameters	design	achieved
Injecting beam energy	Up to 80 keV/Z	38,04 – 72,89 keV/Z
A/Z	4÷7.5	4,4($^{40}Ar^{+7}$) ÷6,9($^{48}Ca^{+7}$)
Energy	4÷8 MeV/n	4,01 – 7 MeV/n
Ion (for DECRIS-PM)	4-136	12 ($^{12}C^{+2}$) – 84 ($^{84}Kr^{+14}$)
Intensity (A~50)	>10 pμA	10,4 pμA ($^{40}Ar^{+7}$);
Magnetic field level	0.6÷1.3 T	0.8÷1.23 T
K factor		280
Dee voltage	2x130 kV	130 kV
Power of RF generator	2x30 kW	
Accelerator efficiency	>50%	51,9 % ($^{48}Ca^{+10}$ 5 pμA)

Electron Cyclotron Resonance (ECR) source DECRIS-PM is used for production of ions [2, 3]. It has magnetic structure from permanent magnets. It placed on high voltage platform with work voltage up 70 kV for increasing efficiency of initial beam transport and capture to acceleration [4].

In the DC-280 cyclotron, a spiral inflector is used to rotate the beam from the vertical direction of axial injection into the median plane. Both the cyclotron magnetic field and own electrostatic field of inflector rote the ion beam by spiral. To ensure optimal injection conditions for all range of accelerated ions, two versions of the inflector type A and type B with two magnetic radii of 7.5 and 9.2 cm are used.

Inflectors with magnetic radii of 7.5 cm and 9.2 cm for the range of accelerated ions with A / Z from 4 to 7 is shown in Fig. 1.

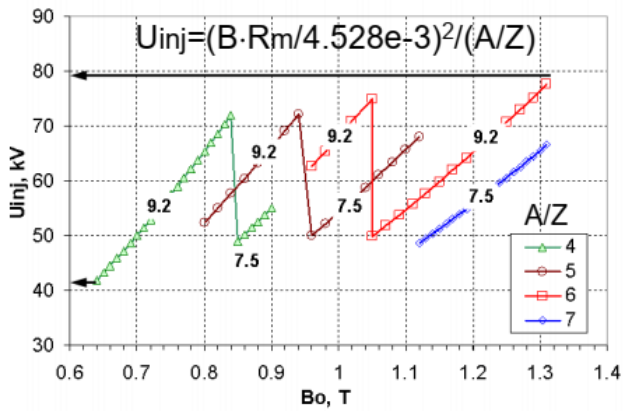

Figure 1: Dependence of the magnetic field on the injection voltage for the inflector A and B.

During experiments both of them were successful tested. There is electrostatic quadrupole lens in central part of cyclotron. Polyharmonic buncher is used for increasing of ions capture to acceleration [4].

Accelerated beam is extracted from cyclotron by electrostatic deflector. It works in conjunction with magnetic channel. Deflector length is 1.3 meters. The work electric field strength in gap between electrodes is up 90 kV/cm [1].

Extracted beam is delivered by transport channel to experimental setups [5]. There are 5 channels connected with 3 isolated halls.

On 26 December 2018, the first accelerated beam was got inside of DC-280 cyclotron [1, 6]. On January 2019, accelerated beam was extracted from cyclotron to transport channel. On September, the new experimental facility Dubna Gas Filled Separator 2 was mounted, and test with accelerator beam was started [7]. On December of 2019, work with beam of ^{48}Ca was initiated. On November 2020, the first experiment on production of ^{115}Mc was started.

† kbgikal@jinr.ru

ISBN: 978-3-95450-240-0 ISSN: 2673-5539 doi:10.18429/JACoW-RuPAC2021-FRA01

The cyclotron has worked 9350 hours during three years. Different mode of work with different ions and energy were explored. The work diagram of DC-280 cyclotron with marks of tested regimes is presented on Fig. 2. The cyclotron has shown reliable and highly effective work. The control and extraction systems were optimized for improving of efficiency and reliable of accelerator.

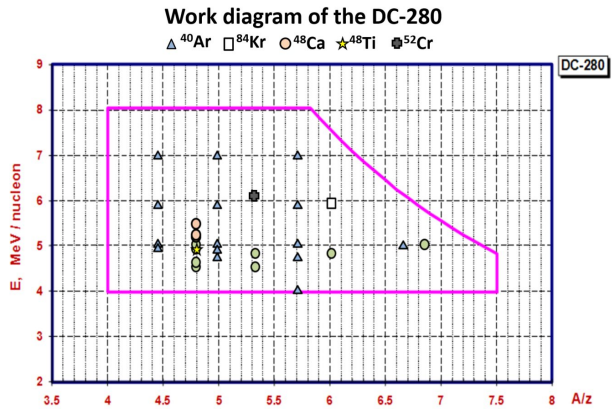

Figure 2: DC-280 work diagram with mark of test modes.

RESULTS

Producing of ^{48}Ca

The six heaviest chemical elements with atomic numbers 113 to 118 that fill the 7th row of Mendeleev's Periodic Table were synthesized in reactions of ^{48}Ca ions with actinide targets in the experimental studies carried out over the recent years. Over 50 new isotopes of elements 104 to 118 with maximum neutron excess were for the first time produced and their decay properties were determined in these investigations. The new isotopes considerably filled up the Chart of the Nuclides and expanded it up to Z = 118 and N = 177 superheavy elements. Fundamental conclusions of the modern theory concerning the limits of existence of nuclear matter have for the first time received experimental confirmation.

The first test experiments on DC-280, were on ^{48}Ca beams with actinide targets.

From the spectrum obtained from the ECR source, ions with charge +7, +10 don't have other ions with the same A / Z. The accelerated beam of $^{48}Ca^{+10}$ with intensity is about 7.1 pμA and $^{48}Ca^{+7}$ with intensity is about 5 pμA were obtained. Due to the lower consumption, $^{48}Ca^{+10}$ was chosen for experiments on the synthesis of superheavy elements.

The intensity of the injected charged particle beam affects its passage through the injection channel and its further capture into acceleration. At the same time, this effect is not observed for the passage along the horizontal part of the axial injection, and on the vertical, with an increase in the intensity from the ion source to 240 μA, we observed a deterioration of the beam transmission through the spherical deflector (Bender) from 94.22% at 150 μA to 79% at 240 μA, and the capture in acceleration decreased from 72.41% to 64.63%, respectively. This may be due to an increase in the space charge of the beam or the tuning of the accelerator as a whole. The efficiency of capture into acceleration at different intensities from an ECR source is shown in Fig. 3.

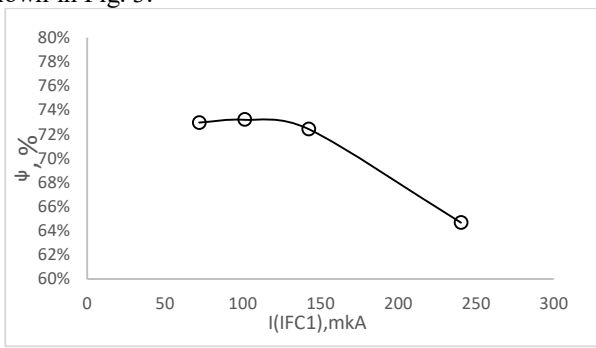

Figure 3: The efficiency of capture into acceleration.

The efficiency of transmission of the $^{48}Ca^{10+}$ beam at different initial currents from the DECRIS-PM ion source is shown in Fig. 4.

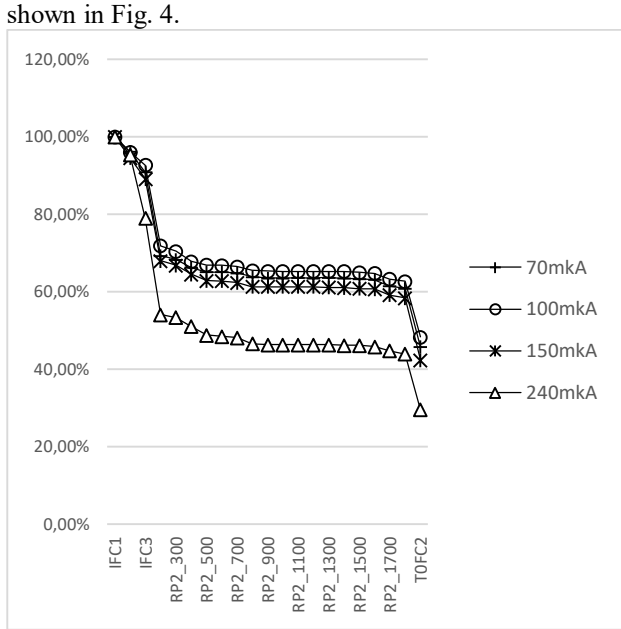

Figure 4: The efficiency of transmission of the $^{48}Ca^{10+}$.

The total efficiency of transporting the ion beam of $^{48}Ca^{10+}$ from the vertical part of the injection to the transport channel is about 50%.

At the moment, the beam is given to the DGFRS-2 experimental setup for a series of test experiments. The efficiency of passing through the transport channel is about 90%.

Producing of ^{48}Ti

For further experiments for super heavy elements will be needed beams of accelerated ions of ^{50}Ti and ^{54}Cr. For development of technology, we have accelerated their naturally occurring isotopes ^{48}Ti and ^{52}Cr.

From the spectrum obtained from the ECR source, the ions of ^{48}Ti with a charge of +7, +10 do not have other ions with the same A / Z and we can use them in experiments on the synthesis of SHE.

ISBN: 978-3-95450-240-0 ISSN: 2673-5539 doi:10.18429/JACoW-RuPAC2021-FRA01

The beam of $^{48}Ti^{+10}$ from ECR source with intensity is about 2.5 pμA and $^{48}Ti^{+7}$ with intensity is about 3.14 pμA were obtained and accelerated with intensity 1,0 pμA and 0,93 pμA respectively.

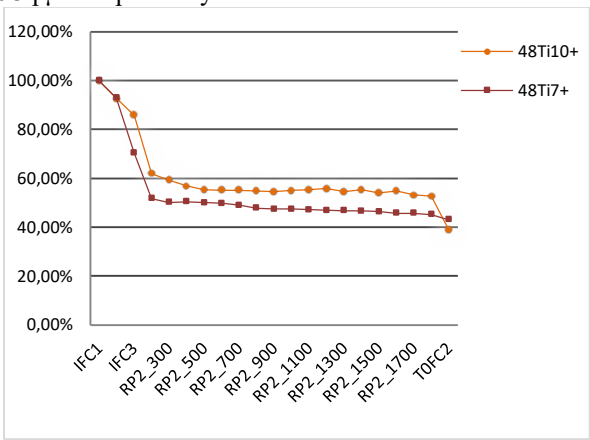

Figure 5: The efficiency of transmission of the $^{48}Ti^{10+,7+}$.

As we can see from Fig. 5, the total efficiency of transporting the ion beam of $^{48}Ti^{10+,7+}$ from the vertical part of the injection to the transport channel is about 40-45%.

Producing of ^{52}Cr

From the spectrum obtained from the ECR source, the ions of ^{52}Cr with a charge of +7, +8, +10 do not contain other ions with the same A / Z, but we cannot accelerate ions with a charge of +7 and +8 to the energy required for the experiment.

The beam of $^{52}Cr^{+10}$ from ECR source with intensity is about 6,3 pμA and accelerated with intensity 2,6 pμA.

We compared the passage of the beam through the cyclotron for different operating modes of the ECR source.

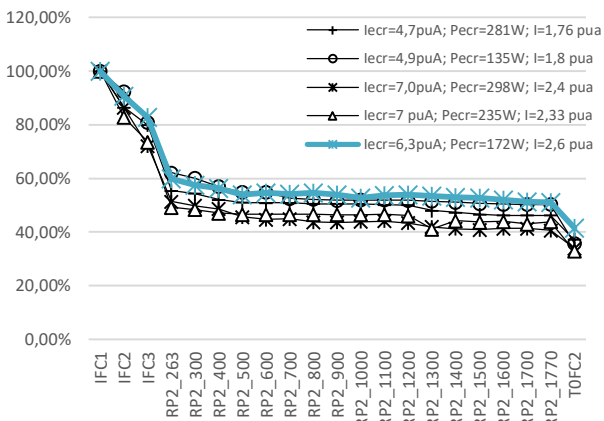

Figure 6: Comparison of normalized ^{52}Cr beam intensity in different points of cyclotron for different beam intensities.

The comparison of normalized intensity distribution for ^{52}Cr ion beam in acceleration process is presented on Fig. 6. There are data for different intensities of beam and different ECR source regimes.

We can see, that efficiency of acceleration worsen then we increase power input to ECR source [8].

The total efficiency of transporting the ion beam of $^{52}Cr^{10+}$ from the vertical part of the injection to the transport channel is about 50%.

CONCLUSION

The beams of $^{48}Ca^{7+,10+}$, $^{48}Ti^{+7,+10}$ and $^{52}Cr^{10+}$ were accelerated and extracted from the DC-280 to the beam transport channel. Maximum intensity of accelerated ^{48}Ca ion beam is 10,6 pμA and 7,1 pμA were extracted. The efficiency of acceleration for ^{48}Ca is about 50 %. The beam is given to the DGFRS-2 experimental setup for a series of test experiments.

The beams of accelerated $^{52}Cr^{10+}$ and $^{48}Ti^{7+,10+}$ ions with intensity 2,6 pμA and 1 pμA respectively were extracted from the DC-280 to the beam transport channel. The efficiency of acceleration for $^{52}Cr^{10+}$ and $^{48}Ti^{7+,10+}$ in range 40-50 %. Carried out only the first experiments dedicated to the production of $^{52}Cr^{10+}$ and $^{48}Ti^{7+,10+}$. At the first experiments, for the ion beam of ^{48}Ti and ^{52}Cr the intensity is limited by ion current from ECR source. We work to improve of the method of ion production and optimize the ECR source work mode.

REFERENCES

[1] I.V. Kalagin *et al.*, "SHE factory: cyclotron facility for Super Heavy Elements Research" In *proc. 22nd International Conference on Cyclotrons and their Applications* Cape Town, South Africa, 2020. doi: 10.18429/JACoW-Cyclotrons2019-THC01

[2] V. Mironov *et al.*," Optimization of the Metal Ion Production by Electron Cyclotron Resonance Ion Sources", ISSN 1547-4771, *Phys. Part. Nucl. Lett.*, Vol. 18, No. 3, pp. 370–377, 2021. doi:10.1134/S1547477121030092

[3] S. L. Bogomolov *et al.,* "Production of High-Intensity Ion Beams from the DECRIS-PM-14 ECR Ion Source", *ISSN 1547-4771, Phys. Part. Nucl. Lett,* Vol. 15, p. 878–881, 2018. doi: 10.1134/S1547477118070191

[4] G.G. Gulbekian *et al.*, "The project of the HV axial injection for the DC-280 cyclotron at the JINR FLNR" *Phys. Part. Nucl. Lett.,* Vol. 11, No. 6, pp. 763–773, 2014. doi: 10.1134/S1547477121030092

[5] I.V. Kalagin *et al.,* "The project of the beam transportation lines for the DC-280 cyclotron at the JINR FLNR", In *Proc. of RuPAC-2014 Int. Conf.,* paper TUP014, p.p. 336-338, Obninsk, Russia, 2014. http://accelconf.web.cern.ch/AccelConf/rupac2014/papers/thpsc09.pdf

[6] B.N. Gikal *et al.*, "Start-Up of the DC-280 Cyclotron, the Basic Facility of the Factory of Super heavy Elements of the Laboratory of Nuclear Reactions at the Joint Institute for Nuclear Research", *Nuclear Research Physics of Particles and Nuclei Letters,* Vol. 16, p.866-875, 2019. doi: 10.1134/S1547477119060177

[7] A.G. Popeko, "On-line separators for the Dubna Super heavy Element Factory", *Nucl. Inst. Meth.Phys. Res. B* 376, 144–149, 2016. doi: 10.1016/j.nimb.2016.02.025

[8] Semin V.A. *et al.,* "DC-280 cyclotron for Factory of Super Heavy Elements experimental results", In *Proc. of 12th Int. Particle Acc. Conf. IPAC2021* p.p. 4126-4129, 2021. doi:10.18429/JACoW-IPAC2021-THPAB182

ISBN: 978-3-95450-240-0 ISSN: 2673-5539 doi:10.18429/JACoW-RuPAC2021-FRA02

CYCLOTRON OF MULTICHARGED IONS

Yu.K. Osina†, A.A. Akimova, Yu.N. Gavrish, A.V. Galchuck, S.V. Grigorenko, V.I. Grigoriev, M.L. Klopenkov, R.M. Klopenkov, L.E Korolev., K.A. Kravchuck, A.N. Kuzhlev, I.I. Mezhov, V.G. Mudrolyubov, K.E Smirnov., Yu.I. Stogov, S.S. Tsygankov, M.V. Usanova,
JSC «NIIEFA», 196641, St. Petersburg, Russia

Abstract

The JSC "NIIEFA" is designing a cyclotron system intended to accelerate ions with a mass-to-charge ratio of 3-7 in the energy range of 7.5-15 MeV per nucleon. The variety of ions, the range of changes in their energy, and the intensity of the beams provide conditions for a wide range of basic and applied research, including for solving a number of technological tasks.

The cyclotron electromagnet has an H-shaped design with a pole diameter of 4 meters and a four-sector magnetic structure. In the basic mode, the dependence of the induction on the radius corresponding to the isochronous motion is realized by turning on the main coil only through the shape of the central plugs, sector side plates, and sector chamfers. For other modes of isochronous acceleration, the current in the main coil is changed and correction coils are tuned. The resonance system consists of two resonators with an operating frequency adjustable from 13 to 20 MHz. The final stage of the RF generator is installed close to the resonator and is connected to it by a conductive power input device.

The external injection system generates and separates ions with a given A/z ratio. The injection energy is chosen such that the Larmor radius is constant, which allows using an inflector of unchanged geometry for the entire list of ions.

The transportation system forms beams of accelerated ions with specified parameters and delivers them to sample irradiation devices. Computer control of the cyclotron is provided.

MAIN TECHNICAL FEATURES

A distinctive feature of heavy ions' interaction with a substance is high specific energy loss and, as a consequence, more localized dependence of the penetration depth on energy compared to light ions.

This property of heavy ions allows a broad range of applications from fundamental research in nuclear physics and sold- state physics to applied technological tasks, namely, deep layer-to-layer implantation, simulation of radiation damages of different materials, etc.

A cyclotron system producing multicharged ions is under designing in the JSC "NIIEFA". The system includes a cyclotron with an external injection system, a system to form and transport beams of accelerated ions, a sample irradiation system and utilities.

This cyclotron system is intended to generate and accelerate ions with a mass-to-charge ratio (A/z) of 3 - 7 in the energy range of 7.5-15 MeV per nucleon as well as to use this set of ions in practical applications.

Table 1 presents the calculation results of boundary accelerating modes of C, O, Ne, Si, Ar, Fe, Kr, Ag, Xe and Bi ions. For light ions, higher energies are possible.

Table 1: Boundary Modes Of Ions' Acceleration

Element	Charge	Induction in the center of the magnet, T	Energy, MeV per nucleon
Bi_{209}	35	1.29	7.28
	43	1.6	16.94
Xe_{136}	23	1.29	7.43
	28	1.56	16.12
Ag_{107}	18	1.29	7.35
	21	1.6	15.41
Kr_{84}	14	1.29	7.21
	18	1.5	16.5
Fe_{56}	9	1.41	7.53
	11	1.6	15.44
Ar_{40}	6	1.46	7.5
	10	1.29	16.2
Si_{28}	4	1.5	7.18
	6	1.49	15.93
	9	1.42	32.1
Ne_{20}	3	1.43	7.19
	4	1.56	15.22
	6	1.43	27.9
O_{18}	3	1.33	7.11
	4	1.46	15.44
O_{16}	3	1.29	9
	3	1.6	13
	5	1.42	32.1
C_{12}	2	1.29	7.21
	3	1.29	16.23
	4	1.42	34.4

The variety of ions, range of their energy and intensity variation allow us to adjust a so-called coefficient of the linear energy transfer over a broad range, which is especially important for applied researches.

ELECTROMAGNET

The iron core of the electromagnet is of an H-shaped design and of a four-sector magnetic structure. The pole diameter equals 4m. The magnet is equipped with the main coils and a set of additional radial and azimuthal coils.The induction in the center of the magnet varies in the limits of 1.29-1.6T for different types of ions. The mode with the

† npkluts@luts.niiefa.spb.su

ISBN: 978-3-95450-240-0 ISSN: 2673-5539 doi:10.18429/JACoW-RuPAC2021-FRA02

1.42 T induction in the center of the magnet was chosen as the basic mode.

In the basic mode, the induction dependence on the radius corresponding to the isochronous motion is realized by turning on the main coils only through the shape of the central plugs, sector side plates, and sector chamfers. For other modes of isochronous acceleration, the current in the main coils is changed and correction coils are tuned.The beam is extracted from a fixed final radius of 1800 mm using a deflector and magnet channel.

The model of the magnet is shown in Fig. 1 and its main parameters are given in Table 2.

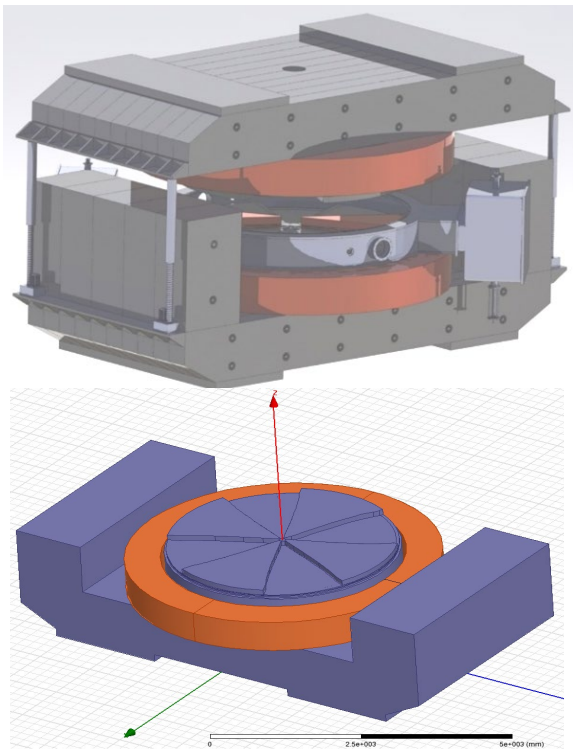

Figure 1: The electromagnet model.

Table 2: Parameters of the Electromagnet

Iron core sizes, mm	8100x4000x4300
Pole diameter, mm	4000
Number of sectors (per pole)	4
Lifting height of the upper movable half-yoke, mm	1000
Induction in the center of the magnet, T	1,29 – 1.6
Final acceleration radius, mm	1800
Sector angular length, degrees	51
Air gaps, valley/hill, mm	370/ 80
Consumed power, kW, no more than	262
Magnet mass (Fe/Cu), t	870/72
Number of radial coils Number of azimuthal coils Consumed power, kW, no more than	11×2 4×4 20

More detailed information is given in a poster report.

The vacuum chamber of the electromagnet consists of a titanium body and two covers, which are pole pieces of the iron core. Free access to the in-chamber equipment is provided by lifting up the upper movable half-yoke of the magnet.

RESONANCE SYSTEM

The resonance system consists of two mirror- symmetrical resonators galvanically coupled near the electromagnet axis. Each resonator is a quarter-wave coaxial line with conductors of variable cross-section. The frequency is controlled by changing the wave resistance of a part of the line near to the shorting flange using single-section panels.

The layout of the resonance system is shown in Fig. 2. The vertical section of the resonator with panels´ drives is given in Fig. 3.

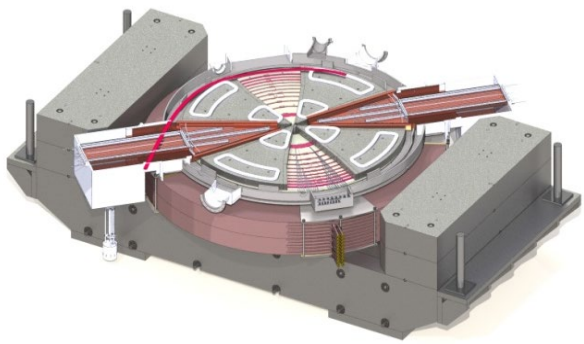

Figure 2: Layout of the resonance system.

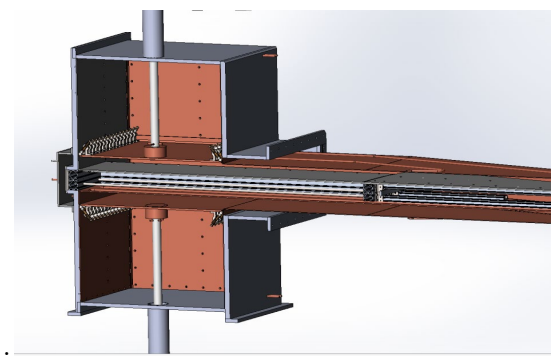

Figure 3: Resonator. Vertical section.

The resonance system includes two AFT trimmers and an RF-probe, which design is similar to that of corresponding units of cyclotrons produced by the JSC “NIIEFA”. The design power of active losses in the resonance system at the highest frequency of the range is approximately 40 kW and at the lowest frequency it is 60 kW.

RF-POWER SUPPLY SYSTEM

The RF power supply system operates in the frequency range of 13 – 20 MHz. Structurally, the equipment of the system is divided into 3 units, namely, the cabinet housing the main equipment, the amplifier final stage and the high-voltage power supply. The final stage of the amplifier developed on the basis of GU - 66 generator triode is located in the direct vicinity to the resonance system. RF – power is 60 kW.

ISBN: 978-3-95450-240-0 ISSN: 2673-5539 doi:10.18429/JACoW-RuPAC2021-FRA02

In the light of a significant change in characteristics of the resonance system in the frequency range, the conductive power input device is used. In this version, the resonance system simultaneously functions as the final stage anode loop.

EXTERNAL INJECTION SYSTEM

The external injection system is located in the vault under the cyclotron and consists of vertical and horizontal sections. The horizontal section includes ion sources, switching magnet, devices for beam preliminary forming, diagnostics and vacuum pumping means. Two ECR sources and two electron-beam sources will be manufactured and tested, three of which will be applied in the external injection system. A 90° analyzing magnet providing separation of ions of necessary charge is installed between these two sections of the external injection system. The vertical section is equipped with solenoids, correcting magnets, diagnostics, vacuum pumping devices and a spiral inflector.

The injection energy is chosen such that the Larmor radius is constant (30.4 mm), which allows using an inflector of unchanged geometry for the entire list of ions.

BEAM TRANSPORT SYSTEM

In this project, a modular beam transport system is considered, which delivers a beam of ions to separately located target rooms (any in number). Switching and correcting magnets, quadrupole lens (shown in Figs. 4 and 5), diagnostic unit with the Faraday cup and the beam profile sensor are used as standard modules.

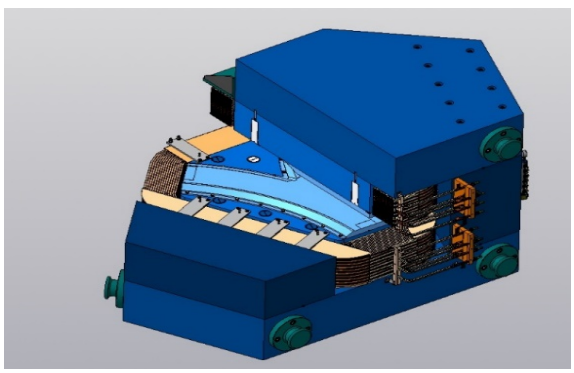

Figure 4: Switching magnet.

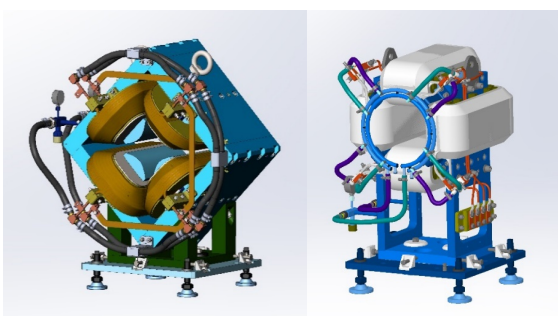

Figure 5: Quadrupole lens (left) and correcting magnet (right).

In addition, the system can include a set of collimators and diaphragms, which form a preset irradiation field, and irradiation chambers. The irradiation chambers are equipped with a special equipment for positioning and fixing of samples to be irradiated, monitoring and control of irradiation conditions, diagnostics of low-intensity ion beams.

UTILITIES

The power supply and water cooling systems are traditional for cyclotrons designed and produced in the JSC «NIIEFA ».

The vacuum system must meet special requirements to minimize the intensity loss of multicharged ions. The operating pressure not more than 10^{-7} torr should be maintained in all vacuum volumes of the external injection system, cyclotron and beamlines.

To strengthen the reliability of the system, it is divided into 3 sub-systems, namely, the vacuum system of the external injection system, the vacuum system of the cyclotron and the vacuum system of beamlines. All these sub-systems can operate autonomously.

High-vacuum pumping in the external injection system is performed with eight turbomolecular pumps and five cryogenic pumps. In the vacuum chamber of the cyclotron, two cryogenic pumps are used with a pumping rate of 6500 l/s for hydrogen and a turbomolecular pump. In beamlines (with three irradiation chambers), operate eight turbomolecular pumps and six cryogenic pumps.

Possible isolation of separate vacuum volumes (ion sources, the external injection system, irradiation chambers, and some sections of beamlines) is provided to perform routine and preventive maintenance of the equipment located inside these volumes.

The cyclotron system is completely automated. An operator performs turn on/off of the cyclotron system and choice of an operating mode.

The automated control system provides a necessary consequence of turn on/off operations of the equipment, monitoring of the state of all the systems; the information obtained is visualized on screens of monitors. In an emergency situation, either separate equipment or the whole cyclotron system is automatically turned off.

CONCLUSION

This cyclotron system of multicharged ions can serve as the basis for a nuclear-physical center undertaking large-scale fundamental and applied research and solving particular tasks in the field of the radiation materials science including modification of surface layers of different articles.

Nowadays, the designing of the system is being completed and the production of the main units and systems has been started.

ISBN: 978-3-95450-240-0 ISSN: 2673-5539 doi:10.18429/JACoW-RuPAC2021-FRA03

SIMULATION AND DESIGN OF THE PERMANENT MAGNET MULTIPOLE FOR DC140 CYCLOTRON

V. Kukhtin†, A. Firsov, M. Kaparkova, E. Lamzin, M. Larionov, A. Makarov,
A. Nezhentzev, I. Rodin, N. Shatil, JSC "NIIEFA", St. Petersburg, Russia,
G. Gulbekyan, I. Ivanenko, N. Kazarinov, I. Kalagin, N. Osipov, JINR, Dubna, Russia,
N. Edamenko, D. Ovsyannikov, S. Sytchevsky, St.Petersburg State University, Russia

Abstract

Permanent magnet (PM) multipoles are very attractive for beam transportation and focusing in accelerators. The primary advantages over electromagnets are no power supply and no cooling systems, better maintainability.

A PM quadrupole is supposed to be utilized in the DC140 cyclotron destined for acceleration of heavy ions which is under construction in JINR, Dubna. The extracted ion beam passes through a region where the stray field reduces sharply. Horizontal focusing of the beam line will be provided with a passive magnetic channel (MC1) and a PM quad (PMQ) in the strong and low field regions, respectively.

REQUIRED PMQ PARAMETERS

Table 1 lists design parameters of the quad.

Table 1: PMQ Design Parameters

Field gradient (G_0)	8.1 T/m
Working region (hor. × vert.)	64 mm × 25 mm
Aperture (hor. × vert.)	80 mm × 32 mm
Overall sizes (hor. × vert.)	170 mm × 106 mm
Effective lenght* (L_{eff0})	299.26 mm
Error in working region** ($\Delta_{x,y}$)	±1%

*The effective length of the quad is calculated as:

$$L_{eff\,0} = \frac{1}{G_0}\int_{-L/2}^{L/2} \frac{\partial B_y(0,0,z(s))}{\partial x} dz(s)$$

**A linear approximation error in the horizontal and vertical directions is evaluated as:

$$L_{eff\,0}\Delta_x = \frac{1}{G_0 x}\int_{-L/2}^{L/2}\left[B_y(x,y,z) - \frac{\partial B_y(0,0,z)}{\partial x}x\right]dz = L_{effx} - L_{eff\,0}$$

$$L_{eff\,0}\Delta_y = \frac{1}{G_0 y}\int_{-L/2}^{L/2}\left[B_x(x,y,z) - \frac{\partial B_x(0,0,z)}{\partial y}y\right]dz = L_{effy} - L_{eff\,0}$$

Also, additional criteria should be considered together with the above magnetic specification, see Table 2.

Table 2: PMQ Operating Conditions

External field	0.35 T
Vacuum	10^{-7} Torr
Operating temperature	30-40 °C
Temperature range	20-70 °C
Life time	10-15 years

† kukhtin-sci@yandex.ru

The DC140 quad will be located near the dees and designed as a set of identical PMs rigidly fixed in a non-magnetic housing encircling the aperture.

Additional aspects of the quad specification include:

- simple PM shape, preferably cuboidal bricks,
- minimized number of PM in assembly,
- minimized nomenclature,
- commercial availability of PM

STAGES OF PMQ DESIGN

The initial quad design is selected from an analytical study with the use of a simplified 2D model [1]. At this stage the number and positions of PMs are determined. Then the chosen configuration is optimized in iterative 2D and 3D parametric simulations with realistic PM shape and magnetic characteristics in mind. Simulated data are used to select candidate magnet materials, number, dimensions, and tolerated mechanical and magnetic errors of PM blocks. As a result, the quad design is finalized, and an assembly procedure is proposed. Additional adjustment may be required on the basis of measurements of supplied PM. The assembled quad is magnetically inspected to make sure the desired field requirements are reached.

SIMPLIFIED 2D MODEL OF PMQ

An initial configuration has been generated with the use of 2D analytical models [1] based on the mathematically strict reasoning:

- In the absence of degaussing (the magnetization **M** = const), a field integral of PM with a finite length L_{PM} is equal to a two-dimensional field $\mathbf{B}_{2D}$ generated by an infinite PM multiplied by L_{PM}:

$$\int_{-\infty}^{+\infty} \boldsymbol{B}_{3D}(x,y,z)\,dz = \boldsymbol{B}_{2D}(x,y)\cdot L_{PM}$$

  So, the 2D approximation is quite suitable to determine the initial PM quad configuration which then will be corrected with respect to the demagnetization.
- With distance, the field generated by an infinite PM of an arbitrary shape is approaching the field of an infinite PM cylinder with the same dipole magnetic moment. Thus, the cylindrical representation is applicable for the initial study of magnetic performance. At the next stage, modifications are introduced reasoning from practical implementation.

ISBN: 978-3-95450-240-0 ISSN: 2673-5539 doi:10.18429/JACoW-RuPAC2021-FRA03

Particularly, the PM shape has been adjusted for cuboidal bricks.

- The field of a radially magnetized PM cylinder is described with a simple analytical expression:

$$\boldsymbol{H} = \frac{(\boldsymbol{n},\boldsymbol{m})\boldsymbol{n} - \boldsymbol{m}/2}{\pi r^2}$$

where $\boldsymbol{m} = \boldsymbol{M} \cdot \pi R^2$ – dipole magnetic moment per unit length; $\boldsymbol{M}$ – magnetization vector, R – magnet radius; $r = |\boldsymbol{r}|$ – distance between the magnet center and an observation point, $r > R$; $\boldsymbol{r}$ – position vector to the observation point; $\boldsymbol{n} = \boldsymbol{r}/r$ – unit vector from the magnet center to the observation point. The cylindrical representation is convenient to use as the field generated by the magnet cylinder depends on the product of its area and magnetization, not on these parameters individually.

Finally, the simplified 2D model of the PM quad is composed as a set of infinite rods magnetized in the radial direction and placed around the aperture. At the next stage orientations and positions of the magnets are optimized in order to ensure desired field quality.

Field Quality Criteria

Field quality criteria is deduced from two assertions:

- Linear approximation errors in the horizontal and vertical directions, Δ_x and Δ_y, (see Table 1) are below the field gradient error ε_G:

$$|\Delta_{x,y}| \le \varepsilon_G = \frac{|\boldsymbol{G} - \boldsymbol{G}_0|}{|\boldsymbol{G}_0|}, \quad \boldsymbol{G} = \nabla B_y$$

- The beam in the magnet aperture is localized within a region of the elliptical shape.

Therefore, the field quality of the quad is assessed through the maximal deviation of the field gradient from the required level of 8.1 T/m within the ellipse inscribed in the 64 mm × 25 working region.

PMQ Optimization Using 2D Model

– PM rods with unknown dipole magnetic moments are positioned over the XY plane around the aperture.

– Unknown components (m_x, m_y) of the dipole magnetic moments form the vector of unknowns X.

– Inside the working region a set of reference points is taken with a step $\Delta\varphi = 1°$ over the line $x = a_x \cos\varphi$, $y = a_y \sin\varphi$, $0 \le \varphi \le \pi/2$, $a_x = 32$ mm, $a_y = 12.5$ mm.

– Target values of the field gradient $\mathbf{G}_0 = \nabla B_{0y} =$ (8.1, 0) T/m at the reference points create the right-hand vector Y_0.

– Values of field gradient at the reference points which are linearly dependant on X form vector Y = AX, where A is the matrix with coefficients derived from the field generated by a cylindrical magnet.

The aim is to find vector X (i.e combination of the dipole moments **m**) that provides Y=AX (gradient **G** at the reference points) as close to Y_0 (the required $\mathbf{G}_0$) as possible. The optimal solution is searched through minimizing the functional

$$\Phi = \max_k |\boldsymbol{m}_k|^2 = \max_k \left\|X^{(k)}\right\|_2^2$$

at given

$$\Psi = \max_l |\boldsymbol{G}_l - \boldsymbol{G}_0|^2 = \max_l \left\|Y^{(l)} - Y_0^{(l)}\right\|_2^2 = \text{const}$$

The research and optimization lead to a set of 26 identical PM, 11mm × 11mm each, positioned around the aperture with different orientations, see Fig. 1. Fig. 2 shows calculated field deviations from the ideal distribution. Field gradient error in the elliptical region was found to be below 0.07%.

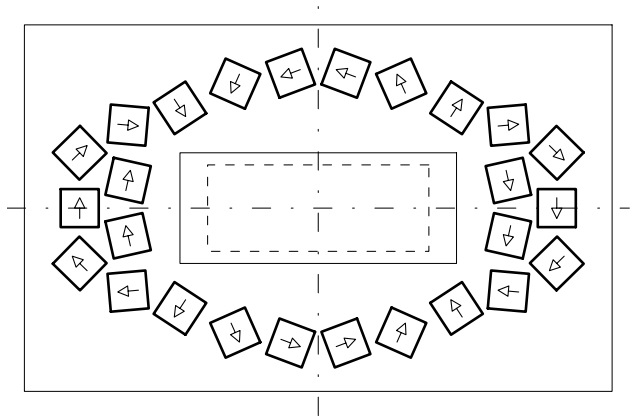

Figure 1: Quad formed with 26 identical 11 mm ×11 mm PM bricks each magnetized to 1.1402T. Arrows indicate PM orientations, dashed lines bound 64mm × 25mm working region, solid lines are for 80mm × 32mm aperture and 170mm × 106mm overall sizes.

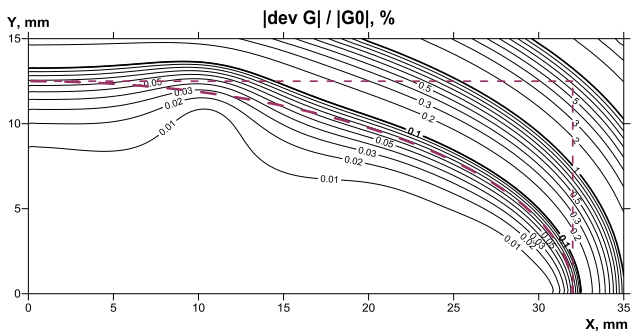

Figure 2:Relative gradient error $\varepsilon_G = |\delta\boldsymbol{G}|/|\boldsymbol{G}_0|$ (%). Dashed lines indicate 64mm × 25mm working region with inscribed elliptical region.

CORRECTION FOR REALISTIC PM

The selected configuration is then used in 2D and 3D field simulations, performed with KOMPOT and KLONDIKE codes [2, 3]. The quad model is fully parametrized and accommodated to influential parameters of actual PM blocks, primarily: realistic 3D geometry of PM, remanent field Br and magnetic susceptibility $\varkappa$ (anisotropic, if that is the case). Sensibility of the simulated field to various perturbing factors is presented in Table 3 in terms of the gradient error ε_G.

ISBN: 978-3-95450-240-0 ISSN: 2673-5539 doi:10.18429/JACoW-RuPAC2021-FRA03

Table 3: Max Gradient Error ε_G in Elliptical Region

Perturbing factor	max ε_G
Unperturbed system	0.07%
Square PM cross-section	0.5%
Intrinsic PM degaussing ($\varkappa$=0.1)	5%
Mutual PM magnetization ($\varkappa$=0.1)	0.6%
Anisotropy $\varkappa$ ($\varkappa_{\parallel M}$=0.1, $\varkappa_{\perp M}$=0)	0.3%
3D representation ($\varkappa$=0.1)	0.17%

Simulations have demonstrated that the influence of any of the perturbing factor is described by a smooth, weakly variable function at low variations of the relevant criterion. This was used as a basis for iterative optimization of the quad design in order to neutralize the perturbing factors.

Iterative Optimization of PMQ Design

At every iteration k (k = 0, 1, …):

- The target gradient value $\boldsymbol{G}_{targ}$ is prescribed at the reference points: $\boldsymbol{G}_{targ,k} = \boldsymbol{G}_0 - \Delta\boldsymbol{G}_{corr,k-1}$ (at k = 0: $\boldsymbol{G}_{targ,0} = \boldsymbol{G}_0$).
- Using $\boldsymbol{G}_{targ,k}$, optimization with the simplified 2D model is performed to determine: (a) orientation and magnetic moments $\mathbf{m}_k$ for every PM, (b) optimized gradient map: $\boldsymbol{G}_{simp,k}$.
- The obtained $\mathbf{m}_k$ are then used in 2D/3D simulation with perturbing factors involved. The simulated data represent expected gradient distribution $\boldsymbol{G}_k$.
- Finally, influence of the perturbing factors is estimated as $\Delta\boldsymbol{G}_{corr,k} = \boldsymbol{G}_k - \boldsymbol{G}_{simp,k}$

It took 2 iterations to determine the PM parameters enabling the desired field quality accurate to ε_G = 0.08%. In the calculations magnetic susceptibility of the Nd-Fe-B PM $\varkappa$ = 0.1 was applied.

As a result, the optimized PM quad specification was generated (Table 4). The numerical study also defines tolerances for the PM geometry and orientation (Table 5).

The proposed design (Fig. 3) envisages assembly technologies and long-term vacuum operating conditions.

CONCLUSIONS

The iterative numerical study has been used to optimize the PM quad design and assess sensitivity of its magnetic specification to various factors. However, any procured batch of PM may have fluctuations from the specified characteristics. The remanent field of commercial PM typically deviates up to 3%. Magnetic susceptibility and PM dimensions may also vary over the batch. This necessitates additional correction with respect to results of the acceptance inspection. The iterative optimization of the quad design should be repeated with the detected imperfections as inputs.

Temperature characteristics of the PM material (typically B_r – 0.1%/°C) and possible long-term decay of magnetic properties must be kept in mind in the design. The final design will reflect all latest modifications.

Table 4: PM Parameters at Operating Temperature

Remanent field B_r	1.1853 T
Magnetic susceptibility $\varkappa$	0.1
Linear piece of B-H curve	up to 1200 kA/m
Nd-Fe-B grade	N35SH, N35UH
PM cross-section	11 mm × 11 mm
PM length L_{PM}	300 mm
Total number of PM	26

Table 5: Geometrical and Magnetic Tolerances

PM dimensions	± 0.05 mm
Remanent field $\lvert B_r \rvert$:	
- average over batch	± 3%
- single PM	±1-1.5%
Magnetization direction	± 1°
Positioning:	
- X, Y, Z coordinates	± 0.05 mm
- orientation	± 0.3°

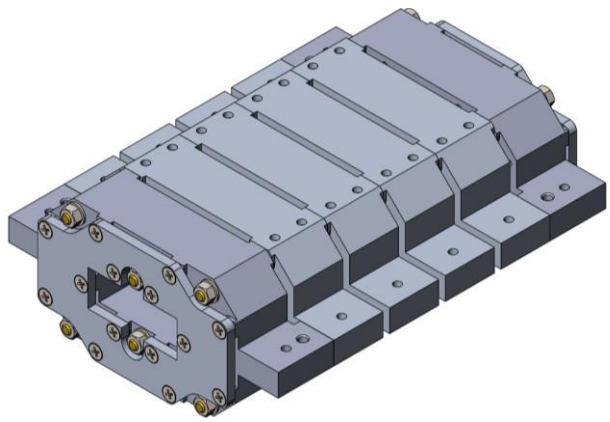

Figure 3: Proposed PM quad design.

REFERENCES

[1] V.M. Amoskov *et al.*, "Modelling and design of permanent magnet multipoles for beam transport and focusing. I: Selection of optimal design and parameters" *Vestnik of Saint Petersburg University. Applied Mathematics. Computer Science. Control Processes*, vol. 17, no. 4, 2021 (in press)

[2] V. Amoskov *et al.*, "Computation technology based on KOMPOT and KLONDIKE codes for magnetostatic simulations in tokamaks", *Plasma Devices Oper.*, vol. 16, no.2, pp.89-103, 2008, doi:10.1080/10519990802018023

[3] V.M. Amoskov *et al.*, "Magnetic model MMTC-2.2 of ITER tokamak complex", *Vestnik of Saint Petersburg University, Applied Mathematics. Computer Science. Control Processes*, vol. 15, no. 1, pp. 5-21, 2019, doi:10.21638/11702/spbu10.2019.101

ISBN: 978-3-95450-240-0 ISSN: 2673-5539 doi:10.18429/JACoW-RuPAC2021-FRA04

THE EXPERIMENTAL RESEARCH OF CYCLOTRON DC-280 BEAM PARAMETER

V.A. Semin†, S.L. Bogomolov, K. Gikal, G.G. Gulbekyan, I.A. Ivanenko, I.V. Kalagin, N.Yu. Kazarinov, V.I. Mironov, L. Pavlov, A.A. Protasov, K.B. Gikal,
Joint Institute for Nuclear Research, Dubna, Russia

Abstract

The DC-280 is the high intensity cyclotron for Super Heavy Elements Factory in FLNR JINR. It was successful commissioned in 2018 [1] and the design parameters were obtained [2,3]. It was designed for production of accelerated ions beam with intensity up 10 pμA to energy in range 4 - 8 MeV/n. The beam power is up 3,5 kW. The diagnostics elements shall be capable of withstanding this power. Moreover such intensity beam required continuous control for avoid of equipment damage. Special diagnostic equipment were designed, manufactured and commissioning. During the design the calculation of thermal loads was made. Some of them were tested before installation on cyclotron. Diagnostic elements used on DC-280 cyclotron are described in this paper.

The special Faraday cup was designed for beam current measurement. The moving inner probe and multylamellar probe are inside the cyclotron. The Scanning two-dimension ionization profile monitor was produced for space distribution analysis of accelerated high intensity beam. Inner Pickup electrode system with special electronic was created for beam phase moving analysis. Time of flight system based on two pick-up electrodes for energy measured was placed in transport channel. These and over diagnostic system were commissioned and tested. The results present in report.

THE TEST OF THERMAL LOADS RESISTANCE

The DC-280 is the high intensive accelerator with beam power up 3,5 kW. For predicting the damage from hitting of the beam on elements, the modeling [4] and testing of prototypes of elements with the electron gun were carried out. It was collaboration of Flerov laboratory of nuclear reaction (JINR) and the Faculty of Mechanical Engineering of the Brno University of Technology (FME BUT During this work the Faraday cup was tested [4].

We heated the sample by electron beam with energy 100 keV. The power was concentrated in the spot with size Ø8 mm. Vacuum level was 10^{-6} Torr. In the process of experiments the temperature in different point of the cup were controlled. The visual monitoring of the beams hitting points was provide. The test results were compared with model ones.

We provide test of the normal work mode, the emergency modes: the hitting of the high intensity beam on the element and work without the water cooling. Series of repeating of high intensity beam and cooling for testing of construction resistance to repeating loads were produced.

† seminva@jinr.ru

The tests show, that this construction of the Faraday cup head from Al is able to withstand power 3500 W without of the damage in area Ø8 mm. The surface of Faraday cup was started destroyed only under beam with power 4200 W. Furthermore the test show the efficiency of cooling with half of cooling water flow. The construction does not damage after series of periodic thermal loads. Thus the construction correspond to requirements.

FARADAY CUP CONSTRUCTION

The design of Faraday cup was presented in [4] in frame of DC-72 project was updated for DC-280. The cup was changed for reduce of distance between the inner surface of cup and water cooling channel. The design was optimization for decreasing of mistakes of current measuring by secondary electron emission on the edge of cup. The magnet system on permanent magnets, part of the design, was moved closer to entry. The magnet system on permanent magnets, part of the design, was moved closer to entry diaphragm. The diaphragm size was reduced, the taper angle was enlarge up to 80^0. The design was optimized by FLNR constructors. The sketch of Faraday cup present on Fig. 1. The new construction was successfully tested and is used on DC-280.

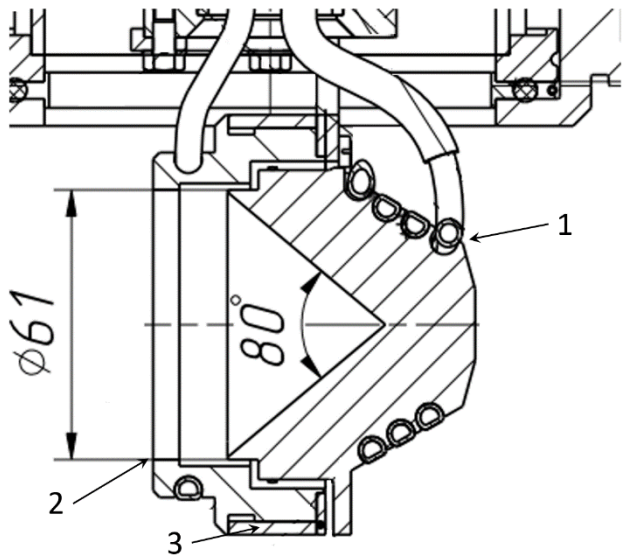

Figure 1: Sketch of the Faraday cup: 1- Water cooling channel; 2- diaphragm; 3- magnet system.

INNER CYCLOTRON PTOBES

For measuring of ions beam current inside the cyclotron two moving probe are used. One is placed before the entry to deflector second is diametrically opposite. They

ISBN: 978-3-95450-240-0 ISSN: 2673-5539 doi:10.18429/JACoW-RuPAC2021-FRA04

mark PR2 and PR1 respectively. The probe moving in radius range from 263 to 1800 mm. It have water cooling system and possible to take the ion beams with power up 1500 W. The linear moving system based by servo motor with reduction gear is used for moving. It give accuracy of position better them 0,5 mm.

Special plate bellows with high work length is used for separation of vacuum part. Moreover there is the sliding seals for moving the probe head in to the gateway. It gives us possibility for operative service, moreover we can place on head of probe the foil for imprinting of the beam form.

Diagnostic head is placed in grounded screen for protect from RF interference. Probe head have special form with sides which hinder moving the electrons from diagnostic part to ground screen. The sides high is 4 mm. These sides and the strong vertical magnetic field exclude the error from the charge getting with moving the secondary electrons from diagnostic head to ground screen.

The moving multylamellar probe is used for control of beam trajectory between the deflector and magnet channel. It have 5 lamella with width 5 mm and one on external radius with width 25 mm. We can put on the probe on a beam trajectory by a pneumatic actuator. The dependence between the place of the lamella and intensity of beam gives us information about the place and size of ion beam after deflector.

The schema of cyclotron diagnostic elements is presented on Fig. 2.

CONTROL OF BEAM CURREN DURING ACCELATION

The described earlier devices are used for control of beam current in different points of cyclotron on various stage of acceleration. Three Faraday cups are placed in axial injection system. One is on HV part and two on ground part. They provide the control efficiency of ions transportation from ECR source to center of cyclotron. They mark IFC1-IFC3.

Moreover IFC1 together with bending magnet IM90 are used for analysis beam from the source and separation the needed ion with needed A/Z ratio. The IM90 have bending radius 90 cm. The collimator placed before the IFC1 can be used for increasing resolution.

We use the moving probe PR2 for control the intensity of the beam. It is earlier, than PR1, on the beam way and last before extraction. The needed ion is divided from impurity on radius 400mm. The rotation beam current between IFC3 and PR2 (R=400) gives us efficiency of capture to acceleration. For improving of capture we use Polyharmonic buncher [5]. The simulation predict the capture efficiency up 70%.The experimental results presented in [1-3] match with it.

Comparing the beam intensity on different radius we define the efficiency of acceleration. We try to get maximum intensity on each radius during the tuning of cyclotron. Thus we fine tune radial correction coils to produce the magnetic field correspond to isochronic regime.

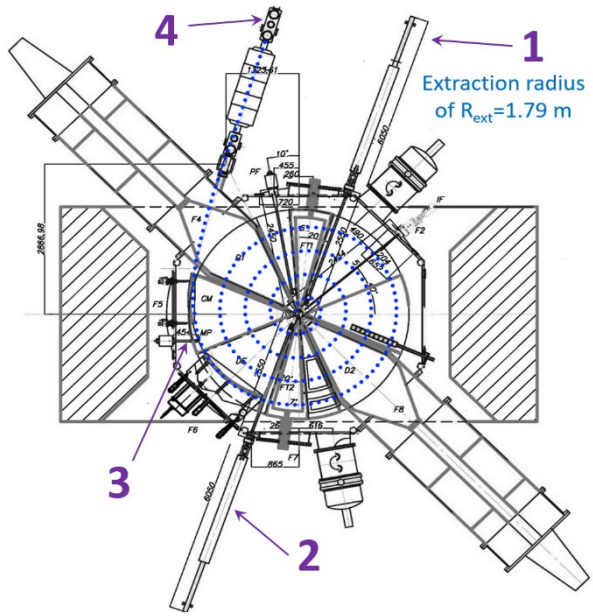

Figure 2: Schema of cyclotron diagnostic elements: 1, 2-inner moving probes PR1and PR2. 3 Multylamellar probe; 4-Faraday cup T0FC1.

We can define the shift of the beam orbit center along inner probe move direction use combination of PR1 and PR2 probes. There are four couple of azimuthal correction coils inside the cyclotron for correction beam orbit center place.

During the experiments we obtain the efficiency of acceleration inside the cyclotron more than 90%.

We use the Faraday cups placed on transport channel for measuring the intensity. There are 7 Faradays cups: Two, T0FC1 and T0FC2 in beginning part, and 5, T1FC3-T5FC3 after commuting magnet [6]. Moreover, the 4 section loss monitor placed along channel in important places. They have overture Ø60 mm. It indicate on the exit of the beam from channel aperture and protect the equipment from thermal damage.

During the experiments we obtain the efficiency of transport more than 90%. The full efficiency of acceleration from Ion source to experimental setup is about 50%.

Moreover the algorithm of automatically measure of intensity on different stage of acceleration was made to simplify the regular using.

BEAM PROFILE CONTROL

For control of beam profile an axial injection system we use the moved luminophore combine with camera. Luminophore have the pneumatic actuator identical to Faraday cup. The Luminophore placed in water cooling holder, rotated to 45^0 to beam direction. Camera placed opposite the luminophore. In axial injection system, there ion have low energy, we use the quartz glass. Then luminophore is put on, we can see the luminous spot. The brightness is correspond to intensity, so we can see profile.

ISBN: 978-3-95450-240-0 ISSN: 2673-5539 doi:10.18429/JACoW-RuPAC2021-FRA04

There is luminophore on the transport channel to. But there it made from Al_2O_3. In spite of the water cooling of holder, the plate luminophore can work with beam intensity up 20 pnA. The luminophore destroyed under more intensive beam.

The Scanning two-dimension ionization profile monitor was designed for control of high intensity beam [7]. It based on the collection of products of the residual gas ionization by a passing beam. It give us profile of the beam in real time without of destroy of beam structure. It give us possibility to evaluate of beam current during experiments.

MEASURING OF ENERGY

For measuring of energy we use TOF method. There are two capacity ring Pick up electrodes in beginning part of transport channel. The signal go through amplifier and couple calibrated cable line to analyzing electronics. The long of fly base is 2203 mm. System of treatment of signal promptly give information about the ions energy. System successful works. The measured energy matches with calculation results and other systems results.

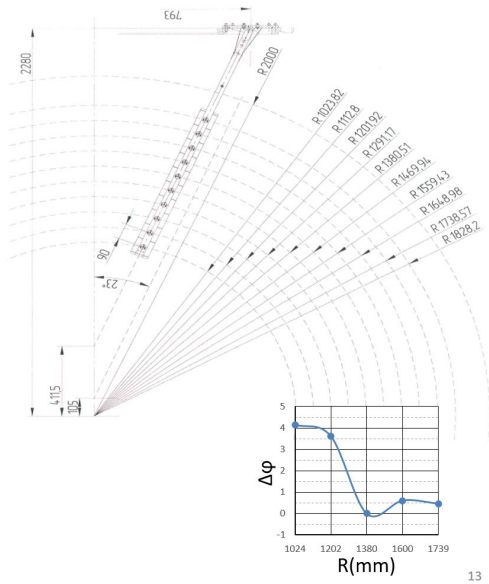

Figure 3: Placing of phase moving control system, and example of analisis for $^{40}Ar^{+7}$ (F=8.51 Hhz; E=5.2 MeV/n).

PHASE MOVING CONTROL

For analysis of phase moving of beam during the acceleration the special system was created. It based on ten pair of capacity Pick-up electrodes. It placed in special holder inside cyclotron. One electron from each pair under the median plane second above. The scheme of place of system in cyclotron is presented on Fig. 3.

We use the second harmonic filter to divide the useful from signal. Comparing the signals we get the shift in time of moving the beam bunch on different radius. After calibrate amendments we get information about phase moving during the acceleration.

Similarly compare the signals from two electrodes from one pair we can evaluate the shift beam trajectory from median plane. But this requires high accuracy of placing of systems and control of identical of electrodes in pair. We preparing system to this experiment end plane to test it soon.

We provided series test and find some problems with electronics and we upgrading it now. Moreover we create the software for operational processing signals.

CONCLUSION

Since end of 2018, then DC-280 start to work, main diagnostic elements were tested. Some of them, as Faraday cups, were modernized. The system of phase moving control is commissioning now.

Moreover experiments showed the need of additional diagnostics system. We are going to place the nondestructive intensity probe before each experimental setup. We are planning to estimate the emittance using existing possibility and compare with measuring by special systems.

REFERENCES

[1] B.N. Gikal *et al.,* "Start-Up of the DC-280 Cyclotron, the Basic Facility of the Factory of Super heavy Elements of the Laboratory of Nuclear Reactions at the Joint Institute for Nuclear Research", *ISSN 1814-5957, Nuclear Research Physics of Particles and Nuclei Letters,* Vol. 16, p.866-875 2019. DOI:10.1134/S1547477119060177

[2] I.V. Kalagin *et al.,* "SHE factory: cyclotron facility for Super Heavy Elements Research" In *Proc.: International Conference on Cyclotrons and their Applications,* Cape Town, South Africa 2020 DOI:10.18429/JACoW-Cyclotrons2019-THC01

[3] V.A. Semin *et al.,* "DC-280 cyclotron for Factory of Super Heavy Elements experimental results." *In Proc. of 12th Int. Particle Acc. Conf. (IPAC2021)* p.p. 4126-4129, 2021. doi:10.18429/JACoW-IPAC2021-THPAB182

[4] I.V. Kalagin *et al.,* "A device for beam current measuring in the channels for transporting external beams of the DC-72 cyclotron." JINR; P9-2002-164. http://www.jinr.ru/publish/Preprints/2002/164(P9-2002-164).pdf

[5] G.G. Gulbekian *et al.,* "The project of the HV axial injection for the DC-280 cyclotron at the JINR FLNR" *Physics of Particles and Nuclei Letters,* Vol. 11, No. 6, pp. 763–773, 2014. https://inis.iaea.org/search/search.aspx?orig_q=RN:46024650

[6] I.V. Kalagin *et al.,* "The project of the beam transportation lines for the DC-280 cyclotron at the JINR FLNR", *In Proc. of RuPAC-2014 Int. Conf.,* Obninsk, Russia, p.p. 336-338, 2014, paper THPSC09.

[7] Yu.G. Teterev, A.T. Isatov, S.V. Mitrofanov and A.I. Krylov, "Upgrading the Scanning Two-Dimensional Ionization Profile Monitor in Beam Transport Lines", *Instruments and Experimental Techniques,* Vol. 63, No. 6, pp. 795–800, 2020. DOI: 10.1134/S002044122005036X

ISBN: 978-3-95450-240-0 ISSN: 2673-5539 doi:10.18429/JACoW-RuPAC2021-FRA05

CYCLOTRON SYSTEM C-250

K.E. Smirnov†, Yu.N. Gavrish, A.V. Galchuck, S.V. Grigorenko, V.I. Grigoriev, R.M. Klopenkov, L.E. Korolev, K.A. Kravchuck, A.N. Kuzhlev, I.I. Mezhov, V.G. Mudrolyubov, Yu.K. Osina, Yu.I. Stogov, M.V. Usanova,
JSC «NIIEFA», 196641, St. Petersburg, Russia

Abstract

JSC "NIIEFA" is designing a cyclotron system that generates intensive proton beams with final energy in the range of 30-250 MeV. We have adopted a non-standard technical solution: at the energy of less than 125 MeV negative hydrogen ions are accelerated with the extraction of protons by the stripping device; at higher energies protons are accelerated, and the beam is extracted by a deflector and a magnetic channel. The isochronous dependence of the magnetic field on the radius for different final energies is provided by changing the current in the main coil and tuning the correction coils.

The cyclotron electromagnet has an H-shaped design with a pole diameter of 4 meters, a four-sector magnetic structure, and high spirality sectors. The dees of the resonance system are formed by delta electrodes and placed in the opposite valleys; stems are brought outwards through holes in the valleys. The operating frequency range is 24-33.2 MHz. The power of the RF generator is 60 kW.

The cyclotron complex is equipped with a branched beam transport system and target devices for applied research on the radiation resistance of materials. Computer control of the cyclotron and its associated systems is provided.

MAIN TECHNICAL FEATURES

The JSC "NIIEFA" is designing a cyclotron system comprising a proton cyclotron, a developed system of beamlines, samples' irradiation system and utilities. The most complicated problem of this project is construction of a unique cyclotron generating proton beams with an energy varied in the range of 30-250 MeV. Cyclotrons with the energy variation over such a wide range are not available nowadays.

The method of negative ions' acceleration with the extraction of protons with a stripping device, which is standard for low-energy cyclotrons, cannot be applied as the binding energy of an additional electron is lower than 0,8 eV. With an increase in the energy of a negative ion when it is moving in a strong magnetic field, rapidly grows the probability of this electron detachment, and, consequently, a decrease in the beam intensity.

To reduce losses, it is necessary to lower significantly the induction of the electromagnet, which will result in a corresponding increase in the diameter of magnet poles. Therefore, at energies higher than 100 MeV, protons are used as accelerated particles. To provide the isochronous motion of protons with different final energy, it is necessary to change the magnetic field induction and its dependence on the radius over wide limits corresponding to the relativistic increase in the proton mass.

To make less stringent requirements to the magnetic field forming, a non-standard decision was adopted. We decided to use negative hydrogen ions as particles to be accelerated in the final energy range of 30-125 MeV; at energies of 125-250 MeV, protons are used.

The ion source is an inner radial Penning-type cold-cathode source.

ELECTROMAGNET

The iron core of the electromagnet is of an H-shaped design, a four-sector magnetic structure and high helicity sectors. The mode with the 1.08 T induction in the center of the magnet and 1.35 T at the final acceleration radius corresponding to the final energy of 250 MeV was chosen as the basic mode. In this mode, the induction dependence on the radius corresponding to the isochronous motion is realized by turning on the main coil only through the shape of the central plugs, sector side plates, and sector chamfers.

To vary the final energy over the range of 250-125 MeV, the isochronous dependence of the magnetic field on the radius is provided by decreasing the current in the main coil and turn on of correction coils located on sectors. The beam is extracted from a fixed final radius by means of a deflector and magnetic channel.

At lower final energies, we used the magnetic field formed for an proton´s energy of 125 MeV (with reversal of the polarity). A beam of required energy is extracted by moving the stripping device with a thin carbon foil.

The electromagnet is shown in Fig. 1 and its parameters are given in Table 1.

Figure 2 shows trajectories of extracted beams. Green color shows protons after passing the deflector; in red are shown negative hydrogen ions and in blue are given protons at the output of the stripping device foil. The deflector is located in the upper left valley; the stripping device foil can be moved over the gap between left sectors.

† npkluts@luts.niiefa.spb.su

ISBN: 978-3-95450-240-0 ISSN: 2673-5539 doi:10.18429/JACoW-RuPAC2021-FRA05

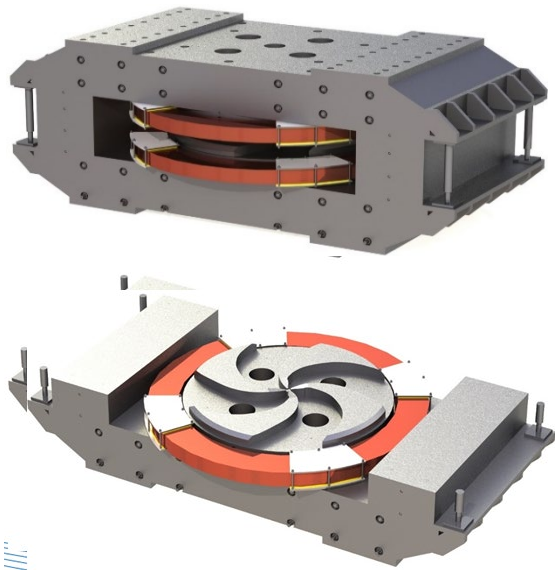

Figure 1: Electromagnet.

Table 1: Parameters of the Electromagnet

Magnet sizes, mm	8100×5360×3600
Pole diameter, mm	4000
Number of sectors (per pole)	4
Lifting height of the upper movable half-yoke, mm	1000
Induction in the center of the magnet, T	0.8-1.08
Final acceleration radius, mm	1800
Helicity at the final acceleration radius	54°
Air gaps, sector/ valley, mm	100/500
Consumed power, kW, no more than	104
Magnet mass (Fe/Cu), t	720/34
Number of correction coils	15×8
Consumed power, kW, no more than	16

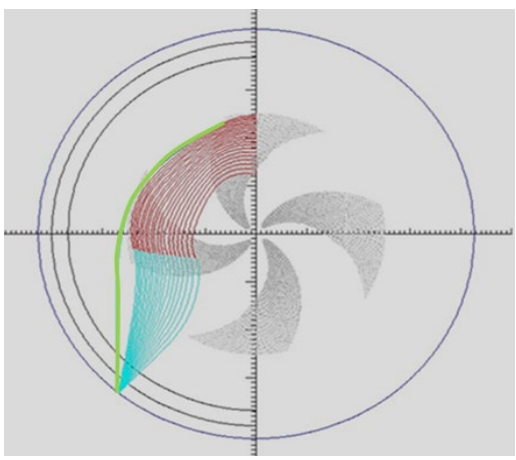

Figure 2: Trajectories of extracted beams.

To align axes of beams with different energies with the axis of the beamline ion tube, a matching magnet is used. The center of the magnet coincides with the point, in which intersect trajectories of proton beams with different energies.

RESONANCE SYSTEM

From Fig. 2 it is seen that trajectories of proton beams with energies in the range of 30-125 MeV practically completely occupy a part of the valley near to the pole edge. This circumstance makes us to use the resonance system with delta-electrodes and dee stems located in through holes made in the magnet valleys.

In such a version, the resonance system includes four coaxial resonators. Each of these resonators consists of a dee cover (a δ-electrode) and corresponding valley cladding as well as a short-circuited section of the coaxial line formed with a dee stem and a tank.

Figure 3 shows the layout of the resonance system in the electromagnet. The dee with stems and a pair of resonators are given in Fig. 4.

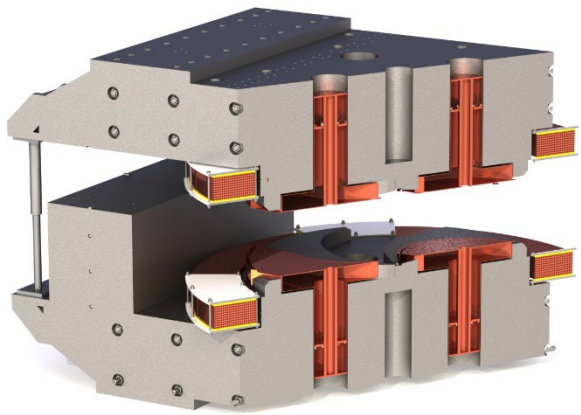

Figure 3: Layout of the resonance system.

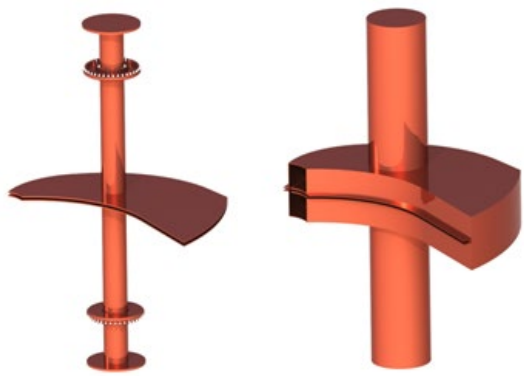

Figure 4: Model of a pair of resonators.

The in-phase operation of all resonators is provided due to a galvanic contact between pairs of ‘’the upper and bottom dee covers” and between dees in the center of the magnet (a puller).

To vary the frequency in a specified range of 24-33.2 MHz, we change the length of coaxial sections by moving synchronously shorting flanges with ball contacts.

ISBN: 978-3-95450-240-0 ISSN: 2673-5539 doi:10.18429/JACoW-RuPAC2021-FRA05

The maximum active loss power in the resonance system with the RF-voltage amplitude at the final radius of 100 kV is about 50 kW. The resonance system is equipped with an RF-power capacitance input device, an RF probe and two electromechanically-driven trimmers.

RF-POWER SUPPLY SYSTEM

The RF-power supply system operates in the frequency range of 24-33.2 MHz. Structurally the equipment of the system is divided into 3 units, namely, cabinet of the main equipment, amplifier final stage and high-voltage power supply.

The main equipment cabinet houses master oscillator, preamplifier, amplifier pre-final stage as well as system for monitoring, control, protection and measurements and ancillary equipment. The cabinet is shown in Fig. 5.

Figure 5: Cabinet of the main equipment.

The amplifier final stage (Fig. 6) in a separate cabinet will be installed in a direct vicinity to the resonance system. The final stage is developed on the basis of the GU – 66A generator triode with an output power up to 100 kW. The RF power is output from the final stage through an isolating capacitor and connector. The final stage is connected to the device of the RF- power input to the resonance system either directly or with a short section of a coaxial feeder.

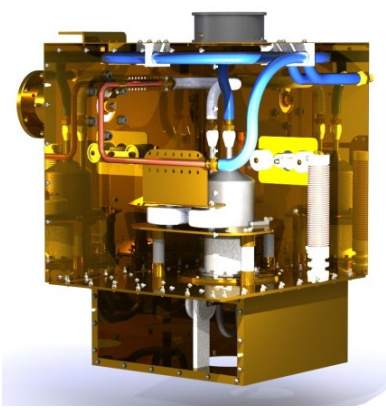

Figure 6: Model of amplifier final stage.

We plan to construct a high-voltage power supply of the inverter type with the output voltage of 10 kV, current of 13 A and voltage stability of 5×10^{-3}.

BEAM TRANSPORT SYSTEM

In the project worked out in the JSC «NIIEFA», the system of beamlines providing the delivery of the proton beam to three separately located target rooms is considered (Fig. 7).

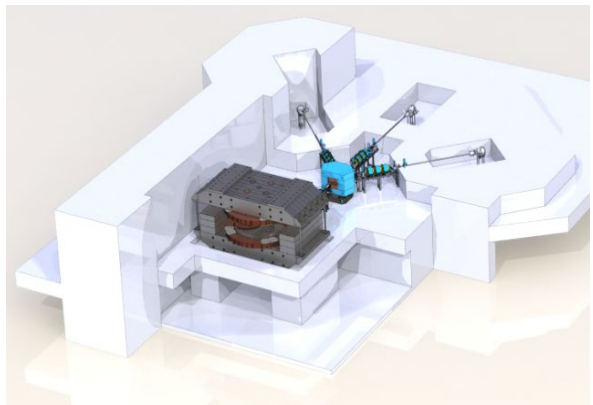

Figure 7: Layout of the cyclotron system main equipment (project).

The beam transport system comprises a matching magnet, electromagnetic lenses, correcting magnets and diagnostics. The central beamline can be equipped with a neutron converter.

UTILITIES

The cyclotron system is automatically controlled. The automated control system should provide monitoring, diagnostics and control of the operation of the cyclotron and all its associated systems. In an emergency situation, either separate equipment or the whole cyclotron system should be automatically turned off.

CONCLUSION

The cyclotron system with control of proton energy and beam current over such a wide range is a unique experimental instrument to be applied for research in the field of radiation material science and for studying the radiation strength of materials. It is for the first time that researches will get an opportunity to use proton and neutron beams to form irradiation fields with a wide range of energies and intensities. As a result, new experimentally-proved knowledge in the field of radiation physics will be obtained.

Nowadays, designing of the system is being completed, and production of the main units and systems has been started.

ISBN: 978-3-95450-240-0 ISSN: 2673-5539 doi:10.18429/JACoW-RuPAC2021-FRB01

ADVANCES IN THE DEVELOPMENT OF A VACUUM INSULATED TANDEM ACCELERATOR AND ITS APPLICATIONS*

S.Yu. Taskaev†, T.A. Bykov, A.A. Ivanov, D.A. Kasatov, Ia.A. Kolesnikov, A.M. Koshkarev, A.N. Makarov, G.M. Ostreinov, I.M. Schudlo, E.O. Sokolova, I.N. Sorokin
Budker Institute of Nuclear Physics, 630090 Novosibirsk, Russia
Novosibirsk State University, Novosibirsk, Russia

Abstract

A compact accelerator-based neutron source has been proposed and created at the Budker Institute of Nuclear Physics in Novosibirsk, Russia. An original vacuum insulated tandem accelerator (VITA) is used to provide a proton/deuteron beam. As a result of scientific research and modernization, the power of the ion beam was increased, an operation mode without high-voltage breakdowns was achieved, and the operation of the accelerator in a wide range of changes in the energy and current of ions was ensured. The proton/deuteron beam energy can be varied within a range of 0.6 – 2.3 MeV, keeping a high-energy stability of 0.1%. The beam current can also be varied in a wide range (from 0.3 mA to 10 mA) with high current stability (0.4%). VITA is used to obtain epithermal neutrons for the development of boron neutron capture therapy, thermal neutrons for the determination of impurities in ITER materials by activation analysis method; fast neutrons for radiation testing of materials; 478 keV photons to measure the ^{7}Li(p,p'γ)^{7}Li reaction cross section, etc. VITA is planned to be used for boron imaging with monoenergetic neutron beam, for characterizing of neutron detectors designed for fusion studies, for in-depth investigation of the promising ^{11}B(p,α)αα neutronless fusion reaction, for studying the crystal structure of materials by neutron diffraction, etc.

INTRODUCTION

To develop a promising procedure for treating tumors (boron-neutron capture therapy, BNCT [1]), an accelerator-based epithermal neutron source has been prepared and designed in the BINP [2]. Neutrons are generated as a result of the ^{7}Li(p,n)^{7}Be threshold reaction by directing a proton beam, which is produced in an original design tandem accelerator, onto the lithium target.

Significant progress in the development of the accelerator and a significant expansion of its applications have been achieved recently. The report provides a description of the accelerator and its operating parameters, highlights the features of the accelerator, gives the examples of its application and declares plans.

EXPERIMENTAL FACILITY

The neutron source comprises an original design tandem accelerator, solid lithium target, a neutron beam shaping assembly, and is placed in two bunkers as shown in Fig. 1. The facility has the ability to place a lithium target in 5 positions; they are marked as positions *A*, *B*, *C*, *D*, *E*.

The original design tandem accelerator, which was named as Vacuum Insulated Tandem Accelerator (VITA), has a specific design that does not involve accelerating tubes, unlike conventional tandem accelerators. Instead of those, the nested intermediate electrodes (*1b*) fixed at single feedthrough insulator (*1d*) is used, as shown in Fig. 1. The advantage of such an arrangement is moving ceramic parts of the feedthrough insulator far enough from the ion beam, thus increasing the high-voltage strength of the accelerating gaps given high ion beam current. A consequence of this design was also a fast rate of ion acceleration—up to 25 keV/cm.

RESULTS AND DISCUSSION

The potential is supplied for the high-voltage electrode and five intermediate electrodes of the accelerator from a sectioned rectifier (*1e*) through a feedthrough insulator (*1d*) in which a resistive voltage divider is mounted. For the compactness of the accelerator, the average electric field strength on the insulator was chosen to be 14 kV/cm, which is 1.5 times higher than the recommended one. This led to breakdowns along the surface of smooth ceramic insulators with a height of 73 mm, from which the feedthrough insulator was assembled. Such breakdowns occurred approximately once every 10 – 20 min; they did not lead to a decrease in the electric strength of the accelerator, but required 15 s to restore the parameters of the ion beam. To eliminate breakdowns along the vacuum surface of insulators, smooth ceramic insulators were replaced with corrugated insulators of the same height.

A beam of negative hydrogen ions with an energy of 20 – 30 keV is injected into the tandem accelerator. Since VITA is characterized by a fast ion acceleration rate, the entrance electrostatic lens is strong. For this reason, the injected ion beam must be refocused to the entrance to the accelerator. To focus the ion beam at the entrance of the accelerator, we used a magnetic lens. Since the transport and focusing of a relatively low energy ion beam is accompanied by a spatial charge, a wire scanner OWS-30 (D-Pace, Canada) is used to control the position and size of the ion beam at the entrance to the accelerator.

The position and size of the ion beam in the accelerator are controlled by two pairs of video cameras overseeing the input and output diaphragms of the external accelerating electrode. Cameras register visible radiation caused by interaction of ions with residual and stripping gases, and heating of diaphragms.

* Work supported by Russian Science Foundation, grant No. 19-72-30005
† taskaev@inp.nsk.su

ISBN: 978-3-95450-240-0 ISSN: 2673-5539 doi:10.18429/JACoW-RuPAC2021-FRB01

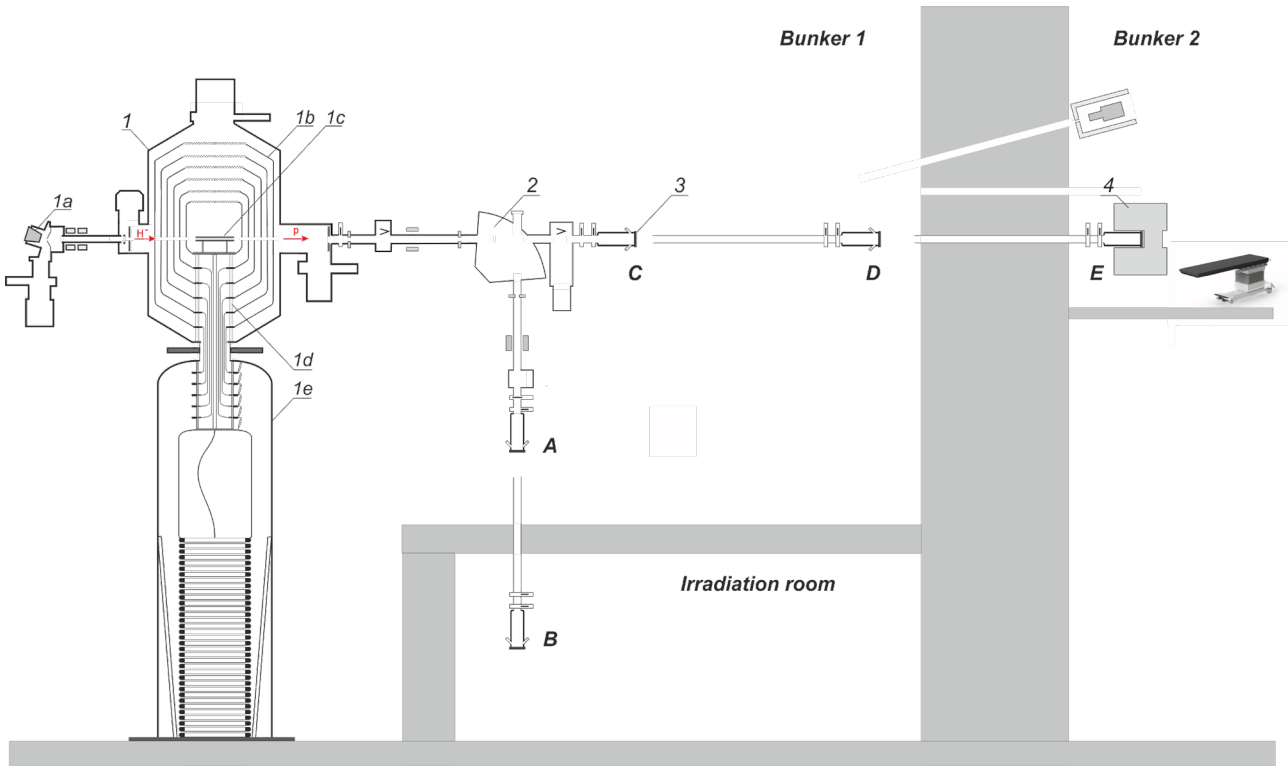

Figure 1: Layout of the experimental facility: 1 – vacuum-insulated tandem accelerator (1a – negative ion source, 1b – intermediate- and high-voltage electrodes, 1c – gas stripper, 1d – feedthrough insulator, 1e – high-voltage power supply), 2 – bending magnet, 3 – lithium target, 4 – beam-shaping assembly. A, B, C, D, E – lithium target placement positions.

A gas stripper *(1c)* is used for stripping negative hydrogen ions into protons. The stripper is a cooled tube with argon inlet through a hole in the middle. The presence of a gas stripper in a tandem accelerator is often considered a disadvantage. We managed to neutralize the disadvantages and turn the use of a gas stripper into an advantage. The additional gas flow makes it possible to visualize the beam for diagnostics of its position and size and improves the high-voltage strength of the accelerating gaps. Of course, additional gas injection increases the undesirable flux of secondary charged particles, but this flux is reduced to an acceptable level by improving vacuum pumping and suppressing secondary electron emission from the walls of the vacuum chamber. The flux of positive argon ions formed inside the gas stripper and penetrating into the accelerating gaps turned out to be extremely low: it was 2000 times less than the proton beam current.

Typically, a gas stripper provides 95% conversion of negative ions to positive ones. Although a larger injection of argon leads to an increase in the proton current, the current of secondary charged particles grows much more strongly. Inside a stripping tube 16 mm in diameter, the ion beam has a size of about 5 mm and a divergence of ±2 mrad. The size of the ion beam and the divergence were determined from measurements of the phase portrait of the neutral flux measured with a cooled diaphragm scanning the beam and a wire scanner located behind the scanning diaphragm and a bending magnet turned on to deflect ions.

The proton beam obtained inside the stripper is focused by an electrostatic lens due to the penetration of the electric field through the diaphragm into the high-voltage electrode, is accelerated in the accelerating gaps, and is slightly defocused by the output electrostatic lens. At a distance of 1.86 m from the center of the accelerator, the proton beam has a characteristic size of 11 mm, a divergence of ±1.5 mrad, and a normalized emittance of 0.23 mm mrad. The peculiarity of the proton beam, which is attractive for its transportation, lies in its sharp border – there is no beam at a distance of 2σ from the beam axis. This is due to the effect of the space charge during the transport and focusing of a beam of negative hydrogen ions and the small size of the diaphragms – 10 mm in the entrance and 20 mm in the accelerating gaps.

Two cooled copper diaphragms with four thermocouples evenly spaced in azimuth inside are installed before the bending magnet. These diaphragms are used to optimize the production of the ion beam. By a magnetic focusing lens and a corrector in the low-energy beam path, the passage and acceleration of the ion beam are achieved such that the input diaphragm of the first accelerating electrode is heated rather weakly (diagnosed by video cameras) and the cooled diaphragms in front of the bending magnet are also heated weakly and symmetrically. Stronger focusing of negative ions makes it possible to obtain a smaller proton beam at the exit from the accelerator and with a lower divergence, but this mode is accompanied by a greater heating of the entrance diaphragm of the first accelerating electrode due to the broadening of the ion beam here. Weaker focusing of negative ions, on the contrary, does not lead to heating of the entrance diaphragm of the first

ISBN: 978-3-95450-240-0 ISSN: 2673-5539 doi:10.18429/JACoW-RuPAC2021-FRB01

accelerating electrode, but makes the proton beam more divergent. Since the accelerator operates in a wide range of ion energies and currents, as well as the type of ions—protons or deuterons, this procedure is used to optimize the production of an ion beam.

The spatial charge does not influence the transport of the proton beam, therefore, the proton beam can be transported relatively simply and without loss to a lithium target 10 cm in diameter in whatever position it is installed. So, with the bending magnet turned off, the size of the proton beam on the surface of the lithium target in position *C* is 20 mm, in position *D* – 28 mm, *E* – 38 mm. To direct the proton beam downward, a bending magnet with a decay rate of 0.5 is used, which ensures the same focusing of the proton beam in the direction along and across the magnetic field. The proton beam is transported in the vertical part when its divergence is ±8 mrad. On the surface of the lithium target at position *A*, the transverse dimension of the proton beam is 30 mm and can be increased by turning on the scanner; at position *B*, the transverse dimension of the proton beam is predicted to be 70 mm.

As a result, the facility produces a beam of protons or deuterons, the energy of which can be varied within a range of 0.6 – 2.3 MeV, keeping a high-energy stability of 0.1%. The beam current can also be varied in a wide range (from 1 pA to 10 mA) with high current stability (0.4%).

The facility is capable of producing a powerful neutron flux of various energy ranges: thermal, epihermal, over-epithermal, monoenergetic, and fast; 478 keV photons in ^{7}Li(p,p'γ)^{7}Li reaction, 511 keV photons in ^{19}F(p,αe^{+}e^{-})^{16}O reaction, α-particles in ^{7}Li(p,α)α and ^{11}B(p,α)αα reactions, and positrons in ^{19}F(p,αe^{+}e^{-})^{16}O reaction.

APPLICATIONS

The initial application of such an accelerator was to generate neutrons for BNCT, and this application was realized. The developed neutron source commercialized by TAE Life Sciences (USA) is installed in new BNCT Center (one of the first six BNCT clinics in the world) at Xiamen Humanity Hospital in Xiamen, P.R. China in 2020. It is planned to start treatment in early 2022. The manufacture of two more neutron sources began this year: for National Oncological Hadron Therapy Center (CNAO) in Pavia, Italy, and for National Medical Research Center of Oncology in Moscow, Russia. The neutron source in BINP is used for the development of dosimetry methods in BNCT [3,4], testing of boron delivery drugs [5,6], measurements of neutron yield in lithium [7], and it is planned to be used for boron imaging in cooperation with the University of Pavia (Italy) and characterization of the epithermal neutron field in cooperation with the Laboratory of Subatomic Physics and Cosmology CNRS-IN2P3, Grenoble-Alpes University (France) and the Laboratory of Micro-Irradiation, Metrology, and Neutron Dosimetry, IRSN (Cadarache, France).

Another important application of the facility is to gain fundamental knowledge. A ^{7}Li(p,p'γ)^{7}Li reaction cross section and 478 keV photon yield from a thick lithium target at proton energies from 0.65 MeV to 2.225 MeV were measured with high precision [8]. Now an experiment is being prepared to study the energy and angular characteristics of products of the promising neutronless fusion ^{11}B(p,α)αα reaction.

Recently, the source was used to measure the content of hazardous impurities in boron carbide samples developed for thermonuclear fusion reactor ITER [9]. The neutron source is planned to be used for radiation tests of fibers of the laser calorimeter calibration system of the Compact Muon Solenoid electromagnetic detector developed for the High-Luminosity Large Hadron Collider in CERN. The facility is also planned to be used to obtain a beam of cold and ultracold neutrons and to carry out elemental analysis of the surface of materials by backscattered protons.

CONCLUSION

A compact original design tandem accelerator VITA has been proposed and created at the BINP. The accelerator is used to provide the high neutron flux in various energy ranges, from thermal to fast, the 478 keV and 511 keV photons, α-particles, and positrons for research in various fields including boron neutron capture therapy and thermonuclear fusion.

REFERENCES

[1] W. Sauerwein, A. Wittig, R. Moss, Y. Nakagawa (Eds.), Neutron Capture Therapy: Principles and Applications. Springer, 2012. doi:10.1007/978-3-642-31334-9

[2] S. Taskaev *et al.*, "Neutron Source Based on Vacuum Insulated Tandem Accelerator and Lithium Target", *Biology*, vol. 10, 350, Apr. 2021. doi:10.3390/biology10050350

[3] T. Bykov *et al.*, "Initial trials of a dose monitoring detector for boron neutron capture therapy", *J. Instrum.,* vol. 16, P01024, 2021. doi:10.1088/1748-0221/16/01/P01024

[4] M. Dymova *et al.*, "Method of measuring high-LET particles dose", *Radiat. Res.*, vol. 196, pp. 192-196, Aug. 2021. doi:10.1667/RADE-21-00015.1

[5] M. Vorobyeva *et al.*, "Tumor cell-specific 2'-fluoro RNA aptamer conjugated with closo-dodecaborate as a potential agent for boron neutron capture therapy", *Int. J. Mol. Sci.*, vol. 22, 7326, July 2021. doi:10.3390/ijms22147326

[6] A. Zaboronok *et al.*, "Gold nanoparticles permit in situ absorbed dose evaluation in boron neutron capture therapy for malignant tumors", *Pharmaceutics*, vol. 13, 1490, Sept. 2021. doi:10.3390/pharmaceutics13091490

[7] M. Bikchurina *et al*., "The measurement of the neutron yield of the ^{7}Li(p,n)^{7}Be reaction in lithium targets", *Biology*, vol. 10, 824, Aug. 2021. doi:10.3390/biology 10090824

[8] S. Taskaev *et al*., "Measurement of the ^{7}Li(p,p'γ)^{7}Li reaction cross-section and 478 keV photon yield from a thick lithium target at proton energies from 0.65 MeV to 2.225 MeV", *Nucl. Instrum. Methods Phys. Res., Sect. B*, vol. 502, pp. 85-94, June 2021. doi:10.1016/j.nimb.2021.06.010

[9] A. Shoshin *et al*., "Test results of boron carbide ceramics for ITER port protection", *Fusion Eng. Des*., vol. 168, 112426, March 2021. doi:j.fusengdes.2021.112426

ISBN: 978-3-95450-240-0 ISSN: 2673-5539 doi:10.18429/JACoW-RuPAC2021-FRB02

ACCELERATORS OF ELV SERIES: CURRENT STATUS AND FURTHER DEVELOPMENT

D.S. Vorobev, E.V. Domarov, M.G. Golkovskii, Y.I. Golubenko, A.I. Korchagin, D.A. Kogut. N.K. Kuksanov, R.A. Salimov, A.V. Semenov, S.N. Fadeev, A.V. Lavrukhin, P.I. Nemytov,
The Budker Institute of Nuclear Physics (BINP), Novosibirsk, 630090, Russia

Abstract

For many years, Budker Institute of Nuclear Physics produces medium-energy industrial electron beam accelerators. Flexible (due to the possibility of completing with different systems) and reliable accelerators cover the energy range from 0.3 to 3 MeV, and up to 130 mA of beam current, with power up to 100 kW.

New accelerators of the ELV type are also being developed. Namely ELV-15 with energy range up to 3.0 MeV and power up to 100 kW. At present time accelerator was assembled and tested in Novosibirsk.

In addition, an accelerator was developed and tested with a new model of extraction device of a focused electron beam into the atmosphere. At present, various experiments are run using the installation with a new device for the extraction of the concentrated electron beam into the atmosphere for the production of nanopowders, surfacing of powder materials for metals, etc.

ELV ACCELERATORS

The ELV industrial accelerators [1] are widely used due to a number of advantages:

- High electron beam power in wide energy range
- High efficiency of electron beam (70-80%), which important for long term operation
- High stability of electron beam parameters
- Extra-long lifetime and high reliability: 24/7 mode of operation
- Wide set of underbeam equipment: for the film, and cables irradiation, nanopowders manufacturing, liquids, and gases treatment and crosslinking

Table 1 represent parameters of the most popular ELV accelerators. As you can see, a new accelerator appears here: ELV-15 with max energy 3 MeV. Also, the current range for the ELV-8 accelerator was increased up to 60 mA. The common view of the ELV type accelerators is shown on Fig. 1. Actually, the ELV accelerators are well described in [2].

Deliveries of last years

More than 200 accelerators were delivered and installed by now. Even for the last three years, under the significant influence of COVID-19, we had delivered 17 accelerators to our customers. For 2022 is about 15 accelerators now in the queue.

Two accelerators, ELV-8 and ELV-4 were delivered to Russia in 2020. One of them (ELV-8) is installed into a new foam film plant. The plant is located in the Kotovsk city, Tambov region, and is currently reaching production parameters. It should be noted that the delivery of this accelerator was carried out jointly with our partner, the Chinese company "Shanxi Yuridi". The electron beam crosslinking underbeam technology line was supplied by this company.

Table 1: Models of the ELV Accelerators

Name	Energy, MeV	Max current, mA	Power, kWt
ELV-0.5-130	0.3-0.5	130	65
ELV-0.5-70	0.4-0.8	70	50
ELV-4-1	0.7-1.0	100	100
ELV-4-1.5	1.0-1.5	67	100
ELV-8	1.0-2.5	60	100
ELV-15	1.5-3.0	50	100

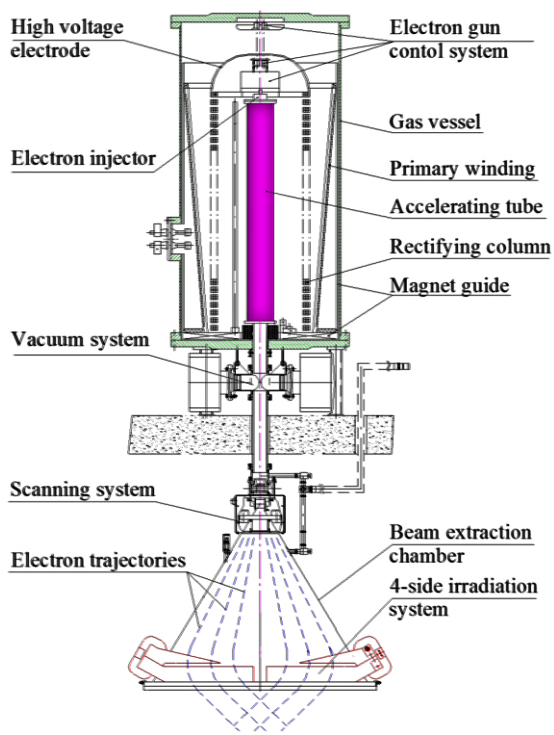

Figure 1: The ELV type accelerator view.

ISBN: 978-3-95450-240-0 ISSN: 2673-5539 doi:10.18429/JACoW-RuPAC2021-FRB02

ELV-15

The most important achievement in 2021 is the ELV-15 accelerator. We and our partners have long had a desire to make an accelerator with an energy of 3 MeV. Increasing the energy up to 3 MeV expands the application possibilities.

Design

The high-voltage rectifier of the ELV-8 accelerator, with a maximum energy of 2.5 MeV and a power of 100 kW, was taken as a basis. After that, the diameter and height of the primary winding, the number of turns of the primary winding, the diameter of the secondary winding coils (sections) were increased. The number of rectifying sections has also been increased (i.e. column height).

Even though the diameter of the sections for ELV-15 has been increased, nevertheless, it remains possible to use standard sections of the ELV secondary winding. In this configuration, the accelerator was successfully assembled and tested. The accelerating tube consists of 4 x 90cm parts, the number of rectifying sections is 80, the number of primary windings is 2 (the height and diameter are increased).

As a voltage sensor, as in ELV-8, a rotary voltmeter is used. The beamline, optical, and extraction system did not undergo significant changes. In the power supply system (power supply cabinet), the ability to change the frequency of the primary winding power supply depending on the requested energy has been added (to simplify the operation of the matching circuit).

Accelerating tube view and the common view of the ELV-15 accelerators are shown on Figs. 2 and 3.

Figure 2: The ELV-15 accelerating tube.

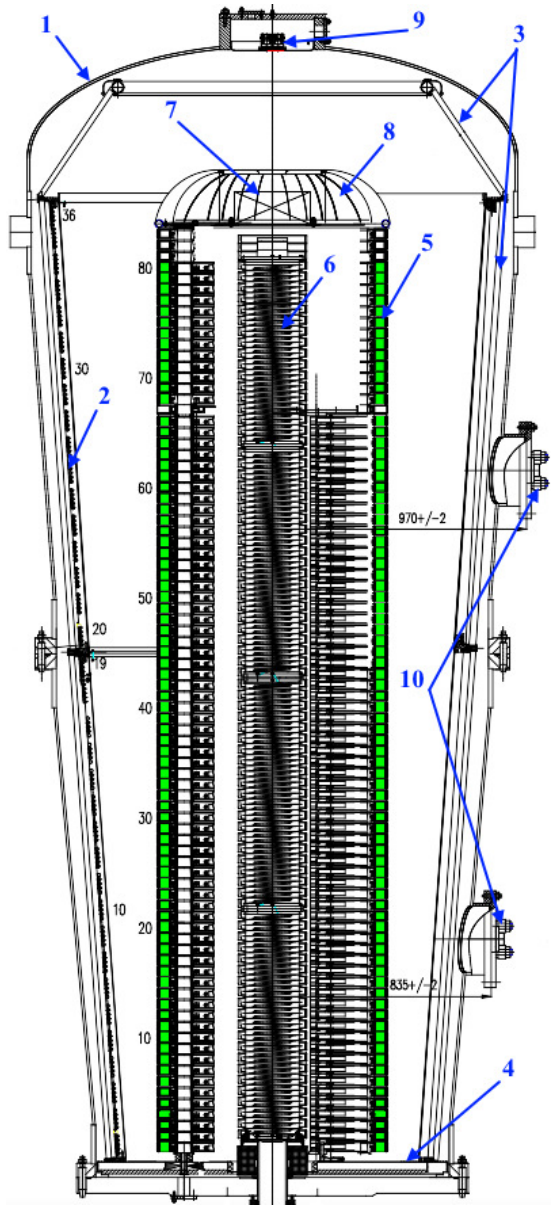

Figure 3: The ELV-15 view. 1 - vessel; 2 - primary windings; 3.4 - magnetic guides; 5 - rectifier sections; 6 - accelerating tube; 7 - injector control unit; 8 - high voltage electrode; 9 - optical channels for injector control; 10 - primary winding feedthrough.

Testing

In August 2021, all tests of the ELV-15 accelerator were completed. The maximum parameters were obtained: maximum power (100 kW) at an energy of 3 MeV with a current of 33.3 mA, and 50 mA at lower energies (2 MeV and less). Also accelerator was tested on maximum energy 3.3 MeV without load (beam).

Upon completion of the tests, the accelerator was disassembled, packaged and shipped to customers in China.

The topic of the ELV-15 accelerator will be covered in more detail in future articles.

ISBN: 978-3-95450-240-0 ISSN: 2673-5539 doi:10.18429/JACoW-RuPAC2021-FRB02

ELV-8 IMPROVEMENT

For the ELV-8 accelerator, the maximum current was increased to 60 mA. The maximum power remains the same - 100 kW. This improvement allows you to work with a current of 60 mA in the energy range 1.0 - 1.66 MeV. Such an improvement required a slight upgrade in the cooling of the power cabinet choke and the addition of the ability to change the capacitance of the matching circuit during operation. In the aftermath, it turned out that a more accurate tuning of the matching circuit elements allows the accelerator to operate in the entire range without retuning or changing the capacitance/frequency.

FOCUSED ELECTRON BEAM INTO THE ATMOSPHERE

A new type of gas-dynamic extraction device was designed and pre-tested. It can efficiently extract a focused electron beam into the atmosphere [3].

During the tests, stable operation was achieved at a beam power of 70 kW and a short-term operation at 100 kW. After long-term operation of the accelerator at a power of 50 kW, the diameters of the holes in the diaphragm did not change. Diaphragm hole diameter on the extraction device output is 2-2.5 mm.

4M EXTRACTION DEVICE

In cooperation with Shanxi Yuridi company, at 2019, an extraction device with a window width of 4 meters was manufactured, and tested. Such a wide electron beam raster was required to irradiate a polyethylene film up to 4 meters wide. The ELV-8 accelerator equipped with this extraction device was successfully delivered and installed to a Chinese company in Anhui province.

The four meters width extraction device shown on Fig. 4.

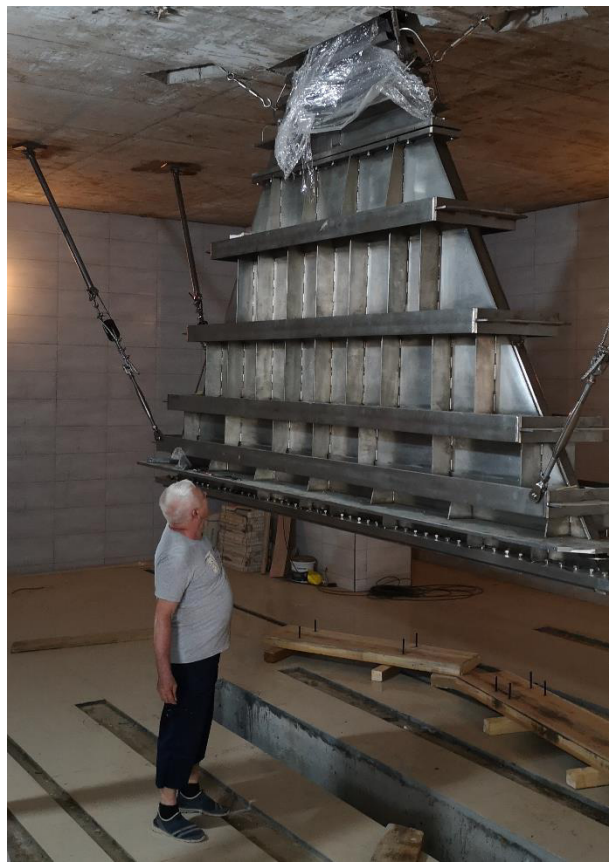

Figure 4: Four meters width extraction device.

REFERENCES

[1] N. K. Kuksanov *et al.*, "ELV accelerators are a tool for innovation", in *Proc. RUPAC'18*, Protvino, Russia, Oct 2018, pp. 261-263. doi:10.18429/JACoW-RUPAC2018-TUPSA55

[2] R. Salimov *et al.*, "D.C. high power electron accelerators of ELV-series: status, development, applications", *Radiat. Phys. Chem Methods*, vol. 57, pp. 661-665, 2000. doi:10.1016/S0969-806X(99)00486-7

[3] E. V. Domarov *et al.*, "Upgrated the extraction device of focused electron beam into the atmosphere", presented at the RUPAC'21, Alushta, Russia, Sep-Oct 2021, paper FRB03, this conference.

ISBN: 978-3-95450-240-0 ISSN: 2673-5539 doi:10.18429/JACoW-RuPAC2021-FRB03

UPGRATED THE EXTRACTION DEVICE OF FOCUSED ELECTRON BEAM INTO THE ATMOSPHERE

E. V. Domarov, N. K. Kuksanov, R. A. Salimov, A. I. Korchagin, S. N. Fadeev, A. V. Lavrukhin, V. G. Cherepkov, Y. I. Golubenko, I. K. Chakin, M. G. Golkovsky, A,V, Semenov P. I. Nemytov,
Budker Institute of Nuclear Physics SB RAS, Lavrentyev av. 11 Novosibirsk, 630090 Russia

Abstract

This article deals the factors affecting the diameter and angle of divergence of the electron beam at the exit from the accelerator tube of an industrial ELV series accelerator. Measurements of the parameters of a high-power electron beam were carried out up to a power of 100 kW. On the basis of the data obtained, a new type of gas-dynamic extraction device was designed and pre-tested, which can efficiently output a focused electron beam to the atmosphere.

INTRODUCTION

For more than 30 years at the Institute of Nuclear Physics (INP SB RAS), on ELV-6 accelerator has been successfully operating a multi-stage gas-dynamic extraction device through which a focused electron beam is released into the atmosphere. It uses an accelerating tube with permanent magnets. The design and manufacture of such accelerating tubes are rather complicated. At present, ELV accelerators use simpler and more reliable accelerating tubes without magnetic accompaniment. They have a large aperture of 100 mm and are mass-produced [1]. Since the reliability of serial accelerating tubes is high, and the technology for manufacturing tubes with permanent magnets has been lost. The task was posed of a possible replacement of the accelerating tube with permanent magnets with an accelerating tube with a large aperture without permanent magnets for the ELV-6 accelerators.

BEAM MOTION ANALYSIS

The beam size and its angular divergence at the exit of the accelerating tube are influenced by the following main factors:

1. Longitudinal electric field: carries out the main focusing of the beam;
2. Influence of the magnetic field of heating coil (the beam acquires an azimuthal momentum Pφ0);
3. The space charge of the beam;
4. The ripples of the accelerating voltage;
5. Aberrations of electromagnetic lenses. They also affect the optimal hole size in the outlet diaphragms;
6. Transverse component of the magnetic field of the primary and secondary windings, which leads to oscillations of the beam, and leads to increase the holes in the diaphragms

The calculations were carried out using the SAM program developed at the BINP SB RAS [2]: the effect of the intrinsic magnetic field of the incandescence was taken into account, the influence of the potential of electrodes with an aperture of 20 mm on the parameters of the beam, embedding of the LaB6 pellet and the shape of the cathode electrode was checked.

The potential distribution along the accelerating tube is shown in Fig. 1. A so-called "electric-gate" is formed near the high-voltage edge of the tube; a minimum of potential is created, which prevents the acceleration of secondary particles appearing as a result of ion bombardment of electrode with an aperture of 20 mm.

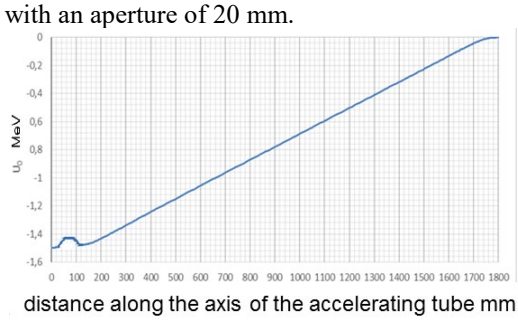

Figure 1: Distribution of potential along the axis of the accelerating tube.

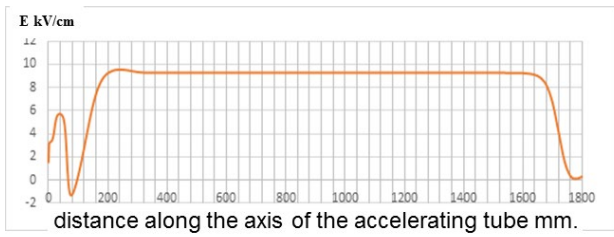

Figure 2: Distribution electric field along the axis of the accelerating tube.

The distribution of the electric field on the tube axis is uneven (see Fig. 2). With an increase the electric field, the beam is focused, and with a decrease the field, the beam is defocused. Three characteristic areas can be distinguished. The cathode is located at point 0. The first section is from 0 to 200 mm. In this section, the beam successively undergoes focusing, defocusing, and focusing. Integrally, this section is strongly focusing and has the greatest effect on the beam parameters at the tube exit. In the second section (200-1700 mm), the electric field is uniform and there is no focusing. In the third section - the tube exit - the electric field decreases to 0 and a defocusing lens is formed with a focal length of about 4 Ltr (where Ltr is the tube length), i.e. about 7 meters. Figure 3 shows the calculated beam envelopes for the optimal geometry of the electric field.

ISBN: 978-3-95450-240-0 ISSN: 2673-5539 doi:10.18429/JACoW-RuPAC2021-FRB03

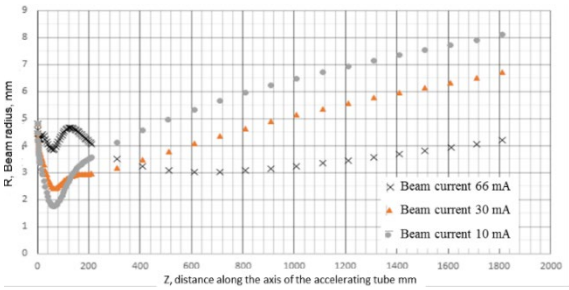

Figure 3: The envelopes for different beam currents at an energy of 1.5 MeV, the length of the accelerating tube is 1800 mm.

The beam current in ELV accelerators is regulated by changing the cathode temperature. The cathode is heated by a tungsten coil, since the spiral is a solenoid, then its magnetic field extends to the emitting tablet and beyond (see Fig. 4).

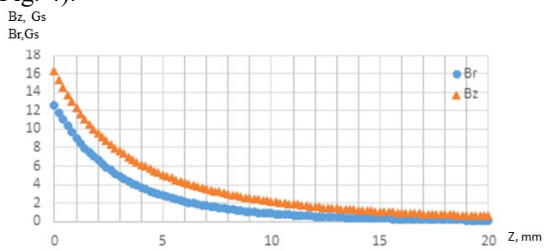

Figure 4: Electron injector heater coil magnetic field. Coordinate z = 0 corresponds to the emitting surface of the tablet.

Because of the magnetic field of the heating coil, the electron acquires an azimuthal momentum Pφ0 of about 4.4 Gs·cm.With a trajectory radius of 5 mm, the angular momentum is obtained 2,2 Gs·cm^2.

$$\Delta r_{\min} = \frac{1}{2} \cdot F \cdot \frac{P_{\phi 0} \cdot r}{P_0} = 0.33mm \qquad (1)$$

P_0 – momentum of electrons, F- is the focal length of the lens, $P_{\phi 0} \cdot r$ - is the angular momentum.

The minimum focused beam diameter Δr_{min} is approximately 0.3 mm.

Let us consider the effect of the emittance associated with the cathode temperature on the beam diameter in the plane of the diaphragm. The value of the temperature emittance:

$$\varepsilon_T = \frac{d_k \cdot \Delta P_k}{P_0} = d_k \cdot \alpha_k, (\alpha_k = \frac{\Delta P_k}{P_0}) \qquad (2)$$

where d_k is the diameter of the cathode, ΔP_k is the spread of transverse momenta due to the temperature of the cathode, and P_0 is the final momentum of electrons. The divergence of the beam in the crossover at its total energy after the lens is equal to d_L/f_L; where d_L is the diameter of the beam at the entrance to the lens, and f_L is the focal length of the lens, therefore

$$d_{\min} = \frac{\varepsilon_T \cdot f_L}{d_L} = 0,05mm \qquad (3)$$

With d_L = 10 mm, $f_л$= 180 mm and ε_T = 3 10^{-3} rad mm, we have $d_{min} \approx$ 0.05 mm. This value is negligible.

The ripples of the accelerating voltage in this electron accelerator were initially assumed to be 5%. The energy ripple causes the focal length of the lens to change with the pulsation frequency, which leads to an increase in the beam diameter in the crossover.

$$d_{\min} = d_{lens} \frac{\Delta f}{f} \qquad (4)$$

Where d_{min} is the minimum diameter of the focused beam cm, d_{lens} is the diameter of the beam at the entrance to the lens, which is 10 mm.

At an energy of 1.5 MeV, $\frac{\Delta f}{f} \approx \frac{\Delta U}{U}$ then, at an energy ripple of $5 \cdot 10^{-2}$, the effective beam diameter in the first diaphragm at the exit from the outlet will be ≈ 0.5 mm

The tube, which is located inside the high-voltage rectifier and the primary winding, is penetrated by a transverse magnetic field associated with the tilt or misalignment of the accelerating tube and the primary or secondary windings of the transformer. Its value can reach $B_\perp$ = 0.2 G. This leads to the appearance of variable angles Δα at the exit from the accelerating tube

$$\Delta\alpha = \frac{B_\perp \cdot L_{tr}}{B\rho_0} = 5.5 \cdot 10^{-3} \qquad (5)$$

Where is the transverse magnetic field of the primary winding, L_{tr} is the length of the accelerating tube, which is 1800 mm, B·ρ0 is the electron momentum, which is $6.5 \cdot 10^3$ G·cm for a beam energy of 1.5 MeV

$\Delta d_{min} = f_L \cdot \Delta\alpha$. Where f_L is the focal length of the lens 180 mm. In our case, the oscillations of the beam in the output diaphragm will be $\Delta dmin \approx 5 \cdot 10^{-3} \cdot 18 = 9 \cdot 10^{-2}$ cm= 0,9 mm.

This increases the area of the opening in the diaphragm through which the gas passes.

If we sum up all the above effects, then the minimum beam size at the exit from the extraction device will be about 2 mm.

MEASUREMENT OF BEAM PARAMETRS

For a more accurate measurement of the beam parameters, a water-cooled diaphragm with a whole diameter of 16 mm was fabricated. The size was determined by touching the diaphragm with the beam at points located at opposite ends of the diaphragm opening. The magnitude of the current on the diaphragm was 10^{-3} of the total beam current. It was necessary to fix the currents of the deflecting (correcting) coils. They were preliminarily calibrated.

The results of measurements of the beam diameter with an energy of 1.5 MeV, at beam currents of 10, 30, 66 mA, and different currents of the focusing electromagnetic lens are shown in the graphs (see Fig. 5).

ISBN: 978-3-95450-240-0 ISSN: 2673-5539 doi:10.18429/JACoW-RuPAC2021-FRB03

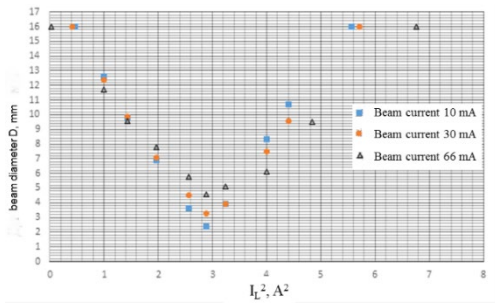

Figure 5: Dependence of the beam size in the diaphragm on the focusing lens current at an energy of 1.5 MeV.

Figure 6 shows a simple scheme that allows you to determine d_L from the dependence D_{beam} $(1/f_L)$, which is equivalent to the dependence D_{beam} (I_L^2) in Fig. 5.

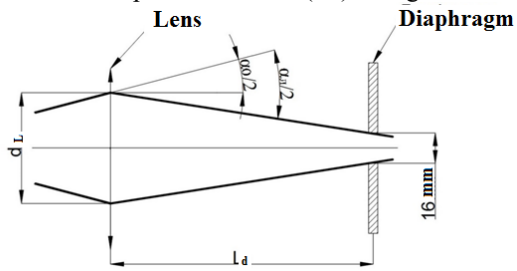

Figure 6: d_L is the diameter of the beam in the lens. D - measuring diaphragm with a hole diameter of 16 mm. D_{beam} is the beam diameter in the diaphragm, L_d is the distance from the lens to the diaphragm, which is 940 mm.

From the Fig. 6 shows that

$$D_{beam} = d_L - (\alpha_L - \alpha_0) \cdot L_D \qquad (6)$$

Where α_0 -is the angle of divergence or convergence of the beam at the entrance to the lens;

$\alpha_L = d_L / f_L$

Focal length of an electromagnetic lens

$$f_L = \frac{4(B\rho)^2}{I^2 \int B_{1A}^2 \cdot dl} \qquad (7)$$

Bρ - electron momentum at the exit from the accelerating tube G·cm; I_L is the current of the electromagnetic lens A. $\int B_{1A}^2 dl$- integral of the magnetic field strength for an electromagnetic lens.

Since D_{beam} linearly depends on I_L^2, then from the slope of the curve D_{beam} (I_L^2) one can find d_L: taking the derivative with respect to I_L^2 from the right-hand side of formula (6).

$$d_L = \frac{\Delta(D_{beam})}{\Delta(I_L^2)} \frac{4(B\rho)^2}{(\int B_{1A}^2 \cdot dl) \cdot L_D} \qquad (8)$$

From the same curve, as can be seen from (6), it is possible to find the divergence of the beam at the entrance to the lens. To do this, it is necessary to extrapolate the left side of the curve D_{beam} (I_L^2) to $D_{beam} = 0$.Then from (6)

$$\alpha_0 = d_L \frac{f_L - L_D}{L_D \cdot f_L} \qquad (9)$$

The beam diameter at the exit from the accelerating tube is d_L=9 mm. The divergence of the beam at the exit from the accelerating tube $\alpha_0 = 7 \cdot 10^{-3}$ rad.

MAIN RESULTS

Based on the measurements carried out in the fall of 2018, a device was designed and manufactured for extraction a focused electron beam into the atmosphere from the ELV accelerator, which has a tube with a large aperture equal to 100 mm.

A general view of extraction device is shown on Fig. 7.

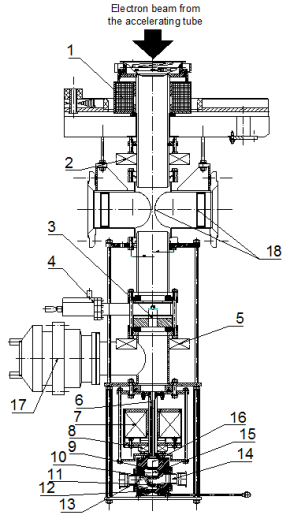

Figure 7: 1 - Upper lens L1; 2 - upper correctors C1; 3 - water-cooled diaphragm with a hole diameter of 7mm D6; 4- Gate valve; 5- average correctors C2; 6 - water-cooled diaphragm with a hole diameter of 10mm D5; 7 - Lower lens L2; 8- lower correctors C3; 9- diaphragm with a hole diameter of 4 mm D4; 10- diaphragm with a hole diameter of 3.5 mm D3: 11- diaphragm with a hole diameter of 2.5 mm D2; 12 - diaphragm with a hole diameter of 2mm; 13 - the first stage of pumping (pump AVZ-90); 14 - the second stage of pumping (pump AVZ-90); 15 - the third stage of pumping(pump RUTS ZJ-150+AVZ-20); 16 - fourth stage (turbomolecular pump NVT-450); 17 - fifth stage (turbomolecular pump NVT-450); 18 - sixth stage (two pumps NMD-0.4).

During the tests, stable operation was achieved at a beam power of 70 kW and a short-term operation at 100 kW. After long-term operation of the accelerator at a power of 50 kW, the diameters of the holes in the diaphragm did not change. Diaphragm hole diameter on the extraction device outlet has 2-2.5 mm.

REFERENCES

[1] R.Salimov *et al.*, "D.C. high power electron accelerators of ELV-series: status, development, applications", *Radiat. Phys. Chem Methods*, vol. 57, pp. 661-665, 2000. doi:10.1016/S0969-806X(99)00486-7

[2] M. Tiunov. *BEAM. 2D Code Package for Simulation of High Perveance Beam Dynamics in Long Systems*. Novosibirsk, 1998.

ISBN: 978-3-95450-240-0 ISSN: 2673-5539 doi:10.18429/JACoW-RuPAC2021-FRB04

A LINEAR ACCELERATOR FOR PROTON THERAPY

V.V. Paramonov†, A.P. Durkin, A.A. Kolomiets
Institute for Nuclear Research of the RAS, 117312,Moscow, Russia

Abstract

For applications in Proton Therapy (PT), linear accelerators can provide beam performances not achievable with cyclic facilities. The results of the development of a proposal for a linac, operating in a pulsed mode, with the maximal proton energy of 230 MeV, are presented. Possibilities of fast, from pulse to pulse, adjustment of the output energy in the range from 60 MeV to 230 MeV, formation and acceleration to the output energy of a 'pencil-like' beam are shown. Optimized solutions, proposed for both the accelerating-focusing channel and the technical systems of the linac make it possible to create a facility with high both functional, economic and operational features. Special attention, due to the selection of proven in long-term operation parameters of the systems, is paid to ensuring the reliability of the linac operation. The feasibility of linac is substantiated on the basis of mastered, or modified with a guarantee, industrial equipment.

INTRODUCTION

Advantages of linacs for PT are known and one can see it in reviews [1,2]. Now the mostly advanced, in the stage of construction, is the LIGHT project [3]. To meet the high requirements for such linacs for applied purpose, sometimes system parameters are set that are more suitable in record-breaking linacs for research purposes. In this report we present the physical justification for the proton linac with wide functional possibilities but conservative, well mastered systems parameters.

RATIONALITY AND FEASIBILITY

The cornerstones of this linac proposal are:

- - wide functionality for both practical and research proton medicine;
- - operational reliability through conservative systems parameters, proven in long-term operation;
- - cost reduction, size reduction;
- - deep mutual optimization, balance and feasibility of proposals for beam dynamics, accelerating and focusing elements;
- - focus on well mastered level of technologies and elements parameters confidently mastered in high-tech industry (or with guaranteed parameters upgrade);
- - to be placed in regional PT centres.

To meet all requirements, everyone will come to the concept of high-frequency, multi-cavity, low-current, pulsed proton linac with pencil-like proton beam. The main solutions and features are briefly discussed below.

† paramono@inr.ru

SCHEME AND PARTICULARITIES

The linac is built according to classical scheme for proton linear accelerators at medium, up to 200 MeV, proton energies, Fig. 1.

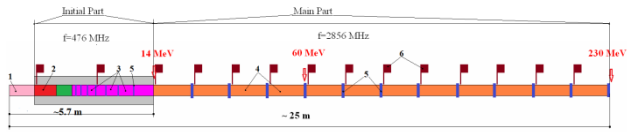

Figure 1: Linac scheme. 1 - proton source, 2 – RFQ, 3 – IH DTL structure, 4 – TW structure, 5 – focusing elements, 6 – RF sources.

The proton source provides 60 keV continuous proton beam with transverse emittance ~0.1 π mm mrad. Such beam can not be formatted, but confidently can be collimated from more powerful beam.

Further accelerator is in two parts. The initial part, operating with frequency 476 MHz, includes RFQ cavity, matching section and accelerating cavities. RFQ cavity provides pre-acceleration and formation of bunches with the small longitudinal emittance. Subsequent elements provide beam matching, allowing beam collimation at energies < 7 MeV, acceleration to energy ~14 MeV and preservation of emittance growth, both in transverse and in longitudinal directions. Operating frequency is selected as a compromise between beam dynamics requirements, parameters of accelerating elements and RF sources, taking into account further acceleration in the main part. As the result, at output of initial part we expect pencil beam with envelope of ~1 mm and extremely small, for such proton energies, phase length of bunches, ~4 degrees, see Fig. 2. In more details initial part of the linac is considered in [4].

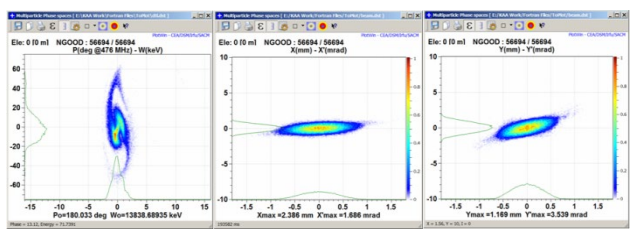

Figure 2: The phase space bunch portraits at the output of linac initial part.

In the main part, operating at frequency of 2856 MHz, protons will be accelerated for the maximal energy of 230 MeV. The value of operating frequency is selected both from commercial availability of RF hardware and parameters of accelerating strictures. In the main part the output proton energy can be changed fast in the range from 60 MeV to 230 MeV.

ISBN: 978-3-95450-240-0 ISSN: 2673-5539 doi:10.18429/JACoW-RuPAC2021-FRB04

RF CAVITIES

The relatively short, ~1 in length, RFQ has a good, ~8 MHz, separation in frequency with dipole modes and provides bunch formation and pre-acceleration to energy ~1.6 MeV with the maximal electric field strength at the electrodes surface up to 1.57 Ek, where Ek is Kilpatrick threshold value, and RF pulsed power consumption up to ~ 125 kW, [4].

The beam pulse length of the linac is defined mainly by RF pulse length of klystrons in the main part. As for initial part, the length of beam pulse is much less as compared to field rise time in accelerating cavities. To decrease rise time, which is necessary but not useful, in initial part we need an accelerating structure with relatively low quality factor Q but with high effective shunt impedance Ze. Different structures were compared in [5] and Inter-digital H-type structure was selected. In initial part 11 relatively short, $4\beta\lambda$, from 155 mm to 410 mm in length, IH DTL cavities are applied, [4].

In the main part Travelling Wave (TW) accelerating structure is applied. For protons acceleration we can not allow strong field decay, typical for constant impedance TW option and constant gradient TW option is strongly preferable from proton dynamics. TW structure represents the simple disk loaded waveguide with magnetic coupling. It decouples the control over group velocity β_{gr} and Ze value. The simplest shape of cells confidently allows production with modern NC equipment realising required ~10 mm precision. There are 12 accelerating modules, consisting from accelerating structure, RF source and focusing elements. In the beginning of main part TW structure operates with n=-1 backward harmonic of accelerating field. Practical proposal for protons acceleration with n=-1 harmonic was formulated in 90-th of previous century, [6]. Particularities of n=-1 harmonic application for protons acceleration was analysed in [7]. Now there are a lot of papers dedicated to development and tests of such option. With the average accelerating rate over TW structure of ~13.2 MV/m the ration of maximal electric field at the surface Es all time is lower Kilpatrick threshold Ek~45 MV/m for frequency 2856 MHz, see Fig. 3.

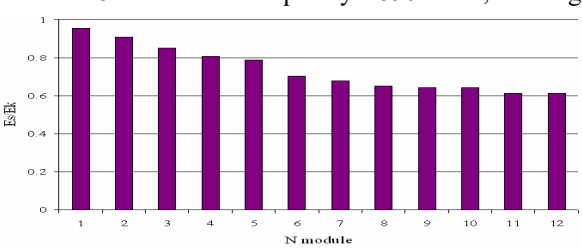

Figure 3: The maximal values of Es/Ek ratio for accelerating modules in the main linac part.

Such conservative Es value ensures, after short commissioning, stable structure operation without RF breakdowns. With such structure parameters we are far below from effects of pulsed RF heating, which can occur for higher accelerating gradient in the structure. Additionally, requirements for surface treatment during cells manufacturing are typical for S-band accelerations structures.

RF SOURCES

With a reasonable, from practice, safety margins we need for initial linac part it total ~520 kW of pulsed RF power, with RF pulse length ~80 μs, non uniformly distributed between 12 RF channels. With duty factor value of ~250 the average RF power ~2 kW is rather low. Unified architecture and declared parameter limits of solid state RF amplifiers, described in [8], meet this specification.

For TW structure in the main linac part we need in total ~144 MW of pulsed, or ~ 220 kW average RF power. Multi Beam Klystrons (MBK) are very attractive due to lower cathode voltage ~60 kV. Commercially available are MBK with PMQ focusing and output RF power ~6 MW, [9]. But 24 klystrons for such short linac is not the best solution. Development of klystrons with different parameters is continuous process and MBK with 12 MW output RF power is quite realistic, [10]. For modulators there is interesting development of solid state units also with unified modular architecture, [11].

FOCUSING ELEMENTS AND LATTICE

Both in initial and in main linac parts as focusing elements PMQ lenses with SmCo5 permanent magnets are applied. Due to a small aperture radius ~4 mm, according simulations, focusing gradient G up to 260 T/m can be achieved. There is example of practical PMQ realisation with G~200 T/m, [12].

In initial part PMQ doublets are applied with 70 T/m < G < 120 T/m, [4]. For the main part lattice options are investigated in [13]. In any case for PMQ in main part G < 215 T/m, showing a sufficient reserve with respect to calculated values.

FRONT-END SIMULATIONS

Front-end simulations for beam dynamics are performed from RFQ input to linac output by using TRANS-IT code [14]. Phase space beam portraits at the linac output are shown in Fig. 4. The beam has a small pencil-like diameter trough the total linac. In the current option transmission from DTL input to TW output is of ~95%. The bottle-neck points for these small particle losses are fixed and transmission will be improved in further development.

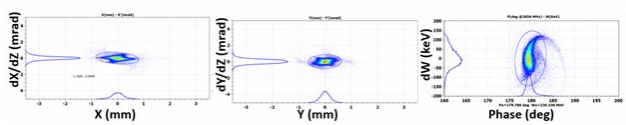

Figure 4: Phase space beam portraits at the linac output.

Space charge forces are essential in the linac beginning, especially RFQ, and affect mainly longitudinal motion. Short estimations have shown no essential changes in beam parameters for pulse beam current up to ~2 mA.

ISBN: 978-3-95450-240-0 ISSN: 2673-5539 doi:10.18429/JACoW-RuPAC2021-FRB04

ENERGY REGULATION

The simplest method of proton energy regulation is the manipulations from RF pulse to pulse with the phase in one accelerating module, with switched off subsequent modules. This case from pulse to pulse we can get any energy between lower and upper energy limits for active module. The last module has wider control ability and even can decelerate protons, Fig. 5.

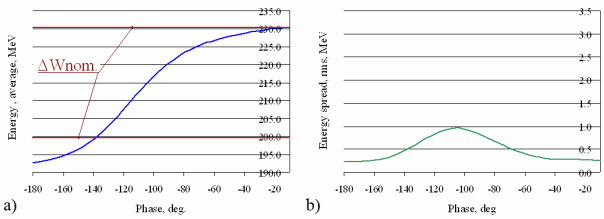

Figure 5: Dependencies of output energy , (a), and rms energy spread, (b), on the phase of RF field in the last accelerating module.

More sophisticated methods for output energy regulation are under development.

MAIN FEATURES

Radiological effect of proposed linac has been estimated in [15]. With different operating modes, direct pencil-like or fluffy beams, short or long beam pulses and low, ~ μA scale, or medium, ~ mA scale, the dose both for practical PT and for FLASH mode can be delivered in required time. This parameters range is foreseen for proposed linac.

The summarized features of this linac proposal are:

- - wide functionality for both practical and research proton medicine;
- - the maximal proton energy – 250 MeV;
- - the total length ~ 25.5 m;
- - the range of output energy regulation – 60 MeV - 230 MeV;
- - the maximal time for energy regulation < 20 ms;
- - the maximal pulse beam current - up to 2 mA;
- - beam pulse length - up to 15 μs;
- - operational reliability through conservative systems parameters;
- - use of mastered level of technologies and elements parameters confidently mastered in high-tech industry (or with guaranteed parameters upgrade);

SUMMARY

The physical substantiation of a proton linac for use in PT proton therapy is presented. The functional capabilities ensure its use in both practical and research medicine. To provide broad functionality, both traditional solutions are optimized and new proposals for accelerator systems are justified. Conservative, long-term proven system parameters ensure reliable stable operation. For the construction of linac equipment, the mastered level of technologies and the characteristics of the equipment, achieved in the national high-tech industry are sufficient. The feasibility of the desired improvements is beyond doubt. In terms of a complete set of functional, economic and operational parameters, the proposed linac surpasses both cyclic facilities and advanced foreign competitors.

ACKNOWLEDGEMENTS

The authors are grateful to INR colleagues, especially L. Kravchuk, A. Feschenko, S. Akulinichev, for their support, discussions and useful recommendations. We also are grateful to DESY PITZ group for access, in framework of the collaboration, to the CST software [4].

REFERENCES

[1] U. Amaldi *et al.*, "Accelerators for hadrontherapy: From Lawrence cyclotrons to linacs", NIM A, vol. 620, p. 563, 2010, doi:10.1016/j.nima.2010.03.130.

[2] U. Amaldi *et al.*, "High frequency linacs for hadrontherapy", Reviews of Accelerator Science and Technology, vol. 2, p. 111, 2009.

[3] A. Degiovanni et al., "LIGHT- a Linear Accelerator for Proton Therapy", in *Proc. NAPAC2016*, Chicago, IL, USA, 2016, paper FRB1IO02.

[4] V. Paramonov, A. Durkin, A. Kolkmiets, "Initial Part of a Compact Proton Linac for Applied Purposes", PHPL, vol. 17, p. 624, 2020, doi:10.1134/S1547477120040366

[5] V. Paramonov, A. Durkin, "Comparison of Accelerating Structures with High Operating Frequency for Low Energy Protons Acceleration", in *Proc. LaPLas2019*, p. 122, Moscow, Russia, 2019.

[6] D. Tronc, "Travelling Wave Acceleration of Protons", *Nucl. Instr. Meth.* A327, p. 253, 1994.

[7] V. Paramonov, "Limitations for Acceleration of Intermediate Mass Particles with Travelling Wave Structure", in *Proc. LINAC2014*, Geneva Switzerland, 2014, paper TUPP121.

[8] G. Sharkov *et al.*, "Unified Line of Solid-State Amplifiers for Light and Heavy Ion Accelerators", in *Proc. LaPLas2021*, p. 368, Moscow, Russia, 2021

[9] https://toriy.ru/upload/iblock/e49/KIU_268.pdf

[10] Yu. Paramonov, Toriy, private communication, 2021.

[11] A. Zavadtsev *et al.*, "Modular Compact Solid-State Modulators for Partice Accelerators", Journal of Physics: Conference Series, vol. 941, p. 012095, 2016, doi:10.1088/1742-65/96/941/1/012095

[12] C. Ronsvalle *et al.*, "Simple Characterization Method of Small High Gradient Permanent Magnet Quadrupoles", in *Proc. IPAC2014*, Dresden, Germahy, 2014, doi:10.18429/JACoW-IPAC2014-TUPRO091

[13] A. Durkin *et al.*, "Analysis of Focusing Schemes in the Main Part of a Linear Proton Accelerator for Medicine", in *Proc. LaPLas2021*, p. 308, Moscow, Russia, 2021.

[14] A. Kolomiets *et al.*, "TRANSIT Code for Beam Dynamic Simulation", in *Proc. RuPAC2014*, Obninsk, Russia, 2014, paper TUPSA07.

[15] L. Ovchinnikova *et al.*, "Effect of a Proton Beam From a Linear Accelerator for Radiation Therapy", Presented at RuPAC2021, Alushta, Russia, paper MOPSA41, this conference.

ISBN: 978-3-95450-240-0 ISSN: 2673-5539 doi:10.18429/JACoW-RuPAC2021-FRB05

UPDATED STATUS OF PROTOM SYNCHROTRONS FOR RADIATION THERAPY

V.E. Balakin, A.I. Bazhan, V.A. Alexandrov, V.I. Chashurin, P.A. Lunev, A. A. Pryanichnikov†, A. E. Shemyakov, M. A. Belikhin, A.I. Shestopalov
Lebedev Physical Institute RAS, Physical-Technical Center, Protvino, Russian Federation
and Protom Ltd., Protvino, Russian Federation

Abstract

Physical-Technical Center of P.N. Lebedev Physical Institute of RAS and Protom Ltd. are engaged in development and implantation of synchrotrons for proton therapy into clinical practice. There are two proton therapy complexes “Prometheus” in Russia. That are fully developed and manufactured at Physical-Technical Center and Protom. Every day patients with head and neck cancer get treatment using "Prometheus" at the A. Tsyb Medical Radiological Research Center. At the moment these facilities together have accumulated more than 5 years of clinical experience. Two facilities are based on the Protom synchrotrons in the USA. One operates at the McLaren Hospital PT Center, it started to treat patients in 2018. Another one is as a part of the single-room proton therapy system “Radiance330” in Massachusetts General Hospital that went into clinical operations in 2020. The first Israel proton therapy complex based on Protom synchrotron was launched in 2019. Protom facilities provide full stack of modern proton therapy technologies such as IMPT and pencil beam scanning. Key features of Protom synchrotron: low weight, compact size and low power consumption allow it to be placed in conventional hospitals without construction of any special infrastructure.

This report presents current data on accelerator researches and developments of Physical-Technical Center and Protom Ltd. In addition, it provides data on the use of Protom based proton therapy complexes under the clinical conditions.

INTRODUCTION

Proton therapy (PT) is one of the most accurate and modern methods of radiotherapy and radiosurgery. [1, 2]. Protons can reduce the radiation load on surrounding tissues up to 30-50% in comparison with gamma rays. The use of a proton beam for tumors located near critical organs, such as the brain stem, optic nerves, etc. are particularly effective. Therefore, in cases of head and neck cancer, proton therapy is the most advantageous of the available types of treatment for many patients. Given the advantages of this type of treatment over radiation therapy, using gamma radiation and electron beams, proton therapy is increasingly being used in the treatment of cancer. There is an increase of PT centers around the world.

In the world, active work is being carried out aimed at increasing the accuracy of dose delivery to the tumor, reducing the time that patients stay under the influence of radiation and increasing the availability of this method for a larger range of patients. New proton accelerators, as well as more cost-effective and accurate immobilization systems for patients are being developed for these purposes [3].

Protom Ltd. is a manufacturer of the equipment for Proton Therapy (PT). Protom can provide full range of the technologies for PT including the accelerator complex based on the compact synchrotron, pencil beam scanning beam delivery system, patient positioning and immobilization system, treatment planning system and all needed software. The Protom synchrotron [4,5] – one of the most advanced medical accelerators in the world. It is the most compact synchrotron, the outer diameter is 5 m and the weight is 15 tons. This kind of accelerator does not use absorbers for proton range correction. That fact makes Protom synchrotron is radiation clean accelerator (radiation is produced only during patient irradiation session). Protom synchrotron is energy efficient facility. The average power consumption of all accelerator complex during treatment is 30 kW. The maximum energy of 330 MeV makes proton tomography of full patient body available [6].

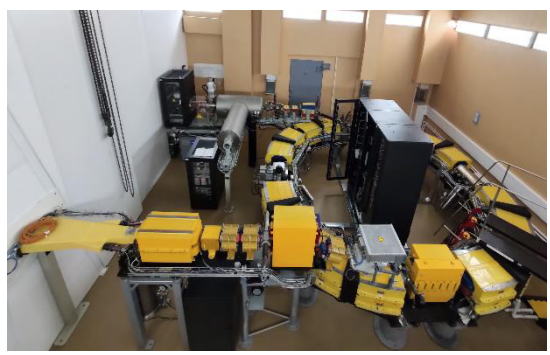

Figure 1: Protom Synchrotron-based Accelerator Complex “Prometheus” in MRRC, Obninisk, Russia.

The first technical run of the prototype of Proton Synchrotron was in 2003. The technical runs of facilities based the synchrotron were performed in 2010 in Protvino City Hospital, Protvino, Russia and Central Military Hospital, Ruzhomberok. In 2011 the technical facility in McLaren Hospital, Flint, MI, USA was successfully performed too. Nowadays proton therapy facilities based on Protom Syn-

† pryanichnikov@protom.ru

ISBN: 978-3-95450-240-0 ISSN: 2673-5539 doi:10.18429/JACoW-RuPAC2021-FRB05

chrotron has been successfully used under clinical conditions more than 5 years. The first patient was irradiated in Protvino City Hospital in 2015. Since 2017 the proton therapy facility works only on biological research [7]. In 2016 treatment process was started in the A. Tsyb Medical Radiological Research Center Obninsk [8,9], Russia, in 2018 in the McLaren Hospital and in 2020 in the Massachusetts General Hospital. The clinical accelerator in MRRC is presented in Fig. 1. Up to date more than 1000 patients were irradiated worldwide most of which have been treated in Russia.

PROTON THERAPY SOLUTIONS OVERVIEW

Protom synchrotron currently is implemented in several proton therapy complexes. Protom synchrotron works as a part of Russian proton therapy complex "Prometheus", US "Radiance 330" complex, and Israel P-Cure facility that is shown in Fig. 2.

Table 1: Proton Therapy Solutions Based on the Protom Synchrotron

Prometheus	Radiance 330	P-Cure Proton Therapy Solution
Protom Ltd.	Protom International	P-Cure
Russian local granted CE is ongoing	FDA proved CFDA is ongoing	FDA is ongoing Israel is ongoing CFDA is ongoing
Obninsk, Russia Protvino, Russia Ruzhomberok, Slovakia	Flint, MI, USA Boston, MA, USA Middleton, MA, USA	Shilat, Israel

Basic information about these complexes is shown in the Table 1, where there first row is name of the facility, the second one consists of main manufacturers, the third one consists of permissions to treat, and the last one – locations of these facilities. Any synchrotron-based medical facility consists of beam injection system including ion source and linear or tandem accelerator, main accelerator – the synchrotron, beam extraction and transfer channels, medical part including one or several treatment rooms with patient immobilization, positioning and imagine systems.

Figure 2: Protom Synchrotron-based Accelerator Complex in P-Cure, Shilat, Israel.

INJECTORS

Protom Synchrotron uses 3 types of injectors. Two of them are Tandem accelerators produced by Protom ltd. and the last one is RFQ produced by AccSys Technology, Inc. The Table 2 consists of brief comparison of this injectors.

Table 2: Injector Types for Proton Synchrotron

Tandem v.1	AccSys Technologies RFQ	Tandem v.2
Injection energy 0.9 MeV	Injection energy 1.6 MeV	Injection energy 1.1 MeV
Film recharge (Carbon)	No recharge	Gas recharge (Nitrogen)
"Prometheus" 1st gen	"Radiance 330"	P-Cure PT Solution "Prometheus" 2nd gen

Since 2017 the process of update facilities used Tandem v.1 started. Using Tandem v.2 allows to increase the number of injected and captured protons.

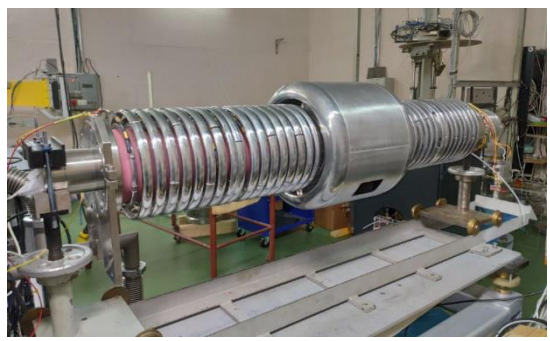

Figure 3: Accelerator tube assembly for Tandem v.2.

The key difference from the previous version was increased injection energy and change of recharge type. Gas recharge made the full system more reliable and allowed to get away from the procedure of changing carbon recharge film. That should be performed at least a few times per year. The Tandem v.2 is shown in Fig. 3.

THE SYNCHROTRON

The synchrotron serves to accelerate the proton beam from the injection energy to the required energy in a given range. The synchrotron provides a high rate of particle acceleration equal to 250 MeV per 0.9 s.

To simplify the design of the accelerator and reduce its dimensions, separate focusing elements are excluded from the magnetic synchrotron system, and edge focusing is introduced into the rotary magnets, which is provided by cuts of magnets from the side of the free gaps. One of the main advantages of this magnetic system is the low power consumption compared to analogues. During the calculation period, measurements of the power consumed by the magnetic system were made. The average value is 30 kW. Main parameters of Protom Synchrotron are shown in Table 3.

ISBN: 978-3-95450-240-0 ISSN: 2673-5539 doi:10.18429/JACoW-RuPAC2021-FRB05

Table 3: Main Parameters of Protom Synchrotron

Range of accelerated proton energies, MeV	30 - 330
Range of energies for treatment, MeV	70 - 250
Acceleration time for 250 MeV, sec	0.9
Intensity of extracted beam, protons per cycle	up to 4×10^9
Outer diameter of the ring, m	5
Accelerator weight, tons	15
Average energy consumption during treatment, kW	30

EXTRACTION CHANNEL

The beam extraction from the synchrotron occurs according to the following scheme: the buildup of betatron oscillations is initiated with subsequent scattering by the internal target.

After that beam enters the electrostatic deflector from the changed orbit, where it is radially thrown from into the Lambertson magnet. In the channel, the focusing lenses and the position correcting magnets are installed. Observation of the beam is carried out from the phosphor-coated screens using the system of visual control. The key parameters of extraction channel variation are presented in Table 4.

Table 4: Parameters of Extraction Nozzles and Scanning System

	Prometheus 1st gen	**P-Cure, Prometheus 2nd gen**
Horizontal field size, mm	700	400
Vertical field size, mm	90	400

Each of Protom synchrotron-based proton therapy facility has active pencil beam scanning system with IMPT mode. Table 5 shows typical beam sizes for several energies.

Table 5: Typical Beam Sizes

Energy [MeV]	**Transverse beam size, σ_x for Gaussian distribution, mm**	**Transverse beam size, σ_y for Gaussian distribution, mm**
70	5,0	5,0
100	3,3	3,3
150	2,6	2,6
250	1,9	1,9

PROTOM MEDICAL SYSTEM

The system includes an armchair designed to fix the patient and move him to the irradiation zone, an x-ray unit represented by a small-dose X-ray tube and a digital X-ray panel (detector).

With their help, the X-ray photographs are taken with a subsequent process of reconstructing them into a three-dimensional image for subsequent irradiation planning. The individual radiograph mode has been put into place in order to verify the patient's position before the start of the treatment [10].

There is a unique Treatment Planning System (TPS) that has been developed by Protom Ltd. It is based on Monte Carlo calculation. The Protom TPS takes into account Multiple Coulomb scattering and proton losses on nuclear interactions. It supports parallel computing technology and is able to use GPU. This TPS is a part of proton therapy complex “Prometheus”. It is used in MRRC as a main TPS.

CONCLUSION

Physical-Technical Center and Protom Ltd. has full range of the technologies for proton therapy that are successfully used under clinical conditions over 5 years. Physical-Technical Center and Protom Ltd. are improving existing solution and developing new ones that are focusing on accuracy of dose delivery and decreasing patient treatment time.

Each of proton therapy facilities based on Protom Synchrotron supports full intensity modulated proton therapy (IMPT) option with high beam delivery accuracy and active pencil beam scanning (PBS) option. Both of these features are native technologies for Protom Synchrotron, there is no need in additional facility updates. Protom Synchrotron was initially designed to support proton radiography and tomography. The last researches have shown that intensity level that is necessary for radiography implementation can be reached with no constructive changes.

According to 5 years of clinical use Proton Synchrotron demonstrated high level of reliability. Downtime for the synchrotron was less than 1%.

All of these parameters together with low cost of the accelerator, low power consumption, fast installation process, absence of radiation in inactive mode let Protom Synchrotron successfully compete other PT commercial solutions. Nowadays more and more hospitals choose proton therapy facilities based on Protom Synchrotron.

REFERENCES

[1] A. P. Chernyaev *et al.*, “Proton Accelerators for Radiation Therapy”, *Medical Radiology and Radiation Safety*, vol. 64, no. 2, pp. 11–22, 2019. doi:10.12737/article_5ca5a0173e4963.18268254

[2] H. Paganetti, “Proton Beam Therapy”, *IOP Publishing*, P. 33, 2017. doi:10.1088/978-0-7503-1370-4

[3] K.B. Gordon *et al.*, “Proton Therapy in Head and Neck Cancer Treatment: State of the Problem and Development Prospects (Review)”, Sovremennye tehnologii v medicine, vol. 13, no. 4, pp. 70–81, 2021. doi: 10.17691/stm2021.13.4.08

ISBN: 978-3-95450-240-0 ISSN: 2673-5539 doi:10.18429/JACoW-RuPAC2021-FRB05

[4] A. A. Pryanichnikov *et al.*, "Status of the Proton Therapy Complex Prometheus", in *Proc. 26th Russian Particle Accelerator Conf. (RuPAC'18)*, Protvino, Russia, Oct. 2018, pp. 135-138. doi:10.18429/JACoW-RuPAC2018-FRXMH03

[5] A. A. Pryanichnikov *et al.*, "Clinical Use of the Proton Therapy Complex "Prometheus"", *Phys. Part. Nuclei Lett.,* vol. 15, no. 7, pp. 981-985, 2018. doi:10.1134/S1547477118070592

[6] A. A. Pryanichnikov *et al.*, "New beam extraction mode on Protom synchrotrons for proton tomography", *Int. J. Part. Ther.,* vol. 7, no. 4, P.158, 2021. doi:10.14338/IJPT.20-PTCOG-7.4

[7] V.E. Balakin *et al.*, "The Effect of Low and Medium Doses of Proton Pencil Scanning Beam on the Blood-Forming Organs during Total Irradiation of Mice", *Dokl. Biochem. Biophys.,* vol. 49, no. 4, pp. 231–234, 2020. doi:10.1134/S1607672920050026

[8] K. Gordon *et al.*, "Proton re-irradiation of unresectable recurrent head and neck cancers", *Rep Pract Oncol Radiother* vol. 26, no. 2, pp. 203-210, 2021. doi:10.5603/RPOR.a2021.0029

[9] K. Gordon *et al.*, "A Clinical Case of 5 Times Irradiated Recurrent Orbital Hemangiopericytoma", *Case. Rep. Oncol.*, vol. 14, no. 1, pp. 78-84, 2021. doi: 10.1159/000513030

[10] V. E. Balakin *et al.*, "Clinical Application of New Immobilization System in Seated Position for Proton Therapy" *KnE Energy*, vol. 3 np. 2, pp. 45–51, 2018. doi:10.18502/ken.v3i2.1790

ISBN: 978-3-95450-240-0 ISSN: 2673-5539 doi:10.18429/JACoW-RuPAC2021-FRB06

THE RESULTS OBTAINED ON "RADIOBIOLOGICAL STAND" FACILITY, WORKING WITH THE EXTRACTED CARBON ION BEAM OF THE U-70 ACCELERATOR

V.A Pikalov, Y.M. Antipov, A.V. Maximov, V.A. Kalinin, A. Koshelev, A.P. Soldatov, M.K. Polkovnikov, M.P. Ovsienko and A.G. Alexeev,
NRC "Kurchatov Institute" – IHEP, Protvino, Russia

Abstract

This report provides an information of present status of the «Radiobiological stand» facility at the extracted carbon ions beam of the U-70 accelerator. The results of the development of the RBS facility are presented. A plans for development an experimental medical center for carbon ion therapy on the basis of the U-70 accelerator complex are also reported.

INTRODUCTION

The experimental facility «Radiobiological Stand» (RBS) is in operation on the extracted from the U-70 accelerator complex beam of carbon nuclei since 2014 [1]. The installation is to conduct physics and radiobiological experiments at the ion energies up to 450 MeV/u. Development of the oncology treatment technology and training of domestic experts are the main goals of these radiobiological studies. The first cancer treatments with the beam of carbon nuclei can be the another primary goal of these studies. The RBS installation has been certified as a Center of Collective Use [2] in 2017 under the number 507813 with the following reference: http://www.ihep.ru/pages/main/6580/8769/index.shtml. The RBS installation [3] is in the continuous process of run-to-run development: beam parameters and beam control systems are being improved, systems of active and passive modification of the carbon beam are being developed. This report presents today's RBS and describes its nearest perspectives.

RBS STATUS

The slow extraction of the carbon beam from U-70 into the channel No. 25 is being done with use of the scheme proposed by O. Piccioni and B.T. Wright in 1954–1955 [4]. The scheme is based on the beam energy moderation passing through a solid target. Currently 6 fixed energies are available for RBS: 450, 400, 350, 300, 250 and 200MeV/u. The channel No. 25 consists of septum magnet SM34, three dipoles BM1-BM3, two sets of quadrupoles: Q1-Q4 with the aperture of 75 mm and Q5-Q7 with the aperture of 100 mm, horizontal corrector and the beam stop. It is instrumented by three TV-boxes with remotely operated scintillation screens. The channel vacuum of 10^{-2} bar (not worse) starts from SM34 and ends up after Q7. The target station (see Fig. 1) consists of two target blocks with four Beryllium targets each.

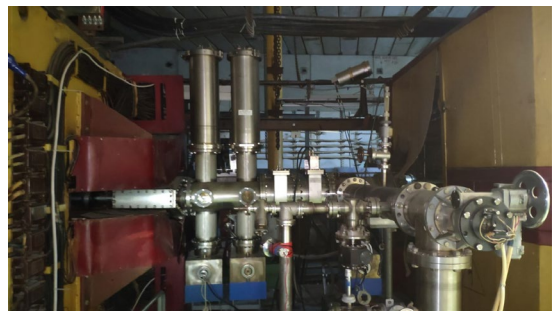

Figure 1: Target station of the channel No. 25.

Figure 2 presents the measured by RBS Bragg peaks in water.

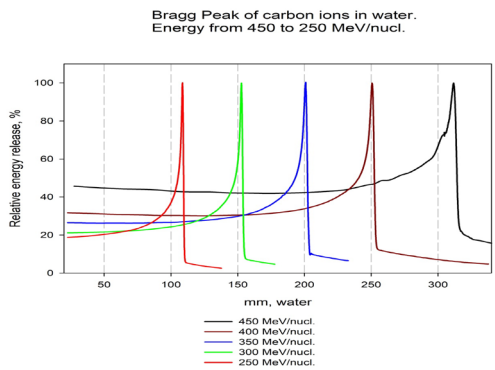

Figure 2: Bragg peaks for different energies of extracted carbon beam.

The shielded area of RBS consists of two zones: experimental and medical, as it can be seen in Fig. 3, with the common system of access control. These zones are separated from each other by a concrete wall with the intermediate collimator. The collimator aperture can be varied manually from 50x50 to 150x150 mm with use of special inserts.

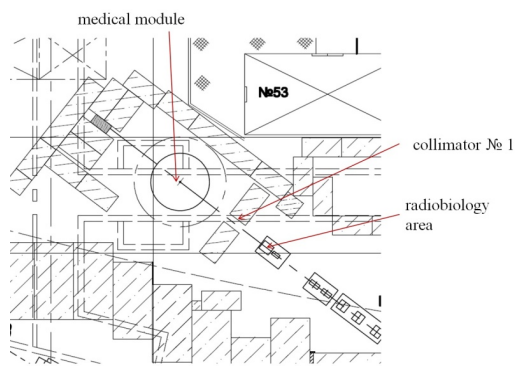

Figure 3: The schematic top view of the RBS installation.

ISBN: 978-3-95450-240-0 ISSN: 2673-5539 doi:10.18429/JACoW-RuPAC2021-FRB06

For the future patients there is a 6-axis table in the medical zone, see Fig. 4. The table was designed and manufactured at IHEP. The deck is made of carbon plastic. Accuracy of the table positioning in Cartesian coordinates is not worse than 0.5 mm.

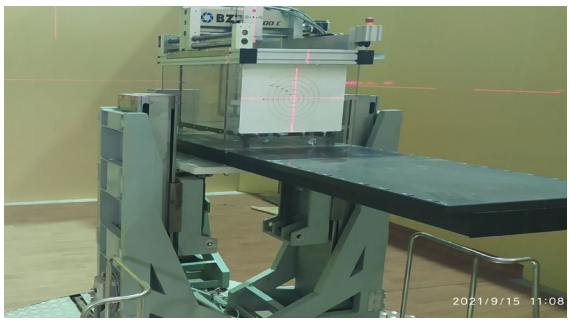

Figure 4: The 6-axis table in the medical module.

Recently developed and manufactured electromagnetic system of beam leveling is shown in Fig. 5. This system replaces the previous one with permanent magnets [5]. The system consists of the vertical and horizontal dipole magnets and their power supplies (Fig. 5).

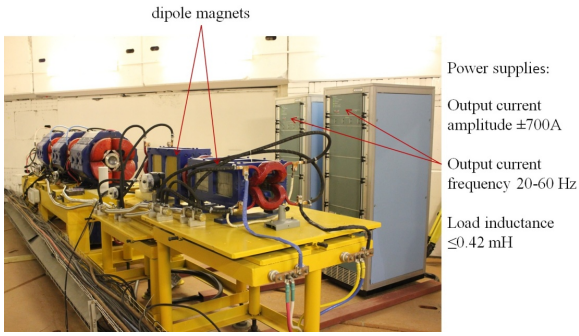

Figure 5: Electromagnetic scanning system.

The shapes of the dipole currents and the transverse distributions of the dose are shown in Fig. 6 and Fig. 7.

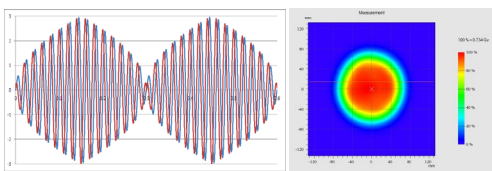

Figure 6: Currents and doses at helical scan.

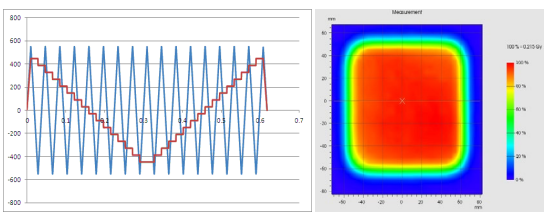

Figure 7: Currents and doses at Cartesian scan.

The automatic energy degrader inserts PMMA plates with thickness from 1 to 63 mm to moderate the beam energy smoothly. Ripple filters [6] are used to modify the Braggs peak. One of these filters is shown in Fig. 8 along with the corresponding Braggs peak in water.

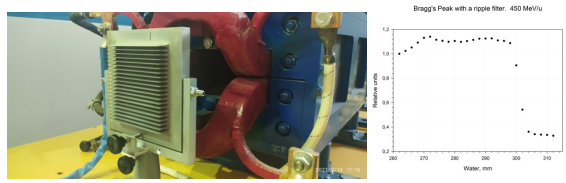

Figure 8: Aluminium ripple filter 16 mm on the left and Bragg's Peak on the right.

A certain work is done for the instrumentation of irradiation. A beam-content-meter is made to measure the beam composition wherever measured. The results of such a measurement are shown in Fig. 9.

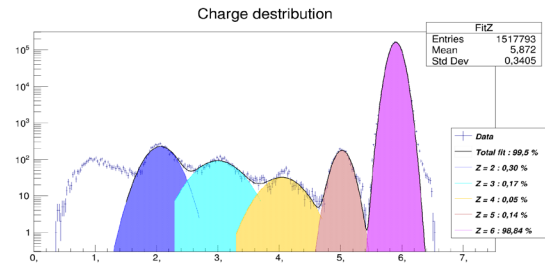

Figure 9: Carbon ion beam composition. 300 MeV/u.

To measure the 2D dose distributions the special mosaic ionization chamber was developed and manufactured. Schematic plot of the chamber and the screen shot of the measurement results are shown in Fig.10.

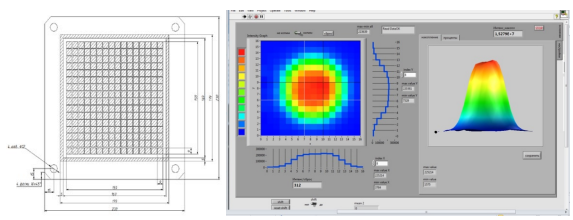

Figure 10: Mosaic 256-cell plane-parallel ionization chamber.

PLANS

The closest plans assume the new center of ion therapy on the base of U-70. Currently the new channel No. 26 is the candidate. Preliminary view of this new channel is shown in Fig. 11. The magnetic elements of this new channel have been designed and the prototypes are under the test program.

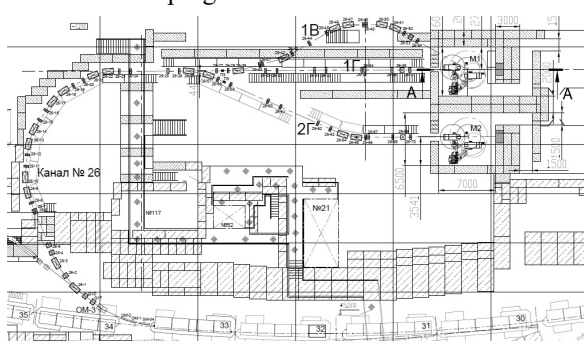

Figure 11: Schematic view of the channel No.26.

ISBN: 978-3-95450-240-0 ISSN: 2673-5539 doi:10.18429/JACoW-RuPAC2021-FRB06

CONCLUSION

The Radiobiological Stand Facility :

- works in continuous mode;
- according to the results obtained, 21 articles were published over the last 3 years;
- developed and implemented an electromagnetic beam leveling system (wobbler system);
- beam diagnostics tools were developed and manufactured;
- now has slow extraction of 200, 250, 300, 350, 400, 455 MeV per nucleon of $^{12}C^{6+}$ beam for radiobiology and future prior-to-therapy studies.

On the basis of the government decree No. 287 of 04.16.2020, work is underway to design the Ion Radiation Therapy Complex.

REFERENCES

[1] G. Britvich *et al.,* "First Results of Experiments with the Extracted Carbon Beam at the U-70 Accelerator", *in Proc. RuPAC2014,* Obninsk, Kaluga Region, Russia, 2014, pp. 197-199, WEPSB19.

[2] V.A. Pikalov and Y.M. Antipov, "Experimental Facility "Radiobiological Test Setup on Accelerator U-70" as Centers for Collective Use (CCU)", in *Proc. RUPAC'18,* Protvino, Russia, Oct 2018, pp. 253-255. doi:10.18429/JACoW-RUPAC2018-TUPSA50.

[3] Y. Antipov, V.A. Pikalov, "Carbon Beam from U-70 for Radiobiology", presented at the 25th Russian Particle Accelerator Conf. (RuPAC'16), St. Petersburg, Russia, Nov. 2016, paper THYMH01, unpublished.

[4] M. Antipov *et al., Instr. and Exp. Techn.,* v.64, n.3, pp. 343-351, 2021. DOI: 10.1134/S00204412210201 OX.

[5] Y.M. Antipov *et al., Instr. and Exp. Techn.,* v.58, n.4, pp. 552-561, 2015. DOI:10.1134/s0020441215040016.

[6] A. Solovev *et al.,* "3D-printed beam modifiers for radiobiological experiments in monoenergetic carbon ion beam." *Int. J CARS* Vol. 11, Suppl. 1, 2016, P. 58-59.

ISBN: 978-3-95450-240-0 ISSN: 2673-5539 doi:10.18429/JACoW-RuPAC2021-FRB07

TRANSMISSION STUDIES WITH ION BEAMS WITHIN FAMA*

Z. Jovanović†, N. Nešković, I. Telečki, M. Ćosić, and R. Balvanović
Laboratory of Physics, Vinča Institute of Nuclear Sciences, University of Belgrade, Serbia

Abstract

FAMA is a user facility for materials science with low-energy ion beams in the Vinča Institute of Nuclear Sciences, Belgrade, Serbia. It includes a heavy ion source, a light ion source, two channels for modification of materials, and two channels for analysis of materials. Recently, the designing of a channel for transmission studies within FAMA has begun. The initial studies to be undertaken in this channel are related to the rainbow effects with very thin electrostatic lenses and two-dimensional materials.

INTRODUCTION

FAMA is a facility for materials science with low energy ion beams. It is the low energy part of the TESLA Accelerator Installation, a large user infrastructure for production, acceleration and use of ion beams in science, technology, medicine and education. Currently, FAMA includes a heavy ion source, a light ion source, and a small proton cyclotron complex. The heavy ion source delivers multiply-charged heavy ions of energies of 10–20 keV per charge unit, while the light ion source produces positive or negative light ions of energies of 10–30 keV. These beams are used in two channels for modification of materials. The cyclotron complex delivers protons of energies between 1 and 3 MeV, and they are employed in two channels for analysis of materials. Recently, the designing of the channel for transmission studies (C3) of FAMA has begun, in which the ion beams from the heavy and light ion sources will be used.

INITIAL TRANSMISSION STUDIES

The first planned series of experiments in the C3 channel is related to ion transmission through very thin electrostatic multipolar and rainbow lenses (VTELs) [1–3]. The focusing properties of these lenses are fully determined by the rainbow effect. In the first measurements, the projectiles will be H^+ ions of energy of 15 keV from the light ion source and $^{40}Ar^{12+}$ ions of energy of 180 keV from the heavy ion source while the targets will be the quadrupole and square rainbow lenses [2, 3]. The beams should come on the targets closely parallel with the diameters of about 15 mm. The experiments will be performed in the high vacuum conditions.

The second planned series of measurements in the C3 channel is based on using the rainbow effect for specific characterization of 2D materials – by ion transmission [4–6]. In the first experiments, the projectiles will be 10 keV H^+ ions from the light ion source and 20 keV $^4He^{2+}$ ions from the heavy ion source. The ion beams should come on the targets closely parallel with the diameters of about 10 μm. The targets will be the flakes of graphene. The measurements require the ultra-high vacuum conditions.

CHANNEL FOR TRANSMISSION STUDIES

A scheme of the C3 channel is depicted in Fig. 1. It is connected to the mass analyser of one of the channels for modification of materials (C2). The transport elements of the channel are: two steering magnets, to be used to correct the ion beam direction toward the target if needed, and three magnetic quadrupole lenses, making a quadrupole triplet, to finally shape the beam impinging on the target. The characteristics of the magnetic quadrupole triplet have been determined on the basis of the transport calculations for the above specified ion beams, to be used in the first experiments. The transport line of the C3 channel, extending down to its interaction chamber, contains two diagnostic boxes, both being high vacuum cylindrical chambers made of stainless steel, each including a variable circular ion beam collimator, to be used to generate a closely parallel beam. The standard diameters of the collimators are 5 mm in experiments with VTELs and 2 mm in the experiments with 2D materials. In the measurements with 2D materials, the differential pumping apertures with the standard diameters of 2 mm are placed at the entrance and exit of the interaction chamber.

The transport calculations have been conducted using the first-order matrix formalism and the Ion Beam Simulator computer code. As a result, we have adopted 2.0 T/m as the maximal magnetic field gradients on the axes of the magnetic quadrupole lenses. Besides, we have adopted 14 mT as the maximal horizontal and vertical components of the magnetic induction on the axes of the steering magnets.

The interaction chamber of the C3 channel is an ultra-high vacuum cylindrical chamber made of stainless steel. There are two target holder assemblies in the interaction chamber – for VTELs and 2D materials. The former assembly includes a three-axis manipulator while the letter assembly comprises a five-axis goniometer and a sample acceptor stage, enabling one to remove the irradiated target from the interaction chamber for analysis. An electrostatic deflector is placed immediately after the target holder assembly for 2D materials, to be able to move away from the axis of the channel the ions that remained charged upon the interaction with the crystal, and thus record the angular distribution of neutralized ions. The deflector will also enable one to measure the charge state distribution of transmitted ions. The crystal structure of the chosen 2D material will be determined using a reflection high energy electron diffraction (RHEED) system, attached to the interaction chamber.

* Work supported by the Ministry of Education, Science and Technological Development of the Republic of Serbia
† zjovanovic@vinca.rs

ISBN: 978-3-95450-240-0 ISSN: 2673-5539 doi:10.18429/JACoW-RuPAC2021-FRB07

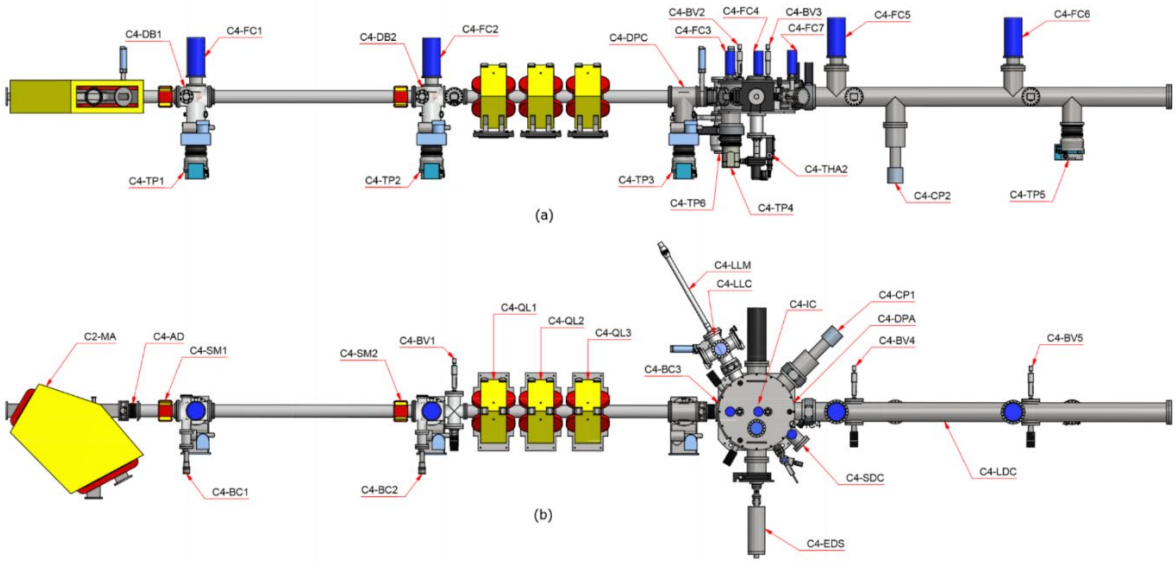

Figure 1: Vertical and horizontal projections of a scheme of the C3 channel – (a) and (b), respectively: C2-MA – the mass analyser of the C2 channel; C3-AD – the alignment device; C3-SM1 and C3-SM2 – the steering magnets; C3-DB1 – the first diagnostic box; C3-BC1 and C3-FC1 – the first beam collimator and the first Faraday cup; C3-TP1 – the first turbomolecular pump; C3-DB2 – the second diagnostic box; C3-BC2, C3-FC2 and C3-BV1 – the second beam collimator, the second Faraday cup and the first beam viewer; C3-TP2 – the second turbomolecular pump; C3-QL1, C3-QL2 and C3-QL3 – the magnetic quadrupole lenses making the quadrupole triplet; C3-DPC – the differential pumping chamber; C3-TP3 – the third turbomolecular pump; C3-IC3 – the interaction chamber; C3-DPA1, C3-FC3, C3-BC3, C3-FC4, C3-BV2, C3-FC5 and C3-DPA2 – the entrance differential pumping aperture, the third Faraday cup, the third variable circular beam collimator, the fourth Faraday cup, the second beam viewer, the fifth Faraday cup and the exit differential pumping aperture; C3-THA2 – the target holder assembly for 2D materials; C3-LLC – the load-lock chamber; C3-LLM – the load-lock manipulator; C3-EDS – the electron diffraction system; C3-CP1, C3-TP4 and C3-TP6 – the first cryogenic pump, the fourth turbomolecular pump and the sixth turbomolecular pump; C3-DC – the detector chamber; C3-FC6 and C3-BV3 – the sixth Faraday cup and the third beam viewer; C3-CP2 – the second cryogenic pump; C3-FC7 and C3-BV4 – the seventh Faraday cup and the fourth beam viewer; and C3-TP5 – the fifth turbomolecular pump, respectively.

The C3 channel also contains a load lock chamber and a detector chamber, both being high vacuum cylindrical chambers made of stainless steel. The former chamber enables one to introduce a 2D material in the interaction chamber. In the latter chamber, there will be two 2D position-sensitive detectors. The larger detector, with the diameter of 40 mm, will be used for measuring the spatial distributions of ions transmitted through the chosen VTEL at different distances from it while the smaller detector, with the diameter is 25 mm, will be employed for recording different parts of the angular distribution of ions transmitted through the chosen 2D material. The larger detector, placed in the interaction chamber, will be also used to measure the charge state distribution of transmitted ions.

The vacuum system of the C3 channel will include five turbomolecular pumps of the pumping speed of about 700 l/s, one turbomolecular pump of the speed of about 300 l/s, and two cryogenic pumps of the speed of about 1200 l/s. The aim is to ensure the pressure of 5×10^{-8} and 5×10^{-10} mbar in the interaction chamber in the experiments with VTELs and 2D materials, respectively.

The control and safety system of the C3 channel will be composed of the Group 3 Control hardware and the WonderWare InTouch software.

ACKNOWLEDGEMENTS

The research was funded by the Ministry of Education, Science and Technological Development of the Republic of Serbia (project “Physics and chemistry with ion beams”). The authors would like to acknowledge the contribution of the FAMA team from the Laboratory of Physics, Vinča Institute of Nuclear Sciences.

REFERENCES

[1] N. Nešković, P. Beličev, I. Telečki, and S. Petrović, *Advances in Imaging and Electron Physics,* Vol. 182, Academic Press, Elsevier, Waltham, p. 123–186, 2014.

[2] N. Nešković, I. Telečki, M. Ćosić, S. Grujović Zdolšek, and P. Beličev, *Nucl. Inst. Meth. Phys. Res.* A985, 164670, 2021.

[3] S. Grujović Zdolšek, N. Nešković, I. Telečki, M. Ćosić, and P. Beličev, submitted for publication.

[4] N. Nešković, S. Petrović, and M. Ćosić, Rainbows in Channelling of Charged Particles in Crystals and Nanotubes, Springer, Cham, 2017.

[5] M. Ćosić, S. Petrović, and N. Nešković, *Nucl. Inst. Meth. Phys. Res.* B 422, 54, 2018.

[6] M. Ćosić, M. Hadžijojić, R. Rymzhanov, S. Petrović, and S. Bellucci, *Carbon* 145, 161, 2019.

ISBN: 978-3-95450-240-0 ISSN: 2673-5539 doi:10.18429/JACoW-RuPAC2021-FRC01

NEUTRON FIELD MEASUREMENTS BY GFPC BASED MONITORS AT THE CARBON BEAM OF IHEP U-70 PROTON SYNCHROTRON

I.L.Azhgirey, I.S. Bayshev, V.A. Pikalov and O.V. Sumaneev, NRC "Kurchatov Institute" – IHEP, Protvino, Russia

Abstract

Neutron monitors with gas filled proportional counter (GFPC) as a sensitive element were presented at RuPAC-2018. These monitors have been used recently to measure fast neutron fluxes near the carbon beam based experimental facility at IHEP. The experimental facility "Radiobiological test setup at the U-70 accelerator" was built at NRC "Kurchatov Institute" - IHEP, Protvino, to carry out radiobiological and physical experiments with the extracted beam of carbon nuclei with an energy up to 450 MeV/nucleon. The measurements were compared with the CERN FLUKA code simulations.

INTRODUCTION

Neutron detection by GFPC monitors [1] is based on thermal neutron capture reaction by a 10B nucleus with emission of α particle. Incident neutrons are moderated to thermal energies by a moderator layer surrounding a corona counter SNM-14. The internal surface of the counter is covered with amorphous boron, with the 10B isotope content enriched up to 80-85%. The counter is filled with argon at atmospheric pressure. A signal is formed mainly after ionization of argon by ions of 4He or 7Li ions. The SNM-14 corona counter in these monitors is operated in proportional mode.

A pair of monitors can be more efficient for detecting high-energy neutrons, provided the response curve of the complementary (light) monitor is close to the response curve of the main (heavy) monitor below 100 keV and much lower at high energies. Each of the types of monitors can work independently as a neutron flux counter. Efficiency of the separate monitor will be determined by its response function and neutron spectrum in the monitor location. Pair of monitors works as a simplest spectrometer dividing the neutron spectrum in two groups.

The monitors are intended to work without intervention for a long period of time. They are controlled via a single coaxial cable (for both data and power supply) and are relatively small. The monitors themselves and their front-end electronics are radiation hard, and their operation is not affected by the magnetic field.

The main goal of these measurements was testing of the recently developed neutron monitors in a typical high energy neutron field at the Radiobiological Stand (RBS) facility [2]. The RBS layout is shown in Fig. 1, where big letters C point to the carbon beam axis at the entrance to and at the exit from the RBS area. The height of the beam axis with respect to the concrete floor is 215 cm.

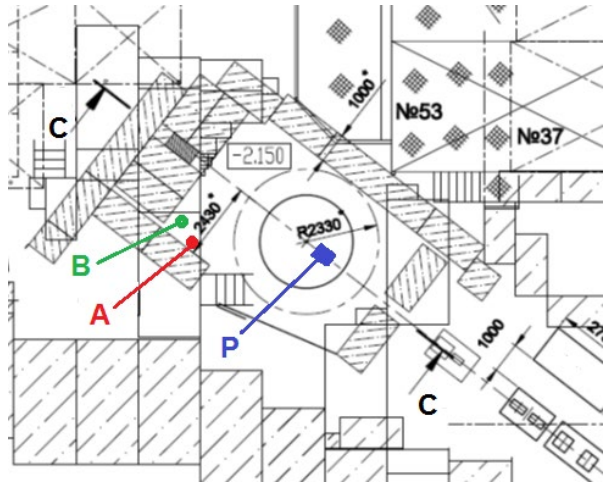

Figure 1: Schematic top view of the RBS facility. A and B – pair of the neutron monitors, C – ion beam, P – water phantom.

The wide beam passes through the collimator opening of 5×5 cm and approximately 50% of the beam hits the water phantom installed on the top of the medical bench. The main source of neutrons is the beam interaction with phantom and interactions with collimator material produce background source.

Passed beam is monitored by a flat air-filled ionization chamber of 20×20 cm area. The beam energy is 434 MeV/nucleon. Irradiation was done with 236 cycles, consisting of 0.6 s long pulses with 8 s spacing between them. The RBS area is surrounded by concrete shielding blocks and the monitors were placed inside shielding but not too close to the beam axis. Monitor coordinates are given in the Table 1.

Table 1: Transverse X, Vertical Y and Longitudinal Z Coordinates of the Monitor Centers With Respect to the Phantom Center

Monitor	X, cm	Y, cm	Z, cm
A	196	-103	332
B	167	-103	361

The main (heavy) monitor (monitor A through this report and in Fig.1) measured the fluence of fast neutrons (with energy greater 100 keV). The complementary (light) monitor (B through this report and in Fig.1) was used for the correction of the monitor A readings.

ISBN: 978-3-95450-240-0 ISSN: 2673-5539 doi:10.18429/JACoW-RuPAC2021-FRC01

MEASUREMENTS

Figure 2 shows the dependence of the measured count rates on the beam intensity (blue and black dots for monitors A and B respectively). The dependence of the measured rates N'A and N'B is linear within 3% at the count rates below 6000 counts/cycle or 10 kHz. At higher rates the effect of the counter "dead time" breaks this linearity.

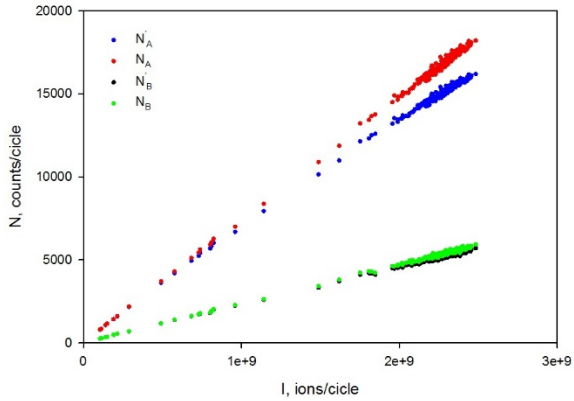

Figure 2: Monitor count rate as a function of the ion beam intensity.

For GFPC the effect of the "dead time" can be expressed as follows:

$$\frac{N'}{T} = \frac{N}{T} \times \exp(-S \times \frac{N}{T}),$$

where T is the pulse duration, S is the "dead time", N'/T is the measured count rate and N/T is the "true" count rate. Then the ratio of the measured counts of the monitors A and B can be derived as:

$$r(N_B) = \frac{N'_A}{N'_B} = \frac{N_A}{N_B} \times \exp\left(-N_B \times \frac{S}{T} \times \left(\frac{N_A}{N_B} - 1\right)\right) = R \times \exp\left(-N_B \times \frac{S}{T} \times (R-1)\right),$$

where r and R are the ratios of the measured and "true" counts respectively. Let's fit the dependence $r(N_B)$ by the function $a \times \exp(-b \times N_B)$, where $a = R$, $b = S / T \times (R - 1)$ and iterate N_B. The iteration results are shown in the Fig. 3 and presented in the Table 2.

Finally, the estimated "dead time" S equal to 3.87 μs was used to convert the measured counts to the "true" ones. These "true" counts of monitors A and B are presented in Fig. 2 by the red and green dots respectively. Their dependence on the beam intensity is quite linear even at high count rates. Green dots are almost coinciding with black ones.

Based on the "true" counts of the monitor A value of the fast neutron fluence at the location of the monitor A is equal to 7.4×10^{-6} n/cm^2 per one beam ion.

SIMULATIONS

Neutron energy spectra were calculated on the base of Monte Carlo simulations of nuclear cascades initiated by the ion beam in the RBS. CERN FLUKA code v.4-1.1 [3] was used for these simulations. Calculated spectra at the location of our monitors A and B are shown in Fig. 4. They were used to obtain the value of the fast neutrons fluence. In combination with the response functions of our monitors from [1] they allow to estimate the monitor count rates.

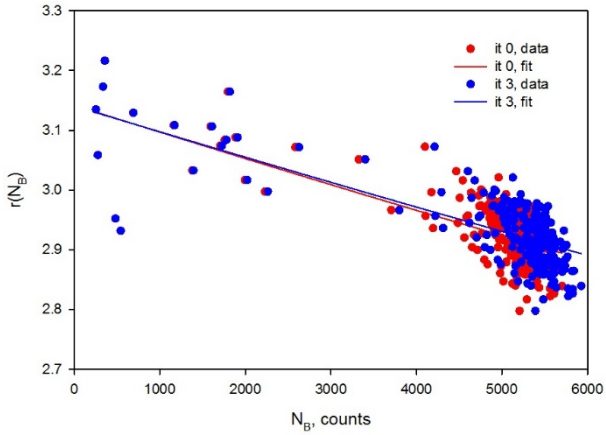

Figure 3: Ratio of the monitor counts as a function of number of "true counts" of the monitor B.

Table 2: The Iteration Results

#	<N_A/I> × 10^6	<N_B/I> × 10^6	<N_A/N_B>	R	S/T × 10^6
0	6.64	2.27	2.921	3.142	6.724
1	7.42	2.36	3.152	3.141	6.455
2	7.39	2.35	3.141	3.141	6.465
3	7.39	2.35	3.141	3.141	6.464

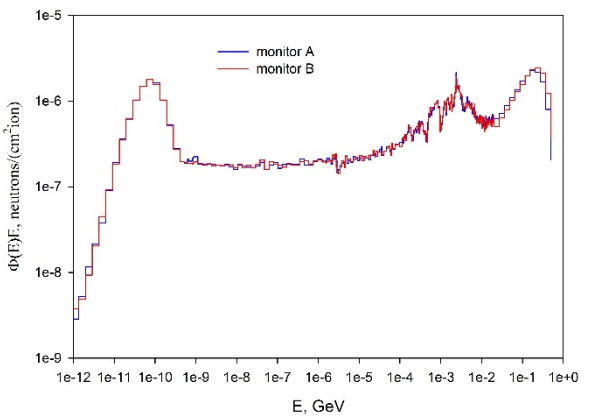

Figure 4: Neutron energy spectrum at the location of monitors A and B.

Results of these calculations are presented in the Table 3 along with the measured values.

The measured value of the fast neutron fluence at the location of the monitor A corresponds to the calculated one within 15%.

CONCLUSION

System of two recently developed GFPC neutron monitors was used for measurements of the neutron field around the Radiobiological Stand facility at IHEP. The monitor A (heavy, or main) was used to measure the fluence of fast

ISBN: 978-3-95450-240-0 ISSN: 2673-5539 doi:10.18429/JACoW-RuPAC2021-FRC01

neutrons, the monitor B (light, or complementary) - to estimate the GFPC "dead time" and thus to correct the readings of monitor A at the count rates exceeding 10 kHz. A good agreement of the measured and simulated with FLUKA code values gives us a preliminary validation of our interpretation of the main monitor as a fluence meter, though the interpretation efforts must be continued for other types of the neutron spectra.

Table 3: Comparison of the Calculated and Measured Values

Type	Fast neutron fluence, n/cm2/ion	Calculated, counts/ion	Measured, counts/ion
A	7.69×10^{-6}	7.91×10^{-6}	7.39×10^{-6}
B	8.43×10^{-6}	2.04×10^{-6}	2.35×10^{-6}

REFERENCES

[1] I. L. Azhgirey, I. S. Bayshev, I. A. Kurochkin, V. S. Lukanin, V. A. Pikalov, and O. V. Sumaneev, "Neutron Monitors for High Energy Accelerators", in *Proc. 26th Russian Particle Accelerator Conf. (RuPAC'18),* Protvino, Russia, Oct. 2018, p. 224. DOI:10.18429/JACoW-RuPAC2018-TUPSA38.

[2] Y.M. Antipov *et al.,* "Transversally-flat dose field formation and primary radiobiological exercises with the carbon beam extracted from the U-70 synchrotron,", *Instrum. Exp. Tech.,* v.58, n.4, pp. 552-561, 2015. DOI:10.1134/s0020441215040016.

[3] G. Battistoni *et al.,* "Overview of the FLUKA code", *Annals of Nuclear Energy,* v.82, pp.10-18, 2015. DOI:10.1016/j.anucene.2014.11.007.

ISBN: 978-3-95450-240-0 ISSN: 2673-5539 doi:10.18429/JACoW-RuPAC2021-MOPSA02

EXPERIMENTAL TESTS OF CW RESONANCE ACCELERATOR WITH 7.5 MeV HIGH INTENSITY ELECTRON BEAM

L.E. Polyakov, N.V. Zavyalov, Ya.V. Bodryashkin, M.A. Guzov, A.I. Zhukov, I.V. Zhukov, I.A. Konyshev, V.V. Kuznetsov, N.N. Kurapov, I.A. Mashin, V.R. Nikolaev, A.M. Opekunov, G.P. Pospelov, S.A. Putevskoj, M.L. Smetanin, A.V. Telnov, A.N. Shein, I.V. Shorikov, RFNC-VNIIEF, Sarov, Russia

Abstract

CW resonance accelerator with high average power electron beam is developed at RFNC-VNIIEF. Electron energy range is varied from 1.5 to 7.5 MeV and average beam current is up to 40 mA.

In this paper we present the results of electron beam dynamics simulation. The operating parameters of RF system, beam optics and bending magnets are determined. These parameters permit to obtain output beam with minimal current losses on each accelerating stage.

As a result of carried out tests 7.5 MeV electron beam was obtained after five passes of accelerating cavity. The electron energy spectrum, average beam current, transverse beam dimensions were determined on each accelerating stage. Common beam current loss is under 10 %.

INTRODUCTION

CW electron accelerator is aimed to obtain beams with the electron energies – 1.5, 3, 4.5, 6 и 7.5 MeV [1]. The accelerator is based on coaxial half-wave cavity (type of oscillations T_1). The electron energy gain up to 1.5 MeV per one pass of the accelerating gap. If it's necessary electrons is returned to the cavity for the subsequent energy gain by bending magnets.

Average beam power at the maximum of energy (7.5 MeV) achieves 300 kW. It becomes possible because of grid-controlled RF gun, which allows to obtain quasicontinuous electron beams with the average current 40 mA and energy 100 keV. RF system of accelerator consists of three independent amplifying cascades and RF power summator. It permits to obtain output RF signal with the average power up to 560 kW at frequency 100 MHz. Main characteristics of CW electron accelerator are shown in Table 1.

Table 1: Characteristics of CW Electron Accelerator

Parameter	Value
Electron energy, MeV	1.5, 3, 4.5, 6, 7.5
Average beam current, mA	40
Operating frequency, MHz	100
Average beam power, kW	300
Average power loss, kW	165
RF system power кВт	560

OPTIMIZATION OF OPERATING MODES

At present accelerator has the ability to product 7.5 MeV electron beams with the average current up to 100 μA. RF system consists of single amplifying cascade with 180 kW of output power. Current scheme of accelerator is shown in Fig. 1.

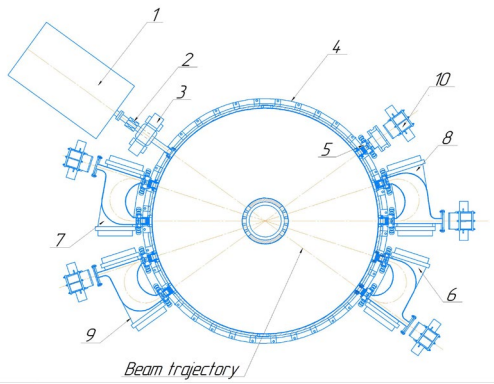

Figure 1: Accelerator scheme (1 – RF injector; 2 – focusing solenoid; 3 – quadrupole lens; 4 – accelerating cavity; 5 – corrector; 6 – 9 – bending magnets; 10 – Faraday cup).

Electron beam dynamics simulation was performed using program code ASTRA (A Space Charge Tracking Algorithm) [2]. Subsequent tests show that optimal beam injection phase into the accelerating cavity vary from - 20 to - 5 degree. Optimal magnetic field in the centre of focusing solenoid (2) is 12 mT. Magnetic quadrupole lens (3) installed in the injection channel is intended to compensate the various effect of transverse components of electric field in the cavity cross-section. Magnetic rigidity of lens is 20 mT [3]. Maximum of electric field inside the cavity is 185 kV/cm.

Calculated electron energy characteristic after each pass of accelerating cavity is shown in Fig. 2. Calculated values of average beam energies and energy spreads is shown in Table 2.

Table 2: Calculated Electron Energies znd Energy Spread

Number of pass	Average energy, MeV	Energy spread, MeV
1	1.5	0.074 (4.9%)
2	3.05	0.098 (3.2%
3	4.51	0.195 (4.3%)
4	6.042	0.311 (5.15%)
5	7.507	0.407 (5.43%)

ISBN: 978-3-95450-240-0 ISSN: 2673-5539 doi:10.18429/JACoW-RuPAC2021-MOPSA02

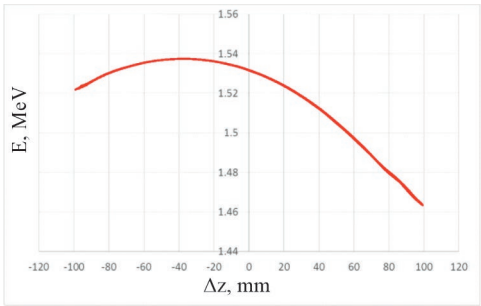

(a)

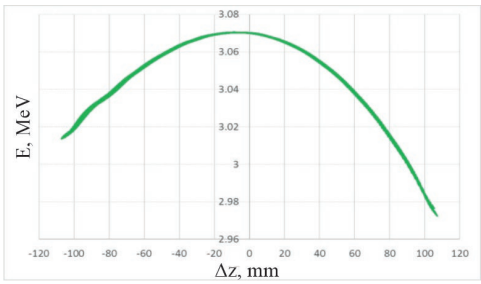

(b)

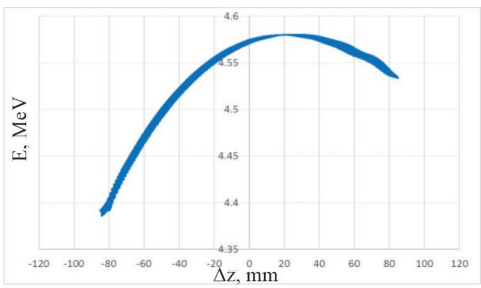

(c)

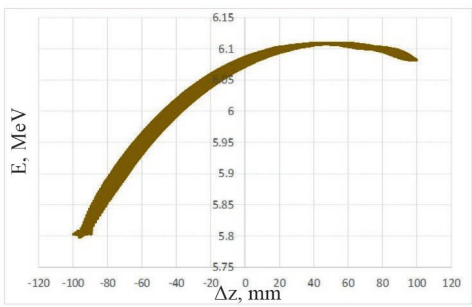

(d)

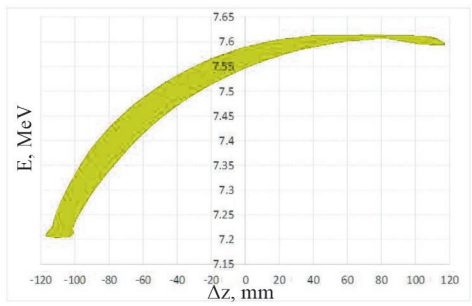

(e)

Figure 2: Calculated energy distributions in electron bunches after the first (a), second (b), third (c), fourth (d) and fifth (e) accelerating stage.

Calculated magnetic induction values of bending magnets are shown in Table 3.

Table 3: Magnetic Induction Values of Bending Magnets

Number of pass	Magnetic induction, mT
1	-
2	35
3	61
4	95
5	123

EXPERIMENTAL RESULTS

The experiment was aimed to optimization and verification of calculated operating parameters and carried out at the pulse-periodic mode in the interests of safety. The RF pulse duration was 2 ms, the pulse repetition period was 30 ms. The average beam current varied from 10 to 100 μA.

Beam loss was minimized because of calculated data and with a help of correcting magnets which are placed in the input and output of vacuum cameras. Thus, total beam current loss amounts to 8%.

The electron energy spectrum measurement was performed using a method of absorbing filters [4, 5]. The measuring assembly is composed of 23 isolated from each other aluminum plates with air gap between them (Fig. 3). The thickness of plates varied from 0.15 mm for 1.5 MeV electrons to 1 mm for 7.5 MeV electrons.

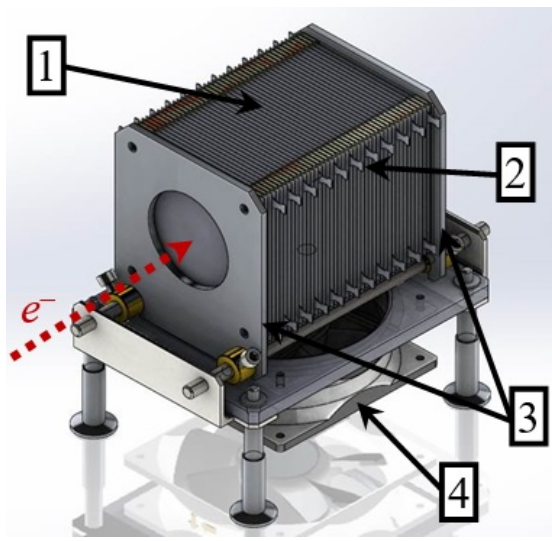

Figure 3: Measuring assembly: 1 – aluminum plates; 2 – current pickups; 3 – retention flanges; 4 – fan.

During experiment beam induced current from each plate was measured, while other plates were grounded. The electric scheme of plate connection is shown in Fig. 4.

ISBN: 978-3-95450-240-0 ISSN: 2673-5539 doi:10.18429/JACoW-RuPAC2021-MOPSA02

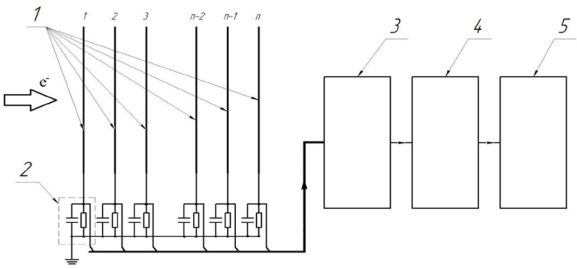

Figure 4: Electric scheme of plate connection in energy detector: 1 – aluminum plates; 2 – smoothing-integrating RC-filter; 3 – analog-digital converter; 4 – controller ; 5 – PC with software; (1…n) – number of absorbing plate.

Using calculated and experimental charge distributions on absorbing plates the electron energy spectrums after each accelerating stage were reconstructed (Fig. 5).

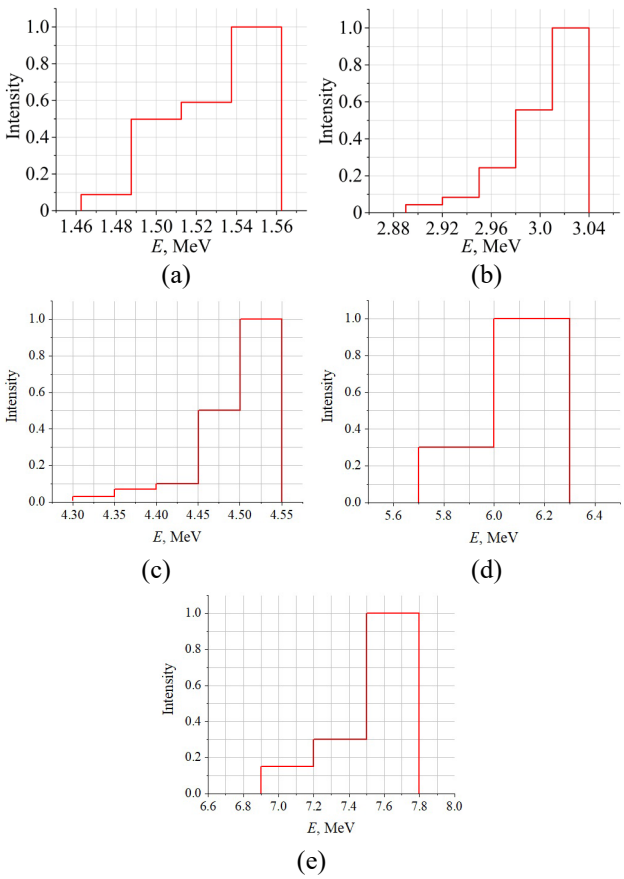

Figure 5: Reconstructed electron energy spectrum after one (a), two (b), three (c), four (d) and five (e) passes of accelerating cavity

Measured electron energy characteristics on each accelerating stage are shown in Table 4.

Table 4: Measured Electron Energies and Energy Spread

Number of pass	Average energy, MeV	Energy spread, MeV
1	1.5	0.100
2	3.05	0.150
3	4.51	0.200
4	6.042	0.310
5	7.5	0.4

CONCLUSION

The simulation series aimed to optimization of accelerator operating parameters were performed. Optimal beam injection phase into accelerating cavity, injection channel parameters, magnetic induction values in bending magnets were precisely determined.

The electron beam was experimentally obtained after each of five passes of accelerating cavity. Beam current loss is under 10%.

Measured and calculated electron energy characteristics are found in good correlation.

REFERENCES

[1] A.V. Telnov, “Status Report of Development of High Power Beam CW Electron Accelerator”, in *Proc. 26th Russian Particle Accelerator Conf. (RuPAC'18)*, Protvino, Russia, Oct. 2018, pp. 72-74. doi:10.18429/JACoW-RUPAC2018-WECAMH04

[2] K. Floettmann. Astra User`s Manual, http://www.desy.de~mpyflo/Astra_documentation

[3] L.E. Polyakov, “Electron Injection System of CW Resonance Accelerator With High Power Electron Beam”, in *Proc. 26th Russian Particle Accelerator Conf. (RuPAC'18)*, Protvino, Russia, Oct. 2018, pp. 292-294. doi:10.18429/JACoW-RUPAC2018-WEPSB07

[4] N.N. Kurapov *et al.* “System of On-line Energy Control of Electron Beam for Accelerators LU-7-2 and LU-10-20”, in *Proc. XVIII Int. Conf. Khariton's topical scientific readings. High energy density physics*, 2017. pp. 222-228.

[5] A. M. Opekunov, “Experimental Studies of Electron Beam Characteristics of High Power CW Resonance Accelerator”, in *Proc. 26th Russian Particle Accelerator Conf. (RuPAC'18)*, Protvino, Russia, Oct. 2018, pp. 289-291. doi:10.18429/JACoW-RUPAC2018-WEPSB06

ISBN: 978-3-95450-240-0 ISSN: 2673-5539 doi:10.18429/JACoW-RuPAC2021-MOPSA03

CALCULATIONS OF ION DYNAMICS AND ELECTRODYNAMIC CHARACTERISTICS OF 800 keV/NUCLON RFQ

M.A.Guzov, N.V. Zavyalov, A.V. Telnov, M.L. Smetanin, A.M. Opekunov, L.E. Polyakov,
Russian Federal Nuclear Center – All-Russia Research Institute of Experimental Physics (RFNC-VNIIEF), Sarov
S.M. Polozov, Yu.Yu. Lozeev, A.I. Makarov, E.N. Indushniy, NRNU MEPhI, Moscow

Abstract

An accelerating structure with radio frequency quadrupole (RFQ) [1] focusing is considered. The RFQ is capable of providing bunching and acceleration of ion beams from H+ to O5+ to energies of the order of 1 MeV/nucleon, with an A/Z ratio from 1 to 3.2. The proton current reaches 2 mA, and the ion current reaches 1 mA.

The calculation of the dynamics of ions has been carried out. An electrodynamic model of a four-vane RFQ with magnetic coupling windows has been created. The dependence of the operating frequency of the cavity on its geometric parameters is found. The geometry of the magnetic coupling windows, which provides the optimal mode separation, is determined. Various types of cavity shells are considered and the corresponding electrodynamic characteristics (EDC) are obtained. The influence of additional frequency tuning elements (plungers and "spacers" of frequency tuning) on the EDC is investigated. As a result, an optimized electrodynamic model of the accelerating structure is obtained.

RESULTS OF CALCULATING THE ION DYNAMICS IN AN ACCELERATING STRUCTURE

The purpose of calculating the dynamics of ions in an accelerating structure is to obtain conditions for accelerating the beam with minimal losses [2]. There are two types of losses: transverse and longitudinal (phase). Transverse losses are eliminated by changing the modulation parameter. Longitudinal losses disappear due to a change in the phase of a synchronous particle, which in turn also depends on modulation. Therefore, the problem of finding the optimal parameters of the accelerating structure, which are interconnected, was solved.

The range of accelerated particles from H+ to O5+ is considered. Particle dynamics were simulated in three stages:

1) preliminary modeling in order to identify the main parameters of the accelerating structure;

2) dividing the structure into periods;

3) modeling the dynamics in the structure, divided into periods.

The initial data for calculating the dynamics of ions are presented in Table 1. The emittance for protons and O5+ ions were obtained (Figs. 1,2). The values of energy, particle velocity, particle current and particle loss are calculated (Table 2). The calculations of the dynamics of ions were carried out with a preliminary bunching device ("buncher") and without it.

Table 1: Parameters for Modeling the Dynamics of a Proton Beam

Ions	p^+	O^{5+}
Length of structure, cm	450,0	
Length of buncher , cm	280,0	
Emittance, π×cm×mrad	0,03	
Transverse beam size (x,y), cm	0,1	0,2
Voltage, kV	40,0	140,0
Frequency, MHz	81,25	
Particle current, мА	2,0	1,0

The calculation was carried out for the phase length of the beam 2π and 1.4π (pre-bunched beam).

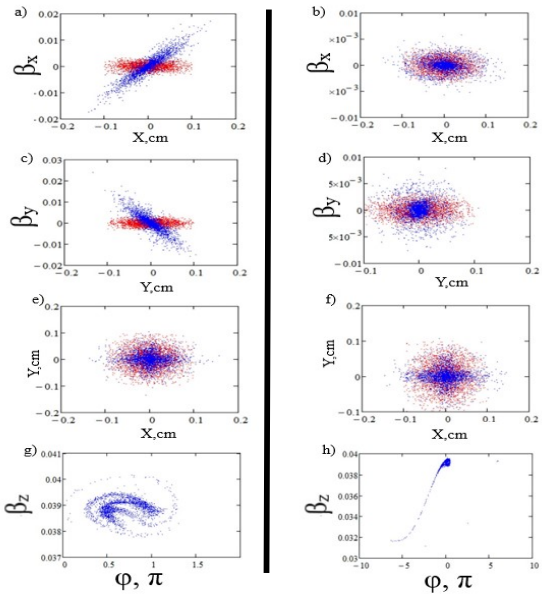

Figure 1: Results of calculations of the dynamics of protons :in RFQ (particles are indicated in red at the beginning of the structure, blue at the end), a - transverse emittance (X), without buncher; b - transverse emittance (X), with a buncher; c - transverse emittance (Y), without buncher; d - transverse emittance (Y), with a buncher; e - cross-section of the beam, without a buncher; f - cross-section of the beam, with a buncher; g - longitudinal emittance, without a buncher; h - longitudinal emittance, with a buncher.

ISBN: 978-3-95450-240-0 ISSN: 2673-5539 doi:10.18429/JACoW-RuPAC2021-MOPSA03

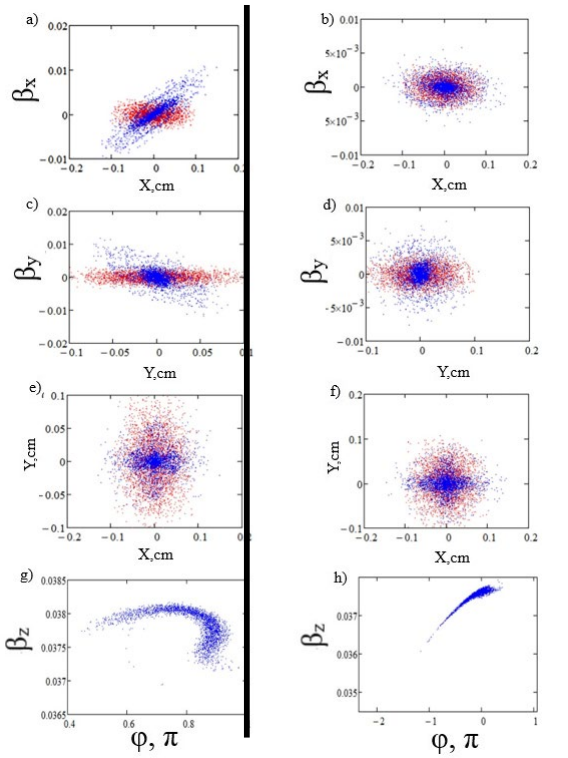

Figure 2: Results of calculations of the dynamics of O5+ in RFQ (particles are indicated in red at the beginning of the structure, blue at the end), a - transverse emittance (X), without buncher; b - transverse emittance (X), with a buncher; c - transverse emittance (Y), without buncher; d - transverse emittance (Y), with a buncher; e - cross-section of the beam, without a buncher; f - cross-section of the beam, with a buncher; g - longitudinal emittance, without a buncher; h - longitudinal emittance, with a buncher.

Table 2: Results of Modeling the Dynamics of Ions

Ions	p^+		O^{5+}	
	with a buncher	without a buncher	with a buncher	without a buncher
Velocity β	0,037	0,037	0,037	0,037
Energy, keV/nuclon	654,3	654,3	654,3	654,3
Current, mA	2,0	1,845	1,0	0,931
Current transmission coefficient, %	100,0	92,2	100,0	93,1
Transverse particles loses, %	0,0	0,0	0,0	0,0
Longitudinal particles loses, %	0,0	7,8	0,0	6,9

As a result of the calculations, a structure with a preliminary buncher was chosen, since it ensures the transportation and acceleration of the beam without losses.

ELECTRODYNAMIC MODEL OF RFQ

The electrodes in the structure under consideration have the same shape and are installed in such a way that the windows in the perpendicular planes are displaced by half a period (Fig. 3) [3].

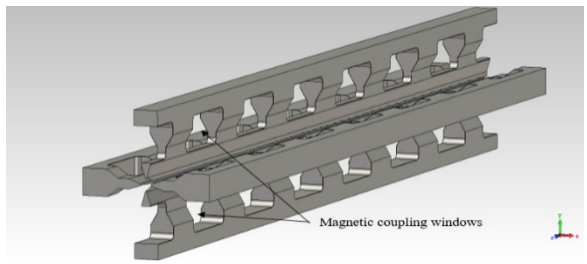

Figure 3: Electrodes with offset magnetic coupling windows

In such structures, windows exist to achieve the following goals:

1) providing frequency separation with the H_{110} wave;
2) simplification of tuning the resonator to the operating frequency;
3) stabilization of the distribution of electromagnetic fields;
4) reducing the size of the resonator by reducing the total inductance.

A structure with seven magnetic coupling windows is considered. Frequency separation was 9.3 MHz. The geometry of the coupling windows with the distribution of the transverse electric field along the resonator axis is shown in Fig. 4.

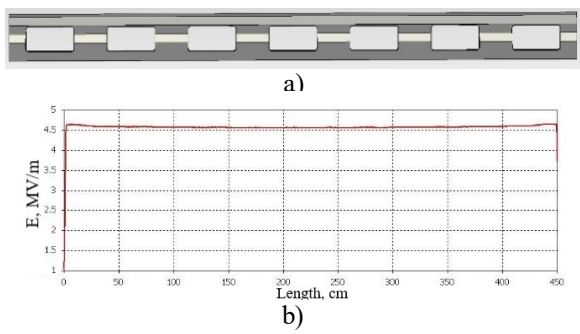

Figure 4: Results of modeling the coupling windows in the electrodes, a - the geometry of the coupling windows in the electrode, b - the distribution of the electric field along the central axis of the resonator

Calculations of quality factor, power losses in the walls and the transverse shunt impedance of the accelerating structure were carried out for three different body shapes (Fig. 5): rectangular (a), round (b) and octagonal (c). The calculated EDCs depending on the shape of the body of the accelerating structure are presented in Table 3.

ISBN: 978-3-95450-240-0 ISSN: 2673-5539 doi:10.18429/JACoW-RuPAC2021-MOPSA03

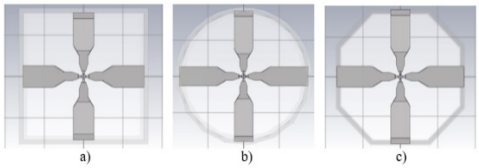

Figure 5: Shapes of the cross-section of the cavity.

Table 3: EDC of Resonators with Different Body Shapes

Type of cross-section of the cavity	Frequency, MHz	Radius of cavity, cm	Quality factor	Voltage, kV		Transverse shunt impedance kOhm/cm
				40	140	
				Power loss, kW		
rectangular	82,30	29,0	15541,0	17,1	208,9	30,0
cylindrical	79,57	34,0	15757,0	17,4	213,2	33,0
octagonal	80,86	32,0	15729,0	17,1	209,6	29,0

As you can see, the EDCs differ insignificantly. Therefore, we will choose a cylindrical resonator (Fig. 5a). This type of form is very popular in the scientific community, and the shell manufacturing technology is quite simple.

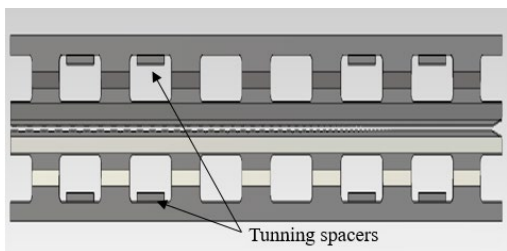

a)

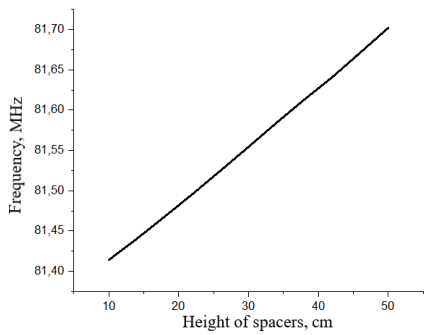

b)

Figure 6: Model of cavity with tuning spacers, a - the location of the "cubes"; b - the dependence of the cavity operating frequency on the height of the "cubes".

In a real cavity, due to various mechanical deformations and inaccuracies in the manufacture of the resonator, the operating frequency differs from the calculated one. In this regard, various options for frequency tuning were considered:

a) frequency adjustment with the help of "tuning spacers" (Fig. 6);

b) frequency control plungers (Fig. 7).

In fig. 6b shows a graph of the change in the operating frequency of the resonator with a change in the height of the "spacers". The sizes of regular "spacers" are 136x380 mm.

In fig. 7 shows the location of the plungers at half of their working stroke of 50 mm (a) and the graph of the dependence of the operating frequency of the cavity on the immersion depth of the plunger (b). diameter of plunger is 145 mm.

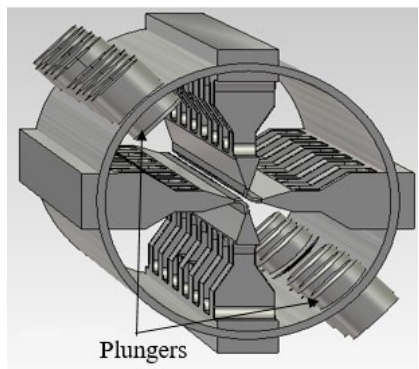

a)

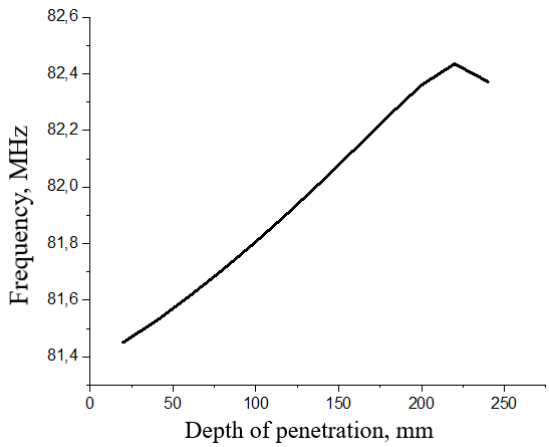

b)

Figure 7: Model of cavity with frequency tuning plungers depth.

CONCLUSION

The calculation of the dynamics of ions has been carried out (Fig. 1, 2). The transverse and longitudinal emittance and the beam cross section view have been obtained. An electrodynamic model of RFQ has been constructed, with the corresponding elements of dynamic and static frequency tuning. The operating frequency of the accelerating cavity is 81.25 MHz. Various shapes of cavity have been calculated, for which EDCs are given (Table 3).

ISBN: 978-3-95450-240-0 ISSN: 2673-5539 doi:10.18429/JACoW-RuPAC2021-MOPSA03

REFERENCES

[1] Kapchinsky I.M. “Linear Resonance Accelerators Theory: Particle Dynamics”, Moscow, Energoatomizdat, 1982.

[2] S.M. Polozov, *Prob. of Atomic Sci. and Tech*., 3(79), 131-136, 2012.

[3] S. M. Polozov, A. E. Aksentyev, and T. Kulevoy, “Beam Dynamics and Accelerating Cavity Electrodynamics' Simulation of CW 2 MeV Proton RFQ”, in *Proc. 5th Int. Particle Accelerator Conf. (IPAC'14)*, Dresden, Germany, Jun. 2014, pp. 3286-3288. doi:10.18429/JACoW-IPAC2014-THPME030

ISBN: 978-3-95450-240-0 ISSN: 2673-5539 doi:10.18429/JACoW-RuPAC2021-MOPSA04

THE TUNING RF PARAMETERS OF 40 MHz RFQ

A. Sitnikov, D. Seleznev, G. Kropachev[1], A. Semennikov, T. Kulevoy,
ITEP – NRC Kurchatov institute, Moscow, Russia
[1]also at JINR/FLNR, Moscow region, Russia

Abstract

The new linac for ions with mass(A)-to-charge(Z) ratio 8 (A/Z=8), output energy 4 MeV/u and 10 mA current is under development at NRC "Kurchatov Institute"-ITEP. The linac consists of Radio-Frequency Quadrupole (RFQ) and two sections of Drift Tube Linac (DTL).

The 40 MHz 11 meters long RFQ is based on a 4-vane structure with magnetic coupling windows [1]. The paper presents results of tuning radio-frequency (RF) RFQ parameters.

INTRODUCTION

The cavity with Radio-Frequency Quadrupole is wide used as an initial part of ion linac [2, 3].

The RFQ accelerating structure is based on H-cavity with four electrodes with modulated tips. Each electrode has one or few coupling windows. In order to minimize field non-uniformity the coupling windows shifted in vertical electrodes line related to horizontal electrodes line (or vice versa) [1]. Thus, the RFQ linac could be divided on odd number separated identical sections with similar RF parameters (front/end sections have an input/output gaps).

The results of RF tuning of the RFQ linac which is under development in NRC "Kurchatov Institute"-ITEP are presented in this paper.

THE RFQ LINAC

According to particles dynamics simulation the RFQ should has vanes length equals to ~11 m, average aperture radius R_0 = 12.5 mm, vane tip radius R_e=0.8* R_0 = 10 mm and operates at f_0 = 40.625 MHz. The RFQ cavity consists of 1000 mm long 11 identical sections and input/output flanges. The shifted windows structure was chosen for RFQ linac. The windows` areas were chosen as bigger as possible in order to minimize the cavity`s inner diameter [4]. The regular RFQ section is shown on Fig. 1. The main dimensions and RF parameters are presented at Tables 1 and 2, correspondently.

THE RFQ LINAC RF PARAMETERS TUNING

It should be mentioned that:

1. All further explanation was done for ideal model;
2. All describing methods of RF tuning have an influence to resonant frequency as well as field distribution.

The RFQ Linac RF Parameters Tuning Under Manufacturing Stage

The simulated RF parameters and measured one could be different to each other because of various reasons such as manufacturing or simulating errors. Thus, in RFQ linac design the special elements which could be modified at manufacturing stage should be provided.

The coupling window (area of coupling window) is the simplest element to be modified at manufacturing stages. It was tried out in [5]. The face of coupling window which could be modified is shown on Fig. 1.

The simulation has shown that resonant frequency has a linear relationship at coupling window`s height as it is shown at Fig. 2. The gradient is equal to $\Delta f/\Delta h$ = -45 kHz/mm. The same simulation was done for coupling window`s length. In this case the gradient is equal to $\Delta f/\Delta l$ = -90 kHz/mm.

Changing the coupling window`s height seems more simple and more precisely compared to changing coupling window`s length.

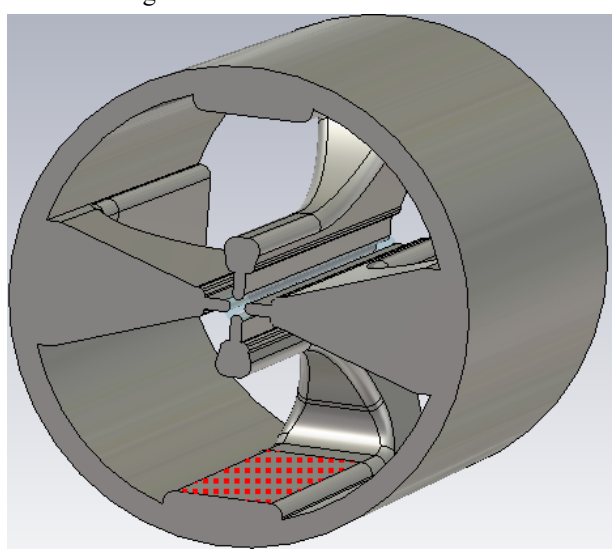

Figure 1: The regular RFQ section (the area for modification is highlighted with red).

Table 1: The Main Dimensions of RFQ Sections

Parameter	Value (mm)
Cavity inner diameter	860
Cavity length	1000
Vane base width	250
Vane base height	37.5
Vane top width	60
Vane window length	770
Vane window height	290
Vane tip height	30

ISBN: 978-3-95450-240-0 ISSN: 2673-5539 doi:10.18429/JACoW-RuPAC2021-MOPSA04

Table 2: The Main RF RFQ Parameters

Parameter	Value
Resonant frequency, MHz	40.625
Resonant frequency of the dipole mode, MHz	53
Inter-vane voltage, kV	170
Self quality factor	14000
RF power losses, kW/m	44
Full RF power losses, kW	484

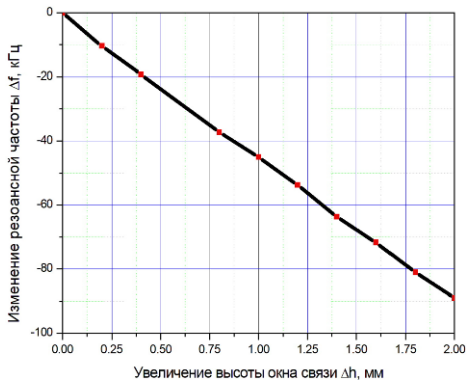

Figure 2: The resonant frequency to coupling window`s height dependence.

The RFQ Linac RF Parameters Tuning by Movable Plungers

The RF tuning of manufactured and assembled RFQ linac would be achieved by different plungers. Plungers should play two main roles – tuning the resonant frequency and change the RF field distribution. Plungers could have different geometry, be motorized or stationary.

The motorized plungers usually injected into cavity through side flanges and use for resonant frequency tuning [6] as it shown on Fig. 3. The resonant frequency relationship on plunger`s diameter and length is shown on Fig. 4. From Fig. 4 one can see that maximal resonant frequency changing is reached at Ø140 mm and $h$ = 120 mm plunger`s diameter and length, correspondently.

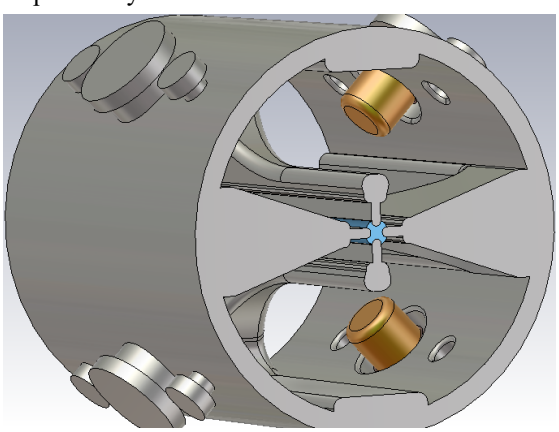

Figure 3: Plungers injected through side flanges.

The plungers which were injected into the RFQ cavity also have an influence to RF field distribution. As an example, four cylindrical plungers with diameter 140 mm and length 100 mm injected into first cell would lead to non-uniformity RF field up to δE = 5% and resonant frequency change Δf = 22 kHz. In order to compensate RF field non-uniformity the additional plungers should be injected into central (four plungers) and last sections (four plungers). In this case, the non-uniformity of the RF field would be decreased to δE = 2.4% while resonant frequency would be changed up to Δf = 65 kHz (see Fig. 5).

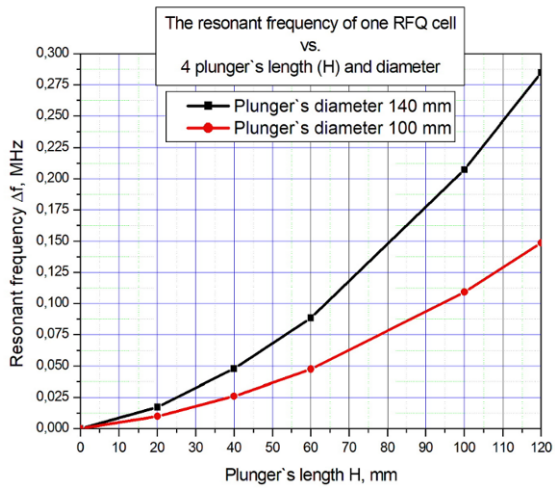

Figure 4: The resonant frequency dependence on plunger`s diameter and length.

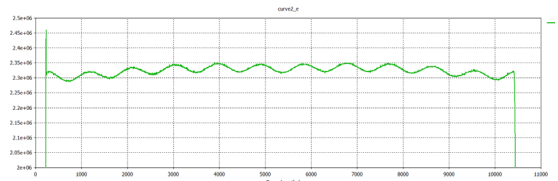

Figure 5: The non-uniformity of the RF field with 4 plungers in the first, last and central sections.

The RFQ Linac RF Parameters Tuning by Stationary Plungers

The rational way is to place stationary plungers inside the cavity do not occupy the side flanges. As an example, the stationary plungers could be made as blocks and mounted inside the coupling windows (see Fig. 6).

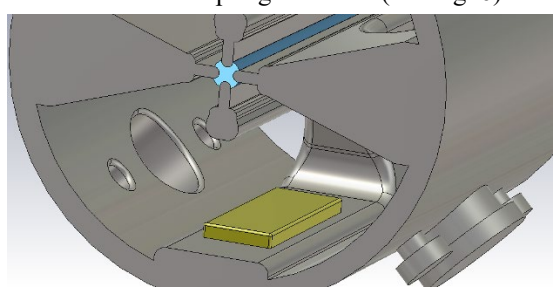

Figure 6: Plunger mounted inside the coupling window.

The dependence of the resonant frequency changing vs. dimensions of four stationary plungers mounted inside the coupling windows is shown on Fig. 7. One can see that

ISBN: 978-3-95450-240-0 ISSN: 2673-5539 doi:10.18429/JACoW-RuPAC2021-MOPSA04

maximum frequency changing is equaled to $\Delta f = 1.8$ MHz and achieved with plunger`s L*W*H = 400*150*100 mm.

If four stationary plungers mounted in the first section the RF field non-uniformity would be rise up to $\delta E = 12\%$ (see Fig. 8) while frequency changing doesn`t exceed $\Delta f = 66$ kHz. In order to compensate such non-uniformity the additional four stationary plungers (in each section) should be mounted in the last section and in two sections nearby central. In this case the non-uniformity of the RF field would be worse than $\delta E \leq 5\%$ while frequency changing $\Delta f = 272$ kHz (see Fig. 9).

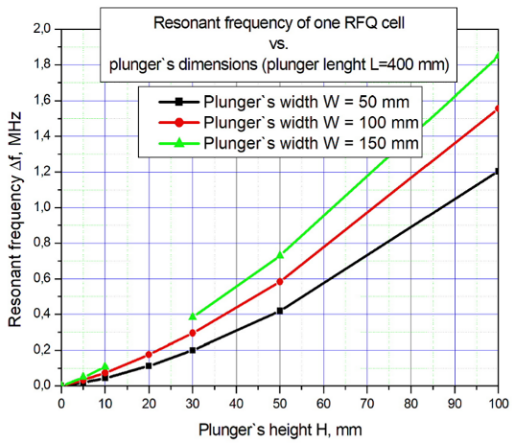

Figure 7: The resonant frequency dependence on plunger`s dimensions.

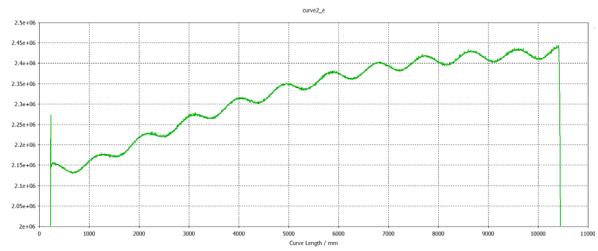

Figure 8: The non-uniformity of the RF field with 4 stationary plungers in the first sections.

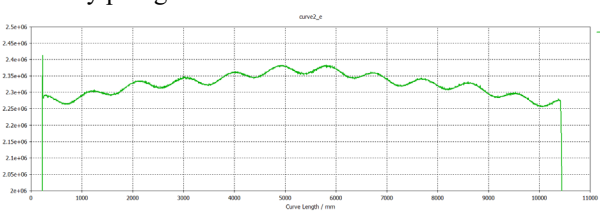

Figure 9: The non-uniformity of the RF field with 4 stationary plungers in the first, last and two nearby central sections.

CONCLUSION

Based on simulation the next conclusion could be done:

1. The RFQ linac design should have elements which could be modified after primary cavity assembling and RF parameters measurement. Particularly, increasing coupling windows lead to decreasing resonant frequency. Thus, RFQ linac design should have a smaller coupling windows compared to simulated one;
2. It is appropriate to tune RF field distribution by stationary plunger taking into account its influence to resonant frequency changing;
3. The motorized plungers should be used for Automatic Frequency Tuning system (AFT).

REFERENCE

[1] V.A. Andreev, G. Parisi, “Field Stabilization and End-Cell Tuning in a 4-vane RFQ”, Presentet at *EPAC’94*, London, June 1994, pp. 1300-1302.

[2] I. M. Kapchinskii and V. A. Teplvakov, *Prib. Tekh. Eksp.* No. 2, 19, 1970.

[3] G. Kropachev, T. Kulevoy and A. Sitnikov, “The Proton LINAC for Compact Neutron Source DARIA”, *J. of Surface Investigation: X-ray, Synchrotron and Neutron Techniques*, Vol. 13, No. 6, pp. 1126–1131, 2019.

[4] A. Sitnikov *et al.*, “The RF Parameters of Heavy Ions Linac”, presented at the *12th Int. Particle Accelerator Conf. (IPAC'21),* Campinas, Brazil, May 2021, paper MOPAB206.

[5] V.A. Koshelev *et al.*, “Design of 4-vane RFQ with Magnetic Coupling Windows for Nuclotron Injector Lu-20”, in *Proc. 28th Linear Accelerator Conf. (LINAC'16)*, East Lansing, MI, USA, Sep. 2016, pp. 575-577. doi:10.18429/JACoW-LINAC2016-TUPLR050

[6] A. Gusarova *et al.,* “Research and Design of a New RFQ Injector for Modernization of the LU-20 Drift-Tube Linac”, *Phys. of Particles and Nucl. Lett.,* Vol.13, No.7, 2016.

ISBN: 978-3-95450-240-0 ISSN: 2673-5539 doi:10.18429/JACoW-RuPAC2021-MOPSA06

PARAMETERS OF THE NORMAL CONDUCTING ACCELERATING STRUCTURE FOR THE UP TO 1 GeV HADRON LINACS

I.V. Rybakov†, A.V. Feschenko, L.V. Kravchuk, V.V. Paramonov, V.L. Serov, Institute for nuclear research of the Russian academy of sciences, Moscow, Russia

Abstract

Compensated bi-periodic accelerating structure Cut Disk Structure (CDS) was developed for accelerating particle beams at β~1. In the papers dedicated to the development of this structure, a significant decrease in Ze was shown for medium energies range, β~0.4-0.5. For high-intensity hadron linacs, this energy range, in which particles are captured to acceleration from the drift tube structure, is of the greatest interest. In this paper, a set of CDS parameters was obtained, which provides a Ze value not lower in the comparison to the proven structures in the medium energy range. By the comparison of the electrodynamic and technological parameters of CDS with these structures, the advantages of its application in multi-section cavities for the up to 1 GeV linacs are shown. The selection of optimal cells manufacturing tolerances, the method of its tuning before brazing and frequency parameters control, and the selection of the method for multipactor discharge suppression are determined. The results of the sketch project of the CDS cavity numerical simulation as a non-uniform coupled system and optimization of the transition part of sections and bridge devices are presented.

INTRODUCTION

Compensated biperiodic structure CDS was proposed for high energy area, β~1 [1,2]. For particle velocities β>0,5 CDS is superior to known analogues in effective shunt impedance Z_e. But in lower energy area, β<0.5, it was difficult to implement internal cooling channels, required for CDS application in hadron linacs with intense beam [3,4]. In recent investigations the cells dimensions were optimized to equalize CDS with analogues in Ze value simultaneously placing internal cooling channels. Also, the techniques for multipacting discharge damping in CDS coupling cells [5], and combining of CDS sections into accelerating cavity [6], were developed. For application in hadron linacs with intense beams and energies up to 1 GeV in the total set of RF and technological parameters CDS surpass [7], known analogues.

CDS STRUCTURE FOR β>0,5

The CDS structure has shown competitive electromagnetic parameters for hadron linacs at comparatively high velocity range 0.4≤ β≤0.8, as it is shown in Fig. 1 [4].

The advantage of CDS in Z_e over proven strictures such as ACS, SCS and DAW decreases with high internal wall thickness at β<0.5. At the same time, it is necessary to place internal cooling channels in them. In high intensity linacs the RF heat load is about 3 kW/m. The RF loss density and temperature distribution is shown in Fig. 2.

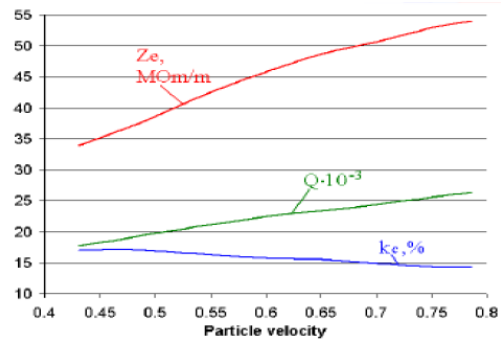

Figure 1: Comparison of the accelerating structures at 991MHz operating frequency.

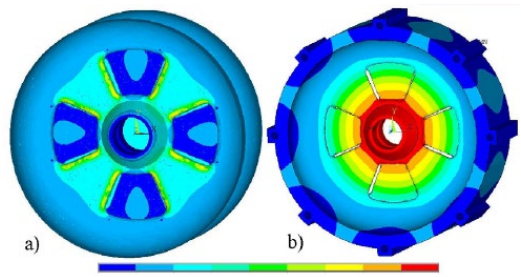

Figure 2: RF loss density (a) and temperature (b) distributions in CDS.

In case of only external cooling channels implemented the drift tube is overheated which causes thermal-stress deformations leading shift of operating frequency.

Calculating a combination of CDS parameters to implement internal cooling channels with maintaining high Z_e value has become the main problem for its application at β<0.5.

CDS OPTIMIZATION FOR β~0,4

To implement internal cooling channels a set of CDS geometrical parameters was calculated, providing both high Z_e value and sufficient internal wall thickness. Comparison of CDS electrodynamic parameters with proven accelerating structures (Fig. 3) at β=0.4313 is shown in Table 1.

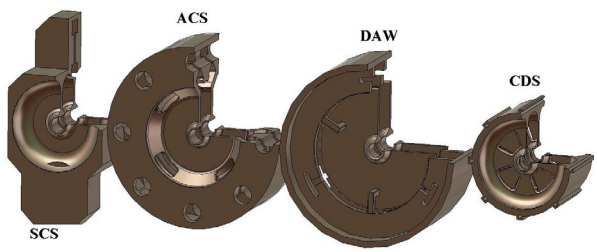

Figure 3: Comparison of the accelerating structures at 991MHz operating frequency.

† irybakov@inr.ru

ISBN: 978-3-95450-240-0 ISSN: 2673-5539 doi:10.18429/JACoW-RuPAC2021-MOPSA06

Table 1: Parameters of Accelerating Structures, β=0,4313

Parameter	DAW	ACS	SCS	CDS
Length, mm			65,24	
Width, mm	425.67	405.35	211.79	211.54
Height, mm	425.67	405.35	465.74	211.54
k_c	0.56	0.054	0.042	0.164
Q	23407	15834	16998	14738
Z_e, Mom/m	30.76	28.66	30.04	31.16

The structures have a similar efficiency of using RF power, determined by the value of Z_e. At the same time, the CDS structure has twice smaller transverse dimensions.

In terms of the coupling coefficient value, the DAW structure has an overwhelming advantage, for which it is more than 0.5. But in the vicinity of the operating mode of the DAW, there are parasitic oscillations with variations of the field along the azimuth, taking into account the splitting from the stems. The suppression of the influence of these oscillations requires the introduction of additional elements into the structure, such as slots, which complicate the manufacturing and tuning of the cavity. At the same time, the CDS structure has a coupling coefficient reaching 0.16, three times higher than that of the ACS and SCS structures, which is an intermediate value [7].

Based on the optimization and of the geometrical parameters of the cells of the sections, a design technical drawing of the CDS structure for the 991 MHz operating frequency and β=0.4313, taking into account the wall thickness for the internal cooling channels, shown in Fig. 4.

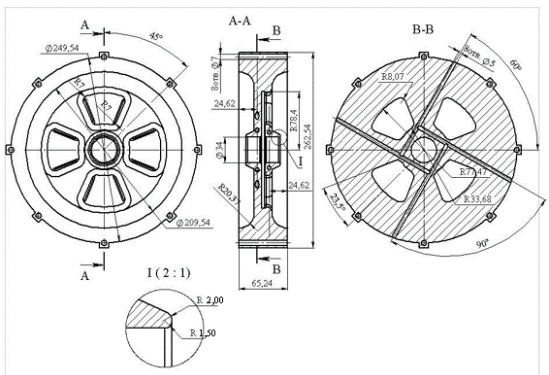

Figure 4: CDS structure design drawing at 991MHz operating frequency, β=0.4313.

The figure shows both external and internal cooling channels. Taking into account the results of comparing the efficiency of the cooling system options used in the CDS cavity, external channels can be excluded from the project to simplify the manufacturing of the structure.

The twice smaller transverse dimensions although allows application of CDS for relatively small operating frequencies ~300 MHz in comparison with widely used π-mode structures (PiMS) CDS shows higher Z_e value as a compensated structure (Fig. 5) [8].

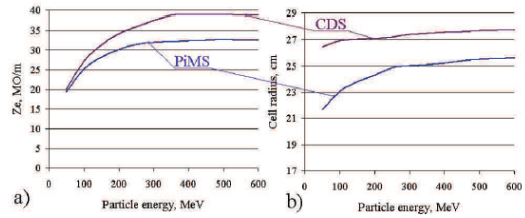

Figure 5: The plots of shunt impedance Ze, (a), and cell radius R_c, (b), for PiMS and CDS.

MULTIPACTING SUPPRESION

Using the example of a CDS structure tuned to a frequency of 991 MHz, acceleration rate of 2.5 MV/m, β=0.4313, the probability of the of a multipactor discharge near the operating field level in the gaps of the coupling cells was shown [9].

To suppress the discharge at the operating field level, a proven method of multipactor suppressing in the structure can be used by introducing alternating detuning of neighboring accelerating cells to create an electric field voltage in the coupling cell that exceeds the upper threshold for the multipactor occurrence. In the CDS structure at frequency of 991 MHz, acceleration rate of 2.5 MV/m, β=0.4313, the value of neighboring accelerating cells detuning is ±1.2 MHz

To preserve the uniformity of the geometric parameters of the structure in the sections and simplify the tuning of the cavity before brazing, a technique of multipactor suppressing is considered, which allows violating the condition of resonant electron motion by changing the geometry of the plane gap of the coupling cell– the distance δl between the lower faces of the planes forming the gap increases, as shown in Fig. 6. The maximum value δl is limited by the conditions of inner cooling channels placement in the drift tubes.

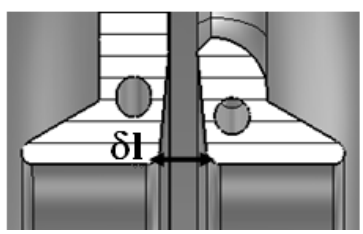

Figure 6: The change of geometry of coupling cells for multipactor suppression in CDS.

With an increase in the δl to 2 mm, the electron flight time decreases to a value below 0.5 of the RF field period and the number of secondary electrons decreases [5].

CDS CAVITY TUNING

Cavities based on normally conducting structures in the main parts of high intensity hadron linacs consist of sections connected by bridge devices. In particular, the first cavity of the main part of the INR linac consists of four sections (18, 20, 21, 19 structure periods, respectively) and three bridge devices made of a standard 220x104 mm waveguide. The total length of the cavity is more than 13.5 meters, as shown in Fig. 7.

ISBN: 978-3-95450-240-0 ISSN: 2673-5539 doi:10.18429/JACoW-RuPAC2021-MOPSA06

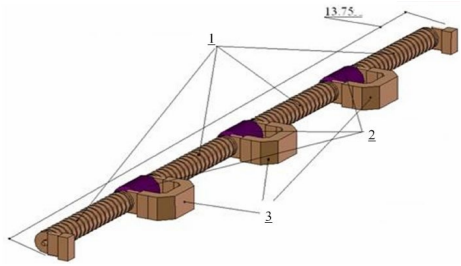

Figure 7: CDS based accelerating cavity. 1 – CDS accelerating sections, 2- focusing elements, 3- coupling bridge devices.

Numerical simulation of a complete cavity by modern software tools with the use of reasonable computing resources will not provide the necessary calculation accuracy. At the same time, individual configuration of sections and bridge devices as a non-uniform system will require multiple iterations of simulation that take a long time.

To simulate the cavity as a system of sections and bridge devices, a technique based on a multimode approximation was used, operating with the integral parameters of the system elements – the eigenfrequencies and the values of the magnetic field of sections and bridge devices on the coupling gap [10]. This technique is a generalization of the single-mode approximation technique. A special feature of the technique is the possibility of using the parameters of the elements of a non-uniform coupled system obtained by direct numerical simulation, which allows to fully take into account the details of their design.

With connection of the CDS section and the bridge device in the form of a rectangular waveguide segment with a transition part, it is necessary to achieve the optimal separation of the operating and two neighbouring modes while maintaining sufficient sensitivity of the frequency of the operating mode to the frequency tuning elements. The presence of sufficient mode separation near the operating frequency is necessary to increase the stability of the field distribution in the cavity sections. Figure 8 shows the dependence of the frequency of the resulting modes of the system depending on the position of the tuning plunger for the case of a CDS section and a bridge device near the operating frequency of 991 MHz

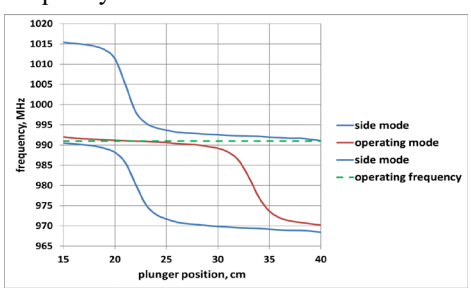

Figure 8: The tuning of CDS cavity sections connected by bridge devices at 991 MHz frequency.

In this case, the distance between the operating mode and neighbouring modes is determined by the value of the coupling coefficient, which depends on the length of the gap.

The presence of a coupling gap between the section and the bridge device leads to a decrease in the frequency of the operating mode of the section, in full accordance with the multi-mode technique. In this regard, it is necessary to adjust the frequency of the ending half cells before brazing the sections.

This ensures both the tuning of the operating frequency and the equal separation of neighbouring oscillations in frequency.

The results obtained show that using a model based on a multi-mode technique, it is possible to analyse and simulate a non-uniform coupled system of four unequal CDS sections connected by three bridge devices with RF power input to the central bridge [6].

CONCLUSION

The problem of implementing the CDS structure for hadron linacs in the area of $0.4<\beta<0.8$ and optimizing its parameters has been completely solved. According to its results, it is not inferior to proven structures in terms of electrodynamic parameters, having twice smaller transverse dimensions and can be used both at frequencies of ~ 1000 MHz and at a lower frequency of ~300 MHz

REFERENCES

[1] V. Paramonov, "The Cut Disk Accelerating Structure for High Energy Linacs", in *Proc. 17th Particle Accelerator Conf. (PAC'97),* Vancouver, Canada, May 1997, paper 4P025, pp. 2962-2964.

[2] V. V. Paramonov *et al.,* "The PITZ CDS Booster Cavity RF Tuning and Start of Conditioning", in *Proc. 25th Linear Accelerator Conf. (LINAC'10),* Tsukuba, Japan, Sep. 2010, paper MOP081, pp. 241-243.

[3] V. V. Paramonov, "The Cut Disk Structure Parameters for Medium Proton Energy Range", in *Proc. 24th Linear Accelerator Conf. (LINAC'08),* Victoria, Canada, Sep.-Oct. 2008, paper THP059, pp. 924-926.

[4] V. V. Paramonov, "The CDS Parameters for Proton Linac with Moderate Heat Loading", in *Proc. 22nd Russian Particle Accelerator Conf. (RuPAC'10)*, Protvino, Russia, Sep.-Oct. 2010, paper TUPSA013, pp. 65-67.

[5] I. Rybakov, V. Paramonov, *Phys. At. Nucl.*, Vol. 81, No. 11, pp. 1652-1655, 2018. doi:10.1134/S1063778818110182

[6] V. Paramonov *et. al.*, *Phys. Part. Nucl. Lett.,* v. 15, n, 7, 2018, pp. 915-918. doi:10.1134/S1547477118070555

[7] I. Rybakov *et al.*, *J. Phys. Conf. Ser.,* v. 747, p. 012073, 2016. doi:10.1088/1742-6596/747/1/012073

[8] V. V. Paramonov, "Comparison of Normal Conducting High Energy Accelerating Structures for a Moderate Operating Frequency", in *Proc. 27th Linear Accelerator Conf. (LINAC'14)*, Geneva, Switzerland, Aug.-Sep. 2014, paper MOPP125, pp. 348-350.

[9] I. V. Rybakov and I. I. Isaev, "Estimation of Multipacting in CDS Structure", in *Proc. 25th Russian Particle Accelerator Conf. (RuPAC'16)*, Saint Petersburg, Russia, Nov. 2016, pp. 288-290. doi:10.18429/JACoW-RUPAC2016-TUPSA035

[10] V. V. Paramonov, "The Common Dispersion Equation for High-Energy Compensated Accelerating Structures", in *Proc. 21st Linear Accelerator Conf. (LINAC'02),* Gyeongju, Korea, Aug. 2002, paper TU442, pp. 410-413.

ISBN: 978-3-95450-240-0 ISSN: 2673-5539 doi:10.18429/JACoW-RuPAC2021-MOPSA07

200 MeV LINEAR ELECTRON ACCELERATOR – PRE-INJECTOR FOR A NEW KURCHATOV SYNCHROTRON RADIATION SOURCE

I. A. Ashanin[1,2], S. M. Polozov[1,2] A. I. Pronikov[1,2] , V. I. Rashchikov[1,2],
V. N. Korchuganov[2], V. A. Ushakov[2]
[1]National Research Nuclear University MEPhI, Moscow, Russia
[2] National Research Center "Kurchatov Institute" Moscow, Russia

Abstract

New linear electron accelerator (linac) with an energy of about 200 MeV (or 300 MeV in a high-energy version) is being proposed for injection into the booster synchrotron, which is being developed for the reconstruction of the SIBERIA-2 accelerator complex with the aim of upgrade to 3rd generation source at the NRC «Kurchatov Institute». A modernized linac and its specific elements layout will described in the report. The modeling of accelerating structure and optimization of electrodynamics characteristics and fields distribution and geometric in order to reduce the beam spectrum at the output of the linac was done. A step-by-step front-to-end beam dynamics simulation results will discuss.

INTRODUCTION

Kurchatov synchrotron radiation source (KSRS) today consists of 80 MeV linac, 450 MeV small booster ring Siberia-1 and 2.5 GeV main ring Siberia-2 [1]. Compact booster ring Siberia-1 uses for intermediate acceleration of electrons from 80 to 450 MeV and injection into the main ring, also a source of synchrotron radiation in the field of vacuum ultraviolet and soft X-ray. At the moment, a 40 keV diode gun and ~ 4 A in a pulse with a duration of ~ 18 ns is used as an injector. The energy spread at the output is about 7%. From the gun electron beam drives to the input of the linear accelerator. Disk-and-washer type accelerating structure has 112 accelerating gaps. After acceleration to 80 MeV, the beam pulse consists of about 50 microbunches following each other at a frequency of 2.8 GHz.

In the version for reconstruction (see Fig. 1), it is proposed to use a classic three-electrode gun with a heated oxide cathode (powered by a single modulator) as an electron source. The linear accelerator will include 4 or 6 sections, each about 2.14 m long, operating on a standing wave (biperiodical accelerating system, BAS) (see Fig. 2). Consequently, after acceleration beam energy will be 200 MeV.

Two bunchers – one short klystron type and one adiabatic – will be placed in front-end of linac, which will include several (4-7) irregular accelerating cells with increasing phase wave velocity and accelerating field amplitude for longitudinal beam bunching.

To increase the current transmission coefficient and to reduce the beam energy spectrum, in addition to the adiabatic buncher, a one- or two-gap buncher can be placed in front of the adiabatic buncher operating at a frequency that is two or four times lower than the operating frequency of the sections [2].

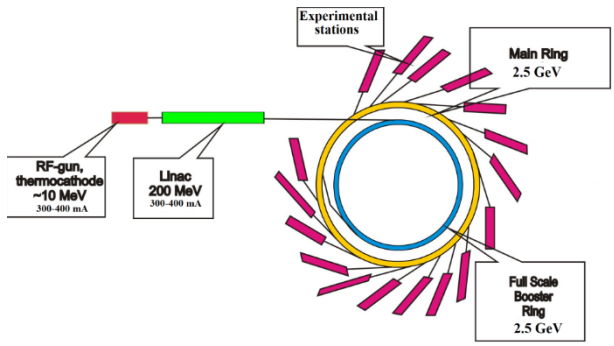

Figure 1: Planned scheme of the accelerator complex.

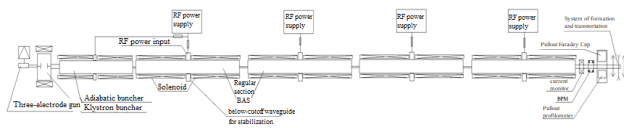

Figure 2: Possible scheme of the linac layout.

All results of the beam dynamics simulation were carried out using the BEAMDULAC-BL code developed at the Department of Electrophysical Facilities of NRNU MEPhI [3-5]. Numerical simulation was carried out in stages, with control of parameters after buncher, after the second, fourth and sixth regular sections.

BEAM DYNAMICS SIMULATION IN THERMIONIC GUN

Simulation shows that the optimal injection energy will be 100–120 keV. The beam current at these parameters was 1.03 A, energy spread 0.76%, beam radius 3.6 mm, transverse emittance 6.5 π (cm-mrad), micropervance 0.03 mkA/B$^{3/2}$ [6]. Transverse beam focusing is carried out using magnetic solenoids on all sections of the linear accelerator and triplets of quadrupole lenses at higher energies.

BEAM DYNAMICS SIMULATION IN ADIABATIC BUNCHER

Linac front-end with a thermionic cathode should provide an energy of ~ 10 MeV. The operating frequency is 2800 MHz. The number of periods is 26.

The adiabatic buncher includes four periods with increasing phase velocity and RF field amplitude. At the

ISBN: 978-3-95450-240-0 ISSN: 2673-5539 doi:10.18429/JACoW-RuPAC2021-MOPSA07

injection energy of 100 keV in the first four cells, it is necessary to change the phase velocity of the wave from 0.64 to 0.90. In this case, the amplitude of the accelerating field will increase from 90 to 150 kV / cm. In the remaining 22 regular cells of the adiabatic buncher, the phase velocity and the field amplitude are constant. The length of the gaps of the accelerating cells in the regular part is approximately $\beta_{ph}\lambda/4$, but can be adjusted if necessary.

The lengths of the coupling cells are chosen the same and equal to 4 mm. The aperture radius for the entire channel is 5 mm. Beam dynamics simulation results at the exit of the adiabatic buncher are presented in Table 1. Transverse beam focusing is realized by solenoid field.

Table 1: Beam Dynamics Simulation Results at the Output of the Adiabatic Buncher

Parameter	Value
Electric field amplitude, E_{max}, kV/cm	150
Output energy W_{out}, MeV	10.15
Output current I_{out}, mA	447
Current transmission coefficient, %	74.5
Longitudinal losses, %	24.5
Transverse losses, %	0.9
Width of the energy spectrum FWHM, %	±1.5

ELECTRODYNAMICS PARAMETERS OF ACCELERATING STRUCTURE

The biperiodical accelerating structure (BAS) operating on a standing wave was chosen as an accelerating structure. The accelerating cells have an optimized Ω-shape and provide the maximum field on the axis of the structure. Coupling cells have a small longitudinal dimension (4 mm gap). The phase shift per cell is π/2, the phase shift between adjacent accelerating cells is π. Geometry of the regular period of the BAS is shown in Fig. 3.

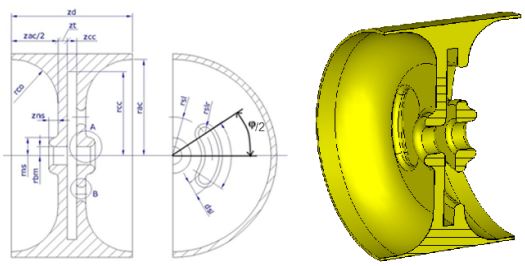

Figure 3: Geometry of the regular period of the BAS.

Electrodynamics parameters of the adiabatic buncher was simulated and geometric parameters was optimized. As a result, the following values of electrodynamics characteristics were obtained: coupling coefficient K_{co} = 11%, effective shunt impedance $r_{sh.ef.}$ = 96 MOhm/m, Q-factor is equal 12800, group velocity is equal 0.165c, surface overvoltage E_{max}/E_{acc} = 3.66. The accelerating structure model used for simulation consists of one whole accelerating cell, two half cells and two coupling cells. Electric field distribution in the cell for the one period presented in Fig. 4.

It is also proposed to use a BAS as a regular section, but consisting of 40 accelerating cells. The length of the last cell should be increased, since the coupling cell will not be located behind it. The RF power input is also organized into one of the central accelerating cells. Because of the high input power, in this case, it is convenient to use a symmetrical two-way RF coupler, which makes us possible to reduce the field strength in waveguides and high-frequency windows by a factor of four. Electric field distribution in the structure consists of four bunching cells and the first 5.5 regular cells is shown in Fig. 5.

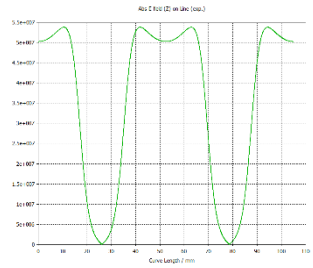

Figure 4: Electric field distribution in the cell for one period.

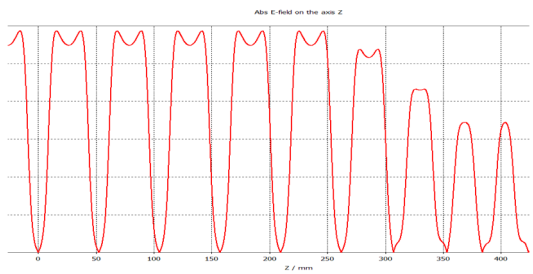

Figure 5: Electric field distribution in the layout of the complete structure (four bunching cells and the first 5.5 regular cells).

BEAM DYNAMICS SIMULATION IN REGULAR SECTION

Beam dynamics simulation results at the exit of the four regular sections depending vs. the injection phase are shown in Table 2. Beam cross and the phase portrait on the phase plane (γ, z) at injection phase -0.75 are shown in Fig. 6. The energy spectrum and beam envelope at the same injection phase are presented in Fig. 7.

Front-to-end simulation leads to following results. The total length of the linac will be about 10 m. The operating frequency is 2800 MHz. Maximum field strength on axis: 450 kV/cm. Output energy is near about 215 MeV. Energy acceleration rate: 50-55 MeV/section. The transverse emittance at the output of the linac will be about 10 nm rad.

ISBN: 978-3-95450-240-0 ISSN: 2673-5539 doi:10.18429/JACoW-RuPAC2021-MOPSA07

Table 2: Beam Dynamics Simulation Results at the Output of the Fourth Regular Section Depending on the Injection Phase

Parameter		Value	
Injection phase, $d\varphi$	0,75	0	-0.75
Full output energy, MeV	196.0	215.7	214.2
Output current I_{out}, mA	354.2	325.3	348.9
Transmission coefficient, %	59.0	54.2	58.2
Longitudinal losses, %	39.7	44.8	40.9
Transverse losses, %	1.2	2.6	1
Width of energy spectrum FWHM, %	±2.6	±2.2	±1.7

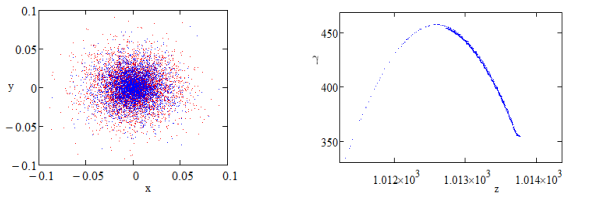

(a) (b)

Figure 6: Beam cross section (the initial distribution is shown in red, at the output - in blue) (a) and the phase portrait on the phase plane (γ, *z*) (b).

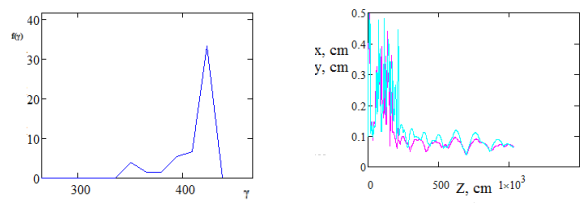

(a) (b)

Figure 7: The energy spectrum (a) and beam envelope at injection phase -0.75.

SPECTRUM OPTIMIZATION

The minimal variation of the matching gap's length *d_z* between the regular sections leads to a significant phase shift of the bunch and can be used for precise tuning of the beam energy spectrum. Variation by 1 mm at a wavelength of 107.14 mm corresponds to a change in the injection phase by 3.4 degrees. With this accelerator adjustment, it is possible to obtain a beam spectrum at the output of less than ± 1% FWHM.

Dependence of the current transmission coefficient and the spectrum width of the beam at the output of the fourth regular section on the length of the matching gap are exposed in Table 3. Phase portraits on the longitudinal phase plane (γ, *z*) and the energy spectrum after the fourth regular section, depending on the length of the matching gap are presented in Fig. 8. The average output energy also increases due to the shorter and denser bunch, which makes it possible to reduce the amplitude of the accelerating field from 450 to 410 kV/cm. This power reduction consumed by the section, and will create 5% margin for compensating for power losses in the microwave path.

Table 3: Dependence of the Current Transmission Coefficient and Beam Spectrum at the Output of the Fourth Regular Section on the Length of the Matching Map

Length of matching gap *d_z*, mm	Average beam energy, MeV	Transmission coefficient %	Width of the energy spectrum FWHM, %
164	225.7	54.7	±0.88
165	230.2	54.3	±1.85
166	228.9	54.1	±2.44

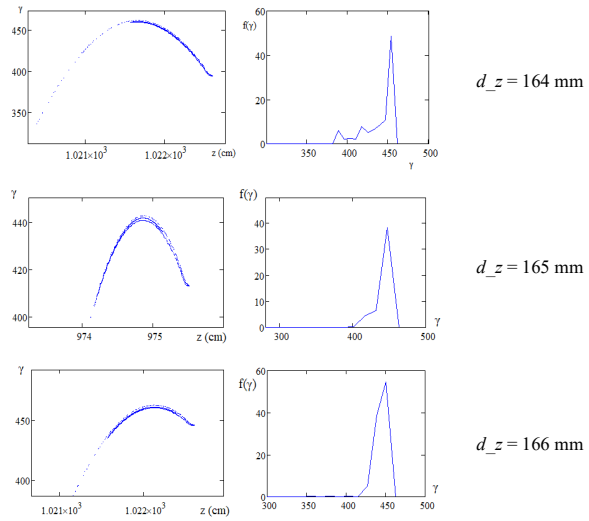

Figure 8: Phase portraits on the phase plane (γ, *z*) and the energy spectrum after the six regular section, depending on the length of the matching gap.

CONCLUSION

It was proposed to use BAS structures in regular part of the KSRS-2 injection linac and to reach the beam energy of 200 MeV, it will be necessary to use four regular sections. Fine tuning of the length of the matching gap between the sections provide to a significant improvement of the spectrum (less than ± 1% FWHM). The total "front-to-end" beam current transmission coefficient is about 58%, which, at an injection current of 600 mA, makes it possible to obtain at the output about 350 mA of a beam accelerated to the maximum energy.

ACKNOWLEDGMENT

Project is realized according to the NRC Kurchatov Institute, Order № 2212 of the 23.10.2020 entitled "Modernization project of Kurchatov synchrotron radiation source" carried out within the framework of the R&D thematic plan of NRC Kurchatov University.

ISBN: 978-3-95450-240-0 ISSN: 2673-5539 doi:10.18429/JACoW-RuPAC2021-MOPSA07

REFERENCES

[1] V. Korchuganov, *et. al.*, "The status of the facilities of Kurchatov's Synchrotron Radiation Source", in *Proc. RuPAC2014*, Obninsk, Russia, Oct. 2014, paper THY02, pp. 290-292.

[2] I. Ashanin, *et. al.*, "Beam dynamics simulation in the linear accelerator used as an injector for the 4th generation Specialized Synchrotron Radiation Source SSRS-4", *Vestnik of Saint Petersburg University. App. Maths. Comp. Sci. Contr. Proc.*, vol. 15, iss. 1, pp. 126–139, 2019.

[3] E. Masunov and S. Polozov, "The new version of BEAMDULAC code for high intensity ion beam dynamics", *Prob. At. Sci. Technology, Ser. Nuc. Phy. Investigations,* vol. 3, no. 47, pp. 119-121, 2006.

[4] E. Masunov and S. Polozov, "BEAMDULAC code for numerical simulation of 3D beam dynamics in a high-intensity undulator linac", *Nucl. Instr. Meth. A*, vol. 558, pp. 184-187, 2006. doi:0.1016/j.nima.2005.11.037

[5] E. Masunov *et al.,* "Calculation of beam dynamics in traveling-wave accelerators taking account of the current load", *At. Energy*, vol. 109, no. 2, p. 106, Nov. 2010. doi:10.1007/s10512-010-9331-y

[6] E. Masunov, S. Polozov, V. Rashchikov and A. Voronkov, "Stationary and transient beam dynamics simulation results comparison for traveling wave electron linac with beam loading", *Prob. At. Sci. Technology,* vol. 4, no. 80, pp. 96-99, 2012. doi:10.21638/11702/spbu10.2019.110

ISBN: 978-3-95450-240-0 ISSN: 2673-5539 doi:10.18429/JACoW-RuPAC2021-MOPSA08

BEAM DYNAMICS SIMULATION IN A LINEAR ELECTRON ACCELERATOR – INJECTOR FOR THE 4TH GENERATION SPECIALIZED SYNCHROTRON RADIATION SOURCE USSR

I. A. Ashanin[1], S. M. Polozov[1] A. I. Pronikov[1] , Yu.D. Kliuchevskaia
National Research Nuclear University MEPhI, Moscow, Russia
[1]also at National Research Center "Kurchatov Institute" Moscow, Russia

Abstract

USSR project (Ultimate Source of Synchrotron Radiation, 4th generation synchrotron light source) is being developed in the NRC «Kurchatov Institute». This Light Source will include both storage ring and soft FEL (Free Electron Laser) and one linac with an energyof 6 GeV, which is planned to be used both for beam injection into storage ring (top-up injection) and as a high-brightness bunch driver for FEL. It is suggested to use two front-ends in this linac: RF-gun with thermionic cathode with adiabatic buncher for injection into storage ring and RF-gun with photocathode will use to generate a bunch train for FEL. The purpose of this work was to development a general layout of the top-up linac with the aim of minimize of the beam energy spread and transverse emittance at the exit and analysis the front-to-end beam dynamics in this linear accelerator.

INTRODUCTION

The 4th generation synchrotron light source called Ultimate Source of Synchrotron Radiation (USSR-4) is under construction at the moment in Russia [1-2]. New 4th generation source design will require the innovations and evolution in the domestic technologies of magnetic and vacuum systems, the solution of new problems in materials science and instrument engineering. New facilities will become one of the biggest world scientific centres conducted researches in a variety of disciplines spanning physics, chemistry, materials science, biology and nanotechnology.

General facility layout includes 6 GeV main storage ring and top-up injection linac. The top-up injection scheme into USSR main storage synchrotron is preferable. Thus it is proposed to use the same linac with two RF-guns. First of them will RF photogun and can be used to generate the drive beam for FEL. The second one will RF-gun with thermionic cathode can be used for injection into storage ring. Such layout leads to two linacs operation modes: 6 GeV beams for injection and 6-7 GeV high-brilliance bunches for FEL. It leads to the same for-injection scheme as it was used for SuperKEK-B and MAX-IV and is proposed for FCC-ee [3-4]. Both injectors will operate with the same regular part of the linac which consists of 80-90 identical sections (see Fig. 1). The planning transverse emittance is 70-100 pm·rad. The length of the circumference of the main storage ring is about 1300 m, it will consist of 40 super periods, including two asymmetric magnetic arches and a gap of about 5 m for the placement of plugg-in devices between them.

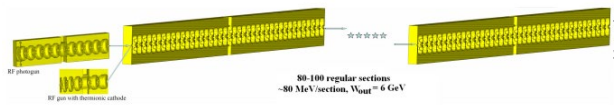

Figure 1: Expected scheme of the 6 GeV top-up injection linac.

The "front-to-end" beam dynamics simulation results in this linear accelerator will discuss in the paper.

All results of the beam dynamics simulation carried out using the BEAMDULAC package developed at the Department of Electrophysical Facilities of NRNU MEPhI [5]. The BEAMDULAC-BL code version was designed to study the beam dynamics in high-intensity electron linacs, it is discussed in detail in [6] and it was tested for a number of e-linac designs [7-8].

RF-GUN'S PARAMETERS COMPARISON

The beam dynamics simulation was done both for RF-guns with photocathode and thermionic cathode (see Table 1) [9]. The beam dynamics simulation in the RF-photogun shows that 250 pC and 10 ps bunch can be easily accelerated by 5.5-cell accelerating structure with comparatively low accelerating gradient of 600 kV/cm [10]. RF-gun with thermionic cathode is a classic adiabatic buncher consists of 26 accelerating cells and 25 coupling cells. First 4 cells are the bunching cells and the phase velocity and the RF field amplitude growth here cell-to-cell. In the other 22 cells this parameters are constant.

Table 1: Comparison of the RF-gun's Parameters

Parameter	Photogun	Thermogun
W_{inj}, keV	100	100-120
E_{acc}, kV/cm	450-600	150
W_{out}, MeV	10.5	10.3
Transmission coeff., %	100	85-90
FWHM, %	±1	±2 %
B, T	0.1	0.035

As the regular section, it is proposed to use a biperiodical accelerating structure (BAS) on a standing wave with a high coupling coefficient in the magnetic field, comparison

ISBN: 978-3-95450-240-0 ISSN: 2673-5539 doi:10.18429/JACoW-RuPAC2021-MOPSA08

of simulation results for structures on standing and travelling wave is held below.

CHOICE OF REGULAR SECTION

Simulations show that TW SLAC section can't be effectively used for injection due to such value of the energy spread and the transverse emittance which will leads to the low injection efficiency. The strong influence of the current loading does not allow accelerating more than 3-5 bunches in one pulse. Comparatively low energy spectrum was obtained in dynamics simulation of the beam at the output of SW BAS [8]. Comparison parameters are presented in Table 2. Beam dynamics simulation results are illustrated in Fig. 2.

Table 2: Comparison of the Beam Dynamics Simulation Results for Regular Part of Accelerator

Parameter	TW SLAC	SW BAS
Length, m	0.305	0.210
Energy gain, MeV/section	91	71
Number of sections	66	86
FWHM, %	±2.5	±0.9
Transverse emittance, nm·rad	1-5	0.3

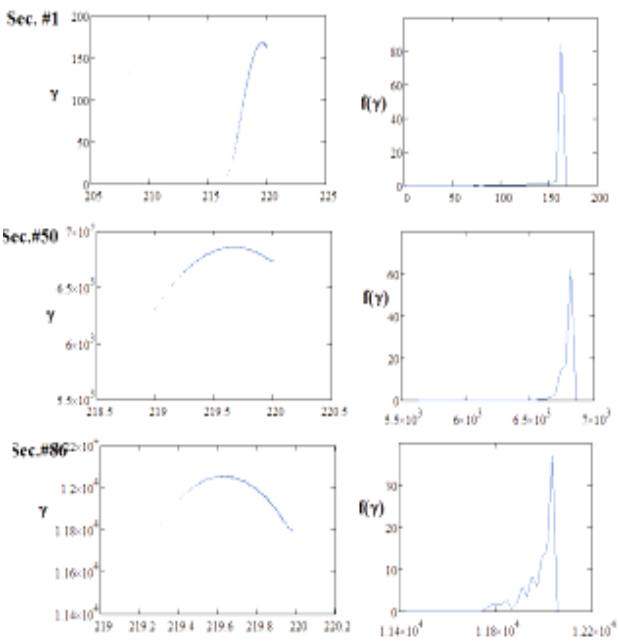

Figure 2: Beam dynamics simulation results for 40-cell BAS: longitudinal phase portraits on the phase plane (γ, z) and the energy spectrum.

ELECTRODYNAMICS CHARACTERISTICS

Regular part

The BAS structure have the following parameters: L = 53.45 cm, coupling coefficient K_{co} = 11.3%, effective shunt impedance $r_{sh.ef.}$ = 116.2 MOhm/m, Q-factor is equal 10571, group velocity is equal 0.165c, E_{max}/E_{acc} = 2.6. The simulation was carried out in the approximation that an energy of 1 J is stored in the cell. General view of regular section and electric field distribution presented in Fig. 3. Then, the optimization of the structure consisting of 10 regular periods was carried out. Q-factor was increased up to 15385 as expected. Electric field distribution of 10 section's structure presented in Fig. 4.

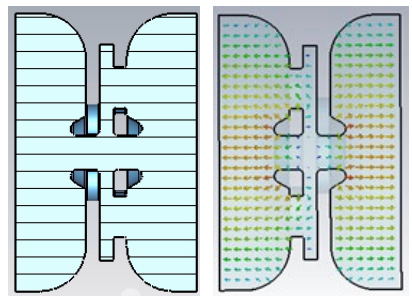

Figure 3: General view of regular section and electric field distribution.

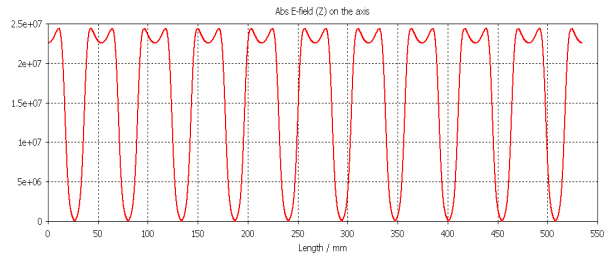

Figure 4: Electric field distribution of BAS structure consists of 10 sections.

Adiabatic Buncher

Also, simulation of the electrodynamics characteristics and optimization of the geometric parameters of the adiabatic buncher and power input were carried out. The buncher cells were configured in layouts identical to the one shown in the Fig. 5. For such cells with a variable length and electric field amplitude, the process of tuning the cells is somewhat different. Here the parameters of one accelerating half-cell are known, and the second is tuned. The ratio of the amplitudes of the accelerating fields in the middle of the half-cells was tuned by changing the solutions of the magnetic coupling gaps in the tuned cell.

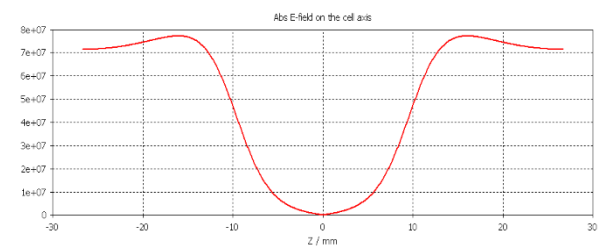

Figure 5: Longitudinal distribution of the electric field on the axis of the structure

ISBN: 978-3-95450-240-0 ISSN: 2673-5539 doi:10.18429/JACoW-RuPAC2021-MOPSA08

For each of the buncher periods, a resonant model was designed and investigated. To determine the requirements for the accuracy of manufacturing, the variation curves of dependences vs the main geometric dimensions of the each regular period were calculated (see Table 3).

Table 3: Dependences vs the Main Geometric Dimensions of the Each Regular Period

Parameter	Value
dF/dR_{ac}, MHz/mm	63.2
dF/dR_{cc}, MHz/mm	0.39
dF/dL, MHz/mm	22.5

Next, the structure, consisting of 4 bunching cells and 4.5 regular cells was optimized. General view of the structure and electric field distributions are shown in Figs. 6 and 7.

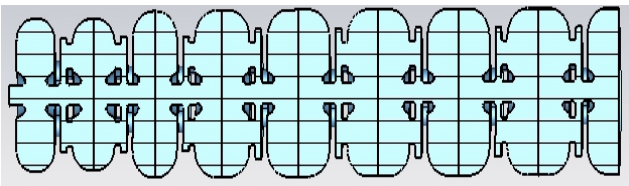

Figure 6: General view of the structure, consists of 4 bunching cells and 4.5 regular cells.

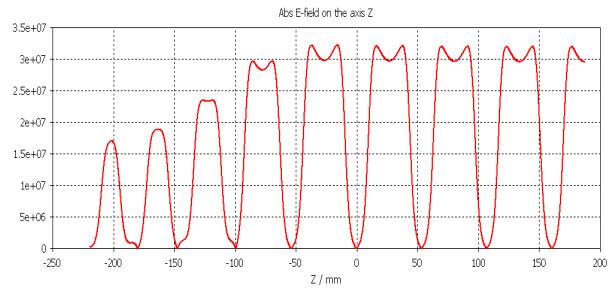

Figure 7: Electric field distribution of 4 bunching cells and 4.5 regular cells.

This structure has the following parameters: L = 407.05 cm, Q-factor is equal 14870, effective shunt impedance $r_{sh.ef.}$ = 103.8 MOhm/m.

RF power input should be injected through the 21st regular cell, therefore the tunable resonant layout consists of a power input cell and two accelerating cells on the sides. On both sides of the cell, rectangular 72x34 mm waveguides are attached for RF power input, connected to the cell by a rectangular window with a variable width.

SPECTRUM OPTIMIZATION

The beam parameters as the geometrical length of the bunch can be reduced and the energy spectrum can be decreased if use the short klystron-type pre-buncher before gentle buncher operating on the half-frequency of 1428 MHz. It was shown that such scheme allows us to control both these parameters using different lengths of short buncher and the different RF field amplitude. Such scheme also provide us also to generate bunches with different geometrical lengths or spectrum [8]. Its application makes it possible to reduce the beam energy spectrum when using RF-gun with thermionic cathode to 0.20 - 0.35%, and the bunch length to 0.8 - 1.0cm. Transverse emittance will be about 1.5 nm · rad, and the beam radius is 0.15 mm (and about 0.25 mm for (4σ)).

The beam dynamics simulation in the regular part of the linac was performed for bunches generated by ptotogun. The current transmission coefficient is near 99.5% after 82th section. In the case of a beam generated by thermogun the current transmission coefficient is near 46.5% after 86th regular section. The beam focusing system is proposed to using solenoids for energies up to 200 MeV, and triplets of quadrupole lenses for higher energies. Front-to-end beam dynamics simulation results are presented in Fig. 8.

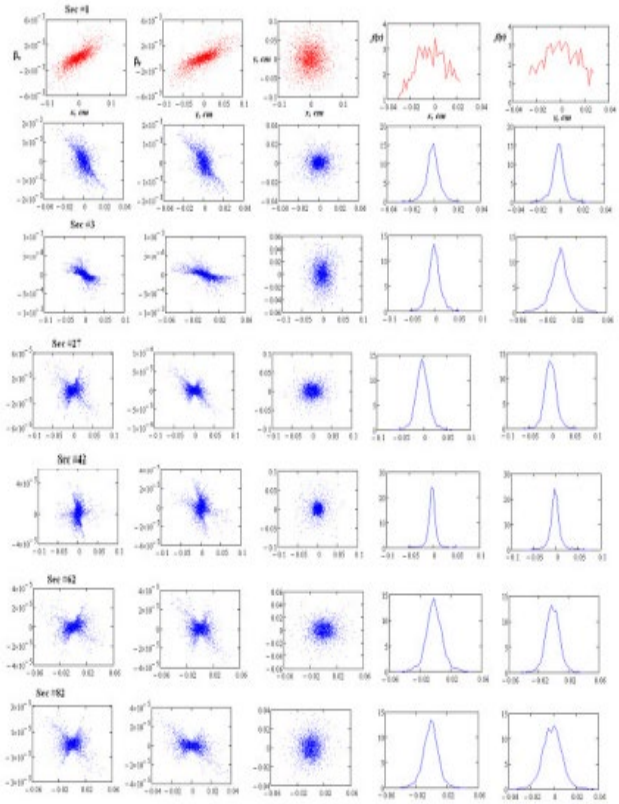

Figure 8: Front-to-end beam dynamics simulation results: beam emittances in both transverse directions, beam cross section and beam distribution along transverse coordinates.

CONCLUSION

The beam dynamics simulation results of two types of RF-gun, of two types of regular part of accelerator were described. Electrodynamics characteristics of adiabatic buncher and regular part were optimized. It was shown that the use of an additional klystron buncher before the adiabatic allows to improve and control the beam energy spectrum and length of the accelerated electron bunch. Front-to-end beam dynamics simulation from the cathode to the exit of the regular part for both variants – with photocathode and thermionic cathode was done.

ISBN: 978-3-95450-240-0 ISSN: 2673-5539 doi:10.18429/JACoW-RuPAC2021-MOPSA08

REFERENCES

[1] Ye. Fomin, V. Korchuganov, "Kurchatov synchrotron radiation source – from the 2nd to the 4nd generation", in *Proc. RUPAC'2018*, Protvino, Russia, Oct. 2018, paper WEZMH02, pp. 84-87.

[2] I. Ashanin, *et al.* "Conceptual Design of a Dedicated Fourth-Generation Specialized Synchrotron Radiation Source (SSRS-4) at the Kurchatov Institute", *Phy. At. Nuc.* vol. 8, no. 11, 2018.

[3] Y. Papaphilippou, "FCC-ee injector complex including Booster", *FCC Meeting 2016*, Rome, Italy, Apr. 2016.

[4] M. Satoh, *et al.*, "Commissioning of SuperKEKB injector linac", in *Proc. of IPAC'16*, Busan, Korea, May 2016, paper THPOY027, pp. 4152-4154.

[5] E. Masunov, S. Polozov, "BEAMDULAC code for numerical simulation of 3D beam dynamics in a high-intensity undulator linac", *Nucl. Instrum. Meth. A*, vol. 558, pp. 184-187, 2006.

[6] T. Bondarenko, E. Masunov and S. Polozov, "BEAMDULAC-BL code for 3D simulation of electron beam dynamics taking into account beam loading and coulomb field", *Prob. At. Sci. Technologies. Ser.: Nuc. Phy. Investigations,* vol. 6 no. 88, pp. 114-118, 2013.

[7] S. Polozov *et al.*, "New 10 MeV high-power electron linac for industrial application", in *Proc. of IPAC'16*, Busan, Korea, May 2016, paper TUPOW023, pp. 1794-1796.

[8] T. Bondarenko, *et al*., "Commissioning and First Tests of the New Standing Wave 10 Mev Electron Accelerator", in *Proc. of RuPAC'16*, St. Petersburg, Russia, Nov. 2016, paper TUCASH02, pp. 173-175.

[9] S. Polozov, *et. al*., Beam Dynamics Simulation Results in the 6 GeV Top-Up Injection Linac of the 4th Generation Light Source USSR, in *Proc. of RuPAC2018*, Protvino, Russia, Oct. 2018, paper WEPSB05, pp. 285-288.

[10] Yu. Kliuchevskaia and S. Polozov, "Optimal RF-photogun parameters for the new injection linac for USSR project", presented at the RuPAC'21, Alushta, Crimea, Sept.-Oct. 2021, paper TUPSB43, this conference.

ISBN: 978-3-95450-240-0 ISSN: 2673-5539 doi:10.18429/JACoW-RuPAC2021-MOPSA11

ROOM TEMPERATURE FOLDING SEGMENT FOR A TRANSFER OF MULTIPLE CHARGE STATES URANIUM IONS BETWEEN SECTIONS OF LINAC-100

V. S. Dyubkov, National Research Nuclear University MEPhI, Moscow, Russia

Abstract

Beam dynamics simulations results of multiple charge states uranium ions ($_{238}U^{59+,60+,61+}$) in a transfer line between two LINAC-100 superconducting sections of DERICA project (JINR, Dubna, Russia) are presented. Transfer line is an advanced magnetic optical system and provides beams bending on 180 degrees. Transfer line options are proposed. Parameters of its optic element are chosen so that dispersion function has zero value at the start and end of the channel for transporting the 35.7 MeV/nucleon ion beams.

INTRODUCTION

Fundamental problems such as studies of neutron matter, searching the borderline of nuclear stability in the major part of the nuclear char, studies of nuclei structure far from "stability valley" requires studies of unstable isotopes synthesized in a laboratory. For this reason a construction of radioactive isotope beam "factories" is the mainstream of the low-energy nuclear physics development. One of the mega science facilities for direct radioactive isotopes studies in electron-ion collisions is a rare isotope beam "factory" of FLNR (JINR) called "Dubna Electron-Radioactive Ion Collider fAcility" (DERICA) [1]. DERICA will consist of a number accelerators. The main of them is quasi-CW superconducting driver LINAC-100 [2, 3] that will accelerate heavy ions and will be used for secondary radioactive ion production. Two-step stripper approach is proposed for LINAC-100 [4]. Numerical simulations of uranium beam stripping shows that only 22% of initial beam intensity for one charge state of uranium ions can be obtained. In order to reach world record of beam current on the target it needs to accelerate charge states of uranium ions closed to central one that is considered to be 60. $_{238}U^{59+}$ and $_{238}U^{61+}$ ions appear in stripping the beam. Doing so one can obtain the three charge states uranium ion beam with intensity is about 60% and total beam current of about 0.6 mA under 1.1 π·mm·mrad normalized transverse beam emittance. A similar technique was used in [5].

There are two options of LINAC 100 layout nowadays. One of them the so called "serial" option, when the second LINAC-100 section is placed straight after the first one. Another one is the so called "parallel" option, when the second LINAC-100 section is placed in parallel to the first one. Diagram of the international accelerator-storage complex DERICA in the case of the "parallel" option is shown in Fig. 1. In this case folding segment (marked by I in Fig. 1) for a transfer of multiple charge states uranium ions between sections of LINAC-100 is required. One of the main restrictions for a transfer line is a demand of a zero dispersion function at the end of it. In this paper folding segment for a transfer of three charge states uranium ions between sections of LINAC-100 is presented.

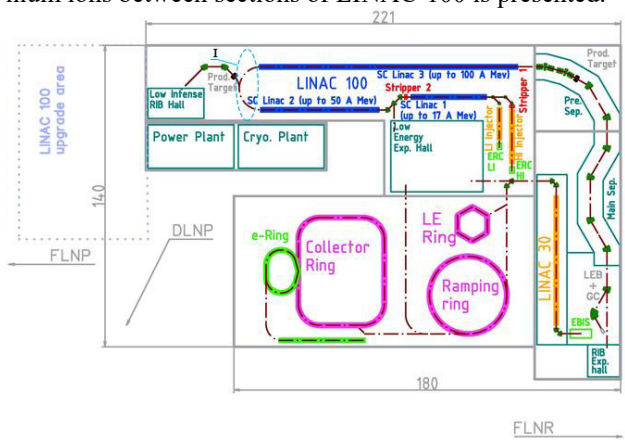

Figure 1: "Parallel" layout option of LINAC-100 for DERICA.

TRANSFER LINE DESIGN

One of a designs for DERICA folding segment was already suggested in [6]. One more option of DERICA folding segment that is called as "current mirror" is presented here. The concept of "current mirror" is widely spread in electron optics. The discussed transfer line layout is presented in Fig. 2.

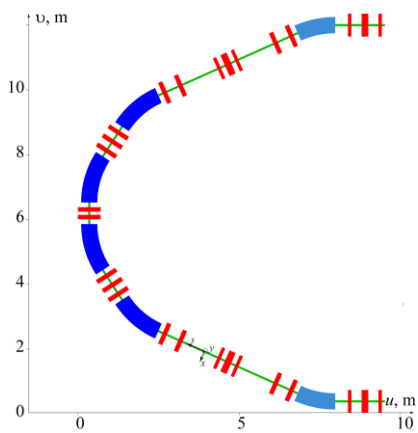

Figure 2: View of the folding segment for heavy ion transfer between sections of LINAC-100.

There are 3 families of quadrupoles and two (33° and 24°) bending magnet families in the transfer line that is a linear achromat. Main magnets parameters are presented in Table 1. Parameters were defined in order to transfer 35.7 MeV/nucleon $_{238}U^{60+}$ ions without transverse size increase and zero dispersion function at the beam exit.

ISBN: 978-3-95450-240-0 ISSN: 2673-5539 doi:10.18429/JACoW-RuPAC2021-MOPSA11

Table 1: Magnet Specifications

Type	Length, cm	Gradient/Feild
Quad type 1	10.0	12.8 T/m
Quad type 1	13.3	0.9 T/m
Quad type 1	13.3	5.3 T/m
Quad type 1	10.0	−1.2 T/m
Quad type 1	10.0	−0.9 T/m
Quad type 2	13.3	0.5 T/m
Quad type 2	13.3	−10.6 T/m
Quad type 2	13.3	−1.2 T/m
Quad type 2	13.3	−0.4 T/m
Quad type 2	13.3	−2.2 T/m
Quad type 2	13.3	−0.8 T/m
Quad type 3	20.0	0.3 T/m
Bend type 1	120.0	1.2 T
Bend type 2	150.0	1.3 T

BEAM TRANSFER SIMULATION

Self-consistent beam dynamics simulations were carried out by means of TraceWin code [7] for hard edge magnets model. Initial $_{238}U^{60+}$ beam particles distributions used for transfer simulations are shown in Fig. 3 (initial transverse beam emittances were 0.18π mm·mrad). Horizontal dispersion function for the suggested channel is presented in Fig. 4. Calculated $_{238}U^{60+}$ beam particles trajectories and its output distributions are shown in Fig. 5 and Fig. 6 correspondingly. Beam current was 0.2 mA.

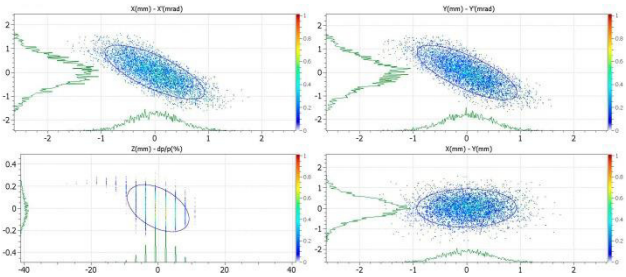

Figure 3: $_{238}U^{60+}$ beam particles distributions at the start.

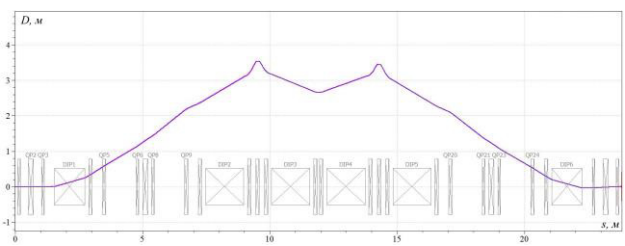

Figure 4: Dispersion function variation along beam path.

After $_{238}U^{60+}$ beam transfer simulation it was performed $_{238}U^{59+}$ and $_{238}U^{61+}$ self-consistent beams transfer simulations. Used initial $_{238}U^{59+}$ (35.3 MeV/u, 1.77 mA) and $_{238}U^{61+}$ (36.1 MeV/u, 1.83 mA) beam particles distributions are shown in Fig. 7 and Fig. 8.

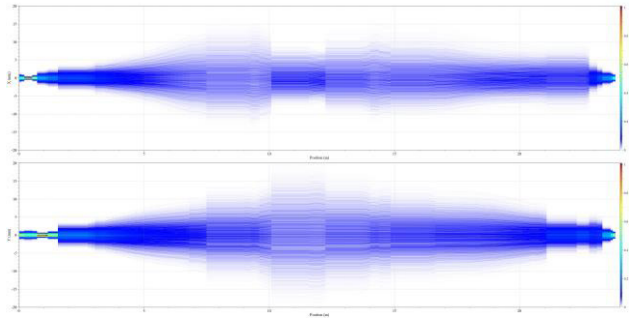

Figure 5: $_{238}U^{60+}$ beam density vs its position.

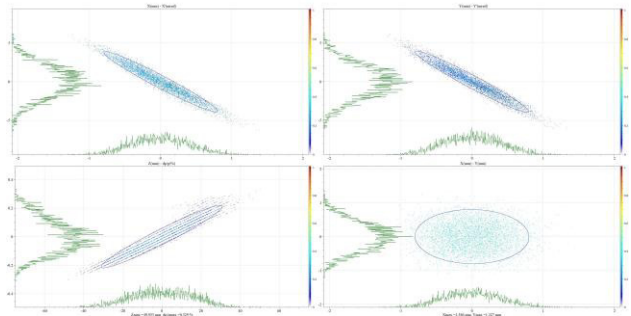

Figure 6: Output particle distribution for $_{238}U^{60+}$ beam.

Calculated results of $_{238}U^{59+}$ beam transfer throughout "current mirror" are presented in Fig. 9, Fig. 10 and Fig. 11. $_{238}U^{61+}$ beam transfer simulation results are shown in Fig. 12, Fig. 13 and Fig. 14. Dispersion function value at the channel end for the $_{238}U^{59+}$and $_{238}U^{61+}$ beam transfer is equal to 2 cm. Maximal deviations of $_{238}U^{59+}$and $_{238}U^{61+}$ beam paths from the path of $_{238}U^{60+}$ beam are ± 6 cm.

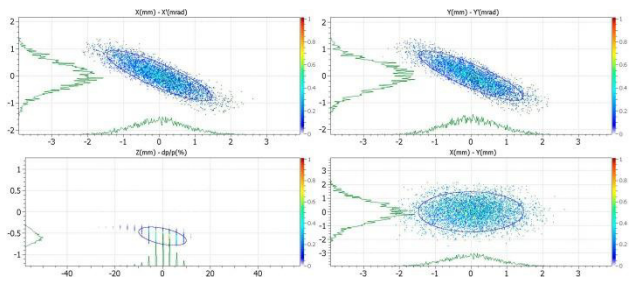

Figure 7: $_{238}U^{59+}$ beam particles distributions at the start.

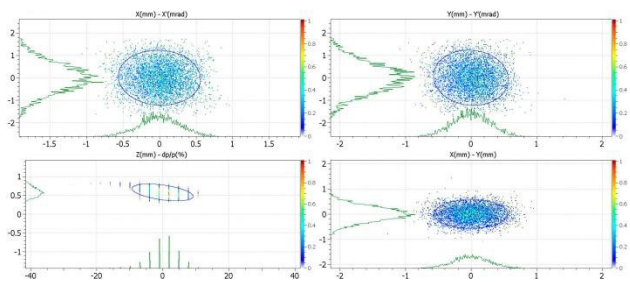

Figure 8: $_{238}U^{61+}$ beam particles distributions at the start.

There are no transverse sizes increase at channel exit for all beams under 100% transmission.

ISBN: 978-3-95450-240-0 ISSN: 2673-5539 doi:10.18429/JACoW-RuPAC2021-MOPSA11

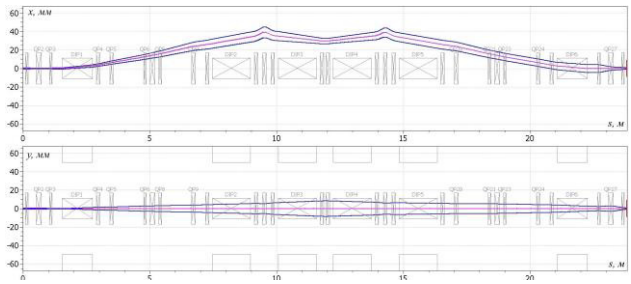

Figure 9: $_{238}U^{59+}$ beam envelopes.

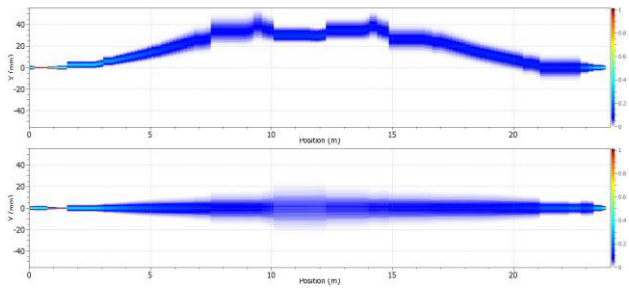

Figure 10: $_{238}U^{59+}$ beam density vs its position.

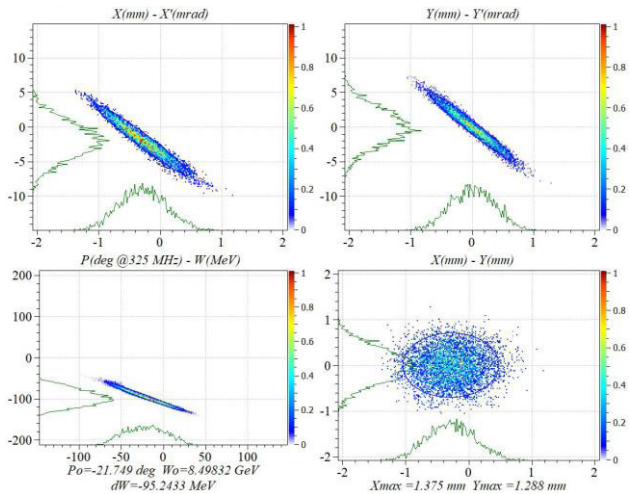

Figure 11: Output $_{238}U^{59+}$ beam particle distribution.

CONCLUSION

Room temperature folding segment for a transfer of three charge states uranium ions between sections of SC LINAC-100 is presented. Suggested transfer line design allow one locate bunchers in the channel in order to manage by beams phase spread. Note, that special care should be taken during magnets design to provide uniform magnetic field of dipoles in the horizontal plane for the region ± 6 cm near central path.

REFERENCES

[1] L.V. Grigorenko *et al.*, "DERICA Project and Strategies of the Development of Low-Energy Nuclear Physics", *Phys. Atom. Nucl.*, vol. 84, no. 1, pp. 68-81, 2021. doi:10.1134/S1063778821010099

[2] L.V. Grigorenko *et al.*, "Design of LINAC-100 and LINAC-30 for new rare isotope facility project DERICA at JINR", in *Proc. HB'18*, Daejeon, Korea, Jun. 2018, pp. 220-225. doi:10.18429/JACoW-HB2018-WEP1WB04

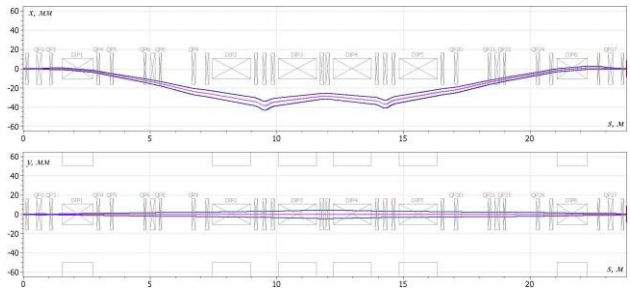

Figure 12: $_{238}U^{61+}$ beam envelopes.

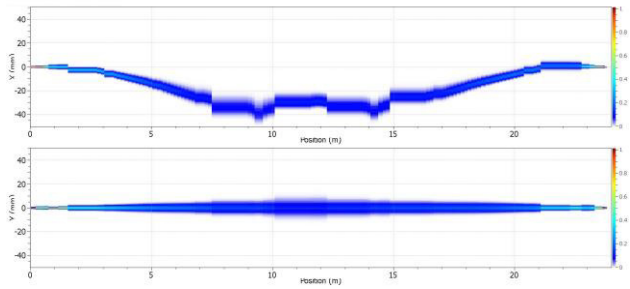

Figure 13: $_{238}U^{61+}$ beam density vs its position.

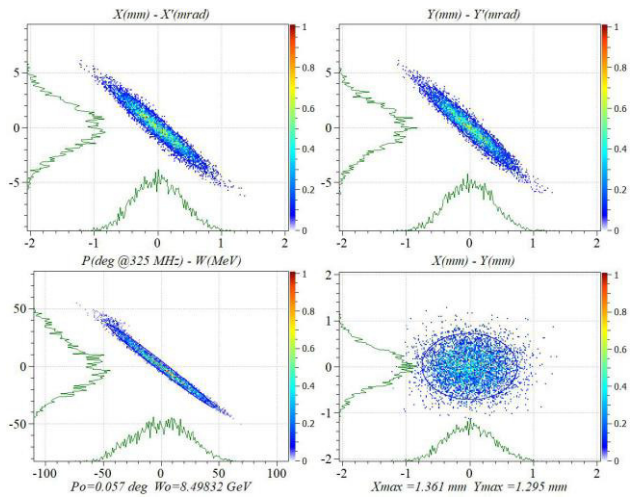

Figure 14: Output $_{238}U^{61+}$ beam particle distribution.

[3] W. Barth *et al.*, "Beam Dynamics Simulation in the LINAC-100 Accelerator Driver for the DERICA Project", *Phys. Atom. Nucl.*, vol. 82, no. 11, pp. 1519-1526, 2020. doi:10.1134/S1063778819110127

[4] W. Barth *et al.*, "Charge stripping at high energy heavy ion Linacs", *J. Phys. Conf. Ser.*, vol. 1350, pp. 012096, 2019. doi:10.1088/1742-6596/1350/1/012096

[5] P.N. Ostroumov *et al.*, "First Simultaneous Acceleration of Multiple Charge States of Heavy Ion Beams in a Large-Scale Superconducting Linear Accelerator", Phys. Rev. Lett., vol. 126, no. 11, pp. 114801, 2021. doi:10.1103/PhysRevLett.126.114801

[6] V.S. Dyubkov and V.Y. Mekhanikova, "Turning channel of uranium ions with suppressed dispersion at the edges for DERICA project", *Phys. Atom. Nucl.*, vol. 83, no. 10, pp. 1471–1477, 2020. doi:0.1134/S1063778820090070

[7] D. Uriot and N. Pichoff, "Status of TraceWin code" // in *Proc. IPAC'15*, Richmond, VA, USA, May 2014, p. 92-94. doi: 10.18429/JACoW-IPAC2015-MOPWA008

ISBN: 978-3-95450-240-0 ISSN: 2673-5539 doi:10.18429/JACoW-RuPAC2021-MOPSA13

COMPUTER SIMULATION OF THE MECHANICAL BEHAVIOR OF THE FFS SUPERCONDUCTING QUADRUPOLE COIL*

Y. Altukhov, A. Ageev, I. Bogdanov, S. Kozub, T. Ryabova, L. Tkachenko, A. Riabchikova,
NRC "Kurchatov Institute" – Institute for High Energy Physics, Protvino, Russia

Abstract

In the frame of the work, carried out at the Research Center of the Kurchatov Institute - IHEP on the development of four wide-aperture superconducting quadrupoles, a mathematical study of the mechanical behavior of the coil block of these magnets was carried out. The quadrupoles are intended for use in the magnetic final focusing system (FFS) of the ion beam in the experiments of the HED@FAIR collaboration [1, 2]. At the design stage of superconducting magnets, it is necessary to perform mathematical modeling to analyze the deformation of coil blocks during the assembly stages, cooling to operating temperature and the influence of ponderomotive forces. The results of computer simulation of changes in the geometry and distribution of forces in the coil block at all these stages are necessary to determine the value of the preliminary mechanical stress in the superconducting coil. The main results of numerical simulation of the mechanics of these magnets are presented in the article.

INTRODUCTION

An international accelerator complex for ions and antiprotons is currently being created (FAIR, Germany, Darmstadt). The HED @ FAIR collaboration will conduct new experiments to study the fundamental properties of high energy density states in matter, generated by intense beams of heavy ions. To carry out these experiments NRC "Kurchatov Institute" - IHEP creates 4 superconducting (SC) quadrupole magnets for the final focusing system (FFS) of the ion beam.

To provide a focal spot of the order of 1 mm, these magnets must have a unique combination of a high magnetic field gradient of 38 T/m and a large inner diameter of the superconducting coil of 260 mm, the operating temperature of the magnets is 4.5 K.

Significant ponderomotive forces arise in the coil of such a magnet, which can transfer it to its normal state. To prevent this transition, the coil is compressed by the bandage with a force sufficient to compensate for the ponderomotive forces. To determine this effort, it is necessary to carry out mathematical modeling of the stress-strain state of the SC coil - bandage system during manufacture and operation.

The main steps taking place with the quadrupole coil block are:

1. Creation of a pre-stressed state under pressure in the coil-bandage system.
2. Fixing the position of the bandage with a key and relieving the press load.
3. Cooling from room to operating temperature.
4. Action on the coil of ponderomotive forces when current is injected into it.

GEOMETRY QUADRUPOLE FFS

Figure 1 shows the cross section of the quadrupole FFS.

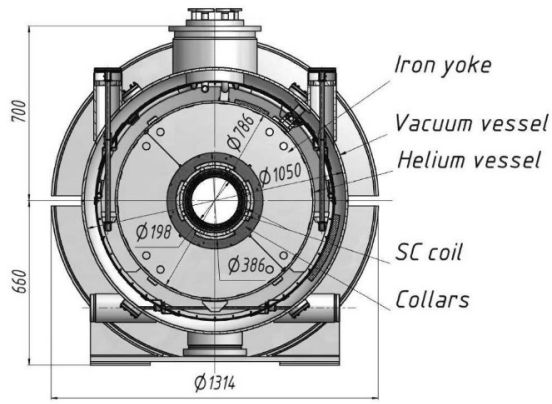

Figure 1: Cross section of the quadrupole FFS.

The main parameters of the quadrupole FFS are presented in Table 1.

Table 1: The Main Parameters of the Quadrupole FFS

Parameter	Value
Operating mode	DC
Inner diameter of the coil	260 mm
Central field gradient	37.6 T/m
Nominal current	5.73 kA
Magnetic field in the coil	5.87 T
Stored energy	1079 kJ
Vacuum vessel length	2400 mm
Vacuum vessel diameter	1400 mm
Cold mass of the quadrupole	~6.5 t
Mass of quadrupole	~10 t

The cold mass inside the helium vessel, with the help of a two-layer superconducting coil, creates a magnetic field, while significant forces arise in the coil, which are compensated by the stainless steel collars (bandage) compressing the coil. Around the collars there is an iron yoke (magnetic shield) made of electrical steel plates. A helium vessel with a cold mass is attached to a vacuum vessel by means of a suspension system; between the walls of the vacuum vessel and the walls of the helium vessel there is a heat shield cooled by a helium flow having a pressure of 13 bar and an inlet temperature of 50 K.

* Work supported by the contract between FAIR and IHEP from 19.12.2016.

ISBN: 978-3-95450-240-0 ISSN: 2673-5539 doi:10.18429/JACoW-RuPAC2021-MOPSA13

DESIGN OF THE COIL BLOCK OF THE QUADRUPOLE FFS

The design of the coil block of the FFS quadrupole consists of 4 coils, consisting of two layers of superconducting cable, which are held in a stressed state at a circular aperture by a laminated bandage. The latter is assembled from identical collars so that it forms a periodic structure with two half rings (8 collars in each) in a period. The connection between adjacent collars in one half-ring is provided by a pin. A key is used as a load-bearing element holding the upper and lower half-rings from the collars in the transverse plane.

Collars are made of stainless steel Nitronic 40. Keys, pins are made of stainless steel 316L. The separators are made of brass. The coils are made of Rutherford-type SC cable, consisting of 28 wires with a diameter of 0.85 mm, transposed at an angle of 15 degrees.

RESULTS OF CALCULATING THE MECHANICAL BEHAVIOR OF THE COIL BLOCK IN A QUADRUPOLE FFS

To study the mechanical behavior of the coil block of the FFS quadrupole, a numerical simulation was carried out with the help of computer code ANSYS [3].

The created finite element model in the first quadrant of the coil block is shown in Fig 2. The model is made in the approximation of a solid collar. Keys and pins are not taken into account.

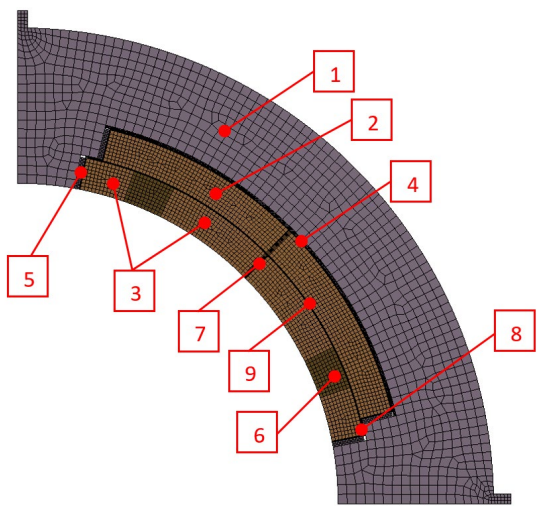

Figure 2: Finite element model in the first quadrant of the coil block. 1- collar, 2- outer coil layer, 3-inner coil layer, 4- protective metal gasket, 5- end metal gasket, 6- separator, 7- body insulation, 8- inner spacer, 9- interlayer gasket.

All contacts between parts were modeled using a sliding contact with a friction coefficient of 0.1. The calculation took into account the mechanical properties of the real superconducting coil. In particular, it was used the measured dependence of the deformation upon the stress of the superconducting coil of the quadrupole FFS, see Fig. 3.

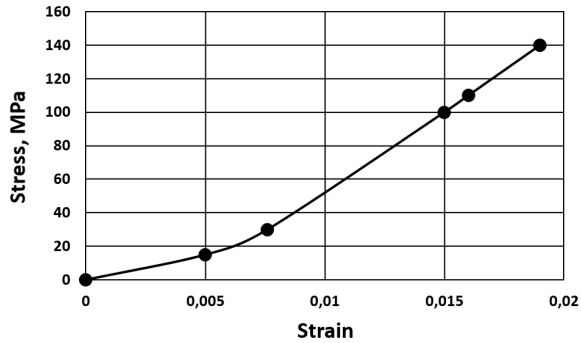

Figure 3: Strain-stress dependence of the superconducting coil of the quadrupole FFS.

Figure 4 shows the magnitude of the stress in the turns of the coil during manufacture and cooling down to 4.5 K. quadrupole FFS.

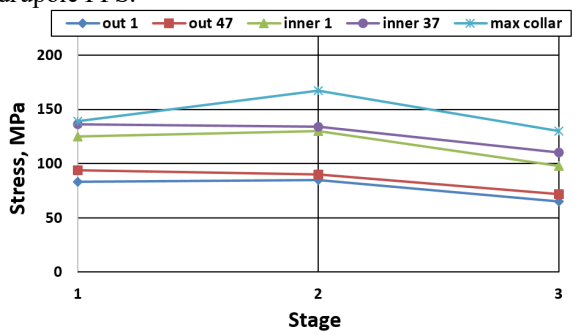

Figure 4: Stresses in the coil at various stages. 1- compression of the coil block with a press, 2- fixing the band with a key and removing the press load, 3- cooling to a temperature of 4.5 K.

RESULTS OF 2D ELECTROMAGNETIC ANALYSIS OF THE COIL BLOCK IN A QUADRUPOLE FFS

As a first approximation of the magnetic properties of the yoke material it was taken the dependence of the magnetic permeability on the magnetic induction for ARMCO steel.

The results of calculation perfomed in code ANSYS the magnetic induction at the current of 5.73 kA in the quadrupole FFS are shown in Fig. 5.

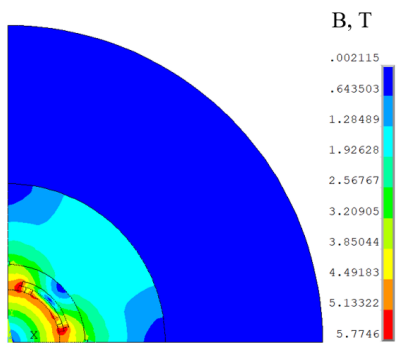

Figure 5: Distribution of magnetic induction for the current of 5.73 kA in the quadrupole FFS.

ISBN: 978-3-95450-240-0 ISSN: 2673-5539 doi:10.18429/JACoW-RuPAC2021-MOPSA13

The results of calculating the pondemotive forces at the current of 5.73 kA in the quadrupole FFS coil are shown in Fig. 6.

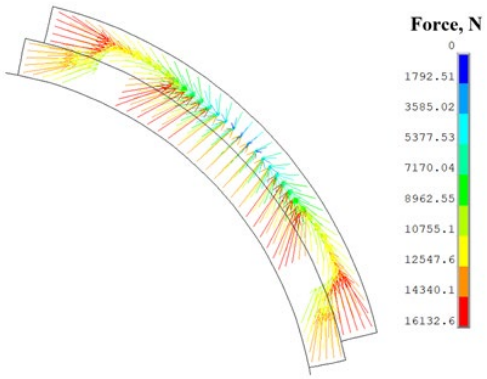

Figure 6: Distribution of pondemotive forces at the current of 5.73 kA in the coil quadrupole FFS.

On the basis of the obtained results of the electromagnetic calculation, it is planned to carry out the calculations of the stress-strain state of the structure of the coil block with the load of the coil by ponderomotive forces, taking into account the previous processes.

RESULTS OF THERMAL- MECHANICAL ANALYSIS OF HELIUM VESSEL QUADRUPOLE FFS

In the process of cooling the cold mass of the quadrupole FFS from a temperature of 290 K to 4.5 K the energy of 5.3×10^8 J must be removed. During cooling, two helium flows are used which is approximately equal in flow rate. One, external, flows through 18 peripheral channels, the other, internal, flows through an internal annular channel. The main amount of the heat of the quadrupole removed during the unsteady cooling mode is contained in the iron yoke. The outer flow is in direct contact with the yoke, whereas between the inner flow and the iron yoke there are two layers of coil with electrical insulation of the SC cable, a layer of body insulation and a layer of stainless steel collars, the thermal conductivity of which is significantly lower than the thermal conductivity of the yoke. As a consequence, the heat transfer from the iron yoke to the outer flow is much greater than the heat transfer from the same yoke to the inner flow.

Therefore, the inner tube will cool faster during the cooling process than the outer shell. As a result, tensile forces will arise in the inner tube, which, at a certain temperature difference between the shell and the inner tube, can cause irreversible deformation of the inner tube. A similar situation is observed during heating, when warm helium is supplied to the cold FFS quadrupole, and compressive forces arise in the inner tube.

In this regard, strength calculations were carried out to determine the permissible difference between the temperature of the outlet end of the outer shell (To) and the temperature of the inlet helium flow (Ti), at which the irreversible deformations in the inner pipe do not yet occurs in the processes of warming and cooling. The results of calculation for the inner tube and for the shell are shown in Fig. 7.

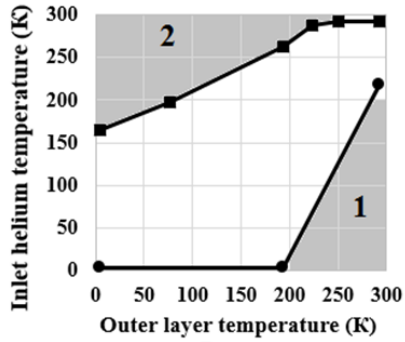

Figure 7: Admissible temperatures of the incoming helium flow Ti at cooling (●) and warming (▪) of the quadrupole as a function of the temperature To of the outlet end of the outer layer. The outer shell is 1.4436 steel, the inner tube is 1.4571 steel. 1 - region of unacceptable temperatures of the input helium flow during cooling. 2 - region of unacceptable temperatures of the input helium flow during warming.

Figure 7 shows that when cooling into a "warm" quadrupole (290 K), the flow of cold helium can be supplied with a temperature of at least 220 K. When the entire outer shell is cooled to a temperature of 280 K, the temperature of the cooling helium flow at the inlet to the quadrupole can be reduced to 190 K, etc. It also follows from this that at a temperature of the entire shell below 190 K, a helium flow can be supplied to the inlet to a quadrupole magnet with a temperature of 4.5 K.

When the cold quadrupole (T≈4.5 K) is warmed up, the initially supplied helium flow should be with a temperature not higher than 165 K. When the outer shell warmed up to 20 K, the temperature of the helium flow at the quadrupole inlet can be increased to 170 K, etc. At a temperature shell 245 K a flow of helium with ambient temperature can be supplied to the quadrupole inlet.

CONCLUSION

A model has been developed and the stress-strain state of the quadrupole FFS coil block has been calculated. The distribution of magnetic induction and ponderomotive forces in the quadrupole coil is obtained. The analysis of mechanical stresses in the helium vessel during the cooling of the superconducting of the quadrupole coil to the operating temperature is carried out and the optimal mode of this process is determined. On the basis of the calculations performed, the drawings of the quadrupole FFS were developed.

REFERENCES

[1] H. Stocker and C. Sturm, “The FAIR start”, *Nuclear Physics A*, vol. 855, pp 506-509, 2011.

[2] H.H. Gutbrod, “FAIR Baseline Technical Report”, Germany, GSI, Sep, 2006.

[3] ANSYS, http://www.ansys.com

ISBN: 978-3-95450-240-0 ISSN: 2673-5539 doi:10.18429/JACoW-RuPAC2021-MOPSA14

THE TECHNOLOGY BEHIND THE PRODUCTION OF DIFFERENT NICA COLLIDER MAGNETS

S. A. Korovkin†, H.G. Khodzhibagiyan, S.A. Kostromin, D.N. Nikiforov,
A.V. Merkurev, V.V. Borisov, M.V. Petrov, Y.G. Bespalov,
JINR, Dubna, Moscow Region, Russia

Abstract

The NICA collider magnetic system includes 70 quadrupole and 80 dipole superconducting (SC) magnets. The serial production and testing of these magnets are near to completion at the Veksler and Baldin Laboratory of High Energy Physics of the Joint Institute for Nuclear Research (VBLHEP, JINR). Manufacturing and assembly technology directly affects the quality of the magnetic field. The article describes the technology behind the production of different type of the NICA collider magnets.

INTRODUCTION

NICA (Nuclotron-based Ion Collider fAcility) is a new acceleration-storage complex. It is under construction in JINR. Collider includes 80 dipole and 70 quadrupole twin-aperture superconducting magnets [1]. The collider is designed to work with operating energies 1.0, 3.0, and 4.5 GeV / nucleon, which correspond to the operating fields of dipole magnets 0.4, 1.2 and 1.8 T, respectively. Serial Production of these magnets started at JINR in 2013 [2]. The magnet includes a cold (4.5K) window frame iron yoke and a SC winding made of a hollow NbTi composite SC cable cooled with a two-phase helium flow.

SC MAGNET PRODUCTION STAGES

The magnet production begins from the fabrication of the SC cable, which show in Fig. 1.

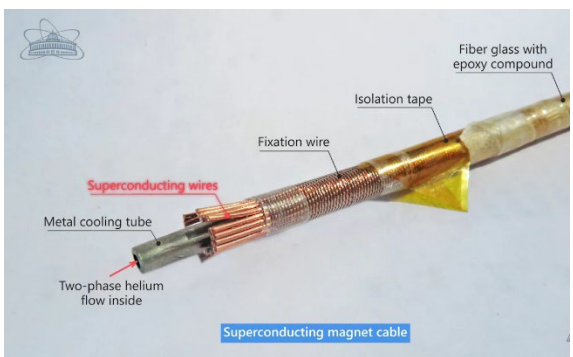

Figure 1: View of the hollow SC cable.

Superconducting wires are wrapped on a cooper- nickel tube and have with cooling tube reliable thermal contact provided by means of fixation wire. The cable is electrically insulated with Kapton tape and fiberglass tape impregnated with epoxy compound. Each SC wire contains 12600 Nb-Ti filaments of 8 microns in a copper matrix. This wire is made in Joint Stock Company "Chepetsk Mechanical Plant". The production of SC cable takes place in LHEP on a special cabling machine (see Fig. 2) when, in one pass, all SC cable components are wind.

Figure 2: Cabling machine for the manufacture of a hollow composite SC cable.

The wet cable is coil on a bobbin and is ready for SC winding production. The wet SC cable on a special rotary table is manually placed in the coil structure and wrapped with prepreg show in Fig. 3.

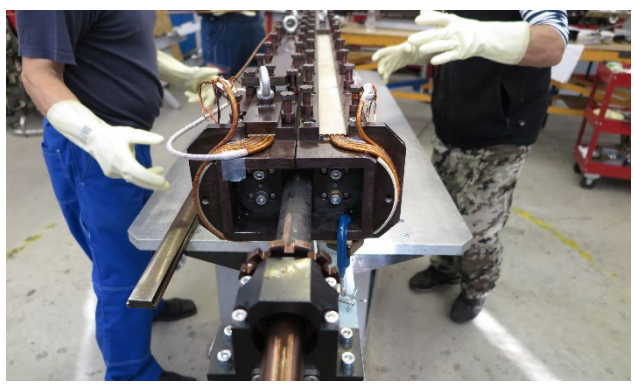

Figure 3: Equipment for baking the SC winding for the NICA collider dipole magnet.

The entire assembly is sent to an oven for baking at a specific temperature regime so that the epoxy compound polymerizes. After baking, the winding is ready for further tests, namely checking the electrical parameters and checking the geometric dimensions.

The iron yoke of the magnet consists of three parts that are bolted together. The yoke is fabricated of the laminated isotropic 0.65 mm thick electrical steel M 530. The laminations are compressed with specific pressure of 5 MPa and clamped together with stainless steel side plates 10 mm thick. The side plates are welded with laminations and 20 mm thick stainless steel end plates. After assembly and welding, yoke is processed on a high-precision machine,

† korovkins@jinr.ru

ISBN: 978-3-95450-240-0 ISSN: 2673-5539 doi:10.18429/JACoW-RuPAC2021-MOPSA14

the manufacturing accuracy is 0.02 mm. All yokes are manufactured by «Stroytekhprogress» Open Joint Stock Company. The yoke of the magnet is received from the manufacturer, after which its basic geometric parameters are checked. Further, the coil and yoke go to the assembly area, where the coil is installed in the yoke. The yoke parts are pulled together with a certain moment, the magnet strapping is mounted. The next step the magnet undergoes warm (at room temperature) magnetic measurements, rotating coil sensors show in Fig. 4.

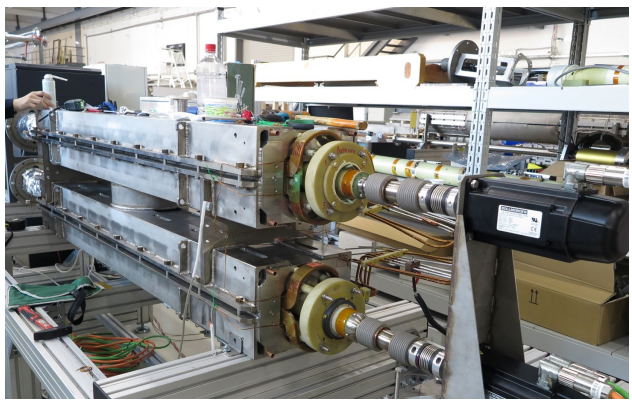

Figure 4: View of the magnetic measurements at room temperature.

The measurement system consists of two measurement shafts, each comprising three identical sections, fixed on plain bearings on the bottom yoke and driven by two servomotors. Detailed description of the magnetic measurement technique is presented in [3]. Warm magnetic measurements allow to detect defects of magnets and check build quality of magnets. The main goal of the warm magnetic measurements is assessment of the quality of the magnetic field in the gape of the magnet.

Figure 5: Preparation the magnet to cryogenic test.

After magnetic measurements, the magnet again enters the assembly site for assembling and brazing helium cooling channels of the winding and bus bars. Brazing takes place with an acetylene-oxygen torch using high-temperature solder show in Fig. 5 After brazing the helium lines, the hydraulic resistance of the helium cooling channels is measured.

The next step is to check the vacuum tightness of the cooling channels. The magnet is placing in a vacuum shell and pumped to 10^{-2} Pa. Then helium is supplied to the helium lines at a pressure of 30 bars. In the case of vacuum tightness of helium lines, the magnet is moved to the cryogenic testing area, where the thermometry and the voltage taps are mounted. Then the magnet is mounted in a vacuum shell and prepared for cryogenic tests show in Fig. 6.

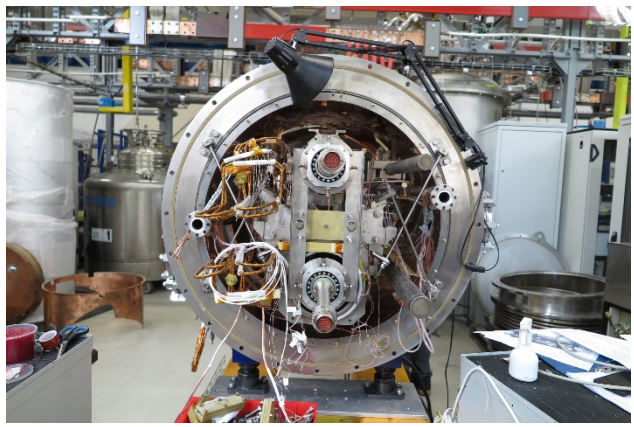

Figure 6: Assembly on a test cryostat for cryogenic testing.

After assembly on a cryogenic stand, tests of the SC magnet are started, "cold" (at 4.6 K) magnetic measurements make it possible to determine the main parameters of the SC magnets at the maximum operating current. These tests are carried out at the operating temperature of the SC magnet and maximum currents. After successfully passing the tests, the magnet is demounted from the vacuum shell and it enters the assembly area. The magnet is completely disassembled, for mounted the High-Vacuum beam pipes. Beam pipes are mounted using measuring equipment Romer Absolute Arm, preliminarily checking the geometric parameters of the beam pipe and its further installation in a SC magnet show in Fig. 7.

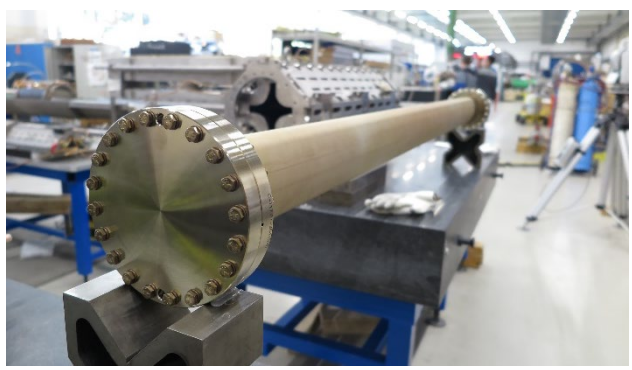

Figure 7: Checking the geometric parameters of the beam pipe and its further installation in a SC magnet.

Precision of the beam pipe mounting in magnet yoke is 0.1mm. The next step is assembling and repeat brazing of helium lines and bus bars. Brazing takes place with an acetylene-oxygen torch using high-temperature solder. After brazing is finished checking the hydraulic resistance of the helium lines of the SC magnet is measured. Again, SC magnet is placed in a vacuum shell and pumped to 10^{-2} Pa, and helium is supplied to the helium lines at a pressure of

ISBN: 978-3-95450-240-0 ISSN: 2673-5539 doi:10.18429/JACoW-RuPAC2021-MOPSA14

30 bars. After successful vacuum tests, the thermometers and the voltage taps are mounted on the magnet, and the magnet is put in a vacuum shell show in Fig. 8.

Figure 8: Assembly and preparation of magnets for shipment to the ring.

After all the checks and final tests, a conclusion is made about the suitability of the magnet and its further sent to the collider tunnel.

CONCLUSION

Manufacturing of the dipole magnets was finished. All of the dipole magnets have successfully passed the cryogenic tests and waiting for arrangement in the tunnel of the NICA Collider. 17 collider lenses are assembled and tested, it remains to test 29 lenses, 12 doublets of quadrupole lenses and produce 12 final focus lenses and 8 magnets for the beams vertical separation.

REFERENCES

[1] Technical Project of NICA Acceleration Complex,Dubna, 2015.

[2] Khodzhibagiyan H. *et al.* "Superconducting Magnets for the NICA Accelerator Collider Complex", *IEEE Trans. Appl. Superconduct.* V. 24, No. 3 P. 1–4, 2014.

[3] M. M. Shandov *et al.*, "First Serial Magnetic Measurements of the NICA Collider Twin-Aperture Dipoles", in Proc. *9th Int. Particle Accelerator Conf. (IPAC'18),* Vancouver, Canada, Apr.-May 2018, pp. 3645-3648. doi:10.18429/JACoW-IPAC2018-THPAL013

ISBN: 978-3-95450-240-0 ISSN: 2673-5539 doi:10.18429/JACoW-RuPAC2021-MOPSA15

THERMODYNAMIC CHARACTERISTICS OF THE SUPERCONDUCTING QUADRUPOLE MAGNETS OF THE NICA BOOSTER SYNCHROTRON

A.A. Bortsova, H.G. Khodzhibagiyan, D.N. Nikiforov,
Joint Institute for Nuclear Research, Dubna, Russia

Abstract

The Booster synchrotron of the NICA accelerator complex in Dubna is designed for acceleration of heavy ions before injection into the Nuclotron. The first run of the Booster synchrotron was carried out in the end of 2020. This work presents calculated and experimental data of static heat leak and dynamic heat releases for quadrupole magnets of the Booster synchrotron with different configuration of the corrector magnets. Obtained results will be taken into account for development of new superconducting magnets and cryogenic installations.

INTRODUCTION

The magnetic system of the booster synchrotron includes 40 dipole magnets, 16 doublets of quadrupole magnets with dipole corrector magnet (DCM) and 8 doublets of quadrupole magnets with multipole corrector magnet (MCM), a reference dipole and a reference doublet of quadrupole magnets.

Correction magnets are designed to correct the orbit and focus the beam. DCM consists of two dipole coils: horizontal and vertical. MCM has 4 coils: sextupole normal, octupole normal, sextupole skew and quadrupole skew.

The magnets produced at JINR are subjected to cryogenic tests, one of the main stages of which is the measurement of static heat leak and dynamic heat releases.

STATIC HEAT LEAK

The calculated total static heat input to the SC magnet is determined as the sum of the heat input by thermal radiation, thermal conductivity of residual gases and along thermal bridges.

Thermal Radiation

For the considered SC magnets, the heat leak includes radiation from the inner surface of the thermal shield at 80 K to the magnet yoke at 4.6 K and the vacuum shell at 300 K to the magnet yoke through the technological holes in the thermal shield for the magnet suspension system and the vacuum system. The heat transmitted by thermal radiation is calculated using the Stefan-Boltzmann Eq. (1) [1]:

$$Q_l = \varepsilon_n C (T_2^4 - T_1^4) A, \quad (1)$$

where ε_n – emissivity; C – Stefan-Boltzmann constant,$\mathrm{W/m^2K}$; T_2, T_1 – temperature of warm and cold surfaces; A– surface area of the thermal radiation, $\mathrm{m^2}$.

Heat Leak by Thermal Conductivity of Residual Gases

The heat leak by thermal conductivity of residual gases for vessels can be calculated using the Eq. (2) [1]:

$$Q_g = 1.82 \cdot 10^5 A_1 \frac{\alpha_1 \alpha_2}{\alpha_2 + \frac{A_1}{A_2}(1-\alpha_2)\alpha_1} \frac{k+1}{k-1} \frac{p(T_2 - T_1)}{\sqrt{MT}}, \quad (2)$$

where A_1, A_2– surface area of the inner and outer vessel, $\mathrm{m^2}$; α_1, α_2– accommodation coefficient for the first and second gas in the vessel; k – adiabatic exponent; p – vessel pressure, Pa; M – molecular weight of gas mixture; T- pressure gauge temperature, K. The mixture of nitrogen and helium is taken as the residual gas in the insulating volume of the vacuum shell.

The calculated value of the heat input by the thermal conductivity of the residual gases is 0.02 W.

Heat Along the Thermal Bridges

Static heat leak through thermal bridges is determined from the heat transfer equation:

$$Q_t = \lambda \Delta T \frac{S}{l}, \quad (3)$$

where λ – thermal conductivity coefficient, $\mathrm{W\,m^{-1}\,K^{-1}}$; S – thermal bridge cross-sectional area, $\mathrm{m^2}$; ΔT – temperature difference, K; l – thermal bridge length, m.

The SC magnets of the NICA accelerator complex are fixed in the cryostat using eight rods. After the magnet cools down to operating temperature, a large temperature gradient from 293 K to 4.5 K appears in the rods. Then the calculated static heat leak to the magnet by eight rods is 2.9 W. To reduce this value, thermal bridge to the thermal shield is provided in the design of the SC magnet (see Fig. 1), due to which the temperature gradient in the rods decreases from 82 K to 4.5 K. This reduces static heat leak to the SC magnet from 2.9 to 1 W.

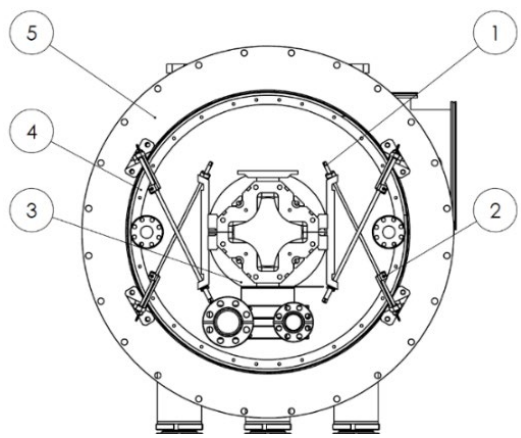

Figure 1: Quadrupole magnet of the booster synchrotron in the cryostat: 1 – rod; 2 – thermal bridge to the thermal shield; 3 – yoke of the SC magnet (4.5 K); 4 – thermal shield (82 K); 5 – vacuum chamber (293 K).

ISBN: 978-3-95450-240-0 ISSN: 2673-5539 doi:10.18429/JACoW-RuPAC2021-MOPSA15

There are copper current leads in quadrupole magnets with DCM and MCM, which are cooled by means of thermal contact with thermal shield. They bring an additional heat leak to the magnet from four DCM current leads of 0.35 W and from eight MCM current leads of 2 W.

The magnetic field in the magnets is measured using a magnetic measurement probe located in the magnet aperture. At helium temperature of the magnet, the measured value of the probe temperature is about 100 K. The calculated value of the heat leak from the magnetic measurement probe to the magnet is about 1.09 W.

The results of a comparative analysis of the calculated and average experimental values of the static heat leak for quadrupole magnets are shown in Fig. 2.

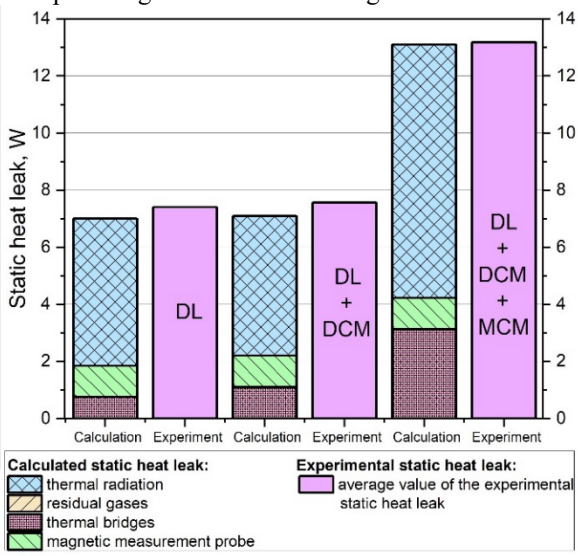

Figure 2: Comparison of the calculated and experimental value of static heat leak for different configurations of the Booster quadrupole magnets.

Figure 2 shows that the calculated and average experimental values of the static heat leak have a slight discrepancy, for quadrupole magnets with DCM – 6 %, with DCM and MCM < 1 %. The heat leak to magnets with and without DCM do not differ much from each other, which is explained by the fact that the DCM is located inside the yoke of quadrupole magnet. Thermal radiation for these configurations of the quadrupole magnet is the same. Therefore, only the DCM current leads determine the difference in static heat leaks.

DYNAMIC HEAT RELEASES

Dynamic heat releases occur in the SC coil and yoke of the magnet. By calculating the heat releases in the SC coil and measuring the total heat releases in the magnet, you can determine the amount of heat releases in the yoke. The Nuclotron type Nb-Ti hollow composite SC cable is used in the coil of the NICA booster synchrotron [2].

The main losses in the SC coil are hysteresis and eddy current losses. Hysteresis losses – magnetization reversal losses of a superconductor. It is possible to reduce the hysteresis losses by decreasing the diameter of the SC filaments. Eddy current losses – ohmic losses that appear as a result of eddy currents flowing in the stabilizing matrix inside the strand. They can be reduced by decreasing the pitch of twisting the SC filaments in the wire and by increasing the ohmic resistance of the matrix material.

The total hysteresis losses in the SC coil can be calculated for one cycle by the relation (4) [3]:

$$Q_G = \frac{8}{3\pi} J_c d_a B_m \lambda V, \quad (4)$$

where Q_G- hysteresis losses, J/cycle; J_c– critical current density, A/m^2; d_a– SC filament diameter, m; B_m – magnetic field amplitude, T; λ – volume fraction of superconducting filaments in a wire; V – wire volume, m^3. For the NICA accelerator complex $B_m = 1.8$ T, the volume fraction of superconducting filaments in the SC strand of λ =0.42. Figure 3 shows the operating cycle of the NICA booster synchrotron. The calculated value of the hysteresis losses for the cycle in Fig. 3 is 1.105 W.

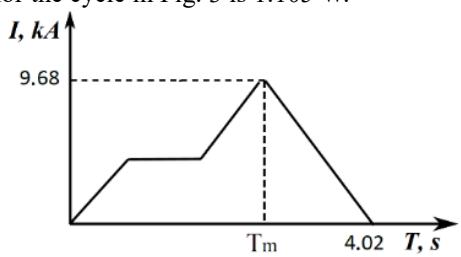

Figure 3: Operating cycle of the Booster synchrotron.

Relation (5) determines eddy current losses [3]:

$$Q_v = \frac{B_m^2}{6\mu_0}\frac{8\tau}{T_m}\lambda V, \quad (5)$$

where Q_v– eddy current losses, J/cycle; τ – time constant of stranded multifilament wire, s (during this time, the screening currents decay after the termination of the change in the external magnetic field); μ_0 – magnetic permeability of vacuum, N/A^2; T_m – field rise time, s. The calculated value of the eddy current losses for the cycle in Fig. 3 is 0.825 W.

The total value of the calculated heat releases in the SC coil is about 1.93 W.

DCM and MCM have current leads on 40 A for DCM and on 80 A for MCM. They are the main source of the dynamic heat releases for DCM and MCM. Detailed calculation and description of their production technology presented in the work [4]. The average experimental value of the dynamic heat releases for the DCM current leads is 0.42 W, and for the MCM is 1.61 W. Figure 4 shows obtained values of heat releases for the quadrupole magnets without DCM and MCM.

ISBN: 978-3-95450-240-0 ISSN: 2673-5539 doi:10.18429/JACoW-RuPAC2021-MOPSA15

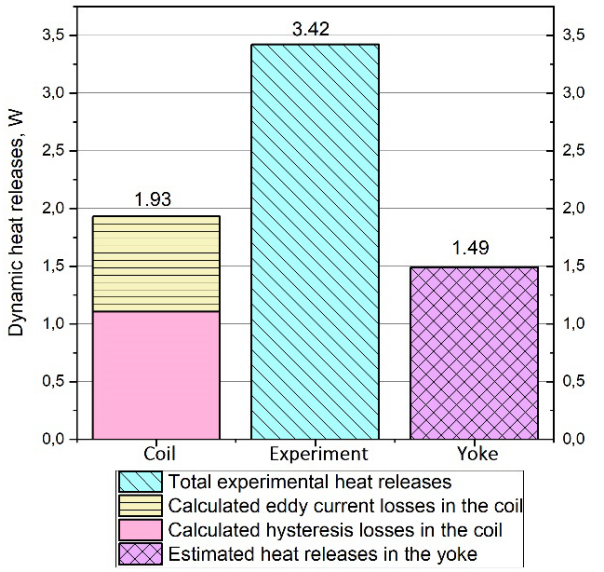

Figure 4: Dynamic heat release of the quadrupole magnets of the Booster synchrotron without DCM and MCM.

From the analysis of the data in Fig. 4 it follows that the yoke accounts for about 44 % of the total dynamic heat releases. It is also seen that hysteresis losses 32 % of the total heat release, prevail over eddy current losses, which equals 24 %.

EXPERIMENT

During cryogenic tests, using the calorimetric method (for more details in [5]), the experimental values of static heat leak and dynamic heat releases in SC magnets are determined.

The static heat leak and dynamic heat releases in the operating cycle of the booster synchrotron for magnets with DCM obtained by the calorimetric method are shown in Fig. 5.

Figure 5 shows that the experimental data have a small scatter, for static heat leak average value equals to 0.6 W and for dynamic heat releases 0.2 W. For static heat leak, this is mainly due to the duration of cooling down and the error of the calorimetric method of about 6 %. Low current leads make the main contribution to the obtained experimental data of dynamic heat releases. Because their technical characteristics have changed.

CONCLUSION

The experimental and calculated values of static heat leak and dynamic heat releases for quadrupole magnets of the Booster synchrotron are presented. The discrepancy between the calculated and experimental mean values for quadrupole magnets with DCM equals to 6 %, with DCM and with MCM <1 %. In addition, based on the analysis of the obtained data, it follows that about 44 % of the released heat falls on the yoke of the SC magnet.

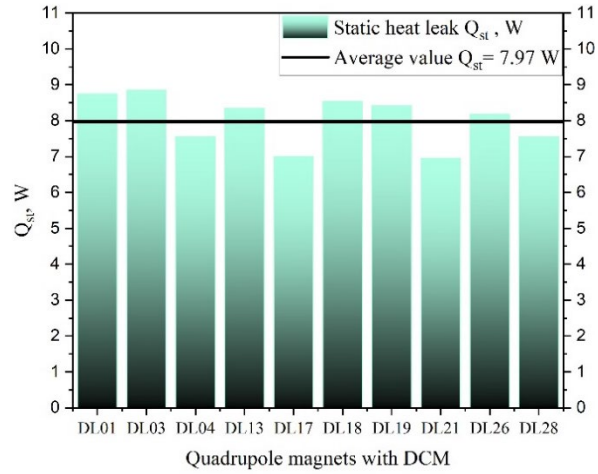

a)

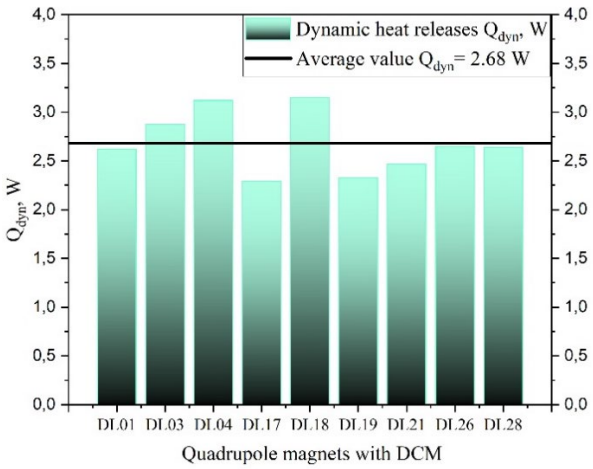

b)

Figure 5: a) Experimental values of heat leak of quadrupole magnets of the Booster synchrotron with DCM; b) Experimental values of dynamic heat releases of quadrupole magnets of the Booster synchrotron with DCM.

REFERENCES

[1] M.P. Malkov *et al.,* "Handbook of cryogenics", "Energoatomizzdat", Moscow, 1985.

[2] A.M. Baldin *et al*., "Superconducting fast cycling magnets of the Nuclotron", *IEEE Trans. Appl. Supercond.*, vol. 5, no. 2, pp. 875-877, 1995.

[3] M.N. Wilson, "Superconducting Magnets," Transl. from Eng. M.: Mir, 1985.

[4] K.V. Loshmanova, D.N. Nikiforov and S.A Smirnov, "Correction magnets for booster of complex accelerator NICA", in *Proc. 15th Cryogenics* 2019, IIR Conf., Prague, 2019. doi:10.18462/iir.cryo.2019.0012

[5] Y.G. Bespalov, *et al.,* "Measurement of static heat leak and dynamic heat releases for NICA SC magnets," in *Proc. 15th Cryogenics* 2019, IIR Conference, Prague, 2019. doi:10.18462/iir.cryo.2019.0016

ISBN: 978-3-95450-240-0 ISSN: 2673-5539 doi:10.18429/JACoW-RuPAC2021-MOPSA16

DESIGN AND CHARACTERISTICS OF CRYOSTAT FOR TESTING OF LOW-BETA 325 MHz HALF-WAVE RESONATORS

D. Bychanok[1]*, S. Huseu, E.Vasilevich, A. Sukhotski, V. Bayev, S. Maksimenko,
Research Institute for Nuclear Problems of Belarusian State University, Minsk, Belarus
M. Gusarova, M. Lalayan, S. Polozov,
National Research Nuclear University MEPhI, Moscow, Russia
A. Shvedov, S. Yurevich, V. Petrakovsky, A. Pokrovsky,
Physical-Technical Institute, Minsk, 220141, Belarus
D. Nikiforov, A. Butenko, E. Syresin, Joint Institute for Nuclear Research, Dubna, Russia
[1]also at Tomsk State University, Tomsk, Russia

Abstract

Design of the cryomodule prototype for testing low-beta 325 MHz half-wave cavities is currently in the process at INP BSU. The cryomodule allows performing intermediate vacuum-, temperature-, and rf-tests during the fabrication of half-wave resonators. The first experimental results of cryomodule cooling down to liquid nitrogen temperatures are presented and discussed. The pressure and temperature control allows us to estimate the main cooling/heating characteristics of the cryostat at different operation stages. The presented test cryomodule will be used for further development and production of superconductive niobium cavities for the Nuclotron-based Ion Collider fAcility (NICA) injector.

INTRODUCTION

The first stages of the fabrication process and properties control of superconductive cavities for high energy particle acceleration are performed at room temperature. The intermediate rf-measurements allow to control of the resonant frequency during initial "warm" tests [1]. Since the niobium-based cavities operate at liquid helium temperatures their resonant frequency significantly differs from intermediate room temperature measurements. The complexity of the half-wave resonators(HWR) geometry and a large number of welds make it difficult to estimate the shrinkage and frequency shift when the resonators are cooled to cryogenic temperatures.

The difference between the cavity's resonant frequency at room and at cryogenic temperatures is one of the most important experimental parameters related to the fabrication of resonators. To determine this parameter, it is necessary to develop a test cryostat that provides temperature and vacuum conditions close to the operational characteristics in the particle accelerator.

The test cryostats are widely used for research purposes in the manufacture of resonators [2, 3]. The present communication is devoted to the cryostat design for testing of low-beta 325 MHz half-wave resonators. In the next sections, we will discuss the main features of the cryostat design and the most important results obtained from a preliminary experiment on cooling to liquid nitrogen temperature.

* dzmitrybychanok@yandex.by

TEST CRYOSTAT DESIGN

The test cryomodule should be designed to effectively perform intermediate vacuum-, temperature- and rf-tests of HWR. Additionally, the geometrical parameters of the cryostat should provide enough space to test different types of frequency tuning systems and other support devices like power coupler, field probe antenna, etc.

The proposed concept of test cryostat consists of standard cryogenic parts [4, 5] including stainless vacuum chamber, liquid nitrogen (LN_2) inputs, liquid helium (LHe) inputs, rf inputs for cavity electromagnetic response measurements, LN_2 shield, etc. The model of the cryostat with a cavity inside is presented in Fig.1 (a-b).

In Fig.1(b) the vacuum chamber providing a protective vacuum (residual pressure ~ 10^{-6} bar) around the resonator. The main heat flux from the environment is screened by a LN_2 shield. It is cooled by a liquid nitrogen subsystem (blue pipes in Fig.1(b)). The integrated helium vessel of HWR is connected to the liquid helium subsystem (yellow pipes in Fig.1(b)). The cavity is mounted inside the cryomodule using two thin stainless steel spokes that are attached to the top cover of the cryostat. The spokes pass through the nitrogen shield and have good thermal contact with it.

The proposed system has an inner length $L = 830$ mm and an inner diameter of $D = 890$ mm. The peripheral devices (power coupler, frequency tuning system, etc.) can also be partially located in the additional volume of the side pipes.

In Fig.2 (a,b) are presented fabricated cryostat and thermal LN_2 shield inside them.

LN_2 shield was fabricated from 3mm thick aluminium type AMc. The copper pipe of the LN_2 system was brazed to the cylindrical part of the LN_2 shield to provide good thermal contact. The outer surface of the LN_2 shield was covered by multilayered thermal isolation. The shape of the copper pipe of the LN_2 system provides gaseous nitrogen to the area of cryogenic inputs on the top of the cryomodule. Vacuum, rf, and electrical inputs are located on the right side of the cryostat.

In the next section, we present the first experimental results of cryostat temperature and pressure tests.

ISBN: 978-3-95450-240-0 ISSN: 2673-5539 doi:10.18429/JACoW-RuPAC2021-MOPSA16

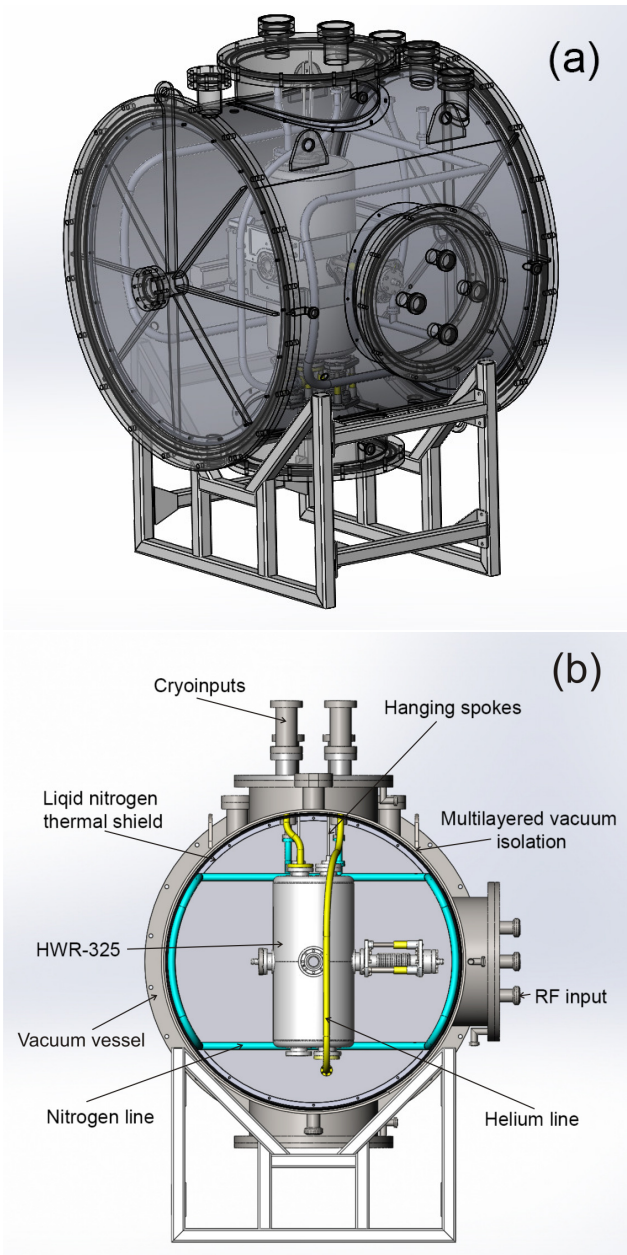

Figure 1: (a) The sketch of test cryostat model with a cavity inside, (b) the main parts and subsystems of the cryostat.

Figure 2: (a) Fabricated test cryostat, (b) the liquid nitrogen shield.

THE EXPERIMENTAL CHARACTERISTICS OF TEST CRYOSTAT

The initial experiments of cryostat temperature and pressure tests were performed without a cavity inside. In the center of the cryostat was placed the platinum resistance thermocouple. The data from this sensor was automatically saved every 3 seconds. Agilent TPS-Compact vacuum system was used for pumping out and pressure control.

The minimal achieved residual pressure inside cryostat at "warm" tests at room temperature was about $5.2 \cdot 10^{-2}$ Pa. The cooling down by adding liquid nitrogen makes it possible to reduce the residual pressure by two orders of magnitude. The minimal residual pressure achieved at temperature below 150 K was about $2.5 \cdot 10^{-4}$ Pa.

Figure 3 is presented the time dependence of temperature in the center of the cryomodule during the first LN_2 tests.

The first experiment began with evacuating air from the cryostat to the fore-vacuum level. After about 2 hours the pressure was about 0.2 Pa and liquid nitrogen began to flow smoothly into the LN_2 system. The intensive cooling at a maximal rate of about 1 degree per minute lasted for about 10 hours. Then the cooling rate was significantly slowed down. The minimal temperature achieved at first tests was -173°C. After about 18 hours the pumps and LN_2 input were

ISBN: 978-3-95450-240-0 ISSN: 2673-5539 doi:10.18429/JACoW-RuPAC2021-MOPSA16

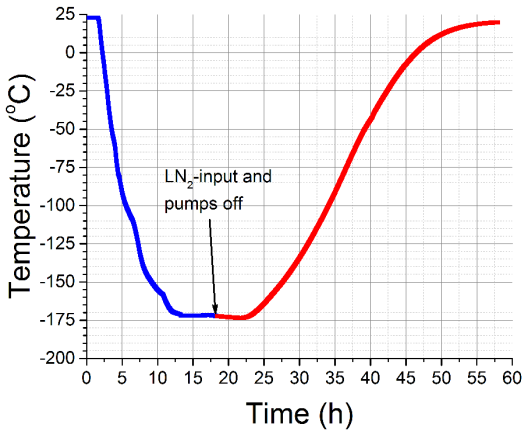

Figure 3: The time dependence of temperature in the center of the cryomodule during the first LN_2 tests.

turned off and the system began to heat up. The heating rate at the middle linear segment was about 0.15 degrees per minute. Heating time to room temperature was about 43 hours. The pressure with the pumps turned off rose to a level of about 0.3 Pa.

The minimal achieved temperature was about 22 degrees above the boiling point of liquid nitrogen. The cooling has slowed down at this point most probably due to some spaces in the multilayered insulation in the area of the end caps of the LN_2 shield. The effectiveness of the multilayer insulation, as well as their effective thermal contact with a cylindrical part, will be verified during the next tests experimentally and numerically.

CONCLUSIONS

The design of the cryostat for testing low-beta 325 MHz half-wave cavities is presented. During the first LN_2 experiments the minimal pressure $P = 2.5 \cdot 10^{-4}$ Pa and temperature $T = 173$°C in the center of cryostat were achieved after about 15 hours of cooling down. During the next steps, additional temperature sensors will be added to separate temperature control of the LN_2 shield. Also, the effectiveness of the multilayered insulation will be revised to decrease the minimal achieved temperature T. After that, the cryostat will be used for intermediate tests on the Nb prototype of HWR-325. Then the liquid helium subsystem will be developed and integrated inside. The presented results will be used for the further development and manufacturing of niobium cavities for the NICA project.

ACKNOWLEDGEMENTS

DB is thankful for support by Tomsk State University Competitiveness Improvement Program. The work was supported by JINR, Russia (Theme 02-0-1065-2007/2023 of Topical plan for JINR research and international cooperation).

REFERENCES

[1] D. Bychanok, *et al.*, "Control of elec-tromagnetic properties during prototyping, fabrication and operation of low-beta 325 MHz half-wave resonators", *J. Phys. D: Appl. Phys.*, 54(25), 255502, 2021, doi:10.1088/1361-6463/abf168.

[2] A. I. Sukhanov *et al.*, "Upgrade of the Fermilab Spoke Test Cryostat for Testing of PIP-II 650 MHz 5-Cell Elliptical Cavities", in *Proc. 19th Int. Conf. RF Superconductivity (SRF'19)*, Dresden, Germany, Jun.-Jul. 2019, pp. 1124–1128. doi:10.18429/JACoW-SRF2019-THP091

[3] J.-L. Biarrotte, S. Blivet, S. Bousson, T. Junquera, G. Olry, and H. Saugnac, "Design Study of a 176 MHz SRF Half Wave Resonator for the SPIRAL-2 Project", in *Proc. 11th Workshop RF Superconductivity (SRF'03)*, Lübeck, Germany, Sep. 2003, paper TUP02, pp. 269–273.

[4] Balshaw, N. "Practical cryogenics and introduction to laboratory cryogenics." 1996.

[5] J. G. Weisend II "Cryostat Design", Springer, 2016.

ISBN: 978-3-95450-240-0 ISSN: 2673-5539 doi:10.18429/JACoW-RuPAC2021-MOPSA17

AUTOMATED SYSTEM FOR HEATING ULTRA-HIGH VACUUM ELEMENTS OF SUPERCONDUCTING SYNCHROTRONS OF THE NICA COMPLEX

A.Sergeev, A.Butenko, A.Svidetelev, JINR, Dubna

Abstract

The Nuclotron-based Ion Collider fAcility that is under construction and commissioning in the Veksler - Baldin Laboratory for High Energy Physics of JINR contains three superconducting synchrotrons, three detectors and several beam transfer lines. All these installations and devices are equipment of high and ultra-high vacuum that requires standard procedure of preparation: preliminarily degassing the "warm" sections of the vacuum systems of the synchrotrons by prolonged heating to remove water vapor from the inner surface of the walls of the beam chamber. The heating system for the "warm" sections of the beam chambers allows one to heat up individual sections of the accelerators with minimal time spent and maximum efficiency. Due to the fact that the Booster and Collider are experimental facilities of original design, they consist of many "warm" areas. Each such element is an experimental, which has an peculiar exterior form and is made of specific composition of materials.

INTRODUCTION

The system being created allows heating elements with an unknown heat capacity and thermal conductivity, which is a very urgent task, since some of the installations are delivered without their own heating system and heating is carried out by the specialists of VBLHEP JINR directly at the place where installation is mounted.

A new method has been developed for correcting the parameters of the power supplied to the heating elements, depending on the temperature of the surface of the heated element. Since in such systems (installations) it is impossible to use high-speed proportional-integral-differentiating controllers (hereinafter PID) due to possible overheating and, consequently, destruction of installation elements due to different coefficients of thermal expansion of different interconnected elements, the algorithm is additionally used correction, which prevents overheating of individual components of the system.

FEATURES OF THE DEVELOPED SYSTEM

- Temperature control of critical elements of the heated system.
- Control of the heating process by introducing feedbacks from temperature sensors, which allows automatically, according to the set parameters of the heating process, to control the speed and intensity of heating of accelerator elements.
- The temperature control of the installation is carried out along the heated surface, which allows evenly heating parts of various shapes and lengths.
- Optimization of the heating process due to the implementation of the connection between the cabinets of different devices, which allows combining several cabinets into a single system that heats up one complex installation as a whole.
- Flexibility of controllability of system parameters, directly in the process of work (warm-up).
- The ability to exclude individual elements from the heating zones, which allows you to concentrate power on certain areas of the heated equipment.
- Automated operational control of a non-staff set of heaters or other equipment (vacuum pumps, gates, etc.).
- Automatic processing of the progress of the heating process and its results, which makes it possible to generate the final product heating certificate.

Within the framework of the NICA project, the following elements of the Booster were heated: numerous high-vacuum posts, RF stations, beam pipe, Septum.

ISBN: 978-3-95450-240-0 ISSN: 2673-5539 doi:10.18429/JACoW-RuPAC2021-MOPSA23

MACHINE LEARNING FOR THE STORAGE RING OPTIMIZATION

Ye. Fomin†, NRC "Kurchatov Institute", Moscow, Russia

Abstract

The design and optimization of new lattices for modern synchrotron radiation sources are for the most part art and highly dependent on the researcher's skills. Since both modern existing and designing storage rings is a very complex nonlinear system the researchers spend a lot of effort to solve their problems. In this work, the use of machine learning technics to improve the efficiency of solving nonlinear systems optimization problems is considered.

INTRODUCTION

There are many methods of optimization. All of them can be divided into three groups: determinate, random (stochastic), and combined. It is advisable to use algorithms from each group to solve their group of problems. Different task solving optimization efficiency using different algorithms is presented in Fig. 1.

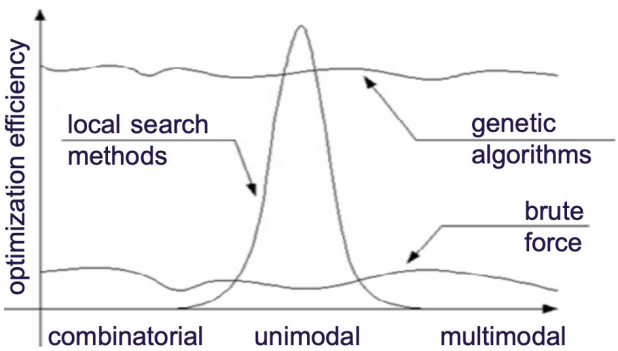

Figure 1: Different task solving optimization efficiency.

Most accelerators and synchrotron radiation sources optimization problems can be attributed to islands of combinatorial problems with many different quality solutions inside an island and between them. An exhaustive search of all solutions or an only subset of solutions is the main feature of combinatorial algorithms. To find the best solution directed, random, and combined an exhaustive search of all possible problem variables is used. Therefore, the search for proper solutions often becomes art. Because very often if you want to optimize nonlinear problem with many variable parameters and restrictions you will face serious difficulties (most rapid and effective optimization methods can't be used, there are many local minima solutions, solving time is directly related to the number of variable parameters, etc.).

So, as you can see in Fig. 1 one of the effective ways to solve multimodal and combinatorial problems within a reasonable time is the use of genetic algorithms. Genetic algorithms are heuristic search algorithms used to solve optimization problems by random selection, combining, and modification of desired parameters using a process like biological evolution. Evolution, as in nature, is an iterative process. The new population from each iteration is referred to as a "generation." The process generally starts with a population that is randomly generated and the fitness of the individuals is evaluated. Individuals with greater/smaller fitness are randomly selected, and their genomes are modified to form the next generation. The average fitness of each generation, therefore, increases/decreases with each iteration of the algorithm. Commonly, the algorithm terminates when either a maximum number of generations has been reached, or a satisfactory fitness level has been achieved for the population.

A genetic algorithm can be used to solve both constrained and unconstrained optimization problems. It likes any other optimization algorithms have their advantages and disadvantages. Their most important advantages may be said to be:

- Any information about the fitness function behavior is not required.
- Discontinuities of the fitness function don't have a significant effect on optimization.
- Methods are relatively stable to fall into local minima.

Their most important disadvantages may be said to be:

- Methods are inefficient for optimizing fitness functions that have a long calculation time.
- A large number of parameters often turns «work with genetic algorithm» to «play with genetic algorithms».
- In the case of simple fitness functions, genetic algorithms are slower than specialized optimization algorithms.

Nowadays, genetic algorithms are powerful computing tools to solve different multidimensional optimization problems. So, the use of genetic algorithms for accelerator and light source optimization allows simplifying and speeds up the search of proper solutions. That's why they have become popular in the accelerator physicist community. The common block diagram for the optimization process using genetic algorithms is shown in Fig. 2.

The long computation time of the fitness function, constraints, and discontinuities are the main features of optimization problems of modern synchrotron radiation sources. When solving this class of problems, any optimization algorithms begin to lose their effectiveness, the time to find satisfactory solutions increases dramatically, and the task of becoming practically unsolvable. To overcome these difficulties, it is necessary to simplify the original problem, divide it into subproblems, reduce the number of variables and the scope of their definition, etc. As a result, the optimization problem becomes solvable but the search time for satisfactory solutions is mainly not reduced.

† yafomin@gmail.com

ISBN: 978-3-95450-240-0 ISSN: 2673-5539 doi:10.18429/JACoW-RuPAC2021-MOPSA23

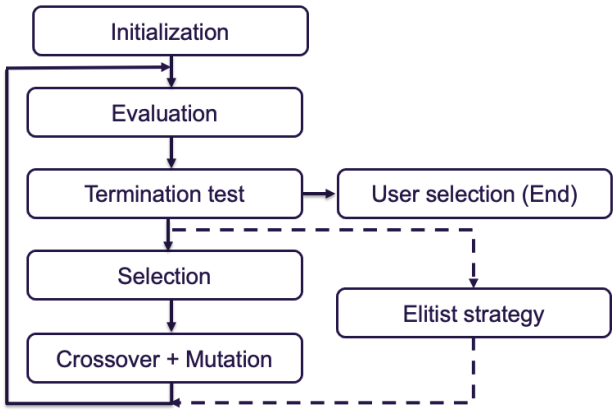

Figure 2: Diagram of the optimization process using genetic algorithms.

So, the main goal of this work is the enhancement of a genetic algorithm to increase the speed and accuracy of searching for solutions to the optimization problem for nonlinear, multidimensional, non-differentiable, multimodal functions with discontinuities in the domain of definition.

DESCRIPTION OF THE PROPOSED METHOD

A specific feature of all genetic algorithms is a lot of fitness function computations at each iteration and a lot of iterations as well. However, to create a new generation of solutions at each iteration, only the solutions obtained at the previous iteration are used. All other previously obtained solutions are no longer used. So, there is a desire to use a large data pool obtained at all previous iterations to speed up the process of solving the optimization problem. One of the best ways to do this is to use machine learning technics and intervene in the evolution process.

Here an intervention method is introduced which is schematically illustrated in Fig. 3. It includes the classification of the search space (unsupervised learning), prediction of the fitness function values (supervised learning), and selection of only potentially best solutions.

In the proposed method the differential evolution algorithm is used [1] as the main global optimization algorithm. Differential evolution uses some of the ideas of genetic algorithms but it does not require working with variables in binary code. This algorithm is simple to implement and can be easily modified anywhere. Also, the differential evolution algorithm was already successfully used to solve the optimization problem in the field of accelerator physics. See [2] for example.

Starting with randomly distributed individuals, the initial population is allowed to produce descendants via the traditional genetic algorithm. After candidates are evaluated at each iteration, all data is accumulated to intervene in the evolution process using machine learning. Next, new candidates of the next generation are created using the tools of differential evolution algorithm. But unlike the conventional approach several crossover and mutation schemes are used. So, n·m·k candidates are created, where n is the population size, m is the number of used crossover and mutation schemes and k is an adjusted integer value.

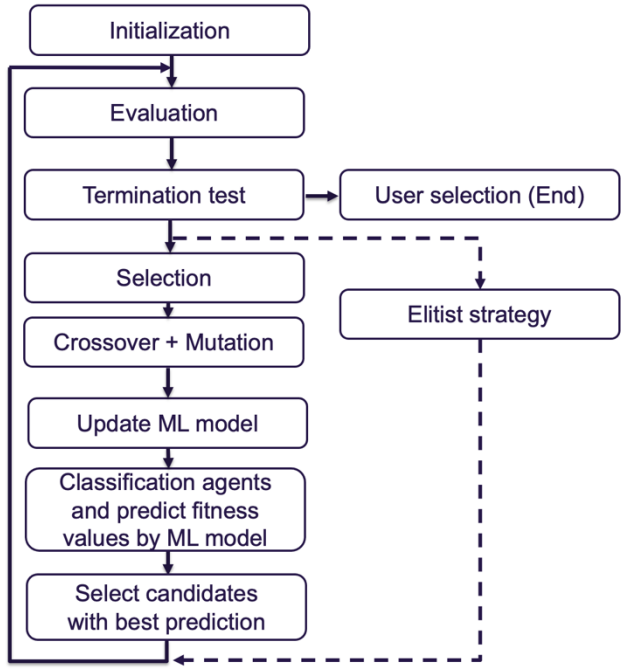

Figure 3: Diagram of the optimization process using genetic algorithms enhanced by machine learning.

On each iteration, the model representation of the fitness function is updated. This model is used to predict fitness function values for n·m·k candidates obtained in the previous step. The value predictions are performed in two steps. In the first step, all candidates are classified into two classes: good and bad. In the second step only for good candidates, the fitness function values are predicted. Next n candidates with the best fitness function values are selected and evaluated. The obtained results are accumulated in the data pool to update the machine learning model of the fitness function.

In the first step SVM [3] and k-NN [4] supervised learning models are used to classify candidates for good and bad. The final decision about the candidate class is made on the results of the two forecasts. In the second step to predict fitness function values for only good candidates the regression model based on the k-NN algorithm is used. Using this approach improves the quality of the final forecast of the fitness function values.

TEST RESULTS

Two different optimization problems are used as an example to demonstrate the application of this method. In the first example, the Rastrigin function is used [5]. This function is very interesting as a performance test problem for optimization algorithms. It is a typical example of a non-linear highly multimodal function, but locations of the minima are regularly distributed and a global minimum is known. Nevertheless, finding the global minimum of this function is a fairly difficult problem.

ISBN: 978-3-95450-240-0 ISSN: 2673-5539 doi:10.18429/JACoW-RuPAC2021-MOPSA23

A comparison of the evolution of average and minimum fitness for both cases with and without machine learning is shown in Fig. 4. In this test number of variables was 10 and the population size was 1000. So, in these conditions, the conventional differential evolution algorithm could not find the global minimum but found a close enough solution. When the differential evolution algorithm is enhanced by machine learning the situation is improving significantly. Although the global minimum is still not found, the found solution has become much better and found much faster.

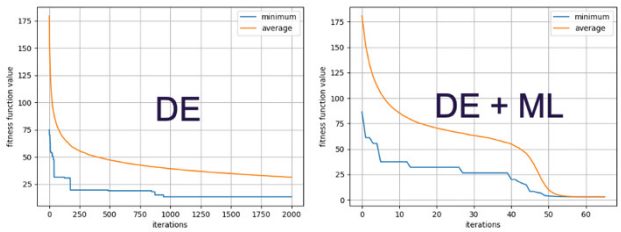

Figure 4: Comparison of the evolution of average (orange) and minimum (blue) fitness (Rastrigin function) without (left) and with (right) machine learning.

In the second example minimization of an electron beam emittance of Kurchatov synchrotron radiation source is used [6]. In this problem, the global minimum is not known and its knowledge is not advisable. Because due to physical and technical restrictions lattice with minimum emittance is not workable. So, in this test number of variables was 6 and the population size was 90 and the results look the same as in the previous test (see Fig. 5). The use of machine learning significantly speeds up the process of solving an optimization problem and allows us to find better solutions.

Note that building machine learning models at each iteration is a time-consuming process and requires significant computational resources especially when a large data pool is used. Therefore, it is not advisable to use machine learning to solve simple problems with fast-calculating fitness functions. In this case, the process of solving an optimization problem will be too long.

Other effective tools for increasing the efficiency of solving optimization problems are a reduction of the dimensionality of the search space for solutions and increasing the efficiency of analysis of the whole search space for solutions.

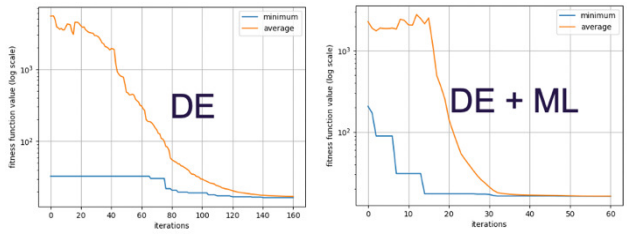

Figure 5: Comparison of the evolution of average (orange) and minimum (blue) fitness (KSRS emittance) without (left) and with (right) machine learning.

SUMMARY AND OUTLOOK

The evolution process of the genetic algorithm significantly speeds up when enhanced by machine learning. Intervention via machine learning not only speeds up evolution but increases the number of elite candidates in the data pool. Greater density of elite candidates allows for the study of the distribution of optimal candidates in the search space.

In this work, the optimizer is driven by the simulated data to realize an offline optimization. Extending it to an online mode would be the next logical step and would be driven by a real storage ring's data.

ACKNOWLEDGMENTS

The reported study was funded by RFBR, project number 19-29-12039.

REFERENCES

[1] R. M. Storn, K. Price, "Differential evolution: a simple and effective adaptive scheme for global optimization over continuous spaces", *Journal of Global Optimization*, vol. 11, pp. 341-359. doi: 10.1023/A:1008202821328

[2] Y. A. Fomin and V. N. Korchuganov, "Differential evolution algorithm for charge particle beam transfer line optic optimization," *2014 20th International Workshop on Beam Dynamics and Optimization (BDO)*, 2014, pp. 1-2. doi: 10.1109/BDO.2014.6890016

[3] https://en.wikipedia.org/wiki/Support-vector_machine

[4] https://en.wikipedia.org/wiki/K-nearest_neighbors_algorithm

[5] https://en.wikipedia.org/wiki/Rastrigin_function

[6] V. Anashin *et al.*, "The dedicated synchrotron radiation source Siberia-2", *Nucl. Instrum. Meth. A,* vol. 282, pp. 369-374, 1989. doi: 10.1016/0168-9002(89)90004-1

ISBN: 978-3-95450-240-0 ISSN: 2673-5539 doi:10.18429/JACoW-RuPAC2021-MOPSA29

APPLIED RESEARCH STATIONS AND NEW BEAM TRANSFER LINES AT THE NICA ACCELERATOR COMPLEX*

A. Slivin†, A. Agapov, A. Baldin, A. Butenko, G. Filatov, A. Galimov, S. Kolesnikov, K. Shipulin, E. Syresin, A. Tikhomirov, G. Timoshenko, A. Tuzikov, V. Tyulkin, A. Vorozhtsov, Joint Institute for Nuclear Research, Dubna, Russia
T. Kulevoy, Y. Titarenko, Institute for Theoretical and Experimental Physics of National Research Centre "Kurchatov Institute", Moscow, Russia
D. Bobrovskiy, A. Chumakov, S. Soloviev, Specialized Electronic Systems (SPELS) and National Research Nuclear University (NRNU) "MEPHI", Moscow, Russia
A. Kubankin, Belgorod State University, Belgorod, Russia
P. Chernykh, S. Osipov, E. Serenkov, Ostec Enterprise Ltd, Moscow, Russia
S. Antoine, W. Beeckman, X. Guy Duveau, J. Guerra-Phillips, P. Jehanno, A. Lancelot, SIGMAPHI S.A., Vannes, France
I. Glebov, V. Luzanov, LLC "GIRO-PROM" (GIRO-PROM), Dubna, Russia

Abstract

Applied research at the NICA accelerator complex include the following areas that are under construction: single event effects testing on capsulated microchips (energy range of 150-500 MeV/n) at the Irradiation Setup for Components of Radioelectronic Apparature (ISCRA) and on decapsulated microchips (ion energy up to 3,2 MeV/n) at the Station of CHip Irradiation (SOCHI), space radiobiological research and modelling of influence of heavy charged particles on cognitive functions of the brain of small laboratory animals and primates (energy range 500-1000 MeV/n) at the Setup for Investigation of Medical Biological Objects (SIMBO). Description of main systems and beam parameters at the ISCRA, SOCHI and SIMBO applied research stations is presented. The new beam transfer lines from the Nuclotron to ISCRA and SIMBO stations, and from HILAC to SOCHI station are being constructed. Description of the transfer lines layout, the magnets and diagnostic detectors, results of the beam dynamics simulations are described given.

INTRODUCTION

NICA (Nuclotron-based Ion Collider fAcility) is a new accelerator complex being constructed at the Laboratory of High Energy Physics of the Joint Institute for Nuclear Research [1]. Within the framework of the NICA project, it is planned to create three experimental stations for conducting of applied research with long-range ion beams extracted from the Nuclotron, and short-range ion beams extracted from the heavy ion linear accelerator (HILAC) [2].

NEW BEAM LINES IN MEASUREMENT HALL OF VBLHEP JINR

Two new areas are organized within the framework of the NICA applied research program.

Special area 1 includes beam channel (Fig. 1) to SOCHI station.

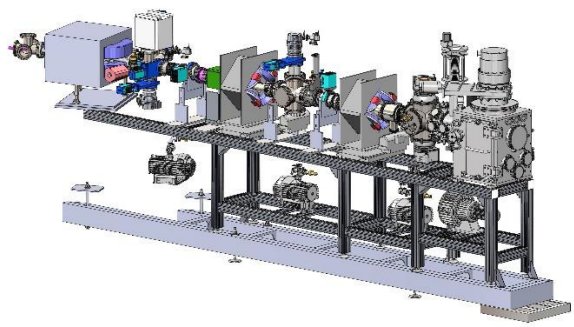

Figure 1: SOCHI beam channel design.

Special area 2 includes two beam channels to SIMBO and ISCRA stations. Beam channels are being developed as part of the JINR-SIGMAPHI collaboration. These channels will be integrated into the existing Nuclotron-to-VP-1 extraction beam line (Fig. 2).

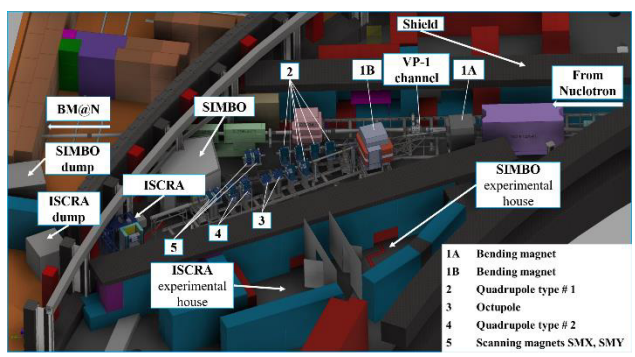

Figure 2: Area 2 infrastructure layout.

BEAM DYNAMICS SIMULATIONS

One of the main conditions required for irradiation of samples is the beam distribution homogeneity at the target area.

* Work supported by grant for young scientists. Unique id 21-102-09
† slivin@jinr.ru

ISBN: 978-3-95450-240-0 ISSN: 2673-5539 doi:10.18429/JACoW-RuPAC2021-MOPSA29

In the SOCHI channel, a 73-mm-wide beam is shaped by quadrupole magnets. The beam envelope in the SOCHI beam line is presented in [3].

In the ISCRA channel two octupole magnets are required to shape the beam profile in the non-scanning mode. The particles distribution on the target was calculated by tracking of 5×10^5 particles in the MAD-X program (Fig. 3).

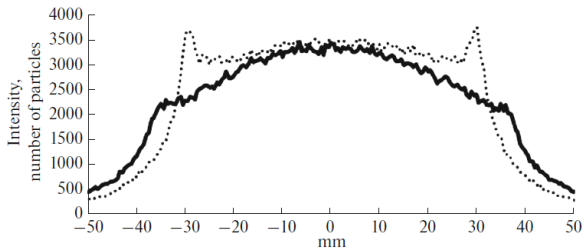

Figure 3: Transverse particle distribution in the horizontal (dotted) and vertical (solid) planes on the target as a function of transverse coordinates.

At the SIMBO station, in addition to quadrupole magnets, a collimator with an adjustable inner diameter from 10 mm to 100 mm will serve to provide a sharp boundary of the irradiation field area in both scanning and non-scanning modes.

MAGNET SYSTEM OF THE NEW BEAM LINES

In addition to the existing dipole magnets that serve to direct the beam from the Nuclotron to the channels [4], the ISCRA and SIMBO channels will be equipped with new scanning magnets, two new families of quadrupoles and new octupole magnets, see Table 1. For the SOCHI channel, two existing quadrupole magnets similar to those in the HILAC-Booster transfer line are used [5].

The detailed technical design of the new magnets has been performed and they are currently under manufacturing at SIGMAPHI. The delivery to JINR is foreseen for summer 2022.

Table 1: Main Requirements on the New Magnet for the ISCRA and SIMBO Channels

	Scanning	Quadrupole		8-pole
Parameter	**SMX/SMY**	**Type 1**	**Type 2**	
# magnets	2+2	6	2	2
Gap/bore Ø (mm)	140	108	160	105
Field/Gradient (T, T/m, T/m^3)	±0.8	0.6-5.4	0.2-1.4	1098
L_{eff} (mm)	356±4	492±2	480±2	505±3
Good Field Region (mm)	H×V 60 x 60	Ø 100	Ø 128	Ø 90
Rel. integrated field error ×10^{-3}	< ±5	< ±5	< ±5	< ±5
Operating mode	Scanning f=0.5-3 Hz	DC	DC	DC

DETECTORS

Three types of detectors will be used for beam diagnostics in the channels in the Measurement Hall: an offline multiwire proportional ionization chamber (1 pcs. 100×100 mm and 2 pcs. 75×75 mm), scintillation-fiber detector (1 pcs. 100×100 mm and 2 pcs. 75×75 mm) and two systems for online diagnostics (4 scintillation-fiber based detectors 20×20 mm). The offline systems duplicate each other to get more reliable results. The diagnostics and corrector system of the HILAC-Booster channel will be used to control the beam in the SOCHI channel [5]. Beam diagnostics in each of the channels will be in conjunction with the beam diagnostics at the stations.

The ion beam diagnostics and control systems of applied stations should be duplicated by the type of detector. All detectors should be placed on stepper motors that transversely move and withdraw detectors from the beam area. The diagnostics equipment is designed to measure and control such beam characteristics as the ion flux density, ion fluence, ion beam linear energy transfer (LET), mean energy, beam profiles, and absorbed dose [6].

SOCHI APPLIED RESEARCH STATION

The SOCHI station (Fig. 4) is designed to research and tests of promising semiconductor micro- and nanoelectronics products for determination of SEE sensitivity to low energy heavy charged particles at the exit from the HILAC.

Figure 4: General 3D view of the SOCHI station.

Table 2 shows the sufficient ion beam parameters for the planned work.

Table 2: Technical Requirements for the Ion Beams at the SOCHI Station

Ion types	$^{12}C^{4+}$, $^{40}Ar^{8+}$, $^{131}Xe^{22+}$, $^{84}Kr^{14+}$, $^{169}Tm^{21+}$, $^{197}Au^{31+}$, $^{209}Bi^{34+}$
Ion energy at the exit from the HILac, MeV/n	3,2
Ion flux density, particles/(cm^2·s)	$10^2..3\cdot10^5$
Maximum irradiation area, mm	Ø29
Beam diameter, mm	Ø73

ISBN: 978-3-95450-240-0 ISSN: 2673-5539 doi:10.18429/JACoW-RuPAC2021-MOPSA29

The equipment for the SOCHI station is being developed as part of the JINR-ITEPh collaboration with participation of SPELS/MEPHI, GIRO-PROM, VST.

The diagnostics system is represented by the following detectors: microchannel plates, system for online diagnostics and control of peripheral ion flux density and fluence (four scintillation-fiber detectors based on multichannel photomultiplier), the fast total-absorption scintillation detector with optical readout, a Faraday cup, fast total absorption phosphor screen. The signals from the detectors are integrated into the general data acquisition system.

ISCRA APPLIED RESEARCH STATION

The ISCRA station (Fig. 5) is designed to research and tests of promising semiconductor micro- and nanoelectronics products for determination of SEE sensitivity to high-energy heavy charged particles.

The equipment for the ISCRA station is being developed as part of the JINR-ITEP collaboration with participation of SPELS/MEPHI, GIRO-PROM.

Figure 5: The positioning system of the ISCRA station (left) and energy degrader (right).

Table 3 shows the sufficient parameters of the ion beam for the planned work.

Table 3: Technical Requirements for the Ion Beams at the ISCRA Station

Ion types, energy MeV/n	$^{197}Au^{79+}$	150-350
	$^{131}Xe^{54+}$	150-367
	$^{12}C^{6+}$	150-392
Ion flux density, particles/(cm2·s)	$10^2..3{\cdot}10^5$	
Irradiation area in the scanning mode/nonscanning mode, mm	200x200/Ø29	
Flux uniformity for the maximum irradiation area in the scanning mode/nonscanning mode, %	15/10	

The diagnostics system is represented by the following detectors: ionization chamber 1, proportional wire ionization chamber 2, miniature gas-filled ionization chamber 3, a scintillation-fiber detector, a silicon detector, an online particle flux density meter based on four scintillators (or four silicon detectors), the absolute measurements of the ion flux density can be performed using 0.1-mm-thick plastic foils as offline detectors at specified points.

SIMBO APPLIED RESEARCH STATION

The SIMBO station is designed for radiobiological research to simulate the effects of heavy charged particles of galactic and solar cosmic rays on the cognitive functions of lower primates and small laboratory animals.

The equipment for the SIMBO station is being developed as part of the JINR-VST collaboration.

Table 4 shows the sufficient parameters of the ion beam for the planned work.

Table 4: Technical Requirements for the Ion Beams at the SIMBO Station

Ion types	$^{12}C^{6+}$, $^{40}Ar^{18+}$, $^{56}Fe^{26+}$, $^{84}Kr^{36+}$
Ion energy at the exit from the Nuclotron, MeV/n	500-1000
Ion flux density, particles/(cm^2·s)	$10^3..10^6$
Radiation dose, Gy	1-3
Irradiation area in the scanning mode/nonscanning mode, mm	100x100/Ø10

The diagnostics system is represented by the following detectors: ionization chamber 1, ionization chamber 2, ionization chamber 3, ionization chamber 4, the thin scintillation counter, a diamond semiconductor detector, the system based on four scintillation detectors for online diagnostics and control.

The mounting and commissioning of the SOCHI station are planned for the autumn of 2021, while the ISCRA and SIMBO stations for spring 2022. First beam experiments at the SOCHI station are planned for spring 2022, experiments at the ISCRA and SIMBO stations are start to autumn 2022.

ACKNOWLEDGEMENTS

Work supported by grant for young scientists. Unique ID 21-102-09.

REFERENCES

[1] G. Trubnikov *et al.*, "Heavy ion collider facility NICA at JINR (Dubna): status and development", in *Proc. ICHEP'12*, Melbourne, Australia, July 2012, pp. 315-328. doi:10.1142/9789814508865_0042

[2] E. Syresin *et al.*, "New Nuclotron beam lines and stations for applied researches", in *Proc. 10th Int. Particle Accelerator Conf. (IPAC'19)*, Melbourne, Australia, May 2019, pp. 449-451. doi:10.18429/JACoW-IPAC2019-MOPMP013

ISBN: 978-3-95450-240-0 ISSN: 2673-5539 doi:10.18429/JACoW-RuPAC2021-MOPSA29

[3] G. Filatov *et al.*, "The beam transfer lines for electronics and radiobiology applications of the NICA project", *Proceedings of the 23rd International Scientific Conference Of Young Scientists And Specialists (Ayss-2019)*, 2019. doi:10.1063/1.5130119

[4] G. Filatov *et al.*, "New Beam Lines for Applied Research at the NICA Facility and Their Beam Dynamics", *Physics of Particles and Nuclei Letters*, vol. 17, no. 4, pp. 434–437, Jul. 2020. doi:10.1134/S1547477120040196

[5] A. Tuzikov *et al.*, "Beam Transfer From Heavy-Ion Linear Accelerator HILAC Into booster of NICA Accelerator Complex", in *Proc. 25th Russian Particle Accelerator Conf. (RuPAC'16)*, Saint-Petersburg, Russia, Nov. 2016, pp. 444–446. doi:10.18429/JACoW-RUPAC2016-WEPSB037

[6] A. Slivin *et al.*, "Development of beam diagnostics systems for applied experimental stations at VBLHEP JINR", in *Proc. AIP*, Oct. 2019, vol. 2163, pp. 080007. doi:10.1063/1.5130122

ISBN: 978-3-95450-240-0 ISSN: 2673-5539 doi:10.18429/JACoW-RuPAC2021-MOPSA39

APPLICATION OF A SCINTILLATION DETECTOR FOR PERIODIC MONITORING OF BEAM PARAMETERS AT MEDICAL PROTON THERAPY COMPLEX «PROMETHEUS»

A.E. Shemyakov†[1], M.A. Belikhin[1,2], A.A. Pryanichnikov[1,2]
Lebedev Physical Institute RAS, Physical-Technical Center, Protvino, Russian Federation
A.I. Shestopalov, Protom Ltd., Protvino, Russian Federation
[1]also at Protom Ltd., Protvino, Russian Federation
[2]also at Lomonosov Moscow State University, Accelerator Physics and Radiation Medicine Department, Moscow, Russian Federation

Abstract

In November 2015 the first domestic complex of proton therapy "Prometheus" start to treat oncology patients. This complex uses a modern technique for irradiation of tumours by scanning with a pencil beam. This technique requires continuous monitoring and regular verification of main beam parameters such as range in water, focusing and lateral dimension. To control these parameters, we developed a waterproof detector for measurements in air and in a water phantom.

The detector system consists of a luminescent screen 5 cm in diameter, a mirror and a CCD camera. When the beam goes through the screen, a glow appears, the reflected image of which is perceived by the camera and analysed. This design is waterproof, which makes it possible to perform measurements in water. To measure the range of protons in water, this detector was fixed on a special positioner, which allows to move the sensor with an accuracy of 0.2 mm. We measured the beams also in comparison with EBT3 dosimetry film for energies from 60 to 250 MeV with a step of 10 MeV. Same measurements of the ranges were carried out using a standard PTW Bragg Peak ionization chamber.

It was shown that this system is a simple and inexpensive tool for conducting regular quality assurance of beam parameters. Unlike the EBT3 dosimetry film, this detector gives an immediate response, which makes it possible to use it when debugging the accelerator and adjusting the beam.

INTRODUCTION

Proton therapy is receiving close attention from radiation oncologists around the world [1]. The research beams of large physics scientific centers adapted for medical purposes have been replaced by specialized medical proton facilities. In November 2015 the first domestic complex of proton therapy "Prometheus" start to treat oncology patients. It is the first specialized medical proton facility put into clinical operation in Russia (Fig. 1). «Prometheus» based on an original synchrotron with a diameter of 5 meters, which makes it possible to obtain proton beams with energy smoothly varying in the range of 30-330 MeV. The active scanning beam of the «Prometheus» synchrotron provides high conformity of the irradiation. This small spots can be used to build intensity modulated proton therapy treatment plans. But this benefit requires accurate tuning and quality assurance procedures of main beam parameters such as range in water, focusing and lateral dimension. For these purposes, a number of special equipment is used in radiation therapy. There are devices for determining the exact range of the particles, such as variable water column “Peakfinder” (PTW) or multi-layer ionisation chamber “Giraffe” (IBA Dosimetry). To assess the size of the beam and its symmetry, film dosimetry or scintillation screen detectors are mainly used [2-7]. All this devices have some limitations. For example, it requires scanning and processing of film dosimetry, which significantly increases the time of the study.

We developed a waterproof detector for measurements in air and in a water phantom that can be used in routine practice.The purpose of this work was to investigate the performances of own development scintillator detector with comparison of PTW Bragg Peak ionisation chamber and EBT3 film dosimetry.

Figure 1: Proton therapy facility «Prometheus».

MATERIALS AND METHODS

For calibration procedures we developed a detection system for measuring the geometric parameters of the beam spot in the energy 50-330 MeV. It consists of 50 mm diameter scintillation screen based on gadolinium oxysulfide, installed perpendicular to the proton beam, a mirror and a CCD camera (Fig. 2). The distance between the camera and the mirror is large enough to minimize the distortion of the

† alshemyakov@yandex.ru

ISBN: 978-3-95450-240-0 ISSN: 2673-5539 doi:10.18429/JACoW-RuPAC2021-MOPSA39

image. Image resolution 0.12 mm/pix. This design is waterproof to make possible to perform measurements in water. For measuring the proton range in water, this detector were fixed on a special 2D positioner, which allows to move the sensor with accuracy of 0.2 mm. The detector was preliminarily characterized in terms of stability and linearity with the delivered amount of protons in range from 3e+8 to 2e+9 protons per second.

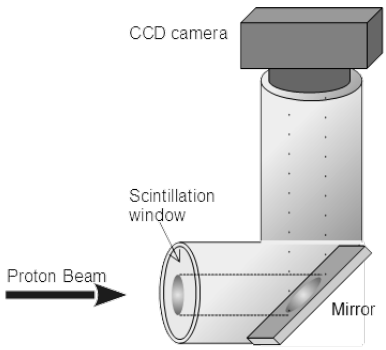

Figure 2: Scheme of scintillation detector.

To minimize induced radioactivity of materials and radiation tarnishing of scintillator and mirror, measurements in each points we performed by single 300ms proton shoot repeated 3 to 5 times to improve accuracy.

CCD camera operation synchronized with beam extraction to maximize image intensity. The signal from the camera is read by a specially developed program. In this program grayscale image is processed by median filter and colored. When the brightness center is found, which coincides with the center of the beam, the signal is approximated by a normal distribution along the horizontal and vertical axes (Fig. 3). The characteristic of the beam size is the sigma parameter of the normal distribution fitted on both axes.

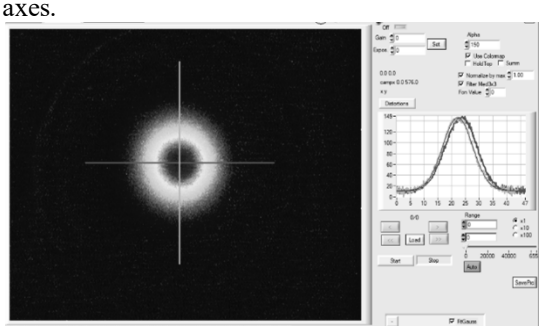

Figure 3: View of the program for beam analysis.

Beam Profile Shaping

One of the important tasks for the device is to help with adjusting the accelerator extraction channel to obtain a focused medical proton beam at the energy range of 30-330 MeV with a step of 10 MeV. Measurements performed in the isocenter of the patient's immobilization system. Figure 4 shows beam with energy 160 MeV before and after this tuning procedure. When launching a new facility and preparing for medical use, it is necessary to adjust the beam release in order to preserve the focus and symmetry of the beam in the entire range of energies used.

Adjustment performs by three quads and two pairs of horizontal and vertical correctors. Configured parameters of magnets current for each energies saved in the config file and restored when the corresponding energy is turned on.

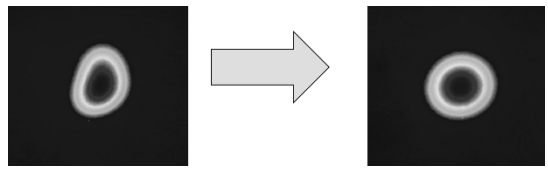

Figure 4: 160 MeV proton beam shape before and after calibration.

Accurate Beam Profile Measurements

Pencil beam technique used in «Prometheus» requires beam characteristics to be carefully assessed and periodically checked to guarantee patient safety. Main task for detector is accurate measurements of beam profile. Due to high sensitivity we can collect important parameters such as spot size in air and in water for further use of this data in the treatment planning system.

RESULTS

We measured beam size both with detector and EBT3 film for proton energies 40 to 200 MeV, see in Table 1. Unlike scintillation detector on which we used single protons shots, EBT3 film were irradiated in dose near 1Gy to have a good signal.

Table 1: Comparison of Scintillation Detector and EBT3 Film Measurements of Beam Size

E,	Detector		EBT3	
MeV	σX, mm	σY, mm	σX, mm	σY, mm
40	8.87	8.85	8.99	9.12
50	7.55	7.04	7.87	7.39
60	6.40	6.20	6.50	6.48
70	5.63	5.18	5.69	5.25
80	5.12	4.78	5.34	4.93
90	5.01	4.36	5.17	4.53
100	4.55	4.47	4.65	4.56
110	4.25	4.10	4.44	4.27
120	3.92	3.98	4.07	4.19
130	3.55	3.61	3.7	3.78
140	3.41	3.43	3.56	3.52
150	3.05	3.00	3.10	3.12
160	2.84	2.89	2.92	2.94
170	2.64	2.68	2.71	2.72
180	2.69	2.84	2.72	2.97
190	2.69	2.75	2.79	2.84
200	2.65	2.68	2.76	2.78

We took the sigma value of the Gaussian as the parameter of the beam size. Measured value ratio is shown in Fig. 5. The ratio of the values of two methods was ≤5%. Thus, size of the beam measured by EBT3 film was bigger at average 3% than the same for scintillation detector. Such

ISBN: 978-3-95450-240-0 ISSN: 2673-5539 doi:10.18429/JACoW-RuPAC2021-MOPSA39

discrepancy may be associated with the calibration of the film or caused by a higher radiation dose, in contrast to the detector.

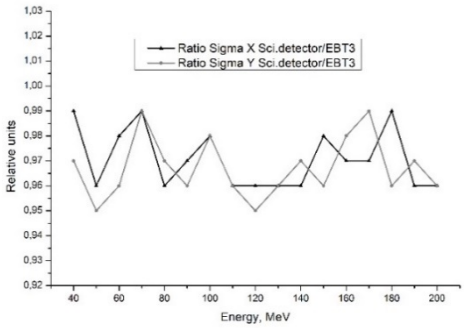

Figure 5: Ratio of measured values for beam σ at X and Y axes.

For measuring the proton range in water, this detector were fixed on 2D positioner, and pictures of the beam were measured as a function of depth in the water. By analyzing the signal amplitude of all pictures, we can determine the proton range in water with high accuracy.

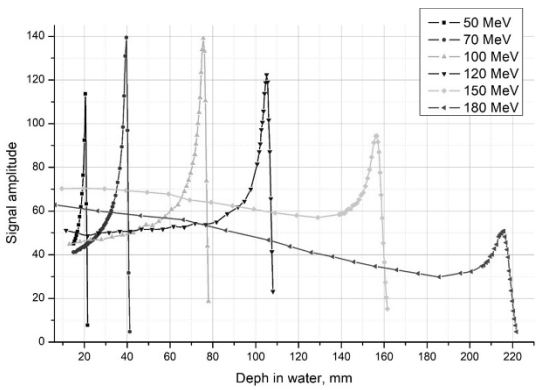

Figure 6: Bragg Peak curves measured by scintillation detector.

Figure 6 shows Bragg curves obtained by analyzing the amplitude of the signal from the scintillation detector for beams with energies 50-180 MeV. We compared this data with the same, received by PTW Bragg Peak chamber in the same water phantom. As the range of protons we used the distance to R80 – the 80 percent level behind the Bragg peak. This distance corresponds to the mean projected range of a proton, i.e. the range at which 50% of the protons have stopped. Thus, the R80 is independent of the initial energy spread of the proton beam. Differences between R80 for detector and Bragg peak ionization chamber were less than 1 mm. Figure 7 shows comparison for 150 MeV proton measurements. For this energy difference was near 0.5 mm.

CONCLUSION

Developed scintillation detector is a simple and inexpensive tool for conducting regular beam quality assurance procedures. Detector combines properties of EBT film dosimeters useful for beam shape analyses and parallel plate ionization chambers used for percentage depth dose measurements in water and proton range verification. Unlike the EBT3 dosimetry film, this detector gives an immediate response, which makes it possible to use for debugging extraction channel and adjusting the beam. The beam parameters obtained during the initial tuning and calibration of the accelerator extraction channel could be used in subsequent beam quality control procedures.

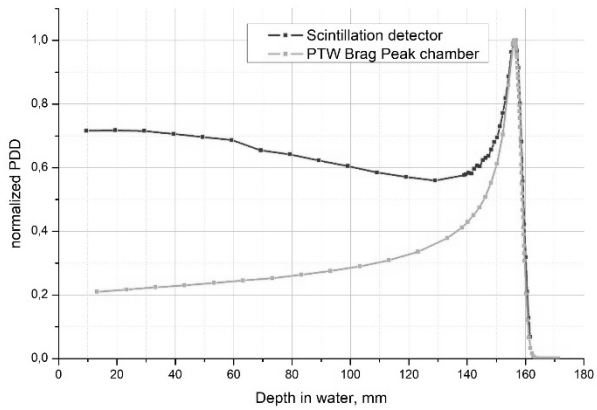

Figure 7: Depth dose curve for 150 MeV proton beam in water measured by scintillation detector and PTW Bragg Peak chamber.

REFERENCES

[1] A. P. Chernyaev *et al.*, "Proton Accelerators for Radiation Therapy", *Medical Radiology and Radiation Safety*, vol. 64, no. 2, pp. 11–22, 2019. doi:10.12737/article_5ca5a0173e4963.18268254

[2] A. A. Pryanichnikov *et al.*, "Clinical Use of the Proton Therapy Complex "Prometheus"", *Phys. Part. Nuclei Lett.* vol. 15, no. 7, pp. 981-985, 2018. doi:10.1134/S1547477118070592

[3] E. Takeshita *et al.*, "A fluorescent screen + CCD system for quality assurance of therapeutic scanned ion beams", *Nucl. Instrum. Methods Phys. Res. Sect. B.* 269 (24) pp. 2936-2940, 2011. doi:10.1016/j.nimb.2011.04.043

[4] S. Russo *et al.*, "Characterization of a commercial scintillation detector for 2-D dosimetry in scanned proton and carbon ion beams", *Physica Medica*, vol.34, pp. 48-54, 2017. doi:10.1016/j.ejmp.2017.01.011

[5] Liyong Lin *et al.*, "A novel technique for measuring the low-dose envelope of pencil-beam scanning spot profiles", *Phys. Med. Biol.* Vol. 58 n. 12, 2013. doi:10.1088/0031-9155/58/12/N171

[6] A. Mirandola *et al.*, "Dosimetric commissioning and quality assurance of scanned ion beams at the Italian National Center for Oncological Hadrontherapy", *Medical Physics*, vol. 42, iss 9, pp. 5287-5300, 2015, doi:10.1118/1.4928397

[7] C. Bäumer, "Dosimetry intercomparison of four proton therapyinstitutions in Germany employing spot scanning", *Z Med Phys.* 27(2) pp. 80-85, 2017. doi:10.1016/j.zemedi.2016.06.007

ISBN: 978-3-95450-240-0 ISSN: 2673-5539 doi:10.18429/JACoW-RuPAC2021-MOPSA40

THE PIPLAN PROTON-CARBON ION RADIATION THERAPY PLANNING SYSTEM

A. A. Pryanichnikov†[1,2], A. S. Simakov[1],
Lebedev Physical Institute RAS, Physical-Technical Center, Protvino, Russian Federation
I. I. Degtyarev, F. N. Novoskoltsev, O. A. Liashenko, E. V. Altukhova, R.Y. Sinyukov
Institute for High Energy Physics named by A.A. Logunov of NRC "Kurchatov Institute", Protvino, Russian Federation
[1]also at Protom Ltd., Protvino, Russian Federation
[2]also at Lomonosov Moscow State University,
Accelerator Physics and Radiation Medicine Department, Moscow, Russian Federation

Abstract

This paper describes the main features of newest version of the Proton-Carbon Ion Radiation Therapy Planning System (PIPLAN). The PIPLAN 2021 code was assigned for precise Monte Carlo treatment planning for heterogeneous areas, including lung, head and neck location. Two various computer methods are used to modeling the interactions between the proton and carbon ion beam and the patient's anatomy to determine the spatial distribution of the radiation physical and biological dose. The first algorithm is based on the use of the RTS&T 2021 high precision radiation transport code system. The second algorithm is based on the original Ulmer's method for primary proton beam and adapted Ulmer's algorithm designed for primary carbon ion beam with energy in the range 100-450 MeV/u.

INTRODUCTION

Today in Russia there are no heavy ion accelerators used in cancer therapy [1]. On the basis of SRC IHEP of NRC "Kurchatov institute" Accelerator Complex U-70 it is planned to create a Ion Beam Therapy Center using the 200-450 MeV/u $^{12}C^{6+}$ ion beams. Currently, a Radiobiological Workbench (RBC) U-70 was created and successfully operated It is shown in Fig. 1.

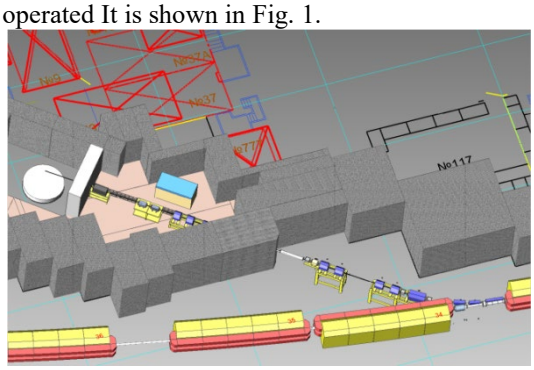

Figure 1: Layout of equipment in the RBC beam transfer line of the U-70 Accelerator Complex.

One of the important areas is the creation of a Radiotherapy Treatment Planning system. The purpose of Radiotherapy Treatment Planning systems is to estimate the dose absorbed by a patient in a radiotherapy session, so that tumors can be irradiated with the strictly necessary dose. Many publications have proved Monte Carlo techniques as a highly accurate dose calculation tool, having the only limitation of computing time cost. Several Monte Carlo based treatment planning systems have been developed and tested at the IHEP U-70 facility for carbon ion therapy. The irradiation of the water phantom has been simulated with the RTS&T and PIPLAN codes.

† pryanichnikov@protom.ru

ION BEAM TREATMENT PLANNING SYSTEM (PIPLAN 2021)

The PIPLAN 2021 Treatment Planning System consist 2 independent methods to Monte Carlo simulation the spatial distribution of the radiation physical and biological dose.

The RTS&T 2021 Precision Simulation Algorithm

The RTS&T [2] code (Radiation Transport Simulation and Isotopes Transmutation Calculation) was assigned for detailed Monte Carlo simulation of many particle types (γ, $e^{\pm}$, p, n, $\pi^{\pm}$, $K^{\pm}$, K_L^0,, antinucleons, muons, ions and etc.) transport in a complex 3D geometry's with composite materials in the energy range from a fraction eV to 20 TeV and calculation of particle fluences, radiation field functionals and isotopes transmutation problem as well. A direct using of evaluated nuclear data libraries (data-driven model) (ENDF/B, JENDL, ROSFOND, BROND, TENDL etc. - total 14 libraries) to N, d, t, ^{3}He,^{4}He particles transport and isotopes transmutation modeling in low and intermediate (E<200 MeV) energy regions is the idea of the RTS&T code construction. In general, this approach is limited by the available evaluated data to particle kinetic energies up to 20 MeV, with extensions up to 30 MeV or 200 MeV.

Adapted Ulmer's Fast Simulation Algorithm

The original Ulmer's method that is designed for incident proton beam up to 400 MeV [3] was adapted for primary carbon ion beam up to 450 MeV/u. We have developed a model for carbon ion depth dose and lateral distributions based on Monte Carlo highly accurate calculations (RTS&T 2021 code). The model accounts for the transport of primary particles, the creation of recoil pro-

ISBN: 978-3-95450-240-0 ISSN: 2673-5539 doi:10.18429/JACoW-RuPAC2021-MOPSA40

tons, secondary protons and heavy nuclei as well as lateral scattering of these contributions [4,5].

The RTS&T Geometry Module (New Version Announcement)

The current version of the RTS&T geometry module included in the RTS&T 2021 code contains a "synthetic" (combinatorial-voxel) scheme for describing the geometry of the object with a choice of the boundary localization method (analytical, iterative, or their combination). The capabilities of the geometric module allow to visualize the geometry of complex material structures of an arbitrary degree of complexity and the distribution of calculated functionals in them. The example of volumetric image is shown in Fig. 2. The example of pixel imaging in Fig. 3.

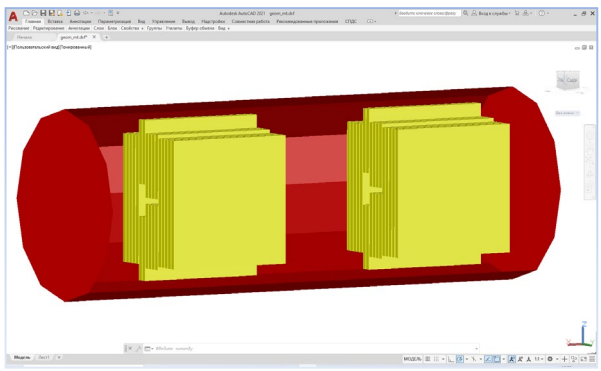

Figure 2: Volumetric image in toning mode of collimator with T-shaped profile.

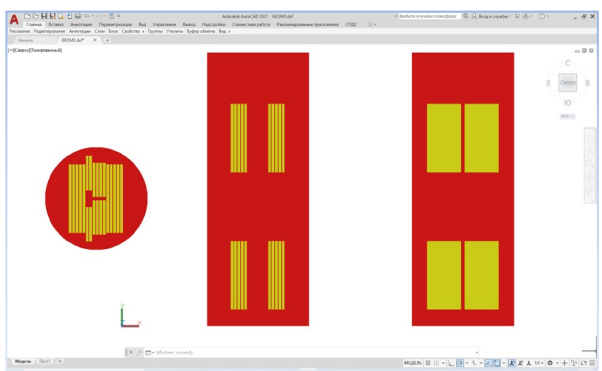

Figure 3: Pixel imaging of a collimator with a T-shaped profile.

BIOLOGICAL MODELING

The RTS&T 2021 code included a versions of the Microdosimetric Kinetic Model (MKM) [6] and Local Effect Model (LEM I-III) with 12 sets of input parameters for various lines of radiosensitive cells, that allows to calculate:

- averaged over the flow (trajectories) and absorbed dose of linear energy transfer (LET);
- relative biological radiation efficiency (RBE) for different levels of cell structure survival (S,%);
- biological dose.

DOSE DISTRIBUTION VERIFICATION

Figures 4-9 represent the results of measurements and Monte Carlo simulations of dose distribution in water phantom for monoenergetic carbon ion sources in the energy range of 200-430.1 MeV/u using the PIPLAN 2021 and RTS&T 2021 codes. In the RTS&T simulation, the CASCADE 1.0 and JQMD 2.0 hadronic generators were used for inelastic hA- and AA-events simulation. The energy losses of incident $^{12}C^{6+}$ ion were calculated using the ATIMA v.1.4.1 [7] code.

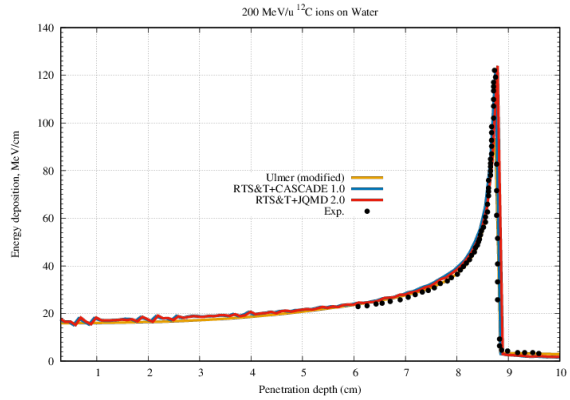

Figure 4: The total absorbed dose versus depth inside water phantom at 200 MeV/u of incident ^{12}C beam (R_{csda}=8.575 g/cm^2).

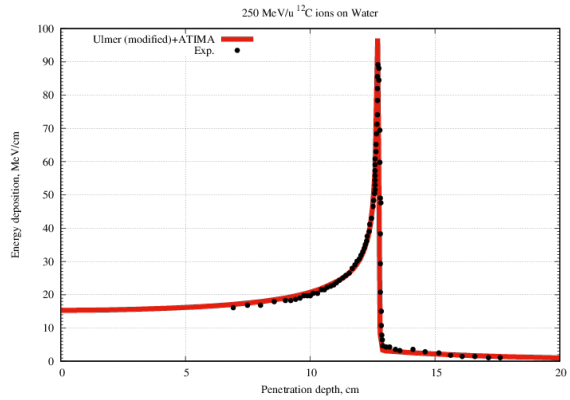

Figure 5: The total absorbed dose versus depth inside water phantom at 250 MeV/u of incident ^{12}C beam (R_{csda}=12.527 g/cm^2).

Figure 4 corresponds to ^{12}C beam energy equal 200 MeV/u, Fig. 5 corresponds 250 MeV/u. Data for carbon ion beam energy of 300 MeV/u is presented in Fig. 6. Depth-dose distribution for 350 MeV/u energy is shown in Fig. 7. The same curve for 400 MeV/u energy is shown in Fig. 8. Maximum energy for experimental data was 430.10 MeV/u, it is presented in Fig. 9. It can be seen from the figures presented above that the results of our calculations are in good agreement with the experimental data.

ISBN: 978-3-95450-240-0 ISSN: 2673-5539 doi:10.18429/JACoW-RuPAC2021-MOPSA40

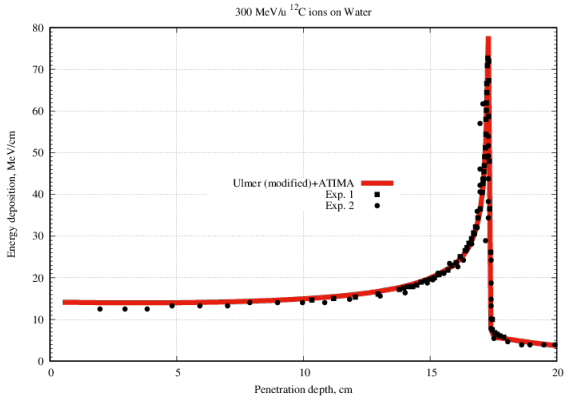

Figure 6: The total absorbed dose versus depth inside water phantom at 300 MeV/u of incident ^{12}C beam (R_{csda}=16.983 g/cm^2).

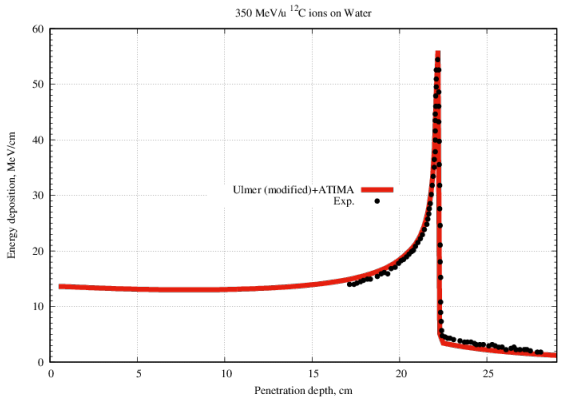

Figure 7: The total absorbed dose versus depth inside water phantom at 350 MeV/u of incident ^{12}C beam (R_{csda}=21.872 g/cm^2).

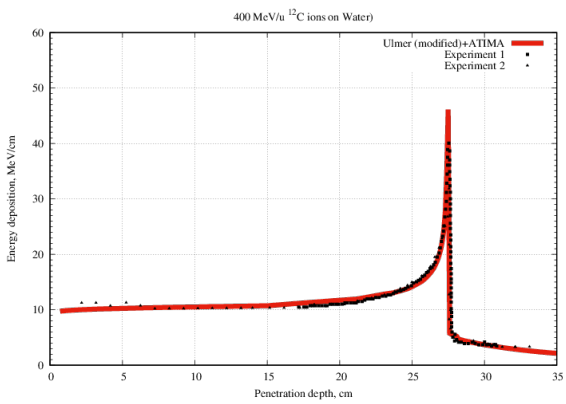

Figure 8: The total absorbed dose versus depth inside water phantom at 400 MeV/u of incident ^{12}C beam (R_{csda}=27.135 g/cm^2).

CONCLUSION

The developed PIPLAN 2021 (Proton-Ion Therapy Treatment Planning System) can be implemented in hardware and software system of Carbon-Ion Therapy Center based on the IHEP Accelerator Complex. Models that are used in PIPLAN can be implemented in already existed Russian proton therapy complexes [8, 9].

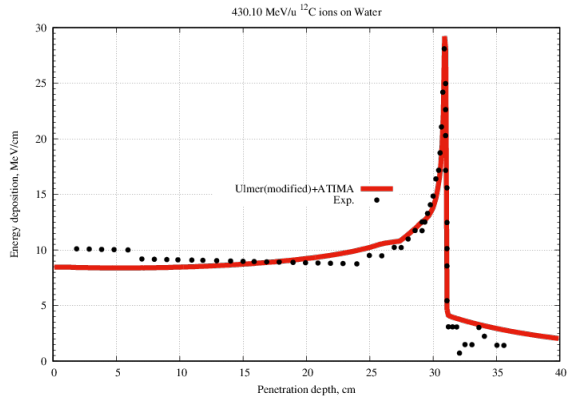

Figure 9: The total absorbed dose versus depth inside water phantom at 430.10 MeV/u of incident ^{12}C beam (R_{csda}=30.463 g/cm^2).

REFERENCES

[1] A. P. Chernyaev *et al.*, "Proton Accelerators for Radiation Therapy", *Medical Radiology and Radiation Safety*, vol. 64, no. 2, pp. 11–22, 2019. doi:10.12737/article_5ca5a0173e4963.18268254

[2] I.I. Degtyarev *et al.*, "The RTS&T-2014 code status", *Nuclear Energy and Technology*, vol. 1, no. 3, pp. 222-225, 2015. doi:10.1016/j.nucet.2016.02.006

[3] Varian Medical Systems, "Eclipse Proton Algorithms Reference Guide", P1026475-001-A, 2019.

[4] L. Sihver, D. Schardt, and T. Kanai, "Depth-Dose Distributions of High-Energy Carbon, Oxygen and Neon Beams in Water", *Japan. J. Med. Phys.*, vol. 18 no. 1, pp. 1-21, 1998. doi:10.11323/jjmp1992.18.1_1

[5] E. Haettner, H. Iwase, and D. Schardt, "Experimental fragmentation studies with ^{12}C therapy beams", *Radiation Protection Dosimetry*, vol. 122, no. 1-4, pp. 485–487, 2006. doi:10.1093/rpd/ncl402

[6] A.A. Pryanichnikov *et al.*, "The RTS&T Code Coupled with the Microscopic Kinetic Model for Biological Calculations in Multi-Ion Therapy", *Phys. Part. Nuclei Lett.,* vol. 17, no. 4, pp. 629–634, 2020. doi:10.1134/S1547477120040378

[7] K. Parodi *et al.*, "Monte Carlo simulations to support start-up and treatment planning of scanned proton and carbon ion therapy at a synchrotron-based facility". *Phys. Med. Biol.* vol. 57, no. 12, p. 3759, 2012. doi:10.1088/0031-9155/57/12/3759

[8] A. A. Pryanichnikov *et al.*, "Status of the Proton Therapy Complex Prometheus", in *Proc. 26th Russian Particle Accelerator Conf. (RuPAC'18)*, Protvino, Russia, Oct. 2018, p. 135-138. doi:10.18429/JACoW-RuPAC2018-FRXMH03

[9] A. A. Pryanichnikov *et al.*, "Clinical Use of the Proton Therapy Complex "Prometheus"", *Phys. Part. Nuclei Lett.,* vol. 15, no. 7, pp. 981-985, 2018. doi:10.1134/S1547477118070592

ISBN: 978-3-95450-240-0 ISSN: 2673-5539 doi:10.18429/JACoW-RuPAC2021-MOPSA41

EFFECT OF A PROTON BEAM FROM A LINEAR ACCELERATOR FOR RADIATION THERAPY

L. Ovchinnikova*[1], S. Akulinichev, A. Durkin, A. Kolomiets, V. Paramonov
INR RAS, Moscow, Russia
A. Kurilik, Moscow, Russia
[1]also at Ferrite Domen Co., St. Petersburg, Russia

Abstract

Linear accelerators can provide beam characteristics that cannot be achieved by circular accelerators. We refer to the concept of a compact linac for creating a proton accelerator with a maximum energy of 230 MeV, operating in a pulsed mode. The linac is designed to accelerate up to 10^{13} particles per 10 to 200 seconds irradiation cycle and is capable of fast adjustment the output energy in the range from 60 to 230 MeV, forming a pencil-like beam with a diameter of ~2 mm. Simulation of dose distribution from a proton beam in a water phantom has been performed. The radiological effect of the linac beam during fast energy scanning is considered, and the features for providing the high dose rate FLASH radiation therapy are specified. The possibility of a magnetic system for increasing the transverse dimensions of the beam-affected region is discussed.

INTRODUCTION

Cancer

Cancer is the second leading cause of death worldwide, as noted by the World Health Organization [1]. The probability of cancer in general population is dependent on genetic predisposition, gender, age, environmental factors, lifestyle and past illnesses [2, 3]. Various preventive strategies, early diagnosis, efficiency and accessibility of applicable types of treatment contribute to the odds of a favorable outcome.

Proton Therapy

Radiation therapy is one one of the most widely used non-surgical methods of malignant tumor treatment. External beam radiation therapy is the method of choice when dealing with deep pathological foci. Gamma rays from various radiation sources, bremsstrahlung photons and electrons produced by electron accelerators, and protons, neutrons and ions originating from hadron accelerators provide the required penetration into body tissue. Proton beams allow to achieve good localization of therapeutic dose delivery while minimizing collateral damage to healthy tissue [4].

Linac Advantages

Linear accelerators provide numerous advantages over circular accelerators. Combination with gantry is possible [5]. This type of accelerator enables precise beam energy modulation while eliminating the necessity for auxiliary energy changes. It also eliminates the losses, parasitic material activation and elevated background radiation levels associated with beam extraction from circular orbits. In this work, we focus on the linear proton accelerator concept, as described in [6].

DOSE DELIVERY

There are several methods of dose distribution forming in patient's body, used throughout the long-standing history of proton therapy, passive scattering being the most traditional one, and involving the use of collimation and compensation equipment. This method causes excessive patient irradiation by nuclear reaction products and necessitates safe storage of single-use collimators and compensators before disposing or recycling.

Beam scanning method eradicates these inconveniences and allows to apply almost arbitrary dose distribution [7, 8]. Also, proton arc therapy is promising [9, 10].

BEAM MANIPULATION

Most of the units put in operation over the past five years in the USA make use of gantries and Pencil Beam Scanning [11]. In this work, we focus on Pencil Beam Scanning with energy up to 250 MeV. Consequently, beam transportation and dose distribution forming are the most important research objectives.

Non-linear magnetic systems are often used to achieve uniform lateral dose distribution. A single non-linear magnet can be used for uniform dose distribution in a single plane [12]. Such magnets are designed for specific mean-square beam radius, [13] describing an auxiliary mechanical device for additional field tuning. Such device allows a beam be stretched into a line in a single plane, e.g. horizontal. This way, scanning can be used in a vertical plane, facilitating strip scanning, similarly minibeam [14, 15].

We also consider the use of dual scanning magnets in vertical and horizontal planes [16], this type of installation providing the most simple and versatile irradiation method. We also take into account that additional simulation is necessary when choosing the best method to achieve the desired distribution when dealing with distant tumor patches. A magnetic multipole combination [17–20] should be used when uniform distribution is desired. Such combination allows for wide beam energy range, facilitating beam width modulation. One can also use permanent magnets when designing achromatic turn only beam transportation system [21].

* lub.ovch@yandex.ru

ISBN: 978-3-95450-240-0 ISSN: 2673-5539 doi:10.18429/JACoW-RuPAC2021-MOPSA41

GEANT4 SIMULATION PROCEDURE

PSTAR [22] data was used for preliminary projected proton range estimation depending on the kinetic energy. The ~158 mm range corresponds to the mean energy of 150 MeV. Geant4 was used to simulate proton dose distributions in a volume [23]. Beam dynamics simulation results described in [6] were used to estimate the accelerator beam parameters and the resulting dose field parameters. TRANSIT [24] output files have been converted to input for Geant4. Particles at the accelerator nozzle were used. Beam radius used in simulation was $r_{RMS} < 0.35$ mm, with energy deviation $e_{RMS} < 0.057$ %. As for our task, dose calculation can be performed with accelerator beam approximated as an monoenergetic pencil beam.

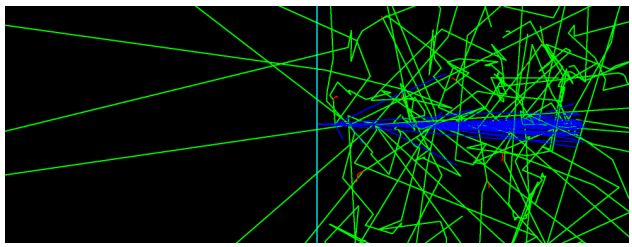

Figure 1: Trajectories visualization in Geant4. Neutral particle tracks shown in green, positively charged particle tracks shown in blue, negatively charged particle tracks shown in red, cyan line marks water phantom boundary.

It was assumed that the simulated particle beam immediately enters the half-space filled with water (Fig. 1). The absorbed dose accumulation is performed in 1 mm steps in the area of ± 50 mm on X and Y axes, 0 to 400 mm on Z axis. X axis is pointing to the right, Y axis is pointing up, Z axis coincides with beam vector.

SIMULATION RESULTS

Depth Dose Distribution

A uniform depth dependency was initially used with the aim of assessing the capability of the described accelerator [6] to form the uniform dose distribution. A spread out Bragg peak with absorber-modulated energy is usually used is such cases. In our case, energy is modulated by the accelerator itself. The sum of the Bragg curves and the corresponding scale factors k are shown in the Fig. 2. The dose characteristics are shown in the Table 1.

Table 1: Characteristics of Absorbed dose distribution by depth

Characteristic	Value
Accumulated pulse duration (μs)	48.2
Protons per 1 μs	10^{10}
Average dose (Gy)	6.52
Dose standard deviation (%)	2.24
Dose Uniformity Ratio = Dmax / Dmin	1.11

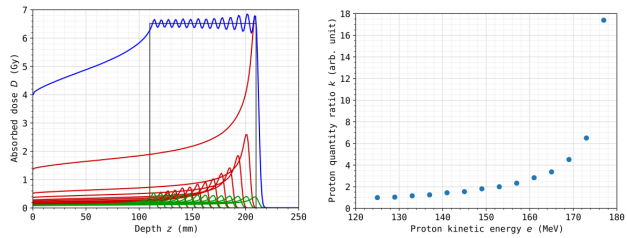

(a) (b)

Figure 2: Uniform dose distribution by depth, consisting of several Bragg curves — (a). The curves are obtained by averaging the volumetric dose in a volume with 100 × 100 mm transverse dimensions. Irradiation volume limited by 110 to 220 mm depth along Z axis is shown in grey color. Bragg curves of 122 up to 177 MeV protons with 4 MeV increment are shown in green color. There are 14 energies in total. The number of protons is 10^{10} for each energy. Bragg curves multiplied by scale factors are shown in red. Accumulated dose is shown in blue. Scale factors — (b).

For the lowest energy of 125 MeV the scale factor $k = 1$, which corresponds to the number of protons 10^{10}. The highest energy 177 MeV corresponds to $k = 17.4$, or $17.4 \cdot 10^{10}$ protons. That means that the higher the energy, the more protons are needed to achieve the desired dose. The sum of scale factors is 48.2, or $48.2 \cdot 10^{10}$ protons in total. Therefore, the total dose in a volume of $100 \times 100 \times 100$ mm^3 is 6.52 Gy when using passive beam scattering, and that dose is delivered over 48.2 microseconds of accumulated accelerator pulse duration.

3D Dose Distribution

We have simulated the filling of $100 \times 100 \times 100$ mm^3 volume using Pencil beams with spot step 4 mm and Gaussian distributed beams with $\sigma = 11$ mm and spot step 25 mm in transverse plane. The inhomogeneity of the spatial distribution of the absorbed dose should be small [25].

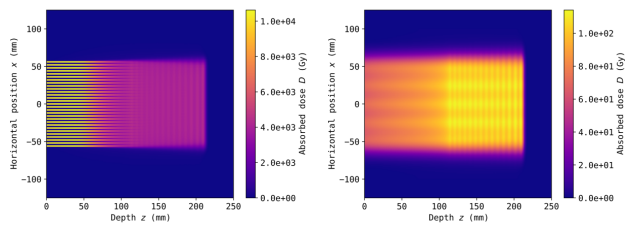

Figure 3: The dose distribution in ZX plane intersecting in dose peaks. Left — Pencil beams, right — Gaussian distributed beams with $\sigma = 11$ mm.

The Fig. 3–8 and Table 2 show the calculation results. Our calculations point out that pencil beams deliver very high average dose, which is orders of magnitude higher than the required therapeutic dose. With wide gaussian beams the average dose can be lowered to FLASH mode levels when using wide beams. FLASH mode requires shortening of irradiation time to 0.5 seconds [26]. Thus, the particle

ISBN: 978-3-95450-240-0 ISSN: 2673-5539 doi:10.18429/JACoW-RuPAC2021-MOPSA41

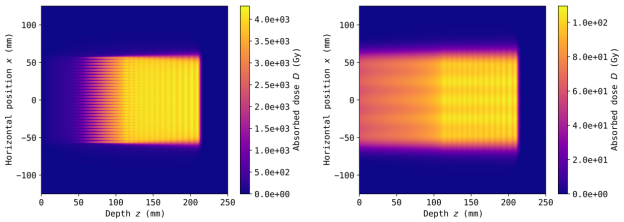

Figure 4: The dose distribution in ZX plane intersecting in dose valley. Left — Pencil beams, right — Gaussian distributed beams with σ = 11 mm.

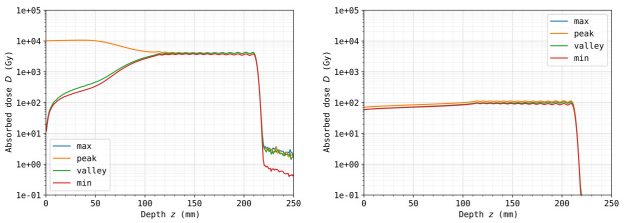

Figure 5: Dose distributions as functions of depth in dose peak and dose valley. Left — Pencil beams, right — Gaussian distributed beams with σ = 11 mm.

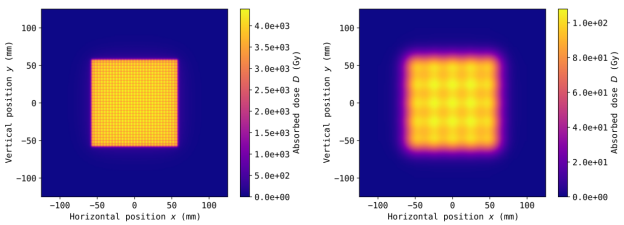

Figure 6: XY plane dose distribution for 110 mm depth. Left — Pencil beams, right — Gaussian distributed beams with σ = 11 mm.

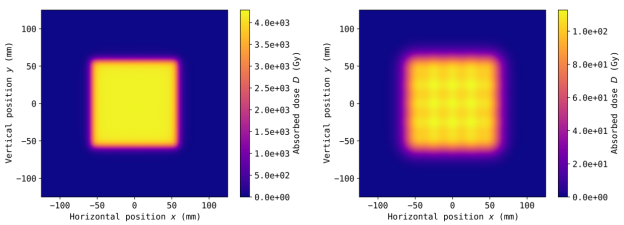

Figure 7: XY plane dose distribution for 210 mm depth. Left — Pencil beams, right — Gaussian distributed beams with σ = 11 mm.

accelerator under consideration can provide FLASH mode irradiation to a volume less than 100 × 100 × 100 mm^3.

CONCLUSIONS

- In order to meet FLASH mode requirements when using beam scanning technique, the accelerator beam can be widened and flattened using nonlinear magnetic elements.
- Alternatively, pulse charge can be lowered and pulse frequency increased accordingly.

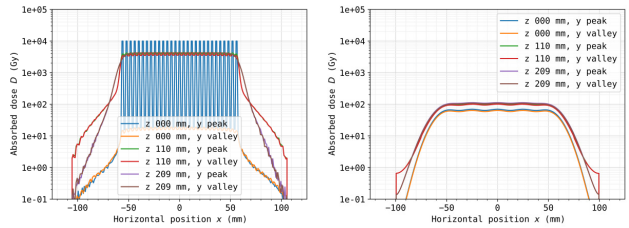

Figure 8: Dose as a function of x along peak and valley for different depth values. Left — Pencil beams, right — Gaussian distributed beams with σ = 11 mm.

Table 2: Absorbed dose distribution characteristics in 100 × 100 × 100 mm^3 volume

Characteristic	Pencil beams	Gaussian beams
Spot step (mm)	4	25
Spots num	841	25
Accumulated pulse duration (μs)	40536	1205
Average dose (Gy)	4006	102
Minimal dose (Gy)	3300	83.4
Maximal dose (Gy)	4481	114
Dose standard deviation (%)	3.36	4.27
Dose Uniformity Ratio = Dmax / Dmin	1.36	1.37

- It should be taken into account that FLASH therapy has some time–dependent limitations [27, 28].
- It is necessary to simulate the beam spread in the vacuum window and in the air between nozzle and water phantom [29, 30].

ACKNOWLEDGEMENTS

The authors thanks colleagues in INR RAS for fruitful discussions and valuable comments. Especially thanks to L. Kravchuk and A. Feschenko for their support of the work, useful discussions and recommendations.

REFERENCES

[1] World Health Organization, *WHO report on cancer: setting priorities, investing wisely and providing care for all*. World Health Organization, 2020, 149 p. ISBN: 978-92-4-000129-9.

[2] American Cancer Society, *Global Cancer Facts & Figures 4th Edition*. Atlanta: American Cancer Society, 2018.

[3] American Cancer Society, *Cancer Treatment & Survivorship Facts & Figures 2019–2021*. Atlanta: American Cancer Society, 2019.

[4] H. Paganetti, *Proton Beam Therapy*, ser. 2399-2891. IOP Publishing, 2017. DOI: 10.1088/978-0-7503-1370-4.

[5] C. Cuccagna *et al.*, "Beam parameters optimization and characterization for a TUrning LInac for Protontherapy," *Physica Medica*, vol. 54, pp. 152–165, 2018. DOI: 10.1016/j.ejmp.2018.08.019.

ISBN: 978-3-95450-240-0 ISSN: 2673-5539 doi:10.18429/JACoW-RuPAC2021-MOPSA41

[6] V. Paramonov, A. Durkin, and A. Kolomiets, "A Linear Accelerator for Proton Therapy", presented at RuPAC'21, September 2021, paper FRB04, this conference.

[7] T. Haberer, W. Becher, D. Schardt, and G. Kraft, "Magnetic scanning system for heavy ion therapy," *Nuclear Instruments and Methods in Physics Research Section A: Accelerators, Spectrometers, Detectors and Associated Equipment*, vol. 330, no. 1, pp. 296–305, 1993. DOI: 10.1016/0168-9002(93)91335-K.

[8] E. Pedroni *et al.*, "The 200-MeV proton therapy project at the Paul Scherrer Institute: Conceptual design and practical realization," *Medical Physics*, vol. 22, no. 1, pp. 37–53, 1995. DOI: 10.1118/1.597522.

[9] S. Ferguson, S. Ahmad, and I. Ali, "Simulation study of proton arc therapy with the compact single-room MEVION-S250 proton therapy system," *Journal of Radiotherapy in Practice*, vol. 19, no. 4, pp. 347–354, 2020. DOI: 10.1017/S1460396919000888.

[10] X. Ding, X. Li, J. M. Zhang, P. Kabolizadeh, C. Stevens, and D. Yan, "Spot-Scanning Proton Arc (SPArc) Therapy: The First Robust and Delivery-Efficient Spot-Scanning Proton Arc Therapy," *International Journal of Radiation Oncology*Biology*Physics*, vol. 96, no. 5, pp. 1107–1116, 2016. DOI: 10.1016/j.ijrobp.2016.08.049.

[11] Particle Therapy Co-Operative Group, *Particle therapy facilities in clinical operation*. https://www.ptcog.ch/index.php/facilities-in-operation

[12] A. J. Jason, B. Blind, and K. Halbach, "Beam expansion with specified final distributions," in *PAC'97 Proceedings*, 1998, pp. 3728–3730. https://accelconf.web.cern.ch/pac97/papers/pdf/9P052.PDF

[13] G. Gu and W. Liu, "Uniformization of the Transverse Beam Profile by a New Type Nonlinear Magnet," in *Proc. 6th International Particle Accelerator Conference (IPAC'15), Richmond, VA, USA, May 3-8, 2015*, (Richmond, VA, USA), ser. International Particle Accelerator Conference, Geneva, Switzerland: JACoW, Jun. 2015, pp. 272–274. DOI: 10.18429/JACoW-IPAC2015-MOPWA065.

[14] J. Reindl and S. Girst, "pMB FLASH - Status and Perspectives of Combining Proton Minibeam with FLASH Radiotherapy," *Journal of Cancer Immunology*, vol. 1, pp. 14–23, Aug. 2019. DOI: 10.33696/cancerimmunol.1.003.

[15] A. Mazal *et al.*, "FLASH and minibeams in radiation therapy: The effect of microstructures on time and space and their potential application to protontherapy," *The British Journal of Radiology*, vol. 93, no. 1107, p. 20 190 807, 2020. DOI: 10.1259/bjr.20190807.

[16] J. Kolski, "Proposed Varying Amplitude Raster Pattern to Uniformly Cover Target for the Isotope Production Facility (IPF) at LANSCE," in *Proceedings of HB2014*, 2014, pp. 148–150. https://accelconf.web.cern.ch/HB2014/papers/mopab46.pdf

[17] N. Tsoupas *et al.*, "Uniform beam distributions at the target of the NASA Space Radiation Laboratory's beam line," *Phys. Rev. ST Accel. Beams*, vol. 10, p. 024 701, 2 Feb. 2007. DOI: 10.1103/PhysRevSTAB.10.024701.

[18] Y. Yuri, N. Miyawaki, T. Kamiya, W. Yokota, K. Arakawa, and M. Fukuda, "Uniformization of the transverse beam profile by means of nonlinear focusing method," *Phys. Rev. ST Accel. Beams*, vol. 10, p. 104 001, 10 Oct. 2007. DOI: 10.1103/PhysRevSTAB.10.104001.

[19] Y. Yuri, I. Ishibori, T. Ishizaka, S. Okumura, and T. Yuyama, "Uniform Beam Distribution by Nonlinear Focusing Forces," in *Proceedings of IPAC'10*, 2010, pp. 4149–4151. https://accelconf.web.cern.ch/IPAC10/papers/thpec041.pdf

[20] I. Ivanenko, I. Kalagin, V. Kazacha, and N. Kazarinov, "Getting Uniform Ion Density on Target in High-Energy Beam Line of Cyclotron U-400M with Two," in *Proceedings of Cyclotrons2013*, 2013, pp. 335–337. https://accelconf.web.cern.ch/CYCLOTRONS2013/papers/weppt007.pdf

[21] D. Trbojevic, S. Brooks, T. Roser, and N. Tsoupas, "Superb Fixed Field Permanent Magnet Proton Therapy Gantry," in *Proc. IPAC'21*, (Campinas, SP, Brazil), ser. International Particle Accelerator Conference, JACoW Publishing, Geneva, Switzerland, Aug. 2021, TUPAB030, pp. 1405–1408. DOI: 10.18429/JACoW-IPAC2021-TUPAB030.

[22] NIST Physical Measurement Laboratory. "Stopping-power & range tables for electrons, protons, and helium ions." (2017), https://www.nist.gov/pml/stopping-power-range-tables-electrons-protons-and-helium-ions

[23] J. Allison *et al.*, "Recent developments in Geant4," *Nuclear Instruments and Methods in Physics Research Section A: Accelerators, Spectrometers, Detectors and Associated Equipment*, vol. 835, pp. 186–225, 2016. DOI: 10.1016/j.nima.2016.06.125.

[24] A. Kolomiets, A. Plastun, and T. Tretyakova, "TRANSIT code for beam dynamic simulation," in *Proceedings of RuPAC2014, Obninsk, Kaluga Region, Russia*, Oct. 2014, pp. 51–53. https://accelconf.web.cern.ch/rupac2014/papers/tupsa07.pdf

[25] H. Shu *et al.*, "Scanned Proton Beam Performance and Calibration of the Shanghai Advanced Proton Therapy Facility," *MethodsX*, vol. 6, pp. 1933–1943, 2019. DOI: 10.1016/j.mex.2019.08.001.

[26] S. Akulinichev *et al.*, "Possibilities of Proton FLASH Therapy on the Accelerator at the Russian Academy of Sciences' Institute for Nuclear Research," *Bulletin of the Russian Academy of Sciences: Physics*, vol. 84, pp. 1325–1329, Nov. 2020. DOI: 10.3103/S1062873820110039.

[27] W. Zou *et al.*, "Current delivery limitations of proton PBS for FLASH," *Radiotherapy and Oncology*, vol. 155, pp. 212–218, Feb. 2021. DOI: 10.1016/j.radonc.2020.11.002.

[28] M. Kang, S. Wei, J. I. Choi, C. B. Simone, and H. Lin, "Quantitative Assessment of 3D Dose Rate for Proton Pencil Beam Scanning FLASH Radiotherapy and Its Application for Lung Hypofractionation Treatment Planning," *Cancers*, vol. 13, no. 14, 2021. DOI: 10.3390/cancers13143549.

[29] U. Weber and G. Kraft, "Comparison of Carbon Ions Versus Protons," *Cancer journal*, vol. 15, pp. 325–32, Jul. 2009. DOI: 10.1097/PPO.0b013e3181b01935.

[30] D. Schardt, T. Elsässer, and D. Schulz-Ertner, "Heavy-ion tumor therapy: Physical and radiobiological benefits," *Rev. Mod. Phys.*, vol. 82, pp. 383–425, 1 Feb. 2010. DOI: 10.1103/RevModPhys.82.383.

ISBN: 978-3-95450-240-0 ISSN: 2673-5539 doi:10.18429/JACoW-RuPAC2021-MOPSA42

COMPACT S-BAND ACCELERATING STRUCTURE FOR MEDICAL APPLICATIONS

A.A. Batov, R.A. Zbruev, M.A. Gusarova, M.V. Lalayan, S.M. Polozov,
National Research Nuclear University MEPhI, Moscow, Russia

Abstract

This paper describes electromagnetic design results for the compact 6.3 MeV electron linac for the radiation therapy facility. Linac is based on S-band biperiodic accelerating structure with inner coupling cells with an increased coupling coefficient.

INTRODUCTION

Biperiodic accelerating structures with on-axis coupling cells with high cell-to-cell coupling coefficients have been developed in NRNU MEPhI since 2010 [1-5]. The joint team of CORAD and MEPhI has constructed a linear electron accelerator for industrial applications based on the developed structures [6, 7]. That accelerator was successfully launched, tested and put into operation in 2015 [8]. Linac has high electrical efficiency, narrow beam energy spectrum, provides energy regulation, and low accelerated beam losses. It is based on 2856 MHz biperiodic accelerating structure for the energy range from 7.5 to 10 MeV and beam power up to 20 kW. The klystron TH2173F (Thales Electron Devices) was used for linac RF feed. It provides up to 5 MW of pulse power for 17 μs RF pulses duration and up to γ 6 kW of averaged power. Another two accelerators have been manufactured, installed at EB-Tech Company site in Daejeon, Republic of Korea, and at "Rodniki" Industrial Park, Ivanovo Region, Russia, and successfully tested [8].

This paper presents biperiodic accelerating structure with inner coupling cells with an increased coupling coefficient. It was developed for compact 6.3 MeV electron linac for radiation therapy facility. The power source that is planned to use is 3 MW magnetron MI456B or E2Vmg7095. The operating frequency of these sources are 2997.8 MHz. Since the accelerating structures should be tuned to the source frequency, the operating frequency of the linac should be set at 2997.8±1.0 MHz.

The structure was based on the MEPhI and CORAD designed S-band linac operated at 2856 MHz design with relatively large cell-to-cell coupling coefficient [3]. Structures operating at frequency of 2856 MHz have one more advantage: the production technology was earlier developed and is ready [8]. However, the 2856 MHz structures cannot be used in the facility under development due to the fact that operating frequency does not correspond to power source one. For this reason, the accelerating structure geometry was scaled in order to reach the 2997.8 MHz RF frequency, while keeping the coupling coefficient of at least 8% and reach the highest possible shunt impedance.

The optimization of the structure in order to increase the shunt impedance is necessary because of power source limitations and necessary beam parameters to be met.

Accelerating section of this linac has been designed under the strict limitations on the facility length and ratio of electromagnetic fields values in bunching cells. Linac technical requirements are summarized below in the Table 1.

The geometry of the structure is developed according to the beam dynamics simulation results and the electrodynamic parameters requirements. The longitudinal dimensions were calculated from beam dynamics. The angle and depth of the drift tube cones and the diaphragm thickness were selected on the basis of the original structure and were kept unchanged due to the fact that the overvoltage factor value in the base structure was low enough for fast conditioning and stable operation.

Table 1: Technical Requirements for Accelerating Structures of the Compact 6.3 MeV Electron Linac for Radiation Therapy Facility

Parameter	Value	Unit
Total length	400<	mm
Number of bunching cells	3	
Number of regular cells	5	
Operating frequency	2997.8	MHz
Coupling coefficient	8…10	%
Shunt impedance	65…90	MΩ/m
Total Loss	1.6<	MW
Ratio of EM field values in buncher	0.4…1	
RF Power source	3	MW

REGULAR CELLS

Dimensions of regular cells were adjusted by scaling [5] the original structure [3] in order to achieve the required values of the cell operating frequency, shunt impedance and the coupling coefficient. Then the particular dimensions were adjusted to make the result more precise. Fine tune was done using electromagnetic field simulation software CST Studio Suite [9]. The cell tuning was considered successful when the value of the accelerating field in the coupling cells turned out to be zero upon reaching the above parameters.

The coupling coefficient and the shunt impedance values were adjusted using the position and the area of the coupling slots. The obtained electrodynamic characteristics are presented in Table 2.

The geometry of the regular cell, electric field topography and the accelerating field distribution along the tuned cavity axis for 1 J of stored energy respectively are presented on the Fig. 1.

ISBN: 978-3-95450-240-0 ISSN: 2673-5539 doi:10.18429/JACoW-RuPAC2021-MOPSA42

Table 2: RF Parameters of the Regular Cavity

Parameter	Value	Unit
Operating frequency	2997.8	MHz
Coupling coefficient	8.1	%
Q-factor	15200	
Effective Shunt Impedance	79,05	MΩ/m
Overvoltage factor	2.28	

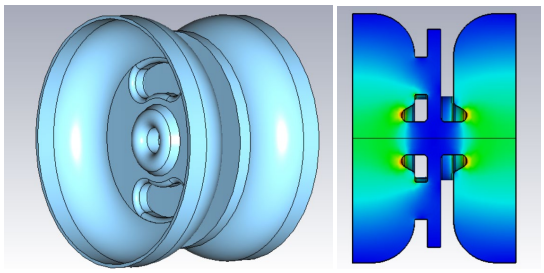

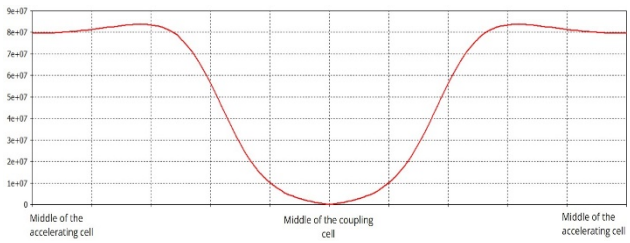

Figure 1: Geometry of the regular cell (*a*); Electric field topography (*b*); The distribution of the longitudinal component of the electric field on the cell axis for 1 J of stored energy (*c*).

BUNCHING CELLS

According to the requirements of the beam dynamics calculation accelerating structure includes 3 bunching cells. Ratio of electromagnetic fields values are in the range of 0.4 to 1 from the beginning of the bunching part. The electromagnetic fields ratio can be set up by changing the ratio between areas of the coupling gaps of the buncher. For this reason, it is necessary to take into account the margin in the area of the coupling slots in order to establish the required ratio of the accelerating fields in the buncher when designing the regular part.

An attempt was made to increase the area of coupling slots in order to get the coupling coefficient as high as 10%. However, the creation of a buncher without depriving the first two cells of noses was not possible. The deprivation of two buncher cells of noses would lead to a noticeable deterioration in the shunt impedance of the structure, below the minimum possible value. Therefore, it was decided to create a compromise option with a coupling coefficient of 8% and an acceptable shunt impedance.

The first bunching cell was designed without a nose in order to achieve the necessary electromagnetic field distribution. The sectional side view of the bunching part is presented on the Fig. 2.

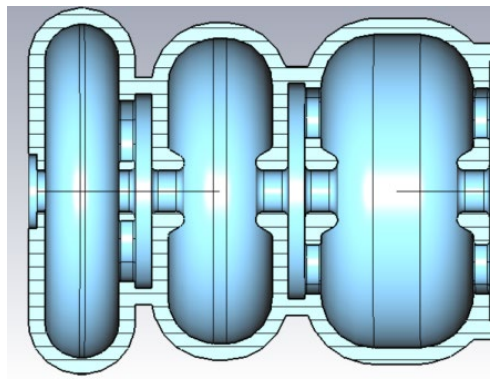

Figure 2: Sectional side view of the bunching part.

THE WHOLE STRUCTURE

According to the requirements of the beam dynamics calculation the accelerating structure consists of 3 bunching and 5 regular cells. The geometry of the whole structure is presented on the Fig. 3.

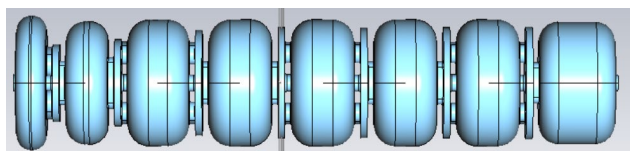

Figure 3: Side view of the S-band accelerating structure.

The electric field topography and the distribution of the module of the longitudinal component of the electric field on the axis of the tuned structure for 1 J of stored energy respectively are presented on the Fig. 4.

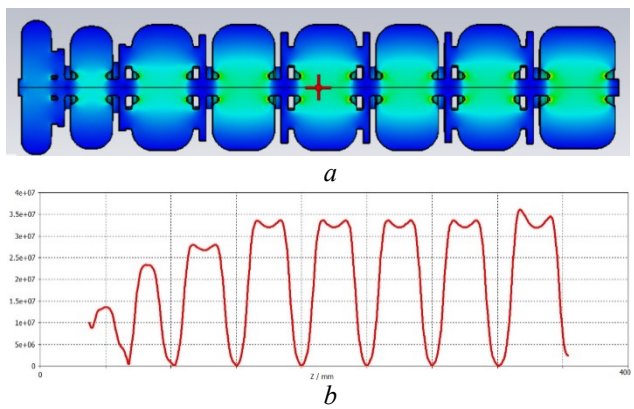

Figure 4: Electric field topography (*a*) and the distribution of the module of the longitudinal component of the electric field on the axis of the tuned structure for 1 J of stored energy (*b*).

ISBN: 978-3-95450-240-0 ISSN: 2673-5539 doi:10.18429/JACoW-RuPAC2021-MOPSA42

The first and last cells of the structure have coupling gaps only on the one side. For this reason, they were additionally tuned to achieve the symmetric electric field distribution.

To obtain the precise operating frequency for the whole linac structure, the radius of each cell was individually slightly modified after all preliminary tuned cells of the structure were put together.

The electrodynamic characteristics of the structure are presented in Table 3. The obtained cell-to-cell coupling coefficient value is relatively large at the optimal shunt impedance value for the power supply system.

Table 3: Electrodynamic Characteristics of an Optimized S-Band Accelerating Structure

Parameter	Value	Unit
Operating frequency	2997.8	MHz
Q-factor	15300	
Effective Shunt Impedance	68,89	MΩ/m
Overvoltage factor	2.64	

THE INPUT COUPLER

The accelerating structure is fed with RF power through power coupler of traditional design. Feeding WG10 (72*34mm) rectangular waveguide is coupled to accelerating cell via rectangular coupling slot.

Overcoupling factor of about 2.4 without beam loading provides near to critical coupling at specified beam current. Electromagnetic field in coupler cell is symmetrised by additional cut-off waveguide used also as vacuum pumping port. Accelerating structure with the power coupler is presented on the Fig. 5.

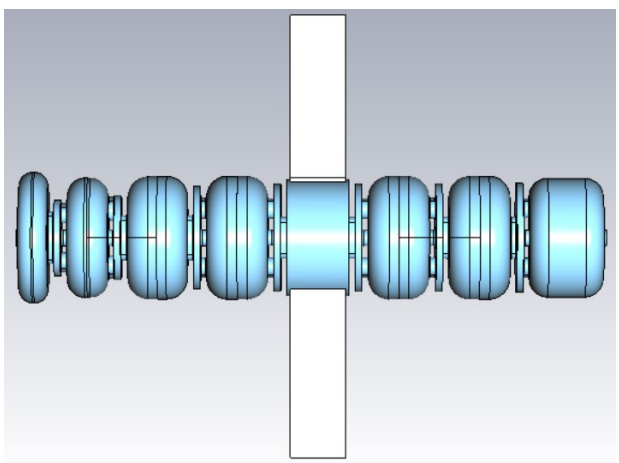

Figure 5: Side view of the S-band accelerating structure with the power coupler.

CONCLUSION

A 2997.8 MHz biperiodic accelerating structure for the compact 6.3 MeV electron linac for the radiation therapy facility was successfully designed. The final optimized geometry of the e-linac structure is presented in Fig. 3 and its electrodynamic characteristics are summarized in Table 3. The structure was optimized to produce a symmetric electric field with a ratio of electromagnetic fields values in the range of 0.4 to 1 in the bunching part as shown in Fig. 4.

The position of the power input device was selected, taking into account the infrastructure of the project. The optimal value of the coupling coefficient has been calculated.

The electron gun for the radiation therapy complex project is also in the design process.

REFERENCES

[1] N.P. Sobenin *et al.*, "Biperiodic accelerating structure with inner coupling cells with an increased coupling coefficient", in *Proc. XXIII Russian Particle Accelerator Conference (RuPAC 2012),* Peterhof, St. Petersburg, Russia, 24 - 28 September 2012, pp 458 – 460.

[2] R.A. Kostin *et al.*, "Thermal Calculation of Accelerating Structures in Electron Linacs", *Technical Physics*, Vol. 58, No. 4, pp. 601–607, 2013. doi:10.1134/S1063784213040105

[3] E.A. Savin and N.P. Sobenin, "Biperiodic accelerating structure with internal coupling cells with an increased coupling coefficient", *Technical Physics*, volume 83, issue. 5, p 12, 2013. doi: 10.1134/S1063784213050198

[4] S.M. Polozov and A.I. Pronikov, "Influence of the Frequency Detuning to Electrodynamics Parameters of an Electron Linac", *Journal of Physics: Conference Series*, 1238:012076, 2019. doi: 10.1088/1742-6596/1238/1/012076

[5] R. Zbruev *et al.*, "Analysis of restrictions on the value of the maximum accelerating field for the biperiodic structure of the linear accelerator of the injection complex of the SILA project", *in Proc 7th Int. Conference Laser, plasma research and technologies (LaPlas-2021)* Moscow, Russia, 23-26 march 2021, pp 414-417. ISBN 978-5-7262-2767-2

[6] S.M. Polozov, V.I. Rashchikov and M.I. Demsky, "Beam dynamics in new 10 MeV high-power electron linac for industrial application", in *Proc. 25th Russian Particle Accelerator Conference (RuPAC 2016)*, St. Petersburg, Russia, 21 - 25 November 2016, pp. 493–495. doi:10.18429/JACoW-RuPAC2016-WEPSB057

[7] T.V. Bondarenko *et al.*, "New 10 MeV high-power electron linac for industrial application", in Proc. *7th International Particle Accelerator Conference (IPAC'16)*, BEXCO, Busan, Republic of Korea, 8-13 May 2016, pp. 1794-1796. doi: 10.18429/JACoW-IPAC2016-TUPOW021

[8] D.S. Basyl *et al.*, "Commissioning and first tests of the new standing wave 10 MeV electron accelerator", in *Proc. 25th Russian Particle Accelerator Conference (RuPAC 2016)*, St. Petersburg, Russia, 21 - 25 November 2016, pp. 173-175. doi: 10.18429/JACoW-RuPAC2016-

[9] CST STUDIO SUITE, https://www.3ds.com/products-services/simulia/products/cst-studio-suite/?utm_source=cst.com&utm_medium=301&utm_campaign=cst

ISBN: 978-3-95450-240-0 ISSN: 2673-5539 doi:10.18429/JACoW-RuPAC2021-MOPSA44

CONCEPTUAL PROJECT OF THE PROTON BEAM LINES IN THE NUCLEAR MEDICINE PROJECT OF THE "KURCHATOV INSTITUTE" - PNPI

D.A. Amerkanov, S.A. Artamonov, E.M. Ivanov, V.I. Maximov, G.A. Riabov, V.A. Tonkikh†, NRC KI-PNPI, Gatchina, Russia

Abstract

The paper presents the calculation and layout of the beam transport lines to the target stations, the operation mode of the magnetic elements and beam envelopes. The method of the proton beam formation for ophthalmology and its parameters are described.

INTRODUCTION

The project of a nuclear medicine complex based on the isochronous cyclotron of negative hydrogen ions C-80 is being developed at the National Research Centre "Kurchatov Institute"-PNPI. The project provides for the design of a building, the creation of stations for the development of methods for obtaining new popular radionuclides and radiopharmaceuticals based on them. The commercial component is not excluded. The project also provides for the creation of a complex of proton therapy of the eyesight. For these purposes, the modernization of the beam extraction system of the cyclotron C-80 is planned: a project for the simultaneously two beams extraction systems is being developed. The one for the production of isotopes with an intensity up to 100 mkA and an energy of 40-80 MeV and the second - for ophthalmology with an energy of 70 MeV and intensity up to 10 mkA.

The initial conditions for both beams at the output window from the accelerator were obtained using the Orbita-1 program [1].

A blueprint of the project and beam transfer lines is shown in Fig. 1.

BEAM TRANSPORT LINES

Radio Isotope Complex

The isotope complex (direction A, Fig. 1) includes four target stations. Target stations will be equipped with special devices for removing highly radioactive targets, loading them into protective containers for safe transportation to storage sites or to hot chambers for further processing.

When designing the line for the production of radionuclides for each energy of the proton beam in the range of 40-80 MeV, the optimal parameters of the magnetic elements of the beam were found under conditions of minimal losses of particles in the transportation path, and so that the beam size on the target was at least 20 mm.

The optimization of the beam transfer lines was carried out using the PROTON_MC program created at the NRC KI-PNPI [2]. The calculation algorithm consists in tracing the proton beam trajectories along the transport channel from the source to hitting the experimenter's target or the aperture of the magnetic elements. The initial conditions of the particles are chosen random within normal distribution. The beam from the accelerator is presented in the form of a multidimensional Gaussian distribution in x, x', z, z', Δp/p phase spice. In the case when an absorber is installed in the transport channel the beam parameters after the absorber are calculated using the GEANT4 program [3].

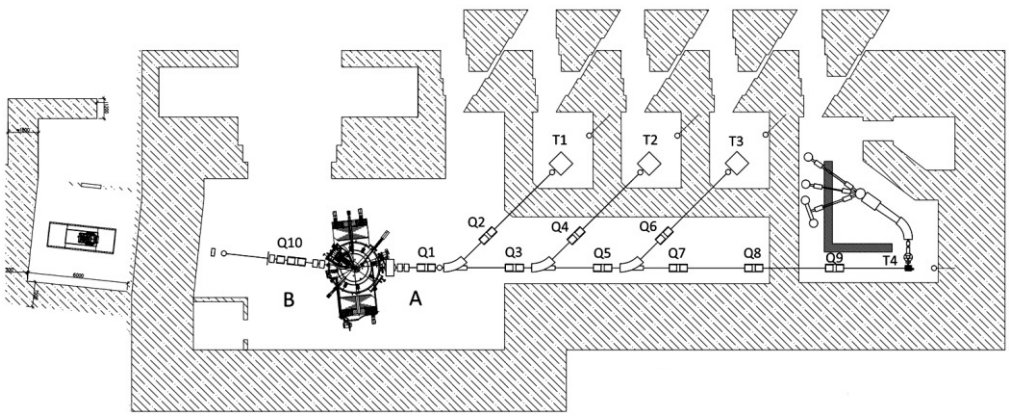

Figure 1: Blueprint of the project and beam transfer lines: (Right) A - beam line for radioisotope part, Q1-Q9 - lens doublets, T1-T4 - target stations. (Left) B - beam line for the ocular oncology complex, Q10 - triplet lenses.

† tonkikh_va@pnpi.nrcki.ru

ISBN: 978-3-95450-240-0 ISSN: 2673-5539 doi:10.18429/JACoW-RuPAC2021-MOPSA44

The output file of this program may be used as the source for the program. The program includes a block for optimizing the any beam parameters presented in a functional form. The random search method is used for obtaining the global maximum of a function of many variables.

Figure 2 shows the results of calculating the beam envelopes in the horizontal (X) and vertical (Z) planes for the target stations T1, T2, T3, T4, respectively. The energy of the protons is E = 70 MeV.

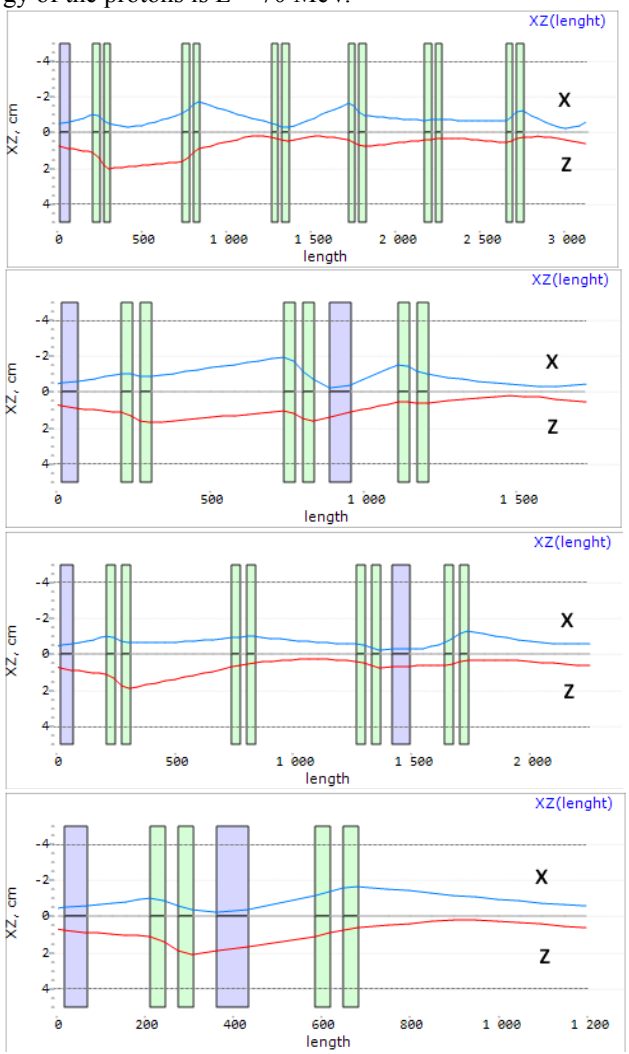

Figure 2: Beam envelopes in horizontal (X) and vertical (Z) planes for stations T1-T4. The upper and lower horizontal lines are the beam aperture.

Figure 3 shows a beam portrait for the most distant T4 direction as an example of the beam quality.

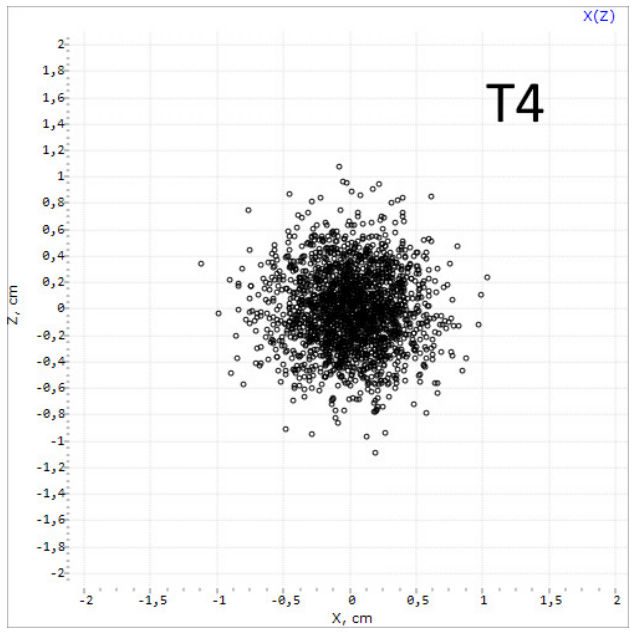

Figure 3: Beam size on the T4 target.

Ophthalmic Oncology Beam Line

Another area of application of the C-80 cyclotron is proton therapy for oncological eye diseases. For this purpose, a beam line was designed for the formation and delivery of a proton beam from the cyclotron to the treatment room, where patients are irradiated (direction B, Fig. 1). Line meets special requirements: beam energy 60-70 MeV; beam diameter at the entrance to the treatment room ≈ 60 mm; beam divergence angle ≈ 1 mrad; the uniformity of the beam in the area of Ø60 mm is not less than 90%.

A challenge in the design of medical tract was the requirement of medical physicists about the simultaneous and independent operation of the two beams of isotopes and medicine. On a cyclotron accelerating H- ions, it turned out the opportunity to provide simultaneous operation of two beams of different intensities and energies - one for the production of isotopes with an intensity of 100 μA and an energy of 40-80 MeV and the second - for ophthalmology with an energy of 60 MeV and intensity 10 mkA.

To implement this idea, it turned out to be necessary to extract the beams in two directions (see Fig. 1) and select a complex configuration of stripping foils.

To obtain a homogeneous beam, a well-known method of beam scattering and sampling of its homogeneous central part were applied.

To implement these conditions, a beam line with a passive scatterer made of tantalum (Ta) foil 300 mkm thick was constructed. The scheme of the beam path is shown in Fig. 4.

ISBN: 978-3-95450-240-0 ISSN: 2673-5539 doi:10.18429/JACoW-RuPAC2021-MOPSA44

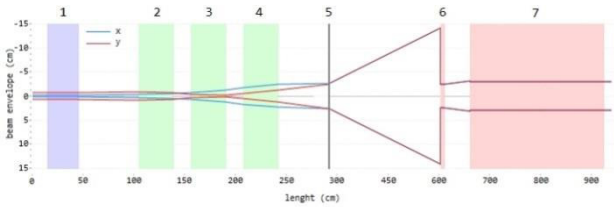

Figure 4: Ophthalmic beam line scheme and beam envelopes: 1 - corrector magnet, 2,3,4 - triplet lenses, 5 - tantalum scatterer 300 mkm thick, 6 - collimator, 7 - protective wall in front of the irradiation room.

The proton beam E = 70 MeV, extracted from the accelerator, is transported to the Ta foil, on which a beam size of ~ Ø30 mm is formed by a triplet lens. The optimization of the proton beam transport line in this section was also carried out using the PROTON_MC program. The results of the passage of protons through a Ta foil with a thickness of 300 mkm, obtained using the GEANT4 program, were the initial conditions of the PROTON_MC program during further transport of the diverging proton beam in free space of ~ 3.7 m. The phase ellipses of the beam at the entrance and exit from the foil are shown in Fig. 5.

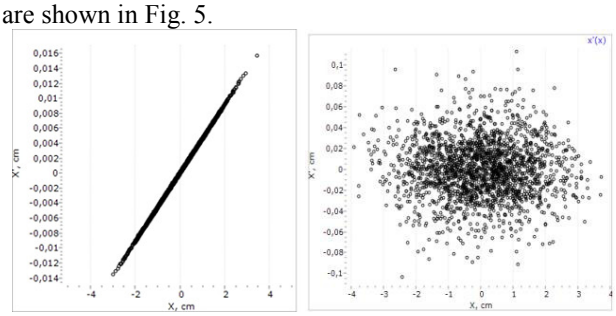

Figure 5: Phase ellipses of the beam (x-x ') at the entrance and exit from the foil, respectively.

A collimator with an optimal beam length of 100 mm and a diameter of 50 mm, installed in front of the protective wall, finally forms a beam with specified conditions as shown by Fig. 6.

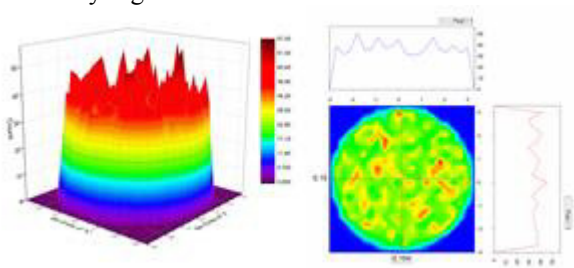

Figure 6: Distribution of the intensity of the proton flux in the beam at the entrance to the irradiation room of patients.

CONCLUSION

Within the framework of this project, the radioisotope and onco-ophthalmological beam line for the transport of the proton beam were designed. We managed to place the necessary equipment within the allocated area.

Calculations show that this configuration of the channels will provide a proton beam with the required parameters.

ACKNOWLEDGMENT

The authors express their sincere gratitude to all colleagues from the PNPI who participated in development of the radiation test facilities at the SC-1000 synchrocyclotron.

REFERENCES

[1] N. K. Abrosimov, G. A. Ryabov, A. N. Chernov, Preprint PNPI-2851, Gatchina, 2010.

[2] D. A. Amerkanov, E. M. Ivanov, G. A. Ryabov, and V. A. Tonkikh , “Calculation and optimization of high-energy beam transfer lines by the Monte Carlo method”, presented at the 27th Rus. Particle Accelerator Conf. (RuPAC’21), Alushta, Russia, 26 September – 2 October 2021, paper TUPSB16, this conference

[3] GEANT4, https://geant4.web.cern.ch

ISBN: 978-3-95450-240-0 ISSN: 2673-5539 doi:10.18429/JACoW-RuPAC2021-MOPSA45

EXPERIMENTAL SIMULATION OF VOLUME REPAINTING TECHNIQUE AT PROTON SYNCHROTRON IN CONTEXT OF SPOT SCANNING PROTON THERAPY

M. A. Belikhin†[1], A.A. Pryanichnikov[1], A. E. Shemyakov,
Lebedev Physical Institute RAS, Physical-Technical Center, Protvino, Russian Federation
A.P. Chernyaev, Lomonosov Moscow State University, Accelerator Physics and Radiation Medicine Department, Moscow, Russian Federation
[1]also at Lomonosov Moscow State University, Accelerator Physics and Radiation Medicine Department, Moscow, Russian Federation

Abstract

Reduction the influence of respiration-induced intrafractional motion is one of the main tasks of modern Spot Scanning Proton Therapy (SSPT). Repainting is one of the techniques of motion compensation. It consists in multiple repeated irradiations of the entire volume or individual iso-energy layers with the dose that is a multiple of the prescribed dose. As a result, the dose is averaged which leads to an increase in the homogeneity of the dose field.

The purpose of this study is experimental simulation of volume repainting and dosimetric estimation of its capabilities in the context of SSPT.

Simulation of respiration-like translational motion is performed using a non-anthropomorphic water dynamic phantom. Target of this phantom is compatible with EBT3 films and ion chamber. Estimation of repainting technique is based on the analysis of dose field shape, average dose and dose homogeneity in the Region of Interest (ROI) located within Planning Target Volume (PTV), and dose gradients along the direction of motion. Repainting technique was used for motion with amplitudes of 2, 5, 10 mm with 2, 4, 6, 8 and 10 iterations at the prescribed dose of 6 Gy. For each case values of the average dose, dose homogeneity and dose gradient were calculated and compared with corresponding values in case of no motion.

Repainting removes hot and cold spots and increases the homogeneity in the ROI from 85.9% to 96.0% at amplitude of 10 mm and 10 iterations. The dose gradient is inversely proportional to the motion amplitude and was not improved by repainting. Optimization of the irradiation time, PTV dose and dose field margins is necessary for clinical using of repainting.

INTRODUCTION

Today proton therapy is the most precision and effective method of modern radiation oncology. These advantages are based on the presence of sharp Bragg peak at the end of the path, low lateral scattering and dependence of the beam penetration depth on its energy [1, 2].

However, these advantages can be fully realized only in case of complete immobility of the tumor, for example, in case of head and neck tumors. Respiration-induced intrafractional motion [3] leads to significant distortions of dose distribution and conformity degradation in case of other localizations such as lungs, liver, prostate, breast and etc. Interplay effect between tumor motion and beam delivery dynamic causes hot and cold spots in the target volume, and irradiation of healthy tissues and organs at risk. These factors significantly decrease efficiency of SSPT [4].

Conventional photon radiation therapy has a lot of solution [5] for monitoring, compensation and mitigation of intrafractional motion. However, direct transfer of these techniques to SSPT is difficult and requires additional research [4, 5]. In the main, the difficulties are caused by differences in the interaction principles of proton and photon beams with matter.

Repainting [3] is a specific method of tumor motion compensation used in SSPT. This one increases homogeneity of dose field and eliminates hot and cold spots. Repainting consists in multiple repeated irradiations of the entire volume or individual iso-energy layers with a dose that is a multiple of the prescribed dose. Intensity of the beam for repainting can be calculated as:

$$I = {}^{I_0}/_{N}$$

where I – intensity of the repainting beam, I_0 – total intensity, N – number of scanning iterations. Prescribed dose in the target volume are delivered as a result of the summation of doses from individual rescans. There are several repainting strategies: uniform, random, level, time delay and breath sampling repainting [3]. These methods differ from each other in the sequence of scanning the target volume and optimization of the irradiation time.

MATERIALS AND METHODS

Proton Therapy Complex

The current experiment was carried out on proton therapy complex «Prometheus» [6, 7]. This one is a specialized serial medical installation for particle therapy manufactured by Protom Ltd. This complex consists of proton synchrotron, patient immobilization system in sitting position and X-ray system. Irradiation of tumor is performed by a thin scanning proton beam with energy in the range of 30-330 MeV and with intensity about 10^9 particles per second in spot scanning mode. Also the complex

† mikhailbelikhin@yandex.ru

ISBN: 978-3-95450-240-0 ISSN: 2673-5539 doi:10.18429/JACoW-RuPAC2021-MOPSA45

is equipped with a planning system for treatment plans calculation with Monte-Carlo method.

Dynamic Phantom

Target motion simulation is carried out by the non-anthropomorphic water dynamic phantom (Fig. 1) designed and manufactured by Protom Ltd. This one is optimized for working with «Prometheus». The dynamic phantom consists of a container with water in which a mobile target is placed. Size of the container is 30×20×20 cm^3, and volume of the targets is 6x6x6 cm^3. The targets are made of PLA using 3D-printing with 10%-filling that improves its visibility on CT. The target is moved by a servo along one axis with precision of ±0.1 mm and high repeatability. A specialized controller drives position of the target and sets motion patterns via PC software. The motion patterns (Fig. 2) are based on respiration which consists of phases: inhale, exhale and pause. Standard dosimetry equipment such as dosimetric films and ion chambers is compatible with the targets.

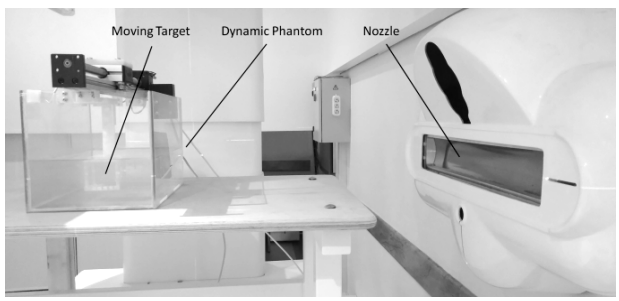

Figure 1: Photo of experimental setup.

Planning

Today used proton therapy complex is not equipped with specialized hardware and software for repainting therefore repainting simulation was carried out manually. For this six irradiation plans with doses: 0.60, 0.75, 1.00, 1.50, 3.00 and 6.00 Gy were calculated in Protom planning system. This set of plans allows to deliver the prescribed dose of 6.00 Gy in 10, 8, 6, 4, 2 and 1 iterations of repainting, respectively. One execution of the plan is equivalent to iteration of repainting. PTV has a cube shape with size of 2×2×2 cm^3 and is located in the target center. The time of 6 Gy plan execution is 1 min 46 sec.

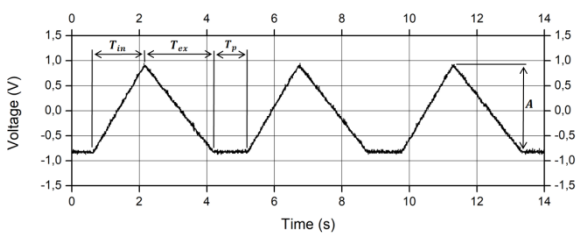

Figure 2: Graph of free breathing motion pattern of the phantom target. Motion was monitored by Protom optical respiration sensor with voltage output.

Irradiation

The dynamic phantom is placed in the immobilization system (Fig. 1) by laser pointers. Verification of phantom position is performed by two orthogonal X-ray snapshots. Free breathing pattern (Fig. 2) is used for target motion simulation. Target moves across the direction of beam propagation. Irradiation is executed in combinations: 1×6.00 Gy, 2×3.00 Gy, 4×1.50 Gy, 6×1.00 Gy, 8×0.75 Gy and 10×0.60 Gy with motion parameters: Inhale=1,5 sec, Exhale=2,0 sec, Pause=1,0 sec, Amplitude=2, 5, 10 mm.

Dosimetry

Dosimetry is carried out by dosimetric films Gafchromic EBT3 and ion chamber PTW PinPoint 3D Chamber 31022. The films and the ion chamber are installed into targets of the phantom. Two-dimensional dose distributions of target cross central layer are measured by the films. Irradiation plans verification in the central point of target is performed by the ion chamber. Irradiated films are processed according to the method described in [8, 9].

Data Analysis

Analysis of dose distributions is performed qualitatively and quantitatively. Qualitative analysis consists in visual inspection of the dose distribution for the presence of distortions such as hot and cold spots, dose field blur. Quantitative analysis consists in evaluation of average dose (Eq. (1)), standard dose deviation (Eq. (2)) and dose homogeneity (Eq. (3)) in the ROI, and dose gradients (Eq. (4)).

$$\langle D_{ROI} \rangle = \frac{\sum_{i=i_1,j=j_1}^{i_2,j_2} D_{ij}}{(i_2-i_1)(j_2-j_1)} \quad (1)$$

$$\sigma_{ROI} = \sqrt{\frac{\sum_{i=i_1,j=j_1}^{i_2,j_2} (D_{ij}-\langle D_{ROI} \rangle)^2}{(i_2-i_1)(j_2-j_1)}} \quad (2)$$

$$H_{ROI} = 100\% - \frac{\sigma_{ROI}}{\langle D_{ROI} \rangle} \cdot 100\% \quad (3)$$

$$\frac{dD}{dx} = \frac{|D_2-D_1|}{|x_2-x_1|} \quad (4)$$

Dose distribution is described by a two-dimensional dose matrix where i_1, j_1, i_2, j_2 – coordinates of the ROI, D_{ij} – element of dose matrix. The dose gradients calculated along the direction of motion on the linear section of dose fall where D_1 and D_2 – dose values at the ends of the linear section, x_1 and x_2 – coordinates of the ends of the linear section. The ROI is selected so that it is less than the PTV therefore size of the ROI is 1.8×1.8 cm. This makes it possible to exclude from the calculations the dose drops at the PTV angles.

RESULTS

The dose distribution images were built in the dose range from 0.00 to 6.50 Gy and in the millimeter coordinate system with resolution of 72 dots per inch (dpi). The calculated quantitative characteristics of dose distributions are presented in Table 1.

ISBN: 978-3-95450-240-0 ISSN: 2673-5539 doi:10.18429/JACoW-RuPAC2021-MOPSA45

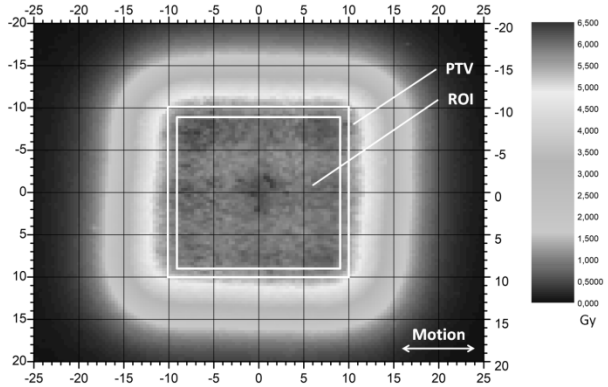

Figure 3: The dose distribution of 6.00 Gy plan without motion and with delineation of PTV, ROI and motion direction (view from nozzle).

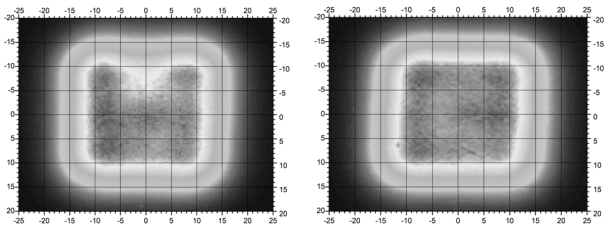

Figure 4: Motion with amplitude of 2 mm: left image – without repainting (4.6 Gy cold spot and no hot spots), right image– 6-iterative repainting.

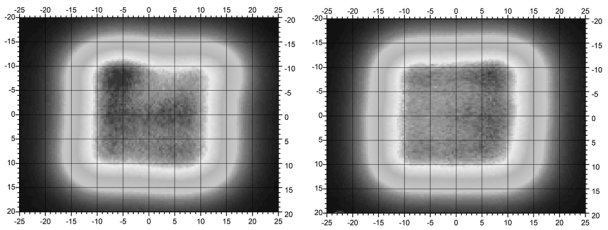

Figure 5: Motion with amplitude of 5 mm: left image – without repainting (6.6 Gy hot and 5.1 Gy cold spots), right image – 8-iterative repainting.

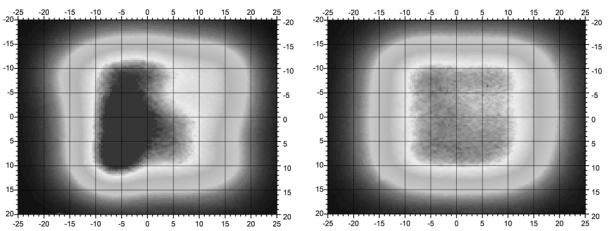

Figure 6: Motion with amplitude of 10 mm: left image – without repainting (7.8 Gy hot and 4.5 Gy cold spots), right image – 10-iterative repainting.

The dose distribution of non-moving target is shown in Fig. 3. This one is characterized by high homogeneity about 97.9% and dose gradient about 0.60 Gy/mm, and no hot and cold spots. The dose distributions of moving target without and with repainting for 2 mm (Fig. 4), 5 mm (Fig. 5) and 10 mm amplitude (Fig. 6) are shown. There are significant distortions of dose distribution without repainting: presence of hot and cold spots with doses of 7.8 Gy and 4.5 Gy (Fig. 6), shape distortion and dose blur along the direction of motion. Dose homogeneity and dose gradient decrease from 97.9% to 85.9% and from 0.60 Gy/mm to 0.44 Gy/mm, respectively, in case of 10 mm motion amplitude.

The images with repainting show that repainting removes hot and cold spots and improves homogeneity from 85.9% to 96.0% in case of 10 mm motion amplitude and 10 iterations. However, the dose gradient is inversely proportional to motion amplitude and is not improved by repainting. This one remains at the same level with ±0.02 Gy/mm fluctuations at a different number of iterations. The average dose in the ROI is lower than the prescribed dose on average 0.3 Gy that may be caused by dose blur along motion direction and film quenching effect [9].

Here the best dose distributions with the least number of repainting iteration are shown. Using more iteration did not improve the dose distribution (Fig. 4,5). The larger the amplitude of motion, the more iteration is needed to achieve acceptable homogeneity.

Table 1: Result of Quantitative Analysis of Dose Distributions

A, mm	N	H, %	Dose, Gy	Gradient, Gy/mm
-	1	97.9	6.0	0.60±0.01
2	1	94.7	5.6	0.59±0.02
	4	97.3	5.8	
	6	97.4	5.7	
5	1	92.1	5.5	0.56±0.02
	6	97.1	5.7	
	8	97.1	5.8	
10	1	85.9	6.2	0.44±0.02
	6	92.5	5.7	
	10	96.0	5.6	

CONCLUSION

Repainting greatly increases the dose homogeneity and removes hot and cold spots when irradiating a moving target. However, the dose gradient along motion direction is inversely proportional to motion amplitude and does not improve by repainting. Average dose in the ROI may decrease due to dose field blur. Thereby, optimization of the irradiation time, PTV dose and dose field margins is necessary for clinical using of repainting.

REFERENCES

[1] M. Durante and S. Galès, "Hadrontherapy", in *Nuclear Physics for Medicine*, NuPECC, pp. 11-56, 2014.

[2] A. P. Chernyaev *et al.*, "Proton Accelerators for Radiation Therapy", *Medical Radiology and Radiation Safety*, vol. 64, no. 2, pp. 11-22, 2019. doi:10.12737/article_5ca5a0173e4963.18268254

[3] T. Kubiak, "Particle therapy of moving targets – the strategies for tumour motion monitoring and moving targets irradiation", *Br. J. Radiol.*, vol. 89, no. 1066, p. 20150275, 2016. doi:10.1259/bjr.20150275

ISBN: 978-3-95450-240-0 ISSN: 2673-5539 doi:10.18429/JACoW-RuPAC2021-MOPSA45

[4] P. Trnková *et al.*, "Clinical implementations of 4D pencil beam scanned particle therapy: Report on the 4D treatment planning workshop 2016 and 2017", *Physica Medica*, vol. 54, pp. 121-130, 2018. doi:10.1016/j.ejmp.2018.10.002

[5] J. Bertholet *et al.*, "Real-time intrafraction motion monitoring in external beam radiotherapy", *Phys. Med. Biol.*, vol. 64, no. 15, 2019. doi:10.1088/1361-6560/ab2ba8

[6] A. A. Pryanichnikov *et al.*, "Clinical Use of the Proton Therapy Complex "Prometheus", *Phys. Part. Nuclei Lett.,* vol. 15, no. 7, pp. 981-985, 2018. doi:10.1134/S1547477118070592

[7] V. E. Balakin *et al.*, "Clinical Application of New Immobilization System in Seated Position for Proton Therapy", *KnE Energy*, vol. 3 no. 2, pp. 45-51, 2018. doi:10.18502/ken.v3i2.1790

[8] D. Cusumano *et al.*, "Sum signal dosimetry: A new approach for high dose quality assurance with Gafchromic EBT3", *J. Appl. Clin. Med. Phys.*, vol. 18, no. 2, pp. 181-190, 2017. doi: 10.1002/acm2.12045

[9] P. Casolaro, "Radiochromic Films for the Two-Dimensional Dose Distribution Assessment", *Appl. Sci.*, vol. 11, no. 5, p. 2132, 2021. doi:10.3390/app11052132

ISBN: 978-3-95450-240-0 ISSN: 2673-5539 doi:10.18429/JACoW-RuPAC2021-MOPSA46

PRELIMINARY STUDY OF THE GANTRY DESIGN FOR THE CENTER OF PROTON RADIATION THERAPY OF THE NRC "KURCHATOV INSTITUTE"

A. N. Chernykh, M. S. Bulatov, G. I. Klenov, V. S. Khoroshkov, NRC “Kurchatov institute”, Moscow, Russia

Abstract

NRC "Kurchatov Institute" is creating a center for proton radiation therapy (PRT), which will include a synchrotron with an energy of 250 MeV, gantry beam installations with a 360° rotation angle and a stationary channel installation. This article presents a block diagram of a gantry beamline installation and a project of a magneto-optical channel of a gantry beam installation with the main magnetic elements. In addition, a turning frame will be presented to accommodate the magnetic elements of the considered project of the gantry beamline installation.

INTRODUCTION

NRC "Kurchatov Institute" is developing a PRT center, which will become part of the Kurchatov Scientific and Educational Medical Center of Nuclear Medicine. In the future, this facility will be used for long-term development of equipment and technologies for new generation PRT and training of personnel (medical physicists and clinicians).

The second purpose of the project and the first product to be introduced into the Russia practical healthcare is a modular clinical center PRT.

A center of PRT will include a synchrotron, two treatment rooms with a 360-degree gantry and a fixed channel. This article presents the main design considerations for the turning frame of the 360-degree gantry and its beamline, which include layout of the beamline with physical and technical characteristics main elements, design and layout of the turning frame.

The main characteristics of the gantry beamline are shown in Table 1.

Table 1: Main Specification of the Gantry Beamline

Parameter	Specification
Energy range from ESS	70 - 250 MeV
Gantry type	±185 degrees
Nozzle type	Combined (Downstream scanning/passive beam)
Virtual SAD	3 m
Max. dose rate	3 Gy/min
Field size	250 mm x 250 mm

Basic requirements for the turning frame: (1) Overall dimensions length no more than 10 m, diameter no more than 13 m; (2) Angle of rotation of the gantry is not less than ± 185° (overlap in the down position); (3) Accuracy of gantry rotation + 0.3°; (4) Isocentricity of gantry rotation <0.5 mm.

IMAGE OPTICS DESIGN FOR THE GANTRY BEAMLINE

Based on the results of modeling various options for the arrangement of the gantry beamline, it is proposed to consider the arrangement made according to the "barrel" type scheme (- 60, + 60, +90 degrees) as a working option. Fig. 1 shows a diagram of a beamline for transporting a proton beam of the gantry facility. MDH 60-1 and MDH 60-2 are two 60-degree dipoles, and MDH 90-1 is a 90-degree dipole with zero angular bevels in the inlet and outlet sections. To focus the proton beam, seven MQ 50-1 - MQ 50-7 quadrupole lenses and three CHV-1 - CHV-3 correctors are installed between the dipole magnets. Five lenses and two correctors on the drift section between 60-degree dipole magnets and two lenses and a corrector on the drift section between 60- and 90-degree dipole magnets, respectively. The longitudinal size of the gantry is 8.2 m, the diameter (along the axis of the proton duct) is 10.24 m.

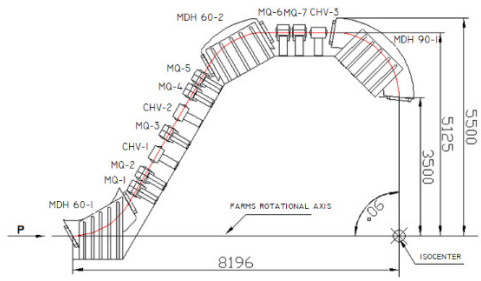

Figure 1: Diagram of the gantry beamline.

The main considerations when choosing the scheme of the gantry beamline are: (1) when an active system for generating a dose field is placed after the MDH 90-1 rotary dipole magnet, large field sizes in the isocenter can be achieved: 250 mm x 250 mm; (2) The arrangement with two 60-degree and one 90-degree dipole magnets reduces the longitudinal dimension of the gantry turning frame and avoids the more complex design of the last dipole.

The diameter of the gantry beamline is largely due to the need to ensure the maximum perpendicularity of the dose distribution entrance into the patient's body, both in the passive and in the active method of its formation. In the case of active method at small distances from the last scanning magnet to the patient's body, the non-parallelism of the beams leads to an increase in the dose on the patient's body surface. To compensate for this effect, a longer SAD L ~ 3.0 m is incorporated in the gantry design. For this

ISBN: 978-3-95450-240-0 ISSN: 2673-5539 doi:10.18429/JACoW-RuPAC2021-MOPSA46

configuration, the maximum deflecting magnet angle of the active dose field formation system can be reduced, which makes it possible to increase the scanning speed.

The beam is transported in a vacuum chamber. The vacuum tube in the gantry starts at the junction with the fixed beam transport route to the gantry, and ends at the exit from the MDH 90-1 dipole magnet. Vacuuming is used to reduce the scattering of the beam in air. In vacuum windows, a Mylar film will be used as the window material, and the air space in the area of the equipment for the dose field formation system can be filled with gaseous helium.

GANTRY BEAMLINE PROJECT

For a gantry with a 360-degree rotation angle, the presence of a transversely symmetric beam at the input is a fundamental condition, this means the equality of the envelopes of the function $\beta x = \beta z = 1.0$, the zero value of the angular deflection function $\alpha x = \alpha z = 0$, and zero variance DX = DDX = 0 in two mutually perpendicular planes OX and OY, respectively [1]. Under this condition, the parameters of the gantry beamline can remain identical for all angles of rotation.

Figure 2 shows the optical functions for the proton beam transport channel at its energies Wmin = 70 MeV and Wmax = 250 MeV, respectively. The calculation of the gantry beamline was carried out using the specialized computational program WINAGILE [2], with the following requirements for the beam parameters: throughout the entire transportation interval from the exit of the 90-degree magnet to the isocenter (the point of intersection of the proton-conductor axis after the 90-degree magnet and the axis of rotation of the gantry) independently from the energy must be formed, an axisymmetric beam with a radius of 5 mm. Taking into account the dependence of the beam emittance on energy, the requirements for optical functions were obtained: for an energy of 70 MeV - $\beta x = \beta z = 9.458$ m; $\alpha x = \alpha z = 0$; for an energy of 250 MeV - $\beta x = \beta z = 18.832$ m; $\alpha x = \alpha z = 0$. Thereby, various distributions of optical functions, depending on the beam energy, are obtained.

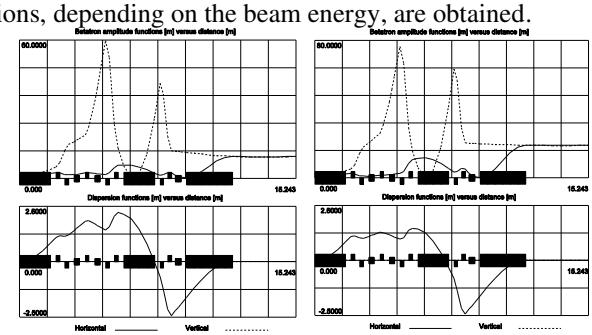

Figure 2: Optical functions of the gantry beamline at energies Wmin = 70 MeV (A) and Wmax = 250 MeV (B).

Figure 3 shows the beam envelopes for energies Wmin = 70 MeV and Wmax = 250 MeV, respectively. In both cases, axisymmetric beams with a radius of 5 mm were obtained. The maximum values of the envelopes are: at an energy of 70 MeV - 10.5 mm horizontally and 12.5 mm vertically; at an energy of 250 MeV - 9.9 mm horizontally and 10.0 mm vertically. In Fig. 3, the dashed curves show the contribution to the envelopes due to dispersion and momentum spread, and the solid curves give the total envelopes taking into account the emittance.

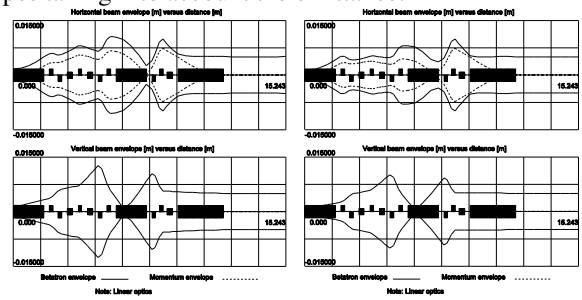

Figure 3: Beam envelopes of the gantry beamline at energy Wmin = 70 MeV (A), Wmax = 250 MeV (B).

MAGNETIC ELEMENTS

The gantry beamline includes 3 dipole, 7 quadrupole and 3 correcting magnets. The detailed characteristics of the magnets are listed in Table 2.

Table 2: Characteristics of Magnetic Elements

Type	Parameter	Specification
MDH-60	Rending radius	1620 mm
	Max field	1,5 T
	Quantity	2
	Tilt angel	0 degree in and out
	Pole distance	50 mm
	Weight	3,7 ton
	Core type	W-shaped
MDH-90	Rending radius	1620 mm
	Max field	1,5 T
	Quantity	1
	Tilt angel	0 degree in and out
	Pole distance	50 mm
	Weight	4,7 ton
	Core type	W-shaped
MQ-50	Aperture	50 mm
	YOKE	
	- height	320 mm
	- width	320 mm
	- length	200 mm
	- weight	135 kg
	WINDING	
	- wire	Copper bus
	- number of turns	22
	Max gradient	19,926 Tl/m
	Max carrent	237.3 A
	Resistance	0,0392 Om
	Voltage	9,7 B
	Max. power	2297 W
	Quantity	7

The main requirements for dipoles and quadrupoles are: (1) Constant quality of the magnetic field for high and low fields, which covers the magnetic rigidity for a proton beam from 70 MeV to 250 MeV (for example, ± 0.08% for integral homogeneity of the field of dipoles); (2) maintaining the linearity of the field, which is important for the

ISBN: 978-3-95450-240-0 ISSN: 2673-5539 doi:10.18429/JACoW-RuPAC2021-MOPSA46

dynamic properties of magnets during fast energy switching for treatment; (3) Compact design of magnetic elements, which can optimize both the total weight of the gantry turning frame and the installation space.

The choice of two 60-degree dipole magnets for parallel transfer of the proton conductor axis is a compromise between the longitudinal length of the gantry (as shown in Fig. 1, the distance between the middle of the entrance of the first MDH 60-1 dipole and the isocenter is about 8.2 m) and the space for the inclined part of the beam channel which contains 5 quadrupoles and 2 correcting magnets.

TURNING FRAME DESIGN

The design of the turning frame is proposed to be realized in the form of a cylindrical tube assembled from three sections. Support rims are located at the outer ends of the outer sections, which are directly placed on roller bearings. The turning frame is set in motion by means of a gear motor with a gear transmission, the driven crown of which is located on one of the supporting rims. The gantry beamline is located on three main support platforms (Fig. 4), which in turn are located on the frame of the cylindrical tube of the turning frame. Adjustment of the position of each magnetic element can be realized using independent fasteners.

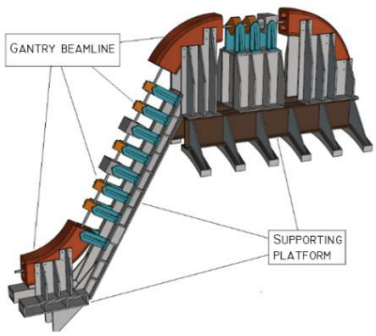

Figure 4: Layout of the gantry beamline and support platforms for magnetic elements.

STATIC ANALYSIS OF STRESSES IN THE TURNING FRAME STRUCTURE

A turning frame with support platforms for placing elements of the magneto-optical gantry channel must withstand a weight of about 30 ~ 50 tons during the working process, therefore, stress analysis in structural elements of the pivot frame at various angles of its orientation is necessary to ensure the rigidity of the proposed structure. A three-dimensional model of a gantry turning frame with the corresponding weight and size characteristics was introduced into the stress analysis module of the Autodesk INVENTOR Professional software (Fig. 5). For the preliminary analysis, two directions of the angular orientation of the turning frame were selected - vertical and horizontal. Figure 5 shows the boundary conditions for the applied load on the frame. The yellow arrow shows the vector of the direction of the gravity force acting on the turning frame in the studied position.

A) B)

Figure 5: The boundary condition for the load on the turning frame in the vertical position (A), in the horizontal position (B).

Figure 6 shows a displacement diagram. Obviously, the maximum displacement of the structure falls on the support platform of the 90-hadus magnet and the rectilinear section of the magneto-optical channel from the 60-degree to the 90-degree magnet for the vertical and horizontal orientation of the turning frame, respectively. The maximum displacement is 0.35 mm and 0.56 mm for vertical and horizontal turning frame orientations, respectively.

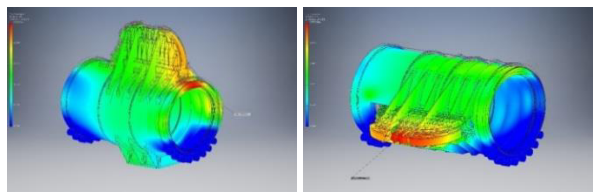

A) B)

Figure 6: Diagram of the displacement of the turning frame structures in the vertical position (A), in the horizontal position (B).

CONCLUSION

The article presents the results of a preliminary study of the gantry design for the PRT center of the NRC "Kurchatov Institute". Based on the analysis of functional requirements, a structural diagram of a beamline for transporting a proton beam in a gantry and a design of a turning frame for placing all magneto-optical elements on it have been developed. The calculation program WINAGILE was used to calculate the beamline, determine the main parameters of the magnetic elements, and obtain axisymmetric beams with a radius of 5 mm for energies of 70 and 250 MeV. Static analysis using Autodesk INVENTOR Professional software has shown the rationality of the proposed design of the turning frame to accommodate of the gantry beamline.

The preliminary studies of the gantry design laid the foundation for the further implementation of the technical project and the manufacture of the main elements of the installation.

This work is supported by the National Research Center "Kurchatov Institute" (order dated 02.07.2020 No. 1059).

REFERENCES

[1] W. Wieszczycka, W.H. Scharf, Proton radiotherapy accelerators, World Scientific Publishing. Co. Ptc. Ltd 2001.

[2] P.J. Bryant, Basic theory for magnetic measurements, CERN 92-05, (Sept., 1992), pp65-69.

ISBN: 978-3-95450-240-0 ISSN: 2673-5539 doi:10.18429/JACoW-RuPAC2021-MOPSA47

VERIFICATION OF A BEAM OF EPITHERMAL NEUTRONS FOR BORON-NEUTRON CAPTURE THERAPY*

G. D. Verkhovod†, D. A. Kasatov, Ia. A. Kolesnikov, A. Koshkarev, A. N. Makarov, I. M. Shchudlo, T. V. Sycheva, S. S. Savinov, S. Yu. Taskaev
Budker Institute of Nuclear Physics, 630090 Novosibirsk, Russia
Novosibirsk State University, Novosibirsk, Russia

Abstract

A promising method of treatment of many malignant tumors is the boron neutron capture therapy (BNCT). It provides a selective destruction of tumor cells by prior accumulation of a stable boron-10 isotope inside them and subsequent irradiation with epithermal neutrons. As a result of absorption of a neutron by boron, a nuclear reaction occurs with the release of energy in a cell containing boron. To measure the "boron" dose, a small-size neutron detector based on a boron-enriched cast polystyrene scintillator was proposed and developed at the BINP. The paper presents the results of changing the boron dose and the dose of gamma radiation in a water phantom and the comparison of these results with the calculated ones. The obtained result is important for irradiation of small laboratory animals with grafted tumors, large domestic animals with spontaneous tumors, and the planned clinical trials of the technique.

INTRODUCTION

A promising method of treatment of many malignant tumors is the boron neutron capture therapy (BNCT) [1]. It provides a selective destruction of tumor cells by prior accumulation of a stable boron-10 isotope inside them and subsequent irradiation with epithermal neutrons. As a result of absorption of a neutron by boron, a nuclear reaction occurs with the release of energy in a cell containing boron. To measure the "boron" dose, a small-size neutron detector based on a boron-enriched cast polystyrene scintillator was proposed and developed [2]. The paper presents the results of measuring the boron dose and the dose of γ-radiation in a water phantom and the comparison of these results with the calculated ones.

In BNCT, it is customary to distinguish four components of the absorbed dose: 1) Boron dose due to α-particles and atomic nuclei of lithium – products of the nuclear reaction $^{10}B(n,\alpha\gamma)^{7}Li$. In the BNCT technique, when boron is accumulated predominantly in tumor cells, the boron dose is therapeutic. 2) The dose of thermal neutrons due to recoil nuclei, mainly protons, of the nuclear reaction of neutron absorption by the atomic nucleus of chlorine $^{35}Cl(n,p)^{35}S$ and nitrogen $^{14}N(n,p)^{14}C$. 3) The dose of fast neutrons due to recoil nuclei during elastic scattering of neutrons on the nuclei of matter. 4) The dose of γ-radiation due to the ionization of atoms of a substance under the influence of γ-radiation. Sources of γ-quantum are a charged particle accelerator, a neutron-generating target, a beam shaping assembly, and an irradiated object (patient).

In the book on neutron capture therapy [1] on page 279 it is written that “the first two components of the dose cannot be measured in principle”. However, for the measurement of the boron dose, a small-sized neutron detector with a cast polystyrene scintillator enriched with boron has been developed [2].

DESIGN OF THE ACCELERATOR

The studies were carried out at the accelerating neutron source of the BINP, constructed for the development of boron neutron capture therapy for malignant tumors [3] (Fig. 1). The neutron source consists of three main units: 1) an electrostatic tandem proton accelerator of an original design (a tandem accelerator with vacuum insulation) to obtain a stationary proton beam with an energy of up to 2.3 MeV and a current of up to 10 mA; 2) a lithium target for generating neutrons in the threshold reaction $^{7}Li(p,n)^{7}Be$; and 3) a system for generating a therapeutic neutron beam for forming an epithermal neutron beam for therapy or a thermal neutron beam for research on cell cultures or small laboratory animals.

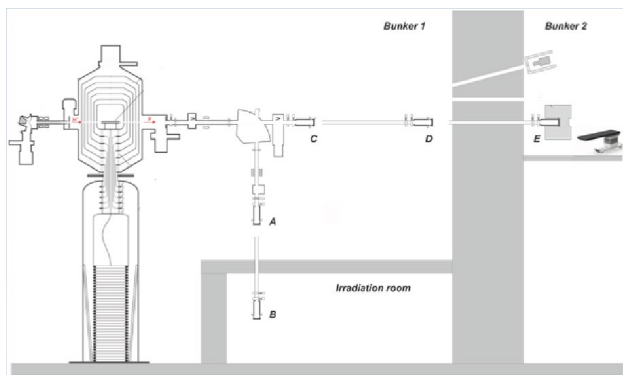

Figure 1: Layout of the experimental facility.

As seen in Fig. 1, the lithium target is placed both in the vertical path (position A) and in the horizontal path (position C) and is planned to be placed in position B for radiation testing of materials with fast neutrons, in position D for boron imaging by the method of instantaneous γ-spectroscopy with a beam monoenergetic neutrons and in position E for clinical trials of the BNCT technique.

In carrying out these studies, preliminary experiments were carried out with the target in position A, the main ones – in position C.

* Work supported by Russian Science Foundation, grant No. 19-72-30005
† g.verkhovod@alumni.nsu.ru

ISBN: 978-3-95450-240-0 ISSN: 2673-5539 doi:10.18429/JACoW-RuPAC2021-MOPSA47

EXPERIMENTAL RESULTS

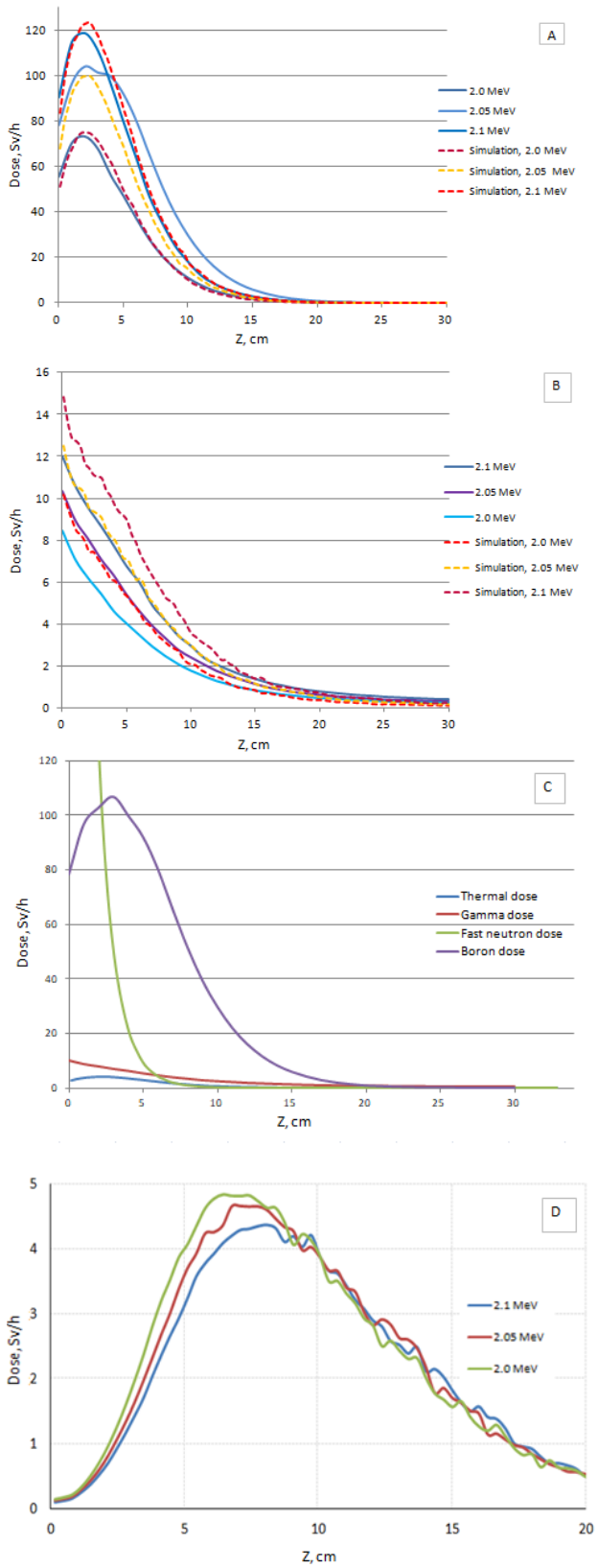

Figure 2: boron dose (a), γ-dose (b), the distribution of all doses along the beam axis (c), the ratio of the "useful" to "harmful" dose (d).

In Fig. 2 shows the dependences of the dose calculated by the detectors on the coordinate along the axis of the proton beam (Z-axis) at three values of the proton energy for: 1) boron dose; 2) γ-ray dose; 3) the ratio of the "useful" to "harmful" dose. On the graphic of the distribution of all doses along the beam axis the data were obtained at an energy of 2.05 MeV. Position Z = 0 corresponds to placing the detector close to the phantom input window; in this case, the distance between the lithium layer and the detector is 5cm. During the experiment, the movable carriage traveled a distance from 0 to 30 cm along the Z axis with a step of 1 cm. The boron and gamma dose plots show the calculated data plotted using the NMC code using the Monte-Carlo method. For subsequent doses of thermal and fast neutrons is calculated in the same way.

The dose distribution graph along the beam axis shows a significant difference in the thermal neutron dose and the gamma dose, in contrast to the boron dose, despite their slow decrease along the beam axis. Considering this contribution of thermal neutrons and gamma radiation, as well as a significant drop in the dose of fast neutrons, we can observe an acceptable ratio of the useful dose to the harmful dose at a distance of 8 cm from the lithium target.

From the obtained ratio of the "useful" dose to the "harmful" dose, it can be noted that the ratio at proton beam energy of 2.1 MeV is lower than at 2.0 and 2.05 MeV. Based on the graph, the most acceptable beam generation mode is 2.0 MeV, but a careful study of the distribution of boron dose along the Z axis, one can notice a significant increase in the useful dose in comparison with the threshold proton energy of 2.05 MeV. Based on this consideration, as well as a slight difference in the graphic of all doses distribution, the most effective mode for boron neutron capture therapy was the neutron generation reaction at proton beam energy of 2.05 MeV.

In addition to the distribution along the axis of the epithermal neutrons beam, the contribution of doses in the transverse plane (Y-axis) was also measured. The carriage with the sensors fixed on it was placed in the position of the maximum boron dose along the Z axis, after which the gamma and boron dose were measured in the plane perpendicular to the axis of the epithermal neutron beam. At each point, 120 measurements were made at energies of the proton beam of the accelerator of 2.05 and 2.1 MeV.

From the graphic shown in Fig.3, we can see that the dose distributions perpendicular to the beam axis take a bell-shaped form. Similar to the readings along the beam axis, the calculated and experimental data for the boron dose practically coincide due to the calibration of the conversion factor for simulation by the Monte Carlo method. It is also worth noting the smoother behavior of the experimental gamma dose data compared to the model, as well as a 10 percent difference in readings.

To compare the value of boron dose with doses of gamma radiation, as well as with doses of fast and thermal neutrons, a general distribution graph was plotted perpendicular to the axis of the neutron beam, also shown

ISBN: 978-3-95450-240-0 ISSN: 2673-5539 doi:10.18429/JACoW-RuPAC2021-MOPSA47

in Fig. 3. It can be seen from the graph that the distribution of all doses takes the form of a Gaussian function. Of the "harmful" doses, fast neutrons make the greatest contribution, but the function rapidly decreases with displacement from the center of the epithermal neutron beam. On the other hand, the dose from thermal neutrons and gamma radiation is almost an order of magnitude less than the readings of the boron dose, but the half-width of their Gaussian functions is large.

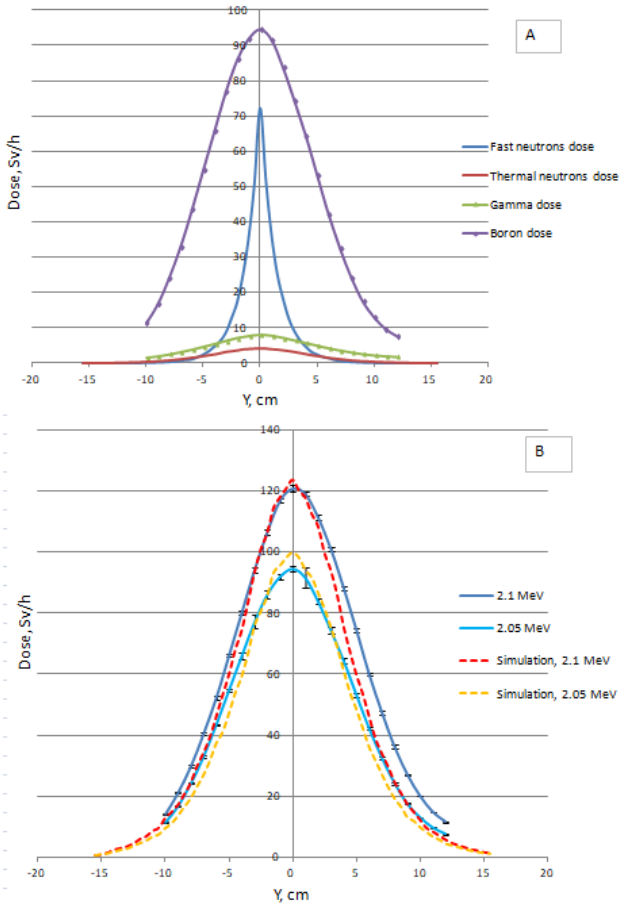

Figure 3: Distribution of doses along the Y-axis: the distribution of all doses (a), the comparison of experimental and calculated data of boron dose (b).

CONCLUSION

In boron neutron capture therapy of malignant tumors, four dose components are distinguished: 1) boron dose, which ensures the destruction of tumor cells due to the selective accumulation of boron in them, 2) a dose of fast neutrons due to elastic scattering of neutrons on atomic nuclei of matter, 3) a dose of thermal neutrons (nitrogen dose) due to $^{14}N(n,p)^{14}C$ reaction and 4) γ-ray dose. The last three doses are non-selective – they damage both tumor cells and healthy tissue cells. The BNCT tends to increase the selective boron dose and decrease the non-selective dose.

The spatial distribution of the boron dose and the γ-ray dose in a water phantom was measured at the accelerator source of epithermal neutrons at the BINP using a specially designed small-size detector with a cast polystyrene scintillator. It was found that the measurement results are in good agreement with the calculated ones. It was shown that at proton energy of 2.05 MeV and a boron concentration in tumor cells of 40 ppm, the selective boron dose is 4 times higher than the sum of non-selective doses, which is acceptable for therapy.

REFERENCES

[1] W. Sauerwein, A. Wittig, R. Moss, Y. Nakagawa (Eds.), *Neutron Capture Therapy: Principles and Applications*. Springer, 2012. doi:10.1007/978-3-642-31334-9

[2] T. Bykov *et al.*, "Initial trials of a dose monitoring detector for boron neutron capture therapy", *J. Instrum.*, vol. 16, P01024, 2021. doi:10.1088/1748-0221/16/01/P01024

[3] S. Taskaev *et al.*, "Neutron Source Based on Vacuum Insulated Tandem Accelerator and Lithium Target", *Biology*, vol. 10, 350, Apr. 2021. doi:10.3390/biology10050350

ISBN: 978-3-95450-240-0 ISSN: 2673-5539 doi:10.18429/JACoW-RuPAC2021-MOPSA48

SIMULATION OF THE ELECTROSTATIC DEFLECTOR OF DC140 CYCLOTRON

A. Zabanov†, K. Gikal, G. Gulbekyan, I. Kalagin, N. Kazarinov, V. Lisov, S. Mitrofanov, V. Semin,
JINR, 141980, Dubna, Russia

Abstract

The main activities of Flerov Laboratory of Nuclear Reactions, following its name - are related to fundamental science, but in parallel a lot of efforts are paid for practical applications. Currently, work is underway to create an irradiation facility based on the DC140 cyclotron for applied research at FLNR. The beam transport system will have three experimental beam lines for testing of electronic components (avionics and space electronics) for radiation hardness, for ion-implantation nanotechnology and for radiation materials science. The DC140 cyclotron is intended to accelerate heavy ions with mass-to-charge ratio A/Z within interval from 5 to 8.25 up to two fixed energies 2.124 and 4.8 MeV per unit mass. The intensity of the accelerated ions will be about 1 pμA for light ions (A<86) and about 0.1 pμA for heavier ions (A>132). The extraction system based on four main elements - electrostatic deflector (ESD), focusing magnetic channel, Permanent Magnet Quadrupole lens and steering magnet. The results of numerical simulation of the ESD of DC140 cyclotron are presented in this this paper.

INTRODUCTION

Flerov Laboratory of Nuclear Reaction of Joint Institute for Nuclear Research carries out the works under the creating of Irradiation Facility based on the DC140 cyclotron [1]. The DC140 will be a reconstruction of the DC72 cyclotron [2, 3].

The ion beam extraction process from the DC140 cyclotron is implemented using the ESD. The azimuthal extension of the ESD is 40° (70° - 110°). Due to the low power of the accelerated ion beams, it was decided that the potential electrode will not have an active cooling system.

The main criteria in the design of the ESD are the absence of electrical breakdowns between the electrodes and the minimum possible particle loss on the surface of the ESD.

This report presents the simulation and comparative analysis of various modifications of the ESD: with a constant gap and variable gap.

THE DETERMINATION OF CURVATURE RADIUS OF THE SEPTUM

The first step of the designing the ESD is determination of curvature radius of the septum. The extraction orbits of ion beams $^{40}Ar^{8+}$, $^{209}Bi^{38+}$ ($W = 4.8$ MeV/u), $^{197}Au^{26+}$, $^{132}Xe^{16+}$ ($W = 2.124$ MeV/u) were used to determine of curvature radius of the septum. The listed ion beams correspond to the corners of the working diagram of DC140 cyclotron (see Fig. 1).

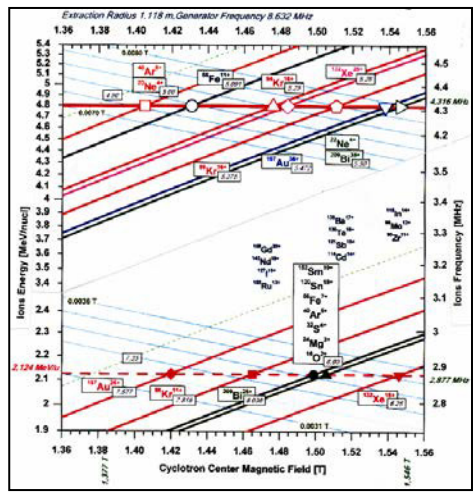

Figure 1: Working diagram of DC140 cyclotron.

The extraction orbit of ion beam in ESD can be represented as circular arc with center coordinates (x_s; y_s). The optimization task is to find the curvature radius of the septum R_s and coordinates of the center (x_s; y_s), which ensure the minimum value of the functional (Eq. 1).

$$\frac{1}{n}\sum_{i=1}^{n}(R_s - R_i)^2 \longrightarrow 0 \qquad (1)$$

where $R_i = \sqrt{(r_i \cdot \cos(\varphi_i) - x_s)^2 + (r_i \cdot \sin(\varphi_i) - y_s)^2}$ is distance from the center coordinates (x_s; y_s) to the i point of the extraction orbit of the ion beam, (r_i, φ_i) are the coordinates of point i of the extraction orbit of the ion beam in cylindrical coordinate system with origin in the cyclotron center.

The optimization results are presented in Table 1.

Table 1: the Optimization Results of the Determination of Curvature Radius of the Septum

Ion	W, MeV/u	x_s, cm	y_s, cm	R_s, cm
$^{40}Ar^{8+}$	4.8	20.87	-200.26	309.28
$^{209}Bi^{38+}$	4.8	19.01	-176.31	285.68
$^{197}Au^{26+}$	2.124	20.6	-198.67	307.68
$^{132}Xe^{16+}$	2.124	19.16	-177.33	286.71

The optimal values of curvature radii of the septum for the ion beams are very different from each other. It is necessary to find the value of curvature radius, which ensures the minimum beam losses. The curvature radius of the septum was chosen $R_s = 301.9$ cm. This value was chosen from geometric and design considerations.

† zabanov@jinr.ru

ISBN: 978-3-95450-240-0 ISSN: 2673-5539 doi:10.18429/JACoW-RuPAC2021-MOPSA48

OPTIMIZATION OF CURVATURE RADIUS OF THE POTENTIAL ELECTRODE

Two modifications of ESD with a variable gap were considered in the work: with a linearly increasing gap and a linearly decreasing electrostatic field. The ratio of the inlet gap to the outlet gap of the ESD g_1/g_n is 6/9 (mm/mm). Let us consider in detail the modification of the ESD with a linearly decreasing field and a gap ratio of 6/9.

For convenience the following consideration will be performed in the local coordinate system $x'y'$. The center of the origin of coordinates of the local system coincides with the center of curvature of the septum. The ordinate axis y' passes through the centre of the septum. The azimuthal extension of the ESD $\Delta\varphi'$ in the local system is 14.73° ([90° - $\Delta\varphi'/2$; 90° - $\Delta\varphi'/2$]).

The field potential $F(r', \varphi')$ which provides a linearly decreasing field, is described by (Eq 2).

$$F(r',\varphi') = \frac{U}{\ln(\frac{R'_1}{R_s})} \cdot \ln(\frac{r'}{R_s}) \qquad (2)$$

where U is potential electrode voltage, R'_1 is distance from the center of coordinates to the inner surface of the potential electrode.

The distance R'_1 can be represented by a function of φ' (Eq. 3).

$$R_1^{'}(\varphi') = R_s + g(\varphi') \qquad (3)$$

The size of the gap $g(\varphi')$ is determined by the (Eq. 4):

$$g(\varphi') = R_s \cdot \exp\left(\frac{1}{C_1 + C_2 \cdot (\varphi' - \varphi'_n)}\right) \qquad (4)$$

where C_1 and C_2 is entered coefficients, $C_1 = \ln\left(\frac{g_n}{R_s} + 1\right)$,

$$C_2 = \left[\frac{1}{\ln\left(\frac{g_1}{R_s}+1\right)} - \frac{1}{\ln\left(\frac{g_n}{R_s}+1\right)}\right] \cdot \frac{1}{\Delta\varphi'}.$$

The optimization task is to find potential electrode radius of curvature R_{pot} and coordinates of the center (x'_{pot}; y'_{pot}), which ensure the minimum value of the functional (Eq. 5).

$$\frac{1}{n}\sum_{i=1}^{n}(R_{pot} - R'_{1i})^2 \longrightarrow 0 \qquad (5)$$

The optimization results are presented in Table 2.

Table 2: the Results of Optimization of Curvature Radius of the Potential Electrode

g_1 [mm]	g_n [mm]	x'_{pot} [mm]	y'_{pot} [mm]	R_{pot} [cm]
6	9	11.64	-36.54	306.28

In Fig. 2 shows the graphs of the deviations δ of the resulting gap in azimuth from the gap for a linearly varying field.

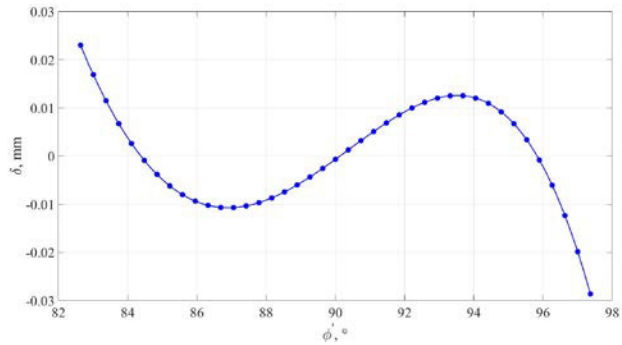

Figure 2: The deviations of the resulting gap in azimuth from the gap for a linearly varying field.

THE ELECTROSTATIC FIELD OF THE ESD WITH VARIABLE GAP

The electric field strength $E_{r'}$ and $E_{\varphi'}$ between the electrodes of the ESD is described by the following system of equations (6)

$$\begin{cases} E_{r'} = -U \cdot (C_1 + C_2 \cdot (\varphi' - \varphi'_n)) \cdot \dfrac{1}{r'} \\ E_{\varphi'} = -\dfrac{U \cdot C_2 \cdot \ln\left(\dfrac{r'}{R_s}\right)}{r'} \end{cases} \qquad (6)$$

The 2D-model of the ESD was calculated using the FEMM 4.2. In Fig. 3 show graphs of the amplitude value of the electric field strength along the central trajectory of the ESD.

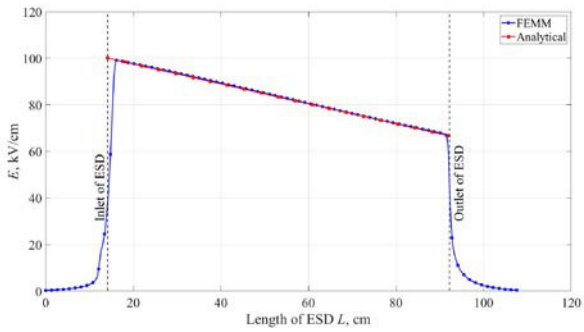

Figure 3: The amplitude value of the electric field strength along the central trajectory of the ESD.

THE COMPARISON OF VARIOUS MODIFICATIONS OF THE ESD

This section provides a comparative analysis of three modifications of the ESD: with constant gap g = 9 mm, with a linearly increasing gap (g_1/g_n = 6/9) and with a linearly decreasing electrostatic field (g_1/g_n = 6/9).

All of above modifications of the ESD deflect the ion beam at a given angle, i.e. integral of the electric field strength along the central trajectory of the ESD is the same for three modifications.

The beam losses is a key comparison criterion. The total beam losses η on the septum surface is the sum of three components:

ISBN: 978-3-95450-240-0 ISSN: 2673-5539 doi:10.18429/JACoW-RuPAC2021-MOPSA48

1. losses at the inlet end face of septum η_{end} (Eq. 7)

$$\eta_{end} = \frac{d_s}{\Delta} \cdot 100\% \quad (7)$$

where d_s is septum thickness at its entry, d_s = 0.5 mm, Δ is casting of ion beam.

2. losses on the inner surface of the septum η_{in} (Eq. 8)

$$\eta_{in} = \frac{\min(\Delta R_s)^2}{4 \cdot \theta_{max} \cdot \Delta \cdot (L_s - L_{loss})} \ 100\% \quad (8)$$

where $\min(\Delta R_s)$ is minimum distance from the septum to the envelope of the extraction orbit, θ_{max} is the angle ion beam makes in the horizontal plane with respect to the assumed central trajectory, L_s is septum length, L_{loss} is distance from the entry ESD to the point at which beam losses begin.

3. losses on the outer surface of the septum η_{out} (Eq. 9)

$$\eta_{s2} = \frac{\min(\Delta R)^2}{4 \cdot l_{min} \cdot \theta_{max} \cdot \Delta} \ 100\% \quad (9)$$

where $\min(\Delta R)$ is the minimum distance from the septum to the envelope of the last acceleration orbit, l_{min} is distance from the entry ESD to the point at which the $\min(\Delta R)$.

The ESD is located according to the following rules:

1. there should be no beam losses at the potential electrode;
2. the centre of curvature of the septum ensures the minimum value of beam losses on the septum.

The orbits and envelopes calculated for ESD with a constant gap were used in calculating the particle losses at the septum. It was assumed that changes in the envelopes for the extraction orbit of ion beams are insignificant.

Figure 4 shows the estimated location of the ESD with a linearly decreasing electrostatic field for ion beam $^{209}Bi^{38+}$.

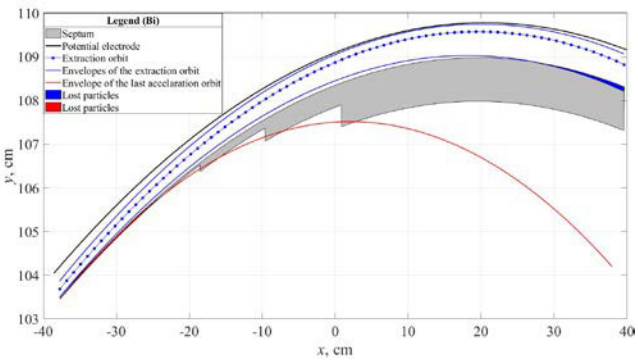

Figure 4: The estimated location of the ESD with a linearly decreasing electrostatic field for ion beam 209Bi38+.

Table 3 shows a comparison of the various modifications of the ESD for ion beam $^{209}Bi^{38+}$ (g_1/g_n = 6/9).

High precision manufacturing of the potential electrode and its installation relative to the septum are important conditions for ensuring the desired change in the variable gap along the length of the ESD.

The ESD with constant gap between electrodes provides the lowest beam losses at the septum compared to the other modifications.

A big value of the beam losses of ion beam $^{209}Bi^{38+}$ is difference between the selected septum radius of curvature R_s = 301.9 cm and obtained as result of optimization for the extraction orbit (R_{Bi} = 285.68 cm).

Table 3: the Comparison of the Various Modifications of the ESD for Ion Beam $^{209}Bi^{38+}$

Parameter	Constant gap	Linearly gap	Linearly field
U [kV]	74	61.67	60.02
E_{max} [kV/cm]	82.22	101.44	99.11
$U \times E_{max}$ [kV^2/cm]	6084.3	6255.8	5948.6
η_{end} [%]	13.93	13.93	13.93
η_{in} [%]	0	9.04	15.75
η_{out} [%]	7.32	6.13	5.28
η [%]	21.25	29.1	34.96

P.S. beam losses are indicated for the ion $^{209}Bi^{38+}$, since they are of the greatest importance in total beam losses.

SUMMARY

The ESD modification with a constant gap was selected based on the minimum values of beam losses at the septum.

REFERENCES

[1] S.V. Mitrofanov *et al.*, "FLNR JINR Accelerator Complex for Applied Physics Researches: State-of-Art and Future", in *Proc. of 22nd Conf. on Cycl. and their Appl. 2019*, Cape Town, South Africa, Sep. 2019, pp. 358-360. doi : 10. 18429/ JACoW CYCLOTRONS2019- FRB02.

[2] B. N. Gikal, "Dubna Cyclotrons – Status and Plans", in *Proc. 17th Int. Conf. on Cyclotrons and Their Applications (Cyclotrons'04)*, Tokyo, Japan, Oct. 2004, paper 20A1, pp. 100-104.

[3] G. Gulbekyan, I. Ivanenko, J. Franko, and J. Keniz, "DC-72 Cyclotron Magnetic Field Formation", In *Proc. of 19th Russian Part. Acc. Conf (RuPAC'04)*, Dubna, Russia, Oct. 2004, paper WENO12, pp. 147-49.

ISBN: 978-3-95450-240-0 ISSN: 2673-5539 doi:10.18429/JACoW-RuPAC2021-MOPSA49

DC140 CYCLOTRON, TRAJECTORY ANALYSIS OF BEAM ACCELERATION AND EXTRACTION

I.A. Ivanenko†, N.Yu. Kazarinov, V.I. Lisov, JINR, Dubna, Russia

Abstract

At the present time, the activities on creation of the new heavy-ion isochronous cyclotron DC140 are carried out at Joint Institute for Nuclear Research. DC140 facility is intended for SEE testing of microchip, for production of track membranes and for solving of applied physics problems. Cyclotron will produce accelerated beams of ions A/Z= 5 – 5.5 and 7. 5 – 8.25 with a fixed beam energy 4.8 MeV/n and 2.124 MeV/n respectively. The variation of operation modes is provided by changing of magnetic field in the range 1.4T – 1.55T with fixed generator frequency 8.632MHz. In this report, the results of design and simulation of the beam acceleration and extraction are presented.

INTRODUCTION

DC140 cyclotron will accelerate the beams from O till Bi in two main operational modes, (see Fig. 1). First mode - for SEE testing of microchips, based on ions with A/Z =5.0 – 5.5 and fixed extraction energy 4.8 MeV/nucl. Second mode - for research works on radiation physics and production of track membranes, based on ions with A/Z= 7.5 – 8.0 and fixed extraction energy 2.1 MeV/nucl. [1].

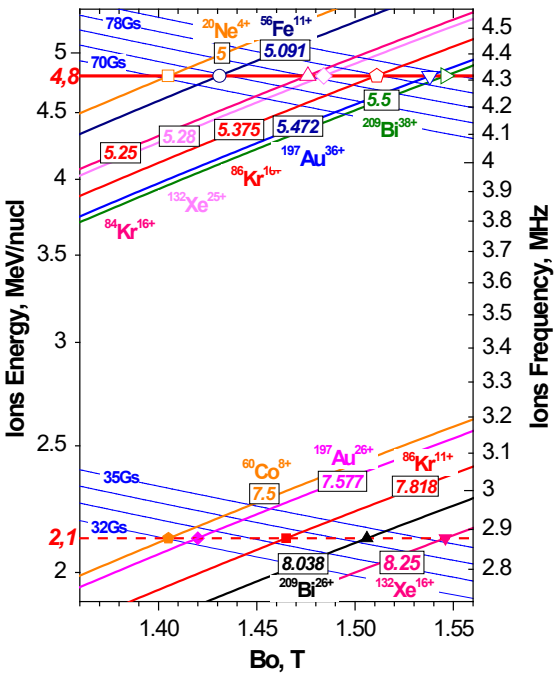

Figure 1: DC140 operational modes diagram.

DC140 cyclotron will be created as a deep reconstruction of DC72 cyclotron. The main parameters of new DC140 cyclotron are presented at Table 1. DC72 main magnet cover the new cyclotron magnetic field range 1.4T – 1.55T and stays without changing. Two 42-degree dees are placed at opposite valleys and provides acceleration voltage up to 60kV. DC140 RF generator works at fixed frequency 8.632 MHz. Acceleration modes operates at 2 and 3 RF harmonics, 4.316 MHz, and 2.877 MHz respectively. The usage of fixed frequency gives the extremely decreases of the time for switching between operation modes that very important in applied physics tasks, especially for SEE testing method.

Table 1: Main Parameters of DC140 Cyclotron

Magnet size, m	5,6x2,7x3,1
Diameter of the pole, m	1.6
Number of sector pairs	4
Number of radial trim coils	10
Number of azimuthal trim coils	4
Magnetic field range, T	1.4 – 1.55
Number of dees	2
RF voltage, kV	60
RF frequency, MHz	8.632
RF harmonic	2 – 3
Ion injection method	axial
Ion source	ECR
Ion extraction method	electrostatic
Deflector voltage, kV	75

CYCLOTRON MAGNETIC FIELD

DC140 is a compact type isochronous cyclotron based on DC72 magnet [2]. Main magnet has H-shape form with 1.6 meter pole diameter.

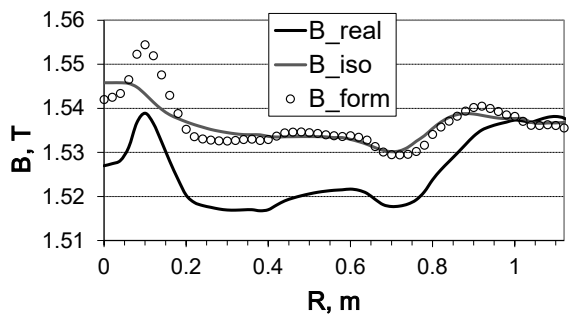

Figure 2: Operational formation of the magnetic field for 209Bi38+ acceleration mode.

Figure 2 demonstrates the usage of 10 radial trim coils for operational formation of isochronous magnetic field for 209Bi38+ acceleration mode. B_real presents base magnetic field, without trim coils. B_iso presents calculated isochronous field for 209Bi38+ acceleration mode. B_form presents final magnetic field, operationally formed with radial trim coils. Formed magnetic field keeps betatron frequencies in the ranges 1.005<Qr<1.05 and

† ivan@jimr.ru

ISBN: 978-3-95450-240-0 ISSN: 2673-5539 doi:10.18429/JACoW-RuPAC2021-MOPSA49

0.2<Qz<0.45, excluded central region, there beam crosses resonance Qr=1, (see Fig. 3). At the first orbits the beam has a high tempo of radius growth and cross Qr=1 resonance area very quickly.

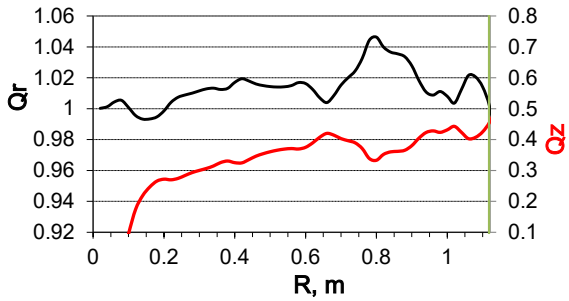

Figure 3: Radial and vertical betatron oscillation frequencies for 209Bi38+ acceleration mode.

INFLECTOR AND CENTRE REGION

Electrostatic spiral inflector with magnetic radius R_{mag}=30mm and electric radius A_e=35mm is used to turn the injected beams onto acceleration region. Because magnetic radius is constant for all operational modes, the injection voltage varies in the ranges 16kV – 20kV for the first main operational mode and 11kV – 13kV for the second.

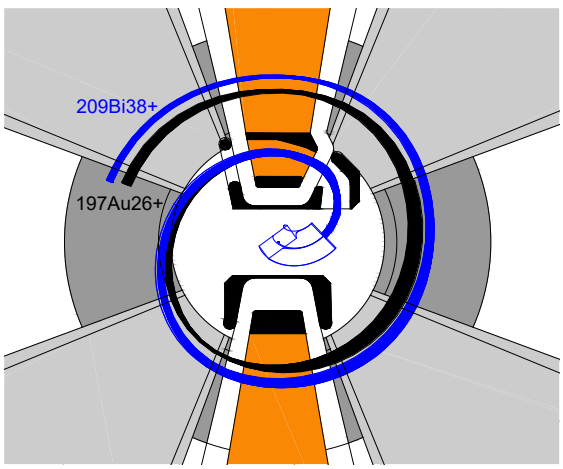

Figure 4: DC140 central region.

Figure 4 demonstrates DC140 central region with calculated first orbits of 197Au26+ (A/Z=7.577) and 209Bi38+ (A/Z=5.5) ions beams. First acceleration gap is placed at angular position 28° from the dee central axis as a compromise between operation modes at 2 and 3 RF harmonics. Figure 5 demonstrates R-R' position of 209Bi38+ beam after inflector and before first acceleration gap. Red line represents the variation of beam R-R' position in depends on inflector angulare rotation. At the start position of calculations, at the inflector entrance, the beam with momentum deviation dp/p=0.01 and phase range ±10° of RF was taken. After crossing the accelerating gaps at the first orbit, the deviation of 209Bi38+ ions energy in the beam become dW/W≈0.07, (see Fig. 6). Phase range increases in about 2 times because different paths of ions during the crossing of first accelerating gap.

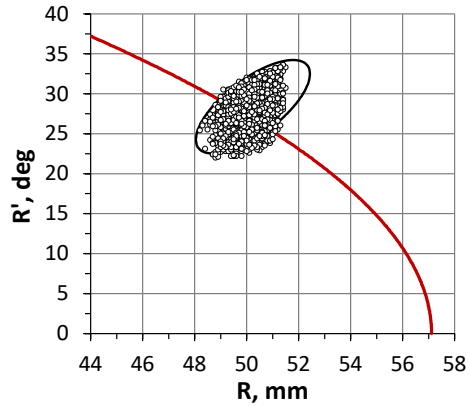

Figure 5: Radial position of 209Bi38+ beam at the entrance of puller (first acceleration gap).

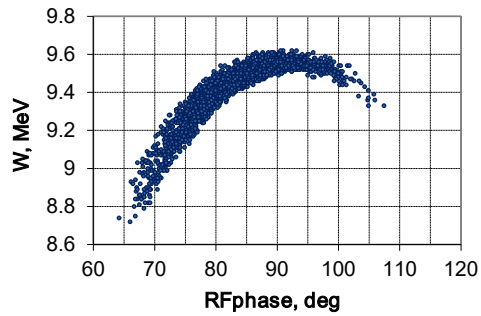

Figure 6: The distribution of ions energy in 209Bi38+ beam at first orbit after injection.

Coefficient of the beam transmission through the cyclotron center is about 16% for total phase range without usage buncher, and about 90% for chosen start phases ±10°.

BEAM ACCELERATION

In DC140 cyclotron the beams pass about 170 orbits up to extraction radius R_{ext}=1.12m. Figure 7 demonstrates the phases of ions in 209Bi38+ beam during acceleration. The criteria of chosen of magnetic field level is a zero phase shifting of the reference ion at the extraction radius, red line at Figure 7.

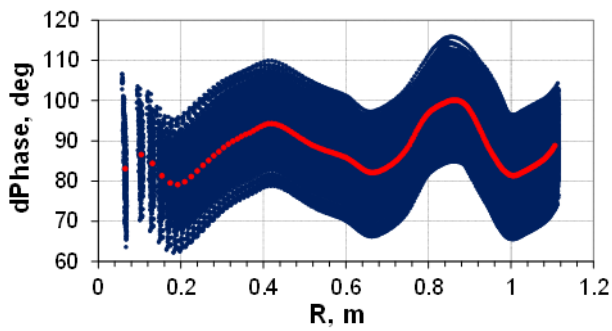

Figure 7: The phases of ions in 209Bi38+ beam during acceleration from cyclotron center to extraction radius.

Figure 8 demonstrates the radial coherent oscillations of ions in 209Bi38+ beam during acceleration from cyclotron center to extraction radius. Red line represents behavior of radial oscillations of reference ion. The main reason of the

ISBN: 978-3-95450-240-0 ISSN: 2673-5539 doi:10.18429/JACoW-RuPAC2021-MOPSA49

increasing of this oscillations at the central radiuses up to value Ar ≈ 0.03m is the compromise angle position of puller accelerating gap for 2 and 3 RF harmonics, (see Fig. 4). Figure 9 demonstrates the vertical behavior of ions in 209Bi38+ beam when it is accelerated from cyclotron center to extraction radius. The coefficient of the beam transmission through acceleration region is about 91%.

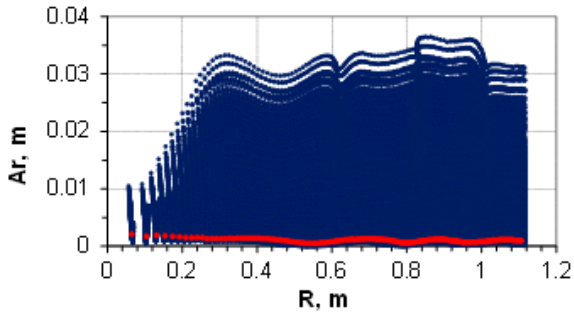

Figure 8: Radial coherent oscillations of ions in 209Bi38+ beam from cyclotron center to extraction radius.

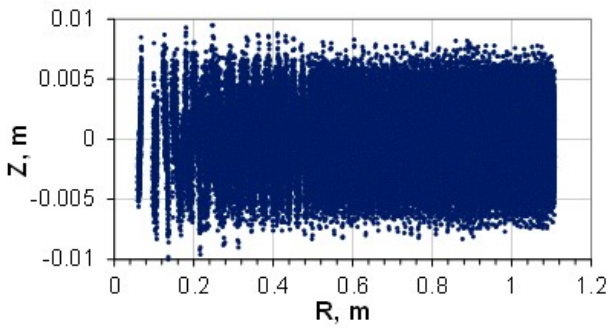

Figure 9: Vertical dimension of 209Bi38+ beam during acceleration from cyclotron center to extraction radius

BEAM EXTRACTION

DC140 beam extraction system consists of electrostatic deflector with maximal extraction voltage 75kV and two correctors (see Fig. 10).

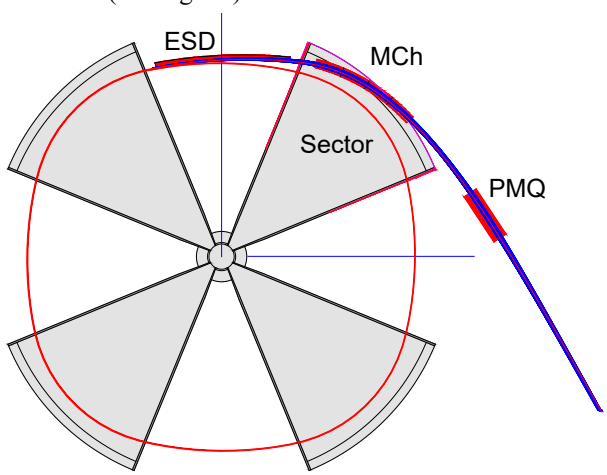

Figure 10: Last orbits and extraction trajectory of 209Bi38+ ion beam.

First corrector, passive magnetic channel MCh, is plased exactly after deflector and compensate the gradient of magnetic field at the sector edge. Second corrector, quadrupole lens PMQ, based on permanent magnets, produce an additional beam focusing in the area of low magnetic field. The distance between neighbor orbits before extraction ≈3.5mm. Because radial coherent oscillations is about 30mm, more then 4 – 5 orbits are accepted at the septum of deflector, as it is shown at the Figure 11. Whereis the deviation of 209Bi38+ ions energy in the extracted beam become dW/W≈0.03.

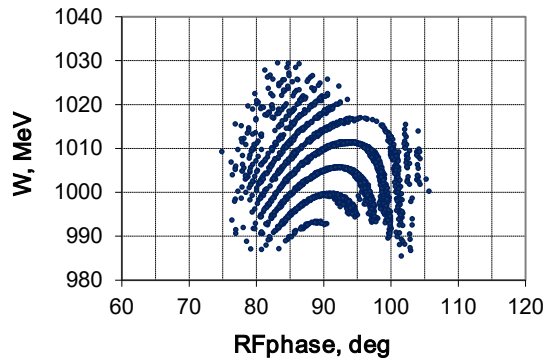

Figure 11: The distribution of ions energy in 209Bi38+ beam at the septum of deflector.

Figure 12 represents radial and vertical envelopes of 209Bi38+ beam when it is passes electrostatic deflector ESD, passive magnetic channel MCh and quadrupole lens PMQ. The efficiency of beam transmission through DC140 extraction system is about 80%.

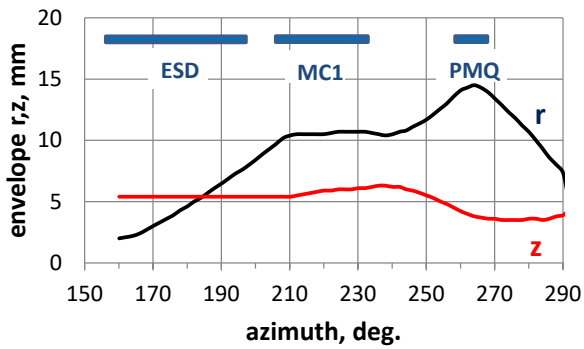

Figure 12: The radial and vertical envelopes of 209Bi38+ extracted beam.

CONCLUSION

DC140 cyclotron will be created as a deep reconstruction of DC72 cyclotron. New cyclotron will produce accelerated beams of ions A/Z= 5 – 5.5 and 7. 5 – 8.25 with a fixed beam energy 4.8 MeV/n and 2.124 MeV/n respectively. Based on results of DC72 magnetic field measurements, the trajectory analysis for DC140 beams was carry out. The results of analysis have shown a good transmission efficiency of injection (≈16% without buncher), acceleration (≈91%) and extraction (≈80%) systems of new cyclotron.

ISBN: 978-3-95450-240-0 ISSN: 2673-5539 doi:10.18429/JACoW-RuPAC2021-MOPSA49

REFERENCES

[1] N. Yu. Kazarinov *et al.*, "Conceptual Design of FLNR JINR Radiation Facility Based on DC130 Cyclotron", in *Proc. 61st ICFA Advanced Beam Dynamics Workshop on High-Intensity and High-Brightness Hadron Beams (HB'18)*, Daejeon, Korea, Jun. 2018, pp. 324-328. doi:10.18429/JACoW-HB2018-WEP2PO028

[2] G. Gulbekian, I. Ivanenko, J. Franko, and J. Keniz, "DC-72 cyclotron magnetic field formation", in *Proc. 19th Russian Particle Accelerator Conf. (RuPAC'04)*, Dubna, Russia, Oct. 2004, paper WENO12, pp. 147-49.

ISBN: 978-3-95450-240-0 ISSN: 2673-5539 doi:10.18429/JACoW-RuPAC2021-MOPSA50

AXIAL INJECTION SYSTEM OF DC140 CYCLOTRON OF FLNR JINR

N.Yu. Kazarinov†, G.G. Gulbekyan, V.V. Bekhterev, I.A. Ivanenko, I.V. Kalagin, V.I. Lisov, S.V. Mitrofanov, N.F. Osipov, V.A. Semin, JINR, 141980, Dubna, Russia

Abstract

Flerov Laboratory of Nuclear Reaction of Joint Institute for Nuclear Research continues the works under creating of FLNR JINR Irradiation Facility based on the cyclotron DC140. The facility will have three experimental beam lines for SEE testing of microchips, for production of track membranes and for solving of applied physics problems. The injection into cyclotron will be realized from the external room temperature 18 GHz ECR ion source. The systems of DC140 cyclotron – axial injection, main magnet, RF- and extraction systems and beam lines are the reconstruction of the DC72 cyclotron ones. The acceleration in DC140 cyclotron is carried out for two values of harmonic number h = 2,3 of heavy ions with mass-to-charge ratio A/Z within two intervals 5 – 5.5 and 7.5 – 8.25 up to two fixed energies 2.124 and 4.8 MeV per unit mass, correspondingly. The intensity of the accelerated ions will be about 1 pmcA for light ions (A≤86) and about 0.1 pmcA for heavier ions (A≥132). The design of the axial injection system of the DC140 cyclotron is presented in this report.

INTRODUCTION

Flerov Laboratory of Nuclear Reaction of Joint Institute for Nuclear Research carries out the works under the creating of Irradiation Facility based on the DC140 cyclotron [1]. The DC140 will be a reconstruction of the DC72 cyclotron [2, 3]. Table 1 presents the main parameters of DC140 cyclotron.

Table 1: Main Parameters of DC140 Cyclotron

Pole (Extraction) Radius, m	1.3 (1.18)	
Magnetic field, T	1.415÷1.546	
Number of sectors	4	
RF frequency, MHz	8.632	
Harmonic number	2	3
Energy, MeV/u	4.8	2.124
A/Z range	5.0÷5.5	7.57÷8.25
RF voltage, kV	60	
Number of Dees	2	
Ion extraction method	electrostatic deflector	
Deflector voltage, kV	73.5	

The irradiation facility will be used for Single Event Effect (SEE) testing of microchips by means of ion beams (^{16}O, ^{20}Ne, ^{40}Ar, ^{56}Fe, ^{84,86}Kr, ^{132}Xe, ^{197}Au and ^{209}Bi) with energy of 4.8 MeV per unit mass and having mass-to-charge ratio A/Z in the range from 5.0 to 5.5.

Besides the research works on radiation physics, radiation resistance of materials and the production of track membranes will be carrying out by using the ion beams with energy of about 2.124 MeV per unit mass and A/Z ratio in the range from 7.577 to 8.25.

The working diagram of DC140 cyclotron is shown in Fig. 1. The acceleration of ion beam in the cyclotron will be performed at constant frequency f = 8.632 MHz of the RF-accelerating system for two different harmonic numbers h. The harmonic number h = 2 corresponds to the maximal and value h = 3 – to minimal ion beam energy. The intensity of the accelerated ions will be 1 pμA for light ions (A≤86) and 0.1 pμA for heavier ions (A≥132).

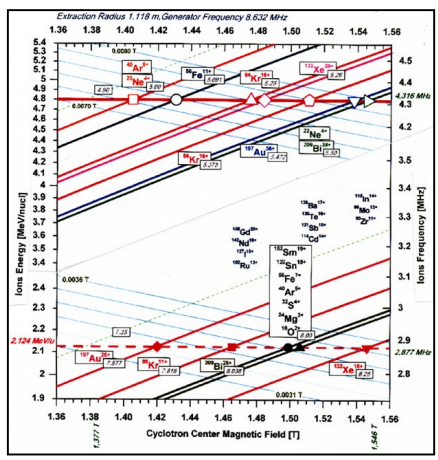

Figure 1: Working diagram of DC140 cyclotron.

The axial injection system of DC140 cyclotron will be adapted from the existing DC72 cyclotron one [4].

This report presents the design and simulation of the beam dynamic in the axial injection beam line of DC140 cyclotron. The simulation was carried out by means of MCIB04 program code [5].

ECR ION SOURCE

The ion beams are produced in room temperature ECR ion source DECRIS-5 designed in Flerov Lab of JINR [6]. The working frequency DECRIS-5 is equal to 18 GHz. It is able to produce the beams of ion from ^{22}Ne to ^{209}Bi.

BEAM LINE ELEMENTS

The scheme of the beam line is shown in Fig. 2. The length of the beam line is equal to 5.065 m. The 90-degree analyzing magnet **M90** separates the injected beam. The solenoidal lenses **S1-4** focus and match beam with the acceptance of the spiral inflector **I** for all level of the cyclotron magnetic field. Two movable diaphragms **CL1, 2** are

† nyk@jinr.ru

ISBN: 978-3-95450-240-0 ISSN: 2673-5539 doi:10.18429/JACoW-RuPAC2021-MOPSA50

used for analysis of the beam spectra. The two-harmonic buncher **BN** increases the beam capture into acceleration.

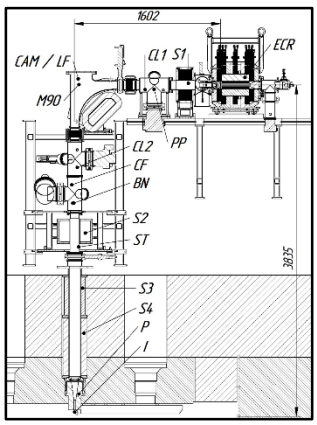

Figure 2: Scheme of the axial injection beam line.

Analyzing Magnet M90

The analyzing magnet **M90** has a bending radius R_M equal to 0.4 m, gap 80 mm and maximum magnetic field 0.2 T. The fluorescent screen **LF** and video camera **CAM** give the possibility to control ion beam size in the magnet.

Solenoids S1-4

The solenoids **S1-4** are the part of existing DC72 cyclotron axial injection beam line [4]. Its on-axis magnetic fields are shown in Fig. 3.

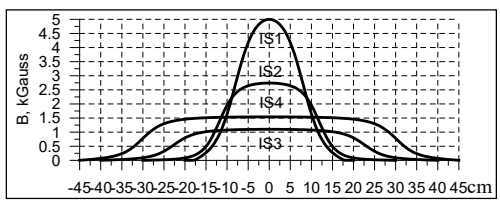

Figure 3: On-axis magnetic field of solenoids.

Diaphragms CL1,2

Two movable diaphragms **CL1,2** is used in the beam spectrum analysis. The first diaphragm **CL1** (see Fig.4) has the form of a square with a side of 10 mm and is located at a distance of 373 mm in front of the **M90** magnet.

The second one **CL2** is a slit with a width of 5 mm<d<10 mm, located at distance equal to 100 mm before Faraday cap **CF**.

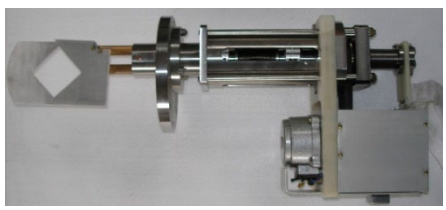

Figure 4: Diaphragm CL1.

Pepper-Pot PP

Pepper-Pot **PP** installed in the horizontal part of the beamline is used for decreasing of the beam current.

Two-Harmonic Buncher BN

To improve the efficiency of beam capture into the acceleration the two-harmonic buncher **BN**, located outside the yoke of the magnet at a distance of 2.341 m from the median plane of the cyclotron, is used. The maximum applied voltage at the grids of buncher is 500 V for the injecting ions having A/Z = 5.5($^{209}Bi^{38+}$). The efficiency of bunching is approximately equal to 2.75 (see Fig. 5).

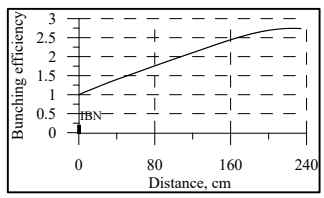

Figure 5: Bunching efficiency.

Beam Stopper ST

The beam stopper **ST** is placed between solenoid **S2** and vacuum gate valve of the main magnet. It has to interrupt completely the ion beam and ensure the safe operation and maintenance of the cyclotron.

Magnetic Plug P

The apertures in the magnetic plug **P** are increased as compare the DC72 cyclotron ones to avoid the possible particle losses.

Spiral Inflector I

To simplify the operation of the cyclotron only one inflector with a magnetic radius of 30 mm is used. In the case of accelerating with harmonic number of h = 2, the injection voltage U_{inj} changes from 17.15 kV to 18.86 kV for the injected ions with A/Z in the range from 5.0 ($^{40}Ar^{8+}$) to 5.5 ($^{209}Bi^{38+}$). In the case of h = 3, the voltage U_{inj} changes from 11.55 kV to 12.58 kV for the injected ions with A/Z in the range from 7.577 ($^{197}Au^{26+}$) to 8.25 ($^{132}Xe^{16+}$).

SIMULATION RESULTS

The calculations of ion injection with the parameters specified in Table 2 were carried out. In all cases, the transfer efficiency is equal to 100%.

A/Z=5.5, B_0=1.546 T, ρ_M=30.0 mm, h=2

Transport of $^{209}Bi^{38+}$ ion beam is considered. In this case the magnetic field at the center of the cyclotron B_0 = 1.546 T is maximal. The horizontal (H) and vertical (V) envelopes of $^{209}Bi^{38+}$ ions in the beam line is shown in Fig. 6 and Fig. 7.

ISBN: 978-3-95450-240-0 ISSN: 2673-5539 doi:10.18429/JACoW-RuPAC2021-MOPSA50

Table 2: Parameters of Ion Beam Used in Simulation

Ions/harmonic number	$^{209}Bi^{38+}/2$	$^{197}Au^{26+}/3$
A/Z	5.5	7.58
ECR voltage Uinj, kV	18.86	11.55
Beam current, μA	1.25	6
Beam diameter, mm	8	8
Emittance, π mm × mrad	220	237

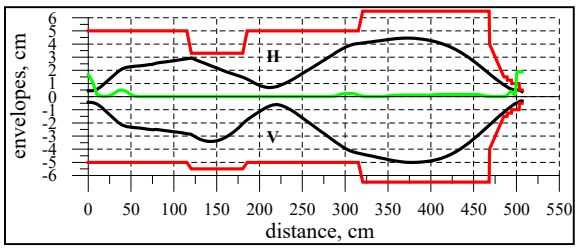

Figure 6: Horizontal (H) and vertical (V) $^{209}Bi^{38+}$ beam envelopes, aperture (red line) and longitudinal magnetic field (green line).

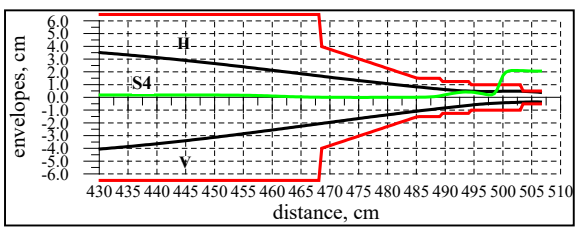

Figure 7: Envelopes of Bi38+ ion beam near inflector.

A/Z=7.58, B_0=1.420 T, ρ_M=30.0 mm, h=3

Transport of $^{197}Au^{26+}$ ion beam is considered. In this case the magnetic field at the center of the cyclotron B_0 = 1.420 T. The horizontal (H) and vertical (V) envelopes of $^{197}Au^{26+}$ ions in the beam line is shown in Fig. 8 and Fig. 9.

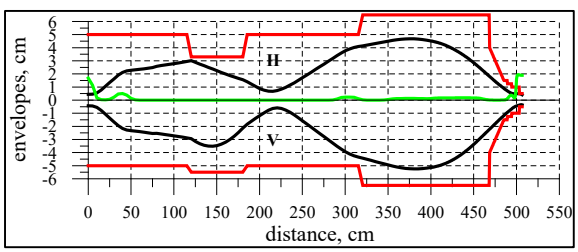

Figure 8: Horizontal (H) and vertical (V) $^{197}Au^{26+}$ beam envelopes, aperture (red line) and longitudinal magnetic field (green line).

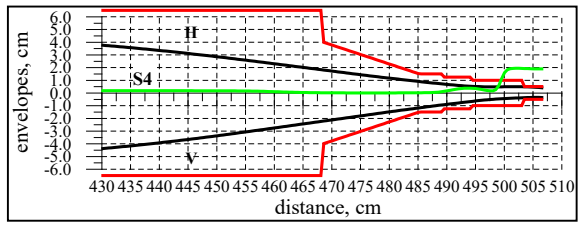

Figure 9: Envelopes of Au26+ ion beam near inflector.

Beam Spectrum Analysis

The beam emittance is decreased at diaphragm **CL1** in 16 times that give opportunity to separate two neighbor charges in the beam spectrum by means of diaphragm **CL2**. The $^{209}Bi^{38+}$ ion beam envelopes are shown in Fig. 10.

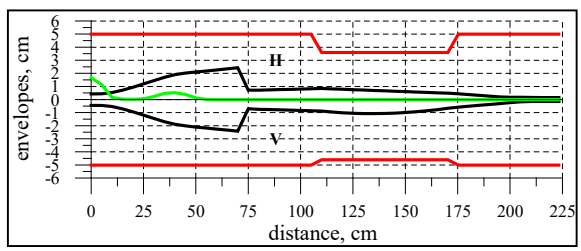

Figure 10: $^{209}Bi^{38+}$ ion beam envelopes.

The distribution of $^{209}Bi^{37+,38+,39+}$ ions and contaminant $^{16}O^{3+}$ ions in front of the diaphragm **CL2** is shown in Fig. 11.

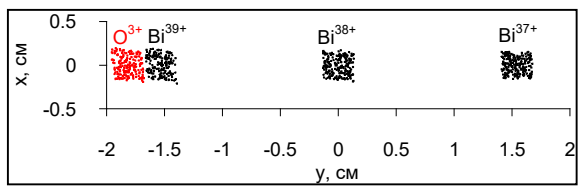

Figure 11: Bi and O ions distribution at slit CL2.

SUMMARY

The axial injection system of DC140 cyclotron allows transporting with of 100% efficiency all ion beams declared in the working diagram of FLNR JINR Irradiation Facility (see Fig. 1).

The proposed system of beam spectrum analysis gives the possibility to separate ion charge up to value Z=38.

The magnitudes of magnetic fields of all beamline optical elements are in the design range.

REFERENCES

[1] S. V. Mitrofanov *et.al.*, "FLNR JINR Accelerator Complex for Applied Physics Researches: State-of-Art and Future", In *Proc. of 22nd Conf. on Cycl. and their Appl.*, Cape Town, South Africa, Sep. 2019, pp. 358-360, doi:10.18429/JACoW-CYCLOTRONS2019-FRB02

ISBN: 978-3-95450-240-0 ISSN: 2673-5539 doi:10.18429/JACoW-RuPAC2021-MOPSA50

[2] B. N. Gikal, "Dubna Cyclotrons – Status and Plans", in *Proc. 17th Int. Conf. on Cyclotrons and Their Applications (Cyclotrons'04)*, Tokyo, Japan, Oct. 2004, paper 20A1, pp. 100-104.

[3] G. Gulbekyan, I. Ivanenko, J. Franko, and J. Keniz, "DC-72 Cyclotron Magnetic Field Formation", In *Proc. of 19th Russian Part. Acc. Conf (RuPAC'04)*, Dubna, Russia, Oct. 2004, paper WENO12, pp. 147-49.

[4] G. G. Gulbekyan, S. L. Bogomolov, V. V. Bekhterev, I. V. Kalagin, N. Yu. Kazarinov, and M. V. Khabarov, "Axial Injection Channel of the DC-72 Cyclotron", in *Proc. 19th Russian Particle Accelerator Conf. (RuPAC'04)*, Dubna, Russia, Oct. 2004, paper WENO11, pp. 144-146.

[5] V. Aleksandrov, N. Kazarinov, and V. Shevtsov, "Multi Component Ion Beam Code-MCIB04", In *Proc. of 19th Russian Part. Acc. Conf (RuPAC'04)*, Dubna, Russia, Oct. 2004, paper THBP09, pp. 201-203.

[6] S. L. Bogomolov *et al.*, "Recent Development in ECR Ion Sources at FLNR JINR", in *Proc. 23rd Russian Particle Accelerator Conf. (RuPAC'12)*, Saint Petersburg, Russia, Sep. 2012, paper FRYOR01, pp. 203-207.

ISBN: 978-3-95450-240-0 ISSN: 2673-5539 doi:10.18429/JACoW-RuPAC2021-MOPSA51

THE EXTRACTION SYSTEM OF DC140 CYCLOTRON

V. Lisov†, K. Gikal, G. Gulbekyan, I. Ivanenko, G. Ivanov, I. Kalagin, N. Kazarinov, S. Mitrofanov, N. Osipov, A. Protasov, V. Semin, A. Zabanov
JINR, 141980, Dubna, Russia

Abstract

The main activities of Flerov Laboratory of Nuclear Reactions, following its name - are related to fundamental science, but, in parallel, plenty of efforts are paid for practical applications. For the moment continues the works under creating irradiation facility based on the cyclotron DC140 which will be dedicated machine for applied researches in FLNR. The beam transport system will have three experimental beam lines for testing of electronic components (avionics and space electronics) for radiation hardness, for ion-implantation nanotechnology and for radiation materials science. The DC140 cyclotron is intended for acceleration of heavy ions with mass-to-charge ratio A/Z within interval from 5 to 8.25 up to two fixed energies 2.124 and 4.8 MeV per unit mass. The intensity of the accelerated ions will be about 1 pμA for light ions (A<86) and about 0.1 pμA for heavier ions (A>132). The following elements are used to extract the beam from the cyclotron: electrostatic deflector, focusing magnetic channel, Permanent Magnet Quadrupole lens and steering magnet. The design of the beam extraction system of DC140 cyclotron are presented in this report.

INTRODUCTION

The DC140 is a sector cyclotron is intended for acceleration of heavy ions [1]. It will be a reconstruction of the DC72 cyclotron [2, 3]. In DC72 beam was extracted by stripping method. In DC140 the extraction will be carried out using an electrostatic deflector.

For beams extraction from the cyclotron is used the electrostatic deflector. The extraction system of the DC140 cyclotron consist a next elements (see Fig. 1):

1. Electrostatic deflector (ESD);
2. Focusing magnetic channel (MC);
3. Permanent Magnet Quadrupole lens (PMQ).

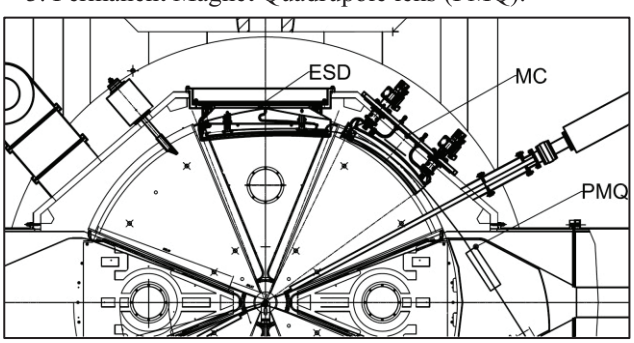

Figure 1: Layout of the elements of extraction system.

The main parameters of DC140 cyclotron are given in Table 1.

Table 1: DC140 Cyclotron Main Parameters

Parameter	Value	
Magnetic field [T]	1.415÷1.546	
Pole (extraction) radius [m]	1.3(1.18)	
Number of sectors	4	
RF frequency [MHz]	8.632	
Harmonic number	2	3
Energy [MeV/u]	4.8	2.124
A/Z range	5.0÷5.5	7.57÷8.25
RF voltage [kV]	60	
Number of Dees	2	
Ion extraction method	electrostatic deflector	
Deflector voltage [kV]	73.5	

NUMERICAL SIMULATION OF THE BEAM EXTRACTION

For numerical simulation the test ion in accordance with working diagram are used [see Fig. 2, 3, 4, 5]. The parameters of this ion are given in Table 2.

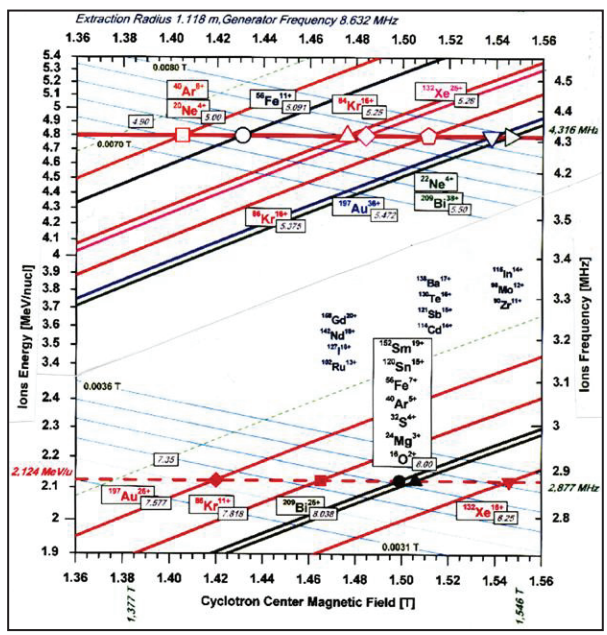

Figure 2: Working diagram of DC140 cyclotron.

† lisov@jinr.ru

ISBN: 978-3-95450-240-0 ISSN: 2673-5539 doi:10.18429/JACoW-RuPAC2021-MOPSA51

Table 2: Parameters of the Test Ions

Ion	$^{209}Bi^{38+}$
A/Z	5.5
B_o [T]	1.5458
B(R) [T]	1.5540
E(R)	4.80
F_{ion} [MHz]	4.316
Harmonic	2
R_{mag} [cm]	3
U_{inj} [kV]	18.86

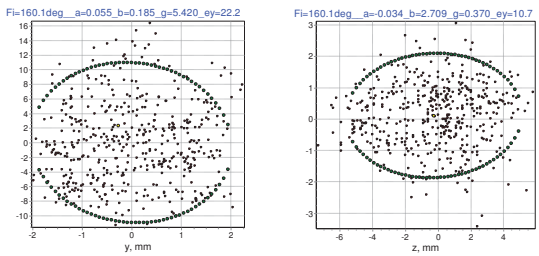

Figure 3: The horizontal and vertical beam emittances at the deflector entrance (A/Z=5.5, Bo=1.55 T).

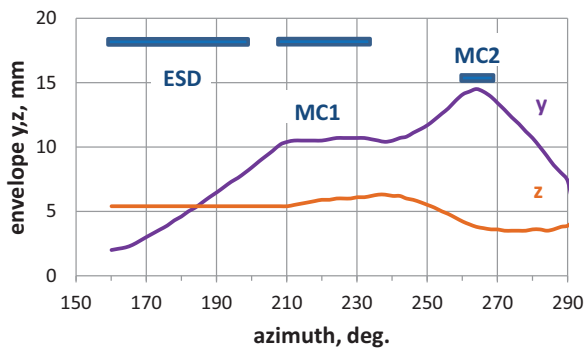

Figure 4: The horizontal and vertical beam envelopes.

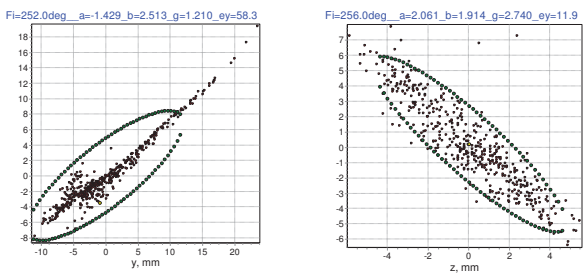

Figure 5: The horizontal and vertical beam emittances at the PMQ entrance (A/Z=5.5, Bo=1.55 T).

ELECTROSTATIC DEFLECTOR

The electrostatic deflector (ESD) consists of two parallel plates (septum plate and potential plate), between which an electric field is created and deflecting the beam from the cyclotron chamber.

The azimuthal position of electrostatic deflector is 40º (70º - 110º). Due to the low power of the accelerated ion beams, it was decided that the potential electrode will not have an active cooling system.

The main parameters of the electrostatic deflector are given in Table 3.

Table 3: Parameters of the Electrostatic Deflector

Parameter	Value
Azimuthal position [deg]	70÷110
Max. Voltage [kV]	73.5
Length of the "potencial" plate [mm]	780
Length of the "septum" plate [mm]	775
Thickness of the "septum" plate [mm]	0.3÷1.0
Material of the "potencial" plate [mm]	Al
Material of the "septum" plate [mm]	W
Gap between plates [mm]	9
Displace of the deflector edges [mm]	± 10

During the design, three modifications of the deflector were considered: with constant gap g = 9 mm, with a linearly increasing gap (g_1/g_n = 6/9) and with a linearly decreasing electrostatic field (g_1/g_n = 6/9).

Modeling of the electrostatic deflector in detail in [4].

The electrostatic deflector with constant gap between electrodes provides the lowest beam losses (η = 21.25 %) at the septum compared to the other modifications (see Fig. 6).

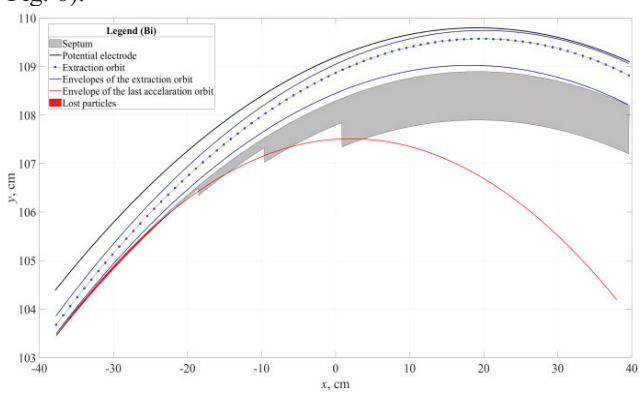

Figure 6: Graph of losses of ion beam $^{209}Bi^{38+}$ in an electrostatic deflector with a constant gap.

ISBN: 978-3-95450-240-0 ISSN: 2673-5539 doi:10.18429/JACoW-RuPAC2021-MOPSA51

FOCUSING MAGNETIC CHANNEL

The focusing magnetic channel (MC) is intended for focusing in the horizontal direction of the heavy ion beam extracted from the cyclotron (see Fig. 7). The MC consists of 4 parts with different cross-sections. Azimuth extent of each section 8.3° (see Fig. 8).

The main parameters of the magnetic channel are given in Table 4.

Table 4: Parameters of Magnetic Channel

Parameter	Value
Azimuthal position [deg]	36÷64
Horizontal aperture [mm]	32
Vertical aperture [mm]	20
Displace of the edges [mm]	± 15
Focusing gradient of the magnetic field [T/m]	13.5

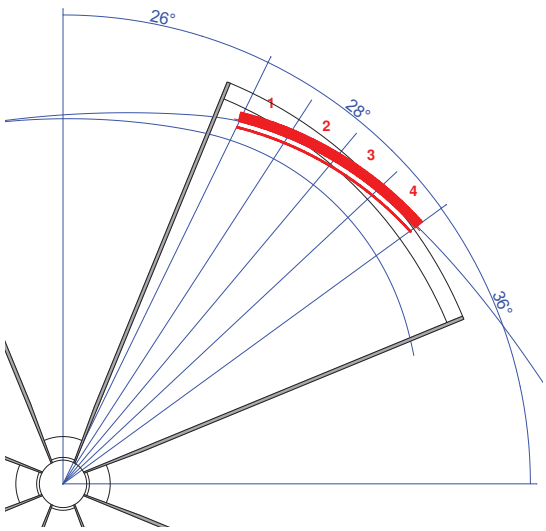

Figure 7: Layout of the magnetic channel in the cyclotron extraction system.

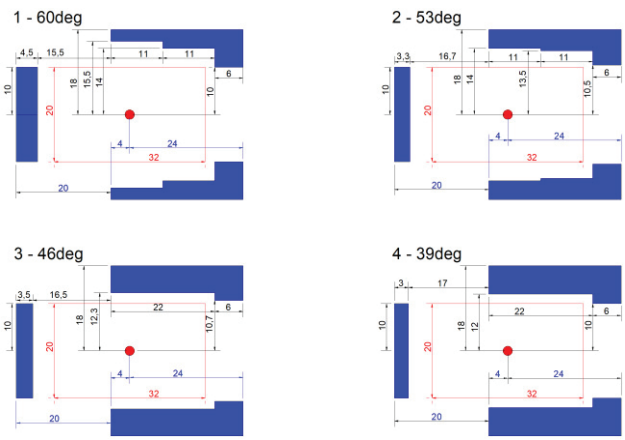

Figure 8: Cross section of four parts of magnetic channel.

PERMANENT MAGNET QUADRUPOLE LENS

The cross-section of the permanent magnet quadrupole lens consisting of 26 permanent magnets is shown in Fig. 9. The main parameters of the permanent magnet quadrupole lens are given in Table 5.

Simulation and design of the PMQ is presented in the work [5].

Table 5: Parameters of PMQ

Parameter	Value
Horizontal aperture [mm]	64
Vertical aperture [mm]	25
Effective length [cm]	29.9
Focusing gradient of the magnetic field [T/m]	8.1

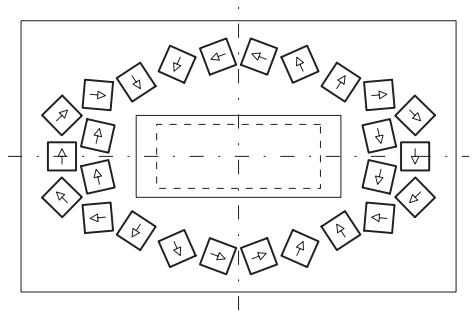

Figure 9: Cross section of PMQ consisting of 26 permanent magnets.

The working area takes into account the horizontal spread of orbits ± 4 mm.

REFERENCES

[1] S. V. Mitrofanov *et al.*, "FLNR JINR Accelerator Complex for Applied Physics Researches: State-of-Art and Future", In *Proc. of 22nd Conf. on Cycl. and their Appl.*, Cape Town, South Africa, Sep. 2019, p. 358-360. doi:10.18429/JACoW-CYCLOTRONS2019-FRB02

[2] B. N. Gikal *et al.*, "Dubna Cyclotrons – Status and Plans", In *Proc. of 17th Conf. on Cycl. and their Appl.*, Tokyo, Japan, Oct. 2004, paper 20A1, p. 100-104.

[3] G. Gulbekyan, I. Ivanenko, J. Franko, J. Keniz, "DC-72 Cyclotron Magnetic Field Formation", In *Proc. of 19th Russian Part. Acc. Conf (RuPAC'04)*, Dubna, Russia, Oct. 2004, paper WENO12, p.147-49.

[4] A. Zabanov et al., "Simulation of the electrostatic deflector of DC140 cyclotron", presented at RuPAC'21, Alushta, Crimea, Sep.-Oct. 2021, paper MOPSA48, this conference.

[5] I. Rodin "Simulation and Design of the Permanent Magnet Multipole for DC140", presented at RuPAC'21, Alushta, Crimea, Sep.-Oct. 2021, paper FRA03, this conference.

ISBN: 978-3-95450-240-0 ISSN: 2673-5539 doi:10.18429/JACoW-RuPAC2021-MOPSA52

MODELING OF THE MAGNETIC SYSTEM OF THE CYCLOTRON OF MULTICHARGED IONS

Yu.K. Osina†, Yu. N. Gavrish, A.V. Galchuck, Yu.I. Stogov,
JSC «NIIEFA», 196641, St. Petersburg, Russia

Abstract

This paper presents the results of the calculation of the magnetic system of the cyclotron for accelerating of multicharged ions developed at NIIEFA JSC. The cyclotron complex is designed to generate ions with a mass-to-charge ratio in the range A/Z= 3÷7, accelerate them to energies in the range of 7.5-15 MeV per nucleon. The cyclotron electromagnet has a four-sector structure, with a pole diameter of 4 m. Radial coils placed on the poles under the sectors are designed to adjust the magnetic field for providing isochronous acceleration conditions for different ions. A group of azimuthal coils designed to correct the first harmonic of the magnetic field and to center the orbits of the accelerated ion, as well as to adjust the position of the axial symmetry plane of the magnetic field is located on the sectors. The required magnetic field topology for ion acceleration was formed in the induction range of 1.29-1.6 T. Calculations were performed for the 1/8 part of the electromagnet. A mode was chosen in which the dependence of induction on the radius, which provides isochronism, is realized due to the shape of "iron". For this mode with an induction in the center of 1.44 T, the shape of side plates, plugs, and sector chamfers was determined. The currents in radial coils and the main dynamic characteristics of the cyclotron magnetic field for ion acceleration in the energy control range were calculated using the obtained magnetic field maps.

INTRODUCTION

According to the design data, the cyclotron of multicharged ions is designed to accelerate ions having a mass-to-charge ratio A/Z=3÷7 (C_{12}^{+3}, O_{16}^{+4}, O_{18}^{+3}, Ne_{20}^{+5}, Si_{28}^{+6}, Ar_{40}^{+10}, Fe_{56}^{+14}, Kr_{84}^{+18}, Ag_{107}^{+22}, Xe_{136}^{+28}, Bi_{209}^{+43}). The electromagnet of the cyclotron will provide the isochronous motion of a wide range of ions in the process of acceleration to energy regulated in the range of 7.5 - 15 MeV/nucleon [1]. Taking into account the significant dimensions of the electromagnet, the H-shaped version of the magnetic circuit with a four-sector magnetic structure was chosen. The diameter of the pole of the electromagnet is 4 m. The air gaps in the "hill" and in the "valley" are 80 mm and 370 mm, respectively. This structure makes it possible to place resonators in the valleys of the electromagnet with the horizontal placement of rods and tanks. The electromagnet is equipped with a set of correcting coils.

Correcting coils are designed for: adjusting the shape of the distribution of the magnetic field over the radius to ensure isochronous conditions for the acceleration of specific ions; adjusting the position of the plane of symmetry of the magnetic field; correcting the first harmonic of the magnetic field and centering the orbits of the accelerated ions.

† npkluts@luts.niiefa.spb.su

MAGNETIC SYSTEM OF THE CYCLOTRON

The magnetic field for the cyclotron of multicharged ions was simulated using the Ansys Maxwell software package [2, 3]. Magnet type is H-shaped. The structure of the magnetic field is four-sector, the angular length of the sectors is 51^0. The formation of the magnetic field was carried out by changing the shape of the boundaries of the sector side plates and correcting coils. As a result of numerical simulation, the magnetic circuit of the multicharged ion cyclotron and the shape of the sector side plates was determined, provided the required ion acceleration mode for A/Z = 4.66. 3D calculation model of 1/8 part of the magnet is shown in Fig. 1.

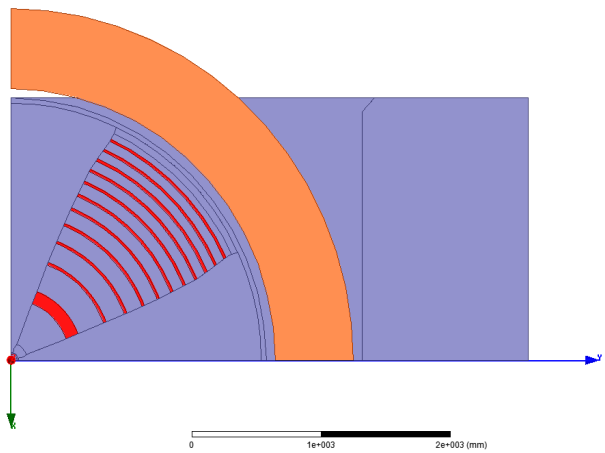

Figure 1: 3D calculation model of 1/8 part of the magnet.

The required maximum of the magnetic field rigidity at the final orbit (Rf.o. = 1.8 m) should reach 2.73 T·m [1].

During the magnetic field formation in the center, there were difficulties due to the effects of the saturation of steel and the complex shape of the surface of the sectors. As a result of numerical modeling, the shape of the sector side plates and the cyclotron central plug was determined, providing an isochronous mode of acceleration for particles with A/Z = 4.66.

Figure 2 shows the calculated magnetic fields for ions with A/Z=3÷7.

ISBN: 978-3-95450-240-0 ISSN: 2673-5539 doi:10.18429/JACoW-RuPAC2021-MOPSA52

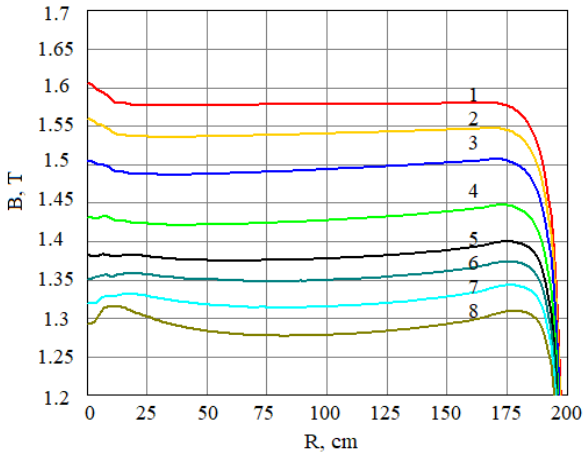

Figure 2: Radial distribution of the average magnetic field for different excitation level of the main coils (1 - 700, 2 - 640, 3 - 570, 4 - 480, 5 - 420, 6 - 390, 7 - 360, 8 - 330 kA·turn).

When changing the energy and/or the type of particles having a different A/Z ratio, it is necessary to adjust the currents in the radial coils. These coils in the amount of 11 pairs are placed in the grooves of the aluminum / or stainless steel disk, which is located between the pole of the cyclotron and the sectors. Additionally, 2 sets of coils are provided for correcting the first harmonic of azimuthal inhomogeneities. This low power correction coils will be housed in vacuum-tight housings (aluminum or stainless steel) located on the sectors. 3D calculation model of 1/2 electromagnet with azimuthal coil housing is shown in Fig. 3. The housing bodies of the correcting coils are water cooled.

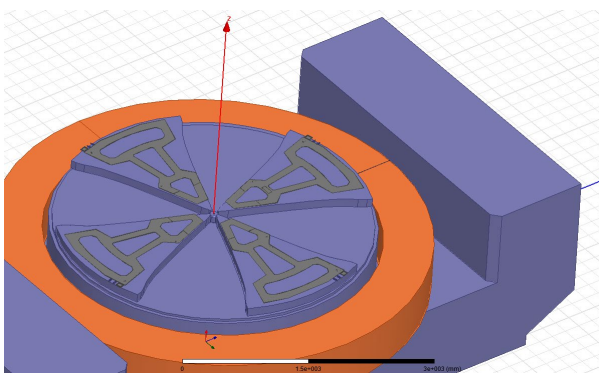

Figure 3: 3D calculation model of 1/2 electromagnet with azimuth coil housings.

Calculations of the correcting coil fields for various levels of the cyclotron magnet excitation have been performed. The radial distribution of the fields of the radial correcting coils at the maximum level of induction in the center of 1.6 T (700 kA·turn) is shown in Fig. 4.

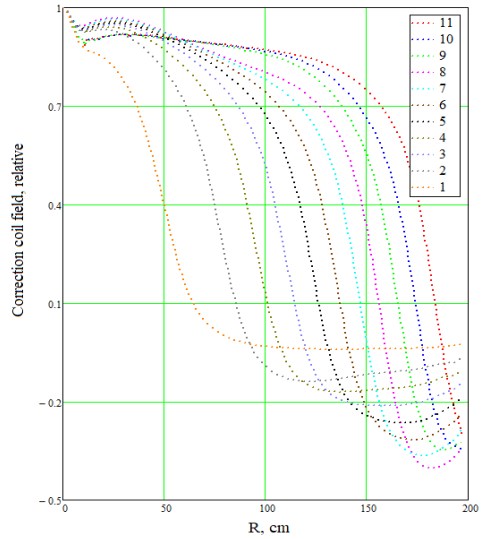

Figure 4: The radial distribution of the radial coil fields at the maximum level of induction in the center 1,6 T (700 kA·turn).

The currents in the correcting coils were determined. The maximum power consumption of the correcting coils will be no more than 20 kW.

Harmonic analysis of the obtained magnetic field was made, and the frequencies of betatron oscillations were calculated for the required set of ions. Figure 5 shows the movement of the operating point of the heaviest accelerated particle (Bi_{209}^{+43}) in the phase diagram.

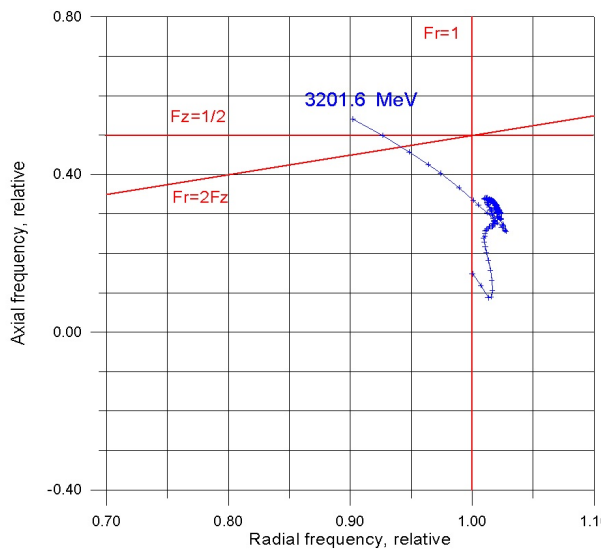

Figure 5: Phase diagram of Bi_{209}^{+43} acceleration at the level of 700 kA·turn.

The calculated phase motion in the resulting magnetic field for the maximum mode of the cyclotron, corresponding to the induction in the center of 1.6 T, is shown in Fig. 6.

The main characteristics of the cyclotron electromagnet are listed in Table 1.

ISBN: 978-3-95450-240-0 ISSN: 2673-5539 doi:10.18429/JACoW-RuPAC2021-MOPSA52

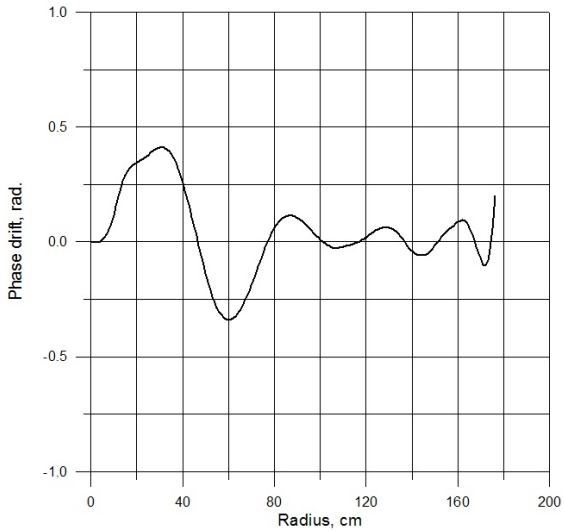

Figure 6: Calculated phase motion in the resultant magnetic field at the level of 700 kA·turn.

Table 1: Main Characteristics of Multicharged Ion Cyclotron Electromagnet

Magnetic core (steel 10)	H-shaped
Outside dimensions of the electromagnet, m	8,1×5,36×4,3
Pole diameter, m	4
Number of sectors per pole	4
Gap "valley"/ "hill", mm	370/80
Sector angular extent, maximum, degrees	51
Induction in the center, range, T	1,29 – 1,6
Main coil power supply, kW, not more	262
Mass of the electromagnet (steel/copper), t	870/72
Number of pairs of radial coils	11
Number of pairs of azimuthal coils	8
Total power consumption of the correcting coils, kW, not more	20

It is worth noting that the technical solutions adopted at the preliminary design stage will allow the acceleration of light ions to energies higher than 15 MeV/nucleon in the cyclotron of multicharged ions. However, the maximum energy of the light ions will be limited by both the parameters of the correcting coils and the required potential of the electrostatic deflector.

CONCLUSION

Thus, an electromagnet of the cyclotron of multicharged ions designed to accelerate ions with the ratio A/Z = 3÷7 to energy regulated in the range of 7.5-15 MeV/nucleon has been developed. As a result of numerical simulation, the parameters of the magnetic system of the multicharged ion cyclotron were determined. Correcting coils have been developed to ensure the isochronous operation of the cyclotron for different types of ions. The power consumption at the maximum excitation current is 262 kW. Each main coil consists of sections, the design of which protects the conductor from damage during transportation, movement, and installation in its working position. The mass of the electromagnet (Fe/Cu) is 870/72 tons, respectively. The formed magnetic field for accelerating ions with A/Z = 3÷7 meets the requirements for the stability of particle motion. Phase diagrams are obtained for the resulting magnetic fields formed for acceleration of ions in the required energy range.

REFERENCES

[1] Yu.K. Osina *et al.,* "Cyclotron complex of multi-charge ions", Nuclear and electrophysical installations - sources of powerful ionizing radiation: a collection of abstracts of the scientific and technical conference", June 15-18, 2021 - Snezhinsk, RFNC-VNIITF, 2021, pp. 5-6.

[2] ANSYS http://www.ansys.com/

[3] Yu. K. Osina *et al.* "Formation of the Magnetic Field in the CC 30/15 Isochronous Cyclotron". *Phys. Part. Nucl. Lett.,* 2020, Vol. 17, No. 4, pp. 494–497. DOI: 10.1134/S1547477120040354.

ISBN: 978-3-95450-240-0 ISSN: 2673-5539 doi:10.18429/JACoW-RuPAC2021-MOPSA53

FOCUSING PROPERTIES OF THE MAGNETIC STRUCTURE OF ISOCHRONOUS CYCLOTRONS WITH LARGE SPIRALITY ANGLE OF POLE TIPS

D.A. Amerkanov, S.A. Artamonov†, E.M. Ivanov, G.A. Riabov, V.A. Tonkikh,
NRC "Kurchatov Institute" - PNPI, Gatchina, Leningrad district, 188300, Russia

Abstract

Magnetic structures with a large spirality angle of pole tips have been investigated in a number of works and are used in superconducting cyclotrons, H^- ion cyclotrons, etc. With the design and construction of an 80 MeV isochronous H^- cyclotron, such studies were continued and extended. In this work, a relatively simple approach for analyzing the spiral structure is proposed.

INTRODUCTION

The magnetic structure with a large spirality angle of the pole tips is used in cases when vertical focusing from the flutter (field difference in the valley and the sector) is insufficient and it is necessary to add the angle focusing. This situation is typical for superconducting cyclotrons and for cyclotrons that accelerate negative hydrogen ions. Moreover, at JINR in Dubna, such structures have been investigated and a cyclotron and a synchrocyclotron with sectors in the form of an Archimedes spiral with a maximum spirality angle of up to 70 degrees were built. Numerical calculations of the magnetic field for an isochronous superconducting cyclotron with spiral sectors in the approximation of their uniform magnetization were carried out [1].

Two effects were noted: a decrease in the flutter in the central region with the introduction of spirality and a mismatch between the spirality of the sector Irion and the magnetic field. However, calculations made for a specific geometry are not applicable in the case of a different design. With the construction of an isochronous cyclotron for accelerating H-ions up to 40-80 MeV [2, 3], studies of the focusing properties of spiral structures were continued and expanded. Modern 3D software codes simplify the design of the magnetic field of any configuration by using trial- and- error method. However, to speed up the procedure and reduce the number of options for 3D analysis, it is useful to first perform a simplified and visual analysis of the system and estimate the importance of various parameters in the framework of a simpler 2D approximation.

OPTIMIZATION OF THE MAGNET GAPS

As a first approximation, the hill and the valley gaps have been chosen using the 2D POISCR code calculations with the fill factor method. In this method, a 3D problem is reduced to a 2D one. The iron rings or the so-called shims mounted on the magnet poles and providing an isochronous rise in the field are calculated using a 2D program with a reduced value of the magnetic permeability $\mu_{new}(B) = \mu(B) \cdot C$. The permeability is reduced by a factor C – so-called filling factor equal to the ratio of the azimuthal length of the sector to the length of the periodicity element at a radius r. The gap of the magnet obtained in this way corresponds to the gap of the hill, and there is no additional shim in the valley. Thus, two variants of the gaps of the main magnet and the gaps of the hills and the valleys were analyzed. The parameters of these variants are presented in the caption to Fig. 1.

FLUTTER

The azimuthal variation of the magnetic field [1] is determined by the so-called flutter $F(r)$:

$$F(r) = <(B - <B>)^2> / <B>^2, \quad <...> = (2\pi)^{-1} \int_0^{2\pi} ... d\theta$$

Flutter can be represented as a Fourier harmonics expansion of the azimuthal variation of the magnetic field. The fundamental contribution to the expansion is made by the general focusing harmonic associated with the number of sectors and periodicity elements (in our case, $N = 4$). If we denote the value of the fundamental focusing harmonic $f = B_N / <B>$, then $F = f^2/2$.

Analytical calculation of flutter is a complex problem and therefore approximate methods have been used. In particular, in [4], an expression was obtained for the general harmonic of the magnetic field variation in an isochronous cyclotron in the approximation of uniform magnetization of the sectors of a magnet

$$B_N = 8M \sin(\frac{2\pi a}{d}) \exp(-\frac{2\pi g_h}{d}),$$

where $2a$ is the length of the sector along the azimuth for a given radius r, $2g_h$ is the gap in the hill, d is the period of the structure, equal to the total length of the hill and valley, $4\pi M$ = 21kG. It follows from this expression that for an isochronous cyclotron with a period of the magnetic field structure equal to $d = 2\pi r / N$, where N is the number of sectors, the flutter grows with increasing radius according to the law

$$F \sim B_N^2 / 2 \sim \exp(-2/x), \quad x = r / N \cdot g_h \qquad (1)$$

Although this approximation is insufficient for obtaining accurate quantitative estimates, it allows, in a unified manner, to get an idea of the relationship between the different parameters of the magnetic structure. Moreover, the introduction of the dimensionless parameter x enables the comparison of different variants of structures. In particular, flutter rises as the gap in the hill decreases and falls as the number of sectors increases.

†artamonov_sa@pnpi.nrcki.ru

ISBN: 978-3-95450-240-0 ISSN: 2673-5539 doi:10.18429/JACoW-RuPAC2021-MOPSA53

The maximum flutter value corresponds to the case when the azimuthal extent of the sector and the valley are equal. In this case, $a = 0.25d$ and $\sin(\pi/2) = 1$. For the case when the parameter x becomes less than 0.5, the flutter drops very sharply, i.e., at radii $r \le 0.5 \cdot N \cdot g_h$, azimuthally variation becomes ineffective, and focusing tends to zero. The results of these calculations are shown with curve 3 in Fig. 1.

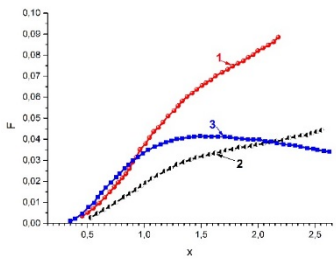

Figure 1: The dependence of flutter on the dimensionless parameter $x = r / N \cdot g_h$, where $N = 4$, for two options: 1- $2g_v = 386$ mm, $2g_h = 170$ mm, $h1 = 108$ mm; 2 - $2g_v = 284$ mm, $2g_h = 145$ mm, $h2 = 69$ mm; 3 - a variant of uniform magnetization for the case of the geometry of the first variant.

The dependence of flutter on the radius can be calculated using 3D programs. However, in our case, to speed up and simplify the calculations, we used approximate calculations. Flutter can be estimated using a 2D program if we replace the calculation of the edge effect along the azimuth with the calculation of the edge effect along the radius of the two-dimensional magnet with a gap in the form of teeth and valleys along the radius. In this case, gap variation of 2D-magnet along radius corresponds to the length and gaps of the sector and valley along the azimuth of the investigated magnet.

The simple estimates carried out for the C-80 cyclotron show that the structure with straight sectors does not provide the necessary vertical focusing; therefore, it is necessary to use the next effect.

SPIRALITY EFFECT

As it is well known, the frequency of vertical oscillations, which determines the vertical focusing, can be expressed using the following approximation:

$$\nu_z^2 \approx -k + F \cdot S(r,\gamma), \quad S(r,\gamma) = 1 + 2tg^2\gamma, \qquad (2)$$

where k is the rate index of average magnetic field growth along the radius

$$k = (r / \langle B \rangle)(d\langle B \rangle / dr) \approx 2W / E_0 .$$

W is the kinetic energy, $E_0 = 938$ MeV is the rest mass of the proton, γ is the spirality angle. The frequency of axial oscillations is determined by two oppositely acting terms - the defocusing of the isochronous rise of the mean-field and the focusing action of the azimuthal variation of the field. The task is to select F and γ for each value of the energy W so that ν_z^2 remains greater than zero during acceleration. At the same time, to limit the dissociation of negative ions, it is necessary to strive for the minimum possible value of the magnetic field in the hill, i.e. to the minimum flutter value. The spiraling sector provides an increase in focusing force due to the non-perpendicular angle of particle entry into the sector region. Effectively, the flutter F is multiplied by the coefficient $S(r,\gamma)$; however, in a structure with a large spirality angle, the increase in focusing force is noticeably less [1] than could be expected from the above formula. This is due to a decrease of flutter when the spirality angle is introduced and a mismatch between the iron and the magnetic spirality angles.

There is a simple geometric explanation for the first effect. With a large spirality angle, the difference between the sector length along the azimuth (AB in Fig. 2) and the width of the A_1B_1 sector determined by the perpendicular to its centerline becomes significant.

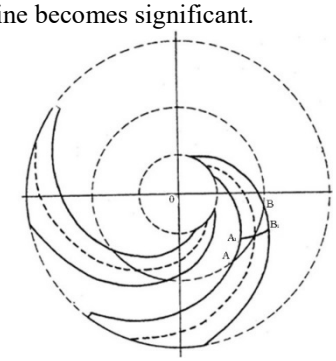

Figure 2: There is a difference between the sector length along the azimuth AB and the "effective" length A_1B_1 at large spiraling angles. The effective width of the sector long the perpendicular to the sector centerline is equal $A_1B_1 \approx AB \cdot \cos\gamma$.

In the case of straight sectors, the flutter is determined by the magnetic field difference in the hill and the valley. In this case, the field falls off along the azimuth. When a spiraling angle is introduced, the distance between the sectors along a line perpendicular to the centerline of the sector is much smaller than the distance along the azimuth. This leads to a decrease in the effective length of sector A_1B_1 and, accordingly, to a decrease in the length of the valley. From geometric considerations, we can conclude that the effective length of the A_1B_1 sector is approximately equal to the length of the sector along the azimuth AB multiplied by a factor equal to $\cos\gamma$, i.e. $A_1B_1 \approx AB \cdot \cos\gamma$. With a decrease in the length of the sector, the effective length of the valley and the period of periodicity decrease. In this case, the dimensionless parameter x, introduced in expression (1) and related to the length of the periodicity period, will also decrease and become $x_{\text{eff}} = x \cdot \cos\gamma$. According to Fig. 1, a decrease in the value of the parameter $x_{\text{eff}} = x \cdot \cos\gamma$ leads to a shift along the graph towards lower flutter values. At intermediate and large radii, the spirality causes an increase in edge focusing and a decrease in flutter and the total effect leads to an overall increase in focusing. However, at small radii, the introduction of spiraling reduces the effective sector length and this can lead to a very sharp drop in flutter and a total decrease in focusing. The total effect of the introduction of

ISBN: 978-3-95450-240-0 ISSN: 2673-5539 doi:10.18429/JACoW-RuPAC2021-MOPSA53

the spiral sectors can be characterized by a parameter that is the product of two factors: flutter F and S (r, γ). However, at small radii, the introduction of spiraling reduces the effective sector length and this can lead to a very sharp drop in flutter and a decrease in focusing. The total effect of the introduction of the spiraling sectors can be characterized by a parameter that is the product of two factors: flutter F and S (r, γ). Since the flutter drops sharply at $x_{\text{eff}} < 0.5$, the introduction of spiraling in the central region leads to a decrease in focusing. For each radius, it is possible to calculate the limiting value of the spiraling angle, exceeding which spiraling does not give an increase in focusing. This value for each value of the parameter x can be estimated to be by finding a solution for the following expression:

$$U(x,\gamma) = (F(x\cos\gamma)/F(x))\cdot(1+2tg^2\gamma)-1=0, \qquad (3)$$

where $F(x)$ is a function of the type shown in Fig. 1.

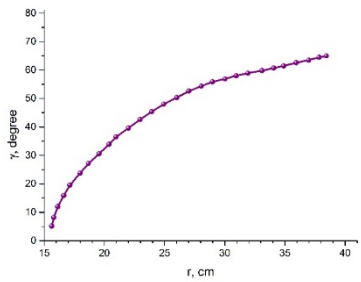

Figure 3: Ultimate spirality angle for C-80 cyclotron in dependence on the radius for $2g_v = 386$ mm, $2g_h = 170$ mm, $N = 4$.

Figure 3 shows the limiting spiraling angle calculated by the formula (3) depending on the radius for the case of the C–80 cyclotron. According to the Fig. 3, spiraling leads to the decreasing of vertical focusing at radii smaller than 35 cm, and it is advisable to use a structure with a large spirality angle at radii greater than 35 cm. Thus, a structure with a large spiraling angle is effective only at radii larger that the hill gap value.

3D COMPUTATION AND EXPERIMENT

When choosing the spiral angle in the cyclotron design, it is necessary to take into account the fact that the magnetic field does not completely repeat the iron sector geometry.

According to the Fig. 4, there is the effect of magnetic spirality "penetration" into the region of straight sectors. And this effect leads to a decrease in vertical focusing at radii smaller than 35 cm. This effect explains the widespread use of direct sectors in the central region. It is also seen that at radii of ~ $75 \le r \le 88$ cm there is a "lag" between the magnetic field spiraling angle the geometrical one. The maximum lag reaches 7º, which at a spirality angle of 65º leads to a 30% decrease in focusing.

After preliminary assessments related to the choice of the parameters of the magnetic structure, the final variants were calculated in detail using the 3D MERMAID program.

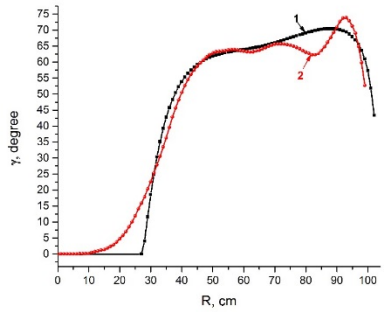

Figure 4: The spirality angle $-\gamma$ (deg.) in dependence on the radius of the cyclotron: 1 - the data of the sector geometry spirality, 2 – the spirality of the fourth focusing harmonic of the magnetic field, obtained in 3D calculations and measurements of the magnetic field.

In the calculations, to achieve maximum accuracy, the magnetic structure was described using ~ 20.5 million straight prisms. During the design process, two variants of the magnetic structure were considered at a finite radius: flutter $F = 0.04$, spirality angle $\gamma = 55$ ° and $F = 0.025$ with $\gamma = 65$ °, and field variation amplitudes of 4.14 and 3.28 kG, respectively. Ultimately, the second option was adopted, providing a lower field in the hill, at which the loss of H minus ions due to electrodissociation does not exceed 2.6%.

CONCLUSION

The analysis of the structure of the magnetic field of a cyclotron with a high spirality angle, presented in this work, makes it possible to investigate the effect of different parameters of the structure and promptly compare various options. Such an approach provides the means to qualitatively analyze the effect of a decrease in the vertical focusing of the spiral structure at the center of the cyclotron. It is expedient to use the structure with a large spiraling angle only at radii larger than the gap in the hill. In the central region, it is advisable to use direct sectors. The paper presents a technique that was used in the design of the magnetic structure of the C-80 cyclotron. The use of the limiting large values of the spirality angle in the C-80 cyclotron made it possible to obtain limiting energy as high as 80 MeV in a magnet with a diameter of 2 meters at an extraction radius of 0.9 m. The magnetic structure allows us to limit the of negative ions electrodissociation to less than 3%.

REFERENCES

[1] H.G. Blosser and D.A. Jonson, “Focusing properties of superconducting cyclotron magnets” *Nucl. Instrum. Methods*, vol. 121, pp. 301, 1974. doi:10.1016/0029-554X(74)90080-9

[2] Yu. N. Gavrish *et al.*, “Physical Start-up of the C-80 Isochronous Cyclotron”, in *Proc. 25th Russian Particle Accelerator Conf. (RuPAC'16),* Saint Petersburg, Russia, Nov. 2016, pp. 180-182. doi:10.18429/JACoW-RUPAC2016-TUCASH04

[3] N.K. Abrossimov, S.A. Artamonov, V.A. Eliseev, G.A. Riabov, Preprint PNPI-2049, Gatchina, 1995.

[4] V.I. Danilov, Preprint JINR-R-409, Dubna, 1959.

ISBN: 978-3-95450-240-0 ISSN: 2673-5539 doi:10.18429/JACoW-RuPAC2021-MOPSA54

CALCULATION OF DOSE FIELDS AND ENERGY SPECTRA OF SECONDARY RADIATION IN THE EXTRACTION ZONE OF A SYNCHROTRON ACCELERATOR FOR PROTONS WITH ENERGIES UP TO 700 MeV

R.P. Truntseva, N.V. Zavyalov, A.V. Telnov, A.M. Opekunov, N.N. Kurapov,
FSUE "RFNC-VNIIEF", Sarov, Russian Federation

Abstract

The possibility of using a multipurpose synchrotron accelerator for studying the processes of interaction of heavy charged particles with various materials is considered. The accelerator provides proton energies up to 700 MeV. At the design stage of the experimental room, it is necessary to evaluate the emerging dose fields. In this case, it is important to evaluate the dose environment, energies and types of secondary radiation that may enter the adjacent rooms.

This paper presents the results of the radiation environment evaluation in the radiation extraction zone of the synchrotron accelerator. Simulation results of secondary radiation energy spectra near the walls, which separate the irradiation zone from adjacent rooms, are presented. Proton energies are equal to 60, 85, 110 and 700 MeV are considered. Simulation was performed by the Monte Carlo method in a program developed using Geant4 libraries.

INTRODUCTION

Dose distribution estimation can be performed in different ways: experiment; simulation; comparison. At experimental rooms development stage estimation of arising dose fields is performed in simulation method. The extraction zone of a synchrotron accelerator which provide proton energies up to 700 MeV for studying the processes of heavy charged particles interaction with matter is considered. Apart from dose field estimation it is necessary to define type and energy of radiation which may enter the adjacent rooms. Against this characteristics can be adjust such parameters as: time spent in adjacent rooms, working hours in additional rooms, biological shielding thickness at the border of two rooms.

Simulation results of dose distribution estimation and energy spectra in experimental room by Monte-Carlo method in Geant4 [1] based software are presented. Primary particles energies are 60, 85, 110 and 700 MeV.

SIMULATION DESCRIPTION

The major mechanisms of proton interaction with the target material are: elastic scattering, excitation and ionization of atoms in the medium and nuclear reactions. Other interaction mechanisms have minor contribution [2, 3]. The package of physical processes "FTFP_BERT" [4] was used. This package includes the functions of the FRITIOF [5] model, the compound-nucleus model and the Bertini intranuclear cascade model [6]. The major nuclear reactions are: (p, *MpNn*), where M and N are integers; (p, $x\alpha$); (p, xd); (p, xt); (p, γ) [2, 7]. Reactions of type (p, *MpNn*) and in a less degree (p, $x\alpha$); (p, xd); (p, xt); (p, γ) are expected in simulation with protons energy up to 110 MeV. Also arising of muons and different ions is expected in simulation with proton energy equal to 700 MeV.

Simulation geometry is shown in Fig. 1. The air volume 495×600×810 cm is divided to cells 45x45x50 cm. Concrete walls (ρ = 2.3 g/cm^3) 50 cm wide are set around the air volume. At h = 150 cm height from the floor and distance d = 70 cm from the wall iron cylinder with 10 cm diameter and length is located. At 10 cm distance from cylinder the monodirectional proton source with 3 cm diameter is placed (energy distribution - Gaussian).

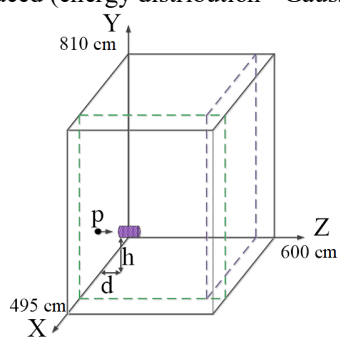

Figure 1: Simulation geometry.

Simulation results were: absorbed dose distribution in volume elements per one primary particle and secondary radiation energy spectra in areas specified by green and purple dotted lines in Fig. 1 (layers of air with 10 cm thickness). Further, coordinate denomination (according to Geant4 geometry): x – room width, y – height a, z – length.

In energy spectra calculation were registered: p, γ, n, e^- и e^+, μ–mesons, α and other types of secondary radiation ("other"). Width of energy bin for all cases is equal to 100 keV.

DOSE FIELD CALCULATION

The resulting dose field was divided into key sections. The following describes the simulation result for one of these sections (Fig. 2, near the side wall).

Maximum absorbed dose (90-180 cm in height and 0-50 cm in length) is: 60 MeV - 3 158 · 10^{-18} Gy; 85 MeV - 4.934 · 10^{-18} Gy; 110 MeV - 7 284 · 10^{-18} Gy per one primary proton. Minimum values (720-810 cm

ISBN: 978-3-95450-240-0 ISSN: 2673-5539 doi:10.18429/JACoW-RuPAC2021-MOPSA54

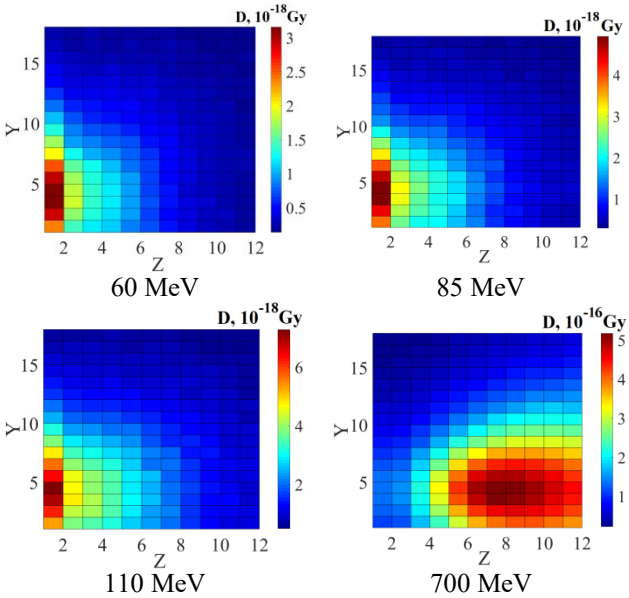

Figure 2: Absorbed dose distribution, $x = 0$.

in height and 500-600 cm in length), respectively: 60 MeV - 0.134 · 10^{-18} Gy; 85 MeV - 0.293 · 10^{-18} Gy; 110 MeV - 0.484 · 10^{-18} Gy per one primary proton. At 700 MeV - maximum value (135-180 cm in height and 300-350 cm in length) 5.172 · 10^{-16} Gy; minimum (765-810 cm in height and 0-50 cm in length) - 0.217 · 10^{-16} Gy per one primary proton. Total absorbed dose per one primary proton: 60 MeV – 116,350·10^{-18} Gy; 85 MeV – 215,461·10^{-18} Gy; 110 MeV – 354,334·10^{-18} Gy; 700 MeV – 423,951·10^{-16} Gy.

1) Absorbed dose maximum values in sections near the floor and ceiling are observed in the region of primary radiation propagation. Absorbed dose maximum value in near the floor section is 25-46 times more than in near the ceiling section. This difference becomes smaller with increasing of primary protons energy. Minimum absorbed dose in near the floor section is 41-77% higher than in near the ceiling section. This difference increase with increasing of primary protons energy. Absorbed dose minimum value in near the floor section is 5 times higher than near the ceiling, when the energy of primary protons is 700 MeV. Minimum values of absorbed dose in near the floor section are located in corners of room. Total absorbed dose in near the floor section is 6-7.5 times higher than near the ceiling, when the energy of the primary protons is 110 MeV; at 700 MeV - 15.4 times higher.

2) Maximum values of absorbed dose in the near front and back walls sections are observed in region of primary radiation propagation. Maximum value is observed in the area where the object is located at when energy of primary protons up to 110 MeV. In the front wall section, maximum and total values are 3 orders of magnitude greater than the same at the rear wall section. At 700 MeV, the propagation of radiation is predominantly forward. Maximum absorbed dose in near the front wall section is 17.5 times less than in near the back wall section.

3) In sections near the side walls at energies up to 110 MeV, maximum value is observed at the level of the source location (90-180 cm in height and 0-50 cm in length); at 700 MeV - in the middle of the room length. Minimum absorbed dose is recorded in cells in the corners of the ceiling near the back wall of the room.

SECONDARY RADIATION ENERGY SPECTRA

Figure 3 shows the energy spectra of secondary radiation in the layers $z = z_{max}$ and $x = x_{max}$. Thickness of the layers is 10 cm, the energy of primary protons (E_{pr}) is 60 MeV.

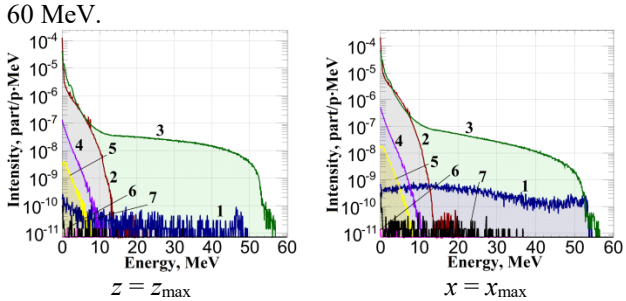

Figure 3: Secondary radiation energy spectra, E_{pr} = 60 MeV (1 – p, 2 – γ, 3 – n, 4 – e^-, 5 – e^+, 6 – α; 7 – "other").

Table 1 shows the average energies of secondary radiation in the air near the back and side walls of the room, depending on the primary protons energy; *ot* - other types of secondary radiation.

Table 1: Secondary Radiation Average Energies, E_{pr} up to 110 MeV

	E, MeV					
	$z = z_{max}$			$x = x_{max}$		
	60	85	110	60	85	110
p	14,541	17,607	22,047	20,066	21,475	23,186
γ	0,518	0,573	0,620	0,812	0,819	0,831
n	1,090	1,766	2,662	1,136	1,457	1,790
e^-	1,160	1,189	1,219	1,140	1,150	1,162
e^+	1,571	1,605	1,646	1,479	1,509	1,551
α	5,880	4,349	6,630	3,125	4,603	4,686
ot	3,895	8,188	13,944	7,282	9,379	12,398

Until nuclear interactions begin to prevail over other processes in the interaction of primary protons with matter, the total energy spectra differ slightly. Increasing of average α energy with increasing of primary particles energy is not observed in Table 1 because of its insignificant amount in total energy spectra (from 8,3 · 10^{-6} to 3,87 · 10^{-5} %).

Figure 4 shows the energy spectra of secondary radiation in the layers $z = z_{max}$ and $x = x_{max}$. Thickness of the layers is 10 cm, energy of primary protons is 700 MeV. Table 2 shows the average energies of secondary radiation in the air near the back wall at the primary proton energy equal 700 MeV; *ot* - other types of secondary radiation.

ISBN: 978-3-95450-240-0 ISSN: 2673-5539 doi:10.18429/JACoW-RuPAC2021-MOPSA54

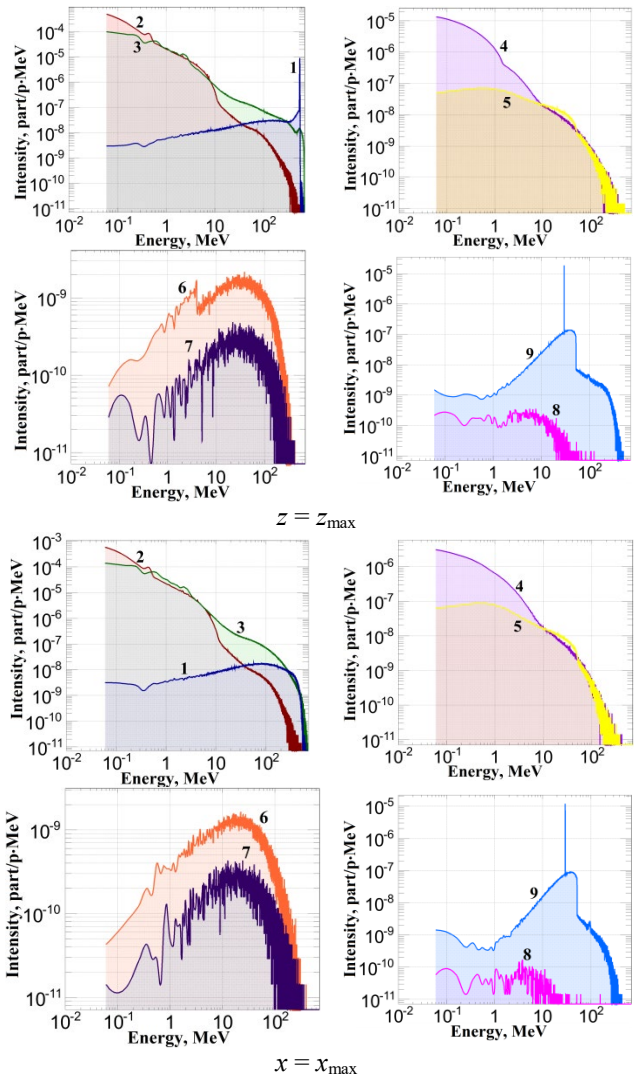

Figure 4: Secondary radiation energy spectra, E_{pr} = 700 MeV (1 – p, 2 – γ, 3 – n, 4 – e^-, 5 – e^+, 6 – μ^+, 7 – μ^-, 8 – α, 9 – "other").

In the layer near the back wall of the room, the main contributions to the total energy spectrum are made by protons (19.24%), gammas (40.58%) and neutrons (36.35%). In near the side wall layer, the main contributions are made by gammas (47.99%) and neutrons (49.14%).

Table 2: Secondary Radiation Average Energies, E_{pr} = 700 MeV

	$z = z_{max}$	$x = x_{max}$
p	511,284	182,114
γ	1,693	1,247
n	25,869	8,724
e^-	2,626	4,487
e^+	24,539	19,626
μ^+	86,112	56,755
μ^-	84,836	57,189
α	11,036	8,032
ot	41,838	36,592

CONCLUSION

With proton energies up to 110 MeV, the maximum dose load occurs along the propagation region of the primary radiation, mainly in the lower part of the room. The minimum absorbed dose in near the floor section is recorded in the corners.

Front and back walls of the room. At proton energies up to 110 MeV, the highest absorbed dose is observed in the area of the irradiated object. At 700 MeV, the maximum dose load occurs near the back wall of the room.

Side walls of the room. At energies of primary protons up to 110 MeV, the maximum absorbed dose is observed at the level of the radiation source projection. At 700 MeV, maximum absorbed dose is observed in coordinates corresponding to the projection of the middle of the room; minimum value is for the corners under the ceiling of the room near the back wall.

When the primary particles energy is up to 110 MeV, it is necessary to provide radiation protection primarily from n and γ. Their contributions to the total energy spectra: from 39.6 to 42.9% for γ, from 55.8 to 60.2% for n. At 700 MeV, secondary protons begin to make an additional contribution (near the back wall of the room).

REFERENCES

[1] Geant4, https://geant4.web.cern.ch/node/1

[2] A.P. Chernyaev, A.V. Belousov, E.N. Lykova, "Interaction of ionizing radiation with matter: a tutorial", Moscow: Phys. fac., Moscow State University, 2019. ISBN 978-5-6042768-5-3

[3] V.A. Egorova, M.E. Zhukovskiy, S.V. Podolyako, I.A. Tarakanov, "Mathematical model of the interaction between protons and matter", Preprints of the Institute of applied Mathematics M.V. Keldysh, № 138, 2017. doi:10.20948/prepr-2017-138.

[4] Geant4 Physics List Guide. Release 10.7, https://geant4-userdoc.web.cern.ch/UsersGuides/PhysicsListGuide/html/index.html

[5] B. Nilsson-Almqvist and Stenlund. *E. Comp. Phys. Comm.* 1987, № 43, p. 387.

[6] M.P. Guthrie, R.G. Alsmiller and H.W. Bertini, *Nucl. Instr. Meth*, № 66, p. 29, 1968.

[7] I.V. Racobolskaya, "Nuclear Physics: a tutorial", Under ed. of Petukhov, Moscow University press, 1971.

ISBN: 978-3-95450-240-0 ISSN: 2673-5539 doi:10.18429/JACoW-RuPAC2021-MOPSA55

BEAM-INDUCED BACKGROUND SIMULATIONS FOR THE CMS EXPERIMENT AT THE LHC

I. Azhgirey, I. Bayshev, I. Kurochkin, A. Riabchikova*, NRC "Kurchatov Institute" - IHEP, Protvino, Russia
A. Dabrowski, CERN, Geneva, Switzerland
S. Mallows, KIT, Karlsruhe, Germany

Abstract

Beam-induced background (BIB) comes from interactions of the beam and beam halo particles with either the residual gas in the vacuum chamber of accelerator or the collimators that define the beam aperture. Beam-induced processes can potentially be a significant source of background for physics analyses at the Large Hadron Collider (LHC).

This contribution describes the simulation software environment used for this part of the Compact Muon Solenoid (CMS) experiment activity and recent beam-induced background simulation results for the Phase-2 CMS operation design.

INTRODUCTION

The LHC [1] will be upgraded to enable baseline operation for the High Luminosity LHC (HL-LHC) [2] period (Phase-2) at an instantaneous luminosity of 5×10^{34} cm^{-2} s^{-1}. The accelerator will operate at energy of 7 TeV per beam and a distance between bunches of 25 ns. This will allow to the CMS experiment [3] to collect integrated luminosity order 300 fb^{-1} per year and up to 3000 fb^{-1} during the HL-LHC projected lifetime of ten years, assuming machine efficiency is around 50%. The consideration of the radiation effects is a key to the overall success of the CMS experiment.

The Beam Radiation Instrumentation and Luminosity (BRIL) Project is responsible for the simulation and monitoring of the BIB in the CMS. The collaboration needs to understand and take into account all sources of the BIB and kinematic parameters of BIB particles entering the experimental cavern from the LHC tunnel.

BIB FORMATION ANF EFFECT

BIB comes from interactions of the beam or beam halo particles either with the residual gas in the beam pipe or with the collimators that define the beam aperture. We can divide BIB into three different types based on their origin.

The first one is the local inelastic beam-gas interactions (LBG). This is the dominant source of BIB in the CMS near-beam region. The main locations of inelastic beam gas collisions are the superconducting parts of the beam pipe in the Long Straight Section 5 (LSS5). Cold sections have a relatively high rate of the residual gas pressure compared to warm ones. The most important is the final focus triplet cryostat just upstream of the CMS hall.

The second source is the distant Beam Halo (BH). BH particles are produced when off-orbit components of the beam scrape one of the collimators in the cleaning sections of the LHC, and the resulting collision products are absorbed downstream by the tertiary collimators (TCT), which are about 150 m upstream of the interaction point 5 (IP5). The products of hadronic and electromagnetic showers started in the TCT can reach the CMS cavern.

The third source is the distant elastic beam gas interactions (DBG) that occur anywhere around the ring. Elastically scattered particles can make several turns before they hit a collimator. When they interact with the TCT, they can produce particle showers similar to those produced by the BH.

In the HL-LHC time the BIB will differ in several aspects from what is currently experienced at the LHC. The cold section of the final focus triplet will be extended and thus a longer degraded vacuum section is expected there. The higher luminosity and the beam current will also amplify the degradation of the vacuum in the beam pipe in the forward regions of the CMS. In addition, the aperture of the final focus triplet and the Target Absorber Secondaries collimator (TAS) will be larger, and this will allow more BIB particles to enter the CMS cavern at a low radius. Most of the BIB particles that enters the CMS inner tracker volume is originating from interactions of the previous generations of the BIB particles with the beam pipe material. Thus, compared to the current conditions, where the beam pipe in the CMS is partially sheltered from background particles by the TAS, highly energetic BIB particles will be able to travel through the TAS aperture and interact with the beam pipe in the central part of the detector, resulting in a higher level of background.

Low-radius BIB mainly affects pixel and strip trackers in CMS, where it induces spurious hits in detectors, increasing dead time and adversely affecting track reconstruction. The main impact arises when a muon produced in a decay of mesons created by the interaction of the beam or beam halo particles upstream of the detector interacts with the CMS detector and produces an energy deposition that can mimic the signatures of particles originating from central collisions in the IP5, also introducing a large imbalance in the measured total transverse momentum.

The rate of BIB events was typically a few Hz during Phase-1 Run 2 data taking.

* Anastasiia.Riabchikova@cern.ch

ISBN: 978-3-95450-240-0 ISSN: 2673-5539 doi:10.18429/JACoW-RuPAC2021-MOPSA55

SIMULATION SOFTWARE

The Beam Radiation Instrumentation and Luminosity (BRIL) project of CMS is responsible for maintaining and improving the radiation simulation infrastructure of the CMS experiment. This software infrastructure is used by the BRIL to estimate the radiation levels in the CMS detector and experimental cavern.

Simulations are performed by the BRIL Radiation Simulation group (RadSim) using specialized software based on a complex dynamic model of the CMS experiment, its infrastructure and interface with the LHC. RadSim uses two Monte Carlo (MC) simulation packages, FLUKA [4, 5] and MARS [6], to transport particles through the CMS and to calculate radiation levels in the detectors and the CMS cavern.

It is also important to estimate the BIB radiation relative to the Collision Induced Background (CIB) at locations of various radiation detectors, which are operated by the BRIL project and are used to monitor the BIB rate and luminosity during the LHC operation [7].

BIB simulation uses an external set of input data. For LBG input source at the interface plane between LHC and CMS cavern can be calculated with FLUKA or MARS using residual gas profiles in the LSS5 beam pipe, preliminary simulated by the LHC Vacuum Group.

For DBG source should be calculated in two steps. Elastic beam-gas interactions along the cold LHC ring and the intermediate source at TCT are calculated using the STRUCT tracking code [8], and then the particle transport from TCT to the entrance of the CMS was simulated using MARS [9].

For BH source was also prepared in two steps. Intermediate source – hits map at the TCT - was determined using the SixTrack tracking code [10], and the particle transport to the CMS was simulated using FLUKA code [11].

Actual geometry models of the CMS and LSS5 are important parts of the simulation soft. There are include description of the CMS sub-detectors, LHC elements (vacuum chambers, vacuum equipment, interface of experiment with accelerator, magnetic elements in the LSS5), experimental cavern with CMS infrastructure. Magnetic structure description should include not only field in magnet apertures, but also field inside material of magnets and scattered field around it. It should provide correct description of trajectories of the charged products of cascades, initiated in the SS5.

SIMULATION AND RESULTS

The BIB particles transport simulation through the CMS detector was performed with CERN FLUKA v.4-1.1 and CMS FLUKA Model v.6.0, that represents the CMS Phase-2 configuration. In the Fig. 1 MC estimation of the flux of all charged particles produced by proton-proton collisions in the CMS experimental cavern is shown.

Two most modern BIB source files for HL-LHC were used, for BH and LBG. BIB particles are coming from the right side starting from interface plane at Z = 22.6 m. In Fig. 2 and Fig. 3 results of the simulations are shown for the same particle type and scale as in Fig. 1. Background from proton-proton collisions (CIB) dominates over the BIB, and the outgoing BIB particles (at negative Z side) cannot be distinguished from CIB ones. But the incoming BIB particles are in antiphase with the outgoing CIB, and at some locations can be clearly separated from CIB and measured. Such measurements are used for the control of the LHC beam conditions and beam abort signal elaboration if it is necessary for detector safety.

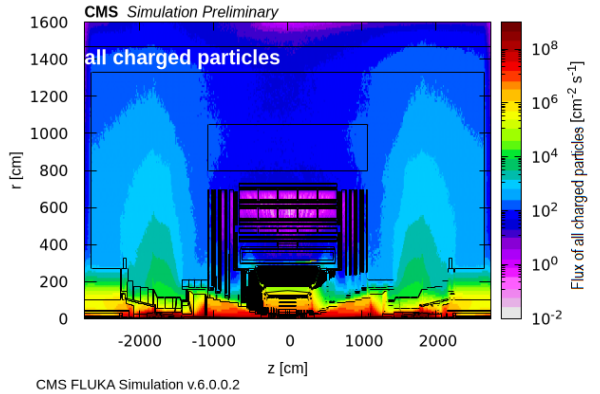

Figure 1: MC estimation of the flux of all charged particles in the CMS detectors and cavern at nominal HL-LHC luminosity 5×10^{34} cm^{-2}s^{-1}.

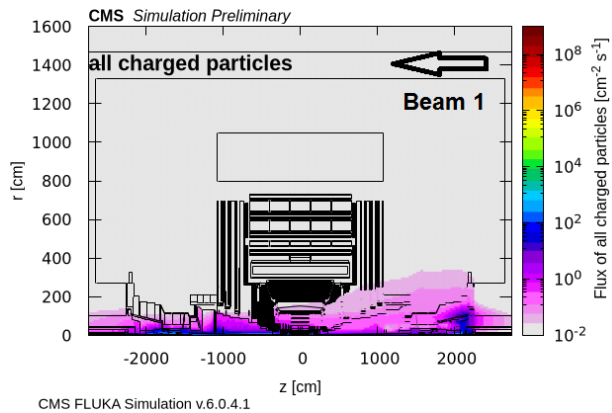

Figure 2: MC estimation of the flux of all charged particles in the CMS detectors and cavern from BH BIB source.

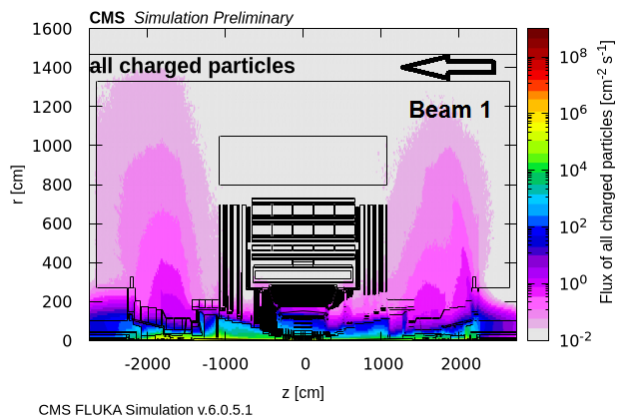

Figure 3: The same as for Fig. 2, but for LBG BIB source.

In Fig. 4 and Fig. 5 the flux of muons is presented for the same two BIB sources. The flux of BH initiated muons at

ISBN: 978-3-95450-240-0 ISSN: 2673-5539 doi:10.18429/JACoW-RuPAC2021-MOPSA55

small radius is much less intense than the flux from LBG, but BH source can give perceptible contribution to the total BIB at radius greater than 1 m.

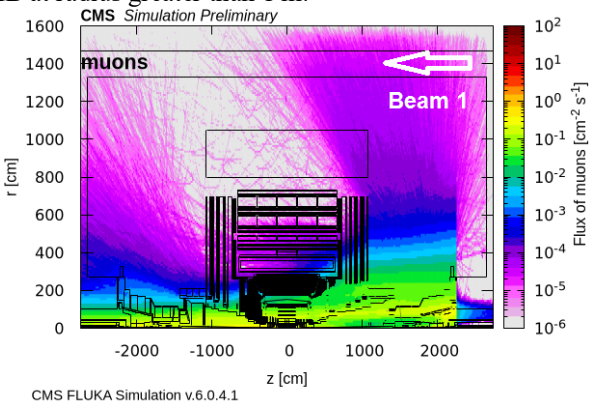

Figure 4: MC estimation of the flux of muons in the CMS detectors and cavern from BH BIB source.

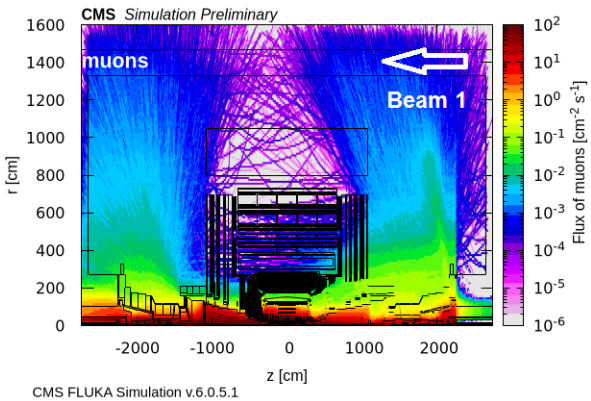

Figure 5: The same as for Fig.4, but for LBG BIB source.

In Fig. 6 and Fig. 7 radial distributions of the flux of all charged particles of BIB are presented for locations of the BRIL near beam detectors, designed to control BIB intensity and beam conditions. BCML is a Beam Condition Monitor that includes two pairs of stations located at different distance from IP (Z = 0). While the rates of the incoming background are relatively low, the outgoing background particles interact with detector material inside CMS and the central beam pipe (both cylindrically shaped central and conically shaped sections) and thus produces showers that generate much larger numbers of hits in the detector. However, unless bunches are noncolliding, these showers are fully superimposed over the collision products and thus are not distinguishable in the data.

TEPX D4R1 (part of the CMS end cap pixel detector) and FBCM (Fast Beam Condition Monitor) will also be used for measuring of the BIB intensity and distribution at the HL-LHC.

CONCLUSION

The software and approaches used by the CMS BRIL RadSim group for BIB simulations in the CMS experiment at HL-LHC are presented in this report. The first data of BIB simulation for modern version of the CMS Phase-2 FLUKA Model v.6.0 are presented.

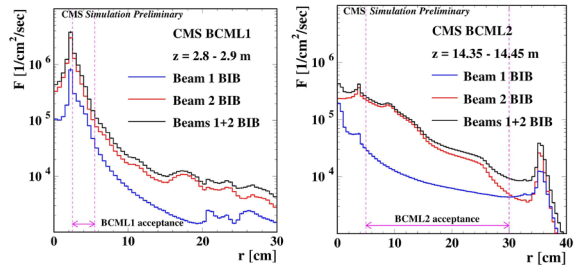

Figure 6: MC estimation of the radial distribution of the flux of all charged particles of BIB in CMS BCML1 (left) and BCML2 (right) detectors per one second of HL-LHC operation.

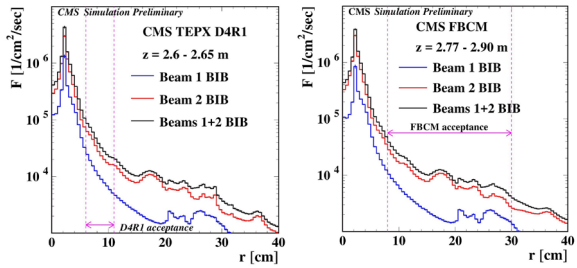

Figure 7: The same as for Fig. 6, but for CMS TEPX D4R1 (left) and FBCM (right) detectors.

ACKNOWLEDGMENTS

We would like to thank the CMS Technical Coordination and the CMS Integration Office for their support of the BRIL Radiation Simulation, and the LHC Background Working Group for the fruitful discussions.

REFERENCES

[1] L.Evans and P.Bryant, *JINST* 3, S08001, 2008. doi:10.1088/1748-0221/3/08/S08001.

[2] G. Apollinary *et al.*, Technical Report CERN-2015-005, 2015, doi:10.5170/CERN-2015-005.

[3] CMS Collaboration, *JINST* 3, S08004, 2008 doi:10.1088/1748-0221/3/08/S08004.

[4] G. Battistoni *et al., Annals of Nuclear Energy* 82, 10-18, 2015, doi:10.1016/j.anucene.2014.11.007.

[5] T.Bohlen, *et al.*, *Nuclear Data Sheets* 120, 211-214, 2014 doi:10.1016/j.nds.2014.07.049.

[6] I. Azhgirey and V. Talanov, in *Proceedings, XVIII Charged Particle Accelerator Workshop*, Protvino, Russia, volume 2, p. 184, 2000.

[7] A. Dabrowski, *Nucl. Phys. B* 273-275, p. 1147-1154, 2016. doi:10.1016/j.nuclphysbps.2015.09.180.

[8] I. Baishev, A. Drozhdin, and N. Mokhov, SSCL-MAN-0034, 1994.

[9] S. Mallows *et al.*, *Nucl. Instr. and Meth.* A824, p. 30-32, 2016. doi:10.1016/j.nima.2015.11.044.

[10] R. Robert-Demolaize, R. Assmann, S. Redaelli and F. Schmidt, *Conf. Proc.* C 0505161, 4084, 2005.

[11] R. Bruce *et al., Nucl. Instr. Meth.* A 729, 824-840, 2013. doi:10.1016/j.nima.2013.08.058.

ISBN: 978-3-95450-240-0 ISSN: 2673-5539 doi:10.18429/JACoW-RuPAC2021-MOPSA56

UPGRADES OF A VACCUM INSULATED TANDEM ACCELERATOR FOR OBTAINING REQUIRED VOLTAGE WITHOUT BREAKDOWNS

I. Sorokin†, Ia. Kolesnikov, A. Makarov, I. Schudlo, S. Taskaev,
Budker Institute of Nuclear Physics, 630090 Novosibirsk, Russia and
Novosibirsk State University, Novosibirsk, Russia

Abstract

Epithermal neutron source based on an electrostatic tandem accelerator of a new type - Vacuum Insulation Tandem Accelerator, and lithium neutron target has been proposed and developed at BINP for Boron Neutron Capture Therapy - promising method for treatment of tumors. 2 MeV proton beam was obtained in the accelerator, the neutron generation carried out with bombardment of lithium target by protons, successful experiments on irradiation of cell cultures incubated in boron medium have been carried out, human glioblastoma grafted mice were cured. It is necessary to increase proton energy from 2 to 2.3 MeV to form a neutron beam suitable for the treatment of deep-seated tumors and to provide the high-voltage strength of the accelerator at a potential of 1.2 MV in order to suppress dark currents to an acceptably small value. Two upgrades to obtain the required potential were consistently implemented. At first, the glass rings of the feedthrough insulator were replaced by smooth ceramic ones doubled in height which made it possible to refuse placing the resistive divider inside. Then the smooth ceramic rings were replaced by the new ceramic rings with a ribbed outer surface. Modernization made it possible to obtain the required voltage of 1.15 MV in the accelerator without breakdowns. The report describes in detail the modernizations carried out, presents the results of the studies.

INTRODUCTION

The source of epithermal neutrons based on a tandem accelerator with vacuum isolation and a lithium target [1] for the development of boron neutron capture therapy [2] of malignant tumors was proposed and created at the BINP. A stationary proton beam with energy of 2 MeV was obtained, neutrons were generated, and the effect of neutron radiation on cell cultures [3] and laboratory animals [4] was studied. An increase in proton energy up to 2.3 MeV [5] is required for a neutron beam suitable for the treatment of deep-seated tumors. The purpose of this work was to modernize a feedthrough insulator to increase a high-voltage strength of the accelerator when receiving a voltage of 1.2 MV.

ACCELERATOR DESIGN

Figure 1 shows a vacuum-insulated tandem accelerator. A beam of negative hydrogen ions is injected into the accelerator and accelerated to 1 MeV. In the gas (argon) stripping target 7, which has installed inside the high-voltage electrode 1, negative hydrogen ions are converted into protons. Then, protons are accelerated to energy of 2 MeV by the same potential of 1 MV [5]. Gas is pumped by a turbomolecular pump 10 installed at the output of the accelerator and a cryogenic pump 4 through a jalousies 3 in the electrodes.

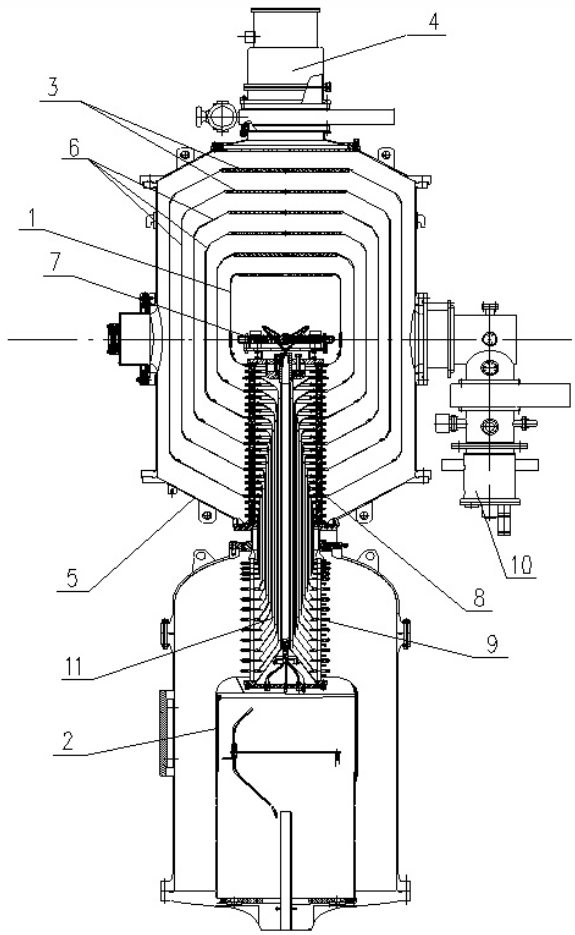

Figure 1: General cross-section view of the electrostatic 6-gap accelerator-tandem with vacuum insulation: 1 - high-voltage electrode of the accelerator-tandem; 2 - high-voltage electrode of high-voltage rectifier; 3 - jalousies of electrodes; 4 - cryogenic pump; 5 - vacuum tank of the accelerator; 6 - intermediate electrodes of the tandem-accelerator; 7 - gas stripping target; 8 - vacuum part of feedthrough insulator; 9 - gas part of feedthrough insulator; 10 - turbomolecular pump; 11 - internal coaxial cylinders.

One of the basic elements of the vacuum-insulated tandem accelerator is a sectionalized disassemble feedthrough insulator through which the voltage from the high-voltage rectifier 2 is fed to the central electrode of accelerator 1.

† I.N.Sorokin@inp.nsk.su

ISBN: 978-3-95450-240-0 ISSN: 2673-5539 doi:10.18429/JACoW-RuPAC2021-MOPSA56

Electrodes of same potential of the lower (gas) 9 and upper (vacuum) 8 parts of the feedthrough insulator are connected by a system of internal coaxial cylinders 11 of different length and diameter. The distribution of the potential over the intermediate electrodes 6 was determined by the new resistive voltage divider, which after replacing single glass rings with a height of 35 mm with ceramic rings with a smooth surface with a height of 35 mm and 70 mm, is completely located outside the lower gas part of the feedthrough insulator. The previous resistive voltage divider was originally located inside the upper and outside the lower part of the feedthrough insulator. The insulator of the lower gas part remained the same. The total height of the feedthrough insulator has not changed.

After a series of experiments, the purpose of which was to obtain a voltage at the accelerator of 1.15 MV with an upgraded feedthrough insulator made of smooth ceramics, the accelerator was disassembled. Large number visible traces of discharges were found over the entire surface of smooth ceramics (Fig. 2).

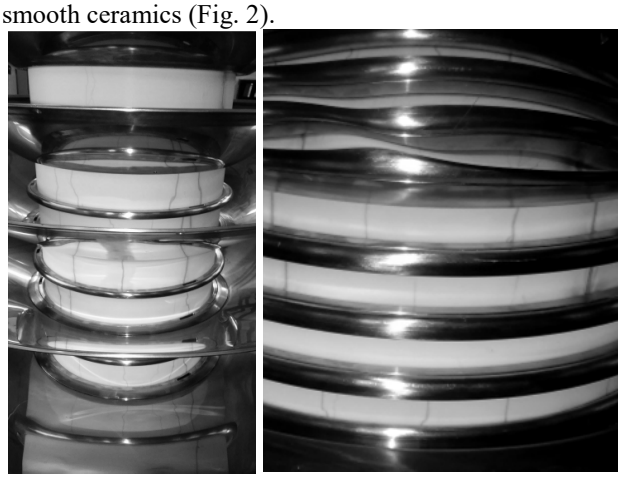

Figure 2: Smooth ceramic surface after training (left, right) with breakdown traces.

The appearance of breakdown traces is the result of a training during which the electric field strength on the ceramic surface was ~ 15 kV/cm.

Experience with accelerators showed that for it to work without breakdowns, it is necessary that the electric field strength on the surface of ceramic accelerator tubes be ~ 10 kV/cm. In our case, the voltage was exceeded by 1.5 times, while the accelerator was stable at a voltage of 1.15 MV (~ 13.7 kV/cm). However, traces of discharges may be the cause of subsequent breakdowns in the future.

There are two options for solving this problem. First, it is necessary to increase the height of individual insulators by 1.5 times, which will lead to an increase in the dimensions of the accelerator. The second option is to change the surface shape of the vacuum part of the ceramic rings

Studies of insulators with different geometry of the outer surface showed that a ribbed surface with radii of ribs and depressions from 0.5 to 1 mm provides an increase in electrical strength up to 1.5 times compared to a smooth surface. With the same height of the insulators, the surface length of the ribbed insulator is $\pi/2$ times longer than that of a smooth insulator. The developed processing technology for inorganic insulators allows the realization of ribbed surface geometry.

Based on the obtained experimental data [6], we upgraded the feedthrough insulator. Ceramic insulators with a ribbed outer vacuum surface were made (Fig. 3), which replaced smooth ceramic insulators with a height of 35 mm and 73 mm. The radius of the ribs and troughs has chosen 1 mm, based on the previously obtained results.

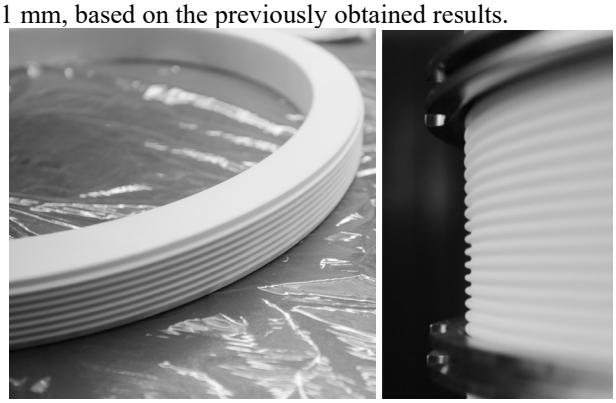

Figure 3: Ribbed ceramic surface 35 mm insulator (left) and 70 mm insulator (right) before training.

The height of the new individual ribbed ceramic insulators has not changed. The total height of the feedthrough insulator remained the same.

EXPERIMENTAL RESULTS

The new feedthrough insulator with an outer ribbed vacuum surface of ceramic rings has installed. After opening to the atmosphere standard training has performed. The voltage of 1 MV was obtained over a time that was 2 times less and with a smaller number of breakdowns than at the feedthrough insulator with a smooth ceramic surface (Fig. 4).

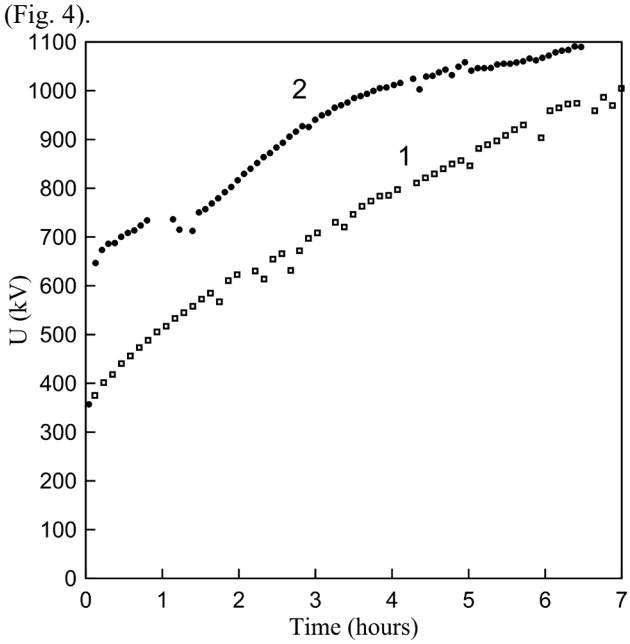

Figure 4: Graphs of the first increase in voltage at the accelerator after modernization: 1 - smooth ceramic, 2 - ribbed ceramic.

ISBN: 978-3-95450-240-0 ISSN: 2673-5539 doi:10.18429/JACoW-RuPAC2021-MOPSA56

In the third series of experiments, the voltage of 1200 kV has reached (Fig. 5). Note that the average electric field strength on an insulator with a smooth surface was ~ 14 kV/cm, and on an insulator with a ribbed vacuum surface, taking into account an increase in its length by π/2, it was ~ 9 kV/cm. It value is given in literary sources as a value providing the required electric strength.

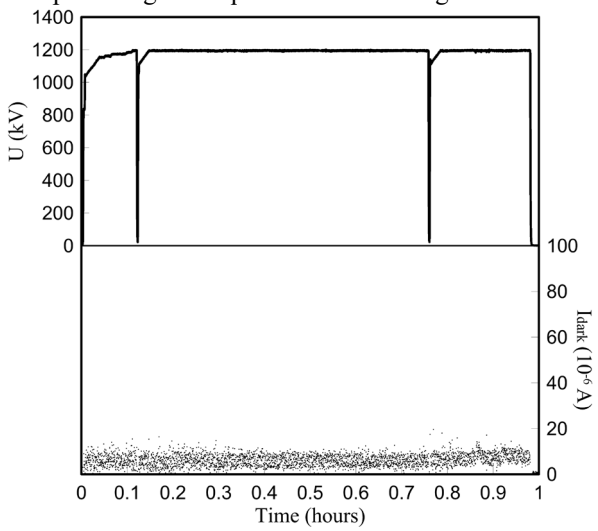

Figure 5: Graphs of the voltage U and dark current I_{dark} at the accelerator versus time.

After receiving 1200 kV, the voltage was reduced to a working 1150 kV and the mode without breakdowns was reached (Fig. 6). In this case, the average electric field strength on the vacuum surface of the feedthrough insulator was ~ 8.3 kV/cm, taking into account increase in its length by π/2. Also, decrease in the dark current value and the level of the X-rays dose to minimum values was observed.

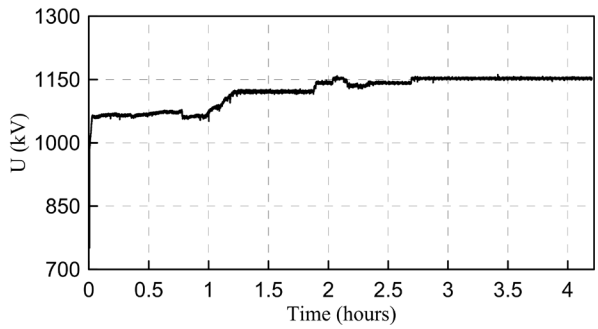

Figure 6: Graph of the voltage dependence of the accelerator when increasing and standing at a voltage of 1150 kV.

After several months of operation of the accelerator, during which there was no situation associated with violations in the operation of the feedthrough insulator, traces of breakdowns have not found on the ribbed vacuum surface of the feedthrough insulator (Fig. 7).

Thus, it has established experimentally that the use of single insulating rings of double height with a ribbed vacuum surface and the refusal to use part of the resistive voltage divider inside the feedthrough insulator is justified - the voltage of 1.15 MV has obtained and the working reliability of the feedthrough insulator is increased.

Figure 7: Ribbed ceramic surface (left, right) after training without breakdown traces.

CONCLUSION

An epithermal neutrons source based on the vacuum insulated tandem accelerator and a lithium target is operating at BINP. A modernization of the feedthrough insulator is proposed and implemented. Ceramic insulators with a ribbed surface replace ceramic ring insulators with a smooth surface. It has found that the upgraded feedthrough insulator provides greater reliability compared to the previous one. The required voltage of 1.15 MV was obtained in the vacuum insulated tandem accelerator after the upgrade. The operating mode without high-voltage breakdowns was maintained, which is important for using a neutron source in therapy and for other applications.

ACKNOWLEDGMENT

The study has supported by the Russian Science Foundation (project No. 19-72-30005) and by the Budker Institute of Nuclear Physics.

REFERENCES

[1] S. Taskaev, "Accelerator based epithermal neutron source", *Phys. Part. Nucl.*, vol. 46, no. 6, pp. 956-990, Nov. 2015. doi:10.1134/S1063779615060064

[2] W. Sauerwein *et al.*, *Neutron Capture Therapy: Principles and Application*. Springer, 2012. doi:10.1007/978-3-642-31334-9

[3] E. Sato *et al.*, "Radiobiological response of U251MG, CHO-K1 and V79 cell lines to accelerator-based boron neutron capture therapy", *J. Radiol. Res.*, vol. 59, no. 2, pp. 101-107, March 2017. doi:10.1093/jrr/rrx071

[4] S. Taskaev, "Development of an Accelerator-Based Epithermal Neutron Source for Boron Neutron Capture Therapy", *Phys. Part. Nucl.*, vol. 50, no. 5, pp. 569-575, Sept. 2019. doi:10.1134/S1063779619050228

[5] L. Zaidi *et al.*, "Beam Shaping Assembly Design of ^{7}Li(p,n)^{7}Be Neutron Source for Boron Neutron Capture Therapy of Deep-seated Tumor", *Appl. Radiat. Isotopes*, vol. 139, pp. 316-324, Sept. 2018. doi:10.1016/j.apradiso.2018.05.029

[6] Ya. Kolesnikov *et al.*, "Electrical strength of the high-voltage gaps of the tandem accelerator with vacuum insulation", in *Proc. 27th ISDEIV*, Suzhou, China, vol. 2, pp. 778-781, 2016. doi:10.1109/DEIV.2016.7764033

ISBN: 978-3-95450-240-0 ISSN: 2673-5539 doi:10.18429/JACoW-RuPAC2021-MOPSA57

EXPERIMENTAL INVESTIGATION THE SYNTHETIC CRYSTAL DIAMOND PLATES OF METHODS OF POSITRON ANNIHILATION SPECTROSCOPY

M.K. Eseev, I.V. Kuziv, Northern (Arctic) Federal University named after M.V. Lomonosov, Arkhangelsk, Russia
A.G. Kobets[1], I.N. Meshkov, O.S. Orlov, A.A. Sidorin, K. Siemek[2], Joint Institute for Nuclear Research, Dubna, Moscow Region, Russia
[1]also at Institute of Electrophysics and Radiation Technologies, NAS of Ukraine, Kharkov, Ukraine
[2]also at Institute of Nuclear Physics Polish Academy of Sciences, Krakow, Poland

Abstract

Nowadays positron annihilation spectroscopy is a powerful technique of microstructure investigations of crystalline materials. Doped diamonds were studied by Positron annihilation spectroscopy and Infrared spectroscopy. As a result of the experiments, data show the effect of nitrogen doping of diamonds on the occurrence of defects in a doped diamonds.

INTRODUCTION

Synthetic crystal diamond plates are used in scientific and technical fields and in new materials. Various defects and types of defects in diamond plates can changed its properties. Investigation the defects of diamond plated is very important for use diamond plates for fully solving applied problems in roentgen-optical systems and quantum sensorics. The investigation included three different spectroscopy types. First type is Positron annihilation spectroscopy (PAS). PAS is unique non-destructive instrument to detect open-volume defects, such as vacancies, vacancy clusters, microvoids or dislocations. PAS can define defects in the near-surface layer of materials with thickness up to 10…100 nm. It can be used in cases where other popular methods such as scanning electron microscopy (SEM) or X-ray diffraction are not applicable [1,2]. The second type of spectroscopy which used in this investigation is Infrared spectroscopy. This technique allows to define types of diamond defects such as A type and C type. The third type is Raman spectroscopy. It is valuable method because it provides readily distinguishable signatures of each of the different forms of carbon.

MATERIALS AND METHODS

Generation of the synthetic crystal diamond plates was conducted by HTHP method with addition of nitrogen in different concentrations (12,5 ppm, 75 ppm, 88 ppm). Defects in the atomic structure of diamond plates are responsible for this colour. Transparent sample contained 12 ppm, yellow - 7 ppm, pink - 88 ppm. Then diamonds were cut by laser. Several series of paired samples of the diamond plates with 0,8 mm in height and different side size were studied (Fig. 1).

One sample from each group was cut along and across and left for investigation by Infrared and PAS spectroscopy methods.

Simultaneously one sample from each group was left for investigation by Raman spectroscopy method. Pink sample contained NV^0 (575 nm) and NV^- (637 nm) defects.

Figure 1: Synthetic crystal diamond plates.

First part of experiment consisted in measurement the positron annihilation lifetime spectroscopy (PALS). PALS measurements were conducted using digital spectrometer APU-8702RU and the BaF_2-based scintillator (Fig. 2).

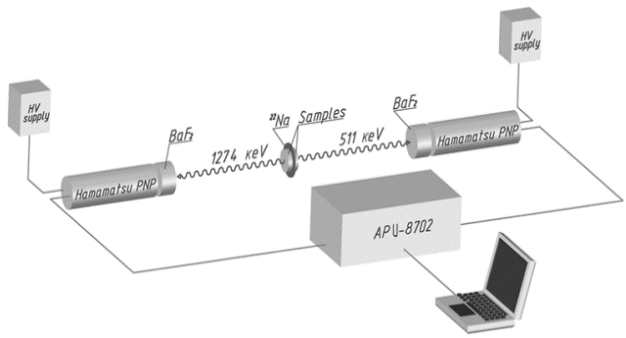

Figure 2: PALS instruments.

The timing resolution equaled 250 ps. The typical sandwich geometry was used, where the positron source located between two identical samples. The ^{22}Na isotope with an activity of 850 kBq was used as a positron source. It was placed between two identical samples. The positron source consisted of $^{22}NaCl$ salt between two titanium foils (10 μm).The measurements were carried out at room temperature.

This method shows average lifetime of the positron in diamond plates. The positron lifetime gives information

ISBN: 978-3-95450-240-0 ISSN: 2673-5539 doi:10.18429/JACoW-RuPAC2021-MOPSA57

about the electron density. Electron density inside the defect is lower in comparison with bulk area what in tern reflects in the mean positron lifetime.

Doppler broadening spectroscopy of annihilation radiation (DB) measurements were performed using ORTEC HPGe detector model GEM25P4-70 with energetic resolution FWHM 1.20 keV for energy 511 keV. Each obtained spectrum was analyzed to calculate S and W parameters by SP-16K program.

The Doppler Broadening method is based on slow monoenergetic positron beam with positrons energies ranging up to 35 keV working at JINR in Dubna, Russia (Fig. 3) [3].

The second part of the experiment consisted in the study of samples by Infrared spectroscopy. Infrared spectroscopy measurements were conducted using Bruker HYPERION 3000 Spectrometer.

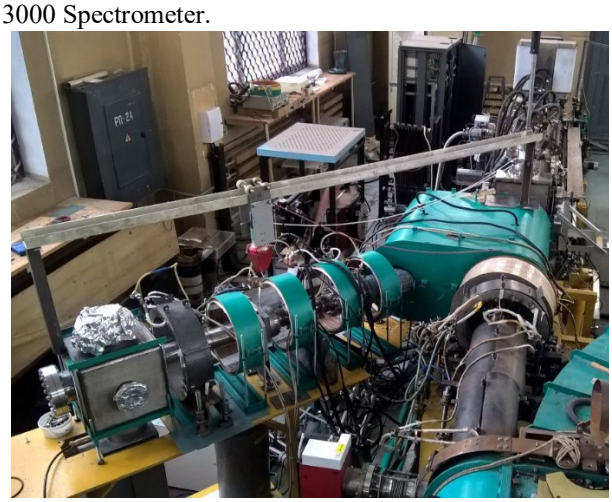

Figure 3: Doppler Broadening instruments.

RESULTS AND DESCUSSION

PALS measurements revealed two lifetime components. The total number of coincident events, accumulated in the spectrum for each pair of samples, equals to $3*10^6$. The analysis of spectra was conducted using LT 10.2 program.

The annihilation rate λ is a reciprocal value of mean positron lifetime.

$$\lambda = \frac{1}{\tau} = \pi r_0^2 c n_e \,, \qquad (1)$$

Dependence positron lifetime from nitrogen concentration of samples are shown in Table 1. τ_1 and τ_2 represent positron lifetime components and I_1 and I_2 its intensities, respectively. τ_{av} is a mean positron lifetime.

Table 1: Dependence Positron Lifetime From Nitrogen Concentration Of Samples

Nitrogen concentration, ppm	τ_1, ps	I_1, %	τ_2, ps	I_2, %	τ_{av}, ps
12,5	153 ± 1	55,9	258 ± 1	44,1	199 ±1
75	171 ± 1	68,7	332 ± 1	31,3	220 ±1
88	207 ± 1	79,4	350 ± 1	20,6	236 ±1

The positron lifetime for bulk (τ = 100-100 ps) was reported by Uedono A. [4] and for monovacancy (τ = 140-150 ps) was reported by Pu A [5].

The results of lifetime method is shown in Fig. 4.

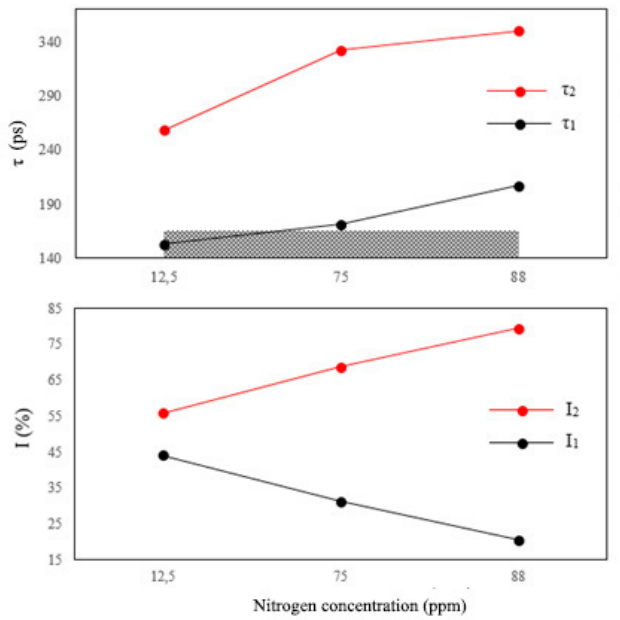

Figure 4: Dependence of the positron lifetime on nitrogen concentration.

The Doppler broadening measurement were used to study defect profiles beneath the surface.

Each obtained spectrum was analyzed to calculate S and W parameters by SP-16K program. The S parameter reflects annihilations with low momentum electrons taking place in defects. It is sensitive to open-volume defects like vacancies, vacancy cluster or jogs at dislocation lines.

Doppler broadening show that defect concentrations increase with increasing nitrogen concentration at the depth of 40-400 nm, then defect concentration decrease (Fig. 5).

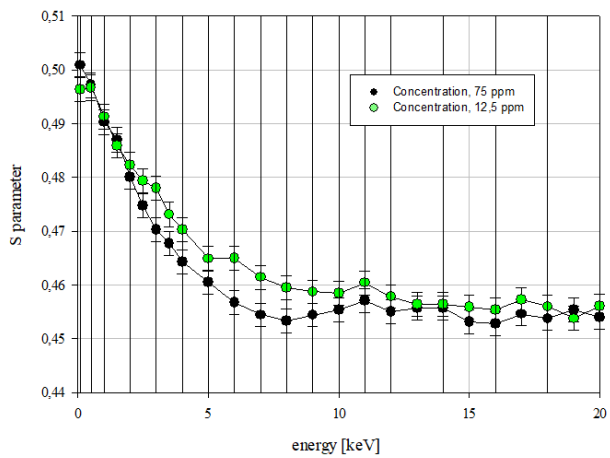

Figure 5: Dependence of the S parameter in samples (12,5 ppm and 75 ppm) on positron energy.

Infrared spectrum of transparent sample which was cut along shown in Fig. 6 and which was cut across shown in Fig. 7.

ISBN: 978-3-95450-240-0 ISSN: 2673-5539 doi:10.18429/JACoW-RuPAC2021-MOPSA57

Concentration of A defects in transparent sample which was cut along - 91,63±5,63 ppm.

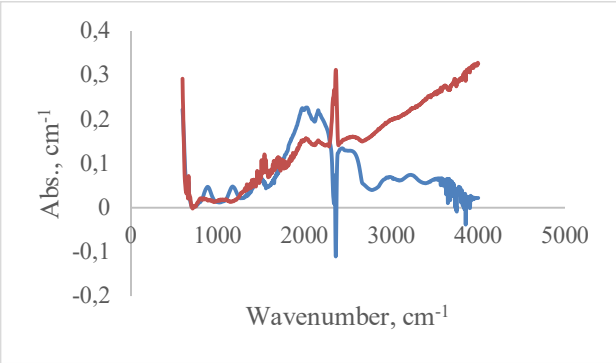

Figure 6: Infrared spectrum of transparent sample. Blue line – before cutting, red line – after cutting.

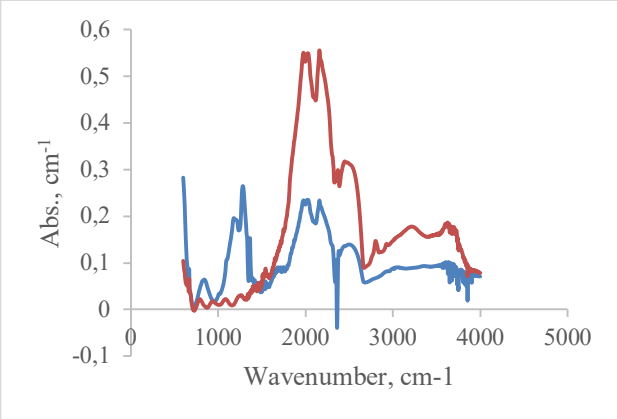

Figure 7: Infrared spectrum of transparent sample. Blue line - before cutting, red line - after cutting.

Infrared spectrum of yellow sample which was cut along shown in Fig. 8 and which was cut across shown in Fig. 9.

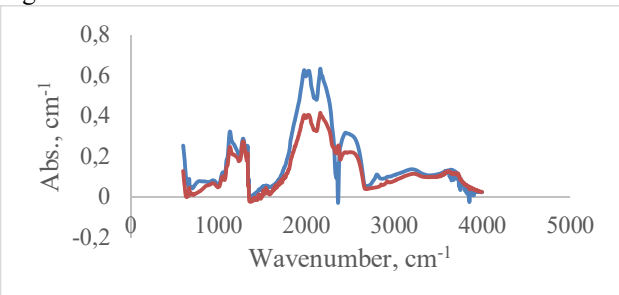

Figure 8: Infrared spectrum of yellow sample. Blue line – before cutting, red line – after cutting.

Concentration of C+ defects in yellow sample before cutting (along) - 64,40±11,69 ppm. Concentration of C+ defects in yellow sample after cutting (along) - 153,44± 27,78 ppm.

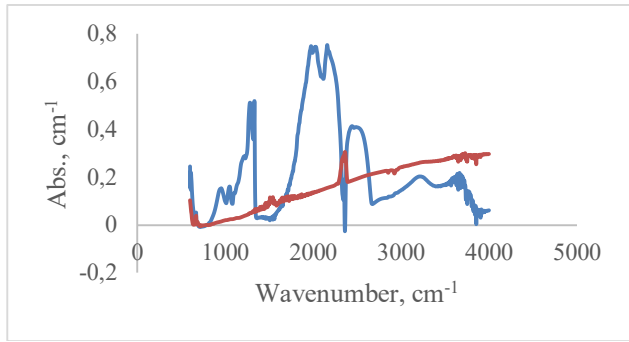

Figure 9: Infrared spectrum of yellow sample. Blue line - before cutting, red line - after cutting.

Concentration of C+ defects in yellow sample before cutting (along) - 110,31±20,06 ppm.

CONCLUSION

This PAS investigation reveals that all samples have defects. All the defects are of the vacancy-type such as monovacancy, divacancy and vacancy clusters. Dependence of the amount of such defects is also in accordance with the depth of the layer in diamond plate. Positron annihilation spectroscopy is a unique method for detection the structural defects.

Raman spectroscopy shows that pink sample contained NV defects (NV^0 (575 nm) and NV^- (637 nm) defects).

Infrared spectroscopy shows that transparent sample (Nitrogen concentration - 12,5 ppm) has just A-type defect and yellow sample (Nitrogen concentration - 75 ppm) C+-type defect.

This work was supported by the state order of the Ministry of Education and Science of the Russian Federation No. 075-00940-21-05. We would like to thank AGD Daimonos JSC for the presented samples.

REFERENCES

[1] I. Prochazka, "Positron annihilation spectroscopy", *Materials Structure*, vol. 8, number 2, pp. 55-60, 2001.

[2] P. Horodek, M. Eseev and A. Kobets, "Studies of stainless steel exposed to sandblasting", *Nukleonika*, vol. 60, pp. 721-724, 2015.

[3] A.A. Sidorin *et al.*, "The LEPTA facility for fundamental studies of positronium physics and positron spectroscopy", *Materials Science Forum*, vol. 733, pp. 291-296, 2013.

[4] A. Uedono *et al.*, "Positron annihilation in silicon in thermal equilibrium at high temperature" *J. Phys.: Condens. Matter*, vol. 12, p.719, 1999/

[5] Pu. A. Bretagnon T *et al.*, "Positron annihilation investigation of vacancies in as-grown and electron-irradiated diamonds", *Diamond Relat. Mater.*, vol. 9, pp.1450-1463, 2000.

ISBN: 978-3-95450-240-0 ISSN: 2673-5539 doi:10.18429/JACoW-RuPAC2021-MOPSA58

SOURCES OF ULTRASHORT X-RAY PULSES IN THE INVESTIGATION OF THE STRUCTURE AND DYNAMICS OF NANOSYSTEMS

M. K. Eseev†, D. N. Makarov, Northern Arctic Federal University, Arkhangelsk, Russia

Abstract

Free electron lasers are today one of the main sources of ultrashort X-ray pulses. The installations used in the world today are presented and the results of experiments and calculations with various nanosystems are presented.

INTRODUCTION

Free Electron Lasers (FELs) were invented by Madey [1] and then experimentally demonstrated by his group at Stanford University in the 1970s. These lasers use relativistic electrons propagating through a periodic system of magnets (undulator) to generate and amplify coherent electromagnetic radiation.

Initially, the operation of such lasers was demonstrated in infrared mode. After that, work continued on expanding the FEL in the direction of EUV and X-ray modes. To solve this problem, the radiation was additionally amplified using the spontaneous emission self-amplification (SASE) mode. In the SASE mode, the particles of the electron beam are grouped into microbunches when they pass through the undulator and interact in it with the radiation of the beam itself. It is these FELs that are currently actively used in SAR and have great prospects for further improvement.

FELs have the widest frequency setting range and can generate very high peak and average laser powers. The formation of attosecond X-ray pulses on XFELs is currently being reported [2]. The possibility of creating zeptosecond pulses has been reported [3]. The extremely high power, coupled with the excellent lateral coherence of these XFELs, provides a dramatic increase in peak brightness.

The advent of XFELs has ushered in a new era in X-ray and X-ray studies. A large number of such lasers have been built in the last 15 years.

FLACH is the first XFEL facility for photons with energy in the extreme ultraviolet (EUV) region and was built in 2005 at DESY, Hamburg. LCLS is the first hard X-ray FEL built in 2009 at the SLAC National Accelerator Laboratory, USA. The SACLA plant in Japan and the FERMI plant in Trieste represent the first generation of XFELs, which have demonstrated tremendous scientific potential and influence in broad fields of science. XFEL installations are currently expanding worldwide: PAL-XFEL in South Korea, SwissFEL in Switzerland, European XFEL (EuXFEL) in Germany, etc.

DIFFRACTION ANALYSIS USING X-RAY USP

One of the most common approaches that can be used to observe an object in four dimensions x, y, z, t is time-dependent femtosecond crystallography (TR-SFX).

Measuring the temporal dynamics of such processes includes 2 stages, see Fig.1. The first is the launch of the studied dynamic process, and the second is the collection of diffraction patterns with different time delays by irradiating the ultrashort pulses of the studied system. To study such processes, ultrashort pulses of high brightness are used, since a pulse of even shorter duration τ is required to study dynamic processes with characteristic times τ_T, i.e., the condition $\tau << \tau_T$ must be satisfied. A very bright USP source is necessary because in the short time τ of interaction of the pulse with the system under study, a sufficient amount of radiation has been scattered so that it can be detected. To implement this concept, difficulties arise due to the destruction of the sample under study due to the high brightness of the ultrashort pulses. Despite this, in 2000 Janos Hajdu and his colleagues showed how this difficulty can be overcome [4]. They calculated that a molecule exposed to an X-ray pulse would begin to explode on a time scale of about 10 femtoseconds. Thus, shorter light pulses can pass through the molecule, capturing information about the virtually unperturbed structure. And pulses bright enough will give rise to continuous diffraction patterns strong enough to be measured.

The first stage can be implemented in several ways. The most common method is the so-called *pump-probe*. This method, suitable for studying quantitatively reproducible dynamics, is based on the creation of a time-delayed sequence of two short pulses: a "pump" pulse (usually an optical laser or the first XFEL pulse) unbalances the substance, and a "probe" X-ray pulse is used to create or taking "snapshots" of the structure of a substance at a specific point in time during the dynamic response of the substance. The structural response of the system can then be traced as a function of time by repeatedly applying these two impulses to the substance with different relative delays.

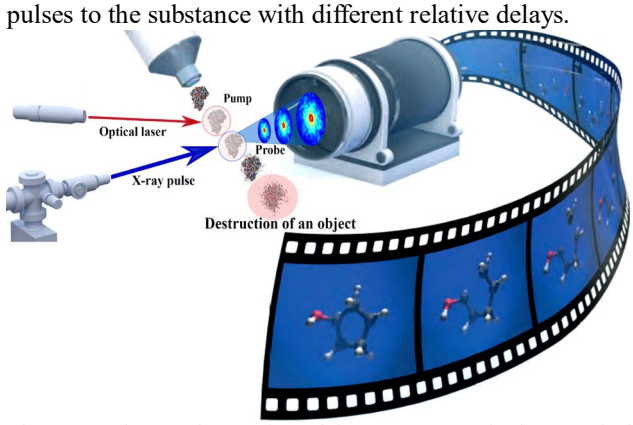

Figure 1: Scheme of operation of the TR-SFX method. Instead of an optical laser (Pump), there can be an X-ray pulse (the first pulse is Pump, and the second is Probe) [5].

† m.eseev@narfu.ru

ISBN: 978-3-95450-240-0 ISSN: 2673-5539 doi:10.18429/JACoW-RuPAC2021-MOPSA58

SCATTERING SPECTRA OF ULTRA-SHORT PULSES ON NANOSTRUCTURES

In [6-8], a theory of scattering of X-ray ultrashort pulses by nanostructures consisting of identical atoms was developed. In this theory, the basic expressions for calculations were obtained:

$$\frac{d^2W}{d\omega d\Omega_{\mathbf{k}}} = \frac{1}{(2\pi)^2}\frac{1}{c^3\omega}\left(N_a \mathrm{N}_e S(\omega,\mathbf{n},\mathbf{n}_0) + \delta_N(\mathbf{p})\mathrm{N}_e(\mathrm{N}_e-1)\mathrm{F}(\omega,\mathbf{n},\mathbf{n}_0)\right),$$

$$S(\omega,\mathbf{n},\mathbf{n}_0) = G(\omega,\mathbf{n},\mathbf{n}_0) - F(\omega,\mathbf{n},\mathbf{n}_0), \mathrm{G}(\omega,\mathbf{n},\mathbf{n}_0) = \frac{1}{N_e}\int \rho(\mathbf{r})\left|\mathbf{f}(\mathbf{r})\right|^2 d\mathbf{r},$$

$$F(\omega,\mathbf{n},\mathbf{n}_0) = \frac{1}{N_e^{\,2}}\left|\int \rho(\mathbf{r})\mathbf{f}(\mathbf{r})e^{-i\mathbf{kr}}d\mathbf{r}\right|^2, \mathbf{f}(\mathbf{r}_a) = \left[\tilde{\mathbf{E}}(\omega)\times\mathbf{n}\right],$$

$$\tilde{\mathbf{E}}(\omega) = \int_{-\infty}^{+\infty}\left(\mathbf{E}(\mathbf{r}_{a,e},t) - \frac{1}{2}\nabla_a\left(\frac{\mathbf{E}(\mathbf{r}_{a,e},t)}{c}\right)^2\right)e^{i\omega t}dt, \delta_N(\mathbf{p}) = \left|\sum_a e^{i\mathbf{p}\mathbf{R}_a}\right|^2. \quad (1)$$

Summation in Eq. (1) is carried out over all atoms of the considered system. We will use the electronic density $\rho(\mathbf{r})$ of the Dirac-Hartree-Fock-Slater model [9].

As an example, we present the results of calculations of the scattering spectra of USP on graphene. For this, we first need to determine the $\delta_N(\mathbf{p})$ factor, which is equal to [8]:

$$\delta_N(\mathbf{p}) = \frac{4\sin^2\left(\frac{\sqrt{3}}{2}L\mathbf{p}jd\right)}{\sin^2\left(\frac{\mathbf{p}id}{2}\right)\sin^2\left(\frac{\sqrt{3}}{2}\mathbf{p}jd\right)} \quad (2)$$

$$\left\{\cos\left(\frac{\mathbf{p}jd}{\sqrt{3}}\right)\sin\left(\frac{\mathbf{p}idN}{2}\right) + \cos\left(\frac{\mathbf{p}jd}{2\sqrt{3}}\right)\sin\left(\frac{\mathbf{p}id(N+1)}{2}\right)\right\}^2,$$

where L is the number of graphene ribbons, N is the number of the cells in graphene tape, d is the distance between atoms along the x axis, and $\boldsymbol{i}$ and $\boldsymbol{j}$ are unit vectors along the x and y axes, respectively, see Fig. 2.

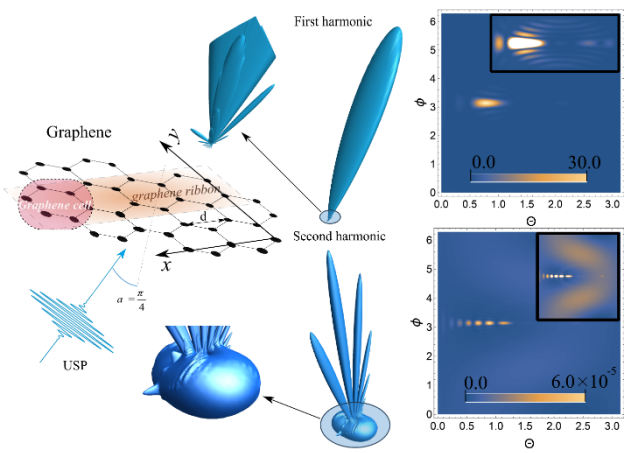

Figure 2: 3D radiation pattern of the scattering spectra USP (see Eq. (1)) and the contour plot for the spectra, where θ and ϕ are angles (in radians) with a spherical coordinate system, i.e. polar and azimuth angles, respectively. Inserts in contour plots show an enlarged (more contrasting) scatter spectrum. The first harmonic is in the figures above, and the second harmonic is below. A USP was selected with a frequency ω_0=100 au, a pulse duration γ corresponding to 43 as and amplitude E_0 = 1000 au. The numbers of the graphene ribbons and cells are $L=10$, $N=10$, respectively The angle of incidence α between $\mathbf{n}_0$ and the z axis was selected as $\alpha=\pi/4$ [8].

CONCLUSION

As a result, we obtain two diffraction patterns on the fundamental and second harmonics, both of which were derived from the same USP and on a given polyatomic system. As a result, diffraction analysis can be carried out by studying two diffraction patterns at once, which allows you to get more details about the research object.

ACKNOWLEDGEMENTS

The study was supported by a grant from the President of the Russian Federation (# МД-4260.2021.1.2); state assignment of the Russian Federation (# 0793-2020-0005).

REFERENCES

[1] J. M. J. Madey, "Stimulated emission of Bremsstrahlung in a periodic magnetic field", *J. Appl. Phys.* vol. 42, p. 1906, Feb. 1971. doi.org/10.1063/1.1660466

[2] P. K. Maroju *et al.* "Attosecond pulse shaping using a seeded free-electron laser", *Nature*, vol. 578, p. 386, Feb. 2020. doi.org/10.1038/s41586-020-2005-6

[3] D. Dunning, B. W. J. Mcneil, N. R. Thompson, "Few-cycle pulse generation in an x-ray free-electron laser", *Phys. Rev. Lett.* vol. 110, 104801, Mart 2013. doi:10.1103/PhysRevLett.110.104801

[4] R. Neutze et al. "Potential for biomolecular imaging with femtosecond x-ray pulses", *Nature*, vol. 406, p. 752, August 2000. doi.org/10.1038/35021099

[5] M. K. Eseev, V. I. Matveev, D. N. Makarov, "Diagnostics of nanosystems using ultrashort X-ray pulses: theory and experiment (Mini-review)", *JETP Letters,* vol. 114, issue 7, p. 444, August 2021, doi:10.31857/S1234567821190034

[6] D.N. Makarov, M.K. Eseev, K.A. Makarova, "Analytical wave function of an atomic electron under the action of a powerful ultrashort electromagnetic field pulse", *Optics Letters,* vol. 44, p. 3042, June 2019. doi.org/10.1364/OL.44.003042

[7] M.K. Eseev, A.A. Goshev, D.N. Makarov, "Scattering of Ultrashort X-ray Pulses by Various Nanosystems", *Nanomaterials*, vol. 10, p. 1355, July 2020. doi.org/10.3390/nano10071355

[8] M.K. Eseev, A.A. Goshev, K.A. Makarova, D.N. Makarov, "X-ray diffraction analysis of matter taking into account the second harmonic in the scattering of powerful ultrashort pulses of an electromagnetic field", *Scientific Reports*, vol. 11, 3571, Feb. 2014. doi.org/10.1038/s41598-021-83183-3

[9] F. Salvat, J. D. Martinez, R. Mayol, and J. Parellada. "Analytical Dirac-Hartree-Fock-Slater screening function for atoms (Z = 1-92)", *Phys. Rev.* A, vol. 36, p. 467, Jul 1987. doi: 10.1103/physreva.36.467

ISBN: 978-3-95450-240-0 ISSN: 2673-5539 doi:10.18429/JACoW-RuPAC2021-TUPSB04

FEATURES OF THE ELECTRON COOLING SYSTEM OF THE NICA BOOSTER

S.A. Melnikov†, E.V. Ahmanova, A.V. Butenko, A.G. Kobets, I.N. Meshkov, O.S. Orlov, K.G. Osipov, S.V. Semenov, A.S. Sergeev, A.A. Sidorin, A.O. Sidorin, E.M. Syresin,
Joint Institute for Nuclear Research, Dubna, Russia
A.V. Ivanov, The Budker Institute of Nuclear Physics, Novosibirsk, Russia

Abstract

The report presents the results obtained during the commissioning the Electron Cooling System (ECS) of the Booster (Fig. 1), the first in the chain of three synchrotrons of the NICA accelerator complex. The work was performed without an ion beam and with a circulating ion beam He^{1+} and $^{56}Fe^{14+}$. In the work with a circulating ion beam He^{1+}, the effect of reducing the lifetime of the circulating ions was observed when the velocities of the cooling electrons and the cooled ions coincide. The dependences of the electron beam current on the ECS parameters for different electron energy values were experimentally obtained. The specific features of operation of electron gun of the NICA Booster are hollow beam formation and the phenomenon of virtual cathode creation confirmed both experiments and by numerical simulation. In conclusion section the results of first experiments on electron cooling of $^{56}Fe^{14+}$ ion electron cooling are presented.

INTRODUCTION

The main tasks of the Booster synchrotron of heavy ions are the accumulation of $2 \cdot 10^9$ gold ions $^{197}Au^{31+}$ or other low-charged heavy ions and their acceleration to the maximum energy (578 MeV/u for $^{197}Au^{31+}$), which is sufficient for their subsequent stripping to the state of bare nuclei. The use of electron cooling in a Booster at ion energy of 65 MeV/u makes it possible to significantly reduce the 6D emittance of the beam.

SCHEME OF THE ELECTRON COOLING SYSTEM OF THE NICA BOOSTER

The ECS is constructed according to the classical scheme proposed and implemented in the early 1970s in the Institute of Nuclear Physics of SB of USSR Academy of Science [1].

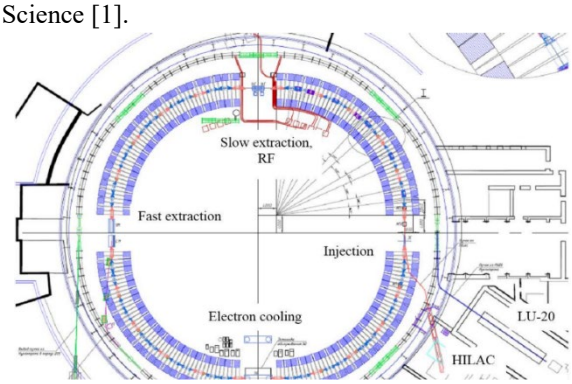

Figure 1: Booster Scheme with Built-in ECS.

In electron cooling set-up (Fig. 2), an electron beam passes from the cathode of the electron gun to the collector in a uniform longitudinal magnetic field. A short rectilinear solenoid allows one to form an electron beam with the necessary parameters in a gun with special optics. The toroidal sections of the Cooler magnetic system are used to transport the beam to straight solenoid – the cooling section.

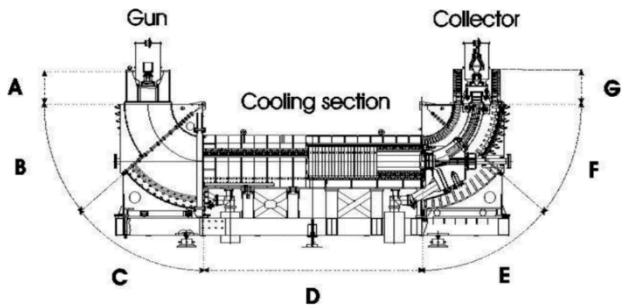

Figure 2: A, G–the solenoids of the gun and the collector, B, C, E, F - the sections of the toroidal solenoids, D-the cooling section solenoid.

In the ECS of the NICA Booster (Table 1), the homogeneity of the magnetic field of this solenoid is made at the level of $3 \cdot 10^{-5}$ (straightness of the magnetic field line) that provides the design value of the cooling time. The energy of the ECS electrons variates in this range of 1.0 – 50.0 keV.

Table 1: Parameters of the Booster ECS

Electron energy E, keV	1.5 – 50
Electron beam current I, A	≤ 1
Accuracy of energy adjustment and its stability, $\Delta E/E$	$\leq 1 \cdot 10^{-5}$
Beam current stability, $\Delta I/I$	$\leq 1 \cdot 10^{-4}$
Electron beam loss current, $\delta I/I$	$\leq 3 \cdot 10^{-5}$
The strength of the ECS longitudinal magnetic field, kGs	1 – 2
Permissible inhomogeneity of the longitudinal magnetic field in the cooling area, $\Delta B/B$	$\leq 3 \cdot 10^{-5}$ on the length 15 cm.
Transverse temperature of electrons in the cooling section (in the particle system), eV	≤ 0.3
Correction of the ion orbit at the input and output of ECS	offset, mm $\leq 1{,}0$ angular deviation, mrad $\leq 1{,}0$

† smelnikov@jinr.ru

ISBN: 978-3-95450-240-0 ISSN: 2673-5539 doi:10.18429/JACoW-RuPAC2021-TUPSB04

PARKHOMCHUK'S ELECTRON GUN

The ECS electron gun invented by V. V. Parkhomchuk, (Fig. 3) consists of three-electrode [2], which are cathode (1), a cathode electrode ("grid") (2) and an anode (3). The grid potential relative to the cathode can vary from -1 to +2 kV. The electrons from the cathode of the gun to the collector move in a longitudinal homogeneous magnetic field of a strength up to 1000 Gs. The cathode of a diameter of Ø 30 mm has a convex shape. The grid is necessary for the formation of a hollow electron beam (see below).

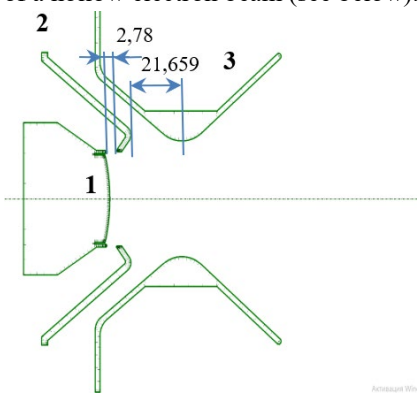

Figure 3: The Booster ECS gun scheme.

TESTING THE ECS

Experiments without a circulating ion beam in the Booster were performed at the ECS installation in the period from June 2019 to November 2020. During this time, the maximum design current values (1.0 A) were obtained for various values of the beam energy, the current-voltage functions of the gun were obtained (Fig. 4), and the formation of a virtual cathode (hollow beam) was investigated. These dependencies were verified by numerical modeling with help of SAM code (BINP of SB of RAS.

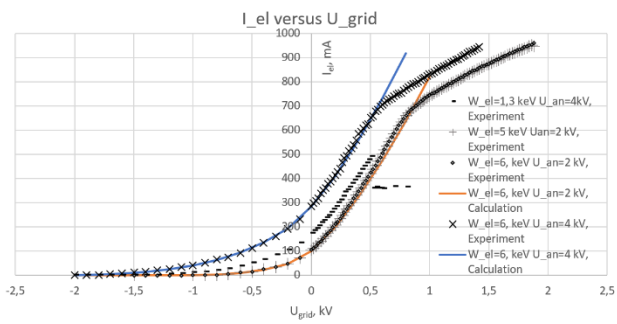

Figure 4: The volt-ampere characteristics of the gun for the electron beam energy of 5 and 6 keV. The potential difference between the cathode and the anode is 2 and 4 kV. Calculations were fulfilled for electron energy 6 keV and potential difference between the cathode and the anode was 2 and 4 kV (red and blue curves respectively) and are in a good agreement with the experimental values.

As follows from Fig. 4, influence of electron energy outside the gun (the gun cathode potential relatively to ground) on electron beam current is very weak – «+» curve (5 keV) and «•» curve (6 keV) coincide practically. At the same time, influence of anode potential is rather significant.

It can be seen from the volt-ampere characteristic that the beam current begins to grow at the ratio |Ugrid/Uan| = 0.5. At current values (≈ 0.7 A), the field of the space charge of the beam forms a "sag" of the potential, which in turn leads to deceleration of the beam and some part of them that comes to zero (relatively to the cathode) potential area is reflected back to the cathode. As result, the perveance of the gun decreases (the bend of the curves in Fig. 4) and a region free of electrons appears. This is so-called "hollow electron beam" based on virtual cathode formation (Fig. 5). This mode of cooling electron beam operation is preferable when ion recombination with cooling electrons is significant.

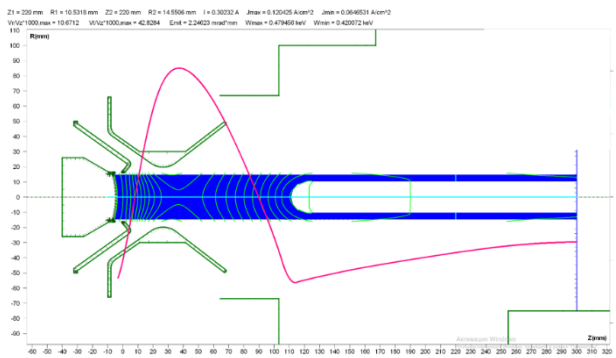

Figure 5: Formation of the hollow beam Potential values: φ_{cath} = -1.3 kV, U_{an}=4 kV, U_{grid} = 0.5 kV. Longitudinal magnetic field is equal to 0.1 T. The red curve gives the electron beam potential distribution at the axis relatively to ground.

FIRST ION ELECTRON COOLING EXPERIMENT

During the first Booster session in December 2020, an experiment was conducted to commission the ECS with a circulating He^{1+} helium ion beam with an energy of 3.2 MeV/u (injection energy into the Booster) (Table 2). In this experiment the only diagnostic devices that allowed observing the cooling effect were used: the A. A. Baldin ionization profilometer [3] and a parametric current transformer (PCT) measuring ion beam current.

Table 2: Experiment Parameters

Ion type	He1+
Ion energy, Mev/u	3.2
Electron energy, keV	1.73 – 1.8
Electron beam current, A	0.1 – 0.2
Electron beam diameter, mm	28

ISBN: 978-3-95450-240-0 ISSN: 2673-5539 doi:10.18429/JACoW-RuPAC2021-TUPSB04

During the experiment, the electron beam was not hollow, which was confirmed by further numerical modeling, as well as the results of measuring the beam profile on an electron gun similar to the one in the Booster ECS [2]. Therefore, during the experiment, a significant decrease in the lifetime of the circulating beam was observed, due to, probably, strong recombination.

The ion beam profile was also recorded by an ionization profilometer that was operated in summing mode the counting rate of all the MCP channels registering the vertical distribution of the beam density (relative counts – RC), and the time dependence RC(t) was measured. Then the results were summed over several injection cycles ⟨RC(t)⟩ (Fig. 6).

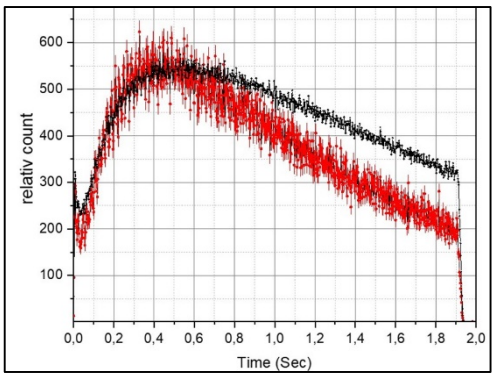

Figure 6: ⟨RC(t)⟩ with the electron current off (black curve) and on (red curve). The electron energy is 1.78 keV, the electron beam current 150 mA. The latter is the optimum electron energy for electron cooling equal to $(E_e)_{opt} = (m_e/m_{nucleon})\times E_{ion}$, where E_e is electron energy (not corrected to electron beam space charge potential!), E_{ion} is the ion energy per nucleon.

SECOND ION ELECTRON COOLING EXPERIMENT

During the second run of the Booster in September 2021, an experiment was conducted to electron cooling of ions $^{56}Fe^{14+}$ beam circulating at injection energy of 3.2 MeV/u. A Schottky spectrometer was used as the main detecting device (Fig. 7), as well as a profilometer used during first experiment.

After the appearance of a wide signal of the ion beam injected into the Booster (Fig. 7a) with a large frequency spread Δf/f0, the signal narrows, its amplitude increases but its area insignificantly decreases in accordance with the beam life time. Thus, there is a decrease in the peak width, i.e decrease of the ion momentum spread of the beam. Such a signal behavior demonstrates definitely effect of electron cooling.

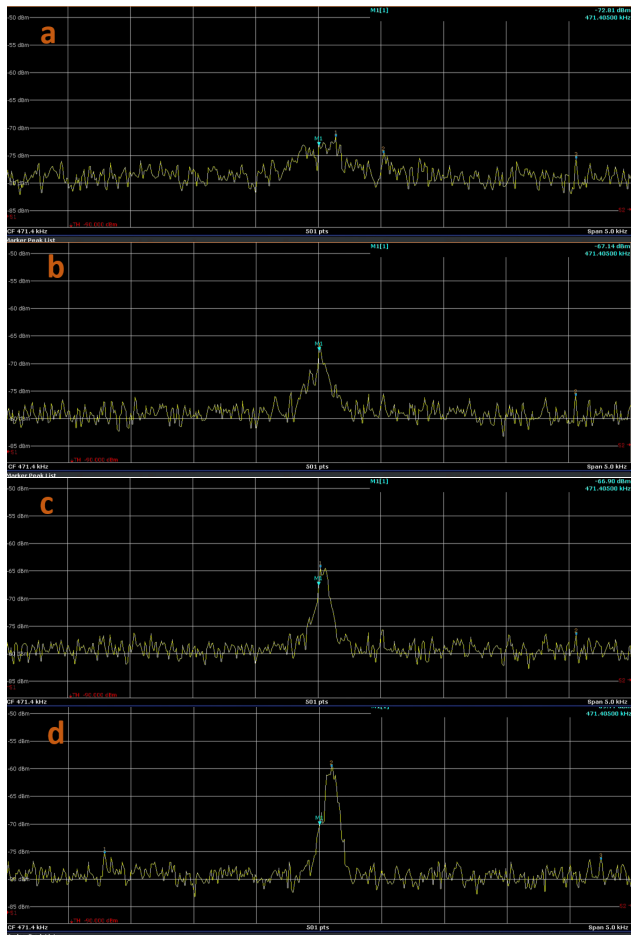

Figure 7: The signal from the Schottky spectrometer. a) is the signal of injection of an ion $^{56}Fe^{14+}$ beam into the Booster ring, b), c), d) are the cooling of the ion beam by an electron beam.

Thus, we can say that the first electron cooling of a heavy ion beam was observed in the Russian Federation.

REFERENCES

[1] I. N. Meshkov *et al.,* "Commissioning of the installation for electron cooling experiment", Preprint of G.I.Budker INP, Novosibirsk, USSR, vol. 72-706, 1970.

[2] A. V. Ivanov *et al.,* "The Electron Gun with Variable Beam Profile for Optimization of Electron Cooling", in *Proc. 8th European Particle Accelerator Conf. (EPAC'02)*, Paris, France, Jun. 2002, paper WEPRI049.

[3] A. A. Baldin *et al.*, "Non-destructive diagnostics of accelerated ion beam with MCP-based detectors at the NICA accelerator complex. Experimental results and prospects", in *Proc. 27th Russian Particle Accelerator Conf. (RuPAC'21)*, Alushta, Russia, Sep. 2021, paper WED05, this conference.

ISBN: 978-3-95450-240-0 ISSN: 2673-5539 doi:10.18429/JACoW-RuPAC2021-TUPSB05

LONGITUDINAL IMPEDANCE OF THE NICA COLLIDER RING AND ION BEAM STABILITY

S. Melnikov†, E. Ahmanova, M. Korobitsina, I. Meshkov, K. Osipov,
Joint Institute for Nuclear Research, Dubna, Russia

Abstract

The report presents the results of optimization of the longitudinal coupling impedance of the NICA collider ring using numerical simulation of its individual elements by the CST Studio. Based on the obtained results, analytical estimates of the stability of the ion beam in the ring are obtained for one value of the ion mode energy – 3 GeV/u.

INTRODUCTION

The project of the Nuclotron-based Ion Collider fAcility (NICA) accelerator complex [1] is being developed at JINR. The ion Collider, which is the main part of it, will allow us to study the collision processes of gold ions with a kinetic energy of 1 – 4.5 GeV/u ($\sqrt{s} \leq 11$ GeV/u) and polarized protons with energy of 2 – 12.6 GeV ($\sqrt{s} \leq 27$ GeV). One of the criteria determining the stability of the motion of charged particles inside the beam chamber is the value of its impedance, which is most important for high-intensity beams.

The interaction of the charged particle beam with the accelerator beam chamber leads to the appearance of electromagnetic fields induced in the chamber (wake-fields) and their reverse effect on the beam, leading to coherent instabilities in the longitudinal and transverse directions. The value $W_{||}(r_1, s) = \frac{1}{q_1}\int_{-\infty}^{\infty} E(r_1, z, t)_{t=(s+z)/c} dz$is called the longitudinal Wake potential. Its transverse component can be found according to the Panofsky-Wenzel theorem: $W_{\perp}(r_1, s) = -\nabla_{\perp}\int_{-\infty}^{s} W_{||}(r_1, s')ds'$. The coupling impedance is the Fourier image of the Wake potential

$$Z_{\parallel}(\omega) = \frac{\int_{-\infty}^{\infty} W_{\parallel}(s)e^{-i\omega s}ds}{\int_{-\infty}^{\infty} \lambda(s)e^{-i\omega s}ds}$$
$$Z_{\perp}(\omega) = i\frac{\int_{-\infty}^{\infty} W_{\perp}(s)e^{-i\omega s}ds'}{\int_{-\infty}^{\infty} \lambda(s)e^{-i\omega s}ds} \quad (1)$$

where λ (s) is the charge distribution normalized by q_1.

The longitudinal and transverse impedances can excite instabilities of the beam particle motion in the Collider. In addition, the real part of the longitudinal impedance determines the contribution to the growth of energy dissipation in the walls of the vacuum chamber, which, with a high-intensity beam, can cause significant heating of individual elements of the superconducting Collider.

Each of the Collider rings (Fig. 1) is a racetrack type accelerator and consists of two rotary arches and two long straight sections. The perimeter of the Collider 503.04 m is equal to two perimeters of the Nuclotron.

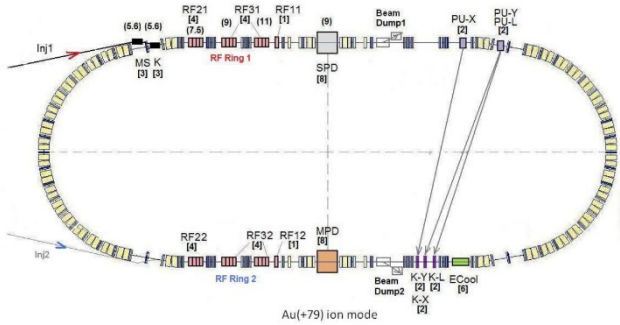

Figure 1: Scheme of the Collider ring. Here Inj1, 2 – injection channels; RFij – RF-stations with i – number of station, j – number of the ring; SPD – spin physics detector, MPD – multipurpose detector, PU-X,Y,L and K-X,Y,L – pick-up stations and kickers for stochastic cooling; ECool – electron cooling system; MS – septum magnet; K – injection kicker.

CALCULATION OF IMPEDANCE

After the initial calculation, changes were made to its design for each element to minimize the value of $Z_{||}$ /n, where n is the circulation frequency harmonic.

In this work, the calculation of Wake-potentials was performed in the CST Studio program. To minimize the contribution of the impedance to the particle dynamics, it is possible to change the design of the element to reduce the amplitude of low-frequency resonances, or to shift them up in frequency. In other words, changes were made to minimize the value of $Z_{||}$ /n. The choice of a design change is helped by the wakefield picture calculated by CST Studio, which displays the excitation of the electromagnetic field in various cavities of the chamber elements.

The biggest changes were made to the collimator unit, kicker of feedback system and pick-up stations in Collider arches (Beam Position Monitor – BPM).

Collimator Unit

The collimator unit consists of scraper and absorber, having a similar design, so we will limit ourselves to considering changes in the design only on the example of a scraper (Fig. 2).

†smelnikov@jinr.ru

ISBN: 978-3-95450-240-0 ISSN: 2673-5539 doi:10.18429/JACoW-RuPAC2021-TUPSB05

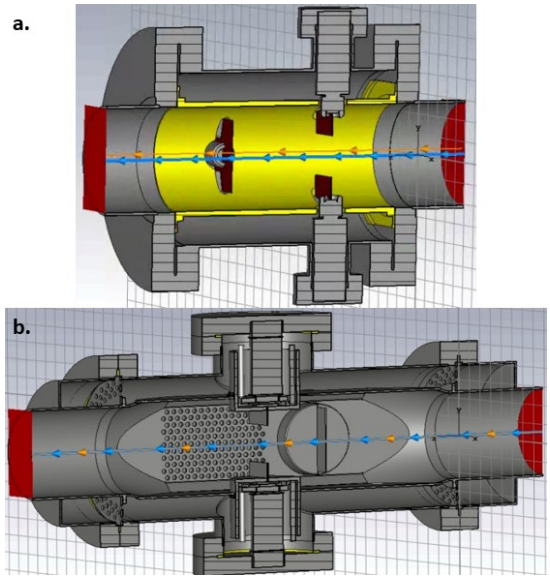

Figure 2: The design of the scraper a) initial model and b) modified.

Shielding “cups” were installed around the scraper plates, connected to the aperture insert by a sliding contact to avoid the penetration of an electromagnetic field into the volume of the vacuum chamber. For the same purpose, end screens were added. The total length of the structure increased from 230.8 mm to 400 mm, due to the expansion of the pipes of the stepper mechanism (for placing "cups"). To ensure the necessary vacuum conditions, a pumping pipe was added (located in the horizontal plane and not visible in the figure) and a perforation was made in the aperture insert. All this made it possible to shift the resonant frequencies upwards (Fig. 3).

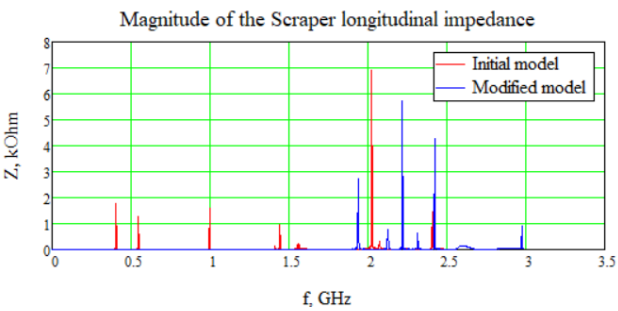

Figure 3: The longitudinal impedance of the scraper for the collimation mode before (red curve) and after (blue curve) design changes.

Kicker of the Feedback System

The feedback kicker (Fig. 4) should work in the frequency band 0.7 to 3.2 GHz. Therefore, in this case, it was necessary not only to reduce the values of $Z_{\parallel}/n$, but also to prevent resonances from entering the kicker's working frequency band (Fig. 5).

The kicker plates were elongated and bent at the edges right next to the flange, which in the updated design has a beveled face. All this ensured the suppression of the resonant amplitudes by 30 or more times in a given frequency band.

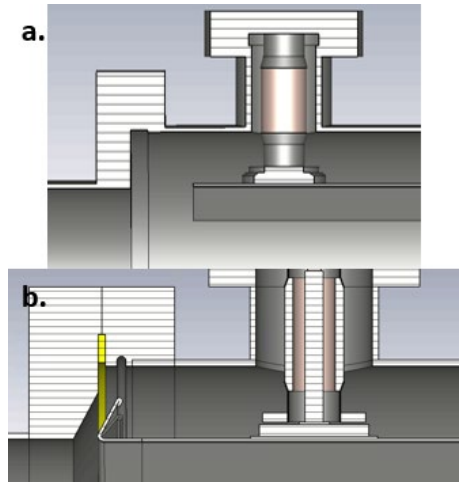

Figure 4: The design of the feedback kicker a) initial model and b) modified.

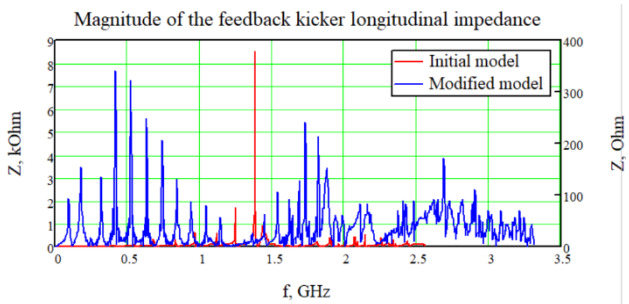

Figure 5: The longitudinal impedance of the feedback kicker before (red curve) and after (blue curve) design changes.

Beam Position Monitor

In total, 46 BPMs are installed in the arches of one Collider ring – 23 horizontal and vertical (4 for betatron oscillation period). Each BPM (Fig. 6) has a measuring electrode 1 of elliptical cross-section with a diagonal cut, which is separated on both sides from the rest of the beam tube by guard electrodes 2. Each BPM is located in a common vacuum chamber with a pumping pipe and bellows.

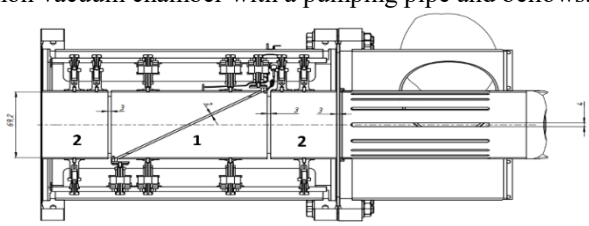

Figure 6: Sketch of the initial BPM and pumping pipe.

The main changes added to the design of the BPM are shielding “clamps” that close the gaps between the measuring and guard electrodes, and end screens with cooper ”springs” installed on the guard electrodes and closing the gaps between them and the bellows chamber and the pumping pipe unit, respectively (Fig. 7). This made it possible to get rid of all resonant frequencies, except for one arising from the diagonal cut in the measuring electrode (Fig. 8).

ISBN: 978-3-95450-240-0 ISSN: 2673-5539 doi:10.18429/JACoW-RuPAC2021-TUPSB05

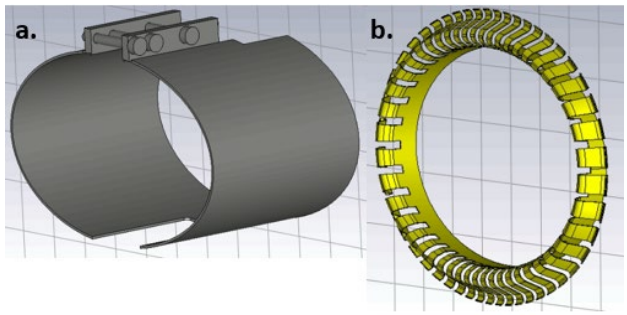

Figure 7: a) Shielding “clamp” and b) “springs”.

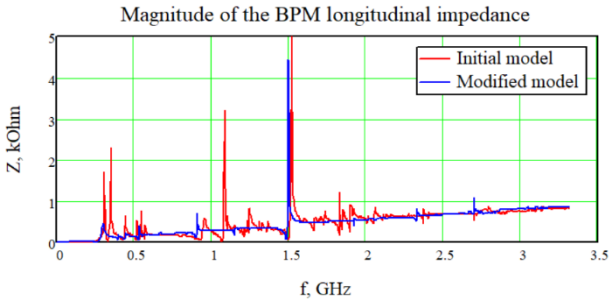

Figure 8: The longitudinal impedance of BPM in Collider arches before (red curve) and after (blue curve) design changes.

ANALYSIS OF ION BEAM STABILITY

The total impedance of the ring consists of the impedances of its individual elements. The total impedance of the NICA Collider ring is represented by Fig. 9 for two operating modes – the beam collimation mode (collimators are put in working position) and the mode when collimators are in retracted position. For both modes, the results are presented for the initial and shielded design of BPM.

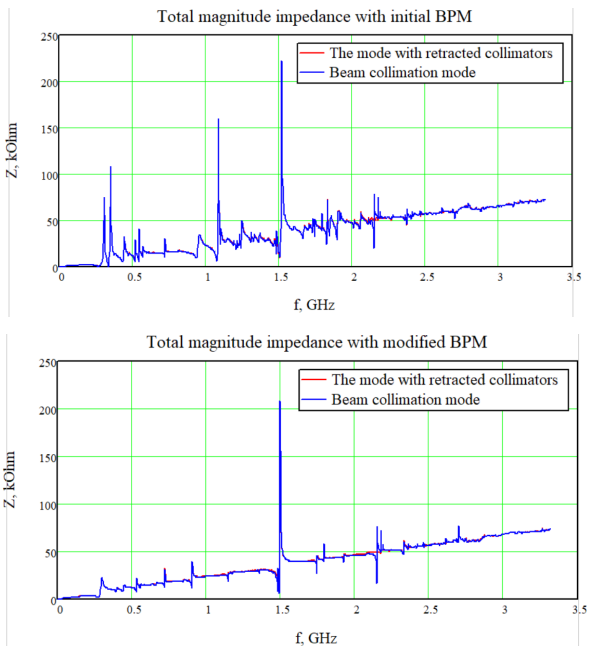

Figure 9: Total impedance of the ring with initial (top) and modified (bottom) BPM design.

As can be seen from the Fig. 9, the main contribution to the total impedance is given by BPM and there is practically no difference between the collimation mode and the mode with retracted collimators, therefore we will limit ourselves in the future only to the collimation mode.

Using the results published in CERN Accelerator School [2], a function was obtained that determines the boundary of the region of stable longitudinal motion for a coasting beam in the ring of the NICA Collider.

The real and imaginary values of the ring impedance are superimposed on this graph and are added to the impedance of the spatial charge and the resistive wall (Fig. 10). The beam motion is stable if the point is located inside the region.

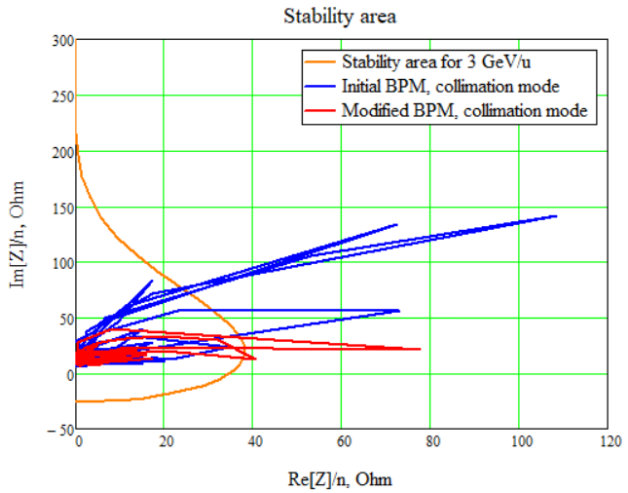

Figure 10: Influence of the initial and shielded BPM model on the beam stability.

Thus, application of the RF shielding of the BPMs reduces impedance contribution to the instability of the beam motion.

REFERENCES

[1] D. Kekelidze *et al.*, “Three stages of the NICA accelerator complex”, *The European Phys. Journal A*, vol. 52, no. 8, 2016. doi:10.1140/epja/i2016-16211-2

[2] J. L. Laclare, “Coasting beam longitudinal coherent instabilities”, in *CERN Accelerator School: Course on General Accelerator Physics*, Jyvaskyla, Finland, Sep. 1992, pp. 349-384.

ISBN: 978-3-95450-240-0 ISSN: 2673-5539 doi:10.18429/JACoW-RuPAC2021-TUPSB07

PARTICLE COLLIMATION IN THE NICA COLLIDER

O.Kozlov, Yu.Gusakov, I.Meshkov, I.Semenova, E.Syresin, JINR, Dubna, Russia

Abstract

The system of particles collimation developed for the NICA collider is considered. The main collimation goal is the beam halo cleaning to minimize the background for experiment. The main mechanisms of particle losses, including the ion recombination in electron cooler, are also reviewed.

INTRODUCTION

The Nuclotron-based Ion Collider fAcility (NICA) [1] is a new accelerator complex being constructed at JINR. Two collider rings are designed to achieve the required luminosity up to 10^{27} $cm^{-2}s^{-1}$ at two interaction points (IP). The first IP is connected with Multipurpose detector (MPD) for the ion-ion (Au^{+79}) collider experiments in the energy range of 1÷4.5 GeV/u. The second IP is aimed for the polarized proton-proton and deuteron-deuteron collisions. The collider must obtain the required luminosity taking into account the certain conditions: luminosity lifetime limitation by intrabeam scattering in a bunch (IBS), space charge tune shift, threshold of microwave instability, slippage factor optimization for efficient stochastic cooling, maximum required RF voltage amplitude. This article considers the $^{197}Au^{+79}$ ion mode of the facility operation.

LATTICE OF THE RINGS

Collider lattice was developed and optimized [2] with some constraints: ring circumference, a number of the dipole magnets in an arc, convenience of the beam injection into the ring. The rings are vertically separated (32 cm between beam axes) and use two-aperture superconducting magnets (dipoles and quadrupoles). Rings have the racetrack shape with the bending arcs and long straight section. Bending arc comprises 12 FODO cells. The cells with empty dipoles are used for horizontal dispersion suppression and convenient beam injection and extraction (dumping) schemes. The long straight sections matched to the arcs contain the RF stations, electron and stochastic cooling devices, BPMs, superconducting quadrupole blocks and collimation elements as well. The optics in these sections produces the betatron tune variation, vertical beam separation in the rings and conditions for colliding beams in interaction points (IP). The project parameters of the collider ring are presented in Table 1. The placement of collimation system elements in both collider rings is possible only in the western superperiod (Fig. 1). The eastern part of the collider is designed to accommodate the modules of the acceleration system.

Table 1: Main Parameters of the Collider Rings

Ring circumference	503.04 m	
Number of bunches	22	
Rms bunch length	0.6 m	
β-function in the IP	0.35 m	
Betatron tunes, Q_x/Q_y	9.44/9.44	
Chromaticity, $Q'_{x,0}/Q'_{y,0}$	-33/-28	
Acceptance	40 π·mm·mrad	
Long. acceptance, Δp/p	±0.010	
Gamma-transition, γ_{tr}	7.088	
	Dipole	Quadrupole
Number of magnets	80+8(vert.)	86+12(fin.foc)
Max. magnetic field	1.8 T	23 T/m
Effective length	1.94 m	0.47 m
Beam pipe (h/v)	120mm/70mm	

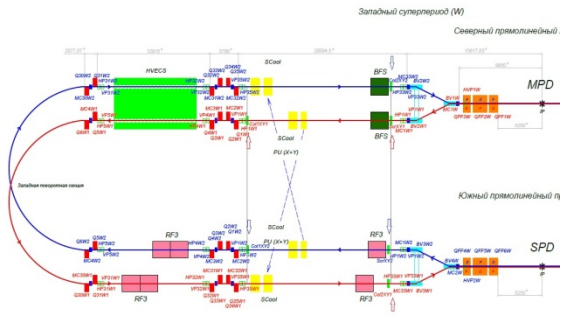

Figure 1: Positioning of the collimation elements in the collider lattice (shown by thick arrows).

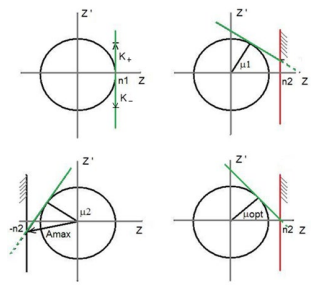

Figure 2: Principle of two-stage collimation in transversal phase space.

STATUS OF THE SYSTEM OF PARTICLE COLLIMATION

The collimation system is designed to clean the beam halo [3], the particles that have get maximum amplitudes (comparable to acceptance) due to intrabeam scattering or nonlinearities of the magnetic field, to reduce it interaction with the walls of the vacuum chamber and, especially, to protect the detector from additional background.

ISBN: 978-3-95450-240-0 ISSN: 2673-5539 doi:10.18429/JACoW-RuPAC2021-TUPSB07

A two-stage particle collimation scheme is considered, consisting of a scraper and two interceptors or collimators of scattered particles for each ring (Fig. 2). The arrangement of the collimators corresponds to the optimal betatron phase advance between these devices. The separate device contains horizontal and vertical movable elements limiting the beam aperture. Scraper - a thin foil (for example, W) is located at the acceptance border (6σ). Halo particles passing through it obtain an additional transverse angle due to multiple Coulomb scattering. For example, the characteristic W foil thickness of 0.1÷1 mm is required for the scattering angle of 0.5÷1 mrad. Collimators (interceptors) - extended devices located outside the acceptance limits, provide the absorption of the energy of scattered particles. The process of particle scattering is considered depending on the foil material and particle energy. The chosen scheme of collimation is the relatively dependent on of the scrappers and collimators locations (Fig. 3). The scattered particles envelopes were traced (Fig. 4) and the possible locations of the thick collimators were determined. The required longitudinal lengths of the devices for ion stopping were calculated. The characteristic longitudinal length for the absorber plates (Fe, W, Inconel) reserved for the collimator design is less than 10 cm.

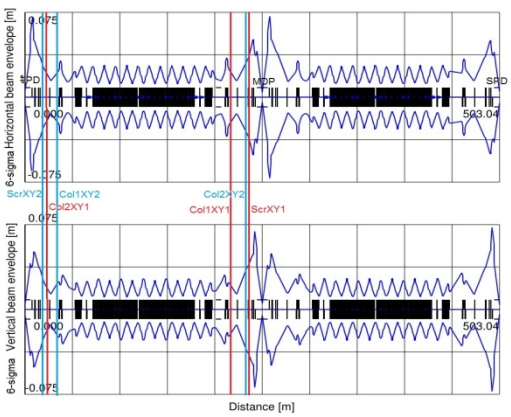

Figure 3: Locations of the collimation elements and acceptances of the rings in horizontal and vertical planes.

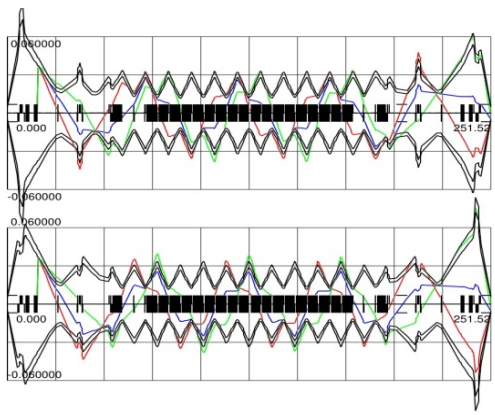

Figure 4: Scattered particles envelopes tracking. Beam envelopes (6σ and 7σ, black curves) are shown in horizontal (top) and vertical (bottom) planes.

An extensive study of the interaction of high-energy ions with matter was carried out (angles of multiple Coulomb scattering in the foil, ion energy losses in the collimator material). The Fig. 5 shows examples of energy loss by an ion in a thick collimator.

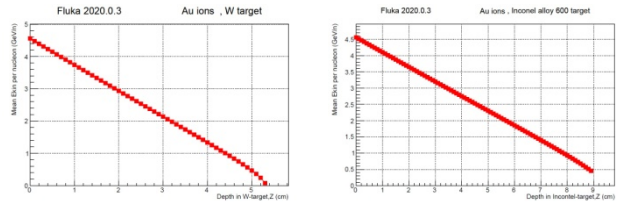

Figure 5: The average energy of Au^{+79} ions in absorber (W and Inconel) depth. The initial ion energy is E_k=4.5 GeV/n.

The designs of the scraper and collimator for the collider have been developed. The Fig. 6 shows the design of a combined device that allows to control the movement of horizontal and vertical plates (or foil in scraper). The device combines collimator functions for both rings.

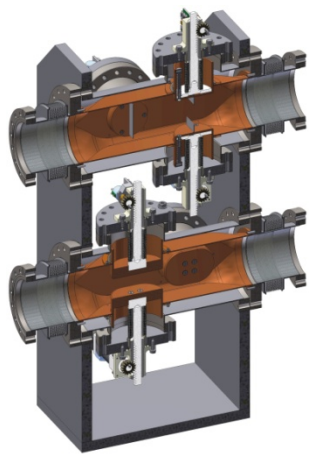

Figure 6: Horizontal and vertical collimator design for two-level collider rings.

CHARGE EXCHANGE EFFECTS IN THE COLLIDER

Losses of ions in the rings of the collider can occur due to the change in the charge state by the ion, the capture of an electron. Three relevant effects were estimated for the collider: charge exchange due to residual gas, bounded-free pair production and recombination in electron cooler.

The rate of recombination of the ions $Au^{+79} \rightarrow Au^{+78}$ in the section of the electron cooling system was calculated by the well-known approach.

The time constant (lifetime) of recombination is represented as

$$\tau_{rec} = \frac{\gamma^2}{\alpha_{rec} n_e \eta}, \quad (1)$$

ISBN: 978-3-95450-240-0 ISSN: 2673-5539 doi:10.18429/JACoW-RuPAC2021-TUPSB07

where γ is the gamma factor of the ion, n_e is the density of the electron beam in the laboratory coordinate system, $\eta=C_{cool}/C_{ring}$ is the ratio of the electron cooler length to the collider perimeter, and the coefficient is written as [4]:

$$\alpha_{rec} = 1.92\times10^{-13}\frac{Z_i^2}{\sqrt{T_e}}\left[\ln\left(\frac{5.66Z_i}{\sqrt{T_e}}\right)+0.196\left(\frac{T_e}{Z_i^2}\right)^{1/3}\right]. \quad (2)$$

Calculations using the above formulas for the corresponding parameters of the ion beam of the collider and the electron beam are given in Table 2 for maximal ion kinetic energy of E_i=4.5 GeV/n, the number of bunches in the ring of n_b=22 , the electron energy of E_e=2.5 MeV, electron beam current of I_e=1 A, the electron beam diameter of d_e=1 cm, where N_i is the intensity of the ion beam, T_e is the transverse electron temperature.

Table 2: Time Constants and Recombination Rates of Au^{+79} Ions

N_i	T_e,eV	α_{rec}, cm^3/s	τ_{rec}, s τ_{cool},s	$\Delta N=n_b N_i/\tau_{rec}$, ions/s
$2.3\cdot10^9$	100	$5.36\cdot10^{-10}$	3383 35	$1.50\cdot10^7$
$2.3\cdot10^9$	10	$1.98\cdot10^{-9}$	910 25	$5.56\cdot10^7$

For the expected parameters of the electron beam at T_e=100 eV, the estimated lifetime is 1 hour. The corresponding flow of recombined ions is $1.5\cdot10^7$ ions per second. With a practically attainable parameter T_e=10 eV, this flux will be about $6\cdot10^7$ ions per second. The characteristic cooling times are rather weakly dependent on T_e. Without additional collimation the recombined ions will be lost in the very specific places in the bending arcs of both rings of the collider. The power will be dissipated in vacuum chamber, superconducting coil and yoke. The values of the dissipated power of the order of 0.01÷0.05 W corresponding to the typical parameters of electron cooler (Table 2) are rather acceptable for the superconducting wire operation.

To estimate the charge exchange of an ions on residual gas molecules in the NICA collider, one were used the theoretical calculations of radiactive electron capture in reactions of heavy nuclei with light target atoms, scaling law of the radiactive electron capture cross sections as a function of the atomic numbers of the incident ion and the target, the relationship between the parameters of the residual gas (partial pressures) and the parameters of the circulating beam [5]:

$$P_i=3.3\cdot10^{-21}\,\alpha T/(\mu_i\,\sigma_{i,tot}(E_k, Z)\beta)\cdot1/\tau, \quad (3)$$

where P_i is the partial pressure of the i-th component of the gas (nTorr), μ_i is the number of atoms in a gas molecule, $\sigma_{i,tot}$ is the total cross section for charge exchange, T is the absolute temperature, E_k, β are the beam parameters, α is the permissible losses during charge exchange, τ is the beam circulation time. Using the above relation, the pressure in the beam pipe (hydrogen) during, for example, 2 hours circulation of Au^{+79} ions (E_k=4.5 GeV/n), with an acceptable loss of intensity of 5% should be no worse than P_i=0.2 nTorr.

The effect, bounded-free pair production [6], observed at colliders was also evaluated. Theoretical estimates are used for the reaction cross sections at the collider interaction point: $Z_1+Z_2\rightarrow Z_1+e^+(Z_2+e^-)_{1s1/2}$, ($Z_1=Z_2=79$). The rate of generation of $Au^{+79}\rightarrow Au^{+78}$ in the reaction of beams collision at the project luminosity of 10^{27} $cm^{-2}s^{-1}$ is rather negligible due to small total cross-sections of the reaction (<50 mb) for the collider energy range.

CONCLUSION

The scheme of a beam halo collimation system in the collider is described. The system must ensure the elimination of unnecessary particle background during the physical experiment. Other sources of losses in the collider associated with ion charge exchange processes are also considered. In particular, the effect of ion recombination in the section of electron cooling was estimated.

REFERENCES

[1] G.V. Trubnikov *et al.,* "Status of NICA Project at JINR", in *Proc. of International Particle Accelerator Conf. (IPAC 2014),* Dresden, Germany, 2014, pp. 1003-1005.

[2] O.S. Kozlov *et al.,* "NICA Collider lattice optimization", *in Proc. of Russian Particle Accelerator Conf. (RuPAC 2016),* St. Petersburg, Russia, 2016, pp. 166-168.

[3] O. Kozlov, "Beam Collimation in the Collider", XIth Session of the NICA Machine Advisory Committee, Dubna, Russia, 2020, https://indico.jinr.ru/event/1335/.

[4] I. Ben-Zvi *et al.,* "Electron Cooling for RHIC", *in Proc. of Particle Accelerator Conf. (PAC 2001),* Chicago, USA, 2001, pp. 48-50.

[5] I.S. Dmitriev, G.L. Saksagansky, I.A. Shukeilo, Preprint NIIEFA, B-0407, Leningrad, 1978.

[6] D.A. Bauer, D.V. Karlovets, V.G. Serbo, "Bound–free pair production in relativistic nuclear collisions from the NICA to the HE LHC colliders", *Eur. Phys. J.* A (2020) 56:200.

ISBN: 978-3-95450-240-0 ISSN: 2673-5539 doi:10.18429/JACoW-RuPAC2021-TUPSB08

MAGNETO-OPTICAL STRUCTURE OF THE NICA COLLIDER WITH HIGH CRITICAL ENERGY

S. Kolokolchikov, Yu. Senichev, INR RAS, Moscow, Russia
E. Syresin, JINR, Dubna, Russia

Abstract

For proton option of NICA collider, it is necessary to cross the transition energy ($\gamma_{tr} = 7{,}1$). For this reason, a magneto-optical structure with a high critical energy ($\gamma_{tr} = 15$) is considered. In this case, methods of increasing the critical energy for the proton option of the NICA collider are investigated. The method of superperiodic modulation of quadrupole gradients is applied. The selection of sextupoles is carried out to suppress the natural chromaticity and compensate the sextupole component. The Twiss parameters for the proposed structures are given, as well as the dynamic apertures and working points are investigated.

SUPERPERIODIC MODULATION

The momentum compaction factor is defined in general as

$$\alpha = \frac{1}{\gamma_{\mathrm{tr}}} = \frac{1}{C}\int_0^C \frac{D(s)}{\rho(s)}\,ds \qquad (1)$$

where C – the length of a closed equilibrium orbit, $D(s)$ – horizontal dispersion function, $\rho(s)$ – radius of curvature of the equilibrium orbit. And taking into account equation for dispersion function with biperiodic focusing:

$$\frac{d^2D}{ds^2} + [K(s) + \varepsilon k(s)]D = \frac{1}{\rho(s)} \qquad (2)$$

where $K(s) = \frac{e}{p}G(s)$, $\varepsilon k(s) = \frac{e}{p}\Delta G(s)$, $G(s)$ – gradient of magneto-optical lenses, $\Delta G(s)$ – superperiodic gradient modulation. Thus, MCF depend on the functions: the curvature of the orbit $\rho(s)$, gradient and modulation of quadrupole lenses respectively $G(s)$, $\Delta G(s)$.

In the NICA structure, the regular arrangement of dipole magnets eliminates the possibility of modulating the curvature of the orbit. Therefore, to change transition energy use only the modulation of dispersion function by modulating the strength of quadrupole lenses over the superperiod. For one superperiod, the MCF is determined [1]:

$$\alpha_s = \frac{1}{\nu_{x,\,\mathrm{arc}}^2}\left\{1 + \frac{1}{4}\left(\frac{\bar{R}_{\mathrm{arc}}}{\nu_{x,\,\mathrm{apk}}}\right)^4 \sum_{k=-\infty}^{\infty} \frac{{g_k}^2}{\left(1-\frac{kS}{\nu_{x,\,\mathrm{arc}}}\right)\left[1-\left(1-\frac{kS}{\nu_{x,\,\mathrm{arc}}}\right)^2\right]^2} \ldots\right\} \qquad (3)$$

where $\overline{R}_{arc}$ – the average value of the curvature, $\nu_{x,arc}$ – the number of horizontal betatron oscillations on the length of the arc, S – number of superperiods per arc length, g_k – k-th harmonic of the gradient modulation in the Fourier series expansion of the function $\varepsilon k(s) = \sum_{k=0}^{\infty} g_k\, cos(k\phi)$. First harmonic $k = 1$ has a dominant influence and for 12 FODO cells, the condition is implemented $S = 4$, $\nu_{x,\mathrm{apk}} = 3$, where 3 FODO cells are combined into one superperiod as shown on Fig. 1. Thus, due to the tune of betatron oscillations of a multiple of 2π, the arc has the properties of a first-order achromat [2].

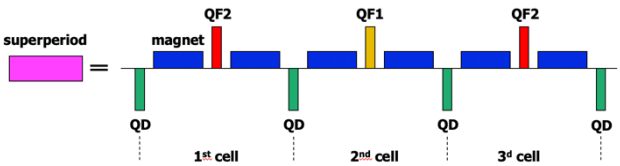

Figure 1: Superperiod contains 3 FODO cells.

DISPERSION SUPPRESSION

An important requirement in the design of a magneto-optical structure is to ensure zero dispersion in straight sections to ensure the movement of particles along the equilibrium orbit in these sections. This requirement is easily implemented in the case of creating regular arcs composed of identical superperiods. In this case, by providing a zero dispersion value $D = 0$ (as well as the derivative of the dispersion $D' = 0$) at the entrance to the arc, due to the regularity, the output of the arc will also have zero values of the dispersion and its derivative, and therefore on the entire straight section. However, the peculiarity of the given structure of the NICA collider, the presence of missing magnets on the two extreme cells does not make it possible to create a completely regular arc of 4 identical superperiods. Thus, it is necessary to ensure the suppression of dispersion at the edges of the arc.

Two possible cases of dispersion suppression are considered and shown on Fig. 2.

- Dispersion suppression is carried out by using two edge FODO cells located symmetrically on both sides.
- Dispersion suppression by arc, by selecting the gradients of the quadrupoles of the two families.

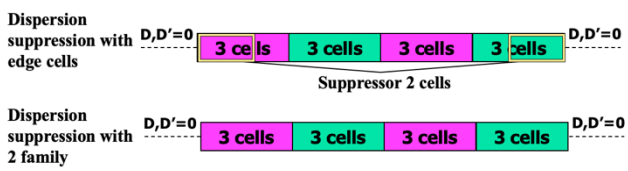

Figure 2: Principal scheme of arc for different dispersion suppression.

Edge suppressor. The edge superperiod has a missing magnet in 2 cells, thus making the collider arcs not regular and there is a need to suppress the dispersion in straight sections using 2 additional families of QFE1 and QFE2 quadrupoles on the edge of the arc. The scheme of arc with β-function and dispersion function of all entire ring are shown on Fig. 3.

ISBN: 978-3-95450-240-0 ISSN: 2673-5539 doi:10.18429/JACoW-RuPAC2021-TUPSB08

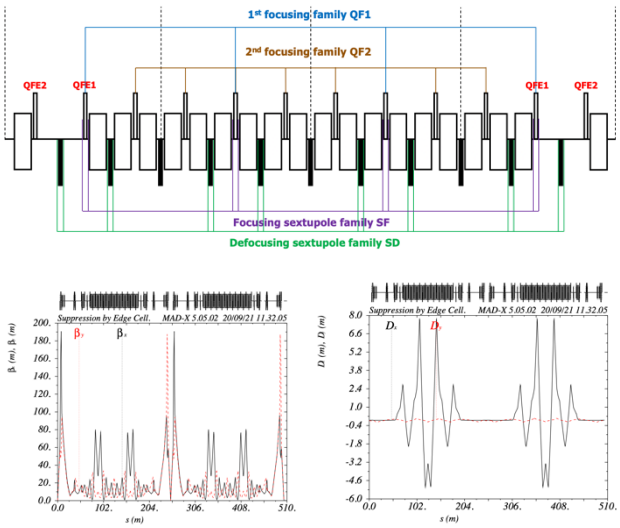

Figure 3: Edge Suppressor. Top – principal scheme of arc with edge quadrupoles. Bottom left – β-function, bottom right – dispersion function.

Sextupole Correction

The tune shift on the arc is equal to $\nu_{x\ arc} = 3, \nu_{y\ arc} = 3$. Thus, at each superperiod, a tune shift occurs $0{,}75\pi$, including the edge ones. In the described case there is peaks of β-function on arc at quadrupoles QF2. Thus, the phase difference between the QF2 quadrupoles of the first and third (second and fourth superperiod) is not a multiple of $\pi/2$. Simultaneously, the number of betatron oscillations between the central quadrupoles (QF1 or QFE1) of 1 and 3 or 2 and 4 superperiods $\nu_{1-3} = \nu_{2-4} = 1{,}5$. Thus, by placing the sextupoles of the same family next to the central quadrupoles, it will be possible to ensure mutual suppression of the sextupoles [3].

Dynamic Aperture

Working point for the entire ring $9{,}44 \times 9{,}44$, same as for regular structure in heavy ion option. Dynamic aperture on Fig. 4 for $dp/p = 5 \times 10^{-3}$ in x-plane: $500\ \text{mm} \times mrad$; in y-plane: $40\ \text{mm} \times mrad$.

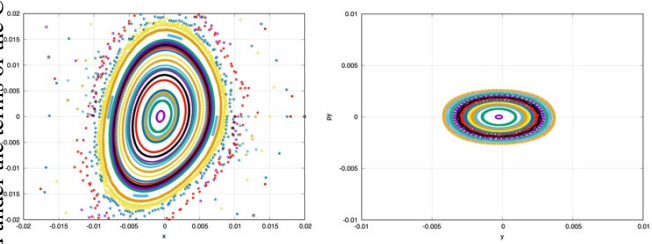

Figure 4: Dynamic aperture for edge suppression scheme in both planes for $\mathrm{dp/p} = 5 \times 10^{-3}$.

Arc suppressor. This case differs from the first, all the quadrupoles of the arc belong to the first or second family, and the suppression of dispersion is also provided by only 2 families. The scheme of arc with β-function and dispersion function of all entire ring are shown on Fig. 5. But to achieve the required critical energy value, it is necessary to provide a greater modulation of the quadrupole gradients

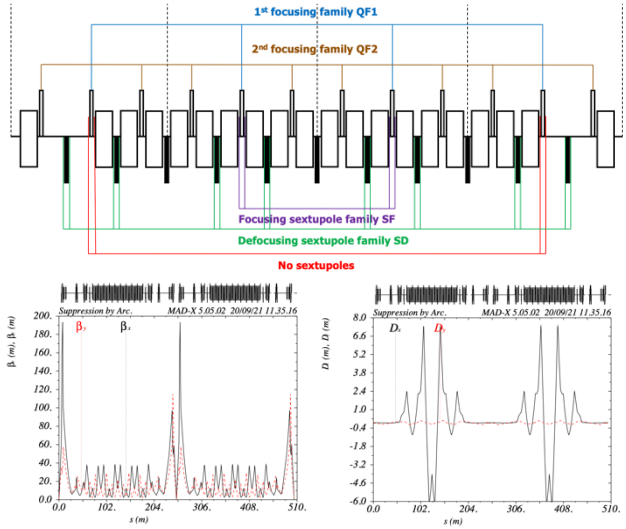

Figure 5: Arc Suppressor. Top – principal scheme of arc with only 2 families. Bottom left – β-function, bottom right – dispersion function.

than in the case of dispersion suppression by edge superperiods. In this case the phase shift on the arc becomes equal to $\nu_{x\ arc} = 2{,}72, \nu_{y\ arc} = 3$.

Sextupole Correction

Due to the fact, that tune shift on arc not a multiple of 2π, and also between the central quadrupoles is not a multiple $\pi/2$, and is equal to 1,41, it turns out that the sextupoles do not compensate each other exactly. The arrangement of sextupoles for this case is different from the arrangement of sextupoles in the case of dispersion suppressors at the edges of the arc. The SF family is located next to the central quadrupoles of the superperiod QF1, and SD is located next to the defocusing quadrupoles QD, but only those that surround QF1 on the left and right. However, there are no sextupoles of the focusing family in the edge superperiods. This is done to reduce the influence of sextupoles on the dynamic aperture. The suppression of chromaticity is also possible without them, since the main contribution is made by sextupoles 2 and 3 of the superperiod.

Dynamic Aperture

The working point for the entire ring is $9{,}44 \times 9{,}44$, the same as for the regular structure. Figure 6 shows the dynamic aperture for this working point in both planes for

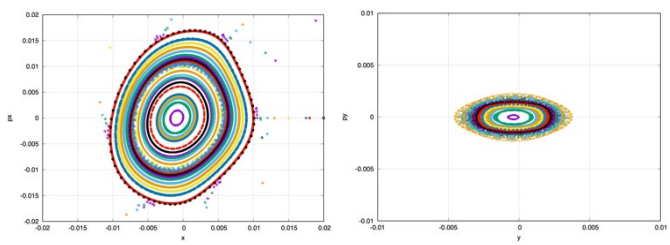

Figure 6: Dynamic aperture for arc suppression scheme in both planes for $\mathrm{dp/p} = 5 \times 10^{-3}$.

ISBN: 978-3-95450-240-0 ISSN: 2673-5539 doi:10.18429/JACoW-RuPAC2021-TUPSB08

$dp/p = 5 \times 10^{-3}$. Dynamic aperture in x-plane: 500 $mm \times mrad$; in y-plane: 30 $mm \times mrad$;

ION MODE

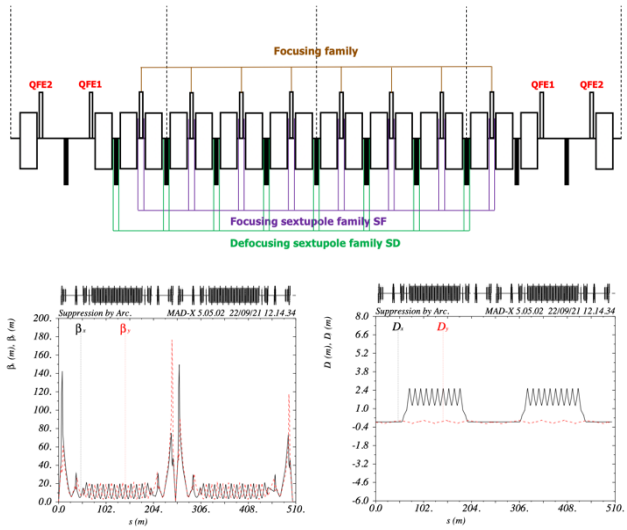

Figure 7: Ion mode. Top – principal scheme of arc with edge quadrupoles. Bottom left – β-function, bottom right – dispersion function.

Ion mode structure is regular and have 12 FODO cells and contains 2 families: focusing and defocusing. Dispersion suppressed by two edge FODO cells which have a different focusing quadrupole strength when quadrupole strength in focusing family. The scheme of arc with β-function and dispersion function of all entire ring are shown on Fig. 7.

Sextupole Correction

As structure is regular there is no problems with sextupole correction. Focusing and defocusing sextupoles located near focusing and defocusing quadrupoles in the central cells.

Dynamic Aperture

Working point for the entire ring 9,44 × 9,44, same as for regular structure in heavy ion option. Dynamic aperture on Fig. 8 for $dp/p = 5 \times 10^{-3}$ in x-plane: 500 mm × $mrad$; in y-plane: 50 mm × $mrad$.

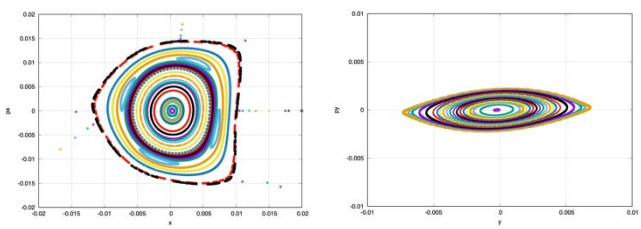

Figure 8: Dynamic aperture for ion mode scheme in both planes for dp/p = 5×10^{-3}.

CONCLUSION

For proton mode of NICA collider applied method of superperiodic modulation to increase transition energy (change γ_{tr} from 7,1 to 15). In this case two options of dispersion suppression on the edges of arc can be considered: suppression with edge superperiods and suppression with only two families of quadrupoles. Each option has it is own features, but both of them can be used on NICA collider.

REFERENCES

[1] Yu. V. Senichev and A. N. Chechenin, "Theory of "Resonant" Lattices for Synchrotrons with Negative Momentum Compaction Factor", *Journal of Experimental and Theoretical Physics,* Vol. 105, No. 5, pp. 988–997, 2007.

[2] Yu. V. Senichev and A. N. Chechenin, "Construction of "Resonant" Magneto-Optical Lattices with Controlled Momentum Compaction Factor", *Journal of Experimental and Theoretical Physics*, Vol. 105, No. 6, pp. 1141–1156, 2007.

[3] P.J. Bryant, "Planning Sextupole Families in a Circular Collider", *Advanced accelerator physics.* Proceedings, 5th Course of the CERN Accelerator School, Rhodos, Greece, September 20-October 1, Vol. 1, 2, 1993.

ISBN: 978-3-95450-240-0 ISSN: 2673-5539 doi:10.18429/JACoW-RuPAC2021-TUPSB09

RESONANCE SLOW EXTRACTION FROM ION SYNCHROTRON FOR TECHNOLOGICAL APPLICATION

M. F. Blinov, I.A. Koop, V. A. Vostrikov, Budker Institute of Nuclear Physics, Novosibirsk, Russia

Abstract

Third-order resonance slow extraction from synchrotron is the most common use extraction method for external target experiments nuclear physics, proton and heavy ion therapy, since it can provide relatively stable beams in long time. The principle of third-order resonant slow extraction is intentionally exciting the third-order resonance by controlling detuning and sextupole strength to gradually release particles from inside to outside stable separatrix. BINP develop the ion synchrotron for wide range of technological application. The present paper describes slow extraction method with exiting betatron oscillations by the transverse RF-field. Such extraction technique provides stable current extraction for entire extraction time. The paper present simulation of slow extraction driving RF-knockout.

INTRODUCTION

The synchrotron will produce beams of protons accelerated up to 4 GeV and wide range of ion species including $^{209}Bi^{41+}$ up to 36 MeV/n respectively (see Table 1).

Table 1: Synchrotron Specifications

Characteristics	Value
Circumference, m	168.37
Beam injection energy proton/$^{209}Bi^{41+}$, MeV/n	700 / 36
Maximum energy proton/$^{209}Bi^{41+}$, MeV/n	4000 / 400
Magnetic rigidity, T·m	16.2
Max dipole field, T	1.6
Critical γ	6.39
Tune, Q_x/Q_z	6.65 / 4.61
Natural chromaticity, ξ_x/ξ_z	-10.2 / -10.1
Acceptance hor/ver, π cm·mrad	7.5 / 1.9
Beam intensity, protons/$^{209}Bi^{41+}$	10^{12} / 10^{8}
Momentum compaction factor	0.024
Proton beam emittance under injection, π cm·mrad	0.52
Frequency revolution proton/$^{209}Bi^{41+}$, MHz	1.46 ÷ 1.75 / 0.48 ÷ 1.27

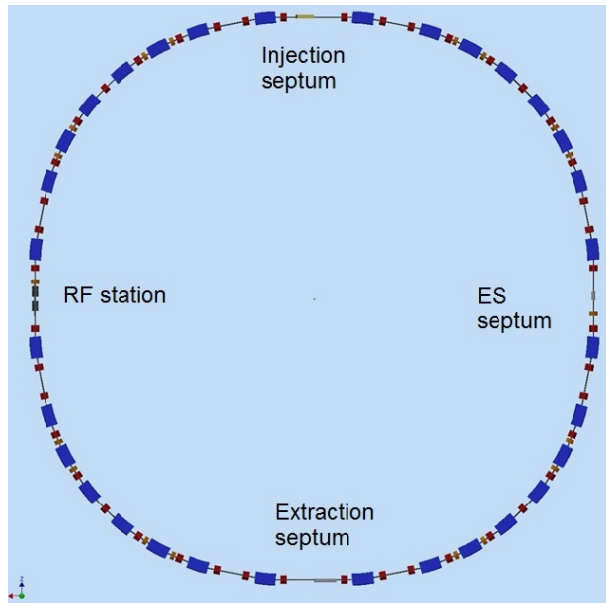

Figure 1: General layout of synchrotron.

The general layout of synchrotron is presented in Fig.1. The synchrotron optics is characterized by four super periods and four closed dispersion bumps (see Fig. 2). The injection and extraction septum magnets, RF-cavity and electrostatic septum located in free dispersion drifts. One resonance sextupole used for extraction is located close to RF-cavity. For slow extraction convenience the synchrotron operates below critical energy in the entire range of energy.

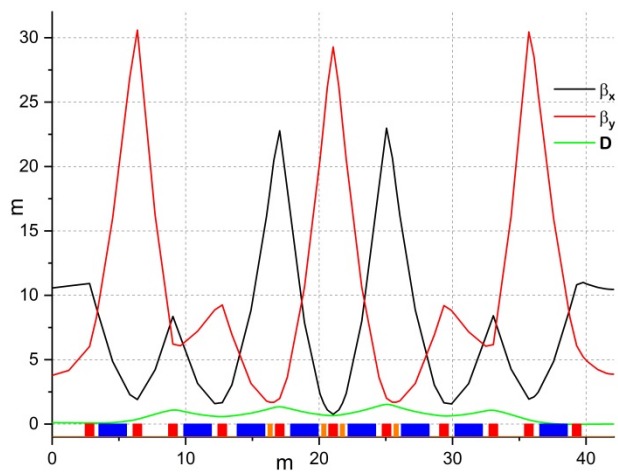

Figure 2: Lattice function of synchrotron quarter.

SLOW EXTRACTION

The slow extraction from synchrotron based on the third order horizontal resonance. The sextupole magnet excites resonance harmonics. When the excitation achieves a cer-

ISBN: 978-3-95450-240-0 ISSN: 2673-5539 doi:10.18429/JACoW-RuPAC2021-TUPSB09

tain level, the circular trajectories in phase space are distorted into triangular trajectories. After exceeds of certain level the triangular trajectories become open. The area of the single particle stable triangle is the acceptance and its value:

$$\epsilon_{stable} = \frac{48\sqrt{3}\pi^2}{S^2}(\delta Q)^2, \quad (1)$$

where δQ is particle detuning. The normalized sextupole strength in thin lens approximation:

$$S = \frac{1}{2}\beta_x^{3/2}\frac{l_s}{B\rho}\left(\frac{d^2B_z}{dx^2}\right) \quad (2)$$

The useful representation of the beam is provided by the amplitude-momentum space, called the Steinbach diagram (see Fig. 3).

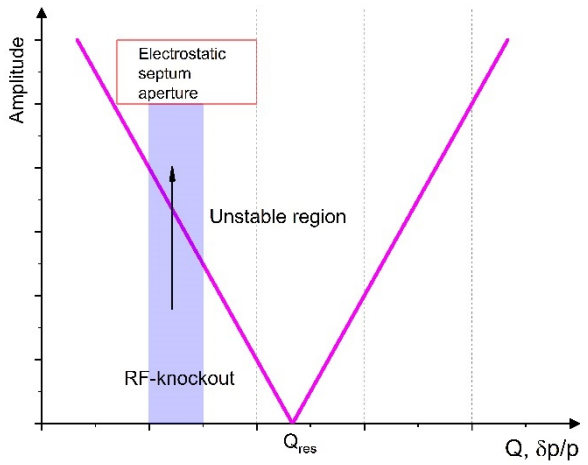

Figure 3: Steinbach diagram show RF-knockout driving mechanism.

In RF-knockout extraction [1] the beam is excited in the horizontal phase space by a radio frequency or by stochastic noise with right range of the frequency. The amplitude of betatron oscillation increase and, without changing the tune of the particles, they go from the stable region. The beam will gradually leave the triangle stable region without changing energy. The momentum spread of the extracted beam is equal to the momentum spread of the circulating beam, unlike the case of extraction by the betatron core.

LAYOUT OF THE EXTRACTION SCHEME

To initiate slow extraction the horizontal closed orbit locally distorted in the electrostatic and magnetic septums azimuths. The local orbit bump creates by eight dipole correctors - four regular correctors and four special bump magnets (see Fig. 4), which ensures the electrostatic septum limits the synchrotron horizontal aperture during the extraction process. After that horizontal betatron tune shifts to resonance value Q_x=20/3 with small detuning and switch on the resonance sextupole. Finally, RF-knockout extraction method applying without varying ring optics. In electrostatic septum the extracted particles gets horizontal kick inside ring. The performance of electrostatic septum with 0.1 mm titanium foil indicates in Table 2. The spill in x-s plane between electrostatic and magnet septums is shown in Fig. 5.

Table 2: Electrostatic Septum Specifications

Kick angle, mrad	1.0
Distance from foil to closed orbit, mm	42
Gap, mm	9
Effective length, mm	500
Max voltage, kV	-90
Overall length, mm	720
Spiral step, mm	8
Beam loss, %	~2
Total mass, kg	~150

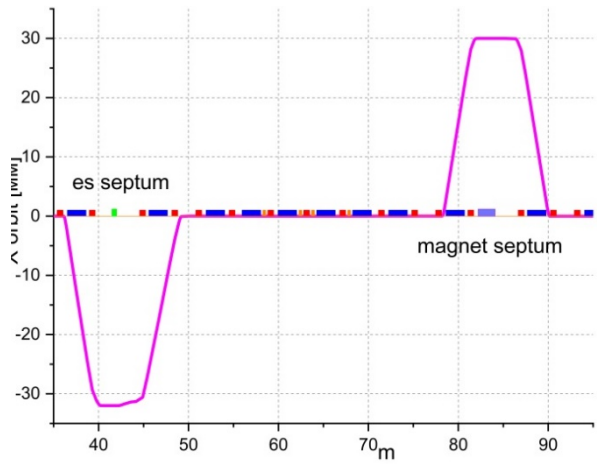

Figure 4: Closed orbit bumps in electrostatic and magnet septum azimuths.

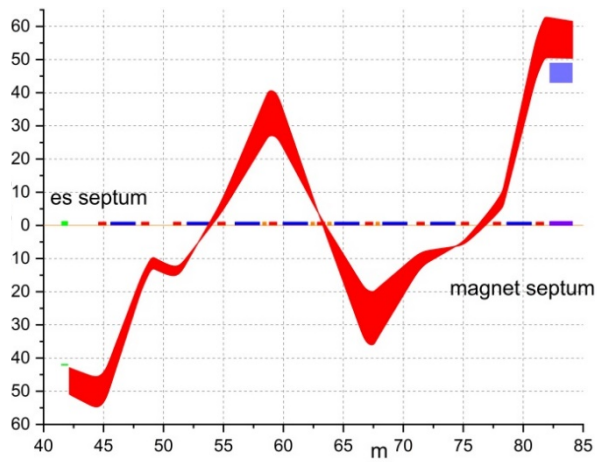

Figure 5: Spill position between electrostatic and magnet septums.

The phase space portrait in the entrance and exit of Lambertson type magnetic septum is shown on Fig. 6. The gap between circulating and extraction beams is about 8 mm that sufficient for magnetic septum with thickness 5 mm.

TIME STRUCTURE OF SPILL

For research of extracted beam spill structure the particle tracking code was developed. The 6D tracking of the particles through the lattice of synchrotron is performed calculating the corresponding first order transfer matrices.

ISBN: 978-3-95450-240-0 ISSN: 2673-5539 doi:10.18429/JACoW-RuPAC2021-TUPSB09

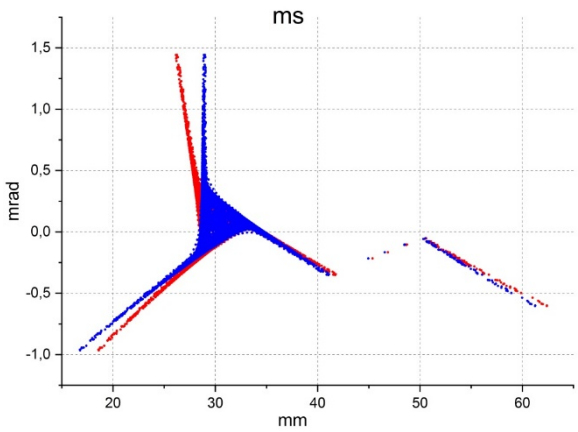

Figure 6: Phase space portrait beam at slow extraction in entrance (red) and exit (blue) of magnetic septum.

The tracking through the sextupoles and kicker is performed with thin lens approximation. The RF signal waveform can be defined by the user. Initially the normal distribution in the horizontal and vertical phase space is generated. The horizontal particle coordinate at the electrostatic septum is verified. If the particle position exceed septum knife the particle marked as extracted and turn number and coordinates are stored in the output file.

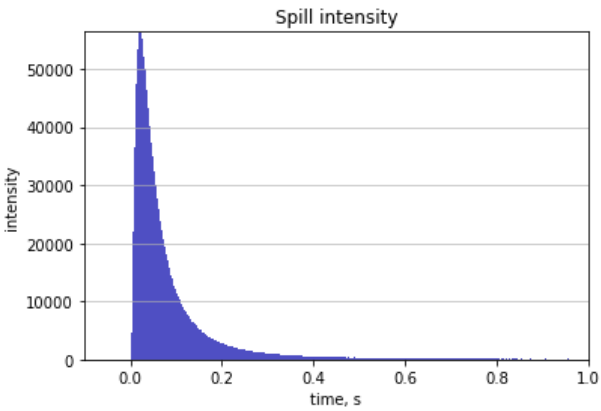

Figure 7: Spill structure for constant amplitude of RF-knockout.

The spill structures for constant amplitude of RF which provide kick angle 0.2 μrad is shown in Fig. 7. Such intensity fluctuation not acceptable for beam irradiation application. For this purpose, it was considered optimizing the AM function of RF-knockout. The radial distribution function in normalized phase space can be expressed by using the Reyleigh distribution function as [2]:

$$p(r) = \frac{2r}{\sigma^2} e^{\left[-\frac{r^2}{\sigma^2}\right]}, \quad (3)$$

where σ is the standard deviation. The σ increases through in RF-knockout slow extraction. Thus, the number of the extracted particles can be expressed as:

$$\frac{dN_{ext}}{dn} = N_0 \frac{d\sigma^2(n)}{dn} \frac{r_0^2}{\sigma^4(n)} exp\left[-\frac{r_0^2}{\sigma^2(n)}\right], \quad (4)$$

where r_0 is a separatrix size. In order to provide a flat spill Eq. 3 should be kept constant during extraction.

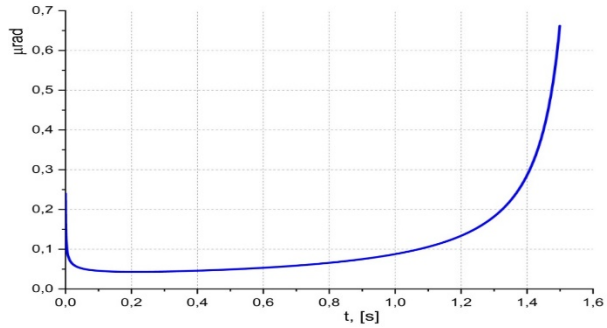

Figure 8: AM function in kick angles values of RF-knockout vs extraction time.

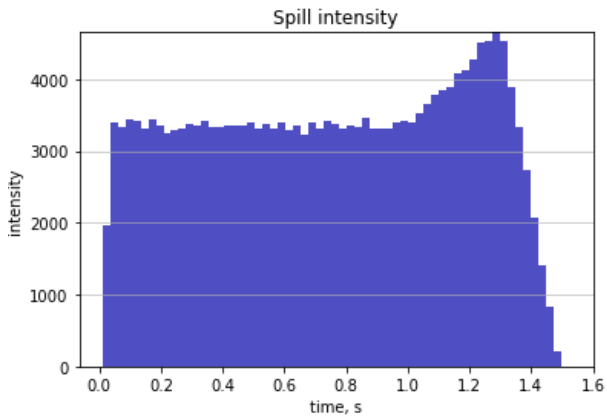

Figure 9: Spill structure for new AM function.

For extraction time 1.5 s the derived AM function for flat spill is presented in Fig. 8. The tracking simulation with determined AM modulation was carry out. The spill structure for this case is shown in Fig. 9. Clear that spill is flat up to 1 sec extraction within 5 % fluctuation. For kick angle ~0.7 μrad the electric field strength is 3.3 kV/m for 1m length deflection plate. This value is moderate and rf power amplifier for such RF knockout is available.

CONCLUSION

After analysis and evaluation, the feasibility of the RF-knockout extraction in the synchrotron for technological application has been developed. A flat spill is possible with an amplitude modulation of the signal. The simulation showed that for the first part of extraction the beam intensity is constant within a fluctuation less than 5 %. In order to get constant extraction also for the last part, the feedback system could be useful.

REFERENCES

[1] N. Carmignani *et al.*, "RF-knockout Extraction System for the CNAO Synchrotron", in *Proc. 1st Int. Particle Accelerator Conf. (IPAC'10)*, Kyoto, Japan, May 2010, paper THPEB007, pp. 3891-3893.

[2] T. Furukawa *et al.*, "Global spill control in RF-knockout slow-extraction", *Nucl. Instr. Meth.* A522, 2004.

ISBN: 978-3-95450-240-0 ISSN: 2673-5539 doi:10.18429/JACoW-RuPAC2021-TUPSB10

MODELING OF THE SPIN-NAVIGATOR METHOD FOR MANIPULATING THE BEAM POLARIZATION IN A SPIN-TRANSPARENT STORAGE RING

A. E. Aksentev[1]*, A. A. Melnikov, Y. V. Senichev,
Institute for Nuclear Research of the Russian Academy of Sciences, Moscow, Russia
V. P. Ladygin, Joint Institute for Nuclear Research (JINR), Dubna, Russia
[1]also at National Research Nuclear University "MEPhI," Moscow, Russia

Abstract

A method for manipulating the orientation of the beam polarization axis based on using the so-called "spin-navigator" technique in a storage ring operating in the spin-transparent regime has been modelled. The beam particles' spin- and orbital dynamics have been numerically investigated with the purpose of determining the method's feasibility; the latter's effect on spin-decoherence has been studied also.

INTRODUCTION

In the projected method for the manipulation of the beam polarization, the spin-transparent (ST) regime is effected by means of "Siberian snakes" which set the beam particles' spin precession frequencies close to zero (in the beam rest frame). Practically, this means that the spin-vector of a particle on the closed orbit (CO) coincides with itself after passing the accelerator lattice sequence (see Fig. 1). The additionally used "spin-navigating" solenoids (Fig. 2) have a two-fold purpose: not only to orientate the polarization axis, but also to stabilize this orientation by slowly turning the beam particles' spin-vectors about it, thus offsetting the "zero spin precession frequency" condition [1].

However, the finiteness of the beam phase space volume prevents the simultaneous satisfaction of the "zero precession frequency" condition by all beam particles. Due to the differences in their spin-orbit motion the particles' spin-vectors diverge (which phenomenon is termed "spin-decoherence"), which causes depolarization of the beam. One must meet certain conditions, homogenizing the distribution of the spin-precession axis over the beam phase space, in order to preserve the polarization.

The purpose of the present work was to study the beam particles' spin-orbital dynamics in the neighborhood of the zero spin resonance and the determination of whether the spin-navigator method for manipulating the orientation of the beam polarization axis is a feasible option. To that end, the COSY INFINITY modeling environment was used [2]. Depolarization mechanisms, in particular those specific to the proposed polarization manipulation method, have been considered.

MODELLING RESULTS

Numerical modeling has been done using the COSY INFINITY [2] modelling environment. We used three bunches

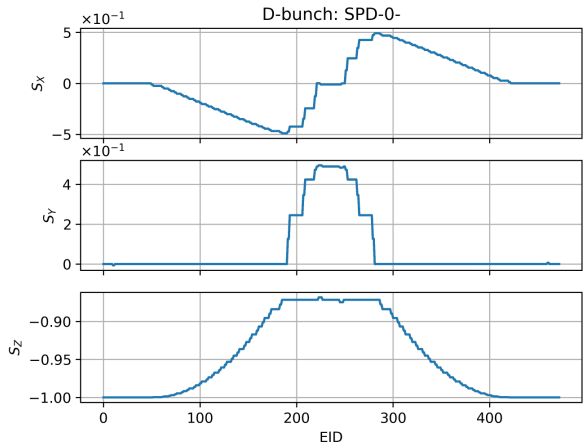

Figure 1: Transformation of the reference particle's spin-vector coordinates during one revolution in the accelerator lattice. The ordinal numbers (EID) on the horizontal axis indicate the element just passed. The particles whose spin-vector coordinates are represented in the figure have only energy deviation $\delta = {}^{\Delta K}/_{K}$ from the reference particle at injection, which is indicated by the words "D-bunch"; the words "SPD-0-" indicate that the spin-vectors of all particles pointed backwards along the reference particle's momentum vector.

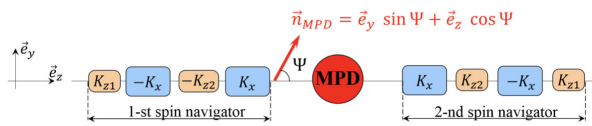

Figure 2: Spin-navigator placement scheme in the MPD-detector section [1].

of $N = 300$ particles each for a sufficiently precise beam polarization estimate

$$\boldsymbol{P} = \frac{1}{N}\sum_{j=1}^{N} \boldsymbol{s}^{(j)}.$$

Particles were uniformly distributed in phase space at injection:

1. X- and Y- bunches: $x, y = \pm 2$ mm respectively (the other phase-space coordinates set to zero);
2. D-bunch: $\delta = {}^{\Delta K}/_{K} = \pm 2 \cdot 10^{-4}$ (same as above).

* a.aksentyev@inr.ru

ISBN: 978-3-95450-240-0 ISSN: 2673-5539 doi:10.18429/JACoW-RuPAC2021-TUPSB10

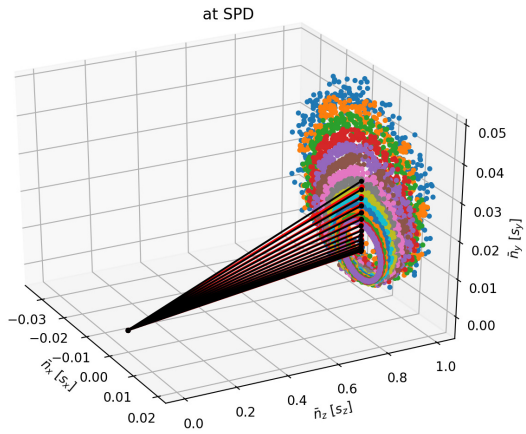

Figure 3: Mean spin-vector $\langle \boldsymbol{s} \rangle$ (or, what is the same, invariant spin axis $\bar{n}$) orientations at the SPD-detector for particles with varying initial offsets from the closed orbit in the radial direction at injection. Colored dots indicate the ellipses the spin-vectors describe during precession.

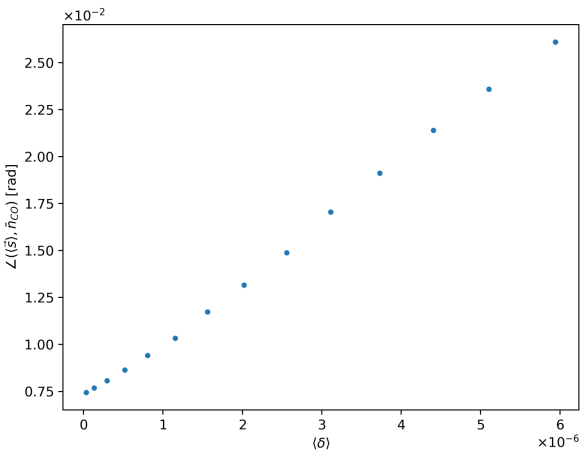

Figure 4: The angle of tilt of a non-reference particle's invariant spin axis from that of the reference particle as a function of the offset particle's mean kinetic energy offset.

The study results can be summarized in the following: a beam particle's spin-vector precesses along the surface of a cone (Fig. 3) whose **(a)** spray angle, as well as the **(b)** angle of deviation of its axis from the direction defined by the invariant spin axis $\bar{n}_{CO}$ of the particle on the closed orbit (Fig. 4), depend on the mean value of its kinetic energy deviation $\langle \delta \rangle = \langle \Delta K / K \rangle$. This value also determines the **(c)** spin precession frequency. The three parameters **(a)**, **(b)**, **(c)** also determine, in the general case, the rapidity of the beam depolarization process caused by spin-decoherence. Initially, four major cases of orientation of the beam polarization axis had been checked: up, down, forward (along the momentum vector), backward. In the majority of observed cases, spin-decoherence was not an issue (see Fig. 5 for a typical simulation result); however, a case of rapid depolarization (Fig. 6) was observed for the "polarization-up" case.

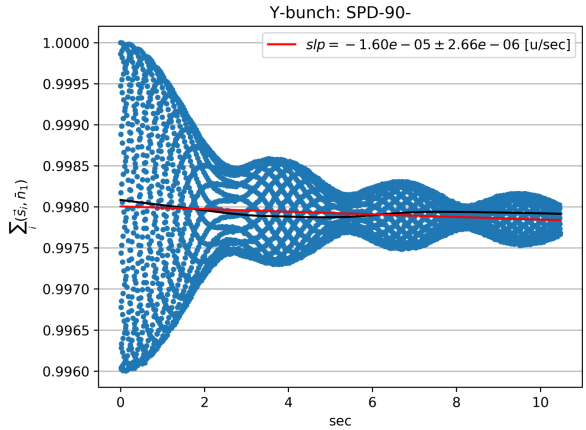

(a) The beam polarization as a function of time. The legend specifies the depolarization speed as estimated by the slope of a linear regression fit (red line) of the simulation data.

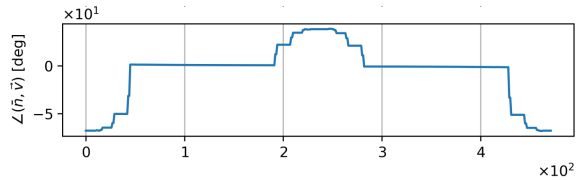

(b) The $\bar{n}$ tilt distribution within the lattice sequence. The distribution is *symmetric* with respect to the lattice sequence's median.

Figure 5: The stable case.

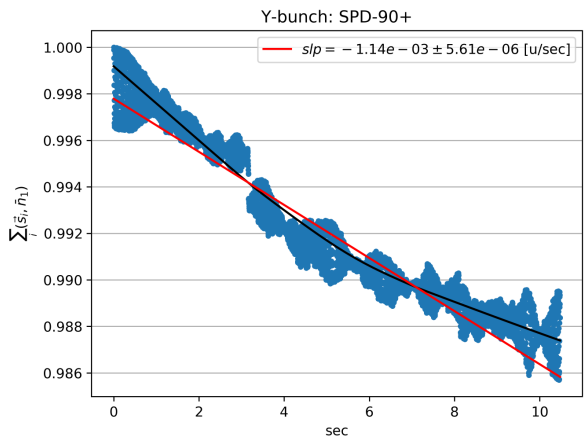

(a) The beam polarization as a function of time.

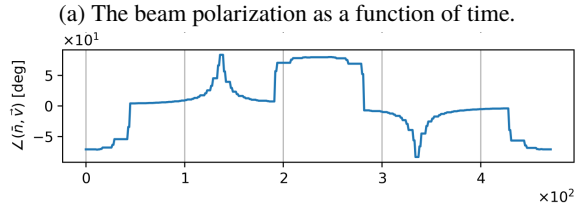

(b) The $\bar{n}$ tilt distribution within the lattice sequence. The distribution is *asymmetric* with respect to the lattice sequence's median.

Figure 6: The unstable case.

ISBN: 978-3-95450-240-0 ISSN: 2673-5539 doi:10.18429/JACoW-RuPAC2021-TUPSB10

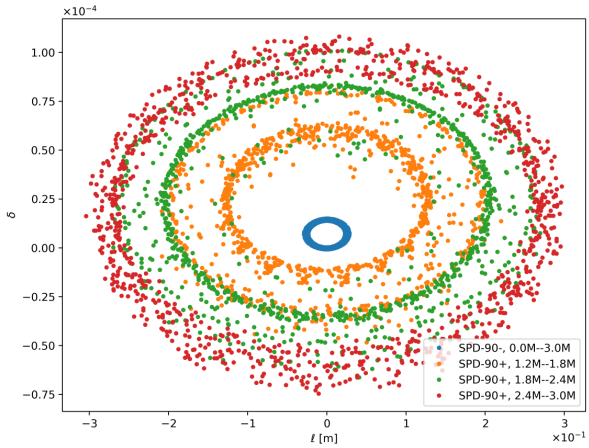

Figure 7: Longitudinal beam phase-space ellipse in the stable and unstable cases, with the latter split into three beam-revolution subranges, denoted by color.

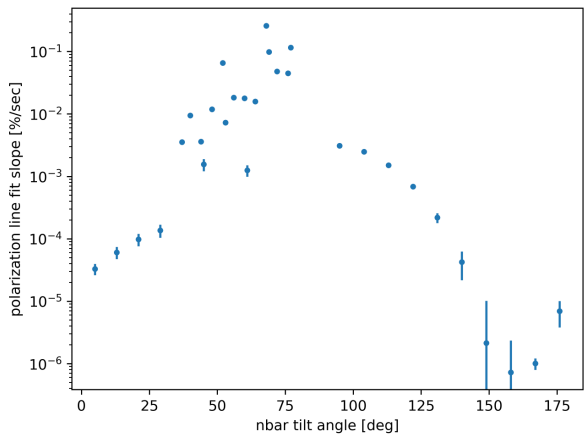

Figure 8: Meta-study results showing the dependence of depolarization rapidity as a function of the orientation of the polarization vector at the SPD-detector.

STUDY OF INSTABILITY

Upon encountering a case of phase-space instability (see Fig. 7), an additional meta-study checking a range of orientations was carried out (Fig. 8). The study suggests phase-space instabilities might be effected by the spin-navigators' mode of operation: the latter operate by creating an asymmetry in the magnetic field distribution in the straight sections of the storage ring. In Figs. 5b and 6b the polarization axis distributions along the beam line are presented. The distribution in Fig. 6b shows an asymmetry with respect to the median element in the lattice's sequence, which asymmetry is lacking in the stable case (Fig. 5). In fact, the meta-study appears to suggest that there is a direct correlation between the degree of asymmetry in the $\bar{n}(z - z_{median})$ distribution and the depolarization speed. Since the production of the asymmetry is *the means* by which the spin-navigators manipulate the polarization axis, we conclude that there is a definite domain of applicability of the spin-navigator method.

CONCLUSION

The feasibility of using the spin-navigator technique for manipulating the orientation of the beam polarization axis in a storage ring operating in the spin-transparency mode has been confirmed, although its applicability domain appears restricted on account of phase-space stability.

REFERENCES

[1] A. M. Kondratenko *et al.*, "Polarized ions in the NICA facility," Tech. Rep., Dubna, Aug 2018.

[2] M. Berz, "Symplectic Tracking Through Circular Accelerators with High Order Maps" in *Proc., Workshop on Nonlinear Problems in Future Particle Accelerators*, Capri, Italy, April 19-25, 1990, pp. 288-296.

ISBN: 978-3-95450-240-0 ISSN: 2673-5539 doi:10.18429/JACoW-RuPAC2021-TUPSB11

NUMERICAL INVESTIGATION OF THE ROBUSTNESS OF SPIN-NAVIGATOR POLARIZATION CONTROL METHOD IN A SPIN-TRANSPARENT STORAGE RING

A. Melnikov[1†], A. Aksentyev[1,2], Y. Senichev[1], V. Ladygin[3]
[1]Institute for Nuclear Research of the Russian Academy of Sciences, Troitsk, Moscow, Russia
[2]National Research Nuclear University "MEPhI," Moscow, Russia
[3]Joint Institute for Nuclear Research, Dubna, Moscow region, Russia

Abstract

The robustness of spin-navigator based method for manipulating the beam polarization axis has been investigated with respect to bend magnet installation errors. Toward that end, variation of the invariant spin axis components along the beamline of an imperfect storage ring operating in the spin-transparent mode has been estimated. The beam polarization vector behavior in the given lattice has been investigated. Conclusions are made regarding the feasibility of using "spin navigator" solenoids for defining the beam polarization axis in the detector region.

INTRODUCTION

In the proposed method of polarization control in a spin-transparent (ST) mode spin precession frequency is set close to zero with the help of "siberian snakes". Since particles are in the vicinity of an integer resonance, "navigator" solenoids with weak fields are used for stabilization of polarization direction (Fig. 1) [1]. They consist of solenoids with longitudinal field and magnets with radial field rotating spin-vectors of particles by small angles. In ST method one can obtain any polarization direction at any point of an orbit for arbitrary beam energy.

This method of polarization control is highly sensitive to errors. That is why it is necessary to investigate its robustness in the numerical simulation. The stabilizing influence of navigator solenoids in the vicinity of an integer resonance should be larger than the influence of effects arising from lattice imperfections. Spin-orbit dynamics simulations using NICA lattice were made below to estimate the influence of magnet tilts on the ability to guide polarization direction with navigator solenoids in the detector.

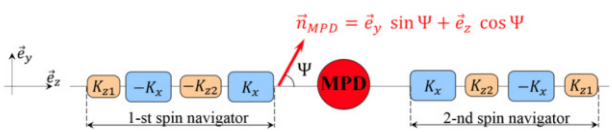

Figure 1: The scheme of navigator solenoids location close to MPD detector [1].

† alexei.a.melnikov@gmail.com

METHOD "SPIN-KICK"

When the bending magnets are rotated around the optical axis it is necessary to compensate the vertical component of the guiding field to preserve the closed orbit. The latter will not be flat if the radial components of magnetic field are present. In the simulation a simplifying assumption was used that orbital dynamics does not change with magnet tilts but spin transfer matrix of an element is rotated by an angle depending on a tilt. All the results obtained with this assumption can be interpreted without the loss of generality in the frame of estimation of ST method robustness and feasibility.

Spin dynamics of particles in a laboratory frame is described by T-BMT equation:

$$\frac{d\vec{S}}{dt} = \vec{S} \times (\vec{\Omega}_{MDM} + \vec{\Omega}_{EDM}),$$

$$\vec{\Omega}_{MDM} = \frac{q}{m\gamma}\left[(\gamma G + 1)\vec{B}_{\perp} + (1+G)\vec{B}_{\parallel} - \gamma\left(G + \frac{1}{\gamma+1}\right)\frac{\vec{\beta}\times\vec{E}}{c}\right],$$

$$\vec{\Omega}_{EDM} = \frac{q\eta}{2m}\left[\vec{\beta}\times\vec{B} + \frac{\vec{E}}{c}\right],$$

where $\vec{\Omega}_{MDM}$ and $\vec{\Omega}_{EDM}$ are spin-vector $\vec{S}$ precession frequencies, caused by the presence of magnetic and electric dipole moment of particles – MDM and EDM respectively. G is the anomalous magnetic moment, γ – Lorentz factor. $\vec{B} = \vec{B}_{\parallel} + \vec{B}_{\perp}$, $\vec{B}_{\parallel} = \frac{\vec{v}\cdot\vec{B}}{v^2}\vec{v}$.

In the case of a purely magnetic lattice ($E = 0$) and taking into account that $\Omega_{EDM} \ll \Omega_{MDM}$, in the rest frame:

$$\vec{\Omega}_{MDM} = \frac{q}{m\gamma}[\gamma G\,\vec{B}_{\perp} + (1+G)\vec{B}_{\parallel}].$$

In the case of bend magnet tilts around the optical axis of the accelerator $B_{\parallel} = 0$. In linear approximation the vertical precession frequency does not change. The radial component $\Delta\Omega_{MDM}$ emerges that is equivalent to spin-vector rotation around the radial axis by an angle ψ:

ISBN: 978-3-95450-240-0 ISSN: 2673-5539 doi:10.18429/JACoW-RuPAC2021-TUPSB11

$$\psi = \frac{\alpha R}{v} \cdot \Delta\Omega_{MDM} = \frac{\alpha R}{v} \cdot \frac{qG}{m} B sin(\varphi),$$

where α and R – the angular size and trajectory radius of a particle in the magnet, B – guiding field, φ – random angle of a tilt around the longitudinal axis.

NUMERICAL INVESTIGATION OF SPIN-ORBITAL DYNAMICS

For numerical modeling the program software COSY INFINITY was used. It is based on differential algebraic approach for optimization of transfer map calculation. The latter are calculated for orbital and spin motion separately.

In the model the beam consisting of 100 deuterons was injected with $\gamma = 1.14$. The particles were uniformly distributed from -2 to 2 mm in a transverse radial direction. The initial polarization is longitudinal.

Dipole magnets were rotated by angles $\varphi \sim N(0, 10^{-4})$. The RMS error $\sigma(\varphi)$ is expressed through the error of magnet installation heights $\sigma(h)$ and the length of a magnet L: $\sigma(\varphi) = \sigma(h)/L$. With $\sigma(h) \sim 100$ um and $L \sim 1$ m, $\sigma(\varphi) \sim 10^{-4}$.

In the setting with $\varphi \sim N(0, 10^{-4})$ the relative change of a spin-tune and longitudinal polarization $\Delta\nu/\nu \sim 10^{-3}$, $\Delta P/P \sim 10^{-5}$. These values are caused by nonzero realization of math. expectation value in a finite sampling and, as a consequence, the emergence of nonvanishing Y projection of invariant axis N_y in the detector region. It can be explained in the following way: vertical polarization arises from magnet tilts along the ring. Then the latter is rotated into the ring plane by a half-snake solenoid before detector region. This is equivalent to rotation of spin-vectors around Y axis after one turn or $\Delta N_y \neq 0$ in a detector.

The expectation value of tilt angles was shifted by $\pm 10^{-3}$ rad to investigate the robustness of spin dynamics. In this setup $\Delta\nu/\nu \sim 10^{-2}$, $\Delta P/P \sim 10^{-4}$, $\Delta N_y \sim 10^{-2}$ (Fig. 2, 3, 4).

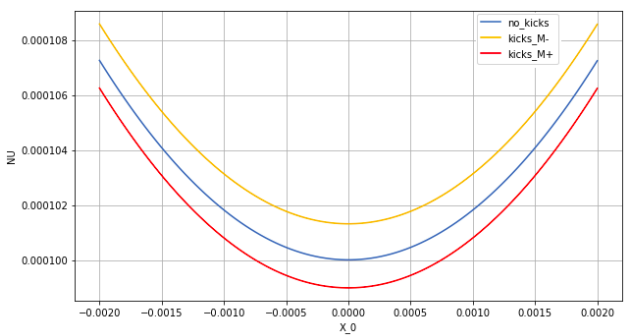

Figure 2: Spin-tune for different transversely offset particles for ideal lattice and with magnet tilts around the longitudinal axis $\varphi \sim N(\pm 10^{-3}, 10^{-4})$.

In Fig. 2 the spin-tune of a reference particle coincides with the necessary value 10^{-4} set by navigator solenoids to provide stable polarization control [1]. The parabolic dependence of spin-tune on a particle transverse position in a bunch comes from the orbit lengthening effect. It leads to different effective energies and spin-tunes due to synchronous acceleration principle [2].

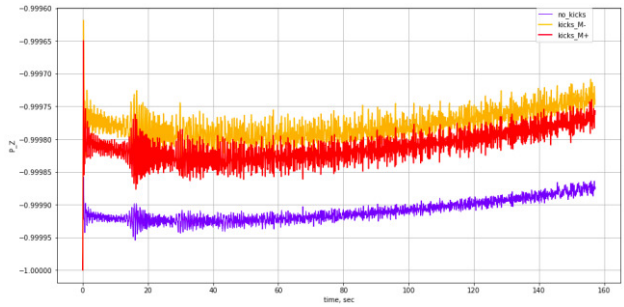

Figure 3: The time dependence of a longitudinal beam polarization in the detector point for ideal lattice and with magnet tilts around the longitudinal axis $\varphi \sim N(\pm 10^{-3}, 10^{-4})$.

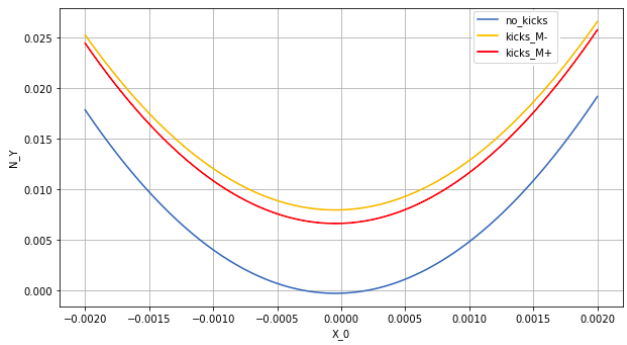

Figure 4: The dependence of a vertical component of the invariant axis N_y in the detector point for different transversely offset particles for ideal lattice and with magnet tilts around the longitudinal axis $\varphi \sim N(\pm 10^{-3}, 10^{-4})$.

CONCLUSION

The principal ability of beam polarization control with navigator solenoids was demonstrated in a structure with lattice imperfections such as bending magnet rotations. The main effect arising from magnet tilts is the emergence of a vertical component of invariant spin axis in the detector point. It was explained first and then shown in the numerical experiment. The qualitative character of spin dynamics is preserved that means that the spin motion remains stable in the vicinity of an integer spin resonance corresponding to ST regime.

REFERENCES

[1] A. Kondratenko, M. Kondratenko, Y. Filatov, A. Kovalenko, A. Butenko, V. Mikhailov, E. Syresin, S. Shimansky, "Polarized ions at NICA complex. Project description", Dubna, Technical report, Aug. 2018.

[2] Y. Senichev, A. Aksentev, A. Ivanov, E. Valetov, "Frequency domain method of the search for the deuteron electric dipole moment in a storage ring with imperfections", arXiv:1711.06512v1.

ISBN: 978-3-95450-240-0 ISSN: 2673-5539 doi:10.18429/JACoW-RuPAC2021-TUPSB12

DEVELOPMENT OF A PROGRAM CODE FOR CALCULATION OF CHARGED PARTICLE DYNAMICS IN RFQ

A.S. Boriskov, N.V. Zavyalov, A.V. Telnov, M.L. Smetanin, A.M. Opekunov, L.E. Polyakov,
RFNC-VNIIEF, Sarov, Russia

Annotation

The code for the beam dynamics simulation in radio-frequency quadrupole (RFQ) accelerating structure was written in the C++ programming language. Charged particle beam dynamics was simulated in RFQ structure aimed to accelerate ion beams up to energies of 1.25 MeV / nucleon.

The characteristics of the beam at the exit of the structure (velocity, particle capture coefficient, beam profile, transverse emittances, longitudinal phase portrait) were determined.

INTRODUCTION

The considered accelerating structure is intended for the initial acceleration of ions with an A/Z ratio from 1 to 3.2 (A is the mass number, Z is the charge of the ion). Particles from H to O fall within the specified range.

In order for the capture coefficient in the acceleration mode to be high, it is necessary to use systems that are effective at a low initial particle velocity. These requirements are met by accelerating structures in which acceleration, grouping and focusing of charged particles by a radio-frequency (RF) electromagnetic field occur simultaneously.

RFQ ACCELERATOR

Focusing systems use conventional electrostatic or magnetic quadrupole lenses. To focus the beam in two transverse directions, it is necessary to change the polarity of the poles. When using an alternating RF field, it is possible to use a quadrupole system of electrodes, which is uniform along the axis of the accelerator [1]. Such a system is shown in Fig. 1.

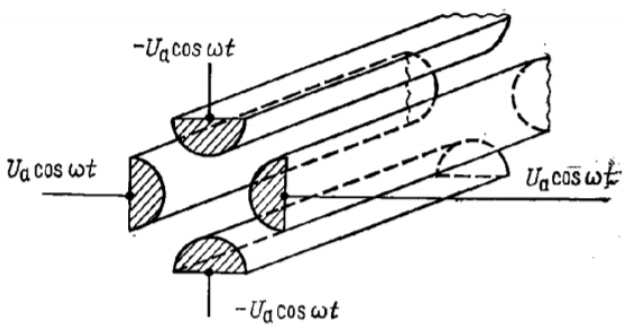

Figure 1: Quadrupole symmetric four-wire line.

The value $2U_a$ is the amplitude value of the voltage between adjacent electrodes. Since an RF voltage is applied to the electrodes, the particles, when moving along the axis, successively experience the action of fields with an alternating sign of the gradient.

The longitudinal accelerating component of the electric field in a four-wire line is created if the distance between opposite electrodes of the same polarity changes periodically along the axis [2]. The spatial period of the change in the distance between the electrodes should be equal to the path that the equilibrium particle travels during the RF period, and the phases of the change in the distances in the perpendicular planes are shifted by half a period.

PROTON AND LIGHT ION BEAM DYNAMICS SIMULATION

The selection of the parameters of any accelerating structure for calculating the particle dynamics begins with the selection of the operating frequency. It is selected based on the condition of the minimum length of an accelerator with a RFQ.

The closest to the optimal value is the widely used frequency of 81.25 MHz from the range of frequencies from 40.625 to 972 MHz.

Taking into account the literature data on the recommended field strength on the surface of the electrodes [3], the value of the Kilpatrick criterion was chosen 1.85.

A pre-buncher is usually placed between the ion source and the accelerating structure. Taking into account the buncher, the phase length of the beam at the entrance to the structure with the RFQ is set equal to 1.4 π.

EQUATION OF MOTION IN THE APPROXIMATION OF ANALYTICALLY GIVEN FIELDS

To simulate the action of an electromagnetic field on accelerated particles in the equation of motion, it is sufficient to take into account only the electric component of the RF field:

$$\frac{d\vec{p}}{dt} = e\vec{E}(r,t)\,. \qquad (1)$$

In the Cartesian coordinate system, the expression for the accelerating potential in the RFQ structure on the axis of beam motion in the one-wave approximation has the form [3]:

$$U(x,y,z,t) = \frac{U}{2}\left[A_{01}(x^2-y^2) + A_{10}I_0\left(k\sqrt{x^2+y^2}\right) \cdot \sin(kz)\right]\cos(\omega t), \qquad (2)$$

where U – voltage between electrodes;
k – wave number;
ω – RF field frequency;
I_0 – modified Bessel function;
A_{01} и A_{10} – focusing and accelerating parameters respectively.

ISBN: 978-3-95450-240-0 ISSN: 2673-5539 doi:10.18429/JACoW-RuPAC2021-TUPSB12

Using expression (2), we find the electric field strength. Next, we substitute in (1) and pass into Cartesian coordinates and obtain the equations of motion:

$$\begin{cases} \frac{dp_x}{dt} = \frac{eU}{2}\left[2A_{01}x + A_{10}I_1\left(k\sqrt{x^2+y^2}\right)\cdot\frac{kx}{\sqrt{x^2+y^2}}\cdot\sin(kz)\right]\cos(\omega t) \\ \frac{dp_y}{dt} = \frac{eU}{2}\left[2A_{01}y - A_{10}I_1\left(k\sqrt{x^2+y^2}\right)\cdot\frac{ky}{\sqrt{x^2+y^2}}\cdot\sin(kz)\right]\cos(\omega t) \\ \frac{dp_z}{dt} = \frac{eU}{2}\left[A_{10}I_0\left(k\sqrt{x^2+y^2}\right)\cdot k\cos(kz)\right]\cos(\omega t) \end{cases} \quad (3)$$

NUMERICAL SIMULATION OF ION DYNAMICS

At the first stage, the simulation of ion dynamics was carried out in the BEAMDULAC-RFQ program [4], [5].

Own program code for particle dynamics simulation has been written. When writing, a wide analysis of methods for calculating the dynamics of particles taking into account the space charge effect was carried out. The most interesting are the CIC method (Cloud in Cell) and the "large particle method". The latter method is easier to implement and allows direct calculation of the action of Coulomb forces without preliminary calculation of the potentials and intensities at the grid nodes. This calculation, in turn, imposes a certain error on the calculation results.

In the BEAMDULAC-RFQ program, the Runge-Kutta method of the 4th order is used to solve equations (3), and the CIC method is used to take into account the effect of space charge.

DEVELOPING OUR OWN PROGRAM CODE

Using the C ++ programming language, a physico-mathematical model of the ion beam motion in an accelerating structure with a RFQ has been created. To simulate the action of the RF field on the dynamics of particles, the equations of motion are used (3).

The developed program uses a direct calculation of the space charge "by the method of large particles" [6]. The particle beam is represented as a set of bunches located on the axis of the accelerating structure. Each bunch is represented by N uniformly charged balls of radius R (large particles). The force acting on the i-th particle from the j-th is calculated by the formula [6]:

$$F_{ij} = \begin{cases} \frac{q^2}{4\pi\varepsilon_0(2R)^2}\cdot\left(\frac{2R}{r_{ij}}\right)^3\cdot\frac{r_{ij}}{2R}, & r_{ij} \geq 2R \\ \frac{q^2}{4\pi\varepsilon_0(2R)^2}\cdot\left[\begin{matrix} 2\left(\frac{2R}{r_{ij}}\right)^3 \\ -9\left(\frac{2R}{r_{ij}}\right)+8 \end{matrix}\right]\cdot\frac{r_{ij}}{2R}, & 0 \leq r_{ij} < 2R \end{cases} \quad (4)$$

Thus, summing up the forces for each particle, we obtain the influence of the remaining particles of the bunch on it:

$$F_i = \sum_j^N F_{ij} . \quad (5)$$

Taking the superposition of the forces acting on the particle from the RF field (3) and the forces of the own field of the particles (4), equation (1) is solved.

The counting time starts to grow noticeably when a larger number of particles are specified. However, the use of a hybrid computational model allows the use of a parallel (GPU) computation mode, for which the problem of calculating particle dynamics is ideally suited.

ION BEAM DYNAMICS SIMULATION RESULTS

The calculation of the dynamics of ions was carried out using the initial data presented in Table 1.

Table 1: Initial Data for Modeling Dynamics

Parameter	Value	
Ion type	H^+	O^{5+}
Frequency, MHz	81.25	
Structure length, mm	5043	
Emittance (x, y), π × cm × mrad	0.03	
Longitudinal pulse spread,%	± 0.1	
Beam size (x, y), mm	1	2
Voltage between adjacent electrodes, kV	40	140
Beam initial phase	-0.2 π	-0.2 π
Final phase of the beam	1.2 π	1.2 π
Minimum aperture, mm	7	
Particle current, mA	2	0.2

Figure 2 shows the velocities of an equilibrium particle during it's propagation along accelerating structure, calculated in different programs. It can be seen that the curves repeat each other perfectly. The discrepancy between the calculation results in the two programs is less than 0.1%. This fact makes it possible to use the developed code for solving problems of charged particle dynamics simulation in RFQ.

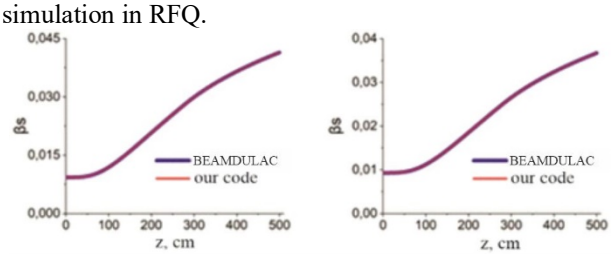

(a) (b)

Figure 2: Equilibrium particle velocity for protons (a) and ions O^{5+} (b).

As a result of calculations, phase portraits were obtained in all planes for protons (Fig. 3) and O^{5+} ions (Fig. 4).

ISBN: 978-3-95450-240-0 ISSN: 2673-5539 doi:10.18429/JACoW-RuPAC2021-TUPSB12

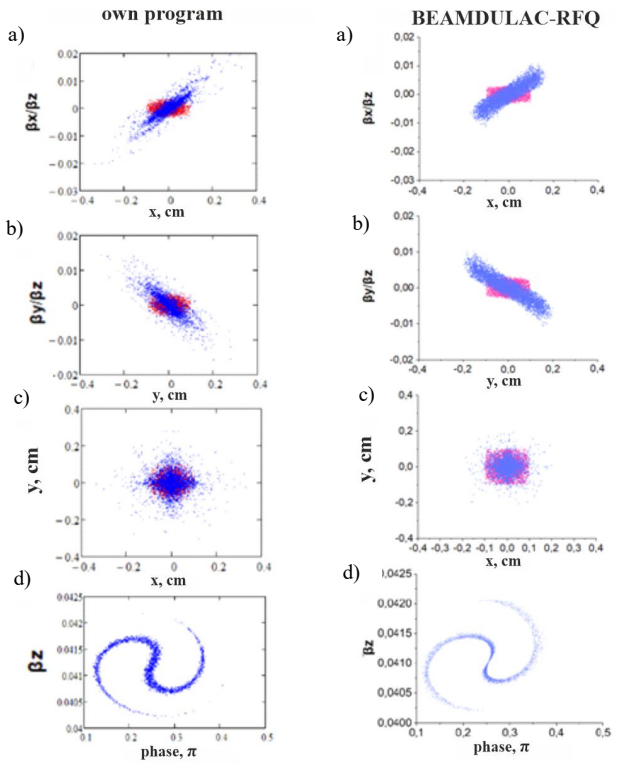

Figure 3: Results of proton dynamics simulation: on the left - in your own program; on the right - BEAMDULAC-RFQ (red dots - particles at the beginning of acceleration, blue dots - particles at the end of acceleration). a, b – transverse phase portraits; c – bunch cross-section; d – longitudinal phase portrait.

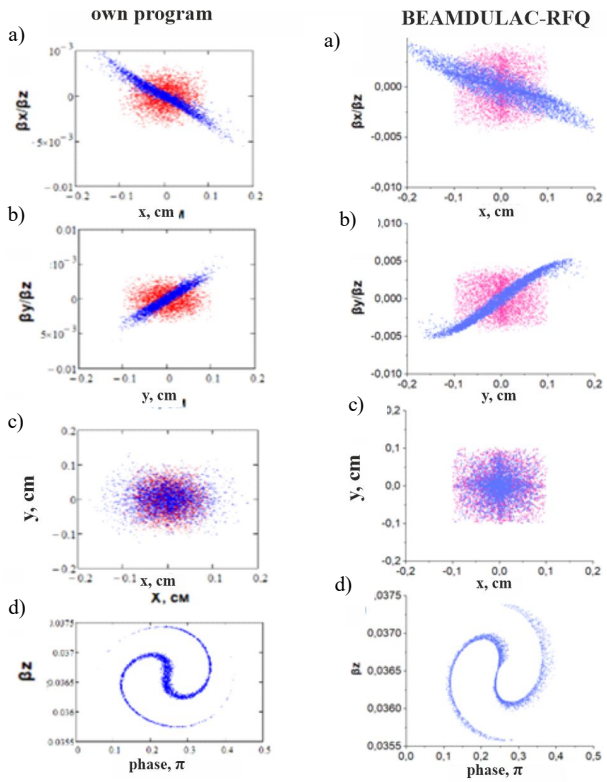

Figure 4: Results of O^{5+}dynamics simulation: on the left - in your own program; on the right - BEAMDULAC-RFQ (red dots - particles at the beginning of acceleration, blue dots - particles at the end of acceleration. a, b – transverse phase portraits; c – bunch cross-section; d – longitudinal phase portrait.

CONCLUSION

A program code has been developed for the ion beam dynamics simulation taking into account the space charge effect using a hybrid computation model, based on the "method of large particles" to estimate the intrinsic field of the beam. To verify the obtained results, control calculations were performed in the BEAMDULAC-RFQ program, which has proven itself in the accelerating community. The dynamic parameters of ions (Figs. 3 and 4), obtained as a result of simulation in our own program, are in full agreement with similar results obtained in the BEAMDULAC-RFQ program, despite different methods for calculating the space charge of the beam. At the exit from the accelerating structure, the phase length of the beam is 0.3 π at the initial 1.4 π, which indicates a successful longitudinal bunching. Thus, it was shown that the developed program code is in no way inferior to the analogue in terms of the counting time and allows to do charged particle dynamics simulation in the RFQ accelerating structures.

ACKNOWLEDGEMENT

The team of authors would like to acknowledge Sergei Polozov from MEPhI, Moscow for providing the opportunity to use BEAMDULAC-RFQ program in the work on this paper.

REFERENCES

[1] E.S. Masunov, S.M. Polozov, Workshop by course “Electrophysical installations and technologies”, p.1. Linear accelerators. Tutorial, Moscow, MEPhI, 2004.

[2] I.M. Kapchinsky, “Linear Resonance Accelerators Theory: Particle Dynamics”, Moscow, Energoatom-izdat, 1982.

[3] V.A. Teplyakov, “Study of the possibility of creating the initial part of a continuous mode accelerator with an energy of 5 MeV”, Protvino, 2000.

[4] E.S. Masunov, S.M. Polozov, “The New Version of BEAMDULAC Code for High Intensity Ion Beam Dynamics”, *Problems of Atomic Science and Technology*, ser. “*Nucl. Phys Inv.*”, N. 3 (47), p. 119-121, 2006.

[5] E.S. Masunov, S.M. Polozov, “BEAMDULAC Code for Numerical Simulation of 3D Beam Dynamics in a High-intensity Undulator Linac”, *Nucl. Instr. and Methods in Phys. Res.*, A, 558, p. 184–187, 2006.

[6] D.A. Ovsyannikov, Y.A. Svistunov, “Modeling and Optimization of Charged Particle Beams in Accelerators”, St. Petersburg, 2003.

ISBN: 978-3-95450-240-0 ISSN: 2673-5539 doi:10.18429/JACoW-RuPAC2021-TUPSB13

CHARGED PARTICLE DYNAMICS OPTIMIZATION IN DISCRETE SYSTEMS

E. D. Kotina†, D. A. Ovsyannikov, St. Petersburg State University, St. Petersburg, Russia

Abstract

Discrete optimization methods of dynamic systems are widely presented in the scientific literature. However, to solve various problems of beam dynamics optimization, it is necessary to create special optimization models that would take into account specifics of the problems under study. The paper proposes a new mathematical model that includes joint optimization of a selected (calculated) motion and an ensemble of perturbed motions. Functionals of a general form are considered, which make it possible to estimate various characteristics of a charged particle beam and the dynamics of the calculated trajectory. The optimization of a bundle of smooth and nonsmooth functionals is investigated. These functionals estimate both integral characteristics of the beam as a whole and various maximum deviations of the parameters of the particle beam. The variation of a bundle of functionals is given in an analytical form, that allows us to construct directed optimization methods. The selected trajectory can be taken, for example, as the trajectory of a synchronous particle or the center of gravity of a beam (closed orbit). We come to discrete models when we consider the dynamics of particles using transfer matrices or transfer maps. Optimization problems can be of orbit correction, dynamic aperture optimization, and many other optimization problems in both cyclic and linear accelerators of charged particle beams.

INTRODUCTION

Discrete systems are becoming increasingly important in theory and practical application in optimal control and optimization problems [1-5]. This is due to the fact that many problems are described by discrete equations, since in practice information about the state of the process comes discretely, and control of the dynamic process is implemented most often at discrete moments of time. The standard approach to the design of various control systems involves the initial calculation of the selected motion and the subsequent study of perturbed motions using equations in deviations. This approach, however, does not always lead to the desired results. When analyzing perturbed motions, it turns out that their dynamic characteristics are not always satisfactory from one point of view or another. This is a consequence of the significant dependence of the perturbed motions on the selected motion. In this paper, a mathematical model is proposed that allows simultaneous optimization of the selected motion and the ensemble of perturbed motions in discrete systems. In this case, the simultaneous optimization of smooth and nonsmooth functionals is considered.

† e.kotina@spbu.ru

The classical formulations of optimal control problems in discrete systems are quite well known and studied [1]. These problems can be considered as tasks of single trajectories control. Along with them, non-standard problems of the theory of optimal control are being developed. In particular, the control problems of ensembles of trajectories (beams) were considered under various cost functionals in continuous and discrete-time systems [2]. Further, non-standard problems of joint optimization of program motion and perturbed motions in continuous systems [6, 7], as well as in discrete ones [3-5] were developed. The problems of simultaneous optimization of smooth and nonsmooth functionals defined on a program motion and a beam of perturbed trajectories in continuous and discrete systems were further developed [8-10].

This article is devoted to the construction of new methods for optimizing the bundle of smooth and nonsmooth functionals in discrete systems.

PROBLEM STATEMENT

In this paper a dynamic system is described by the discrete equations of the following type

$$x(k+1) = f\big(k, x(k), u(k)\big), \quad (1)$$

$$y(k+1) = F\big(k, x(k), y(k), u(k)\big), \quad (2)$$

$$k = 0, \dots, N-1,$$

where $x(k) - n-$ dimensional phase vector, characterizing the state of the system, $y(k) - m-$ dimensional phase vector, $u(k) - r-$ dimensional vector, $f(k) = f\big(k, x(k), u(k)\big)$ is $n-$dimensional vector function, $F(k) = F\big(k, x(k), y(k), u(k)\big) - m-$ dimensional vector function. We suppose that $f(k)$ is defined and continuous in $\Omega_x \times U(k)$ by the arguments $\big(x(k), u(k)\big)$ for $k = \overline{1, N}$ along with their partial derivatives. We also assume that $F(k)$ is defined and continuous in $\Omega_x \times \Omega_y \times U(k)$ by the arguments $\big(x(k), y(k), u(k)\big)$ for $k = \overline{1, N}$ along with their first and second partial derivatives. Here $\Omega_x \subset R^n$, $\Omega_y \subset R^m$, $U(k)$ – a compact set in R^r, $k = \overline{1, N}$. We suppose that for a given vector $u(k)$, the vector $x(k)$ and the vector $y(k)$ uniquely determine the phase state $y(k+1)$ of the perturbed particle at the $k-$th step and vice versa, by $y(k+1) -$ the state of the perturbed particle at the previous step.

Equation (1) describes the dynamics of the selected motion. Equation (2) describes the perturbed motion.

We assume, that $x(0) = x_0$, $(x_0 \in \Omega_x \subset R^n)$ and the initial state of the system (2) is described by set $M_0 -$ a compact set of nonzero measure in R^m, the sequence of vectors $\{u(0), u(1), \dots, u(N-1)\}$ we will call control and denote u for brevity, $x = \{x(0), x(1), \dots, x(N)\} =$

ISBN: 978-3-95450-240-0 ISSN: 2673-5539 doi:10.18429/JACoW-RuPAC2021-TUPSB13

$x(x_0, u)$ – the trajectory of selected motion corresponding to the control u and the initial state x_0, $x(k) = x(k, x_0, u)$ – the state of the system at the step k, $y = \{y(0), y(1), \dots, y(N)\} = y(x, y_0, u)$ – the trajectory of perturbed motion, $y(k) = y(k, x, y_0, u)$ – the state of the system at the step k. The set of trajectories $y(x, y_0, u)$ corresponding to the initial state x_0, the control u and different initial states $y_0 \in M_0$ we will call a beam of trajectories or simply the beam. State of the beam at the k –th step is the cross-section of trajectories ensemble denoted as $M_{k,u} = \{y(k): y(k) = y(k, y_0, x, u), y_0 \in M_0\}$. The controls satisfying conditions $u(k) \in U(k)$, $k = \overline{1, N-1}$ we call admissible.

On the trajectories of the system (1)-(2), we introduce cost functionals that allow us to evaluate the dynamics of the calculated and perturbed motion and to carry out their joint optimization:

$$I_1(u) = \sum_{k=1}^{N-1} g\big(k, x(k)\big) + g(N, x(N)), \quad (3)$$

$$I_2(u) = \max_{y(N) \in M_{N,u}} \Phi\big(y(N)\big), \quad (4)$$

$$I(u) = I_1(u) + I_2(u). \quad (5)$$

Here $g_k = g\big(k, x(k)\big)$, $k = 0,1, \dots, N-1$ and $g_N = g(N, x(N))$ continuously differentiable functions by x, $\Phi(y(N))$ – a non-negative continuously differentiable function with respect to y.

We consider the problem of functional (5) minimization for all admissible controls.

FUNCTIONAL VARIATION

Let u – admissible control. We will consider the following variation of this control:

$$\tilde{u}_\varepsilon = u + \varepsilon \Delta u. \quad (6)$$

We suppose, that $\tilde{u}_\varepsilon$ is an admissible control, when $\varepsilon \epsilon [0, \bar{\varepsilon})$, $\bar{\varepsilon} > 0$, in this case, we will call Δu the permissible direction of the control variation.

The trajectory increment at the k –th step $\Delta x(k) = \tilde{x}(k, x_0, \tilde{u}_\varepsilon) - x(k, x_0, u)$ and the trajectory increment of perturbed motion at the k –th step $\Delta y(k) = \tilde{y}(\tilde{x}, y_0, \tilde{u}_\varepsilon) - y(x, y_0, u)$, for control in Eq. (6), can be represented as [1]

$$\Delta x(k+1) = \varepsilon \delta x(k+1) + o(\varepsilon),$$
$$\Delta y(k+1) = \varepsilon \delta y(k+1) + o(\varepsilon),$$

where $k = \overline{1, N}$ and variations δx и δy satisfy the equations [10]:

$$\delta x(k+1) = \frac{\partial f(k)}{\partial x(k)} \delta x(k) + \frac{\partial f(k)}{\partial u(k)} \Delta u(k), \quad (7)$$

$$\delta y(k+1) = \frac{\partial F(k)}{\partial x(k)} \delta x(k) + \frac{\partial F(k)}{\partial y(k)} \delta y(k) + \frac{\partial F(k)}{\partial u(k)} \Delta u(k), \quad (8)$$

$$k = 0, \dots, N-1.$$

At the same time, the initial conditions take place $\delta x(0) = 0$ and $\delta y(0) = 0$.

The increment of the functional in Eq. (5) can be written as

$$I(\tilde{u}_\varepsilon) - I(u) = \varepsilon \delta I + o(\varepsilon) = \varepsilon \delta I_1 + \varepsilon \delta I_2 + o(\varepsilon), \quad (9)$$

where δI_1 – functional (3) variation, δI_2 – functional (4) variation, δI – functional (5) variation.

Variation of the Functional $I_1(u)$

We write out a variation of the functional (3) using Eq. (7). We get

$$\delta I_1 = \sum_{k=1}^{N-1} \frac{\partial g_k}{\partial x_k} \delta x_k + \frac{\partial g_N}{\partial x_N} \delta x_N.$$

Variation δI_1 can be converted to the form

$$\delta I_1 = \sum_{k=0}^{N-1} \left[\beta^T(k+1) \frac{\partial f(k, x(k), u(k))}{\partial u(k)}\right] \Delta u(k), \quad (10)$$

using the following auxiliary vector functions

$$\beta^T(N) = \frac{\partial g_N}{\partial x_N},$$
$$\beta^T(k) = \beta^T(k+1) \frac{\partial f(k)}{\partial x(k)} + \frac{\partial g_k}{\partial x(k)}, \quad (11)$$
$$k = 1, \dots, N-1.$$

Variation of the Functional $I_2(u)$

We write down a variation of the functional $I_2(u)$

$$\delta I_2 = \max_{y_0 \in Y_0(u)} \left\{\frac{\partial \Phi(y_N)}{\partial y_N} \delta y_N\right\},$$

where $Y_0(u)$ is defined as follows [10]:

$$Y_0(u) = \Big\{y_0 \in M_0 : \Phi\big(y(N)\big) = \Phi(y(N, x(x_0, u), y_0, u)) = \max_{y_N \in M_{N,u}} \Phi(y_N)\Big\}.$$

The variation of the functional $I_2(u)$, using equations (8), can be converted to the form

$$\delta I_2 = \max_{y_0 \in Y_0(u)} \left\{\sum_{k=0}^{N-1} \left[\xi^T(k+1) \frac{\partial f\big(k, x(k), u(k)\big)}{\partial u(k)} + \gamma^T(k+1) \frac{\partial F(k, x(k), y(k), u(k))}{\partial u(k)}\right] \Delta u(k)\right\}, \quad (12)$$

using the following vector functions

$$\xi^T(N) = 0, \quad \gamma^T(N) = \frac{\partial \Phi(y_N)}{\partial y_N},$$
$$\xi^T(k) = \gamma^T(k+1) \frac{\partial F(k)}{\partial x(k)} + \xi^T(k+1) \frac{\partial f(k)}{\partial x(k)}, \quad (13)$$

ISBN: 978-3-95450-240-0 ISSN: 2673-5539 doi:10.18429/JACoW-RuPAC2021-TUPSB13

$$\gamma^T(k) = \gamma^T(k+1)\frac{\partial F(k)}{\partial y(k)},$$

$$k = 1, \dots, N-1.$$

Variation of the Functional $I(u)$

Let us consider the functional $I(u)$. It follows from Eq. (9) and Eq. (10), Eq. (12) that the variation of the functional $I(u)$, using auxiliary functions (11), (13), can be represented as

$$\delta I_2 = \max_{y_0 \in Y_0(u)} \left\{ \sum_{k=0}^{N-1} \left[\xi^T(k+1)\frac{\partial f(k,x(k),u(k))}{\partial u(k)} + \beta^T(k+1)\frac{\partial f(k,x(k),u(k))}{\partial u(k)} + \gamma^T(+1)\frac{\partial F(k,x(k),y(k),u(k))}{\partial u(k)} \right] \Delta u(k) \right\}. \quad (14)$$

Thus, expression (14) gives us an analytical representation of the variation of the functional. On the basis of this representation, it is possible to build effective optimization methods taking into account the dynamics of program motion and perturbed motions. This may be important when optimizing the dynamics of charged particles in linear and cyclic accelerators.

CONCLUSION

When optimizing only the functional $I_1(u)$, the control choice does not depend on the perturbed movements, and they do not affect this choice. When optimizing the functional $I_2(u)$ we see from Eq. (12) that the controls depend on both the selected motion and the perturbed motions, and only the "worst" particles are taken into account in the perturbed motions. When studying the functional $I(u)$, equal to the sum of the functionals $I_1(u)$ and $I_2(u)$, we simultaneously optimize both the dynamics of the selected motion and the dynamics of perturbed motions, namely, we estimate the dynamics of the "worst particles", i.e. the greatest deviations from the selected motion. This approach can be effective in solving various problems of optimizing the dynamics of charged particles in accelerators and beam formation systems [8, 9, 11]. We especially note the problems and the need to optimize the dynamic aperture (DA) in cyclic accelerators and colliders [12, 13]. The proposed approach makes it possible to construct new optimization methods. Note that DA is understood as the deflection (in the x or y plane) of the particle that is most distant from the center of the beam (from the trajectory of the central particle), but at the same time remains within the aperture of the accelerator channel. The definition of DA directly implies the need to optimize the dynamics of the "worst particle" in the beam, which leads to a functional of type (4). We also note that transfer matrices or transfer maps can be used to obtain discrete equations of particle dynamics [14].

REFERENCES

[1] A. I. Propoj, Elements of the Theory of Optimal Discrete Processes. Moscow: Nauka, 1973 (In Russian).

[2] D. A. Ovsyannikov, Modeling and Optimization of Charged Particle Beam Dynamics. Leningrad: Leningrad State University Publishing House, 1990 (In Russian).

[3] E. D. Kotina and A. D. Ovsyannikov, "On simultaneous optimization of programmed and perturbed motions in discrete systems", in *Proc. 11th Int. IFAC Workshop on Control Applications of Optimization (CAO 2000)*. St. Petersburg, Russia, July 2000, pp. 183-185.

[4] E. D. Kotina, "Control discrete systems and their applications to beam dynamics optimization", in *Proc. 1st Int. Conf. Physics and Control (PhysCon 2003)*. St. Petersburg, Russia, August 2003, pp. 997–1002, 12370411

[5] E. D. Kotina, "Discrete optimization problem in beam dynamics", *Nucl. Instrum. Methods*, vol. 558, no. 1, pp. 292-294, 2006.

[6] A. D. Ovsyannikov, "Control of program and disturbed motions", *Vestnik of Saint Petersburg University. Series 10. Applied Mathematics. Computer Science. Control Processes*, no. 4, pp. 111-124, 2006.

[7] D. A. Ovsyannikov *et. al*., "Beam dynamics optimization: models, methods and applications", *Nucl. Instrum. Methods,* vol. 558, no. 1, pp. 11-19, 2006.

[8] M. Yu. Balabanov, M. A. Mizintseva and D. A. Ovsyannikov, "Beam dynamics optimization in a linear accelerator", *Vestnik of saint Petersburg University. Applied Mathematics. Computer Science. Control Processes*, vol. 14, no. 1, pp. 4-13, 2018.

[9] D. A. Ovsyannikov *et. al*., "Optimization of dynamics of trajectory bundles using smooth and nonsmooth functionals. Part 1", *Vestnik of Saint Petersburg State University. Applied Mathematics. Computer Science. Control Processes.* vol. 16, no. 1, pp. 73-84, 2020. doi.org /10.21638/11702/spbu10.2020.107

[10] E. D. Kotina and D. A. Ovsyannikov, "Mathematical model of joint optimization of programmed and perturbed motions in discrete systems", *Vestnik of Saint Petersburg State University. Applied Mathematics. Computer Science. Control Processes.* vol. 17, no. 2, pp. 213-224, 2021. doi.org /10.21638/11701/spbu10.2021.210

[11] A. A. Poklonskiy, D. NeuJJer, M. Berz, D. A. Ovsyannikov and A. D. Ovsyannikov, "Optimizing buncher and phase rotator for Neutrino Factory", *Vestnik of Saint Petersburg University. Series 10. Applied Mathematics. Computer Science. Control Processes*, no. 1, pp. 64-76, 2006.

[12] P. V. Snopok, D. A. Ovsyannikov, A. D. Ovsyannikov, C. J. Johnstone and M. Berz, "High-order simulation of muon collider interaction region", *Vestnik of Saint Petersburg University. Series 10. Applied Mathematics. Computer Science. Control Processes*, no. 1, pp. 77-83, 2006.

[13] A. V. Bogomyagkov et. al., "Dynamic aperture of the NICA collider optimized with a genetic algorithm", Physics of Particles and Nuclei Letters, vol. 16, no. 1, pp. 21-29, 2019. doi: 10.1134/S1547477119010060

[14] M. Berz, Modern Map Methods in Particle Beam Physics. San Diego, USA: Academic Press, 1999.

ISBN: 978-3-95450-240-0 ISSN: 2673-5539 doi:10.18429/JACoW-RuPAC2021-TUPSB16

CALCULATION AND OPTIMIZATION OF HIGH-ENERGY BEAM TRANSFER LINES BY THE MONTE CARLO METHOD

D.A. Amerkanov†, E.M. Ivanov, G.A. Riabov, V.A. Tonkikh, NRC "Kurchatov Institute" - PNPI, Gatchina, Leningrad district, 188300, Russia

Abstract

The calculation of high-energy beam lines consists of tracing of the proton beam trajectories along the transport channel from the source. The PROTON_MK program code was developed to carry out such calculations using the Monte Carlo method. The beam from the accelerator is introduced in the form of a multivariate Gaussian distribution in x,x', z,z', dp/p phase space. In the case when an absorber (absorber, air section, window in the channel, etc.) is installed in the transport channel the beam parameters after the absorber are calculated using the GEANT4. The output file of this code can be used as input for the program. The program allows calculation of any beam parameters - intensity, spatial or phase density, energy distribution, etc. The program includes a block for the optimization of beam parameters presented in a functional form. Random search method with learning for search correction based on analysis of intermediate results (so-called statistical gradient method) is used for obtaining the global maximum of a function of many variables. The program has been tested in calculations of the beam transport lines for IC-80 cyclotron and for the development of the beam line for ophthalmology.

INTRODUCTION

There is a many of programs in the world for calculating the optics of high-energy beams [1, 2]. In most of them, the ion source is represented in the phase space in the form of a multidimensional ellipsoid, inside which particles and their initial parameters are uniformly distributed while there are no particles outside. Moreover, it is assumed that the beam emittance is conserved during the transport of the beam along the channel, which means that there are no beam losses in the channel. In particular, it is not possible to compute the effect of collimators on the intensity and other parameters of the beam. These assumptions greatly facilitate the mathematical formulation of the problem, but they do not quite reflect the experimental situation. In this work, a more adequate representation of the ion source is proposed.

REPRESENTATION OF SOURCES

In the experiment, the beam profile i.e. the distribution of the beam intensity over the transverse coordinates is well approximated by the Gaussian distribution, and the beam spot, i.e. intensity distribution in x, z-plane is an ellipse. This situation is typical for a multivariate Gaussian distribution, where any marginal or partial distribution along any axis is also described by a Gaussian distribution. Let's assume that the beam in the ion source can be described by a five-dimensional normal distribution with a distribution function in space (x, x', z, z', δ):

$$f(X,Z,s,\delta)=\frac{1}{(2\pi)^{5/2}|\Sigma|^{1/2}}\exp\left\{-\frac{1}{2}\begin{pmatrix}X\\Z\\\delta\end{pmatrix}^{T}\Sigma^{-1}\begin{pmatrix}X\\Z\\\delta\end{pmatrix}\right\}$$

where $\sum$ is a 5x5 symmetric matrix, which is the covariance matrix of the adopted distribution, i.e. the mathematical expectation of the distribution and its elements are of interest, X is a vector (x, x '), Z is a vector (z, z'). The components of the matrix Σ have the form where $\sigma_{k\ell} = \langle y_k \cdot y_e \rangle$ y_k, y_e are the components of the random vector (x, x', z, z', δ).

In most cases, the movements along x and z are independent and then $\sum_{xz}$=0.In the case when the magnetic analysis takes place only in the x-plane $\sum_{zp}$=0.Based on the general properties of the multivariate normal distribution, it is possible to write the bivariate Gauss distribution in x, x' space in the form:

$$f(X)=\frac{1}{(2\pi)\left|\sum_{xx'}\right|^{1/2}}\exp\left\{-\frac{1}{2}X^{T}\sum_{xx'}^{-1}X\right\}$$

The elements of the correlation matrix Σ_{xx} are the mathematical expectations of the vector (x_i x_j') i.e. M (x_i x_j), where i, j = 1, 2 and x_1 = x, x_2 = x'. The matrix Σ_{xx} has the form:

$$\sum_{xx'}=\begin{pmatrix}M(x^2) & M(xx')\\ M(xx') & M(x'^2)\end{pmatrix}=\begin{pmatrix}\sigma_x^2 & \rho\sigma_x\sigma_{x'}\\ \rho\sigma_x\sigma_{x'} & \sigma_{x'}^2\end{pmatrix}$$

where M (x, x') = $\rho\sigma_x\sigma_{x'}$ by definition of the correlation coefficient ρ.

Then the bivariate Gaussian distribution on the plane takes the form:

$$f(x,x')=\frac{1}{2\pi\sqrt{1-\rho^2}\,\sigma_x\sigma_{x'}}\exp\left\{-\frac{1}{2\left(1-\rho^2\right)}\lambda^2\right\}$$

where σ_x $\sigma_{x'}$ are the standard deviations and ρ is the correlation coefficient. From the general form of the probability density of two random variables, it follows that the probability density is constant in all points of the xx' plane at which

$$\lambda^2=\left(\frac{x^2}{\sigma_x^2}-2\,\rho\,\frac{xx'}{\sigma_x\sigma_{x'}}+\frac{x'^2}{\sigma_{x'^2}}\right)$$

where λ is an arbitrary value.

The curve on the xx' plane, defined by the equations above, is the so-called ellipse of equal probabilities. In the case of a Gaussian distribution, instead of one ellipse, there is a set of concentric ellipses each of which corre-

† amerkanov_da@pnpi.nrcki.ru

ISBN: 978-3-95450-240-0 ISSN: 2673-5539 doi:10.18429/JACoW-RuPAC2021-TUPSB16

sponds to the fraction of the beam particles lying inside the ellipse contour. Let's denote by P(λ) the probability of a beam particle to fall inside an ellipse with a given value of λ parameter and F(λ) the area of this ellipse in phase space.

$$P(\lambda) = \iint_{\lambda} f(x,x')\,dx\,dx' = 1 - \exp\left(-\lambda^2\right),$$

$$F(\lambda) = \iint_{\lambda} dx\,dx' = \sigma_x\,\sigma_{x'}\,\lambda^2 \Big/ \sqrt{1-\rho^2}$$

If δ is a fraction of particles outside the ellipse, then

$$P(\lambda) = 1-\delta,\ \lambda^2 = -2\ln\delta(1-\rho^2)$$

The area of the ellipse F (λ) divided by π determines the emittance of the beam enclosed within the ellipse. The emittance of the beam increases with an increase in the amount of the beam contained within the ellipse. The results presented in the Table 1. demonstrate a relationship between the probability of a beam particle to fall inside an ellipse with a given value of the parameter λ and the beam emittance for the case of a straight ellipse i.e. when ρ = 0.

Table 1: Inside an Ellipse Probability of a Beam Particle

λ^2	δ	P (λ)	F(λ)/ π
1	0.61	0.39	$\sigma_x\ \sigma_{x'}$
2	0.37	0.63	$2\,\sigma_x\ \sigma_{x'}$
3	0.22	0,74	$3\,\sigma_x\ \sigma_{x'}$
4	0.14	0.86	$4\,\sigma_x\ \sigma_{x'}$
6	0.05	0.95	$6\,\sigma_x\ \sigma_{x'}$

Gaussian distribution parameters can be determined by characteristic points of the ellipse. The ellipse of the beam and its three characteristic points x_1, x_2 and x_2' is shown in Fig. 1.

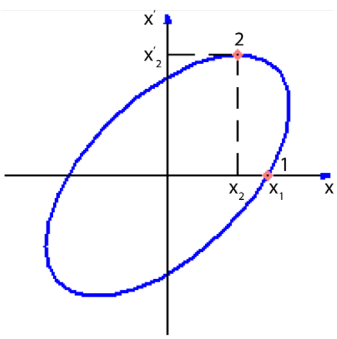

Figure 1: Ellipse of the beam.

$$\sigma_x = x_2 \Big/ \rho\sqrt{-2\ln\delta},\ \sigma_{x'} = x_2' \Big/ \sqrt{-2\ln\delta},\ \rho = x_2^2 \Big/ x_2^2 + x_1^2$$

The sign of ρ corresponds to the sign of x_2. If $x_2 > 0$ then the beam diverges and ρ > 0. If $x_2 < 0$ then ρ< 0 and the beam converges. In the case of ρ = 0, the beam is described by a straight ellipse.

GEANT CODE USAGE

Another way of the generation of the particle source is used when an energy degrader, scattering foil or vacuum window is presented in the channel.

In this situation, the beam behavior in the degrader material is calculated by using the GEANT code. On the output of the program, a file containing the energy, transverse coordinates and velocities of the particles is produced. The file is used as input for further tracing of trajectories through the channel.

THE BEAM TRANSPORT ALONG A CHANNEL

The calculation algorithm is as follows: a five-dimensional vector (x, x′, z, z′, dp/p) randomly generated according to Gaussian distribution determines the initial conditions for a particle at the entrance of the channel. Then the particle with the chosen initial conditions is traced along the channel. The transport channel consists of standard magnetic elements located in different positions: quadruple lenses, various types of magnets, which provide deflection of the beam in different directions. In a linear approximation, the relationship between the input and output coordinates and velocities in the transport element can be obtained using the transition matrix, which is different for each element.

The mathematical expression for the transition matrices has been formulated in many works. In this work, we used the coordinate system and transition matrices from Steffen's monograph [3]. The calculation of the trajectory of a particle along the channel is carried out step-by-step by application of transition matrices for magnetic elements. At the output of each element, the x and z coordinates are compared with the apertures. If a particle falls out of the aperture, then its transport is stopped and it is counted as a lost particle. As a result of multiple repetitions of this procedure (several thousand times), the beam parameters are evaluated at the output of each element.

OPTIMIZATION

In addition to the problem of calculating the beam parameters in a channel with a given configuration, it is often necessary to obtain the optimal value of some beam parameters by varying the magnetic field in channel elements or configuration of the channel. This problem is solved in this work by using the Monte Carlo method. The different beam parameters such as intensity, energy distribution and so on are calculated using the above technique. In our case, one of the random search methods, the statistical gradient method, was used for optimization. The calculation algorithm is as follows. A sequence of random vectors is selected whose components are variable parameters with a normal distribution.

$$\vec{X}^K = (x_1^K, x_2^K, x_3^K, \ldots x_n^K), \quad K = 1,2,\ldots n$$

With dispersions σ_i and mean value X_0. For each set of randomly selected parameters, i.e. for each vector, the

ISBN: 978-3-95450-240-0 ISSN: 2673-5539 doi:10.18429/JACoW-RuPAC2021-TUPSB16

quality function $\Phi(\vec{X}^K)$ is calculated, the maximum $\Phi_m = \max \Phi(X)$ and the vector $\vec{X}^M$ at which $\Phi = \max \Phi$ are found. Then the statistical weight of each variable element is calculated.

$$g_i = \frac{1}{N}\sum_{K=1}^{N}(\Delta\Phi^K \cdot \Delta x_i^K)/\sigma_i^2,$$

$$\Delta\Phi^K = \Phi^K - \Phi^0, \quad \Delta x_i^K = x_i^K - x_i^0$$

It is convenient to use normalized statistical weights

$$y_i = g_i / \sqrt{\sum_{i=1}^{n} g_i^2},$$

where n is the number of variables. Based on a series of trial calculations of the quality function, an attempt is made to move to a point with a larger value of maximum obtained at random search

$$x_i^r = x_i^m + \varepsilon \cdot y_i$$

where ε is a pre-selected factor. Then the function $\Phi^r = \Phi(\vec{X}^r)$ is calculated and compared with Φ_m. If $\Phi m < \Phi^r$, then one more step is made in the direction of the gradient, but if $\Phi_m \geq \Phi^r$, then Φ_m is taken equal to the original Φ_0 and a new cycle of calculations is performed. To reach a better precision it is envisaged to reduce the range of random vectors by reducing values of σ_i and step ε. The process is repeated until the change in Φ or all parameters x_i becomes smaller than a predetermined value.

Constraints on the parameter ranges are easily included in the procedure that is not always possible with regular search methods. As shown in [4], in the presence of constraints on the range of parameter variation in the form:

$$\varphi_j(\vec{X}) \geq 0, \quad j = 1 \ldots m$$

The global maximum search algorithm remains unchanged, and the quality function Φ is assumed to be equal to zero when the coupling condition is violated.

ALGORITHM REALIZATION

Based on the described algorithm, a code with a graphical interface PROTON_MK was developed. The program was written in C ++ and can be compiled to produce an executable file for Windows.

PROTON_MK provides the following opportunities:

- Calculation of the high energy beam transport lines which consist of quadruple lenses, bending magnets, free space, collimators.
- Generation of the particle source - the sample of N particles with the axial momentum of the channel p_0 and parameters of the Gaussian distribution σ_0, σ_x ,σ_x ', σ_z, σ_z', ρ_x, ρ_z, $\Delta p / p$.
- Beam import after the absorber according to GEANT4 calculation.
- The output of beam parameters at any channel element.
- Variation of the operation modes of a large number of optical elements of the channel to optimize the output beam parameters.
- The calculation results are presented in the output report.

The program was tested during the development of the beams with energy of 50–900 MeV by decelerating the primary proton beam with energy of 1000 MeV in a copper absorber. Good agreement of calculation results with experimental data was achieved. Another example of the application of the program was the design of the beam for ophthalmology with a high degree of homogeneity [5] at the IC-80 accelerator. A beam with an intensity of 10 μA is extracted from the accelerator and then is focused onto a thin 300 μm tantalum scattering plate. The collimator after the foil preserves the central and uniform part of the scattered beam in such a way that a beam with a diameter of 60 mm and an intensity of 10^{10} s^{-1} falls into the patient's irradiation room with a 5% uniformity in intensity and a minimum divergence. The beam line for ophthalmology and the beam envelopes are shown in Fig. 2.

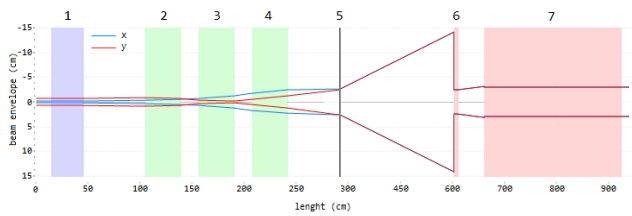

Figure 2: Ophthalmic beam line and beam envelopes on the level 95% of the intensity. 1 - corrector magnet, 2,3,4 – quadruple lenses triplet, 5 - tantalum scattering foil 300μm thick, 6 - collimator, 7 – radiation shielding wall in front of the irradiation room.

REFERENCES

[1] Karl L. Brown, "A First and Second Order Matrix Theory for the Design of Beam Transport Systems and Charged Particle Spectrometers", *SLAC REPORT NO. 75,* no. 1, 1968, pp. 71-134.

[2] K.R. Crandall, D.P. Rusthoi, "TRACE 3-D Documentation" LA-UR-97-886, 1997.

[3] K. Steffen, "High-energy beam optics", 1965.

[4] D.M. Kuzmenkov, V.I. Chernetsky, "Method of searching for global extreme in linear and nonlinear programming problems under arbitrary constraints", *Algorithms and Programs for Random Search ed. Knowledge*, Riga, 1969, p. 145.

[5] D.A. Amerkanov, S.A. Artamonov, E.M. Ivanov, G.A. Ryabov, and V.A. Tonkikh, "Conceptual project of proton beam lines in the nuclear medicine project of the "Kurchatov Institute" - PNPI", presented at the 27th Rus. Particle Accelerator Conf. (RuPAC'21), Alushta, Russia, 26 September – 2 October 2021, paper MOPSA44, this conference.

ISBN: 978-3-95450-240-0 ISSN: 2673-5539 doi:10.18429/JACoW-RuPAC2021-TUPSB17

INVESTIGATIONS OF CHARGE PARTICLE DYNAMICS IN SPACE CHARGE FIELDS

A.S. Chikhachev[1], All-Russian Electrotechnical Institute, 111250, Moscow, Russia

Abstract

The paper studies the nonstationary dynamics of single-component systems. The problem of the dynamics of a plane layer is considered. The classical collisionless system described by the "Meshchersky integral" and the "conjugate" integral of motion is considered. States characterized by a constant charge in nonstationary coordinates are obtained.

INTRODUCTION

The study of non-stationary systems that intensively interact with their own field is of great interest from both experimental and theoretical points of view. In this paper, we will use the nonstationary Hamiltonian, which follows from Meshchersky's work [1]. A similar Hamiltonian was used in [2,3,4], in which, apparently, the problem of exact accounting for the eigenfield was solved for the first time. It should be noted that the model Hamiltonian of a nonstationary system can be used both for a quantum mechanical system and for a classical one. In this paper, the classical system is considered.

CLASSIC COLLISIONLESS SYSTEM

Let us first consider a one-dimensional system of charged particles described by a collisionless kinetic equation. Let x be the coordinate and t be the time. A one-dimensional system can be described by the following nonstationary Hamiltonian:

$$H=\frac{p^2}{2m}+\frac{1}{\xi^2(t)}U\left(\frac{x}{\xi(t)}\right) \tag{1}$$

Where $p=m\dot{x}$, $\xi(t)$ - the characteristic function that satisfies the equation $\ddot{\xi}=\frac{\lambda}{\xi^3(t)}$, Where λ - constant.

If, next, enter new variables $x_*=\frac{x}{\xi(t)}$, $\tau=\int\frac{dt'}{\xi^2(t')}$, then from (1.1) we can obtain an expression for the integra of motion:

$$I=\frac{m}{2}\left(\frac{dx_*}{d\tau}\right)^2+\frac{m\lambda}{2}x_*^2+U(x_*). \tag{2}$$

Potential function $U(x_*)=q\xi^2\Phi\left(\frac{x}{\xi}\right)$, where is the elementary charge , is the electrostatic potential. In variables, the expression (2) is essentially the Hamiltonian of a stationary (i.e., independent of) systems, and the role of the potential is played by the expression $\frac{m\lambda x_*^2}{2}+U(x_*)$.

In addition to (2), there is a conjugate integral:

$$J_I^{\pm}=\pm\int_0^{x_*}\frac{dx_*'\sigma\left(\frac{2}{m}(I-U(x_*'))-\lambda x_*'^2\right)}{\sqrt{\left(\frac{2}{m}(I-U(x_*'))-\lambda x_*'^2\right)}}-\tau,$$

here σ is the Heaviside function. The velocity of a particle can be represented as the sum of the portable (or nasal) velocity - this is the magnitude $x\frac{\dot{\xi}}{\xi}$ and relative-

$$\upsilon_x'=\pm\sqrt{\frac{2}{m}(I-U(x_*))+\frac{x_*^2}{4\tau_0^2}}.$$

In this case, the relative movement in the positive and negative directions of the axis is possible x. Consider the case of relative forward motion: $\upsilon_x'>0$, then

$$J_I^{=}=\int_0^{x_*}\frac{dx_*'\sigma\left(\frac{2}{m}(I-U(x_*'))-\lambda x_*'^2\right)}{\sqrt{\left(\frac{2}{m}(I-U(x_*'))-\lambda x_*'^2\right)}}-\tau.$$

Performing equality $\frac{dJ_I^+}{d\tau}\equiv 0$ is trivial.

Previously, conjugate integrals of motion, apparently for the first time, were considered in [2].

There are, further, two possibilities: to study the dynamics of a clot with an increasing and decreasing function $\xi(t)$. Let us first consider the case of a decreasing $\xi(t)=\sqrt{\xi_0^2-\frac{t}{\tau_0}}$. In this case,

[1]churchev@mail.ru

ISBN: 978-3-95450-240-0 ISSN: 2673-5539 doi:10.18429/JACoW-RuPAC2021-TUPSB17

$\xi(\tau)=\xi_0\exp\left(-\frac{\tau}{2\tau_0}\right)$. Let, further, the density $n=\int d\dot{x}f\left(I,J_I^+\right)$, potential - $U\left(\frac{x}{\xi}\right)=U\left(x_*\right)$.

Poisson equation

$$\frac{d^2U\left(x_*\right)}{dx_*^2}=-4\pi q^2\xi^3\int\frac{dIf\left(I,J_I^+\right)}{\sqrt{\frac{2}{m}\left(I-U\right)-\lambda x_*^{'2}}}.$$

Complete self-consistency is achieved when the integral on the right side is proportional to ξ^{-3}. It is enough to take the distribution function in the form :

$$f=\kappa_*\delta\left(I-I_0\right)\exp\left(-\frac{3}{2\tau_0}J_I^+\right) \tag{3}$$

Note that $\exp\left(\frac{\xi_0^3}{\xi}\right)=\frac{\xi_0^3}{\xi^3}$ In this case, the density is as follows:

$$n=\frac{\kappa}{\xi^4\sqrt{\frac{2}{m}\left(I_0-U\right)-\lambda x_*^2}}\exp\left\{-\frac{3}{2\tau_0}\int_0^{x_*}\frac{dx_*'\sigma\left(\frac{2}{m}\left(I_0-U\left(x_*'\right)\right)-\lambda x_*^{'2}\right)}{\sqrt{\frac{2}{m}\left(I_0-U\left(x_*'\right)\right)-\lambda x_*^{'2}}}\right\}$$

The Poisson equation is reduced to the form:

$$U''\left(x_*\right)=-4\pi q^2\xi_0^3\frac{\kappa}{\sqrt{\frac{2}{m}\left(I_0-U\left(x_*\right)\right)-\lambda x_*^2}}\times \tag{4}$$

$$\exp\left\{-\frac{3}{2\tau_0}\int_0^{x_*}\frac{dx_*'\sigma\left(\frac{2}{m}\left(I_0-U\left(x_*'\right)\right)-\lambda x_*^{'2}\right)}{\sqrt{\frac{2}{m}\left(I_0-U\left(x_*'\right)\right)-\lambda x_*^{'2}}}\right\}$$

Denote, next,

$$\upsilon_0^2=\frac{2I_0}{m},s=\frac{x_*}{2\tau_0\upsilon_0},s_0=\frac{x_{*0}}{2\tau_0\upsilon_0},y=\frac{2U}{m\upsilon_0^2},$$

$$u(s)=\int_{s_0}^{s}\frac{ds'\sigma\left(1-y\left(s'\right)+s'^2\right)}{\sqrt{1-y\left(s'\right)+s'^2}}.$$

Then the Poisson equation follows:

$$y''\left(s\right)=-\kappa_1u'\left(s\right)\exp\left\{-3u\left(s\right)\right\},$$

$$u'\left(s\right)=\frac{\sigma\left(1-y\left(s\right)+s^2\right)}{\sqrt{1-y\left(s\right)+s^2}}. \tag{5}$$

Note that the current density consists of two terms - the first of which is the "nose" type, independent of the field. The second term-defined by the relative velocity, $\upsilon_*=\sqrt{\frac{2}{m}\left(I_0-U\right)-\lambda s^2}$, depends on the field.

The density and current density are: $n=\frac{n_0}{\xi^4}u'\exp\left\{-3u\right\},j_x=\frac{n_0v_0}{\xi^5}\left(1-su'\right)\exp\left\{-3u\right\}.$

Let's rewrite the system (5) in the following form:

$$y'=\frac{\kappa_1}{3}\exp\left\{-3u\left(s\right)\right\}-C_0,$$

$$u'\left(s\right)=\frac{\sigma\left(1-y\left(s\right)+s^2\right)}{\sqrt{1-y\left(s\right)+s^2}}. \tag{6}$$

in this case, the value κ_1 determines the boundary condition: $y_0'=\frac{\kappa_1}{3}+C_0$.

Figure 1 shows the solution of this system when $\kappa_1=3,y\left(0\right)=0,u\left(0\right)=0,C_0=-1,$ and Fig. 2 shows the dependence of the total charge of the clot (layer) and the current from s.

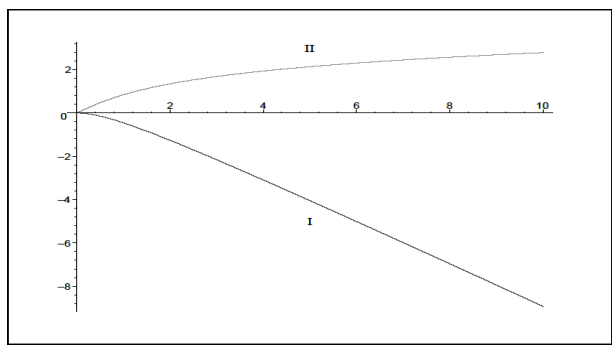

Figure 1: Dependencies y(s) (I) and u (s) (II).

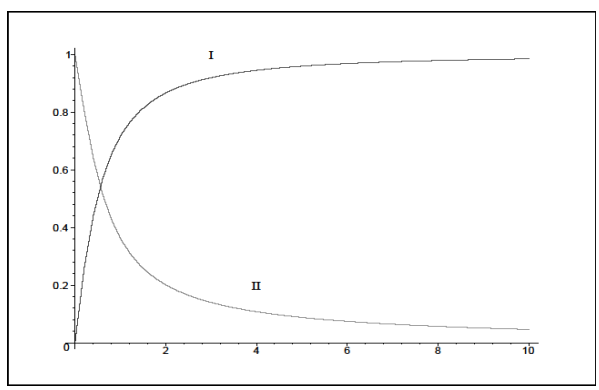

Figure 2: Dependence of the total charge.

ISBN: 978-3-95450-240-0 ISSN: 2673-5539 doi:10.18429/JACoW-RuPAC2021-TUPSB17

layer from s (I) and current from s (II).

The curve I in Fig. 2 shows the output to the state with the full charge of the layer in the variables S, τ. In the variables x, t this corresponds to the decrease in the charge of the layer and its size proportionally $\xi(t) = \sqrt{\xi_0^2 - \frac{t}{\tau_0}}$. In the case of a growing function $\xi(t)$ when the charges move in the negative direction of the axis x, then the total charge of the layer, constant in the variables in the variables x, t will grow. Note that the constant charge of the layer in non-stationary variables can be obtained only in the case when the transport and relative velocities have opposite directions.

CONCLUSION

In this paper, we study nonstationary self-consistent solutions for the potential of a flat layer and a spherical cluster of charges interacting with an eigenfield. The collisionless kinetic problem was solved.
The results of numerical solutions for the density and potential as functions of a self-similar variable are presented.

It is shown that it is possible for a collisionless system to reach a state with a constant charge in nonstationary coordinates x_*, τ. The rate of change of the total charge in the variables is determined by the time parameter τ_0 by $\tau_0 \to \infty$ the charge can remain almost constant. It is possible that the considered problem is interesting when solving the problem of accumulation of large charges.

Previously, solutions of problems in systems interacting with an eigenfield were considered in [2,3,4].

REFERENCES

[1] J. Mestschersky, “Uber die Integration der Bewegungs-gleichungen im Probleme zweier Korper von verandlicher Masse”, *Astron.Nachr.*, v.159, p.229, 1902.

[2] A.S. Chikhachev, “Nonstationary self-consistent model of an ensemble in its own field”, *Technical Physics*, vol. 59, No. 4, p. 474, 2014.

[3] A.S. Chikhachev “Dynamics of electric charges in a self-consistent field in a spherical-symmetric system”, *PEPAN*, vol. 17, No. 3, pp. 325-327, 2020.

[4] A.S. Chikhachev, “System of charges in an eigenfield” *IISJ*, vol. 20, pp.8-17, 2020.

ISBN: 978-3-95450-240-0 ISSN: 2673-5539 doi:10.18429/JACoW-RuPAC2021-TUPSB20

SELECTION OF A SYSTEM FOR CORRECTING THE ENERGY SPREAD OF RELATIVISTIC ELECTRON BUNCHES FOR A FREE ELECTRON LASER

A. M. Altmark†, N. A. Lesiv, K. Mukhamedgaliev, Saint-Petersburg Electrotechnical University "LETI", Saint-Petersburg, Russia

Abstract

The object of this work is a device called dechirper, which is used to decrease energy spread in relativistic electron bunch for free electron laser application. This system is based on cylindrical dielectric waveguide with vacuum channel needed for electron bunch passing. The Vavilov-Cherenkov radiation excited in waveguide is used to profile electromagnetic field inside the bunch and therefore to achieve the required energy distribution. The work includes numerical modeling of the electron beam passage through a waveguide structure, the generation of wake radiation and the interaction of this radiation with an electron bunch. We made original code to carry out numerical modeling, where the method of macroparticles and the method of Green's function are implemented. The dependences of the energy compression coefficient and the length at which the maximum energy compression coefficient is achieved on various parameters of the dielectric waveguide structure and the physical parameters of electron bunches were identified. Various recommendations were also made on the choice of a waveguide used as a dechirper.

INTRODUCTION

The use of undulators for the generation of monochromatic laser radiation is related with energy spread reducing inside electron bunch, implemented with the help of dechirpers. The main advantage of plasma-based dechirpers [1] is the high values of the generated fields, but the realization of such a scheme is associated with high cost of technical implementation and plasma nonstability. Widespread dechirpers based on rectangular dielectric waveguide [2] due to simplicity manufacturing technology of waveguide as well as possibility of adjustment distances between plates. Dielectric rectangular structures are used in STFC Daresbury Laboratory developing Free Electron Laser (FEL) CLARA [3]. Th structure consisting of pairs of flat, metallic, corrugated plates is used in SLAC [4] which, despite its simplicity, has a significant limitation in the form of a low breakdown voltage. This work is concentrated on reducing of energy spread of bunch in cylindrical dielectric waveguide, as it becomes possible to generate higher fields compared to rectangular structure with the same charge and bunch length. In addition, in this case, there are no problems of instability of the structure that accompanies the plasma waveguide.

† aaltmark@mail.ru

INITIAL PARAMETERS

Dechirper is a part of a FEL that serves for energy spectrum correction of relativistic electron bunch, Fig. 1.

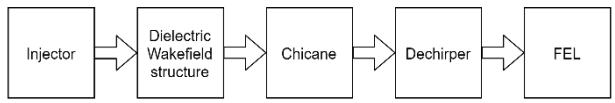

Figure 1: Beam preparation scheme for FEL.

After being generated in the injector, the bunch enters in the wakefield dielectric structure where it is placed in field of another bunch, called "driver". The bunch is placed at a point in the field to create an energy distribution along the bunch when the energy of "head" is less than the energy of the "tail", Fig. 2. This energy distribution is needed for chicane (system of dipole magnets), where it is compressed and then enters in the dechirper. Last one is represented by cylindrical dielectric waveguide (CDW), Fig.2, where the bunch creates a wakefield within itself to profile the energy with minimum spread. There is a clear dependence of its radiation spectrum on the energy distribution along the bunch length. A higher monochromaticity of FEL radiation is observed with a more uniform distribution of energy.

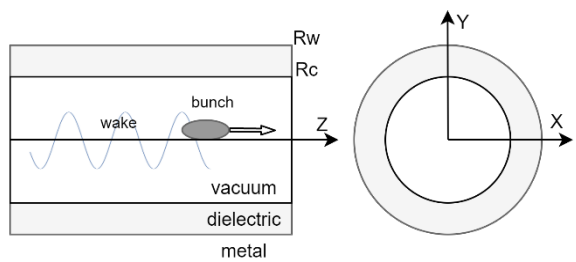

Figure 2: Dechirper based on cylindrical dielectric waveguide.

This paper considers a problem in which a relativistic electron bunch with a given energy distribution along the length enters in CDW(*Rc* – inner radius, *Rw* – external radius, ε – dielectric constant), Fig.2, with dielectric filling and physical parameters of the bunch: *Q* – charge of bunch; *W* – bunch energy; Δ*W* – the spread of the energy; *offset_x* – dismission of the bunch along the *X*-axis, σ_x, σ_y, σ_z is the standard deviation of Gaussian bunch along the corresponding direction.

The monoenergetic coefficient *C* is obtained from the ratio of the maximum energy difference of the particles in the bunch (ΔW_{max}) and the average energy of the bunch *W*. The energy compression coefficient (ECC) *D* is obtained from the ratio of C_0 in start of calculation and C_f at

ISBN: 978-3-95450-240-0 ISSN: 2673-5539 doi:10.18429/JACoW-RuPAC2021-TUPSB20

the end of calculation. The distance at which the maximum of ECC is reached will be denoted by L_{Dmax}.

We used Euler's numerical method and the macroparticle method [5] to calculate the beam dynamics along a cylindrical waveguide. The main equations are the equations of relativistic kinematics.

ANALYSIS OF RESULTS

The dependence of the ECC on W in a cylindrical waveguide is present for next parameters of CDW: Rc = 0.5 cm, Rw = 0.6 cm, ε = 3.75. The plot on Fig.3 shows the dependence of the distance L_{Dmax} on energy W. The ECC practically does not change. The efficiency of energy redistribution between particles decreases due to difference between the speed of the bunch and the phase velocity of the electromagnetic wave in the medium, therefore L_{Dmax} depends on W as linear function.

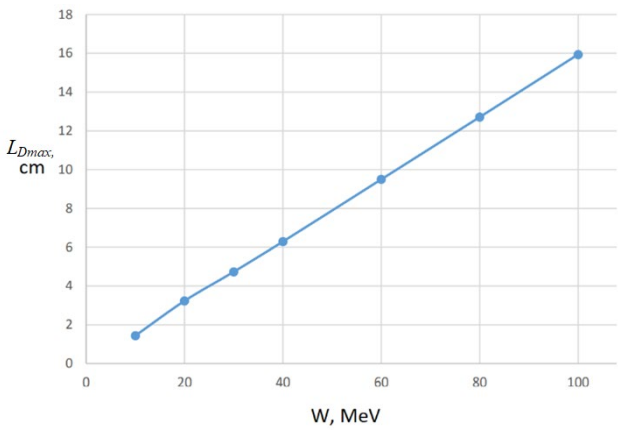

Figure 3: Dependence of L_{Dmax} on energy.

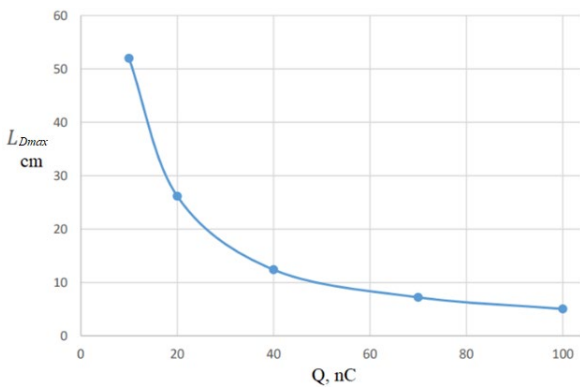

Figure 4: Dependence of L_{Dmax} on bunch charge.

From the plot on Fig. 4, the L_{Dmax} is decreases sharply as a function of Q due to proportionality of charge and wakefield amplitude. The value of wakefield limits the distance L_{Dmax}. The ECC changes in a small range of quantities since the field structure does not change with variation of bunch charge.

Table 1 shows the dependence of D_{max} on the ε, which is determined by superposition of modes in the wakefield for next parameters: Rc = 0.5 cm, Rw = 0.6 cm, Q = 100 nC, W = 50 MeV, ΔW = 5 MeV, $\sigma_x = \sigma_y$ = 0.00035 cm, σ_z = 0.001 cm. Symmetrical modes make the main role in the formation of the field structure after value of ε = 5. The values of D_{max} depending on the ε at *offset_x* = 0. 002 cm decreases after the value of ε = 5 due to the excitation of a greater number of asymmetric modes.

Table 1: Calculation Results for Different Values of ε

ε	*offset* = 0 cm		*offset* = 0.002 cm	
	D_{max}	L_{Dmax}, cm	D_{max}	L_{Dmax}, cm
2	1.03972	9. 35	1.03511	6.54
2.25	1. 0468	10. 91	1.04235	8.69
2.5	1. 4086	9. 47	1.03957	7.19
3	1.36150	8. 36	1.03747	6.80
5	1.03278	7. 88	1.03328	6.95
8	1.03500	9. 38	1.03279	6.98
12	1. 3688	11. 21	1.03295	7.76
20	1.03622	13. 19	1.03094	8.81

The values of D_{max} and L_{Dmax} increase with the thickness of the dielectric, which is also explained by the growing of excited modes (see Table2). This calculations were made for next parameters: Rw = 2 cm, Q = 100 nC, W = 50 MeV, ΔW = 5 MeV,$\sigma_x = \sigma_y$ = 0.00035 cm, σ_z = 0.001 cm.

Table 2: Calculation Results Different Values of Rc

Rc, cm	D_{max}	L_{Dmax}, cm
1.0	1.01920	12.80
1.1	1.01952	14.29
1.2	1.01997	16.03
1.3	1.02181	19.39
1.4	1.02124	20.32
1.5	1.02111	21.76
1.6	1.02113	23.47
1.7	1.02118	25.27
1.8	1.02118	27
1.9	1.02170	29.73

With the growth of the transverse bunch displacement *offset_x* from the waveguide axis, the number of excited asymmetric modes also grows. Therefore, the field amplitude module and its structure are changed, which in this case leads to an increase in the value of D_{max} and a decrease *of* L_{Dmax}, Fig 5. However, the bunch location nearby dielectric layer leads to Beam BreakUp Instability (BBU) [6] due to the transverse effect of asymmetric fields.

CONCLUSION

Based on the obtained dependencies, we give some recommendations for choosing a waveguide structure used as a dechirper. During the analysis, it was obtained that the value *of* L_{Dmax} is influenced by the energy, charge, and bunch displacement from the axis of the waveguide, as well as the thickness of the dielectric layer.

The selection of these parameters can achieve the desired length of the dechirper. It must be considered that in dechirpers of small length (about 3-5 cm) the wakefield

ISBN: 978-3-95450-240-0 ISSN: 2673-5539 doi:10.18429/JACoW-RuPAC2021-TUPSB20

will not have time to fully form and, accordingly, the dechirping effect will not be observed.

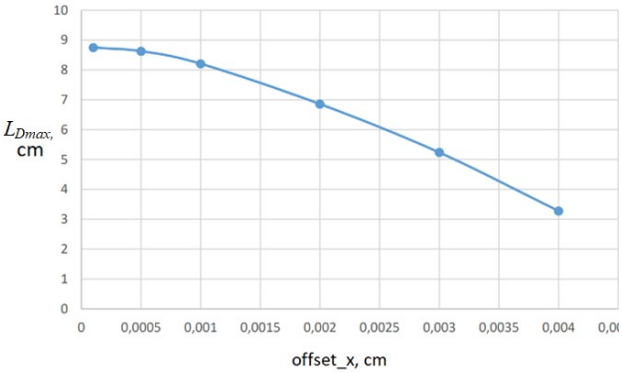

Figure 5: Dependence of L_{Dmax} on transverse displacement.

Low values of energy and charge lead to the instability of the bunch and the formation of a field with a weak amplitude. These parameters practically do not change the structure of the field. So, it is possible to achieve the desired length of the dechirper almost without changing the structure of the field. By changing the dielectric permeability, dielectric thickness, and bunch displacement, it is possible to achieve a suitable ECC, but it should be borne in mind that changing several of these parameters at once does not always lead to an increase in the ECC.

REFERENCES

[1] Y. P. Wu *et al.*, "Phase space dynamics of a plasma wakefield dechirper for energy spread reduction", *Phys. Rev. Lett.*, vol. 122, no. 20, p. 204804, Apr. 2019. doi:10.1103/PhysRevLett.122.204804

[2] F. Reimann, U. van Rienen, U. Lehnert, and P. Michel, "Wakefield-based dechirper structures for ELBE", in *5th International Particle Accelerator Conference (IPAC'2014)*, Dresden, Germany, Jun. 2014, pp. 2882-2884. doi:10.18429/JACoW-IPAC2014-THPRO012

[3] M. Colling, D. Dunning, B. Fell, T. Pacey and Yu. Saveliev, "Mechanical design of a dielectric wakefield dechirper system for CLARA", in *10th International Particle Accelerator Conference (IPAC'2019)*, Melbourne, Australia, May 2019, pp. 1912-1915. doi:10.18429/JACoW-IPAC2019-TUPRB108

[4] J. Zemella *et al.,* "Measurements of wake-induced electron beam deflection in a dechirper at the Linac Coherent Light Source", *Phys. Rev. Accel. Beams*, vol. 20, no. 10, p. 104403, Aug. 2017. doi:10.1103/PhysRevAccelBeams.20.104403

[5] Eun-San Kim, A. Sessler and J. Wurtele, "Analysis of the longitudinal collective behavior in a 50 GeV × 50 GeV muon collider ring", *Phys. Rev. Accel. Beams*, vol. 2, p. 051001, May 1999.

[6] D. Shchegolkov, "Suppressing parasitic effects in a long dielectric wakefield accelerator", *AIP Conf.Proc.*, vol. 1777, p. 070009, Oct. 2016. doi:10.1063/1.4965652

ISBN: 978-3-95450-240-0 ISSN: 2673-5539 doi:10.18429/JACoW-RuPAC2021-TUPSB21

SYSTEM FOR CORRECTING THE LONGITUDINAL LENGTH OF ELECTRON BUNCHES FOR GENERATION A FREE ELECTRON LASER

A. M. Altmark†, N. A. Lesiv, K. Mukhamedgaliev, Saint-Petersburg Electrotechnical University "LETI,", Saint-Petersburg, Russia

Abstract

The chicane is device for longitudinal compression of electron bunch for generation of coherent radiation in free electron laser. It is present a numerical simulation of beam dynamics passing through system which consist dielectric waveguide and four dipole magnets. The simulations made with use the modified Euler method based on Green-function knowledge for electromagnetic field. We researched influence of various physical parameters of the electron bunch, as well as the chicane parameters on the change in the longitudinal bunch length. The optimal parameters of the focusing system were proposed for a relativistic particle beam with given initial bunch parameters. Recommendations for the selection of chicane parameters are also presented.

INTRODUCTION

The beam compression is necessary for a variety of applications, such as, for example, the generation of short X-ray pulses [1]. To implement the compression of beams can, for example, using Laser Wake Field Accelerator (LWFA), which forms the necessary energy profile for the further use of this beam in a free electron laser (FEL) [2,3]. Also, for profiling of beam energy it is used Plasma Wake Field Accelerator (PWFA) [4]. The scientists of Argonne Wakefield Accelerator (AWA) employees are developing a compression system to generate a sequence of beams [5], which can then be used to produce THz radiation. The problem of generating a short beam in Stanford Linear Accelerator (SLAC) is solved using a periodic structure [6], where the wakefield creates a profile of the beam energy necessary to create the Linac Coherent Light Source (LCLS), which is part of FEL project. The purpose of this work is to obtain the recommended parameters of the chicane, based on bunch dimensions and the distribution of energy inside the bunch.

INITIAL PARAMETERS

A relativistic bunch of charged particles with a given linear distribution of energy and bunch length flies through chicane – a system consisting of four two-half magnets.

Simple scheme of chicane illustrated on Fig.1 and consists of four dipole magnets. The high-energy particles located in the "tail" of the bunch move along a short path and catch up with low-energy particles located in the "head" of the bunch, which move along a longer path, thus compressing the bunch.

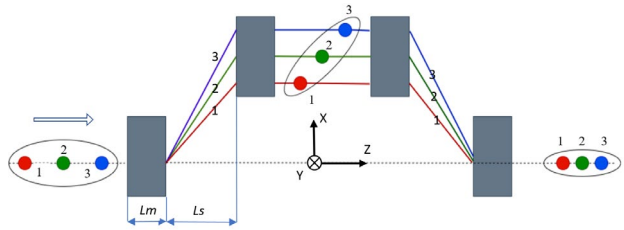

Figure 1: Schematic representation of a chicane consisting of four two-way magnets (1 – "tail" head of bunch and 3 – "head" of bunch).

It is necessary to determine the final length of the bunch, after the flight of the chicane, as well as to consider the influence of the bunch parameters and the parameters of the magnetic system on it. We use a qualitative characteristic of bunch, which is called a compression coefficient along the bunch length A. It is defined as:

$$A = \frac{l_0 - l_f}{l_0} 100\%,$$

where l_0 is initial bunch length, l_f is final bunch length.

It is also important to note that the height of the magnetic sections is infinite during chicane modeling. Therefore, we exclude in our numerical modeling the situation when particles do not fall into dipole magnets.

In this paper, to calculate the beam dynamics in chicane, two numerical based on macroparticle method [7] and the Euler method. According to macroparticle method the bunch is represented by number of interacting identical particles. This way allows significantly increase the speed of calculations. This method is quite simple to implement and less expensive compared to other methods of calculation. Also, we used modified Euler method was chosen to the simulation.

We choose initial data for numerical simulations: a magnetic system consisting of four dipole magnets arranged symmetrically with a magnetic field B = 1 T, length of magnetic section Lm = 2 cm, the distance between the magnetic sections Ls = 2 cm, the charge of the bunch Q = 0.16 fC, transverse dimensions (σ_x and σ_y) = 0.01 mm, longitudinal size of the bunch (standard deviation) σ_z = 0.1 mm, radial displacements along the axes X and Y (*offset_x*, *offset_y*) = 0 cm, bunch energy W = 1000 MeV, relative energy spread $\varkappa$ = 5 %.

It has been shown that the modified Euler method is stable with a sufficiently large number of particles, so it can be used for numerical modeling. Minimum number of *Nopt* lies in the range of 1000 or more particles. For present experiments, this number of particles will be used.

The first experiment is made to identify the dependence

† aaltmark@mail.ru

ISBN: 978-3-95450-240-0 ISSN: 2673-5539 doi:10.18429/JACoW-RuPAC2021-TUPSB21

of coefficient *A* from the bunch energy with the fixed parameters of the bunch and chicane. It can be seen from calculation results (see Table 1) that energy growing causes a sharp decline of coefficient *A*.

Table 1: Dependence of the Compression Coefficient on the Energy of the Bunch

W, MeV	A, %
10	1.99025
100	0.082693
500	0.022229
1000	0.000216
10000	0.000002

This phenomenon is caused by the fact that if a bunch has a lot of energy, then the magnitude of the magnetic field B = 1 T is not enough to deflect the particles to the required trajectory and the electrons fly almost along their initial trajectory. It follows that small bunch energy causes strong influence of the magnetic field. In this case, the particles start to rotate inside magnetic section.

The next stage of the experiments was to determine the dependence coefficient *A* the bunch on the relative energy spread $\varkappa$, Fig. 2.

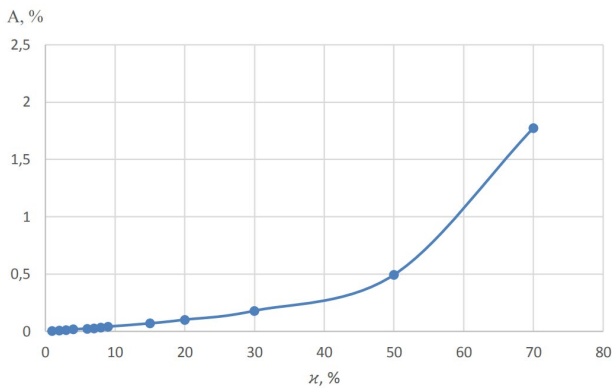

Figure 2: Dependence of the compression coefficient on the energy spread.

Based on this plot, it can be concluded that in the range of $\varkappa$ from 7% to 70%, there is an increase in the compression. This can be explained by the circumstance that large energy spread leads to growing of particles with high-energy. This fact increasing the probability of compression of the bunch.

Table 2: Dependence of the Compression Coefficient on the Longitudinal Length of the Bunch

$\sigma_{z,\ um}$	A, %
0.1	19.711600
1	1.784560
100	0.021851
1000	0.001933
1250	0.001190

The influence of bunch sizes on compression shows that the change in the transverse dimensions (σ_x, σ_y) does not affect *A*. Conversely, the increase of longitudinal bunch length (see Table 2) leads to sharp decline of compression coefficient *A* along the length. This is since at low values of σ_z, the distance between the electrons decreases, thereby reducing the time the flight of high-energy particles relative to low-energy particles. As a result of this process the "fast" particles catch up with the "slow" during the flight in chicane.

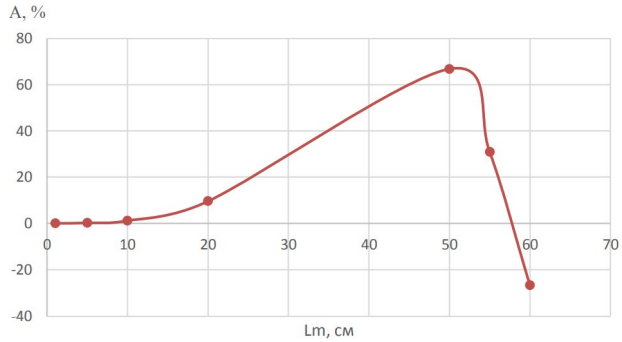

Figure 3: Dependence of the compression coefficient on the length of the magnetic section.

The dependency *A* (*Lm*), Fig. 3, explained by the fact that with an increase of magnetic section the bunch flight length also grows. It follows that high energy particles have time to catch up with low energy particles and the longitudinal length of the bunch becomes minimal. However, with large values of *Lm*, the "fast" particles begin to overtake the "slow" ones, which lead to stretch of bunch along the *Z* axis.

Analyzing the dependence of *A* (*Ls*), Fig.4, we can say that the increase in the value of *A* occurs for similar reasons as in the case of a change in the length of magnets *Lm*. That is, based on the same geometric considerations (increasing the length of the path of the particles), the bunch is pulled along the *Y* axis.

Because the phase volume should be conserved in time (Liouville's theorem on the conservation of the phase volume in space), it can be concluded that the projection of the bunch on the Z axis should decrease, which is what happens in this case.

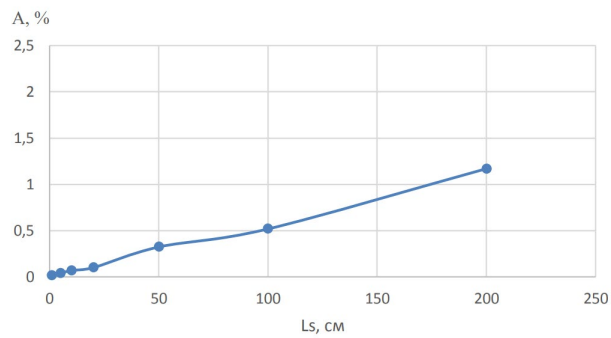

Figure 4: Dependence of the compression coefficient on the distance between the magnetic sections.

In the future, with a sufficiently large distance between the magnets, the value of *A* will drop sharply, because there will be a similar effect as when changing the length *Lm*. Given the above, it is necessary to select the distanc-

ISBN: 978-3-95450-240-0 ISSN: 2673-5539 doi:10.18429/JACoW-RuPAC2021-TUPSB21

es between the sections for certain lengths of magnets to achieve the optimal value of the compression coefficient *A*.

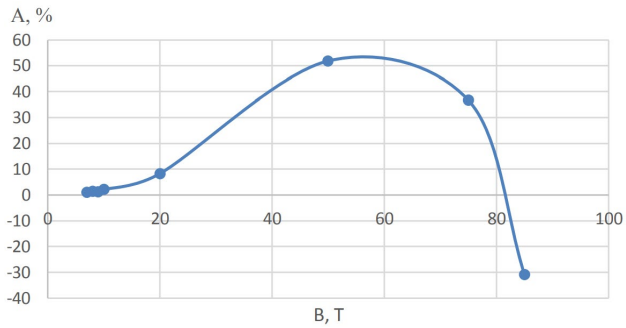

Figure 5: Dependence of the compression coefficient on the magnetic field value of the magnetic section.

When analyzing the dependence $A(B)$, Fig.4, it can be seen that at high values of magnetic induction, the compression coefficient A takes negative values. This is since some of the particles either fly away at a sufficiently large distance, or are reflected, thus, the magnetic section plays the role of a magnetic "wall". At low values of the magnitude of field B, the magnetic sections have practically no effect. As a result, the value of A takes on small values.

CONCLUSION

For a relativistic electron bunch with given initial physical parameters, the optimal parameters of the magnetic system were selected to achieve maximum compression of the longitudinal bunch length (see Table 3).

Table 3: Recommended Pattern Parameters for a Clump of Electrons with Specified Parameters

Parameter	Value	Parameter	Value
N	1000	σ_z, cm	100
Q, fC	16	Lm, cm	10
W, MeV	100	Ls, cm	10
$\varkappa$, %	5	B, T	6
σ_x, cm	10	A, %	97.5
σ_y, cm	10		

As a result of the analysis, it was revealed that the change in A is strongly influenced by such physical parameters of the beam as the energy of the bunch, the spread of energy in the electron bunch, the initial longitudinal length of the relativistic bunch, as well as the parameters of the stain. It is necessary to consider the fact that some values of the compression coefficient along the length at certain parameters of the bunch were achieved by modeling bulky magnetic systems with large magnetic field values, which in real life is quite impractical to use.

As a result of the analysis of the calculation results, it was revealed that the change in A is strongly influenced by such physical parameters of the beam as the bunch energy W, the relative spread of energy $\varkappa$, the initial longitudinal length, and the chicane parameters. It is necessary to consider the fact that some values of the compression ratio along the length at certain parameters of the bunch were achieved by simulating bulky magnetic systems with high magnetic field values, which in real life is rather inappropriate to use.

REFERENCES

[1] L. Bentson, P. Emma and P. Krejci, "A new bunch compressor chicane for the SLAC linac to produce 30-fsec, 30-kA, 30-GeV electron bunches", in *8th European Particle Accelerator Conference (EPAC'02)*, Paris, France, May 2002, pp. 683-685.

[2] A. Loulergue *et al.*, "Beam manipulation for compact laser wakefield accelerator based free-electron lasers", *New J. Phys.*, vol. 17, no. 2, p. 023028, Feb. 2015. doi:10.1088/1367-2630/17/2/023028

[3] V. Afonso Rodriguez *et al.*, "Design optimization for a non-planar undulator for the JETI-laser wakefield accelerator in Jena", in *2th International Particle Accelerator Conference (IPAC'11)*, San Sebastian, Spain, Sep. 2011, pp. 1452-1454.

[4] J. Pfingstner, E. Adli, C. Lindstrøm, E. Marín and D. Schulte, "Considerations for a drive beam scheme for a plasma wakefield linear collider", in *7th International Particle Accelerator Conference (IPAC 2016)*, Busan, Korea, Jun. 2016, pp. 2565-2568. doi:10.18429/JACoW-IPAC2016-WEPMY010

[5] G. Ha et al., "High-charge-short-bunch operation possibility at Argonne Wakefield Accelerator Facility", in *6th International Particle Accelerator Conference (IPAC'15)*, Richmond, Virginia, USA, May 2015, pp. 89-91. doi:10.18429/JACoW-IPAC2015-WEPWA034

[6] K. Bane et al., "Measurement of the longitudinal wakefield in the SLAC linac for extremely short bunches", in *Particle Accelerator Conference (PAC'03)*, Portland, OR, United States, May 2003. doi:10.1109/PAC.2003.1289836

[7] P. Baxevanis and G. Stupakov, "Novel fast simulation technique for axisymmetric plasma wakefield acceleration configurations in the blowout regime", *Phys.Rev.Accel.Beams*, vol. 21, no. 7, p. 071301, Jul. 2018. doi:10.1103/PhysRevAccelBeams.21.071301

ISBN: 978-3-95450-240-0 ISSN: 2673-5539 doi:10.18429/JACoW-RuPAC2021-TUPSB22

WAKEFIELD UNDULATOR BASED ON A SINUSOIDAL DIELECTRIC WAVEGUIDE*

I. L. Sheinman†, O. S. Alekseeva, Saint-Petersburg Electrotechnical University "LETI", Saint-Petersburg, Russia

Abstract

The idea of creating an undulator based on the wake principle by passing a beam through a sinusoidal dielectric waveguide is proposed. A numerical analysis of the dynamics of a short electron beam in a wake undulator on a bending wave of a waveguide with a dielectric filling is carried out. The possibility of reducing the instability of the beam by choosing the initial phase of the flexural wave and the initial transverse positioning of the beam is considered.

INTRODUCTION

Undulators are key elements of free electron lasers [1]. They are devices in which the electron beam in the process of movement experiences the action of transverse periodic force. The oscillations of particles arising under the force in the transverse direction are accompanied by accelerated motion of the particles, which, in turn, generates electromagnetic radiation in the direction of the beam movement. To create a transverse force, electromagnetic fields created by periodically located dipole magnets are used. Undulator radiation also arises when particles move through a periodic lattice of crystals, where the local fields of atoms play the role of deflecting fields.

Undulators have a number of features that make them attractive for creating free electron lasers: a large beam aperture; short undulator period, the ability to generate waves of both circular and plane polarization, dynamic control of the wavelength and undulator coefficient.

Linear charged particle accelerators are used as sources of electron bunch sequences for free electron lasers. An intensively developing direction in recent years is the use of linear wakefield accelerating structures with dielectric filling. They are based on the principle of excitation of Cherenkov radiation in dielectric waveguides by a high-current relativistic electron beam.

The leading bunch (driver) with a large charge, moving along the axis of the vacuum channel of the dielectric waveguide, generates behind itself a wake electromagnetic wave of Cherenkov radiation, the phase velocity of which is equal to the speed of the driver. This wave has a longitudinal field component, which is used to accelerate the witness bunch.

A significant drawback of this approach is the exponentially increasing displacement of the beam relative to the waveguide axis, associated with the interaction of the beam with the wakefield generated by it itself, as a result of which the particles are attracted to the waveguide wall, and at high energy they can destroy its integrity.

In [2-5], it was proposed to use the parasitic effect of beam deflection from the waveguide axis in a wakefield accelerating structure to create a wakefield undulator. The use of the bunch-generated intrinsic transverse fields in a microwave cavity to create an undulator effect was proposed in [2]. In [3], it was proposed to create an alternating transverse electromagnetic field for the generation of undulator radiation with the oncoming motion of the generator and undulator bunches. However, due to significant deflecting fields acting on the generator bunch, the range of its flight turned out to be limited [4], which reduced the effectiveness of the method.

An alternative idea is to use a sinusoidal bent waveguide to create transverse beam oscillations [5]. In such a waveguide, the tail of the main beam or the secondary beam of charged particles, being attracted either to one wall or to the other, will vibrate in the transverse direction (Fig. 1). Due to such oscillations, the beam electrons will move with transverse acceleration and generate electromagnetic waves, which is a necessary condition for creating a free electron laser.

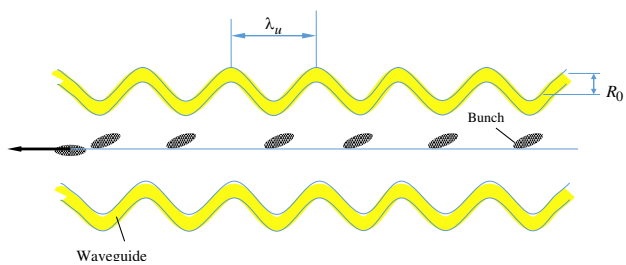

Figure 1: Wakefield undulator.

Modern undulators based on an alternating magnetic field are very expensive and require precise tuning. The proposed approach assumes the use of a bent waveguide with correctly selected parameters as a terminal device for an accelerator for a free electron laser, which will significantly reduce the cost of creating undulators.

BEAM DYNAMICS IN A WAKEFIELD WAVEGUIDE

To describe the beam dynamics with deviations from the waveguide axis not exceeding $R_c/2$, it is possible with a good degree of accuracy to take into account only the first transverse mode of the wake waveguide with a linear dependence of the transverse force on the distance from the particle generating the force to the waveguide axis.

Let us first consider a filamentary electron bunch (beam) with a longitudinal charge profile $f(\zeta)$ moving

* Work supported by Baltic Science Network powerhouse.
† ishejnman@yandex.ru

ISBN: 978-3-95450-240-0 ISSN: 2673-5539 doi:10.18429/JACoW-RuPAC2021-TUPSB22

parallel to the waveguide axis with a displacement $r(\zeta, t)$. We will assume that the charge in the bunch is uniformly distributed in the longitudinal direction $f(l) = 1/l$, where l is the length of the bunch. The change in the magnitude of the relativistic factor with time can be neglected.

In the case when the amplitude of the first mode dominates over the others, the radial dynamics of the beam in a regular waveguide is described by the equation [4-6]

$$\frac{\partial^2 r(\zeta,t)}{\partial t^2} - A\int_0^{\zeta} \sin\left(k_z(\zeta-\zeta_0)\right) r(\zeta_0,t)\,d\zeta_0 = 0,$$

where $A = -\dfrac{eq}{4m_e\gamma_0} k_\perp \psi_{F\perp} > 0$, noting that electron beam charge is negative, q is the charge of the electron beam ($q<0$), k_z and $k_\perp$ are the longitudinal and transverse wavenumbers of the first mode of the waveguide, $r(\zeta,t)$ is the displacement of the bunch from the axis of the waveguide, $\psi_{F\perp}$ is the series coefficient in the expansion of the radial force for the first mode, depending on the geometry and dielectric constant waveguide.

In the case of a point charge, which flies in without an initial radial velocity into the field of action of a transverse harmonic force, only the cosine dependence of the force ensures the finite motion of the particle in the transverse direction. The dependence of the force according to the sine law leads to the average displacement of the particle, which increases linearly with time. However, in the case of an extended bunch, as will be shown below, there is an accumulation of action from the head of the bunch, and the purely cosine dependence of the waveguide bend gives rise to instability of the beam, leading to its exit from the waveguide channel.

In this regard, the bending of the axis of the waveguide relative to the longitudinal axis z will be taken into account by adding to the expression for the force an additional periodic displacement of the beam relative to the axis of the waveguide: $R_{0c}\cos(\kappa z)$ or $R_{0s}\sin(\kappa z)$, where $\kappa = 2\pi/\lambda_u$, λ_u is the flexural wavelength. By introducing a parameter $\chi = \mathrm{arctg}\left(R_{0s}/R_{0c}\right)$ characterizing the initial phase of the flexural wave and varying χ, using the numerical simulation, it is possible to select conditions that correspond to the optimal ratio between the flight distance and the amplitude of the bunch oscillations.

For electron bunches with a length less than a quarter of the wavelength of the Cherenkov wake radiation of the waveguide $\Lambda = 2\pi/k_z$, the sine under the integral can be replaced by its argument. Then the equation of radial dynamics with single-mode excitation of a bent waveguide takes the form:

$$\frac{\partial^2 r_c(\zeta,t)}{\partial t^2} - A\int_0^{\zeta} f(\zeta_0)\left(k_z(\zeta-\zeta_0)\right)\left(r(\zeta_0,t) + R_{0c}\cos(\kappa z)\right)d\zeta_0 = 0,$$

$$\frac{\partial^2 r_s(\zeta,t)}{\partial t^2} - A\int_0^{\zeta} f(\zeta_0)\left(k_z(\zeta-\zeta_0)\right)\left(r(\zeta_0,t) + R_{0s}\sin(\kappa z)\right)d\zeta_0 = 0$$

with initial conditions

$$r(\zeta,0) = r_0,\ \left.\frac{dr(\zeta,t)}{dt}\right|_{t=0} = v_{r0} = 0.$$

The combined analytical solution of the obtained equations has the form:

$$r(\zeta,t) \approx r_{free}(\zeta,t) + r_{\sin}(\zeta,t) + r_{\cos}(\zeta,t),$$

where the term

$$r_{free}(\zeta,t) \approx \frac{r_0}{2}\left(I_0\left(2\sqrt{\sqrt{Ak_z}\zeta t}\right) + J_0\left(2\sqrt{\sqrt{Ak_z}\zeta t}\right)\right) +$$
$$+\frac{v_{r0}}{2\sqrt{\sqrt{Ak_z}\zeta}}\left(I_1\left(2\sqrt{\sqrt{Ak_z}\zeta t}\right) + J_1\left(2\sqrt{\sqrt{Ak_z}\zeta t}\right)\right)$$

represents the free movement of a bunch under the influence of forces created by it itself,

$$r_{\cos}(\zeta,t) \approx \frac{AR_{0c}k_z}{\left(Ak_z - \kappa^4 v^2\right)} \times$$
$$\left(\cos\left(\frac{\sqrt{Ak_z}\zeta}{\kappa v}\right)\cos\kappa v t - \frac{\kappa^2 v}{\sqrt{Ak_z}}\sin\left(\frac{\sqrt{Ak_z}\zeta}{\kappa v}\right)\sin\kappa v t - \cos\left(\kappa\zeta + \kappa v t\right)\right) +$$
$$+R_{0c}\frac{Ak_z\zeta^2}{\kappa^2 c^2}\sum_{n=0}^{\infty}\left(\frac{\left(\dfrac{Ak_z(\zeta L)^2}{c^2}\right)^n}{(2n+1)!(2n+3)!}\left((2n+3)(2n+1) - \kappa^2 L\zeta\right)\right),$$

$$r_{\sin}(\zeta,t) \approx \frac{AR_{0s}k_z}{\left(Ak_z - \kappa^4 v^2\right)} \times$$
$$\left(\cos\left(\frac{\sqrt{Ak_z}\zeta}{\kappa v}\right)\sin\kappa v t + \frac{\kappa^2 v}{\sqrt{Ak_z}}\sin\left(\frac{\sqrt{Ak_z}\zeta}{\kappa v}\right)\cos\kappa v t - \sin\left(\kappa\zeta + \kappa v t\right)\right) +$$
$$+R_{0s}\frac{Ak_z\zeta^2}{\kappa^2 c^2}\sum_{n=0}^{\infty}\left(\frac{\left(\dfrac{Ak_z(\zeta L)^2}{c^2}\right)^n}{(2n+1)!(2n+3)!}\left(\kappa L(2n+3) + \kappa\zeta(2n+1)\right)\right).$$

describe the forced motion of a bunch under the influence of a force periodically changing in space.

RESULTS OF NUMERICAL SIMULATION OF BEAM DYNAMICS

Let us present the results of modelling the flight dynamics for a beam energy of W = 10 GeV, a charge q = 100 nC, a length of l = 60 μm, and a base frequency of the waveguide f = 300 GHz.

The calculation results for a single uniformly distributed bunch along the length of the bunch for the cosine dependence of the waveguide bend are shown in Fig. 2. The initial displacement of the beam particles from the waveguide axis was taken equal to $r_0 = 10$ μm, the initial radial velocity was assumed to be zero, and the waveguide bend amplitude $R_0 = 0.5R_c$.

ISBN: 978-3-95450-240-0 ISSN: 2673-5539 doi:10.18429/JACoW-RuPAC2021-TUPSB22

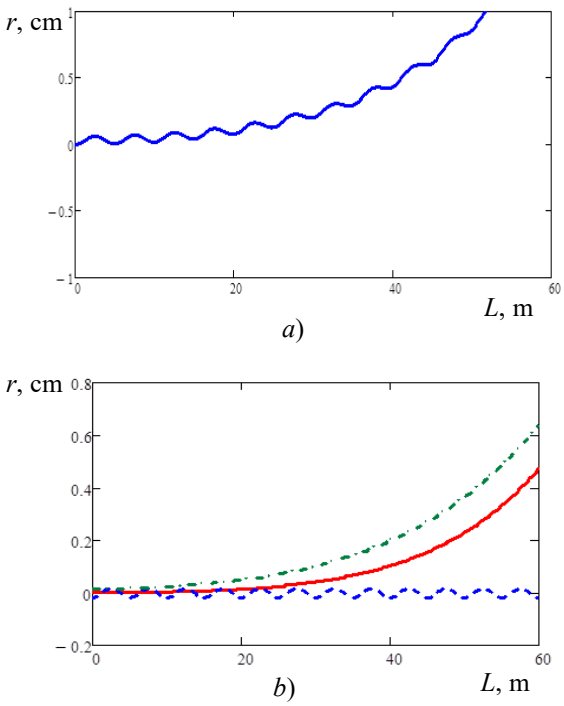

Figure 2: Results of modelling the beam dynamics for the cosine dependence of the waveguide bending: *a*) the beam trajectory, *b*) the effect of individual terms (red solid line is r_{free}, blue dashed line – the first term of $r_{\cos}$, green dash-dotted line – the second term of $r_{\cos}$).

As can be seen from Fig. 2, the solution without taking into account the initial phase is unstable, and the bunch quickly "settles" on the wall. Fig. 2b shows that the second term in $r_{\cos}$ leads to the deflection of the beam from the waveguide axis.

The introduction into the equation of dynamics of an additional term with a displacement that changes according to the sine law, and the selection of the initial phase of the flexural wave make it possible to achieve a much greater flight range.

The simulation results taking into account the correction by selecting the initial phase of the waveguide bending ($\chi = -0.085$) are shown in Fig. 3. The effects of the initial displacement of the bunch from the axis r_{free} and the second term $r_{\cos}$ cancel each other out, which makes it possible to increase the flight range by more than 2 times.

The inverse formulation of the problem is also possible: selection of the transverse positioning and radial velocity of the bunch at the entrance to the curved wake waveguide to maximize the flight range of the beam with a constant waveguide profile.

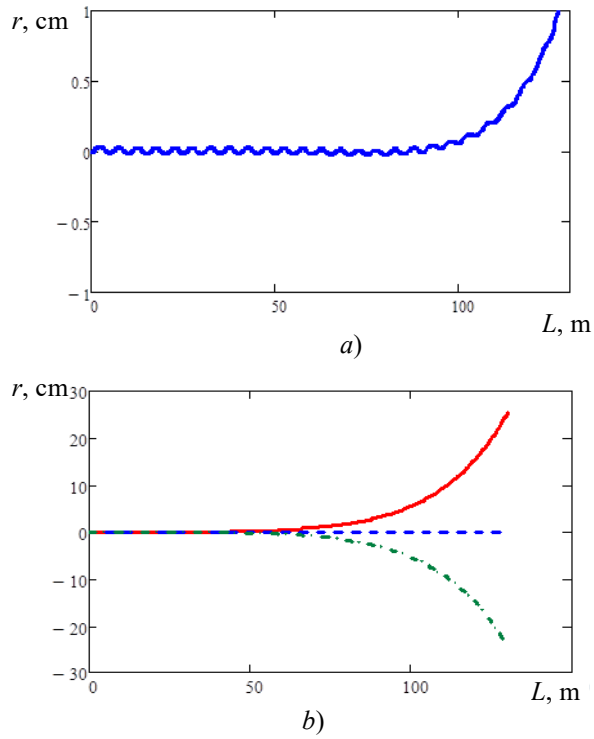

Figure 3: Beam dynamics simulation results with correction by introducing bias with sine ($\chi = -0.085$).

CONCLUSION

The choice of the initial phase of the bending of the waveguide and its matching with the axial positioning of the bunch at the entrance to the undulator make it possible to achieve a significant increase in the range of the beam flight and, thereby, to increase the emitted power of X-ray radiation.

REFERENCES

[1] C. Pellegrini, A. Marinelli, and S. Reiche, "The physics of x-ray free-electron lasers", *Rev. Mod. Phys.*, vol. 88, p. 015006, 2016. doi:10.1103/RevModPhys.88.015006

[2] S. Tantawi *et al.*, "Experimental demonstration of a tunable microwave undulator", *Phys. Rev. Lett.*, vol. 112, p. 164802, 2014. doi:10.1103/PhysRevLett.112.164802

[3] C. Jing, S. S. Baturin, A. Kanareykin, P. Schoessow, and A. Zholents, "A beam-driven microwave undulator for FEL", in *Proc. of IPAC2014*, Dresden, Germany, June 2014, paper WEPRO008, pp. 1956-1958. doi:10.18429/JACoW-IPAC2014-WEPRO008

[4] I. L. Sheinman, "Beam dynamics in dielectric structure when using it as undulator", in *Proc. Int. Conf. "Stability and Control Processes" in Memory of V. I. ZUBOV (SCP) joined with 21st Int. Workshop on Beam Dynamics and Optimization (BDO)*, Saint-Petersburg, Russia, Oct. 2015, pp. 201-204. doi:10.1109/SCP.2015.7342093

[5] I. L. Sheinman, "Undulator effect on a bending acoustic wave of the wakefield waveguide", in *Wave electronics and its application in information and telecommunication systems (WECONF-2019)*, Saint-Petersburg, Russia, June 2019. doi:10.1109/WECONF.2019.8840619

ISBN: 978-3-95450-240-0 ISSN: 2673-5539 doi:10.18429/JACoW-RuPAC2021-TUPSB25

STORAGE RING DESIGN AND BEAM INSTABILITIES INVESTIGATION FOR MEPhI's PHOTON SOURCE*

V. S. Dyubkov†, S. M. Polozov, National Research Nuclear University MEPhI, Moscow, Russia

Abstract

There is a design of a compact photon source based on inverse Compton scattering at NRNU MEPhI. Updated synchrotron lattice, electron dynamics simulation and beam instabilities studies are presented.

INTRODUCTION

Photons of 5-30 keV and flux of about 10^{10}-10^{12} γ/s are used for materials science, research of nano - and biosystems, medicine and pharmacology, physics and chemistry of fast-flowing processes. There are a few ways of 5-30 keV photon production. This project aims to development of a compact system for generating radiation in a next-generation light undulator in the photon energy range of 5-30 keV for ring and linear sources based on inverse Compton scattering.

A number of facilities based on inverse Compton scattering effect are under design or operation today: MuCLS [1], LyCLS [2], ThomX [3], ODU CLS [4], SLEGS [5], SPARC_LAB [6], LUCX [7], LESR [8], Daresbury Compton Backscattering X-ray Source [9]. Compton light source is supposed to be built on the NRNU MEPhI site. Two operating modes of the compact light source are possible: the storage ring Compton source design and the linac-based Compact-XFEL.

STORAGE RING

In order to generate 5-30 keV X-rays in light ondulator it is suggested that compact storage synchrotron will be used with top-up injection from normal conducting S-band linac with tuneable energy in the range of 20-60 MeV.

The use of a storage ring provides the following advantages: high intensity of the generated photon flux, high brightness, electron beam energy tuning in a wide range, high degree of monochromaticity and coherence of the generated photons.

In order to get horizontal rms beam size at interaction point (IP) with laser photons of 30 μm for electron horizontal emittance $\varepsilon_{x,\mathrm{rms}}$ of 100 nm the horizontal beta-function value should be equal to 30 cm in accordance with

$$\beta_x = \sigma^2_{x,\mathrm{rms}} \big/ \varepsilon_{x,\mathrm{rms}}.$$

The same value should have the vertical beta-function at IP. Dispersion function D_x should have a zero value at IP to minimize e-bunch size because

$$\sigma^2_{x,\mathrm{rms}} = \beta_x \varepsilon_{x,\mathrm{rms}} + D_x^2 \left[(p - p_0)/p_0 \right],$$

where $\sigma_{x,\mathrm{rms}}$ – horizontal rms beam size, β_x – horizontal beta-function, p – momentum of electron, p_0 – equilibrium momentum.

Furthermore, the length of storage ring straight section should be of 1.5 m to increase interaction efficiency between electron bunch and laser photons head-on collision as well as feasibility of laser positioning. The updated version of synchrotron magnetic lattice is presented in Fig. 1. Storage ring circumference is 10.661 m. The quadrupole gradients were calculated numerically by means of AT [10] to satisfy requirements above. Figure 2 shows obtained optic functions. From Fig. 2 it is seen that β_x is 24.12 cm and β_y is 14.62 cm at IP. Momentum compactification factor is equal to 0.0645 at 60 MeV, betatron horizontal and vertical tunes are 3.762 and 2.794 correspondingly. Also it was estimated dynamic aperture (DA) (Fig. 3). DA is equal to ±4.3 mm which is sufficient value for 30 μm beam-size.

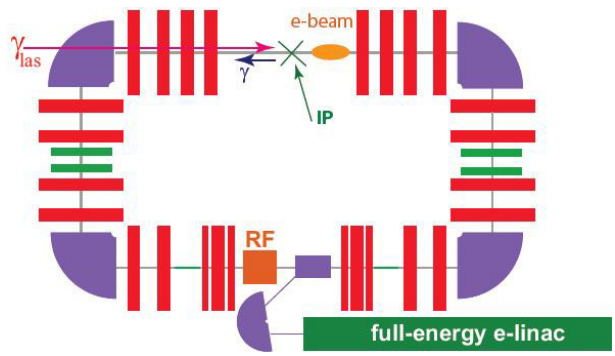

Figure 1: Basic magnet lattice of storage ring.

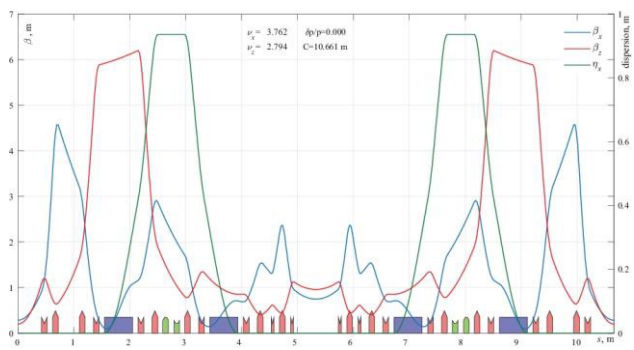

Figure 2: Twiss functions and dispersion.

Two families of sextupoles were arranged in the dispersion function maximum to correct chromaticities.

* Work supported by Russian Foundation for Basic Research, grant no. 19-29-12036
† vsdyubkov@mephi.ru

ISBN: 978-3-95450-240-0 ISSN: 2673-5539 doi:10.18429/JACoW-RuPAC2021-TUPSB25

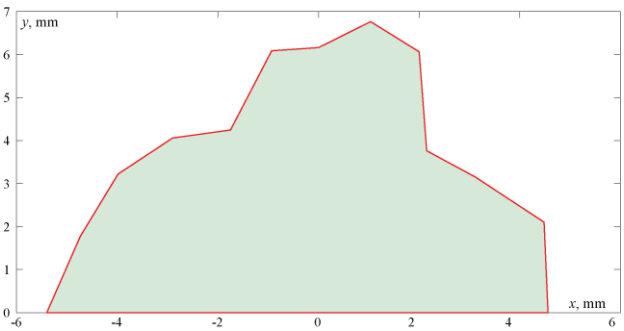

Figure 3: Dynamic aperture (for 1000 turns).

LIFE TIMES, INSTABILITIES, NON-LINEAR EFFECTS AND LIMIT CURRENTS

Following the study of different non-linear effects, instabilities and space charge limitations are started. It is necessary to define the final value of beam lifetime and the bunch current (charge). These parameters are crucially important to further design both injector and laser systems. First we estimate values of radiation integrals [11] for the lattice [12]: I_1=1.17, I_2=7.48 1/m, I_3=14.48 1/m^2, I_4=2.27 1/m. Such values of radiation integrals and small radiation energy losses (due to the low beam energy of 10-60 MeV losses are equal to $3\cdot10^{-1}$ eV/turn) give us very high value of the radiation times τ_x=3200 and τ_y=2230 s correspondently for horizontal and vertical motion. The calculation of the Touschek lifetime (TLT) give the representative value about 1-10 ms for the different beam energy, bunch charge, and the energy acceptance (see Figs. 4-7). We should estimate TLT and decide will it be the main factor limiting the lifetime for the low energy beam in small-circumference ring. It is obviously from our general suggestions for beam dynamics in low-energy rings and it was shown by simulation for MEPhI project.

It is clear the optimal bunch charge should be not greater than 300 pC and we have to increase the momentum acceptance up to 2-3 % to reach biger value of TLT.

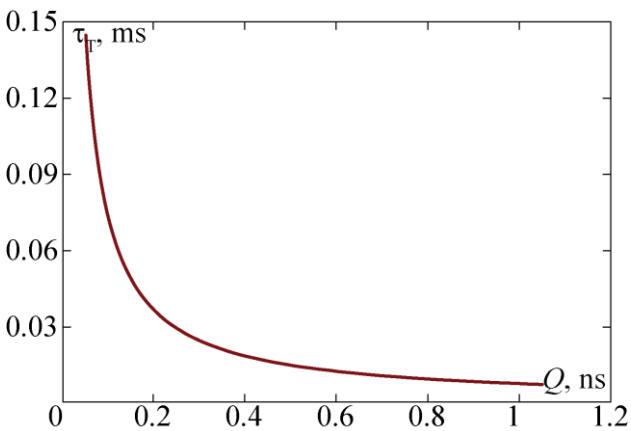

Figure 4: TLT vs bunch charge.

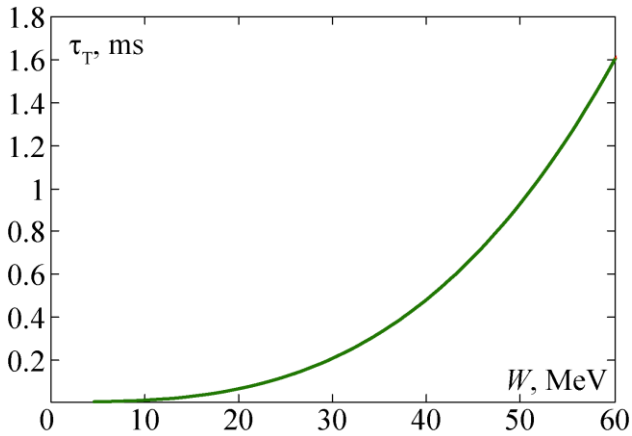

Figure 5: TLT vs beam energy.

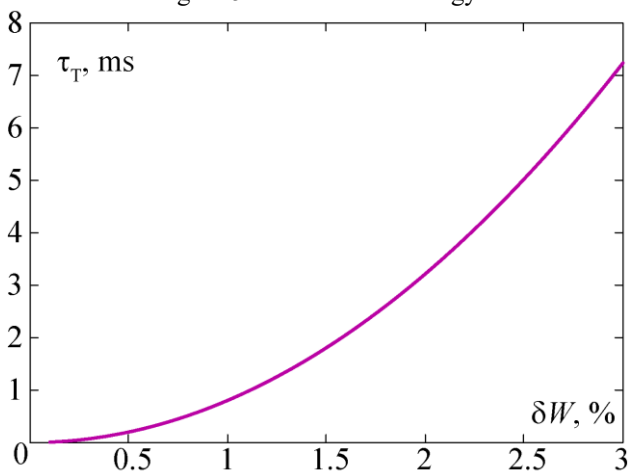

Figure 6: TLT vs energy acceptance (Q = 1 nC).

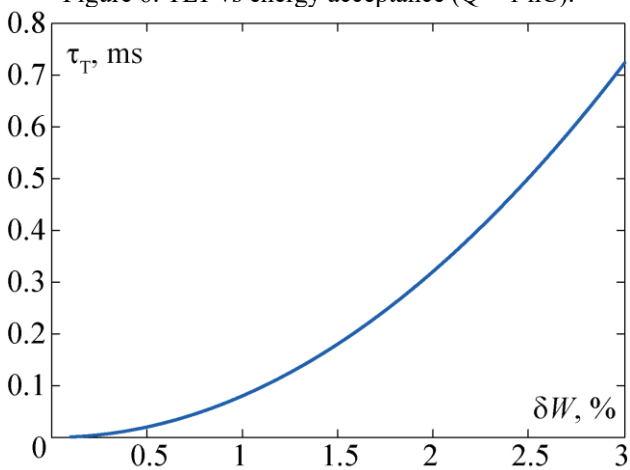

Figure 7: TLT vs energy acceptance (Q = 100 pC).

Following the intra-beam scattering (IBS) was simulated and the IBS time was defined [13]. It is equal to ~150 s for horizontal motion and is very high for vertical and longitudinal ones. The threshold bunch current calculated for longitudinal motion using the finite fine filament technique is equal to 630 A (or 600 nC in 1 ps bunch). The limit calculated for transverse motion (by uniformly charged ellipsoid technique and with the accelerating potential 300 kV and the vacuum chamber size 20×100 mm) is ~830 pC.

ISBN: 978-3-95450-240-0 ISSN: 2673-5539 doi:10.18429/JACoW-RuPAC2021-TUPSB25

As it was shown under such values (< 1 nC) of the bunch charge the batatron tune shift will very small $\Delta\nu_x$=-2.02·10^{-13} and $\Delta\nu_x$=−2.21·10^{-12} per turn.

Finaly the estimation of the microwave instability life times were done. It was chosen the accelerating cavity frequency about 3000 MHz (T_{turn}/T_{RF}=105) and energy acceptance 3 %. The vacuum chamber form was supposed to be similar to USSR4 (ESRF-EBS synchrotron vacuum chamber) project to define the vacuum chamber impedance. The beam current will be limited by ~400 A due to microwave instability. Characteristic times will be equal to 23 and 4.2 ms for horizontal and vertical motions correspondently.

CONCLUSION

Current activities on physical models design of a compact monochromatic radiation source in the x-ray range based on inverse Compton scattering are presented. A circumference of the storage ring is supposed to be about 11 m. Simulations were done to define the bunch life times and to study basic non- linearity effects. It was shown Touschek lifetime will the main limiting factor for the designed low-energy ring. Estimation gives us TLT is about 0.1-1.0 ms for different bunch charge, beam energy and energy acceptance values and it is the lowest from the set of key lifetimes. The bunch charge should be limited by 300-400 pC/bunch to have high TLT and weakly influence on the bunch dynamics.

REFERENCES

[1] M. Dierolf, “The Munich Compact Light Source – a laboratory-scale synchrotron facility for biomedical research”. http://www.e17.ph.tum.de

[2] J. Rifkin *et a1*., “Apparatus, system and method for high flux, compact Compton X- ray source”, US patent 7277526 B2. Oct. 2, 2007.

[3] A. Variola *et al.,* “ThomX Technical Design Report”, France, Rep. SOLEIL/SOU-RA-3629, Mar. 2014. http://hal.in2p3.fr/in2p3-00971281

[4] K.E. Deitrick *et al*., “High-brilliance, high-flux compact inverse Compton light source”, *Phy. Rev. Accel. Beams*, vol. 21, p. 080703, Aug. 2018. doi:10.1103/PhysRevAccelBeams.21.080703

[5] Q.Y. Pan *et al*., “A Future Laser Compton Scattering (LCS) γ-Ray Source: SLEGS at SSRF”, *Synchr. Rad. News*, vol. 22, no. 3, p. 11, Jun. 2009. doi:10.1080/08940880902959759

[6] C.Vaccarezza *et al*., "The SPARC_LAB Thomson source", *Nucl. Instrum. Meth. A*, vol. 829, no. 1, p. 237, Sep. 2016. doi:10.1016/j.nima.2016.01.089

[7] K. Sakaue *et al*., “Development of a compact X-ray source based on laser-Compton scattering with a pulsed-laser super-cavity”, in. *Proc. 11th Eur. Particle Accelerator Conf. (EPAC’08)*, Genova, Italy, Jun. 2008, paper TUPP156, pp. 1872-1874.

[8] P. Gladkikh, “Lattice and beam parameters of compact intense x-ray sources based on Compton scattering*”, Phy. Rev. Accel. Beams*, vol. 8, p. 050702, May 2005. doi:10.1103/PhysRevSTAB.8.050702

[9] D. Laundy *et al*., “Results from the Daresbury Compton backscattering X-ray source”, *Nucl. Instrum. Meth. A*, vol. 689, p. 108, Oct. 2012. doi:10.1016/j.nima.2012.05.054

[10] AT, http://atcollab.sourceforge.net/docs.html

[11] E.B. Levichev, “Low emittance electron storage rings”, *Phy.-Uspekhi*, vol. 61, no. 1, pp. 29-51, 2018. doi:10.3367/ufne.2016.12.038014

[12] V.S. Dyubkov *et al.*, “Beam Dynamics Investigation for a New Project of Compton Back Scattering Photon Source at NRNU MEPhI”, in *Proc. IPAC’21*, Campinas, SP, Brazil, May 2021, pp.186-188. doi:10.18429/JACoW-IPAC2021-MOPAB042

[13] J.D. Bjorken and S.K. Mtingwa, “Intrabeam Scattering”, *Part. Accel*., vol. 13, pp. 115-143, 1983.

ISBN: 978-3-95450-240-0 ISSN: 2673-5539 doi:10.18429/JACoW-RuPAC2021-TUPSB26

LATTICE OPTIONS WITH REVERSE BENDING MAGNETS FOR USSR HMBA STORAGE RING

V. S. Dyubkov[1†], E. D. Tsyplakov[2], T. V. Kulevoy[2], National Research Center "Kurchatov Institute", Moscow, Russia
[1]also at National Research Nuclear University MEPhI, Moscow, Russia
[2]also at ITEP-NRC Kurchatov institute, Moscow, Russia

Abstract

The 4th generation light source, the Ultimate Source of Synchrotron Radiation (USSR4) is under design, to be built in Moscow region (Russia). It will be a 6 GeV and about 1100 m circumference storage ring synchrotron [1-3]. Baseline lattice of the USSR4 for now is a scaled version of the ESRF-EBS Hybrid Multi-Bend Achromat (HMBA) lattice that was successfully commissioned in 2020 [4-7]. Its natural horizontal electron beam emittance is about 70 pm·rad. Further reduction of beam emittance can be achieved with the use of reverse bending magnets. The evolution of the envisaged lattices for the USSR4 storage ring, including options with reverse bends is presented.

INTRODUCTION

Today third- and fourth-generation synchrotron radiation (SR) sources and X-ray free-electron lasers (FEL's) have many different applications in materials science, molecular biology and biochemistry, biomedical studies, crystallography, spectroscopy, studies of fast processes and other fields of scientific and applied research. For such applications the main problem is reaching the diffraction limit for a given beam energy of 3-6 GeV: thereby, an object can be imaged with high contrast and sharpness once its size is comparable to the wavelength of the synchrotron or undulator radiation. It was assumed that transverse emittance value below 100 pm·rad is necessary for the fourth generation light source to reach new horizons in the research by using SR. For a long time it was assumed that such values of the emittance could be reached only with FEL's driven by high-brightness electron linacs. A few years ago, it was demonstrated that low horizontal emittances can be achieved in storage synchrotrons as well and first beams with emittances about 100 pm·rad were generated at MAX-IV (Sweden) [8] and ESRF-EBS (France) [7] synchrotron light sources. Several similar facilities are under design and construction stages [9, 10] but today's trend is the existing SR sources upgrade to the fourth generation.

It is proposed that USSR4 facility will include both the 6 GeV storage synchrotron and FEL(s). The choice of this layout leads to the complication of injection system based on the full-energy linear accelerator. This linac will be used both for top-up injection into storage ring and for a generation of the high-brightness drive bunches for FEL.

SYNCHROTRON RING LATTICE

Baseline lattice of the USSR4 for now is a scaled version of the ESRF-EBS 40-fold symmetry HMBA lattice that consists of 7 bends for each cell, 4 of them being the so-called LGB magnets, 2 are combined-function magnets (DQ) and "triplet of the magnets" at the centers of the 38 standard cells (Fig. 1). The main difference of this lattice from ESRF-EBS one is the presence of 5 cm long short bend (SB) with high field (~0.86 T) at the cell center. This lattice ensures the designed horizontal emittance 70 pm·rad together with Touschek lifetime (TLT) is equal to 28.9 h for zero current approximation, momentum acceptance (MA) is equal to ±6% at the center of the straight section and sufficient off-momentum dynamic aperture (DA) for off-axis injection schemes (± 1 cm in horizontal plane and about 3 mm in the vertical one) [2]. An advantage of that lattice is the scaling of the commissioned ESRF-EBS storage ring synchrotron and needs minimal changes of components (magnets, chambers) to start its construction in a short time.

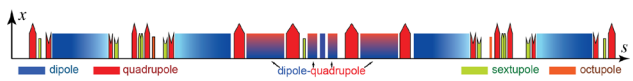

Figure 1: Layout of baseline lattice.

However, equilibrium electron beam horizontal emittance ε_x already now in 1.5-2 times lower than 70 pm for the similar projects [9, 10] in view of energy and circumference of SR sources. It is well known that the next step towards lower ε_x values is anti-bends (reverse bends) implementation [11-13] together with mentioned LGB magnets under constant beam energy. So, the expected ε_x value is about 45 pm for 1104 m long 6 GeV APS-U project [10]. The APS-U lattice is the scaled and modified ESRF-EBS HMBA lattice with six reverse bend (RB) gradient dipoles.

Firstly, an attempt was made by authors to re-optimize USSR baseline lattice by means of re-tune magnets parameters to reduce ε_x value up to 50 pm. The problem could not be solved without significant modification of the baseline lattice or RB introduction.

The next step toward the solution of the mentioned problem was the considering of RB introducing into baseline lattice by corresponding shifts of the existing quadrupoles in the horizontal plane from the closed orbit. An example of USSR4 lattice with reverse bends is presented in Fig. 2 (we considered lattice without SB at the cell center and with one DQ there).

The main tasks for the lattice optimization were:

1. ε_x value is about 50 pm or lower.

† Dyubkov_VS@rrcki.ru

ISBN: 978-3-95450-240-0 ISSN: 2673-5539 doi:10.18429/JACoW-RuPAC2021-TUPSB26

2. Zero dispersion at centres of straight sections.
3. Realization of "–*I* transformation" conditions.
4. Acceptable DA value for off-axis injection.
5. MA and TLT comparable with that are for baseline lattice or bigger.
6. Fields of magnets should not exceed the upper limits designed for ESRF-EBS magnets.

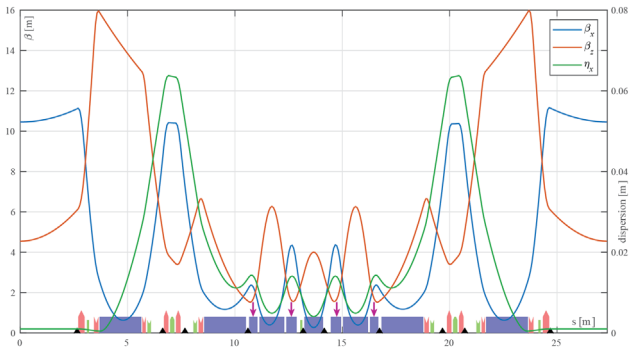

Figure 2: Layout of considered lattice with RB.

Lattice optimization was carried out by means of MADX [14], AT [15], Pyhton [16]. With the help of Nelder-Mead simplex method [17] it was obtained a set of ε_x values for different absolute value of the bending angle ψ of reverse bend that is presented in Fig. 3. Note that the fields of LGB magnets was changed too. A dependence of horizontal partition number J_x [18] on ψ values is shown in Fig. 4. From this figures one can find that ε_x value lower than 50 pm corresponds for $|\psi|$ values greater than 2 mrad and, consequently, J_x values closed to 2. Typical distribution of fields of dipoles along the cell, for instance for the lattice with ε_x = 50 pm, shown in Fig. 5. DA for that lattice is shown in Fig. 6. It follows that DA sizes in the horizontal and vertical plane are about ±3 mm and 3 mm that is still not enough for off-axis injection. Note, that DA sizes for APS-U project with swap-out injection in the horizontal and vertical plane is about ±3 mm and 3 mm correspondingly.

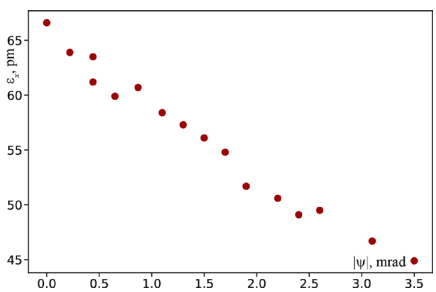

Figure 3: Dependence of ε_x on $|\psi|$.

The supposition that was made during RB introducing into baseline lattice is vacuum chamber geometry the same as for ESRF-EBS one. It is clear that RB can change beam orbit so that vacuum chamber geometry will need to be redesigned and, consequently, to perform gas loads and impedance calculations, beam instabilities investigation and so on. The required shifts of RB gradient dipoles can be estimated by means of following expression

$$|\psi_{RB}| = |k_1 l \Delta x|, \quad (1)$$

where k_1 is the the quadrupole strength, l is its length, Δx is its horizontal shift.

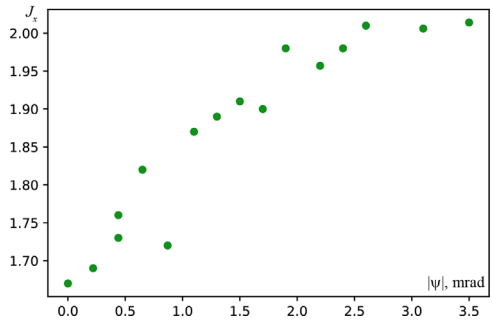

Figure 4: Dependence of J_x on $|\psi|$.

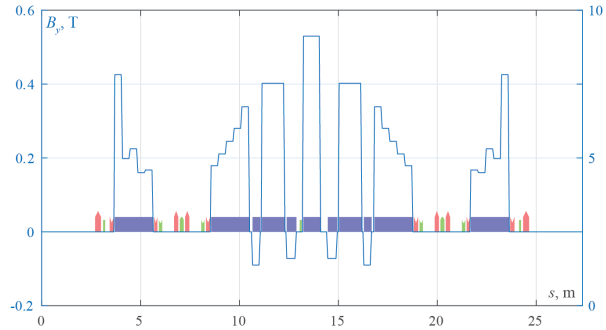

Figure 5: Typical distribution of dipoles fields.

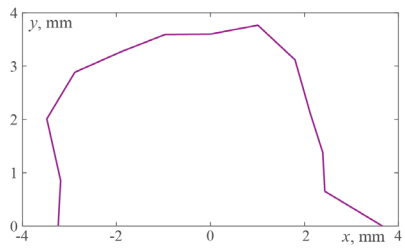

Figure 6: Example of DA for the lattice option with RB.

A graph of a dependence of absolute value of closed orbit shift on absolute value of shift of RB gradient dipole is presented in Fig. 7. It follows that possible Δx value is lower than 0.7 mm because of horizontal dimension of vacuum chamber cross section. That dimension is supposed to be equal to 16.5 mm for the cell central region. In turn, this means that $|\psi|$ value is less than 1.2 mrad and, in accordance with Fig. 3, ε_x is greater than 60 pm.

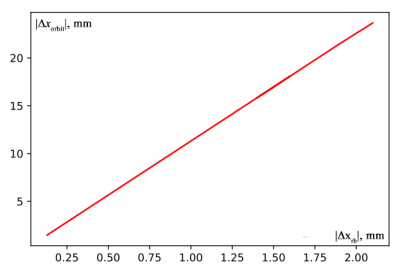

Figure 7: Dependence of absolute value of closed orbit shift on absolute value of RB shift.

ISBN: 978-3-95450-240-0 ISSN: 2673-5539 doi:10.18429/JACoW-RuPAC2021-TUPSB26

CONCLUSION

The evolution of the envisaged lattices for the USSR storage ring, including options with reverse bends is presented. It is pointed that it is not possible to reduce equilibrium horizontal beam emittance down to 50 pm by means of reverse bend gradient dipoles implementation under condition that vacuum chambers should be the same as for ESRF-EBS main ring. Nevertheless, reverse bends allow one to reach equilibrium horizontal emittance lower than 50 pm·rad, but it will need to redesign significant amount of the magnets, vacuum chambers, etc.

REFERENCES

[1] I. A. Ashanin *et al.*, "Conceptual design of a dedicated fourth-generation Specialized Synchrotron radiation Source (SSRS-4) at the Kurchatov Institute", *Phys. Atom. Nuclei*, vol. 81, no. 11, pp. 1646-1651, 2018. doi:10.1134/S1063778818110030

[2] S.M. Liuzzo *et al.*, "USSR HMBA Storage Ring Lattice Options", presented at IPAC'21, Campinas, Brazil, May. 2021, paper TUPAB049, unpublished.

[3] T.V. Kulevoy *et al.*, "USSR - the Project of the Ultimate Synchrotron Radiation Source in Russia", presented at IPAC'21, Campinas, Brazil, May 2021, paper TUPAB055, unpublished.

[4] "EBS Storage Ring Technical Report", ESRF, Grenoble, France, 2019. https://www.esrf.eu/files/live/sites/www/files/about/upgrade/documentation/Design%20Report-reduced-jan19.pdf

[5] S.M. Liuzzo *et al.*, "Preparation of the EBS beam commissioning", *J. Phys.: Conf. Ser.*, vol. 1350, p. 012022, 2019. doi:10.1088/1742-6596/1350/1/012022

[6] S.M. Liuzzo *et al.*, "Hybrid multi bend achromat at 3 GeV for future 4th generation light sources", in *Proc. IPAC'16*, Busan, Korea, May 2016, pp. 2822-2825. doi:10.18429/JACoW-IPAC2016-WEPOW006

[7] S. White *et al.*, "Commissioning and restart of ESRF-EBS", presented at IPAC'21, Campinas, Brazil, May 2021, paper MOXA01, unpublished.

[8] "MAX IV Facility Detailed Design Report", Lund, Sweden, Aug. 2010. https://www.maxiv.lu.se/accelerators-beamlines/accelerators/accelerator-documentation/max-iv-ddr

[9] G. Xu, X.H. Cui, Z. Duan, Y.Y. Guo, "Progress of the lattice design and physics studies on the high energy photon source", in *Proc. IPAC'19*, Melbourne, Australia, May 2019, pp. 2697-2699. doi:10.18429/JACoW-IPAC2019-TUPGW046

[10] R.O. Hettel, "Status of the APS-U Project", presented at IPAC'21, Campinas, Brazil, May 2021, paper MOXA02, unpublished.

[11] J.-P. Delahaye and J.P. Potier, "Reverse bending magnets in combined function lattice for the CLIC damping ring", in *Proc. PAC'89*, Chicago, Illinois, March 1989, pp. 1611-1613. doi:10.1109/PAC.1989.72869

[12] A. Streun, "Use of reverse bending magnets in multi-bend achromat lattices", presented at IPAC'20, Caen, France, May 2020, paper WEVIR01, unpublished.

[13] A. Streun, "The anti-bend cell for ultralow emittance storage ring lattices", *Nucl. Instrum. Methods in Phys. Research A*, vol. 737, pp. 148-154, 2014. doi:10.1016/j.nima.2013.11.064

[14] L. Deniau, H. Grote, G. Roy, *The MAD-X Program User's Reference Manual Version 5.03.07*. http://cern.ch/madx/releases/last-rel/madxuguide.pdf

[15] W. Rogers *et al.*, "pyAT: A Python build of Accelerator Toolbox". in *Proc. IPAC'17*, Copenhagen, Denmark, May 2017, pp. 3855-3857. doi:10.18429/JACoW-IPAC2017-THPAB060

[16] G.V. Rossum and F.L. Drake, *Python 3 Reference Manual*, CreateSpace, Scotts Valley, CA, USA, March 2009.

[17] J. Nelder and R. Mead, "A simplex method for function minimization", *Comput. J.*, vol. 7, pp. 308-313, 1965. doi:10.1093/COMJNL/7.4.308

[18] M. Conte and W.W. MacKay, *An introduction to the physics of particle accelerators*. Singapore: World Scientific Publishing, 2008.

ISBN: 978-3-95450-240-0 ISSN: 2673-5539 doi:10.18429/JACoW-RuPAC2021-TUPSB28

X-RAY THOMSON INVERSE SCATTERING FROM PERIODICALLY MODULATED LASER PULSES*

D. Yu. Sergeeva†, A. A. Tishchenko, National Research Nuclear University MEPhI, 115409 Moscow, Russia
also at National Research Center "Kurchatov Institute", 123098 Moscow, Russia
also at Belgorod National Research University, 308015 Belgorod, Russia

Abstract

Being a compact source of x-rays based on the Thomson backscattering, Thomson source has potential to be used in medicine and biology and in other areas where narrow band x-ray beams are essential. We propose and investigate theoretically the idea to use laser pulses modulated with a short period in Thomson backscattering. The coherent radiation is obtained with intensity proportional to the squared number of micro-pulses in the whole laser pulse.

INTRODUCTION

Thomson (or Compton) backscattering happens when a laser pulse scatters off with a counter propagating relativistic free electron. Thomson backscattering underlies a bright and compact X-ray source. The sizes of such source are much smaller, than synchrotron's sizes, while the brightness is comparable with that. The general layout of this process is shown in Fig. 1.

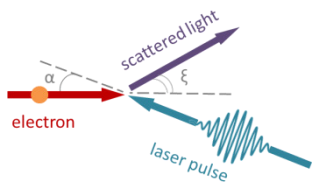

Figure 1: Layout of Thomson backscattering: laser pulse scattering on a moving relativistic electron.

The frequency of the scattered light is defined as without recoil effect:

$$\omega = \omega_0 \frac{1+\beta\cos\alpha}{1-\beta\cos\xi}, \tag{1}$$

where ω_0 is the frequency of incident laser pulse, $\beta = v/c$ with c being the speed of light in vacuum and v being the initial speed of the electron, α is an angle of interaction, ξ is the angle between the electron's trajectory and the propagation direction of the initial laser pulse.

The number of X-ray photons depends on the number of oscillations of electrons in the external field, i.e. the laser pulse duration T:

$$N_{\text{ph}} = f\left(N_{\text{oscillations}}\right) \propto T. \tag{2}$$

Increasing T leads to incoherent enhancement of radiation. It is similar to incoherent radiation from a long electron beam [1]:

$$I = I_0\left(N + N^2 F\right). \tag{3}$$

Here the first summand describes incoherent radiation, while the second one describes the coherent radiation. In order to switch on coherence effects we propose to use the laser with periodical longitudinal profile, the layout see in Fig. 2.

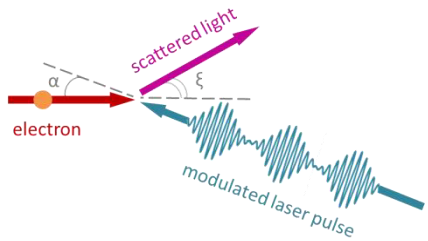

Figure 2: Periodically modulated laser pulse is scattered on a relativistic electron beams, giving rise to the radiation with frequency higher than initial laser.

As the first approximation the laser wave can be considered as a plane wave:

$$\mathbf{E}^{\text{ext}}\left(\mathbf{r},t\right) = \mathbf{E}_0\cos\left(\omega t - \mathbf{kr} + \varphi_0\right), \tag{4}$$

where ω is the laser frequency, $\mathbf{k}$ is its wave-vector, $\mathbf{E}_0$ is the laser amplitude, φ_0 is the initial phase. The modulated laser pulse can be described by [2]:

$$\mathbf{E}^{\text{ext}}\left(\mathbf{r},t\right) = \mathbf{E}_0\left(t\right)\cos\left(\omega t - \mathbf{kr} + \varphi_0\right). \tag{5}$$

For periodically modulated beam $\mathbf{E}_0\left(t+t_0\right) = \mathbf{E}_0\left(t\right)$. It means that instead of wave with a modulated profile we can use the set of N short laser pulses each of which is described by the field of a plane wave, see Fig. 3.

* This work was supported by the RFBR grant 19-29-12036
† dysergeyeva@mephi.ru

ISBN: 978-3-95450-240-0 ISSN: 2673-5539 doi:10.18429/JACoW-RuPAC2021-TUPSB28

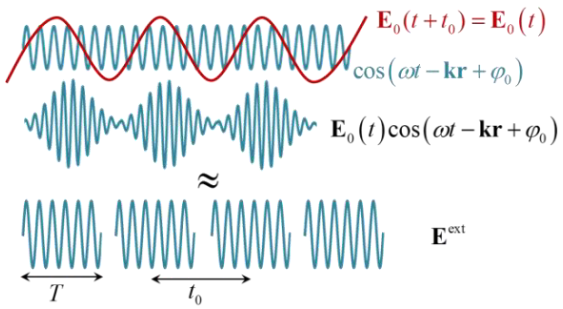

Figure 3: Different ways to perform the modulated laser pulse.

In this paper, we propose the new way to increase the intensity of X-ray inverse Compton source significantly, using the modulated laser pulses.

GENERAL THEORY

The energy of light scattered on the relativistic electron per the unit frequency and per unit solid angle is

$$\frac{dW_1(\mathbf{n},\omega)}{d\Omega d\omega}=\frac{e^2\omega^2}{4\pi^2c^3}\left|\int_0^T dt e^{i\omega t}e^{-i\mathbf{kR}(t)}\left[\mathbf{n},\mathbf{v}(t)\right]\right|^2, \quad (6)$$

where e is the electron's charge, $\mathbf{k}$ is the wave-vector of scattered light, $\mathbf{k}=\mathbf{n}\omega/c$ with $\mathbf{n}$ being the unit wave-vector, T is the duration of a single laser pulse, $\mathbf{R}(t)$ and $\mathbf{v}(t)$ are the trajectory and the velocity of the electron in the external field (laser). As the electron having the initial speed starts to oscillate in the external field, $\mathbf{R}(t)$ describes this periodical motion along with drift motion in a single laser pulse [3].

If an external field is periodical (modulated laser pulse), the electron's trajectory repeats in every period of the external field t_0. So, for the electron moving in the modulated laser pulse we can write $\mathbf{R}(t)=\mathbf{R}(t+t_0)$ and $\mathbf{v}(t)=\mathbf{v}(t+t_0)$. It means that in the case of scattering of the modulated laser pulse on the electron the integral in Eq.(6) reads

$$\frac{dW(\mathbf{n},\omega)}{d\Omega d\omega}=\frac{e^2\omega^2}{4\pi^2c^3}\left|\sum_{n=0}^{N-1}\int_{nt_0}^{T+nt_0} dt e^{i\omega t}e^{-i\mathbf{kR}(t)}\left[\mathbf{n},\mathbf{v}(t)\right]\right|^2, \quad (7)$$

where N is the number of periods of the external field.

ELECTRON MOTION

In order to find the coordinates and the velocity of the electron in the electromagnetic field of laser beam one need to solve the system of motion equations:

$$\frac{d\mathbf{p}}{dt}=e\mathbf{E}+\frac{e}{c}\left[\mathbf{v},\mathbf{H}\right], \quad \frac{d\varepsilon}{dt}=e\mathbf{vE}, \quad (8)$$

where $\mathbf{E}$ and $\mathbf{H}$ are the electric and magnetic fields of laser wave, which are related as $\mathbf{H}=\left[\mathbf{n},\mathbf{E}\right]$, $\mathbf{p}$ is the momentum of the electron moving under action of the laser pulse, ε is its energy. Wave function describing the motion of the electron in the field of the plane wave was calculated strictly by Volkov proceeding from Dirac equation [4]. Later, the solution for the momentum was obtained by Ritus in form of four-vectors [5]:

$$p_\mu=p_{0\mu}-\frac{e}{c}A_\mu+k_\mu\left(\frac{e}{c}\frac{pA}{kp}-\frac{e^2}{c^2}\frac{A^2}{2kp}\right), \quad (9)$$

where $p_\mu=(\varepsilon/c,\mathbf{p})$, $p_{0\mu}=(\varepsilon_0/c,\mathbf{p}_0)$, $\mathbf{p}_0$ coincides with the electron's momentum when there is no the external field, $\mathbf{A}_\mu=(0,\mathbf{A})$ with $\mathbf{A}$ being the vector-potential: $\mathbf{H}=rot\mathbf{A}$, $\mathbf{E}=-(1/c)\partial A/\partial t$, $k_\mu=(\omega_0/c,k_0)$, $pA=-\mathbf{p}_0\mathbf{A}$, $kp=-\mathbf{k}_0\mathbf{p}_0+\varepsilon_0\omega_0/c^2$. The similar solution can be obtained solving Eqs.(8)-(9) by classical methods like it was done in [3, 2].

Let the external wave propagate along z-axis. Then the wave-vector is $\mathbf{k}_0=\mathbf{e}_z\omega_0/c$, the vector-potential can be written in form [6] $\mathbf{A}=\mathbf{e}_xA_0\cos(\omega_0t-k_{0z}z)$, where $\mathbf{A}_0$ is the amplitude, and, consequently, the electrical and magnetic fields are

$$\begin{aligned}\mathbf{E}^{\text{ext}}&=\mathbf{e}_xA_0k_0\sin(\omega_0t-k_0z),\\ \mathbf{H}^{\text{ext}}&=\mathbf{e}_yA_0k_0\sin(\omega_0t-k_0z).\end{aligned} \quad (10)$$

Let us introduce the laser strength parameter $a_0=eA_0/(mc^2)$, where e and m are the electron charge and mass correspondingly. In order to avoid nonlinear effects below we will consider the case $a_0<<1$, that means that it means that the terms proportional to a_0^2 will be further excluded from our consideration. Second approximation is $\Delta p_z<<p_z$, where Δp_z is the additional momentum induced by the electromagnetic field: $\Delta p_z=p_z-p_{0z}$. Taking into account these two approximations we can write the expressions for the electron's trajectory:

$$\mathbf{R}(t)=\mathbf{R}_0+\mathbf{v}_xt-\frac{a_0c}{\gamma_0\omega_0}\frac{\sin(t\eta)-t\eta}{1-\beta_{0z}}\left\{1,0,\frac{\beta_{x0}}{1-\beta_{0z}}\right\}, \quad (11)$$

where $\eta\approx\omega_0(1-\beta_{0z})$. In order to calculate the energy of scattered radiation per unit frequency and per unit solid angle one needs to find the velocity of the electron in external field:

$$\mathbf{v}=\mathbf{v}_{0x}-\frac{a_0c}{\gamma_0}(\cos(t\eta)-1)\left\{1,0,\frac{\beta_{x0}}{1-\beta_{0z}}\right\}. \quad (12)$$

INTENSITY OF RADIATION

Substituting the obtain expressions for the velocity and trajectory of the electron in the external field (i.e. Eqs. (11)-(12)) in Eq. (7) we obtain:

ISBN: 978-3-95450-240-0 ISSN: 2673-5539 doi:10.18429/JACoW-RuPAC2021-TUPSB28

$$\frac{dW(\mathbf{n},\omega)}{d\Omega d\omega}=\frac{e^2\omega^2}{4\pi^2c^3}\left|\sum_{n=0}^{N-1}e^{iD}\times\right.$$
$$\left.\times\int_{t_0 n}^{T+t_0 n}dt e^{iB\sin\eta t}e^{iAt}\left(\mathbf{H}+\mathbf{K}\cos\eta t\right)\right|^2, \quad (13)$$

where we designate

$$A=\omega-\omega\left(\mathbf{n}\mathbf{v}_0c^{-1}+a_0\gamma_0^{-1}\left[n_x+n_z\beta_{x0}/\left(1-\beta_{0z}\right)\right]\right), \quad (14)$$

$$B=\omega\left[n_x+n_z\beta_{x0}/\left(1-\beta_{0z}\right)\right]a_0\gamma_0^{-1}\omega_0^{-1}\left(1-\beta_{0z}\right)^{-1}, \quad (15)$$

$$\mathbf{K}=\frac{a_0c}{\gamma_0}\left[\frac{\beta_{x0}}{\left(1-\beta_{0z}\right)}\left(\mathbf{e}_yn_x-\mathbf{e}_xn_y\right)-\left(\mathbf{e}_yn_z-n_y\mathbf{e}_z\right)\right], \quad (16)$$

$$\mathbf{H}=\left[\mathbf{n},\mathbf{v}_0\right]-\mathbf{K},\qquad D=-\mathbf{n}\mathbf{R}_0\,\omega/c. \quad (17)$$

Integration can be performed with help of the following formula:

$$e^{ix\sin y}=\sum_{s=-\infty}^{\infty}e^{isy}J_s(x), \quad (18)$$

where $J_s(x)$ is the Bessel function of the s-th order. As a result we find:

$$\frac{dW(\mathbf{n},\omega)}{d\Omega d\omega}=\frac{e^2\omega^2}{4\pi^2c^3}\left|\sum_{s=-\infty}^{\infty}F(s,t_0)\frac{\sin\left(T\left(A+s\eta\right)/2\right)}{\left(A+s\eta\right)/2}\times\right.$$
$$\left.\times e^{i\frac{Nt_0-t_0+T}{2}\left(A+s\eta\right)}\left[\mathbf{H}J_s(B)+\frac{\mathbf{K}}{2}\left(J_{s-1}(B)+J_{s+1}(B)\right)\right]\right|^2, \quad (19)$$

where the factor $F(s,t_0)$ defines the coherent effect due to the modulation of the laser pulse

$$F(s,t_0)=\frac{\sin\left(N\left(A+s\eta\right)t_0/2\right)}{\sin\left(\left(A+s\eta\right)t_0/2\right)}. \quad (20)$$

Actually, $F(s,t_0)$ is proportional to N and being squared is proportional to N^2, which is maximal coefficient enhancing the radiation. The condition of maximal enhancement is

$$\omega=\frac{2m\pi-s\omega_0t_0\left(1-\beta_{0z}\right)}{t_0\left[1-\frac{\mathbf{n}\mathbf{v}_0}{c}-\frac{a_0}{\gamma_0}\left(n_x+n_z\frac{\beta_{x0}}{1-\beta_{0z}}\right)\right]},\ l=0,\pm1,.... \quad (21)$$

For $l=0$ the radiation is maximal, what follows from maximum of relation of the sine to its argument in Eq. (19):

$$\omega=\frac{-s\omega_0\left(1-\beta_{0z}\right)}{1-\frac{\mathbf{n}\mathbf{v}_0}{c}-\frac{a_0}{\gamma_0}\left(n_x+n_z\frac{\beta_{x0}}{1-\beta_{0z}}\right)}. \quad (22)$$

In this case these two factors are maximal simultaneously and, consequently, the maximal enhancement of radiation can be observed.

CONCLUSION

In this paper, we propose the new way to increase the intensity of X-ray inverse Compton source significantly, using the modulated laser pulses. We construct the theory describing the radiation in all its spectral and angular details. Also, we obtain the conditions of the coherent enhancement of radiation.

REFERENCES

[1] D. Yu. Sergeeva, A. P. Potylitsyn, A. A. Tishchenko, M. N. Strikhanov, "Smith-Purcell radiation from periodic beams", *Optics Express*, vol. 25, pp. 26310-26328, 2017. doi:10.1364/OE.25.026310

[2] S. A. Akhmanov and S. Yu. Nikitin, *Physical Optics*. Oxford, Great Britain: Clarendon Press, 1997.

[3] S. N. Andreev *et al.*, "On the motion of a charged particle in a plane monochromatic electromagnetic wave", *Quantum Electronics*, vol. 39, pp. 68-72, 2009. doi:10.1070/QE2009v039n01ABEH013968

[4] D. M. Wolkow, "Über eine Klasse von Lösungen der Diracschen Gleichung", *Zeitschrift für Physik*, vol. 94, pp. 250-260, 1935. doi:10.1007/BF01331022

[5] V. I. Ritus, "Quantum effects of the interaction of elementary particles with an intense electromagnetic field", *Journal of Soviet Laser Research*, vol. 6, pp. 497-617, 1985. doi:10.1007/BF01120220

[6] B. M. Bolotovskii and A. V. Serov, "Special features of motion of particles in an electromagnetic wave", *Physics-Uspekhi*, vol. 46, pp. 645-655, 2003. doi:10.1070/PU2003v046n06ABEH001349

ISBN: 978-3-95450-240-0 ISSN: 2673-5539 doi:10.18429/JACoW-RuPAC2021-TUPSB29

GEANT4 FOR INVERSE COMPTON RADIATION SOURCE SIMULATIONS*

A. A. Savchenko†, A. A. Tishchenko, D. Yu. Sergeeva, National Research Nuclear University MEPhI, 115409 Moscow, Russia
also at National Research Center "Kurchatov Institute", 123098 Moscow, Russia
also at Belgorod National Research University, 308015 Belgorod, Russia

Abstract

In this paper, creation and implementation of the Compton backscattering module into the Geant4 package are under consideration. Created module of Compton backscattering has been implemented as a discrete physical process and operates with a fixed light target (a virtual volume with the properties of a laser beam), with which a beam of charged particles interacts producing x-rays. Such a description allows user to flexibly change necessary parameters depending on the problem being solved, which opens up new possibilities for using Geant4 in the studied area.

INTRODUCTION

Compton backscattering or inverse Compton scattering (ICS) [1, 2] is a promising mechanism for engineering of a bright, compact and versatile X-ray source: with dimensions being significantly smaller, the brightness of this source is comparable with that of synchrotron radiation. Nowadays, active researches are underway on various aspects of this phenomenon [3, 4] aiming at increasing of radiation intensity and quality. In modern science, such kind of research is necessarily accompanied by the computer simulations. In this paper, we are discussing creation and implementation of the Compton backscattering module into the Geant4 package [5-7], which is the leading simulation toolkit in high-energy physics [8], accelerator physics [9], medical physics [10], and space studies [11]. This paper is organized as follow. First, we show brief theoretical description of the ICS process, and then some issues of ICS implementation into Geant4 are considered. We finish with Geant4 simulation results and conclusion.

BRIEF THEORETICAL DESCRIPTION

Let us adduce theoretical description of scattering process shown in Fig. 1. We consider here collision of electron and laser beams under arbitrary angle α. In this case ICS photon spectral-angular distribution reads

$$\frac{d^2N(\mathbf{n},\omega)}{d(\hbar\omega)d\theta}=\frac{\sin(\theta)d\phi}{137}\frac{\omega}{4\hbar\pi^2c^2}\times \times\left|\sum_{s=1}^{\omega/\omega_0}\frac{\sin\left((A-s\eta)NT/2\right)}{(A-s\eta)/2}\frac{J_s(B)}{(-1)^{-s}}\left\{\mathbf{H}-s\frac{\mathbf{K}}{B}\right\}\right|^2, \quad (1)$$

where

$$A=\omega-\frac{\omega}{c}\left[n_x\left(v_{0x}+\frac{a_0c}{\gamma}\right)+n_yv_{0y}+ +n_z\left(v_{0z}+\frac{a_0v_{0x}}{\gamma(1-\beta_{0z})}\right)\right], \quad (2)$$

$$B=\frac{\omega}{c}\left[n_x\frac{a_0c}{\omega_0\gamma(1+\beta_{0z})}+n_z\left(\frac{a_0v_{0x}}{\omega_0\gamma(1-\beta_{0z}^2)}\right)\right], \quad (3)$$

$$T_{\text{int}}=NT=N\frac{2\pi}{\omega_0(1+\beta_{0z})}, \quad (4)$$

$$\mathbf{H}=(\mathbf{e}_xn_y-\mathbf{e}_yn_x)\left(v_{0z}+\frac{a_0v_{0x}}{\gamma(1-\beta_{0z})}\right)+ +(\mathbf{e}_yn_z-\mathbf{e}_zn_y)\left(v_{0x}+\frac{a_0c}{\gamma}\right)+(\mathbf{e}_zn_x-\mathbf{e}_xn_z)v_{0y}, \quad (5)$$

$$\mathbf{K}=(\mathbf{e}_xn_y-\mathbf{e}_yn_x)\left(-\frac{a_0v_{0x}}{\gamma(1-\beta_{0z})}\right)+ +(\mathbf{e}_yn_z-\mathbf{e}_zn_y)\left(-\frac{a_0c}{\gamma}\right), \quad (6)$$

$$\eta=\omega_0+\frac{k_{0z}z}{t}\simeq\omega_0(1+\beta_{0z}), \quad (7)$$

$$n_x=\sin\theta\cos\varphi,\ n_y=\sin\theta\sin\varphi,\ n_z=\cos\theta. \quad (8)$$

Here ω is the frequency of the scattered photon, ω_0 is the laser frequency, γ is the electron Lorentz factor (here we consider moderately relativistic electrons), c is the speed of light, $\beta_{0z}=v_{oz}/c$ is longitudinal component of the reduced speed of electron, with v_{0x},v_{0y},v_{0z} being electron velocity projections; $\mathbf{e}_x,\mathbf{e}_y,\mathbf{e}_z$ are unit axes, θ is the polar angle of observation, φ – is the azimuthal angle of observation, $\hbar$ is the Planck constant, N is the number of electron oscillations in the laser field, T – is the laser wave period, a_0 is the nonlinearity parameter of laser beam. In this paper we consider only linear scattering i.e. $a_0\to 0$.

The frequency of a scattered photon (in a head-on collision of laser and electron beams) is determined by the relation

* This work was supported by the RFBR grant 19-29-12036
† aasavchenko1@mephi.ru

ISBN: 978-3-95450-240-0 ISSN: 2673-5539 doi:10.18429/JACoW-RuPAC2021-TUPSB29

$$\omega \approx \frac{4\gamma^2\omega_0}{1+\gamma^2\theta^2}, \quad (9)$$

with the cutoff frequency of the radiation (in the case of scattering in the direction of the pulse of the primary electron)

$$\omega_{max} = 4\gamma^2\omega_0. \quad (10)$$

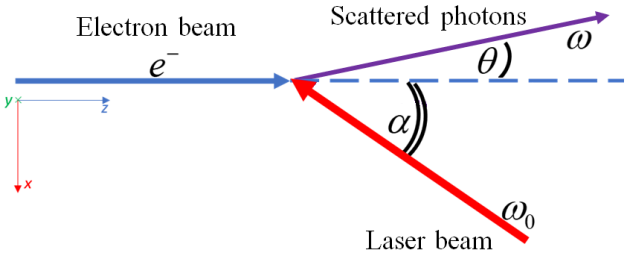

Figure 1: Layout of the ICS. Electron beam (blue) collides with laser beam (red) under angle α producing x-rays (magenta).

ICS IMPLEMENTATION INTO GEANT4

The current version of Geant4 (Geant 10.07.p02) includes several x-ray production processes such as X-ray transition radiation, synchrotron radiation, bremsstrahlung, particle induced x-ray emission. To add ICS physics into Geant4 we took as a basis x-ray transition radiation module (G4VXTRenergyLoss class) developed by Grichine and others [12-15]. Thus, created module of Compton backscattering has been implemented as a discrete physical process. Instead of real laser beam we introduce a so call fixed light target (a virtual volume with the properties of a laser beam), with which a beam of charged particles interacts (see Fig. 2). We start with the estimation of the total number of ICS photons using Poisson distribution with mean value obtained via numerical integration of Eq. (1) over energies and angles. In case when we have non zero number of photons, angular and energy physical tables from the base class G4BackCompton can be filled with corresponding values calculated from Eq. (1). ICS photons production is described by a family of classes shown in Fig. 3. The base class also contains PostStepDoIt function providing ICS photon generation when relativistic charged particle enters the G4LogicalVolume LightTarget. ICS photons are generated randomly along the particle trajectory with random energy and angle taken from corresponding physical tables. Number of photons generated on particle trajectory is defined by GetMeanFreePath function exploiting information about total number of photons and target length. Photon energies is subtracted from the kinetic energy of the incident particle.

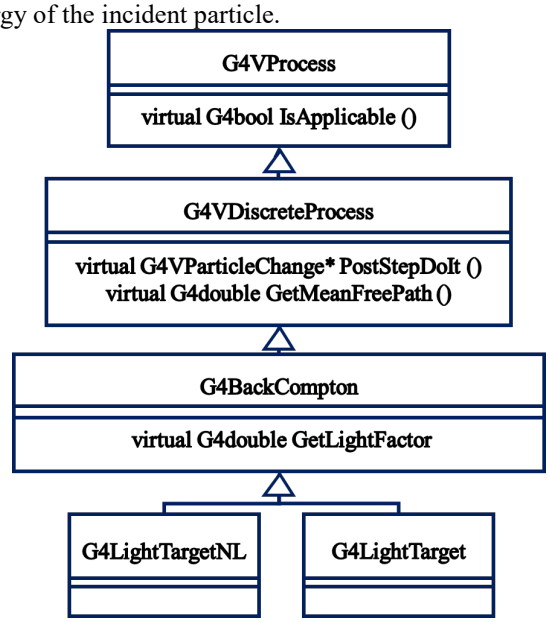

Figure 3: Inheritance diagram for GEANT4 classes describing ICS photon generation from the Light Target. The base class G4BackCompton inherits from G4VDiscreteProcess. G4LightTarget and G4LightTargetNL (not constructed yet) implement pure virtual function GetLightTarget for laser beam parameters transfer.

ICS SIMULATIONS IN GEANT4

In Fig. 4 one can see the results of a ICS simulation using the created module described above. These distributions were obtained for an observation angle θ of 3 mrad relative to the initial trajectory of the 20 MeV electron beam in a head-on collision with a laser beam with wavelengths of 532 and 1064 nm and a pulse time of 9 ns, $a_0 = 0.03$. The figure shows distinct peaks with energies precisely determined by the expression (9) and coincided with experimental data (see Figure 6a from [16]).

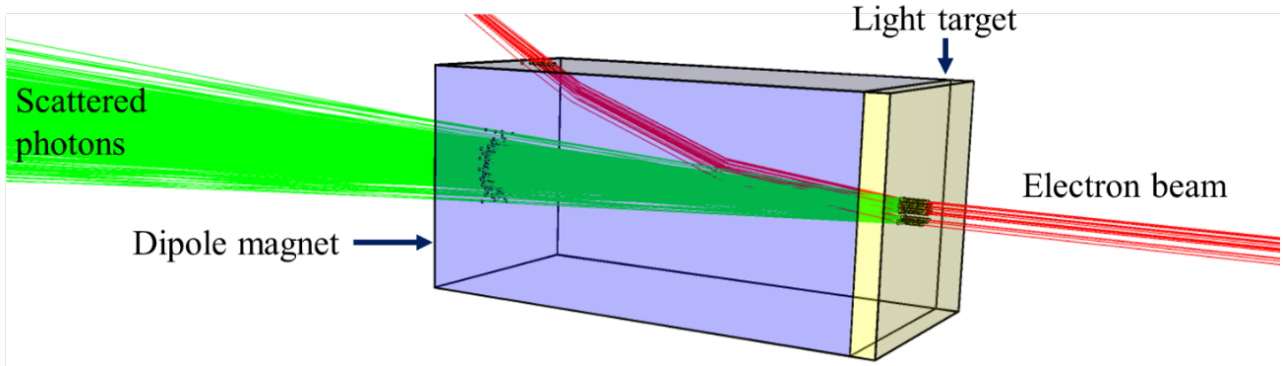

Figure 2: Visualisation of ICS process in Geant4. Electron beam interact with light target producing x-rays, and then it is being declined by dipole magnet.

ISBN: 978-3-95450-240-0 ISSN: 2673-5539 doi:10.18429/JACoW-RuPAC2021-TUPSB29

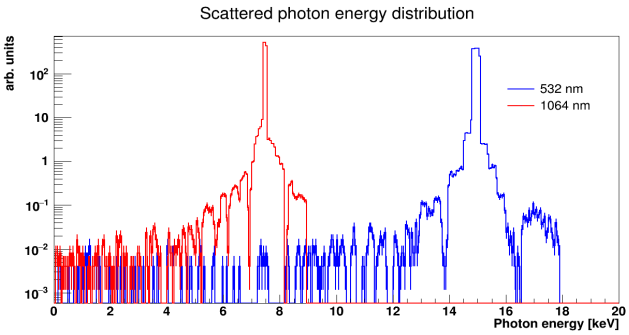

Figure 4: Geant4 simulation of ICS. Head-on collision of the 20 MeV electron beam with a laser beam with wavelengths of 532 (blue) and 1064 (red) nm, pulse time is 9 ns, $a_0 = 0.03$, observation angle θ is 3 mrad relative to the initial trajectory of electrons.

Figure 5 shows the case of electron beam laser collision under angle $\alpha = 7°$ with other conditions being the same like it was for Fig. 4. One can see that peak positions move to lower energies as well as intensities decrease. Such a result shows correct behaviour of ICS module. Indeed the energy and number of photons should decrease with increasing of α.

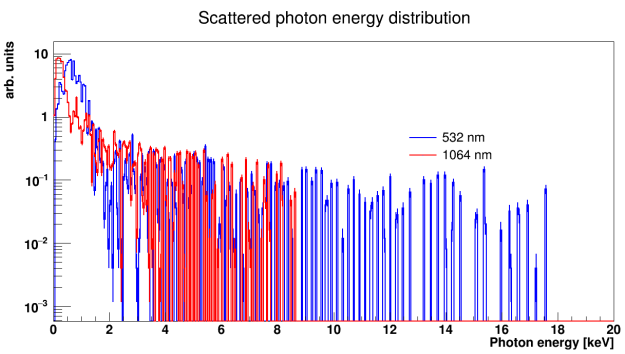

Figure 5: Geant4 simulation of ICS. Collision of the 20 MeV electron beam with a laser beam with wavelengths of 532 (blue) and 1064 (red) nm, pulse time is 9 ns, $a_0 = 0.03$, collision angle $\alpha = 7°$, observation angle θ is 3 mrad relative to the initial trajectory of electrons.

CONCLUSION

We constructed a basis for new discrete physical process in Geant4 using G4FastSimulation principles. It has been shown that the created physical module provides predictable results. Next step is to add a model for non-linear scattering regime, validate created code via comparison with pure theory and experimental data, and after that officially apply for merging with Geant4.

REFERENCES

[1] K. T. Phuoc *et al.*, "All-optical Compton gamma-ray source", *Nat. Photonics*, vol. 6, pp. 308–311, 2012. doi:10.1038/nphoton.2012.82

[2] G. Sarri *et al.*, "Ultrahigh brilliance multi-MeV gamma symbol-Ray beams from nonlinear relativistic Thomson scattering", *Phys. Rev. Lett.*, vol. 113, p. 224801, 2014. doi:10.1103/PhysRevLett.113.224801

[3] K. Dupraz *et al.*, "Design and optimization of a highly efficient optical multipass system for γ-ray beam production from electron laser beam Compton scattering", *Phys. Rev. ST Accel. Beams*, vol. 17, p. 033501, 2014. doi:10.1103/PhysRevSTAB.17.033501

[4] A. Ovodenko *et al.*, "High duty cycle inverse Compton scattering X-ray source", *Appl. Phys. Lett.*, vol. 109, p. 253504, 2016. doi:10.1063/1.4972344

[5] J. Allison *et al.*, "Recent developments in Geant4", *Nucl. Instrum. Meth. A*, vol. 835, pp. 186-225, 2016. doi:10.1016/j.nima.2016.06.125

[6] J. Allison *et al.*, "Geant4 developments and applications", *IEEE Transactions on Nuclear Science*, vol. 53, pp. 270-278, 2006. doi:10.1109/TNS.2006.869826

[7] S. Agostinelli *et al.*, "Geant4 - a simulation toolkit", *Nucl. Instrum. Meth. A*, vol. 506, pp. 250-303, 2003. doi:10.1016/S0168-9002(03)01368-8

[8] U. Husemann, J. Mechnich, and A. Salzburger, "Simulation strategies using FATRAS and GEANT4 for a future upgrade of the ATLAS tracking", *Journal of Physics: Conference Series*, vol. 219, p. 032021, 2010. doi:10.1088/1742-6596/219/3/032021

[9] D. D. DiJulio, C. P. Cooper-Jensen, H. Björgvinsdóttir, Z. Kokai, and P. M. Bentley, "High-energy in-beam neutron measurements of metal-based shielding for accelerator-driven spallation neutron sources", *Phys. Rev. Accel. Beams*, vol. 19, p. 053501, 2016. doi:10.1103/PhysRevAccelBeams.19.053501

[10] S. Incerti, M. Douglass, S. Penfold, S. Guatelli, and E. Bezak, "Review of GEANT4-DNA applications for micro and nanoscale simulations", *Physica Medica*, vol. 32, pp. 1187-1200, 2016. doi:10.1016/j.ejmp.2016.09.007

[11] K. Murase, K. Ioka, S. Nagataki, and T. Nakamura, "High-energy cosmic-ray nuclei from high- and low-luminosity gamma-ray bursts and implications for multimessenger astronomy", *Phys. Rev. D*, vol. 78, p. 023005, 2008. doi:10.1103/PhysRevD.78.023005

[12] J. Apostolakis, S. Giani, M. Maire, A. V. Bagulya, and V. M. Grichine, "Parameterization models for X-ray transition radiation in the GEANT4 package", *Comput. Phys. Commun.*, vol. 132, pp. 241-250, 2000. doi:10.1016/S0010-4655(00)00154-5

[13] V. M. Grichine, "Generation of X-ray transition radiation inside complex radiators", *Phys. Lett. B*, vol. 525, pp. 225-239, 2002. doi:10.1016/S0370-2693(01)01443-5

[14] V. M. Grichine and S. S. Sadilov, "GEANT4 models for X-ray transition radiation", *Nucl. Instrum. Methods A*, vol. 522, pp. 122-125, 2004. doi:10.1016/j.nima.2004.01.031

[15] V. M. Grichine, "Angular distribution of X-ray transition radiation from regular radiators", *Nucl. Instrum. Methods A*, vol. 696, pp. 141-143, 2012. doi:10.1016/j.nima.2012.09.002

[16] K. Chouffani, D. Wells, F. Harmon, J. Jones, and G. Lancaster, "Laser-Compton scattering from a 20 MeV electron beam", *Nucl. Instrum. Methods. A*, vol. 495, pp. 95-106, 2002. doi:10.1016/S0168-9002(02)01580-2

ISBN: 978-3-95450-240-0 ISSN: 2673-5539 doi:10.18429/JACoW-RuPAC2021-TUPSB32

EMISSION OF PHOTONS AT THE INTERACTION OF A HIGH ENERGY POSITRON BEAM WITH A PERIODICALLY DEFORMED CRYSTAL*

A. A. Yanovich†, A. G. Afonin, G. I. Britvich, A. A. Durum, M. Yu. Kostin, I. S. Lobanov, V. I. Pitalev, I. V. Poluektov, Yu. E. Sandomirsky, M. Yu. Chesnokov, Yu. A. Chesnokov, NRC "Kurchatov Institute" – IHEP, 142281 Protvino, Russia

Abstract

Periodically deformed crystals have long attracted attention as "crystalline undulators" [1-8]. In the experiment carried out at the U-70 accelerator, the radiation of positrons moving in a periodically deformed crystal was observed. Experimental evidence has been obtained for an undulator peak in a radiation spectrum, which is qualitatively consistent with calculations. It is shown that most of the emitted energy is due to hard photons with energies of tens of MeV as a result of channeling and reflection of particles, whose spectral density is several times higher than the radiation in an amorphous target.

INTRODUCTION

Intense X-rays are currently used for research in biology, medicine, materials science, and many other areas of science and technology. The traditional way to obtain such beams (with energies of several keV and higher) is the use of special magnets - undulators at accelerators [9]. The energy of the photons generated in the undulator is proportional to the square of the Lorentz factor of the gamma particle and inversely to the period of the undulator L.

Unlike conventional undulators with a period of several centimeters, "crystal undulators" have a period of the submillimeter range and are capable of generating photons hundreds of times harder. In [10], a crystalline undulator was created for the first time, and in [11], an indication was obtained of the existence of an undulator peak in radiation. At the same time, background radiation from channeled particles with higher radiation energies was observed. Later it was shown that unchanneled above-barrier particles emit strongly on trajectory segments that are close to tangents to curved crystallographic planes (as a result of the "volume reflection" process [12-14]). In this work, we tried to measure the emission spectrum in a wide range of energies and to understand what proportion of this spectrum is undulator radiation. Figure 1 shows the difference between the trajectories of channeled particles in a crystalline undulator and trajectories in a conventional undulator. In a crystal, the sinusoidal motion of particles with a period of the deformation of the planes (~ 100 μm) is modulated by frequent oscillations (with a period ~ 1 μm) during channeling between curved crystallographic planes. The radiation due to channeling with frequent oscillations is many times tougher, but its spectral density is lower than undulator radiation due to the deformation of the planes.

* Work supported by Russian Science Foundation (grant 17-12-01532).
† yanovich@ihep.ru

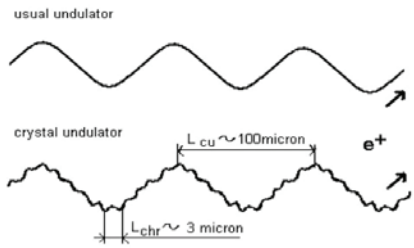

Figure 1: Particle trajectories in a conventional undulator (top) and in a crystalline undulator (bottom).

In addition, as noted above, the above-barrier particles, when their trajectories reach tangents to curved planes, perform aperiodic oscillations (Fig. 2) and also radiate strongly [12]. The techniques described below were used to measure the emission energy spectrum in a wide range.

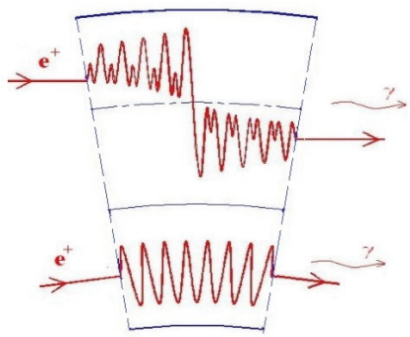

Figure 2: Trajectories of above-barrier particles near the tangent to curved planes (top); the trajectories of channeled particles in the same section are shown below.

CRYSTALLINE TARGET

In [10], the possibility of creating a crystalline undulator — a periodically bent crystal — by double-sided application of mechanical grooves was shown for the first time. A schematic of an undulator with applied grooves, developed at IHEP according to this principle, is shown in Fig. 3. The period of double-sided application of grooves d must be no less than the thickness of the crystal plate h so that sinusoidal deformations penetrate in deep into the entire thickness of the crystal, according to the Saint-Venant principle, known from the theory of elasticity [15]. The first data on radiation with a crystal undulator were obtained with a positron beam with an energy of 10 GeV at IHEP [11]. However, most electron accelerators, where crystal undulators can be used, operate at energies below 6 GeV.

ISBN: 978-3-95450-240-0 ISSN: 2673-5539 doi:10.18429/JACoW-RuPAC2021-TUPSB32

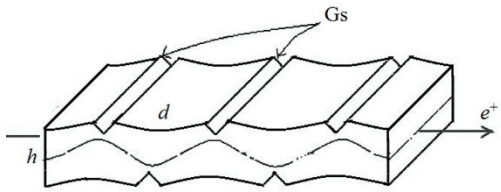

Figure 3: Schematic representation of a crystal undulator: Gs - grooves, d - period of grooving, h - thickness of the crystal plate, e+ - positron beam. The sinusoid shows curved crystallographic planes in the thickness of the crystal.

We have prepared new samples of crystalline undulators (Fig. 4a), optimized for lower energies of positrons, which can be achieved at operating electron accelerators. To capture most of the beam, several identical grooved plates were combined into an array in one holder (Fig. 4b). The experiment with new samples of undulators was carried out on the CRYSTAL setup at a positron energy of 6 GeV. With the achieved parameters, namely, a period of 0.4 mm, an amplitude of 50 Å, the number of periods is 8, it was planned to obtain an undulatory peak of photons about 0.6 MeV (experimental and calculated data will be presented below).

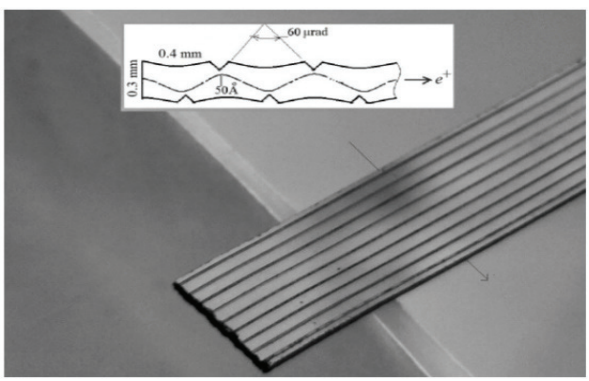

a

b

Figure 4: Crystalline undulator for a 6 GeV positron beam: a - its photograph and a schematic representation of its cross section (inset); b - appearance of the array of plates in one holder (crystal target in the assembly).

EXPERIMENTAL SETUP AND RESULTS

The experiment was performed in the 4a beamline of the U70 accelerator (Fig. 5). A positron beam with an energy of 6 GeV and an intensity of ~ 10^4 particles per cycle was directed to a crystalline device located in a goniometer.

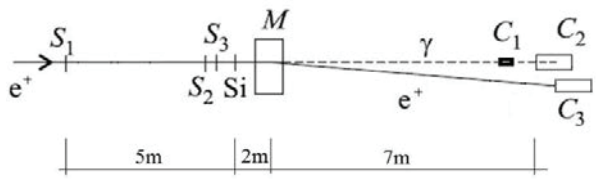

Figure 5: Schematic of the Crystal setup. S_1 – S_3 scintillation counters, C_1 – C_2 calorimeters for determining the energy of generated photons, C_3 – calorimeter for determining the energy of positrons after the magnet M. Si – crystal radiator in the goniometer.

The goniometer step was 0.02 mrad for horizontal rotation. The telescope of scintillation counters S_1, S_2, S_3 separated the fraction of particles entering the crystal radiator and formed an angular divergence $\sigma_x \sim 0.5$ mrad and $\sigma_y \sim 1.0$ mrad. Moreover, the last counter had a cross section of 2 × 30 mm, which coincides with the transverse dimension of the crystal assembly, and was mounted at the end of the radiator and could move with it in the goniometer due to the fiber-optic connection to the PMT. A vertically deflecting magnet M with a magnetic-path length Bl = 0.33 T×m separated the emitted photons and interacting positrons. The C_1 yttrium calorimeter was adapted to register photons in the 60 keV - 2 MeV region, the main BGO detector C_2 could register gamma quanta with energies of several MeV and above (the calorimeters were not used at the same time). In addition, the C_3 - Shashlyk electromagnetic calorimeter [16] registered positrons. The energy spectrum of the positron beam was measured with a Shashlyk calorimeter with a resolution of several percent. The C_1 calorimeter was also used to quickly find the planar orientation of a crystal target.

First, the main plane (111) was found, along which silicon strips were cut and bent, by rotating the horizontal angle φ_x. In Figure 6 shows the orientation dependence of the C_1 count on the horizontal angle of the goniometer.

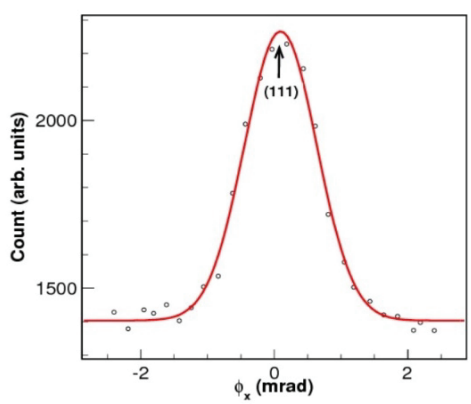

Figure 6: C_1 counting rate depending on the horizontal angle of crystal rotation.

ISBN: 978-3-95450-240-0 ISSN: 2673-5539 doi:10.18429/JACoW-RuPAC2021-TUPSB32

The spectra of emitted energy and energy losses of positrons were measured for two positions of the goniometer: in-plane orientation and disoriented state of the crystal target. In the case of a disoriented state, the crystal is equivalent to an amorphous radiator with a length of 3.5% of the radiation length. In Figure 7 shows the spectra of the emitted energy E × dN / dE for the above two cases of orientation of the crystal target, measured by the calorimeter C_2. The spectrum of the radiated energy for the disoriented state is shown by the horizontal line as for an amorphous medium. For an oriented state of a crystalline target, the emitted energy increases several times due to the generated photons with energies of the MeV range. Calculations show that channeling radiation predominates up to ~100 MeV; above this energy, radiation from above-barrier particles predominates in the spectrum.

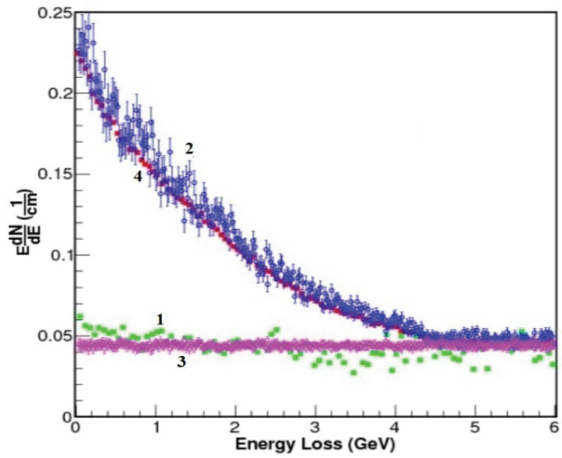

Figure 7: Measured spectra of the radiated energy in different positions of the crystal radiator: 1 - disoriented state, 2 - in-plane orientation; 3, 4 - the corresponding calculation results are shown.

Against this background of high emitted energy and processes of multiple photon production, undulator radiation in the soft spectral region is not visible. To register undulator radiation, it was decided to use another calorimeter based on yttrium aluminate $YAlO_3$. The signal at the yttrium detector adapted for recording undulator radiation was distorted. Calculations show that these distortions arise due to the presence of accompanying coherent radiation during channeling and reflection of particles. At a positron energy of 6 GeV in channel 4a, this creates a multiplicity factor of about 3, which is much higher than 1. Thus, most of the undulator events (0.5 photons per 1 positron) are accompanied by several photons of higher energy and are recorded with distortions. However, using a special selection of events with low energy losses of the primary positron using the Shashlyk calorimeter (about 10% of all statistics), we obtained spectra that are experimental confirmation of the existence of an undulator peak in the 0.6 MeV energy region.

The data on the emitted energy in the C_1 calorimeter, taking into account our selection criterion, are presented in Fig. 8 in comparison with the calculation results confirming the presence of a radiation peak at this energy. This comparison is possible only at a qualitative level, since the instrumental function of the detector was not taken into account (limited detection efficiency of gamma and Compton tail). It should be noted that the calculations of undulator, channeled, and above-barrier radiation were carried out using algorithms and programs [12, 17], where they are described in detail.

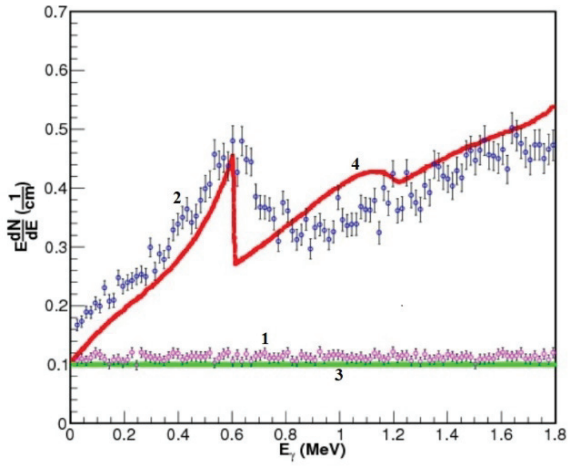

Figure 8: Spectra of the emitted energy in a crystalline target: 1 - experiment, 3 - calculation for the disoriented case; 2 - experiment, 4 - calculation for the oriented case of crystal target.

The setup scheme used will be upgraded in the next sessions of the accelerator operation. In particular, it is planned to use a narrow collimator to limit the angular distribution of gamma radiation. It is also proposed to apply the Compton scattering technique in order to restore the undistorted gamma spectrum.

CONCLUSION

The experiment observed the emission of positrons in a periodically deformed crystal. Under high background conditions of a due to the process of multiple production of photons, we received an experimental indication of the existence of an undulator peak in radiation at a qualitative level, which was confirmed by calculations. It is shown that most of the emitted energy is due to hard photons with energies of tens of MeV as a result of channeling and reflection of particles whose spectral density is a multiple of the radiation in an amorphous target. It is shown that most of the emitted energy is due to hard photons with energies of tens of MeV as a result of channeling and reflection of particles, whose spectral density is several times higher than the radiation in an amorphous target. It is this property of a periodically deformed crystal that makes it a promising source of radiation of high-energy photons and can be used in accelerators (for example, for transillumination of thick objects). The developed crystal radiators also have the prospect of being used for collimating beams at large electron-positron colliders [18], and can be used in special electromagnetic calorimeters (for example, in space).

ISBN: 978-3-95450-240-0 ISSN: 2673-5539 doi:10.18429/JACoW-RuPAC2021-TUPSB32

REFERENCES

[1] V. V. Kaplin, S. V. Plotnikov, and S. A. Vorobiev, "Radiation by charged particles channeled in deformed crystals", *Zh Tekh. . Fiz. (J. Appl. Phys)*, vol. 50, pp. 1079-1081, 1980.

[2] V. G. Baryshevsky, A. O. Grubich, and I. Ya. Dubovskaya, "Generation of gamma-quanta by channeled particles in the presence of a variable external field", *Phys. Lett. A*, vol. 77, pp. 61-64, 1980.

[3] H. Ikezi, Y. R. Lin-Liu, and T. Ohkawa, "Channeling Radiation in a Periodically Distorted Crystal", *Phys. Rev. B*, vol. 30, pp. 1567-1568, 1984.

[4] S. A. Bogacz and J. B. Ketterson, "Possibility of obtaining coherent radiation from a solid state undulator", *J. Appl. Phys.*, vol. 60, pp. 177-188, 1986.

[5] G. B. Dedkov, "Channeling radiation in a crystal undergoing an action of ultrasonic or electromagnetic waves", *Phys. Stat. Sol. (b)*, vol. 184, pp. 535-542, 1994.

[6] A. V. Korol, A. V. Solovev, and W. Greiner, "Photon emission by an ultra-relativistic particle channeling in a periodically bent crystal", *Int. J. Mod. Phys. E*, vol, 8, pp. 49-100, 1999.

[7] U. Mikkelsen and E. Uggerhoj, "A crystalline undulator based on graded composition strained layers in a superlattice", *Nucl. Instr. Methods. B*, vol. 160, pp. 435-439, 2000.

[8] R. O. Avakian, K. T. Avetyan, K. A. Ispirian, and E. G. Melikyan, "Method for preparation of crystalline undulators" *Nucl. Instr. Methods A*, vol. 492, pp. 11-13, 2002.

[9] C. Pellegrini and J. Stohr, "X-ray Free Electron Laser", SLAC *Beam Line*, vol. 32, iss. 1, pp. 32-41, 2002.

[10] S. Bellucci, S. Bini, V. M. Biryukov *et al.*, "Resummed photon spectrum in radiative γ decays", *Phys. Rev. Lett.*, vol. 90, p. 034801, 2003.

[11] V. T. Baranov, S. Bellucci, V. M. Biryukov *et al.*, "First results of investigation of radiation from positrons in a crystalline undulator", *JETP Letters*, vol. 82, pp. 562-564, 2005.

[12] Yu. A. Chesnokov, V. I. Kotov, V. A. Maisheev, and I. A. Yazynin, "Radiations photons in process of charged particle volume reflection in bent monocrystal", *J. Instrum.*, vol. 3, p. P02005, 2008.

[13] A. G. Afonin, V. T. Baranov, G. I. Britvich *et al.*, "Investigation of the emission of photons induced in the volume reflection of 10-GeV positrons in a bent silicon single crystal", *JETP Lett.* 88, pp. 414-417, 2008.

[14] W. Scandale, A. Vomiero, S. Baricordi, *et al.*, "Experimental study of the radiation emitted by 180-GeV/c electrons and positrons volume-reflected in a bent crystal", *Phys. Rev. A*, vol. 79, p. 012903, 2009.

[15] S. P. Timoshenko, J. N. Goodier, Theory of elasticity, McGraw-Hill, New-York, 1951.

[16] G. S. Atoian, V. V. Issakov, O. V. Karavichev, *et al.*,"Development of Shashlyk calorimeter for KOPIO", *Nucl. Instrum. Methods A*, vol. 531, pp. 467-480, 2004.

[17] S. Bellucci and V. A. Maisheev, "Calculations of intensity of radiation in crystal undulator", *Nucl. Instrum. Methods B*, vol. 252, pp. 339-346, 2006.

[18] A. Seryi, "Future prospects of accelerator science for particle physics", *Nucl. Instrum. Methods A*, vol. 623, pp. 23-28, 2010.

ISBN: 978-3-95450-240-0 ISSN: 2673-5539 doi:10.18429/JACoW-RuPAC2021-TUPSB33

2.5 GeV BOOSTER SYNCHROTRON FOR A NEW KURCHATOV SYNCHROTRON RADIATION SOURCE

A.S. Smygacheva, V.N. Korchuganov, Ye.A. Fomin, V.A. Ushakov, A.G. Valentinov
NRC «Kurchatov Institute», Moscow, Russia

Abstract

The Project of complete modernization of the current accelerator complex is in progress in the NRC «Kurchatov Institute». A new booster synchrotron is a part of the injection complex for a new 3-d generation synchrotron light source. The booster has to ensure reliable and stable operation of the upgraded main storage ring. The paper presents the final design of the new booster synchrotron and its main parameters.

INTRODUCTION

The Kurchatov synchrotron radiation source consists of the 2.5 GeV main storage ring, the 450 MeV booster synchrotron and the 80 MeV linac [1]. The current main ring is the second generation light source with electron beam emittance of 98 nm×rad. The accelerator complex has been in operation for over 20 years in its current configuration. Improvement of the qualities of synchrotron radiation beams is associated with the modernization of the entire accelerator complex and the replacement of the main ring with the 3-d generation source [2].

The need to increase the spectral flux and brightness of a light source demands the creation of a new structure with low electron beam emittance (~1–10 nm×rad) for the main ring. A feature of a low-emittance structure is a high natural chromaticity and a small dynamic aperture. A small aperture can lead to a significant decrease in the efficiency of the electron beam injection from the current booster synchrotron with the high-emittance structure into the new main ring. The need to ensure long-term spatial and temporal stability of photon beams dictates high requirements for temperature stabilization of the main ring (±0.1°C). These requirements can be achieved with constant currents in the magnets and the accelerating RF structure, i.e. when the storage ring is operating at the same energy. In addition, with the possibility of injection at full energy and periodic sub-accumulation of electrons from the booster synchrotron, it becomes possible to carry out experiments on synchrotron radiation without interruptions for re-accumulation of electrons and energy rise in the main storage ring. These conditions do not allow using the current booster synchrotron with electron beam emittance of 800 nm×rad and energy of 450 MeV as an injector for the new low-emittance main ring.

The new booster synchrotron must have a symmetrical structure with a periodicity equal to or multiples of the main ring structure. The length of the main drift spaces must be about 2 m to accommodate the magnets of the beam transport channels and the RF cavity. The booster lattice must have relatively small values of Twiss parameters along a beam orbit and the natural emittance from 40 to 60 nm×rad at the energy of 2.5 GeV.

BOOSTER LATTICE

The booster magnet lattice is based on the modified DBA structure with 12 cells. The total number of magnets is the 24 dipoles, the 60 quadrupoles, the 48 sextupoles and the 24 correctors. The booster synchrotron will be located in the same tunnel with the main storage ring. The main lattice parameters are given in Table 1. The optics functions are shown in Fig. 1.

Table 1: The Booster Lattice Parameters

Energy, GeV	0.2 – 2.5
Circumference, m	110.9
Operating frequency, Hz	1
RF-frequency, MHz	181.168
Harmonic number	67
Beam current, mA	10 – 15
Tunes x/y	7.178/4.367
Nat. Chromaticity x/y	-9.0/-8.6
Nat. emittance at 2.5 GeV, nm×rad	43.4
Momentum compaction factor	0.01
Energy spread at 2.5 GeV	8.4×10^{-4}
Energy loss per turn at 2.5 GeV, keV	539
Damping time x/y/s at 2.5 GeV, msec	3.5/3.4/1.7

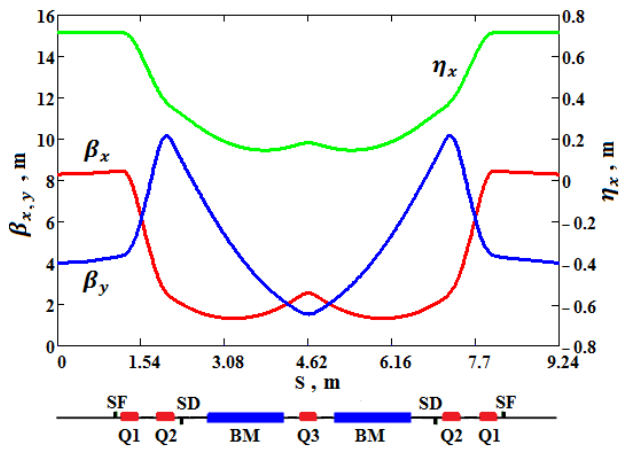

Figure 1: Twiss parameters for one booster cell.

The booster lattice provides the natural emittance of 43.4 nm×rad at the energy of 2.5 GeV. The horizontal and vertical tunes are located far from structure resonances. The dynamic aperture, taking into account chromaticity corrections, is in horizontal from -93 to +129 mm and in vertical of ±105 mm at the center of the main drift. It's

ISBN: 978-3-95450-240-0 ISSN: 2673-5539 doi:10.18429/JACoW-RuPAC2021-TUPSB33

higher than the physical aperture, defined by the vacuum chamber in horizontal of ±25 mm and in vertical of ±10 mm.

The main contribution to the electron beam lifetime of the booster synchrotron is the elastic scattering. The minimum lifetime of 45 sec is at the injection energy of 200 MeV and gas residual pressure of 100 nTorr. This lifetime is sufficient for the optimal booster operation, since immediately after injection the electrons are accelerated from energy of 200 MeV to 2.5 GeV. But to reduce the induced radioactivity it is necessary to provide the residual pressure not higher than 10 nTorr. Note that the minimum lifetime determined by the Touschek effect for one bunch with current of 10 mA is 2 hours at the energy of 1.6 GeV.

LATTICE ERRORS

Alignment errors of the magnets and the magnetic fields errors lead to displacements of the equilibrium orbit and shifts of the betatron tunes. The booster lattice with and without errors was studied using the MAD-X program [3]. 1000 sets of random errors with a Gaussian distribution bounded by an interval of ±2σ were included in calculations. As a result the values of permissible errors for magnets of the booster synchrotron were determined. The permissible errors are: shifts of magnets in three directions – 0.2 mm, turns around three axes – 0.1 mrad, the dipole field relative error – 10^{-4}, the relative dipole field gradient error – 2×10^{-4}, the relative quadrupole field gradient error – 5×10^{-4}.

According to calculations, the mean values of the deviation of the equilibrium orbit are in horizontal of 7.5 mm and in vertical of 6.9 mm. The largest contribution to orbit distortions is made by the alignment errors of the quadrupole magnets in the horizontal and vertical directions.

To correct orbit in the booster synchrotron 24 correctors and 24 correction coils of dipole magnets will be used. To calculate closed orbit correction the SVD algorithm was used in the MAD-X program [4]. As a result, the average value of the maximum strength of the correctors is in horizontal of 0.3 mrad and in vertical of 0.48 mrad. The average value of the maximum strength of the correction coils is in horizontal of 0.19 mrad. The strength corresponds to the rotation angle of the particle trajectory in the magnet. After the correction, the residual orbit deviations are in horizontal of 0.12 mm and in vertical of 0.14 mm.

According to calculations, the betatron tunes is shifted towards the difference resonances of the 3-d and 4-th orders. The betatron tunes and lines of the resonances are shown in Fig. 2. The largest contribution to tunes shifts is made by the alignment errors of the quadrupole and sextupole magnets in the horizontal direction, the quadrupole field gradient error and the dipole field gradient error. However the dynamic aperture remains larger than the physical aperture (Fig. 3).

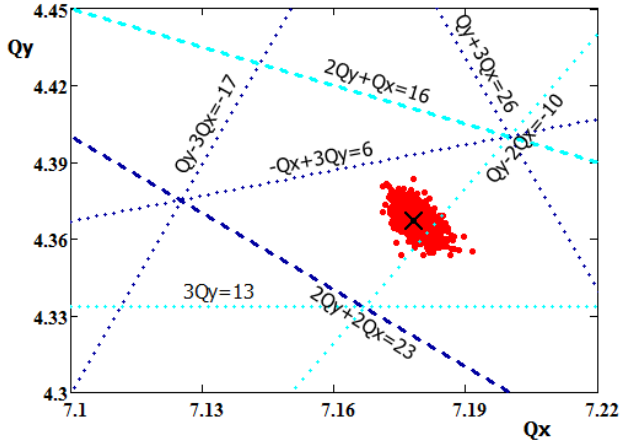

Figure 2: The betatron tunes diagram: the black cross – tunes for the lattice without errors, read points – tunes for the lattice with 1000 sets of random errors.

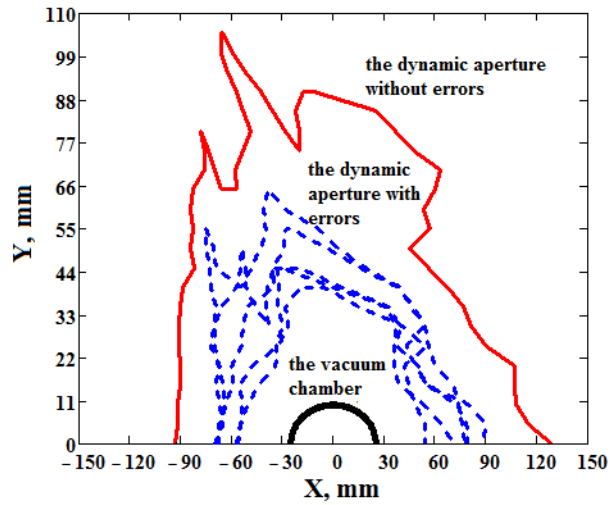

Figure 3: Dynamic aperture for the booster lattice.

MAGNETS

The booster synchrotron will operate in a cyclic mode with a frequency of 1 Hz in the energy range from 200 MeV to 2.5 GeV. The presence of alternating magnetic fields determines the manufacturing technology of the magnets of the booster synchrotron. The yoke of each magnet will be laminated, i.e. will be assembled from 1 mm thick magnetic steel sheets. To ensure high quality of the magnetic field, the profile of each sheet must be made with an accuracy of 10–20 μm. The entire internal geometry of the magnet yoke must be maintained with the same accuracy during assembly. At present, stamping is a proven technology for producing sheets.

The dipole magnet of the booster synchrotron must provide a 15-degree angle of rotation of the particle trajectory over the entire range of operating energies. In this case, the magnetic field in the pole gap varies from 0.1 to 1.3 T. The pole gap is 24 mm. The length of the magnet in the magnetic field (the effective length) required to obtain the indicated rotation angle is 1679.363 mm with a bending radius of 6415 mm and a

ISBN: 978-3-95450-240-0 ISSN: 2673-5539 doi:10.18429/JACoW-RuPAC2021-TUPSB33

magnet yoke length of 1674 mm. The ends of the magnet are parallel to each other.

The quadrupole magnets of the booster synchrotron are grouped into three families: two families of focusing lenses and one family of defocusing lenses. The magnets must provide the required magnetic field gradients with an effective length of 320 mm. The maximum gradients of the quadrupole field at energy of 2.5 GeV are 21.12 T/m, 20.89 T/m, and –23.55 T/m, respectively. The radius of the circle inscribed between the poles of the quadrupole is 25 mm. The yoke length of the quadrupole is 300 mm.

The booster synchrotron sextupole magnets are divided into two families: lenses for correcting horizontal chromaticity and lenses for correcting vertical chromaticity. The required gradients of the sextupole field at energy of 2.5 GeV are 90 T/m^2 and -215 T/m^2, respectively. The effective length and the length of the magnet yoke are 100 mm. The radius of the circle inscribed between the poles of the sextupole is 30 mm.

The correcting magnet combines the functions of a horizontal and a vertical corrector and is a frame dipole magnet. The corrector has to provide a maximum angle of rotation of the particle trajectory of 0.48 mrad with a magnet yoke length of 100 mm.

Direct current sources are required to power the magnetic elements of the booster synchrotron. These sources must operate with inductive loads with time constants of about 0.5 s for dipole magnets, about 0.2 s for quadrupole and sextupole magnets, 20–50 ms for correcting magnets. The booster synchrotron will operate in a cyclic mode; therefore, the source current at both levels and during the rise of the beam energy must be stabilized with high accuracy. In addition, the sources must have a sufficiently high output voltage for the forced increase and decrease of the current in the magnets and ensure operation with periodically oscillating high voltage of both polarities.

Coils of magnets are connected to the electrical network sequentially by families. It is possible to divide the magnets into groups within the same family. For example, not all 24 dipole magnets can be powered from one source, but 12 or 6 magnets. This approach reduces the requirements for the power characteristics of power supplies and increases the safety of the installation as a whole. The final decisions on the scheme for connecting the magnets will be made at the stage of engineering studies of the communications of the accelerator complex.

To achieve a high quality of the magnetic field and the required magnets parameters, the geometry of all magnets is determined by 2D- and 3D-simulations of magnetic fields. For more information on magnets design, see a paper [5] at this conference.

RF SYSTEM

The RF system of the booster synchrotron is assumed to be similar to that currently operating at the main storage ring of the Kurchatov synchrotron radiation source [6]. It is based on the one RF generator and the one accelerating cavity. The operating frequency of the booster RF system is taken to be equal to the RF frequency of the main storage ring – 181 MHz, which corresponds to the 67th harmonic of the circulation frequency in the booster synchrotron (2.704 MHz). This choice is optimal from the point of view of the best synchronization of both accelerators, the transfer of electron bunches into predetermined separatrices without losses and increasing the coherent oscillations.

The RF generator is based on an output stage with a tube module (tetrode). The long-term operating output power of the RF generator is 200 kW in continuous mode at the frequency range from 180 to 182 MHz. Power is transmitted from the RF generator to the cavity via a 75 Ohm coaxial waveguide (feeder). The cavity of the booster synchrotron has a design similar to the cavities of the operating main storage ring. The design feature of the cavity is the presence of tuners for automatic frequency control of the fundamental mode and tuners for manual control of the frequencies of the high order modes. The stability of the RF system under load by the beam current is provided by a feedback system, with the help of which it is possible to set and stabilize the accelerating voltage and the phase difference between the feeder current and the accelerating voltage.

The RF system of the booster synchrotron will ensure the capture of electrons into the acceleration mode with a current of 10-15 mA and an energy spread of ± 1.5% when a beam is injected from the linac and provide an energy acceptance within 0.5% at an energy of 2.5 GeV to establish a reasonable beam lifetime, and also compensate for losses energy by electrons for synchrotron radiation. The energy losses per turn are 22.1 eV at 200 MeV and 538.7 keV at 2.5 GeV.

CONCLUSION

The booster lattice based on modified DBA structure satisfies the requirement of placing the synchrotron in the same tunnel with the main storage ring. It consists of 12 cells, each with mirror symmetry about the center of the cell. This lattice significantly reduces the strength of machine resonances in the working range of betatron frequencies and is stable against various kinds of magnetic field errors within the permissible values. The structure of the booster synchrotron has a large dynamic aperture with compensated natural chromaticity and low natural emittance, which is necessary and sufficient for efficient transfer of the electron beam from the booster synchrotron to the main storage ring with minimal particle losses.

REFERENCES

[1] V. Korchuganov *et al.*, “Status of the Kurchatov synchrotron radiation source”, in *Proc. RuPAC’18*, Protvino, Russia, Oct. 2018, pp. 81-83. doi:10.18429/JACoW-RUPAC2018-WEZMH01

[2] Ye. Fomin and V.N. Korchuganov, “New Lattice Design for Kurchatov Synchrotron Radiation Source”, presented at

ISBN: 978-3-95450-240-0 ISSN: 2673-5539 doi:10.18429/JACoW-RuPAC2021-TUPSB33

RuPAC'21, Crimea, Russia, Sep. 2021, paper TUPSB34, this conference.

[3] MAD-X, http://madx.web.cern.ch/madx/.

[4] W. Herr, "Implementation of new closed orbit correction procedures in the MAD-X program", CERN, Geneva, Switzerland, Rep. CERN-SL-2002-48 (AP), Oct. 2002.

[5] A.S. Smygacheva, V.N. Korchuganov, and Ye.A. Fomin, "Magnets Design for 2.5 GeV Booster Synchrotron", presented at RuPAC'21, Crimea, Russia, Sep. 2021, paper WEPSC20, this conference.

[6] I.K. Sedlyarov *et al.*, "Upgrade of the RF system of Siberia-2 electron storage ring/SR source", in *Proc. PAC'09*, Vancouver, BC, Canada, May 2009, paper WE5PFP015, pp. 2018-2020.

ISBN: 978-3-95450-240-0 ISSN: 2673-5539 doi:10.18429/JACoW-RuPAC2021-TUPSB34

NEW LATTICE DESIGN FOR KURCHATOV SYNCHROTRON RADIATION SOURCE

Ye. Fomin†, V. Korchuganov, NRC "Kurchatov Institute", Moscow, Russia

Abstract

Nowadays the upgrade project of the 2nd generation synchrotron radiation source operating at NRC "Kurchatov Institute" has been ongoing. The main aim of the project is to create a new synchrotron radiation source with the same 124 m circumference and providing synchrotron radiation properties inherent to the 3rd generation sources (emittance ~3 nm·rad). The new machine will consist of a new storage ring with 2.5 GeV electron energy, full energy booster synchrotron, and 0.2 GeV linac. The mandatory requirement for the project is to keep all currently operating beamlines.

In this article, we present the design challenges and approaches for this machine, the conceptual design, and the baseline lattice.

INTRODUCTION

Kurchatov synchrotron radiation source is a 2nd generation source with 2.5 GeV electron beam energy and 98 nm·rad emittance. The circumference of the main storage ring is 124.13 m. The main storage ring lattice is based on a modified DBA type lattice and consists of 6 cells, each of which contains two 3 m straight sections [1].

Currently, 13 beamlines operate regularly and 4 more are under construction. The main source of synchrotron radiation is bending magnets with 1.7 T magnetic fields. The characteristic photon energy is 7 keV and the full spectral range of synchrotron radiation is 0.1 – 2000 Å. To expand the facility's experimental opportunities 3 superconductive wiggles were installed in the straight sections of the main storage ring (one with 7.5 T and two with 3 T maximum fields).

Improving qualities of photon beams primarily associated with an increase in their intensity and brightness requires the upgrade of the facility completely. So, after such upgrade, the facility must have an electron beam emittance less than 5 nm·rad and provide synchrotron radiation beams with properties close to properties of the beams generated by the 3rd generation sources. For this apart from the development of a new main storage ring, it is necessary to develop a new full energy booster synchrotron and a new linac. Moreover, a mandatory requirement for the upgrade project is the preservation of all currently operating beamlines.

MAIN REQUIREMENTS

DBA type lattice was designed in the mid-1970s by R. Chasman and G. Green and formed the basis of the 2nd and 3rd generation synchrotron radiation sources [2]. The development of technologies for creating magnet, RF, vacuum systems, software, and hardware for 3D simulations have created opportunities for the construction of new synchrotron radiation sources based on MBA lattice. The use of complex and high-precision magnet elements in MBA lattice makes it possible to reduce electron beam emittance up to 2 orders and even more than in DBA lattice. While the circumferences of both storage rings are about the same. The first successfully commissioned such projects are MAX-IV [3] and ESRF upgrade project – ESRF EBS [4]. Also, deserve attention projects such as the SLS-2 project [5] and one of the most ambitious to date – the PETRA-IV project [6].

Based on the last progress in accelerator physics and technologies and on world scientific community experience in an upgrade of working synchrotron radiation sources we have formulated the main requirements for the new Kurchatov synchrotron radiation lattice:

- Preservation all currently operated beamlines.
- Achievement the electron beam emittance less than 5 nm·rad.
- Preservation spectral range of synchrotron radiation.
- Preservation ring symmetry and zero-dispersion straight sections.
- Providing the possibility of electron beam injection and storing.
- Beam lifetime more than 10 hours.
- Preservation of the main storage ring circumference.
- Compliance with technological limitations.

NEW LATTICE

Kurchatov synchrotron radiation source is one of the compact sources in the world. The small circumference of the main storage ring is achieved through the use of bending magnets with a high magnetic field (1.7 T). This imposes very strict limitations from the technologies side.

To reduce electron beam emittance and simultaneously minimize a storage ring circumference, it is advisable to use special magnets with combined functions (like sandwich type magnets) and antibend magnets [7, 8]. Based on the results of the conducted research the modified 3BA type lattice is optimal for the new Kurchatov synchrotron radiation source. This half of lattice formed from 3 bending magnets with 2.0 T magnetic field, 4 combined functions magnets, 4 magnets with antibend, 2 doublets of quadrupole lenses, 6 chromatic and 1 harmonic sexupoles. In the new lattice, there are no octupoles. A comparison of current and new lattices of the Kurchatov synchrotron radiation source is illustrated in Fig. 1.

† yafomin@gmail.com

ISBN: 978-3-95450-240-0 ISSN: 2673-5539 doi:10.18429/JACoW-RuPAC2021-TUPSB34

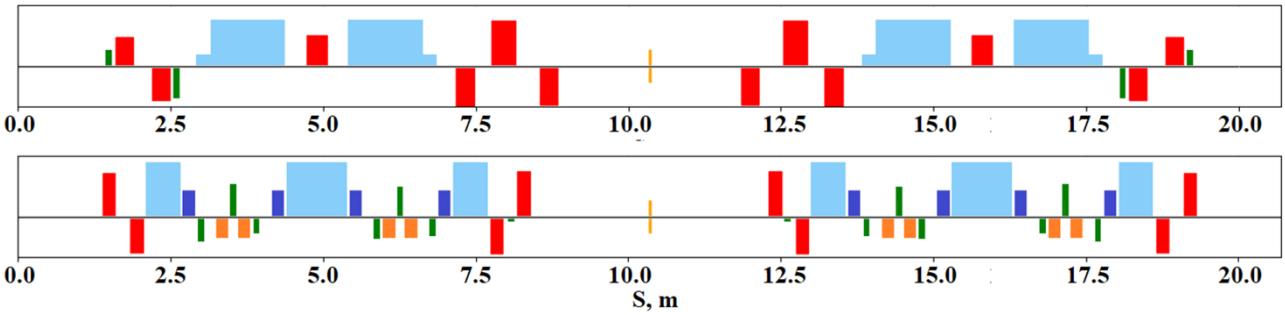

Figure 1: A comparison of current (top) and new (bottom) lattices of the Kurchatov synchrotron radiation source. Light blue – main bending magnets with 2 T magnetic field, blue – special magnets with combined functions, orange – antibend magnets, red – quadrupoles, green – sextupoles.

To reduce electron beam emittance as much as possible in the new lattice a few requirements above was dropped. Namely circumference of the main storage ring and the position of straight sections are not saved exactly. Since the fulfillment of these requirements does not allow obtaining the emittance of the electron beam less than 10 nm·rad. In addition, to increase the space between magnetic elements, the field in bending magnets was increased from 1.7 to 2.0 T. Avoiding strict compliance with these requirements is a compromise between achieving a low emittance and technical difficulties of a new project.

Optics functions of the new lattice are illustrated in Fig. 2.

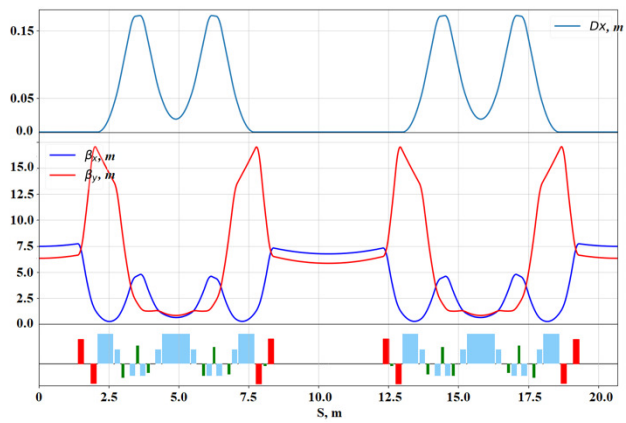

Figure 2: Optics functions.

A distinctive feature of the new lattice is the increased length of the straight section with zero dispersion in the current lattice. This will make it possible to install longer insertion devices into it. The second straight section in the new lattice has also zero dispersion and can be used for insertion devices installation too. As well horizontal and vertical betafunctions in the straight section are approximately the same. This will allow to tune machine to operate in special mode with round beams of synchrotron radiation from insertion devices. All of this will expand the facility's performance.

Achieving low emittances requires lattices with more strong quadrupoles, which leads to an increase in natural chromaticity and to an increase in the strengths of sextupoles used to compensate for it. This leads to a stronger nonlinear motion of electrons, the appearance of a large number of resonances, and a decrease in the size of the dynamic aperture. To compensate for natural chromaticity, increase the size of the dynamic aperture and minimize the betatron tunes shifts 6 chromatic and 1 harmonic sextupole families are used. The strengths of sextupoles have been optimized with the help of genetic algorithms enhanced by machine learning [9] to minimize nonlinear effects on the electron beam dynamics.

The dynamic aperture in the middle of the injection straight section is presented in Fig. 3. The vertical size of the dynamic aperture without any errors is ±12 mm and horizontal size – ±16 mm. This dynamic aperture size is sufficient to inject an electron beam using an off-axis injection scheme with 4 kickers.

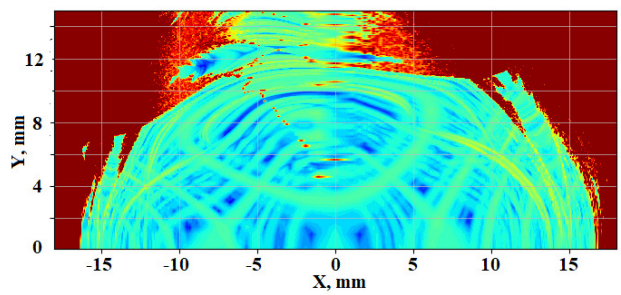

Figure 3: The dynamic aperture in the middle of the injection straight section.

A tune diagram for the good field region (±11 mm in horizontal and ±8 mm in vertical planes) is shown in Fig. 4. The working point was removed from low-order resonances at a sufficient distance to ensure stable betatron oscillations with an amplitude of up to 10-15 mm and an energy spread of up to 3.5 %.

The projected parameters of the new Kurchatov synchrotron radiation source are summarized in Table 1.

The influence of errors on the dynamic aperture is shown in the Fig. 5, closed orbit in Fig. 6 and Fig. 7. Here all elements have errors in a magnetic field, gradient, horizontal and vertical displacement, and tilt.

After the correction dynamic aperture restores almost to the reference aperture without errors. A similar situation with compensation for closed orbit distortion. After correction, residual distortions do not exceed 20 μm in both planes.

ISBN: 978-3-95450-240-0 ISSN: 2673-5539 doi:10.18429/JACoW-RuPAC2021-TUPSB34

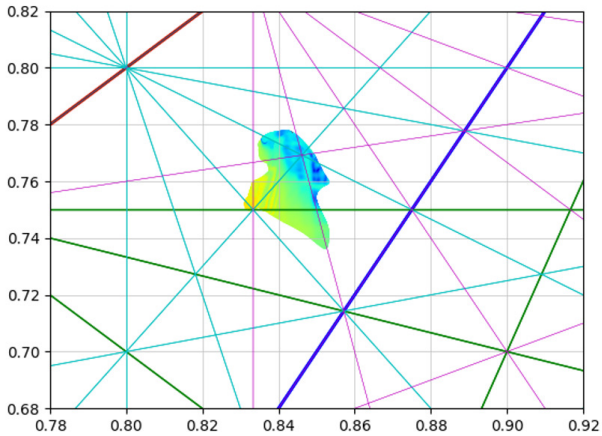

Figure 4: Tune diagram.

Table 1: Main Parameters

Parameter	Value
Energy	2.5 GeV
Circumference	124.169 m
Emittance	2.86 nm·rad
Beam current	up to 200 mA
Tunes	14.8529 / 6.7551
Chromaticity	-29.3 / - 27.1
Energy loss	925.4 keV
Dumping times	0.955/2.238/3.404 ms
RF frequency	181.078 MHz

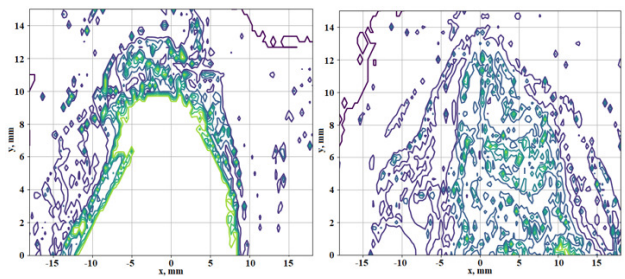

Figure 5: Dynamic aperture with errors. $\sigma_{x/y}$ is 35 μm on the left and 100 μm on the right.

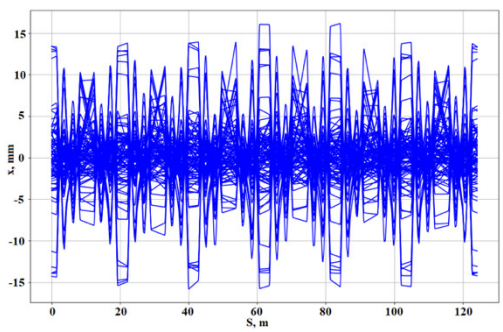

Figure 6: Horizontal orbit distortions, $\sigma_{x/y}$ is 50 μm.

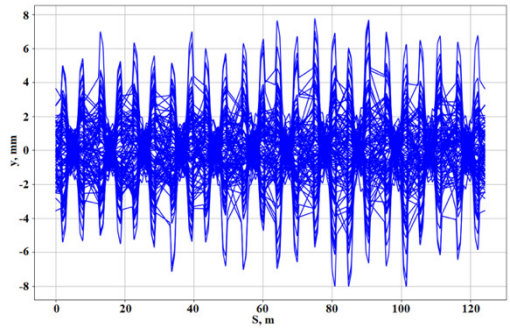

Figure 7: Vertical orbit distortions, $\sigma_{x/y}$ is 50 μm

SUMMARY AND OUTLOOK

Design study for the Kurchatov synchrotron radiation source upgrade is ongoing and a reference lattice is in place. Projected baseline parameters are 200 mA current, 2.86 nm·rad emittance. Tolerance studies and commissioning simulations are ongoing, R&D on technical subsystems has been launched. Despite all the difficulties the project looks quite real from a technical point of view.

ACKNOWLEDGMENTS

The reported study was funded by RFBR, project number 19-29-12039.

This work has been carried out using computing resources of the federal collective usage center Complex for Simulation and Data Processing for Megascience Facilities at NRC "Kurchatov Institute".

REFERENCES

[1] V. Anashin *et al.*, "The dedicated synchrotron radiation source Siberia-2", *Nucl. Instrum. Meth. A,* vol. 282, pp. 369-374, 1989. doi: 10.1016/0168-9002(89)90004-1

[2] R. Chasman, G. K. Green and E. M. Rowe, "Preliminary Design of a Dedicated Synchrotron Radiation Facility", in *IEEE Transactions on Nuclear Science*, vol. 22, no. 3, pp. 1765-1767, June 1975, doi: 10.1109/TNS.1975.4327987

[3] MAX-IV Conceptual Design Report, MAX-lab.

[4] ESRF upgrade program phase II (2015 - 2022) Technical Design Study, ESRF, 2014.

[5] SLS-2 Conceptual Design Report, PSI-Bericht, 2017.

[6] I. V. Agapov, R. Brinkmann, Y.-C. Chae, X. N. Gavaldà, J. Keil, and R. Wanzenberg, "Lattice Design for PETRA IV: Towards a Diffraction-Limited Storage Ring", in *Proc. 60th ICFA Advanced Beam Dynamics Workshop on Future Light Sources (FLS'18)*, Shanghai, China, Mar. 2018, pp. 12-16. doi:10.18429/JACoW-FLS2018-MOP1WB01

[7] Ye. Fomin and V. Korchuganov, "Kurchatov Synchrotron Radiation Source - From the 2nd to the 4th Generation", in *Proc. 26th Russian Particle Accelerator Conf. (RuPAC'18)*, Protvino, Russia, Oct. 2018, pp. 84-87. doi:10.18429/JACoW-RUPAC2018-WEZMH02

[8] E. B. Levichev, "Low emittance electron storage rings", *Physics-Uspekhi*, vol. 61, pp. 29-51. doi: 10.3367/ufne.2016.12.038014

[9] Ye. Fomin, "Machine learning for the storage ring optimization", presented at the RuPAC-2021, Alushta, Crimea, October 2021, paper MOPSA23.

ISBN: 978-3-95450-240-0 ISSN: 2673-5539 doi:10.18429/JACoW-RuPAC2021-TUPSB35

3D SIMULATION STUDY AND OPTIMIZATION OF MAGNETIC SYSTEM OF DECRIS ION SOURCE WITH THE PUMPING FREQUENCY 28 GHz

V. Amoskov†, E. Gapionok, V. Kukhtin, A. Labusov, E. Lamzin, A. Makarov, I. Rodin, A. Safonov, N. Shatil, D. Stepanov, E. Zapretilina, JSC NIIEFA, St. Petersburg, Russia
S. Bogomolov, A. Efremov, JINR, Dubna, Russia
S. Sytchevsky, Saint Petersburg State University, Russia

Abstract

A superconducting magnet system for a 28 GHz ECR ion source (DECRIS) was studied in order to select its parameters and optimize performance.

Parametric magnetic models were performed for two design configurations, conventional ("sextupole-in-solenoid") and reversed ("solenoid-in-sextupole"). For both configurations, the magnetic effect of the booster and the steel poles on the magnet performance was investigated from the point of view of critical parameters of the system – currents, fields, and forces.

Results of the parametric computations were used to optimize the geometry and sizes of the magnet as well as the magnetic shield, the booster, and the poles.

A comparison of the obtained parameters was used to select the candidate magnet configuration for further design and manufacture.

INTRODUCTION

A 28 GHz ECR ion source DECRIS will be used for the Superheavy Elements Factory (SHE) at JINR, Dubna, which allows to ensure desired mass and energy ranges and the beam intensity in accelerators.

Operation at the 28 GHz demands efficient magnetic configuration capable to provide the axial field as high as 4 T at the injection side in the plasma region.

In order to generate high confining fields DECRIS utilizes a superconducting magnetic system. Efremov Institute is responsible for the magnetic system (MS) design and optimization. Key parameters of the magnetic system are listed in Table 1.

Table 1: Key Parameters of the Magnet System

Warm bore diameter	142 mm
Plasma chamber internal diameter	125 mm
Field peak-to-peak axial distance	420 mm
B_{inj} on axis	4 T
B_{extr} on axis	2÷2.5 T
Minimal axial field B_{min}	0.5÷0.8 T
Field module $\|\mathbf{B}\|$ at R = 62 mm	2.02 T

The magnet system consists of two groups of coils capable to generate min-B confining fields in the plasma region. The axial mirror field is produced by a segmented solenoid. The radial field is generated by a sextupole formed with six racetrack coils assembled in a circle so that their poles alternate.

RESULTS FOR TWO MODELS

Two principal coil layouts are briefly discussed focusing on optimal magnetic performance: a *conventional* ("sextupole-in-solenoid") configuration and a *reversed* ("solenoid-in-sextupole") option. In the "sextupole-in-solenoid" design racetrack coils of the sextupole are located inside the solenoid (Fig. 1a). In the "solenoid-in-sextupole" design the coils arrangement is reversed (Fig. 2a). Both configurations have been well proven in existing ECR sources. Particularly, VENUS for the Facility for Rare Isotope Beams at LBNL utilizes "sextupole-in-solenoid" magnets [1]. An example of the "sextupole-in-solenoid" magnet design is SECRAL-II for the Heavy Ion Facility in Lanzhou, China [2].

Figures 1b-2b show similar models with iron. The racetrack coils contain steel poles. All the coils are enveloped with a steel booster. All steel components are saturated during operation.

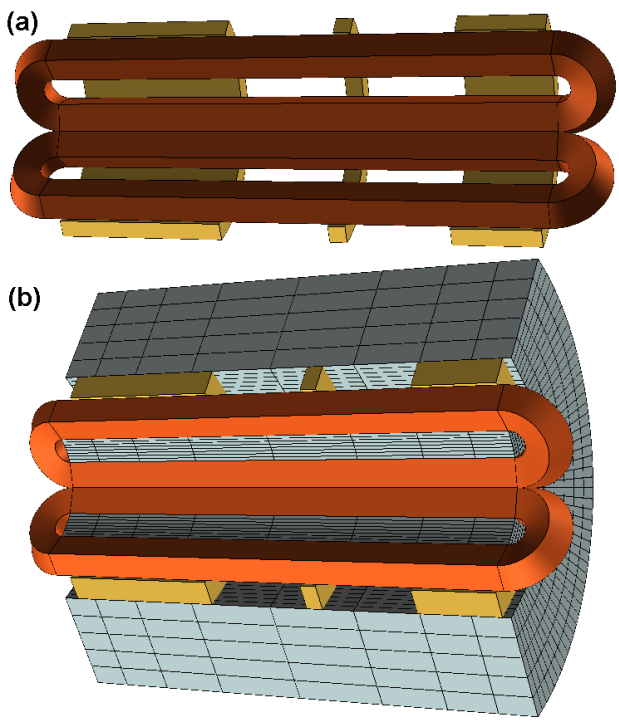

Figure 1: Conventional (sextupole-in-solenoid) magnetic system. Model without (a) and with (b) iron.

† avm@sintez.niiefa.spb.su

ISBN: 978-3-95450-240-0 ISSN: 2673-5539 doi:10.18429/JACoW-RuPAC2021-TUPSB35

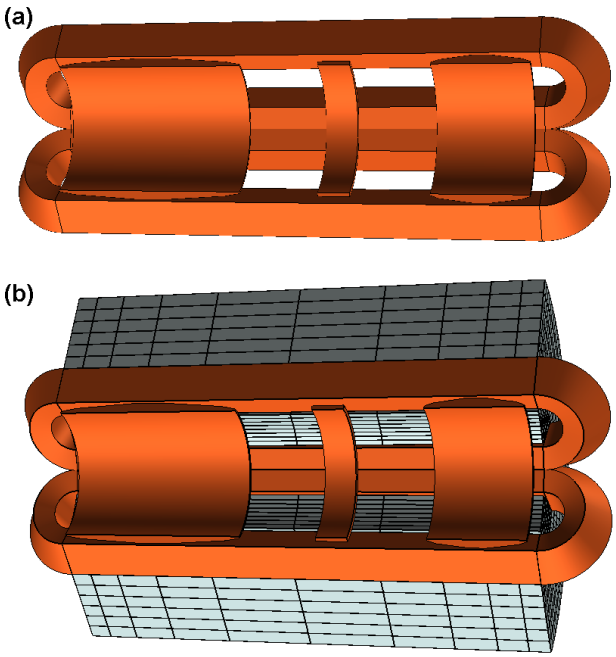

Figure 2: Reversed (solenoid-in-sextupole) magnetic system. Model without (a) and with (b) iron.

Table 2 summarizes the achieved magnetic parameters of these systems.

Table 2: Total Current I_t, Current Density J_e, and Maximum Field B_{max} in Conductor for Considered Options

Parameter	Conventional		Reversed	
	Fig. 1a	Fig. 1b	Fig. 2a	Fig. 2b
Sextuple				
I_t, kAt	353	288	622	482
J_e, A/mm^2	316	258	304	235
B_{max}, T	8.0	7.6	8.6	7.8
Solenoid from injection side				
I_t, kAt	1088	961	865	842
J_e, A/mm^2	218	192	416	405
B_{max}, T	7.3	7.3	7.3	7.1

As seen from Table 2, the steel components sufficiently decrease the field in conductor and coil current.

Parametric simulations were performed for two design options to investigate magnetic effect of the booster and the poles on the magnet performance. Results of computations were used to optimize the geometry and sizes of the magnet.

For better reliability and validation of the result, computations were performed with two codes, KOMPOT and KLONDIKE, utilizing the differential and integral formulations, respectively [3, 4]. The obtained parameters allowed selection of a candidate magnet configuration for further design and manufacture. Table 3 summarizes comparative evaluation of the basic parameters for both design options.

Table 3: Magnetic Parameters for Two Options

Parameter	Conventional, Fig. 1b	Reversed, Fig. 2b
Max field in conductor, T		
Sextuple	7.6	7.8
Solenoid	7.3	7.1
conductor current density, A/mm^2 (calculated/ NbTi design)		
Sextuple	258/264	**235/222**
Solenoid	192/270	**405/369**
Others		
Stored energy, kJ	135	230
Conductor length, km	9.3	6.0

Figure 3 presents the current density in a NbTi cable as a function of the field.

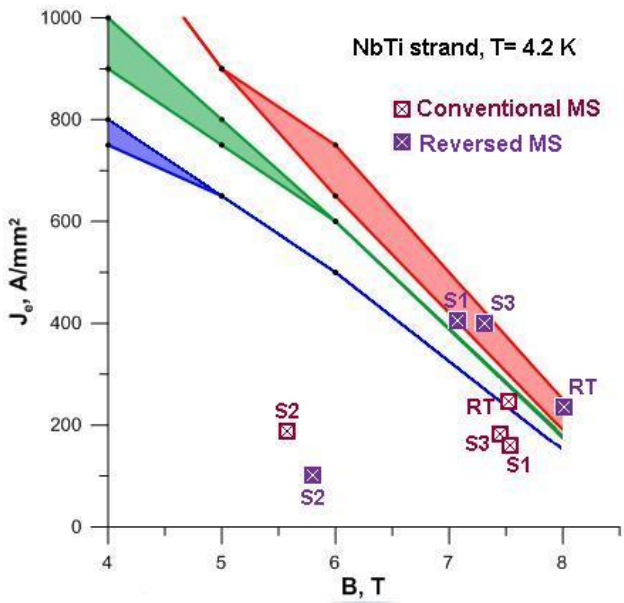

Figure 3: Current density J_e vs. magnetic field B in superconducting ECR magnets. S1, S2, S3 – solenoids, RT – racetrack coil.

The blue, green, and red lines outline, respectively, the reliable, recommended, and risky mode of operation. Markers show the achieved values of current density. Figure 3 shows, that conventional design is favourable and allows using an NbTi conductor for the winding.

Figures 4 and 5 demonstrate field maps (in T) in two planes X = 0 and Y = 0, corresponding to racetrack poles centre and racetrack outer boundary. ECR heating zone R < 62 м is marked in yellow. Solenoid cross-sections are purple, racetracks – orange, and racetrack poles – grey.

Conceptually the conventional option is presented in Fig. 6.

ISBN: 978-3-95450-240-0 ISSN: 2673-5539 doi:10.18429/JACoW-RuPAC2021-TUPSB35

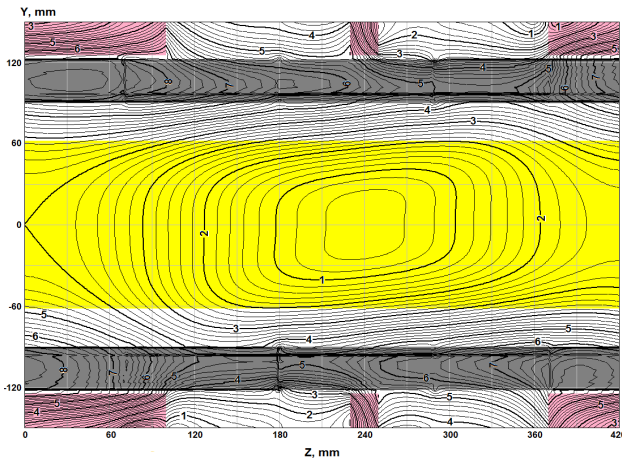

Figure 4: Simulated field map in plane X = 0.

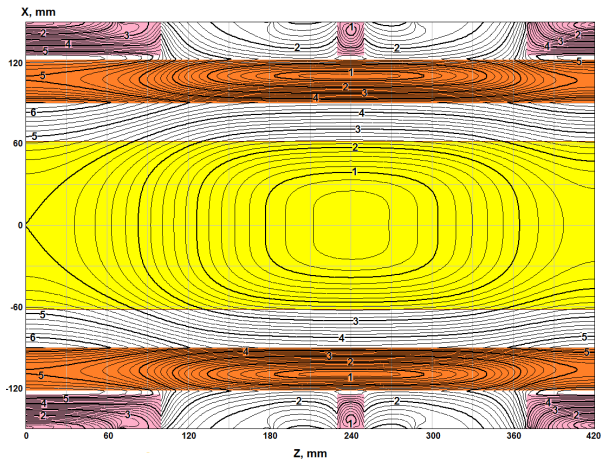

Figure 5: Simulated field map in plane Y = 0.

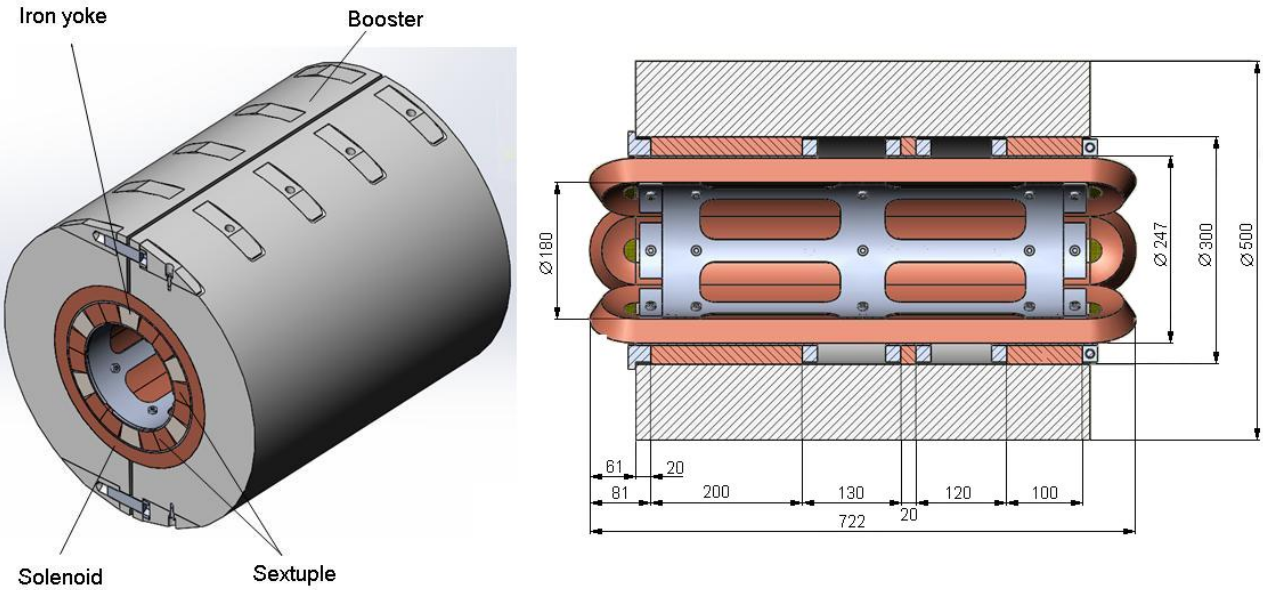

Figure 6: Conceptual design of magnetic system.

CONCLUSION

The simulations have revealed that even with the optimized design the operating current in the "solenoid-in-sextupole" configuration is close to the critical value. This greatly increases conductor loading and deteriorates reliability of the ECR source operation.

For this reason, the conventional "sextupole-in-solenoid" design has been proposed as preferable for further development and construction.

REFERENCES

[1] D. Leitner *et al.*, "Status report of the 28GHz superconducting electron cyclotron resonance ion source VENUS", *Rev. Sci. Instrum.*, vol. 77, no. 3, Art.no. 03A302, 2006, doi:10.1063/1.2149298

[2] H.W. Zhao *et al.*, "Intense highly charged ion beam production and operation with a superconducting electron cyclotron resonance ion source", *Phys. Rev. Accel. Beams*, vol. 20, Art.no. 094801, 2017, doi:10.1103/PhysRevAccelBeams.20.094801

[3] V. Amoskov *et al.*, "Computation technology based on KOMPOT and KLONDIKE codes for magnetostatic simulations in tokamaks", *Plasma Devices Oper.*, vol. 16, no.2, pp.89-103, 2008, doi:10.1080/10519990802018023

[4] V.M. Amoskov *et al.*, "Magnetic model MMTC-2.2 of ITER tokamak complex", *Vestnik of Saint Petersburg University, Applied Mathematics. Computer Science. Control Processes*, vol. 15, no. 1, pp. 5-21, 2019, doi:10.21638/11702/spbu10.2019.101

ISBN: 978-3-95450-240-0 ISSN: 2673-5539 doi:10.18429/JACoW-RuPAC2021-TUPSB36

HIGH INTENSITY CALCIUM, CHROMIUM AND TITANIUM ION BEAMS FROM THE PERMANENT MAGNET ECR ION SOURCE DECRIS-PM

D.K. Pugachev†, S.L. Bogomolov, V.E. Mironov, A.A. Efremov, V.N. Loginov, A.N. Lebedev, A.E. Bondarchenko, K.I. Kuzmenkov, K.B. Gikal, A.A. Protasov, Flerov Laboratory of Nuclear Reactions, Joint Institute for Nuclear Research, Dubna, Russia

Abstract

The first experiment on synthesis at the Superheavy Elements Factory (SHE) was launched at the end of 2020. The result of the experiment with a calcium ion beam and an Americium target is more than 100 events of the synthesis of Moscovium. Two years of operation have shown good capabilities of the Factory. These results allow to start preparing for the synthesis of SHE with atomic number >118. For these experiments we have to use heavier ion beams, such as titanium and chromium. The article describes the method, technique, and last experimental results on the production of metal ion beams such as ^{48}Ca, ^{48}Ti, ^{52}Cr, and ^{54}Cr ion beams from the DECRIS-PM ion source at the DC-280 cyclotron.

INTRODUCTION

For many years, one of the main scientific directions of the FLNR JINR has been the synthesis and study of the properties of superheavy elements. In recent years, almost all the last discovered elements of the Periodic Table have been synthesized using the ^{48}Ca at the U-400 cyclotron in our laboratory.

Further research into the field of superheavy elements requires a new approach and equipment. For these purposes, SHE was built in the FLNR in 2019. Factory is equipped with cyclotron DC-280 (Fig. 1), the main parameters are shown in the Table 1. The main goals of the SHE Factory are experiments at the extremely low cross sections, such as synthesis of new SHE, new isotopes of SHE and study of decay properties of SHE. In addition, experiments requiring high statistics will be conducted, such as nuclear spectroscopy and the study of the chemical properties of SHE [1].

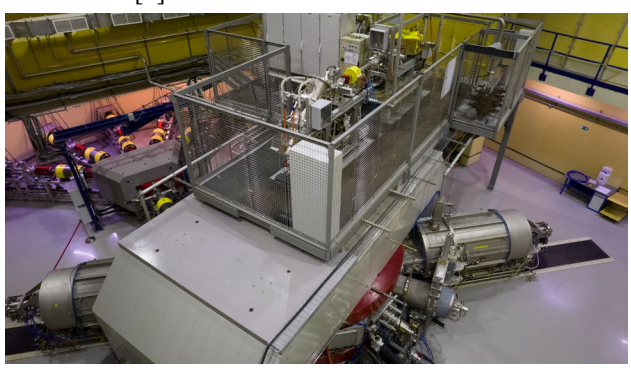

Figure 1: The DC-280 cyclotron.

Table 1: The Main Parameters of DC-280

Ion sources	DECRIS-PM - 14 GHz
Injection energy	Up to 80 keV/Z
A/Z range	4÷7.5
Energy	4÷8 MeV/n
Magnetic field level	0.6÷1.3 T
K factor	280
Magnet weight	1000 t
Magnet power	300 kW
Dee voltage	2x130 kV
RF power consumption	2x30 kW
Flat-top dee voltage	2x14 kV
Deflector voltage	Up to 90 kV

The first experiments at the SHE factory will be performed using ^{48}Ca+$^{242,\,244}$Pu and the ^{48}Ca+^{243}Am reactions. After completion of these experiments, it is planned to start the synthesis of new superheavy elements in reactions of ^{50}Ti and ^{54}Cr ions with ^{248}Cm, ^{249}Bk and $^{249\text{-}251}$Cf isotopes.

DECRIS-PM ION SOURCE

The injector of the cyclotron includes a high-voltage platform to increase the injection energy and thus to reduce the influence of the space charge of the beam. To reduce the power consumption of HV-platform we developed all-permanent magnet ion source DECRIS-PM. The requirements for the ion source are the production of ions with low and medium masses (from He to Kr). The ion source and the high-voltage platform are shown on Fig. 2.

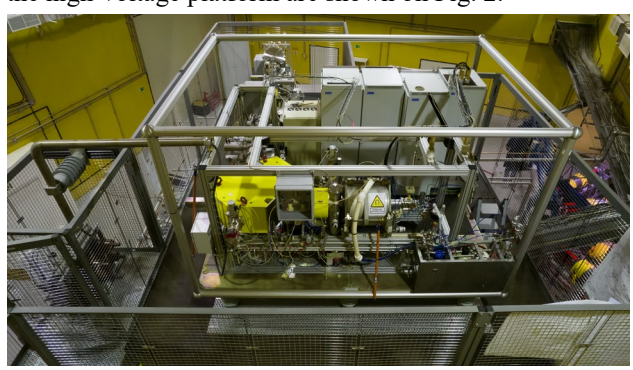

Figure 2: The DECRIS-PM on the high-voltage platform of the DC-280 cyclotron.

The magnetic field of the source is a superposition of an axial magnetic field and a radial magnetic field formed by

† pugachev@jinr.ru

ISBN: 978-3-95450-240-0 ISSN: 2673-5539 doi:10.18429/JACoW-RuPAC2021-TUPSB36

the 24-segment hexapole with a Halbach structure, which provides the creation of a radial magnetic field of 1.05 T on the inner surface of the plasma chamber. In the central part of the source the coil is installed for correction of B_{min} value in the range of ±0.075 T [2]. The magnetic structure and axial magnetic field distribution are shown in Fig. 3.

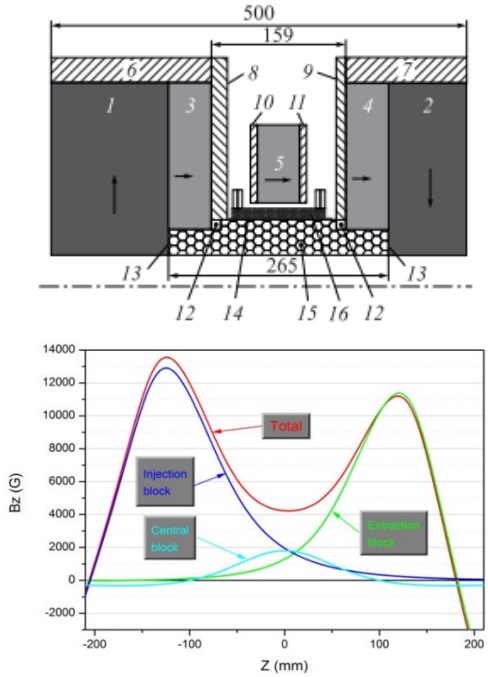

Figure 3: (Top) Magnetic structure of DECRIS-PM 1÷5 – PM rings; 6, 7 – soft iron rings; 8÷11 – soft iron plates, 12÷14 - auxiliary elements, 15 - hexapole, 16 – coil. (Bottom) Axial magnetic field.

PRODUCTION OF ^{48}CA BEAM

The production of calcium beam is described in details in the paper [3]. Therefore, we will present a brief technical description of the equipment.

For stable and long term operation with calcium beam, we use micro-ovens developed in FLNR. Their length is 50 mm, the outer diameter is 6 mm (Fig. 4). A crucible with the working substance is placed inside. The length of the crucible is 30 mm, the inner diameter is 2 mm (Fig. 5). The internal volume is sufficient to load about 100 mg of calcium, which corresponds to several days of continuous work with high beam intensity.

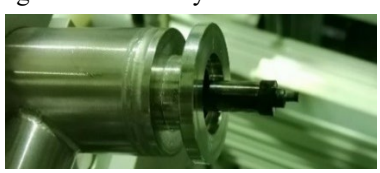

Figure 4: Oven.

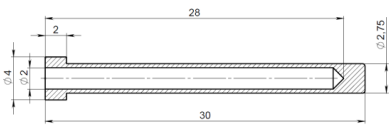

Figure 5: Crucible.

A significant part of the metal vapor evaporated from the oven condenses on the walls of the source chamber and only a small part leaves the source as an ion beam [4]. To prevent deposition of atoms on the water-cooled walls of the chamber, we use a hot tantalum screen (Fig. 6).

Figure 6: DECRIS-PM vacuum chamber, a hot tantalum screen is red.

During the source operation, the screen is heated by the plasma electrons and microwaves that leads to re-evaporation of the atoms condensed on the screen surface. The injected microwave power of 500 W provides the screen temperature of 550 °C, which is quite enough for the evaporation of calcium from the screen surface. [5] The ^{48}Ca ion spectrum, optimized for Ca^{10+} is shown in Fig. 7.

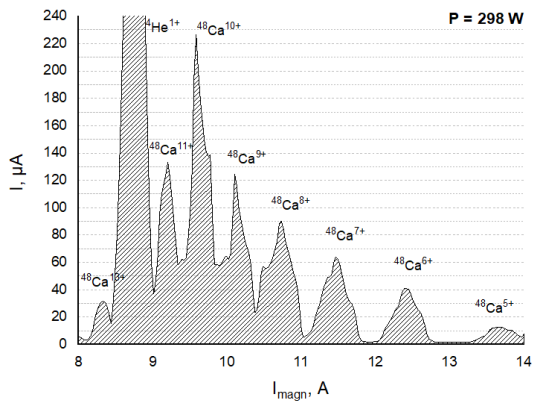

Figure 7: The ^{48}Ca ion spectrum, optimized for Ca^{10+}.

The total operational time with the calcium beam is currently ~ 4500 hours; the average consumption for the entire operation time is 0.67 mg/h excluding regeneration with the average intensity of 8 pμA for Ca^{10+} from the source. The global efficiency of the Ca ion production is 16%, the efficiency of Ca^{10+} production is about of 5%. The dependence of consumption on the ion beam intensity of Ca^{10+} is almost linear (Fig. 8).

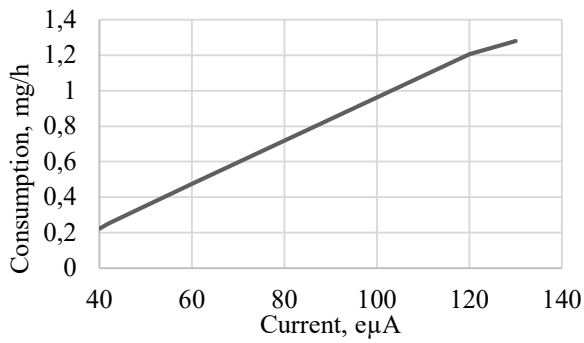

Figure 8: Calcium consumption as a function of Ca^{10+} intensity.

ISBN: 978-3-95450-240-0 ISSN: 2673-5539 doi:10.18429/JACoW-RuPAC2021-TUPSB36

PRODUCTION OF ^{48}TI AND $^{52-54}$CR BEAMS

The working pressure of calcium vapors is achieved at relatively low temperatures, in contrast to the Ti and Cr. Our micro-ovens don't allow us to use the evaporation technique to produce Titanium and Chromium beams.

Up today we have only one solution for production of high-intensity beams of these metals, it is MIVOC method. This method is based on use of organometallic compounds that have a relatively high vapor pressure (~10^{-3} Torr) at the room temperature [6]. Such vapor pressure is sufficient to operate the source providing the high conductivity of the vapor feed channel. We tried to work with different systems of the gas feeding. The best results were achieved with the gas-regulating valve EVR 116 [7]; it has a smooth adjustment of the gas flow and sufficient conductivity, which eliminates clogging of the valve openings by the deposited compound.

To avoid oxidation, the synthesized substance is placed in a vacuum tight container (Fig. 9). All operations are performed in an argon glove box. The excessive pressure of argon prevents the ingress of air and keeps the substance in working condition for a long time. Before feeding the working substance to the ECR, the substance and the feed channel are pre-pumped with argon filling for several times.

Figure 9: Containers with: left - $(CH_3)_5C_5Ti(CH_3)_3$ and right – $C_{10}H_{10}Cr$.

The operational time with the titanium beam at the DC-280 cyclotron currently corresponds to ~720 hours. The global efficiency of ion source for ^{48}Ti is 15 %, the efficiency for the Ti^{10+} is 1.5%. During short experiments it was determined that the vapor of the titanium compound react with aluminum. The compound sticks to the surface without the possibility of re-evaporation from the surface. Replacing the elements with stainless steel made it possible to increase the intensity by factor 2. Anyway, we haven't reached the project values for the intensity of the titanium ion beam. The ^{48}Ti ion spectrum, optimized for Ti^{10+} is shown in Fig. 10.

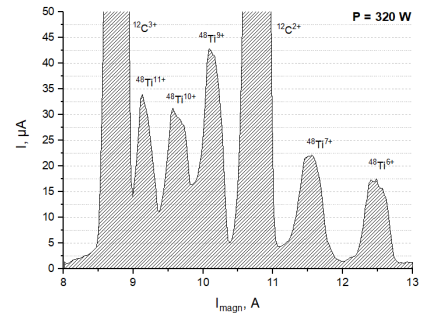

Figure 10: The ^{48}Ti ion spectrum, optimized for Ti^{10+}.

The operational time with the chromium beam at the DC-280 cyclotron currently corresponds to ~1100 hours. The global efficiency of ion source for ^{52}Cr is 10 %, the efficiency for Cr^{10+} is 2%. Chromocene is a very sensitive substance to air, so before starting work, the substance feed channel is pumped out with argon filling more than 5 times. This procedure allows one to get a beam in the shortest possible time. The ^{52}Cr and ^{54}Cr ion spectra, optimized for Cr^{10+} is shown in Fig. 11.

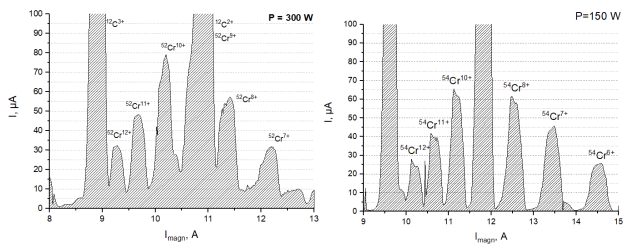

Figure 11: The ^{52}Cr (left) and ^{54}Cr (right) ion spectra, optimized for Cr^{10+}.

CONCLUSION

During the experiments the beams of ^{48}Ca, ^{48}Ti, ^{52}Cr and ^{54}Cr were produced. Calcium ion beam was accelerated with the average transmission from the ion source to output from the cyclotron about of 50%. The average consumption of the Calcium-48 is 0.67 mg/h, for Titanium-48 and Cromium-52-54 the consumption is 0.55-0.65 mg/h.

ACKNOWLEDGMENT

This work was supported by the Russian Foundation for Basic Research under grant № 20-52-53026/20.

REFERENCES

[1] S. N. Dmitriev *et al.*, "SHE Factory: Cyclotron Facility for Super Heavy Elements Research", in *22nd Int. Conf. on Cyclotrons and their Applications, Cyclotrons'19*, Cape Town, South Africa, JACoW Publishing, pp. 305-310. doi:10.18429/JACoW-Cyclotrons2019-THC01A

[2] Efremov *et al.*, *AIP Conf. Proc.* 2011, 040016 (2018). doi:10.1063/1.5053290

[3] Bogomolov *et al.*, "Production of ^{48}Ca and ^{48}Ti ion beams at the DC-280 cyclotron", *24th Int. Workshop on ECR Ion Sources* 2020, USA, September 2020, To be published.

ISBN: 978-3-95450-240-0 ISSN: 2673-5539 doi:10.18429/JACoW-RuPAC2021-TUPSB36

[4] A.A. Efremov *et al.*, "All-permanent Magnet ECR Ion Source DECRIS-PM", in *Proc. HIAT'18*, Lanzhou, China, Oct. 2018, pp. 89-91. doi:10.18429/JACoW-HIAT2018-TUOXA01

[5] V. B. Kutner *et al.*, "Production of intense 48Ca ion beam at the U-400 cyclotron", *Rev. Sci. Instrum.*, vol. 71(2), p. 860, 2000. doi:10.1063/1.1150313

[6] H. Koivisto, J. Arje, and M. Nurmia, "Metal ion beams from an ECR ion source using volatile compounds", *Nucl. Instrum.* Methods Phys. Res., Sect. B, vol. 94, pp. 291–296, 1994. doi:10.1016/0168-583X(94)95368-6

[7] Pfeiffer Vacuum https://www.pfeiffer-vacuum.com

ISBN: 978-3-95450-240-0 ISSN: 2673-5539 doi:10.18429/JACoW-RuPAC2021-TUPSB37

MODERNIZATION OF THE ECR ION SOURCE DECRIS-2M. RESULTS OF THE FIRST TESTS

A.E. Bondarchenko†, S. Bogomolov, A. Efremov, V. Loginov, A. Lebedev, V. Mironov, D. Pugachev, Joint Institute for Nuclear Research, FLNR, Dubna, Russia

Abstract

The article describes the design of the modernized ECR ion source DECRIS-2M. The upgrade consists in increasing the magnetic field to improve plasma confinement and enhance the source performance. The modernization also made it possible to increase the inner diameter of the plasma chamber and replace the coaxial microwave power input by a waveguide. Redesigned injection chamber significantly expands the possibilities of production ions of solids using different methods.

The article also presents the first results of experiments production of Ar, Xe and Bi ion beams from a modernized ion source. The results demonstrate substantial increase of the ion beams intensity, especially in the case of high charge states.

INTRODUCTION

The ECR ion source DECRIS-2m [1] was developed at FLNR JINR in 2001 and is a CAPRICE-type source with a coaxial microwave input of 14 GHz power. The magnetic structure of this source consists of two independent windings with an iron yoke to form an axial field; the radial magnetic field is created by a hexapole (permanent NdFeB magnet with "Halbach structure"). The main parameters of the ECR ion source DECRIS-2m are presented in Table 1.

Table 1: Main Parameters of the ECR Ion Source DECRIS-2m

Frequency (GHz)	14
Magnetic field in the inj. region B_{inj} (T)	1.25
Magnetic field in the extr. region B_{extr} (T)	1.05
Plasma chamber diameter (mm)	64
Number of coils	2
I_{max} (A)	1300
Hexapole parameters	
Material	NdFeB
Inner diameter (mm)	70
Rad. field on the plasma chamber wall (T)	>1.0

The source allows one to produce beams of ions of gaseous and solid substances with medium charges and moderate intensities up to Xe. The disadvantages of the source design include the following:

- in the microwave power input system, a transition from a rectangular waveguide to a coaxial line is used, which leads to losses of microwave power, causing uncontrolled gas desorption in the injection region. This method of microwave power input also requires the use of a special tuning mechanism;
- the size of the evaporator for producing solid ions is limited by the diameter of the inner conductor of the coaxial line;
- there is no room to install additional elements in the plasma chamber, because the injection part of the chamber is used as a coaxial waveguide.

UPGRADED ECR SOURCE DECRIS-2M

During the development of the project, the experience of the mVINIS ECR source modernization was used [2]. The main goal of the modernization was to replace the coaxial input of microwave power with a standard rectangular waveguide. For this, the outer diameter of the plasma chamber was increased from 64 to 74 mm. This entailed changes in the magnetic system of the source, in particular, a new hexapole with an inner diameter of 80 mm was made, and the configuration of the magnetic inserts in the injection region was changed. The new hexapole consists of 24 identical trapezoidal sectors with the corresponding direction of magnetization. Each sector is made from a single piece of magnetic material, thus avoiding magnetic field irregularity along the hexapole poles.

The design of the injection chamber was changed, which made it possible to significantly expand the possibilities for placing devices for supplying solids (evaporators, sputtering electrodes) in the ionization chamber.

In Fig. 1 a cross-section of the upgraded source is shown.

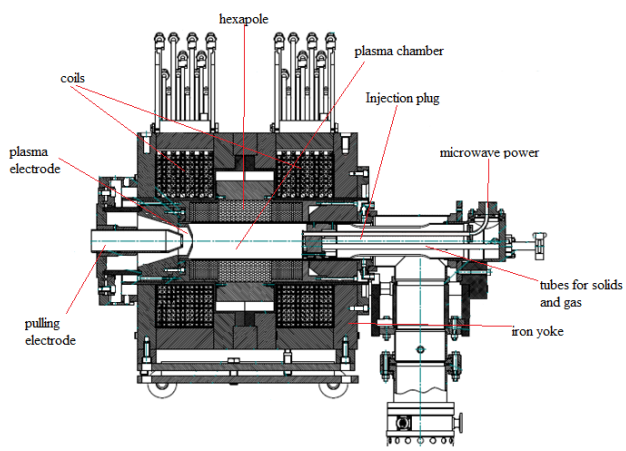

Figure 1: Upgraded DECRIS-2M.

† bondarchenko@jinr.ru

ISBN: 978-3-95450-240-0 ISSN: 2673-5539 doi:10.18429/JACoW-RuPAC2021-TUPSB37

The main parameters of the upgraded ECR source DECRIS-2M are presented in Table 2.

Table 2: Main Parameters of the Modernized ECR Ion Source DECRIS-2M

Frequency (GHz)	14
Magnetic field in the inj. region B_{inj} (T)	1.25
Magnetic field in the extr. region B_{extr} (T)	1.05
Plasma chamber diameter (mm)	74
Number of coils	2
I_{max} (A)	1300
Hexapole parameters	
Material	NdFeB
Inner diameter (mm)	80
Rad. field on the plasma chamber wall (T)	1.05 - 1.15

The new design of the injection chamber allows the microwave power to be injected directly into the plasma chamber through a standard waveguide. Two identical stainless steel tubes are used for gas supply and micro-evaporator inlet for evaporation of solids. The bias-electrode is made of tantalum and is attached to a soft magnetic iron insert. The dimensions and shape of the electrode are selected so as to exclude the interaction of the magnetic insert with the plasma. The location of these elements is shown in Fig. 2.

Figure 2: Injection plug of the DECRIS-2M ion source with new inputs: microwave power, gas and solids.

PRODUCTION OF ION BEAMS FROM THE ECR SOURCE DECRIS-2M

The upgraded ECR source DECRIS-2M was tested at the ECR sources test bench for the production of argon, xenon, and bismuth ions. During the experiments, the operation of the source was stable and reproducible. The obtained results have shown a substantial increase of ion beam currents, especially in the case of high charge states.

Figure 3 to 8 shows the spectra of Ar, Xe and Bi ions. The spectra were produced at an extraction voltage of 20 kV on average. Oxygen was used as a mixing gas for production of Xe, Bi and Ar^{12+} ions, for production of Ar^{8+} ions helium was used as a mixing gas.

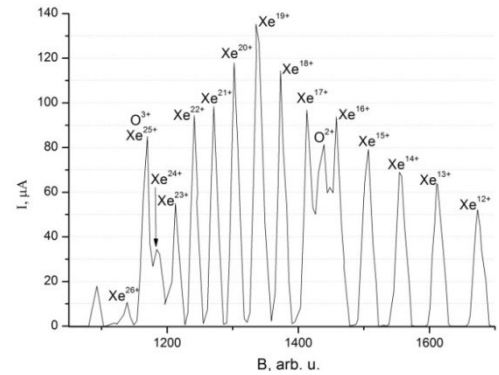

Figure 3: Xe ion spectrum. The operating mode is optimized to produce $^{132}Xe^{20+}$. Microwave power 308 W.

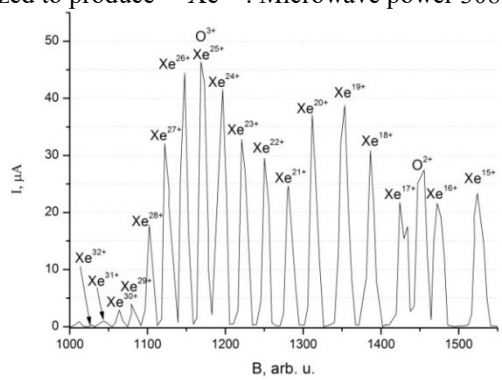

Figure 4: Xe ion spectrum. The operating mode is optimized to produce $^{132}Xe^{27+}$. Microwave power 290 W.

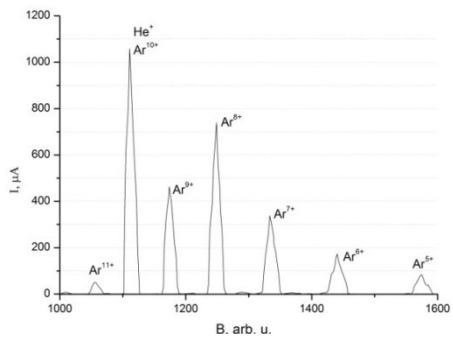

Figure 5: Ar ion spectrum. The operating mode is optimized to produce $^{40}Ar^{8+}$. Microwave power 274 W.

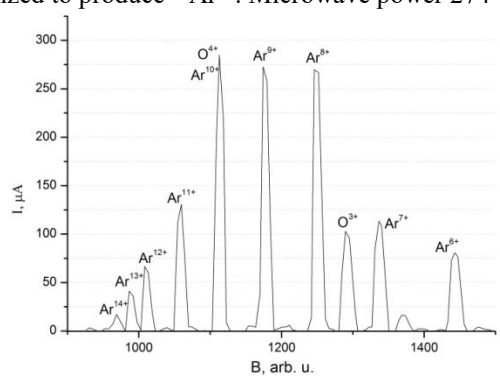

Figure 6: Ar ion spectrum. The operating mode is optimized to produce $^{40}Ar^{12+}$. Microwave power 309 W.

ISBN: 978-3-95450-240-0 ISSN: 2673-5539 doi:10.18429/JACoW-RuPAC2021-TUPSB37

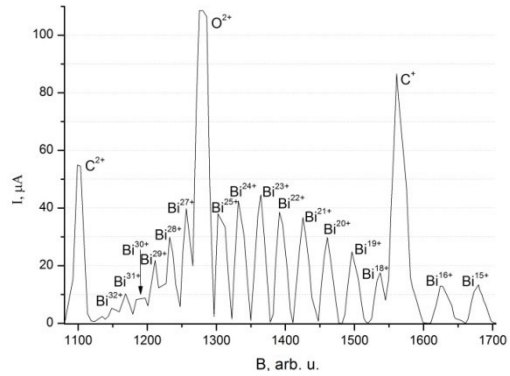

Figure 7: Bi ion spectrum. The operating mode is optimized to produce $^{209}Bi^{27+}$. Microwave power 220 W.

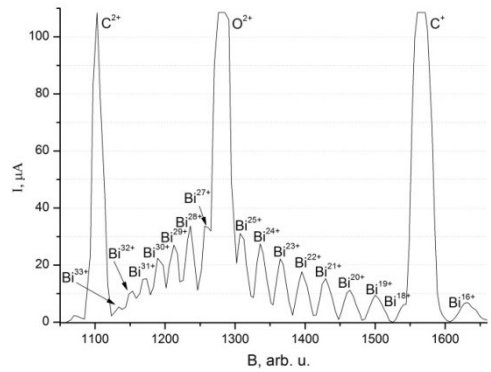

Figure 8: Bi ion spectrum. The operating mode is optimized to produce $^{209}Bi^{32+}$. Microwave power 221 W.

A comparison of the results produced from the ECR ion source before and after the upgrade are shown in Table 3. The results shown for the DECRIS-2m source before the upgrade were produced at an extraction voltage of 16 kV.

Table 3: Comparison of ion currents obtained from ECR sources DECRIS-2m and upgraded DECRIS-2M

Ion	Ion current, μA	
	DECRIS-2m	DECRIS-2M
$^{40}Ar^{8+}$	480	750
$^{132}Xe^{18+}$	30	114
$^{132}Xe^{20+}$	23	118
$^{132}Xe^{27+}$	-	32
$^{209}Bi^{27+}$	-	40
$^{209}Bi^{32+}$	-	11

CONCLUSION

The results obtained during the tests of the modernized source DECRIS-2M demonstrate substantial increase of the ion beams intensity, especially in the case of high charge states. The operating modes of the upgraded source are stable and reproducible.

Research and development of stable modes for obtaining high-intensity ion beams of solid substances will be continued at the ECR sources test bench.

ACKNOWLEDGMENTS

This work was supported by the Russian Foundation for Basic Research, grant no. 20-52-53026 / 21.

REFERENCE

[1] V. Loginov *et al*., "First beam from the DECRIS 14-2m ion source for Slovak republic", *NUKLEONIKA 2003*; Volume 48 (Supplement 2), p. S89-S92.

[2] A. Efremov *et al*., "Upgrading of the CAPRICE type ECR ion source", *AIP Conference Proceedings* 2011, 040017, 2018, doi:10.1063/1.5053291

ISBN: 978-3-95450-240-0 ISSN: 2673-5539 doi:10.18429/JACoW-RuPAC2021-TUPSB38

MAGNETIC SYSTEM WITH VARIABLE CHARACTERISTICS FOR A 2.45 GHz ECRIS

M. S. Dmitriyev†, M. I. Zhigaylova, K. G. Artamonov, O. A. Ivanov National Research Nuclear University MEPhI (Moscow Engineering Physics Institute), Moscow, Russia

Abstract

The study considers the development of the magnetic system of the 2.45 GHz ECRIS for the production of protons and double-charged helium ions. The magnetic field configuration is shown to be based on permanent magnets. The results of the simulation made by the Finite Element Method have been performed. To adjust the axial magnetic field profile the configuration with the alternating position of the ring magnets was analyzed. The double series construction of the bar magnets provides the adjustment of the radial magnetic field B_{rad} at the chamber wall. Additional solenoids were introduced to the system for a corrective tuning of theB_{inj} and B_{ext} parameters and the axial profile minimum B_{min} of the magnetic field distribution. Thus, the magnetic system is appeared to provide the mode switching between the ECR and the microwave operating modes.

INTRODUCTION

A new ECR ion source for the light ion linac is under development at MEPHi. It is designed for the generation of both protons and double charged helium ions. The choice of the operating frequency of 2.45 GHz is specified by several factors: the wide range of elements available at the microwave wavelength, working experience in this frequency range, the compactness of the magnetic system as well as the adjustment ability of the magnetic field distribution inside the plasma chamber.

In order to obtain the required proton intensity and ensure the helium production at the frequency of 2.45 GHz, two types of microwave plasma ion sources were considered as a fundamental base for the development of a new 2.45 GHz ion source with variable characteristics of the magnetic system.

Depending on the ion parameters required, ion sources based on the electron-cyclotron resonance (ECR) or the microwave discharge can be used. The ECR ion sourceprovides the interaction between electromagnetic field and plasma at the frequency of electron-cyclotron resonance and under the vacuum conditions.Unlike the first type, the microwave source does not require the resonance conditions to provide the field-plasma interaction; moreover, gas pressure inside the plasma chamber is several times higher than for the first type. According to the factors of plasma generation ion beam parameters can differ for these two types. ECR ion sources produce multiply charged ions with lower beam currentsin comparison with microwave sources, which provide high beam currents of protons.

The aim of this research is to design a new ECRIS for producing double-charged ions of helium and protons. This aim will be accomplished by meeting the following objectives: developing a magnetic system and calculating the magnetic field parameters to determine the most feasible configuration of the source in order to provide the operation in both ECR and microwave modes.

BASIC PARAMETERSOFECR AND MICROWAVE ION SOURCES

Microwave discharge sources are usually feasible for generating the single-charged ion beams or proton beams with the current up to 100 mA and low emittance in both pulse and continuous-wave operation mode. High magnetic fields are used to increase the ion density.

This type of a source can be distinguished by the frequency that is higher than for the ECR type. In contrast to the magnetic system of the ECR type, the microwave source configuration does not include hexapole magnets to confine plasma in the ECR region.

The magnetic field profile is important for the plasma generation as well as for the operation stability of the application. The magnetic field for this configuration is usually generated by two solenoids with variable currents.

To accomplish the ion parameters required microwave plasma sources were considered according to the following advantages: stability, long lifetime, high ion concentration, small energy spread in the beam, low emittance, compactness and ease of operation.

As compared to the microwave source magnetic system, the ECR source configuration is usually based on permanent magnets instead of solenoids. Sources with the stepped ionization are needed to generate the multiple-charged ion beams. Electrons are gradually knocked out from the external shell of the ionized atoms by electrons accelerated in an alternating field. Along with that, relatively slow ions continue to lose electrons because of the ionization, caused by the second time accelerated electrons. Slow electrons are confined by the magnetic field of the source.

The efficiency of the RF power transmission into the plasma chamber depends on the magnetic plasma density distribution inside the chamber, which affects the dielectric parameters of the chamber space and consequently the effectiveness of the field-plasma interaction. This research is based on the most optimal configuration principles known as the “ECRIS Standard Model”.

† msdmitriyev@mephi.ru.

ISBN: 978-3-95450-240-0 ISSN: 2673-5539 doi:10.18429/JACoW-RuPAC2021-TUPSB38

THE MAGNETIC SYSTEM CONFIGURATION DEVELOPMENT

This section describes the main steps of the 2.45 GHz ECRIS magnetic system development. The numerical simulation of the magnetic field parameters was made by the Finite Element Method (FEM). The initial model of the magnetic system was described in the previous papers [1,2]. Further optimization of the magnetic system design was made to adjust the minimum of the axial field B_{min}. Three solenoids were added to the model of the system to adjust the axial field profile. The initial model is presented in the Fig. 1. The simulation results are presented in the Fig. 2.

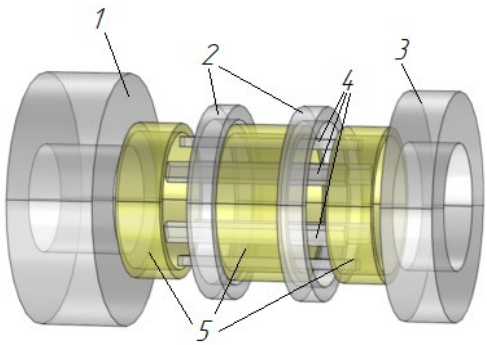

Figure 1: The model of the magnetic system of the 2.45 GHz ECRIS. (1)Injection ring magnet.(2)Middle ring magnet. (3)Extraction ring magnet. (4)Hexapole magnet. (5) Solenoids

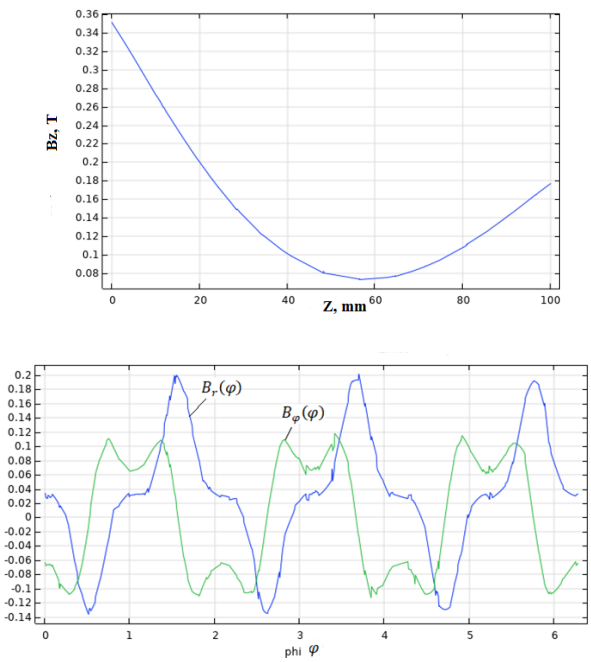

Figure 2: Magnetic flux density distributions of thesystem with the solenoids.

The model of the magnetic system was calculated provided that the material of the magnets is selected to be NdFeB. The length of the hexapole bars was selected as 100 mm, which is equal to the length of the plasma chamber. The plasma chamber diameter is 50 mm, while the other dimensions were determined to keep the system compact. The optimization of the magnetic system was carried out by changing the size of the magnets and their relative position. Table 1 presents the magnetic system characteristics after the optimization.

Table 1: Optimized Parameters of the Magnetic System

	B_{inj}, T	B_{min}, T	B_{rad}, T	B_{ext}, T
Optim.	0.350	0.058 < $\|B\|_{min}$< <0.087	0.193	0.175
Calc.	0.342	0.036	0.190	0.171

THE SYSTEM MODIFICATION

The solid rings with a small inner diameter and radial magnetization are quite complicated for the manufacturers to be produced. According to these technological peculiarities, ring magnet assembly made of trapezoidal elements is more technologically applicable than the whole ring magnets. The configuration suggested in this paper is also expected to avoid longitudinal displacement of the ring magnets, described in the previous papers, as the magnetic assembly provides the radial tuning of the magnet elements position instead. This design prevents the exceedance of the longitudinal space limits and also reduces the size of the whole magnetic system assembly. The central ring magnets are composed of the rectangular magnet bricks to provide the adjustment of the axial magnetic field minimum by the radial or axial displacement of the magnets. Finally, the more accurate profile tuning can be reached by the geometrical adjustment or the additional solenoids currents selection.

Figure 3 shows a model view of the magnetic assembly with solenoids. Axial field distribution for the ECR operation mode is presented in the Fig. 4.

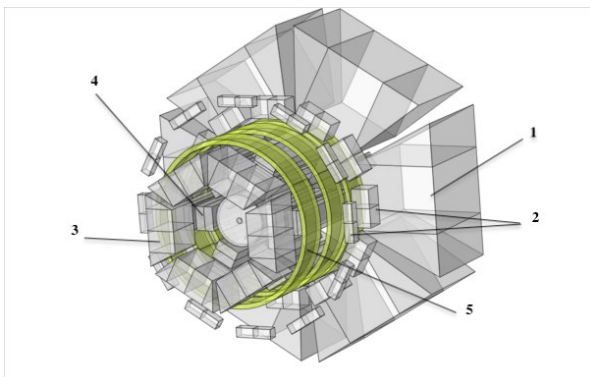

Figure 3: The model of the ECR mode magnetic system. (1) Injection ring magnet. (2)Middle ring magnets. (3) Extraction ring magnet. (4) Hexapole magnet. (5) Solenoids.

The resulting currents of the solenoids are: 70, 0 and -100 A. Current research appears to reveal the slight discrepancy between the simulation results for the described modifications of the system: the minimum of

ISBN: 978-3-95450-240-0 ISSN: 2673-5539 doi:10.18429/JACoW-RuPAC2021-TUPSB38

the system assembly resulting profile exceeds the optimal parameter given above. Further investigation is needed to adjust the lowest point of the axial magnetic field.

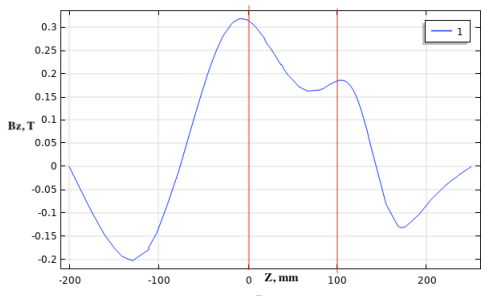

Figure 4: Magnetic flux density distributions of the system with the solenoids.The red lines depict the plasma chamber boundaries.

Table 2 presents the magnetic system characteristics in the ECR operation mode.

Table 2: Magnetic System Parameters

	B_{inj}, T	B_{min}, T	B_{ext}, T
Optim.	0.350	$0.058 < \|B\|_{min} < 0.087$	0.175
Calc.	0.321	0.163	0.178

THE MICROWAVE MODE MODIFICATION

Figure 5 depicts the simulation model of the magnetic system of the microwave mode.

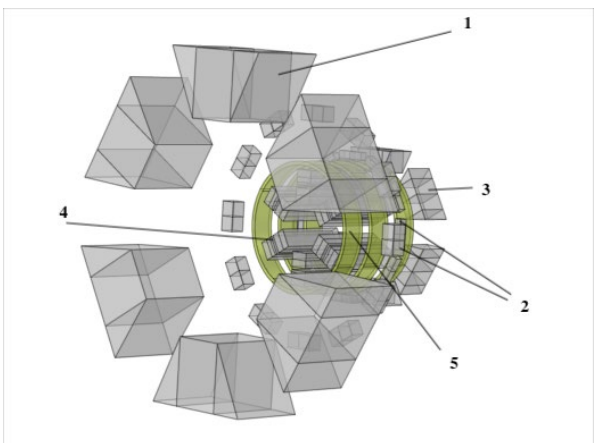

Figure 5: The model of the microwave mode system modification. (1) Injection ring magnet. (2) Middle ring magnets. (3) Extraction ring magnet. (4) Hexapole magnet. (5) Solenoids.

The results of simulation of the microwave mode modification are presented in the Fig. 6. The distribution adjustment in the microwave mode was also carried out by solenoid currents, so that the magnetic field at the edges of the chamber corresponds to the electron cyclotron resonance. The resulting solenoid currents are: 5, 0, and 45 A. Table 3 presents the magnetic system characteristics in microwave operation mode after the final optimization.

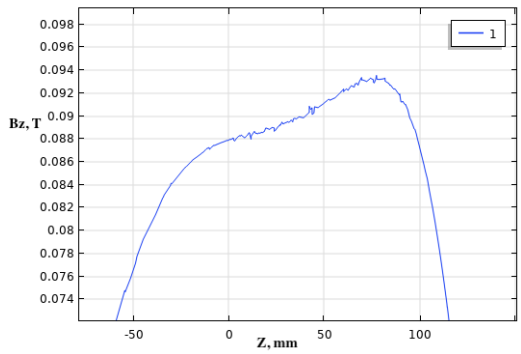

Figure 6: Axial magnetic field profile of the microwave source operating mode with the adjustable position of the ring magnets.

Table 3: Optimized Parameters of the Magnetic System in the Microwave Operation Mode

	B_{inj}, T	B_{ext}, T
Optim.	0.087	
Calc.	0.088	0.087

CONCLUSION

A new ECR ion source with the operating frequency of 2.45 GHz is under development. The magnetic system with the variable parameters was calculated to provide the operation in two modes: ECR and microwave modes. To improve the parameters of the magnetic system the modification with the magnetic assemblywas considered and calculated. The resulting system satisfies the required parameters; however, the lowest point of the field distribution in the ECR mode needs to be adjusted.The solenoid currents provide an accurate magnetic field tuning and displacement of the magnet assembly elements keeps the possibility of the mode selection.

REFERENCES

[1] M.S. Dmitriyev *et al.,* "The simulation of the ECR ion sources magnetic system", in *LaPlas-2021 proceedings*, p. 423, 2021.

[2] M. S. Dmitriyev, K. G. Artamonov, M. V. Dyakonov, and M. I. Zhigailova, "Magnet System for a Proton/helium ECR Ion Source", presented at the *12th Int. Particle Accelerator Conf. (IPAC'21),* Campinas, Brazil, May 2021, paper WEPAB191.

ISBN: 978-3-95450-240-0 ISSN: 2673-5539 doi:10.18429/JACoW-RuPAC2021-TUPSB39

STUDY OF SPACE CHARGE COMPENSATION PROCESS OF A 400 KeV PULSED HYDROGEN ION BEAM

A. S. Belov, S. A. Gavrilov, O. T. Frolov, L. P. Netchaeva, A. V. Turbabin, V. N. Zubets,
Institute for Nuclear Research of the Russian Academy of Sciences, Moscow, Russia

Abstract

A three grid energy analyzer of slow secondary ions with a twin analyzing grid is described. The analyzer has cylindrical geometry and π angle for recording of the slow ions. The analyzer has been used for measurements of degree of space charge compensation (SCC) of a pulsed hydrogen ion beam with energy of 400 keV and peak beam current of 60 mA. Results of the measurements are presented and compared with theoretical estimations based on model in which the SCC degree is limited by heating of electrons in collisions with fast ions of the beam.

INTRODUCTION

Transport of high intensity ion beams in low energy beam transport (LEBT) for injection into linear accelerators is usually space charge dominated. The space charge field can be reduced by process of gaseous SCC. The SCC process consists in the fact that the ions of the beam ionize the residual gas, and the electrons that arise during the ionization of gas molecules compensate the space charge of the beam of positive ions. The slow ions arising due to gas molecules ionization are accelerated in radial direction and acquire energy that determined by the space charge electric field of the ion beam. The degree of SCC can be determined by measurement of the energy distribution of slow ions produced in the beam region.

Electrostatic ion energy analyzers are used to measure slow ions energy spectra [1, 2]. A three grid electrostatic energy analyzer (TGA) has been used to measure SCC of hydrogen ion beam produced by a proton injector of Moscow INR linac [3, 4]. The hydrogen ion beam has peak current of up to 70 mA, energy of 400 keV, pulse duration of 200 μs and repetition rate of 50 Hz. The beam consists mainly from protons (~80%) and H_2^+ ions.

In this paper the TGA improvement and calibration is described, and results of study of the SCC process for different ion beam density are presented.

THE TGA DESCRIPTION

The TGA cross section view is shown schematically in Fig. 1. The analyzer has cylindrical geometry and π angle for recording of the slow ions. The TGA consists of three grids, a collector and a heater. First grid of the TGA is grounded to eliminate influence of electric fields on the ion beam. Second grid is analyzing one. The second grid is twin to decrease effect of electric field penetration through the grid cells. It is under positive potential relative the ground. Retarding field between the first and second grids leads to deceleration of slow ions and to partial decrease or to complete stopping of the slow ion current to the collector in accordance with the slow ions energy spectra.

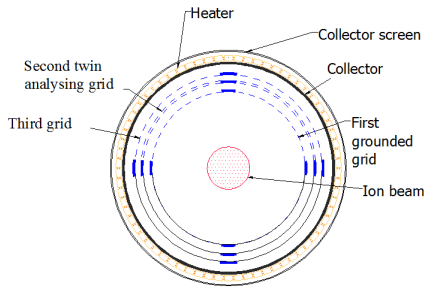

Figure 1: Schematic drawing of the TGA cross-section.

Third grid is under a negative potential (typically -300 V). It is necessary for suppression of secondary electrons from the collector and electrons from the ion beam. The grids have rectangular cells of 0. 5 x 0. 5 mm.

Heating of the TGA is necessary to eliminate systematic error connected with shifting of the TGA characteristics due to charging of the surface layers of the TGA electrodes by the slow ions [2].

Residual gas pressure in vacuum chamber (mainly hydrogen and water vapor) with the TGA was $1.1 \cdot 10^{-5}$ mbar.

Electric field of the TGA as well as ion transport from ion beam to the collector was simulated with COMSOL MP. Figure 2 shows electric field map near the TGA analyzing grid.

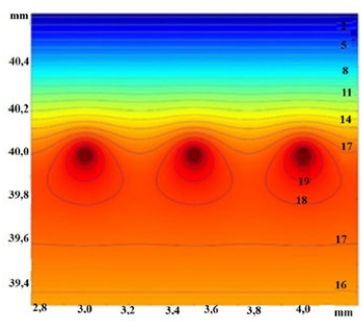

Figure 2: Electric field map of the TGA region near the analyzing grid. Ug2 = 20 V. Ug3 = -300 V.

TheTGA energy resolution is reduced due to the effect of field penetration through the grids and, as the simulation shows, is about 2 eV.

ISBN: 978-3-95450-240-0 ISSN: 2673-5539 doi:10.18429/JACoW-RuPAC2021-TUPSB39

THE TGA CALIBRATION

The TGA has been calibrated with slow electrons using low current electron gun with tungsten filament thermo cathode. The gun has been placed near axis of the TGA. Electrons were accelerated by voltage applied between the filament and grounded extraction electrode. The electrons energy dispersion of 1.5 eV arises due to potential drop at the thermo cathode filament. Negative potential has been applied to the analyzing grid for the recording of electrons spectrum.

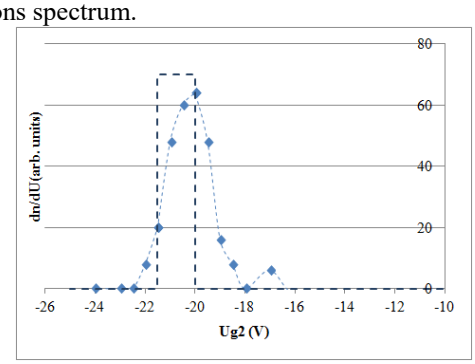

Figure 3: Measured spectrum of electrons with the gun accelerating voltage of 20 eV. U_{g3} = -10 V. The dashed line is the expected electron spectrum; the points are results of the measurements. Temperature of the TGA was 100°C.

It was found that the recorded spectrum changes with change of the TGA temperature. Temperature above 100°C makes no further change of the spectra.

The example of electron energy spectrum measured with the TGA is shown in Fig. 3 for accelerating voltage of 20 eV. The expected spectrum is shown in Fig. 3 by a dashed line. Resolution of the TGA as follows from the data is about 2 eV as expected from a simulation of the TGA electric field distribution.

RESULTS AND DISCUSSION

Complete compensation of positive ion beam space charge by electrons is limited by heating of the electrons in Coulomb collisions with fast ions of the beam [5, 6]. It is follows from the model that potential difference in an ion beam with compensated space charge is proportional to the square root of ion density of the fast ion beam:

$$\Delta\varphi_{comp} \propto {n_b}^{1/2}$$

We have measured the dependence of the SCC degree of a pulsed hydrogen ion beam with a peak current of 60 mA on the beam density using the TGA described. The ion beam density was changed by changing the focusing voltage of the lens installed downstream the duoplasmatron type ion source. The radial distribution of the ion beam current density was measured by a slit profilometer with a current collector of a cut-out ion stream and suppression of secondary electrons. The recorded ion beam profiles were fitted assuming Gaussian type ion densitydistribution. The characteristic radiuses of ion beam density distribution found this way are shown in Fig. 4.

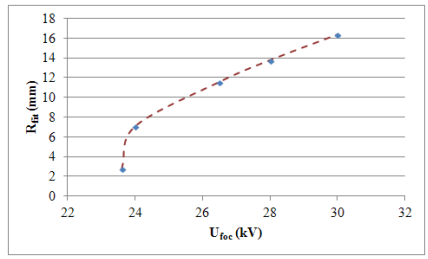

Figure 4: Characteristic radius of the ion beam density distribution vs. focusing voltage of the ion source.

Averaged ion beam density changes from $4.5 \cdot 10^7$ cm^{-3} for focusing voltage of 30 kV to $1.5 \cdot 10^9$ cm^{-3} for focusing voltage of 23.6 kV.

Respective dependences of the TGA collector slow ion current on the potential of the analyzing grid (TGA characteristics) are shown in Fig. 5. We determined degree of SCC of the ion beam using next formula:

$$f_e = 1 - \frac{\varphi_{b\,comp}}{\varphi_{b\,noncomp}},$$

where fe is degree of SCC of an ion beam, $\varphi_{b\ comp}$ is potential difference between axis of the ion beam with compensated space charge and grounded transport tube wall and $\varphi_{b\ noncomp}$ is the potential difference for the ion beam with non compensated space charge.

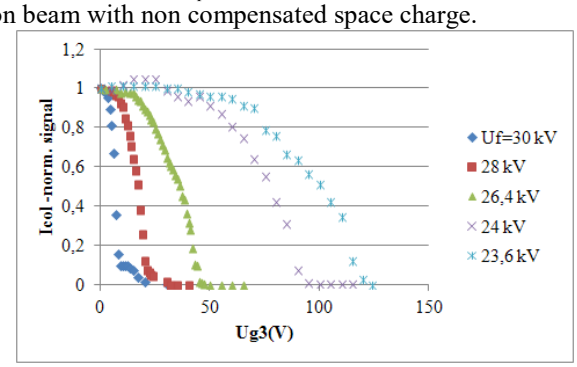

Figure 5: Characteristics of the TGA for different focusing voltage of the ion source.

Value of $\varphi_{b\ comp}$ was determined from the TGA characteristics using fit of the recorded data assuming Gaussian ion beam density distribution.

An example of a TGA characteristic with the fit is shown in Fig. 6. We determined $\varphi_{b\ comp}$ as point where the fitting curve crosses the horizontal axis (20.9 V for Fig. 6). The $\varphi_{b\ noncomp}$ value was determined by solving Poisson equation with known ion current and radial ion density distribution.

The Gaussian fit shown in Fig. 6 is satisfactory except for the "tail" of the current of higher-energy ions. A similar "tail" was observed in [2]. Among possible explanations made in [2] was decay of excited H_2 molecules to charged particles with energy of ~10 eV or collective oscillations in the ion-beam plasma.

ISBN: 978-3-95450-240-0 ISSN: 2673-5539 doi:10.18429/JACoW-RuPAC2021-TUPSB39

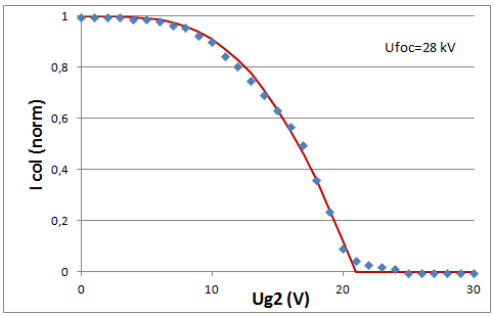

Figure 6: The TGA characteristic for U_{foc} = 28 kV. Points are recorded data; solid line is a fit with Gaussian ion beam density distribution.

We assume that the "tail" origin for our measurements is connected with anomalous ion beam density distribution near the ion beam axis region. The ion beam radial density distribution for case where the "tail" is most pronounced (U_{foc} = 30 kV) is shown in Fig. 7.

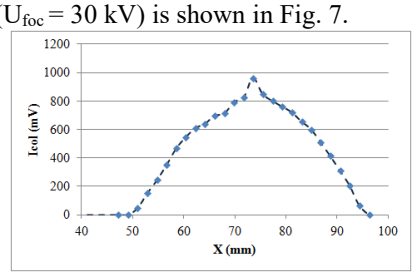

Figure 7: Radial profile of the hydrogen ion beam for Ufoc = 30 kV.

The distribution has characteristic peak at the ion beam axis. The distribution shape can probably be explained by the influence of a weak magnetic field in the ion source plasma expander on the plasma density distribution.

The measured degree of SCC of the hydrogen ion beam was compared with theoretical estimation based on Gabovich – Soloshenko model [5, 6].

Dependences of measured and calculated degree of SCC of hydrogen ion beam on ion beam density are shown in Fig. 8.

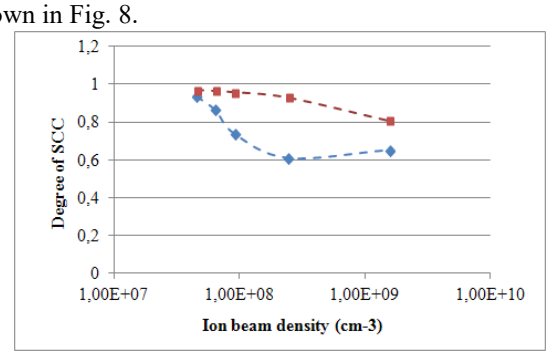

Figure 8: Measured and calculated data for degree of SCC of hydrogen ion beam with peak current of 60 mA and energy of 400 keV vs. the ion beam density. Brown squares are calculation from Gabovich-Soloshenko formula, blue diamonds are results of the measurements.

There is a significant difference between the measured and calculated data. One of the reasons for the discrepancy may be approximation of homogeneous ion beam accepted in the Gabovich-Soloshenko model. For comparison with measurements the model has to be extended to include non homogeneous ion beam density distribution. An ion beam simulation which takes into account complicated processes of SCC [7] is an alternative method for prediction of the SCC degree.

Another factor that reduces degree of SCC may be dynamic decompensation. However, our hydrogen ion beam has a low current noise level. Faraday cup has used to measure the noise value of the ion beam current. It was found that the noise is less than 1% of the ion beam current amplitude. That makes dynamic decompensation an insignificant factor for the ion beam SCC.

CONCLUSION

The three grid energy analyzer of slow secondary ions with the twin analyzing grid is described. The analyzer has been used for measurements of degree of SSC of hydrogen ion beam with peak current of 60 mA and energy of 400 keV. The measurement results qualitatively coincide with the predictions made by the ion beam decompensation model due to the heating of compensating electrons in Coulomb collisions with fast beam ions (model of Gabovich- Soloshenko). But the numerical discrepancies with the model are significant.

REFERENCES

[1] P. Kreisler, H. Baumann, and K. Bethge, "Measurements of Space Charge Compensation of Ion Beams", *Vacuum* 34, p. 215, 1984. doi.org/10.1016/0042-207X(84)90130-1

[2] R. Ferdinand, J. Sherman, R. R. Stevens, Jr., and T. Zaugg, "Space-charge neutralization measurements of a 75 keV, 130 mA hydrogen-ion beam", *in Proceedings of the 1997 Particle Accelerator Conf. (PAC'97)*, Vancouver, BC, Canada, May 1997, *IEEE Trans. on Nucl. Sci.* 3, p. 2723, 1998. Doi: 10.1109/PAC.1997.752744

[3] A.S. Belov, S.A. Gavrilov, O.T. Frolov, L.P. Netchaeva, E.S. Nikulin, and V.N. Zubets, "High responsivity secondary ion energy analyzer". *JINST* 4, T05001, May 2, 2018. Doi: 10.1088/1748-0221/13/05/T05001

[4] A. S. Belov *et al.*, "A Secondary Ion Energy Analyzer for Measuring the Degree of Compensation of the Ion Beam Space Charge", *Instruments and Experimental Techniques,* Vol. 62, No. 5, pp. 609–614, 2019.

[5] M.D. Gabovich, "Ion beam plasma and transport of intense compensated ion beams", *Uspehi Fizicheskih Nauk,* 121, 259, 1977.

[6] I.A. Soloshenko, "Physics of Ion Beam Plasma and Problems of Intensive Ion Beam Transportation", *Rev. Sci. Instrum.* 6, p. 1646, 1996. Doi:10.1063/1.1146909

[7] S.X. Peng *et al.*, "Study on Space Charge Compensation of Low Energy High Intensity Ion Beam In Peking University", *in Proc. 57th ICFA Advanced Beam Dynamics Workshop on High-Intensity and High-Brightness Hadron Beams(HB2016),* Malmö, Sweden, 3-8 July 2016, WEPM6Y01.

ISBN: 978-3-95450-240-0 ISSN: 2673-5539 doi:10.18429/JACoW-RuPAC2021-TUPSB40

He^+ ION SOURCE FOR THE NICA INJECTION COMPLEX

A.M. Bazanov, A.S. Bogatov, B.V. Golovenskiy*, D.E. Donets, K.A. Levterov, D.S. Letkin, D.O. Leushin, A.V. Mialkovsky, V.A. Monchinskiy, D.O. Ponkin, I.V. Shirikov,
Joint Institute for Nuclear Research, Dubna, Russia

Abstract

A mono-ion source of single-charged helium of high intensity has been created to confirm the declared parameters of Heavy Ion Linear Accelerator (HILAC) [1, 2] and for the injection into superconducting synchrotron (SC) Booster during the first run.

The paper presents the design of the He^+ ion source, test bench for the TOF measurements and acceleration beam developed at VBLHEP, JINR. The results of the tests of the source are presented. During the tests the intense beams of ions 50 mA of He^+ were produced.

HELIUM ION SOURCE

For designing helium ion source the proton ion sources described in [3, 4] were taken as a prototype. Ion source with cold magnetron cathode and magnetic plasma compression consists of the two basic parts: plasma generator, system of ions extraction and beam formation. There are three basic space may be attributed to plasma generator: space of auxiliary discharge between magnetron cathode and magnetron anode, space of the main discharge between magnetron cathode and anode, and area of plasma expansion (see Fig. 1).

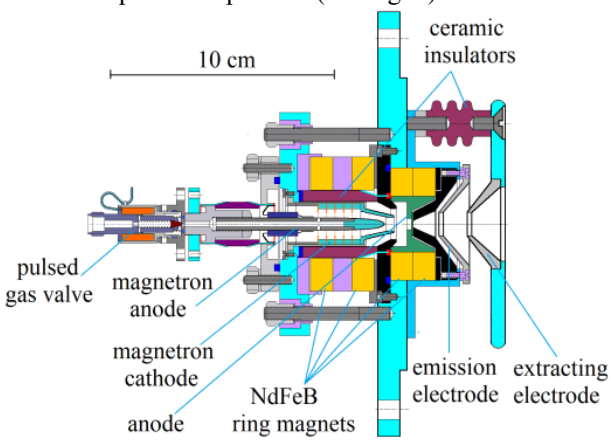

Figure 1: Helium ion source design.

The entire cathode block is placed in a longitudinal magnetic field (see Fig. 2). The magnetic field is organized using four ring neodymium magnets. Two of them with consistent polarity form a longitudinal field in the region of the magnetron cathode. The next two magnets with opposite polarity create a strong non-uniform magnetic field that compresses the plasma into a 1 mm emission hole.

From the region of magnetic compression, the plasma enters the expander and expands in it. A concave plasma boundary (meniscus) is formed, which forms an ejected beam. Extraction of ions from the plasma is carried out by applying a pulsed voltage of up to -40 kV to the extracting electrode.

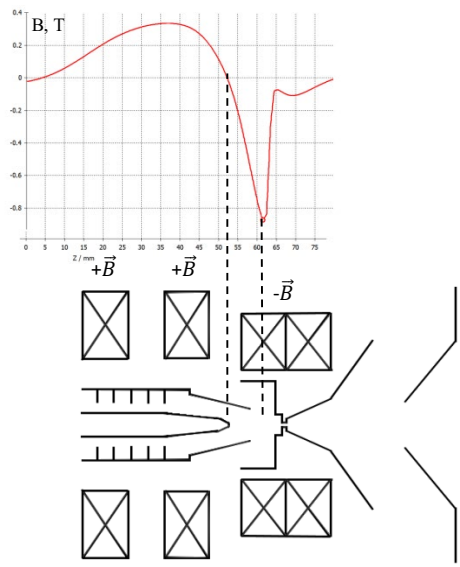

Figure 2: Equivalent diagram and graph of the magnetic field distribution along the axis.

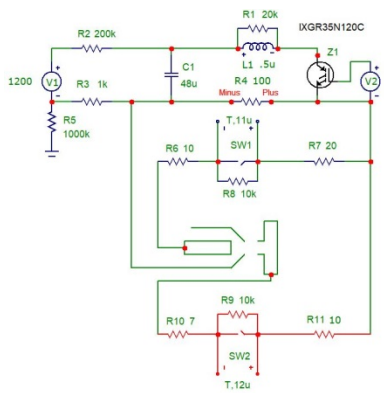

Figure 3: Scheme discharge modulator.

Gas system provides pulsed gas injection into space of magnetron discharge. Pulsed voltage up to 1 kV in the gaps between magnetron anode and magnetron cathode,

* golovenskiy@jinr.ru

ISBN: 978-3-95450-240-0 ISSN: 2673-5539 doi:10.18429/JACoW-RuPAC2021-TUPSB40

and between magnetron cathode and anode was provided with the generator of HV pulses (see Fig. 3).

The auxiliary discharge current in the magnetron region at a voltage of about 450 V reached 3 A. The current of the main discharge, contracted by the magnetic field, reached 15 A (see Fig. 4).

The combustion mode of the main discharge was easily reconfigured by changing either the value of the ballast resistance in the power circuit, or the amount of working gas supplied to the volume of the gas-discharge chamber in portions using an electromagnetic valve.

The ion source operates in a pulsed mode with a repetition rate of 0.25 to 1 Hz and a pulse duration of up to 100 μs.

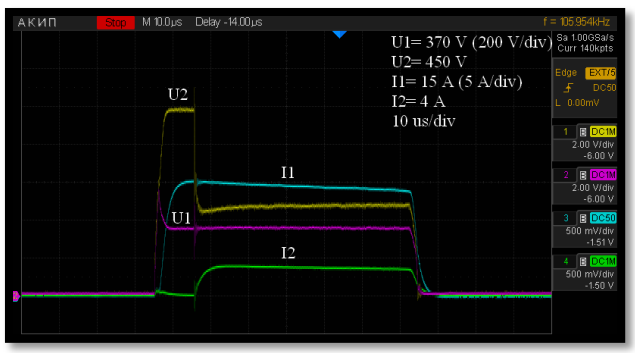

Figure 4: Oscillograms of voltage and current in auxiliary (U_2, I_2) and main discharges (U_1, I_1).

TEST BENCH FOR TOF STUDIES

For test bench extraction voltage was supplied with the pulsed transformer and applied to the terminal whereas extraction electrode had a ground potential. Test bench for the TOF studies had three Faraday cups, beam modulation electrode and drift space ~1.8 m (see Figs. 5 and 6). The total ion current was estimated with the signal from FC1 and the value observed was up to 50 mA. There was the aperture 8 mm diameter in the bottom of the FC1 for the beam passing. About 25 cm behind the extracting electrode Faraday cup 2 and beam modulation electrode mounted together in one assembly could be placed manually on the beam way. The signals registered by Faraday cup 1 and Faraday cup 2 were used for the source tuning.

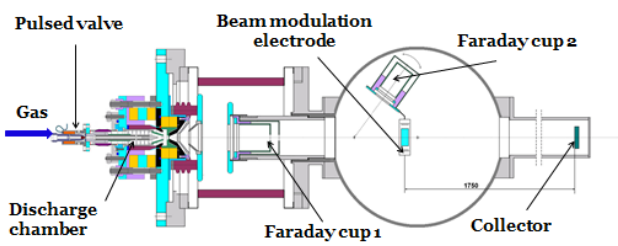

Figure 5: Test bench layout for the TOF measurements.

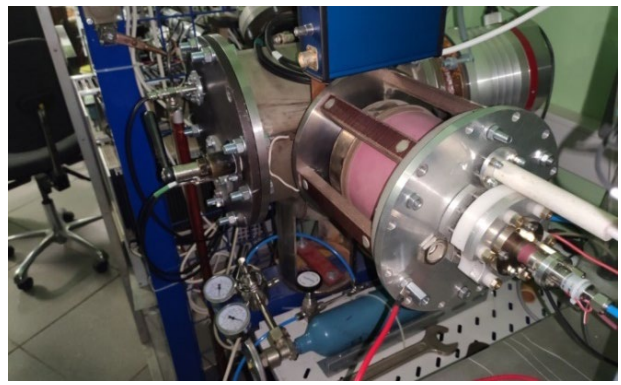

Figure 6: Helium ion source at the test bench.

For the beam modulation the 1 kV pulses 50 ns duration were applied to the electrode. Collector's signals were registered to obtain TOF spectrum. He^+ ions were the main species in the beam produced. Traces of impurities of carbon, oxygen and nitrogen were observed also (see Fig. 7).

The emissivity of the source, at a main discharge current of ~ 10 A, is about 50 mA He^+. The proportion of hydrogen, hydrocarbons, nitrogen and oxygen is reduced by training the source. In the process of improving the parameters of the source, the fraction of He^+ 90% was reached. He^{2+} ions are absent.

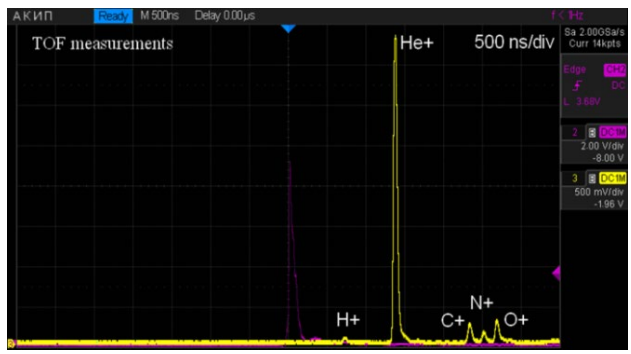

Figure 7: TOF spectrum obtained at the test bench for the helium ion source.

FORMATION THE BEAMS He^+ WITH THE LEBT

To provide with the He^+ beams the first run of the SC Booster helium ion source was placed on the HV terminal and fixed to the LEBT of HILAC (see Fig. 8). Beam was formed by two focusing electrode with the ability to adjust the duration of the ion beam in the range of 3 - 15 μs and accelerated in electrostatic tube up to RFQ input energy 17 keV/u. Two solenoids were used for beam focusing at the RFQ input. Steerers bend the beam in vertical and horizontal planes if needed (see Fig. 9).

ISBN: 978-3-95450-240-0 ISSN: 2673-5539 doi:10.18429/JACoW-RuPAC2021-TUPSB40

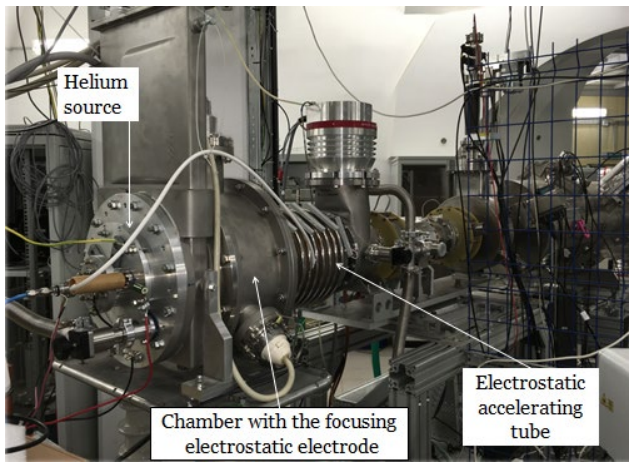

Figure 8: Helium ion source on the HV terminal fixed to the LEBT.

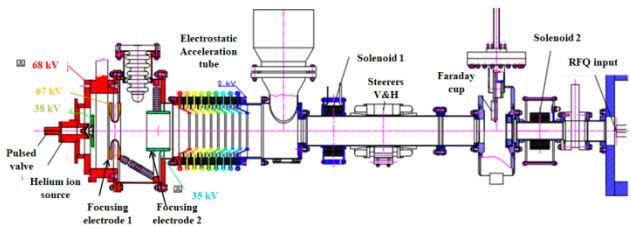

Figure 9: LEBT layout.

Pulse transformer provided HV terminal with electrical pulsed potential up to 100 kV of amplitude at the 200 us of the total pulse duration. To match the He^+ beam energy to RFQ input energy the value 68 kV of electrical potential was provided at the terminal during accelerating run. Beam intensity up to 25 mA at the injection point into RFQ was varied by solenoids (see Fig. 10).

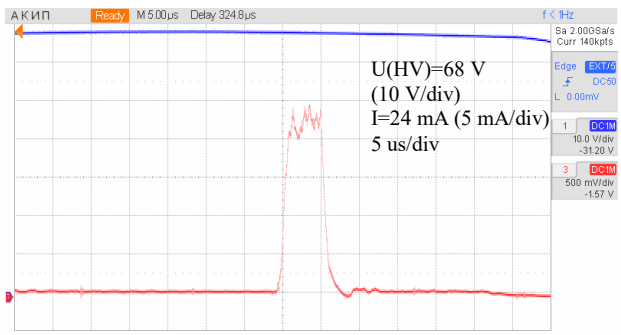

Figure 10: Signal Faraday Cup at LEBT (red), signal from divider of the HV pulsed transformer (blue).

CONCLUSION

To confirm the HILAC parameters, a need arose for a source of singly charged helium. A compact, lightweight, economical (gas flow) ion source with a cold magnetron cathode and magnetic plasma compression at the emission hole is created. A new ion source requires fewer power sources than a duoplasmotron. He^+ source does not need cathode glow power sources and electromagnet power sources due to the use of a cold cathode and permanent ring magnets.

Ion source produced the beams He^+ with current up to 50 mA was developed and used for Booster commissioning successfully.

The results of the work of the source at the stand with beams of protons, deuterium were also obtained.

REFERENCES

[1] A. V. Butenko *et al.*, "Commissioning of the New Heavy Ion Linac at the NICA Project," in *Proc. 25th Russian Particle Accelerator Conf. (RuPAC'16),* Saint Petersburg, Russia, Nov. 2016, pp. 157-160. doi:10.18429/JACoW-RuPAC2016-FRCAMH03

[2] A. V. Butenko *et al.*, "Injection Complex Development for the NICA-project at JINR," *in Proc. 29th Linear Accelerator Conf. (LINAC'18)*, Beijing, China, Sep. 2018, pp. 663-665. doi:10.18429/JACoW-LINAC2018-TH1P02

[3] L. P. Veresov and O. L. Veresov, "Ion source with a cold magnetron cathode and magnetic plasma compression" *Technical Physics*, vol. 48, no. 10, pp. 1338–1345, Oct. 2003. doi:10.1134/1.1620132

[4] L.P. Veresov, O.L. Veresov, A.F. Chachakov, "Hydrogen ion source with a cold magnetron cathode and magnetic plasma compression", *Technical Physics*, vol. 51, no. 1, 130–133, 2006. doi.org/10.1134/S1063784206010208

ISBN: 978-3-95450-240-0 ISSN: 2673-5539 doi:10.18429/JACoW-RuPAC2021-TUPSB43

OPTIMAL RF-PHOTOGUN PARAMETERS FOR THE NEW INJECTION LINAC FOR USSR PROJECT

Yu. D. Kliuchevskaia, S. M. Polozov[1]
National Research Nuclear University Moscow Engineering Physics Institute, Moscow, Russia
[1]also at NRC "Kurchatov Institute", Moscow, Russia

Abstract

The beam dynamics analysis of the RF-gun with photocathode for Russian 4th generation light source Ultimate Source of Synchrotron Radiation (USSR-4) was done to chose the optimal length of the section and cell's number and also to define optimal accelerating gradient and injection phase. The simulation of electrodynamics characteristics and fields distribution in the RF-gun based on 3.5-, 5.5- and 7.5-cell π-mode standing wave accelerating structure at operating frequency 2800 MHz was done. The influence of the beam loading effect on the field amplitude and beam dynamics was the main purposes of study also. The beam dynamics simulation results will present in the report and optimal RF-gun parameters will discuss.

INTRODUCTION

The scheme of the proposed linear electron accelerator which will be used as an injector to the main ring (top-up injection) is similar to the structure of the injector for the CERN FCC-ee: two RF-guns (with a photocathode and a thermionic cathode) and several tens of identical regular sections (see Fig. 1) [1-2]. The development was carried out within the design framework of the 4th generation Ultimate Source of Synchrotron Radiation (USSR-4) for the National Research Center "Kurchatov Institute". In this paper beam dynamics simulation results in RF-gun with photocathode are presented. The beam dynamics analysis in the accelerator was done by using of BEAMDULAC-BL code [3]. The program allows to take into account the beam loading effect and quasi-static components of the beam self-coulomb-field.

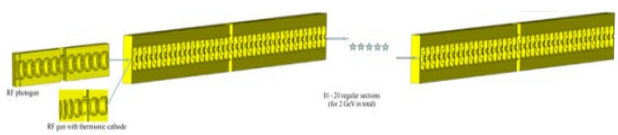

Figure 1: Possible scheme layout of linear accelerator-injector.

BEAM DYNAMICS SIMULATION IN RF-PHOTOGUN

Beam dynamics simulation in RF-gun with photocathode with intensity of 250 pC per bunch for duration of 10 ps was carried out. To achieve the minimum energy spectrum, the parameters of several versions of the photogun (3.5-, 5.5- and 7.5-cell) were optimized (see Fig. 2). Simulation results depending on the field amplitudes in the cells (E_1 – E_4, kV/cm) are presented in Table 1, and taking into account the beam loading in Table 2.

Table 1: Simulation Results Depending on the Field Amplitudes in the Cells

E_1, kV/cm	E_2, kV/cm	E_3, kV/cm	E_4, kV/cm	$\frac{\delta W}{W}$, %	Max E_{out}, MeV
1000	1000	1000	1000	2.5	9.439
900	**1000**	**1000**	**1000**	**1.7**	**9.438**
800	1000	1000	1000	2.2	8.678
750	1000	1000	1000	2.2	8.437
700	1000	1000	1000	2.2	8.181
900	900	1000	1000	3.0	8.390
800	**900**	**1000**	**1000**	**2.0**	**8.808**

According to results the 5.5-cell photogun provides the required minimum value of the energy spectrum for bunches with a charge of 250 pC per bunch and duration of 10 fs.

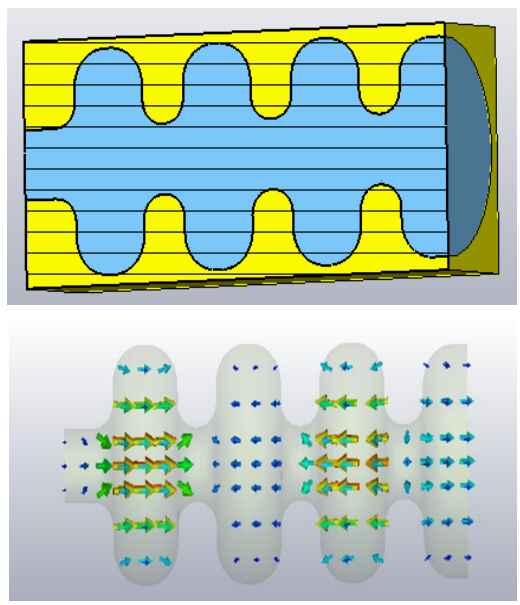

Figure 2: 3.5-cell RF-gun view and electrical field distribution.

The output beam spectrum at different electric field amplitudes (700-1000 kV/cm) in the cells of RF-photogun are shown in Fig. 3. Output longitudinal emittance and beam cross section are shown on Figs. 4 and 5.

ISBN: 978-3-95450-240-0 ISSN: 2673-5539 doi:10.18429/JACoW-RuPAC2021-TUPSB43

Table 2: Beam Dynamics Simulation Results Taking into Account the Beam Loading at $I = 20$ A

E_1, kV/cm	Cells number	$\frac{\delta W}{W}$, %	E_{max}, MeV	Beam Energy Spread, %
600	3.5	2.0	6.2	1.8
600	**5.5**	**2.7**	**8.1**	**0.9**
700	5.5	2.8	8.2	1.2
600	7.5	2.7	4.8	2.2
600	7.5	2.5	4.8	2.0

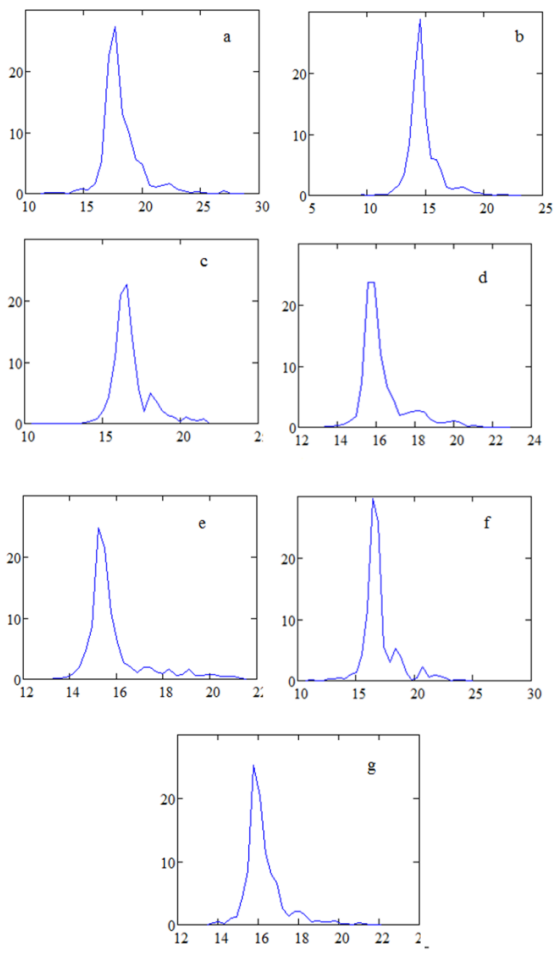

Figure 3: The output beam spectrum at different electric field amplitudes in the cells of RF-photogun.

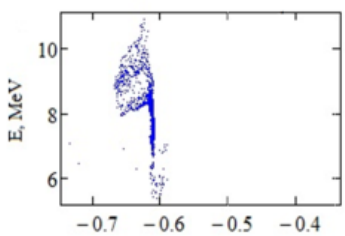

Figure 4: Output longitudinal emittance.

During steps of dynamics simulation preformed electron beam and accelerated in a 5.5-cell photogun was injected into the first regular section and completely captured. Such bunch can be accelerated with an increase of energy slightly higher than for a beam generated by RF-gun with a thermionic cathode.

This is possible because its length less by an order than for a bunch formed by thermionic cathode and the average acceleration rate will be higher.

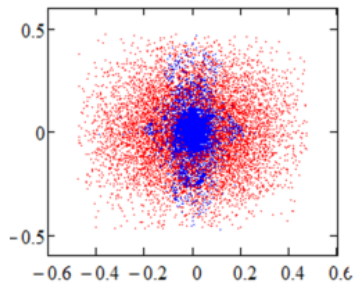

Figure 5: Beam cross section (the initial distribution is shown in red, at the output - in blue).

Table 3: Beam Dynamics Simulation Results Depending on the Field Amplitudes and Injection Phase in the 5.5-cell Photogun

Electric field, kV/cm	Injection phase, $\delta\varphi$	W_{out}, МэВ	Transmis-sion coeff., %	Output energy spectrum FWHM %
400	3.0	6.54	100.0	±2.8
500	3.1	8.36	99.9	±4.6
600	3.2	10.46	99.9	±3.1

Thus, the bunch acceleration generated by the photocathode can be performed at field strength of about 575 kV/cm rather than 600, or the output energy will be slightly higher about 6.3 GeV. Beam dynamics simulation shows that the energy spectrum for a bunch with a charge of 250 pC will be very low after the regular part of the accelerator (~ 0.08%) [4]. The transverse emittance will be ~ 0.3 nm · rad. It has also been shown that the current transmission coefficient is ~ 99.5% (see Fig. 6).

BEAM LOADING EFFECT

One of the purposes of the simulation was study of the beam loading effect on the distribution of the RF field amplitude and the beam dynamics in the «bunch-to-bunch» mode, at which the bunch loads the accelerating structure and the following train of bunches should receive a smaller increase of energy. It was shown that a bunch with a charge of 150 pC (current 15 A with a bunch duration of 100 fs) has no significant effect on the amplitude of the accelerating field. The maximum amplitude decrease is observed in the middle of the accelerating cell, but it is only 1.7% (see Fig. 7).

Simulation also showed that the Coulomb field practically has no effect on the dynamics, leading only to an insignificant increase (up to 0.15 mm or 30%) of the beam envelope in the bunching cells (see Fig. 8).

ISBN: 978-3-95450-240-0 ISSN: 2673-5539 doi:10.18429/JACoW-RuPAC2021-TUPSB43

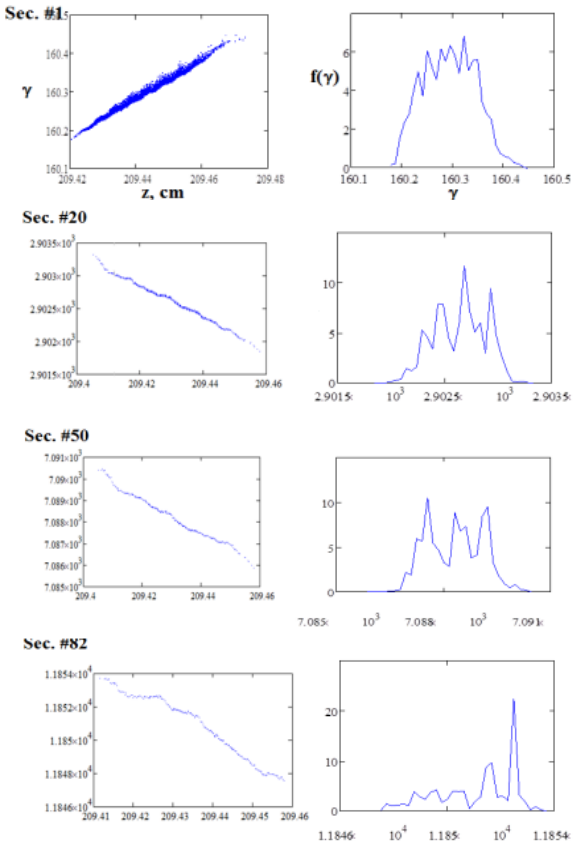

Figure 6: Beam dynamics simulation results in regular part of accelerator-injector for bunch with 250 pC charge, generated by RF photogun. Phase portraits on the phase plane (γ, z) and the energy spectrum.

It has also seen that the size of the envelope differs by 0.0529 mm inside the section, but at the exit the size of the beam is the same.

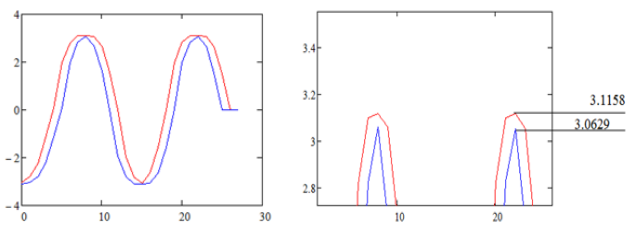

(a) (b)

Figure 7: Dimensionless amplitude of the accelerating field $\hat{e} = eE / 2\pi W_0$ in the center of the cell before the first bunch pass (red curve) (a) and taking into account the introduced disturbance (b).

For a beam generated by a photogun, it is possible to accelerate up to 12 bunches with a charge of 250 pC per bunch with an energy drop from the first bunch to the last less than 1.5%.

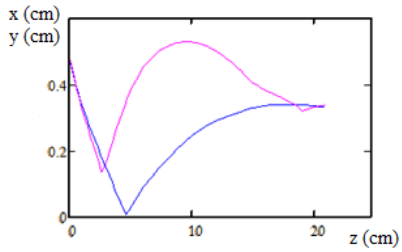

Figure 8: The beam envelope with and without beam loading.

Such beam loading can be compensated, first, by RF power supply system, which makes it possible to pump energy into regular sections, and by a small field's phase displacement, in which a laser pulse is applied to the cathode, from bunch to bunch.

ACKNOWLEDGEMENT

Project is realized according to the NRC Kurchatov Institute, Order № 2212 of the 23.10.2020 entitled "Modernization project of Kurchatov synchrotron radiation source" carried out within the framework of the R&D thematic plan of NRC Kurchatov University.

CONCLUSION

The beam dynamics simulation results of the RF-photogun, as one of the options for the new injection linac was described. Geometric parameters and electrodynamics characteristics were optimized. A 5.5-cell photogun provides the required minimum value of the energy spectrum (~ 0.08%) for bunches with a charge of 250 pC per bunch and duration of 10 fs. It was shown that the beam loading has no significant effect on the beam dynamics.

REFERENCES

[1] Ye. Fomin and V. Korchuganov, "Kurchatov synchrotron radiation source – from the 2nd to the 4nd generation", in *Proc. RUPAC'2018*, Protvino, Russia, Oct. 2018, paper WEZMH02, pp. 84-87.

[2] Y. Papaphilippou, "FCC-ee injector complex including booster", *FCC Meeting 2016*, Rome, Italy, Apr. 2016.

[3] T. V. Bondarenko, E. S. Masunov and S. M. Polozov, "BEAMDULAC-BL code for 3D simulation of electron beam dynamics taking into account beam loading and coulomb field", *Prob. At. Sci. Technologies. Ser. Nucl. Phy. Investigations*, vol. 6, no. 88, pp. 114-118, 2013.

[4] I. A. Ashanin, Yu. D. Kliuchevskaia, S. M. Polozov *et.al.*, "Beam Dynamics Simulation Results in the 6 GeV Top-Up Injection Linac of the 4th Generation Light Source USSR", in *Proc. RuPAC'2018*, Protvino, Russia, Oct. 2018, paper WEPSB05, pp. 285-288.

ISBN: 978-3-95450-240-0 ISSN: 2673-5539 doi:10.18429/JACoW-RuPAC2021-TUPSB44

DESIGN AND SIMULATION OF AN S-BAND RF PHOTOGUN FOR A NEW INJECTOR OF THE ACCELERATOR LINAC-200 AT JINR

Y.A. Samofalova, M.A. Nozdrin, V.V. Kobets, A.S. Zhemchugov, JINR, Dubna, Russia
A.M. Barnyakov, BINP, Novosibirsk, Russia

Abstract

A new 1.5-cell 2.856 GHz S-band RF photogun is simulated for the generation of ultrashort electron beams at the Linac-200 accelerator at JINR. The beam parameters at the photogun output are determined to meet the requirements of the Linac-200 injection. The general design of the photogun is presented. The electrodynamic parameters are determined and the accelerating field distribution is calculated. The particle dynamics is simulated and analysed to obtain the required beam properties.

Introduction

Commissioning of a new electron test beam facility Linac-200 [1] comes to the end at JINR (Dubna, Russia). The facility is based on the MEA accelerator that was transferred from NIKHEF to JINR at the beginning of the 2000s. Linac-200 provides electron beams with energy up to 200 MeV, beam current as much as 40 mA. The principal purpose of the facility is providing test beams for particle detector R&D, studies of novel approaches to the beam diagnostics, and training and education of students. Increasing the charge in the bunch from replacement the injector will give the opportunity to use the accelerator as a driver for a source of terahertz, synchrotron, and transition radiation in the soft X-ray range and to study the characteristics of image detectors, drastically expanding the range of available applied.

RF Photogun Concept

The design of the electron injector of the accelerator Linac-200 includes such elements as a triode type DC electron gun with a thermionic cathode, a chopper, a prebancher and a buncher, which is a short section of the accelerating structure designed for bunching a beam. The parameters of the gun and injector of the Linac-200 accelerator are presented in Table 1. The beam charge is 120nC in a 3 us pulse.

Table 1: Linac-200 Accelerator Injector Parameters

Parameter name	Injector	Electron gun
Pulse current, mA	60	200
Output energy, MeV	6	400

It is proposed to replace the existing injector with a 1.5-cells RF photogun with a cathode integrated into the end wall of the RF cavity. Significant advantages of the photogun include minimization of the emittance growth due to nonlinear components of the transverse electric and magnetic fields owing to the choice of optimal geometry of the accelerating structure.

The design is based on a 1.5-cell RF S-band photogun, similar to the design of the Budker Institute gun [2]. The gun is simulated for the existing laser (Fig. 1) developed by IAP RAS [3], the impulse characteristics are shown in Table 2.

Table 2: IAP RAS Laser Parameters

Parameter name	Value
Wavelength, nm	262
Bunch train repetition rate, Hz	10
Bunch train duration, us	800
Bunches in train	8000
Bunch duration, ps	10
Bunch energy, uJ	1.5

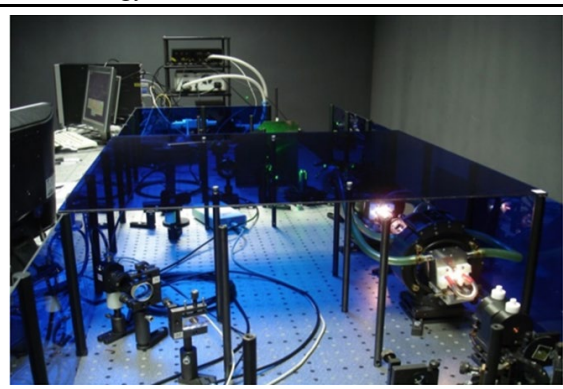

Figure 1: External view of the IAP RAS laser.

One can expect to obtain up to 960 nC in a 3 us pulse using this laser and assuming 10% quantum efficiency of a photocathode.

Simulation of a High Frequency Photogun

The simulation of the RF photogun design model is realized by the software CST Studio Suite 2021 [4] (hereinafter the software). In this work the calculations of the electric and magnetic fields, photoelectron emission and the dynamics of high-frequency ultrashort beams of the photogun were performed using the software. The design model of the RF photogun is 1.5 accelerating cells operating at a 2856 MHz frequency with a π mode oscillation. Microwave power is injected into the cavity by means of a rectangular waveguide and a coaxial line. The calculated standing wave factor is $\rho = 1.1$, the Q-factor is 15000. The estimated output beam energy reaches the set value (Fig. 2) and can regulated by the input power, which indicates the correct operation of the calculation model. Figure 3 shows the layout of the simulation model of the photogun and the simulation results with the electric field distribution along the axis of the cavities.

ISBN: 978-3-95450-240-0 ISSN: 2673-5539 doi:10.18429/JACoW-RuPAC2021-TUPSB44

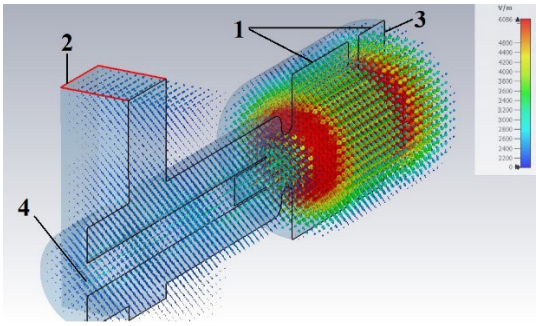

Figure 2: RF photogun layout (1-accelerating cavities; 2-RF power input; 3-cavity wall with a photocathode; 4-cavity for laser input and beam output).

The electric field in the accelerating cavities corresponds to an input microwave power of 4 MW.

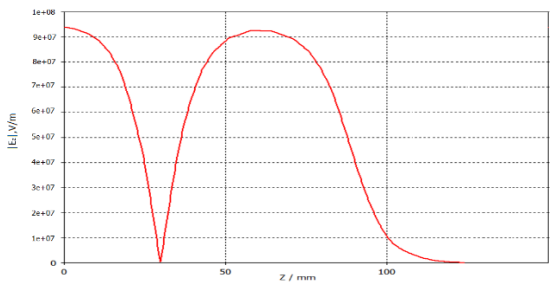

Figure 3: Dependence of the amplitude of the accelerating field on the axis of the cavities on the longitudinal coordinate.

Beam Dynamics in an RF Photogun

Beam dynamics are simulated for the developed computational model using a specialized software module. For these purposes, an idealized electron source with an initial energy corresponding to the photoelectron energy and a temporal structure set according to the specified laser parameters (Tab. 2). The results of beam simulation are presented in Fig. 4.

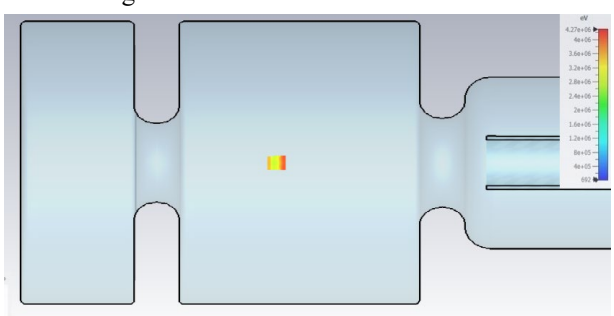

Figure 4: Beam acceleration in the cavity.

The correct operation of the model also required to determine with high accuracy many parameters that directly affect the energy characteristics of the installation as a whole. In particular, to achieve the best performance of the accelerating structure, time moment (the initial phase of microwave power oscillations), in which the electric field with the maximum accelerating potential develops, was coordinated with the transit time of the laser pulses. Then, in order to obtain time-stable energy characteristics of the computational model it was necessary to determine with high accuracy the interval be-tween micro- and macropulses, based on which, taking into account the duration of the microwave power pulse, the number of macro pulse bunches was determined. The obtained matched electron beams versus time are shown in Fig. 5. In the calculation, the electron yield from the photocathode was assumed to be equal to 32nC.

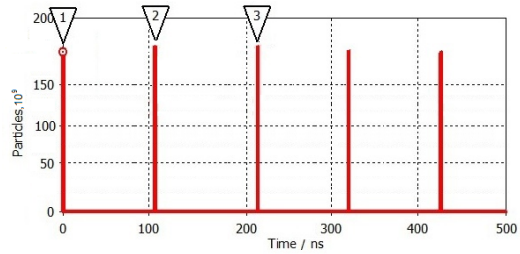

Figure 5: Distribution of beams at the cavity exit as a function of time, when the cavities are already filled.

The results of beam dynamics computational modeling by using the software (Fig. 4 and Fig. 5) demonstrate the expected acceleration electron bunch in accordance with the structure concept, as well as a high degree of agreement between the oscillations of the injected microwave power and the pulse characteristics of the laser.

CONCLUSION

In this work, we propose an RF photogun based on a one-and-a-half-cell high-frequency accelerating structure of the S-band accelerating structure and a powerful pulsed laser, which can be used as an electron source driver for the Linac-200 linear accelerator.

A computational model of the selected accelerating structure has been developed, which makes it possible to evaluate the high-frequency electromagnetic field in the structure and the electron beam dynamics. The parameters of the idealized source, the electrodynamic characteristics of the structure, and the distribution of the accelerating electric field are estimated. For the selected beam parameters, the particle dynamics analysis was performed, the results demonstrated the characteristics of the gun with this laser, close to the expected parameters.

REFERENCES

[1] M. A. Nozdrin *et al.*, "Linac-200: A New Electron Test Beam Facility at JINR", presented at the 12th Int. Particle Accelerator Conf. (IPAC'21), Campinas, Brazil, May 2021, paper WEPAB042.

[2] D. A. Nikiforov *et al.*, "Simulation of a Radio-Frequency Photogun for the Generation of Ultrashort Beams", *Technical Physics,* Vol. 63, No4, pp. 585-592, 2018. doi:10.1134/S1063784218040163

[3] E. I. Gacheva *et al.*, "Laser Driver for a Photoinjector of an Electron Linear Accelerator", *IEEE Journal of Quantum Electronics,* Vol.50, No7, pp. 522-529, 2014. doi:10.1109/JQE.2014.2323472

[4] https://www.cst.

ISBN: 978-3-95450-240-0 ISSN: 2673-5539 doi:10.18429/JACoW-RuPAC2021-TUPSB47

STABILITY CONDITIONS FOR A PENNING TRAP WITH ROTATING QUADRUPOLE OR DIPOLE ELECTRIC FIELDS

A. D. Ovsyannikov†, Saint-Petersburg State University, Saint-Petersburg, Russia

Abstract

The dynamics of particles in a Penning-Malmberg-Surko trap with Rotating Wall (rotating quadrupole and/or dipole electric field) and a buffer gas is considered. Electromagnetic traps are widely used for the accumulation and confinement of charged particles during various experiments in nuclear and accelerator physics, mass spectroscopy, and other fields. Traps are the main element of sources of charged particles in accelerators. An especially important role is played by traps with efficient accumulation during operation (in a cyclic mode) of ion synchrotrons and colliders with short-lived isotopes. The purpose of this work was to develop algorithms for constructing regions of stability (according to Lyapunov) in the space of parameters describing additional rotating electric fields, and to determine the analytical conditions that must be satisfied by the trap parameters to achieve a given degree of stability. The influence of the space charge of a beam of accumulated particles on the stability of the system is also investigated. The calculation results and the proposed models can be used in the selection and adjustment of the main parameters of the designed traps of the considered type.

INTRODUCTION

Electromagnetic traps are used to accumulate charged particles for various purposes in accelerator physics, mass spectroscopy, nuclear physics, and some other areas of scientific research. Traps are especially important part of charged particles sources in synchrotrons and colliders with short-lived isotopes. The essence of their action is the localization of charged particles in a limited area of space for a sufficiently long time. For this, special combinations of electromagnetic fields are formed that provide the required behaviour of charged particles inside the trap. The most famous traps of the Paul and Penning type, as well as their various modifications. A detailed review of the main known types of traps and the principles of their action is presented in [1].

In this paper, we consider the dynamics of charged particles in a Penning trap with additional rotating dipole electric field (so called Rotating Wall — RW) and a buffer gas or rotating quadrupole electric field without buffer gas, studied earlier in [2-5]. Note also that the investigated model of motion can be used in the analysis of the Penning-Malmberg-Surko trap - an open cylindrical trap and its modifications [1]. The results of the analysis of the influence of the rotating field, obtained earlier, were either insufficiently rigorous from the mathematical point of view [3, 5], or were insufficiently complete [4]. In [6-9], general approaches were proposed that are applicable to the analysis of stability and the construction of numerical-analytical solutions of the equations of motion of the system under study for arbitrary values of its parameters. Examples of such an analysis were given in the works [10, 11]. In this paper the model of dynamics includes also influence of the space charge of a beam of accumulated particles and combination of dipole and quadrupole rotating electric field.

It should be noted that the work investigates the motion of single particles in ideal (linear) fields. Interest in this formulation of the problem arises from attempts [1, 3] to explain the observed in experiments [2] effect of compression of a bunch of accumulated particles by a rotating field at extremely low concentrations of accumulated particles. In this case, the focusing effect should follow from the analysis of the solution of the equations of motion of single particles in the fields of forces acting in the trap [1].

EQUATIONS OF MOTION

The dynamics of charged particles in a Penning trap with an additional rotating electric field is considered. Charged particle dynamics is considered in the field of the potentials and homogeneous longitudinal magnetic field:

$$\Phi(r,\theta,z) = \frac{m}{q}\left(\frac{\omega_z^2}{2}\left(z^2 - \frac{r^2}{2}\right) - \frac{(q_r r^2 + q_z z^2)}{2} + azr\cos(\theta + t\omega_r) + b\frac{r^2}{2}\cos 2(\theta + t\omega_r + \theta_0)\right),$$

$$\vec{B} = \vec{e}_z B.$$

Here m and q are the mass and the charge of the particle, ω_z is the frequency of the particle longitudinal oscillations in the axially symmetric electric field of the trap electrodes; a, b and ω_r are amplitude related parameters and the frequency of the rotating electric dipole and quadrupole fields, θ_0 is initial phase parameter of rotating quadrupole field; q_r and q_z are the parameters associated with the space charge, which determine the linear part of the potential of the axially symmetric accumulated beam; z, r and θ are the axial, radial and angular coordinates with the axis coinciding with symmetry axis of the trap electrodes.

The charged particle motion in these fields is described by the following systems of equations correspondingly:

$$\ddot{x} = \left(\frac{\omega_z^2}{2} + q_r\right)x + \Omega_c\dot{y} - k\dot{x} - az\cos(t\omega_r) - b(x\cos 2(t\omega_r + \theta_0) - y\sin 2(t\omega_r + \theta_0)),$$

$$\ddot{y} = \left(\frac{\omega_z^2}{2} + q_r\right)y - \Omega_c\dot{x} - k\dot{y} + az\sin(t\omega_r) + b(y\cos 2(t\omega_r + \theta_0) + x\sin 2(t\omega_r + \theta_0)),$$

$$\ddot{z} = (q_z - \omega_z^2)z - k\dot{z} - a(x\cos(t\omega_r) - y\sin(t\omega_r)).$$

† ovs74@mail.ru, a.ovsyannikov@spbu.ru

ISBN: 978-3-95450-240-0 ISSN: 2673-5539 doi:10.18429/JACoW-RuPAC2021-TUPSB47

Here $\Omega_c = qB/m$ is the particle cyclotron frequency, the parameter k presents the friction force related to the particle scattering by the trap buffer gas molecules. In this work, we considered a modification of the Penning trap, a Penning-Malmberg-Surco trap with an rotating electric field along the entire length of the trap.

REDUCTION TO EQUATIONS WITH CONSTANT COEFFICIENTS

In what follows we confine ourselves to analyzing the solution in the approximation corresponding to the typical experimental values of the parameters:

$$\Omega_c \gg \omega_z \gg \omega_m \approx {\omega_z}^2/2\Omega_c \gg k > 0.$$

Here ω_m is the magnetron frequency, which describes the oscillations of particles in crossed longitudinal magnetic and radial electric fields.

To study particle motion for arbitrary values of a, we introduce new complex variable

$$\psi = (x + iy)e^{i(t\omega_r)}.$$

Then $u = \mathrm{Re}\psi = x\cos(t\omega_r) - y\sin(t\omega_r)$, $v = \mathrm{Im}\psi = y\cos(t\omega_r) + x\sin(t\omega_r)$. It means transition to a moving coordinate system obtained from a stationary by uniform rotation in a transverse plane with a frequency ω_r around the axis z.

As a result, in the new variables we obtain a stationary, with constant coefficients system of equations:

$$\ddot{\psi} + \left(k + i(\Omega_c - 2\omega_r)\right)\dot{\psi} + \left(\omega_r(\Omega_c - \omega_r - ik) - \frac{\omega_z^2}{2} - q_r\right)\psi + az + be^{-i(2\theta_0)}\bar{\psi} = 0,$$

$$\ddot{\bar{\psi}} + \left(k - i(\Omega_c - 2\omega_r)\right)\dot{\bar{\psi}} + \left(\omega_r(\Omega_c - \omega_r + ik) - \frac{\omega_z^2}{2} - q_r\right)\bar{\psi} + az + be^{i(2\theta_0)}\psi = 0,$$

$$\ddot{z} + k\dot{z} + (\omega_z^2 - q_z)z + \frac{a}{2}(\psi + \bar{\psi}) = 0.$$

The characteristic numbers of the system are the roots of the polynomial:

$$\chi(\lambda) = \det\begin{pmatrix} \mathrm{P}(\lambda) & be^{-i(2\theta_0)} & a \\ be^{i(2\theta_0)} & \overline{\mathrm{P}}(\lambda) & a \\ \frac{a}{2} & \frac{a}{2} & Q(\lambda) \end{pmatrix} =$$

$$Q(\lambda)(\mathrm{P}(\lambda)\overline{\mathrm{P}}(\lambda) - b^2) - \frac{a^2}{2}(\mathrm{P}(\lambda) + \overline{\mathrm{P}}(\lambda) - 2b\cos 2\theta_0),$$

where

$$Q(\lambda) = \lambda^2 + k\lambda + {\omega_z}^2 - q_z,$$

$$R(\lambda) = \lambda^2 + (i\Omega_c + k)\lambda - \frac{{\omega_z}^2}{2} - q_r,$$

$$\bar{R}(\lambda) = \lambda^2 + (-i\Omega_c + k)\lambda - \frac{{\omega_z}^2}{2} - q_r,$$

$$P(\lambda) = R(\lambda - i\omega_r),\ \bar{P}(\lambda) = \bar{R}(\lambda + i\omega_r).$$

The distance on the complex plane from the imaginary axis to the characteristic number with the maximum real part, taken with the corresponding sign, will be called the degree of stability and denoted by γ. The degree of stability will be taken with a positive sign if all roots of the characteristic polynomial are in the left half-plane (the case of asymptotic stability of the system). If there is at least one root in the right half-plane, the value of the degree of stability will be taken with a negative sign (the case of an unstable system). If the rightmost root (or roots) are located on the imaginary axis, the degree of stability is zero. The degree of stability of the system under study cannot exceed $\gamma_{max} = k/2$.

CONSTRUCTION OF THE STABILITY REGION

Let us introduce the parameter α, with the help of which we will estimate the degree of stability of the system under study. Let $\mu = \lambda + \alpha$. Let us make the corresponding change in the characteristic polynomial:

$$\tilde{\chi}(\mu) = \chi(\mu - \alpha) = d_0\mu^6 + d_1\mu^5 + d_2\mu^4 + d_3\mu^3 + d_4\mu^2 + d_5\mu + d_6.$$

Here $d_0 = 1$, $d_1 = (3k - 6\alpha)$,… The d_j coefficients can also be calculated from the Taylor formula:

$$d_j = \chi^{(6-j)}(-\alpha)/(6 - j)!\,,\ j = 0,1,\ldots,6.$$

The asymptotic stability test of the polynomial $\tilde{\chi}(\mu)$ for various values of the parameter α can be organized using the necessary and sufficient Routh – Hurwitz conditions (or its modification — the Lienard-Chipard criterion). The fulfillment of these conditions for the polynomial $\tilde{\chi}(\mu)$ with the selected value of the parameter α will mean that the degree of stability of the polynomial $\chi(\lambda)$ will be greater than the selected value: $\gamma > \alpha$.

STABILITY CONDITIONS

Let us compose the Hurwitz matrix for the polynomial $\tilde{\chi}(\mu)$ and consider its odd principal minors:

$$\Delta_1 = d_1,\quad \Delta_2 = \begin{vmatrix} d_1 & d_0 & 0 \\ d_3 & d_2 & d_1 \\ d_5 & d_4 & d_3 \end{vmatrix},$$

$$\Delta_5 = \begin{vmatrix} d_1 & d_0 & 0 & 0 & 0 \\ d_3 & d_2 & d_1 & d_0 & 0 \\ d_5 & d_4 & d_3 & d_2 & d_1 \\ 0 & d_6 & d_5 & d_4 & d_3 \\ 0 & 0 & 0 & d_6 & d_5 \end{vmatrix}.$$

As a result, we obtain the system of inequalities

$$d_j > 0,\quad j = 1,\ldots,6;\quad \Delta_3 > 0,\ \Delta_5 > 0,$$

the fulfillment of which guarantees that the degree of stability γ of the polynomial $\chi(\lambda)$will lie in the range:

$$\alpha < \gamma \le \frac{k}{2}.$$

CALCULATION EXAMPLES

The calculations were carried out for electron with the following values of the main parameters: $\Omega_c = 4.4$ Grad/s, $\omega_z = 59.6$ Mrad/s, $k = 1400\ \mathrm{s}^{-1}$.

In Figures 1 and 2 the found regions of asymptotic stability in the space of parameters a and ω_r are marked with different colors with an estimate of the range of values for the degree of stability of the system. For exam-

ISBN: 978-3-95450-240-0 ISSN: 2673-5539 doi:10.18429/JACoW-RuPAC2021-TUPSB47

ple, red means that the degree of stability is more than 10 percent (but not more than 20), green means more than 20 (but not more than 30), etc. (see the legend of the corresponding figure), where $\gamma_{max} = k/2$ is taken as 100 percent. Figure 1 shows stability area with switched off rotating quadrupole field. Figure 2 shows the effect of adding a rotating quadrupole electric field to the system with dipole rotating field.

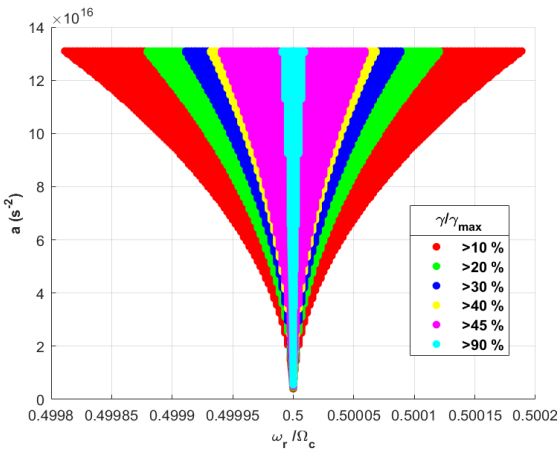

Figure 1: Areas with different ranges of values of the degree of stability (b=0).

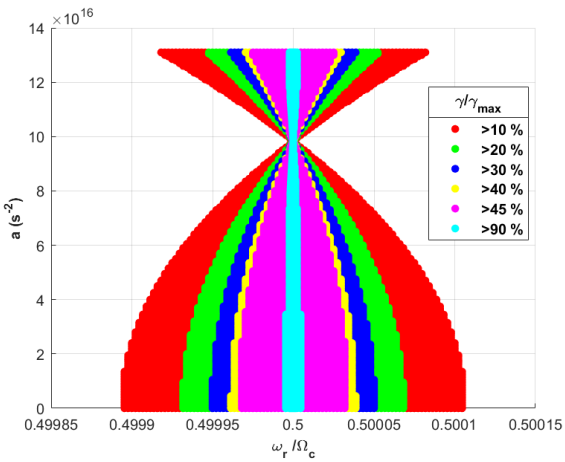

Figure 2: Areas with different ranges of values of the degree of stability ($b = 10^{15}$ s^{-2}, $\theta_0 = \pi/2$).

CONCLUSION

The dynamics of particles in a Penning trap with a rotating quadrupole and/or dipole electric field and a buffer gas is considered. Using the Lienard-Chipart modification of the Routh-Hurwitz stability criterion, an analysis is carried out and regions in the space of parameters of the trap of the asymptotic stability of particle motions (according to Lyapunov) are found. The influence of the space charge of a beam of accumulated particles on the stability of the system is also investigated. Various models of an axially symmetric beam are considered. The stability regions are constructed in the space of parameters characterizing the additional rotating electric field.

Appropriate software has been developed to find and graphically represent areas of stability. In the algorithm for constructing stability regions, stability criteria for families of polynomials linear in the parameter are also used.

The calculation results and the proposed models can be used in the selection and adjustment of the main parameters of the designed traps of the considered type.

REFERENCES

[1] M. K. Eseev, I. N. Meshkov, "Traps for storing charged particles and antiparticles in high precision experiments", *Phys.-Usp.*, vol. 59, no. 3, p. 304317, 2016. doi:10.3367/UFNe.0186.201603f.0321

[2] C. A. Isaac, C. J. Baker *et al.*, "Compression of positron clouds in the independent particle regime", *Phy. Rev. Lett.*, vol. 107, Iss. 3, p. 033201, 2011. doi:10.1103/PhysRevLett.107.033201

[3] C. A. Isaac "Motional sideband excitation using rotating electric fields", *Phy. Rev. A*, vol. 87, Iss. 4, p. 043415, 2013. doi:10.1103/PhysRevA.87.043415

[4] I. N. Meshkov, M. K. Eseev, A. D. Ovsyannikov, D. A. Ovsyannikov, and V. A. Ponomarev, "Analysis of the Particle Dynamics Stability in the Penning-Malmberg-Surko Trap", in *Proc. 25th Russian Particle Accelerator Conf. (RuPAC'16),* Saint Petersburg, Russia, Nov. 2016, pp. 65-67. doi:10.18429/JACoW-RUPAC2016-WECAMH03

[5] T. Hasegava, M. J. Jensen, J. J.Bollinger "Stability of a Penning trap with a quadrupole rotating field", *Phy. Rev. A*, vol. 71, Iss. 2, p. 023406, 2005. doi:10.1103/PhysRevA.71.023406

[6] A. D. Ovsyannikov, M. A. Raikonen, "Algorithm of approximate calculation of multiplicators for one periodic system", *Vestnik of the Saint Petersburg State University of technology and design. Series 1. Natural and technical Sciences*, Iss. 3, p.10-14, 2017.

[7] I. N. Meshkov, A. D. Ovsyannikov, D. A. Ovsyannikov, M. K. Eseev, "Study of the stability of charged particle dynamics in a Penning-Malmberg-Surko trap with a rotating field", *Dokl. Phys.*, vol. 62, no. 10, p. 457-460, 2017. doi:10.1134/S1028335817100093

[8] A. D. Ovsyannikov, "Analysis of the dynamics of charged particles in an ideal Penning trap with a rotating field and a buffer gas", *Vestnik of Saint Petersburg University. Applied Mathematics. Computer Science. Control Processes*, vol. 15, Iss. 1, p. 62-75, 2019. doi:10.21638/11702/spbu10.2019.105

[9] A. D. Ovsyannikov, I. N. Meshkov, D. A. Ovsyannikov *et al.*, "Analysis and Modeling of the Charged Particle Beam Dynamics in the Charlton Trap", *Phys. Part. Nuclei Lett.*, vol. 15, p. 754-757, 2018. doi:10.1134/S1547477118070543

[10] A. D. Ovsyannikov, A. I. Shlokova, A. A. Komarova, "Construction of Stability Regions in the Parameter Space in a Penning Trap with a Rotating Electric Field", *Bulletin of Irkutsk State University, Series Mathematics*, vol. 35, p. 49-59, 2021. doi:10.26516/1997-7670.2021.35.49

[11] A. D. Ovsyannikov, A. A. Komarova, A. I. Shlokova, "Search for Stability Regions in the Space of Coefficients in a Penning-Malmberg-Surko Trap with a Rotating Electric Quadrupole Field", *Vestnik of the Saint Petersburg State University of technology and design. Series 1. Natural and technical Sciences*, Iss. 4, p. 3-6, 2020. doi:10.46418/2079-8199_2020_4_1

ISBN: 978-3-95450-240-0 ISSN: 2673-5539 doi:10.18429/JACoW-RuPAC2021-TUPSB48

OPTIMIZATION OF THE MASTER OSCILLATOR LASER BEAM PARAMETERS IN THE MULTI–PASS AMPLIFIER

T. V. Kulevoy*, A. N. Balabaev, I. A. Khrisanov, A. A. Losev, V. K. Roerich, Yu. A. Satov, A. V. Shumshurov, A. A. Vasilyev, NRC «Kurchatov Institute» – ITEP, 117218, Moscow, Russia

Abstract

Some results devoted to development of the ITEP laser–plasma ion source for a charged particle accelerator are presented. In our case, the laser radiation source is a high-power repetition rate CO_2 laser system based on the nonlinear interaction of a light with a multi-pass amplifier medium. The laser chain consists of a master oscillator [1], gas absorber cell, and a four–pass amplifier.

The efficiency of the laser ion source depends on by the output power of laser setup. The output power of such a laser setup is determined by the efficiency of energy extraction from the amplifying medium.

The spatial parameters of a laser beam at the amplifier input are optimized by numerical simulation. The results obtained for fixed master oscillator pulse and amplifying medium parameters. The maximum output energy is achieved with certain laser beam profile at the amplifier input. For this purpose, only central part of the beam with a Gaussian spatial profile, which is close to uniform in intensity, is injected into the telescopic amplifier. The optimal choice of beam diameter ensures the maximum laser efficiency.

INTRODUCTION

A laser-plasma generator of multiply charged ions based on a CO_2 laser is useful for a wide range of practical applications, including as a source for an particle accelerator. A such repetitive rate laser has a relatively low cost and is capable of emitting a pulses with a power of over 5 GW and an energy of over 100 J. A low operating costs, a relatively weak requirements for cleanliness degree, thermal stabilization and dust–free premises is a undeniable advantage of a such laser.

The laser–plasma generator based on a CO_2 laser was developed for the lead ion source for the CERN accelerator [2] and for the ITEP–TWAC facility [3]. In the above examples, a laser–optical scheme based on nonlinear effects during propagation of radiation pulses in absorbing and amplifying resonant media [4] was used.

EXPERIMENTAL SETUP

The optical scheme of the experimental setup is in the Fig. 1. The master oscillator (1) is based on a self-sustained discharge module at atmospheric pressure with UV preionization. The hybrid generation scheme of the generator is required to form single–frequency laser pulses with a smooth temporal shape and an FWHM pulse duration of 80 ns and energy up to 200 mJ for the P(20) line in the 10-μmetre band. The sectioned absorber gas cell (2) [5] of 90 cm length is filled with a mixture of SF_6/N_2 and is used to modify the master oscillator pulse front edge. The grating (3) separates the master oscillator and the amplifier medium for the entire spectral range except the desired spectral line.

The spatial parameters of the laser beam are defined by a spatial filter that consists of a pair of confocal mirrors (4, 6) and diaphragm (5). The laser beam formed by the filter is close to a Gaussian beam. In the laser setup a four–pass amplification chain is applied. It is arranged with flat mirrors and a pair of mirrors (8, 10) of a Cassegrain off–axis telescope with multiplication $M = 5.5$.

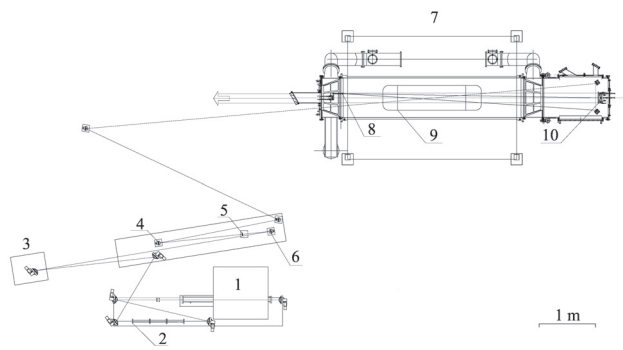

Figure 1: Experimental setup. 1 — master oscillator; 2 — absorbing cell; 3 — diffraction grating; 4 — short–focus mirror of the spatial filter; 5 — spatial filter diaphragm; 6 — long–focus mirror of the spatial filter; 7 — wide-aperture four–pass amplifying module; 8 — small telescope mirror; 9 — active medium; 10 — large telescope mirror.

SPATIAL PARAMETERS OF THE LASER BEAM CALCULATION

The computer program FOCUSD [2] for analysis of the laser beam spatial distribution in the laser beam shaping scheme describes the distribution of the light energy density in the 1D diffraction approximation in the case of cylindrical symmetry and integrally over time. Active medium gain is uniformly $g_0 = 2.5 \times 10^{-2}\,\mathrm{cm}^{-1}$. An absorbing cell influence is described according to the previously developed phenomenological model of an absorbing medium [6].

* kulevoy@itep.ru

ISBN: 978-3-95450-240-0 ISSN: 2673-5539 doi:10.18429/JACoW-RuPAC2021-TUPSB48

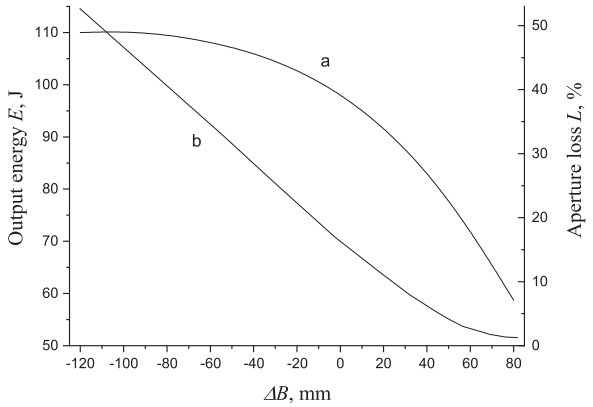

Figure 2: The calculated output energy (a) and aperture losses at the small mirror of the amplifier telescope (b) in dependence on the the spatial filter base detuning ΔB.

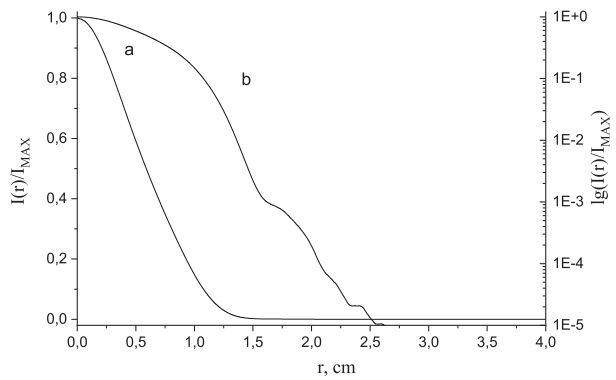

Figure 3: The calculated laser beam energy density distributions on the small mirror of the amplifier telescope. The spatial filter base detuning is +80 mm.
a — in a linear scale; b — in a logarithmic scale.

RESULT AND DISCUSSIONS

The calculated output energy and aperture losses at the small mirror of the amplifier telescope in dependence on the the spatial filter base detuning is presented in Fig. 2.

The radial energy distributions of the beam at the small mirror of the telescope for the different spatial filter detuning is presented in Fig. 3 (a converging beam) and Fig. 5 (a diverging beam). The radius of the small mirror of the telescope is 15.5 mm. The corresponding radial energy distributions of the beam at the amplifier output is presented in Figs. 4 and 6. In this cases, the output energy is 59 and 110 J respectively.

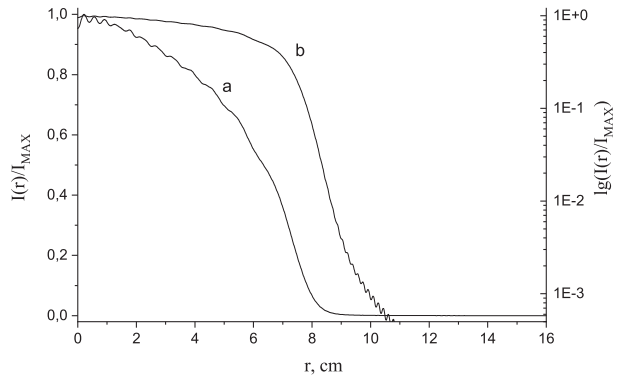

Figure 4: The calculated laser beam energy density distributions at the amplifier output. The spatial filter base detuning is +80 mm.
a — in a linear scale; b — in a logarithmic scale.

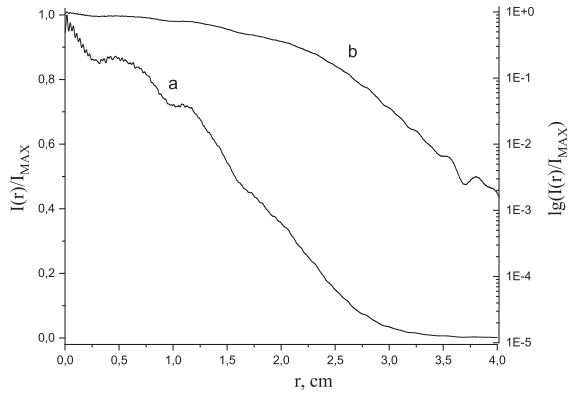

Figure 5: The calculated laser beam energy density distributions on the small mirror of the amplifier telescope. The spatial filter base detuning is −100 mm.
a — in a linear scale; b — in a logarithmic scale.

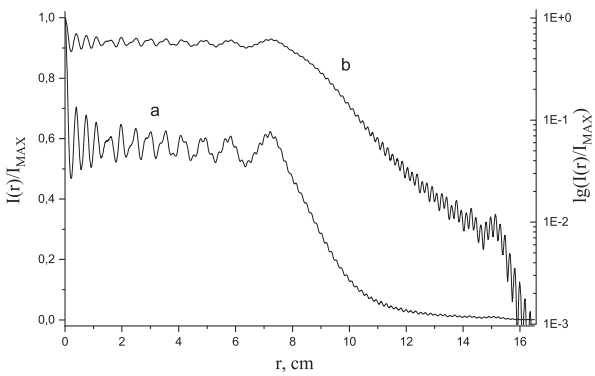

Figure 6: The calculated laser beam energy density distributions at the amplifier output. The spatial filter base detuning is −100 mm.
a — in a linear scale; b — in a logarithmic scale.

ISBN: 978-3-95450-240-0 ISSN: 2673-5539 doi:10.18429/JACoW-RuPAC2021-TUPSB48

CONCLUSION

The results of diffractional calculation of the laser optical scheme have shown that the maximum output beam energy is obtained with a certain beam diameter on the small mirror of the telescope.

The optimal tuning is reached with an increase of beam diameter relative to the diameter of the small mirror, so that the input beam acquires a more uniform profile due to using of the central part of the Gaussian master oscillator beam, despite the increasing aperture losses. Further improvement of uniformity of beam energy density profile is achieved in this geometry of the amplification circuit in saturated passages of the amplifier.

As calculations in earlier works have shown, in this case, a pulse duration "compression" is more efficient and a higher output power is achieved. Output power of a laser pulse is crucial in applied problems such as ion beams generating in a laser–plasma ion sources. It determines of a laser plasma ionization degree and the number of generated ions.

Actual laser scheme differs from the model of amplifying medium used in numerical calculations by significantly inhomogeneous gain coefficient profile over the active medium cross section, results of calculations are in qualitative agreement with observed effects.

REFERENCES

[1] Yu. A. Satov *et al.*, "A stabilized pulsed repetition–rate CO_2 laser for a laser-plasma generator of multiply charged ions", *Instrum. Exp. Tech.*, vol. 55, no. 3, pp. 399–406, 2012-05.

[2] Yu. A. Satov *et al.*, "High-Power CO_2 Laser System with Repetition Rate Operation for High Current Multicharged Heavy Ion Generations", *J. Russ. Laser Res.*, vol. 25, no. 3, pp. 205–216, May 2004.

[3] N. N. Alexeev, *et al.*, "ITEP-TWAC renewal and upgrading program", in *Proc. RUPAC'2012*, Saint|–Petersburg, Russia, Sep. 2012, pp. 112–116.

[4] K. N. Makarov *et al.*, "Study of the dynamics of propagation of CO_2 laser pulses in a chain of nonlinear absorbing and amplifying media", *Quantum Electronics*, vol. 31, no. 1, pp. 23–29, Jan. 2001.

[5] Yu. A. Satov *et al.*, "Device and method for formation of high-power short CO_2 pulses", Federal service for intellectual property (Rospatent), No. RU2653568C1, May 11, 2018.

[6] N. N. Alexeev *et al.*, "Development of a laser system for a heavy–ion injector and its improvement prospects", *ITEP preprint*, no. 1, 2014.

ISBN: 978-3-95450-240-0 ISSN: 2673-5539 doi:10.18429/JACoW-RuPAC2021-TUPSB51

MEASUREMENT OF NEUTRON FIELD FUNCTIONALS AROUND A NEUTRON CONVERTER OF 50 GeV PROTONS

Ya. N. Rascvetalov†, Yu. V. Beletskaya, A. G. Denisov, A. A. Durum, V. L. Ilyukin, A. M. Mamaev, V. N. Peleshko, I. N. Piryazev, E. N. Savitskaya, M. M. Sukharev, S. E. Sukhikh, A. A. Yanovich, NRC "Kurchatov Institute" - IHEP, 142281 Protvino, Russia

Abstract

The experiment was performed on a pulsed neutron source of the "Neutron" research bench, being created at the U-70 accelerator at National Research Center "Kurchatov Institute" - IHEP, Protvino. Neutrons were generated by the 50 GeV proton beam in the special converter.

As a measurement method, neutron activation analysis was used with a set of threshold activation detectors made of C, Al, Nb, In, Bi materials. The neutron energy thresholds of these detectors are in the range from 1 MeV to 75 MeV. The aluminium activation foils were used to calculate the absolute values of the proton quantities in the exposures.

The results of measurements and calculations are presented in the form of the following functionals: nuclides activity of threshold reactions in detectors at the end of the exposure; reaction rate; neutron fluences with energies greater than the threshold. To estimate these values, the spectra of neutrons, protons and pions were calculated using the particle transport codes MARS and HADRON with the FAN15 as a low-energy block. It was found that neutrons dominate up to 100 MeV, and the charged hadrons contribution to the total reaction rate for a particular nuclide formation can range from 4% to 46%.

INTRODUCTION

Pulsed neutron sources based on high-energy proton beams have a wide range of applications – from transmutation of long-lived radioactive elements to neutronographic studies of materials and rapid processes kinetics. Information of the parameters of the neutron field around the proton converter is necessary for these tasks. Similar problems were studied at IHEP (1999 - 2000) with proton beam energy of 1 and 70 GeV [1]. A special research bench "Neutron" was created in 2019 for the extracted 50 GeV proton beam.

The measurements were performed in the field of secondary hadrons, emitted from the side surface of the converter of the bench "Neutron". The converter consists of a lead core 50 × 50 × 300 mm^3 and 40 mm thick polyethylene block surround of the sides. A proton beam with transverse size of 8 mm horizontally and 14 mm vertically dropped on the end face of the lead core along the longitudinal axis. But the beam impact point was shifted horizontally from core center to the right by ~ 8 mm. The intensity of the beam was 1 - 2 bunches per 8.7 s accelerator cycle ($3 \cdot 10^{11}$ protons are in each bunch). As a measurement method, neutron activation analysis was used with a set of threshold activation detectors made of C, Al, Nb, In, Bi materials. The characteristics of the detectors, the threshold reactions, and the identified lines of gamma quanta are fully described in [1].

The aluminium activation foils were used to calculate the number of protons in the exposures. The experiment was performed for three U-70 accelerator runs in the period 2019 - 2021.

RESULTS

The detectors were irradiated in a series of exposures at the points 1, 2, 3 on the thin aluminium substrate placed on the upper converter surface as shown in Fig. 1. The substrate was cut along the beam axis into 12 rectangles (50 × 65 × 0.2 mm^3). The activity A_0 of the ^{22}Na nuclide in these samples at the end of irradiation (a total of $1.3 \cdot 10^{13}$ protons onto converter) is shown in Fig. 2.

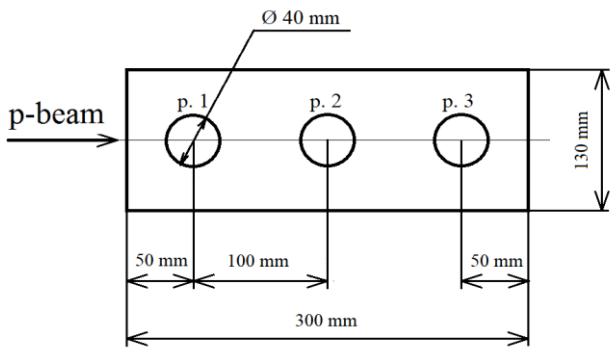

Figure 1: Detectors placement points (p. 1, p. 2, p. 3) on the thin Al substrate.

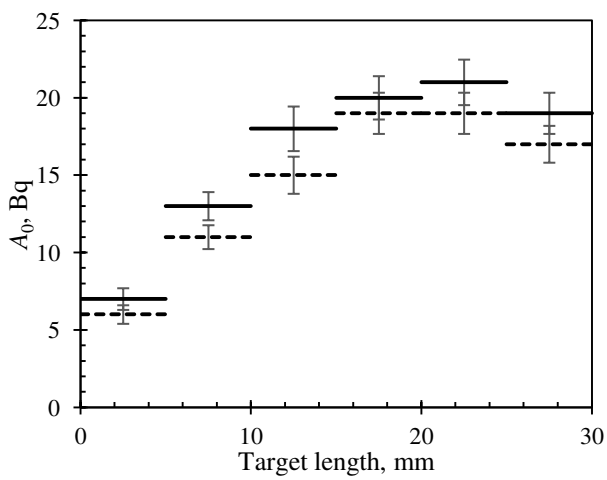

Figure 2: The activities of Na22 in the substrate.

† Jaroslav.Rascvetalov@ihep.ru

ISBN: 978-3-95450-240-0 ISSN: 2673-5539 doi:10.18429/JACoW-RuPAC2021-TUPSB51

Table 1: Experimental Reaction Rates and Their Relation to the Calculated Reaction Rates for 50 GeV Protons Energy

Detector → radionuclide	R_{exp}, 10^{-28} proton^{-1}			R_{exp}/R_{cal}		
	p.1	p.2	p.3	p.1	p.2	p.3
Al →^{24}Na	11.0±6.9%	18.3±6.7%	16.8±6.9%	0.90	0.89	0.93
Al →^{22}Na	2.48±6.5%	5.23±6.5%	5.74±6.5%	2.28	1.93	1.60
Al →^{7}Be	0.125±6.9%	0.454±6.5%	0.709±6.7%	4.11	2.97	2.40
Nb→^{92m}Nb	64±8.2%	111±7.4%	104±7.5%	1.66	1.73	1.73
C →^{11}C	2.68±7.3%	5.82±7.3%	6.43±7.5%	1.30	1.08	0.89
C →^{7}Be	0.884±6.9%	2.02±7.0%	2.43±6.6%	1.21	1.21	1.22
In→^{115m}In	150±6.5%	194±6.5%	171±6.5%	1.02	0.83	0.89
Bi →^{201}Bi	6.47±13.4%	13.9±11.1%	12.3±11%	2.35	1.62	1.02
Bi →^{202}Bi	14.7±8.3%	31.4±8.1%	28.9±8.1%	4.62	3.29	2.18
Bi →^{203}Bi	27.3±15.2%	47.8±12.5%	47.7±12.5%	5.20	3.38	2.58
Bi →^{204}Bi	66.6±8.8%	115±8.8%	96.8±8.8%	8.40	6.03	4.13
Bi →^{206}Bi	69.9±18%	93.5±17.1%	113±15.2%	2.30	1.70	2.01

It should be noted that in this case and for other detectors also, charged hadrons (protons and pions) can make a noticeable contribution to the value of A_0, in addition to neutrons.

The activity A_0 depends on the detector size, the proton beam intensity, the proton energy, the irradiation time, the converter geometry, and the detector position relative to the converter. It is convenient to use the reaction rate R_{exp} to compare the results of repeated or similar experiments. This value is essentially the probability of a particular nuclide formation in the secondary radiation field of one primary proton, normalized to one detector atom. It depends only on the proton energy, the converter geometry, the detection point and experimentally determinates by the formula:

$$R_{exp} = \frac{A_0 \cdot T_0}{N_{at} \cdot N_p(1 - e^{-\lambda T_0})},$$

where T_0 is the irradiation time, N_{at} is the number of atoms in the detector, N_p is the number of protons dropped onto the converter during irradiation, λ is the decay constant.

The reaction rate is also determined by the convolution of the fluences $\Phi(E)$ of neutrons, protons and pions at the detection point with the energy dependences of the cross sections $\sigma(E)$ for the formation of a nuclide in the reactions of these particles with the detector nuclei:

$$R_{cal} = \sum_{i=n,p,\pi} \int \sigma_i(E)\Phi_i(E)\, dE. \qquad (1)$$

The experimental reaction rates R_{exp} and the results of calculations by the Eq. (1) in the form of ratios of experimental R_{exp} to the calculated R_{cal} reaction rates are presented in Table 1. The errors of R_{exp} in Table 1 are included measurement errors of A_0 only.

Smooth $\sigma(E)$ dependences were obtained on the basis of experimental cross sections from the EXFOR database [2]. $\Phi(E)$ is the results of calculations using the MARS code [3] provided by I. L. Azhgirei.

From the analysis of Table 1, it follows that acceptable agreement with the calculation is observed for the reactions Al → ^{24}Na, C → ^{11}C, and In → ^{115m}In, but the difference is up to two or more times for remaining nuclides. The accuracy of calculated R_{cal} strongly depends on the availability of correct cross sections for neutrons and charged hadrons, which are clearly insufficient in the literature. A sufficient amount of information is available in EXFOR for the production of ^{22}Na and ^{24}Na nuclides in aluminium and ^{11}C in carbon in the n-, p- and π-reactions, although the data scatter from different authors can reach several tens of percent. There are no data on the cross sections for π-reactions for remaining reactions. To estimate the contributions of pions to the Bi isotopes production, the corresponding cross sections were calculated using the HADRON code [4].

The calculated contributions of hadrons to the experimental reaction rates R_{exp} are shown in Fig. 3.

We made the assumption that, in practice, R_{exp} can be used to estimate the neutron fluence above the thresholds of the corresponding reactions, i.e.

$$\Phi_{exp}(E > E_b) = \int_{E_b}^{E_m} \Phi_{exp}(E)dE \approx \frac{R_{exp}}{\sigma_{av}} \frac{p_n}{100\%},$$

where p_n is the partial contribution of neutrons to the reaction rate R_{exp} in %, E_b and E_m are the threshold and maximum energies. The effective cross sections σ_{av} can be obtained by averaging σ_b over the selected basic set of N neutron fluences spectra $\Phi(E)$, typical for the conditions of the experiment. The value σ_b is determinate as:

$$\sigma_b = \int_{E_b}^{E_m} \sigma(E)\Phi(E)dE \Big/ \int_{E_b}^{E_m} \Phi(E)dE. \qquad (2)$$

The fluence spectra for proton energy of 50 and 10 GeV were used to calculate σ_b according to Eq. (2). Neu-

ISBN: 978-3-95450-240-0 ISSN: 2673-5539 doi:10.18429/JACoW-RuPAC2021-TUPSB51

tron spectra for proton energy of 10 GeV were calculated for the same geometry as for 50 GeV protons by HADRON code with a low-energy cluster FAN15 [5]. The threshold energies E_b in Eq. (2) were determined from the point of increasing $\sigma(E)$ from 0 to 0.1 of their maximum values. The results of calculating the cross sections σ_b by Eq. (2) are shown in Fig. 4 and σ_{av} – in Table 2.

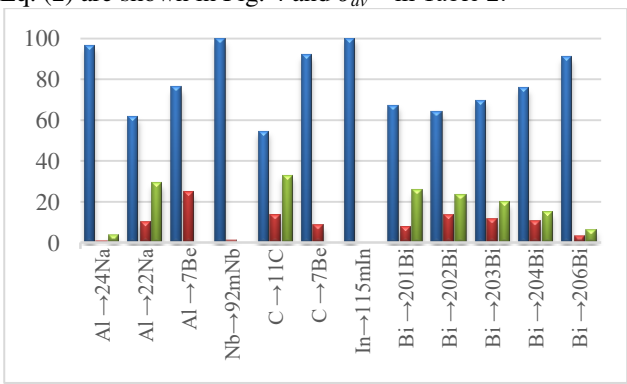

Figure 3: Calculated contributions of hadrons to the reaction rates in %. Neutrons contribution shows by blue colours, protons – red, pions – green.

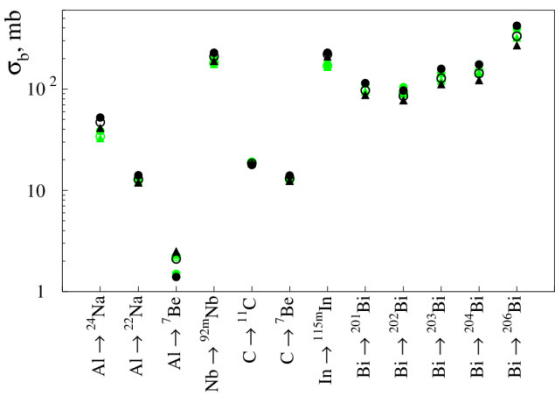

Figure 4: The neutron reactions cross sections weighted by the calculated fluence spectra at three points. Green points correspond to 10 GeV proton beam, black – 50 GeV. (●, ● – p. 1; ○, ○ – p. 2; ▲, ▲ – p. 3).

The average cross sections for three points on the converter surface are close despite the fact that the energy distributions of neutron fluences at these points differ from each other. Averaging over the neutron fluences for 10 GeV proton beam gives to us very close results. The obtained average cross sections can be used to estimate the above-threshold neutron fluences also for other targets with different proton beam energies. The results are shown in Table 2.

As it can be seen from the data in Table 2, the experimental fluences agree with the calculation for the reactions In → ^{115m}In (12%), Al → ^{24}Na (9%), C → ^{11}C (4%), C → ^{7}Be (11%), Bi → ^{201}Bi (29%). The difference reaches factor two and higher for remaining reactions. Under the assumption that the neutron fluences emitted from other side surfaces of the converter are close to the data in Table. 2, it is possible to estimate the total lateral neutron yield also.

Table 2: Neutron Fluences Above the Threshold Energies, Averaged Over Three Points

Reaction	E_b, MeV	σ_{av}, mb	$\Phi(E>E_b)$, n/cm^2/p	
			Calculated	Experiment
In→^{115m}In	0.8	220	8.78E-02	7.82E-02
Al→^{24}Na	6.8	47	3.46E-02	3.18E-02
Nb→^{92m}Nb	9.6	210	2.61E-02	4.47E-02
C →^{11}C	22	18	1.39E-02	1.45E-02
Bi →^{206}Bi	26	341	1.22E-02	2.59E-02
Al →^{22}Na	30	13	1.11E-02	2.12E-02
C →^{7}Be	31	4	1.10E-02	1.24E-02
Bi →^{204}Bi	45	146	8.29E-03	4.93E-02
Bi →^{203}Bi	55	133	7.04E-03	2.23E-02
Bi →^{202}Bi	64	86	6.25E-03	1.90E-02
Bi →^{201}Bi	75	99	5.42E-03	7.59E-03
Al →^{7}Be	114	2	3.62E-03	1.48E-02

CONCLUSION

Experimental data for the hadrons yields from the neutron converter lateral surface of known geometry have been obtained with acceptable accuracy for 50 GeV proton beam energy. Reaction rates R_{exp} can use to check of the adequacy of calculated cross sections threshold. An application of methods of effective cross sections and threshold reactions has been attempted to estimate the above-threshold neutron fluences. The hadrons component compositions at the measurement points and their contributions to R_{exp} have been calculated.

An application of methods of effective cross sections and threshold reactions has been attempted to estimate the above-threshold neutron fluences. Acceptable agreement between the experimental and calculated fluences of above-threshold neutrons has been obtained for the reactions In → ^{115m}In, Al → ^{24}Na, C → ^{11}C, C → ^{7}Be, Bi → ^{201}Bi. The discrepancies for remaining reactions are mainly explained by the lack of reliable data on the cross sections. Experimental fluences have been used to estimate the total lateral neutron yields. The values of 122, 50, 23, 19 and 12 neutrons per proton have been received for the neutron yields above the threshold of 0.8, 6.8, 22, 31 and 75 MeV, respectively.

REFERENCES

[1] G. Krupnyi et al., "Field of Secondary Radiation from the Surface of Heavy Targets Irradiated with Medium-Energy Protons (Ep ~ 1 GeV)", *Atomic Energy*, vol. 90, pp. 254–259, 2001.

[2] Experimental Nuclear Reaction Data (EXFOR) https://www-nds.iaea.org/exfor/

[3] I. Azhgirey and V. Talanov, "The MARS Code Status" in *Proc. of XVIII Workshop on the Charged Particle Accelerators*, Protvino, Russia, 2000, v. 2, p. 184.

[4] A. Sannikov and E. Savitskaya, "Physics of the HADRON Code: Recent Status and Comparison with Experiment", *Nucl. Instr. Meth. Phys. Res.*, vol. A450, pp. 127-137, 2000.

ISBN: 978-3-95450-240-0 ISSN: 2673-5539 doi:10.18429/JACoW-RuPAC2021-TUPSB51

[5] E. Savitskaya and A. Sannikov, "FAN15 Software Code for Calculating Low-Energy Photon and Neutron Transfer in Arbitary Media", *Atomic Energy*, vol. 122, pp. 51-57, 2017.

ISBN: 978-3-95450-240-0 ISSN: 2673-5539 doi:10.18429/JACoW-RuPAC2021-TUPSB52

MEASUREMENT OF THE ARGON IONS CURRENT ACCOMPAYNING AT THE ACCELERATING SOURCE OF EPITHERMAL NEUTRONS*

I. A. Kolesnikov†, Yu. M. Ostreinov, P. D. Ponomarev, S. S. Savinov, I. M. Shchudlo, S. Yu. Taskaev
Budker Institute of Nuclear Physics, 630090 Novosibirsk, Russia
Novosibirsk State University, Novosibirsk, Russia

Abstract

For the development of a promising method for the treatment of malignant tumors - boron neutron capture therapy - the accelerator-based epithermal neutrons source has been proposed and created in the Budker Institute of Nuclear Physics. Argon ions formed during stripping of a beam of negative hydrogen ions to protons are accelerated and, in parallel with the proton beam, are transported along the high-energy path of the facility. Depending on the relative number of argon ions, their effect can be from negligible to significant, requiring their suppression. In this work, the current of argon ions reaching the beam receiver in the horizontal channel of the setup was measured. It was determined that the argon beam current accompanying the proton beam is 2000 times less than the proton beam current. This makes it possible not to apply the proposed methods of its suppression.

INTRODUCTION

Charged particle accelerators are widely used in scientific research, medicine, and other applications. Tandem accelerators are high-voltage electrostatic accelerators in which the high-voltage potential is used twice: first to accelerate negative ions, and then, after changing the polarity of their charge in the high-voltage terminal, to accelerate positive ions. Thin foils are used for the conversion of the ion charge, or, at a higher ion current, gas stripping targets similar to the argon target in the tandem accelerator of the Budker Institute of Nuclear Physics of the Siberian Branch of the Russian Academy of Sciences. The stripping gas target provides effective stripping of the negative ion beam; however, its use leads to the formation of an undesirable beam of argon ions, which are formed in the stripping target as a result of argon ionization by the ion beam and penetrate into the accelerating channel. The aim of this work was to measure the current of an argon ion beam in a tandem accelerator with vacuum insulation.

THE EXPERIMENTAL SCHEME

The studies were carried out at the accelerator neutron source of the Budker Institute of Nuclear Physics (Novosibirsk, Russia). The source diagram is shown in Fig. 1 and its detailed description was given in [1]. A tandem accelerator with vacuum insulation was used to obtain a stationary proton beam with an energy of 0.6 to 2.3 MeV and a current of 0.3 to 10 mA, that is, a tandem accelerator of charged particles with an original design of electrodes. In it, unlike traditional accelerators, there are no accelerating tubes; the high-voltage electrode and electrodes with an intermediate potential are embedded in each other and fixed on a single feedthrough insulator, as shown in Fig. 1. This configuration of the accelerator made it possible to improve the high-voltage strength of the accelerating gaps and, as a consequence, to increase the proton current. One of the main elements of the tandem accelerator is the stripping target 4 placed inside the high-voltage terminal. It provides the conversion of negative hydrogen ions to protons with a high efficiency, usually at the level of 95%. The target is a 400-mm long cooled cylindrical copper tube with an inner hole diameter of 16 mm [1]. The interaction of a hydrogen ion beam with a gas target leads to its partial ionization, and a weakly ionized plasma is formed inside the stripping tube. Since electrons are more mobile than argon ions, the plasma assumes a positive potential to maintain quasineutrality.

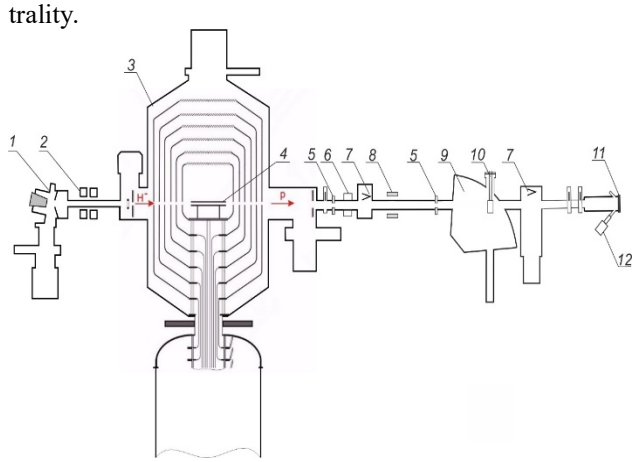

Figure 1: A diagram of an accelerator based source of epithermal neutrons. 1 - a source of negative hydrogen ions; 2 - magnetic lens, 3 - vacuum-insulated tandem accelerator; 4 - gas stripping target; 5 - cooled diaphragm; 6 - contactless current sensor Bergoz (France); 7 - Faraday cups; 8 - corrector; 9 - bending magnet; 10 - cooled beam receiver with a diaphragm; 11 - lithium target; 12 - Hikvision video camera (China).

Under the action of the positive potential, part of the argon ions leaves the stripping tube, enters the accelerating channel, and forms a beam of argon ions. Simple estimates of the argon ion current give values from commensurate to negligible in comparison with the proton

* Work supported by the Russian Foundation for Basic Research, project no. 19-32-90118.
† Ya.A.Kolesnikov@inp.nsk.su

ISBN: 978-3-95450-240-0 ISSN: 2673-5539 doi:10.18429/JACoW-RuPAC2021-TUPSB52

current. It is difficult to reliably estimate the magnitude of the argon ion current due to the inhomogeneity of the converted beam and secondary plasma along the target, the possibility of the development of beam-plasma instability, the penetration of the electric field of the accelerating gaps into the high-voltage terminal, and many other parameters that are not reliably known. To suppress the penetration of argon ions into the accelerating gaps, it was proposed to place metal rings under a negative or positive potential in front of and after the stripping target, or to deflect the ion beam by a magnetic field inside the high-voltage terminal [2]. The formation of an argon ion beam was indicated by two experimental facts. First, the secondary ion current flowing along the periphery towards the accelerated beam of negative hydrogen ions was previously measured with a ring detector [3]. It is possible that argon ions escaping from the stripping target also contribute to this current. However, it is more likely that the main contribution to this current is made by the positive ions formed in the accelerator gaps as a result of the ionization of the residual or stripping gas by the hydrogen ion beam. In this case, positive ions are formed mainly in the first accelerating gap due to its length and high ionization cross section at a relatively low velocity of negative hydrogen ions. Second, when studying the radiation blistering of metals upon implantation of protons with an energy of 2 MeV [4], an earlier formation of blisters of a smaller than expected size from the implantation of protons was observed. This effect was explained by the presence of a beam of argon ions with an energy of 1 MeV; these penetrate the metal to a shallower depth than protons and can deform a metal surface faster with smaller blisters.

RESULTS AND DISCUSSION

The measurements were carried out at a proton beam current of 760 ± 10 μA, an energy of 1.850 ± 0.002 MeV, and a transverse beam size of approximately 1 cm.

The method of mass spectroscopy was used to measure the argon ion current. Inside the bending magnet 9 (see Fig. 1) a cooled diaphragm was inserted 10 with a 5 × 20 mm slot. Since the mass of an argon ion is 40 times greater than the mass of a proton and the kinetic energy is two times lower, the Larmor radius of an ion in a magnetic field is √20 times less than the Larmor radius of the proton and the bending magnet will deflect argon ions by an angle √20 times smaller than the angle of deflection of protons. The separation of the ion beam components is clearly visible on the surface of a lithium target, when the interaction of ions with lithium leads to luminescence recorded by a video camera 12 [5]. Figure 2 shows two examples of a video camera image: without a magnetic field and with a magnetic field. It can be seen that turning on the magnetic field divides the beam into three components: the flux of neutrals 1, the argon ion beam 2, and the proton beam 3.

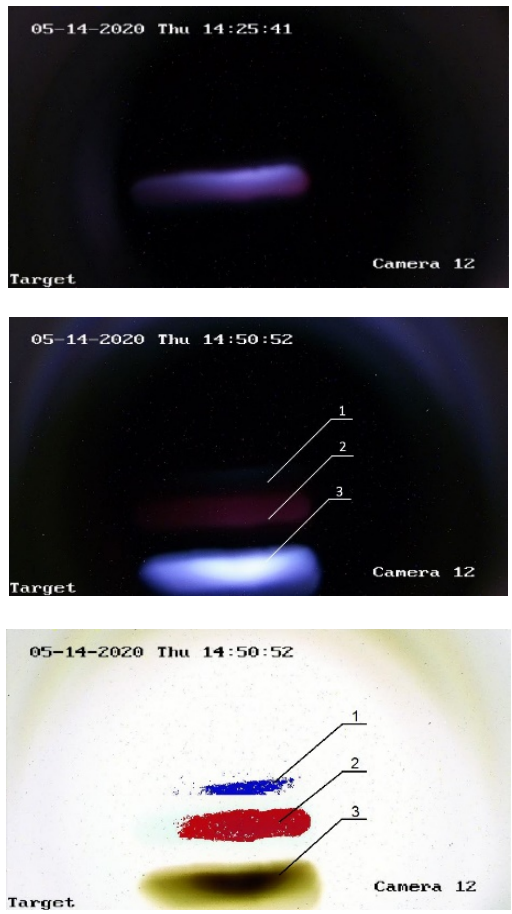

Figure 2: Images from a video camera looking at the surface of a lithium target at a bending magnet current of (a) 0 and (b) 14 A and (c) 14 A with partially inverted colors. 1, glow caused by neutrals (hydrogen atoms); 2, argon ions; 3, protons.

The scenario for measuring the argon ion current consisted in placing the diaphragm below the axis of the accelerator, directing the argon ion beam into the diaphragm opening with the magnetic field of the bending magnet, and deflecting the proton beam below. In fact, at a current of 68.5 A in the bending magnet coil, only a beam of argon ions passes through the diaphragm, which, upon hitting the lithium target, causes a characteristic luminescence recorded by a video camera. According to Fig. 3, at a current of 10 A in the bending magnet coil, an argon beam and a proton beam are visually visible on the surface of a lithium target, while at a current of 68.5 A, there is no proton beam; only beams of argon and neutral ions are visible.

ISBN: 978-3-95450-240-0 ISSN: 2673-5539 doi:10.18429/JACoW-RuPAC2021-TUPSB52

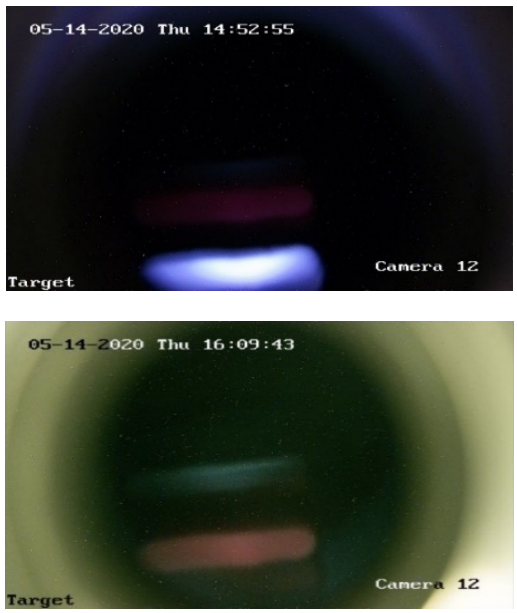

Figure 3: Images from a video camera looking at the surface of a lithium target: (a), with a current in the bending magnet coil of 10 A; (b), 68.5 A.

In this mode, at a current of 68.5 A, the current of charged particles passing through a hole in the diaphragm and hitting the surface of the lithium target was measured; it was 150 ± 70 nA. The current is measured by an ohmic voltage divider connected to the target unit (11 in Fig. 1), electrically isolated from the facility. Without the visualization of an argon ion beam by its luminescence on the surface of a lithium target, such a small value of the recorded current could be mistakenly considered as noise. The result we obtained was unexpected, since it was previously assumed that the current of argon ions is of course less than the current of protons, but not by very much. Since the maximum proton current that passed through the slit of the diaphragm is 286 ± 3 μA, then, assuming the sizes of the beams of argon ions and protons to be equal, we obtain that the current of argon ions is 2000 times less than the proton current. This result is the main result of this study. At such a value, the argon ion beam current does not pose a danger either as a source of additional heating of the lithium target, or as an additional load of a high-voltage power source, and therefore does not require means for its suppression. We will confirm the reliability of this result by an additional experiment and evaluation. For this purpose, we will double the frequency of opening the valve that supplies argon to the stripping target. A larger supply of stripping gas, as it should, leads to an increase in the argon ion current to 670 ± 150 nA and more intense luminescence, which can be seen from a comparison of the images in Figs. 3b and Fig. 4. As well, a larger gas supply leads to better stripping of the beam of negative hydrogen ions, which entails a decrease in the neutral flux, as can be seen from a comparison of the images in Figs. 3b and 4. We note that a two-fold increase in the supply of argon to the stripping target leads to an almost four-fold increase in the argon ion current, which is possible, since the outflow of ions from the stripping target depends on many processes and parameters. Even in this case, the argon ion beam current is very small compared to the proton current.

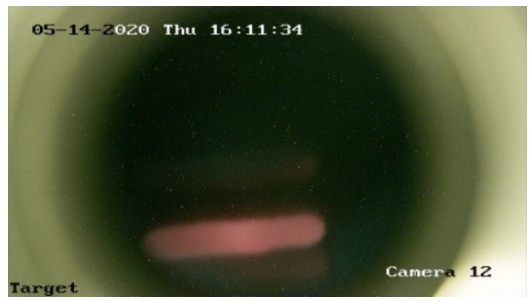

Figure 4: The argon beam glow and a beam of neutral atoms caused by the luminescence of the target lithium layer upon a twofold increase in the argon flow in the stripping target.

CONCLUSION

The Budker Institute of Nuclear Physics operates a vacuum insulated tandem accelerator, in which a gaseous argon stripping target is used to strip a beam of negative hydrogen ions into protons. The interaction of the ion beam with the stripping gas leads to partial ionization of argon, penetration of argon ions into the accelerating channel, and the formation of an accelerated beam of argon ions accompanying the proton beam. The magnitude of the argon ion beam current was measured by mass spectroscopy using a bending magnet and a cooled diaphragm; it is 2000 times smaller than the proton beam current. The reliability of the measurement is provided by visualization of an argon ion beam on the surface of a lithium target, as confirmed by an experiment with increased gas injection and an estimate of the possible contribution of the proton beam. Such a small value of the current of the argon ion beam poses no danger either as an additional heating of the lithium target or as an additional load of a high-voltage power supply and therefore does not require the previously proposed suppression means.

REFERENCES

[1] S. Taskaev *et al.*, "Neutron Source Based on Vacuum Insulated Tandem Accelerator and Lithium Target", *Biology*, vol. 10, 350, 2021. doi:10.3390/biology10050350

[2] A. Makarov *et al.*, "Modification of the argon stripping target of the tandem accelerator", *Appl. Radiat. Isot.*, vol. 106, 2015. doi:10.1016/j.apradiso.2015.07.046

[3] A. Ivanov *et al.*, "Suppression of an unwanted flow of charged particles in a tandem accelerator with vacuum insulation", *J. Instrum.*, vol. 11, 2016. doi:10.1088/1748-0221/11/04/P04018

[4] A. Badrutdinov *et al.*, "In Situ Observations of Blistering of a Metal Irradiated with 2-MeV Protons", *Metals*, vol. 7, 2017. doi:10.3390/met7120558

[5] A. Makarov *et al.*, "The luminescence of a lithium target under irradiation with a proton beam", *Instrum. Exp. Tech.*, vol. 64, 2021. doi:10.1134/S0020441220060184

ISBN: 978-3-95450-240-0 ISSN: 2673-5539 doi:10.18429/JACoW-RuPAC2021-TUPSB53

MEASUREMENT OF PARAMETERS OF NEUTRON RADIATION ON THE ACCELERATOR-BASED EPITHERMAL NEUTRON SOURCE*

M. I. Bikchurina, T. A. Bykov, D. A. Kasatov, Ia. A. Kolesnikov, I. M. Shchudlo, S. Yu. Taskaev,
BINP and Novosibirsk State University, Novosibirsk, Russia
K. A. Martianov, LLC "BINP-Plasma", Novosibirsk, Russia

Abstract

Treatment of oncological diseases using Boron Neutron Capture Therapy (BNCT) is an important issue of our time. Cancer cells accumulate a boron-containing drug, after which they are irradiated with a beam of epithermal neutrons, a nuclear reaction $^{10}B(n,\alpha)^{7}Li$ occurs, and the products of a nuclear reaction destroy these cells. In BNCT, it is generally accepted that the total dose of ionizing radiation consists of four components: boron dose, dose from fast neutrons, dose from thermal neutrons, and dose of gamma radiation. Dose values and their ratio strongly depend on the neutron flux; therefore, the measurement of the neutron flux (yield) is an urgent task. In this work, the neutron yield was measured by the activation of the target with the radioactive isotope beryllium-7, which is formed in the reaction of neutron generation $^{7}Li(p,n)^{7}Be$. It was found that the neutron yield from a specifically manufactured lithium target is in good agreement with the calculated one, which is important for planning therapy.

INTRODUCTION

An accelerator based epithermal neutron source for the development of boron neutron capture therapy (BNCT), a promising method for the treatment of malignant tumors, is proposed, created and is functioning at the Budker Institute of Nuclear Physics [1,2]. The neutron source consists of a tandem accelerator of charged particles of an original design, a lithium neutron-generating target, for generating neutrons as a result of the $^{7}Li(p,n)^{7}Be$ reaction, and a system for forming a therapeutic beam of epithermal neutrons. The total dose of ionizing radiation consists of four components: boron dose, dose from fast neutrons, dose from thermal neutrons, and dose of gamma radiation. Dose values and their ratio strongly depend on the spectrum and neutron flux.

DESIGN OF THE ACCELERATOR

The neutron source consists of a tandem accelerator of charged particles of an original design, a lithium neutron-generating target and a system for forming a therapeutic beam of epithermal neutrons, Fig. 1.

In a tandem accelerator, a surface plasma source using a Penning discharge with hollow cathodes is used to generate negative hydrogen ions. A beam of negative hydrogen ions with an energy of 20-23 keV and a current of up to 10 mA is focused with magnetic lenses and injected into a tandem electrostatic accelerator. In an accelerator, negative hydrogen ions are accelerated by a voltage applied across six high-voltage electrodes. In a gas stripping target made in the form of a cooled tube with argon inlet in the middle and installed inside a high-voltage electrode, negative ions lose electrons and turn into protons, which are accelerated to an energy equal to twice the potential. Then the proton beam is delivered to the lithium target for neutron generation as a result of the threshold nuclear reaction $^{7}Li(p,n)^{7}Be$.

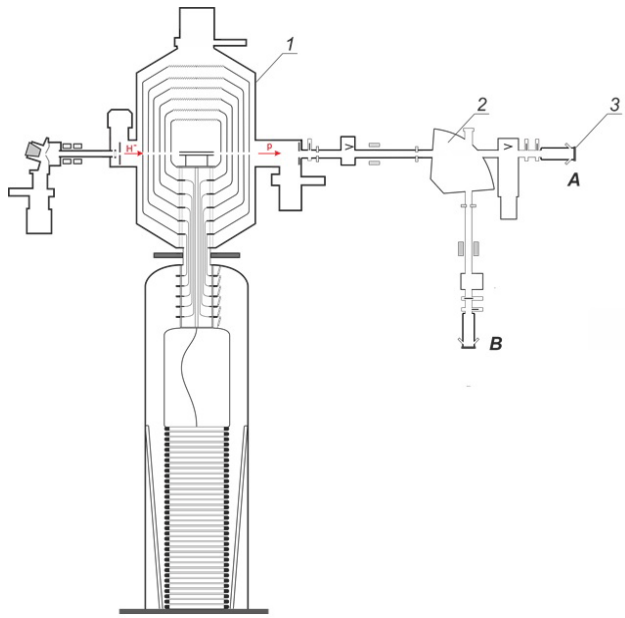

Figure 1: Tandem accelerator with vacuum insulation: 1 – accelerator, 2 – bending magnet, 3 – lithium neutron generating target. The lithium target is placed in the horizontal proton beam transport path (position A) or in the vertical (position B).

EXPERIMENTAL RESULTS

A total of 15 sessions of neutron generation were carried out; used 13 lithium targets. In the manufacture of all 13 targets, only a new copper substrate was used and a new lithium layer was always deposited.

Since the products of the $^{7}Li(p,n)^{7}Be$ reaction are not only a neutron, but also a radioactive atomic nucleus beryllium-7, measuring the number of ^{7}Be nuclei makes it possible to unambiguously determine the number of generated neutrons.

The radioactive atomic nucleus ^{7}Be, as a result of electron capture, is converted back to lithium-7 with a half-life of 53.22 days. In 10.3% of cases, decay is accompanied

*Work supported by grant from the Russian Science Foundation (grant no. 19-72-30005), the Budker Institute of Nuclear Physics and the Novosibirsk State University

ISBN: 978-3-95450-240-0 ISSN: 2673-5539 doi:10.18429/JACoW-RuPAC2021-TUPSB53

by the emission of a 478 keV photon. If we do not allow the propagation of beryllium from a lithium target, then measuring the activation of the target makes it possible to determine the number of produced ^{7}Be nuclei, which is equal to the number of generated neutrons, which was done. Before the measurement, the target assembly is removed from the setup, disassembled, the actual lithium target is taken out of it, which is placed in a transparent plastic bag and placed along the spectrometer axis so that the surface of the lithium layer is directed towards the spectrometer and the distance between the surface of the lithium layer and the entrance window of the detector was equal to 1854 mm. According to the law of radioactive decay, the number of non-decayed atoms at time t is related to the initial (at time t = 0) number of atoms by the ratio $\frac{N(t)}{N_0} = e^{-\frac{0{,}693\ t}{t_{1/2}}}$.

The dependence of the neutron yield in the ^{7}Li(p,n)^{7}Be reaction on the proton energy is given in [3] and can be calculated using the PINO program using reference [4] given in [5]; they are shown in Fig. 2.

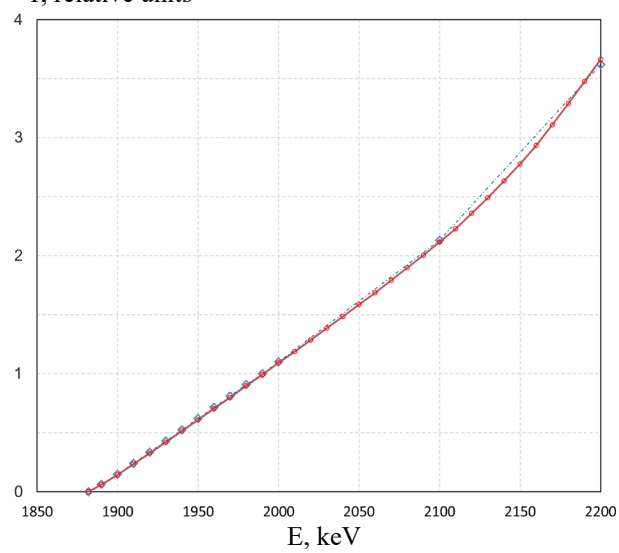

Figure 2: Dependence of the neutron yield Y on the proton energy E in the ^{7}Li(p,n)^{7}Be reaction: ◊ – from [3], ○ – calculated by the PINO program [4].

Since the ^{7}Li(p,n)^{7}Be reaction is threshold (the reaction threshold is 1882 keV), the neutron yield strongly depends on the proton energy. So, with a decrease in the energy of protons from 2 MeV by 1%, the neutron yield decreases by 18%, and from 2.2 MeV – by 11%.

The energy calibration of the accelerator neutron source was carried out using two threshold reactions: ^{7}Li(p,n)^{7}Be – 1.882 MeV, ^{9}Be(p,n)^{9}B – 2.057 MeV. For the second reaction, a beryllium disk 32 mm in diameter and 9.7 mm thick was tightly attracted to the copper substrate of the target through an indium-gallium alloy and irradiated with a proton beam in position A. A neutron detector with a GS20 lithium-containing scintillator (The Saint-Gobain Crystals, USA) installed in front of the target was used to measure the dependence of the recorded signal on the proton energy. The measurement results and the dependence of the neutron yield on energy calculated by the PINO program are shown in Fig. 3.

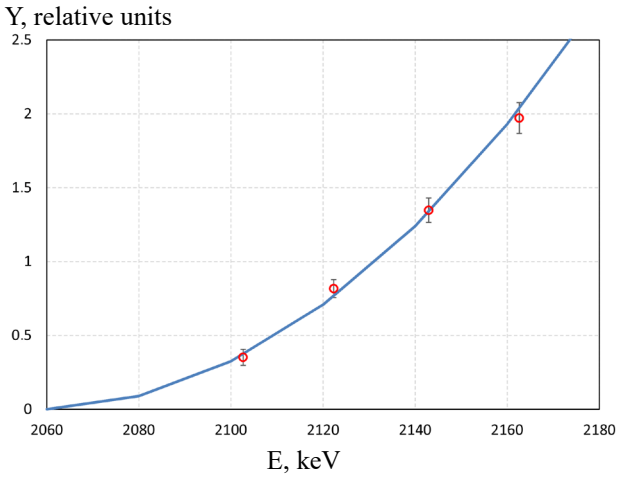

Figure 3: Dependence of the neutron yield Y on the proton energy E in the ^{9}Be(p,n)^{9}B reaction: ○ – measured, solid line – calculated by the PINO program [4].

Subsequently, a bending magnet was used as an energy analyzer. The position of the proton beam in the center of the target was controlled by the following diagnostic tools: i) a video camera recording luminescence of lithium under the bombardment of protons [6], ii) five thermocouples placed inside the copper disk of a lithium target, one in the center, the other four at a distance of 18 mm from the center, uniformly spaced in azimuth, and iii) as indicated by two small-sized neutron detectors with a boron-enriched polystyrene cast scintillator glued to the vacuum chamber of the target assembly near the lithium target. The proton beam on the target surface had a characteristic size of 3 cm.

When calculating the neutron yield, three corrections were taken into account. First, the percentage of lithium-7 was taken into account. For deposition, we used natural or lithium enriched with the isotope lithium-7, produced by the Novosibirsk plant of chemical concentrates. In the batch of natural lithium, the lithium content was 99.95%; in enriched lithium, the atomic fraction of lithium-7 was 99.988%. Secondly, the used natural lithium contains impurities at a concentration of 0.044%. The weighted average value of the atomic number of impurities, in accordance with the product passport, is 15. This value is 5 times higher than the atomic number of lithium, therefore, the deceleration of a proton, determined by interaction with electrons, is 5 times more effective on impurities than on lithium. This means that impurities in a concentration of 0.044% reduce the neutron yield by 0.22%. In lithium enriched with the isotope lithium-7, the concentration of impurities is 0.012%, which means that their presence reduces the neutron yield by 0.06%. Third, let us take into account the secondary emission of electrons when measuring the proton current; the measured proton fluence is overestimated by 1%. The result is graphically shown in Fig. 4 [7].

ISBN: 978-3-95450-240-0 ISSN: 2673-5539 doi:10.18429/JACoW-RuPAC2021-TUPSB53

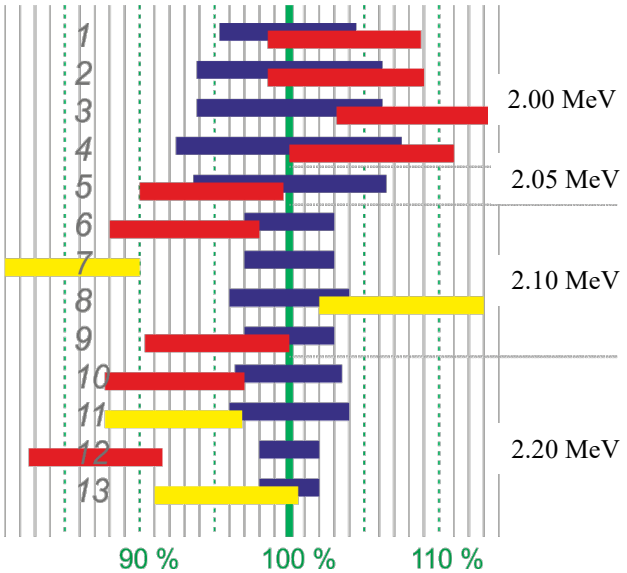

Figure 4: The result of the study comparing the measured neutron yield with the calculated one: from top to bottom - targets in order, blue rectangles - intervals of the calculated number of neutrons, red and yellow – intervals of the measured number of neutrons (red – natural lithium, yellow – enriched with lithium-7 isotope). On the right are the characteristic values of the proton energy.

It can be seen that the measured amount of beryllium-7 is always slightly higher than the calculated one if the target is placed in the horizontal channel (sessions 1-3 and 8) and almost always less if the target is placed in the vertical channel (sessions 4 – 7 and 9 – 13). Perhaps this is due to the large size of the proton beam and its displacement over the target surface, due to which part of the proton beam could fall into the region outside the region of lithium deposition.

PROSPECTS

The obtained result is planned to be used in determining the dose received by patients during therapy at the BNCT clinic in Xiamen (China), equipped with an accelerating neutron source manufactured by TAE Life Sciences (USA).

CONCLUSION

For the first time, the neutron yield from a lithium target was measured by its activation with the radioactive isotope beryllium-7 using a γ-radiation spectrometer based on a semiconductor detector made of highly pure germanium The agreement of the measured yield to the calculated one is shown, which is important when planning boron neutron capture therapy.

REFERENCES

[1] W. Sauerwein, A. Wittig, R. Moss and Y. Nakagawa (Eds.), *Neutron Capture Therapy: Principles and Applications*. Springer, 2012. doi:10.1007/978-3-642-31334-9

[2] S. Taskaev *et al.*, "Neutron Source Based on Vacuum Insulated Tandem Accelerator and Lithium Target", *Biology*, vol. 10, 350, Apr. 2021. doi:10.3390/biology10050350

[3] C. Lee and X. Zhou, "Thick Target Neutron Yields for the ^{7}Li(p,n)^{7}Be Reaction near Threshold", *Nucl. Instrum. Methods Phys. Res., Sect. B*, vol. 152, pp. 1-11, 1999. doi:10.1016/S0168-583X(99)00026-9

[4] https://exp-astro.de/pino/

[5] R. Reifarth, M. Heil, F. Käppeler and R. Plag, "PINO – a tool for simulating neutron spectra resulting from the ^{7}Li(p,n) reaction", *Nucl. Instrum. Methods Phys. Res., Sect. A,* vol. 608, pp. 139-143, 2009. doi:10.1016/j.nima.2009.06.046

[6] A. Makarov, E. Sokolova, S. Taskaev, "Luminescence of a lithium target irradiated with a proton beam", *Instrum. Exp. Tech.*, vol. 64, pp. 30-33, Jan. 2021. doi:10.1134/S0020441220060184

[7] M. Bikchurina *et al.*, "The measurement of the neutron yield of the ^{7}Li(p,n)^{7}Be reaction in lithium targets", *Biology*, vol. 10, 824, Aug. 2021. doi:10.3390/biology10090824

ISBN: 978-3-95450-240-0 ISSN: 2673-5539 doi:10.18429/JACoW-RuPAC2021-WEPSC01

UNIT FOR MATCHING A DRIVING WAVEGUIDE WITH A CAVITY

V.V. Paramonov†, Institute for Nuclear Research of the RAS, 117312, Moscow, Russia

Abstract

To match the driving WaveGuide (WG), usually operating in the fundamental TE10 wave, with the accelerating structure, a device is required that performs the function of a wave-type transformer. In the microwave region, transforming devices with matching windows are usually used, the field distribution in which can also be described as TE-type. At the ends of the window from the side of the structure, regions with an increased density of Surface Currents (SC) inevitably arise, leading to an increase in the surface temperature in a place that is difficult to access for cooling. There are various solutions for matching windows, in order to reduce the maximum SC from the side of the structure, briefly mentioned in the report. A solution based on the dispersion properties of the TE10 wave, providing a significant additional decrease in the SC density, is considered. This solution can be implemented for C-band and lower frequency ranges.

INTRODUCTION

To transmit RF power from RF source to a cavity at frequencies > 300 MHz rectangular WG's, operating with TE10 wave, are usually used. Reasons are in the higher RF power capability and lower attenuation. The simplest solution for appropriate matching of a cavity with waveguide schematically is shown in Fig. 1. Also may be modifications in waveguide dimensions near matching slot, slot shape an so on. A solution, based on dispersion properties of TE10 wave in driving WG is considered below.

MOTIVATION

We can consider cavity excitation by tangential electric field $E\tau s$ of the matching slot [1], and expand cavity field in the set over own modes Ecn :

$$\vec{E}_c = \sum_n e_{cn}\vec{E}_{cn}, \mathrm{e}_{cn} = i\frac{\omega_{cn}}{\omega^2-\omega_{cn}^2}\frac{\int_{Ss}\left[\vec{E}_{\tau s}\overrightarrow{H_{cn}}\right]d\vec{S}}{\mu_0\int_{Vc}\vec{H}_{cn}\vec{H}^*_{cn}dV}, \quad (1)$$

where ωcn are frequencies of own cavity modes. Here and below subscripts *c,s,w* are connected to the cavity, slot and WG respectively. In the same style we can consider excitation of the slot by tangential magnetic fields of the cavity $H\tau c$ and WG $H\tau w$:

$$\vec{E}_s = \sum_m u_{sm}\vec{E}_{sm},$$

$$\mathrm{u}_{sm} = i\frac{\omega}{\omega^2-\omega_{sm}^2}\frac{\int_{Ssd}\left[\vec{E}^*_{sm}\overrightarrow{H_{\tau c}}\right]d\vec{S}+\int_{Sst}\left[\vec{E}^*_{sm}\overrightarrow{H_{\tau w}}\right]d\vec{S}}{\varepsilon_0\int_{Vs}\vec{E}_{sm}\vec{E}^*_{sm}dV} \quad (2)$$

For the field in the slot is known the model of shortened transmission line [2].

† email address paramono@inr.ru

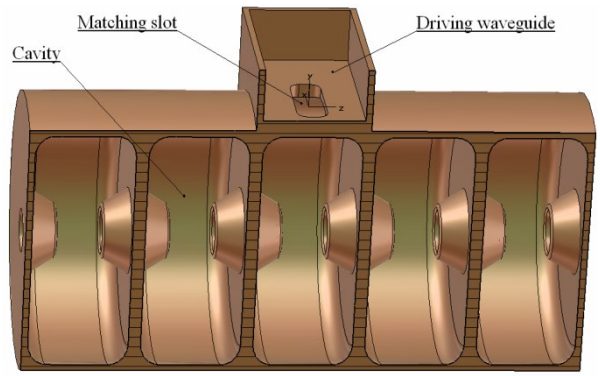

Figure 1: Schematic drawing of the cavity – slot – WG system to be matched.

More descriptive is the slot model, proposed in [3]. The slot is considered as the cavity, bounded by 'magnetic wall' boundary conditions from sides of cavity and WG, Fig. 2.

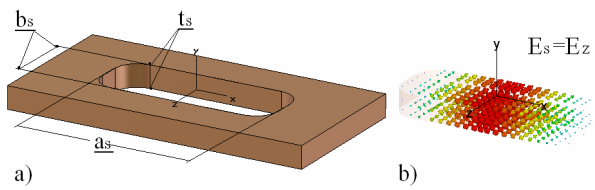

Figure 2: The slot model with dimensions definition, (a), and electric field of fundamental TE10 mode, (b).

In this approximation the field and frequency for fundamental TE10 in the slot are:

$$\vec{E}_{s1} \approx \mathrm{E}_{z0}\cos(\frac{\pi x}{a_s}), \omega_{s1} \approx \frac{\pi c}{a_s} >> \omega, \mathrm{E}_{z0} = 2\sqrt{\frac{W_0}{\varepsilon_0 a_s b_s t_s}}, \quad (3)$$

Supposing fields of own modes in the cavity *Enc* and in the slot *Esm* to be normalized to stored energy *W0=const*, single mode (n=1, m=1), lossless approximations for cavity and slot, after transformation, from Eq. (1) – Eq. (3) one gets:

$$E_{c1} \approx \frac{4\omega_{c1}\omega a_s^2 b_s H_{c\tau}}{W_0(\omega^2-\omega_{c1}^2)\pi^4 c^2\varepsilon_0 t_s}(H_{c\tau}+BH_{w\tau}),$$

$$B = \frac{2}{\pi}\left(\frac{\sin(\frac{\pi}{2}(1+\frac{a_s}{a_w}))}{(1+\frac{a_s}{a_w})}+\frac{\sin(\frac{\pi}{2}(1-\frac{a_s}{a_w}))}{(1-\frac{a_s}{a_w})}\right)\approx\frac{2}{\pi}. \quad (4)$$

Relations in Eq. (4) approximately describe well known correlations and effects. For effective matching the slot should be posted in the region with strong magnetic field of the cavity. The first term in the right hand side of Eq. 4 reflects inevitable reduction of cavity frequency with slot opening.

ISBN: 978-3-95450-240-0 ISSN: 2673-5539 doi:10.18429/JACoW-RuPAC2021-WEPSC01

From Eq. 4 one can see straightforward indication for coupling enhancement – increasing of the slot length a_s. But it is directly connected with enhancement of magnetic field at the slot edges from the side of a cavity, Fig. 3a. And related density if RF losses at the slot edge rises very fast with a_s increasing, Fig. 3b

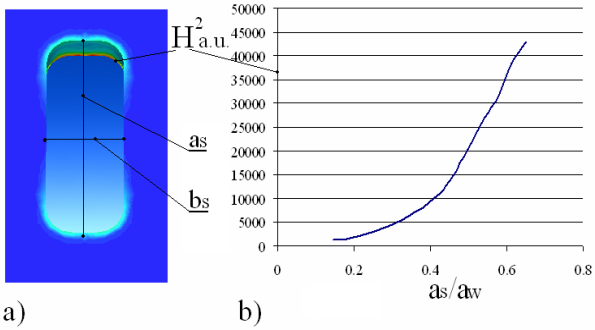

Figure 3: Magnetic field enhancement at the slot edges from the side of a cavity, (a) and rise of RF loss density with slot opening, (b).

Slot edges must be rounded, but RF loss density enhancement still remains. It leads to temperature increasing in a vicinity of slot edges.

As one can conclude from a schematic drawing of the cavity – slot – WG system, the vicinity of a slot is not convenient for placing of cooling channels close to the slot. It provides difficulties for cavities, operating with a high heat load due average dissipation of RF power, for example operating in Continuous Wave (CW) mode. Stress value, associated with high temperature, can exceed elastic limit, leading to slot deformation.

For cavities operating with relatively short RF pulse, but with strong fields, an effect of RF pulsed heating takes place, leading to the same results at slot edges.

Relations in the Eq. 4 show also well known ways to reduce slot length for required matching. It is either increasing of the slot width b_s, or increasing of tangential magnetic field $H\omega\tau$ from the side of WG at the slot position.

WG TAPERING

The simplest method to increase the tangential magnetic field $H\omega\tau$ from the side of WG at the slot position is a gradual reduction in the WG height from b_w to h_w, $b_w > h_w$, Fig. 4a, so called WG tapering. Calculated surface for tangential magnetic enhancement is shown in Fig. 4a. To each specified h_w value corresponds the optimal length of tapering l_w to realize the maximal field enhancement.

As one can see from Fig. 4b, the maximal field enhancement is of ~2.4 for $h_w < 0.2b_w$. But residual WG height h_w should be sufficient for slot placing with rounded edges for comfortable mechanical treatment. The practical value of field enhancement is of ~1.6 for $h_w \sim 0.2b_w$.

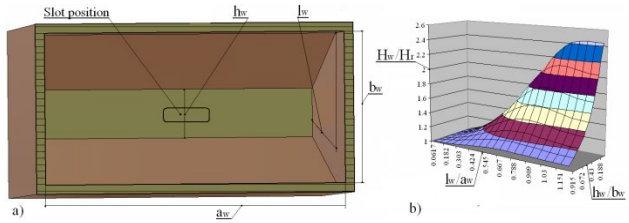

Figure 4: Well known tapering for rectangular WG height, (a), and calculated surface for tangential magnetic field enhancement, (b).

For this usual tapering in the height of rectangular WG symmetry of tapering is not so important. Similar results can be obtained when tapering in height is applied only from one side.

Additional tapering in the WG width a_w provides opposite effect – field enhancement decreases.

T-LOAD

The negative effect of rectangular WG tapering in the width exists due to positive dispersion of TE10.

$$k_z = \sqrt{k^2 - \frac{\pi^2}{a_w^2}}, \frac{dk_z}{dk} > 0, f_{cut} = \frac{c}{2a_w}$$

where k_z is the wave-number of TE10 wave in the direction of propagation and k is the wave-number for cavity operating frequency. Decreasing the WG width we increase the local, in the plane $z=const$, cut-off frequency f_{cut} in this tapered WS part with respect to regular WG parts. Due to positive dispersion of TE10 wave the field strength in WG parts with reduced width is lower.

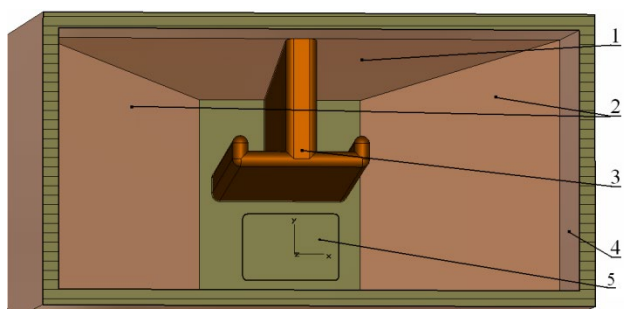

Figure 5: Schematic drawing of WG, tapered in both directions, with T-load. 1- non-symmetric tapering in WG height, 2- tapering in WG width, 3 – T-load, 4- regular WG part, 5- slot position.

Another solution of increasing for tangential field is schematically shown in Fig. 5. An additional element with T-like shape, is introduced into WG near matching slot. This element is placed in antinode of electric field for TE10 wave and provides a capacitive load, resulting in decreasing of local cut-off frequency. Below this element is named as T-load.

The strong reduction in f_{cut} in vicinity of T-load with respect to regular WG part is not required and compensated by WG tapering in width. This case improvement in field enhancement is achieved mainly due to reduction of

ISBN: 978-3-95450-240-0 ISSN: 2673-5539 doi:10.18429/JACoW-RuPAC2021-WEPSC01

surface of WG cross section near slot. Additionally a comfortable window for slot placing remains, Fig. 5.

This element has several degrees of freedom for optimization. Any analitical estimations for T-load optimization for maximal field enhancement, at least at a moment, are not known. This task can be solved with modern software CST, [4]. For geometry, shown in Fig. 5, a typical result, illustrated in Fig. 6, is the field enhancement of ~2.54.

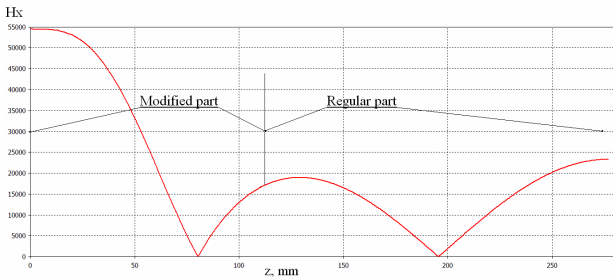

Figure 6: Dependence of tangential magnetic field component *Hx* along WG. Line *x=0, y=0*, see. Fig. 5.

The distribution of tangential magnetic field component at the inner surface of modified WG is shown in Fig. 7. As one can see, tangential field has the maximum not in the place of slot. But at the position of slot placing the distribution is uniform enough. As for high tangential magnetic field at the surface of T-load, it is only requirement of reliable contact between T-load body and WG surface.

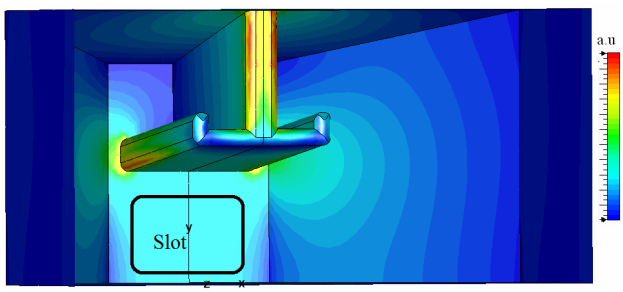

Figure 7: Distribution of tangential magnetic field at the inner surface in modified WG.

For matched case with three cells cavity in Fig. 8 is illustrated the distribution of RF loss density at the surface of modified WG part, slot surface and a part of cavity surface. For the matched case the strength of magnetic field inside cavity is essentially lower, as compared to the filed in the driving WG. The heat load at modifies WG parts, including T-load, is negligible and additional cooling is not necessary. As one see from distribution in Fig. 8, RF loss density at the slot end's from WG side doesn't exceeds density at cavity surface.

Modified WG part is shaped as truncated pyramid and sufficient space is foreseen for matching slot. Together with enhanced magnetic field, it allows to form a wide and short slot with $b_s \sim a_s \ll a_w$. It weakens difficulties with strong magnetic field at the slot edges, see Fig. 3, both for average and pulsed RF heating. Additionally it reduces frequency shift of the cavity due to matching slot, see Eq. (4).

According to design idea, T-load can be implemented into rectangular WG for arbitrary frequency range. But realistically, taking into account T-load dimensions, it can be implemented into WG for L-band, S-band ranges and probably for C-band frequency range.

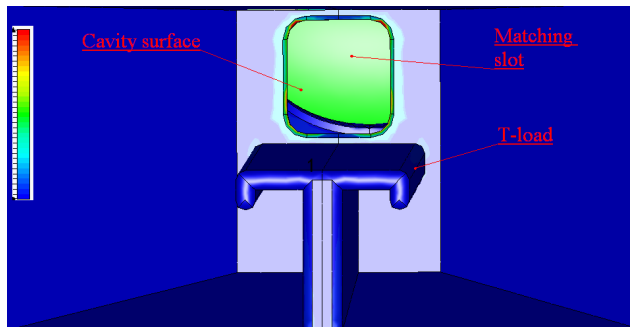

Figure 8: The resulting effect of T-load implementation – distribution of RF loss density in the total system near slot vicinity.

SUMMARY

The new element T-load is suggested to be implemented into driving WG in the vicinity of matching slot. Providing the strong enhancement of tangential magnetic field at WG side in the place of the slot, T-load allows comfortably form shorter slots, resulting in essential reduction of increased magnetic field at slot edges. This case the cooling problem for slot vicinity is essentially relaxed both for average and pulsed RF heating.

ACKNOWLEDGEMENTS

The author is grateful to DESY PITZ group for access, in framework of the collaboration, to the CST software [4].

REFERENCES

[1] J.C. Slater, "Microwave electronics", New York, NY, USA: Van Nostrand Company INC., 1950.

[2] M.A. Allen, G.S. Kino, "On the theory of Strongly Coupled Cavity Chains", *IRE Trans. MTT*, vol. MTT 8, p. 362, 1960.

[3] V. Kaljuzni, "Parameters calculations for accelerating structures with narrow coupling slots", *Journal of Technical Physics,* vol. 48, n. 6, p. 1228, 1978.

[4] https://www.cst.com

ISBN: 978-3-95450-240-0 ISSN: 2673-5539 doi:10.18429/JACoW-RuPAC2021-WEPSC03

MULTIPACTOR DISCHARGE IN SHORT 5-GAP 80 MHz IH STRUCTURES

M. M. Bulgacheva†, M. Gusarova, M. Lalayan, MEPhI, National Research Nuclear University, 115409 Moscow, Russia

Abstract

The results of numerical simulations of multipacting discharge in accelerating Interdigital H-type (IH) cavities are presented in this paper. Optimal design parameters were selected to reduce the number of multipactor electrons. The localization of multipactor trajectories in the short 5-gap 80 MHz IH cavities at various levels of accelerating voltage is considered.

INTRODUCTION

The multipactor effect[1-4] is a phenomenon in radio frequency devices, where secondary electron emission in resonance with an alternating electric field leads to exponential electron multiplication, possibly damaging and even destroying the RF device.

Figure 1 shows the 3D models of the considered 5-gap Interdigital H-type cavities: β=0.06 (a) and β=0.1 (b). This paper investigates the location and possible expansion of the multipactor discharge at different voltage levels.

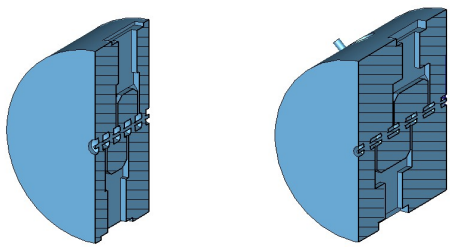

(a) (b)

Figure 1: 3D models of the 80 MHz IH cavities.

In this structure, there are two main areas where a multipactor discharge can occur (see Fig. 2): the gap region at low voltages (up to 10 kV), and the region of the external surface of the resonator and the side walls – at high voltages (up to 4 MV)[5].

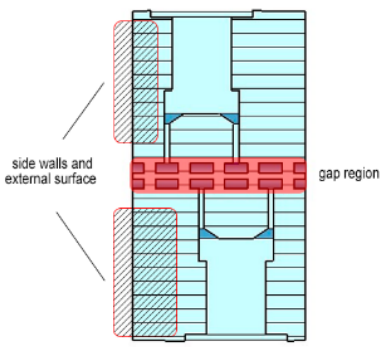

Figure 2: Dangerous areas.

† margaritabulgacheva@gmail.com

GEOMETRICAL MODIFICATION

To decrease the number of multipactor trajectories, the geometry of the drift tube has been modified. The straight angled tubes were replaced with the drift tubes with a bevel (see Fig. 3).

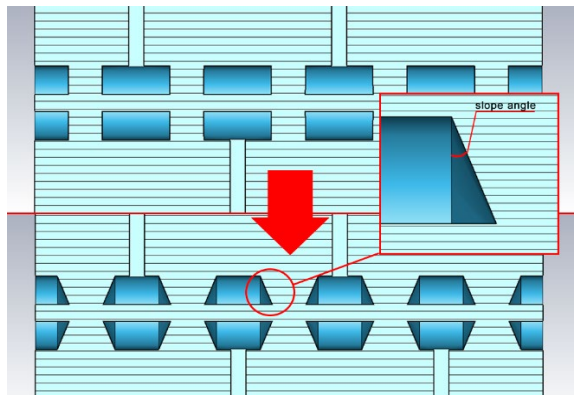

Figure 3: Geometrical modification of the drift tube.

The value of the slope angle of the bevel was selected considering the shunt impedance graph (see Fig. 4).

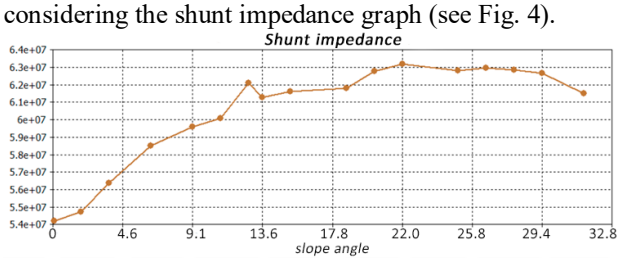

Figure 4: Shunt impedance dependence of the slope angle.

The maximum value of the shunt impedance corresponds to the slope angle of 22°.

THRESHOLD VOLTAGE

The gap voltage [6] at which two-point multipacting of order n can occur can be calculated using expression (1).

$$V = Ed = \frac{d^2(2\pi f)^2 m}{(2n-1)\pi e}. \quad (1)$$

The results of the theoretical calculation of threshold voltage are summarized in Table 1.

Table 1: The Results of Theoretical Calculation of Threshold Voltage Levels

	Short gap	Long gap
Working voltage, MV	1.5	3.5
Threshold voltage (structures without bevel), kV	1.5	5.1
Threshold voltage (structures with bevel), kV	2.3	7.0

ISBN: 978-3-95450-240-0 ISSN: 2673-5539 doi:10.18429/JACoW-RuPAC2021-WEPSC03

It is seen that potentially dangerous gap voltage at which multipacting can occur is up to 7 kV.

NUMERICAL MODELING

For the investigation of multipacting discharge effects the MultP-M code [7-9], developed at MEPhI, has been used. The electromagnetic field is exported from the CST studio [10].

Figure 5(a) shows the number of surviving electrons versus the RF voltage in the IH structure with and without a bevel. The low voltage range was considered separately.

Figure 5(c) shows the diagram RF phase / U. For each pair of RF phase and U, the code tracks the trajectories of 100 electrons randomly distributed over the structure. Each square in Fig. 5(c) corresponds to the voltage level and RF phase electron collision at which multipactor trajectories are detected.

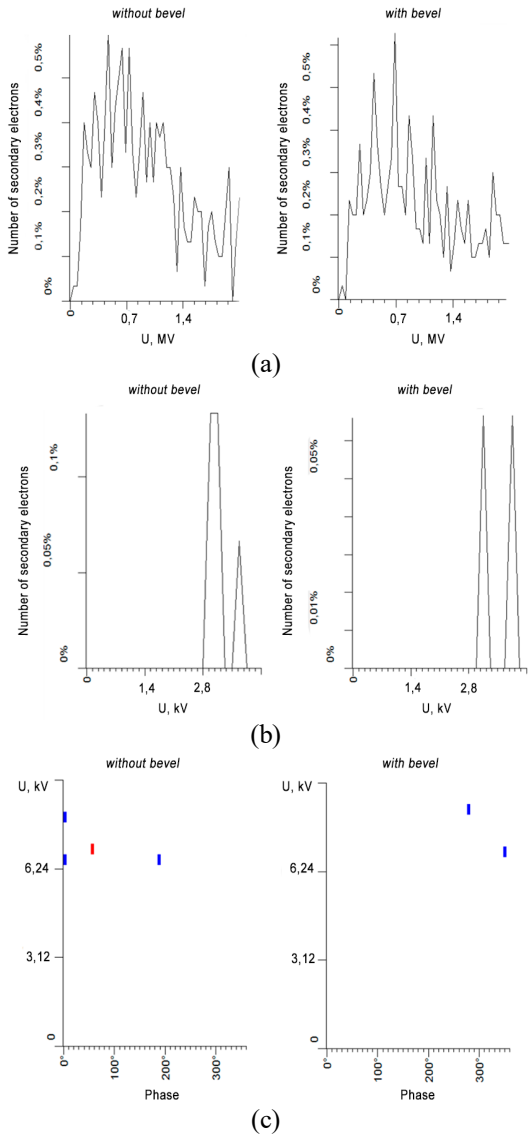

Figure 5: (a) Number of surviving electrons versus voltage level: (a) wide range, (b) low voltage range; (c) diagram RF phase / Voltage.

Thus, in structures with a bevel, there is a smaller increase in the number of particles compared to structures without a bevel. The RF phase / Voltage diagrams show that there is a smaller number of multipactor trajectories in the gap region of structures with a bevel.

Examples of Multipactor Trajectories

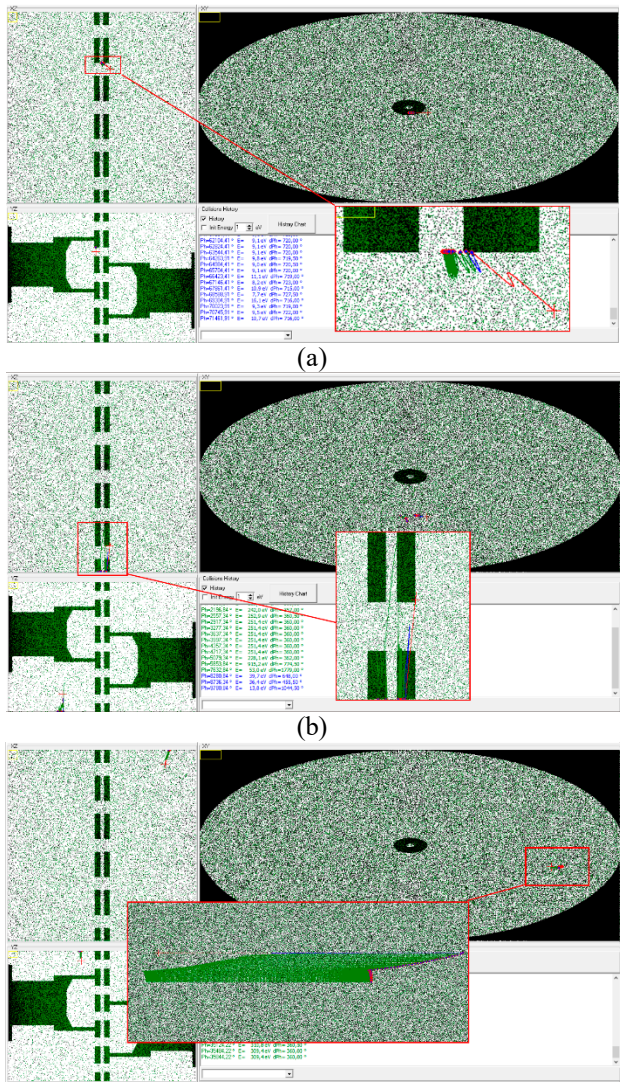

Figure 6: Example of the multipactor trajectories at a different voltage: (a) U=2.8 kV; (b) U=0.47 MV; (c) U=1.97 MV.

It can be seen from Fig. 6 that as the voltage increases, the multipactor trajectories shift closer to the outer surface of the considered 5-gap Interdigital H-type cavities.

CONCLUSION

Thus, the calculation results confirmed the effectiveness of the proposed design change in suppressing the multipactor discharge. Critical regions of multipactor avalanches at different levels of the accelerating voltage are identified.

ISBN: 978-3-95450-240-0 ISSN: 2673-5539 doi:10.18429/JACoW-RuPAC2021-WEPSC03

REFERENCES

[1] S. Brown, Basic Data of Plasma Physics, American Institute of Physics, New York, 1959 reprinted 1994, pp. 202–221.

[2] J.R.M. Vaughan, *IEEE Trans. Electron. Device ED-35* (7), p.1172, 1988.

[3] A. Hatch, H. Williams, *Phys. Rev. 112*, p. 681, 1958.

[4] R. Kishek, Y. Lau, L. Ang, *et al.*, *Phys. Plasmas*, p. 2120, 1998.

[5] V. Shemelin, S. Belomestnykh, Multipactor in Accelerating Cavities, Springer International Publishing, 2020. https://doi.org/10.1007/978-3-030-48198-8

[6] H. Padamsee, J. Knobloch, T. Hays, RF superconductivity for accelerators, John Wiley & Sons, Inc., p. 191, 1998.

[7] S. Khudyakov *et al.*, "Multp-M code geometry import module performance optimization" in *Proc. 24th Russian Particle Accelerator Conference, RuPAC 2014*, Obninsk, Russia, Sep. 2014, pp. 169-171.

[8] M. Gusarova *et al.*, "Evolution of 3D simulation multipactoring code MultP", *Probl. At. Sci. Tech. Ser. Nucl. Phys. Investig,* vol. 49, no. 3, pp. 123-127, 2008.

[9] M. Gusarova *et al.*, "New possibilities of MultP-M code" in *Proc. 5th International Particle Accelerator Conference, IPAC 2014*, Dresden, Germany, Jul. 2014, pp. 433-435.

[10] CST, https://www.cst.com/

ISBN: 978-3-95450-240-0 ISSN: 2673-5539 doi:10.18429/JACoW-RuPAC2021-WEPSC04

ACCELERATING STRUCTURE OF 8 MeV ELECTRON LINAC

A.N. Shein, A.V. Telnov, I.V. Shorikov, RFNC-VNIIEF, Sarov, Russia

Abstract

The paper presents results of three-dimensional electrodynamic calculations of an accelerating section of a resonance electron linear accelerator and input and output matching devices (couplers), as well as its electron dynamics calculation.

INTRODUCTION

Since 1994 a linear electron resonance accelerator LU-10-20 [1], meant for radiation materials processing and radiation processes study has been functioning in RFNC-VNIIEF. Accelerated electron energy – up to 10 MeV, beam average power – up to 12 kW. This accelerator has demonstrated its urgency when conducting radiation studies and tests.

Today modernization of LU-10-20 accelerator, involving an accelerating section and RF power systems, is being conducted. An accelerating section is meant for electron beam acceleration up to nominal energy and represents a complex resonance traveling wave RF structure, consisting of a disk-loaded waveguide and input and output couplers.

ACCELERATING STRUCTURE TYPE

A basic element for any accelerator is a microwave oscillator. To modernize LU-10-20, MI-470 pulsed magnetron manufactured by corporation Scientific Production Enterprise «Toriy» (Moscow) was chosen. Magnetron MI-470 supplies output pulsed power 10 MW with pulse duration from 3 up to 10 μs. Magnetron operation frequency range – (1883÷1889) MHz.

As an accelerating section for LU-10-20 modernization there was chosen structure based on disk-loaded waveguide (DLW) with variable geometry, operating on the traveling wave with mode 2π/3, similar to LU-10-20 current section. Operating frequency of accelerating structure at mode 2π/3 – 1886 MHz. Main arguments for selecting such a structure is experience availability for development and operation of linear accelerators with DLW, simplicity and cheapness of manufacture, availability of aperture for electron beam of larger diameter and simpler feed circuit as compared to structures on standing wave. Using reference data [2] there was determined preliminary geometry of the given accelerating structure, consisting of 10 cells buncher and 32 regular accelerating cells, and electron dynamics calculations were performed in one-particle approximation [3].

CELL GEOMETRY OPTIMIZATION

A purely experimental way for size fitting of accelerating cells from initial approximation to more precise ones represents a long process and is rather a labor-intensive occupation. At that during adjustment each cell undergoes processing on the turner not less than 3..5 times, what inevitably results in degradation of accelerating cell pure working surface. In order to reduce the number of adjustment cycle or to exclude process at all, the accelerating cells preliminary geometry was refined in resonance mock-up model.

To determine resonance frequencies, corresponding to definite oscillation modes, and the following calculated cells geometry adjustment to working frequency, the resonance mock-up electrodynamic model (Fig. 1) was developed. The resonance mock-up uses a property of periodic structures – availability of reflection symmetry planes, perpendicular to translation axis. For the disk-loaded waveguide one of reflection symmetry planes is placed symmetrically to adjacent diaphragms.

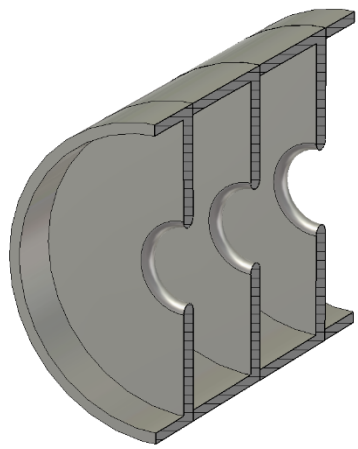

Figure 1: Resonance mock-up model.

In the resonator like that in Fig. 1, consisting of 4 cells, 4 modes become excited. Resonance frequency of the given model on 2π/3 mode was adjusted to the operating frequency 1886 MHz in the frequency band ±40 kHz by changing cell inner diameters (diameter change by 0.01 mm brings to frequency change by 52 kHz). After satisfactory result was achieved one of cells was replaced, and cell adjustments was not continued till all 42 cells were adjusted. Geometry optimization results are given in Fig.2.

ISBN: 978-3-95450-240-0 ISSN: 2673-5539 doi:10.18429/JACoW-RuPAC2021-WEPSC04

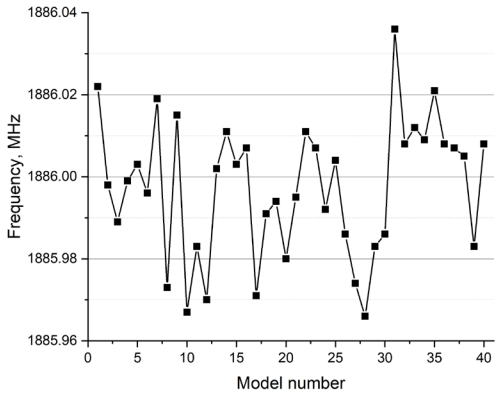

Figure 2: Resonance model adjustment result.

Accelerating field distribution on 2π/3 mode in one of model is given in Fig. 3.

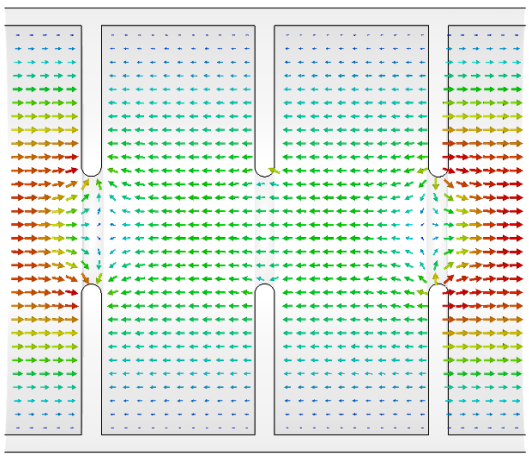

Figure 3: Distribution of accelerating field on mode 2π/3 in the model.

CALCULATION OF ACCELERATING SECTION AND COUPLERS

The traveling wave accelerating structure type, selected as a base for accelerator's modernization, implies usage of input and output matching devices (couplers), which are connected to a rectangular waveguide through coupling window. Couplers have a connecting pipe located symmetrically with regard to the rectangular waveguide to remove electromagnetic field distribution asymmetry in coupling cell axial region, as well as to provide connection of vacuum pumps. Geometry for both couplers was adjusted for operating frequency 1886 MHz by changing its geometry (coupling cell radius and width and thickness of coupling window. Input coupler was adjusted to VSWR value <1.05 at operating frequency and <1.15 in bandwidth ±2 MHz with the aid of a model with first three accelerating cells and arbitrary load. Output coupler was adjusted to the value VSWR not worse than 1.20 in the range ±1.5 MHz from operating frequency in model, involving accelerating structure and input coupler. Final accelerating section design model with input and output couplers is represented in Fig. 4.

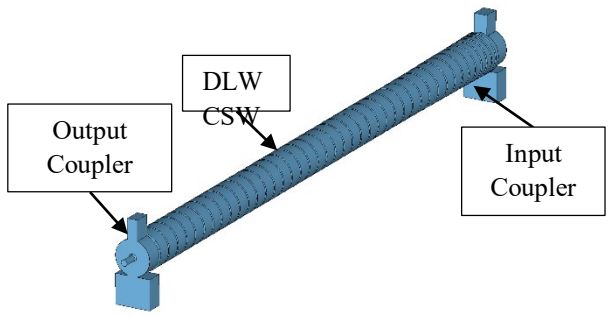

Figure 4: Accelerating structure model.

Quality factor of structure – 17000. The value of calculated shunt impedance is about 55 MOhm/m. Calculated structure filling time by RF power is about 650 ns.

CALCULATION OF ELECTRON DYNAMICS

The obtained three-dimensional model of accelerating section was used for calculation of electron beam dynamics in the accelerator. As transverse focusing there was used a solenoid field 0.1 T.

A single electron bunch with 10 mm radius was injected in accelerating structure during the time corresponding to the period of microwave field (0.53 ns). Electron beam energy – 50 keV. RF power – 8 MW. The calculation took into account losses of RF power on conducting walls.

As a result of calculation the average particle energy was obtained to be 9.1 MeV, capture efficiency by current was – ~60%. Electron spectrum on the accelerator output is given in Fig. 5. Obtained results agree very well with preliminary calculations of electron dynamics [4] (electron energy – 8.79 MeV, capture efficiency – 79%). One can explain a bit smaller particle capture through a negative influence of input coupler, what was neglected in the course of preliminary calculations.

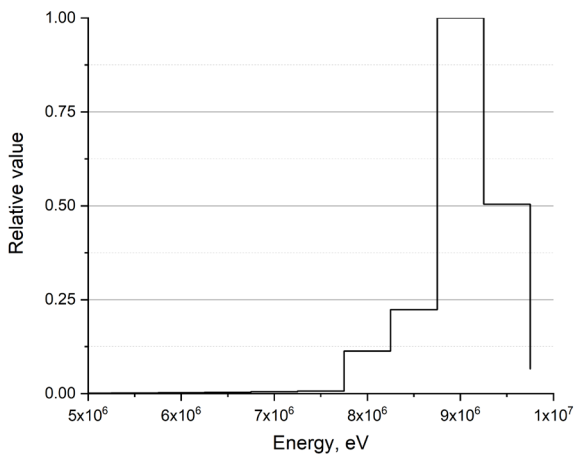

Figure 5: Electron energy spectrum.

ISBN: 978-3-95450-240-0 ISSN: 2673-5539 doi:10.18429/JACoW-RuPAC2021-WEPSC04

CONCLUSION

This paper presents main results of three-dimensional electrodynamic calculation of the accelerating structure of the linear resonance electron accelerator for energy 8 MeV.

A short ground for selecting the accelerating structure type is given.

The accelerating cells geometry was numerically optimized in order to exclude or reduce, if possible, the number of cells after-treatment stages while tuning the accelerating section at the operating frequency. Specified were optimal geometry sizes of input and output matching devices, also providing matching of the accelerating section and RF generator with VSWR not worse than 1.20 at the bandwidth ±1.5 MHz. Structure main electrodynamic characteristics – quality factor, shunt impedance, structure filling time by microwave power were determined.

Electron beam dynamics in the accelerator's model was numerically investigated.

REFERENCES

[1] Zavyalov N.V. *et al.,* "Industrial Linear Electron Accelerator LU-10-20", in. *Proc. XV International Workshop on Charged Particle Linear Accelerators, VANiT, ser. Nucl. Phys. Res*, issue 2, 3 (29, 30), p.39-41, 1997.

[2] O.A. Valdner *et al.* "*Diaphragmatic waveguides: Reference Book*", Moscow, Energoatomizdat, 1991.

[3] A. N. Shein, "Prospects of Creating a Modern Resonance Electron Accelerator", in *Proc. 26th Russian Particle Accelerator Conf. (RuPAC'18)*, Protvino, Russia, Oct. pp. 295-297, 2018. doi:10.18429/JACoW-RUPAC2018-WEPSB08

[4] Telnov A.V. *et al*., "Accelerating Section of Electron Linear Accelerator LU-10-20" in *Proc. XV International Workshop on Charged Particle Linear Accelerators, VANiT, ser. Nucl. Phys. Res,* issue 2, 3 (29,30), p.134-136, 1997.

ISBN: 978-3-95450-240-0 ISSN: 2673-5539 doi:10.18429/JACoW-RuPAC2021-WEPSC05

MODELING OF THE ENERGY COMPRESSION SYSTEM SLED FOR THE LINAC-200 ACCELERATOR

K. Yunenko, M. Gostkin, V. Kobets, A. Zhemchugov, JINR, Moscow Region, Dubna, Russia

Abstract

This paper is devoted to the research of the possibility of increasing the output energy of an electron beam at the LINAC-200 linear accelerator by using the SLED (Stanford Linac Energy Doubler) [1] energy compression system with constant parameters of the storage cavities [2].

In order to select the necessary parameters and characteristics for the successful creation of this system on the accelerator, the SLED system (Fig. 1) structure simulation and the characteristics of cylindrical hollow resonators [3] calculation were conducted using the CST MICROWAVE STUDIO program [4].

INTRODUCTION

The LINAC-200 linear electron accelerator operating at a frequency of 2856 MHz can currently increase the energy of particles to 200 MeV. We continue to build up energy by installing accelerating sections, which according to plans can raise energies up to 800 MeV. However, further increasing the size of the accelerator is difficult, so other approaches have been explored.

Figure 1: SLED energy compression system design from IREN (JINR, LNP).

An energy compression system can be used to increase the energy of an electron beam in a linear accelerator without increasing the size of the installation. In our case, the power multiplication system SLED was chosen [2]. This system consists of several components shown in Fig. 2.

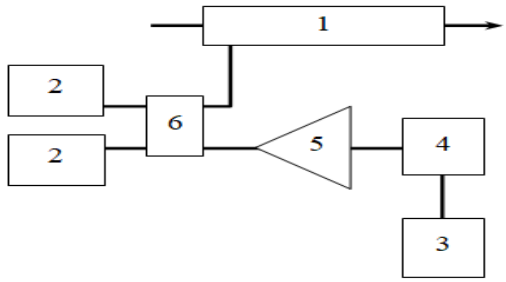

Figure 2: Block diagram of LINAC with an energy compression system SLED (1 - accelerating section, 2 - storage resonators, 3 - master oscillator, 4 - high-speed phase shifter, 5 - power amplifier, 6 - high frequency bridge).

To analyze the structure and obtain results, it is sufficient to consider the process of excitation of a single cavity [1].

PARAMETER ESTIMATION AND CAVITY MODELING IN THE ENERGY COMPRESSION SYSTEM SLED

Pulsed klystrons of the 10 centimeter range are used as microwave power amplifiers, the operating frequency of which corresponds to 2856 MHz. Information on klystrons is specified in the Table 1.

Table 1: Parameters of Klystrons

Type	TH 2129
Company manufacturer	TTE (Thomson Tube Electronics)
Peak power:	
input, W	100
output, MW	20
Average power:	
input, W	0.7
output, kW	20
Pulse duration, μs	4
Frequency of repetition (max), Hz	500

There are 2 types of accelerating sections: short and long (Fig. 3). They have the characteristics specified in the Table 2.

ISBN: 978-3-95450-240-0 ISSN: 2673-5539 doi:10.18429/JACoW-RuPAC2021-WEPSC05

Table 2: Parameters of Accelerating Sections

		short	long
Amount of sections		3	18
Amount of cells in a section		105	210
Length at accelerating intervals, cm		3.673	7.346
Amount of uniform segments per section		11	11
Frequency, MHz		2856	
Type of wave		TW	
Oscillation mode		2π/3	
Acceleration rate, MeV / m		5 (I=40mA) – 7 (I=0)	
Filling time, μs		1.3	
Beam load (total over the entire accelerator), MeV / mA		2.6	
Group speed range velocity, V_γ/c		0.0093 – 0.0389	
Shunt impedance, MOhm		56.5 – 48	
Iris aperture:	diameter, mm	32	
	thickness, mm	5.84	

Figure 3: Long accelerating section A3A.

A high Q factor in copper cavities, at room temperature, can be obtained by using higher-order resonant modes. Taking into account the mechanical stability and frequency separation of higher modes, it can be concluded that the mode with the smallest cavity volume will be the most desirable mode.

Mods from the TE_{01N} family satisfy these requirements. The specific ratio of the diameter D to the length L of the cavity is chosen on the basis of calculations, optimizing the achievement of the maximum frequency resolution between adjacent modes at the highest Q-factor. With an increase in the number of variations N along the length of the cavity, the Q-factor increases, but at the same time, the frequency resolution between adjacent modes decreases. It was decided to use N = 5 [3], the field distribution of which can be seen in Fig. 4.

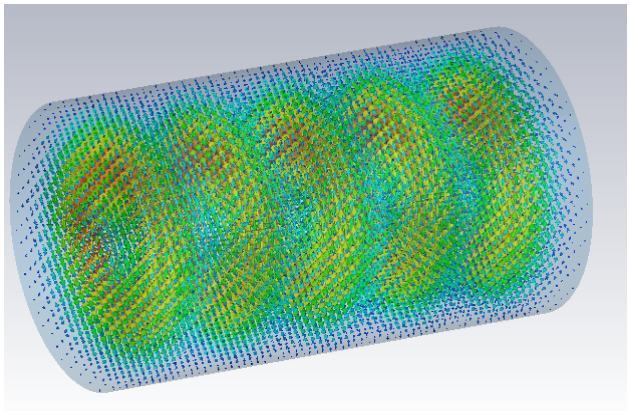

Figure 4: Cavity e- field distribution at selected size.

A cavity was modeled for the well-known structure of the LINAC-200 accelerator, the parameters of which correspond to our needs [1, 2]. The values of the characteristics obtained in the analysis of the SLED system are shown in Table 3.

Table 3: Estimation of the Parameters of the Energy Compression System

Type of wave	$2\pi/3$
Frequency, MHz	2856
Filling time, μs	1.3
Pulse duration, μs	4
Field decay time in section, μs	1.5
Time of pumping out the stored energy, μs	2
Coupling coefficient	4
The coefficient of increase of the collected energy	2.002

The simulation in the CST MICROWAVE STUDIO program resulted in the physical dimensions of the cavity (L = 33.59cm, D = 20.52cm) and its Q factor (Q = 1.002 * 10^5). These data were selected from the obtained modes 1 and 2 (Fig. 5 and Fig. 6) for different cavity sizes.

ISBN: 978-3-95450-240-0 ISSN: 2673-5539 doi:10.18429/JACoW-RuPAC2021-WEPSC05

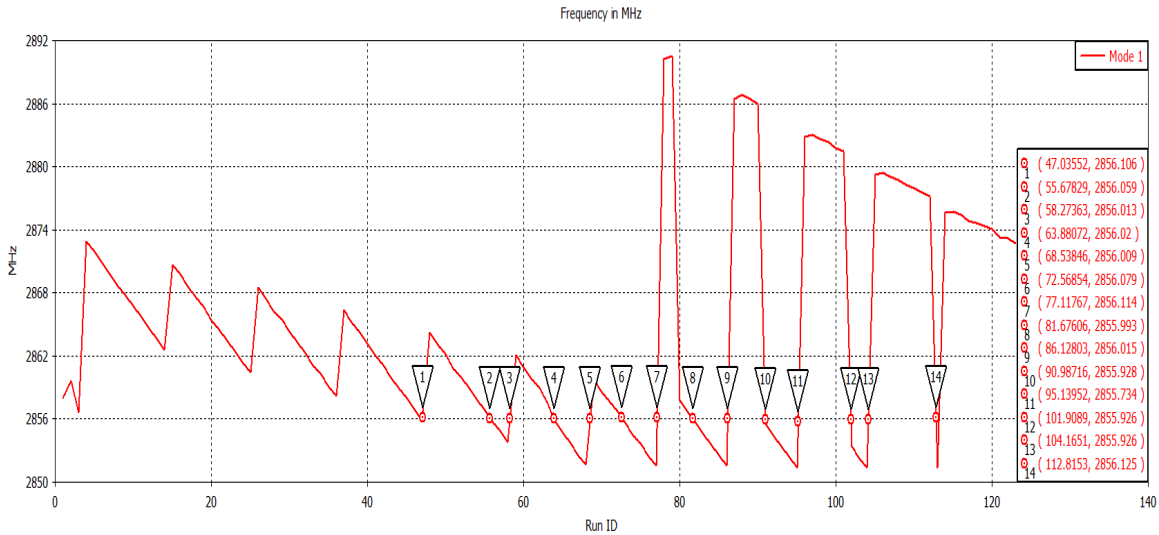

Figure 5: Modes for different cavity parameters (cylinder proportions change).

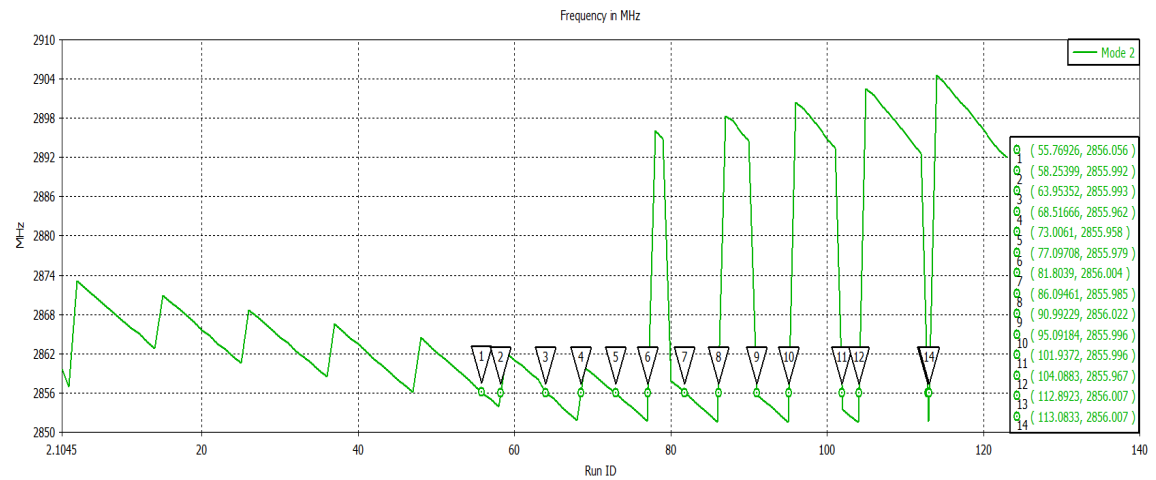

Figure 6: Close modes for different cavity parameters (cylinder proportions change).

CONCLUSION

In the course of the work done, the cavity for the SLED system was modeled, parameters (such as: field decay time in the section, characteristic time of pumping out the stored energy, coupling coefficient, gain of the accumulated energy, Q factor, wave type, resonator diameter, resonator length, material (oxygen-free copper)) which will be suitable for the LINAC-200 accelerator. Based on these values, it can be assumed that an increase in the electron beam energy at the output is possible up to 280 MeV.

REFERENCES

[1] V.M. Pavlov, “Power Multiplier System SLED”, Preprint INP 97-94, Novosibirsk, Nov. 1997, pp. 3-20 (In Russian)

[2] B.Yu. Bogdanovich, V.I. Kaminsky, V.A. Senyukov, “High-frequency Supply Systems of Linear Electron Accelerators with Storage of Microwave Field Energy”, Tutorial ISBN 5-7262-0468-9, MEPHI, Moscow, 2002, pp. 12-23, 54-70 (In Russian)

[3] I.V. Lebedev, “Microwave equipment and devices. T.1”, Textbook, Moscow, Russia, Publ. “Higher School”, 1970 (In Russian)

[4] CST https://www.cst.com/

ISBN: 978-3-95450-240-0 ISSN: 2673-5539 doi:10.18429/JACoW-RuPAC2021-WEPSC06

ASESS INPUT DATA UNCERTAINTIES IN THERMAL-MECHANICAL CALCULATIONS OF THE OUTLET WINDOW MEMBRANE OF THE LUE-200 ACCELERATOR

I. V. Burkov, A. P. Sumbaev, JINR, Dubna, Russia

Abstract

The maximum values of the temperature fields and stress-strain state are calculated for various configurations of the outlet window membrane of the LUE-200 accelerator with assessing uncertainties in input data. The thermo-mechanical parameters are estimated by simulating the electron beam pulsed action mode on the membrane in the computational models based on the mathematical description of the most significant physical processes. The obtained numerical modelling results demonstrated the importance of assessing uncertainties in input data for substantiating the safe operation limits of IREN facility.

INTRODUCTION

The paper clarifies the previously obtained estimates by reducing the error influence in the calculation results, due to the assumptions and approximations adopted in [1], as well as the uncertainty and formalism when specifying the initial data. A change in the approaches in combination with the development of the initial data processing methods are capable of giving a more detailed description of physical processes and contribute to the further improvement of the membrane assembly design [2, 3].

MODEL DESCRIPTION

A thermomechanical problem is focused on evaluating the temperatures field and stress-strain state (SSS) arising on the membrane during the installation operation. The solution of a problem was performed by the method of running finite difference equations reduced to the standard three-diagonal form. The mathematical formulation of the heat conduction problem [4, 5] and the elasticity theory [4, 5, 6] have the following form:

$$\rho \cdot c \cdot \frac{\partial T}{\partial t} = LT + E(E_e, r, h) \cdot I(\tau), \quad (1)$$

$$\rho \frac{\partial^2 U}{\partial t^2} = LU + P + \alpha_{ex} \cdot (3k + 2\mu) \cdot grad\ \theta, \quad (2)$$

where: T is the temperature; U is a deformation; ρ is the density; L is a differentiating operator; E is energy deposition; I is beam current; τ is pulse duration; k and μ are the Lamé constants; α_{ex} is the coefficient of linear thermal expansion of the medium; $\theta = T\text{-}T_0$ – temperature deviation; P is the applied force.

A. A. Samarskii's discretization scheme [4] is used to solve the heat conduction problem. It is stable and has the total approximation property.

Obtained from the measurements of the Rogowski belt beam current the experimental data ($I(\tau)$ diagrams), the normalized distribution of the energy release in the membrane, taking into account the distribution of the current density over the beam cross section [1], the thermos-physical characteristics of structural materials, and the environmental parameters are used as the initial data for calculating the SSS and temperature fields.

Estimation of the Properties

Based on the calculation model work results an assessment of the impulse characteristics of the thermos-mechanical operating mode of the outlet window membrane became available. Let's consider a mode of operation with a limited power level and carry out the necessary calculations. The current IREN facility parameters by neutron yield determine the average electron beam power $P_{av} \sim 1.1$ kW at a pulse duration of $\tau = 250$ ns, the beam current in the pulse $I = 0.63$ A, the electron energy in the beam at the level of $E = 70$ MeV, and the pulse repetition rate $f = 100$ Hz. Single pulse simulation (Fig. 1) was carried out in order to verify the correct operation and applicability of the developed computational model for assessing the thermal-mechanical characteristics of the membrane in a pulsed mode. In that case, the calculation model of the membrane experiences a single pulse action of an electron beam, described by the course of the averaged interpolated curve. The membrane, being previously in a cold state at room temperature, starts to warm up in proportion to the transmitted by the beam power. The cooling rate of the membrane heated after the pulse depends on the membrane material thermal inertia, which is a function of convective heat transfer and thermal conductivity.

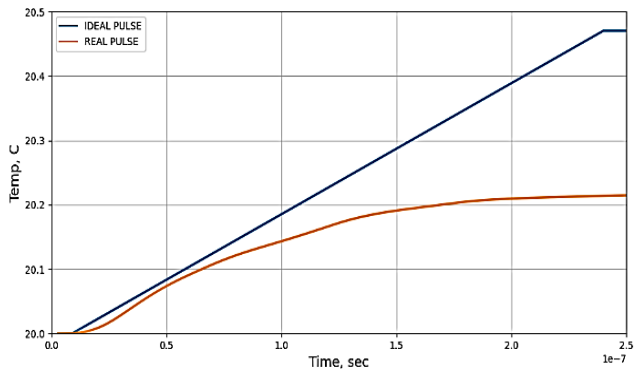

Figure 1: Single pulse.

The subsequent simulation of the installation pulsed operation mode is similar to a single pulse simulation, which is sequentially included in the time series of events f (frequency) times. The steady-state thermo-mechanical characteristics of the membrane for the selected operating mode are shown in Fig. 2 and Fig. 3.

ISBN: 978-3-95450-240-0 ISSN: 2673-5539 doi:10.18429/JACoW-RuPAC2021-WEPSC06

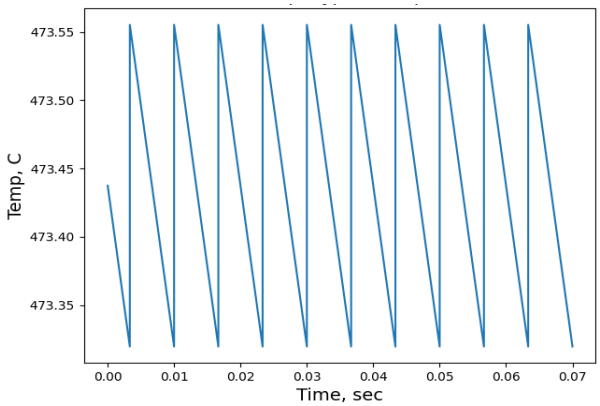

Figure 2: Pulse heating.

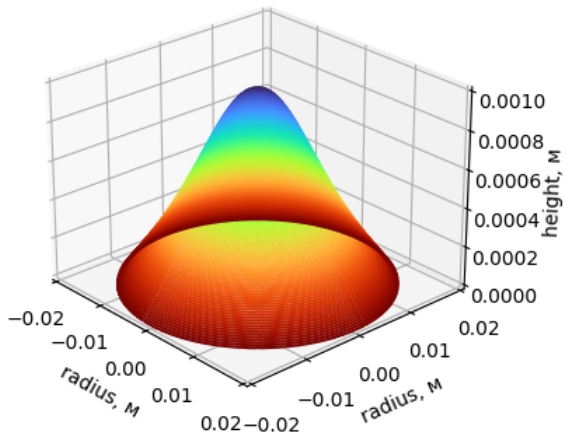

Figure 3: Disposition.

The computational model work results (Fig. 2 and 3) are demonstrate the maximum temperature of 474 C and the height deformation degree of the steel membrane at a given beam power level. It means that results are confirm the negative prediction of the assembly reliability under design conditions made in [1].

Asses

The calculation results errors estimation due to the joint influence of the uncertainties of the initial data is usually named the analysis of errors. First of all, the statistical characteristics of the initial data and the calculation parameters (mathematical expectations, variances and the relative standard deviations corresponding to these variances) need to be estimated or calculated. A series of systematic calculations of «critical» parameters need to then be carried out. The initial data for calculation serials are the values of the input parameters, the influence of the uncertainty of the assignment of which on the calculation result need to be determined.

It should be noted that the electron beam parameters ($I(\tau)$ on Fig. 4 and E on Fig. 5) and the outlet window membrane (R, H) have the most significant influence on the formation of the calculation error. After that the contribution of the uncertainty in setting the error of other initial parameters to the total calculation error (such as characteristics of the ventilation system and the environment) are evaluate.

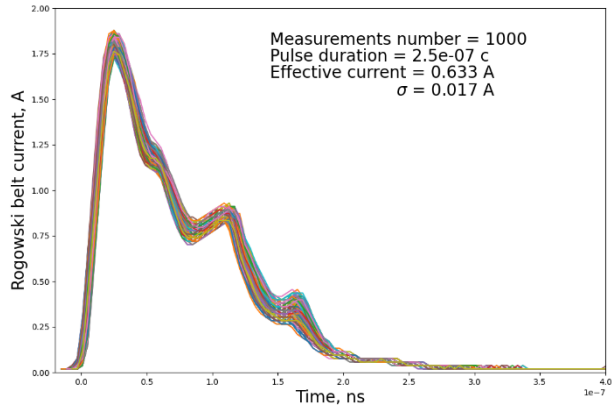

Figure 4: $I(\tau)$ – diagrams.

The presence of the energy release proportional dependence on the parameters of the electron beam and the membrane thickness is obvious. In fact, despite the fact that both input parameters are clearly included in the input data set for estimating energy release, there are no relationship between them. Nevertheless, the uncertainty in setting the energy release should be analyzed in a similar way and additionally determined the values of its inherent corresponding sensitivities. Thus, the desired value is characterized by the deviations of the beam parameters under the selected operating mode for the first case and by the quality of manufacture of the outlet window membrane, determined with a random error and a measuring instruments systematic error.

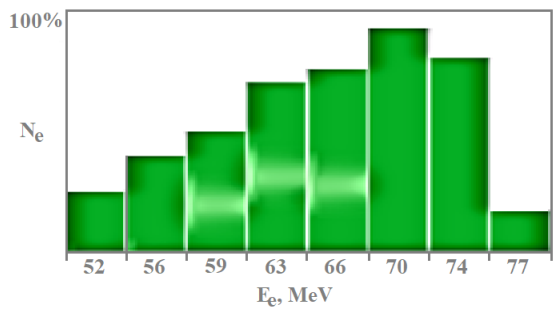

Figure 5: Energy spectrum of electrons.

From the results presented at the stage of the simulation follows that the «critical» parameters are the maximum temperature of the most heated membrane region $F_1 = T[max]$, and the mechanical stresses arising in the metal $F_2 = S[max]$. Thus, it is assumed in the work that the errors in determining the functional F_1 and F_2 the most significantly depend on W, E, L, α, P.

The sensitivity coefficients of the considered functional to changes in the initial parameters of the calculations were determined by sequentially varying one of them while maintaining the values corresponding to their mathematical expectations by other parameters. This is followed by a series of functional calculations with the initial data changed in this way. Then, the functional sensitivity coefficients to changes in the initial data in the point vicinity determined by the values of the mathematical expectations are numerically estimated. The evaluating results the sensitivity coefficients for the maximum temperature of the

ISBN: 978-3-95450-240-0 ISSN: 2673-5539 doi:10.18429/JACoW-RuPAC2021-WEPSC06

most heated outlet window membrane region (F_1) and the mechanical stresses arising in the metal (F_2) to a change in the initial calculation data are presented in a Table 1.

Table 1: Sensitivity Coefficients

Parameter name	$P_{T,i}$	$P_{U,i}$
Beam current	0.804	0.927
Electron energy	0.017	0.020
Membrane tick	0.456	-0.731
Press	0.000	0.135
Heat transfer	-0.280	-0.387

The uncertainties in setting the electron beam parameters are calculated by the results of the experimental data processing (Fig. 4). Foil thicknesses is regulated by industry standards. The analysis of the uncertainties in setting the initial data characterizing the ventilation system operation was carried out in accordance with the methodological recommendations [7], according to which deviations from the design data should not exceed 10% in terms of air flow (with a probability of 95%). The air pressure in the operation hall is formed due to the differences in the power of the supply and exhaust ventilation systems. That indicates the complete dependence of the uncertainty in setting this parameter on the uncertainty in setting the air flow rate. In the same way and for simplicity, we will take as an assumption the linear dependence of the heat transfer coefficient value (α) on the parameters of the ventilation system.

The RMS values (σ), characterizing the total errors in the functional calculation and introduced by the uncertainty of the initial data, were determined by the formula [8]:

$$\frac{\delta F}{F} = \sqrt[2]{\sum_{i=1}^{N}\left[\left(P_{Fi}\cdot\frac{\Delta i}{i}\right)^2\right]}. \qquad (4)$$

The obtained values of the errors (σ) of the maximum temperature T of the most heated outlet window steel membrane region (F_1) and mechanical stresses arising in the metal (F_2) are 4.19% and 6.04%, respectively. Thus, the relative errors values in the determination of the «critical» parameters considered in the paper for the 95% confidence interval should be taken equal to 8.39% and 12.08%, respectively.

CONCLUSION

One of the numerous stages of substantiating the reliability of the design of the outlet window membrane of the LUE-200 accelerator has been carried out. A software has been developed that evaluates the membranes thermomechanical characteristics in continuous and pulsed operating modes. The features of the tool include tools for flexible customization of the solver and the ability to adapt the code for other tasks.

For the selected «critical» parameters, the sensitivity coefficients to the initial calculation data were calculated. As a result, the errors were calculated by evaluating the uncertainties of the beam current and electrons energy, the membrane geometry deviation during manufacture, and the operating characteristics of the supply and exhaust ventilation.

The obtained results have moderately high thermomechanical characteristics of the membrane assembly current configuration in operation at the maximum power level postulated in a paper. However, extreme caution should be exercised when operating the installation in such a parameters. The expected mechanical stress on the membrane is close to the ultimate strength of the material.

REFERENCES

[1] I. V. Burkov *et al.,* "Development of a Technique for the Express Assessment of Temperature Fields on the Outlet Window Membrane of the LUE-200 Accelerator", *Phys. Part. Nucl. Lett.,* Vol. 17. No4, pp. 561-566, 2020. doi:10.1134/S1547477120040159.

[2] A. Sumbaev *et al.,* "LUE-200 accelerator - A photo-neutron generator for the pulsed neutron source "IREN", *J. Instrum.* Vol. 15. No11. p. T11006, 2020. doi:10.1088/1748-0221/15/11/T11006

[3] E. A. Golubkov *et al.,* "Pulsed neutron source Iren at Frank laboratory of neutron physics, JINR, Fundamental interactions & neutrons, nuclear structure, ultracold neutrons, related topics", Proceedings of the XXVI International Seminar on Interaction of Neutrons with Nuclei, Xi'an, China, 28 may 2018. Xi'an, China, JINR, 2018. – p. 147-157.

[4] A.A. Samarskiy, Difference Scheme Theory, M.: Nayka, P. 656, 1977.

[5] K. Vasidzu, Variational Methods in Theory of Elasticity and Plasticity, Moscow, Mir Publ., p. 542, 1987.

[6] V. D. Kupradze *et al.,* "Dynamical problems of the theory of elasticity and thermoelasticity", *Itogi Nauki i Tekhniki. Ser. Sovrem. Probl.* Mat. 7, VINITI, Moscow, pp. 163–294, 1975.

[7] Organization of ventilation at radiation facilities. Methodical instructions, MU 2.2.8/2.6.1.67-02, MINATOM, 2002, (in Russian).

[8] A.V. Kuryndin *et al.,* "Using APROS6 code to assess input data uncertainty in thermalhydraulic calculations of SNF storage pool", Life cycle management technologies, № 2(16), pp. 21-37, 2019.

ISBN: 978-3-95450-240-0 ISSN: 2673-5539 doi:10.18429/JACoW-RuPAC2021-WEPSC07

MEDIUM ENERGY IONS TRANSPORT CHANNEL FOR A PULSED LINEAR ACCELERATOR

V. S. Dyubkov†, National Research Nuclear University MEPhI, Moscow, Russia

Abstract

For a transportation and matching proton and light ion beams (the maximal value A/Z is about 3.2) between RFQ and groups of IH-cavities it is suggested medium energy ions transfer line. That line should provide 100% beam transmission under negligible beam envelope increase and small longitudinal beam size growth during particle transport. MEBT consists of two parts. One of them provides ion transfer with energy of 820 keV/u and the second one provides ion transfer with energy of 2.46 MeV/u.

INTRODUCTION

New linear injector of proton and light ion beams is under design at NRNU MEPhI [1]. This injector will accelerate protons and ions up to oxygen to an energy of 7.5 MeV/nucleon with mass-to charge ratio $A/Z < 3.5$. The main part of linear injector are RFQ linac and two groups of short 5-gaps IH-cavities independently powered. Beams transfer from RFQ linac to the first set of IH-cavities will be done with the help of medium energy beam transport line (MEBT-1). Beams transfer between the first and the second set of IH-cavities will be done by means of MEBT-2. For both transfer lines it is considered to use beam bunchers to control the bunch length and to chop the bunch tails.

MEBT-1 DESIGN

In order to transfer beams of particles from RFQ linac output to the entrance of the first set of IH-cavities MEBT-1 will be used. The suggested layout of the MEBT-1 is shown in Fig. 1. It consists of two quadruple doublets and two quads [2] and its total length is 3.62 m. *B*-field components at the center of the quadruple lens are shown in Fig. 2. Magnetic field distribution in the cross-section of the quad at its center is presented in Fig. 3. Quad gradients for ion beam with $A/Z = 3.2$ are presented in Table 1.

Figure 1: Layout of MEBT-1 line.

Table 1: Quad Parameters

Name	*G*, T/m	*L*, cm
QF1	7.3	10
QD1	-7.3	10
QF2	9.0	10
QD2	−11.3	10

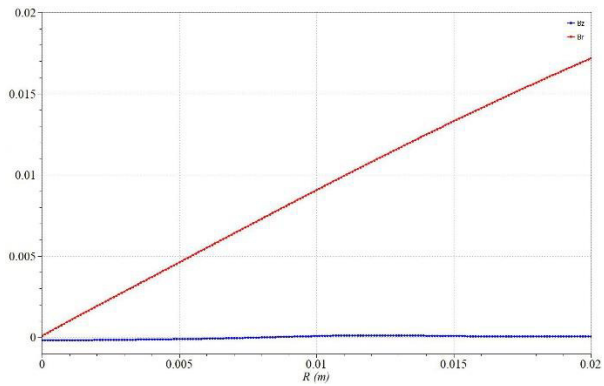

Figure 2: B_z (blue) & B_r (red) field components.

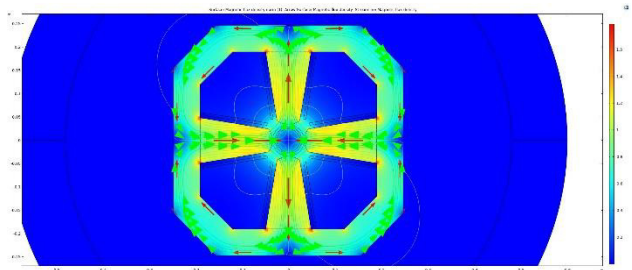

Figure 3: Quad cross-section & B-field distribution. Courtesy to I. Yurin [3].

Also it is supposed that beam buncher will be located in the drift space between doublets. Typical view of that buncher, designed by M. Gusarova, is shown Fig. 4.

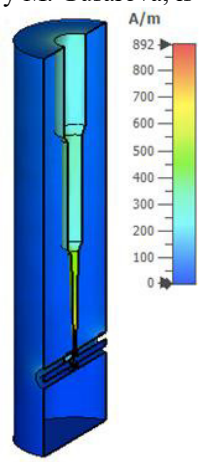

Figure 4: Buncher for MEBT-1.

Self-consistent ion beam dynamics simulation in the calculated 3D fields of MEBT-1 line was carried out by means

† vsdyubkov@mephi.ru

ISBN: 978-3-95450-240-0 ISSN: 2673-5539 doi:10.18429/JACoW-RuPAC2021-WEPSC07

of [4]. Beam current were equal to 2 mA, normalized transverse emittace was equal to 0.04 π·μm·rad. Initial particle distribution used for simulation is presented in Fig. 5. Calculated RMS beam envelopes are presented in Fig. 6 and particle density along the transfer line is shown in Fig. 7. Ion beam at the end of MEBT-1 is shown in Fig. 8.

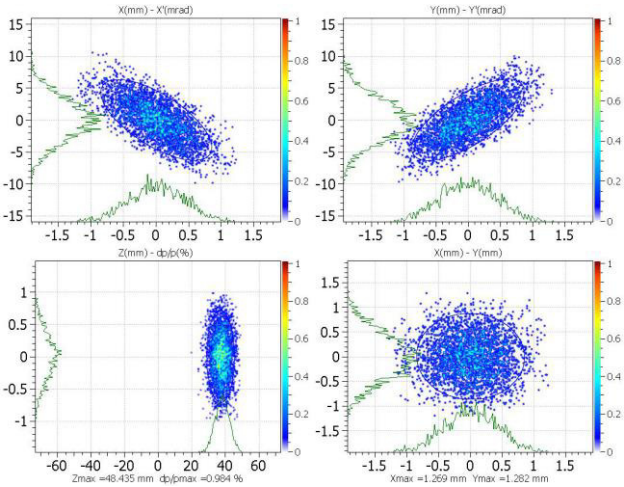

Figure 5: Beam at the MEBT-1 start.

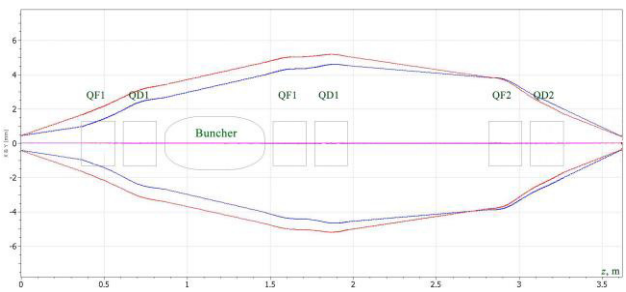

Figure 6: Beam envelope (x - blue, y - red) in MEBT-1.

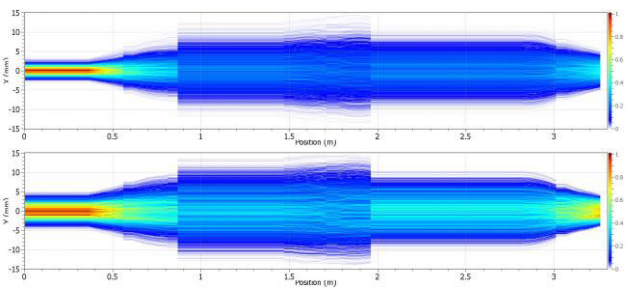

Figure 7: Particle density along the transfer line: x – top; y – bottom.

One can see that beam size at MEBT-1 output does not increase in comparison with its start under 100% transmission. Vacuum chamber diameter should be not smaller than 30 mm.

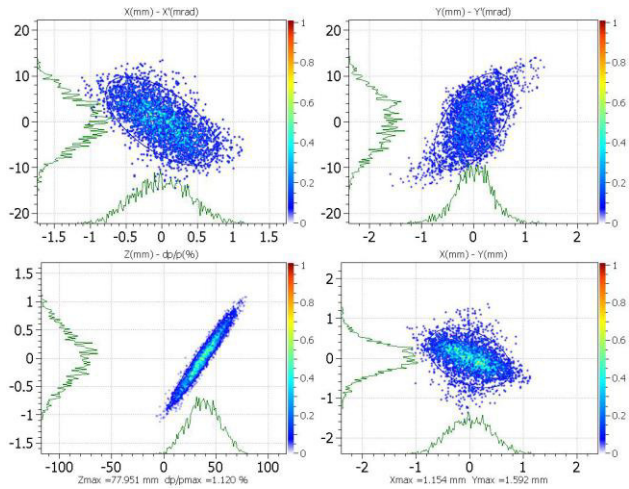

Figure 8: Beam at the MEBT-1 end (buncher is switched off).

MEBT-2 DESIGN

MEBT-2 will be used for beam transfer from the output of the first set of IH-cavities to the input of the second set of IH-cavities at with energy of 2.46 MeV/u. MEBT-2 consists of three identical quadruple doublets. Lenses have the same length as for MEBT-1. Its gradients are 14.7 T/m and −11.6 T/m correspondingly. Length of MEBT-2 line is equal to 3.29 m. Buncher similar to that is for MEBT-1 can be used in MEBT-2. Self-consistent ion beam dynamics simulation in the calculated 3D fields of MEBT-2 line was carried out in the same way as for MEBT-1. Initial particle distribution used for simulation here is presented in Fig. 9. Calculated RMS beam envelopes are presented in Fig. 10 and particle density along the transfer line is shown in Fig. 11. Ion beam at the end of MEBT-2 is shown in Fig. 12.

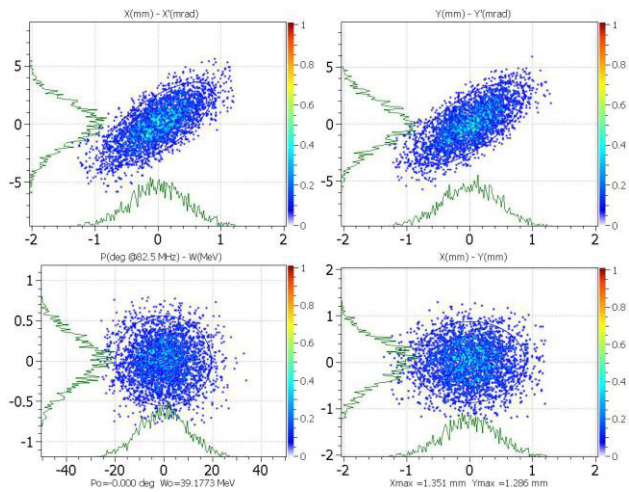

Figure 9: Beam at the MEBT-2 start.

ISBN: 978-3-95450-240-0 ISSN: 2673-5539 doi:10.18429/JACoW-RuPAC2021-WEPSC07

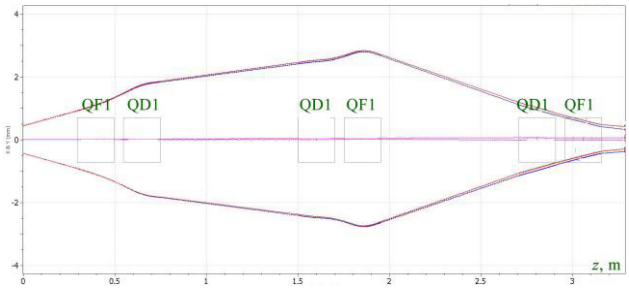

Figure 10: Beam envelope (x - blue, y - red) in MEBT-2.

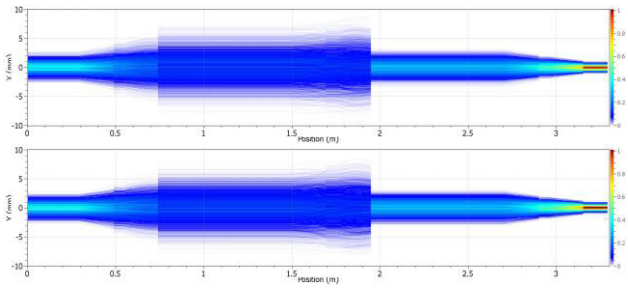

Figure 11: Particle density along the transfer line: x – top; y – bottom.

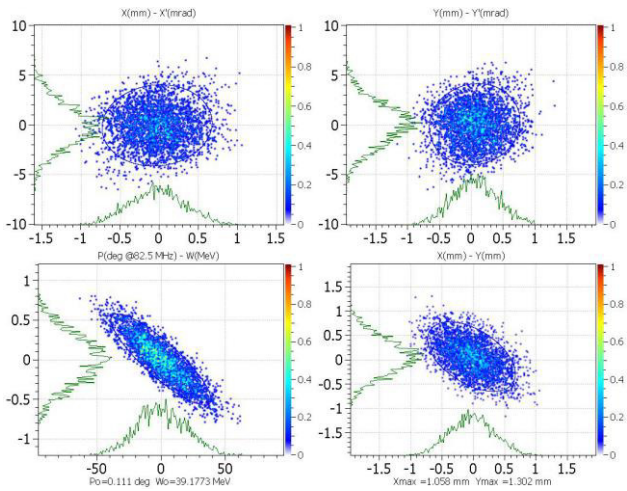

Figure 12: Beam at the MEBT-2 end.

Beam size at the MEBT-2 output does not increase in comparison with its size at the start 100% transmission. Vacuum chamber diameter can be equal to 20 mm.

CONCLUSION

Design of MEBT-1 and MEBT-2 lines for ion beam transfer with mass-to charge ratio $A/Z < 3.5$ is suggested. Self-consistent ion beam dynamics simulations in the "real" 3D fields are performed. Defined parameters of the quads provide 100% beam transmission.

REFERENCES

[1] S.M. Polozov *et al.*, "The conceptual design of the 7.5 MeV/u light ion injector", presented at the 27th Russian Particle Accelerator Conf. (RuPAC'21), Alushta, Crimea, Russian Federation, Sep. 2021, paper TUB07, this conference.

[2] K.G. Steffen, High energy beam optics, New York, USA: Interscience Publishers, 1965.

[3] I. Yurin, "Light Ion Accelerator Magnets", presented at the 27th Russian Particle Accelerator Conf. (RuPAC'21), Alushta, Crimea, Russian Federation, Sep. 2021, paper WEPSC21, this conference.

[4] D. Uriot and N. Pichoff, "Status of TraceWin code", in *Proc. IPAC'15*, Richmond, VA, USA, May 2014, p. 92-94. doi:10.18429/JACoW-IPAC2015-MOPWA008

ISBN: 978-3-95450-240-0 ISSN: 2673-5539 doi:10.18429/JACoW-RuPAC2021-WEPSC08

VACUUM CONDITION SIMULATIONS FOR VACUUM CHAMBERS OF SYNCHROTRON RADIATION SOURCE

S. M. Polozov[1], V. S. Dyubkov[1], V. L. Shatokhin[1], A. S. Panishev, National Research Nuclear University MEPhI (Moscow Engineering Physics Institute), Moscow, Russia
[1]also at National Research Center «Kurchatov Institute», Moscow, Russia

Abstract

Analysis of gas loads for the vacuum system chambers of the 6GeV synchrotron radiation (SR) source are carried out. The main source of gas loads is the photostimulated desorption induced by SR. The influence of storage ring lattice, geometric dimensions and beam parameters on the vacuum conditions in SR-source prototype chambers is studied. The geometric model of the storage ring chamber designed for simulation is considered. The simulation of the radiation flux parameters generated by the charged particles passing through the section of the vacuum chamber has been performed. The technique of calculating the parameters of SR and photostimulated desorption by means of Synrad+ and Molflow+ codes is applied.

MODELING METHODS

During the operation of the SR-source, an intense flux of photon radiation is generated inside the storage ring. Most of this radiation will fall on the inner surface of the vacuum chambers, which leads both to an increase in thermal loads and to the appearance of synchrotron-stimulated desorption. In order to reduce the negative effects of incident radiation, special absorbers are installed in places with a high radiation load. The main part of the heat load is removed with their aid. They are made from a copper alloy (for example CuCrZr) and water cooling is provided in their design. With the change in the parameters and the storage ring geometry, the characteristics of the radiation flux density distribution in separate sections of the vacuum chambers will also change. The parameters of the vacuum system and absorbers must be calculated for these changes.

It is necessary to determine the relationship of changes in SR parameters with new requirements for radiation absorbers. Approaches to determining the characteristics of the radiation flux in the storage ring of the SR-source are considered. For this aim the capabilities of the SynRad + software module and its joint use with the Molflow + package for numerical simulation of accelerator complexes vacuum systems were studied [1].

Synrad+ [2] is a program for determining the parameters of the SR incident on the chambers walls (radiation flux, power, spectrum) by the Monte Carlo method. It calculates the power distribution of the synchrotron radiation incident on the surface. The use of this program in one package with Molflow+ makes it possible to calculate the desorption gas flow from the inner surface of the chambers by SR distribution. Thus, it is possible to determine the effect of changes in the storage ring geometry and optical system parameters on the vacuum level.

VACUUM SYSTEM

ESRF-EBS research accelerator complex, 4th generation synchrotron radiation source was taken as a prototype of the designed SR-source - Ultimate Source for Synchrotron Radiation (USSR, formerly known as “SSRS-4”).

Improvement of the developed SR source parameters, such as high spatial coherence and brightness, required changes in the magnetic system of the facility. This, in turn, led to a change in the lengths of individual sections of the storage ring and vacuum chambers. The structure of the projected SR-source vacuum system was designed. The storage ring perimeter includes identical standard cell sections with identical vacuum chambers (see Fig. 1).

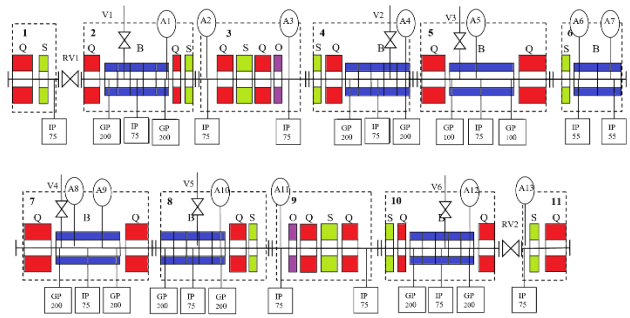

Figure 1: Standard cell: vacuum chambers 1-11, vacuum pumps IP and GP, absorbers A1-13.

Taking into account the change in the geometric parameters of the storage ring, the pressure profiles on the beam axis were modelled (see Fig. 2). There is an insignificant increase in pressure in the region of the chambers length increasing. This is due to an increase in the chambers walls surface area and a slight increase in the total thermal outgassing.

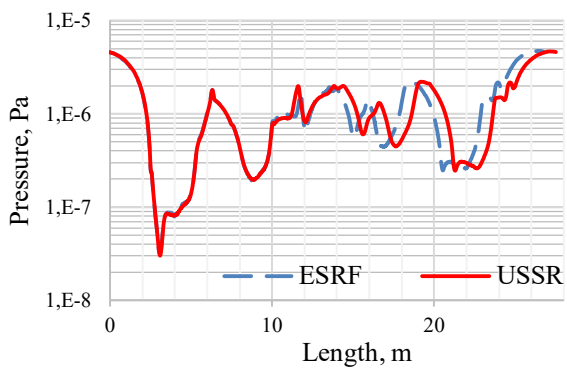

Figure 2: Influence of geometry changes.

ISBN: 978-3-95450-240-0 ISSN: 2673-5539 doi:10.18429/JACoW-RuPAC2021-WEPSC08

Additionally, the stability of the SR-source vacuum system to the dynamic growth of the gas load from the absorbers surface was evaluated. Different levels of the absorbers gas desorption in the three central chambers of the section were simulated (the boundaries of the chambers in Figure 3 are marked with dashed lines). The results of a proportional increase in pressure in the selected areas are explained by the dominant role of stimulated desorption from the absorbers surfaces in comparison with the background gas load from the inner surfaces of vacuum chambers that are not exposed to radiation.

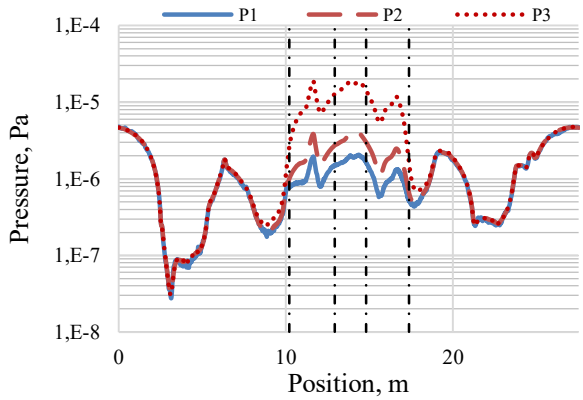

Figure 3: Pressure in the standard cell with different levels of absorbers outgassing; P1 – no changes, P2 – 2x gas desorption, P3 – 4x gas desorption.

SYNCHROTRON RADIATION

The method of modelling the characteristics of synchrotron radiation and photo-stimulated desorption was studied. For one cell of the prototype storage ring [3] simulation of the electron beam passage through the structure of the accelerator is performed. The influence of the SR flux power, generated by the bending magnet DL1, on the stimulated gas desorption of absorbers was investigated.

According to the technical description of the ESRF-EBS storage ring [3], the parameters of the electron beam (see Fig. 4) and the magnetic system (see Table 1) were determined.

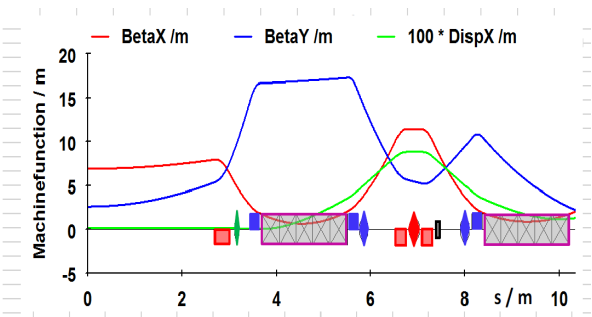

Figure 4: Beam property.

Table 1: Magnet System

Type	Symbol	Magnetic field, T	Length, м
drift			2,7
quadrupole	QF1	50,8	0,295
drift			1,02
quadrupole	QD1	-53,413	0,212
drift			0,37
dipole	DL1-1	0,62481	0,3804
dipole	DL1-2	0,4113	0,3504
dipole	DL1-3	0,30169	0,3573
dipole	DL1-4	0,22665	0,365
dipole	DL1-5	0,16731	0,3722
drift			0,37
quadrupole	QD3	-48,0415	0,162
drift			0,75
sextupole	SD1	-568,898	0,166

Applying Optics Builder [4] this data was added to the calculation model. The synchrotron radiation was generated by a 6 GeV electron beam with a current of 200 mA. The distribution of the absorbed SR flux is obtained for all radiation absorbers located in the selected area. The absorbed power density was on average up to 160 W/cm^2, and for some absorbers it was up to 278 W/cm^2.

The calculation results for the incident SR flux were exported from Synrad+ to Molflow+. Through the stimulated desorption coefficient, the SR power distribution was transformed into a stimulated desorption stream from the surface of the absorbers. For a radiation dose of 100 Ah, the level of gas desorption from these surfaces was $8 \cdot 10^{-8}$ - $6 \cdot 10^{-7}$ mbar·l/s·cm^2. The desorption value for other sections of the vacuum chambers was 10^{-11} mbar l/s cm^2. The obtained outgassing values were compared with the technical data of the prototype parameters [3] (see Table 2).

Table 2: Stimulated Desorption

Absorber	ESRF, mbar·l/s	model, mbar·l/s
ABS CH2-1-1	1.05e-07	8.2E-08
ABS CH3-1-1 Crotch	6.39e-07	9.9E-07
ABS CH4-1-1	3.94e-07	1.7E-07
ABS CH5-1-1	4.03e-07	6.2E-07
ABS5-1-1 H9	1.07e-08	1.3E-08
ABS5-1-1 H11	3.47e-08	9.6E-08

The considered modeling technique was also used in the further calculation of the designed SR source parameters.

The calculation of the generated radiation parameters for the bending magnet of the camera № 2 (DL1) has been carried out for the designed facility and for the prototype on the nominal operating parameters. Comparison of the results is necessary to assess the effect of changes in the characteristics of the magnet system.

ISBN: 978-3-95450-240-0 ISSN: 2673-5539 doi:10.18429/JACoW-RuPAC2021-WEPSC08

For each option, a computational model was created and the total power and angular distribution of the radiation generated by the electron beam when passing through the magnet were calculated (see Fig. 5). The absorption of the generated SR radiation by a section of the vacuum surface - a rectangular face 80x25 mm in size, located 50 mm from the exit from the magnet was simulated.

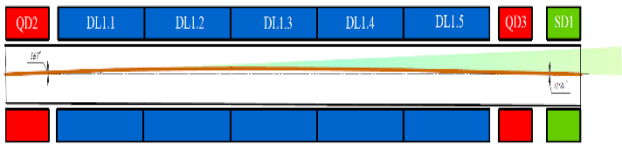

Figure 5: Synchrotron radiation of a bending magnet DL1.

Figures 6,7 and 8 show the results of the density and SR spectrum calculation for the prototype model and for the model of the constructing SR-source.

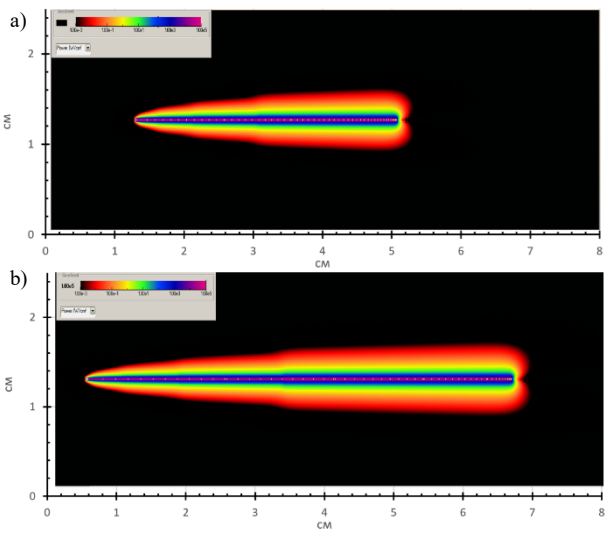

Figure 6: Synchrotron radiation of a DL1 dipole magnet, a) ESRF-EBS; b) USSR.

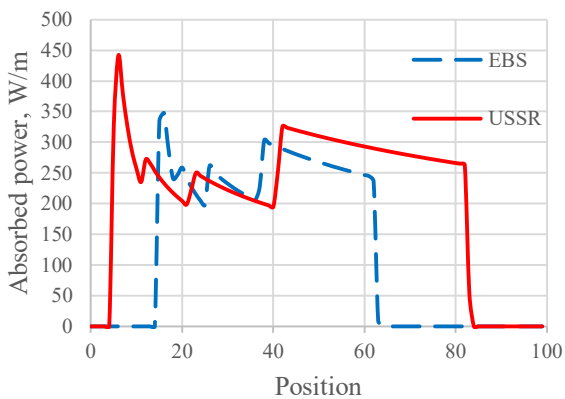

Figure 7: Linear distribution of absorbed power.

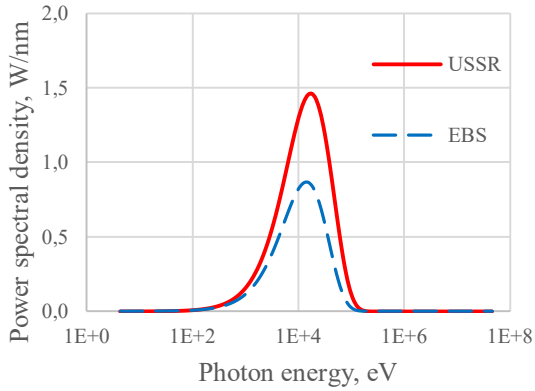

Figure 8: Spectrum of incident radiation.

The obtained results for the designed SR-source were compared with the calculation for the ESRF-EBS prototype. An increase in the length of the storage ring section and of the magnet field magnitude in the magnet sectors, together with a decrease in the beam emittance, led to an increase in the horizontal radiation angle and to an increase in SR power. Therefore, it will require clarification of the absorbers parameters and vacuum equipment.

CONCLUSION

The simulating model of the SR parameters and synchrotron-stimulated desorption based on the Monte Carlo method is considered. A modification of the magnet and vacuum systems elements dimensions and of the beam parameters will lead to different conditions for the radiation flux passage in the new geometry of the SR-source storage ring. Under these conditions, it will be necessary to design a new structure for the distribution of absorbers across the chambers, making changes to their design. It is also possible that the issues of correcting pumping systems will need to be considered.

REFERENCES

[1] M. Ady, R. Kersevan, "Recent developments of Monte-Carlo codes MolFlow+ and SynRad+", in Proc. *10th Int. Particle Accelerator Conf. (IPAC'19)*, Melbourne, Australia, May 2019. doi:10.18429/JACoW-IPAC2019-TUPMP037

[2] Synrad+ A Monte-Carlo Simulator package, CERN https://molflow.web.cern.ch/content/about-molflow

[3] ESRF Upgrade Program Phase II (2015-2022) - "EBS Storage Ring Technical Report", 2018.

[4] Optics Builder documentation, https://molflow.web.cern.ch/content/opticsbuilder-documentation

ISBN: 978-3-95450-240-0 ISSN: 2673-5539 doi:10.18429/JACoW-RuPAC2021-WEPSC10

OPTIMIZATION OF ACCELERATORS VACUUM STRUCTURES PUMPING

S. M. Polozov, A. S. Panishev, V. L. Shatokhin, National Research Nuclear University MEPhI (Moscow Engineering Physics Institute), Moscow, Russia

Abstract

The pumping features for the complex parts of the accelerator vacuum system are modelled to growth the efficiency of vacuum pumping. The vacuum system of a 7.5 MeV/nucleon proton and light ion (A/Z<3.2) accelerator-injector was considered. The Monte Carlo method is suitable for molecular flow modelling in high vacuum. The Molflow+ program was used for this aim. The pressure distribution simulation over the RFQ, IH resonators chambers volume, connecting vacuum pipes and extended vacuum tracts is carried out. The influence of parameters of individual structural elements changes was investigated to define the vacuum conditions inside the accelerators vacuum chambers. The vacuum system configuration and parameters are selected basing on these results to obtain the required vacuum level.

VACUUM SYSTEM FEATURES

Molflow+ software package is used to determine the parameters of the linear accelerator vacuum equipment. This is a Monte Carlo simulator intended to calculate pressure profiles and conductance in ultra-high vacuum [1].

To determine the characteristics of the vacuum it is necessary to specify the geometry of the internal vacuum surfaces, gas loads and the parameters of the pumping equipment in the simulation model.

The vacuum requirements are determined by the allowable degree of the beam destruction via capture and loss of electrons, nuclear reactions, Coulomb scattering due to the interaction with residual gas. Based on the loss evaluation the pressure along the channel, providing a stable ion beam passing through the structure should be of the order of 10^{-5} Pa. At this pressure the molecules will move independently of each other and the simulation of these conditions by the statistical tests method is possible.

In stationary conditions, the molecules desorption from the vacuum chambers walls is the main source of pumping gas loads. The value of thermal outgassing is chosen 10^{-6} Pa·m^3/s·m^2, which is typical for the initial level of vacuum constructional materials outgassing.

The sections of the linear accelerator structure are independent vacuum systems separated by insulating vacuum gates. This includes ion sources, RFQ section, beam transport sections at low energy LEBT, medium MEBT1, 2 and high HEBT, H-type resonator sections IH1, 2 (see Fig. 1).

VACUUM PORT

The vacuum pumps are connected to the resonator chambers using vacuum ports (see Fig. 2).

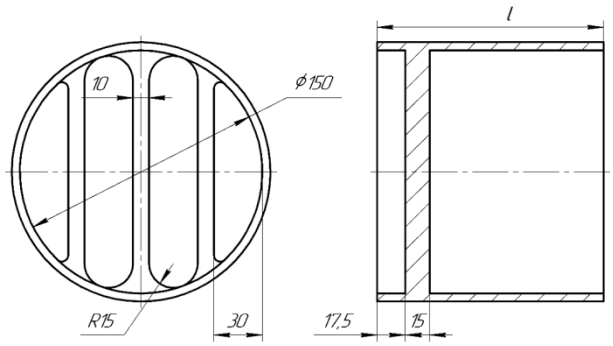

Figure 2: Vacuum port diagram.

Grilles are installed in ports to limit the penetration of microwave power outside the resonator chamber. Vacuum valves are also attached. These construction features affect the vacuum conductivity and reduce the efficient pumping speed. Their conductivity was modelled in the operating mode. The conductivity of the DN 150 port with RF grill according to the simulation results is shown in Table 1.

Table 1: Port conductivity Values

Port height *l*	Conductivity
55 mm	1050 l/s
75 mm	990 l/s
100 mm	911 l/s

RFQ CHAMBER

The model of the RFQ resonator vacuum chamber was used to calculate the pressure distribution along the beam axis and over the volume of the resonator chamber. Vacuum surface model for Molflow+ created from CAD 3D model of the resonator chamber with internal electrodes, plungers, vacuum and RF ports (see Fig. 3).

Figure 1: Block diagram of linear accelerator sections.

ISBN: 978-3-95450-240-0 ISSN: 2673-5539 doi:10.18429/JACoW-RuPAC2021-WEPSC10

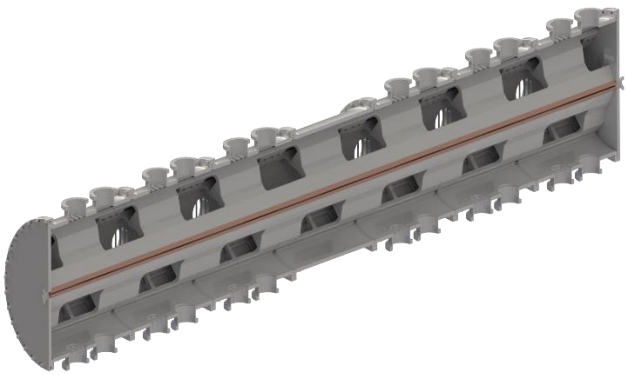

Figure 3: RFQ model.

The influence of the conductivity of internal cavities configuration in the electrode structure on the pressure distribution uniformity over the cavity volume was estimated. Situations with connection of pumps to the vacuum port in various quantities and configurations were simulated. Fig. 4 demonstrates the pressure distribution profile along the resonator axis with full pumping through all resonator ports with 300 l/s pumps. The inner surface of the resonator with a total area of about 34 m^2 is copper coated. The calculated pressure was up to $1.3 \cdot 10^{-5}$ Pa, while its relative fluctuations are insignificant.

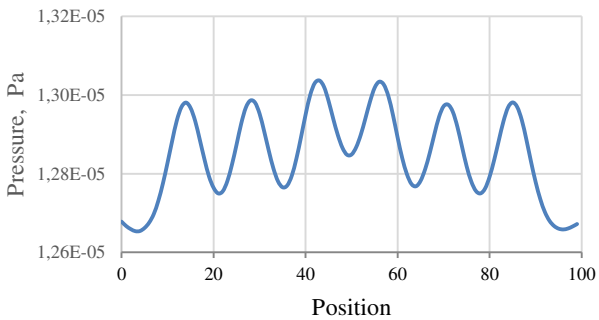

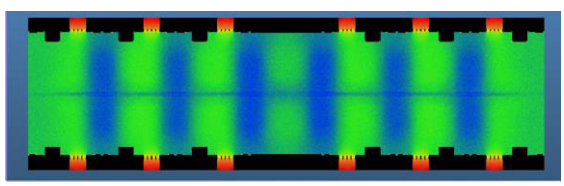

Figure 4: RFQ pressure profile.

When 6 pumps were turned off on one side of the resonator, the total pressure increased due to a decrease in the effective pumping speed, however, no significant disruption of the pressure uniformity in the resonator was observed. It can be seen that the slotted electrodes have good molecular conductivity. Various pump connection schemes can be used. For example, when using the combination of TMP and IP pumps (see Fig. 5). According to this scheme, the TMP provides pumping of significant dynamic gas loads and can be stopped in stationary pumping regime. IP pumps keep vacuum conditions at low thermal gas flows.

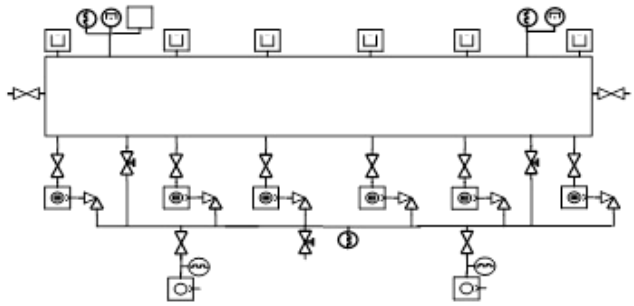

Figure 5: RFQ vacuum system.

H-TYPE RESONATOR SECTIONS

The design of the vacuum section with H-type resonators consists of several resonators and intermediate channels between them. Models of vacuum surfaces were also created from a CAD 3D model of the resonator chamber with internal equipment of electrodes, plungers, vacuum and RF ports (see Fig. 6).

Figure 6: H-type resonator model.

Using a model of a vacuum system of resonators the pressure distribution along the beam axis was calculated on the resonator chambers and intermediate pipelines. Based on the symmetry of the structure, a section with a resonator and adjacent channels was considered as a model. A resonator with two half-length sections of pipes on each side was taken (see Fig. 7).

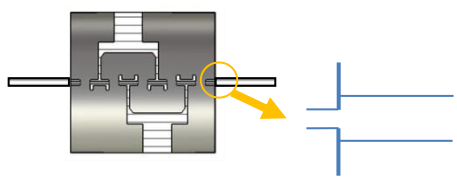

Figure 7: Output channel diagram.

There was an increase in pressure in the connecting pipeline between the resonators (see Fig. 8, a). This is explained by the design feature of the electrode at the inlet tract to the resonator. The channel in the inlet electrode has a very low conductivity (about 5 l/s). In aim to reduce this effect, the analysis of gas flows at the resonator inlet depending on the pumping speed was carried out on the calculation model. Various forms of the electrode that can increase its conductivity are considered. Models of channels with straight bore internal (see Fig. 8, b) diameter and cone bore (see Fig. 8, c) reduced the pressure in the pipeline.

ISBN: 978-3-95450-240-0 ISSN: 2673-5539 doi:10.18429/JACoW-RuPAC2021-WEPSC10

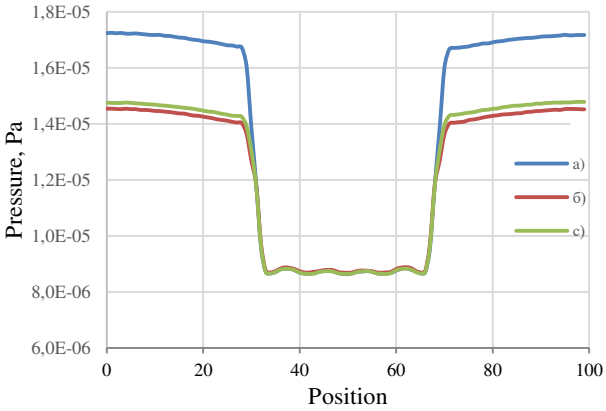

Figure 8: Pressure distribution along the axis of the resonator and pipelines.

In addition, the possibility of reducing outgassing flows by reducing the pipeline internal surface area was considered. The dependence of the pressure in the connecting pipeline on its diameter is investigated. Taking into account the considered factors, possible variants of the pumping scheme with a combination of high-vacuum pumps types were proposed. Pumping is modeled for each structure and pressure distribution profiles in the structures along the beam path are obtained (see Fig. 9).

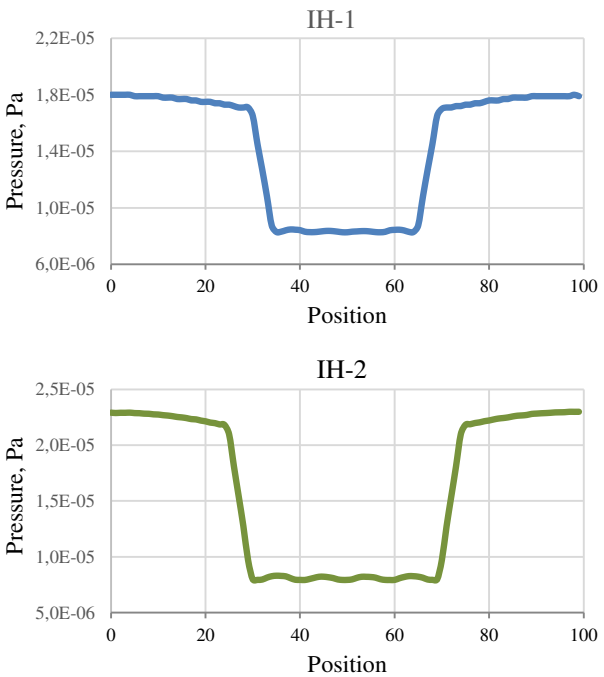

Figure 9: Pressure in H-type resonators and pipelines.

BEAM TRANSPORT CHANNELS

The conditions of pumping of bunchers vacuum chambers and extended beam transport channels were studied separately. For bunchers chambers pumping a system with local vacuum groups are proposed. The pipelines length of LEBT and MEBT channels is relatively small. This made it possible to pump them out through the diagnostic chambers and bunchers resonators.

Modelling has been used to optimize the connection period of IP pumps in HEBT channels. The modelled results were compared with the analytical calculation data. Taking into account the selected distance between the pumps of about 2 m, a model of the vacuum channel was compiled and the pressure distribution along all sections of the channel was obtained (see Fig. 10).

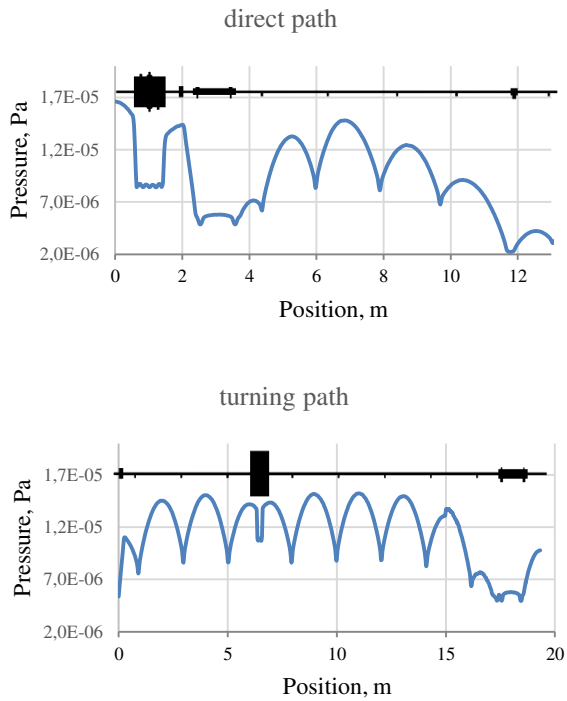

Figure 10: Pressure distribution in the HEBT channels.

CONCLUSION

Based on the results of pumping simulation in the Molflow+ program, pressure distributions were obtained for different resonators structures, and the influence of the pumps location on the pressure profiles was investigated. The selected vacuum schemes and the efficiency of the pumping equipment allow us to provide the necessary vacuum conditions in all sections of the designed accelerator. The presence of local pressure increases is not critical, this small increase will not affect the beam passing.

REFERENCES

[1] Molflow+ A Monte-Carlo Simulator package, CERN. https://molflow.web.cern.ch/content/about-molflow

ISBN: 978-3-95450-240-0 ISSN: 2673-5539 doi:10.18429/JACoW-RuPAC2021-WEPSC12

PRELIMINARY CALCULATION OF THE POWER COUPLER FOR THE SYLA STORAGE RING RF CAVITY

S. V. Matsievskiy*, M. A. Gusarova, M. V. Lalayan, Ya. V. Shashkov
NRNU MEPhI, Moscow, Russia and NRC KI, Moscow, Russia

Abstract

Several new accelerator facilities will be built in Russia in the next few years. One of those facilities is a 6 GeV storage ring light source, the Ultimate Source of Synchrotron Radiation to be built in Protvino, near Moscow.

This paper considers storage ring RF cavity power coupler design issues and provides preliminary calculations of the device.

INTRODUCTION

6 GeV Ultimate Source of Synchrotron Radiation is planned to be built in Protvino, Russia. Storage ring scheme is based on the ESRF-EBS design [1]. Thus, many design patterns are copied from the aforementioned project, including the RF system, consisting of a number of a mono-cell normally conducting HOM-damped cavities (HOM mitigation is discussed in other paper in this conference) [2].

Cavity properties are presented in Table 1. Continuations were carried out for the accelerating voltage value for all cavities $V_{cav\ all} = 3$ MV.

Table 1: RF Cavity Properties

Property	Value
f, MHz	357
Q, $\times 10^3$	41
$R_{sh\ eff}$, MΩ	10
W_{rad}, MeV turn^{-1}	3
I_{beam}, A	0.25

POWER COUPLER

RF cavity with the attached magnetic loop is presented in Fig. 1.

Calculation of the generator power P_g and coupling coefficient β was done by using conventional equations for cavity voltage [3]

$$V_{cav} = \frac{2\sqrt{P_g}\sqrt{R_{sh\ eff}}\sqrt{\beta}\left(-\frac{I_{beam}\sqrt{R_{sh\ eff}}}{2\sqrt{P_g}\sqrt{\beta}}+1\right)}{\beta+1} \quad (1)$$

and optimal coupling [4]

$$\beta = \left(\frac{I_{beam}\sqrt{R_{sh\ eff}}}{2\sqrt{P_g}} + \sqrt{\frac{I_{beam}^2 R_{sh\ eff}}{4P_g}+1}\right)^2. \quad (2)$$

* svmatsiyevskij@mephi.ru

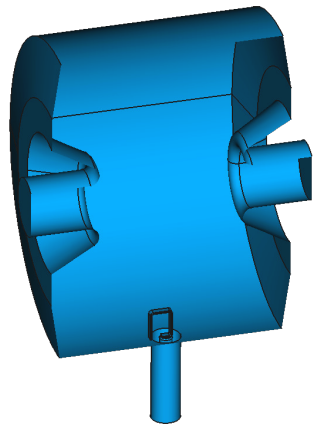

Figure 1: RF cavity with coupling loop.

Substituting Eq. (2) into (1) yields a simple equation for the optimally coupled cavity supply power

$$P_g = \frac{V_{cav}\left(I_{beam}R_{sh\ eff} + V_{cav}\right)}{R_{sh\ eff}}. \quad (3)$$

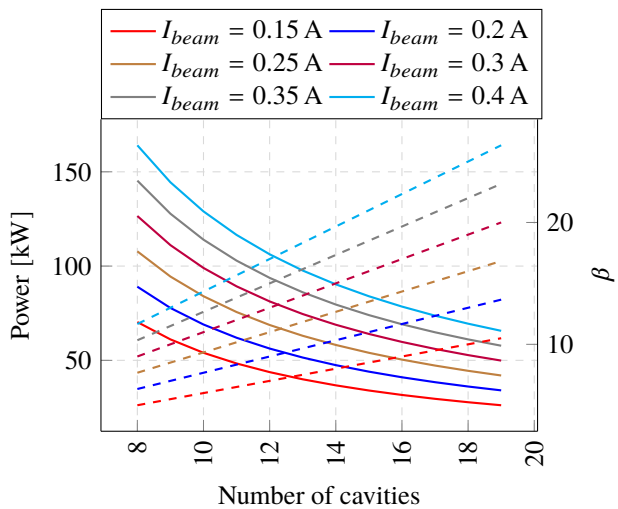

Figure 2: Optimal supply power (solid lines) and coupling coefficient (dashed lines) for different number of cavities.

Equation (3) was used in calculation of Fig. 2. For the operation under 100 kW number of cavities should be greater then 9. Considering a possible cavity failure and operation under higher current a number of cavities in the ring was chosen $N = 14$. Further calculations were done for the constant coupling coefficient value β corresponding to the beam current $I_{beam} = 0.25$ A.

ISBN: 978-3-95450-240-0 ISSN: 2673-5539 doi:10.18429/JACoW-RuPAC2021-WEPSC12

Solving Eq. (1) for P_g yields the equation for the cavity supply power with the fixed coupling coefficient

$$P_g = \frac{I_{beam}V_{cav}}{4\beta}\left(\frac{I_{beam}R_{sh\,eff}}{V_{cav}} + 2\beta + 2\right) + \\ + \frac{V_{cav}^2}{4R_{sh\,eff}}\left(\frac{1}{\beta} + \beta + 2\right). \quad (4)$$

Using this equation cavity power balance was calculated (Fig. 3). In this figure RF cavity power loss was determined using the conventional shunt impedance equation $R_{sh\,eff} = V_{cav}^2/P_{loss}$ and the conservative one $R_{sh\,eff} = V_g^2/P_{loss}^*$. Filled regions on the plot represent difference between the two. Based on the obtained value of generator power P_g standard CF50 flange was chosen as a power coupler interface.

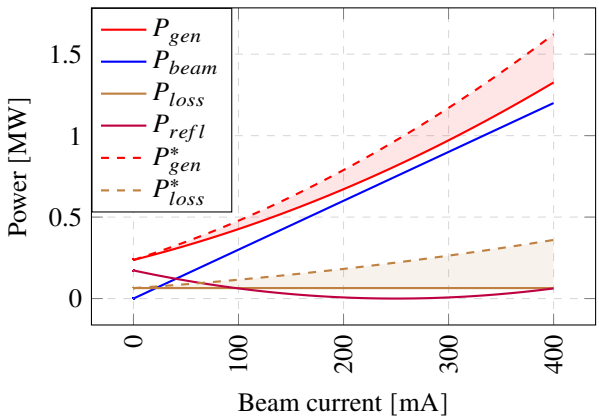

Figure 3: Cavity power balance. Filled regions represent difference between precise values of P_g and P_{loss} and the conservative ones P_g^* and P_{loss}^*.

For the model presented in Fig. 1 dependence of the coupling coefficient β on the magnetic loop immersion depth is shown in Fig. 4.

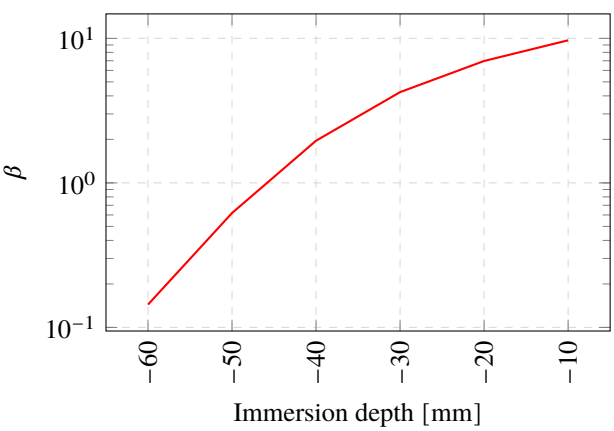

Figure 4: Coupling coefficient over the magnetic loop immersion depth.

RF WINDOW

One of the big concerns for the power supply system is the ceramic RF window. Such a window with a 6 mm alumina ceramic disc was designed and matched. Reflection from the device in frequency range is shown in Fig. 5.

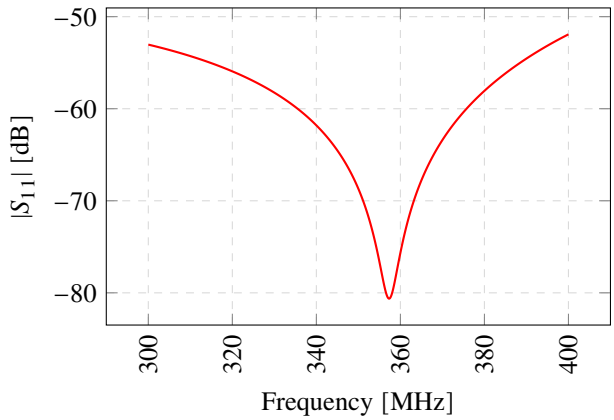

Figure 5: RF window reflection coefficient.

Temperature in the ceramic window was calculated for the CW operational regime with the 140 kW of the transmitted power (Fig. 6). For the simulation temperatures of the inner and outer conductors of the regular line were fixed. Convectional cooling from the atmosphere side was assumed. Even in this case the temperature of the ceramic window is quite large and exceed 380 K.

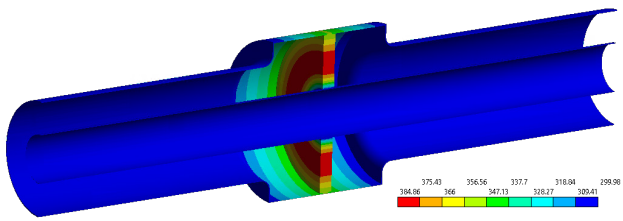

Figure 6: RF window temperature.

Not surprisingly, high temperature gradient lead to the high mechanical stress in the ceramics. It is shown in Fig. 7.

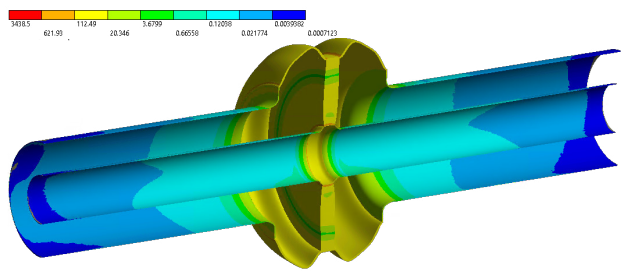

Figure 7: RF window mechanical stress.

For the alumina ceramics mechanical safety factor is shown in Fig. 8. The dangerous values of $f_S < 5$ may be observed on the ceramics inner connection ring, which has high probability of failure. Therefore, lowering the ceramics

ISBN: 978-3-95450-240-0 ISSN: 2673-5539 doi:10.18429/JACoW-RuPAC2021-WEPSC12

temperature is necessary. One of the possible solutions is to use beryllium based ceramics, which has lower RF losses and higher heating transfer coefficient, but is very toxic.

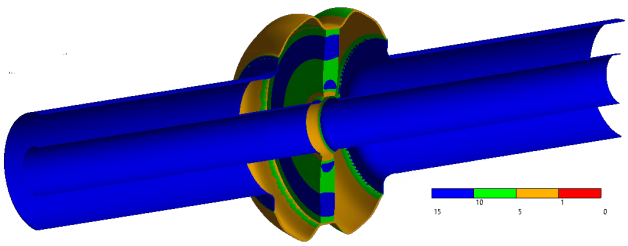

Figure 8: RF window safety margin.

CONCLUSION

In this paper power coupler preliminary calculations were carried out. Number of RF cavities was chosen $N = 14$, CF50 vacuum flange was selected as an RF coupler interface.

Simulation of the simplified RF window model was done. It showed an excessive temperature on the ceramics window, which lead to the unacceptably large mechanical stress in the copper to ceramics brazing region. Usage of the beryllium based ceramics is currently under consideration.

REFERENCES

[1] L. Hoummi *et al.*, "Optimization and error studies for the USSR HMBA lattice," in *Proc. IPAC'21*, (Campinas, SP, Brazil), paper MOPAB224, May 2021 DOI: 10.18429/JACoW-IPAC2021-MOPAB224.

[2] L. Farvacque, Ed., *ESRF-EBS design report*, 2018.

[3] P. V. Wilson, "High energy electron linacs: Applications to storage ring RF systems and linear colliders," SLAC, Accelerator Center, SLAC, 2575 Sand Hill Rd., Menlo Park, CA 94025, USA, Nov. 1991. https://www.slac.stanford.edu/pubs/slacpubs/2750/slac-pub-2884.pdf

[4] V. I. Kaminskii, N. P. Sobenin, and M. V. Lalayan, *Uskoryayushchiye struktury*. 2005, 294 pp., (in Russian), ISBN: 5-7262-0588-X.

ISBN: 978-3-95450-240-0 ISSN: 2673-5539 doi:10.18429/JACoW-RuPAC2021-WEPSC13

ACCELERATING CAVITIES WITH HOM DAMPING FOR USSR-4 STORAGE RING

N.Yu. Samarokov, Ya.V. Shashkov[1†], M.V. Lalayan[1], M.A. Gusarova[1],
NRNU MEPhI, Moscow, Russia,
[1]also at NRC KI, Moscow, Russia

Abstract

Preliminary results on accelerating cavities for USSR-4 facility (also known as SYLA - SYnchrotron and free-electron LAser) project are presented. This facility is under development by collaboration hosted by National Research Center "Kurchatov Institute". SYLA is synchrotron radiation facility based on injector linac and 6 GeV storage ring. Beam energy loss in storage ring is to be compensated by several modified pillbox cavities. Cavity geometry features, its operation frequency choice and induced HOM parameters are discussed. HOM damping technique using corrugated cylindrical waveguides were studied. Longitudinal impedance values of HOM are presented for initial accelerating cavity and structure with waveguides.

INTRODUCTION

6 GeV Ultimate Source of Synchrotron Radiation is planned to be built in Russia. Storage ring scheme is based on the ESRF-EBS design [1-3]. For sources of synchrotron radiation, large values of beam currents are required. Excitation of Higher order modes (HOM) can lead to multibunch instabilities, emittance growth, beam breakup, etc. [4,5].

The general view of the accelerating cavity with an operating frequency of 357 MHz is shown in Fig. 1.

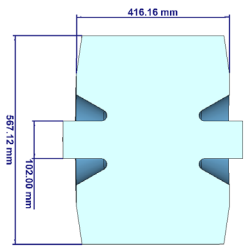

Figure 1: General view of an accelerating cavity at 357 MHz.

For an accelerating cavity the electrodynamic characteristics (EDC) [6] of the fundamental mode (Table 1) and HOM were carried out [7].

Table 1: EDC of Accelerating Cavity

EDC	Values
f, MHz	357
Q, $\times 10^3$	41
$R_{sh\ eff}$, MΩ	10

The frequency dependence of the longitudinal shunt impedance for monopole HOMs is shown in Fig. 2.

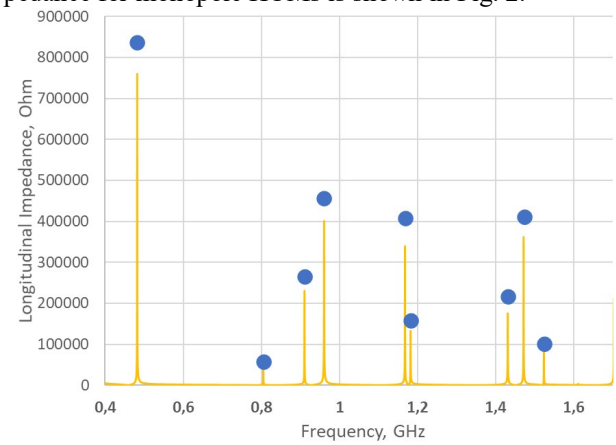

Figure 2: Frequency dependence of the longitudinal shunt impedance for monopole modes for an accelerating cavity at 357 MHz. Graph – result of wakefield simulations, dots – results of eigenmode simulations.

From Fig. 2 one could see that that the shunt impedance of parasitic HOMs accelerating cavity can reach values of up to 10^6 Ohm.

One of the requirements for EBS-ESRF cavity design was to ensure unconditional beam stability up to currents of 1000 mA. For EBS-ESRF longitudinal coupled bunch instability threshold at 200 mA is $R_{HOM} \cdot f_{HOM} = 16$ kW·GHz (Fig. 3) [4].

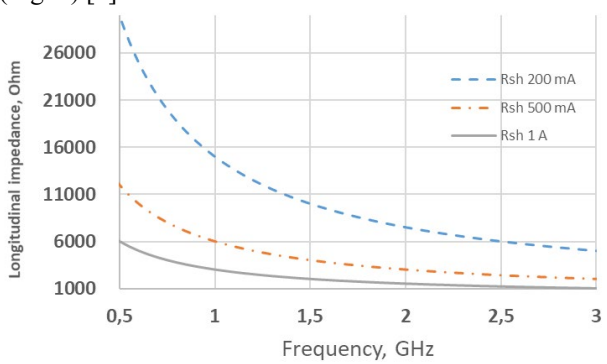

Figure 3: Threshold for longitudinal impedance necessary for unconditional beam stability for 200, 500 and 1000 mA beam current.

From Fig. 2 and 3 we can see that it is necessary to significantly decrease the shunt impedance values of HOMs. To reduce these values, it is proposed to add HOM couplers to the system.

† yvshashkov@mephi.ru

ISBN: 978-3-95450-240-0 ISSN: 2673-5539 doi:10.18429/JACoW-RuPAC2021-WEPSC13

HOM DAMPING USING CORRUGATED WAVEGUIDES

As a baseline design for HOM damping it is proposed to use the design options applied in BESSY and ESRF (Fig. 4) [8]. This design assumes three corrugated waveguides for power output, located at an angle of 120 degrees with respect to each other. The presence of three waveguides is a prerequisite for damping all polarizations of higher order modes [9,10].

Figure 4: Accelerating cavity of the BESSY accelerator (left) and ESRF (right).

In such systems, dipole and parasitic monopole mode will excite an TE11-type mode in the waveguide (Fig. 5). The cutoff frequency should be above 357 MHz (to prevent fundamental mode damping) but below 442 MHz (first monopole frequency). The height of the corrugation ribs and the diameter of the waveguide will determine the cut-off frequency of the TE11 mode (the rest of the parameters have no significant effect on this parameter).

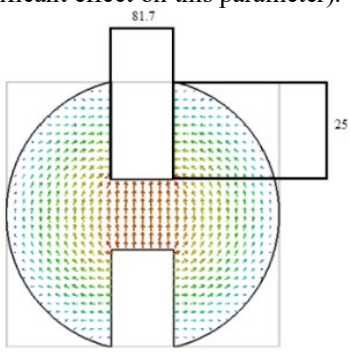

Figure 5: Distribution of TE11 mode electric field in a corrugated cylindrical waveguide.

The graph of the dependence of the cutoff frequency of the TE11 mode on the outer radius of the waveguide, as well as the height and width of the corrugation, is shown in Fig. 6.

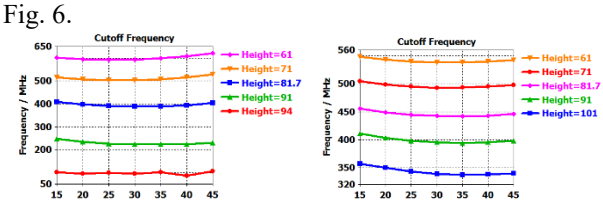

Figure 6: Dependence of the cutoff frequency of the TE11 mode on the outer radius of the waveguide, as well as the height and width of the corrugation.

The waveguide diameter is 220 mm, the corrugation height is 81.7 mm, and their thickness is 25 mm, since with these parameters the cutoff frequency is 437 MHz.

The lengths of the HOM dampers are dimensioned such that the non-propagating decaying fields at 357 MHz are sufficiently low at the HOM absorbers not to affect the quality factor of the accelerating mode (Fig. 7).

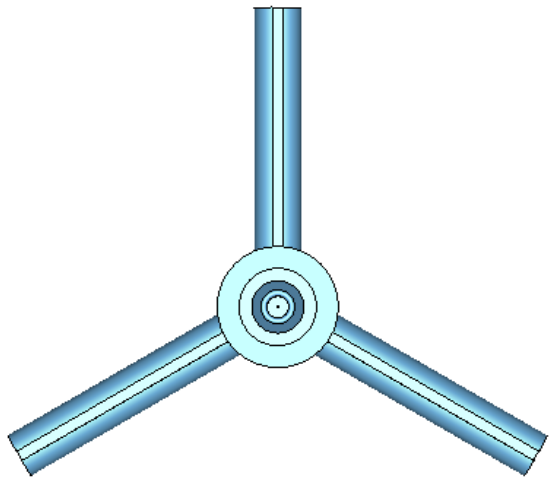

Figure 7: General view of an accelerating cavity with three HOM output devices.

The dependence of the longitudinal and transverse shunt impedance for monopole and transverse modes of oscillations on frequency for an accelerating cavity at 357 MHz with HOM waveguides and a comparison of the damping results are presented in Fig. 8.

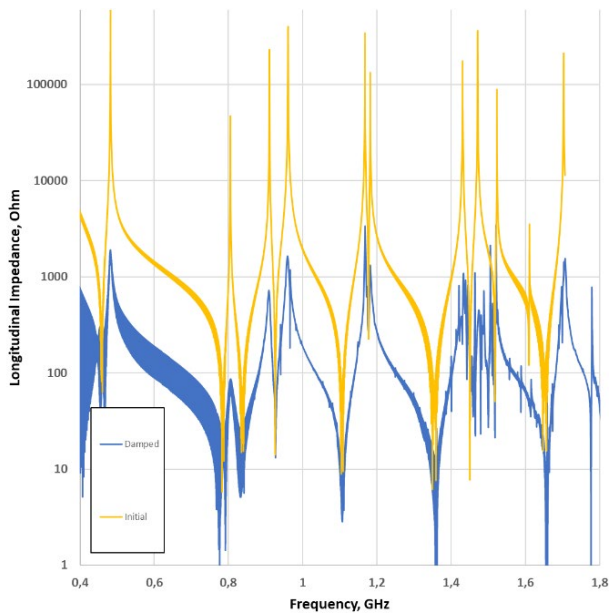

Figure 8: Comparison of the longitudinal shunt impedance for monopole HOMs for an initial accelerating cavity and with HOM waveguides.

From Fig. 8 we can see that longitudinal impedance values of HOMs were reduces by 2-3 orders of magnitude.

Comparison of longitudinal shunt impedance for monopole HOMs for accelerating cavity with HOM waveguides

ISBN: 978-3-95450-240-0 ISSN: 2673-5539 doi:10.18429/JACoW-RuPAC2021-WEPSC13

with threshold longitudinal shunt impedance values necessary for unconditional beam stability for 200, 500 and 1000 mA presented on Fig. 9.

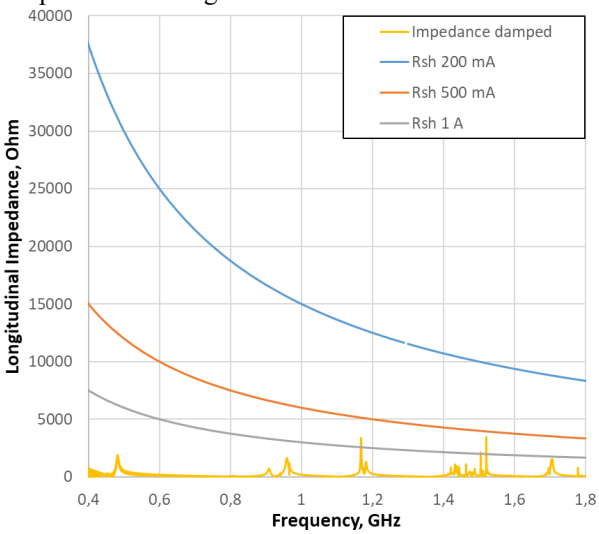

Figure 9: Longitudinal shunt impedance for monopole HOMs for accelerating cavity with HOM waveguides and threshold longitudinal shunt impedance values necessary for unconditional beam stability for 200, 500 and 1000 mA.

From Fig. 9 we can see that achieved impedance values satisfy conditions for unconditional beam stability for currents up to 500 mA. However, it is necessary to conduct further studies in order to achieve stability up to 1000 mA. Field distributions of HOMs that exceed 1000 mA threshold are presented on Fig. 10.

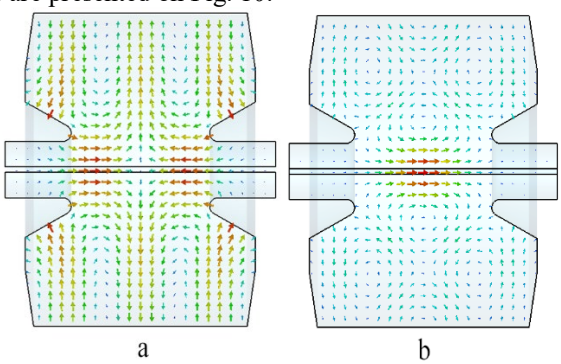

Figure 10: Electromagnetic field distribution of HOMs. (a) – 1168 MHz mode, (b) – 1528 MHz mode.

CONCLUSION

Achieved impedance values satisfy requirements for unconditional beam stability for currents up to 500 mA. However, it is necessary to conduct further studies in order to achieve stability up to 1000 mA. Further research is currently underway.

REFERENCES

[1] L. Hoummi *et al.,* "Optimization and error studies for the USSR HMBA lattice," in Proc. IPAC'21, (Campinas, SP, Brazil), ser. International Particle Accelerator Conference, Aug. 2021, MOPAB224, pp. 730–733, doi:10.18429/JACoW-IPAC2021-MOPAB224.

[2] S.M. Polozov *et al.*, "Current Results of the 4th Generation Light Source USSR (Former SSRS4) Development", presented at the *26th Russian Particle Accelerator Conf. (RUPAC'18)*, Protvino, Russia, Oct 2018, paper MOXMH04.

[3] T.A. Lozeeva, A.S. Fomichev, L.V. Grigorenko, T. Kulevoy, S.M. Polozov, and A.V. Samoshin, "Beam Dynamics Simulation for LINAC-100 - Heavy Ion "Driver" for DERICA Project", presented at the *26th Russian Particle Accelerator Conf. (RUPAC'18),* Protvino, Russia, Oct 2018, paper WEPSB03.

[4] L. Farvacque, Ed., *EBS Storage Ring Technical Report*, 2018

[5] Ya.V. Shashkov *et al.* "Comparison of Higher Order Modes Damping Techniques for 800 MHz Single Cell Superconducting Cavities", *Nucl. Instr. Meth.* A, v. 767, p 271–280, 2014.

[6] N.Sobenin and B.Zverev, "Electrodynamic Characteristics of Accelerating Cavities", Foundation for International Scientific and Education Cooperation. Gordon and Breach Science Publishers S.A. 1999.

[7] S.V. Matsievskiy *et al.,* "Preliminary calculation of the power coupler for the SYLA storage ring RF cavity", presented at the 27th Russian Particle Accelerator Conference (RuPAC 2021), September 2021, paper WEPSC12, this conference.

[8] E. Weihreter, "Status of the European HOM Damped Normal Conducting Cavity", in *Proc. 11th European Particle Accelerator Conf. (EPAC'08),* Genoa, Italy, Jun. 2008, paper THXM03, pp. 2932-2936.

[9] Ya.V. Shashkov *et al*., "Suppression of higher order modes in an array of cavities using waveguides", *Journal of Physics: Conference Series,* Volume 74, p. 116-123, 2016.

[10] Ya. V. Shashkov, A.A. Mitrofanov, N.P. Sobenin, V.L. Zvyagintsev, "Analysis of higher order modes damping techniques in 9 cell cavity with modified drift tubes", *Journal of Physics: Conference Series,* Volume 74, p. 124-131.

ISBN: 978-3-95450-240-0 ISSN: 2673-5539 doi:10.18429/JACoW-RuPAC2021-WEPSC14

BOOSTER RF SYSTEM FIRST BEAM TESTS

A.Yu. Grebentsov, O.I. Brovko, A.V. Butenko, V.A. Gerklotts, A.M. Malyshev, V.D. Petrov, O.V. Prozorov, E. Syresin, A.A. Volodin JINR, Dubna, Russia
A.M. Batrakov, S.A. Krutikhin, G.Y. Kurkin, V.M. Petrov, A.M. Pilan[2], E. Rotov[1], A.G. Tribendis[2], Budker INP, Novosibirsk, Russia
G.A. Fatkin[1], Cosylab Siberia, Novosibirsk, Russia
[1]also at Novosibirsk State University, Novosibirsk, Russia
[2]also at Novosibirsk State Technical University, Novosibirsk, Russia

Abstract

The project NICA is being constructed in JINR, to provide collisions of heavy ion beams in the energy range from 1 to 4.5 GeV/u at the luminosity level of $1 \cdot 10^{27}$ $cm^{-2} \cdot s^{-1}$.

A key element in the collider injection chain is the Booster a cycling accelerator of ions $^{197}Au^{31+}$. The injection energy of particles is 3.2 MeV/u, extraction energy is 600MeV/u.

Two Booster RF stations provide 10 kV of acceleration voltage. The frequency range from 587 kHz to 2526 kHz at the operation of the stations in the injector chain.

The RF stations were fabricated in the Budker Institute of Nuclear Physics. The main design features and parameters of the first beam tests of the Booster RF system are discussed in this paper.

RF SYSTEM

The RF System for Booster consists of two resonators, power amplification cascades, and low-voltage electronic, intellectual controller, and tester module. Main parameters of the RF cavity is presented in Table 1.

Acceleration of particles in the Booster will be made in two stages. The operational frequency range corresponds to 0.5 - 2.5 MHz.

The accelerating cavity is formed by two parts of the short-circuited coaxial lines divided by the accelerating gap (Fig. 1). A vacuum-tight ceramic insulator 6 is installed in the gap. Only the stainless-steel beam pipe and the gap ceramic are under vacuum, the remaining cavity is operated in the air [1].

Table 1: Main Parameters of the RF Cavity

Parameter	Value
Frequency range, MHz	0.5 – 5.5
Gap voltage, kV	5.0
Beam pipe diameter, mm	160
Residual gas pressure, Torr	$< 5.5 \cdot 10^{-11}$
Outside station diameter, m	1.2
Installation length, m	1.4
Real part of conductance at the cavity gap, Ohm	> 1000

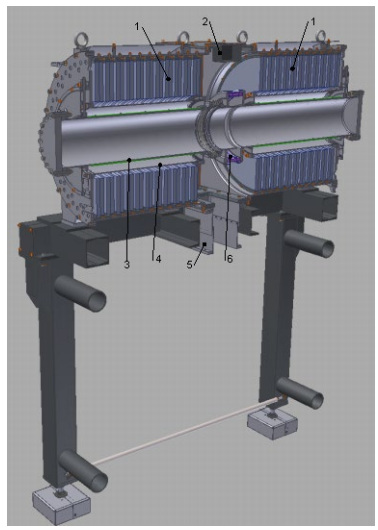

Figure 1: Accelerating cavity of RF station. 1. Amorphous alloy rings, 2. Gap voltage pickup, 3. Beam pipe, 4. Coaxial inner conductor, 5. Connecting nipple, 6. Ceramic insulator.

RF POWER AMPLIFIER

The output stage of the power amplifier employs two tetrodes GU-36B-1. The tubes are driven in the push-pull mode in the common cathodes schematic. Air-cooling of the tubes is used.

The anodes of tubes are connected directly to an accelerating gap of the cavity through the blocking capacitors C_b (Fig. 2).

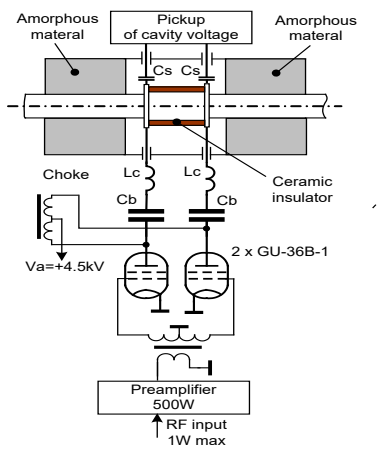

Figure 2: Block diagram of RF power amplifier.

ISBN: 978-3-95450-240-0 ISSN: 2673-5539 doi:10.18429/JACoW-RuPAC2021-WEPSC14

The anode power supply voltage $V_a = +4.5$kV is applied to anodes through the inductance choke. The choke is made of two ferrite rings with dimensions of 180x110x20mm. The magnetic permeability of the rings material is 1000. The type of the used winding also allows suppressing even harmonics of the accelerating voltage at the cavity accelerating gap. A semi-conductor preamplifier with a peak output power of 500 W drives the tubes. The maximum input power of the preamplifier is 1W. During testing of the stations, the maximum output power of the preamplifier does not exceed 200 W [1].

CONTROL SYSTEM

Intellectual Controller for RF stations based on CPU module SAMA5D31-CM. The primary function of the controller is a generation of master frequency for the RF stations which deepens on the current value of the magnetic field. The frequency is generated by 2-channel DDS, each of the channels driving one station. The controller measures a magnetic field using an induction coil and provides corresponding real-time tuning of frequency according to non-linear law with a 20 μs period and better than $2 \cdot 10^{-4}$ relative accuracy.

The controller has DAC's that produce reference voltages to control the accelerating voltage and DC component of anode currents. It also employs ADC's for the measurement of the operating regimes of the stations.

The tester module is used to generate a sequence of events and signals imitating the acceleration cycle. It imitates signals from the magnetic field sensor and necessary synchronization pulses in different acceleration modes.

The tester module is intended to allow regular RF system checks. Additional software for the second Booster run was made to control the RF stations more effectively [2].

ACCEPTANCE TESTS IN DUBNA

Two Booster RF stations were delivered to Dubna in 2014 and tested at the test bench that was built for that reason (Fig. 3).

The project parameters of the RF stations such as output current from the tetrodes and output RF voltage were achieved. After that tests the Booster RF system was installed into the second straight section of the Booster ring and was tested again.

Figure 3: Booster RF station at the test bench in Dubna.

The system was tested in operating modes, the output signals from the first RF station are shown in Fig. 4.

The additional control rack was built to provide safe remote control operating.

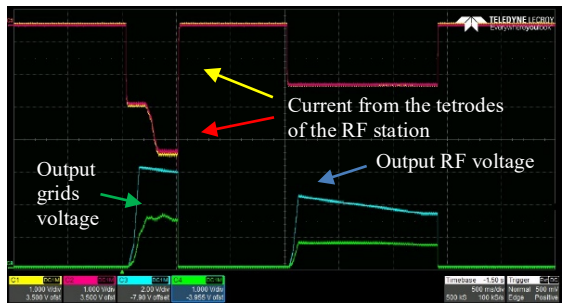

Figure 4: The main parameters of the first Booster RF station during tests.

FIRST EXPERIMENTS WITH ACCELERATING BEAMS IN BOOSTER

The installation of the Booster cryomagnetic equipment was started in September 2018. The first technical Booster run was done in November-December 2020.

At the first steps, the insulating vacuum volume and beam pipe were assembled and tested. After this, the cooling of the cryomagnetic system, commissioning of thermometry, quench protection systems, tuning of power supply, and HILAC-Booster beam transfer line systems were done.

Then the beam was injected into the Booster on the plateau of the magnetic field corresponding to the injection energy. The beam circulation was achieved without the orbit correction system. Turn-by-turn measurements were used for injection optimization. The efficiency of beam injection was achieved at the level of about 75%.

After the orbit correction and tuning of the injection system, the intensity of the circulating beam was achieved up to 7×10^{10} ions or 1.3 mA. The charge of these ions is equal to the charge of 2×10^{9} Au^{31+} ions.

The He^{+} ion lifetime of about 1.3 s corresponds to the average pressure in the beam pipe of about 3×10^{-10} Torr.

The beam current transformer signal at ion acceleration up the energy of 100 MeV/u is shown in Fig.5. The choice of maximal ion energy was defined by the radiation safety conditions at Booster operation without its extraction system.

The next Booster run with its extraction system and the Booster – Nuclotron transfer line was realized in September 2021 [3].

All the standard preparation and procedures of RF stations were performed.

The results of the second Booster run are given bellow. The beam current transformer signal at ion acceleration up the energy of 200 MeV/u is shown in Fig. 6.

The efficiency at adiabatic beam capture was achieved at the level of about 99%.

ISBN: 978-3-95450-240-0 ISSN: 2673-5539 doi:10.18429/JACoW-RuPAC2021-WEPSC14

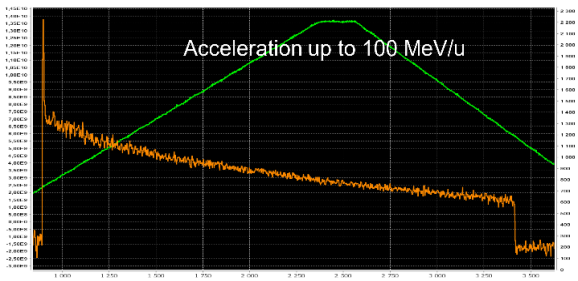

Figure 5: Beam current transformer signal at ion acceleration, first Booster run in December 2020.

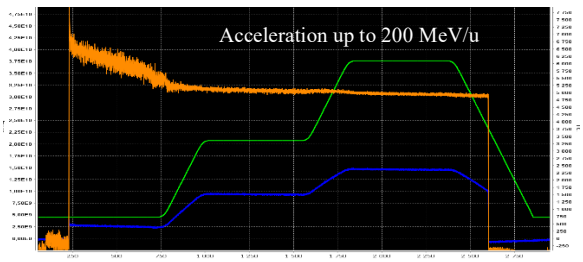

Figure 6: Beam current transformer signal at ion acceleration, second Booster run in September 2021.

The maximum energy of accelerated ions Fe^{+14} corresponds to the energy of 578 MeV/u.

The RF voltage was applied adiabatically on the table of injection magnetic field, which gives a high-quality beam capture. The beam was accelerated on the fifth RF harmonic after the first table of the magnetic field. The beam was recaptured on the first RF harmonic on the second table of the magnetic field (Fig. 7).

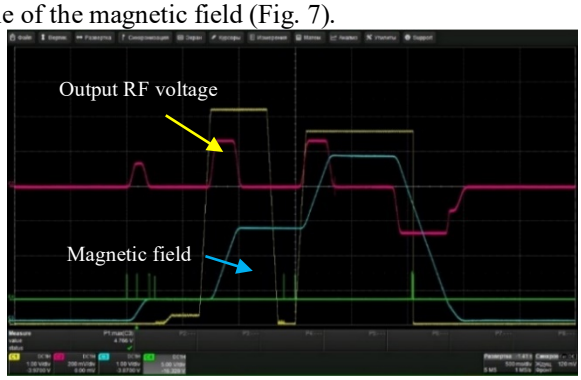

Figure 7: RF station parameters during adiabatic beam capture.

The impact of the applied adiabatic voltage on the beam is shown below (Fig.8).

One of the major goals that were reached is the possibility to use RF voltage to decelerate the Fe^{+14} particles on the falling magnetic field (Fig.9). It would improve the radiation safety conditions at Booster operation without beam extraction.

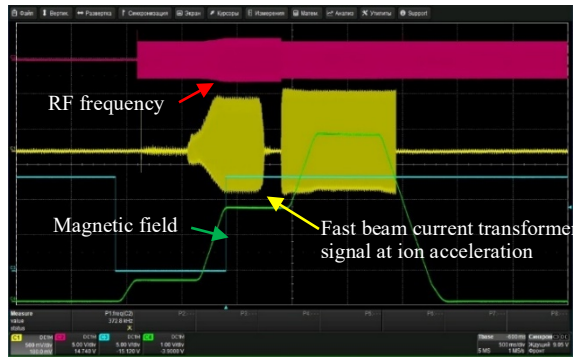

Figure 8: RF adiabatic voltage impact on the beam.

Figure 9: RF voltage applied to the falling magnetic field.

CONCLUSION

Two Booster RF accelerating stations were fabricated in Budker Institute of Nuclear Physics for Booster. The stations were tested in two Booster runs in operating mode.

The designed accelerating voltage in the frequency range of 0.5 – 2.5 MHz was obtained during the beam runs.

Due to the flexible control system, it was possible to work with adiabatic beam capture and achieve a level of efficiency of about 99%.

REFERENCES

[1] G. Y. Kurkin *et al.*, "RF System of the Booster of NICA Facility", in Proc. 24th Russian Particle Accelerator Conf. (RuPAC'14), Obninsk, Russia, Oct. 2014, paper TUCB02, pp. 26-28.

[2] G. A. Fatkin, A. M. Batrakov, I. V. Ilyin, G. Y. Kurkin, A. M. Pilan, and M. Yu. Vasilyev, "Controller for RF Stations for Booster of NICA Project", in *Proc. 24th Russian Particle Accelerator Conf. (RuPAC'14),* Obninsk, Russia, Oct. 2014, paper THPSC29, pp. 383-385.

[3] A. V. Butenko *et al.,* "First Experiments with Accelerated Ion Beams in the Booster of NICA Accelerator Complex", presented at *the 12th Int. Particle Accelerator Conf. (IPAC'21)*, Campinas, Brazil, May 2021, paper MOPAB025.

ISBN: 978-3-95450-240-0 ISSN: 2673-5539 doi:10.18429/JACoW-RuPAC2021-WEPSC15

BARRIER STATION RF1 OF THE NICA COLLIDER. DESIGN FEATURES AND INFLUENCE ON BEAM DYNAMICS

A.M. Malyshev, A.A. Krasnov, Ya.G. Kruchkov, S.A. Krutikhin, G.Y. Kurkin, A.Yu. Martynovsky, N.V. Mityanina[1], S.V. Motygin, A.A. Murasev[1], V.N. Osipov, V.M. Petrov, A.M. Pilan[2], E. Rotov[1], V.V. Tarnetsky[1], A.G. Tribendis[2], I.A. Zapryagaev[1], A.A. Zhukov, Budker INP, Novosibirsk, Russia
O.I. Brovko, I.N. Meshkov[3], E. M. Syresin, JINR, Dubna, Russia
[1]also at Novosibirsk State University, Novosibirsk, Russia
[2]also at Novosibirsk State Technical University, Novosibirsk, Russia
[3]also at Saint-Petersburg State University, Saint-Petersburg, Russia

Abstract

This paper reports on the design features and construction progress of the barrier bucket RF systems for the NICA collider being built at JINR, Dubna. Each of two collider rings has three RF systems named RF1 to 3. RF1 is a barrier bucket system used for particles capturing and accumulation during injection, RF2 and 3 are resonant systems operating at 22nd and 66th harmonics of the revolution frequency and used for the 22 bunches formation. The RF systems are designed by Budker INP. Both RF1 stations were manufactured, delivered to JINR and tested at the stand. The test results are presented in the article, as well as some results of calculating the effect of the RF1 system on the beam dynamics.

INTRODUCTION

The Nuclotron based Ion Collider fAcility (NICA) [1], operating in its heavy ion collision mode is aimed at the experiments with colliding beams of $^{197}Au^{79+}$ ions at energies from 1 to 4.5 GeV/u per beam. Budker Institute of Nuclear Physics contributes to several parts of the project, including its RF systems – barrier bucket and harmonic. Barrier bucket system, RF1, is used to capture the particles injected from the Nuclotron and to accumulate the required number of ions. This is done using moving barriers technique. RF1 also can accelerate the accumulated beam if the injection energy is lower than that of the experiment. Harmonic systems, RF2 and 3, are used to form 22 bunches with required parameters. Each collider ring has one RF1 station, four RF2 and eight RF3 stations.

The RF1 system generates 2 pairs of ±5 kV pulses (accelerating and decelerating in each pair) at the bunch revolution frequency thus forming the two separatrices – injection and stack. A bunch from the Nuclotron is shot into the injection separatrix, moved and added to the stack by switching off the pulses separating the two separatrices and so merging the two bunches. If the combined bunch length exceeds the half-ring perimeter it is compressed by moving the barrier pulses. Ion accumulation process is accomplished by the electron cooling. The accumulated ions trapped between the two barrier pulses may be accelerated, if needed, by ±0.3 kV meander voltage generated by the RF1 as well [2].

RF1 BARRIER BUCKET SYSTEM – INDUCTION ACCELERATOR

The barrier station is a coaxial line filled with 84XB-M grade amorphous iron rings. Pulse voltages generated by transistors operating in a switching mode are applied to the rings. These voltages are summed up at the accelerating gap of the station.

The station is cooled by water. There are channels for water flow between the rings of amorphous iron. Figure 1 shows the details of the RF1 station.

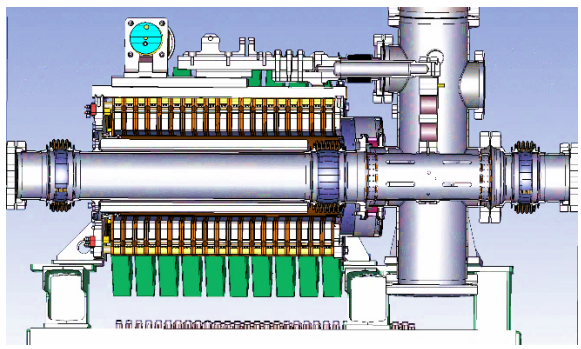

Figure 1: Details of the RF1 station.

To form the barrier voltage, 16 sections 6-20 are used, 3 accelerating sections 5-3, and one damping section.

At the moment when RF1 does not work, the accelerating gap is short-circuited by a contactor.

Figure 2 shows the appearance of the RF1 station.

Figure 2: Appearance of the RF1 station.

† alexmal94@mail.ru

ISBN: 978-3-95450-240-0 ISSN: 2673-5539 doi:10.18429/JACoW-RuPAC2021-WEPSC15

Stacking Algorithm

During injection of particles into the collider ring, particles are accumulated between the first and second pulses. In the interval between the third and fourth pulses, particles are injected. After the second and third pulses are turned off after their contraction, the accumulated bunch and the injected bunch are combined. The fourth voltage pulse becomes the second. Then it is necessary to switch on the third and fourth impulses accordingly in order to return to the initial location. The duration of the barrier voltage pulse can be adjusted from 80 ns to 10 ns.

If it is necessary to increase the energy, the accelerating voltage is switched on and at the same time, the magnetic field in the collider ring rises. Accelerating voltage (blue solid line on Fig. 3) - meander (0-300) V.

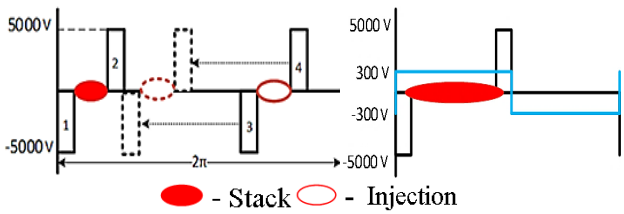

Figure 3: Barrier voltage (left) and acceleration (right).

TEST RESULTS OF RF1 STATION

Full load tests were carried out at a water temperature of + 30 ° C, a pressure drop (inlet-outlet) of 3.5 atm. and flow rate ~ 70 l / min. The maximum temperature in the pulse generators was + 47 ° C. The maximum temperature in amorphous iron was + 33 ° C. The heating protection threshold for output transistors is set at +60 ºC.

The operability of the power supplies of the accelerating and barrier sections for the equivalent and as part of the station has been checked. The accuracy of the output voltage is +/- 1%.

Oscillograms of the accelerating and barrier voltages were obtained, see Fig. 4, Fig 5.

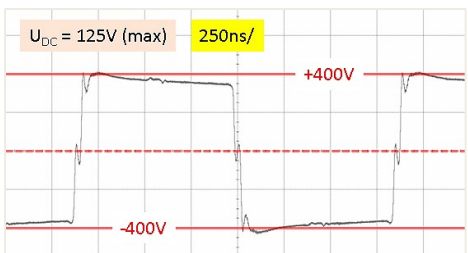

Figure 4: Accelerating voltage of RF1 station.

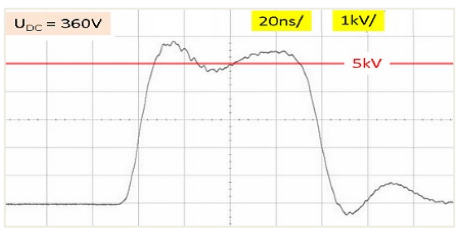

Figure 5: Barrier voltage of RF1 station.

INFLUENCE OF THE BARRIER SYSTEM ON BEAM DYNAMICS

Figure 6 shows a sketch of the entire RF1 station and a diagram of the connection of the RF1 station rings to the accelerating gap with rectangular voltage sources.

On equivalent circuits (Fig. 6, Fig. 7, Fig. 8) numbers 1-6 indicate parts of the rings: 1 – key (pulse generator); 2 - primary loop (from pulse generator to amorphous iron); 3 - amorphous iron; 4 - secondary loop (parasitic gap around the inductor); 5 - coaxial; 6 - accelerating gap.

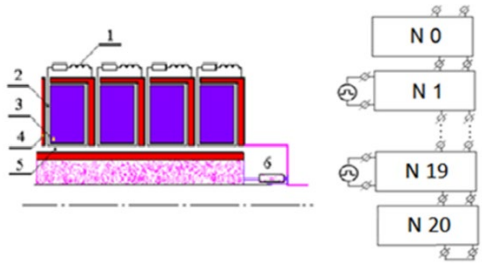

Figure 6: Connection of the RF1 station rings to the accelerating gap.

3D modeling of the RF1 station is impossible due to the complexity of the design, since it is necessary to take into account not only geometric, but also electrical parameters.

Therefore, the simulation of output voltage and impedance were carried out using equivalent circuits on Fig. 7, Fig.8. Figure 7 shows the equivalent circuit one ring for the rings with numbers N=1-19.

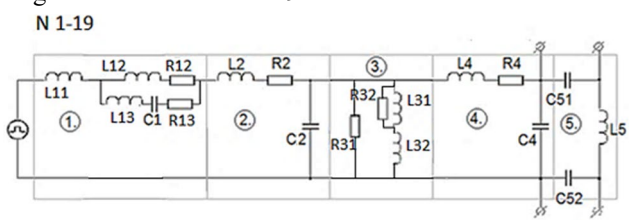

Figure 7: Equivalent circuit of one ring (from the 1st to the 19th).

Circuit of the last ring (N20) and accelerating gap (N0) are shown in Fig. 8.

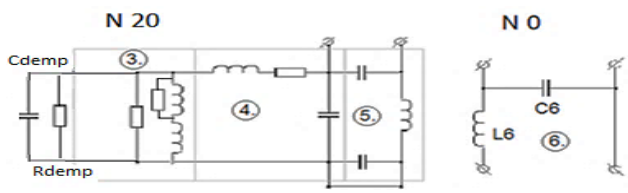

Figure 8: Last ring and accelerating gap.

The measurements of the station and calculations of its model with the estimated parameters were carried out.

Using the equivalent circuit, the signal transmission through the structure (Fig. 9) and the impedance (Fig. 10) are calculated.

Parameters of equivalent circuit are estimated with independent inductances and capacitances (quasistatic approach) and corrected so that simulation of output voltage was in sufficient accordance with measured one (Fig. 9).

ISBN: 978-3-95450-240-0 ISSN: 2673-5539 doi:10.18429/JACoW-RuPAC2021-WEPSC15

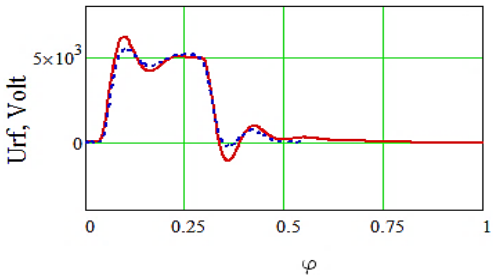

Figure 9: Comparison of measured (blue dash-dotted line) and calculated (solid red line) output pulse.

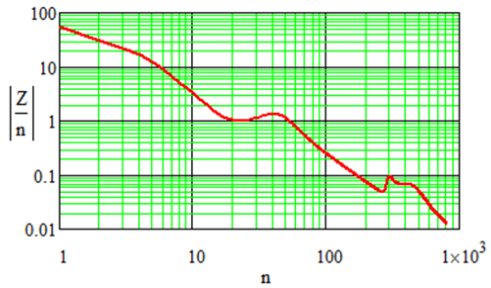

Figure 10: System impedance calculated by equivalent circuit impedance, Z_{out}/n.

The RF voltage affecting the particle dynamics includes the RF system output voltage Urf (obtained above, Fig. 9), the beam-induced voltage Uind, taking into account the output impedance of the station RF1 and the harmonics of the beam longitudinal distribution function, and the space charge field voltage, proportional to this distribution function:

$$U(\varphi) = U_{rf}(\varphi) + U_{sc}(\varphi,\rho) + U_{ind}(\varphi,\rho)$$

The beam particles undergo phase motion in the potential of this voltage:

$$W(\Delta\varphi) = k_0 \frac{Z_{Au}}{A_{Au}} e \int_0^{\Delta\varphi} (U(\varphi_s + \Delta\varphi) - U(\varphi_s)) d\varphi$$

$$k_0 = \frac{q_{rf}}{2\pi} \frac{\omega_0 \eta}{R_s p_s} > 0, \qquad \eta = \gamma_s^{-2} - \alpha$$

The stationary (Boltzmann) distribution is defined with account of the total potential:

$$\rho(\varphi) = C \cdot \exp\left(-\frac{W_{rf}(\varphi) + W_{sc}(\varphi,\rho) + W_{ind}(\varphi,\rho)}{\delta_{p\,av}{}^2 (\omega_0 \eta)^2} \right)$$

$$\int_0^{2\pi} \rho(\varphi) d\varphi = Q = I_0 / f_0, \quad \delta_{p\,av}{}^2 = \left\langle (\Delta p / p_s)^2 \right\rangle$$

The (self-consistent) longitudinal distribution is found by solving the self-consistent problem by iterations (Fig. 11), in which the initial approximation is calculated without taking into account the induced voltage and the space charge field (black dash-dotted line on Fig. 11).

As a result, with the maximum possible spread of longitudinal pulses, we obtain a longitudinal distribution and the shape of a potential well at a beam current of 0.4 A. and an ion energy of 3 GeV/u. These calculations shows that the stationary longitudinal distribution of the beam 0.4A can exist.

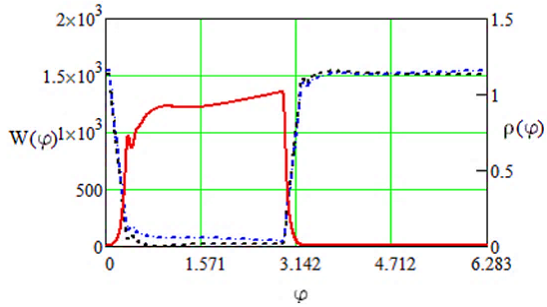

Figure 11: Longitudinal distribution (solid red line); RF potential - black dash-dotted line; total Self-Consistent Potential - blue dash-dotted line.

Microwave Instability

A table of threshold values of the beam current at energies from 1 to 4.5 GeV/u was calculated (Table 1, φbb = 10/12π).

$$I_0 \le \varphi_{bb} \frac{(A_{Au} E / Z_{Au} e) |\eta| \delta_{p\,av}{}^2}{|Z_{out}(n\omega_0)/n|_{\max}}$$

RF1 impedance (max 60ohm, see Fig. 10) at 0.4A does not cause microwave instability.

Table 1: Microwave Instability Threshold

Energy, GeV/u	**1**	**3**	**4.5**
$\Delta p_{sep}/3$, 10^{-3}	0.24	0.37	0.6
Threshold current, A, at $\lvert Z/n\rvert_{\max} = 60\ Ohm$	2.6A	2.2A	0.8A

CONCLUSION

The results of testing the station at the stand are obtained.

An equivalent circuit diagram of the station was compiled, taking into account the design features and measurements of the finished station. The parameters of the station were measured and simulations were carried out.

The calculations of the beam dynamics have been carried out, which show that the stationary longitudinal distribution of the beam 0.4A can exist and no microwave instability arises during the operation of the station.

REFERENCES

[1] D. Kekelidze *et al.*, "Three stages of the NICA accelerator complex", *Eur. Phys. J.* A (2016) 52: 211. doi:10.1140/epja/i2016-16211-2

[2] A. G. Tribendis *et al.*, "Construction and First Test Results of the Barrier and Harmonic RF Systems for the NICA Collider", presented at the *12th Int. Particle Accelerator Conf. (IPAC'21),* Campinas, Brazil, May 2021, paper MOPAB365.

ISBN: 978-3-95450-240-0 ISSN: 2673-5539 doi:10.18429/JACoW-RuPAC2021-WEPSC16

NUMERICAL RESEARCH OF DESIGN SOLUTIONS FOR THE BENDING MAGNETS OF THE ELECTRON BEAM FACILITY GESA-1M

N. Kazachenko†, E. Gapionok, V. Kukhtin, I. Rodin, K. Tkachenko,
JSC "NIIEFA", St. Petersburg, Russia
D. Ovsyannikov, S. Sytchevsky, St.Petersburg State University, Russia

Abstract

Comparative simulations of magnet configurations have been performed searching for the optimum design of bending magnets for the intense pulsed electron beam facility GESA-1M. The beam trajectory through electric and magnetic fields was simulated for three candidate configurations of the bending magnets. A comparison was focused on the expected power density and divergence angle at the target. The most efficient concept was found to be two pairs of coils arranged orthogonally to each other. This configuration produces highly uniform distribution of the current density at the target, the divergence angle being as low as several degrees. An important advantage is that the initial beam power can be intensified by a 20% at the target.

INTRODUCTION

GESA-1M is used for improvement of material surface properties and is capable to generate a 120 kV, 10 A/cm^2, 50 μs electron beam with the diameter of 10 cm. One of specific concerns is to prevent the beam path from micro-contaminations from the irradiated surface. To overcome this problem a system of bending magnets is used to guide and deflect particles. The best efficiency is observed when the electron beam is deposited normally to the surface, and a constant power density is kept across the beam spot. The study has been carried out for three candidate design options illustrated in Fig. 1.

COMPUTATIONAL PROCEDURE

All electrons in a pulse were assumed to have the same energy of 120 keV. Each electron trajectory was taken tangentially to a field line at the starting point. The starting points were taken on a horizontal plane on the upper surface of the top coil at $Z = 42$ cm. The vertical electron momentum is directed opposite to the axis Z.

An electron moves according to the Newtonian equations of motion. Using the Gaussian system of units, the electron motion can be represented in a vector form as

$$\begin{cases} d\vec{p}/ds = \vec{E}'/\beta + [\vec{\beta}, \vec{H}']/\beta \\ d\vec{r}/ds = \vec{p}'/p' \end{cases}$$

Here $\vec{p} = \vec{\beta}/\sqrt{1-\beta^2}$ is the relativistic momentum, $\vec{\beta}$ is the electron velocity, s is the trajectory length, $\vec{r}$ is the position vector, $\vec{E}' = e\vec{E}/E_0$ and $\vec{H}' = e\vec{H}/E_0$ are respective vectors of relative electric and magnetic field strength, e is the electron charge, E_0 is the self-energy.

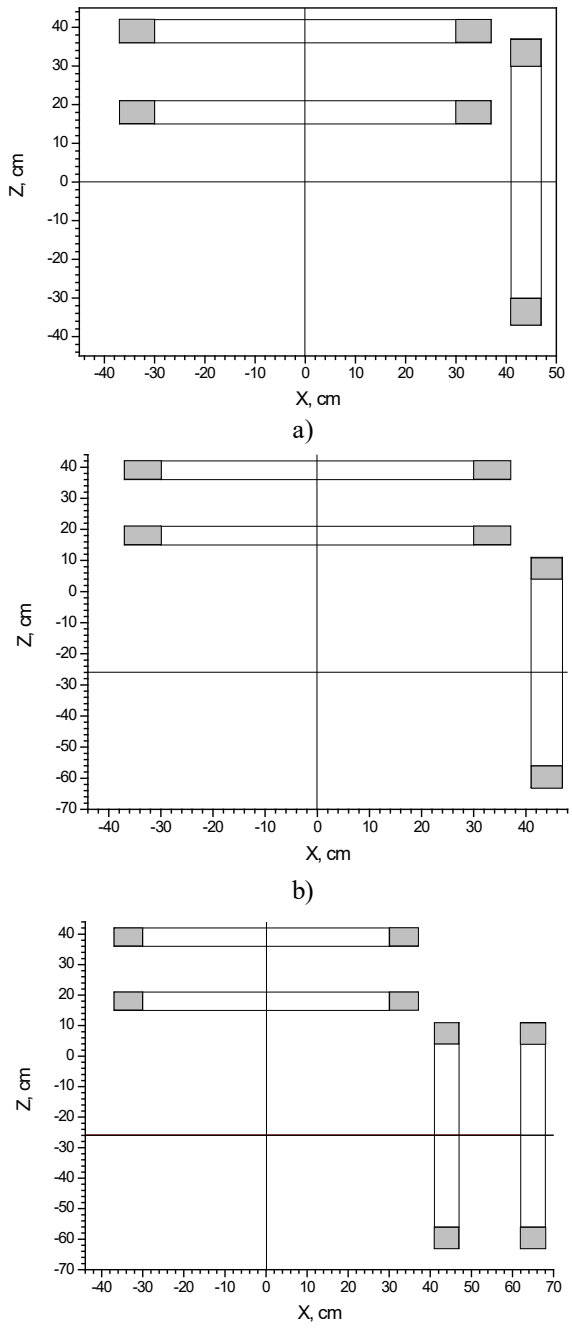

Figure 1: Bending magnet. a) Design option #1, b) Design option #2, c) Design option #3.

A space charge electric field was taken zero assuming magnetic field of the bending magnet is high enough to

† kazachenko-sci@yandex.ru

ISBN: 978-3-95450-240-0 ISSN: 2673-5539 doi:10.18429/JACoW-RuPAC2021-WEPSC16

neglect space-charge repulsion. The total momentum p' was assumed constant.

The starting points were taken on concentric circles with the radius R_0 varying in the range from 0 to 5 cm. The point coordinates were determined as in the $x_0 = R_0 \cdot \cos\varphi$, $y_0 = R_0 \cdot \sin\varphi$, $z_0 = 42$ cm, where φ is the angle between the position vector of a starting point and axis X ranging from 0 to 2π. Components of the total momentum at every starting point were determined as $p'_{x0} = -p' \cdot \left(\frac{H_x}{H}\right)$, $p'_{y0} = -p' \cdot \left(\frac{H_y}{H}\right)$, $p'_{z0} = -p' \cdot \left(\frac{H_z}{H}\right)$, where H_x, H_y, H_z, H were observed at the origin of coordinates (x_0, y_0, z_0). The electron trajectory was derived by solving the above system of equations using Adams' method [1,2]. Field strength components H_x, H_y, H_z were evaluated in simulations with electromagnetic code KLONDIKE [3, 4].

The every trajectory was ended at the target surface. At the end point components of the total momentum of an electron and its incident angle were calculated. The target surface was located normally to the axis X at a 1 cm distance away from the vertical coil at the exit of the bending magnet (see Fig. 1). The beam energy density was evaluated over 4 trajectories started from the vertices of a small quadrangle on the $Z = 42$ cm plane. The quadrangle area was pre-determined in test simulations. The starting quadrangle was projected on the target surface with controllable curvature. Observation points were taken over the projection. The energy density on the irradiated surface was evaluated via the ratio of the starting and projected areas.

RESULTS OF TRAJECTORY SIMULATIONS

Plots on Figs. 2, 3, 4 present incident angles calculated for 3 design options of the bending magnet. Option #1 demonstrates the most non-uniform angular distribution. The highest deflection is detected near the beam periphery reaching 13°. The incident angle above the admissible value of 10° occurs for almost a half of electrons. Asymmetry of the angular distribution is resulted from the electron drift due to the field inhomogeneity. Option #2 provides the incident angles below 7°. For Option #3 the incident angle as low as 4° is observed over the entire irradiated surface. Weak asymmetry of the angular distribution occurs with respect to the plane Y = 0.

Figs. 5, 6, 7 illustrate simulated current density over the target. Again, Option #1 demonstrates the most non-uniform distribution of the current density. Options #2, #3 provide good uniformity of the current density distribution. A 30% reduction of the current density on the target surface as compared to the emitted beam is observed for Option #2. This means that the beam spot on the target is larger than the aperture. For Option 3 the current density remains unchanged.

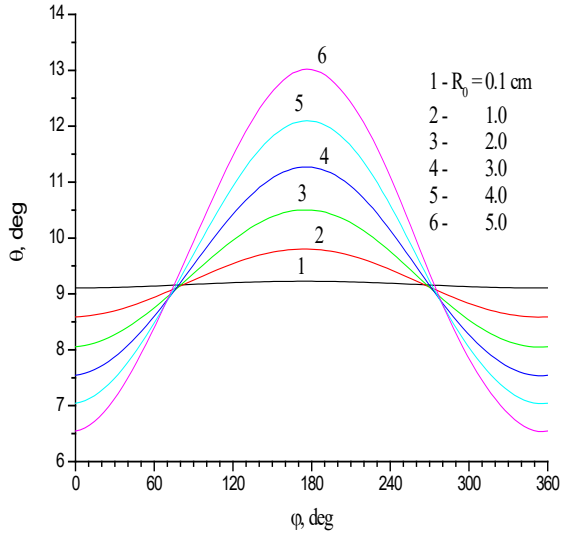

Figure 2: Incident angle θ vs. polar angle φ, for various trajectories. Design option #1.

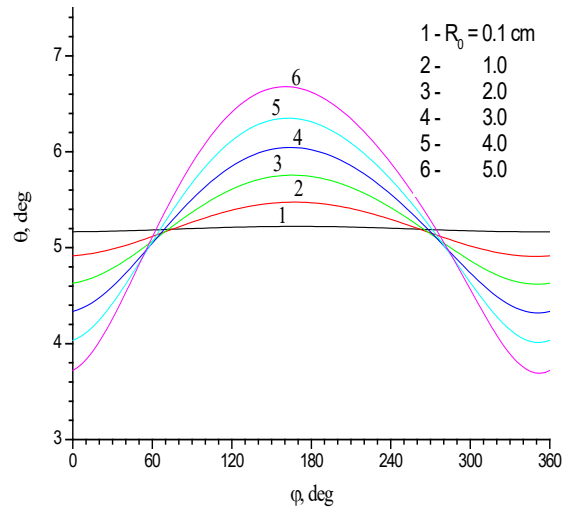

Figure 3: Incident angle θ vs. polar angle φ, for various trajectories. Design option #2.

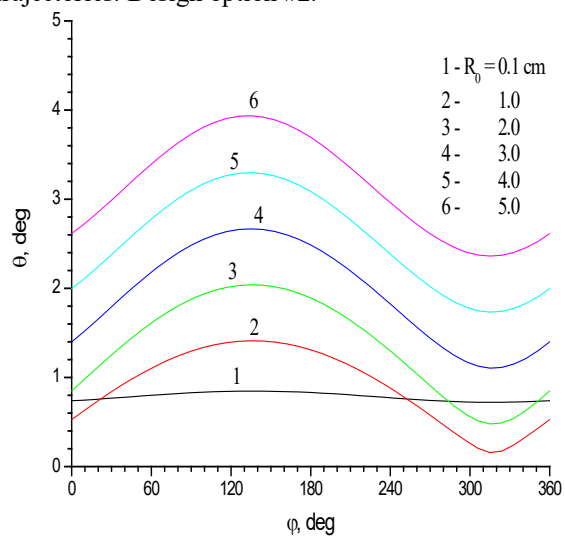

Figure 4: Incident angle θ vs. polar angle φ, for various trajectories. Design option #3.

ISBN: 978-3-95450-240-0 ISSN: 2673-5539 doi:10.18429/JACoW-RuPAC2021-WEPSC16

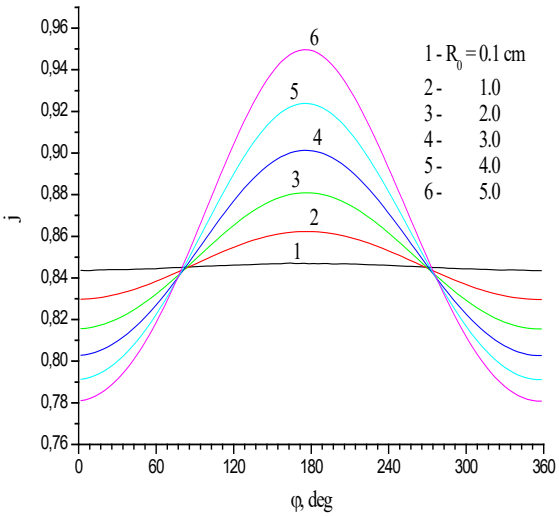

Figure 5: Current density on target surface for various trajectories. Design option #1.

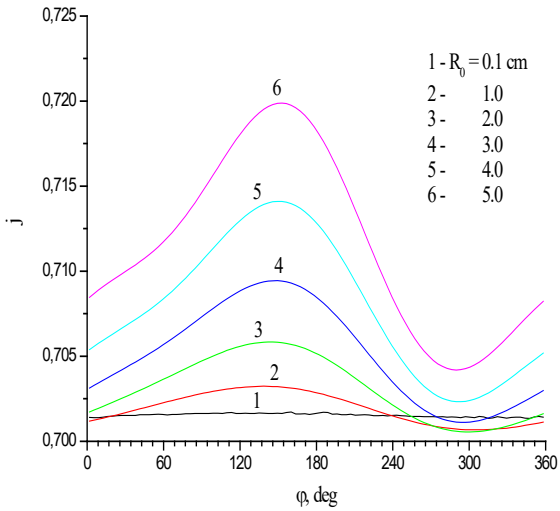

Figure 6: Current density on target surface for various trajectories. Design option #2.

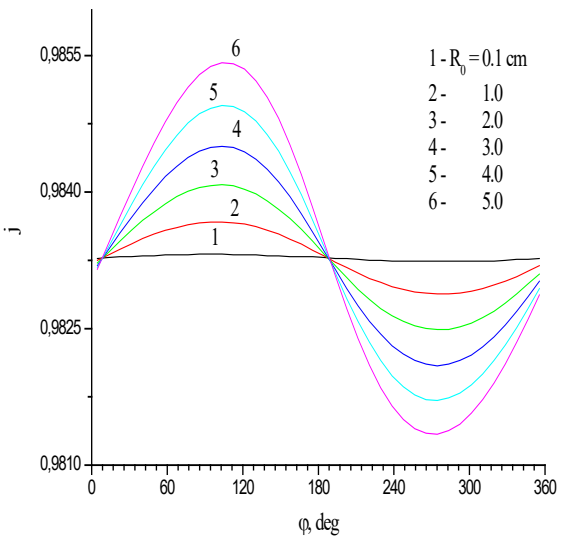

Figure 7: Current density on target surface for various trajectories. Design option #3.

CONCLUSIONS

The most efficient concept was found to be configuration #3 with two pairs of coils arranged orthogonally to each other. Such bending magnet provides highly uniform distribution of the current density at the target with the incident angle as low as 4°.

These evaluations have been obtained assuming the initial electron velocity at the starting point is co-directed with the field line. Also, space-charge repulsion was neglected. A further study is necessary to assess the error introduced with these assumptions.

REFERENCES

[1] N.Kalitkin. Numerical methods (in Russian), Moscow, Nauka Publ., 1978.

[2] O.Arushunyan, S.Zalyotkin. Numerically solving ordinary differential equation in FORTRAN (in Russian), Moscow, Moscow State University Publ., 1990.

[3] V. Amoskov *et al.*, "Computation technology based on KOMPOT and KLONDIKE codes for magnetostatic simulations in tokamaks", *Plasma Devices Oper.*, vol. 16, no.2, pp.89-103, 2008, doi:10.1080/10519990802018023

[4] V.M. Amoskov *et al.*, "Magnetic model MMTC-2.2 of ITER tokamak complex", *Vestnik of Saint Petersburg University, Applied Mathematics. Computer Science. Control Processes*, vol. 15, no. 1, pp. 5-21, 2019, doi: 10.21638/11702/spbu10.2019.101

ISBN: 978-3-95450-240-0 ISSN: 2673-5539 doi:10.18429/JACoW-RuPAC2021-WEPSC17

VIBRATING WIRE SYSTEM FOR FIDUCIALIZATION NICA BOOSTER SUPERCONDUCTING QUADRUPOLE MAGNETS

T. Parfylo, V. Borisov, M. Kashunin, H. Khodzhibagiyan, B. Kondratiev, S. Kostromin, V. Mykhailenko, M. Shandov
Joint Institute for Nuclear Research, Dubna, Russia

Abstract

The NICA (Nuclotron-based Ion Collider fAcility) is a new accelerator complex under construction at the Laboratory of High Energy Physics (LHEP) JINR. The facility includes two injector chains, two existing superconducting synchrotrons Nuclotron and a new Booster, under construction superconducting Collider, consisting of two rings. The lattice of the Booster includes 48 superconducting quadrupole magnets that combined in doublets. Each doublet must be fiducialized to the calculated trajectory of the beam. Alignment of the magnetic axis is necessary for properly install the magnets at the beam trajectory. The vibrating wire technique was applied to obtain the the magnetic axis position of quadrupoles. A new measurement system has been worked out and produced at the LHEP. The magnetic axis positions of the quadrupole doublets are determined at the ambient temperature. The paper describes design of the measurement system, measuring procedure and results of the magnetic axis position measurements.

INTRODUCTION

The NICA (Nuclotron-based Ion Collider fAcility) is a new accelerator complex under construction at the Laboratory of High Energy Physics (LHEP) JINR [1]. The facility includes two injector chains, two existing superconducting synchrotrons Nuclotron and a new Booster, under construction superconducting Collider consisting of two rings. The Booster have been put into operation at 2020. Main goals of the Booster are accumulation of 2×10^9 Au^{31+} ions acceleration of the heavy ions up to energy required for effective stripping; forming of the required beam emittance with electron cooling system. It has 210.96 m circumference and includes 48 superconducting quadrupole magnets that combined in doublets. All superconducting magnets for the NICA Booster have been assembled and tested at the test facility at the Laboratory of High Energy Physics. According to the technical specifications [2], the magnetic axis position must be measured with an accuracy less than 0.1 mm.

The vibrating wire technique was applied to achieve the precision of measuring the magnetic axis position. The vibrating wire technique based on Lorentz forces between alternating current flowing through the taut wire and transverse magnetic field excite the mechanical wire vibrations. If the frequency of driving current is close to one of the wire resonance frequencies the effect will be especially strong. The wire position can be obtained by moving the wire across the magnet aperture and measuring the wire vibrating amplitude [3, 4].

DOUBLET OF QUADRUPOLE MAGNETS

The Booster quadrupole magnets are Nuclotron-type include cold iron yoke with hyperbolic poles, shaped the magnetic field and a coil made of a hollow superconductor. The doublet of quadrupole magnets is a single rigid mechanical construction of about 1.8 m length. It's consists of defocusing and focusing quadrupoles, cylinder for rigid mounting magnets with each other, as well as two beam position monitors within cylinder. The doublet has a removable design that allows splitting it into two parts for assembly-disassembly halves of yoke and coil [5].

The main parameters of the NICA Booster quadrupole magnets are shown in Table 1.

Table 1: The Main Parameters of the NICA Booster quadrupole Magnets

Parameter	Unit	Value
Number of magnets	pieces	48
Maximum field gradient	T/m	21.5
Effective magnetic length	m	0.47
Field error at R = 30 mm		6×10^{-4}
Beam pipe aperture (h/v)	mm	128/65
Pole radius	mm	47.5
Yoke width/height	m	0.226
Weight	kg	110

VIBRATING WIRE SYSTEM

The NICA Booster Vibrating Wire measurement system has been designed, produced and commissioned at the LHEP. The copper-beryllium wire 0.125 mm diameter and length about 5.3 m stretched through the mechanical center of the doublet aperture (see Fig. 1: 2 – defocusing, 3 – focusing magnets) and supported by two stages A and B (4 and 5). Each of them has horizontal and vertical Physik Instrumente linear stages 404.2PD to moving wire (1) across the aperture. The doublet and stages are installed on the balk 6 m along. The geometrical centers of defocusing and focusing magnets are placed at the 3/8 L_w and 5/8 L_w, where L_w – wire length. The wire is fixed on stages and stretched by 0.8 kg weight. Digital wave form generator Keithley 6221 was used to drive alternating current through the wire. Two orthogonal Sharp phototransistors GP1S094HCZ0F (6) were used to detect wire vibrations and National Instruments 24-bit PXIe-4464 module for signal registration from them.

ISBN: 978-3-95450-240-0 ISSN: 2673-5539 doi:10.18429/JACoW-RuPAC2021-WEPSC17

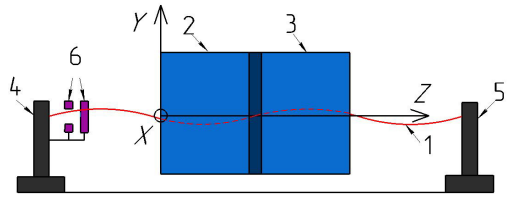

Figure 1: The scheme of the NICA Booster vibrating wire measurement system.

MEASURING PROCEDURE

To begin with, the wire position aligns to the doublet aperture geometrical center. The wire on the stages are adjusted relative to the doublet by Hexagon laser tracker AT402 with ±0.05 mm alignment tolerance. Then operating points are set on the wire position detectors – GP1S094HCZ0F. The output voltage of the phototransistors has a linear dependence on the amplitude of the wire vibrations with the X,Y positions in doublet aperture – $A \sim I_w \times |X, Y| \times L_w / \omega_n \times L_m$, where A – amplitude of the wire vibration, I_w – AC current through the wire, $L_{w,m}$ – wire and magnet length, ω_n – n harmonic of the wire natural frequency. The minimum of the wire vibration amplitude corresponds to the magnetic center position.

According to the position of the magnets, the fourth harmonic of the wire natural frequency is used to find the magnetic center position and also, at the fourth harmonic the wire is unsusceptible to external constant fields. Usually the fourth harmonic is about 104 Hz. The frequency of alternating current through the wire is close to the natural frequency of the wire. Furthermore, to maintain the correct S/N ratio, the wire vibration amplitude must be less than the working area of phototransistors. All measurement procedures are carried out by automatic program written in the LabVIEW programming environment.

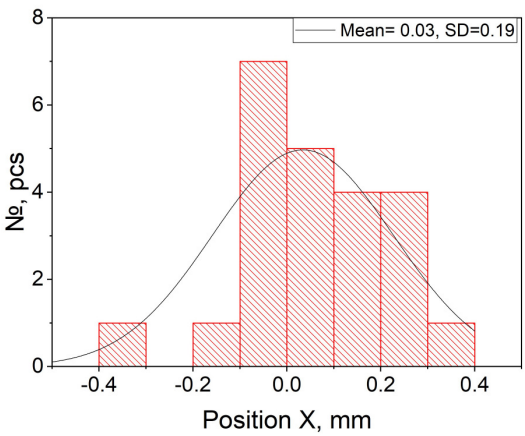

Figure 2: X position of the magnetic center of the defocusing quadrupole.

Initially, the position of the magnetic center determined for defocusing magnet. The wire vibrating amplitude at the detectors position is measured at 11 points on 1 mm length with step 0.1 mm (see Fig. 2, 3). The linear stages are moved in co-directional. The wire operating AC – 0.1 A and magnet DC – 35 A. In order to avoid the influence of the background fields, magnetic measurements were carried out with positive and negative operating currents trough the magnet coil. The mean value of the minimum wire vibration amplitude for negative and positive operating currents through the magnet coil corresponds to the magnetic axis position. The same measurements for the focusing magnet. Two points of the magnetic center for defocusing and focusing magnets defined the line – magnetic axis of the doublet. After magnetic measurements, the position of the magnetic axis was used to adjust the beam position monitors located between defocusing and focusing magnets.

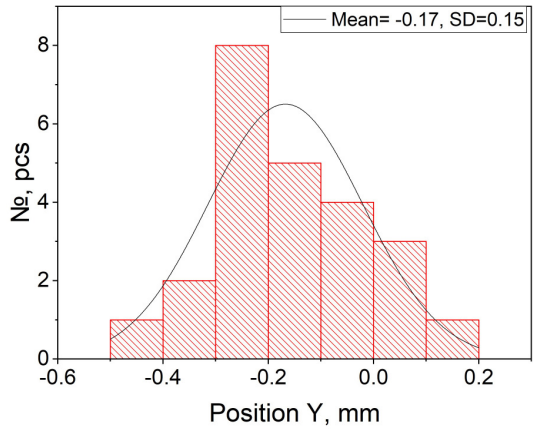

Figure 3: Y position of the magnetic center of the defocusing quadrupole.

MEASUREMENTS REPEATABILITY

With an eye to check out the wire measurement system and disassembly-assembly (D-A) of the doublets the repetitive measurements have been accomplished. The doublet was measured four times with a complete D-A of them. Disassembly involves the separation of the two parts of the doublet iron yoke and the dismantling of the coil. Magnet assembly carried out in reverse order. The results are shown in the Table 2. According to the results of four measurements (three D-A of the doublet) the standard deviation of the magnetic axis position is less than 0.04 mm.

Table 2: Deviation of the Magnetic Axis Positions

№ D-A	Defocusing X/Y mm	Focusing X/Y mm	Doublet X/Y mm
0	-0.02/-0.25	0.10/-0.26	0.04/-0.27
1	-0.07/-0.25	0.07/-0.26	0.00/-0.26
2	-0.03/-0.25	0.06/-0.32	0.02/-0.30
3	0.02/-0.22	0.11/-0.28	0.07/-0.26
mean	-0.03/-0.24	0.09/-0.28	0.03/-0.27
σ	0.04/0.02	0.02/0.03	0.03/0.02

ISBN: 978-3-95450-240-0 ISSN: 2673-5539 doi:10.18429/JACoW-RuPAC2021-WEPSC17

MEASUREMENT RESULTS

Magnetic axes fiducialization of the NICA Booster quadrupole magnets were successfully done. All measurements carried out at the ambient temperature. The typical tolerance of the magnetic axis position is determined below 0.07 mm. The positions of the magnetic axes for all magnets are shown at Fig. 4 and normal distributions of the magnetic axis positions are shown at Figs. 5-8.

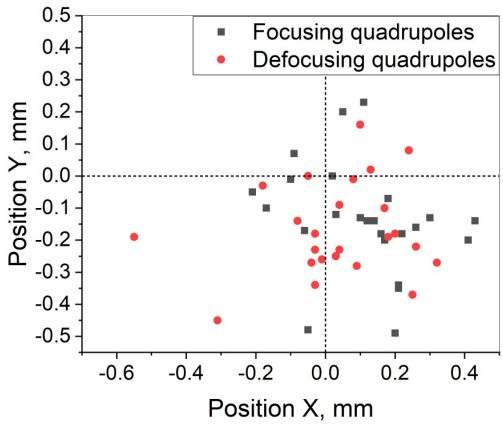

Figure 4: The magnetic axis positions of the NICA Booster quadrupole magnets.

The large spread of deviations of the magnetic axis positions is explained by the choice of the coordinate system of the doublet. Due to the fact that the coordinate system is set at the beginning of the defocusing magnet and the magnetic center is located significantly further along the length of the doublet. If there is a small angle between the defocusing and focusing magnets, this leads to large deviations of the magnetic axis positions.

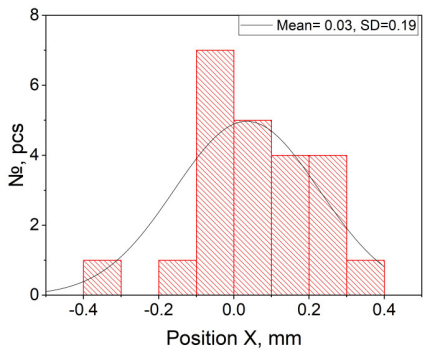

Figure 5: The defocusing quadrupoles normal distribution of the X positions of the magnetic center.

CONCLUSIONS

Vibrating wire technique is high accuracy technique to determine magnetic axis position of the magnet. It can be applied not only for one magnet but also for several magnets at the same time. It was shown that using vibrating wire technique, it's possible to fiducialize the doublet of the magnets at the beam trajectory. An accuracy of the determining magnetic axis below 0.07 mm and repeatability of the results after disassembly-assembly – 0.04 mm. The system also allows to take into account the influence of background fields. The developed vibrating wire system meets the technical requirements for the production of the superconductive magnets for the NICA project. Optimization, improvement, studies of the vibrating wire system and techniques should be continued at the LHEP.

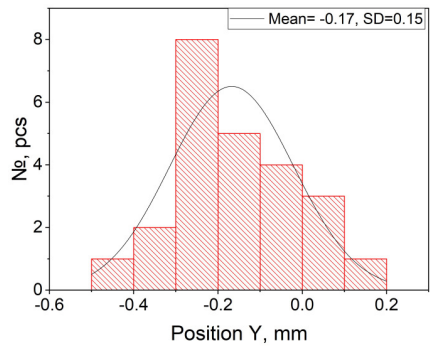

Figure 6: The defocusing quadrupoles normal distribution of the Y positions of the magnetic center.

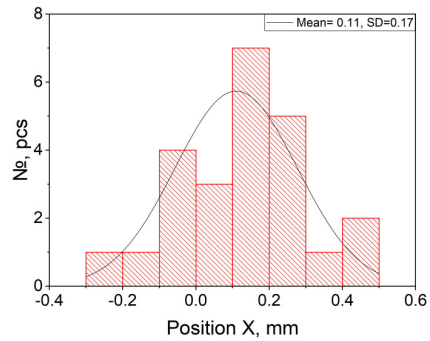

Figure 7: The focusing quadrupoles normal distribution of the X positions of the magnetic center.

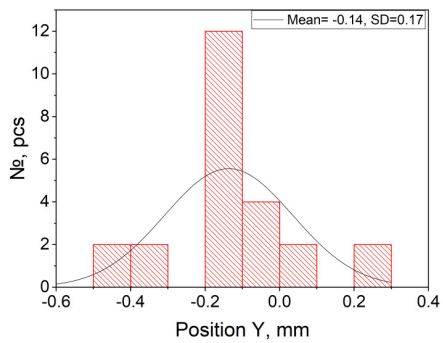

Figure 8: The focusing quadrupoles normal distribution of the Y positions of the magnetic center.

REFERENCES

[1] G. Trubnikov et al., Heavy ion collider facility NICA at JINR (Dubna): status and development, 36th International Confer-

ISBN: 978-3-95450-240-0 ISSN: 2673-5539 doi:10.18429/JACoW-RuPAC2021-WEPSC17

ence of High Energy Physics (ICHEP2012) July 4-11, Melbourne, Australia. doi:10.22323/1.174.0554

[2] Technical Project of NICA Acceleration Complex, Dubna, 2015.

[3] A. Temnykh, The magnetic center finding using vibrating wire technique, 11th International Magnetic Measurement Workshop, 1999.

[4] Z. Wolf, A vibrating wire system for quadrupole fiducialization, SLAC TN 10 087, 2010.

[5] H. Khodzhibagiyan et al., Superconducting Magnets for the NICA Accelerator Collider Complex // IEEE Transactions on Applied Superconductivity. 2014. June. V. 24, no. 3. P. 14.

ISBN: 978-3-95450-240-0 ISSN: 2673-5539 doi:10.18429/JACoW-RuPAC2021-WEPSC18

SERIAL MAGNETIC MEASUREMENTS OF THE NICA COLLIDER TWIN-APPERTURE DIPOLES. THE MAIN RESULTS

D. A. Zolotykh†, V. V. Borisov, I. I. Donguzov, O. Golubitsky, H. G. Khodzhibagiyan, B. Kondratiev, S. A. Kostromin, I. Yu. Nikolaichuk, T. Parfylo, M. M. Shandov, A. V. Shemchuk, E. V. Zolotykh,
JINR, Dubna, Moscow Region, Russia

Abstract

NICA Collider includes 80 dipole twin-aperture superconducting magnets. Totally 80 main and 6 spare magnets were manufactured and tested by a specially designed magnetic measurement system (MMS). Dipole magnets were tested at the ambient and operating (4.5 K) temperatures. This paper contains the main results of magnetic measurements of the NICA Collider twin-aperture dipoles.

INTRODUCTION

NICA (Nuclotron-based Ion Collider fAcility) is a new acceleration-storage complex. It is under construction in JINR. Collider includes 80 dipole twin-aperture superconducting magnets [1]. The operating energies for the Collider are 1.0, 3.0, and 4.5 GeV / nucleon, which correspond to the magnetic fields of 0.4, 1.2 and 1.8 T, respectively. Manufacturing of 80 main and 6 spare magnets is finished now. The main parameters of the dipoles were checked:

- Field in the center of the dipole ($B_1(0)$).
- Effective length (L_{eff}).

$$L_{eff} = \frac{1}{B_1(0)} \sum_{i=1}^{3} B_{1,i} S_i \quad (1)$$

- Median plane angle.

$$\alpha = -arctg \frac{A_1}{B_1} \quad (2)$$

- Relative harmonics up to 10^{th}.

Dipoles were tested at the ambient and operating (4.5 K) temperatures. Maximal operating current at operating temperature is 10.44 kA.

MAGNETIC MEASUREMENTS SYSTEM

Magnetic measurements were completed using the rotating harmonic coil method. Special MMS (see Fig. 1) were designed and manufactured for those tasks. This MMS consists of 3 blocks. Blocks locate in lodgement. Each block (see Fig. 2) includes 3 harmonic coils produced by PCB (printed circuit board) technology. Each coil consists of 400 turns (20 layers of 20 turns) [2,3]. Six MMS were produced and used for the magnetic measurement procedures: 2 for tests at the ambient temperature and 4 for the operating temperature. The basic views (front and rear) of the dipole magnets include MMS are shown in Fig. 3 (before connection with feed box).

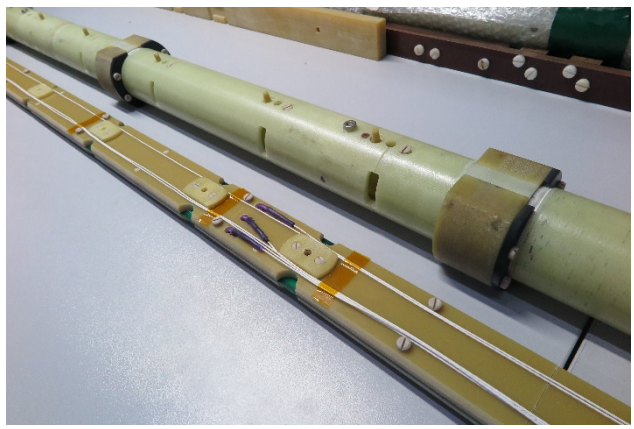

Figure 1: Magnetometer (lodgement and measuring shaft).

Figure 2: Block of the PCB harmonic coils.

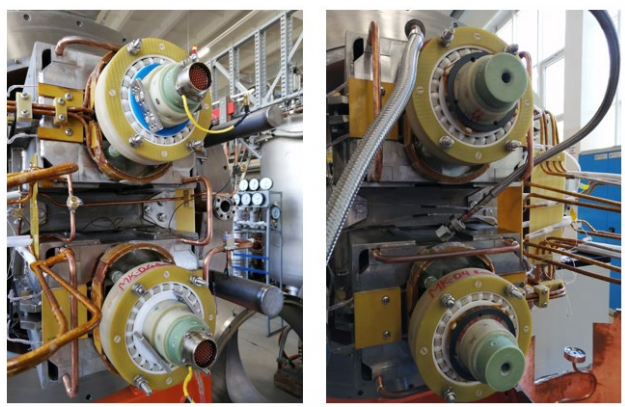

Figure 3: The basic views of dipole magnets.

† zolotykh@jinr.ru

ISBN: 978-3-95450-240-0 ISSN: 2673-5539 doi:10.18429/JACoW-RuPAC2021-WEPSC18

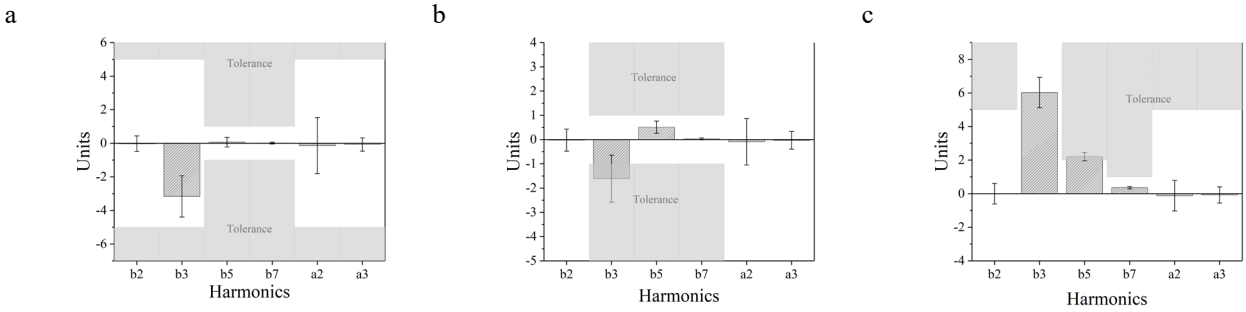

Figure 4: Relative harmonics for 2.3 kA (a), 6.89 kA (b) and 10.44 kA (c).

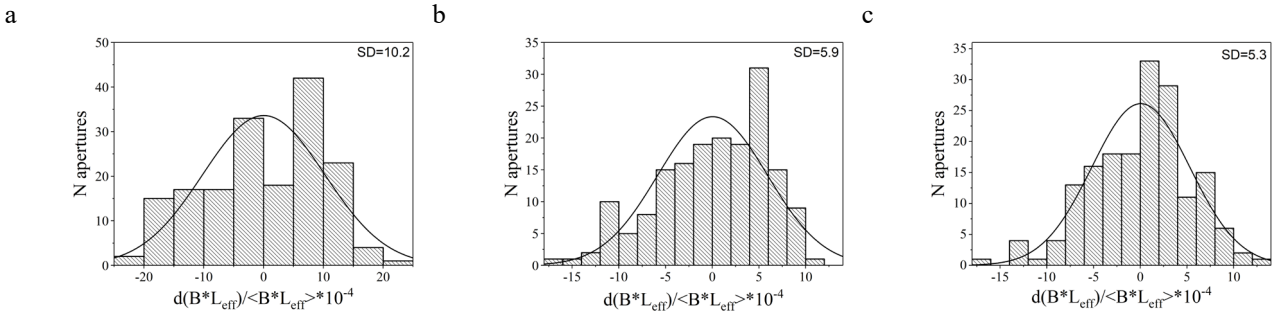

Figure 5: Distributions of relative deviation of the magnetic field integral for 2.3 kA (a), 6.89 kA (b) and 10.44 kA (c).

THE MAIN RESULTS

The procedure of the magnetic measurements of dipole magnets includes «warm» (at the ambient temperature) and «cold» (@ 4.5 K) tests. «Warm» magnetic measurements allow to detect defects of magnets and check build quality of magnets. «Cold» magnetic measurements allow to define the main characteristics of magnets at maximal operating current [4].

The procedure of magnetic measurements at the ambient and operating temperatures consists of 3 steps:

- 1: measurements of «reference» magnetic field (for definition of initial phase).
- 2: measurements of the main field (in the center of magnet) and the effective length.
- 3: measurements of the compensated field (relative harmonics).

Each step was measured clockwise and counterclockwise using step-by-step method.

Relative harmonics spectrums for the operating currents 2.3, 6.89 and 10.44 kA are shown in Fig. 4 (a, b, c). The magnetic field quality of most magnets is within specification. b_3 harmonic at a current of 6.89 kA and b_5 at a current of 10.44 kA slightly exceed the specification for some of the magnets.

The distributions of the relative deviation of the magnetic field integral are shown in Fig. 5 (a, b, c). The dependence of the mean value and standard deviation of the magnetic field normalized integral at the operating currents is shown in Fig. 6. The standard deviation dependence of magnetic field integral on the current is shown at Fig. 7. From the existence of such a dependence, it follows that one of the factors causing the spread of the field integral decreases with increasing magnetic field induction.

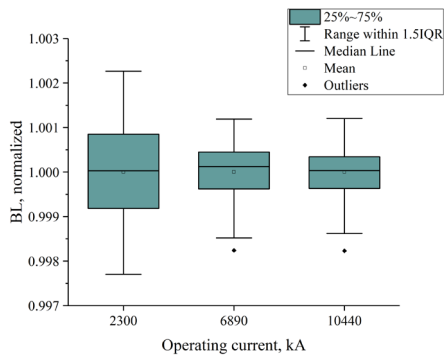

Figure 6: Normalized integral of magnetic field vs. operating current.

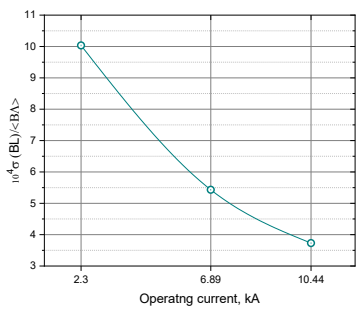

Figure 7: Standard deviation of magnetic field integral vs. operating current.

For the dipole magnets b_3 increases because of iron saturation. In case of the dipole magnets b_3 is allowed. The dependence of b_3 harmonic (mean value) on operating current and standard deviations are shown in Fig. 8.

ISBN: 978-3-95450-240-0 ISSN: 2673-5539 doi:10.18429/JACoW-RuPAC2021-WEPSC18

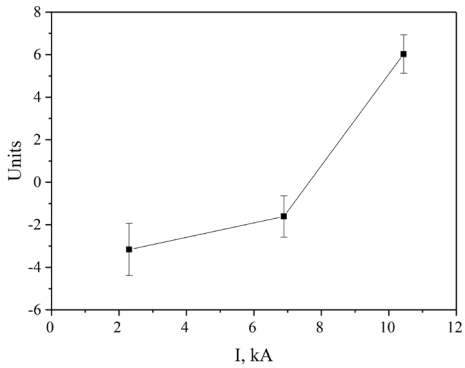

Figure 8: Dependence of b_3 mean value on current.

Relative deviation of integral of the magnetic field on magnets (for blue and red apertures separately) is shown in Fig. 9.

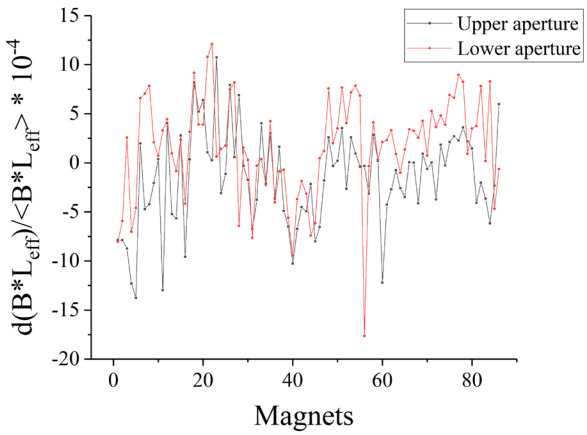

Figure 9: Relative deviation of integral of the magnetic field on magnets.

Specified values were received by relative calibration procedure of all magnetic measurement probe to one.

CONCLUSION

Manufacturing and test of the dipole magnets was finished. All of the dipole magnets have successfully passed the cryogenic tests and waiting for arrangement in the tunnel of the NICA Collider. Absolute calibration of all of the dipole MMS and results of hall probe measurements will be carried out later.

ACKNOWLEDGMENT

The authors would like to thank to those who support our tests at JINR, especially to the staffs of the SCM&T Department of LHEP.

REFERENCES

[1] Technical Project of NICA Acceleration Complex (Dubna, 2015).

[2] M. M. Shandov *et al.*, "The Present Status of the Magnetic Measurements of the NICA Collider Twin-Aperture Dipoles", in *Proc. 26th Russian Particle Accelerator Conf. (RuPAC'18),* Protvino, Russia, Oct. 2018, pp. 349-352. doi:10.18429/JACoW-RUPAC2018-WEPSB32

[3] M. M. Shandov *et al.*, "Magnetic Measurement System for the NICA Collider Dual Dipoles", in *Proc. 25th Russian Particle Accelerator Conf. (RuPAC'16),* Saint Petersburg, Russia, Nov. 2016, paper THPSC005, pp. 547-549. doi:10.18429/JACoW-RUPAC2016-THPSC005

[4] M. M. Shandov *et al.*, "First Serial Magnetic Measurements of the NICA Collider Twin-Aperture Dipoles", in *Proc. 9th Int. Particle Accelerator Conf. (IPAC'18),* Vancouver, Canada, Apr.-May 2018, pp. 3645-3648. doi:10.18429/JACoW-IPAC2018-THPAL013

ISBN: 978-3-95450-240-0 ISSN: 2673-5539 doi:10.18429/JACoW-RuPAC2021-WEPSC20

MAGNETS DESIGN FOR 2.5 GeV BOOSTER SYNCHROTRON

A.S. Smygacheva, V.N. Korchuganov, Ye.A. Fomin
NRC «Kurchatov Institute», Moscow, Russia

Abstract

The Project of complete modernization of the current accelerator complex is in progress in the NRC «Kurchatov Institute». The development of a new booster synchrotron as a part of the injection complex for a new 3-d generation synchrotron light source is included in the Project. The booster synchrotron has 24 dipoles, 60 quadrupoles, 48 sextupoles and 24 correctors. In order to obtain the required field quality, 2D- and 3D-simulations of magnets were carried out. The obtained geometry for each of the magnets is presented in the paper.

INTRODUCTION

The booster synchrotron is based on the modified DBA structure with 12 cells, each with mirror symmetry about the center of the cell [1]. One cell consists of 2 dipoles, 5 quadrupoles, 4 sextupoles and 2 correctors. The booster lattice has a large dynamic aperture with compensated natural chromaticity and low natural emittance (43.4 nm×rad). The structure is stable against various kinds of magnetic field errors within the permissible values.

The sensitivity of the booster lattice to errors and the parameters of the electron beam set the requirements for the quality of the magnetic fields. Optimization of the main characteristics of the field (the integral homogeneity of the field and the effective length) to the required values is carried out by searching the magnet pole geometry in 2D- and 3D-simulations of magnetic fields. The manufacturing technology and the magnetic properties of the steel have to be taken into account during magnet field optimization.

The booster synchrotron will operate in a cyclic mode with a frequency of 1 Hz in the energy range from 200 MeV to 2.5 GeV. The presence of alternating magnetic fields determines the manufacturing technology of the magnets of the booster synchrotron. The yoke of each magnet will be laminated, i.e. will be assembled from 1 mm thick magnetic steel sheets. The steel chosen for the magnet yokes is M940-100A. To ensure high quality of the magnetic field, the profile of each sheet must be made with an accuracy of 10–20 μm. The entire internal geometry of the magnet yoke must be maintained with the same accuracy during assembly.

The paper presents the optimization results of magnetic fields, electrical parameters and geometry of the booster magnets. 2D- and 3D-simulations of magnetic fields were carried out in the CST Studio Suite [2].

DIPOLES

The dipole magnet is a sector bending magnet. The ends of the magnet are parallel to each other. The main dipole parameters are presented in Table 1. The cross section of the dipole is shown in the Fig. 1.

The dipole magnet has also two additional coils for the field correction. The cross-sectional conductor size is 3.15×3.15 mm^2. The maximum current is 10 A in the correction coils.

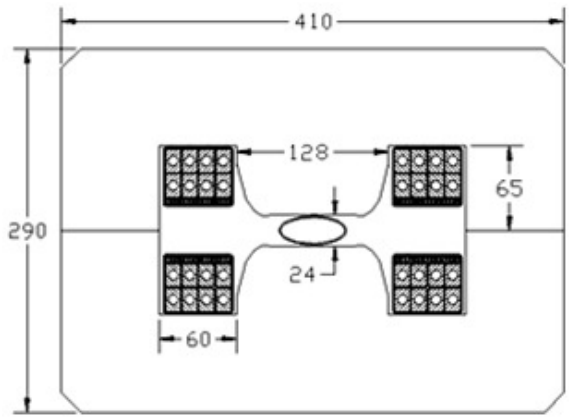

Figure 1: The dipole cross section.

Table 1: Dipole Parameters

Number of magnets	24
Deflection angle, deg	15
Magnetic field, T	0.1-1.3
Magnetic length, mm	1679.363
Yoke length, mm	1674
Curvature radius, mm	6415
Gap, mm	±12
Homogeneity within the GFR	$\leq \pm 2\times10^{-4}$
Number of coils	2
Number of turns per pole	8
Conductor cross section/ Inner hole diameter, mm^2/mm	18×12/ 8
Max. current, kA	1.56
Resistance per magnet, mΩ	6.47
Inductance per magnet, mH	2.86
Max. power loss, W	15.8
Pressure drop, bar	4
Cooling water flow rate, l/min	17.3
Temperature rise, °C	13.1
Magnet weight, kg	1500

The geometry of the pole, obtained in 2D- and 3D-simulations, provides the dipole field homogeneity in the central section of the magnet better than $\pm5\times10^{-5}$ in a good field region (GFR) of 20×40 mm^2 (h×w) and the integral homogeneity of $\pm2\times10^{-4}$ (Fig. 2). To reduce the

ISBN: 978-3-95450-240-0 ISSN: 2673-5539 doi:10.18429/JACoW-RuPAC2021-WEPSC20

magnetic saturation effect in the pole the Rogowski curve [3] was used for forming the transverse profile. To reduce distortions of the dipole field homogeneity in the GFR with increasing energy, the transverse profile has symmetrical shims directed to the horizontal plane of symmetry of the magnet. The magnet pole ends are formed by three planes to make the integral homogeneity symmetrical in the horizontal direction.

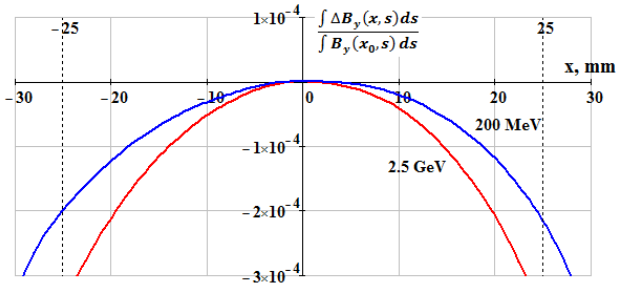

Figure 2: Integral homogeneity of the dipole field.

QUADRUPOLES

The quadrupole magnets of the booster synchrotron are grouped into three families: two families of focusing lenses and one family of defocusing lenses. The main quadrupoles parameters are presented in Table 2. The cross section of the quadrupole is shown in the Fig. 3.

The quadrupole magnet has also the 4 additional coils for field gradient correction. The cross-sectional conductor size is 3.15×3.15 mm^2 for additional coil. The maximum current is 9.3 A.

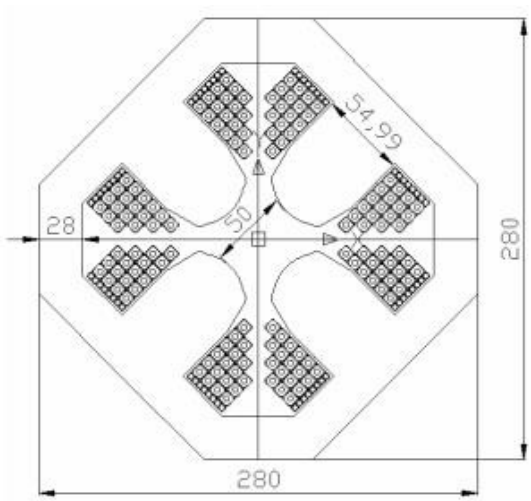

Figure 3: The quadrupole cross section.

The hyperbolic shape of the poles allows maintaining the constancy of the gradient of the quadrupole field in the working area of the magnet. Note, due to the magnetic saturation effect the effective length of the magnet differs at different energy levels. In addition, with the increasing current in the coils nonlinearities of the effective length and the field gradient arise. It is important to keep the product of these quantities at a high energy level (at 2.5 GeV).

The searched geometry of the magnet pole provides the homogeneity of the magnetic field gradient in the central section of the magnet better than ±1×10^{-4} in the GFR and the integral inhomogeneity better than ±5×10^{-4} (Fig. 4). The geometry of the pole ends was chosen so that the effective length is 320 mm at energy of 2.5 GeV.

Table 2: Quadrupole Parameters

Quadrupole magnets	Q1	Q2	Q3
Number of magnets	24	24	12
Max. gradient (2.5 GeV), T/m	21.12	-23.55	20.89
Magnetic length, mm	320		
Yoke length, mm	300		
Homogeneity of gradient within the GFR	≤ ±5×10^{-4}		
Number of coils	4		
Number of turns per pole	18		
Conductor cross section/ Inner hole diameter, mm^2/mm	7×7/ 3.5		
Current at max. gradient, A	292	325	289
Resistance per magnet, mΩ	26		
Inductance per magnet, mH	4.3		
Max. power loss, kW	2.22	2.75	2.17
Pressure drop, bar	4		
Cooling water flow, l/min	5.7		
Water temperature rise, °C	6.6	9.28	8
Bore radius, mm	25		
Magnet weight, kg	70		

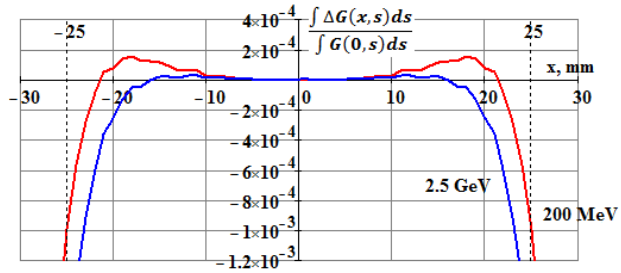

Figure 4: Integral homogeneity of the quadrupole field gradient.

SEXTUPOLES

The main sextupoles parameters are presented in Table 3. The cross section of the sextupole is shown in the Fig. 5.

The geometry of the transverse pole profile is set by a parabola, since the sextupole magnet provides a quadratic growth of the magnetic induction with radius. The pole ends are formed by one plane. The searched pole geometry provides an integral homogeneity of ±1×10^{-3} in the energy range 200 MeV to 2.5 GeV in the GFR (Fig. 6). This value is achieved with an increased homogeneity in the central section: the homogeneity changes in the range from 0 to +2.3×10^{-3} in the GFR at energy of 200

ISBN: 978-3-95450-240-0 ISSN: 2673-5539 doi:10.18429/JACoW-RuPAC2021-WEPSC20

MeV and in the range from 0 to $+1.7\times10^{-3}$ at energy of 2.5 GeV.

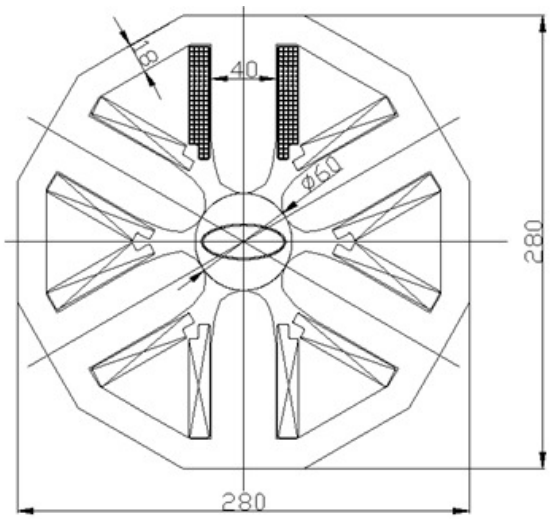

Figure 5: The sextupole cross section.

Table 3: Sextupole Parameters

Sextupole magnets	SD	SF
Number of magnets	24	
Max. sextupole gradient (2.5 GeV), T/m^2	-215	90
Magnetic length, mm	100	
Yoke length, mm	100	
Homogeneity of sextupole gradient within the GFR	$\leq\pm1\times10^{-3}$	
Bore radius, mm	30	
Number of coils	6	
Number of turns per pole	86	
Conductor cross section, mm^2	2.5×2.5	
Current at max. gradient, A	9	3.7
Resistance per magnet, mΩ	397	
Inductance per magnet, mH	66.9	
Max. power loss, W	32.2	5.6
Magnet weight, kg	25	

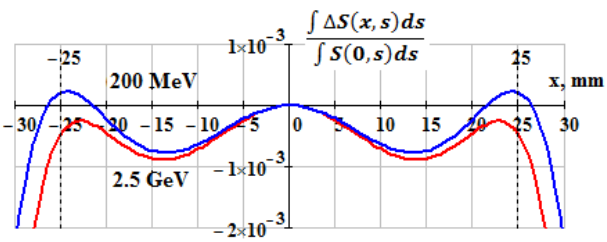

Figure 6: Integral homogeneity of the sextupole field.

CORRECTORS

The correcting magnet combines the functions of a horizontal and vertical corrector and is a frame dipole magnet (Fig. 7). The corrector provides a maximum angle of rotation of the particle trajectory of 0.48 mrad with a magnet yoke length of 100 mm. The effective length is 200 mm.

The corrector has the 4 main excitation coils. The cross-sectional conductor size is 2×2 mm^2. The maximum current is 7.2 A in the coils. The number of turns per coil is 266.

The integral homogeneity of the field is 2×10^{-2} in the GFR (Fig. 8). The sextupole component of the field is 1.78 T/m^2, which is less than the field value in the sextupole.

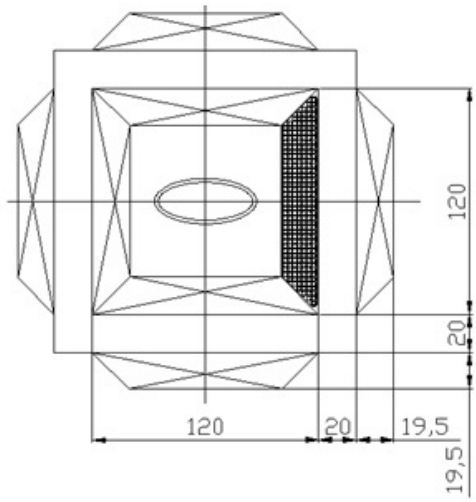

Figure 7: The corrector cross section.

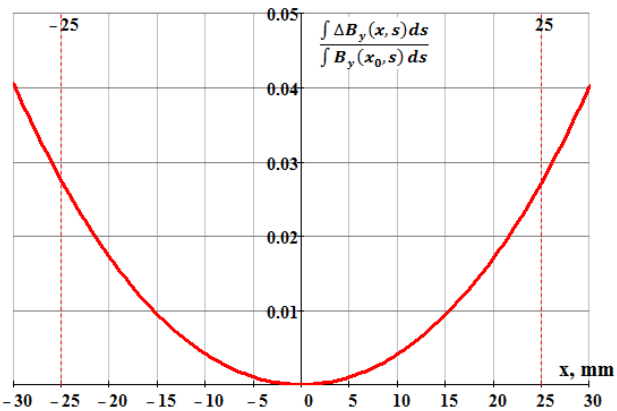

Figure 8: Integral homogeneity of the corrector field.

CONCLUSION

The geometry of each type of magnetic elements of the booster synchrotron is optimized in order to obtain the required parameters and quality of the magnetic field. However, we are considering the possibility of replacing the coils and small changes in the geometry of the dipole magnet due to the dense arrangement of the elements on the ring of the booster synchrotron. Also note, after the prototype is made and the magnetic measurements are carried out the geometry of the poles of each type of magnet can be corrected to achieve the required parameters of the magnetic field.

ISBN: 978-3-95450-240-0 ISSN: 2673-5539 doi:10.18429/JACoW-RuPAC2021-WEPSC20

REFERENCES

[1] A.S. Smygacheva, V.N. Korchuganov, and Ye.A. Fomin, "2.5 GeV booster synchrotron for a new Kurchatov synchrotron radiation source", presented at RuPAC'21, Crimea, Russia, Sep. 2021, paper TUPSB33, this conference.

[2] CST Studio Suite, http://www.3ds.com

[3] W. Rogowski, "Die elektrische Festigkeit am Rande des Plattenkondensators", Archiv f. Elektrotechnik, vol. 12, March 1923, pp. 1-15, https://doi.org/10.1007/BF01656573

ISBN: 978-3-95450-240-0 ISSN: 2673-5539 doi:10.18429/JACoW-RuPAC2021-WEPSC21

MAGNETS FOR LIGHT IONS ACCELERATOR

I. A. Yurin, S. M. Polozov, M. S. Dmitriev, E.N. Indyushnii, National Research Nuclear University MEPhI (Moscow Engineering Physics Institute), Moscow, Russian Federation.

Abstract

At the moment, the National Research Nuclear University (MEPhI) is developing an injector for an accelerator of light ions with an energy of 7.5 MeV / nucleon. The injector uses several tens of quadrupole magnets with a magnetic field gradient of 6-18 T / m and several units of dipole magnets. Key requirements for quadrupole magnets include large aperture, compact transverse dimensions, uniform shape and design, ease of fabrication from a manufacturing standpoint, field accuracy within 0.1%, and low power consumption. This article will describe the requirements, simulation results, and preliminary designs for quadrupole and dipole magnets.

INTRODUCTION

The new project of the injector for the proton and light ion accelerator will have several tens of quadrupole magnets, the range of the magnetic field gradient is 6-18 T / m, the aperture of the transport channel is 66.5 mm, the physical length of the lens is 100 mm, and the pulse repetition rate to 5 Hz. The original concept of a quadrupole magnet was continuous operation, since in any case the inductive component will be large enough and the transient time will not allow reducing the operating time with the power supply turned on. Based on the simulation results, for the maximum value of the magnetic field gradient (18 T / m), the active power of each cooling will be 582 W, and an active liquid system will also be required to maintain an acceptable temperature with a water flow rate of 0.415 liters / minute for each winding. According to the concept, the operating mode of the accelerator system is continuous (24/7), therefore, efficiency in terms of operation is also an important aspect. For example, for 10 quadrupole magnets (with the maximum gradient value), the electricity consumption per week will be 3.9×10^3 kW-hr, and the volume of water pumped will be 167 m^3. The optimal solution was to switch to a pulsed mode of operation.

MAGNET DESIGN

When developing the quadrupole, several important points were taken into account: the power source must be made on existing serial electronic components (in particular, IGBT transistors), the cooling system must be passive, the magnet design for all sections of the injector must be unified. The simulation resulted in a quadrupole magnet with the following parameters in Table 1.

Table 1: Quadrupole Specifications

Parameters	Value	Unit
Quadrupole gradient	18.0	T/m
Physical length	100	mm
Effective length	128.5	mm
Good field region	±15	mm
Number of turns per pole	48	
Conductor dimension	4×8	mm^2
Weight	138.25	kg
Steel	3408	
Operating temperature	48	°C
Total heat dissipation	10.55	W

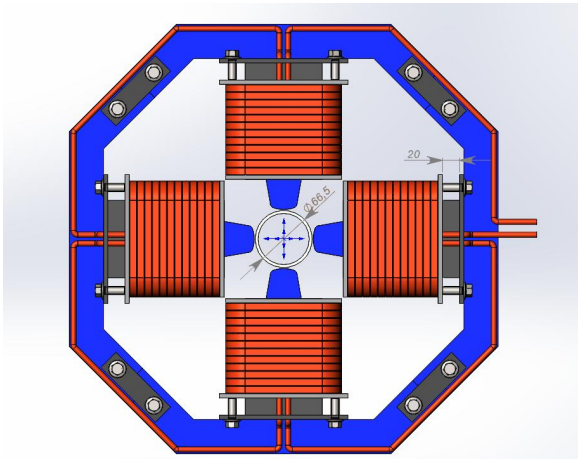

Figure 1: Front view of the pulse quadrupole.

The Pulsed Quadrupole was developed using 3D modeling software. To realize the maximum gradient of 18 T / m, the excitation current must be 180.5 A, the number of turns in coil is 48, the transverse dimensions of the conductor are 4 × 8 mm^2. A sketch of the model is shown in Fig. 1. The inductance of each coil is 3.17×10^{-3} H. The pole shape is built according to the equation [1]

$$xy = \frac{h^2}{2} \quad (1)$$

The magnet yoke is designed out of silicon steel, since this steel has a narrow hysteresis loop and, unlike low-carbon steel, will reduce the transient time by 5-6 times (for this model), in this case, steel grade 3408 is chosen. The yoke design is 4 connecting elements. The elements are packets of laminated steel with a thickness of 0.35 mm, this thickness is due to the decay time of eddy currents [2]

ISBN: 978-3-95450-240-0 ISSN: 2673-5539 doi:10.18429/JACoW-RuPAC2021-WEPSC21

$$\theta = \left(\frac{\sigma^2}{\pi \times \rho_{cm}}\right) \times 10^3 = 1.95\ ms \quad (2)$$

POWER SUPPLY CONCEPT

The power supply is an LC circuit [3], where the pre-charged capacitor C is the source, and the inductance L is the series-connected quadrupole coils. The schematic diagram is shown in Fig. 2.

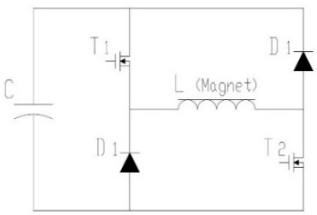

Figure 2: LC circuit.

This connection scheme was chosen in order to refuse from the pulse matching system, as when each coil is powered by a separate source. The pulse times are calculated from the allowable heat dissipation. The maximum allowable amount of heat load per coil is 10.6 W, at this load in steady state the temperature of the coils is 48 degrees Celsius. Temperature distribution is shown in Fig. 3.

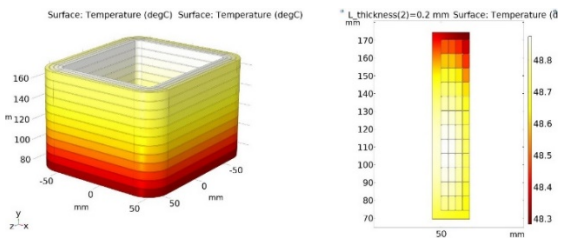

Figure 3: Coil temperature distribution.

For the operation at a frequency of 5Hz, the allowable pulse time is 5 ms, with the required pulse flat top time of 200 μs, the rise time is 2.49 ms. Calculated LC parameters are presented in Table 2 with other parameters.

Table 2: Power Supply Specifications

Parameters	Value	Unit
Magnet current maximum am-	180.6	A
Maximum amplitude of voltage	1510	V
Maximum pulse rep-rate	5	Hz
Pulse time	5	ms
Front time	2.9	ms
Flat top time	200	μs
Capacity	187	μF
Load parameters	13.54	mH, mΩ

PULSE OPERATION MODE SIMULATION

Simulation of the circuit was carried out in the program for modeling electrical circuits, taking into account the inductances and resistances of all sections of the circuit, both the coils themselves and the connecting wires, the fall of the pulse shelf within 200 μs is no more than 0.06%, the simulation results are presented in Fig. 4.

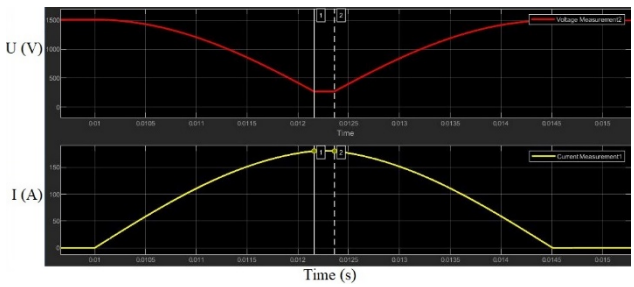

Figure 4: The values of the voltage across the capacitor and the current in the coil during the pulse.

The magnetic field gradient is corrected by shifting of the coil along the pole axis. From the zero point, where the field gradient is 18 T / m, a shift of ± 10 mm is possible, such a shift makes it possible to change the field gradient within 0.94%, which is sufficient since according to production conditions, the permissible deviation for the coils is 1%. The adjustment was simulated in the time domain in a 2D staging. With this technique, it is worth considering the conductivity of the yoke in the longitudinal direction, since the sheets of steel are located perpendicular to this direction. There are several approximations for determining the conductivity of the laminated core [4], according to these approximations, the conductivity in longitudinal direction is taken into account. The simulation results are presented in Fig. 5.

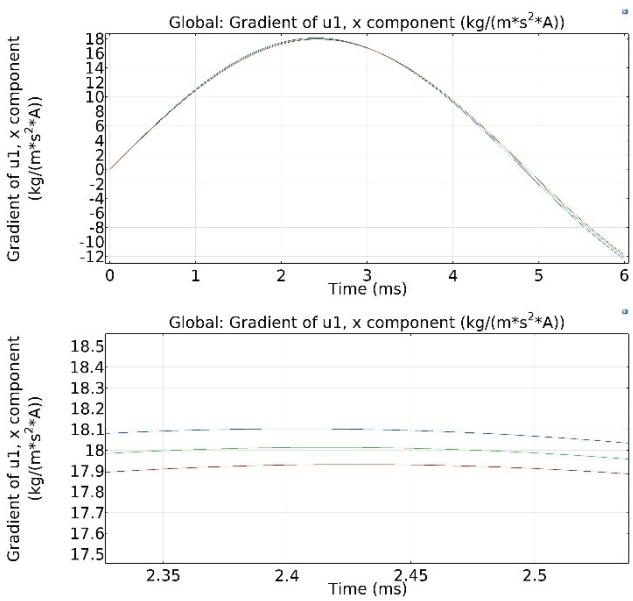

Figure 5: Adjusting the gradient

ISBN: 978-3-95450-240-0 ISSN: 2673-5539 doi:10.18429/JACoW-RuPAC2021-WEPSC21

DIPOLE MAGNETS

Three types of dipole magnets are also being developed for LEBT to compose beam from four ion source and for HEBT to shift the beam after injector to the injection chicane 0.06 T, 0.2 T, 1.19 T. The type version, at 0.06 T will used for composing beams from two ion sources, in view of the relatively low field level, was designed without an active cooling system, cooling only by means of free convection. For the yoke of the magnet low-carbon steel of St 1010 is used, the mass of the yoke is 703 kg, the amount of heat generated per coil is 44 W, the maximum design temperature is 37 degrees Celsius. A sketch of this magnet is shown in Fig. 6.

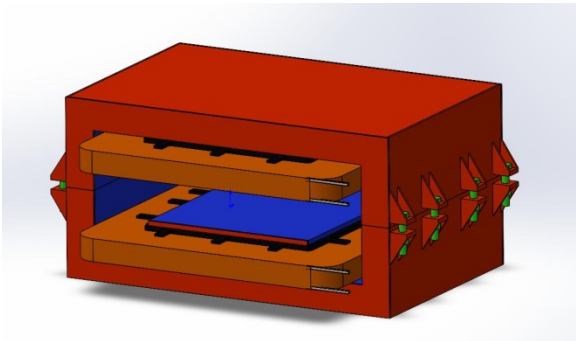

Figure 6: Dipole magnet 0.06 T.

The second dipole, with the field of 0.2 T will be used for composing of two trajectories in the final segment of LEBT. The shape of the dipole is due to the presence of two trajectories passing through the gap of the magnet. The yoke is steel St 1010, the mass of the yoke is ~500 kg, the amount of heat generated per coil is 700 W, the water consumption is 0.96 liters / minute, the maximum design temperature is 33 degrees Celsius. A sketch of magnet is shown in Fig. 7.

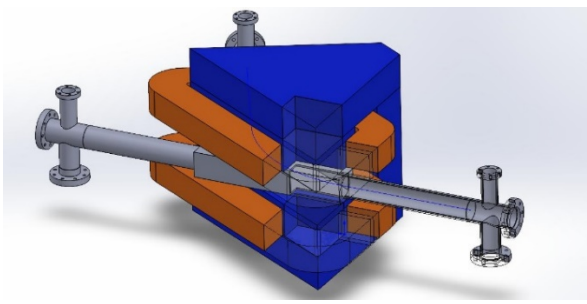

Figure 7: Dipole magnet 0.2 T.

The third dipole with a field level of 1.19 T will used for rotation the beam from the HEBT into the booster and it also uses an active cooling system. The yoke is steel St 1010, the mass of the yoke is 4400 kg, the amount of heat generated per coil is 3500 W, the water consumption is 5.14 liters / minute, the inlet pressure is 3.3 atm. The maximum design temperature is 31 degrees Celsius. A sketch of this magnet is shown in Fig. 8.

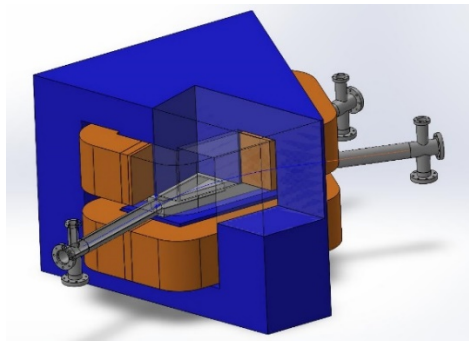

Figure 8: Dipole magnet 1.19 T.

CONCLUSION

The development of a pulsed quadrupole magnet was carried out taking into account the thermal load and the possibility of unifying the magnet for all sections of the accelerator. Requirements for the power supply were determined. Dipole magnets calculated. Further steps are to calculate the beam dynamics using obtained field distributions, example is shown in Fig. 9.

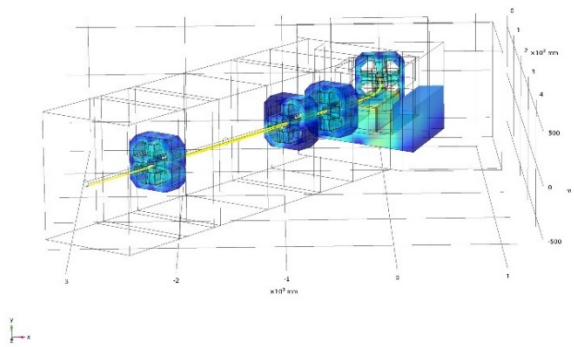

Figure 9: Beam dynamics in structure.

REFERENCES

[1] J. Tanabe, "Iron Dominated Electromagnets Design, Fabrication, Assembly and Measurements". Stanford Linear Accelerator Center, Stanford Synchrotron Radiation Laboratory, Stanford, USA, SLAC-R-754, 2005, p. 44.

[2] A. Ponomarenko, "Powerful impulse technology", MEPhI, Moscow, 2007.

[3] J.Wang *et al*., "Versatile dc/pulse switching mode power supply for an interleaving dipole magnet", in *Proc. EPAC'02,* Paris, France, June 2002, pp. 2508-2510.

[4] H.Neubert *et al., "*Homogenization approaches for laminated magnetic cores using the example of transient 3d transformer modeling", Technische Universität Dresden, Germany, Institute of Electromechanical and Electronic Design, 2ABB AG, Corporate Research Center Germany, Ladenburg, Germany, in *Proc. COMSOL'13,* Rotterdam, Netherlands, October 2013.

ISBN: 978-3-95450-240-0 ISSN: 2673-5539 doi:10.18429/JACoW-RuPAC2021-WEPSC28

OPTICAL DIAGNOSTICS OF 1 MeV PROTON BEAM IN ARGON STRIPPING TARGET OF A TANDEM ACCELERATOR*

A. N. Makarov#, S. S. Savinov, I. M. Shchudlo, S. Yu. Taskaev
Budker Institute of Nuclear Physics, Novosibirsk, Russia
Novosibirsk State University, Novosibirsk, Russia

Abstract

A neutron source for boron neutron capture therapy based on a vacuum-insulated tandem accelerator has been developed and operates at Budker Institute of Nuclear Physics. Conducting a ~10 mm proton beam with a power of up to 20 kW through a system of accelerating electrodes and 16 mm argon stripping tube is not an easy task. Any mistake made by operator or a malfunction of the equipment responsible for the correction of the beam position in the ion beam line can lead to permanent damage to the accelerator when a powerful beam hits the surface of the stripping tube or diaphragms of the electrodes. To determine the position of the proton beam inside the argon stripping tube, optical diagnostics have been developed based on the Celestron Ultima 80-45 telescope and a cooled mirror located at an angle of 45° to the beam axis in the straight-through channel of the bending magnet. The cooled mirror, in addition to the optical function, also performs the function of measuring the neutral current due to the electrical isolation of the mirror and the extraction of secondary electrons from its surface. The luminescence of a beam in the optical range, observed with the help of the developed diagnostics, made it possible for the first time to determine beam size and position inside the stripping tube with an accuracy of 1 mm. The light sensitivity of applied optical elements is sufficient for using a shutter speed from 2 to 20 ms to obtain a color image of the beam in real time. This makes it possible to realize a fast interlock on the event of a sudden displacement of the beam.

INTRODUCTION

Boron neutron capture therapy (BNCT) is currently considered as a promising technique for treatment of malignant tumors [1, 2]. Two clinics using accelerator based BNCT technique began treating patients in 2020 and four more BNCT clinics are ready to start. An accelerator neutron source developed [3] at Budker Institute of Nuclear Physics serves as a prototype for a facility constructed in 2021 for a BNCT clinic in Xiamen (China). It is planned to equip the National Medical Research Center of Oncology (Moscow, Russia) and National Oncological Hadron Therapy Center (Pavia, Italy) with the same vacuum-insulated tandem accelerators (VITA). Safety and durability of the new type of the accelerator are very important in case of 24/7 clinical operation and have not been studied in detail yet. One of the possible reasons that can lead to permanent damage of the accelerator and interrupt normal operation is the situation when a powerful ion beam hits the surface of the stripping tube or diaphragms of the accelerating electrodes. Since 2008, the year we obtained first neutrons at the accelerator [4], the stripping tube and diaphragms were damaged several times by the beam (Fig. 1).

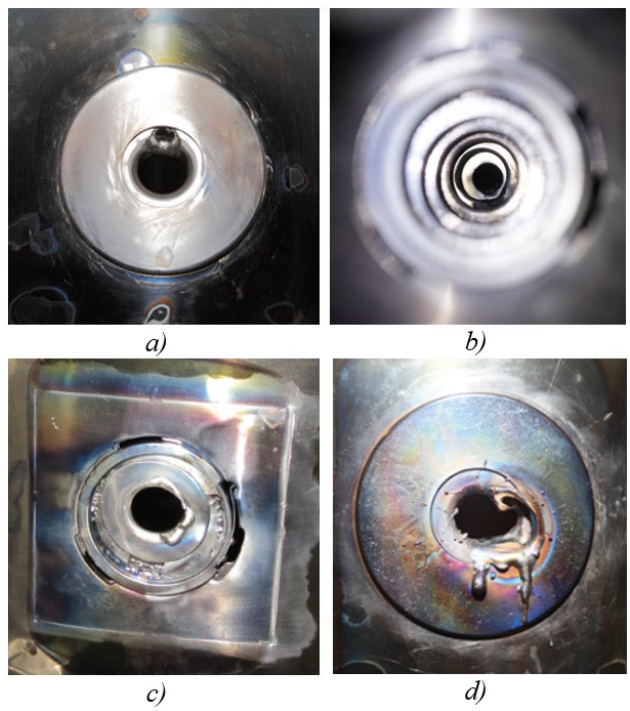

Figure 1: Photos of accelerator diaphragms (diameter is 20 mm) melted by the beam in different times: a) 12.2011, b) 03.2013, c) 03.2015, d) 06.2016.

With a DC current of up to 10 mA and energy of 2 MeV it takes only a few seconds for the beam to melt a diaphragm. In this case, one second of beam displacement will cost 2 weeks of repairing the accelerator. Reasons of sudden beam displacement from the axis can be different: it can be a mistake made by operator, or a malfunction of the equipment responsible for the correction of the beam position, or fast variation in conditions of a gas discharge in the H^- ion source. In this paper we describe an optical diagnostics that is capable to determine the position and size of the proton beam inside the accelerator with an accuracy better than 1 mm in real time. Such diagnostics can improve the reliability of the accelerator in clinical use. Available beam diagnostics, such as optical diagnostics at the entrance to the accelerator [5], calorimetric diagnostics

* This research was supported by Russian Science Foundation, grant No. 19-72-30005
# A.N.Makarov@inp.nsk.su

ISBN: 978-3-95450-240-0 ISSN: 2673-5539 doi:10.18429/JACoW-RuPAC2021-WEPSC28

of a charge-exchange tube, and measurement with a wire scanner [6] do not allow *in situ* estimation of the position, size, and shape of the beam inside the stripping tube. The speed of operation and the accuracy of these diagnostics also do not allow the implementation of fast interlock on the event of a sudden displacement of the beam.

EXPERIMENTAL SETUP

Figure 2 shows the VITA and the high-energy beam transporting channel where the new optical diagnostics is installed. Coming from source *1* the low-energy negative hydrogen ion beam is injected into accelerator *2* and accelerated up to 1 MeV. In argon stripping tube *3* negative hydrogen ions are converted into protons. Then protons are accelerated by the same 1 MV potential to an energy of 2 MeV. Accelerated proton beam is transported through the high-energy beam line and received by the lithium target *5* when the bending magnet *4* is switched on. In this case, thanks to the straight-through channel of the bending magnet, uncharged particles and visible light can pass directly into the vacuum chamber *6*. This property is used to register the glow in the stripping tube. With the help of a cooled mirror installed inside chamber *6* at an angle of 45° to the axis of the accelerator, visible light is directed into telescope *7* Celestron Ultima 80-45.

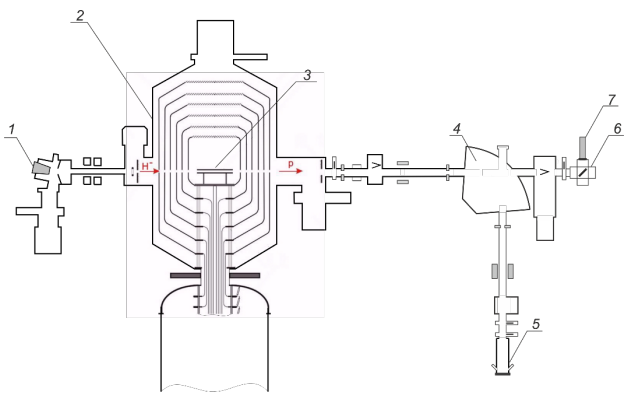

Figure 2: Experimental setup: *1* – negative hydrogen ion source, *2* – accelerator, *3* – argon stripping tube, *4* – bending magnet, *5* – lithium target, *6* – vacuum chamber with cooled 45° mirror, *7* – telescope.

Let us look in detail at the design of the cooled mirror. A typical proton beam charge-exchange rate is about 95%. This means that the power of the neutral H^0 beam hitting the mirror is 2.5% of the power of the proton beam, i.e. up to 500 W/cm^2 at 10 mA 2 MeV proton beam. Such thermal load requires the organization of effective forced cooling. Plus, significant deformations due to thermal expansion of the metal cannot be allowed for the mirror, as well as deformations as a result of the supply of water pressure to the cooling channels. All these considerations formed the basis for the design of the cooled copper mirror (Fig. 3). The mirror is electrically insulated from the facility body. Due to the electrical isolation of the mirror and the extraction of secondary electrons from its surface, it is possible to measure the current of neutrals and the charge-exchange rate in real time [7]. The vacuum window is made of barium fluoride, so it can be used to install an infrared camera instead of a telescope.

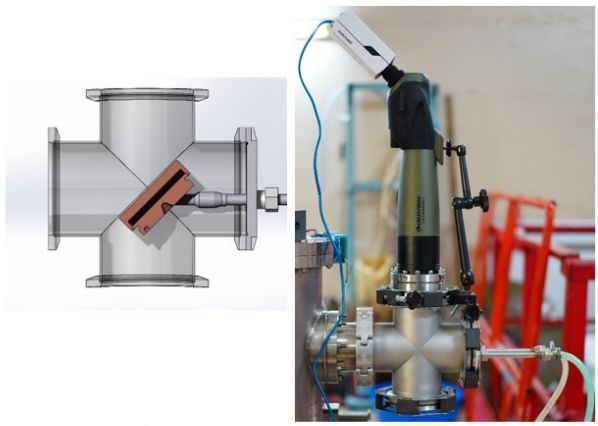

a) *b)*

Figure 3: Construction of the cooled mirror: a) technical drawing, b) photo of the installed diagnostics.

EXPERIMENTAL RESULTS

Before the experimental results were obtained, it was not obvious whether, in principle, it would be possible to get an image of the beam inside the charge-exchange tube. This could be prevented by several phenomena: 1) the glow of the beam in the high-energy beam transporting channel could eclipse the light from the stripping tube, 2) the light sensitivity of the used optical elements could be insufficient. Fortunately, this did not happen and we managed to get an image of the 2 mA beam inside the charge-exchange tube (Fig. 4*a*). At Fig. 4*b*, one can see the moment of displacement of the beam, which occurred due to the breakdown inside the H^- ion source. The beam shifted and returned to its place within less than 20 ms, however, thanks to the fast shutter speed, this moment was captured.

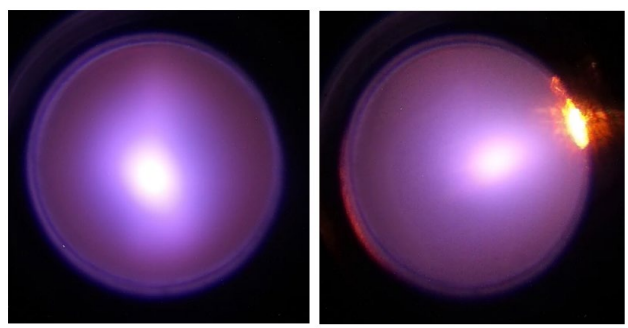

a) *b)*

Figure 4: Photo of the 2 mA proton beam in 16 mm argon stripping tube taken at 1/100 s shutter speed: a) normal operation, b) sudden beam displacement.

Looking at Fig. 4*a*, we get a typical beam size inside the accelerator equal to 3×5 mm. Now we can estimate the minimum time required for the beam to melt the accelerator diaphragm. To heat a part of a stainless-steel

ISBN: 978-3-95450-240-0 ISSN: 2673-5539 doi:10.18429/JACoW-RuPAC2021-WEPSC28

diaphragm with a thickness of 2 mm up to the melting point, it is necessary to spend energy Q equal to:

$$Q = c\, m\, \Delta T = 154 \text{ J},$$

where c is the heat capacity, m is the mass, and ΔT is the temperature of the part of the diaphragm heated by the beam. Accordingly, at 10 kW beam power, this will take at least 15 ms. We assume the energy of the beam and, accordingly, its power, relying on our experience: the entrance diaphragm of the central electrode was damaged most often (see Fig. 1), the beam energy in this case is 1 MeV.

To estimate the minimum melting time, we assume the worst-case scenario, namely, that the entire beam hits the diaphragm of the central electrode without touching other diaphragms. And also, we assume that the size of a 10 mA beam does not exceed 3×5 mm. We also neglect heat transfer along the diaphragm and energy losses due to infrared radiation. A relatively large error can be hidden in the assumption that the diaphragm was not heated previously (by the edge of the beam or accompanying particles). In any case, the speed of the developed diagnostics is sufficient to implement interlock, since the longest time is taken by the frame exposure varying from 2 to 20 ms (depending on the beam current, for a large current – it is smaller), other times are shorter.

CONCLUSION

With the help of developed optical diagnostics, it was possible for the first time to see a beam inside the charge-exchange tube of the VITA. Diagnostics makes it possible to determine in real time the shape of the beam, as well as its displacement from the axis of the accelerator with an accuracy of better than 1 mm. The sensitivity of applied optical elements is sufficient to realize fast interlock when the beam suddenly moves. Such diagnostics can improve the reliability of the VITA in clinical use.

REFERENCES

[1] W. Sauerwein, A. Wittig, R. Moss, Y. Nakagawa (Eds.), *Neutron Capture Therapy: Principles and Applications*. Springer, 2012. doi:10.1007/978-3-642-31334-9

[2] S. Taskaev, V. Kanygin, *Boron Neutron Capture Therapy*, Novosibirsk, Russia: Publisher of SB RAS 216, 2016. doi: 10.1134/S106377882101021X

[3] S. Taskaev *et al.*, "Neutron Source Based on Vacuum Insulated Tandem Accelerator and Lithium Target", *Biology*, vol. 10, 350, Apr. 2021. doi:10.3390/biology10050350

[4] B. Bayanov *et al.*, "First neutron generation in the BINP accelerator based neutron source", *Appl. Radiat. Isot.*, vol. 67, no. 7, pp 285-287, July 2009. doi: 10.1016/j.apradiso.2009.03.077.

[5] T. Bykov *et al.*, "Visualization of a negative hydrogen ions beam in a vacuum insulation tandem accelerator." in *Proc. 18th Int. Congress on Neutron Capture Therapy*, Taipei, Taiwan, Oct.-Nov 2018, , pp. 202-203.

[6] T. Bykov *et al.*, "Use of a Wire Scanner for Measuring a Negative Hydrogen Ion Beam Injected in a Tandem Accelerator with Vacuum Insulation", *Instrum. Exp. Tech.*, 2018, vol. 61, no. 5, pp. 713-718. doi:10.1134/S0020441218050159

[7] Ia. Kolesnikov. *et al.*, "Diagnostics of the Efficiency of a Gas Stripping Target of a Tandem Accelerator with Vacuum Insulation", *Instrum. Exp. Tech.*, 2020, vol. 63, no. 3, pp. 314-318. doi: 10.1134/S0020441220040065

ISBN: 978-3-95450-240-0 ISSN: 2673-5539 doi:10.18429/JACoW-RuPAC2021-WEPSC29

DIAGOSTICS OF THE PROTON BEAM POSITION USING THE LUMINESCENCE OF A LITHIUM NEUTRON-GENERATING TARGET*

E.O. Sokolova†, A.N. Makarov, S.Yu. Taskaev,
Budker Institute of Nuclear Physics, Novosibirsk, Russia
Novosibirsk State University, Novosibirsk, Russia

Abstract

A compact accelerator-based neutron source [1] has been proposed and created at the Budker Institute of Nuclear Physics in Novosibirsk, Russia. An original design tandem accelerator is used to provide a proton beam. The neutron flux is generated as a result of the ^{7}Li (*p, n*) ^{7}Be threshold reaction using the solid lithium target. A beam shaping assembly is applied to convert this flux into a beam of epithermal neutrons with characteristics suitable for BNCT (boron neutron capture therapy) [2]. In addition to the main purpose the neutron source is used to measure the content of impurities in ceramic samples developed for ITER [3], for measurement of the cross section of the reaction of inelastic scattering of a proton on a lithium nucleus. The neutron source is planned to be used for radiation testing of optical fibers of the laser calorimeter calibration system of the CMS [4] for the High Luminosity Large Hadron Collider (CERN). The need to provide the long-term stable generation of neutrons requires the development of diagnostic techniques that display relevant information from various subsystems of the neutron source in real time. We have developed and put into operation diagnostics for monitoring the position of the proton beam on a lithium target, which is also resistant to radiation exposure.

EXPERIMENTAL SETUP

An accelerator-based source of epithermal neutrons (Fig. 1) consists of an ion source *1a*, tandem accelerator with vacuum insulation *1* to obtain a stationary proton beam with an energy of up to 2.3 MeV and a current of up to 9 mA, lithium target *3* to generate neutrons as a result of the ^{7}Li (*p, n*) ^{7}Be threshold reaction. The lithium target is a copper disk, on which a thin lithium layer (usually 60 μm) is deposited from the side of the proton beam, and spiral channels for water cooling occur on the back side. The lithium targets may be installed in various positions: *A* after the bending magnet, *B* inside the irradiation room, *C* with movable system, *D* along the proton beam, *E* along the proton beam in the separate bunker, inside the beam shaping assembly (optionally).

To develop diagnostics for visual monitoring of the position of the proton beam, a lithium target was placed in the position *C* behind the bending magnet, which in this case was turned off. A Hikvision (China) video camera was installed on one of the branch pipe of the target assembly with barium fluoride glass; on the second branch pipe, with fused quartz glass, a darkened adapter was located, to which a CCS200 Compact Spectrometer (Thorlabs, United States) with the wide range (200–1000 nm) was connected through a multimode 5-m-long quartz fiber, with a core diameter of 200 μm and a numerical aperture of 0.22 NA. The spectrometer and PC were placed in the separate bunker to protect the spectrometer from bremsstrahlung radiation and neutrons.

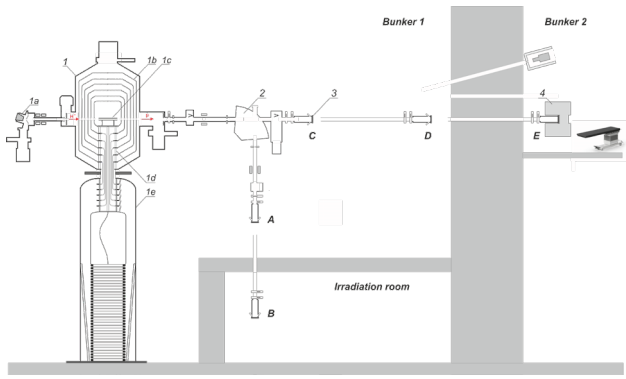

Figure 1: Compact accelerator-based neutron source: *1* – tandem accelerator with vacuum insulation; *2* – bending magnet; *3* – lithium neutron-generating target; *4* – beam shaping assembly.

RESULTS AND DISCUSSION

The emission spectrum of the lithium target was measured with a spectrometer when it was irradiated with a 2 MeV proton beam (see Fig. 2). The 610.3 ± 0.5 nm emission line corresponds to the $1s^2 3d \rightarrow 1s^2 2p$ electronic transition in the lithium atom, while the 670.7 ± 1 nm line corresponds to the $1s^2 2p \rightarrow 1s^2 2s$ transition in the lithium atom, and the 656.3 ± 1 nm line is the H_α spectral line observed for the hydrogen atom.

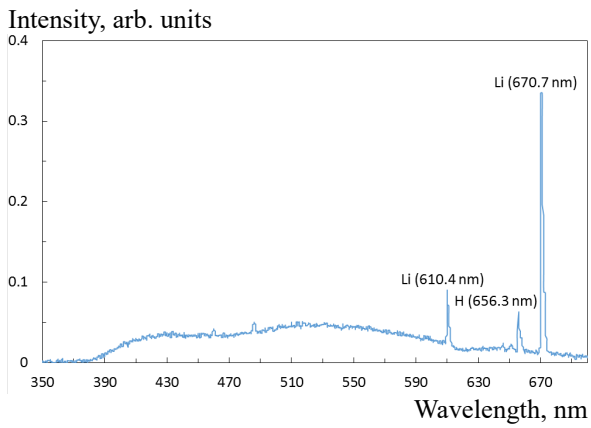

Figure 2: The luminescence spectrum of the lithium target.

* Work supported by supported by the Russian Foundation for Basic Research, project No. 19-32-90119.
† buiya@bk.ru

ISBN: 978-3-95450-240-0 ISSN: 2673-5539 doi:10.18429/JACoW-RuPAC2021-WEPSC29

The luminescence of lithium under the action of high-energy protons is clearly recorded by the video camera. Thus, Fig. 3 shows the images obtained with a Hikvision video camera when the lithium target is connected in *C* position (Fig. 1) through a bellows. The lithium target is irradiated with a proton beam of 2 mm in diameter and is moved using a Bohua actuator (China). The images clearly show a glow in the form of a light oval spot. The shape of the spot is due to the fact that the video camera views the target at an angle of 45°. Visualization of the proton beam on the target was used to measure the spatial distribution of the thickness of the lithium layer by recording the intensity of radiation of 478 keV gamma quanta emitted during inelastic scattering of protons on lithium nuclei [5].

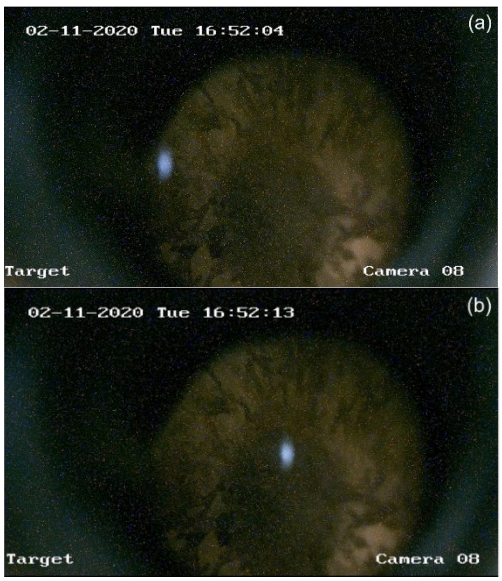

Figure 3: The glow recorded by Hikvision video camera when a lithium target is irradiated with a proton beam 2 mm in diameter in the direction of protons: (a) to the edge of the lithium target, (b) to the center.

The registration of luminescence made it possible to increase the reliability of the results of measuring the current of an argon ion beam that contributes to the flux of secondary charged particles in the accelerator [6]. The measurements were carried out by mass spectrometry using a bending magnet, inside which a cooled collimator with a 4 × 20 mm aperture was introduced through a vertical pipe (see Fig. 1). The charged particles which passed through the hole hit a lithium target which is electrically isolated from the facility and generated a current in the circuit, which was measured.

Figure 4 shows that the supply of a current to the bending magnet leads to the separation of the beam components: if the neutrals (hydrogen atoms) remain in place, then the argon ions and protons are displaced downward. At a certain current of the bending magnet, the proton beam will hit the collimator below the slit, the argon ions will pass through the slit, and their current can be measured. The measured current was so small, at the level of measurement accuracy, that if it were not for the visualization of the argon beam on the lithium target, it could be mistakenly considered zero. Figure 4b shows that only neutrals and argon ions pass through the slit and enter the target. With an increase in the gas injection into the stripping target, the glow intensity caused by argon ions increases, which should be expected, while the intensity of neutrals, that is, hydrogen atoms, on the contrary, decreases, which should also be expected (Fig. 4c).

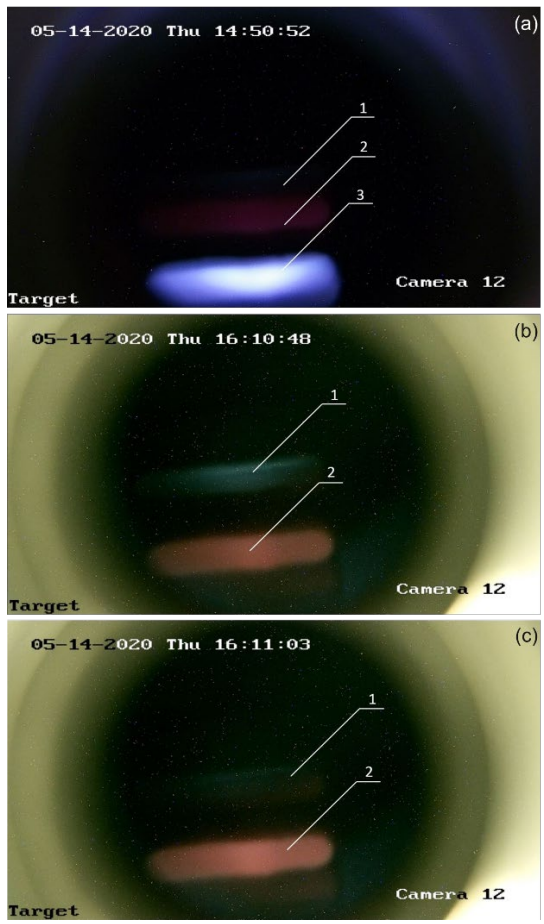

Figure 4: The glow recorded by a Hikvision video camera when a lithium target is irradiated with the components of a charged particle beam, at a bending magnet current of 14 A (a), 68 A (b) and 68 A and double gas injection into a stripping target (c). *1*, glow caused by neutrals (hydrogen atoms); *2*, argon ions; *3*, protons.

CONCLUSION

The accelerator-based epithermal neutron source operates at the Budker Institute of Nuclear Physics. It consists of a vacuum-insulated tandem accelerator for producing a proton beam and a lithium target for generating neutrons as a result of the ^{7}Li (*p, n*) ^{7}Be threshold reaction. The luminescence of lithium was recorded when the target was irradiated with protons using a video camera and a spectrometer. The registered radiation intensity of 610.3 ± 0.5 nm corresponds to the $1s^2 3d \rightarrow 1s^2 2p$ electronic transition in the lithium atom, while the 670.7 ± 1 nm line corresponds to the $1s^2 2p \rightarrow 1s^2 2s$ transition. Based on the results of the study, an optical diagnostic was developed and put into operation for operational monitoring of the position and the

ISBN: 978-3-95450-240-0 ISSN: 2673-5539 doi:10.18429/JACoW-RuPAC2021-WEPSC29

size of the proton beam on the surface of a lithium target used in the neutron generation mode.

REFERENCES

[1] S. Taskaev *et al.*, "Accelerator based epithermal neutron source", *Phys. Part. Nucl.*, vol. 46, no. 6, p. 956, Nov. 2015. doi:10.1134/S1063779615060064

[2] W. Sauerwein, A. Wittig, R. Moss, Y. Nakagawa, Neutron Capture Therapy: Principles and Applications, Ed. Springer, Germany; 2012. doi:10.1007/978-3-642-31334-9

[3] A. Shoshin *et al.*, "Qualification of Boron Carbide Ceramics for Use in ITER Ports", *IEEE Trans. Plasma Sci.*, vol. 48, no. 6, p. 1474, Jun. 2020. doi:10.1109/TPS.2019.2937605

[4] D. Kasatov *et al.*, "A Fast-Neutron Source Based on a Vacuum-Insulated Tandem Accelerator and a Lithium Target", *Instrum. Exp. Tech.*, vol. 63, no. 5, pp. 611-615, Sep. 2020. doi:10.1134/S0020441220050152

[5] D. Kasatov *et al.,*"Method for in situ measuring the thickness of a lithium layer", *J. Instrum*., vol. 15, no 10, p. 10006, Oct. 2020. doi:10.1088/1748-0221/15/10/P10006

[6] A. Ivanov *et al.,* "Suppression of an unwanted flow of charged particles in a tandem accelerator with vacuum insulation", *J. Instrum.*, vol. 11, no. 4, p. 04018, Apr. 2016. doi:10.1088/1748-0221/11/04/P04018

ISBN: 978-3-95450-240-0 ISSN: 2673-5539 doi:10.18429/JACoW-RuPAC2021-WEPSC30

MEASUREMENT OF THE PHASE PORTRAIT OF A 2 MeV PROTON BEAM ALONG BEAM TRANSFER LINE*

T. Bykov, Ia. Kolesnikov, S. Savinov, I. Shchudlo, S. Taskaev,
Budker Institute of Nuclear Physics, 11 Lavrentiev ave., 630090 Novosibirsk, Russia

Abstract

For the development of a promising technique for the treatment of malignant tumors - boron neutron capture therapy - an accelerator source of epithermal neutrons has been proposed and created at the Budker Institute of Nuclear Physics (Novosibirsk, Russia). For future therapy and radiation testing of materials for ITER and CERN with fast neutrons, it is necessary to ensure the transportation of a proton beam in a high-energy path at a distance of 10 meters.

For this purpose, a phase portrait of the proton beam was measured in the vertical and horizontal high-energy paths using a movable diaphragm with a diameter of 1 mm, mounted on a three-dimensional vacuum driver, and a wire scanner.

The software for remote control of the movable diaphragm and data processing of the wire scanner was developed. An algorithm for processing a series of measurements was also developed to reconstruct the image of the phase portrait of the beam and calculate the emittance. This work describes in detail the features of the measuring devices, control algorithms and data processing.

An experiment was carried out to measure the phase portrait and emittance of a proton beam with an energy of 2 MeV and a current of up to 3 mA. A beam of neutral particles was also measured. The effect of a bending magnet on the focusing and emittance of the beam is studied. The invariant normalized emittances calculated from the measured phase portraits make it possible to claim that the beam can be transported over distances of about 10 meters without changes in the current geometry of the high-energy beam line.

INTRODUCTION

Epithermal neutrons source based on a vacuum-insulated tandem accelerator [1] with a lithium target and a neutron Beam Shaping Assembly (BSH) [2] is currently the only experimental facility of this class in the world. It is able to generate a stationary beam of protons or deuterons with an energy range of 0.6 to 2.2 MeV and a current range of 1 pA to 10 mA. Such a wide range of parameters opens up a whole range of applications, in addition to clinical trials and therapy.

For future therapy and radiation testing of materials with fast neutrons [3, 4], it is necessary to ensure the transportation of a proton beam in a high-energy path at a distance of 10 meters. For that purposes a beam phase portrait and emittance was measured.

* The study was supported by a grant from the Russian Science Foundation (project No. 19-72-30005) with the support of the Budker Institute of Nuclear Physics SB RAS.

EXPERIMENTAL SETUP

To measure the phase portrait of the proton beam, the cooled diaphragm and the three-dimensional vacuum driver are placed in the diagnostic chamber in front of the bending magnet, the wire scanner is placed behind the bending magnet, and the luminescence effect of the lithium target is monitored by a video camera (Fig. 1). The wire scanner is placed so that one wire measures the current horizontally and the other vertically.

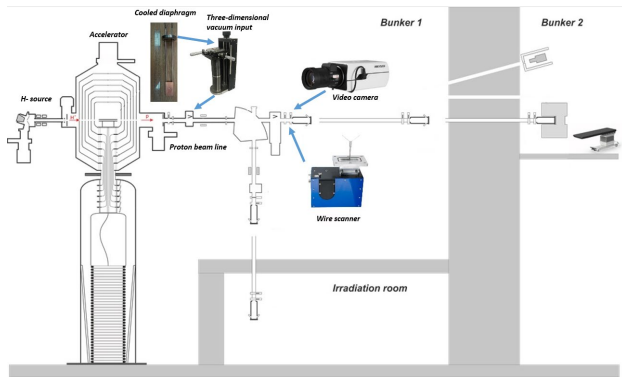

Figure 1: Experimental setup.

First, using a lithium target like a Faraday cup, the center of the beam is found. Further, by entering the motion, one coordinate is left fixed, and the other is moved and the current profile is measured. The same is repeated for the second coordinate.

It should be said that the wire scanner was used not in a standard way. Normally it should be used to measure low-energy charged-particle beam profiles (< 1 MeV) [5]. The use of cooled diaphragm with a hole of 1 mm allows to reduce the heat power generated on the wire probes so that it allows to measure the proton beam current with energy of 2 MeV and current up to 3 mA. During the experiments this constraint were found. A further increasing in current leads to overheating of the tungsten scanner probes and to the ignition of a plasma discharge.

DATA PROCESSING

An example of a measurements made by wire scanner is shown on Fig. 2. Each graph corresponds to the measurement of the beam at a given position of the cooled diaphragm. In this case it can be seen that the beam distribution is measured along the X axis, and the Y axis is fixed. Then the graphs are shifted taking into account the coordinates of the cooled diaphragm.

ISBN: 978-3-95450-240-0 ISSN: 2673-5539 doi:10.18429/JACoW-RuPAC2021-WEPSC30

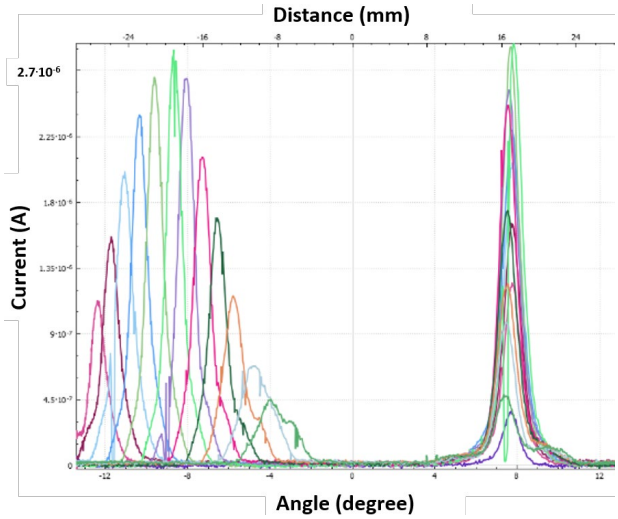

Figure 2: Beam measurements along one coordinate made by wire scanner.

Then all graphs as a whole are shifted to the origin. A mean graph is built between two adjacent graphs, with the values that are the average values between the two values of the corresponding graphs. This operation is repeated several times. As a result, a more continuous, smoother distribution is obtained from a discrete set of curves.

Then a 3D phase portrait is constructed. The examples of phase portrait obtained in this way is shown in Fig. 3.

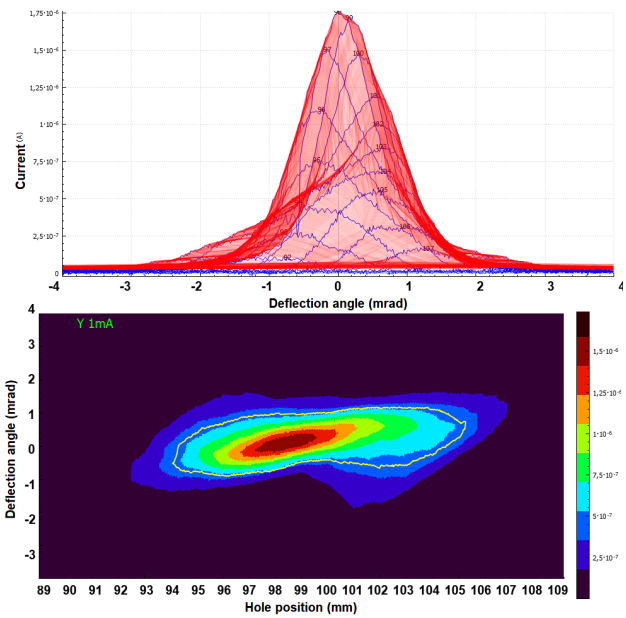

Figure 3: Shifted and augmented graphs and the 3D phase portrait is a result of data processing.

The coordinate of the cooled diaphragm is plotted along the X axis, the deflection angle of a beam is shown along the Y axis, and the current value is indicated by color.

In order to calculate the emittance, the following steps were taken. The area is determined, the total current in which is 2/3 of the total current throughout the portrait, and the area value will be denoted as $\varepsilon_{2/3}$. This area was then multiplied by the relativistic coefficients β and γ, for a proton beam with an energy of 2 MeV they are $\beta = \sqrt{\frac{2T}{E}} = 0{,}065$ and $\gamma = \frac{1}{\sqrt{1-\beta^2}} = 1{,}002$, respectively. Thus, the invariant emittance is $\varepsilon_{inv} = \varepsilon_{2/3}\beta\gamma$. Note that the X axis in most cases lacked the scanning range, so the emittance will be indicated with an inequality sign.

RESULTS AND DISCUSSION

The influence of the proton current on the phase portrait of the beam was studied. The emittance coincides with an accuracy of 10% for proton beam currents from 0.5 mA to 3 mA. The phase portrait depends on the current since the space charge of the beam affects the beam, and a 1.5% change in the magnetic lens current significantly affects the beam transport. The normalized emittance was defined as 0.23 mm mrad.

The effect of the focusing magnetic lenses, which are located in the entrance to the accelerator, on the proton beam after passing through the accelerator was also studied. The current 66 A and 56 A in magnetic lenses is the optimal mode used when conducting a beam with parameters standard for BNCT. In the weak focusing mode (65 A and 55 A), the beam has a large angular divergence in comparison with other modes. In the strong focusing mode (67 A and 57 A), it would seem that the beam size is small and the angular divergence is acceptable. However, with such focusing, the ion beam heats up the entrance diaphragm of the accelerator strongly, which makes this mode unacceptable during long-term operation.

The estimated beam sizes were obtained for the positions of the lithium target. That is 30 mm at position (Fig. 4 A) after going down through the bending magnet. Beam is expanded further down into irradiation room (Fig. 4 B) with the size 55 mm. Beam has the size 20 mm (Fig. 4 C) after the bending magnet going straight through and expand up to 28 mm at the position D (Fig. 4) and 38mm at Bunker 2 at the BSH (Fig. 4 E).

A beam of this size can be delivered to Bunker 2 for clinical trials and in the radiation testing room.

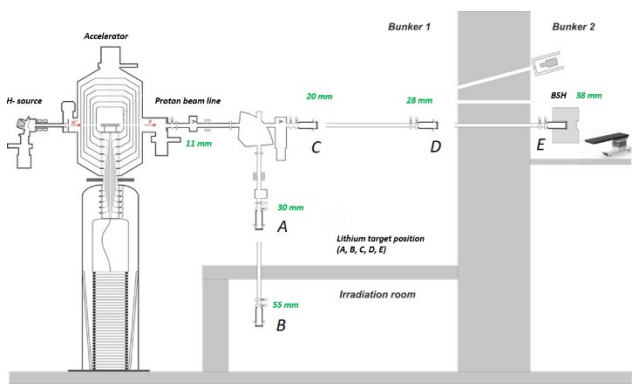

Figure 4: Estimated beam size at different positions of the lithium target.

ISBN: 978-3-95450-240-0 ISSN: 2673-5539 doi:10.18429/JACoW-RuPAC2021-WEPSC30

CONCLUSION

The phase portrait of a proton beam obtained in the vacuum insulated tandem accelerator was measured using a movable diaphragm and a wire scanner. The result obtained made it possible to determine the size of the proton beam in lithium target placement positions.

REFERENCES

[1] S. Taskaev, "Development of an accelerator-based epithermal neutron source for boron neutron capture therapy", *Phys. Part. Nucl.* vol. 50 no. 5, pp. 569–575, 2019. doi:10.1134/S1063779619050228

[2] L. Zaidi *et al.*, "Beam Shaping Assembly Design of ^{7}Li(p,n)^{7}Be Neutron Source for Boron Neutron Capture Therapy of Deep-seated Tumor", *Appl. Radiat. Isot.,* vol. 139, p. 316, 2018. doi:10.1016/j.apradiso.2018.05.029

[3] A. Shoshin *et al.*, "Test results of boron carbide ceramics for ITER port protection", *Fusion Eng. Des.*, vol. 168, 112426, March 2021. doi:10.1016/j.fusengdes.2021.112426

[4] D. Kasatov *et al.*, "Fast-neutron source based on a vacuum-insulated tandem accelerator and a lithium target", *Instrum. Exp. Tech.*, vol. 63, no. 5, pp. 611–615, 2020. doi:10.1134/S0020441220050152

[5] D-Pace Oscillating Wire Scanner Probe, https://www.d-pace.com/?e=70

ISBN: 978-3-95450-240-0 ISSN: 2673-5539 doi:10.18429/JACoW-RuPAC2021-WEPSC31

2D-TOMOGRAPHY OF THE PROTON BEAM IN THE VACUUM INSULATED TANDEM ACCELERATOR*

M .I. Bikchurina†, I A. Kolesnikov, S. S. Savinov, I. M. Shchudlo, S. Yu. Taskaev,
Budker Institute of Nuclear Physics, 630090 Novosibirsk, Russia
Novosibirsk State University, Novosibirsk, Russia

Abstract

For the development of a promising method for the treatment of malignant tumors - boron neutron capture therapy - the accelerator-based epithermal neutrons source has been proposed and created in the Budker Institute of Nuclear Physics [1,2]. With different parameters of the proton beam - the energy and current of the beam, the parameters of the ion-optical system, the parameters of the ion source - the conditions for beam transportation change - its size, angular divergence, and position relative to the axis of the accelerator. For optimal conduction of the beam along the path, two-dimensional tomography of the beam can be used - using a cooled diaphragm with a diameter of several millimeters installed on a vacuum three-dimensional motion input, and a Faraday cup, fast chord measurements are carried out, on the basis of which the beam profile is restored. The beam profile obtained in this way is somewhat different from the profile obtained by measuring the phase portrait of the beam using a wire scanner [3]. The advantage of this method is a relatively short time to restore the profile, depending on the diameter of the cooled diaphragm hole.

INTRODUCTION

Charged particle accelerators are widely used in scientific research, medicine, and other applications. Tandem accelerators are high-voltage electrostatic accelerators in which the high-voltage potential is used twice: first to accelerate negative ions, and then, after changing the polarity of their charge in the high-voltage terminal, to accelerate positive ions. Since power density of the proton beam can reach tens of kW/cm^2 there are mechanisms, influencing on the transportation of the beam, such as parameters of the H^- source (accelerating and extracting potentials, voltage of the discharge), focusing and correctors values and energy of the beam there is a need to diagnostic beam with such power and transport it through the high-energy beam line correctly, without heating vacuum chambers. For solve this task it was proposed and realized fast diagnostic of the beam profile, size and destination – two-dimensional tomography.

THE EXPERIMENTAL SCHEME

The studies were carried out at the accelerator neutron source of the Budker Institute of Nuclear Physics (Novosibirsk, Russia). The source diagram is shown in Fig. 1 and its detailed description was given in [1]. A tandem accelerator with vacuum insulation was used to obtain a stationary proton beam with an energy of 0.6 to 2.3 MeV and a current of 0.3 to 10 mA, that is, a tandem accelerator of charged particles with an original design of electrodes.

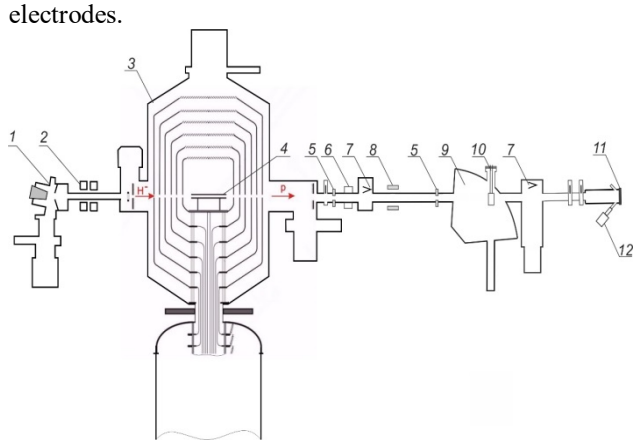

Figure 1: A diagram of an accelerator based source of epithermal neutrons. 1 - H^- source, 2 – magnetic lense, 3 – vacuum-insulated tandem accelerator, 4 – gas stripping target, 5 – cooled diaphragm, 6 –NPCT contactless beam sensor (Bergoz, France), 7 – movable Faraday cup 8 – corrector, 9 – bending magnet, 10 – cooled beam receiver with a diaphragm, 11 – lithium target, 12 – Hikvision video camera.

H^- beam, extracted from H^- source *1*, focusing by a magnetic lense *2* and injected in the accelerator *3*. Inside the accelerator H^- stripping by an argon target *4*, transform into proton with probability 90÷95% [4], and accelerates to the energy equal to the double potential of the accelerator. After the accelerator proton beam goes through cooled diaphragm *5* and its current measuring by a contactless beam sensor *6*. Then proton beam goes through bending magnet *9* and small part of it pass through the cooled diaphragm with aperture of 2 mm *10*, installed on the vacuum three-dimensional motion input. Finally, it comes to the Faraday cup (lithium target *11*, electrically isolated from rest part of the facility). Camera *12* detect luminescence of the lithium target [5], caused by the proton beam bombardment.

Using vacuum three-dimensional vacuum input proton beam current measured and two arrays of the proton currents obtained.

RESULTS

An example of the image obtained given in the Fig. 2. The easier way to obtain necessary information of the proton beam profile is find peak current, passing through

* Work supported by the RFBR project no. 19-72-30005.
† knkstdor@gmail.com

ISBN: 978-3-95450-240-0 ISSN: 2673-5539 doi:10.18429/JACoW-RuPAC2021-WEPSC31

the cooled diaphragm and measure two orthogonal chords, passing through this point. Results of measurements, obtained in three different modes, are given in the Fig. 3. Yellow line obtained for the proton beam current 1 mA, green line obtained for the proton beam current 3 mA and blue line obtained for the proton beam current 3 mA with stronger focusing parameters, set by magnetic lense (*2* in Fig. 1). Solid line are Gaussian distributions, approximated for the measured values, which are shown as dash line.

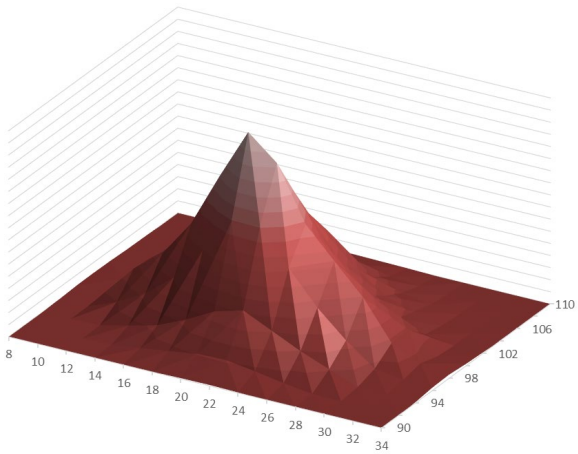

Figure 2: Result of the two-dimensional tomography for the proton current 1.2 mA. X and y axes are coordinates of the diaphragm, z axis is current distribution.

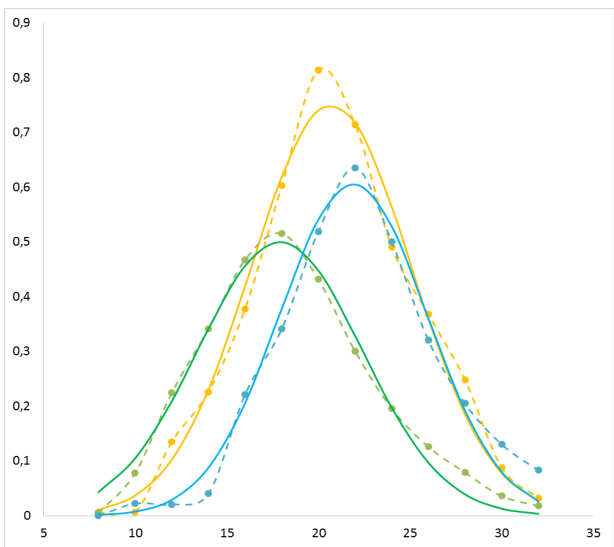

Figure 3: Profile of the proton beam passed through the peak of the beam. Solid line is approximation by the Gauss distribution, dash line are measured values. Yellow line is 1 mA, green one is 3 mA, blue one is 3 mA with a stronger focusing parameters.

CONCLUSION

The Budker Institute of Nuclear Physics operates a vacuum insulated tandem accelerator, in which transporting the proton beam with high power density – it can reach few tens of kW/cm^2. To provide fast measurements of the proton beam profile at bending magnet the two-dimensional tomography diagnostic was implemented. For the measuring two main chords, passing through the peak current, it takes around 1-2 minutes, which is fast relatively to the time of irradiations and experiments in the facility. The beam profile obtained in this way is somewhat different from the profile obtained by measuring the phase portrait of the beam using a wire scanner [3], but it can be used for the adequate estimation of the beam site relatively to the beam transport channel and beam size.

REFERENCES

[1] S. Taskaev *et al.*, "Neutron Source Based on Vacuum Insulated Tandem Accelerator and Lithium Target", *Biology*, vol. 10, 350, Apr. 2021. doi:10.3390/biology10050350

[2] W. Sauerwein, A. Wittig, R. Moss, Y. Nakagawa (Eds.), *Neutron Capture Therapy: Principles and Applications*. Springer, 2012. doi:10.1007/978-3-642-31334-9

[3] T. Bykov *et al.*, "Measurement of the portrait of 2 MeV proton beam along beam transfer line", presented at the 17th Rus. Particle Accelerator Conf. (RuPAC'21), Alushta, Russia, September-October 2021, paper WEPSC30, this conference

[4] Ia. Kolesnikov, A. Koshkarev, I. Shchudlo and S. Taskaev, "Diagnostics of the Efficiency of a Gas Stripping Target of a Tandem Accelerator with Vacuum Insulation", *Instr. and Exp. Tech.*, vol. 63, 314-318, Jan. 2020. doi:10.1134/S0020441220040065

[5] A. Makarov, E. Sokolova and S. Taskaev, "The luminescence of a lithium target under irradiation with a proton beam", *Instr. and Exp. Tech.*, vol. 64, pp. 24-27, Jan. 2021. doi:10.1134/S0020441220060184

ISBN: 978-3-95450-240-0 ISSN: 2673-5539 doi:10.18429/JACoW-RuPAC2021-WEPSC32

PROTON BEAM SIZE DIAGNOSTICS USED IN THE VACUUM INSULATED TANDEM ACCELERATOR*

M .I. Bikchurina, T. A. Bykov, D. A. Kasatov, I A. Kolesnikov†, A. M. Koshkarev, A. N. Makarov, Yu. M. Ostreinov, S. S. Savinov, I. M. Shchudlo, E. O. Sokolova, I. N. Sorokin, S. Yu. Taskaev,
Budker Institute of Nuclear Physics, 630090 Novosibirsk, Russia
Novosibirsk State University, Novosibirsk, Russia

Abstract

For the development of a promising method for the treatment of malignant tumors - boron neutron capture therapy - the accelerator-based epithermal neutrons source has been proposed and created in the Budker Institute of Nuclear Physics [1,2]. After the acceleration phase, a proton beam with an energy of up to 2.3 MeV and a current of up to 10 mA is transported in a high-energy path. With a beam size of 1 cm^2, its power density can reach tens of kW/cm^2. Diagnostics of the size of such a powerful beam is a nontrivial task aimed at increasing the reliability of the accelerator. The paper presents such diagnostics as: 1) the use of the blister formation boundary during the implantation of protons into the metal; 2) the use of thermocouples inserted into the lithium target; 3) the use of the melting boundary of the target lithium layer when it is irradiated with a beam; 4) the use of the activation of the lithium target by protons; 5) the use of video cameras; 6) the use of an infrared camera; 7) the use of the luminescence effect of lithium when it is irradiated with protons; 8) the use of collimators with a small diameter of 1-2 mm; 9) the use of the method of two-dimensional tomography [3].

INTRODUCTION

Charged particle accelerators are widely used in scientific research, medicine, and other applications. Tandem accelerators are high-voltage electrostatic accelerators in which the high-voltage potential is used twice: first to accelerate negative ions, and then, after changing the polarity of their charge in the high-voltage terminal, to accelerate positive ions. Thin foils are used for the conversion of the ion charge, or, at a higher ion current, gas stripping targets similar to the argon target in the tandem accelerator. After the acceleration phase, a proton beam with an energy of up to 2.3 MeV and a current of up to 10 mA is transported in a high-energy path. With a beam size of 1 cm^2, its power density can reach tens of kW/cm^2. Diagnostics of the size of such a powerful beam is a nontrivial task aimed at increasing the reliability of the accelerator.

THE EXPERIMENTAL SCHEME

The studies were carried out at the accelerator neutron source of the Budker Institute of Nuclear Physics (Novosibirsk, Russia). The source diagram is shown in Fig. 1 and its detailed description was given in [1]. A tandem accelerator with vacuum insulation was used to obtain a stationary proton beam with an energy of 0.6 to 2.3 MeV and a current from 1 pA to 10 mA, that is, a tandem accelerator of charged particles with an original design of electrodes.

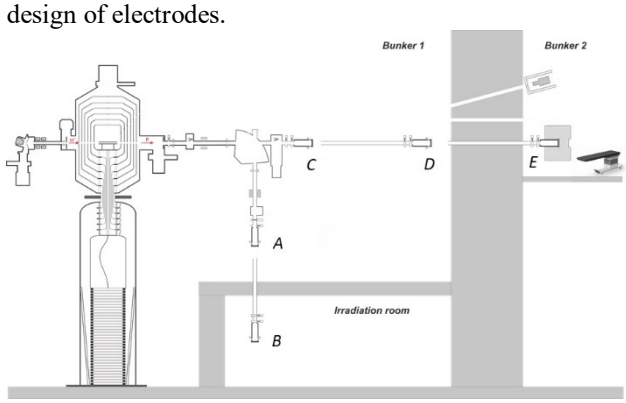

Figure 1: A diagram of an accelerator based source of epithermal neutrons. A-E – sites of the lithium neutron generating target.

RESULTS AND DISCUSSIONS

Below will be briefly discussed 9 implemented at the vacuum-insulated tandem accelerator diagnostics of the proton beam size with a high power density (up to tens of kW/cm^2).

Use a Blistering Effect at Proton Implantation in Metal

Implantation of the protons in the metal cause blistering – deformation of the target surface by the “bubbles” – blisters. Knowing the progress of the blisters appearing we can estimate profile of the proton beam and calculate the proton beam size. Example of this calculations presented in Fig. 2. And details are given in [4]. The effective square of the beam is 0.75±0.07 mm^2.

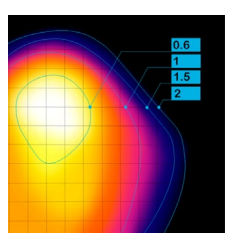

Figure 2: Blistering-covered area of the target versus current fluence (mA·hours).

* Work supported by the Russian Foundation for Basic Research, project no. 19-72-30005.
† Ya.A.Kolesnikov@inp.nsk.su

ISBN: 978-3-95450-240-0 ISSN: 2673-5539 doi:10.18429/JACoW-RuPAC2021-WEPSC32

Use a Thermocouples, Inserted in the Lithium Target

When the target assembly is equipped with thermoresistors it can be used to determine the beam profile, size and destination. The Fig. 3 shows the layout of the thermocouples in the copper disk of the target. In the paper [5] it was discussed, that using proton beam size dependence versus proton beam current, shown at the fig. 3, we claim that there is no effect of the space charge for proton beam in the high-energy beam line.

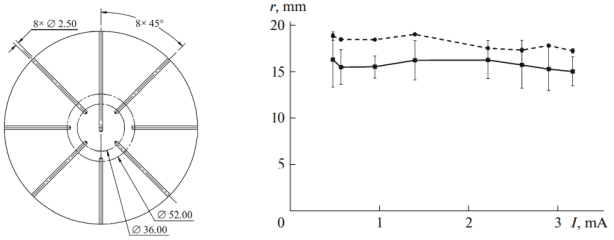

Figure 3: Schematic of thermocouple arrangement in the target copper disk (left). Proton beam radius versus the beam current. Dashed line is plotted according to the data from the thermocouples positioned on a 26-mm radius, solid – 18 mm (right).

Use a Melting of the Lithium Layer of the Target under Powerful Proton Beam

Since the temperature of lithium melting is 180ºC we can estimate the proton beam profile and measure the proton beam size. At Fig. 4 there shown the process of melting lithium layer of the neutrongenerating target under the few kW/cm^2 power density proton beam. The estimation sizes of the ellipse axes on amplitude level 1/e are 10.5 × 8 mm.

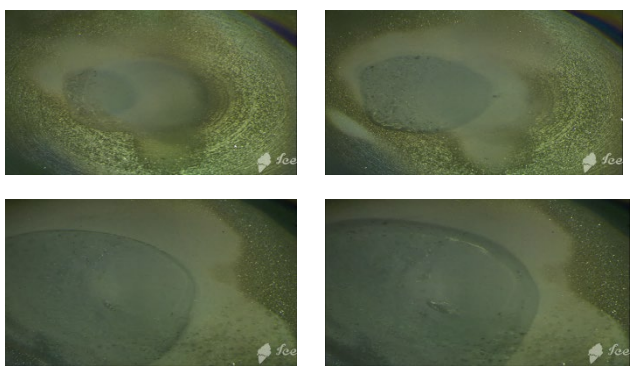

Figure 4: Evolution of the melting lithium layer under bombardment of the proton beam with 2 MeV energy. Upper left is 1.56 mA proton beam current, upper right is 1.81 mA, lower left is 2.59 mA and lower right is 3.05 mA.

Use an Activation of the Lithium Target by Berilium-7

Since radioactive isotope of beryllium is accumulates under proton bombardment of the lithium target, we can measure radioactive target by a gamma-spectrometer and estimate the proton beam profile and size at the lithium target. First results were obtained "by hand" without any automatization [6], so spatial resolution isn't fine. Later gamma-spectrometry complex has been constructed and used, as it shown in the Fig. 5. The results of the automatized measurements with different time of the integration are also shown at the Fig. 5.

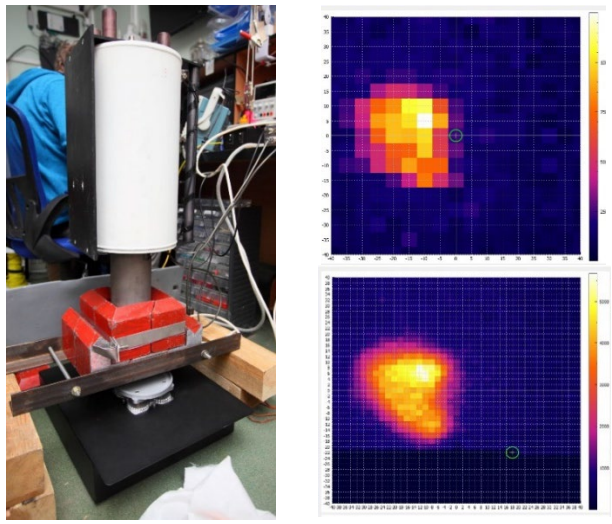

Figure 5: Gamma-spectrometry complex (left) and results of the measurements with 1 hour exposure time (up-right) and 8 hours exposure time (down-right).

Use Video Cameras

One of the features of the tandem accelerators is the need of the gas inlet into the stripping target area. Usually it is considered as disadvantage, but we turned it into advantage – we use video cameras to "see" the beam position, as it shown at Fig. 6 [7]. Using a developed software we also know the actually position of the beam and its size.

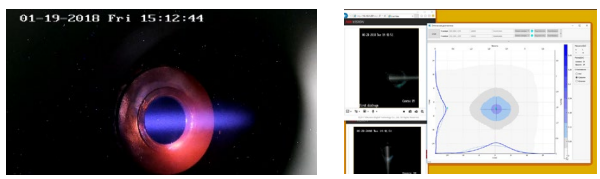

Figure 6: H^- beam entering the accelerator (left) and soft, estimating the proton beam size and profile (right).

Use an Infrared Camera

We using an infrared camera for the monitoring beam position in real-time. This device cannot be used with proton beam energy more than 1882 keV – the energy for the threshold reaction ^{7}Li(p,n)^{7}Be. In the Fig. 7 it is shown the example of determining the proton beam size [5].

ISBN: 978-3-95450-240-0 ISSN: 2673-5539 doi:10.18429/JACoW-RuPAC2021-WEPSC32

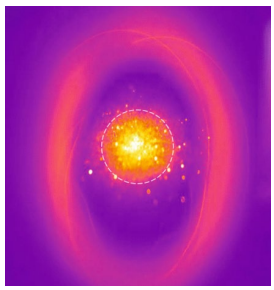

Figure 7: Image obtained from the infrared camera during the target irradiation by a proton beam with a current of 1.4 mA. The dashed circle denotes the diameter of 30 mm.

Use an Effect of the Luminescence of the Lithium under Proton Bombardment

The luminescence of the lithium layer of the target under proton bombardment helps us in all experiments with a lithium target to provide a correct transportation of the proton beam to the target [8]. In the Fig. 8 it is shown typical lithium luminescence under proton beam bombardment. Also, luminescence of the lithium target helped us in an experiment for determining argon beam current, accompanying the proton beam [9].

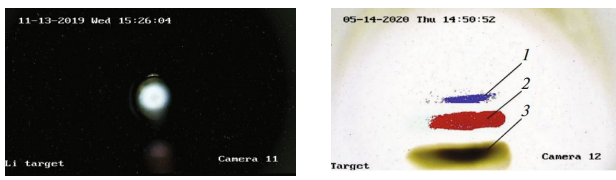

Figure 8: The luminescence recorded by a Hikvision video camera when a lithium target is irradiated with a proton beam (left). Image from a video camera looking at the surface of a lithium target at a bending magnet current of 14 A. *1* - glow caused by neutrals (hydrogen atoms); *2* - argon ions; *3* - protons (colors are partially inverted).

Use a Collimator with 2 mm Aperture

Proton beam was scanned, using a bending magnet or vacuum three-dimensional motion input, cooled collimator with an aperture and Faraday cup [9]. The profile obtained shown in the Fig. 9.

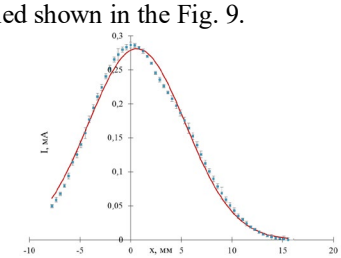

Figure 9: The dependence of the proton beam current, passed through the hole from its coordinate on the collimator and Gaussian distribution, approximated this dependence.

Use Two-Dimensional Tomography

We can use vacuum two-dimensional motion input for obtaining two-dimensional tomography of the proton beam. [3] In Fig. 10 are shown 3d-picture of the proton beam current distribution and profile of the beam along one axe, passing through the current peak.

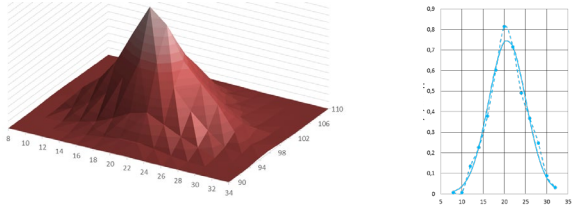

Figure 10: The example of the two-dimensional tomography measurement (left) and chord measurement, passing through the peak current (right).

CONCLUSION

The Budker Institute of Nuclear Physics operates a vacuum insulated tandem accelerator, in which transporting the proton beam with high power density – it can reach few tens of kW/cm^2. To provide stable transportation of the beam from the exit of tandem-accelerator up to lithium neutron generating target there were proposed and implemented 9 diagnostics of proton beam size.

REFERENCES

[1] S. Taskaev *et al.*, "Neutron Source Based on Vacuum Insulated Tandem Accelerator and Lithium Target", *Biology*, vol. 10, 350, Apr. 2021. doi:10.3390/biology10050350

[2] W. Sauerwein, A. Wittig, R. Moss, Y. Nakagawa (Eds.), *Neutron Capture Therapy: Principles and Applications*. Springer, 2012. doi:10.1007/978-3-642-31334-9

[3] M. Bikchurina *et al.*, "2D tomography of the proton beam in the vacuum-insulated tandem accelerator", presented at the 17th Rus. Particle Accelerator Conf. (RuPAC'21), Alushta, Russia, September-October 2021, paper WEPSC31, this conference.

[4] A. Badrutdinov *et al.*, "In Situ Observations of Blistering of a Metal Irradiated with 2-MeV Protons", *Metals*, vol. 7, 558, 2017. doi:10.3390/met7120558

[5] T. Bykov *et al.*, "A study of the spatial charge effect on 2-MeV proton beam transport in an accelerator-based epithermal neutron source", *Tech. Phys.*, vol. 66, pp. 98-102, 2021. doi:10.1134/S1063784221010047

[6] E. Sokolova, D. Kasatov, Ya. Kolesnikov, I. Shchudlo and S. Taskaev, "Measurement of the Proton Beam Profile via an Activation Method of Diagnostics", in *Proc. RuPAC'21,* St. Petersburg, November 2016, pp. 698-699. doi:10.18429/JACoW-RuPAC2016-THPSC070

[7] S. Taskaev *et al.*,"Accelerator neutron source for boron neutron capture therapy", in *Proc. IPAC'18*, Vancouver, Canada, April-May 2018, pp. 550-552. doi:10.18429/JACoW-IPAC2018-MOPML062

[8] A. Makarov, E. Sokolova and S. Taskaev, "The luminescence of a lithium target under irradiation with a proton beam", *Instr. and Exp. Tech.*, vol. 64, pp. 24-27, Jan. 2021. doi:10.1134/S0020441220060184

[9] Ya. Kolesnikov et al., "Measuring the Current of a Beam of Argon Ions Accompanying a Beam of Protons in a Tandem Accelerator with Vacuum Insulation", *Instr. and Exp. Tech.,* vol. 64, pp. 503-507, 2021. doi:10.1134/S0020441221040199

ISBN: 978-3-95450-240-0 ISSN: 2673-5539 doi:10.18429/JACoW-RuPAC2021-WEPSC33

INCREASING QUALITY OF EXPERIMENT INTERPRETATION IN REAL-TIME*

A. M. Koshkarev†, T. A. Bykov, Ia. A. Kolesnikov, A. N. Makarov, E. O. Sokolova, S. Yu. Taskaev
Budker Institute of Nuclear Physics, 630090 Novosibirsk, Russia
Novosibirsk State University, Novosibirsk, Russia

Abstract

An Epithermal neutron source based on an electrostatic tandem accelerator of a new type – Vacuum Insulation Tandem Accelerator, and a lithium neutron generating target has been proposed and developed at the Budker Institute of Nuclear Physics [1] for the Boron Neutron Capture Therapy [2] – the promising method for treatment of tumours and for other applications. This paper proposes and implements a flexible and customizable method for the operational data processing, allowing an operator and physicists to obtain and analyze the information during the experiment without the need of post-processing data. The application of it accelerates the process of obtaining informative data during the experimental research and automates the analysis process. Also it was proposed and implemented a process of automatic distributed journaling of the results of the experiment. As a result of the implementation of the proposed tools the productivity of the analysis of experimental data and the detailing of the experimental journal was increased the developed and implemented system of real-time data processing has shown its effectiveness and has become an integral part of the control system, data collection and data storage of the epithermal neutron source.

INTRODUCTION

One of the most important and time consuming parts of researcher's everyday life is the post-processing of experimental data. Sometimes it takes more than 3 hours, but in some experiments physicists need results in real time. For example: visualization of diagnostics, such as beam position by thermocouples or calculation of average beam currents only when the energy is in the nominal range.

SYSTEM ARCHITECTURE

The developed and implemented accelerator control system consists of many units, such as measurement controllers, server, database, operator's software, software for TVs and physicist-analytics software.

Architecture on Fig. 1. allows collecting data from all units of the accelerator on the server and transfer measurements to clients, that can proceed their own real-time analytics.

Main idea of this architecture is to process data on distributed way on client PC. In this case server only collects data, stores it in database and sends to clients. Also, server checks some low-speed interlocks and calculates some composite diagnostics, like proton fluence or power on the stripping target inside the accelerator.

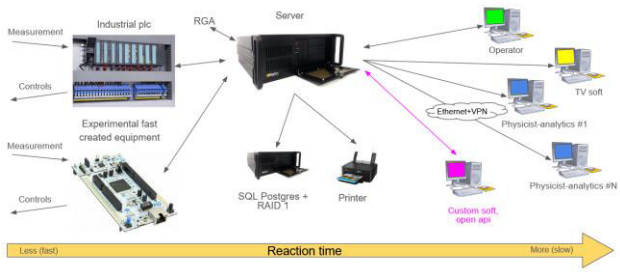

Figure 1: System architecture.

Physicist-Analytics Software

This is a software for physicist-analytics, that allows to proceed a real time analysis, like building a dependence of gamma radiation divided by beam current on the energy (Fig. 2), that was used in the experiment with reactions in lithium targets [3, 4]. Also, this system was used in different experiments [5, 6].

Basic functions are listed below:

1. Plotting the dependences of any measurement channel on another.
2. Time averaging of any channel with displaying "Box plot" on the graph (Fig. 2).
3. Averaging of any channel only by a given condition (example: average if the current is in the selected range).
4. Distribution of the logging status of the experiment with personal notes and an automatic printing at the end of the experiment.
5. Creation of an own channel on the basis of other channels data, for example *(a+b)*c* with all above functions.
6. The program can work from anywhere (via VPN), which can be useful in the case of the new wave of COVID-19.

If this functionality is not enough – programmer can create his own soft, that will process some complex operations and get data with system API.

TV Software

This software is designed to display data on three 50" TVs. During a collaboration experiment with other labs (sometimes international), all physicists who do not have access to the system can see the instantaneous value of the measurements and observe the graph of values.

* Work supported by Russian Science Foundation, grant No. 19-72-30005
† email address: koshi8bit@mail.ru

ISBN: 978-3-95450-240-0 ISSN: 2673-5539 doi:10.18429/JACoW-RuPAC2021-WEPSC33

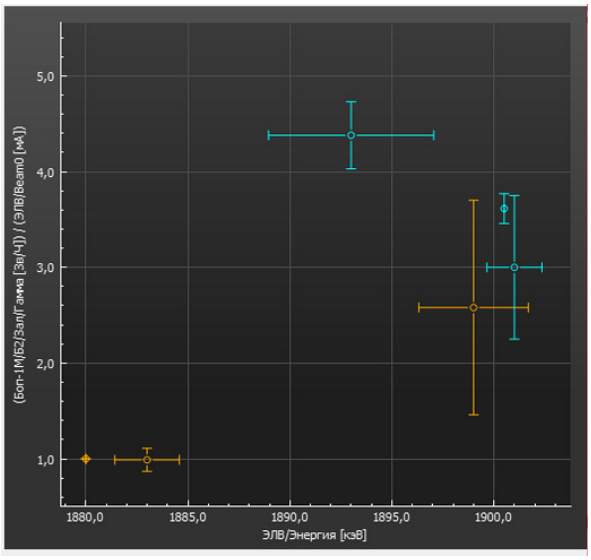

Figure 2: Gamma/Beam current VS Energy with standard deviation

This software allows not only the display of graphs and numerical values, but it is also capable of displaying various visualizations of the beam position, such as the passage of the beam through the chilled apertures (Fig. 3) or the position of the proton beam on the target by thermocouples with different visualization: simple temperature gradient (Fig. 4) and colormap (Fig. 5).

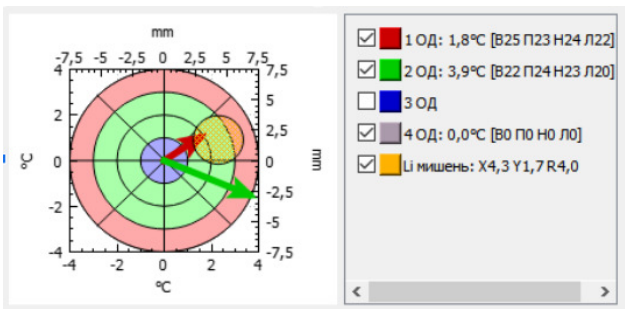

Figure 3: Beam passage through the chilled apertures

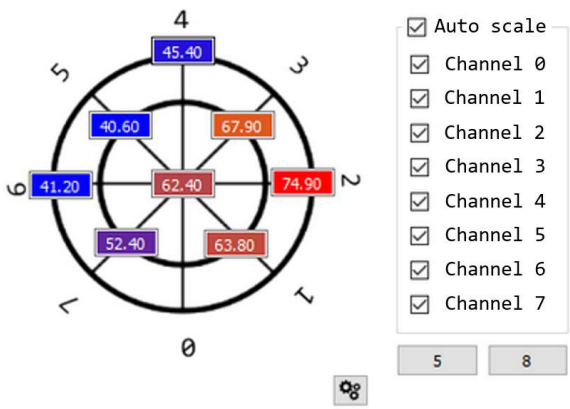

Figure 4: Beam position by temperature (simple gradient)

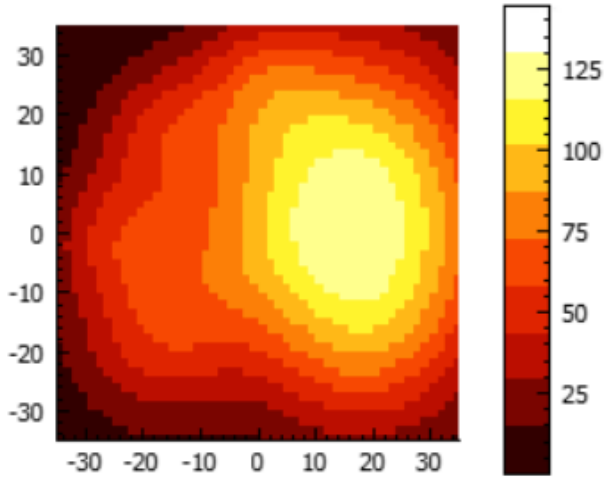

Figure 5: Beam position by temperature (colormap)

Also, in a separate window all participants of the experiment can study the last events recorded in the electronic journal.

Journal

The system includes the possibility of distributed logging from the physicist-analytics software. All logs are stored in the software database and can be printed as a paper anytime and add it in a folder for papers. In the process of filing in a paper journal it is possible to print your own photos or graphs plotted in Excel or other third-party software.

In this way user can easily find the complete information about the experiment in the same folder. This system is in operation since 10 February, 2020 and the thickness of the experimental journal is already 30mm.

CONCLUSION

The developed and tested control system is running on the accelerator and allows to perform some analytics in real time. This can save human efforts, because physicist do not need to extract csv or xlsx files from operator panel and to recall the time of the experiment, it is available during the experiment. Also, journal system allows to find all important data with personal notes very quickly.

REFERENCES

[1] W. Sauerwein, A. Wittig, R. Moss, Y. Nakagawa (Eds.), *Neutron Capture Therapy: Principles and Applications*. Springer, 2012. doi:10.1007/978-3-642-31334-9

[2] S. Taskaev *et al.*, "Neutron Source Based on Vacuum Insulated Tandem Accelerator and Lithium Target", *Biology*, vol. 10, 350, Apr. 2021. doi:10.3390/biology10050350

[3] M. Bikchurina *et al.*, "The measurement of the neutron yield of the ^{7}Li(p,n)^{7}Be reaction in lithium targets", *Biology*, vol. 10, 824, Aug. 2021. doi:10.3390/biology 10090824

[4] S. Taskaev *et al.*, "Measurement of the ^{7}Li(p,p'γ)^{7}Li reaction cross-section and 478 keV photon yield from a thick lithium target at proton energies from 0.65 MeV to 2.225 MeV",

ISBN: 978-3-95450-240-0 ISSN: 2673-5539 doi:10.18429/JACoW-RuPAC2021-WEPSC33

Nucl. Instrum. Methods Phys. Res., Sect. B, vol. 502, pp. 85-94, June 2021. doi:10.1016/j.nimb.2021.06.010

[5] T. Bykov *et al.*, "Initial trials of a dose monitoring detector for boron neutron capture therapy", *JINST,* vol. 16, P01024, Jan. 2021. doi:10.1088/1748-0221/16/01/P01024

[6] A. Badrutdinov et al., "In Situ Observations of Blistering of a Metal Irradiated with 2-MeV Protons", *Metals*, vol. 7, 2017. doi:10.3390/met7120558

ISBN: 978-3-95450-240-0 ISSN: 2673-5539 doi:10.18429/JACoW-RuPAC2021-WEPSC34

TREATMENT OF THE RESULTS MEASUREMENT OF PROFILE BEAM USING WIRE SCANNERS AT ACCELERATOR U-70 IHEP

D. A. Vasiliev †, V. T. Baranov, V. A. Kalinin, O. P. Lebedev, A. V. Louttchev, D. A. Savin, Institute for High Energy Physics in National Research Centre "Kurchatov Institute", 142281 Protvino, Russia

Abstract

The IHEP has developed fast wire scanners based on servomotors with a scanning speed of V=16 m/s. For processing of analog signals from detectors, a digital USB oscilloscope NI USB-5133 manufactured by National Instruments has been chosen. The paper describes methods of data processing from a wire scanner using a program developed in the LabVIEW environment and obtaining information about beam parameters as well. To determine the beam revolution frequency, a fast Fourier transform is used. The measured input signal is integrated at a chosed number of turns of the beam. The amplitude, center position, offset, rms deviation of the resulting distribution and beam sizes at the corresponding energy level are calculated using the Gaussian Peak Fit VI library element. The beam profile data in different modes of accelerator operation are presented.

INTRODUCTION

When setting up and operating the accelerator, it becomes necessary to measure the profile of the circulating beam. At IHEP, a transition was made to modern methods of developing fast wire scanners, taking into account the latest developments in mechatronics and robotics. The choice and justification of this approach were presented in [1]. Some results on the introduction of horizontal and vertical wire scanners U-70 into operation were presented at the RUPAC 2018 conference [2, 3]. This paper presents methods for processing the beam profile data using a program developed in the LabVIEW environment. Also the results of measurements of some parameters of the U-70 accelerator for proton and carbon beams at the speed of the carbon fiber V=16 m/sec are given.

COMPONENTS OF WIRE SCANNERS FOR THE U-70 ACCELERATOR

Two brushless 4490H024BS (Faulhaber) servo motors with RE-10-1-C64 resolvers (LTN Servotechnik) are controlled by ACJ-055-18R controllers through the Copley Motion Explorer CME2 software shell from Copley Controls. CME2 is installed on a computer under Windows.

The system provides double crossing of the carbon fiber the proton beam per one revolution. The speed of movement is used for processing scintillation detectors signals.

† Dmitry.Vasiliev@ihep.ru

PROCESSING OF BEAM PROFILE MEASUREMENT DATA

For automated processing of analog signals from wire scanners on the U-70 accelerator, an ADC with an external trigger, a conversion frequency of at least 50 MHz per channel, 8-bit capacity and with a memory of at least 3 MB per channel is required. A digital USB oscilloscope NI USB-5133 from National Instruments is used.

This converter allows to measure and analyze the amplitude and time parameters of the recorded signals. Using the National Instruments LabVIEW2012 development environment, we have created software for working with the NI USB-5133 oscilloscope. The software algorithm is as follows:

Initialization of the device; Selection of the measurement mode (AC, DC); Configuration of the measurement channels (ADC frequency, input signal range, number of measurement points); Selection of the number of measurement channels (1 or 2); Selection of the number of measurements (ADC buffer size); Setting the ADC operation mode by an external sync pulse; Reading the measured data; Saving the array of measured data to a file for subsequent processing.

The time of a half a revolution of the carbon fiber at a constant speed is determined as:

$$T_{1/2} = \frac{\pi \cdot r}{v},$$

where r is the length of the arm of the measuring frame (R-190 mm x 100 mm, Z-150 mm x 150 mm), v is the linear speed of movement (v=16 m/s), $T_{1/2}$=37.3 ms (R-axis), $T_{1/2}$=29.45 ms (Z-axis)

Minimum ADC buffer size for measuring half a revolution

$$N = f_{ADC} \cdot T_{1/2},$$

where f_{ADC} is the conversion frequency. For a conversion frequency of 100 MHz, the minimum buffer size is 3.7×10^6 (R axis) and 2.9×10^6 (Z axis). To measure the direct passage of the fiber through the beam, the buffer size at the ADC frequency of 100 MHz was set to 2×10^6, to measure the forward and reverse passage – 3.5×10^6.

The program performs:

ISBN: 978-3-95450-240-0 ISSN: 2673-5539 doi:10.18429/JACoW-RuPAC2021-WEPSC34

- Selection of the measurement axis (R or Z), according to this, the radius of the frame arm is selected;
- Setting the speed of uniform fiber movement (by default-16 mm/ms);
- Calculation of the frame rotation time;
- Selecting the ADC conversion frequency;
- Subtracting an array of measured data from a file;
- Determining the length of an array;
- The length of the array determines whether only the forward pass was measured, or the forward and reverse;
- All arrays and indicators are reset after the previous processing.

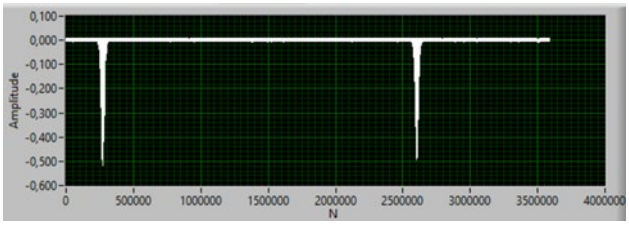

Figure 1: Graphical representation of signal selection during forward and backward pass from the measured data array.

Fragments corresponding to the forward and backward pass of the carbon fiber are selected from the entire data set. Taking into account the value of t_0, arrays are selected for the forward and backward passage of the fiber. The value is determined from the moment of uniform motion of the fiber to the beginning of registration of the beam profile. Since the input signal has negative polarity, the minimums of the input signal in the selected arrays are determined. The difference between the indices in the general array of the found minima is used to determine the real value of t_0. Arrays are selected from the measured data array for forward and backward fiber pass. A graphical representation of signal selection during forward and backward pass from the measured data array is shown in Fig. 1.

At the same time, the average value of the projection of the fiber position on a given axis is calculated. The projection is defined by the formula:

$$x = \sin\left(2 \cdot \pi \cdot \frac{t}{T}\right) \cdot r ,$$

where $t = t_0 + dt \cdot n$ ($dt = 1/F_{ADC}$, n is the number of dimensions in the array), T is the time of a complete revolution of the carbon fiber with a given constant speed, and t_0 is the setting time measured by double measurement of the profile. The output data is an array of mean values of the measured signal and an array of the corresponding projections of the fiber on a given axis. The initial and final values of the arrays of integrals are used to determine the offset from the zero value. The resulting value is subtracted from the array. After that, the arrays of integrals are normalized to unity.

To determine the beam rotation frequency the fast Fourier transform is used. The frequency of the highest amplitude is determined from the frequency spectrum in the selected range of 133–203 kHz. Next, the input measured signal is integrated over a given number of beam revolutions – n_r. Simultaneously, the average value of the projection of the position of the fiber on the given axis is calculated. The output data is an array of mean values of the measured signal and an array of the corresponding projections of the fiber on a given axis.

Then, using the Gaussian Peak Fit VI library element (the least squares method), the normal distribution corresponding to the input arrays is calculated. The amplitude, center, offset and standard deviation (σ) of the obtained distribution are calculated. The plot displays the array of data to be integrated and the corresponding normal distribution for the forward and backward pass. The result of performing the integration and searching for the corresponding normal distribution is shown in Figs. 2 - 4.

The beam size is determined as ±nσ, n is given before the start of the calculation. The beam size in the given example was determined as ±3σ. Similarly to the one described above, the calculation and graphical representation of the dependencies of the input signal on the projection of the fiber position on a given axis for the forward and backward pass is performed.

Before start the program an operator selects several options for making measurements. A given number of beam revolutions is set, during which the signal is integrated. After processing, the program allows selecting several options for the analysis of the beam density distribution: the beam size and its position relative to the center of the vacuum chamber are determined, the shape of the registered signal from the scintillation detector is given taking into account the correction when determining the beam projection in the perpendicular direction relative to the vacuum chamber, the Fourier analysis of the registered signal from the detector is performed.

RESULTS OF MEASUREMENTS

Wire scanners make it possible to measure the dimensions of the proton and carbon beams in various operating modes of the accelerator. Taking into account the need to measure the profile of a carbon beam in the range E=200÷450 MeV/n at an intensity $I=10^{9}\div10^{10}$ ($_{12}C^{6+}$), a carbon fiber 200 μm thick is installed in the profilometers. Below are the results of measurements of the beam profile at the 3σ level at the beam injection energy E_k=1.3 GeV, at E=50 GeV ($I=7\times10^{11}$ p) and for carbon beam at E=450 MeV/n.

ISBN: 978-3-95450-240-0 ISSN: 2673-5539 doi:10.18429/JACoW-RuPAC2021-WEPSC34

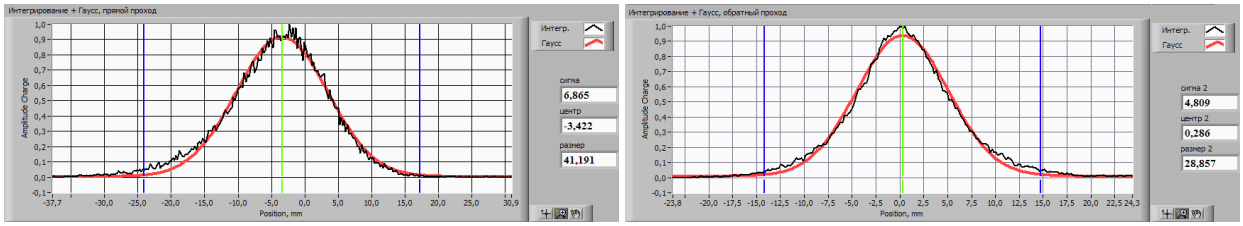

Figure 2: Horizontal (left) and vertical (right) profiles of the proton beam at the injection energy E=1.3 GeV (n_r=5).

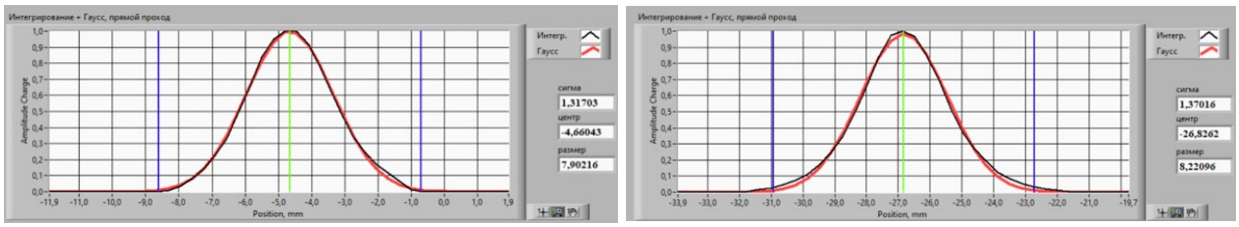

Figure 3: Horizontal (left) and vertical (right) profiles of the proton beam at the energy E=50 GeV (n_r=5).

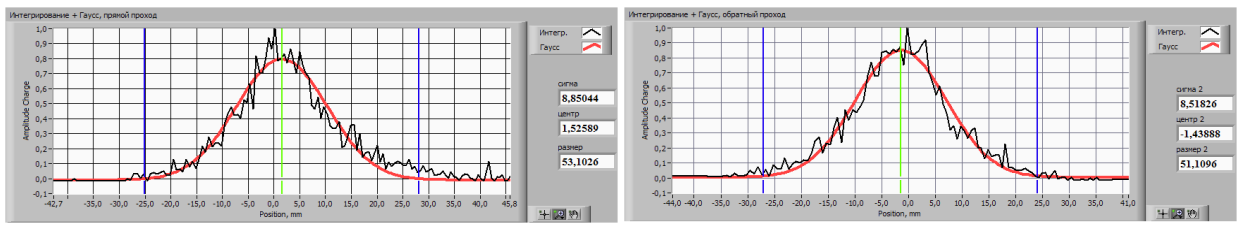

Figure 4: Horizontal (left) and vertical profiles (right) of the carbon beam at E=450 MeV/n, I=3×10^9 ($_{12}C^{6+}$).

At the U-70 accelerator, narrowband analog and wideband digital feedback circuits are used to eliminate errors in beam injection from the booster and to prevent the development of coherent instabilities [4]. Figure 5 shows the results of measurements of the beam profile and Fourier analysis of these data with the feedback circuits on and off.

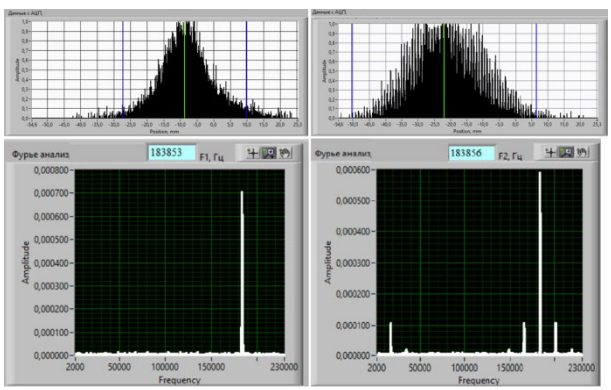

Figure 5: Horizontal profile (top) and Fourier analysis (bottom) with on (left) and off (right) feedback loops.

The local frequency of betatron oscillations is fixed at 17 kHz. This allows us to determine the frequency of betatron oscillations Q_R

$$Q_R = K - \frac{f_l}{F_0},$$

where K - an integer close to the calculated frequency of the betatron oscillations; f_l - local frequency of betatron oscillations; F_0 - frequency of particle circulation in accelerator.

For U-70 IHEP: K=10, F_0=180-200 kHz (for proton beam).

$$Q_R = 10 - \frac{17kHz}{183.8kHz} = 9.9$$

CONCLUSION

The developed program for processing the data for measuring the profile of the circulating beam is successfully used during several sessions of the accelerator for both proton and carbon beams.

REFERENCES

[1] V. T. Baranov, S. S. Makhov, D. A. Savin, V. I. Terekhov, The mechatronic design of a fast wire scanner in IHEP U-70 accelerator, *Nucl. Instr. Methods Phys. Res.,* A: Volume 833, October 2016, pp. 186-191.

[2] V. T. Baranov, V. N. Gorlov, D. A. Savin, and V. Terekhov, "Fast Wire Scanners for U-70 Accelerator of IHEP", in *Proc. 26th Russian Particle Accelerator Conf. (RuPAC'18)*, Protvino, Russia, Oct. 2018, pp. 459-461. doi:10.18429/JACoW-RUPAC2018-THPSC24.

[3] V. A. Kalinin, V. T. Baranov, G. V. Khitev, and O. P. Lebedev, "Experimental Study of the Transverse Beam Size Used a Fast Wire Scanner in the U70 at IHEP", in *Proc. 26th Russian Particle Accelerator Conf. (RuPAC'18)*, Protvino, Russia, Oct. 2018, pp. 480-482. doi:10.18429/JACoW-RUPAC2018-THPSC36.

[4] S. V. Ivanov, N. A. Ignashin, O. P. Lebedev, S. E. Sytov, "Transverse Beam Feedback Systems in the U-70 Synchrotron", IHEP Preprint 2015–11, p. 15.

ISBN: 978-3-95450-240-0 ISSN: 2673-5539 doi:10.18429/JACoW-RuPAC2021-WEPSC36

SIMULATION OF THE COHERENT RADIATION INTERFEROMETRY FOR THE BEAM TEMPORAL STRUCTURE DIAGNOSTICS

M. Toktaganova*, D. Shkitov†, M. Shevelev, S. Stuchebrov
Tomsk Polytechnic University, Lenina ave. 2a, 634050 Tomsk, Russia

Abstract

We consider a mathematical model and computer simulation results describing the interferometry of both diffraction and transition radiation to develop an electron bunch train structure diagnostic method. The results of the autocorrelation function simulation indicate a possibility of diagnosing the bunch number in the train as well as spacing between them in case of using narrowband or broadband detectors. The suggested method will allow rejecting spectrum reconstruction in favor of extracting information directly from the autocorrelation function.

INTRODUCTION

Nowadays, free electron lasers and new facilities that are capable of generating sequences of short electron bunches with a high (THz) repetition rate have widely developed [1]. The existing diagnostic methods for such sequences have limitations or are not applicable. Therefore, it is important to develop new approaches to diagnose the temporal structure of such sequences (trains) in modern accelerators. In this report, we describe a model of coherent radiation interferometry. Based on the analysis of interferometer autocorrelation function (ACF), we can derive the information about temporal structure of the trains.

MODEL DESCRIPTION

In this section, we describe the mathematical model for the ACF simulation underlying the proposed approach. In general case, the intensity of radiation produced by the train registered by the detector after passing through the interferometer is determined by the following expressions:

$$I(\Delta l) = \int_{\nu_1}^{\nu_2} [N + N(N+1)F(\nu)] \frac{d^2W}{d\nu d\Omega} V(\nu)T(\nu)P(\nu)M(\nu)S(\nu),$$

$$F(\nu) = \frac{1}{m^2} e^{-\frac{4\pi^2\nu^2}{c^2}\left(\sigma_x^2 s_x^2 + \sigma_y^2 s_y^2 + \sigma_z^2 s_z^2\right)} \left| \sum_{j=1}^{m} e^{-i\frac{2\pi\nu}{c} l(j-1)s_z} \right|^2,$$

where ν is the radiation frequency, c is the speed of light in vacuum, $\{\nu_1, \nu_2\}$ is the detector sensitivity range, N is the electron number in the train, c is the speed of light, $\frac{d^2W}{d\nu d\Omega}$ is the spectral-angular distribution of radiation from one electron, $F(\nu)$ is the form-factor of a uniform electron bunch train, $S(\nu)$ is the detector sensitivity function, $M(\nu)$ is the interference multiplier, $T(\nu)$ is the multiplier responsible for transmission properties of the vacuum chamber window, $V(\nu)$ is the multiplier responsible for radiation propagation medium and splitter material in the interferometer, $P(\nu)$ is the multiplier responsible for the polarizer characteristics. In [2–4] you can find more information on how to calculate the bunch form-factor. As seen, the model takes into account the train structure parameters and the detector characteristics. The mechanisms of transition radiation (TR) and diffraction radiation (DR) are selected as the radiation source. Note that TR mechanism is invasive and DR one is noninvasive. The geometries of TR and DR generation are illustrated in Fig. 1. However, other type of radiation could be selected as a source (e.g., synchrotron or Cerenkov radiation).

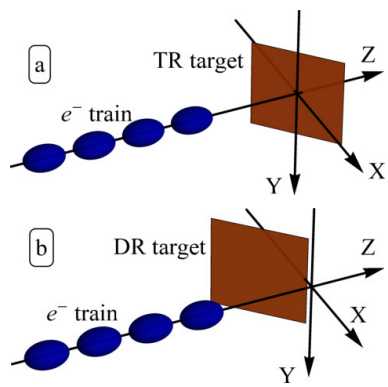

Figure 1: The schematic interaction geometries of the train with the target in cases of TR (a) and DR (b).

In these geometries, only the horizontal component of the radiation polarization is mainly present. It means that $\frac{d^2W}{d\nu d\Omega} \approx \frac{d^2W_z}{d\nu d\Omega}$.

SIMULATION

The simulation of the TR and DR spectra from single electron, illustrated in Fig. 2, was carried out based on the program written on the *Wolfram Language* code [5], developed earlier [6]. For numerical integration, the default method and the Monte Carlo method [7] was used[1]. In the simulation, the target is flat and has a finite size to be acceptable for use in the accelerator path. The θ_0 is the angle between the normal vector and the particle trajectory. The center of the TR target is located at the coordinate system center. The DR target edge is located at the distance equal to

* mmt8@tpu.ru
† shkitovda@tpu.ru

[1] {Automatic, "SymbolicProcessing"->False} and {"MonteCarlo", "MaxPoints"->10^8, Method->{"MonteCarloRule", "AxisSelector"->Random, "Points"->$5 * 10^6$}, "SymbolicProcessing"->False}

ISBN: 978-3-95450-240-0 ISSN: 2673-5539 doi:10.18429/JACoW-RuPAC2021-WEPSC36

the impact parameter from the system coordinate center. For a given value of the impact parameter (which $> 3\sigma$), we can speak of the non-perturbing nature of the interaction of the 0.1-mm transverse size bunch (or less) with the DR target. As the first step, the simulation was carried out for a simple case, the details of which are listed in Table 1. The simulation was conducted for the Michelson interferometer with interference multiplier equals to $M(\nu) = \left|1 + e^{-i2\pi\Delta l\nu/c}\right|^2$, where $\Delta l = 2d$ is the optical path difference and d is the interferometer movable mirror displacement. $M(\nu)$ is illustrated in Fig. 3. The $F(\nu)$ and $S(\nu)$ model components are presented in Fig. 4 with narrowband detector (ND) and broadband detector (BD). Note that the wide variety of THz detectors [8] are currently available.

Table 1: The Simulation Parameters

Target type	Perfect conductor
Target size	50 mm × 50 mm
Distance target center to detector, L	5 m
Impact parameter (for DR only), h	0.5 mm
Spectral frequency range simulation	0.01 –1.5 THz
Tilt angle of target (DR, TR), θ_0	45°, 46.5°
Energy of electrons, E_e	10 MeV
Longitudinal bunch size, σ_z	0.15 ps
Bunch transverse dimensions, σ_x, σ_y	0.1 mm
Charge distribution in the train	Uniform
Charge distribution of bunches	Gaussian
Number of bunches in the train, m	2–10
Train population, N	1000
Bunch spacing, l (BD, ND)	1 –7 ps, 9 –15 ps
BD sensitivity range	0.1 –1.4 THz
ND sensitivity range	0.5 –0.7 THz
$V(\nu)$, $T(\nu)$, $P(\nu)$	1

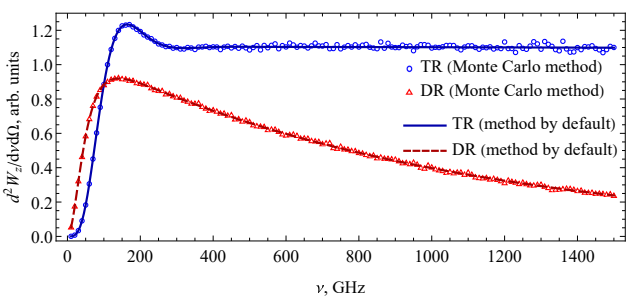

Figure 2: Spectral distributions of TR and DR.

RESULTS AND DISCUSSION

Simulation results for DR are presented in Fig. 5 and 6. Some outliers are due to numerical calculations. In general terms, the ACF represents the intensity dependence from Δl with the packet's set of oscillations. As can be seen, the packet's number connected the bunch number by the relation $m = (k + 1)/2$, where k is the number of oscillation packets in the ACF (see Fig. 5). There is the clear difference between

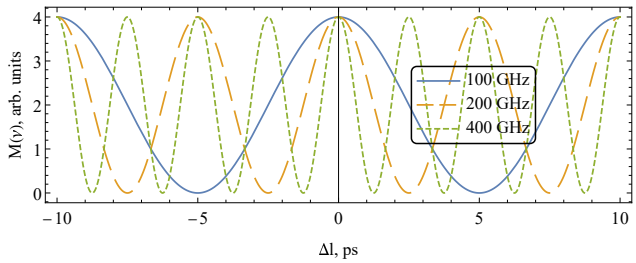

Figure 3: The examples of interference multiplier for different frequencies.

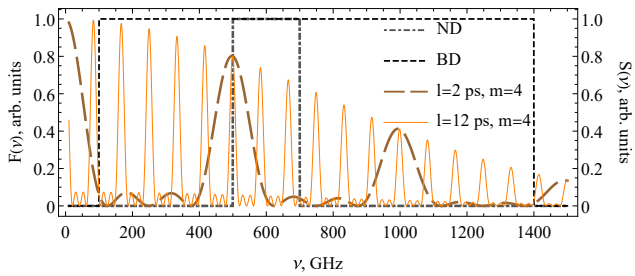

Figure 4: Form-factors of electron trains for two bunch spacing (both TR and DR cases are coincides) and detector sensitivity ranges for both ND and BD cases.

the ACF in case of ND and BD. With BD, we can distinguish the shorter bunch spacing in the train. It is important to have at least two peaks in the detector sensitivity range in order to get the clear packet structure. In Table 2 the comparison of l and estimated l_{est} is presented, where l_{est} is the average value of distance between peaks of ACF envelope curve (see Fig. 6). For TR case, the all findings will be the same.

Table 2: The Estimation of Spacing (in ps) for Fig. 6

ND	l	9	10	11	12	13	14	15
	l_{est}	8.7	10.6	10.8	12.3	12.8	14.4	14.7
BD	l	1	2	3	4	5	6	7
	l_{est}	1.0	2.0	3.0	4.0	5.0	6.0	7.0

CONCLUSION

We have demonstrated the technique for measuring the microbunches separation in a microbunch system by virtue of the coherent TR and DR autocorrelation function simulation. The obtained results are limited by the finite bandwidth of the detector. Thereby, the time delay between microbunches can be determined via measuring of autocorrelation curve employing a detector with an appropriate frequency range. The detection system with the broadband frequency response range allows for the measurement of a short time delay between microbunches. The technique proposed does not dependent on the microbunch train production method and is applicable to any number of microbunches. This technique shows that the usage of coherent diffraction radiation allows to control the time delay between microbunches without destruction of the electron beam.

ISBN: 978-3-95450-240-0 ISSN: 2673-5539 doi:10.18429/JACoW-RuPAC2021-WEPSC36

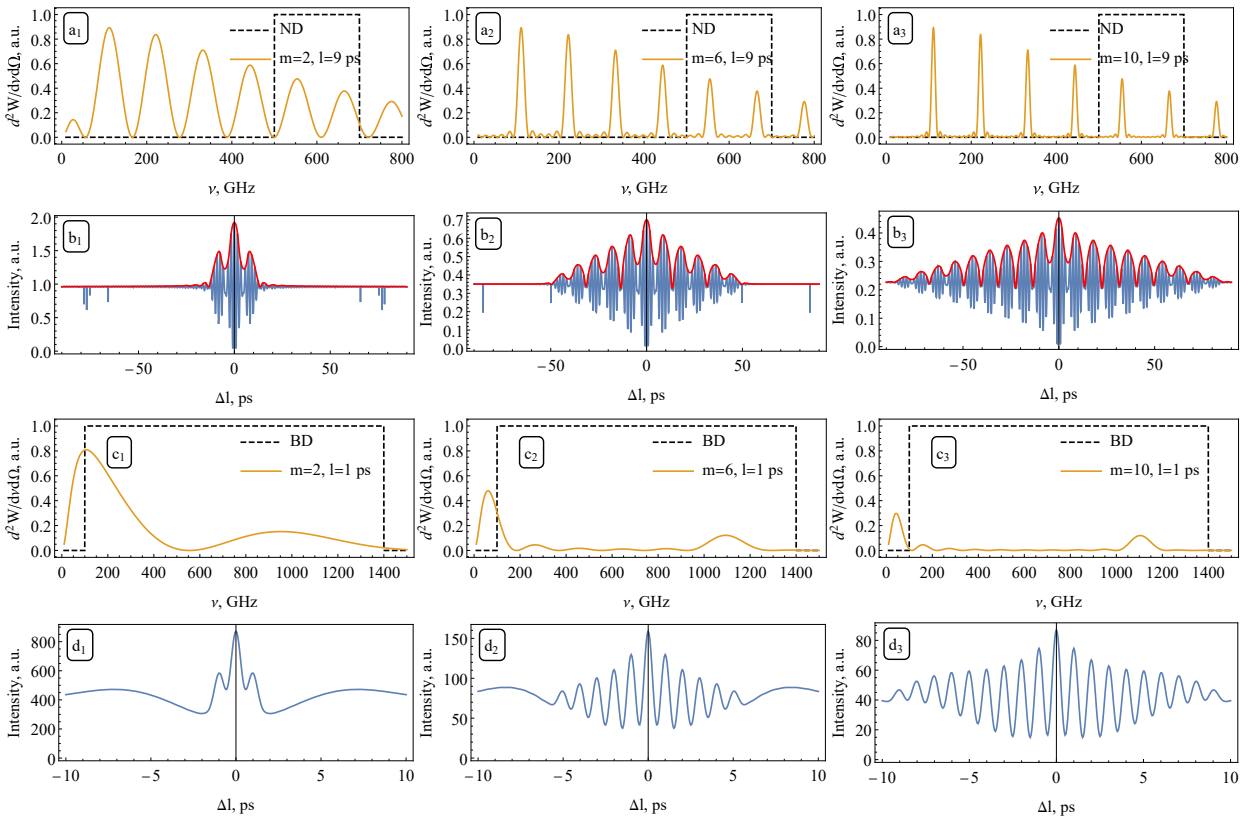

Figure 5: The DR spectra (a, c rows) and autocorrelation function (b, d rows) evolution in depends on increasing bunch number in train for both ND (a, b rows) and BD (c, d rows) case. The red line is the envelope curve.

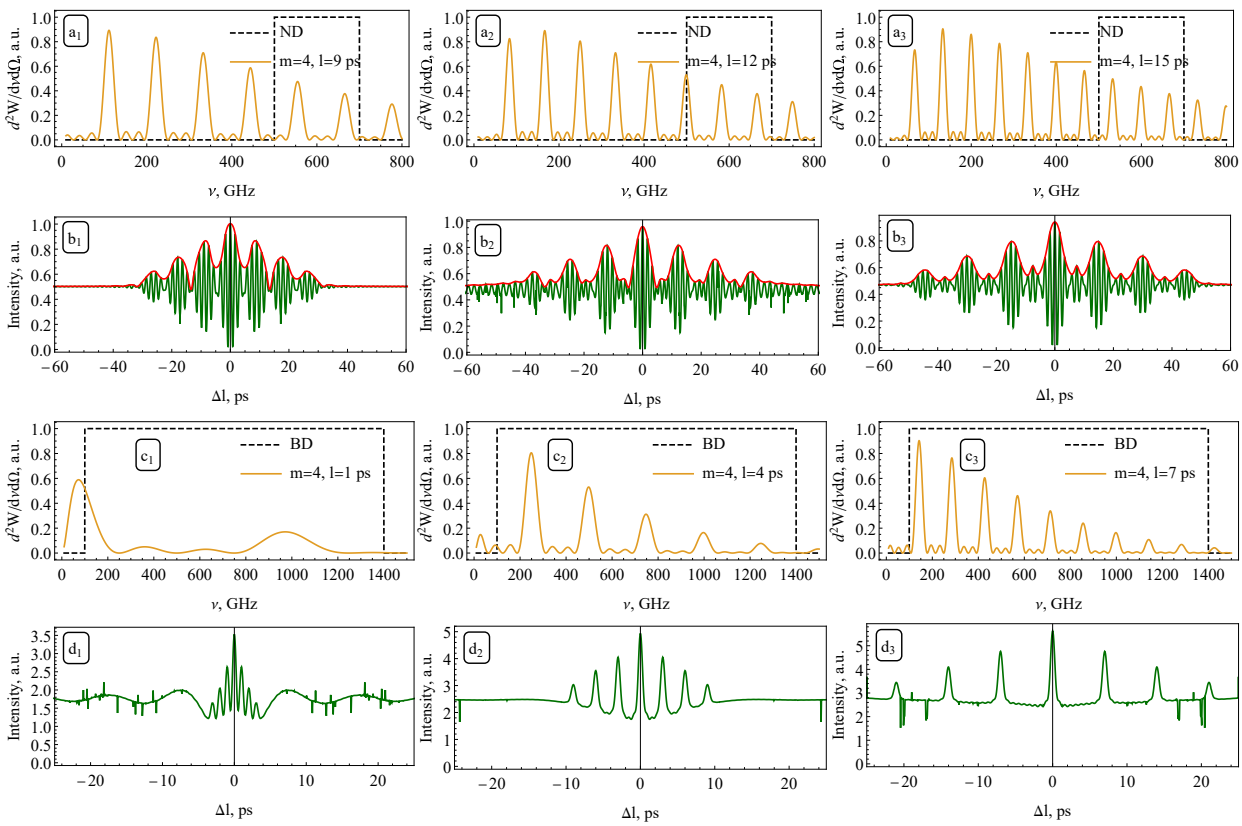

Figure 6: The same caption as on Fig. 5 but in depends on bunch spacing with fixed bunch number.

ISBN: 978-3-95450-240-0 ISSN: 2673-5539 doi:10.18429/JACoW-RuPAC2021-WEPSC36

REFERENCES

[1] S. Antipov *et al.*, "Subpicosecond bunch train production for a tunable mJ level THz source", *Phys. Rev. Lett.*, vol. 111, p. 134802, 2013. doi:10.1103/PhysRevLett.111.134802

[2] G. A. Naumenko, "Form-Factors of Relativistic Electron Bunches in Polarization Radiation", *Advanced Materials Research*, vol. 1084, p. 138, 2015. doi:10.4028/www.scientific.net/AMR.1084.138

[3] A. P. Potylitsyn, "Spatial coherence in transition radiation from short electron bunches", *JETP Lett.*, vol. 103, pp. 669–673, 2016. doi:10.1134/S0021364016110102

[4] Coherent Transition Radiation from Bunches of Charged Particles, https://demonstrations.wolfram.com

[5] Wolfram Language, https://www.wolfram.com/language

[6] D. A. Shkitov, "Code for simulation of diffraction radiation from flat finite surfaces", in *Proc. 26 th Russian Particle Accelerator Conf. (RuPAC'18)*, Protvino, Russia, Oct. 2018, pp. 510–513. doi:10.18429/JACoW-RUPAC2018-THPSC56

[7] NIntegrate Integration Rules, https://reference.wolfram.com/language/tutorial/NIntegrateIntegrationRules.html#430697921

[8] R. A. Lewis, "A review of terahertz detectors", *J. Phys. D: Appl. Phys.*, vol. 52, p. 433001, 2019. doi:10.1088/1361-6463/ab31d5

ISBN: 978-3-95450-240-0 ISSN: 2673-5539 doi:10.18429/JACoW-RuPAC2021-WEPSC39

DATA COLLECTION, ARCHIVING AND MONITORING SYSTEM FOR U70 SYNCHROTRON

V. A. Kalinin†, N. A. Oreshkova, NRC "Kurchatov Institute" - IHEP
(Institute for High Energy Physics), Protvino, Moscow region, Russia

Abstract

This paper describes a data collection, archiving and monitoring system for U70 synchrotron. The system is designed to monitor the operation of the U-70 accelerator and is responsible for the collection of low-frequency (less than 2 kHz) analog signals from the U-70 technological systems, their processing and subsequent sending to the database using the Data Socket technology. The developed complex block diagram is presented. The hardware and its characteristics (number of channels, resolution, bandwidth) and the interface and functionality of the software are described. The results of using this system at the U-70 accelerator complex are presented.

INTRODUCTION

U-70 personnel need to control a large number (more than 100) parameters when controlling the accelerator complex, most of which are represented in the form of low-frequency (frequencies less than 2 kHz) analog signals. To quickly identify malfunctions and improve the efficiency of the accelerator complex, it was decided to create a system for monitoring and archiving low-frequency signals.

HARDWARE

The block diagram of the data collection, archiving and monitoring system for U70 synchrotron is shown in Fig. 1. It includes analog-to-digital converters (ADC), local servers and a database server.

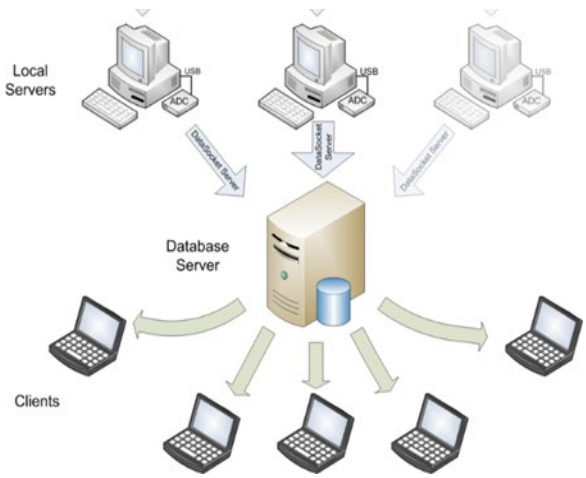

Figure 1: The block diagram of the data collection, archiving and monitoring system for U70 synchrotron.

An analog-to-digital converter (ADC) E-14-140-M is used to digitize the signals. Its characteristics are presented in Table 1. The ADC is connected to the Local server (a PC running the WINDOWS 7 32bit operating system) by a USB cable. The HP proliant dl160 running the Debian 8 operating system is used as a database server (Database server).

Table 1: Characteristics of the ADC E-14-140-M

Number of channels	32 with "common ground"
Resolution	14 bits
Input signal range	±10 V
Conversion frequency	100 kHz

Each ADC operates in the mode of 32 analog channels and 8 digital channels.

The analog inputs of the ADC are supplied with 31 signals from the control outputs of various sources (induction sensor, total voltage of the electric field RF, magnetic field corrections, etc.) (Data Sources) and one synchronization signal (common for all ADCs). The synchronization signal represents two pulses of different amplitudes (8V and 3V). The pulses are linked to the supercycle of the U-70 accelerator with a duration of 8-10s.

The digital channels receive the following signals from the synchronization system [1]:

- NC (start of the accelerating cycle);
- B1 (technological pulse generated on the falling part of the magnetic field of the previous magnetic cycle);
- B2 (the beginning of magnetic field booster plateau stabilization pulse);
- KS1 (end of the booster plateau);
- T0 (the beginning of magnetic field main plateau stabilization pulse);
- KS2 (end of the main magnetic field plateau);
- Reset (service pulse delayed in time relative to the NC pulse);
- Two backup channels of the U-70 timer system.

The parameters of the magnetic cycle are monitored using digital signals.

SOFTWARE

The software is created in LABVIEW and consists of the server and client parts.

†vakalinin@ihep.ru

ISBN: 978-3-95450-240-0 ISSN: 2673-5539 doi:10.18429/JACoW-RuPAC2021-WEPSC39

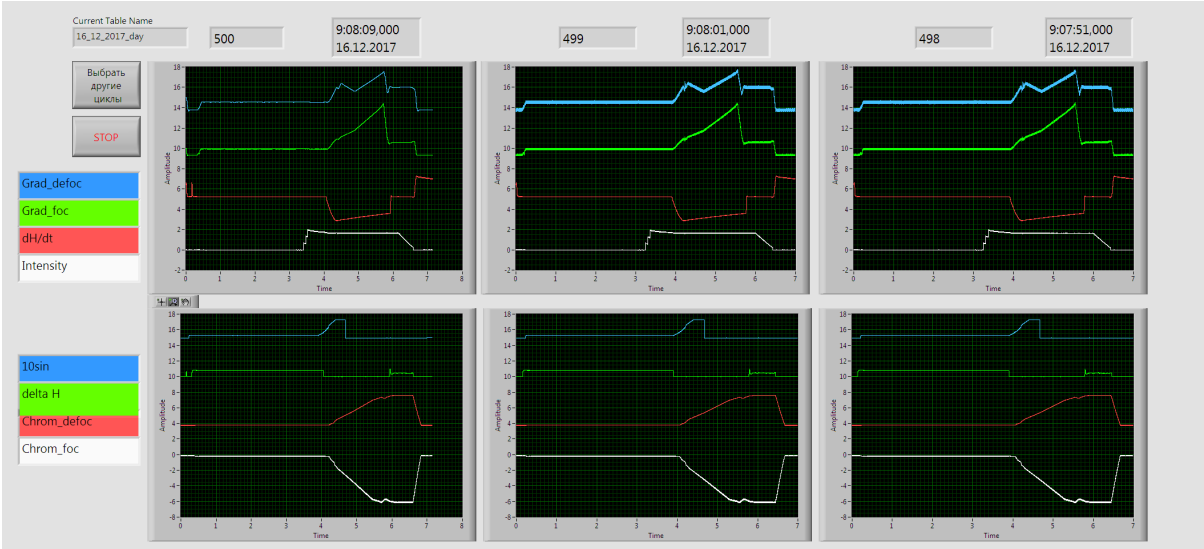

Figure 2: Three cycle monitoring program interface.

The Server Part

When the local server program receives a 3V synchronization pulse (the beginning of the U-70 magnetic cycle booster plateau), it collects data from the ADC until an 8V synchronization pulse is received (the end of the U-70 magnetic cycle main plateau). Then it displays the collected data on the graph and transmits it via DataSocket Transfer Protocol [2] to the Database server.

The database server program receives data from all local servers via the DataSocket Transfer Protocol and writes it to the database. MariaDB 10.2 is used as a database [3].

Each session creates a new database consisting of tables. Tables are created automatically twice a day (the beginning of the shift at 8:00 and the end of the shift at 20:00). Each table contains the following columns: cycle number (from the shift beginning); date and time of data receipt; columns of data from local servers, a column with digital channel data (time intervals between U-70 timer system pulses). To save space, the database stores complete information only for the last seven days. The remaining tables contain data for every tenth cycle and cycles with certain parameters (the work of fast output, the work of a certain physical installation).

The Client Part

Three client programs have been developed: monitoring of the last three cycles, working with the archive and an emergency alerts program (SPY).

Monitoring of 3 cycles The program continuously outputs the last 3 cycles for the 8 selected channels. The cycle number and the date of data receipt are displayed at the top of the screen. The user can change the sensitivity of the signals and their offset relative to each other. It is also possible to bind the signals to one of the pulses on the digital channels. Three cycle monitoring program interface is shown in Fig. 2.

Working with the archive The user can display up to 10 signals from the database. To do this, you need to select the signals of interest and the date when the data was received. The search for a cycle is carried out using the slider on the statistics graph. If the requested data is not found in the database, the message "Table not found" will be displayed. The user can use cursors to measure the time and amplitude characteristics of signals. The cursor color matches the color of the channel whose characteristics the cursor measures. The corresponding fields display measurements of both absolute values (relative to the zero signal level) and the difference values between the cursors.

For more convenient search, buttons (arrows) are organized to scroll the cycles forward and backward with a given step. The user can display the signals of the last cycle recorded in the database on the graph.

The program allows to save the current settings (selected signals, sensitivity, position of signals on the graph, binding to synchronization pulses, cursor selection), the graph (in .png, .jpeg, .bmp formats) and the selected signals in .csv format. The program interface for working with the archive is shown in Fig. 3.

Emergency Alerts Program (SPY). The emergency alerts program signals the occurrence of emergency situations through visual and audible alerts. The program will respond to the following emergency situations:

- The intensity is below the threshold. The source of the intensity signal is the signal of the induction sensor U-70. The threshold is set on the statistics graph (Fig. 4) using the horizontal cursor (intensity threshold).
- Acceleration losses. The difference between the accumulated and accelerated intensity is determined. The accumulated intensity is determined by the pulse T0, the accelerated intensity is determined by the pulse KC2.

ISBN: 978-3-95450-240-0 ISSN: 2673-5539 doi:10.18429/JACoW-RuPAC2021-WEPSC39

Figure 3: The program interface for working with the archive.

- Insufficient intensity for the work of internal targets. In total, three targets are controlled (24, 27 and 35). The user has the opportunity to choose controlled targets. The shortage of intensity is determined by the nature of the current flowing in the additional windings of the blocks of the U-70 ring electromagnet (bumpers), which create a local distortion of the orbit. If the intensity is insufficient, the feedback increases the bump current to the maximum value (Fig. 5). The program monitors a sharp (no more than 10 ms) increase in the current signal to the maximum.
- The remaining intensity in U70 is higher than the set value. The remaining intensity is controlled using the FEP bump.
- The disappearance of the magnetic cycle U-70 is determined by the signal Ḣ. In this case, the program only issues a sound notification.

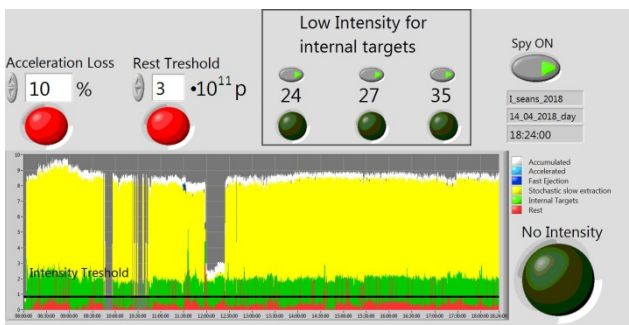

Figure 4: Emergency Alerts Program interface.

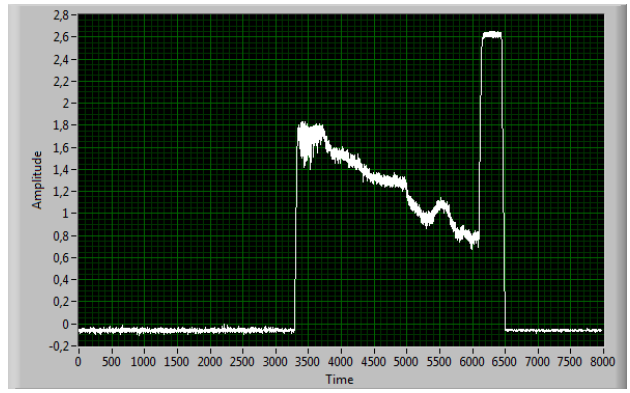

Figure 5: Bump current with insufficient intensity for target operation.

CONCLUSION

A data collection, archiving and monitoring system for U70 synchrotron has been developed. The system was tested on the U-70 accelerator in the first run of 2018. It is planned to increase the number of signals recorded in the database, expand the list of emergency warnings and expand the functionality of client programs (measurement of betatron and synchrotron frequencies).

REFERENCES

[1] O. P. Lebedev, V. I. Serebryakov, Synchronization System for Physical Setups in IHEP Accelerator Booster Mode. IHEP Preprint 86-165, Serpukhov, 1986.

[2] http://www.ni.com/white-paper/3223/en/

[3] https://mariadb.com

ISBN: 978-3-95450-240-0 ISSN: 2673-5539 doi:10.18429/JACoW-RuPAC2021-WEPSC40

DETECTION OF ANOMALIES IN BPM SIGNALS AT THE VEPP-4M

I.A. Morozov*, P.A. Piminov, BINP SB RAS, Novosibirsk, Russia

Abstract

Beam position monitors (BPMs) are widely used for beam diagnostics in particle accelerators. Turn-by-turn (TbT) beam centroid data provide a means to estimate performance-critical accelerator parameters, like betatron frequency and optical functions. Parameter estimation accuracy is heavily related to TbT data quality. BPM faults might lead to erroneous estimation of accelerator parameters and should be accounted for achieving accurate and reliable results. Several anomaly detection methods for TbT data cleaning are considered. Derived features of BPM signals along with their robust dispersion estimation are used to flag faulty BPM signals. Estimated contamination factor is used with unsupervised learning methods (Local Outlier Factor and Isolation Forest). Application of anomaly detection methods for the VEPP-4M experimental TbT data is reported.

INTRODUCTION

The VEPP-4M storage ring [1] is equipped with 54 dual-plane BPMs [2]. The system can provide TbT data with resolution close to 20 µm. TbT data is acquired by excitation of the circulating beam with impulse kickers. To improve the reliability of optics inference, detection of anomalies in BPM signals is required.

Anomaly detection is widely used for TbT data quality control [3, 4]. Anomalies caused by BPM electronics failures might deteriorate the measurements quality of accelerator parameters. To mitigate the effects of anomalies, robust parameter estimators should be used. Flagged BPMs should be excluded at the optics inference stage where it's possible.

Previously BPM signal quality was judged only based on the frequency spread across BPMs during single data acquisition. In this paper extended procedure of anomaly detection at the VEPP-4M is described. This procedure was tested on a large set of measurements and found to be reliable. Results of anomaly detection and classification at the VEPP-4M are reported.

ANOMALY DETECTION LOOP

A schematic view of the anomaly detection loop is shown in Fig. 1. Usable signal length is limited by decoherence. For frequency measurement, 1024 turns are used and 128 turns are used for amplitude and phase computation.

Each signal is split into several overlapping samples of short lengths. This allows generating large data set. Several different features are computed for each normalized sample. These features are used as a measure of samples similarity. Close samples are assumed to have close set of features. Thus, signals with samples containing large deviations of features can be flagged as anomaly candidates. In our case,

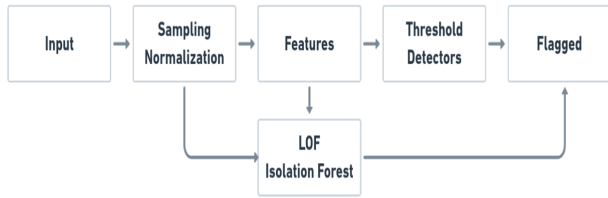

Figure 1: Anomaly detection loop at the VEPP-4M.

eight different derived features were tested. Each feature is also processed separately with a threshold detector. This allows defining anomaly score for each signal as the number of samples from a given signal with a feature value above the defined threshold. Anomaly scores across different features are combined to flag anomaly candidates and to estimate the contamination rate of a given measurement. A combination of threshold detectors performs well for anomaly detection in both simulations and experimental data. Robust estimation of feature spread allows to minimize the number of false positive cases.

For known contamination rate, several unsupervised machine learning (ML) methods can be applied. Local Outlier Factor [5] and Isolation Forest [6] techniques are used as a second layer in anomaly detection. These methods are applied directly to samples and in the feature space. Local Outlier Factor was found to perform well in both cases, while Isolation Forest worked better in feature space.

DERIVED FEATURES GENERATION

For normalized samples, several derived features can be computed. These features are obtained directly from a sample or from a full sample matrix.

Maximum absolute amplitude value in a sample is computed. This feature performs well for identification of spikes in TbT signals. For each sample, the frequency of the largest spectrum peak is computed. Significant frequency deviation across samples might indicate an anomaly and is sensitive to large spikes and noise. Fourier spectrum floor level in a given range of frequencies is used as a next feature. Samples with large noise should have a large spectrum floor level. A selected range of frequencies is assumed to contain no large peaks. Quasiperiodic decomposition reconstruction error is used as a measure of how well a given sample is approximated by several harmonics. From the SVD decomposition of the full sample matrix, the maximum absolute values of SVD space modes are used. Sample noise is also estimated using optimal SVD truncation [7]. Samples with anomalies are assumed to have larger noise estimations. Hankel filter [8] is applied to each sample and a feature is generated as a norm of the difference between filtered and original sample. Robust PCA [9] is used on the full sample matrix.

* I.A.Morozov@inp.nsk.su

ISBN: 978-3-95450-240-0 ISSN: 2673-5539 doi:10.18429/JACoW-RuPAC2021-WEPSC40

Corresponding column norms of the sparse part are used as features. Mean current across BPMs can also be used as an additional feature.

THRESHOLD DETECTORS

Based on a derived feature a simple threshold detector can be constructed. To do this, the median value of sample features is computed or another center tendency estimators can be used. Biweight midvariance is used as a robust estimator of dispersion. The median value is subtracted and absolute values of features are used. Normalization is performed for features and for dispersion estimation. Signal anomaly score is defined the number of samples above certain threshold. In practice, several dispersion values allow reliable separation of outliers. Five dispersion values were used for the VEPP-4M case.

Thus, based on each feature, signals are assigned an anomaly score. Results from all features are combined. If several threshold detectors have zero flagged anomaly candidates, TbT data is considered to be normal. Anomaly scores across detectors are summed and BPMs with total anomaly scores above the given threshold are flagged as anomaly candidates. The contamination rate for a single measurement is estimated based on the flagged signals.

UNSUPERVISED DETECTORS

Local Outlier Factor and Isolation Forest methods are used as an additional layer for anomaly detection. These methods require the expected contamination rate.

The Local Outlier Factor is based on local density estimation. We have tested this method for sample space and derived feature space. It was found to perform well in both cases. For sample space, its performance is influenced by the number of samples. Without splitting BPM signals into a large number of smaller samples, the detection quality was not satisfactory. Several restarts are used to obtain more reliable results.

The Isolation Forest identifies anomalies by isolation. An outlier can be isolated with a smaller number of partitions. When applied to sample space, it was found to produce a large number of false positive results. No such problem was observed for feature space. A random sampling of features with several restarts was used for both methods when applied to features. Instead of using features for each sample, only the largest feature is selected and assigned to the corresponding BPM signal.

ANOMALIES STUDY AT THE VEPP-4M

The above anomaly detection procedure was tested on the VEPP-4M experimental TbT data. Several hundreds of successive data acquisitions were analyzed. Typical examples of BPM signals with anomalies are shown in Fig. 2. Such anomalies are caused by BPM electronics and appear in both planes simultaneously. On average less than 1 % of signals contain such anomalies at beam current in3 mA to 4 mA range and close to 2 % at 1 mA in the first 1024 turns.

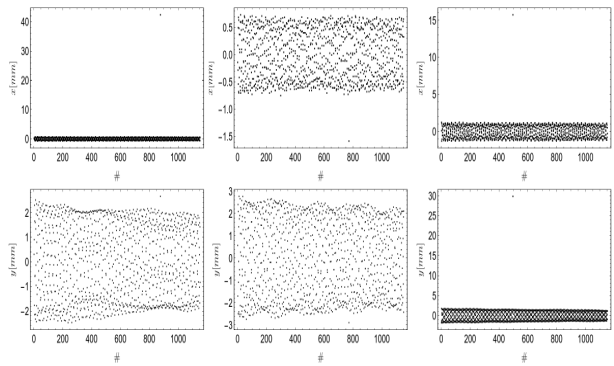

Figure 2: Examples of spike anomalies in TbT signals. Spikes appear in both planes.

In Fig. 3 an example of detected spike anomalies is shown along with derived features for all BPMs. In this measurement, two BPM signals contained spikes in the horizontal plane. As it can be seen, corresponding sample features are well separated from the rest of BPM signals by most of the features. These BPMs were also flagged by ML methods.

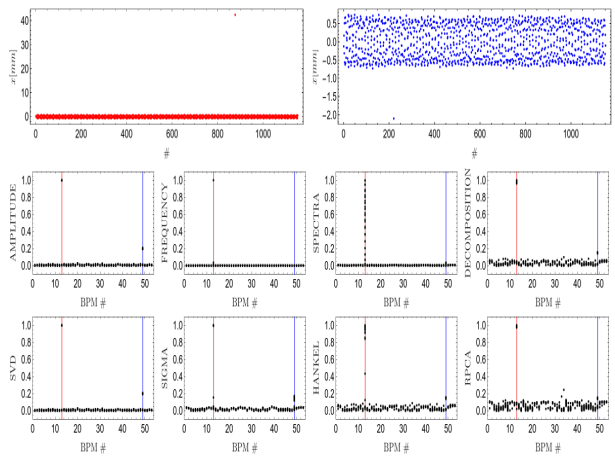

Figure 3: Example of detected spike anomalies from single measurement (top plots). Normalized features for all BPMs (bottom plots). Positions of signals with anomalies are indicated with lines.

Another type of anomalies were observed in both simulations and experimental data in the vertical plane. Several BPM signals were systematically flagged by both layers. These BPMs have small values of vertical β function (1.5 m). And in combination with noise and coupling, they stand out from the rest of BPMs. An example of such systematic anomalies is show in Fig. 4. As it can be seen from feature plots, these signals are separated from other BPMs. Several other BPMs were systematically flagged only by ML methods in the horizontal plane. For these cases, horizontal β function is less than the vertical one. The accuracy of estimated parameters (amplitudes and phases) is poor compared with other BPMs. We exclude these BPMs from the computation of β function based on phase measurement.

ISBN: 978-3-95450-240-0 ISSN: 2673-5539 doi:10.18429/JACoW-RuPAC2021-WEPSC40

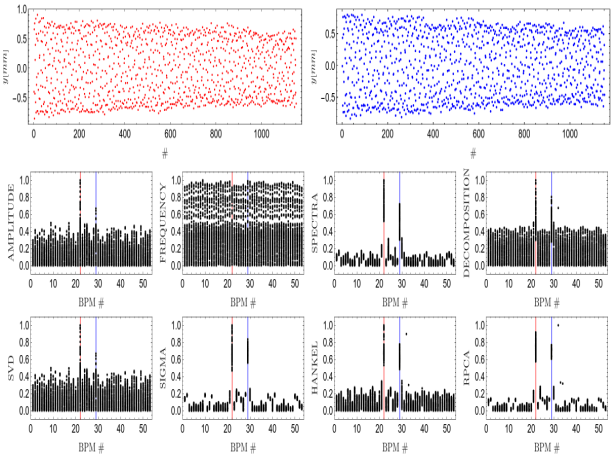

Figure 4: Example of detected systematic anomalies from single measurement (top plots). Normalized features for all BPMs (bottom plots). Positions of signals with anomalies are indicated with lines.

In Fig. 5 the results of 50 successive TbT measurements are shown. BPMs with high counts correspond to systematic anomalies. These BPMs are mostly flagged due to the ratio of β functions. For the horizontal plane, two BPMs stand out. In this case, BPMs are flagged only by ML methods while feature detectors show no sign of anomalies. Normally, since the estimated contamination rate is zero, in this case, used ML methods do not flag any BPMs. But for this study, we have allowed at least one BPM to have an anomaly. For the vertical plane, both layers mostly flag BPMs in the experimental region, where the value of the vertical β function is small compared to the horizontal one.

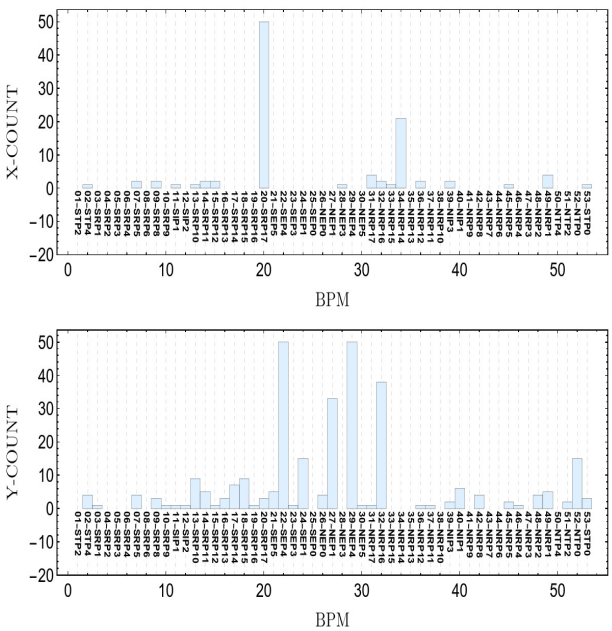

Figure 5: Flagged BPMs for 50 successive measurements. BPMs with high counts correspond to systematic anomalies.

CONCLUSION

The anomaly detection procedure for BPM signals processing at the VEPP-4M was extended. Several methods based on derived features of samples generated from BPM signals were tested. These features along with their robust dispersion estimation have allowed to define anomaly score for BPM signals and to estimate the contamination rate of a given TbT measurement. In combination with unsupervised ML methods, this procedure provides reliable detection of anomalies. An experimental study of anomalies in BPM signals at the VEPP-4M was performed. It was found spike anomalies appear in about 1 % of the signals in a single measurement. Several BPMs were systematically flagged due to different operation conditions. Further improvement and a more detailed study of anomalies are planned in the new season.

REFERENCES

[1] P. Piminov *et al.*, "Vepp-4m collider operation in high energy," *Proceedings of the 12th International Particle Accelerator Conference, IPAC2021, Campinas, Brazil*, May 2021.

[2] E. A. Bekhtenev and G. V. Karpov, "Bpm system for vepp-4m collider," *Physics of Particles and Nuclei Letters*, vol. 15, no. 7, pp. 929–932, Dec. 2018. DOI: 10.1134/S1547477118070154.

[3] R. Calaga and R. Tomás, "Statistical analysis of rhic beam position monitors performance," *Phys. Rev. ST Accel. Beams*, vol. 7, p. 042 801, 4 Apr. 2004. DOI: 10.1103/PhysRevSTAB.7.042801.

[4] E. Fol, R. Tomás, J. Coello de Portugal, and G. Franchetti, "Detection of faulty beam position monitors using unsupervised learning," *Phys. Rev. Accel. Beams*, vol. 23, p. 102 805, 10 Oct. 2020. DOI: 10.1103/PhysRevAccelBeams.23.102805.

[5] M. M. Breunig, H.-P. Kriegel, R. T. Ng, and J. Sander, "Optics-of: Identifying local outliers," in *Principles of Data Mining and Knowledge Discovery*, J. M. Żytkow and J. Rauch, Eds., Berlin, Heidelberg, 1999, pp. 262–270.

[6] F. T. Liu, K. M. Ting, and Z.-H. Zhou, "Isolation forest," in *2008 Eighth IEEE International Conference on Data Mining*, 2008, pp. 413–422. DOI: 10.1109/ICDM.2008.17.

[7] M. Gavish and D. L. Donoho, "The optimal hard threshold for singular values is 4/sqrt(3)," *IEEE Transactions on Information Theory*, vol. 60, no. 8, pp. 5040–5053, Aug. 2014. DOI: 10.1109/TIT.2014.2323359.

[8] I. Morozov, P. Piminov, and I. Yakimov, "Precise analysis of beam optics at the vepp-4m by turn-by-turn betatron phase advance measurement," *Proceedings of the 17th Russian Particle Accelerator Conference, RUPAC2021, Alushta, Russia*, Oct. 2021, this confference.

[9] E. J. Candès, X. Li, Y. Ma, and J. Wright, "Robust principal component analysis?" *J. ACM*, vol. 58, no. 3, May 2011. DOI: 10.1145/1970392.1970395.

ISBN: 978-3-95450-240-0 ISSN: 2673-5539 doi:10.18429/JACoW-RuPAC2021-WEPSC42

RF CAVITY BASED CHARGE DETECTOR FOR A LOW CHARGE ULTRA SORT SINGE ELECTRON BUNCH MEASUREMENT

K.V. Gubin, ILP SB RAS, Novosibirsk, Russia
A.M. Barnyakov, S.L. Samoylov, D.P. Sukhanov[1], BINP SB RAS, Novosibirsk, Russia
[1]also at Novosibirsk State University, Novosibirsk, Russia and Novosibirsk State Technical University, Novosibirsk, Russia

Abstract

Nowadays the project of laser-driven Compton light source started in ILP SB RAS in collaboration with BINP SB RAS. It was expected the production of 1-10 pC electron beams sub-ps time range duration with energies up to 100÷150 MeV as a result of the first stage of the project. It is necessary to have the non-destructive charge detector for on line measurements during experiments. We proposed the detector based on reentrant RF resonator technology. Single circular cylinder geometry of measuring RF cavity is insensitive to electron beam position and size as well as time structure of bunch (on the assumption of sufficiently short bunch). Base data of cavity are close to acceleration section elements of VEPP-5 linac.The prototype of the detector was successfully tested at VEPP-5 electron linac. Measured charge of single bunch reaches down to 1 pC and less. This paper presents the results of development and testing of diagnostics.

INTRODUCTION

At the present time, the impressive progress in laser wakefield acceleration (LWFA) of charged particles gives grounds to consider LWFA as a perspective method of electron beam production in the GeV energy range.

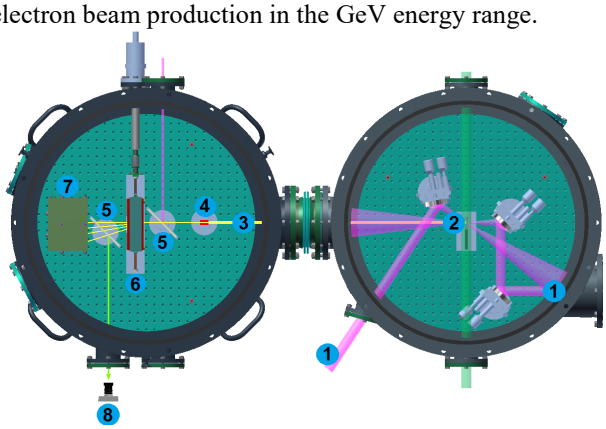

Figure 1: Experimental vacuum chamber. (1) Laser beams, (2) supersonic gas jet, (3) electronic beam, (4) RF beam charge detector, (5) screens, (6) magnet spectrometer, (7) faraday cap, (8) CCD.

The project of laser-driven Compton light source started in ILP SB RAS in collaboration with BINP SB RAS. The first stage of the project is to create a stand for obtaining and studying LWFA-accelerated electron beam inside the supersonic gas jet with energy as high as 100 MeV. At the next stage, it is planned to obtain a high-energy gamma-ray beam by means of Compton backscattering of a probe light beam on LWFA-accelerated electrons [1] (see Fig.1). Expected parameters of the electron beam are: up to 50-100 MeV of energy, 1-10 pC of charge, 1-10 mrad of angular divergence, ≤ 0.1 ps of beam duration.

DETECTOR PURPOSE, DESIGN AND PARAMETERS

Non-destructive beam current measurement is a necessary constituent of any accelerator facility. In our case we propose to use the wide-used diagnostics based on reentrant RF resonator. This kind of detector was realized, for example, [2] as a beam current monitor or beam position monitor [3, 4].

The development of beam charge detector is constrained by the following general demands:

- Compact size (full dimensions not more than ~10 cm) because the device will be placed inside limited volume of experimental vacuum chamber (Fig. 1) with diameter 70 cm and height 50 cm.
- Detector will operate with single bunch condition. Storage methods of measurements are unacceptable because of the electron beam has repetition rate not more 1 Hz. Moreover, expected beam parameters (as charge as beam size and position) will be very unstable between charge pulses.
- Maximum unification of detector parameters with parameters of VEPP-5 RF elements [5].
- Beam charge range is from 100÷500 fC (tuning regime of LWFA experiment) to 1÷5 nC (RF-photogun experiments).
- In any case beam structure can has as one bunch as bunch train structure. But the bunch duration inside the train will be more or less uniform.

According to the fundamental properties of beam loading we can estimate analytically induced wakefield in the cavities of the millimeterwave structure [6, 7]. A pointlike beam induces a voltage (and, therefore, signal amplitude from pickup antenna) linearly depended on beam charge

$$U_p = 2kq \tag{1}$$

For the TM_{010} mode in the cylindrical waveguide with radius R and length L final expression of the loss parameter is

$$k = \frac{LT^2}{2\varepsilon_0 R^2 J_1^2(\nu_{01})} \tag{2}$$

ISBN: 978-3-95450-240-0 ISSN: 2673-5539 doi:10.18429/JACoW-RuPAC2021-WEPSC42

Linear dependence between beam charge q and electrical (and magnetic) field, hence voltage on the detector antenna can us to measure the transverse beam charge.

More accurate modelling by CST Studio gives us the following main results:

- Simple cylindrical geometry of RF cavity is most useful for us. This geometry has minimal sensitivity to beam position, size, transverse angle etc.
- Cavity geometry choose the same with geometry of regular cavities of VEPP-5 linac acceleration section (see Fig. 2).
- Detector sensitivity will be enough high to sub-pC bunch registration.
- Beam charge detector can be used as for LWFA experiment, as for any VEPP-5 application.

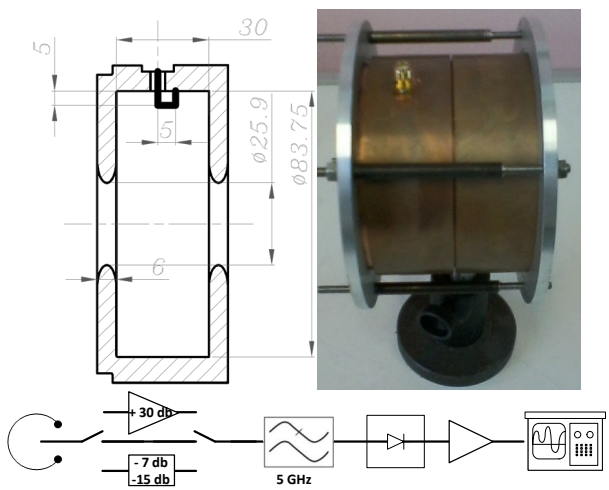

Figure 2: Maquet of cavity based charge detector and measuring circuit.

DETECTOR PROTOTYPE AND MEASURING CIRCUIT

As result of numerical modelling, the simple cylindrical reentrant cavity was chosen for further experimental realization. We use cavity geometry the same to acceleration section cavity of VEPP-5 linac in BINP (see Fig. 2). It simplifies the manufacture, measure and tuning of detector cavity. The prototype of detector based on segment of acceleration section of VEPP-5 linac was manufactured. Goal of prototype development are:

- To study RF characteristics, to choose and complete the measuring circuit.
- To excite cavity by the short electric pulse through the axial stub antenna.
- To excite cavity by VEPP-5 electron beam and to study the detector real parameters (as sensitivity, linearity of characteristics etc.).

Measuring circuit was chosen maximum simple (Fig. 2). It consists of cavity with pickup antenna; RF amplifier or attenuator with bandpass up to 30 GHz; RF filter with bandpass up to 3.2 GHz (necessary for extraction the basic cavity RF frequency of TM_{010} mode); detector head with frequency band up to 20 GHz; video amplifier with bandpass 500 MHz and register oscilloscope.

VEPP-5 LINAC BEAM TEST

Finally, charge detector was tested at electron linac of Injection Complex VEPP-5, BINP. The layout experiment is presented in Fig. 3. The injection complex has 180° magnetic spectrometer placed after the second RF structure as regular beam diagnostics. Detector cavity placed in front of the output port of the spectrometer. To test the detector operation over a wide range of the beam charge, the electron beam was intentionally extra focused/defocused by quadrupole lens/magnetic corrector in front of the first RF structure. The tunable bunch charge was in the range between 4.8 nC ($3 \cdot 10^{10}$ e^-, nominal operational condition of VEPP-5 Injection Complex) and practically down to zero, the repetition rate was 2 Hz.

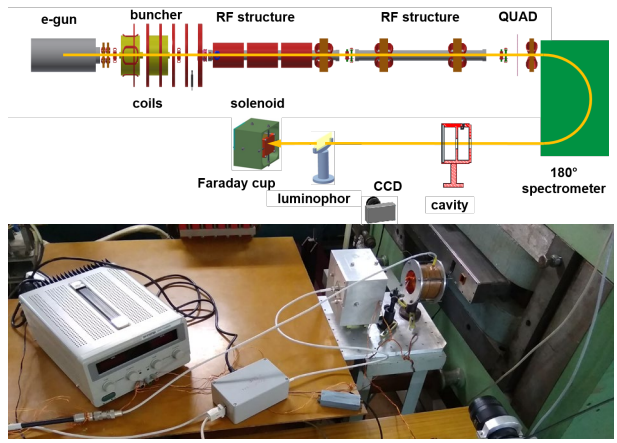

Figure 3: Electron beam line layout of VEPP-5 Injection Complex and the detector in experimental area.

Typical bunch train structure shown in Fig. 4. Beam energy at the FC point was 120-125 MeV, bunch train duration was ~ 5 ns, tunable bunch charge was in the range between 4.8 nC ($3 \cdot 10^{10}$ e^-, nominal operational condition of VEPP-5 Injection Complex) and practically down to zero, repetition rate was 2 Hz.

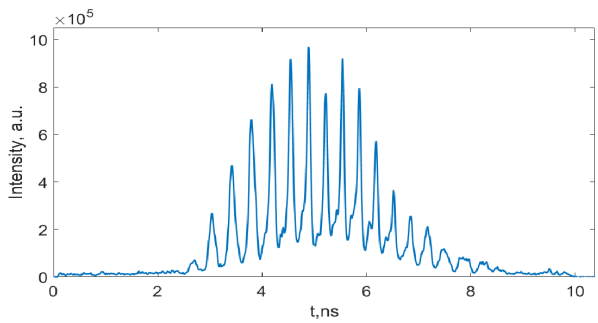

Figure 4: Bunch train structure inside VEPP-5 linac [8].

Detector signal is calibrates by Faraday cup [9]. Luminophor screen with CCD camera [10] use in order visual observation of electron beam. Cavity and FC signals were processed by specially developed amplifiers with wide-variable amplification factor.

ISBN: 978-3-95450-240-0 ISSN: 2673-5539 doi:10.18429/JACoW-RuPAC2021-WEPSC42

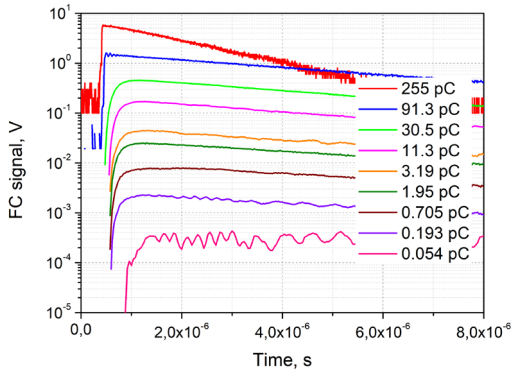

Figure 5: Signals of FC for different charge of electron beam.

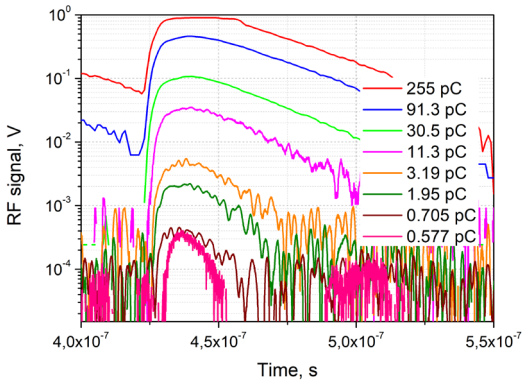

Figure 6: Signals of RF cavity based charge detector for different charge of electron beam.

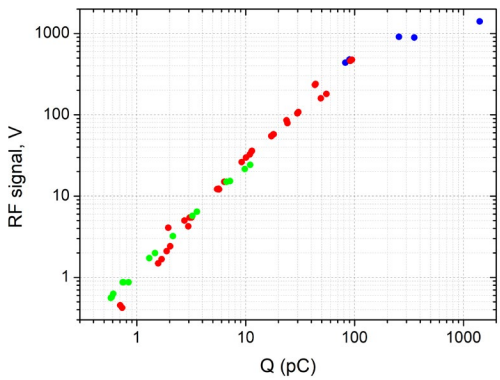

Figure 7: Dependence between detector signal and beam pulse charge.

Typical RF and FC signals from experiment are shown in Figs. 5-6. Final calibration curve of detector - dependence between detector signal and beam pulse charge is presented in Fig. 7.

The stable work of the device with bunch charge from ~ 1 nC down to ~ 0.5 pC was observed, which practically equals to the expected parameters. The experimental data are in good agreement with those of the standard beam diagnostics in Injection Complex VEPP-5. Dependence between detector signal and beam pulse charge is linear, as it was expected. Low charge limit consists ~ 500 fC and is conditioned by the radio- disturbance.

CONCLUSION

Developed charge detector allows measuring the charge of ultrashort ($\tau \leq 1$ ps) low charge (~ 1 pC) electron bunch with high precision without any additional complicated electronics and does not need special calibration procedures. The prototype of beam charge detector manufactured and successfully tested under 120 MeV beam of VEPP-5 accelerator complex at Budker INP, Novosibirsk. Proposed diagnostics can be used in wide range of linear accelerated experiments.

REFERENCES

[1] V.I. Trunov *et al.,* "Laser-driven plasma wakefield electron acceleration and coherent femtosecond pulse generation in X-ray and gamma ranges." *Journal of Physics: Conference Series.* Vol. 793. No. 1. IOP Publishing, 2017.

[2] D. Lipka, J. Lund-Nielsen, and M. Seebach, "Resonator for Charge Measurement at REGAE", in *Proc. 2nd Int. Beam Instrumentation Conf. (IBIC'13),* Oxford, UK, Sep. 2013, paper WEPF25, pp. 872-875.

[3] D. Lipka, M. Dohlus, M. Marx, S. Vilcins, and M. Werner, "Design of a Cavity Beam Position Monitor for the ARES Accelerator at DESY", in *Proc. 7th Int. Beam Instrumentation Conf. (IBIC'18)*, Shanghai, China, Sep. 2018, pp. 269-272. doi:10.18429/JACoW-IBIC2018-TUPB05

[4] C. Simon *et al.*, "Design and Beam Test Results of the Reentrant Cavity BPM for the European XFEL", in *Proc. 5th Int. Beam Instrumentation Conf. (IBIC'16)*, Barcelona, Spain, Sep. 2016, pp. 356-359. doi:10.18429/JACoW-IBIC2016-TUPG17

[5] M.S. Avilov *et al. Atomic Energy* 94. No.1, pp. 50-55, 2003.

[6] M.V. Arsentyeva *et al.*, "Development of the Millimeter-Wave Accelerating Structure", *Physics of Particles and Nuclei Letters* 16.6, pp. 885-894, 2019.

[7] T. P. Wangler, RF Linear accelerators. – John Wiley & Sons, 2008.

[8] V. V. Balakin, D. E. Berkaev, V. M. Borin, F. A. Emanov, and O. I. Meshkov, "Longitudinal Beam Measuruments on Damping Ring BINP's Injection Complex With New Resonator", in *Proc. 26th Russian Particle Accelerator Conf. (RuPAC'18)*, Protvino, Russia, Oct. 2018, pp. 453-455. doi:10.18429/JACoW-RUPAC2018-THPSC22

[9] V.V. Gambaryan *et al.,* "Design and test of a Faraday cup for low-charge measurement of electron beams from laser wakefield acceleration", *Review of Sc.Instr.* 89.6 p. 063303, 2018.

[10] K.V. Gubin *et al.,* "A Spectrometer for Measuring the Characteristics of a Single Laser-Accelerated Electron Bunch with a Small Charge", *Instruments and Experimental Techniques* 63.3, pp. 325-333, 2020.

ISBN: 978-3-95450-240-0 ISSN: 2673-5539 doi:10.18429/JACoW-RuPAC2021-WEPSC44

BEAM LOSS MONITORING SYSTEM FOR THE SKIF SYNCHROTRON LIGHT SOURCE

Yu. I. Maltseva*[1], S. V. Ivanenko, A. Khilchenko, X. C. Ma, O. I. Meshkov[1], A. Morsina[2], E. A. Puryga
Budker Institute of Nuclear Physics SB RAS, Novosibirsk, Russia
[1]also at Novosibirsk State University, Novosibirsk, Russia
[2]also at Novosibirsk State Technical University, Novosibirsk, Russia

Abstract

The Siberian ring source of photons (SKIF) is a new 3 GeV fourth-generation synchrotron light source being developed by the Budker Institute of Nuclear Physics (BINP). In order to ensure its reliable operation, beam loss diagnostics system is required. Two types of beam loss monitors will be installed at the SKIF: 5 fiber-based Cherenkov Beam Loss Monitors (CBLM) for the linac and transfer lines and 128 Scintillator-based Beam Loss Monitors (SBLM) for the storage ring. Sophisticated electronic equipment are employed to use these monitors at different SKIF operating modes. The article describes the design of the SKIF beam loss diagnostics system based on numerical simulations and experimental studies.

INTRODUCTION

The SKIF is the 4th generation synchrotron light source with 3 GeV energy and emittance of 75 pm rad, that is under construction in Novosibirsk, Russia [1]. The SKIF consists of 200 MeV electron linac, linac-to-booster transfer line (LBT), booster synchrotron with maximum energy of 3 GeV and circumference of 158.7 m, booster-to-storage ring transfer line (BST) and storage ring with 16-fold symmetry and 476 m circumference. The storage ring is designed to operate at top-up injection with up to 400 mA beam current. Current stability of 1% is required. The layout of the SKIF accelerator facility is shown in Fig. 1.

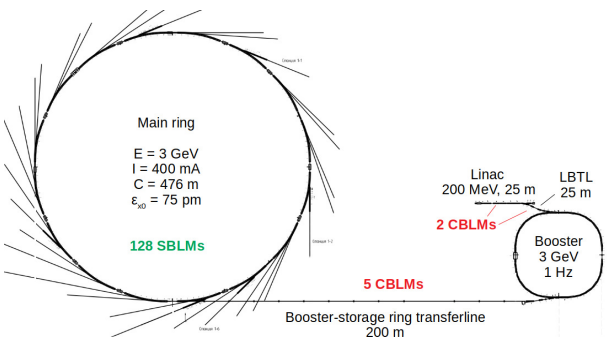

Figure 1: The SKIF layout.

The SKIF is aimed to provide users with syncrotron radiation (SR) almost in 24/7 operation. Therefore, strict requirements on the electron beam stability are imposed. In order to achieve effective SKIF commissioning in the future and its reliable operation and performance in various modes, beam loss diagnostics system is required. This system is an essential tool for real time monitoring of beam losses usually caused by misaligned beam during the machine commissioning or faulty condition of accelerator subsystems or related with beam lifetime [2].

For the linac, LBT and BST where single-bunch mode is available, we proposed to use the CBLMs. For the storage ring in order to control beam losses during machine tuning and operation at top-up mode, the SBLMs were proposed.

CHERENKOV BEAM LOSS MONITOR

The operation principle of the CBLM is based on the registration of the Cherenkov radiation generated by secondary charged particles in the optical fiber attached to the vacuum pipe [3]. The Cherenkov light propagates upstream and downstream along the optical fiber and can be detected usually by a photomultiplier (PMT) at either one or both ends of the fiber. Timing of the PMT signal gives the location of the beam loss and signal intensity is proportional to the number of lost particles.

Simulations and Experimental Studies

The CBLM prototype tests were performed at the operating BINP accelerator [4] with beam parameters similar to the SKIF. As an optimal fiber type in terms of sensitivity, radiation hardness and cost effectiveness, multimode silica fiber with step-index profile FG550UEC by Thorlabs was selected. It has 550 μm core diameter, high OH–, F-doped silica cladding. Measured light dispersion was obtained to be 0.17±0.01 ns/m. In order to achieve desired CBLM spatial resolution of 1 m due to the SKIF magnet spacing, maximum fiber length should be about 40 m.

As a photodetector microchannel plate PMT (MCP-PMT) was selected, with gain over 10^6, dark current less than 1 nA, front rise time of 0.5 ns and the duration (FWHM) of the anode current pulse of at least 1.5 ns. It allows detecting beam losses of ~1 pC corresponding to 1% of the total bunch charge.

The experimental results of 500 MeV beam loss distribution at the downstream and upstream fiber ends are shown in Fig. 2. The upstream signal has 4.2 times better spatial resolution than the downstream one. Taking into account the difference in PMT gains, the downstream signal sensitivity

* yu.i.maltseva@inp.nsk.su

ISBN: 978-3-95450-240-0 ISSN: 2673-5539 doi:10.18429/JACoW-RuPAC2021-WEPSC44

is about 10 times higher than the upstream one, which is consistent with the numerical simulations [5].

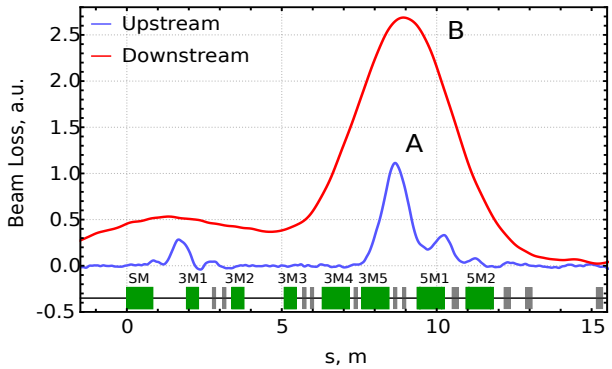

Figure 2: Beam loss distributions of the 500 MeV electron beam at both fiber ends. FWHM of the peak A is 4.2 times smaller than the peak B.

Since the upstream loss measurements provide better monitor spatial resolution and the downstream one – better monitor sensitivity, for the SKIF we decided to perform beam loss measurements from both fiber ends.

Due to the SKIF layout, the designed CBLM system for the linac and LBT consists of a single 30 m long fiber with 2 MCP-PMTs each, 200 m long BST requires 5 fibers of 40 m and 10 MCP-PMTs in total.

SCINTILLATOR BEAM LOSS MONITOR

In its simplest form, the SBLM consists of a plastic scintillator coupled with the PMT [6]. Shower particles e-, e+,γ passing through the scintillator volume excite scintillation. The polystyrene-based SC-205 scintillator manufactured by IHEP was selected. It has a light output equal to 66% of anthracene and decay time of 2.5 ns.

The detector construction has been selected as 10 cm long scintillator rod with 2.5 cm diameter. To maximize light collection the surfaces of the scintillator should be wrapped around with reflective Tyvek paper. The PMT 9107B by ET Enterprises was chosen to match scintillator diameter, moreover, the PMT spectral sensitivity matches the emission spectrum of the scintillator.

The SBLM is placed in a 3 mm steel housing to avoid background signal due to the scattered SR. To perform regular radiation induced calibration of the SBLM signals, a LED is attached to the free end of the scintillator.

SBLM Performance Simulations

Based on FLUKA [7] simulations of the beam loss scenarios we determined optimal amount of the SBLMs and their optimal position at the SKIF storage ring.

Fig. 3 shows an example of simulated distribution of secondary particles caused by the beam loss inside quadrupole. The simulated beam loss scenario is the following: 3 GeV electron beam hits the vacuum pipe with small incident angle relative to equilibrium orbit. Light output is in the range of 10^2-10^4 photons/primary.

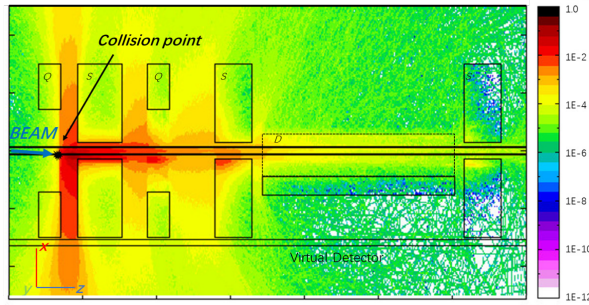

Figure 3: Typical distribution of the secondary charged particles for the beam loss in the SKIF lattice.

Regular losses most likely to occur at the locations with larger beam size which is due to higher beta- or dispersion functions. The simulation result of the SBLM response for a single SKIF superperiod [8] is shown in Fig. 4. 8 SBLMs per superperiod at the locations of the most significant shower peaks to achieve maximum diagnostic efficiency are proposed. Due to the 16-fold symmetry of the ring, a total number of 128 SBLM detectors are planned to be installed around the SKIF storage ring.

BLM ELECTRONICS

CBLM Measuring Module

Measuring modules based on switch capacitor array (SCA) technology are developed to digitize the signal from the PMT. Capacitive storage arrays (such as PSI's DRS4 [9]) are the key elements in such systems. They provide data logging at a sampling rate of several GHz. The following main elements can be distinguished in the developed measurement module for the CBLM (see Fig. 5):

- Programmable gain input amplifiers (PGA);
- DRS4 chip in the configuration with two lines of capacitive storage arrays up to 4096 elementary cells each;
- EA unit that generates signals for carrying out amplitude and time calibration for DRS4 chip;
- Synchronization and timing node, linking DRS4 data recording cycles to external events;
- Digital node based on Intel Cyclone V SoC FPGA.

Bilateral signal registration mode will be organized. The measuring modules placed between the segments of the magnetic structure operate in a two-channel mode. Total amount of 10 modules is required for the SKIF CBLM system.

SBLM Measuring Module

Four-channel measuring modules built on the data recording oscillographic method are proposed to be used for the SBLMs. Each channel of the measuring module will provide data recording with sampling rate of 250 MHz and amplitude resolution of 14 bits. The resources of the Intel Cyclone V FPGA installed on the board of each module will be used for implementing various operation modes of the measuring modules, as well as for receiving, preprocessing and transmitting data via the Ethernet channel. The devel-

ISBN: 978-3-95450-240-0 ISSN: 2673-5539 doi:10.18429/JACoW-RuPAC2021-WEPSC44

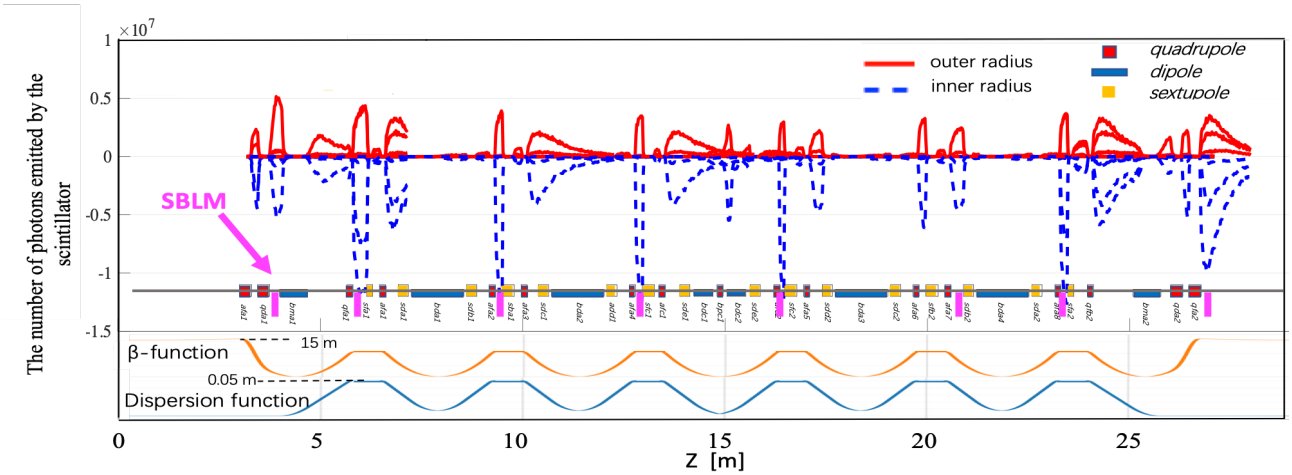

Figure 4: The simulated distribution of optical photons in the scintillator over the SKIF storage ring superperiod. The sign of the vertical axis only has meaning of direction.

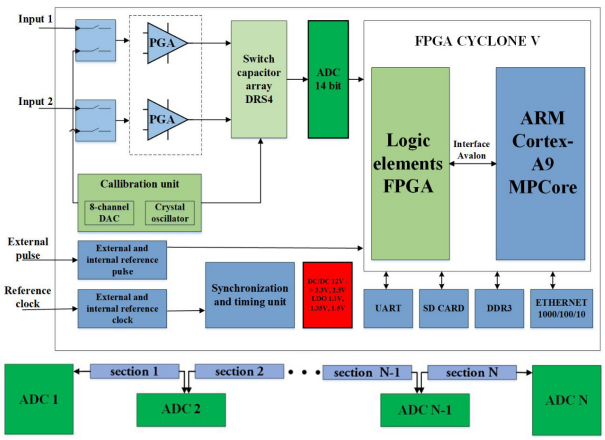

Figure 5: Measuring module for the CBLM (top), scheme of the CBLMs in successive segments of the magnetic structure (bottom).

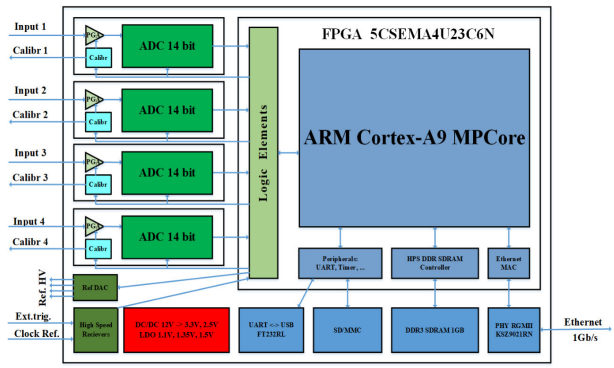

Figure 6: Measuring module for the SBLM.

oped measuring module has four identical measuring tracts (see Fig. 6), each of them includes:

- Wideband input amplifier (0-100MHz) with programmable gain;
- 14-bit ADC with sampling rate up to 250 MHz;
- Synchronization and timing node, built on the basis of PLL (generator with a phase-locked loop) and FPGA elements;
- The generator of the test signal for the SBLM amplitude calibration;

The developed SBLM measuring module will have two operating modes: oscilloscope and counting. Oscilloscope mode allows recording the shape of the detector signals in a sequence of time windows with a duration set by the operator. Counting mode allows fixing signals in a sequence of successive time windows, the duration of which is set in software. For the SKIF storage ring, 32 modules are required.

The CBLM and SBLM measuring modules are combined into the general data acquisition system by the cable synchronization lines that ensure the binding of data acquisition cycles to external events. They interface with a PC-based operator console using a standard switch over Ethernet-1000 communication channels.

CONCLUSION

For the SKIF to achieve effective future commissioning and its reliable operation and performance in various modes, beam loss diagnostics system is critical. The design of the beam loss diagnostics system for the SKIF is completed. The CBLM optimal parameters were selected based on the prototype test results at the operating BINP accelerator. Based on FLUKA simulations, total amount of the SBLMs and their optimal position at the SKIF storage ring were obtained. Further experiments with the SBLM prototype are expected. The measuring modules for the CBLM and the SBLM have been developed. These electronics could be combined into a general data acquisition system and integrated in the SKIF control system for real time operation.

ISBN: 978-3-95450-240-0 ISSN: 2673-5539 doi:10.18429/JACoW-RuPAC2021-WEPSC44

REFERENCES

[1] S. M. Gurov et al., Injection system for the Siberian Ring Source of Photons, *Journal of Surface Investigation: X-ray, Synchrotron and Neutron Techniques* 14, 651-654 (2020). doi:10.1134/s1027451020030271

[2] K. Wittenburg, "Beam Loss Monitoring and Control", in *Proc. 8th European Particle Accelerator Conf. (EPAC'02)*, Paris, France, Jun. 2002, paper THYGB001, pp. 109-113.

[3] Yu.I. Maltseva *et al.*,"Distributed beam loss monitor based on the Cherenkov effect in an optical fiber", *Physics-Uspekhi*, vol. 58, pp. 516–519, 2015. doi:10.3367/ufne.0185.201505m.0553

[4] Yu.I. Maltseva et al., "Current Status of VEPP-5 Injection Complex", presented at the *27th Russian Particle Accelerator Conf. (RuPAC'21)*, Alushta, Russia, Sept.-Oct. 2021, paper TUA02, this conference.

[5] Yu.I. Maltseva, V.G. Prisekin, A.R. Frolov, Beam Loss Measurements Using the Cherenkov Effect in Optical Fiber for the BINP e+e- Injection Complex, in *Proc. 8th Int. Beam Instrumentation Conf. (IBIC'19)*, Malmö, Sweden, Sep. 2019, pp. 233-237. doi:10.18429/JACoW-IBIC2019-TUA003

[6] L. Torino, K. B. Scheidt, "New beam loss detector system for EBS-ESRF", in *Proc. 7th Int. Beam Instrumentation Conf. (IBIC'18)*, Shanghai, China, Sep. 2018, pp. 346-352. doi:10.18429/JACoW-IBIC2018-WEOB01

[7] A. Ferrari, P. R. Sala, A. Fasso, and J. Ranft, "FLUKA: A Multi-Particle Transport Code", United States, Dec. 2005. doi:10.2172/877507

[8] G. N. Baranov et al., "Magnet Lattice Optimization for Novosibirsk Fourth Generation Light Source SKIF", *Siberian Physical Journal*, vol. 15, no. 1, pp. 5-23, 2020. doi:10.25205/2541-9447-2020-15-1-5-23

[9] S. Ritt, "Design and performance of the 6 GHz waveform digitizing chip DRS4", in *Proc. IEEE Nucl. Sci. Symp. Conf. Rec. (NSS)*, Sydney, Australia, Oct. 2008, pp. 1512-1515. doi:10.1109/NSSMIC.2008.4774700

ISBN: 978-3-95450-240-0 ISSN: 2673-5539 doi:10.18429/JACoW-RuPAC2021-WEPSC45

MEASUREMENT OF THE ELECTRON BEAM SPECTRUM BY THE ABSORBING FILTERS METHOD DURING A SINGLE PULSE

A. Drozdovsky, A.Bogdanov, S. Drozdovsky, A.Kantsyrev, A.Khurchiev, V. Panyushkin, S.Savin, A.Skobliakov, S.Visotski, V.Volkov
NRC «Kurchatov Institute» - Institute of theoretical and experimental physics, Moscow, Russia

Abstract

Equipment for measuring the spectrum of an electron beam during a single pulse has been developed and manufactured. We developed a method of processing experimental data and present the obtained results.

INTRODUCTION

The interest in measuring the energy spectrum of electron beams by the method of absorbing filters is due to the technical availability in comparison with magnetic spectrometry. Moreover, the measuring unit is compact, efficient and suitable for various research facilities.

EXPERIMENTAL FACILITY

The task of our work was to determine the spectrum of an electron beam with a maximum energy up to 300 keV during one pulse. We applied elements of the technique by [1] to obtain the spectrum from the absorption curves of the beam. The beam passed through a sequence of metal plates of same thickness located perpendicular to the beam axis at fixed interval, while the charge *Qi* absorbed in each plate is measured for each pulse. The measurement scheme is shown in Fig. 1.

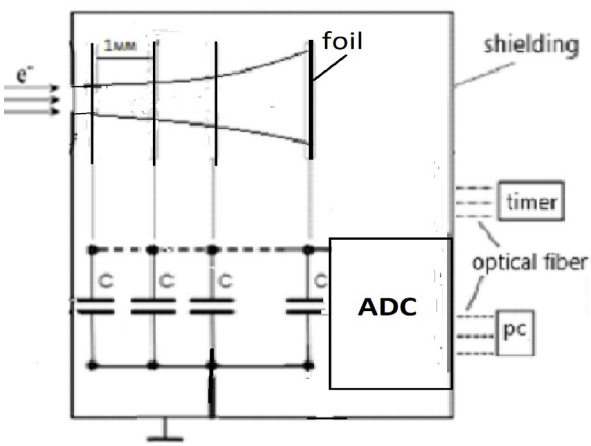

Figure 1: The measurement scheme.

Beams of energy up to 300 keV were emitted from an electron gun [2]. The current collector package consists of 16 insulated identical aluminum foils with the gap of 1 mm between. The thickness of the foils varies from 10 to 25 microns depending on the maximum electron energy. The charge of the foils after passing the beam was measured by an ADC. The charge absorbed by the nth foil $Q_n = V_n C_n$. Each foil is connected to a capacity C_n = 7 nF. The distribution of voltage V_n over the foils of thickness 16 microns after passing an electron beam through at different charging voltages is shown in Fig. 2.

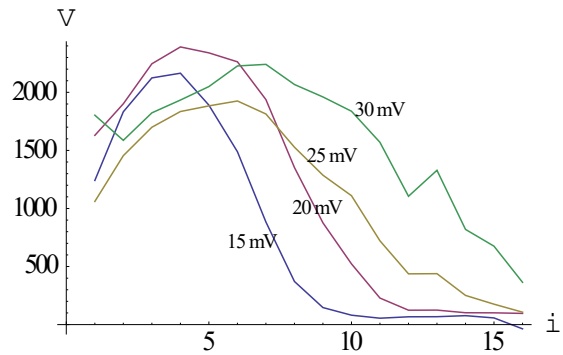

Figure 2: Distribution of voltage V_n over foils at different voltages of the pulse generator of the gun.

Measurements with foils of thickness 16 microns are suitable for the correct determination of the spectrum at charging voltages up to 25 kV. For high voltages the data is incomplete as can be seen from the absorption curves.

METHOD OF SPECTRUM RESTORING

The measurement process is related to the following system of integral equations:

$$\int_{E_{min}}^{E_{max}} K_i(\varepsilon)\, q(\varepsilon)\, d\varepsilon = Q_i\,, \quad i = 1, \ldots, n\,, \qquad (1)$$

where Q_i is the experimentally obtained charge absorbed by the plate number i, $q(\varepsilon)$ is the charge density with respect to the energy (the energy spectrum of the beam), $K_i(\varepsilon)$ is the kernel of the integral transform, with a physical meaning of the probability for a particle with the energy ε to be absorbed in the plate i. The integration is bounded by the interval $\{E_{min}, E_{max}\}$, which limits the range of particle energies in the beam. Our task is to restore $q(\varepsilon)$ from Q_i by solving this system of integral equations. After approximation $q(\varepsilon)$ and $K_i(\varepsilon)$ by step functions, piecewise constant on the intervals $\{\varepsilon_j - \Delta\varepsilon/2, \varepsilon_j + \Delta\varepsilon/2\}$, $\varepsilon_{j+1} - \varepsilon_j = \Delta\varepsilon$, the system (1) takes the discrete form:

* Work supported by R&D Project between NRC "Kurchatov Institute" - ITEP and TRINITI

ISBN: 978-3-95450-240-0 ISSN: 2673-5539 doi:10.18429/JACoW-RuPAC2021-WEPSC45

$\sum_j K_{ij} q_j = Q_i\,, \quad i = 1, \ldots, n\,,\ j = 1, \ldots,$ (2)

where $K_{ij} = \Delta\varepsilon\ K_i(\varepsilon_j)$, $q_j = q(\varepsilon_j)$, or in matrix representation $K\,q = Q$.

The values K_{ij} were calculated by the Monte Carlo method using the Geant4 software package [3]. The charges absorbed in the foils were calculated for monoenergetic beams from 10 to 300 keV with step 10 keV, filling the range quite dense. Figures 3 and 4 show the structure of the array K.

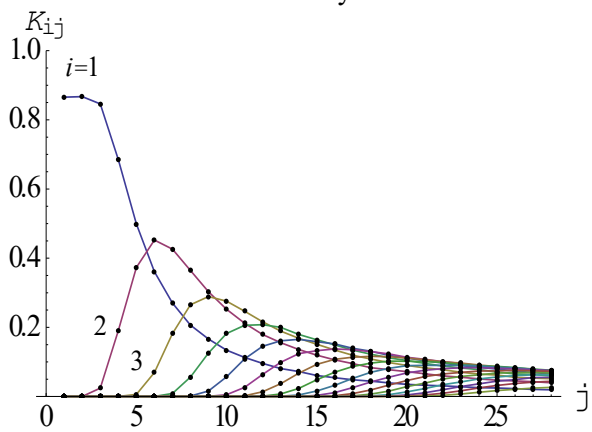

Figure 3: Distribution of absorbed charges overbeams of different energies for each plate i.

The first one shows the distribution of the absorbed charge by energy for each plate (plate – line), the second shows the distribution of the absorbed charge across the plates for each energy (energy – line).

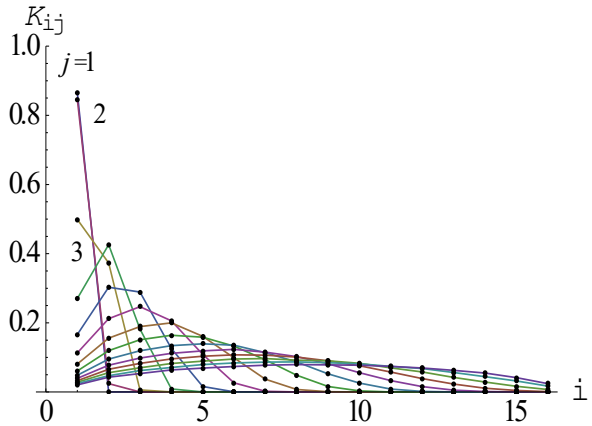

Figure 4: Charge distribution over plates for each beam

On the ordinate axis – the charge in relative units, on the abscissa axis: the first figure – the numbers of energy counts, the second – plate numbers.

The equation (1) or (2) is an ill-posed inverse problem, as well as the most arising in practice.

The related mathematical tool is the theory of correct and incorrect problems by A. N. Tikhonov [4]. To obtain an appropriate solution, Tikhonov regularization is used, which means minimizing the functional

$$\|Kq - Q\|^2 + \alpha\|q\|^2,\ \alpha > 0\,,$$

with respect to q, where $\|\ \|$ denotes the norm of a vector or matrix (operator). The first term is responsible for the fidelity and the second one for the regularity. The larger the regularization parameter α, the higher the regularity and lower the accuracy. $\alpha = 0$ corresponds to the least squares method. In our case, the search for the minimum is carried out by the conjugate gradient method.

It turned out that not the regularization is crucial, but the high-precision fitting of the input data and the transformation kernel by statistical distributions, which make the regularization parameter reduced to almost zero. The data Q is approximated by normal distribution, and the kernel K by normal and log-normal as the energy or plate is fixed respectively.

The fitting of the matrix K is performed as follows. First, for each j (fixed energy), we approximate the one-dimensional array K_{ij} (charge distribution over the plates) by the function

$$\alpha_j P_N(\sigma_j, \mu_j;\ x) + \beta_j,$$

where $P_N(\sigma, \mu;\ x)$ is normal distribution.

Then, for each i (plate is fixed), we approximate the one-dimensional array K_{ij} (charge distribution by energy) by the function

$$\alpha_i P_{LN}(\sigma_i, \mu_i;\ y - \lambda_i),$$

where $P_{LN}(\sigma, \mu;\ x)$ is lognormal distribution. Thus we get the fitted array K_{ij}.

To fit the experimental data, besides the absorption function Q_i, we need the charge passage function $\widehat{Q_i}$. They are related in the following way:

$$\widehat{Q_i} = \sum_{j=1+i}^{n} Q_j\,,\ i = 0, \ldots, n,$$

$$Q_i = \widehat{Q_{i-1}} - \widehat{Q_i}, i = 1, \ldots, n.$$

The fitting of the experimental data is conducted in the following order. First, we calculate $\widehat{Q_i}$ from Q_i as above, then fit the one-dimensional array $\widehat{Q_i}$ by the function

$$\alpha C_N(\sigma, -\mu;\ -x) + \beta,$$

where C_N is the cumulative function for normal distribution. Then, by the inverse we get the fitted Q_i.

All the calculations were performed in Wolfram Mathematica.

RESULTS

We illustrate our method by an example of calculating the spectrum of a beam with the source voltage 17.5 keV. The described above fitting of the

ISBN: 978-3-95450-240-0 ISSN: 2673-5539 doi:10.18429/JACoW-RuPAC2021-WEPSC45

passing function is depicted in the Fig. 5. On the abscissa axis – the plate numbers, on the ordinate axis – the charge in relative units. The points represent the discrete passing function, the line represents the continuous fitting function.

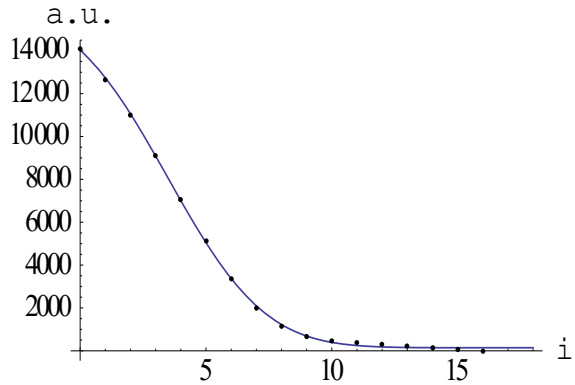

Figure 5: The passing function $\widehat{Q}_i$.

Next, we solve the equation $K\ q = Q$ by Tikhonov regularization with $\alpha = 0$ and get a quite regular and accurate solution, shown in Fig. 6a. On the abscissa axis – the energy in keV, on the ordinate axis – the charge density with respect to the energy.

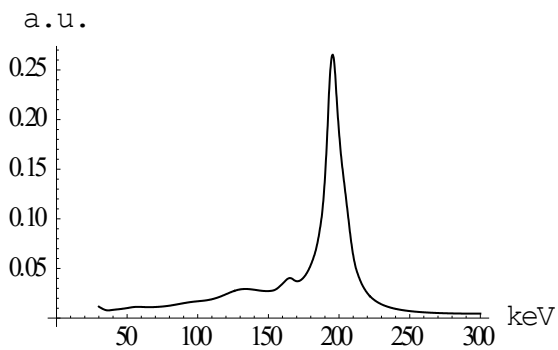

Figure 6a: With fitting.

For comparison, we give the results of processing the same beam with regularization without fitting in Fig. 6b.

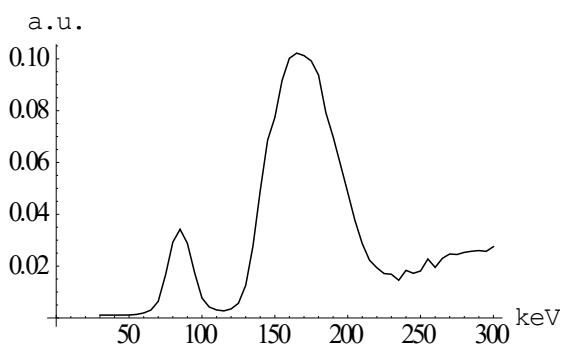

Figure 6b: Without fitting.

A series of measurements, carried out at different operating modes of the accelerator (Fig. 7).

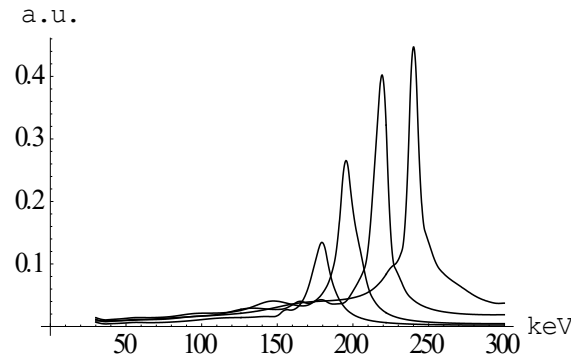

Figure 7: Spectrum at voltage 15, 17.5, 20, 25 kV.

CONCLUSIONS

The validity of the technique applied is confirmed by the fact that the spectrum obtained during charging the voltage of 17.5 kV (Fig. 8a) sufficiently matches the spectrum (Fig. 8b) measured on a magnetic spectrometer [2]. In this case, both the maximum energies of the electrons are almost the same.

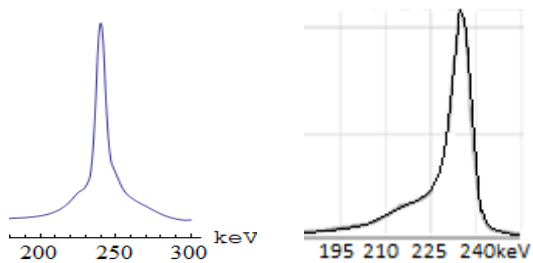

(a) (b)

Figure 8: (a) - The spectrum from the absorbing filters method.; (b)- The spectrum on a magnetic spectrometer.

REFERENCES

[1] N. N. Kurapov *et al*., The system of operational control of the electron beam energy of the accelerators LU-7-2 and LU-10-20. XVIII Kharitonov Readings, Volume 1, p. 222, FSUE "RFNC-VNIIEF", 2016.

[2] A. A. Drozdovsky *et al*., "Electronic gun for physical researches," *Phys. Part. Nucl. Lett.* 11, 577–580, 2014.

[3] Geant4 User's Guide for Application Developers, Geant4 Collaboration.

[4] A. N. Tikhonov, V. Ya. Arsenin. Methods for solving ill-posed problems. Ed. 3, revised, 1986 (in Russion).

ISBN: 978-3-95450-240-0 ISSN: 2673-5539 doi:10.18429/JACoW-RuPAC2021-WEPSC50

ENHANCEMENT OF TRANSVERSE BEAM PHASE SPACE ANALYSIS BY TOMOGRAPHY METHOD AT INR LINAC

A. I. Titov[1†], S. A. Gavrilov[1], S. E. Bragin, O. M. Volodkevich,
Institute for Nuclear Research of the Russian Academy of Sciences, Moscow, Russia
[1]also at Moscow Institute of Physics and Technology (State University), Moscow, Russia

Abstract

The investigation of transverse beam phase space parameters behavior along the accelerator is important for proper accelerator tuning. At INR RAS linac transverse emittance and Twiss parameters are reconstructed from beam profile measurements with quadrupole scan technique at several measurement points along the accelerator. Profile treatment is performed with ordinary transverse profiles method and tomographic reconstruction method. Various experimental data is presented. The comparison of the results obtained by the two methods is done. Features of beam dynamics simulation based on the data from these methods are discussed.

INTRODUCTION

The investigation of transverse beam phase space parameters behavior along the accelerator is important for proper accelerator tuning and beam transport simulation. For low-energy beams direct measurements can be done with slit-grid or pepper pot devices. For high-energy beams direct measurements are impossible and reconstruction method is applied – a quadrupole scan technique (QST). A typical layout of components, required for QST measurements, is presented in Fig. 1.

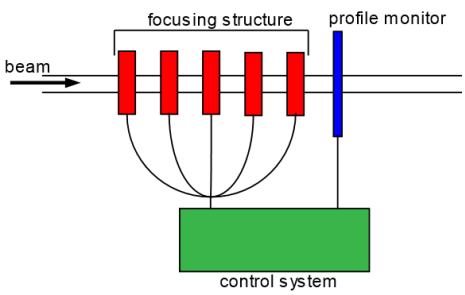

Figure 1: Typical layout of components required for quadrupole scan technique measurements.

QST is a group of methods that in general provides information only about phase ellipse parameters. That is enough for the majority of the beam transfer codes that are used for dynamics simulation. However, if accelerator is not tuned properly, particles distribution in transverse phase space can be non-elliptical. In that case inaccuracy of methods, which reconstruct phase ellipse, grows and so does inaccuracy of the simulation.

One of the methods of beam transverse phase portrait parameters measurements, which can be attributed to QST, is a tomographic reconstruction. It can reconstruct internal structure of the phase space distribution and is applicable for all possible particle distributions in phase space.

† aleksandr.titov@phystech.edu

Beam transfer simulation at INR linac is performed with TRACE 3D code and the main method for phase ellipse parameters measurements at INR linac is a typical QST realization – transverse profiles method (TPM). Also a tomographic reconstruction was implemented as an alternative and enhancement to the TPM.

TRANSVERSE PROFILES METHOD

Transverse profiles method requires rms beam size and beam centre measured for its operation. These values are represented as vertical lines in corresponding phase plane. The disposition of these lines can be transferred to arbitrary point of measuring area by transfer matrix method. Results of the measurement represent a set of lines. The phase ellipse is inscribed in these lines with the iteration algorithm (Fig. 2). Twiss parameters and rms emittance values are then obtained. In more detail TPM is described in [1].

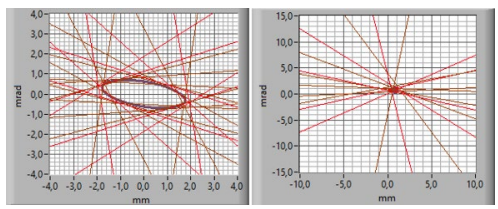

Figure 2: Results of TPM reconstruction. Phase ellipse (on the left) and phase ellipse center (on the right).

TOMOGRAPHIC RECONSTRUCTION

Tomographic reconstruction requires all information about beam profiles for its operation. Obtained profiles are transformed with use of the transfer matrices and converted into a sinogram. The rotation angles in phase space are also obtained from transfer matrices. The sinogram and rotation angles are then transmitted to tomography kernel. The kernel is based on the Simultaneous algebraic reconstruction technique (SART). Result of the tomography is post-processed so it can be used for beam dynamics simulation (Fig. 3). In more detail tomographic reconstruction kernel and post-processing of the results is described in [2].

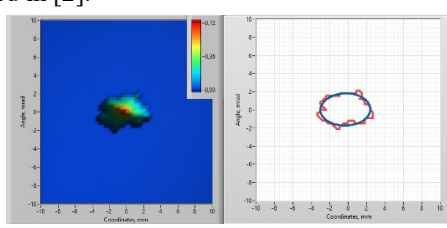

Figure 3: Results of the tomographic reconstruction. On the left – phase portrait. On the right – phase portrait envelope (red) and phase ellipse (blue).

ISBN: 978-3-95450-240-0 ISSN: 2673-5539 doi:10.18429/JACoW-RuPAC2021-WEPSC50

According to widely used emittance conventions that is also used at INR linac, emittance of the full beam, which is reconstructed by tomography, is 5-rms emittance. Due to SART features tomographic reconstruction provides almost the same level of error if phase space rotation angle is greater than 100 degrees (Fig. 4). Because of that not all measurements can be used.

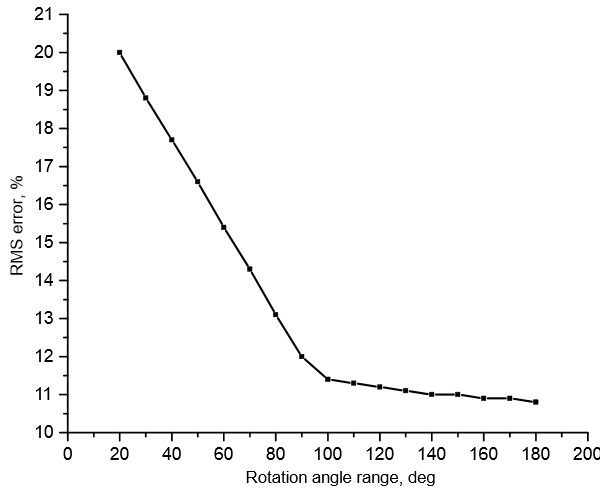

Figure 4: RMS error of the SART depending on rotation angle range.

To check tomography results we simulate the dynamics of the reconstructed phase ellipses and compare the beam position and the size of the reconstructed beams with the measured ones. A standard deviation of the reconstructed value is used as a unit of measurements. If the reconstructed beam size results of the phase ellipse transport simulation differ from the measured values by more than one standard deviation of tomographic method, then the phase portrait is not treated as elliptical and cannot be used for beam dynamics simulation in TRACE-3D codes. Difference between measured and reconstructed profiles is denoted as v_e. In these terms this criterion can be formulated as $v_e \leq 1$.

EXPERIMENTAL RESULTS

During accelerator run in April 2021 beam profiles has been measured at five different points of INR linac (Fig. 5). Measurements were made with two SEM-grids located after RFQ, SEM-grid located after first DTL tank (C1 in Fig. 5), two wire scanners (WS1 and WS2) located near the matching cavity (MC in Fig. 5), Beam Cross-section monitor (BCSM) located at the exit of the linac (C32 in Fig. 5) and SEM-grid located at the end of the Research Complex transport line. There were two measurements made with BCSM: one with 100 μs and other with 32 μs beam pulse length.

For all measurements rotation angle ranges have been checked. For SEM-grids after RFQ and SEM-grid in Research Complex transport line ranges were less than 100 degrees so these measurements were not treated.

Twiss parameters and transverse emittance values for all measurements are presented in Table 1. Data from wire scanners was treated by TPM simultaneously, so there is one column for WS measurements for TPM. Twiss parameter γ can be derived from other parameters so its values are omitted in the table. Underlined values for tomography measurements mean that v_e is greater than 1 so phase portraits cannot be treated as elliptical.

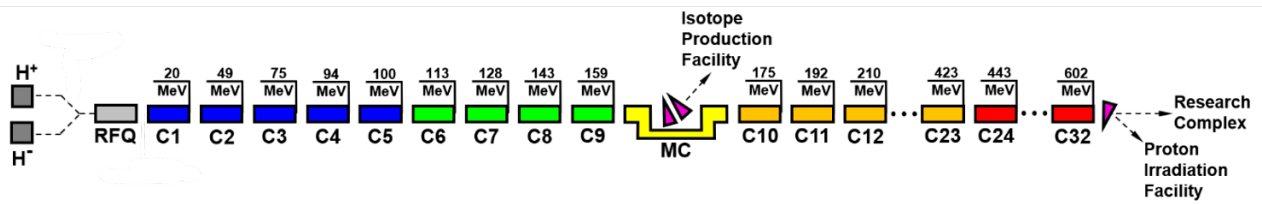

Figure 5: INR RAS linac diagram.

Table 1: Values of Twiss Parameters and Transverse Emittance for Both Methods in Different Measurement Points

Parameter	Tomography					TPM			
	SEM-grid	WS1	WS2	BCSM 32 μs	BCSM 100 μs	SEM-grid	WS	BCSM 32 μs	BCSM 100 μs
x, mm	1.18	-1.75	-0.3	-2.92	-1.98	0.36	-0.32	-3.00	-2.46
x', mrad	0.45	1.19	0.03	1.92	1.30	1.96	0.56	1.78	0.84
α_x	-0.05	0.02	-0.03	-0.46	0.03	-1.36	0.64	-0.18	0.26
β_x, mm/mrad	0.58	1.47	1.53	4.26	4.49	0.57	1.30	3.36	2.38
$\varepsilon_{x\,norm}$, mm*mrad	2.48	2.43	2.60	2.14	2.41	0.52	0.41	0.38	0.77
y, mm	0.84	2.23	0.16	-1.04	-0.60	0.60	0.08	-0.90	-1.42
y', mrad	0.95	-1.64	0.00	-0.01	0.55	0.50	-0.76	0.12	0.84
α_y	0.93	1.72	2.22	0.54	0.84	1.08	2.73	0.86	0.83
β_y, mm/mrad	0.83	4.61	5.4	5.48	5.13	0.93	5.47	5.37	3.49
$\varepsilon_{y\,norm}$, mm*mrad	3.40	2.81	3.63	3.2	4.16	0.62	0.52	0.57	0.85

ISBN: 978-3-95450-240-0 ISSN: 2673-5539 doi:10.18429/JACoW-RuPAC2021-WEPSC50

METHODS COMPARISON

Results from Table 1 show that with tomographic reconstruction not all measurements can be selected for further beam dynamics simulation because they have non-elliptical phase portraits. For elliptical measurements, results differ for these two methods. These results were used for dynamics simulation through the transport line so that reconstructed and real values could be compared.

The dynamics of the beam position and size through the transport line for both methods based on the WS1 data is shown in Fig. 6. Also, the simulated beamline structure is presented. Difference between the experimental and the reconstructed values measured in standard deviations of the tomographic reconstruction method are presented in Table 2. The tomographic method is better at reconstruction beam center than the transverse profiles method. All differences between the measured and the reconstructed beam size for both methods are less than one standard deviation.

Table 2: Difference Between Measured and Reconstructed Beam Parameters Measured in Standard Deviations

Parameter, standard deviations	Tomography	TPM
$position_x$	0.39	2.12
$position_y$	0.20	2.42
$rms\ size_x$	0.86	0.15
$rms\ size_y$	0.11	0.36

Results show a similar behaviour of the normalized emittance values for both methods: it decreases from SEM-grid to WS and then grow from WS to BCSM in case of 100 μs beam (for tomography growth starts from WS1 to WS2). For 32 μs beam there is no significant growth from WS to BCSM.

Behaviour of normalized emittance from SEM-grid to WS can be easily explained with measurements of the beam pulse current near the same points because it decreases along with the emittance values. However current continue to decrease after wire scanners while normalized emittance does not.

There is a possible explanation for this phenomenon, which can explain dynamics of the normalized emittance and the difference between BCSM measurements for different pulse length. The reason could be a problem with beam loading compensation system. This leads to energy divergence of the beam within the pulse. After first wire scanner beam position is corrected with dipole correcting magnets along the accelerator, which push apart differently accelerated parts of the beam. This leads to non-elliptical shapes of phase portrait that can be seen on BCSM. When a 32 μs beam is measured there is no emittance increase due to uniform acceleration of the pulse.

CONCLUSIONS

Transverse phase portrait tomography is implemented at the INR RAS linac as an addition to transverse profiles method. Information about internal structure of particle distribution in transverse phase space can determine if phase portrait can be treated as elliptical or not. Tomographic reconstruction will help to choose the most proper phase ellipse parameters for beam dynamics.

Results of both methods show normalized emittance growth along the accelerator. If a hypothesis connected with beam longitudinal mismatch is right then results of these two methods can be uesd as an indicator of improper accelerator tuning.

REFERENCES

[1] S. Bragin *et al.*, "Transverse Beam Matching and Correction Procedures in INR Linac", in *Proc. 23rd Linear Accelerator Conf. (LINAC'06)*, Knoxville, TN, USA, Aug. 2006, paper TUP077.

[2] A. I. Titov and S. A. Gavrilov, "Transverse Phase Portrait Tomography of Proton Beams at INR RAS Linac", in *Proc. 9th Int. Beam Instrumentation Conf. (IBIC'20),* Santos, Brazil, Sep. 2020, pp. 193-196. doi:10.18429/JACoW-IBIC2020-WEPP37

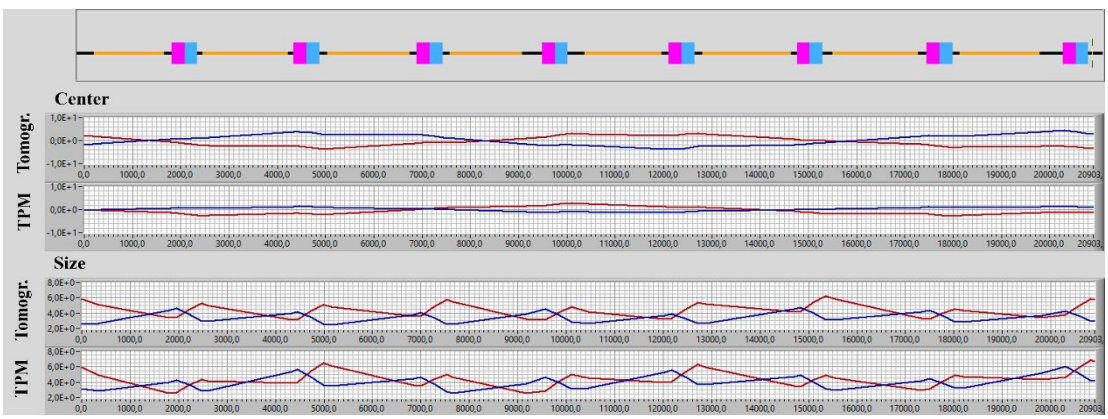

Figure 6: Scheme of the transport line around the matching cavity (on top) and beam position and size dynamics through the simulated transport line. On the scheme pink and blue rectangles are quadrupole lenses, orange lines are accelerating cavities, black lines are drift spaces. On the graphs blue lines are for the X-axis, red lines are for the Y-axis.

ISBN: 978-3-95450-240-0 ISSN: 2673-5539 doi:10.18429/JACoW-RuPAC2021-WEPSC51

CONCEPT OF DECISION SUPPORT SYSTEM FOR INR RAS LINAC BEAM TUNING

A. I. Titov†, S. A. Gavrilov,
Institute for Nuclear Research of the Russian Academy of Sciences, Moscow, Russia and
Moscow Institute of Physics and Technology (State University), Moscow, Russia

Abstract

During the last decade instruments of machine learning are gaining popularity in accelerator control systems. One of these instruments is decision support system (DSS) that is already successfully used in other fields of science. In this article a motivation for implementation of such system for INR RAS linac tuning is discussed. Concept of developed DSS is presented. Changes in INR RAS linac data acquisition system essential for future DSS operation are proposed.

INTRODUCTION

Machine learning (ML) techniques are widespread in modern science, industry and everyday life. ML popularity is explained in its ability to surpass human in such tasks as forecasting based on analysis of huge amount of data, online recommendation based on personal preferences or object recognition, like faces or voices.

Majority of these tasks can be applicated to accelerator physics. For example, now ML algorithms are used to detect faulty BPMs and make orbit correction of the beam at LHC [1] or to determine critical situation at the neutrino beam facility at J-PARC [2].

One of the ML instruments is a decision support system (DSS). These are systems that support decision making activities. DSSs are already successfully used in medicine and help doctors make a diagnosis considering patient's medical history and many other factors.

In theory DSS could be used to help beam operators during accelerator run. However, this system is not used for accelerators. The reason is that new accelerator complexes have precise computer models of the beamline and other ML instruments are used like already mentioned orbit correction system at LHC.

At INR RAS linac the issue of personnel is acute. For the last decade amount of beam operators reduced by half and training of new operators can take years. Moreover, INR linac was constructed almost 30 years ago and does not have a precise model.

In that case DSS, which can help beam operator to analyze the current situation and make decisions to solve problems that arise during accelerator run, is a suitable system that would be extremely helpful for routine operation. Such system would decrease problem solving time and prevent personnel from making wrong decisions during accelerator tuning.

INR LINAC DSS CONCEPT

INR linac DSS is designed as a Bayesian network. It is based on the Bayes' theorem and can be presented as a directed acyclic graph. Its advantage is ability to insert knowledge in it by designing its structure and to determine probabilistic transition values based on the knowledge base. This type of networks is already used for accelerator tuning at LCLS [3].

Input to the DSS will be problems that arise during accelerator operation and output will be ranged list of the most probable solutions for the problems. System has 6 layers. With the increase of a layer number operator need to provide more information about the problem. To work with outer layers information to the inner layer should also be provided. Layered structure of the DSS allows its step-by-step realization. Connection between layers is shown in Fig. 1. Concept scheme of the DSS is shown in Fig. 2.

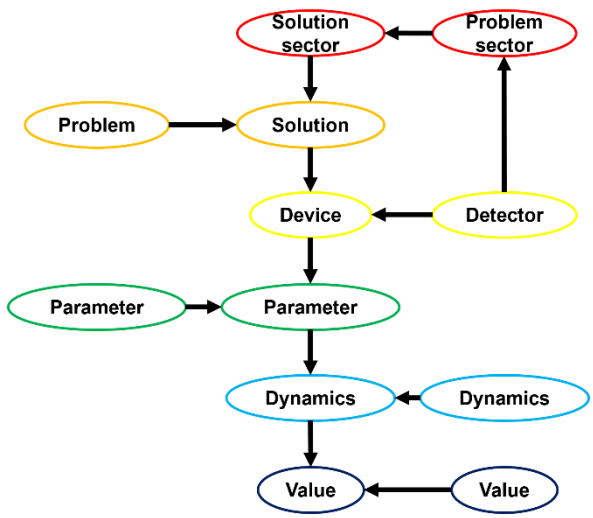

Figure 1: INR linac DSS connections scheme.

Layer 1 is a sector-sector layer. INR linac is divided into 5 sectors and multipurpose research complex (MPC), which is counted as sixth sector. and problem can be attributed to the sector where it occurred. Output of this layer is a sector number where problem solution is located. If problem occurs simultaneously at several sectors DSS should at first provide solution to the sector with the least number.

Layer 2 is a parameter-system layer. Input of this layer is a beam parameter which value is unsatisfactory. As an output DSS should provide type of the linac system, which parameters should be changed to solve the problem. If there are several problems at once, system should solve them in a prescribed way.

† aleksandr.titov@phystech.edu

ISBN: 978-3-95450-240-0 ISSN: 2673-5539 doi:10.18429/JACoW-RuPAC2021-WEPSC51

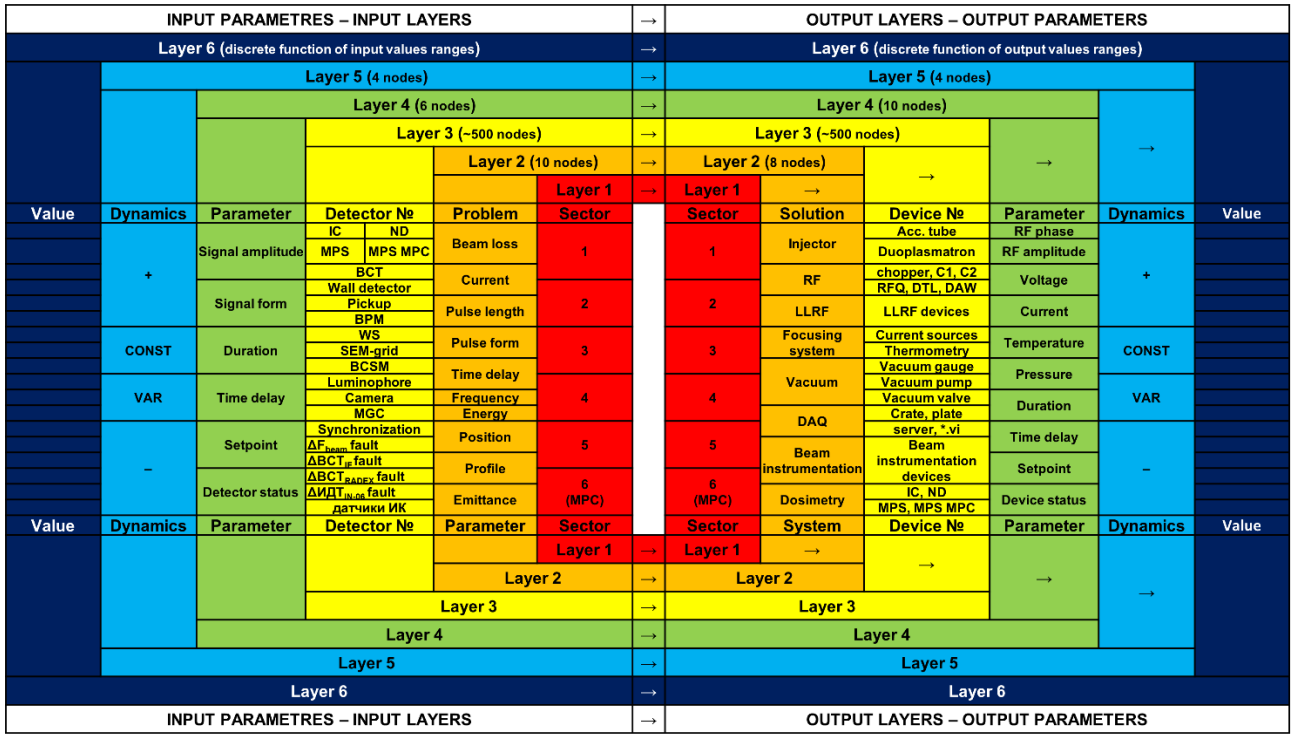

Figure 2: INR linac DSS concept scheme.

Layer 3 is a detector-device layer. Here operator should name the detector on which problem can be seen and number of that detector. To operate with layer 3, operator does not need to fill in sector information because type and number of the detector is enough to determine sector of the accelerator. Output of this layer is a device, which parameters should be changed.

Layer 4 is a parameter-parameter layer. Input is a parameter of the detector, which value is abnormal. Output is a parameter of the device which should be changed.

Layer 5 is a dynamics-dynamics layer. Input is a dynamic characteristic of a parameter which is not satisfactory to the operator. Output is a required dynamic of a device parameter, which should solve the problem.

Layer 6 is a value-value layer. At this layer DSS is planned to operate in an automatic mode. It should monitor all signals acquired by INR linac data acquisition (DAQ) system and check values of these signals. Output is range of values for the device that should be changed.

For the first two layers knowledge base of the DSS can be filled manually. A special option was added to INR linac electronic logbook to acquire data for knowledge base. From layer 3 data analysis should be done in an automatic mode. Data for the analysis should be taken from DAQ system, which should be upgraded.

Change in parameters is chosen as a criterion for a problem and a solution. When some of the beam parameters values become unsatisfactory, data analysis software will start to monitor accelerator systems parameters values. When beam parameters return to satisfactory level, system will record accelerator systems parameters that changed.

INR LINAC DAQ SYSTEM

The INR linac DAQ system is a software package based on the LabVIEW. It consists of DAQ sources running on servers, DAQ receivers running on client computers and DAQ storage server. Data is transmitted via the protocol UDP MultiCast (Fig. 3) [4].

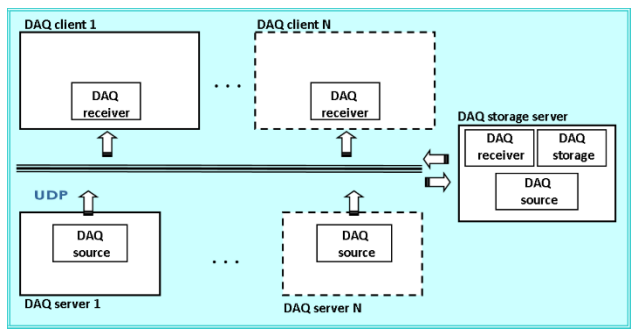

Figure 3: INR linac DAQ system scheme.

DAQ storage server performs data storage and operates as a DAQ source, because it collects data from some servers, which operates on TCP/IP protocol and is not yet implemented into UDP MultiCast system. The period of cyclic polling on the servers is 1...5 seconds. To reduce the network load, not all parameters are transmitted after each survey, but only the changed ones (delta encoding). Once a minute, the entire volume of data is transmitted from the source servers. The data is transmitted in XML format.

Currently, DAQ system consists of 17 source servers,13 servers that transfer data via DAQ storage server and 18 servers, which are not implemented into the system.

ISBN: 978-3-95450-240-0 ISSN: 2673-5539 doi:10.18429/JACoW-RuPAC2021-WEPSC51

DAQ UPGRADE

Currently, INR linac DAQ system stores not all acquired data. System stores information about accelerator systems, such as RF, focusing, vacuum and water-cooling systems and information about accelerator alarms. Beam parameters such as current, position, profiles and beam loss are not stored automatically. For DSS data analysis software all beam parameters should be stored. Also new signals, which are constantly added for accelerator control, should be added to DAQ system.

Examples of DAQ upgrade during last year are presented below. It concerns new diagnostics and upgrade of already existing software. Software for tomographic reconstruction of transverse phase portrait in online mode is shown in Fig. 4.

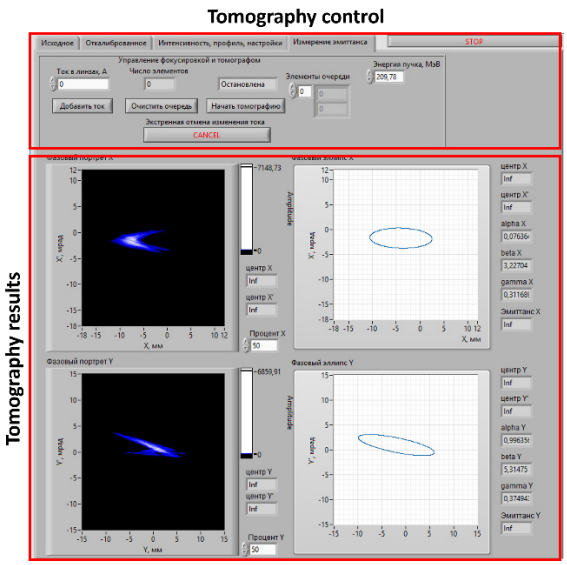

Figure 4: Online tomography software.

During beam tuning this procedure takes 10 minutes and provides Twiss parameters and transverse emittance values. Incorporation of this data into DSS knowledge base can help in future beam tuning.

Upgraded software for beam current and loss monitoring is shown in Fig. 5. Upgraded version has DAQ servers' status control panel and recomposed beam loss distribution panels. All new features were implemented to improve perception of presented information.

CONCLUSIONS

Decision support system is a promising technology that will decrease mental stress on beam operator and problem-solving time. Developed concept of the DSS allows its step-by-step implementation. With proposed INR linac DAQ upgrade this system should become a useful instrument for accelerator tuning.

REFERENCES

[1] E. Fol *et al.*, "Application of Machine Learning to Beam Diagnostics", in *Proc. FEL2019*. doi:10.18429/JACoW-FEL2019-WEB03

[2] K. Nakayoshi *et al.*, "Development of an Expert System for the High Intensity Neutruno", in *Proc. IBIC'18*. doi:10.18429/JACoW-IBIC2018-MOPC18

[3] R. Roussel, A. Hanuka and A. Edelen, "Multiobjective Bayesian optimization for online accelerator tuning", *Phys. Rev. Accel. And Beams,* 24, 062801, 2021. doi:10.1103/PhysRevAccelBeams.24.062801

[4] I.A. Vasilyev, O.V. Grekhov, "Using Data Acquisition System in INR linac", *Problems of atomic science and technology*, 61-63, 2012.

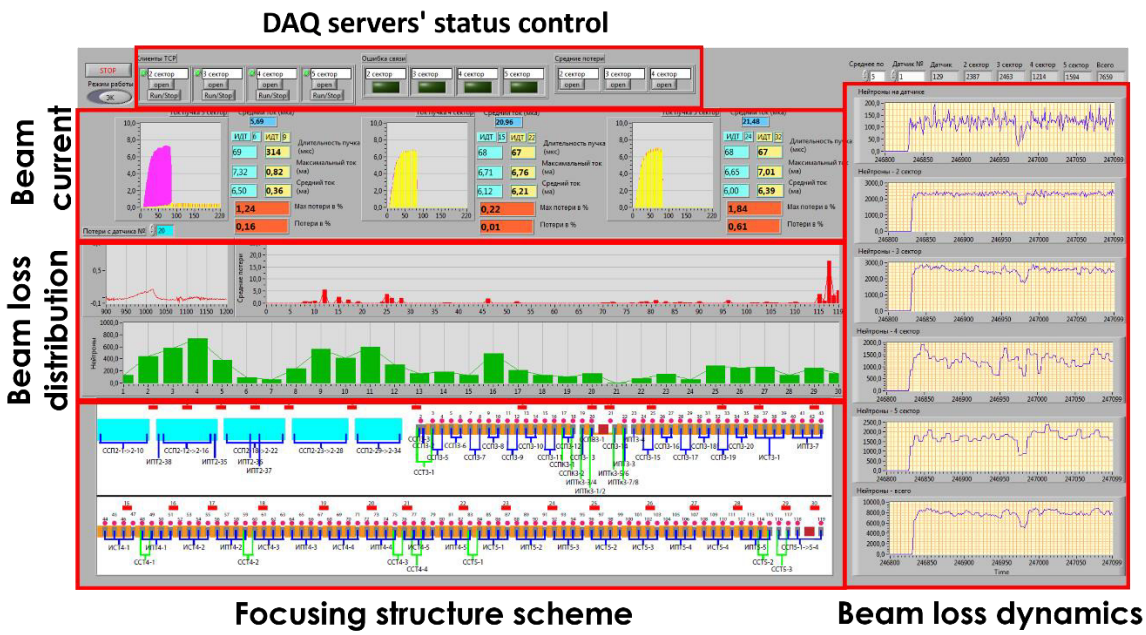

Figure 5: Beam current and loss software.

ISBN: 978-3-95450-240-0 ISSN: 2673-5539 doi:10.18429/JACoW-RuPAC2021-WEPSC55

DEVELOPMENT OF THE LOW INTENSITY EXTRACTION BEAM CONTROL SYSTEM AT PROTOM SYNCHROTRON FOR PROTON RADIOGRAPHY IMPLEMENTATION

A. A. Pryanichnikov†[1,2], P. B. Zhogolev[1], A. E. Shemyakov[1], M. A. Belikhin[1,2],
Lebedev Physical Institute RAS, Physical-Technical Center, Protvino, Russian Federation
A. P. Chernyaev, Lomonosov Moscow State University,
Accelerator Physics and Radiation Medicine Department, Moscow, Russian Federation
V. Rykalin, ProtonVDA, Naperville, USA
[1]also at Protom Ltd., Protvino, Russian Federation
[2]also at Lomonosov Moscow State University,
Accelerator Physics and Radiation Medicine Department, Moscow, Russian Federation

Abstract

Currently, the calculation of the proton range in patients receiving proton therapy is based on the conversion of Hounsfield CT units of the patient's tissues into the relative stopping power of protons. Proton radiography is able to reduce these uncertainties by directly measuring proton stopping power. However, proton imaging systems cannot handle the proton beam intensities used in standard proton therapy. This means that for implementation of proton radiography it is necessary to reduce the intensity of the protons significantly.

This study demonstrates the current version of the new beam control system for low proton intensity extraction. The system is based on automatic removable unit with special luminescence film and sensitive photoreceptor. Using of the removable module allows us to save initial parameters of the therapy beam. Remote automatic control of this unit will provide switch therapy and imaging modes between synchrotron cycles. The work describes algorithms of low flux beam control, calibration procedures and experimental measurements. Measurements and calibration procedures were performed with certified Protom Faraday Cup, PTW Bragg Peak Chamber and specially designed experimental external detector.

The development can be implemented in any proton therapy complexes based on the Protom synchrotron. This allow us to use initial synchrotron beam as a tool for patient verification and to eliminate proton range uncertainties.

INTRODUCTION

Proton therapy is rapidly spreading throughout the world [1]. At present, the calculation of the proton range in patients receiving proton therapy is based on the conversion of Hounsfield CT units of the patient's tissues into the relative stopping power of protons. Uncertainties in this conversion necessitate larger proximal and distal planned target volume margins [2]. These larger margins increase the dose to nearby healthy tissues, causing unwanted and avoidable toxicities [3]. Proton radiography avoids these uncertainties by directly measuring the stopping power of protons, and this can significantly reduce the planned target volume, which directly reduces toxicity [4]. It has the ability to accurately target the patient to the proton beam and quantify anatomical consistency and proton range in the treatment position immediately prior to treatment, resulting in more consistent target coverage, leading to improved patient outcomes [5].

Figure 1: Protom synchrotron-based accelerator complex.

Protom Synchrotron [6-8] is a medical accelerator specially designed for proton therapy. The accelerator complex based on the Protom synchrotron is shown in Fig. 1.

The synchrotron is able to accelerate protons up to 330 MeV. This fact makes proton imaging of the entire human body available without any restrictions. The use of proton imaging will allow us to avoid the uncertainty of the proton range in the patient's body and will make the treatment process more accurate. Moreover, proton radiography can be used as a tool for verification of patient position instead of standard cone beam computed tomography systems. The proton imaging system has a lower equivalent dose to the patient than comparable X-ray imaging systems. However, proton imaging systems cannot handle the proton beam intensities used in standard proton therapy. This means that for implementation of proton radiography it is necessary to reduce the intensity of the protons significantly.

REQUIREMENTS FOR BEAM EXTRACTION MODE

This work was focused on a proton detector prototype being developed by ProtonVDA [9-10]. ProtonVDA has developed a highly efficient and inexpensive proton radiography system based on solid state photomultipliers and fiber detectors. A key feature of this detector is its operation

ISBN: 978-3-95450-240-0 ISSN: 2673-5539 doi:10.18429/JACoW-RuPAC2021-WEPSC55

with single proton events. This implies the development of a special mode for the beam extraction, which is fundamentally different from the therapeutic mode, which requires the maximum intensity of the extracted beam.

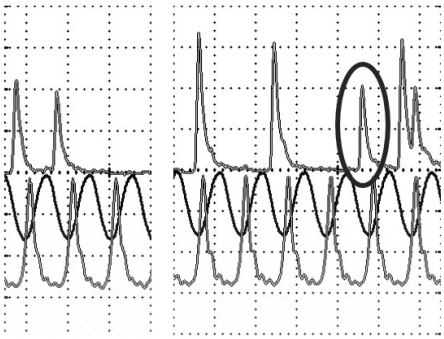

Figure 2: Oscillograms from the external detector: the upper line is a signal from external detector (2 divisions – single proton events, 3 divisions – double protons event); the middle line is an accelerator RF; the bottom line is a beam current inside the synchrotron.

Figure 2 shows low intensity extraction mode at Protom synchrotron. The left oscillogram consists only single proton events, the right one has 2 double proton events, one single (in the ellipse) and one combined (double + single from the same revolution).

LOW INTENSITY BEAM EXTRACTION CONTROL SYSTEM

During the development of the low intensity beam extraction control system, the main conditions were determined that it must satisfy: no effect on the therapeutic beam for proton therapy complexes that are already in clinical practice, a design for integration into existing vacuum system interfaces, an universal design for all proton therapy facilities based on Protom synchrotron. The principal design of the Low Intensity Beam Extraction Control System is shown in Fig. 3.

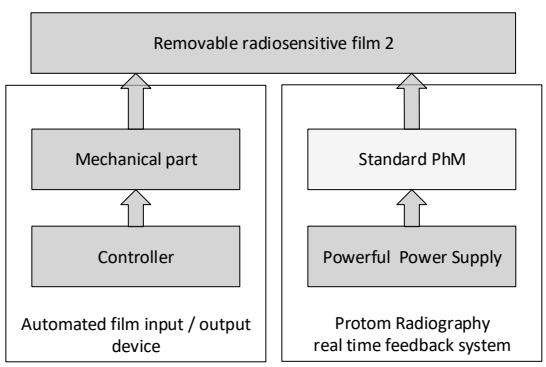

Figure 3: Low Intensity Beam Extraction Control System principle design.

Therefore, it was decided to create a separate module based on the existing system for imaging the proton beam during the transportation through the gantry. This subsystem can be easily implemented in vacuum interfaces; it takes up little space and can be located between the elements of the magnetic optics of the extraction channel. In addition, the removable design makes it possible to avoid changing the beam parameters of already certified installations. The prototype of low intensity beam control unit is shown in Fig. 4.

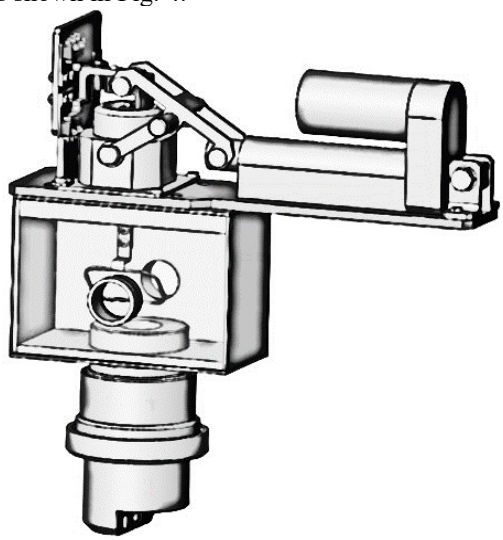

Figure 4: A prototype of low intensity beam control unit with removable film.

The low intensity beam extraction control unit is based on the photomultiplier Hamamatsu R6094 (which is used in standard extraction mode) with an upgraded power supply, as well as films based on the SC-307 scintillator or on gadolinium-terbium oxysulfide.

ACCELERATOR MODE

The standard operating modes of the accelerator have been substantially revised in order to reduce the intensity of the proton beam extraction. Firstly, the number of particles injected into the accelerator was reduced. For this, built-in beam visualization systems consisting of ceramic plates inserted into the vacuum chamber of the injector were used, which significantly reduces the aperture of the vacuum chamber. It was necessary to change the extraction orbit using 16 horizontal electromagnetic correctors operating in a dynamic mode. The values of the acceleration and excitation frequencies were also changed to achieve optimal controllability parameters and beam sizes at the extraction point.

LOW INTENSITY EXTRACTION VERIFICATION

The results of two experiments testing the low intensity extraction mode of the proton radiography implementation on the Protom synchrotron are demonstrated below. A static experimental version Low Intensity Beam Extraction Control System was used for these experiments.

Experimental Measurements of Extracted Particles Number via External Self-made detector

As part of this experiment, it was necessary to be convinced of two things. First of all, there was a need to

ISBN: 978-3-95450-240-0 ISSN: 2673-5539 doi:10.18429/JACoW-RuPAC2021-WEPSC55

demonstrate the correspondence of the calculated values of the extracted protons with real ones. Second thing that should be demonstrated is the presence of single proton events in the structure of the beam extraction, which can be effectively registered by the proton radiography detector system. For these purposes, a detector was assembled based on SC-307 scintillation unit 50 mm thick, photomultiplier PhM-84, power supply Spellman MP5N24 and oscilloscope Aktakom ADS-2114T.

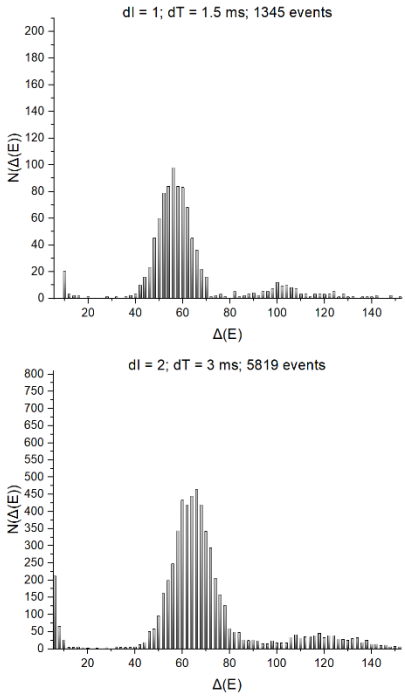

Figure 5: Samples of experimental measurements: the top diagram corresponds the first experimental series, the bottom one – the second series; these diagrams show the total number of detected events (including single protons, from 40 to 80 a.u. dE).

Table 1: Comparison of the Expected and Measured Number of Extracted Protons

Value dI, internal calibration	Expected protons number	Measured protons number
	dT = 1.52 ms	
1	1924	1703
2	3848	4653
10	19242	16167
	dT = 3.04 ms	
1	3848	3536
2	7697	6761
10	38485	37946

Two series of measurement with different timescale was performed. The results of these measurements are presented in Figure 5 and Table 1. The obtained results are in satisfactory agreement with the expected events. The experimental results were used for calibration using an internal Protom Faraday Cup.

Internal Calibration Linearity Check

The purpose of the following experimental measurements is to show the linearity of the Protom Faraday Cup calibrations using an independent detector (dI values in the previous experiment). Table 2 presents the experimental data comparing the PTW Bragg peak chamber readings and the Faraday-calibrated readings of the low-intensity beam extraction control system. The obtained PTW Bragg Peak Chamber data agree with the calibration data of the Protom Faraday Cup up to statistical and instrumental errors.

Table 2: Comparison of Protom Faraday Cup Calibration and PTW Bragg Peak Chamber Readings

Energy, MeV	PTW Bragg Peak Chamber readings, pC	Protom Faraday Cup Calibration number, protons
220	20±2	5×10^6
220	3.8±0.4	1×10^6
220	2.1±0.2	5×10^5
250	19±2	5×10^6
250	3.9±0.4	1×10^6
250	1.9±0.2	5×10^5

CONCLUSION

Within the framework of this study, the basic concept of a low-intensity beam extraction control system is proposed. The system is based on an automatic removable unit with a special luminescent film and a photosensor. The use of a removable module allows us to keep the original parameters of the therapy beam. Remote automatic control of this device will ensure switching between therapy and imaging modes between synchrotron cycles.

A static prototype of a low-intensity beam extraction control unit for the use of the radiographic mode has been developed and manufactured. The performance of this prototype, together with a specially designed low-intensity beam extraction mode, was experimentally confirmed by two series of verification tests. Measurements were performed with certified Protom Faraday Cup, PTW Bragg Peak Chamber and specially designed experimental self-made external detector.

The developed Low Intensity Beam Extraction Control System and a special operating mode of the accelerator can be implemented in any proton therapy complexes based on the Protom synchrotron. This allows us to use the original synchrotron beam as a tool to check the patient's position and eliminate the proton range uncertainties.

REFERENCES

[1] A. P. Chernyaev *et al.*, "Proton Accelerators for Radiation Therapy", *Medical Radiology and Radiation Safety*, vol. 64, no. 2, pp. 11–22, 2019. doi:10.12737/article_5ca5a0173e4963.18268254

ISBN: 978-3-95450-240-0 ISSN: 2673-5539 doi:10.18429/JACoW-RuPAC2021-WEPSC55

[2] H. Paganetti, "Range uncertainties in proton therapy and the role of monte carlo simulations" *Phys. Med. Biol.*, vol. 57, no. 11, pp. 99-117. Jun. 2012 doi:10.1088/0031-9155/57/11/R99

[3] A. J. Lomax "Myths and realities of range uncertainty", *Br. J. Radiol.*, vol. 93, no. 1107, p. 0582, Mar. 2020. doi:10.1259/bjr.20190582

[4] N. Krah *et al.*, "Regularised patient-specific stopping power calibration for proton therapy planning based on proton radiographic images", *Phys. Med. Biol.*, vol. 64, no. 6, p. 065008, Mar. 2019. doi:10.1088/1361-6560/ab03db

[5] U. Schneider, E. Pedroni, "Proton radiography as a tool for quality control in proton therapy", *Med Phys.,* vol. 22, no. 4, pp. 353-363, Apr. 1995. doi:10.1118/1.597470

[6] A. A. Pryanichnikov *et al.*, "Status of the Proton Therapy Complex Prometheus", in *Proc. 26th Russian Particle Accelerator Conf. (RuPAC'18)*, Protvino, Russia, Oct. 2018, pp. 135-138. doi:10.18429/JACoW-RuPAC2018-FRXMH03

[7] A. A. Pryanichnikov *et al.*, "Clinical Use of the Proton Therapy Complex "Prometheus"", *Phys. Part. Nuclei Lett.,* vol. 15, no. 7, pp. 981-985, 2018. doi:10.1134/S1547477118070592

[8] V. E. Balakin *et al.*, "Clinical Application of New Immobilization System in Seated Position for Proton Therapy" *KnE Energy*, vol. 3 np. 2, pp. 45–51, 2018. doi:10.18502/ken.v3i2.1790

[9] C. Miller *et al.*, "Reconstructed and real proton radiographs for image-guidance in proton beam therapy", *J. Radiat. Oncol.*, vol. 8, pp. 97–101, 2019. doi:10.1007/s13566-019-00376-0

[10] C. Sarosiek *et al.*, "Analysis of characteristics of images acquired with a prototype clinical proton radiography system", *Med Phys.*, vol. 48, no. 5, pp. 2271-2278, May 2021. doi:10.1002/mp.14801

ISBN: 978-3-95450-240-0 ISSN: 2673-5539 doi:10.18429/JACoW-RuPAC2021-WEPSC56

BEAM PARAMETERS MEASUREMENT AND CONTROL SOFTWARE TOOLS FOR VEPP-5 INJECTION COMPLEX DAMPING RING

V. V. Balakin*[1], F. A. Emanov[2], D. E. Berkaev, Budker INP, Novosibirsk, Russia
[1]also at Novosibirsk State Technical University, Novosibirsk, Russia
[2]also at Novosibirsk State University, Novosibirsk, Russia

Abstract

Beam parameters control and operation software tools for BINP VEPP-5 injection complex damping ring consisting of two parts were developed. Beam parameters control includes processing of measured turn-by-turn beam coordinates from all damping ring beam position monitors and displaying such features as tunes and beam position into vacuum chamber. This part gives an opportunity to measure damping ring response matrices and carry out its processing too. Beam parameters operation is based on knobs creating. Knob is combination of accelerator control elements, which performs an isolated shift of one selected parameter, e.g. only vertical betatron tune. This part is devoted to their creation and application on VEPP-5 injection complex. This paper presents review of developed software tools and their application result on VEPP-5 injection complex: beam position adjustment via response matrix measurements and quantification the amount of damping ring captured particles during the injection process depending on beam tunes.

VEPP-5 INJECTION COMPLEX

Injection complex VEPP-5 (IC) is a part of VEPP-4 - VEPP-2000 electron-positron colliders complex. It intended for high-energy, nuclear physics and synchrotron radiation experiments conducting. IC (Fig. 1) constists of electron gun, 2 linear accelerators, $e^- \rightarrow e^+$ conversion system, damping ring and transport channels K-500 [1].

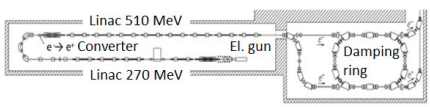

Figure 1: VEPP-5 injection complex scheme.

SOFTWARE TOOLS DESCRIPTION

Beam position monitors (BPM) data processing is a key weapon for obtaining information about beam parameters and their response on accelerator magnetic system changes. Software tools, which includes data obtaining, processing, displaying and keeping, was developed to take advantage of the BPM potential. Software tools are consist from 3 parts:

- Daemons:
  - BPM data processing - *orbitd*
  - knobs service - *knobd*
- GUI-applications for operational staff:
  - damping ring beam positions displaying and keeping in different IC modes - *orbit*
  - turn-by-turn measurements displaying - *turns*
  - tunes displaying and keeping - *tunes*
- GUI-applications for administration:
  - damping ring response matrix collecting - *rmc*
  - magnetization of magnetic system elements - *magn*
  - user application for knob creating and using - *knob*
  - measurement of injected particles number into damping ring vs. tunes - *inj_resp*
  - collected response matrix processing and based on them knob creating - *rmc_proc*

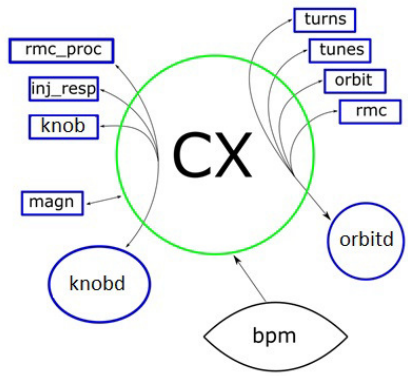

Figure 2: Software tools principal scheme.

Software tools principal scheme is presented on Fig. 2. Black arrows show links between different parts of software, which communicate each other throw CX-server [2].

Program separation into daemons and GUI-applications are conditioned by the need to separate direct processing of data from the display and use of the results of this processing. On the one hand, this gives an opportunity to independenly change each component (logic or visualization) without affecting another part, from other hand, running multiple copies of displaying application requred only one copy of daemon with data processing.

SOFTWARE TOOLS USAGE ON INJECTION COMPLEX

Lattice

Damping ring has 28 quadropole lenses, which means that detecting the tunes shift from varying the current of qudrupole corrector of each lens allows us to measure aver-

* vit.v.balakin@inp.nsk.su

ISBN: 978-3-95450-240-0 ISSN: 2673-5539 doi:10.18429/JACoW-RuPAC2021-WEPSC56

aged beta-function in the lens location [3]. A small change of lens gradient leads to betatron tune shift according to formula $\delta\nu = \frac{1}{4\pi}\int \delta k * \beta(s)ds$. Averaging the beta-function over lens lenght we can get sought value: $< \beta > \approx \frac{4\pi}{L}\frac{\delta\nu}{\delta k}$. Conducting the measure of betatron tunes shift vs. lens gradient becomes possible calculate value of $\frac{\delta\nu}{\delta k}$ via $\nu(k)$ approximation and $< \beta >$ too. Results of such type measurements is shown on Fig. 3.

Analysing the data it becomes clear that the theoretical model prediction (green line on Fig. 3) and beam behavior (blue points) in accelerator based on measurements are different. Now, theoretical model of damping ring is under calibration process.

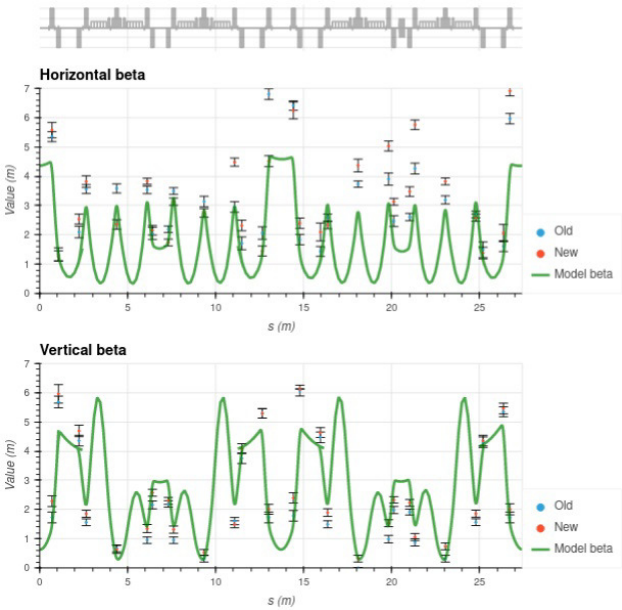

Figure 3: Measured (red points - after beam position correction, blue - before) and model beta-functions.

Responce Matrix

Responce matrix is a table of correspondance between variation of magnetic system element current and change of beam position inside accelerator vacuum chamber [3]. Algorithm of response matrix measurements is the following:

- Magnetizing the elements of the magnetic system of the accelerator to be in the same branch of the iron hysteresis each time. This ensures repeatability of the measurement procedure and further application of the response matrix.
- Selection of the elements necessary for the measurement of the matrix and setting the parameters for the measurement of the matrix. Depending on the objectives of the experiment, these can be quadrupole and dipole correctors or other elements of the magnetic system.
- Conducting a series of beam position measurements depending on choosed elements current. It worth noting the fact, that it is necessary to track power supply status. If it gives adjusted current the algorithm goes further or mark the correctos as unactive otherwise, removing it from response matrix measurement process.
- Based on measurements, formation the sought matrix, matrix with errors of each element calculation of response matrix and information about initial values of magnetic system elements.

Given response matrix can be used for theorethical accelerator model calibration. Calibration is the process of varying theoretical model parameters to achieve equality (with given precision) of the response matrix and theoretical response matrix (calculated the same way, but on the accelerator model).

Another application of the response matrix is to conduct beam position correction. Using SVD with measured response matrix we can get pseudoinverse matrix and calculate the current shift of magnetic elements, which were used in response matrix measurements, to create preassign beam position shift (actually, this operation will create the knob). Figure 4 demonstates the result of above procedure accomplished on injection complex damping ring. The aim of this correction was to minimize horizontal beam coordinates along damping ring perimeter. Blue markers showed beam position before correction using created knob, green - after. Corresponded values of beta-function before and after correction is presented on Fig. 3.

Figure 4: Displaying damping ring beam position. Green marker is the last measured beam coordinate, blue marker is the saved position, red is the inactive BPM's.

Number of Injected Particles vs. Tunes

Beforehand calculated knob for tunes shifting can be use for measuring the amount of captured particles onto damping ring during injection process depending on betatron tunes. For this is nessesary to point tunes in requared position and to make several beam shots from linac to damping ring in order to fix amount of captured beam particles. Next step is to moves tunes to another point by knob and to repeat shot

ISBN: 978-3-95450-240-0 ISSN: 2673-5539 doi:10.18429/JACoW-RuPAC2021-WEPSC56

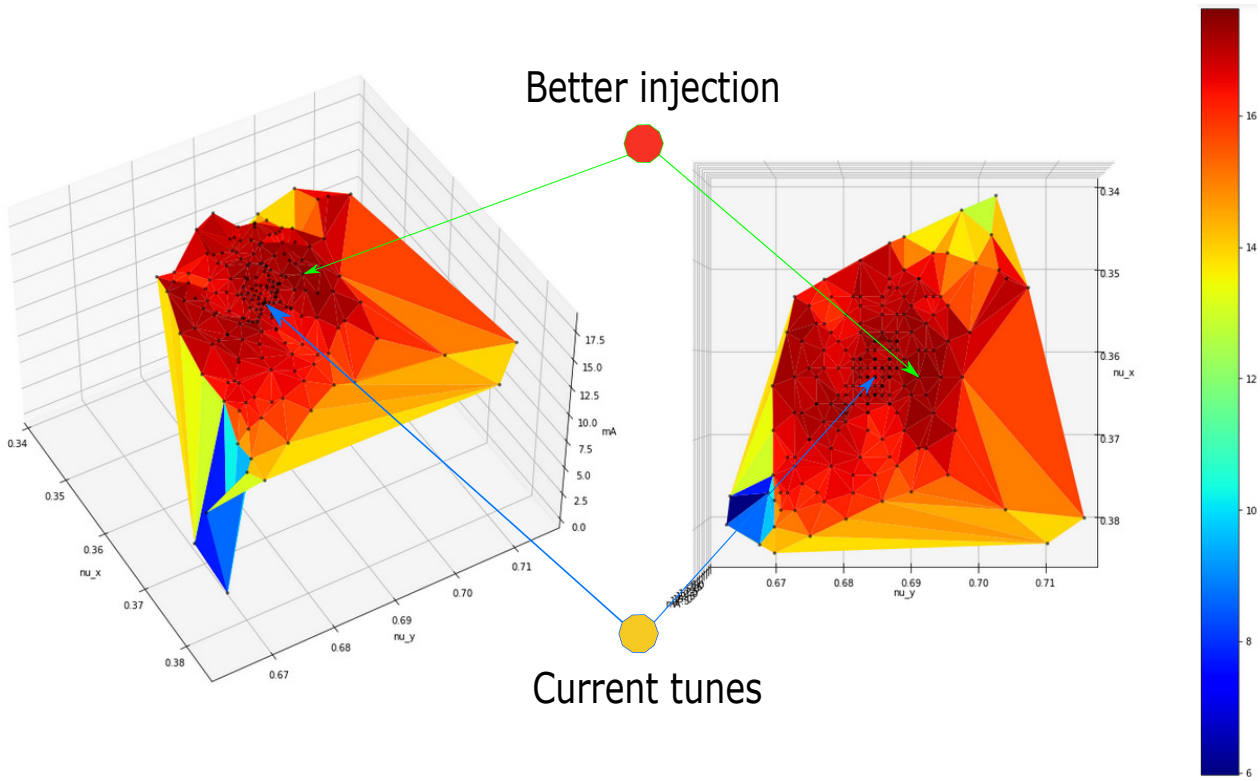

Figure 5: Amount of damping ring captured particles vs. tunes for "VEPP-2000 positron" IC mode.

and fix procedure. As a result of this algorithm usage we will receive desired distribution.

Program *inj_ proc* implements the described algorithm and gives an opportunity to choose one or two knobs for tunes scanning, mesh parameters and shots amount for averaging. Thus, user gets one or two dimensional distribution of captured particles during injection process vs. tunes. Output data has Python-like dictionary format.

Fig. 5 shows plotted distribution for "VEPP-2000 positron" IC mode. It is clearly seen that in the immediate vicinity of the current betatron tunes there is another point, where more particles are captured (moreover, in this new point the amplitude of the betatron beam oscillation beats decrease).

Measurements were made by beforehand calculated knob, which means that we can correct tunes of damping ring with them and get an increase the amount of injected positrons.

CONCLUSION

Beam parameters control and operation software tools for VEPP-5 injection complex were developed. They cover a wide range of tasks: from BPM data processing to response matrix measurements and knobs creating. This software facilitates the injection complex setup process, which includes damping ring energy shifting, creating of local beam position distortion and tunes change.

Using created software were measured damping ring beta-functions, corrected beam position along damping ring perimeter and plotted dependence of damping ring captured particles vs. tunes.

Now such types of measurements and subsequent corrections of magnetic system and beam parameters can be routine procedure for injection complex operational staff.

REFERENCES

[1] K. V. Astrelina et al., "Production of intense positron beams at the VEPP-5 injection complex," in *JETP*, vol. 106, pp. 94-114, doi: 10.1134/S1063776108010068.

[2] D. Bolkhovityanov, F. A. Emanov, "VEPP-5 injection complex control system base software upgrade," in *Proc. RuPAC2018*, 2018, pp. 417-419, doi:10.18429/JaCOW-RUPAC2018-THPS07.

[3] J. Safranek, "Experimental determination of storage ring optics using orbit response measurements," *Nucl. Instrum. Methods A*, vol. 388, pp. 27-36, Mar. 1997, doi: 10.1016/S0168-9002(97)00309-4.

ISBN: 978-3-95450-240-0 ISSN: 2673-5539 doi:10.18429/JACoW-RuPAC2021-WEPSC57

ONLINE MONITORING SYSTEM OF ACCELERATOR ELECTRON BEAM ENERGY

N.N. Kurapov, Ya.V. Bodryashkin, A.V. Tel'nov, A.S. Cherkasov, I.V. Shorikov, RFNC-VNIIEF, Sarov, Russia

Abstract

A necessity for online measurement of the output electron energy arises during start-up, adjustment or operation of an accelerator. For this purpose, there has been developed a system, allowing an online monitoring of energy spectrum accelerated electrons simultaneously with measuring of average beam current. This system is meant for reconstruction of the accelerated electron energy spectrum in the energy range from 1 to 10 MeV at the average beam current from 20 to 150 μA.

The system is based on an absorbing filter method and consists of an assembly, absorbing the accelerated electron beam, and a measuring system.

The developed system tests on the electron accelerator have proved the possibility for its application to monitor electron beam energy in real time.

INTRODUCTION

A number of linear resonance electron accelerators functions in RFNC-VNIIEF. Among these are such accelerators as LU 10 20 [1] and LU-7-2 [2]. These accelerators are meant for generation of intense electron beams and bremsstrahlung and research the radiation hardness of instruments and materials by the means of generating such radiation.

Measurement of the output electron energy is required both during start-up, adjustment or study of accelerator properties, as well as during physical experiments, requiring precise testing of output beam energy. To supply operability and universality (including a capability for application in different accelerators), it was decided to use an absorbing filter method for measurement of the beam energy. As a result, there has been developed a system for measuring beam parameters, consisting of a measuring assembly and a monitoring system. The developed system is portable, compact, and it helps to organize online measurements of accelerated electron beam spectral response inany accelerator with the energy from 1 to 10 MeV in the shortest time

OUTPUT BEAM ENERGY MEASUREMENT USING ABSORBING FILTER METHOD

The simplest way to resolve the problem of measuring the beam energy is to use a method of electron absorption in matter. For aluminum the energy dependence on free path Is of the form [3]:

$$R = 0.412 \cdot W_k^n, \quad \text{for } 0.01 \le W_k \le 3\ МэВ \quad (1)$$

$$R = 0.53 \cdot W_k - 0.106, \text{ for } 3 \le W_k \le 10\ МэВ$$

Where R – free path of electrons in aluminum, g/cm^2;
W_k – kinetic energy, MeV;

$$n = 1.265 - 0.0954 \cdot \ln W_k.$$

One can obtain a full energy response of an accelerated electron beam by restoring energy electron spectrum from current distributions, measured in absorbing assembly plates. A measuring absorbing assembly was developed for this purpose. It represents a set of 20 insulated from each other current-conducting plates of size 100x100 mm and thickness from 0.15 to 1 mm with air gap between plates 2 mm. Appearance of the assembly is shown in Fig. 1.

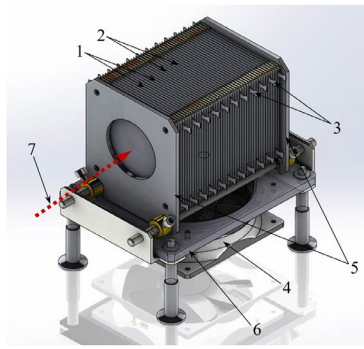

Figure 1: Measuring assembly, 1 - Aluminum plates; 2 - insulation between plates; 3 - leads for current measurement; 4 - fan; 5 - strengthening flanges; 6 - supporting frame; 7 - beam axis direction.

Spectral response of the assembly was calculated in the program C-007 [4] by Monte-Carlo method in the energy range from 1 to 10 MeV in increments of 0.5 MeV. Calculation results are given in Fig. 2.

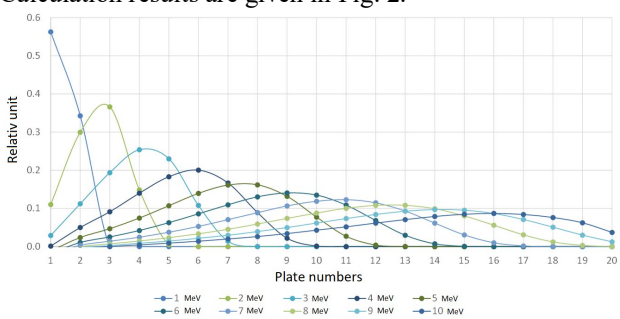

Figure 2: Spectral response of 20 plates assembly.

ENERGY SPECTRUM RECONSTRUCTION PROGRAM REVIEW

To reconstruct the accelerated electron beam spectrum from current distributions over measuring assembly plates, one should solve the system of 20 equations (number of plates) with 19 variables (values of plate current intensities at different beam energies – 1, 1.5, 2, …, 10 MeV). The system in a matrix notation is of the form:

$$\boldsymbol{A} \cdot \boldsymbol{X} = \boldsymbol{B}, \quad (2)$$

ISBN: 978-3-95450-240-0 ISSN: 2673-5539 doi:10.18429/JACoW-RuPAC2021-WEPSC57

To solve the combined algebraic linear equations (CALE) (2) a method of least squares (MLS) has been selected. Solution of the given equation system may contain negative values, which do not satisfy us. Thus, the restriction – $\boldsymbol{X} \geq 0$ was additionally imposed on solutions. Realization of such an algorithm was proposed in paper [5] and applied in developed computer program "Spektr".

The program code is implemented in language C++. The main program window (Fig. 3) is separated into two sections. The left region is meant for visualization of calculated and measured current values, as well as for current distribution output, corresponding to the found energy spectrum. A spectrum and an average beam energy value are presented in the right region.

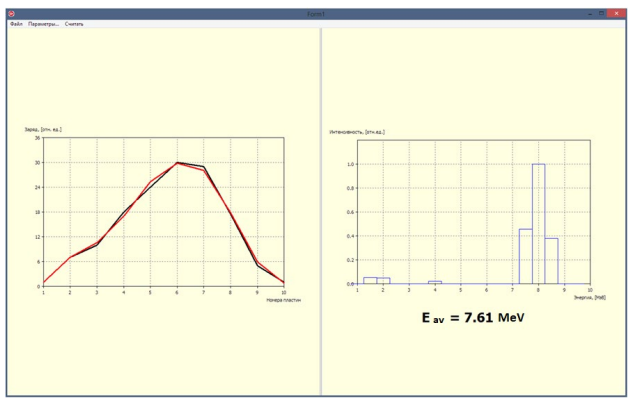

Figure 3: Main window of program "Spektr".

CURRENT MEASUREMENT DESIGN USING ASSEMBLY

When the accelerated electron beam is passing through a detector, a charge is accumulating in the detector plates. The charge accumulated in the detector plates flows down to the ground through a ripple integrating RC-filter, consisting of a resistor and a capacitor. Registered voltages on resistors of each RC-filter arrive at the inputs of a multi-channel a-d converter. Further digitized signals arrive at the inputs the inputs of a multichannel controller, and then the combined signal from the controller output is delivered to the personal computer input. Measurement design for an electron current with the aid of measuring assembly is given in Fig. 4.

RESULTS OF CURRENT MEASUREMENTS AND ENERGY SPECTRUM RESTORATION

Measurement run of accelerated electron beam energy response was conducted using the developed measuring assembly.

Figure 5 shows plate current distributions, normalized to maximal values, obtained at different settings of input accelerator parameters and restored energy spectra corresponding to them. Accelerator settings were changing in such a way, that the maximum current value was in plates with different numbers. According to spectra diagrams one can say that when maximum current is shifted towards plates with a higher number, the average electron energy grows.

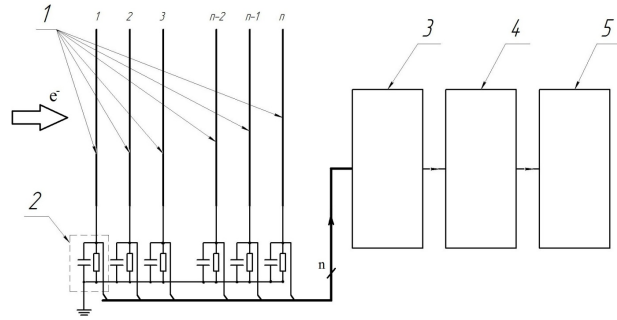

Figure 4: Electron current measuring circuit using the measuring assembly. 1 – electro-conductive absorbers; 2 – ripple integrating RC-filter; 3 – a-d converter; 4 – controller; 5 – personal computer with software.

The most interesting thing was comparison of spectrum, measured by the method of absorbing filters with spectrum, obtained with the aid of magnet spectrometer, namely a scanning magnet. Fig. 6 red line shows a spectrum, measured with the aid of the magnet spectrometer. The histogram reports absorbing filter method measurement results.

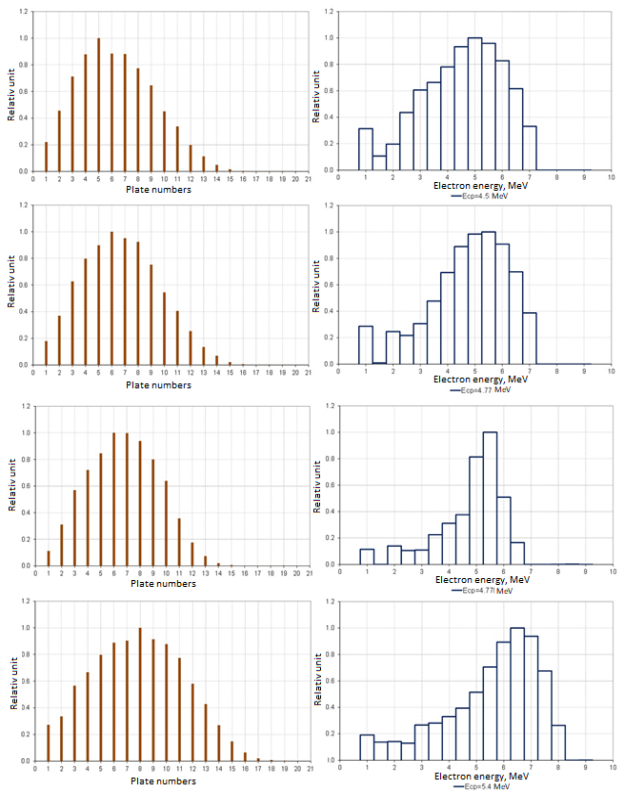

Figure 5: Distribution of currents over plates (left column) and corresponding restored energy spectra (right column)

ISBN: 978-3-95450-240-0 ISSN: 2673-5539 doi:10.18429/JACoW-RuPAC2021-WEPSC57

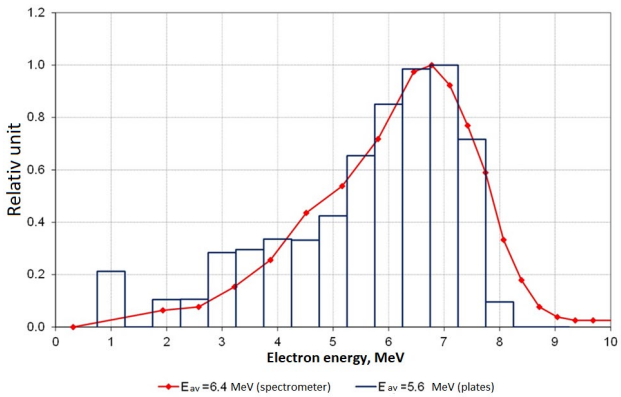

Figure 6: Electron energy spectrum, obtained with the aid of magnet spectrometer and by absorbing filter method.

CONCLUSION

Experimental sample of monitoring system of output electron beam energy was developed and tested.

The following works were performed:

–express control method of output electron beam energy was developed;

– measuring assembly structure was developed;

–calculation of current distribution over the assembly plates at different electron beam energies was carried out;

– the computer program meant for the energy spectrum restoration by distribution of currents in the measuring assembly plates was developed;

– the monitoring system of output energy was developed;

– the energy monitoring system was tested on the accelerator.

From the result obtained it can be concluded, that application of the beam energy monitoring system for operational measurement of accelerated electron beam energy spectrum in the real time mode is possible.

Patent license №2707270 for invention of «Charged particles spectrometer» became a result of the work on development of output electron beam energy monitoring system.

REFERENCES

[1] N.V. Zavyalov *et al.,* "Industrial linear electron accelerator LU-10-20", Materials for XV All-Union Workshop on Linear Charged Particle Accelerator. - *VANiT.- Ser. Yad.- Fiz. Issl.*. Issue 2, 3 (29, 30), P. 39-41, 1997.

[2] N.V. Zavyalov *et al.*, "Simulating and irradiating complexes and installations of RFNC-VNIIEF", 65 years of VNIIEF. *Fiz. i Tekh. Vys.* Plot. En. Issue 1. P. 180-181, 2011.

[3] A.P. Babichev *et al.*, "Physical quantity: Reference book" edited by I.S. Grigorieva, Ye.Z. Meylikhova. Moscow: Energoatomizdat, P. 1232, 1991.

[4] A.K. Zhitnik *et al.,* "Solving technique C-007 by Monte-Carlo method of coupled linear equations for neutron, gamma-quanta, electron and positron transfer", *VANT Ser. Mathem. Model. Fiz. Prots,* Issue 1. P. 17-24, 2011.

[5] Ch. Lowson, R. Henson. Problems computational solution of least square procedure. Moscow: Nauka, 1986. 231 p.

ISBN: 978-3-95450-240-0 ISSN: 2673-5539

List of Authors

Bold papercodes indicate primary authors;

— A —

Afonin, A.G. MOB01, TUPSB32
Agapov, A. MOPSA29, MOPSA32
Agapov, N.N. MOY02
Ageev, A.I. MOPSA13
Aginian, M. WEPSC46
Ahmanova, E.V. TUPSB04, TUPSB05
Akimov, V.P. WEA02 MOPSA01
Akimova, A. FRA02
Aksentyev, A.E. TUB07 **TUPSB10**, TUPSB11, TUB03
Aktershev, Yu. TUY01
Akulinichev, S.V. MOPSA41
Alekseeva, O.S. TUPSB22
Alexandrov, V. FRB05
Alexeev, A.G. FRB06
Alfeev, A.V. MOY02
Ali, M. TUPSB46
Altmark, A. **TUPSB20**, **TUPSB21**
Altukhov, Altukhov,Y.V. MOPSA13
Altukhova, E.V. MOPSA40
Amerkanov, D.A. **MOPSA44**, **MOPSA53**, **TUPSB16**
Amoskov, V.M. **TUPSB35**
Andreev, V. MOY02, WEPSC52
Andrianov, A.V. TUA02, WEA03
Andrianov, S.N. **TUPSB15**
Antipov, Y.M. MOB01, FRB06
Antoine, S. MOPSA29
Antokhin, E.I. **WEPSC23**
Apel, P.Yu. MOPSA28
Arsentyeva, M.V. **WEA03**, WED01
Artamonov, K.G. TUPSB38
Artamonov, S.A. MOPSA44, MOPSA53
Arutunian, S.G. **WEPSC46**
Arzhannikov, A.V. TUC03
Ashanin, I.A. **MOPSA07**, **MOPSA08**
Astakhov, V.I. WED05
Astrelina, K.V. TUA02
Azhgirey, I.L. FRC01, **MOPSA55**

— B —

Balabaev, A. TUPSB48
Balabanov, M.Yu. TUPSB14
Balakin, V.E. FRB05
Balakin, V.V. TUA02, **WEPSC56**
Baldin, A.A. MOY02, **WED05**, MOPSA29, MOPSA30
Balvanovic, R. FRB07
Baranov, G.N. TUA01
Baranov, V.T. WEPSC34
Baričevič, B. THB01
Barnyakov, A.M. TUA02, WEA03, TUPSB44, WEPSC42
Batov, A. MOPSA42
Batrakov, A.M. TUA02, TUB04, WEPSC14
Batranin, A.V. WEPSC38
Bayev, V. MOPSA16
Bayshev, I.S. FRC01, MOPSA55
Bazanov, A.M. MOY02, WEA01, WEA02, MOPSA01, TUPSB40
Bazhan, A.I. FRB05
Beeckman, W. MOPSA29
Bekhtenev, E.A. TUB04, WED01
Bekhterev, V. MOPSA50
Beletskaya, Yu.V. TUPSB51
Belikhin, Belikhin,M.A. MOPSA39, **MOPSA45**, WEPSC55, FRB05
Belikov, O.V. TUY01, TUA02, TUB04
Belkov, A. TUC01
Beloborodov, A.V. WED05
Belousov, V.I. TUC03
Belov, A. **TUPSB39**
Berkaev, D.E. TUY01, TUA02, WEPSC56
Berlev, A.I. MOPSA30
Bespalov, Yu.G. WEB01, WEB03, MOPSA14
Bikchurina, M.I. **TUPSB53**, **WEPSC31**, WEPSC32
Bleile, A. WEB03
Blinov, M.F. **TUPSB09**
Bobrovskiy, D.V. MOPSA29
Bodryashkin, Ya.V. MOPSA02, WEPSC57
Bogataj, L. THB01
Bogatov, A.S. MOPSA01, TUPSB40
Bogdanov, A.V. WEPSC45
Bogdanov, I. MOPSA13
Bogomolov, S.L. FRA01, MOPSA28, TUPSB35, TUPSB36, TUPSB37
Bogomyagkov, A.V. **MOY04**, **MOA01**, TUA01
Bogoslovsky, D.N. WED05
Bokhanov, A. THC02
Bolkhovityanov, D. TUA02
Bondarchenko, A.E. TUPSB36, **TUPSB37**
Borin, V.M. TUA01, WED01, **TUPSB24**
Boriskov, A.S. **TUPSB12**
Borisov, V.V. WEB02, WEB03, MOPSA14, WEPSC17, WEPSC18

ISBN: 978-3-95450-240-0 ISSN: 2673-5539

Bortsova, A.A. **MOPSA15**
Boytsov, A.Y. WEPSC41
Bragin, S. WEPSC50
Britvich, G.I. TUPSB32
Brovko, O.I. MOY02, WEPSC14, WEPSC15
Brukva, A.E. MOB02
Bryzgunov, M.I. **TUB04**
Bubley, A.V. TUB04
Budanov, Yu.A. MOPSA31
Bugaev, V.V. MOY02
Bulatov, M.S. MOPSA46
Bulavskaya, A.A. MOPSA35, MOPSA36, **MOPSA37**, MOPSA38, **WEPSC38**
Bulgacheva, M.M. TUB07, **WEPSC03**
Bunyatov, K. MOPSA33
Burenkov, D.B. TUY01
Burkov, I.V. **WEPSC06**
Butenko, A.V. MOY02, WEA01, THA01, MOPSA16, MOPSA29, WEPSC14, **MOY01**, WEA02, WEC02, MOPSA01, MOPSA17, TUPSB04
Butenko, E.A. **WEPSC41**
Bychanok, D. THA01, **MOPSA16**
Bykov, T.A. FRB01, TUPSB53, **WEPSC30**, WEPSC32, WEPSC33

— C —

Chakin, I. FRB03
Chashurin, V.I. FRB05
Chekavinskiy, V.A. TUB04
Chekmenyov, D.I. WEA03
Cherepennikov, Yu.M. MOPSA35, MOPSA36, MOPSA37, MOPSA38, WEPSC38
Cherepkov, V.G. FRB03
Cherkasov, A.S. WEPSC57
Chernyaev, A.P. MOPSA45, WEPSC55
Chernykh, A.N. **MOPSA46**
Chernykh, P.N. MOPSA29
Chesnokov, M.Yu. TUPSB32
Chesnokov, Y.A. TUPSB32
Chikhachev, A.S. **TUPSB17**
Chubunov, P.A. WEPSC49
Chumakov, A.I. MOPSA29
Chung, M. WEPSC46
Ćosić, M.M. FRB07

— D —

Dabrowski, A.E. MOPSA55
Degtyarev, I.I. MOPSA40
Denisov, A.G. TUPSB51
Denisov, A.P. TUB04
Deryabochkin, O.V. TUB07
Dmitriyev, M.S. TUB07, **TUPSB38**, WEPSC21
Dmitriyeva, V.V. TUB07, TUZ01
Dokutovich, V. WEPSC22
Domarov, E.V. FRB02, **FRB03**
Donets, D.E. MOY02, WEA01, **WEPSC25**, WEA02, MOPSA01, TUPSB40
Donets, E.D. MOY02
Donets, E.E. MOY02, WEPSC41
Donguzov, I.I. WEB02, WEPSC18
Dorokhov, V.L. TUA01, **WED02**
Drozdovsky, A.A. **WEPSC45**
Drozdovsky, S.A. WEPSC45
Druzhinin, V.P. TUY01
Durkin, A.P. FRB04, MOPSA41
Durum, A.A. TUPSB32, TUPSB51
Duveau, X.G. MOPSA29
Dyakonov, M.V. TUB07
Dyubkov, V.S. TUB07, **MOPSA11**, **TUPSB25**, **TUPSB26**, **WEPSC07**, WEPSC08

— E —

Edamenko, N.S. FRA03
Efimov, Y.V. MOPSA24
Efremov, A.A. TUPSB35, TUPSB36, TUPSB37
Egorov, D. WEA02
Eliseev, A.V. MOY02
Eliseev, V.S. WEPSC23
Elkin, V.G. WEPSC52
Emanov, F.A. TUA02, WEPSC56
Eseev, M.K. **MOPSA57**, **MOPSA58**

— F —

Fadeev, S. FRB02, FRB03
Fateev, A.A. WEA01
Fatkin, G.A. WEPSC14
Fedorov, A.N. WED05
Fedorov, K.V. TUPSB46
Fedotov, M.G. TUB04
Feschenko, A. **MOX02**, MOPSA06
Filatov, G.A. MOY02, MOPSA29, MOPSA32
Filimonov, V.V. TUB06
Fimushkin, V.V. MOY02
Firsov, A.A. FRA03
Fischer, E.S. **WEB03**
Fomin, Ye. TUC01, TUC02, **MOPSA23**, TUPSB33, **TUPSB34**, WEPSC20
Franko, J. MOPSA28
Frolov, A.R. TUA02
Frolov, B.A. **MOPSA31**
Frolov, O.T. TUPSB39

ISBN: 978-3-95450-240-0 ISSN: 2673-5539

— G —

Gaidash, V. MOX02
Galchuck, A.V. FRA02, FRA05, MOPSA52
Galimov, A.R. MOY02, WEA01, WEA02, **WEC02**, MOPSA01, MOPSA29, MOPSA32
Gao, D.Q. TUX01
Gapionok, E.I. TUPSB35, WEPSC16
Garaev, D.I. **WED07**
Gavrilov, S.A. WEPSC50, WEPSC51, MOX02, TUPSB39
Gavrish, Yu.N. FRA02, FRA05, MOPSA52
Gerasimenko, A.V. TUB07
Gerasimov, V.V. TUPSB24
Gerklotts, V.A. WEPSC14
Getmanov, Ya.V. TUPSB24
Gikal, K. **FRA01**, FRA04, MOPSA48, MOPSA51, TUPSB36
Ginzburg, N.S. TUC03
Glebov, I.L. MOPSA29
Golkovsky, M. FRB02, FRB03
Golovenskiy, B.V. MOY02, WEA01, WEA02, **MOPSA01**, **TUPSB40**
Golubenko, Yu.I. FRB02, FRB03
Golubev, S. THC02
Golubitsky, O. WEB02, WEPSC18
Goncharov, A.D. TUB04
Gorbachev, E.V. MOY02, WEA01, **WEPSC52**, WEPSC53
Gorchakov, A.A. TUB07
Gorchakov, K. TUY01, TUB04
Gorelyshev, I.V. MOY02, **TUB06**
Gosteyev, V.C. TUB04
Gostkin, M. MOB02, MOPSA21, WEPSC05
Govorov, A. MOY02, WEA01, WEA02, MOPSA01
Grebentsov, A.Yu. MOY02, **WEPSC14**
Grigorenko, S.V. FRA02, FRA05
Grigoriev, V.I. FRA02, FRA05
Grigorieva, A.A. MOPSA35, MOPSA36, MOPSA37, MOPSA38, WEPSC38
Gubin, V. **WEPSC42**
Guerra-Phillips, J. MOPSA29
Gulbekyan, G.G. FRA03, MOPSA28, MOPSA48, MOPSA50, MOPSA51
Gurskiy, S. MOPSA33
Gusarova, M. TUB07, **THA01**, MOPSA16, MOPSA42, WEPSC03, WEPSC11, WEPSC12, WEPSC13
Gusev, I.A. TUB04
Guzov, M.A. TUB07, **MOPSA03**, WEPSC11, MOPSA02

— H —

Harutyunyan, G.S. WEPSC46
He, Y. TUX01
Hodshibagijan, G.G. MOPSA33
Höltermann, H. MOPSA01
Huseu, S. MOPSA16

— I —

Ignashin, N.A. MOB01
Ilukin, V.L. TUPSB51
Ilyin, I.V. TUB04
Indiushnii, E.N. TUB07, MOPSA03, WEPSC11, WEPSC21
Isadov, V. WEPSC52
Issatov, A. FRA04, **WEPSC49**
Ivanenko, I.A. FRA01, FRA03, **MOPSA49**, MOPSA50, MOPSA51
Ivanenko, S.V. WEPSC44
Ivanov, A.A. FRB01
Ivanov, A.V. TUB04, TUPSB04, TUPSB05
Ivanov, E.M. MOPSA44, MOPSA53, TUPSB16
Ivanov, E.V. MOY02
Ivanov, G.N. MOPSA51
Ivanov, O.A. TUPSB38
Ivanov, S.V. ~~MOB01~~
Ivashchuk, O.O. **TUPSB30**, **TUPSB31**, **WEPSC58**
Izotov, I. THC02

— J —

Janezic, E. **WED06**
Jehanno, P.J. MOPSA29
Jovanovic, Z.M. **FRB07**

— K —

Kalagin, I.V. FRA03, FRA04, MOPSA28, MOPSA48, MOPSA50, MOPSA51
Kalinin, V.A. **MOB01**, FRB06, WEPSC34, WEPSC39
Kantsyrev, A.V. WEPSC45
Kaparkova, M. FRA03
Kaportsev, E.V. TUC01, **MOPSA24**
Karamyshev, O. **MOPSA33**
Karamysheva, G.A. MOPSA33
Karataev, P. TUPSB46
Karnaev, S.E. TUA01, THB01
Karpinskii, V.N. **WEC01**
Karpinsky, V. MOY02
Karpov, G.V. TUY01, TUA02,

ISBN: 978-3-95450-240-0 ISSN: 2673-5539

	TUB04, WED01
Karyukina, K.Yu.	TUA01
Kasaev, A.S.	TUY01, TUA02
Kasatov, D.A.	FRB01, MOPSA47, TUPSB53, WEPSC32
Kashunin, M.A.	WEPSC17
Kazachenko, N.I.	**WEPSC16**
Kazarinov, N.Yu.	FRA01, FRA03, FRA04, MOPSA28, MOPSA48, MOPSA49, **MOPSA50**, MOPSA51
Kekelidze, V.	MOY02
Kharyuzov, P.R.	WED05
Kharyuzova, A.P.	WED05
Khilchenko, A.D.	WEPSC44
Khodzhibagiyan, H.G.	MOY01, MOY02, TUB02, WEB01, WEB02, WEB03, MOPSA14, MOPSA15, WEPSC17, WEPSC18, WEPSC19
Khoroshkov, V.S.	MOPSA46
Khramov, D.	WEB02
Khrisanov, I.A.	TUPSB48
Khurchiev, A.	WEPSC45
Kirichenko, A.	MOY02, WEPSC52
Kirpotin, A.N.	TUY01
Kiselev, V.A.	TUA01
Kladov, S.A.	TUY01
Klenov, G.I.	MOPSA46
Kliuchevskaia, Yu.D.	MOPSA08, **TUPSB43**
Klopenkov, M.L.	FRA02
Klopenkov, R.M.	FRA02, FRA05
Kobets, A.G.	MOPSA57, TUPSB03, MOY02, **TUPSB04**
Kobets, V.V.	MOY02, **MOB02**, WEA02, MOPSA01, MOPSA12, MOPSA21, TUPSB44, WEPSC05, WEPSC54
Kogut, D.A.	FRB02
Kolesnikov, Ia.A.	FRB01, MOPSA47, MOPSA56, **TUPSB52**, TUPSB53, WEPSC30, WEPSC31, **WEPSC32**, WEPSC33
Kolesnikov, S.Yu.	WEA01, MOPSA29
Kolokolchikov, S.D.	**TUPSB08**
Kolomiets, A.	FRB04, MOPSA41
Kondakov, A.A.	TUA02
Kondaurov, M.N.	TUB04
Kondratiev, B.Yu.	WEB02, WEB03, WEPSC17, WEPSC18
Konishev, I.I.	MOPSA02
Konstantinov, A.V.	MOY02
Koop, I.	TUY01, TUPSB09
Korchagin, A.I.	FRB02 FRB03
Korchuganov, V.	TUC01, **TUC02**, MOPSA07, TUPSB33, TUPSB34, WEPSC20
Korobitsina, M.Yu.	TUPSB05
Korolev, L.E.	FRA02, FRA05
Korovkin, D.S.	WED05
Korovkin, S.A.	MOY02, WEB01, **MOPSA14**
Korshunov, A.M.	TUB07
Koshelev, A.V.	FRB06
Koshkarev, A.M.	WEPSC32, **WEPSC33**, FRB01
Kostin, M.Yu.	TUPSB32
Kostromin, S.A.	MOY02, **TUB01**, MOPSA14, WEPSC17, MOY01, TUB02, WEB02, WEPSC18
Kot, N.Kh.	TUA02
Kotina, E.D.	**TUPSB13**, TUPSB14
Kotov, E.S.	TUA02
Koubek, B.	MOPSA01
Kovalchuk, M.V.	TUC02
Kovalenko, A.D.	WEA02
Kozlov, A.P.	WEA01, **WEPSC27**
Kozlov, A.V.	TUPSB49
Kozlov, O.S.	MOY02, **TUPSB07**, TUB02, MOPSA32
Kozlovskii, K.I.	TUPSB42
Kozlovskiy, K.I.	TUB07
Kozub, S.	MOPSA13
Krasnov, A.A.	WEPSC15
Krasnov, A.S.	TUB07
Kravchuk, K.A.	FRA02, FRA05
Kravchuk, L.V.	MOPSA06
Kremnev, N.S.	TUB04
Kropachev, G.	MOPSA04, **TUPSB50**, **MOPSA05**
Kruchkov, Ya.G.	WEPSC15
Krutikhin, S.A.	WEPSC14, WEPSC15
Kryachko, I.A.	MOPSA30
Krylov, Y.V.	TUC01
Kubankin, A.S.	MOPSA29, TUPSB46
Kudashkin, A.V.	WEB02
Kukhtin, V.P.	**FRA03**, TUPSB35, WEPSC16
Kuksanov, N.K.	FRB02, FRB03
Kulevoy, T.	**MOY03**, MOPSA04, MOPSA05, MOPSA29, TUPSB26, TUPSB48, TUPSB49, TUPSB50
Kupurzhanov, A.V.	TUY01
Kurakin, V.G.	**THC01**
Kurapov, N.N.	MOPSA02, MOPSA54, **WEPSC57**
Kurilik, A.	MOPSA41

ISBN: 978-3-95450-240-0 ISSN: 2673-5539

Kurkin, G.Y. TUY01, TUA02, WEPSC14, WEPSC15
Kurochkin, I.A. MOPSA55
Kuzhlev, A.N. FRA02, FRA05
Kuzmenkov, K.I. TUPSB36
Kuzmichev, V.G. TUPSB49
Kuznetsov, S.V. **TUPSB18**
Kuznetsov, V.V. MOPSA02
Kwak, D.H. WEPSC46

— L —

Labusov, A.N. TUPSB35
Ladygin, V. TUPSB10, TUPSB11
Lalayan, M.V. THA01, TUB07, MOPSA16, **MOPSA42**, WEPSC03, WEPSC12, WEPSC13
Lamzin, E.A. FRA03, TUPSB35
Lancelot, A. MOPSA29
Lapik, R.M. TUA02
Lapygin, V.G. MOB01
Larionov, M.S. FRA03
Lavrukhin, A. FRB02, FRB03
Lazarev, L.M. WEPSC46
Lazareva, E.G. WEPSC46
Lebedev, N.N. TUA02
Lebedev, O.P. MOB01, WEPSC34
Lesiv, N.A. TUPSB20, TUPSB21
Letkin, D.S. WEA02, MOPSA01, TUPSB40
Leushin, D.O. WEA02, MOPSA01, TUPSB40
Levichev, A.E. TUA02, WEA03, THB01
Levichev, E.B. TUA01
Levterov, K.A. MOY02, WEA01, **WEA02**, MOPSA01, TUPSB40
Levterova, E.A. **MOPSA30**
Liashenko, O.A. MOPSA40
Lisov, V.I. FRA01, MOPSA48, MOPSA49, MOPSA50, **MOPSA51**
Lobanov, I.S. TUPSB32
Loginov, V.N. TUPSB36, TUPSB37
Losev, A.A. TUPSB48
Lozeev, Y. TUB07, MOPSA03, **WEPSC11**
Lozeeva, T.A. TUB07
Lunev, P.A. FRB05
Lutchev, A. WEPSC34
Lutsenko, V.M. **MOPSA20**
Luzanov, V.A. MOPSA29
Lyalin, M.A. TUY01
Lyapin, I.D. MOPSA33
Lysenko, A.P. TUY01
Lyuosev, D.A. MOY02, WEA01, WEA02, MOPSA01

— M —

Ma, X.C. WED01, WEPSC44
Makarov, A. FRA03, TUPSB35
Makarov, A.I. TUB07, MOPSA03, WEPSC11
Makarov, A.N. FRB01, MOPSA47, MOPSA56, **WEPSC28**, WEPSC29, WEPSC32, WEPSC33
Maksimenko, S.A. THA01, MOPSA16
Maksimov, A. MOB01
Malinin, V. MOPSA33
Mallows, S. MOPSA55
Maltseva, Yu.I. **TUA02**, WED01, **WEPSC44**
Malyshev, A.M. **WEPSC15**, MOY02, WEPSC14
Mamaev, A. TUPSB51
Mao, L.J. TUX01
Margaryan, A.V. WEPSC46
Martianov, K. TUPSB53
Martynov, A.A. MOY02, WEA02, MOPSA01
Martynov, G.O. TUPSB24
Martynovsky, A.Yu. TUA02, WEPSC15
Martyshkin, P.V. TUA02
Mashin, I.A. MOPSA02
Maslennikov, K. **WEPSC09**
Matsievskiy, S.V. TUB07, THA01, **WEPSC12**
Maximov, A.V. FRB06
Maximov, V.I. MOPSA44
Melekhov, A.P. TUB07
Melnikov, A.A. TUB03, TUPSB10, **TUPSB11**
Melnikov, S.A. MOY02, TUPSB03, TUPSB04, **TUPSB05**
Meshkov, I.N. MOY02, WEA01, MOPSA57, TUPSB03, TUPSB04, TUPSB05, TUPSB07, MOY01, WEPSC15
Meshkov, O.I. WED02, TUA01, WEA03, **WED01**, TUPSB24, WEPSC44
Mezhov, I.I. FRA02, FRA05
Mialkovskiy, V.V. WEA02, MOPSA01, TUPSB40
Mikhailov, K.I. **MOPSA12**
Mikhailov, V.A. MOY02
Milichenko, Yu.V. MOB01
Miloichikova, I.A. MOPSA35, MOPSA36, MOPSA37, **MOPSA38**, WEPSC38
Minashkin, V.F. WEPSC54

ISBN: 978-3-95450-240-0 ISSN: 2673-5539

Mironov, V. TUPSB36, TUPSB37
Mironov, V.I. FRA04
Mishnev, S.I. TUA01
Mitrofanov, S.V. FRA04, **MOPSA28**, MOPSA48, MOPSA50, MOPSA51, WEPSC49
Mitrofanova, Iu.A. MOY02
Mityanina, N.V. WEPSC15
Mizintseva, M.A. TUPSB14
Moiseev, V.I. TUC01
Monakhov, D.V. WEPSC52, **WEPSC53**
Monchinsky, V.A. MOY02, WEA02, MOPSA01, TUPSB40
Morozov, I.A. TUA01, **WED04**, **WEPSC40**
Morsina, A.A. WEPSC44
Moseev, K. TUC01
Moseiko, N.I. TUC01, **MOPSA25**, **MOPSA26**, **MOPSA27**
Motygin, S.V. TUY01, TUA02, WEPSC15
Mudrolyubov, V.G. FRA02, FRA05
Mukhamedgaliev, K. TUPSB20, TUPSB21
Murasev, A.A. TUA02, WEPSC15
Murygin, O.V. TUB07
Muslivets, V. TUA02
Mykhailenko, V.A. WEPSC17
Myshelovka, L.V. **WEPSC47**
Mytzin, G.V. MOPSA33

— N —

Nazlev, H.P. WEA01, WEPSC52
Nechaeva, L.P. TUPSB39
Nemchenko, R.E. TUB07, THA01
Nemytov, P.I. FRB02, FRB03
Neskovic, N. FRB07
Nesterov, A. MOY02
Nezhentzev, A. FRA03
Nikiforov, D. **WEB01**, WEB02, WEB03, MOPSA14, MOPSA15, MOPSA16, WEPSC19
Nikiforov, D.A. TUA02, TUC03, WEA03, WED01
Nikolaev, I.B. TUA01
Nikolaev, V.R. MOPSA02
Nikolaichuk, I. TUB02, WEPSC18
Novikov, G.G. TUB07
Novikov, M.S. MOPSA33
Novikov-Borodin, A.V. **WEPSC48**
Novoskoltsev, F.N. MOPSA40
Novozhilov, A.E. TUB07
Nozdrin, M.A. MOB02, MOPSA21, TUPSB44, **WEPSC54**

— O —

Odintsov, D.G. TUC01
Okunev, I.N. TUA01
Oleinik, A.N. **TUPSB46**, WEPSC47
Opekunov, A.M. MOPSA02, MOPSA03, MOPSA54, TUPSB12
Oreshkova, N.A. **WEPSC39**
Orlov, O. MOPSA57, TUPSB04
Osina, Yu.K. **FRA02**, FRA05, **MOPSA52**
Osipenkov, A.L. MOY02
Osipov, K.G. MOY02, TUB06, MOPSA01, **TUPSB02**, TUPSB04, TUPSB05
Osipov, N.F. FRA03, MOPSA28, MOPSA50, MOPSA51
Osipov, S. MOPSA29
Osipov, V.N. WEPSC15
Ostreinov, G. FRB01
Ostreinov, Y.M. TUPSB52, WEPSC32
Otboev, A.V. TUY01
Ovchinnikova, L. **MOPSA41**
Ovsienko, M.P. FRB06
Ovsyannikov, A.D. **TUPSB47**, TUPSB14
Ovsyannikov, D.A. TUPSB13, WEPSC16, FRA03, **TUPSB14**

— P —

Pakhomov, A.Yu. WEPSC22
Panasyuk, V.M. TUB04
Panishev, A.S. TUB07, WEPSC08, WEPSC10
Panyushkin, V.A. WEPSC45
Paraipan, M. MOPSA30
Paramonov, V.V. **FRB04**, MOPSA06, MOPSA41, **WEPSC01**
Parfylo, T. TUB02, WEB02, WEB03, **WEPSC17**, WEPSC18
Parkhomchuk, V.V. TUB04
Pashentsev, V.N. TUB07
Pavlenko, A.V. TUY01, TUA02
Pavlov, D.A. **MOPSA43**
Pavlov, L.A. FRA04
Pavlov, O.A. WEA03
Peleshko, V.N. TUPSB51
Perevedentsev, E. TUY01
Peskov, N.Yu. **TUC03**
Pesterev, S.G. TUC01
Petrakovsky, V.S. THA01, MOPSA16
Petrov, M.V. WEB01, WEB03, MOPSA14
Petrov, V.D. WEPSC14
Petrov, V.M. WEPSC14, WEPSC15
Petukhov, A.S. WEA01
Philippov, A.V. MOY02, TUB02, WEC02
Pikalov, V.A. **FRB06**, FRC01
Pilan, A.M. TUA02, WEPSC14, WEPSC15

ISBN: 978-3-95450-240-0 ISSN: 2673-5539

Pilyar, N.V. WEPSC52
Piminov, P.A. **TUA01**, WED04, WEPSC40, **WEPSC43**
Piryazev, I.N. TUPSB51
Pitalev, V.I. TUPSB32
Pivin, R.V. MOY02, **MOPSA18**, **MOPSA19**
Pivovarov, I.L. WEA03
Pobol, I.L. THA01
Pokrovsky, A.I. THA01, MOPSA16
Polkovnikov, M.K. FRB06
Polozov, S.M. **TUB07**, TUC02, **TUZ01**, THA01, THC03, MOPSA03, MOPSA07, MOPSA08, MOPSA16, MOPSA42, MOPSA43, TUPSB25, TUPSB42, TUPSB43, **WEPSC08**, **WEPSC10**, WEPSC11, WEPSC21
Poluektov, I.V. TUPSB32
Polyakov, L.E. **MOPSA02**, MOPSA03, TUPSB12
Ponkin, D.O. MOY02, WEA01, WEA02, MOPSA01, TUPSB40
Ponomarenko, A.G. TUB07
Ponomarev, P.D. TUPSB52
Popov, D. MOPSA33
Pospelov, G. MOPSA02
Prianishnikov, K.E. TUPSB49
Prokopenko, A.V. TUB07
Pronikov, A.I. MOPSA07, MOPSA08
Prosvetov, V.P. TUY01
Protasov, A.A. FRA01, FRA04, MOPSA51, TUPSB36
Prozorov, O.V. WEPSC14
Pryanichnikov, A.A. MOPSA39, **MOPSA40**, **WEPSC55**, **FRB05**, MOPSA45
Pugachev, D.K. FRA01, **TUPSB36**, TUPSB37, WEPSC49
Pureskin, D.N. TUB04
Puryga, E.A. WEPSC44
Putevskoy, S.A. MOPSA02
Putmakov, A.A. TUB04

— R —

Rascvetalov, Ja.N. **TUPSB51**
Rashchikov, V.I. TUB07, **THC03**, MOPSA07
Rassadov, D.N. **TUPSB41**
Ratzinger, U. MOPSA01
Repič, B. THB01
Reva, V.B. TUB04
Riabchenko, K.K. WEPSC22, **WEPSC24**
Riabchikova, A.D. **MOPSA13**, MOPSA55
Riabov, G.A. MOPSA44, MOPSA53, TUPSB16
Rodin, I.Yu. FRA03, TUPSB35, WEPSC16
Rogovsky, Yu.A. TUY01, TUA02
Romanov, S. MOY02, WEPSC52
Rotov, E. WEPSC14, WEPSC15
Rukojatkin, P.A. MOY02
Rukoyatkina, T.V. WEPSC52
Ryabov, T. MOPSA13
Rybakov, I.V. **MOPSA06**
Rybitskaya, T.V. WEPSC22, WEPSC24
Rykalin, V. WEPSC55

— S —

Safonov, A.B. WED05
Safonov, A.V. TUPSB35
Salimov, R.A. FRB02, FRB03
Samarokov, N.Yu. WEPSC13
Samofalova, Y.A. MOB02, **TUPSB44**
Samoshin, A.V. TUB07
Samoylov, S.L. TUA02, WEA03, WEPSC42
Sandalov, E.S. TUC03
Sandomirskiy, Yu.E. TUPSB32
Satov, Yu.A. **TUPSB48**
Savchenko, A.A. **TUPSB29**
Savchik, A.A. TUB07
Savin, D.A. WEPSC34
Savin, S.M. WEPSC45
Savinov, S. TUPSB52, WEPSC30, WEPSC31, WEPSC32, MOPSA47, WEPSC28
Savitskaya, E.N. TUPSB51
Schempp, A. MOPSA01
Sedykh, G.S. WEA01, WEPSC52
Selesnev, D.N. MOPSA04, **TUPSB49**
Seleznev, V.V. WEA01
Semennikov, A.I. MOPSA04
Semenov, A.M. TUY01
Semenov, A.V. FRB02, FRB03
Semenov, S.V. **TUPSB03**, TUPSB04
Semin, V.A. FRA01, **FRA04**, MOPSA28, MOPSA48, MOPSA50, MOPSA51
Senchenko, A.I. TUY01
Senichev, V. **TUB03**, TUPSB08, TUPSB10, TUPSB11
Senkov, D.V. TUB04, WEPSC22
Serdakov, L.E. TUY01
Serenkov, E. MOPSA29
Sergeev, A.S. **MOPSA17**, TUPSB03, TUPSB04
Sergeeva, D.Yu. **TUPSB28**, TUPSB29, WED07
Sergeeva, E.V. **WEPSC19**
Serov, V.L. MOPSA06

ISBN: 978-3-95450-240-0 ISSN: 2673-5539

Shabratov, V. MOB02
Shamov, A.G. TUA01
Shandov, M.M. **TUB02**, WEPSC17, WEB02, WEPSC18
Sharkov, B.Y. **MOX01**
Shashkov, Ya.V. WEPSC12, **WEPSC13**
Shatil, N. FRA03, TUPSB35
Shatokhin, V.L. TUB07, THA01, WEPSC08, WEPSC10
Shatunov, P.Yu. TUY01
Shatunov, Y.M. TUY01
Shchagin, A.V. TUPSB46
Shchudlo, I.M. FRB01, MOPSA47, MOPSA56, TUPSB52, TUPSB53, WEPSC28, WEPSC30, WEPSC31, WEPSC32
Shein, A.N. MOPSA02, **WEPSC04**
Sheinman, I.L. **TUPSB22**
Shemchuk, A.V. **WEB02**, WEPSC18
Shemyakov, A.E. FRB05, **MOPSA39**, MOPSA45, WEPSC55
Shen, G.D. TUX01
Sheng, L.N. TUX01
Shestopalov, A.I. FRB05, MOPSA39
Shevchenko, O.A. TUPSB24
Shevelev, M. WEPSC36
Shikanov, A.E. TUB07, TUPSB42
Shipulin, K.N. MOPSA29, MOPSA32
Shirikov, I.V. MOY02, WEA02, MOPSA01, **MOPSA22**, TUPSB40
Shirkov, G. MOB02, MOPSA33
Shirkov, S.G. MOPSA33
Shkitov, D.A. **WEPSC36**
Shorikov, I.V. MOPSA02, WEPSC04, WEPSC57
Shtro, K.S. TUB04
Shumshurov, A. TUPSB48
Shurygin, A.A. MOY02, **WEPSC26**
Shvedov, A. THA01, MOPSA16
Shvetsov, V.S. WEA01
Shwartz, D.B. TUY01
Sidorin, A.A. MOPSA57, TUPSB04
Sidorin, A.O. MOY02, WEA01, MOY01, TUB06, WEA02, TUPSB04
Sidorov, A.I. WEA01
Siemek, K. MOPSA57
Simakov, A.S. MOPSA40
Simonov, E.A. TUA01
Sinitsky, S.L. TUC03
Sinyatkin, S.V. TUA01, THB01
Sinyukov, R.Yu. MOPSA40
Sitnikov, A. **MOPSA04**, MOPSA05, TUPSB50
Skalyga, V. **THC02**
Skobliakov, A.V. WEPSC45
Skorobogatov, D.N. TUB04
Skovorodin, D.I. TUC03
Skuratov, V.A. MOPSA28
Sledneva, A. **TUPSB01**
Slepnev, V. MOY02
Slivin, A. MOY02, **MOPSA29**, MOPSA32
Smetanin, M.L. TUB07, MOPSA02, MOPSA03, TUPSB12
Smirnov, K.D. TUB07
Smirnov, K.E. FRA02, **FRA05**
Smygacheva, A.S. TUC01, TUC02, **TUPSB33**, **WEPSC20**
Sobenin, N.P. THA01
Sobolev, D.I. TUC03
Sokolova, E.O. WEPSC32, **WEPSC29**, WEPSC33, FRB01
Soldatov, A.P. MOB01, FRB06
Soloviev, S. MOPSA29
Sorokin, I.N. FRB01, **MOPSA56**, WEPSC32
Starostenko, A.A. TUC03, **WEPSC22**, WEPSC24
Starostenko, D.A. **MOY05**
Starostina, E.V. TUA01
Stepanov, D.B. TUPSB35
Stirin, A.I. TUC01
Stogov, Yu.I. FRA02, FRA05, MOPSA52
Strekalovskikh, S.A. MOB01
Stuchebrov, S. **MOPSA35**, **MOPSA36**, MOPSA37, MOPSA38, WEPSC36, WEPSC38
Sukhanov, D.P. WEPSC42
Sukharev, M.M. TUPSB51
Sukhikh, S.E. TUPSB51
Sukhotski, A.E. MOPSA16
Sumaneev, O.V. **FRC01**
Sumbaev, A.P. MOPSA12, WEPSC06
Sun, L.T. TUX01
Svidetelev, A.N. WEA01, WEC02, MOPSA17
Sycheva, T. MOPSA47
Syresin, E. **MOY02**, WEA01, WEA02, THA01, MOPSA16, MOPSA29, TUPSB08, WEPSC14, MOY01, MOPSA01, MOPSA32, TUPSB04, TUPSB07, WEPSC15
Sytchevsky, S.E. FRA03, TUPSB35, WEPSC16
Sytov, S.E. MOB01

ISBN: 978-3-95450-240-0 ISSN: 2673-5539

— T —

Tarnetsky, V.V. WEPSC15
Taskaev, S.Yu. **FRB01**, MOPSA47, MOPSA56, TUPSB52, TUPSB53, WEPSC28, WEPSC29, WEPSC30, WEPSC31, WEPSC32, WEPSC33
Teleski, I. FRB07
Telnov, A.V. TUB07, MOPSA02, MOPSA03, MOPSA54, TUPSB12, WEPSC04, WEPSC57
Telnov, V.I. **TUA03**
Teterev, Yu.G. FRA04, WEPSC49
Tikhomirov, A.M. WEC02, MOPSA29, **MOPSA32**
Timoshenko, G.N. MOPSA29
Timoshenko, M.V. **TUY01**
Tinta, D.T. **THB01**
Tishchenko, A.A. WED07, **TUPSB23**, TUPSB28, TUPSB29
Titarenko, Y.E. MOPSA29
Titov, A.I. **WEPSC50**, **WEPSC51**
Tkachenko, K.I. WEPSC16
Tkachenko, L. MOPSA13
Todyshev, C. TUA01
Toktaganova, M. WEPSC36
Tonkikh, V.A. MOPSA44, MOPSA53, TUPSB16
Topilin, N.D. **WEB04**
Tribendis, A.G. TUA02, WEPSC14, WEPSC15
Trifonov, A. MOB02, **MOPSA21**, WEPSC54
Trubnikov, G.V. MOY01, MOY02, WEA02, THA01, MOPSA33
Truntseva, R.P. **MOPSA54**
Tsarev, G.A. TUB07
Tsygankov, S.S. FRA02
Tsyganov, A.S. WEPSC22
Tsyplakov, E.D. TUPSB26
Tumanov, S.A. TUB07
Turbabin, A.V. TUPSB39
Turgunova, N.D. MOPSA36
Tuzikov, A. MOY02, **WEA01**, MOPSA29, TUB02, WEA02, MOPSA01
Tyulkin, V.I. WEA01, MOPSA29, MOPSA32
Tyurin, N.E. MOB01
Tyutyunnikov, S.I. MOPSA30

— U —

Usanova, M.V. FRA02, FRA05
Ushakov, V.A. TUC01, TUC02, MOPSA07, TUPSB33

— V —

Vakhrushev, R.V. TUB04
Valentinov, A.G. **TUC01**, TUC02, MOPSA24, TUPSB33
Vasilevich, E. MOPSA16
Vasiliev, D.A. MOB01, **WEPSC34**
Vasiliev, S. TUA02
Vasilishin, B. MOY02
Vasilyev, A.A. TUPSB48
Verkhovod, G.D. **MOPSA47**
Vinokurov, N.A. TUPSB24
Visotski, S.A. WEPSC45
Vokhmyanina, K.A. WEPSC47
Volkov, V. WEA03, WED01
Volkov, V. MOY02, WEPSC52
Volkov, V.A. WEPSC45
Volodin, A.A. WEPSC14
Volodkevich, O. WEPSC50
Vorobev, D.S. **FRB02**
Voronin, A.A. MOPSA01
Vorontsov, V.A. **MOPSA34**, **TUPSB19**
Vorozhtsov, A.S. MOPSA29
Vostrikov, V.A. TUPSB09
Vovchenko, E.D. **TUPSB42**
Vybin, S.S. THC02

— W —

Waldt, A. WEB03

— X —

Xu, Z. TUX01

— Y —

Yakimov, I.S. WED04
Yakovenko, S. MOPSA33
Yang, J.C. **TUX01**
Yang, Y.Q. TUX01
Yanovich, A.A. **TUPSB32**, TUPSB51
Yuan, Y.J. TUX01
Yudin, V.D. TUY01, TUA02
Yunenko, K. MOB02, **WEPSC05**
Yurevich, S.V. THA01, MOPSA16
Yurin, I.A. TUB07, **WEPSC21**

— Z —

Zabanov, A.S. **MOPSA48**, MOPSA51
Zaitsev, A.M. MOB01
Zaleski, V.G. THA01
Zapretilina, E.R. TUPSB35
Zapryagaev, I.A. WEPSC15
Zarubin, A. TUPSB49
Zaslavsky, V.Yu. TUC03
Zavyalov, N.V. TUB07, MOPSA02, MOPSA03, TUPSB12, MOPSA54
Zbruev, R.A. MOPSA42
Zemlyansky, I.M. TUY01

ISBN: 978-3-95450-240-0 ISSN: 2673-5539

Zharikov, A.A. TUB04
Zharinov, Yu.M. TUY01
Zhemchugov, A. MOB02, MOPSA21, TUPSB44, WEPSC05
Zhigailova, M.I. TUB07, TUPSB38
Zhilich, V.N. TUA01
Zhilyaev, K.V. WEPSC22
Zhivankov, K.I. TUC03
Zhogolev, P.B. WEPSC55
Zhukov, A.A. TUA01, WEPSC15
Zhukov, I.V. MOPSA02
Zhuravlev, A.N. TUA01
Zolotykh, D.A. WEB02, **WEPSC18**
Zolotykh, E.V. WEB02, WEPSC18
Zorzut, S. THB01
Zubets, V. TUPSB39

ISBN: 978-3-95450-240-0 ISSN: 2673-5539

Institutes List

Allrussian Electrotechnical Institute
Moskow, Russia
- Chikhachev, A.S.

ANSL
Yerevan, Armenia
- Aginian, M.
- Arutunian, S.G.
- Harutyunyan, G.S.
- Lazarev, L.M.
- Lazareva, E.G.
- Margaryan, A.V.

BelSU
Belgorod, Russia
- Ivashchuk, O.O.
- Kubankin, A.S.
- Myshelovka, L.V.
- Oleinik, A.N.
- Vokhmyanina, K.A.

BelSU/LRP
Belgorod, Russia
- Sergeeva, D.Yu.

BEVATECH
Frankfurt, Germany
- Höltermann, H.
- Koubek, B.
- Ratzinger, U.

BINP
Novosibirsk, Russia
- Ma, X.C.
- Meshkov, O.I.
- Ponomarev, P.D.
- Savinov, S.

BINP & NSTU
Novosibirsk, Russia
- Savinov, S.
- Semenov, A.M.

BINP SB RAS
Novosibirsk, Russia
- Aktershev, Yu.
- Andrianov, A.V.
- Antokhin, E.I.
- Arsentyeva, M.V.
- Arzhannikov, A.V.
- Astrelina, K.V.
- Balakin, V.V.
- Baranov, G.N.
- Barnyakov, A.M.
- Batrakov, A.M.
- Bekhtenev, E.A.
- Belikov, O.V.
- Berkaev, D.E.
- Bikchurina, M.I.
- Blinov, M.F.
- Bogomyagkov, A.V.
- Bolkhovityanov, D.
- Borin, V.M.
- Bryzgunov, M.I.
- Bubley, A.V.
- Burenkov, D.B.
- Chakin, I.
- Chekavinskiy, V.A.
- Chekmenyov, D.I.
- Cherepkov, V.G.
- Denisov, A.P.
- Dokutovich, V.
- Domarov, E.V.
- Dorokhov, V.L.
- Druzhinin, V.P.
- Eliseev, V.S.
- Emanov, F.A.
- Fadeev, S.
- Fedotov, M.G.
- Frolov, A.R.
- Getmanov, Ya.V.
- Golkovsky, M.
- Golubenko, Yu.I.
- Goncharov, A.D.
- Gorchakov, K.
- Gosteyev, V.C.
- Gusev, I.A.
- Ilyin, I.V.
- Ivanov, A.A.
- Ivanov, A.V.
- Karnaev, S.E.
- Karpov, G.V.
- Karyukina, K.Yu.
- Kasaev, A.S.
- Kasatov, D.A.
- Khilchenko, A.D.
- Kirpotin, A.N.
- Kiselev, V.A.
- Kladov, S.A.
- Kogut, D.A.
- Kolesnikov, Ia.A.
- Kondakov, A.A.
- Kondaurov, M.N.
- Koop, I.
- Korchagin, A.I.
- Koshkarev, A.M.
- Kot, N.Kh.
- Kotov, E.S.
- Krasnov, A.A.
- Kremnev, N.S.
- Kruchkov, Ya.G.
- Krutikhin, S.A.
- Kuksanov, N.K.
- Kupurzhanov, A.V.
- Kurkin, G.Y.
- Lapik, R.M.
- Lavrukhin, A.
- Lebedev, N.N.
- Levichev, A.E.

ISBN: 978-3-95450-240-0 ISSN: 2673-5539

- Levichev, E.B.
- Lyalin, M.A.
- Lysenko, A.P.
- Makarov, A.N.
- Maltseva, Yu.I.
- Malyshev, A.M.
- Martianov, K.
- Martynov, G.O.
- Martynovsky, A.Yu.
- Martyshkin, P.V.
- Meshkov, O.I.
- Mishnev, S.I.
- Mityanina, N.V.
- Morozov, I.A.
- Morsina, A.A.
- Motygin, S.V.
- Murasev, A.A.
- Muslivets, V.
- Nemytov, P.I.
- Nikiforov, D.A.
- Nikolaev, I.B.
- Okunev, I.N.
- Osipov, V.N.
- Ostreinov, Y.M.
- Otboev, A.V.
- Pakhomov, A.Yu.
- Panasyuk, V.M.
- Parkhomchuk, V.V.
- Pavlenko, A.V.
- Pavlov, O.A.
- Perevedentsev, E.
- Petrov, V.M.
- Pilan, A.M.
- Piminov, P.A.
- Pivovarov, I.L.
- Prosvetov, V.P.
- Pureskin, D.N.
- Putmakov, A.A.
- Reva, V.B.
- Riabchenko, K.K.
- Rogovsky, Yu.A.
- Rotov, E.
- Rybitskaya, T.V.
- Salimov, R.A.
- Samoylov, S.L.
- Sandalov, E.S.
- Savinov, S.
- Semenov, A.M.
- Semenov, A.V.
- Senchenko, A.I.
- Senkov, D.V.
- Serdakov, L.E.
- Shamov, A.G.
- Shatunov, P.Yu.
- Shatunov, Y.M.
- Shchudlo, I.M.
- Shevchenko, O.A.
- Shtro, K.S.
- Shwartz, D.B.
- Simonov, E.A.
- Sinitsky, S.L.
- Sinyatkin, S.V.
- Skorobogatov, D.N.
- Skovorodin, D.I.
- Sokolova, E.O.
- Sorokin, I.N.
- Starostenko, A.A.
- Starostenko, D.A.
- Starostina, E.V.
- Sukhanov, D.P.
- Sycheva, T.
- Tarnetsky, V.V.
- Taskaev, S.Yu.
- Telnov, V.I.
- Timoshenko, M.V.
- Tribendis, A.G.
- Tsyganov, A.S.
- Vakhrushev, R.V.
- Vasiliev, S.
- Vinokurov, N.A.
- Volkov, V.
- Vorobev, D.S.
- Vostrikov, V.A.
- Yakimov, I.S.
- Yudin, V.D.
- Zapryagaev, I.A.
- Zemlyansky, I.M.
- Zharikov, A.A.
- Zharinov, Yu.M.
- Zhilich, V.N.
- Zhilyaev, K.V.
- Zhivankov, K.I.
- Zhukov, A.A.
- Zhuravlev, A.N.

BNRU
Belgorod, Russia
- Savchenko, A.A.
- Sergeeva, D.Yu.
- Tishchenko, A.A.

Budker INP & NSU
Novosibirsk, Russia
- Bykov, T.A.
- Rogovsky, Yu.A.
- Sokolova, E.O.
- Verkhovod, G.D.

Budker Institute of Nuclear Physics
Novosibirsk, Russia
- Ivanenko, S.V.
- Ostreinov, G.
- Puryga, E.A.
- Todyshev, C.

Cancer Research Institute of Tomsk NRMC
Tomsk, Russia
- Miloichikova, I.A.
- Turgunova, N.D.

CERN
Geneva, Switzerland
- Dabrowski, A.E.

ISBN: 978-3-95450-240-0 ISSN: 2673-5539

Ferrite Domen Co.
St. Petersburg, Russia
- Ovchinnikova, L.

GIRO-PROM
Dubna, Moscow Region, Russia
- Glebov, I.L.
- Luzanov, V.A.

GSI
Darmstadt, Germany
- Bleile, A.
- Waldt, A.

I-Tech
Solkan, Slovenia
- Baričevič, B.
- Bogataj, L.
- Janezic, E.
- Repič, B.
- Tinta, D.T.
- Zorzut, S.

IAP
Frankfurt am Main, Germany
- Schempp, A.

IAP/RAS
Nizhny Novgorod, Russia
- Belousov, V.I.
- Bokhanov, A.
- Ginzburg, N.S.
- Golubev, S.
- Izotov, I.
- Peskov, N.Yu.
- Skalyga, V.
- Sobolev, D.I.
- Vybin, S.S.
- Zaslavsky, V.Yu.

IERT
Kharkov, Ukraine
- Kobets, A.G.

IFJ-PAN
Kraków, Poland
- Siemek, K.

IHEP
Moscow Region, Russia
- Afonin, A.G.
- Ageev, A.I.
- Alexeev, A.G.
- Altukhov, Altukhov,Y.V.
- Altukhova, E.V.
- Antipov, Y.M.
- Azhgirey, I.L.
- Baranov, V.T.
- Bayshev, I.S.
- Beletskaya, Yu.V.
- Bogdanov, I.
- Britvich, G.I.
- Budanov, Yu.A.
- Chesnokov, M.Yu.
- Chesnokov, Y.A.
- Degtyarev, I.I.
- Denisov, A.G.
- Durum, A.A.
- Frolov, B.A.
- Ignashin, N.A.
- Ilukin, V.L.
- Ivanov, S.V.
- Kalinin, V.A.
- Koshelev, A.V.
- Kostin, M.Yu.
- Kozub, S.
- Kurochkin, I.A.
- Lapygin, V.G.
- Lebedev, O.P.
- Liashenko, O.A.
- Lobanov, I.S.
- Lutchev, A.
- Maksimov, A.
- Mamaev, A.
- Maximov, A.V.
- Milichenko, Yu.V.
- Novoskoltsev, F.N.
- Oreshkova, N.A.
- Ovsienko, M.P.
- Peleshko, V.N.
- Pikalov, V.A.
- Piryazev, I.N.
- Pitalev, V.I.
- Polkovnikov, M.K.
- Poluektov, I.V.
- Rascvetalov, Ja.N.
- Riabchikova, A.D.
- Ryabov, T.
- Sandomirskiy, Yu.E.
- Savin, D.A.
- Savitskaya, E.N.
- Sinyukov, R.Yu.
- Soldatov, A.P.
- Strekalovskikh, S.A.
- Sukharev, M.M.
- Sukhikh, S.E.
- Sumaneev, O.V.
- Sytov, S.E.
- Tkachenko, L.
- Tyurin, N.E.
- Vasiliev, D.A.
- Yanovich, A.A.
- Zaitsev, A.M.

IMP/CAS
Lanzhou, People's Republic of China
- Gao, D.Q.
- He, Y.
- Mao, L.J.
- Shen, G.D.
- Sheng, L.N.
- Sun, L.T.
- Xu, Z.
- Yang, J.C.
- Yang, Y.Q.

ISBN: 978-3-95450-240-0 ISSN: 2673-5539

- Yuan, Y.J.

INP BSU
Minsk, Belarus
- Bayev, V.
- Bychanok, D.
- Huseu, S.
- Maksimenko, S.A.
- Sukhotski, A.E.
- Vasilevich, E.

Institute of Laser Physics, SB RAS
Novosibirsk, Russia
- Gubin, V.

ISDE
Moscow, Russia
- Chubunov, P.A.

ITEP
Moscow, Russia
- Balabaev, A.
- Bogdanov, A.V.
- Drozdovsky, A.A.
- Drozdovsky, S.A.
- Kantsyrev, A.V.
- Khrisanov, I.A.
- Khurchiev, A.
- Kozlov, A.V.
- Kropachev, G.
- Kulevoy, T.
- Kuzmichev, V.G.
- Losev, A.A.
- Panyushkin, V.A.
- Prianishnikov, K.E.
- Satov, Yu.A.
- Savin, S.M.
- Selesnev, D.N.
- Semennikov, A.I.
- Shumshurov, A.
- Sitnikov, A.
- Skobliakov, A.V.
- Titarenko, Y.E.
- Tsyplakov, E.D.
- Vasilyev, A.A.
- Visotski, S.A.
- Volkov, V.A.
- Zarubin, A.

JAI
Egham, Surrey, United Kingdom
- Ali, M.
- Fedorov, K.V.

JIHT RAS
Moscow, Russia
- Kuznetsov, S.V.

JINR
Dubna, Moscow Region, Russia
- Agapov, A.
- Agapov, N.N.
- Ahmanova, E.V.
- Alfeev, A.V.
- Andreev, V.
- Apel, P.Yu.
- Astakhov, V.I.
- Baldin, A.A.
- Bazanov, A.M.
- Bekhterev, V.
- Beloborodov, A.V.
- Berlev, A.I.
- Bogomolov, S.L.
- Bogoslovsky, D.N.
- Bondarchenko, A.E.
- Borisov, V.V.
- Brovko, O.I.
- Bugaev, V.V.
- Bunyatov, K.
- Butenko, A.V.
- Donets, D.E.
- Donets, E.D.
- Donets, E.E.
- Efremov, A.A.
- Egorov, D.
- Eliseev, A.V.
- Fateev, A.A.
- Fedorov, A.N.
- Filatov, G.A.
- Filimonov, V.V.
- Fimushkin, V.V.
- Franko, J.
- Galimov, A.R.
- Gerklotts, V.A.
- Gikal, K.
- Golovenskiy, B.V.
- Golubitsky, O.
- Gorbachev, E.V.
- Gostkin, M.
- Govorov, A.
- Grebentsov, A.Yu.
- Gulbekyan, G.G.
- Gurskiy, S.
- Hodshibagijan, G.G.
- Isadov, V.
- Ivanenko, I.A.
- Ivanov, E.V.
- Ivanov, G.N.
- Kalagin, I.V.
- Karamyshev, O.
- Karamysheva, G.A.
- Karpinskii, V.N.
- Karpinsky, V.
- Kazarinov, N.Yu.
- Kekelidze, V.
- Kharyuzov, P.R.
- Kharyuzova, A.P.
- Khodzhibagiyan, H.G.
- Kirichenko, A.
- Kobets, A.G.
- Kobets, V.V.
- Kolesnikov, S.Yu.
- Kondratiev, B.Yu.
- Korovkin, D.S.

ISBN: 978-3-95450-240-0 ISSN: 2673-5539

- Korovkin, S.A.
- Kostromin, S.A.
- Kovalenko, A.D.
- Kozlov, O.S.
- Kuzmenkov, K.I.
- Ladygin, V.
- Lalayan, M.V.
- Levterov, K.A.
- Loginov, V.N.
- Lyuosev, D.A.
- Malyshev, A.M.
- Martynov, A.A.
- Melnikov, S.A.
- Meshkov, I.N.
- Mikhailov, V.A.
- Minashkin, V.F.
- Mironov, V.I.
- Mironov, V.
- Mitrofanov, S.V.
- Mitrofanova, Iu.A.
- Monakhov, D.V.
- Monchinsky, V.A.
- Mytzin, G.V.
- Nazlev, H.P.
- Nesterov, A.
- Nikiforov, D.
- Novikov, M.S.
- Nozdrin, M.A.
- Orlov, O.
- Osipenkov, A.L.
- Osipov, N.F.
- Paraipan, M.
- Petrov, M.V.
- Petrov, V.D.
- Philippov, A.V.
- Pilyar, N.V.
- Pivin, R.V.
- Ponkin, D.O.
- Popov, D.
- Prozorov, O.V.
- Pugachev, D.K.
- Romanov, S.
- Rukojatkin, P.A.
- Rukoyatkina, T.V.
- Safonov, A.B.
- Samofalova, Y.A.
- Seleznev, V.V.
- Semenov, S.V.
- Semin, V.A.
- Sergeev, A.S.
- Sergeeva, E.V.
- Shandov, M.M.
- Sharkov, B.Y.
- Shipulin, K.N.
- Shirikov, I.V.
- Shirkov, G.
- Shirkov, S.G.
- Shurygin, A.A.
- Shvetsov, V.S.
- Sidorin, A.A.
- Sidorin, A.O.
- Sidorov, A.I.
- Skuratov, V.A.
- Sledneva, A.
- Slepnev, V.
- Slivin, A.
- Sumbaev, A.P.
- Svidetelev, A.N.
- Syresin, E.
- Teterev, Yu.G.
- Timoshenko, G.N.
- Topilin, N.D.
- Trifonov, A.
- Trubnikov, G.V.
- Tuzikov, A.
- Tyulkin, V.I.
- Vasilishin, B.
- Volkov, V.
- Volodin, A.A.
- Vorozhtsov, A.S.
- Yakovenko, S.
- Yunenko, K.
- Zhemchugov, A.

JINR/DLNP
Dubna, Moscow region, Russia
- Brukva, A.E.
- Lyapin, I.D.
- Malinin, V.
- Siemek, K.

JINR/FLNP
Moscow Region, Russia
- Burkov, I.V.
- Mikhailov, K.I.

JINR/FLNR
Moscow region, Russia
- Issatov, A.
- Kropachev, G.
- Lisov, V.I.
- Pavlov, L.A.
- Protasov, A.A.
- Zabanov, A.S.

JINR/VBLHEP
Dubna, Moscow region, Russia
- Akimov, V.P.
- Bazanov, A.M.
- Bespalov, Yu.G.
- Bogatov, A.S.
- Bortsova, A.A.
- Boytsov, A.Y.
- Brovko, O.I.
- Butenko, A.V.
- Butenko, E.A.
- Donets, D.E.
- Donets, E.E.
- Donguzov, I.I.
- Elkin, V.G.
- Filatov, G.A.
- Fischer, E.S.
- Gorelyshev, I.V.

ISBN: 978-3-95450-240-0 ISSN: 2673-5539

- Kashunin, M.A.
- Khramov, D.
- Konstantinov, A.V.
- Korobitsina, M.Yu.
- Kostromin, S.A.
- Kozlov, A.P.
- Kozlov, O.S.
- Kryachko, I.A.
- Kudashkin, A.V.
- Letkin, D.S.
- Leushin, D.O.
- Levterov, K.A.
- Levterova, E.A.
- Lutsenko, V.M.
- Lyuosev, D.A.
- Martynov, A.A.
- Meshkov, I.N.
- Mialkovskiy, V.V.
- Mykhailenko, V.A.
- Nikolaichuk, I.
- Osipov, K.G.
- Parfylo, T.
- Petukhov, A.S.
- Philippov, A.V.
- Ponkin, D.O.
- Rassadov, D.N.
- Sedykh, G.S.
- Shabratov, V.
- Shandov, M.M.
- Shemchuk, A.V.
- Shirikov, I.V.
- Sidorin, A.O.
- Syresin, E.
- Tikhomirov, A.M.
- Trubnikov, G.V.
- Tuzikov, A.
- Tyutyunnikov, S.I.
- Voronin, A.A.
- Zolotykh, D.A.
- Zolotykh, E.V.

KIT
Karlsruhe, Germany
- Mallows, S.

LETI
Saint-Petersburg, Russia
- Alekseeva, O.S.
- Altmark, A.
- Lesiv, N.A.
- Mukhamedgaliev, K.
- Sheinman, I.L.

LPI
Moscow, Russia
- Kurakin, V.G.

MEPhI
Moscow, Russia
- Aksentyev, A.E.
- Artamonov, K.G.
- Ashanin, I.A.
- Batov, A.
- Bobrovskiy, D.V.
- Bulgacheva, M.M.
- Chumakov, A.I.
- Deryabochkin, O.V.
- Dmitriyev, M.S.
- Dmitriyeva, V.V.
- Dyakonov, M.V.
- Dyubkov, V.S.
- Garaev, D.I.
- Gerasimenko, A.V.
- Gorchakov, A.A.
- Gusarova, M.
- Guzov, M.A.
- Indiushnii, E.N.
- Ivanov, O.A.
- Kliuchevskaia, Yu.D.
- Korshunov, A.M.
- Kozlovskii, K.I.
- Kozlovskiy, K.I.
- Krasnov, A.S.
- Lalayan, M.V.
- Lozeev, Y.
- Lozeeva, T.A.
- Makarov, A.I.
- Matsievskiy, S.V.
- Melekhov, A.P.
- Murygin, O.V.
- Nemchenko, R.E.
- Novikov, G.G.
- Novozhilov, A.E.
- Panishev, A.S.
- Pashentsev, V.N.
- Polozov, S.M.
- Ponomarenko, A.G.
- Prianishnikov, K.E.
- Prokopenko, A.V.
- Pronikov, A.I.
- Rashchikov, V.I.
- Samarokov, N.Yu.
- Samoshin, A.V.
- Savchenko, A.A.
- Savchik, A.A.
- Sergeeva, D.Yu.
- Shashkov, Ya.V.
- Shatokhin, V.L.
- Shikanov, A.E.
- Smirnov, K.D.
- Sobenin, N.P.
- Soloviev, S.
- Tishchenko, A.A.
- Tsarev, G.A.
- Tumanov, S.A.
- Vorontsov, V.A.
- Vovchenko, E.D.
- Yurin, I.A.
- Zbruev, R.A.
- Zhigailova, M.I.

MIPT
Dolgoprudniy, Moscow Region, Russia
- Gavrilov, S.A.

ISBN: 978-3-95450-240-0 ISSN: 2673-5539

- Titov, A.I.
- Tsyplakov, E.D.

MSU
Moscow, Russia
- Belikhin, Belikhin,M.A.
- Chernyaev, A.P.
- Pryanichnikov, A.A.

NArFU
Arhangelsk, Russia
- Eseev, M.K.

NIIEFA
St. Petersburg, Russia
- Akimova, A.
- Amoskov, V.M.
- Firsov, A.A.
- Galchuck, A.V.
- Gapionok, E.I.
- Gavrish, Yu.N.
- Grigorenko, S.V.
- Grigoriev, V.I.
- Kaparkova, M.
- Kazachenko, N.I.
- Klopenkov, M.L.
- Klopenkov, R.M.
- Korolev, L.E.
- Kravchuk, K.A.
- Kukhtin, V.P.
- Kuzhlev, A.N.
- Labusov, A.N.
- Lamzin, E.A.
- Larionov, M.S.
- Makarov, A.
- Mezhov, I.I.
- Mudrolyubov, V.G.
- Nezhentzev, A.
- Osina, Yu.K.
- Rodin, I.Yu.
- Safonov, A.V.
- Shatil, N.
- Smirnov, K.E.
- Stepanov, D.B.
- Stogov, Yu.I.
- Tkachenko, K.I.
- Tsygankov, S.S.
- Usanova, M.V.
- Zapretilina, E.R.

NRC
Moscow, Russia
- Ashanin, I.A.
- Belkov, A.
- Bulatov, M.S.
- Chernykh, A.N.
- Dyubkov, V.S.
- Efimov, Y.V.
- Fomin, Ye.
- Garaev, D.I.
- Gusarova, M.
- Kaportsev, E.V.
- Khoroshkov, V.S.
- Klenov, G.I.
- Korchuganov, V.
- Kovalchuk, M.V.
- Krylov, Y.V.
- Kulevoy, T.
- Maslennikov, K.
- Moiseev, V.I.
- Moseev, K.
- Moseiko, N.I.
- Odintsov, D.G.
- Pesterev, S.G.
- Polozov, S.M.
- Pronikov, A.I.
- Rashchikov, V.I.
- Savchenko, A.A.
- Sergeeva, D.Yu.
- Shatokhin, V.L.
- Smygacheva, A.S.
- Stirin, A.I.
- Tishchenko, A.A.
- Ushakov, V.A.
- Valentinov, A.G.

NRNU MEPHI
Moscow, Russia
- Pavlov, D.A.

NSC/KIPT
Kharkov, Ukraine
- Shchagin, A.V.

NSTU
Novosibirsk, Russia
- Morsina, A.A.
- Tribendis, A.G.

NSU
Novosibirsk, Russia
- Andrianov, A.V.
- Arsentyeva, M.V.
- Balakin, V.V.
- Bekhtenev, E.A.
- Borin, V.M.
- Emanov, F.A.
- Fatkin, G.A.
- Gerasimov, V.V.
- Ivanov, A.V.
- Kasatov, D.A.
- Kladov, S.A.
- Kolesnikov, Ia.A.
- Koop, I.
- Koshkarev, A.M.
- Kotov, E.S.
- Kremnev, N.S.
- Levichev, A.E.
- Lyalin, M.A.
- Maltseva, Yu.I.
- Meshkov, O.I.
- Nikiforov, D.A.
- Pavlenko, A.V.
- Perevedentsev, E.

ISBN: 978-3-95450-240-0 ISSN: 2673-5539

- Reva, V.B.
- Rogovsky, Yu.A.
- Rotov, E.
- Senchenko, A.I.
- Shatunov, P.Yu.
- Shatunov, Y.M.
- Shwartz, D.B.
- Sokolova, E.O.
- Taskaev, S.Yu.

Ostec Enterprise Ltd
Moscow, Russia
- Chernykh, P.N.
- Osipov, S.
- Serenkov, E.

PhTC LPI RAS
Protvino, Russia
- Alexandrov, V.
- Balakin, V.E.
- Bazhan, A.I.
- Belikhin, Belikhin,M.A.
- Chashurin, V.I.
- Lunev, P.A.
- Pryanichnikov, A.A.
- Shemyakov, A.E.
- Shestopalov, A.I.
- Simakov, A.S.
- Zhogolev, P.B.

Physical-Technical Institute of the National Academy of Sciences of Belarus
Minsk, Belarus
- Petrakovsky, V.S.
- Pobol, I.L.
- Pokrovsky, A.I.
- Shvedov, A.
- Yurevich, S.V.
- Zaleski, V.G.

PNPI
Gatchina, Leningrad District, Russia
- Amerkanov, D.A.
- Artamonov, S.A.
- Ivanov, E.M.
- Maximov, V.I.
- Riabov, G.A.
- Tonkikh, V.A.

Private Address
Moscow, Russia
- Kurilik, A.

Protom Ltd.
Protvino, Russia
- Alexandrov, V.
- Balakin, V.E.
- Bazhan, A.I.
- Belikhin, Belikhin,M.A.
- Lunev, P.A.
- Pryanichnikov, A.A.
- Shemyakov, A.E.
- Shestopalov, A.I.
- Zhogolev, P.B.

ProtonVDA
Naperville, Illinois, USA
- Rykalin, V.

RAS/INR
Moscow, Russia
- Aksentyev, A.E.
- Akulinichev, S.V.
- Belov, A.
- Bragin, S.
- Durkin, A.P.
- Feschenko, A.
- Frolov, O.T.
- Gaidash, V.
- Gavrilov, S.A.
- Kolokolchikov, S.D.
- Kolomiets, A.
- Kravchuk, L.V.
- Melnikov, A.A.
- Nechaeva, L.P.
- Novikov-Borodin, A.V.
- Ovchinnikova, L.
- Paramonov, V.V.
- Rybakov, I.V.
- Senichev, V.
- Serov, V.L.
- Titov, A.I.
- Turbabin, A.V.
- Volodkevich, O.
- Zubets, V.

RFNC-VNIIEF
Sarov, Nizhniy Novgorod region, Russia
- Bodryashkin, Ya.V.
- Boriskov, A.S.
- Cherkasov, A.S.
- Guzov, M.A.
- Konishev, I.I.
- Kurapov, N.N.
- Kuznetsov, V.V.
- Mashin, I.A.
- Nikolaev, V.R.
- Opekunov, A.M.
- Polyakov, L.E.
- Pospelov, G.
- Shein, A.N.
- Shorikov, I.V.
- Truntseva, R.P.
- Zavyalov, N.V.
- Zhukov, I.V.

Royal Holloway, University of London
Surrey, United Kingdom
- Karataev, P.

RRC
Moscow, Russia
- Kaportsev, E.V.

Saint Petersburg State University
Saint Petersburg, Russia
- Balabanov, M.Yu.

ISBN: 978-3-95450-240-0 ISSN: 2673-5539

- Kotina, E.D.
- Meshkov, I.N.
- Ovsyannikov, A.D.
- Ovsyannikov, D.A.
- Sidorin, A.O.
- Sytchevsky, S.E.

SIGMAPHI S.A.
Vannes, France
- Antoine, S.
- Beeckman, W.
- Duveau, X.G.
- Guerra-Phillips, J.
- Jehanno, P.J.
- Lancelot, A.

St. Petersburg State University
St. Petersburg, Russia
- Andrianov, S.N.
- Edamenko, N.S.
- Kotina, E.D.
- Mizintseva, M.A.
- Ovsyannikov, A.D.
- Ovsyannikov, D.A.

TPU
Tomsk, Russia
- Batranin, A.V.
- Bulavskaya, A.A.
- Cherepennikov, Yu.M.
- Grigorieva, A.A.
- Miloichikova, I.A.
- Shevelev, M.
- Shkitov, D.A.
- Stuchebrov, S.
- Toktaganova, M.

UNIST
Ulsan, Republic of Korea
- Chung, M.
- Kwak, D.H.

VINCA
Belgrade, Republic of Serbia
- Balvanovic, R.
- Ćosić, M.M.
- Jovanovic, Z.M.
- Neskovic, N.
- Teleski, I.

VNIIEF
Sarov, Russia
- Putevskoy, S.A.
- Smetanin, M.L.
- Telnov, A.V.
- Zavyalov, N.V.

ISBN: 978-3-95450-240-0 ISSN: 2673-5539